Physical Metallurgy

3

Robert W. Cahn and Peter Haasen (†), editors

FOURTH, REVISED AND ENHANCED EDITION

NORTH-HOLLAND

Prof. Robert W. Cahn, editor

PHYSICAL METALLURGY

VOLUME III

LIST OF CONTRIBUTORS

A. S. Argon
E. Arzt
H. K. D. H. Bhadeshia
H. Biloni
J. L Bocquet
W. J. Boettinger
G. Brebec
R. W. Cahn
G. Y. Chin†
T. W. Clyne
R. D. Doherty
H. E. Exner
R. Ferro
D. R. Gaskell
H. Gleiter
A. L. Greer
P. Haasen†
J. P. Hirth
S. Hofmann
E. D. Hondros
E. Hornbogen
G. Kostorz
C. Laird
P. Lejček
W. C. Leslie
Y. Limoge
J. D. Livingston
F. E. Luborsky
T. B. Massalski
J. R. Nicholls
A D. Pelton
D. G. Pettifor
D. P. Pope
M. Rühle
A. Saccone
S. R. J. Saunders
M. P. Seah
W. Steurer
J.-L. Strudel
R. M. Thomson
C. M. Wayman
M. Wilkens
A. H. Windle
H. J. Wollenberger

PHYSICAL METALLURGY

Fourth, revised and enhanced edition

Edited by

Robert W. CAHN
University of Cambridge

Peter HAASEN†
University of Göttingen

VOLUME III

1996

NORTH-HOLLAND
AMSTERDAM—LAUSANNE—NEW YORK—OXFORD—SHANNON—TOKYO

ELSEVIER SCIENCE B.V.
Sara Burgerhartstraat 25
P.O. Box 211, 1000 AE Amsterdam, The Netherlands

ISBN: 0 444 89875 1

This book is printed on acid-free paper.

Printed in The Netherlands

SYNOPSIS OF CONTENTS

Volume 1

Volume 2

Volume 3

CHAPTER 20

DISLOCATIONS

J. P. HIRTH

Mechanical and Materials Engineering Department
Washington State University
Pullman, WA 99164–2920, USA

R. W. Cahn and P. Haasen†, eds.
Physical Metallurgy; fourth, revised and enhanced edition

1. Elementary geometrical properties

The concept of crystal dislocations was introduced by POLANYI [1934], OROWAN [1934] and TAYLOR [1934], although the elastic properties of dislocations in isotropic continua had been known since 1905 (TIMPE, also VOLTERRA [1907]). Dislocations are defects whose motion produces plastic deformation of crystals at stresses well below the theoretical shear strength of a perfect crystal. In fig. 1a, b and c the glide motion of an edge dislocation is shown to cause plastic shear strain. One can imagine a virtual process of cutting the crystal on a glide plane, shearing the cut surface by a shear displacement vector $\boldsymbol{b}$, the *Burgers vector*, and gluing the cut surfaces together, creating the edge dislocation in fig. 1b. The dislocation bounds a slipped area and is a line defect. It is characterized by the Burgers vector $\boldsymbol{b}$ and by a unit vector ξ tangent to the dislocation line at a point in question. The same dislocation could be formed by opening a cut under normal tractions, fig. 1d, and inserting a plane of matter.

In order that the deformation not produce a high energy fault on the cut surface, $\boldsymbol{b}$ is usually a perfect lattice vector as illustrated for an edge dislocation in fig. 2. The choice of the $\pm$ sense of ξ is arbitrary, but once chosen, the $\pm$ sense of $\boldsymbol{b}$ is fixed by the following convention: imagine a perfect reference crystal, select a vector ξ in it, and construct a closed circuit in it, right-handed relative to ξ. Then construct the same Burgers circuit in the real crystal, as shown for example in fig. 2. The vector SF connecting the start of the circuit to the finish is the Burgers vector of a dislocation if it is contained within the circuit. In this operation, the circuit must not pass through the nonlinear core region within an atomic spacing or two of the dislocation line.

For the *edge dislocation*, $\boldsymbol{b}$ is seen to be perpendicular to ξ. In fig. 3 a *screw dislocation* can be imagined to have been created by a cut and displacement operation, or simply by shearing the slipped area by motion of the dislocation in from the surface of a perfect crystal. The screw dislocation has $\boldsymbol{b}$ parallel to ξ. It is right-handed if $\boldsymbol{b}$ points in the same direction as ξ as in fig. 3; left-handed otherwise. In general, fig. 4, the slipped or displaced surface can be arbitrary, the dislocation line can be arbitrarily

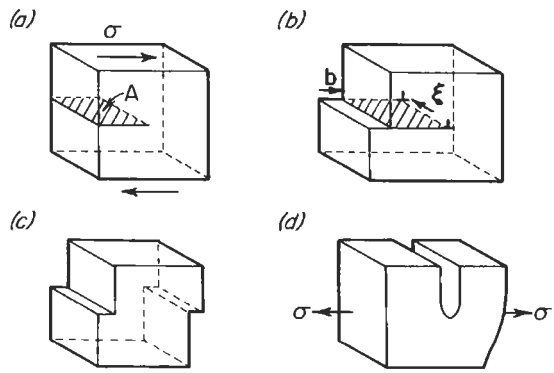

Fig. 1. (a–c) shear of a crystal under a shear stress σ by an amount b by passage of an edge dislocation; (d) creation of same dislocation under normal stress σ once added material is placed in the opened cut.

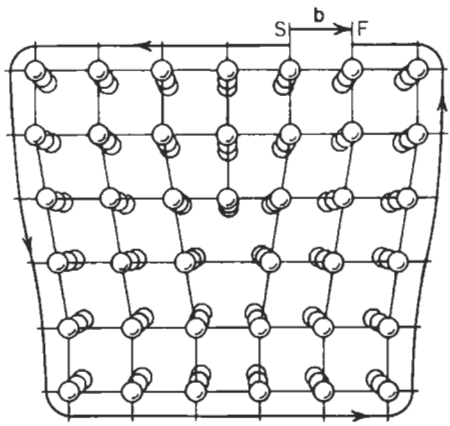

Fig. 2. An edge dislocation in a simple cubic crystal. A Burgers circuit is also shown, projected toward the viewer for clarity so that it passes through the center of atoms not shown. The sense vector ξ points out of the page.

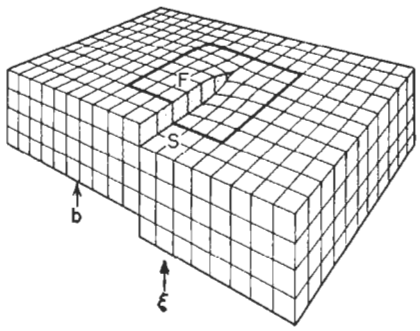

Fig. 3. A screw dislocation in a simple cubic crystal.

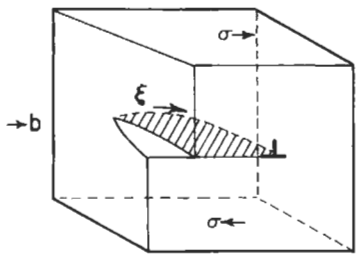

Fig. 4. A mixed dislocation.

References: p. 1872.

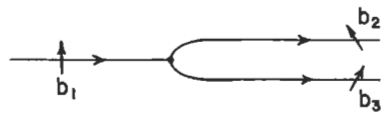

Fig. 5. Three dislocations meeting at a node. Arrows on lines indicate sense of ξ. Equivalent Burgers circuits also shown.

curved, and the dislocation is called *mixed* when the angle β between $\boldsymbol{b}$ and ξ is neither 0 nor an integer multiple of $\pi/2$.

Some other properties follow directly from the above definitions. If ξ is reversed, the sense of $\boldsymbol{b}$ is also reversed as seen from fig. 2 since the circuit is also reversed when ξ is reversed. Since the dislocation line bounds a displaced area, the line cannot end within otherwise perfect crystal but can only end at a free surface, a grain boundary, a second-phase interface, or a dislocation node. A *node* is a point where two or more dislocation lines join. Translation of a Burgers circuit along ξ without the circuit cutting through a dislocation core does not change the vector SF or thus the total $\boldsymbol{b}$ (imagine such an operation for fig. 2); such circuits are called *equivalent* Burgers circuits. Thus, if a dislocation denoted by its Burgers vector, $\boldsymbol{b}_1$, splits into two dislocations $\boldsymbol{b}_2$ and $\boldsymbol{b}_3$, enclosed by equivalent circuits, fig. 5, an analog of Kirchhoff's law applies and $\boldsymbol{b}_1 = \boldsymbol{b}_2 + \boldsymbol{b}_3$. If the ξ for dislocations 2 and 3 are reversed, then the signs of $\boldsymbol{b}_2$ and $\boldsymbol{b}_3$ change by the earlier axiom and: $\Sigma \boldsymbol{b}_i = 0$ for dislocations meeting at a node if all sense vectors ξ are selected to point toward the node.

2. *Elastic fields of dislocations*

2.1. Displacements and stresses

Consider the right-handed screw dislocation with the geometry as indicated in fig. 6. Imagine that the cylindrical region is a portion of an infinite continuum. In cylindrical coordinates, the displacements can be deduced by inspection:

$$u_r = u_\theta = 0, u_z = b\theta/2\pi. \tag{1}$$

Differentiation and the use of Hooke's Law gives the strain and stress fields:

$$\varepsilon_{\theta z} = \frac{1}{2}\left(\frac{1}{r}\frac{\partial u_z}{\partial \theta} + \frac{\partial u_\theta}{\partial z}\right) = \frac{b}{4\pi r}, \tag{2}$$

$$\sigma_{\theta z} = 2\mu\varepsilon_{\theta z} = \mu b/2\pi r, \tag{3}$$

with μ the shear modulus.

The edge dislocation, fig. 7, has displacements u_x and $u_y \neq 0$ but $u_z = 0$. Thus, the solution for this plane-strain problem proceeds by deducing the Airy stress function Ψ. Guided by the screw dislocation result that $\sigma \sim 1/r$ and observing in fig. 2 that $(\sigma_{rr} + \sigma_{\theta\theta}) \sim -\sin\theta$ to give compression above, and tension below the glide plane $\theta = 0$, one finds:

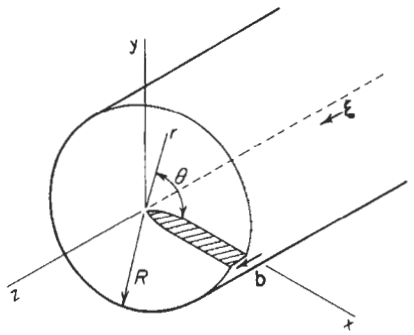

Fig. 6. A right-handed screw dislocation along the axis of a cylindrical region of radius R and length L.

$$\psi = \frac{-\mu b}{\pi(1-\nu)} r \sin\theta \ln r, \tag{4}$$

with ν = Poisson's ratio. Differentiation of eq. (4) gives:

$$\sigma_{rr} = \frac{1}{r}\frac{\partial\psi}{\partial r} + \frac{1}{r^2}\frac{\partial^2\psi}{\partial\theta^2} = -\frac{\mu b \sin\theta}{2\pi(1-\nu)r},$$

$$\sigma_{\theta\theta} = \frac{\partial^2\psi}{\partial r^2} = \sigma_{rr}, \qquad \sigma_{r\theta} = -\frac{\partial}{\partial r}\left(\frac{1}{r}\frac{\partial\psi}{\partial\theta}\right) = \frac{\mu b \cos\theta}{2\pi(1-\nu)r}, \tag{5}$$

$$\sigma_{zz} = \nu(\sigma_{rr} + \sigma_{\theta\theta}).$$

This field has the physical features required by fig. 2; compression above the glide plane, tension below it, and maximum shear stresses on the glide plane $\theta = 0$. The strains are given by Hooke's Law and their integrals give the displacements, see HIRTH and LOTHE [1982].

For the screw dislocation, the strain energy density is $w = \sigma_{\theta z}^2/2\mu$. The total strain energy per unit length in the cylindrical region in fig. 6 is:

$$\frac{W}{L} = \int_{r_0}^{R} wr\,dr\,d\theta = \frac{\mu b^2}{4\pi}\ln\frac{R}{r_0}. \tag{6}$$

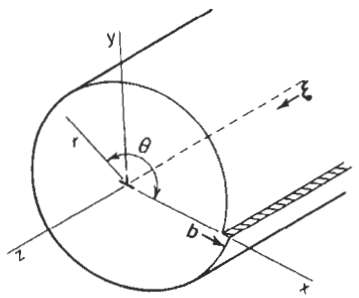

Fig. 7. An edge dislocation.

Here a core cutoff radius r_0 is introduced to avoid divergence. This is necessary because the use of linear elasticity gives an artificial divergence in $\varepsilon_{\theta z}$, eq. (2), as $r \to r_0 \approx b$.

For the edge dislocation, an alternate procedure is simpler. From thermodynamics, the strain energy is equal to the isothermal reversible work done on the system in creating the strain. For fig. 7, imagine creating the dislocation by making a cut on the surface $\theta = 0$, $r > 0$, and displacing it by b, applying stresses $\sigma_{r\theta}$ ($\theta = 0$) to the cut to accomplish the displacement. Since $\sigma_{r\theta} \propto b$ finally, the average stress in the process is $\frac{1}{2}\sigma_{r\theta}$ and the surface work on an element dA is $\frac{1}{2}\sigma_{r\theta}$ ($\theta = 0$)$b\, dA$. The total strain energy per unit length is then given by the integral of this surface work over A:

$$\frac{W}{L} = \int_{r_0}^{R} \tfrac{1}{2}\sigma_{r\theta}(\theta = 0) b \, dr = \frac{\mu b^2}{4\pi(1-\nu)} \ln \frac{R}{r_0}. \tag{7}$$

The displacement and stress field for a mixed dislocation is given by decomposition of $\boldsymbol{b}$ into edge and screw components b_e and b_s and use of the above expressions with $b_e = b \sin\beta$ and $b_s = b \cos\beta$ substituted for b. In general, the strain energy, being quadratic in σ, cannot be superposed, but the screw and edge components of the mixed dislocation have no common stress components, so W/L can also be added,

$$\frac{W}{L} = \frac{\mu b^2}{4\pi(1-\nu)} \left[\sin^2\beta + (1-\nu)\cos^2\beta\right] \ln \frac{R}{r_0} = E(\beta) \ln \frac{R}{r_0}, \tag{8}$$

where $E(\beta)$ is called the *energy factor*.

2.2. Peach–Koehler force

As just discussed, the strain energy is the isothermal reversible work done on the system, which, for a system under constant external pressure, is the Gibbs free energy G of the system. For an isothermal, constant pressure system, ΔG for a hypothetical reversible displacement of the system in some reaction coordinate c_r is a criterion for whether the displacement in the actual case tends to occur spontaneously (forward if $\Delta G < 0$, backward if $\Delta G > 0$, not if $\Delta G = 0$). In a general sense, we define a virtual thermodynamic force as $F = -\partial G/\partial c_r$. Then if $F > 0$, the system tends to change spontaneously in the direction of the reaction coordinate.

We are interested in whether a dislocation will tend to move spontaneously in the presence of a stress field, so the appropriate reaction coordinate is the position $\boldsymbol{r}$ of the dislocation. Imagine the process, fig. 8, of cutting an area $d\boldsymbol{A} = \boldsymbol{n}\, dA = d\boldsymbol{l} \times \delta\boldsymbol{r} = dl(\boldsymbol{\xi} \times \delta\boldsymbol{r})$, displacing the dislocation by $\delta\boldsymbol{r}$, removing or adding matter if necessary, and gluing the surfaces together. If surface forces are needed to prevent the cut from relaxing, work can be extracted ($\Delta G < 0$) as the displacement is accomplished in the hypothetical process. The self-stresses of the dislocation are symmetric and hence do no *net* work in the process. However, any other stresses $\boldsymbol{\sigma}$ acting in the core region *can* extract work. The stresses produce surface forces $\boldsymbol{\sigma} \cdot d\boldsymbol{A}$ and in the displacement $\boldsymbol{b}$ extract an amount of work $-\delta G = \delta W$, given by

$$\delta W = \boldsymbol{b} \cdot \boldsymbol{\sigma} \cdot d\boldsymbol{A} = \boldsymbol{b} \cdot \boldsymbol{\sigma} \cdot (\boldsymbol{\xi} \times \delta\boldsymbol{r}) \delta l = \delta\boldsymbol{r} \cdot (\boldsymbol{b} \cdot \boldsymbol{\sigma} \times \boldsymbol{\xi}) \delta l.$$

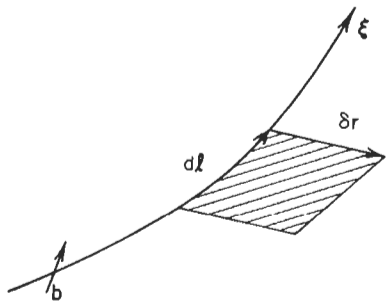

Fig. 8. Displacement of a segment d*l* of dislocation.

But by the definition of the virtual thermodynamic force $\boldsymbol{F}$, $\delta W = \boldsymbol{F} \cdot \delta \boldsymbol{r}$. Thus, the virtual force is (PEACH and KOEHLER [1950]):

$$\frac{\boldsymbol{F}}{L} = \boldsymbol{b} \cdot \boldsymbol{\sigma} \times \boldsymbol{\xi} \qquad \text{or} \qquad \frac{F_k}{L} = -\varepsilon_{ijk} \xi_i \sigma_{jt} b_t, \tag{9}$$

where ε_{ijk} is the permutation operator ($\varepsilon_{ijk} = 1$ or -1 for ε_{123} or ε_{321} or their cyclic permutations, 0 otherwise).

Consider the example of fig. 7, with only $\xi_3 = 1$ nonzero, and with only $b_1 = b$ nonzero. According to eq. (9), a shear stress σ_{21} produces a glide force $F_1/L = \sigma_{21} b_1$; a normal stress σ_{11} produces a climb force $F_2/L = -\sigma_{11} b_1$; other stresses produce no force. For the screw of fig. 6, with $\xi_3 = 1$, $b_3 = b$ a stress σ_{23} produces a glide force $F_1/L = \sigma_{23} b_3$ while a stress σ_{13} produces a (cross-slip) glide force $F_2/L = -\sigma_{13} b_3$.

Thus, the Peach–Koehler equation (9) reveals the direction of prospective spontaneous motion of a dislocation in the presence of stresses σ. *The force is a virtual thermodynamic one and must not be confused with a mechanical force.*

2.3. Dislocation interactions

Interaction forces and energies also can be developed from eq. (9). Consider first the interaction between parallel dislocations A and B in fig. 9, with $\xi_3 = 1$ and $b_1 = b$. Equation (9) then gives for the glide force on B:

$$\frac{F_1^{\mathrm{B}}}{L} = \xi_3^{\mathrm{B}} \sigma_{21}^{\mathrm{A}} b_1^{\mathrm{B}} = \frac{\mu b^2}{2\pi(1-\nu)X}, \tag{10}$$

since $\sigma_{21}^{\mathrm{A}} = \sigma_{r\theta}(\theta = 0,\ x = X) = \mu b / 2\pi(1-\nu)X$. The interaction force is repulsive between like-sign edge dislocations; attractive between opposite-sign dislocations. For more general parallel dislocations, such as A and C in fig. 9 the use of eq. (9) is more complicated, involving more terms. However, in cylindrical coordinates with $r = R$ at dislocation C, the radial interaction force has the simple form

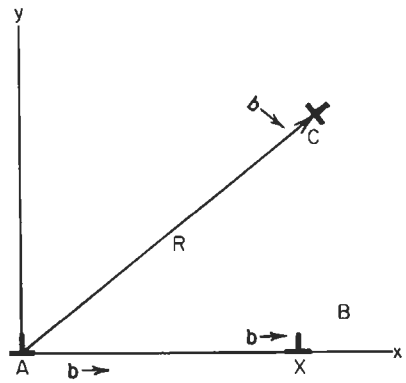

Fig. 9. Parallel dislocations; ξ points out of the page.

$$\frac{F_r}{L} = \frac{\mu}{2\pi R}\left[(\boldsymbol{b}_A\cdot\boldsymbol{\xi}_A)(\boldsymbol{b}_C\cdot\boldsymbol{\xi}_C) + \frac{1}{(1-\nu)}(\boldsymbol{b}_A\times\boldsymbol{\xi}_A)\cdot(\boldsymbol{b}_C\times\boldsymbol{\xi}_C)\right]. \tag{11}$$

Equation (11) is seen to reproduce eq. (10) for the edge case and to give $F_r/L = \mu b^2/2\pi R$ for parallel like-sign screw dislocations. There is a weak oscillating F_θ/L component as well in the general case (NABARRO [1952]).

The interaction energy as a function of R can be determined by integration. For example, for the above screw case

$$W_{int} = \int_{R_a}^{R} \frac{F_r}{L}\,dr = \frac{\mu b^2}{2\pi}\ln\frac{R}{R_a}, \tag{12}$$

where R_a is a reference position and can be chosen to equal r_0, for example.

A procedure for more general interactions is exemplified by the perpendicular screw case of fig. 10. Coordinates are selected for dislocation A so that the stress field can be conveniently and simply expressed by eq. (3), $\sigma'_{\theta z} = \mu b/2\pi r'$. The stress tensor is then transformed to coordinates x, y, z fixed on dislocation B to make the use of eq. (9) easy, giving $\sigma_{yz} = -\mu b\cos^2\theta'/2\pi h$. Equation (9) then readily gives $(F_x^B/L) = -\mu b^2\cos^2\theta'/2\pi h$ for the local value of the interaction force, the locus of which is plotted in fig. 10. This procedure works for defects other than dislocations. Defect A could be a solute atom, a precipitate, or the like, and, provided one can express its stress field, σ^A, the interaction force on B can be determined as above. The equal and opposite nature of the net forces in fig. 10 is fortuitous; in general, Newton's law does not apply for these virtual thermodynamic forces; for example, there can be interaction torques between dislocations.

All of the interaction forces have the characteristic feature that they vary inversely with the spacing of dislocations. This result has important implications for work hardening and macroscopic descriptions of plastic deformation on the basis of dislocation models. The macroscopic flow stress scales inversely with forest dislocation density, or,

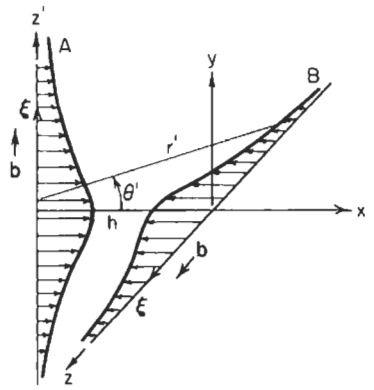

Fig. 10. Two perpendicular right-handed screw dislocations separated by a distance h; light arrows represent the interaction force.

equivalently, directly with the square root of the dislocation density (EMBURY [1971]; LAVRENTEV [1980]), i.e., the total length of dislocation line per unit volume. The exact reasons for such scaling laws remain elusive, but both long-range elastic stresses (the dislocation interaction) and short-range network and junction formation (with Orowan bowing as discussed subsequently) can both produce this behavior. Indeed, both appear to contribute (BASINSKI and BASINSKI [1979]; NABARRO [1986]). Also, the flow stress scales inversely with dislocation cell size (KUHLMANN–WILSDORF [1966]). Recent ideas on the latter relation are critically reviewed by KUBIN [1993] and include the concepts of dislocation mesh lengths and (fractal-like) scaling (KUHLMANN–WILSDORF [1989]; HANSEN and KUHLMANN–WILSDORF [1986]); fractal behavior of slip lines (NEUHÄUSER [1990]); and several reaction-diffusion continuum models.

The examples presented here are all for infinite straight dislocations. Stress, force, and energy expressions are available for generally curved dislocations in the form of line integrals, but, except for special cases such as circles, the integrals can only be solved numerically. Analytical results are available in both the isotropic and anisotropic elastic cases for straight-line segments, angular dislocations and infinitesimal loops. The results are very lengthy, beyond the scope of the present work, and can be found in NABARRO [1967] and HIRTH and LOTHE [1982]. These results are directly applicable to some arrays, such as stacking-fault tetrahedra, and can be used to obtain fairly accurate approximate results for curved arrays such as extended dislocation nodes. The segment approximation is being used currently in the forefront topic of computer simulation of large arrays of interacting dislocations (KUBIN, ESTRIN and CANOVA [1990]; DEVINCRE and CONDAT [1992]).

2.4. Surface effects

At a free surface, equilibrium requires that no forces act on a surface element. If the area element $\boldsymbol{A}$ is defined by a local normal unit vector $\boldsymbol{n}$, the condition is $\boldsymbol{\sigma} \cdot \boldsymbol{A} = A\boldsymbol{\sigma} \cdot \boldsymbol{n} = 0$. For

dislocations in finite media, this surface condition modifies the elastic field. As an example, suppose that the surfaces in fig. 6 are free surfaces bounding the cylinder. The stresses $\sigma_{\theta z}$ from eq. (3) would act on the end surface A_z and produce a net torque on the end. These extraneous stresses are removed by superposing equal and opposite tractions on the surface, solving the elastic problem for a cylinder under such tractions, and adding the resultant strain and displacement field to the infinite medium result. For the case of fig. 6, a net twist appears in the cylinder, the added stresses are $\sigma_{\theta z} = \mu br/\pi R^2$, and the free energy of the system is decreased by $\Delta W/L = -\mu b^2/4\pi$ (ESHELBY [1953]).

Similarly, for the edge dislocation in a finite cylinder, fig. 7, stresses σ_{rr} and $\sigma_{r\theta}$ must be imposed on the cylinder surface $r = R$. In this case the free energy decreases by $\Delta W/L = \mu b^2/8\pi(1-\nu)$. Surface stresses thus characteristically produce energy changes $\sim\mu b^2/10$. These changes are of the order of uncertainties in W/L because of uncertainties in core energy and in the use of isotropic elasticity, so they can consistently be neglected.

When a dislocation is parallel to a free surface, the superposed field often can be determined by an "image" construction. Consider the screw dislocation in fig. 11. Rotation of coordinates shows that eq. (3) gives stresses $\sigma_{xz} = -\mu by/2\pi R^2$ acting on the free surface where $r = R$. A solution which gives opposite stresses which exactly cancel these extraneous stresses is that of an opposite-sign dislocation at the mirror-image position relative to the surface. Thus, the field in the body is that of the real dislocation $\sigma_{\theta z} = \mu b/2\pi r$ and that of the *image dislocation* $\sigma_{\theta' z'} = -\mu b/2\pi r'$. At the site of the real dislocation, the image field is $\sigma_{yz} = -\sigma_{\theta' z'}(\theta = \pi,\ r' = 2\lambda) = \mu b/4\pi\lambda$. Thus, by eq. (9), the free surface exerts an image force

$$F_1/L = \mu b^2/4\pi\lambda, \tag{13}$$

attracting the dislocation to the free surface.

For the edge dislocation, the simple image construction is insufficient and an added stress field is needed to satisfy the free surface boundary condition (HIRTH and LOTHE [1982]). However, the force associated with the free surface tractions is still that of the simple image dislocation. This result is general, Lothe's theorem [1976]; for single dislocations inclined to the surface, the simple image construction gives the correct force

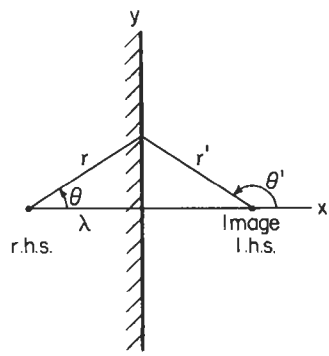

Fig. 11. A right-handed screw dislocation, parallel to and a distance λ from a free surface.

produced by the surface tractions. This theorem has been verified for a number of near-surface dislocation configurations, e.g., SHAIBANI and HAZZLEDINE [1980]. For two or more dislocations near the surface, the simple image construction is insufficient. The added stress field of one dislocation, discussed above for the edge, would produce a force on the other dislocation. Also the theorem is valid only in the linear elastic approximation and breaks down very near the surface where core effects become important (FILLIPOV, GAIDUKOV and MAKSIMOV [1985]).

There are other methods for calculating the fields of dislocations near free surfaces. For example, MUSKHELISHVILI [1975] presents a method of solution of Cauchy integrals. Which method one uses is a matter of taste, but for a single dislocation near a planar surface, the simple image method is straightforward.

2.5. Line tension

For arbitrary dislocations in a deformed crystal, the determination of W/L is a most formidable task. However, a rough approximation can be made. For a random array of dislocations, WILKINS [1969] showed that the outer cutoff R in the self energy exceeds the dislocation spacing. However, the dislocations tend to rearrange to polarize their elastic fields and reduce the energy, with R approaching the interdislocation spacing. On the average, since like-sign dislocations repel while opposite-sign ones attract, a dislocation tends to be surrounded by opposite-sign dislocations at an average spacing λ. In accord with St. Venant's principle, a pair of dislocations of opposite sign are sources of equal and opposite stress fields which should cancel one another over distances greater than $\sim\lambda$ from the pair. Thus, the strain field of the dislocation is limited to a radius $R \approx \lambda$. Hence, since as already discussed, core and surface terms can be neglected, eq. (8) applies roughly for the arbitrary case with $R \approx \lambda$. Moreover, $\lambda \sim \rho^{-1/2}$ where ρ is the dislocation density (m/m^3). Typical values of ρ range from $\sim 10^{10}$ m/m^3 for annealed crystals to $\sim 10^{16}$ m/m^3 for cold worked crystals, corresponding to $10^{-8}\ m < \lambda < 10^{-5}\ m$. With $r_0 \cong b \cong 3 \times 10^{-10}$ m and $\nu \cong 0.3$, the range of W/L in eq. (8) is from 0.28 to 1.18 μb^2.

Since μ and b are constant for a given material, W/L is a constant with the above approximations. A stretched linear-elastic string has a constant energy per unit length W/L numerically equal to the *line-tension* force $\mathcal{S}$ restraining the string, since $\partial W/\partial L = W/L = \mathcal{S}$. In the above approximation the dislocation can be thought of similarly as a stretched line constrained by line tension forces acting parallel to the line:

$$\mathcal{S} = \frac{\partial W}{\partial L} = g\mu b^2. \tag{14}$$

Here g is a numerical factor varying from 0.3 to 1.2 with an average value of roughly 0.7, or in a cruder approximation, 1/2.

The simple line tension analogy is qualitatively useful. For example, in this approximation a bowed-out dislocation or zig-zag dislocation is unstable with respect to a straight dislocation in the absence of stress. Also, the equilibrium angles at a node are determined by the line tensions.

References: p. 1872.

In a more accurate representation, one must account for the variation of W/L with β in eq. (8). $E(\beta)$ is a minimum for the screw orientation $\beta = 0$ or π, so a torque exists tending to twist the dislocation into screw orientation. Including this factor, but retaining the concept that $\mathbb{S}$ is the change in W with change in the total line length of a dislocation, DE WIT and KOEHLER [1959] found:

$$\mathbb{S} = \frac{W}{L} + \frac{\partial^2(W/L)}{\partial\beta^2} = \frac{W}{L}\left[1 + \frac{1}{E(\beta)}\frac{\partial^2 E(\beta)}{\partial\beta^2}\right]. \tag{15}$$

In the simple approximation that $\mathbb{S} = W/L$, the value of $\mathbb{S}$ for an edge exceeds that for a screw, eq. (8), by a factor $1/(1-\nu) \approx 1.4$. With the inclusion of the factor $\partial^2(W/L)/\partial\beta^2$, which tends to stabilize screws and destabilize edges, the situation is reversed and $\mathbb{S}$ for a screw exceeds that for an edge by a factor $(1+\nu)/(1-\nu)(1-2\nu) \approx 4.6$.

Even more accurately, rather than use the rough St. Venant approximation, one should compute the self and interaction energy. This can be done by the straight line segment equations mentioned previously. For the configurations in fig. 12, HIRTH *et al.* [1966] find:

$$\mathbb{S} = \frac{\mu b^2}{4\pi(1-\nu)} \ln\frac{gL}{r_0}, \tag{16}$$

with g a numerical factor equal to 6.41, 1.11, and 0.18, respectively, for cases a, b, and c. The result is understandable qualitatively. In case a, segments A and B are equal and opposite and so work must be done against their attractive interaction force in forming the loop. In case b, segment B is missing, so less work is needed and $\mathbb{S}$ is smaller. In case c, there is even less attractive segment length and $\mathbb{S}$ is lowest. Interestingly, as first noted by MOTT and NABARRO [1948], the line tension of a bowed segment depends on the bowout length L and *not* on the outer cutoff R. This result is important in the theory of bowout in solution-hardened or dispersion-hardened systems.

Advanced solutions of the bowout problem include a many-straight-line-segment, anisotropic elastic calculation by SCATTERGOOD and BACON [1975] and a cubic spline fit line integral solution by DUESBERY *et al.* [1992]. Using an anisotropic elastic version of the straight segment approach, SCHMID and KIRCHNER [1988] found that equilibrium shape of complete dislocation loops was rounder for small loops than for large loops which developed regions of low curvature. The small loop configuration reflects the dominant role of the segment–segment interaction energy, while the large loop shape is controlled by the β dependence in eq. (15).

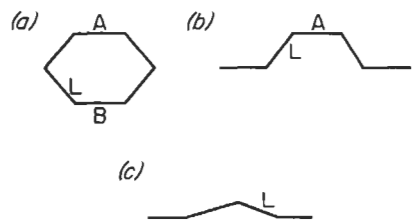

Fig. 12. Bowed-out configurations of an edge dislocation; $\boldsymbol{b}$ is normal to the page.

3. *Crystal lattice effects*

3.1. Peierls barrier

PEIERLS [1940], in a model elaborated by NABARRO [1947], modeled the periodic potential in the glide plane experienced by a straight dislocation lying in a low-index direction. In the model, the bonds across the glide plane were considered to interact by an atomic potential, while the remainder of the lattice was elastic. The model is useful in giving an analytical result that removes the artificial core divergencies of the Volterra dislocation, eqs. (2), (3) and (5). However, as discussed by HIRTH and LOTHE [1982] and by BULLOUGH and TEWARY [1979], the model is physically unrealistic (compared to a cylindrical atomic model centered on the dislocation) and predicts that symmetry positions are positions of energy maxima instead of minima. Nevertheless, atomic calculations indicate that the potential is roughly equivalent to the sinusoidal form of the Peierls–Nabarro result. Also, the prediction of the Peierls–Nabarro result that the magnitude of the energy maxima are greater for screw dislocations than for edge dislocations is supported by the results of nonlinear, anisotropic elastic estimates (PRINZ *et al.* [1983]) and by atomistic calculations (SONDHI *et al.* [1992]). Thus, it is useful to retain their result as an empirical representation of the barrier.

For a dislocation displaced by a distance x from a symmetry position (such as in fig. 2), the potential is:

$$\frac{W}{L} = \frac{W_p}{L} \sin^2 \frac{\pi x}{a}, \tag{17}$$

where a is the period, usually equal to b, and W_p is the *Peierls energy*. The maximum slope of this oscillating potential gives the *Peierls stress*, σ_p, needed to overcome the barrier at 0 K, but the barrier is usually overcome instead by kink formation as discussed below. In the original model the explicit form for W_p for an edge dislocation was

$$\frac{W_p}{L} = \frac{\mu b^2}{2\pi(1-\nu)} \exp\left(-\frac{4\pi\zeta}{b}\right) = \frac{\mu b^2}{2\pi(1-\nu)} \exp\left(-\frac{2\pi d}{b(1-\nu)}\right), \tag{18}$$

where ζ is the *width* of the spreading of the core in the glide plane and d is the glide plane spacing. An equivalent form without the factor $(1-\nu)$ holds for a screw dislocation. This form is not verified in atomic calculations, but the qualitative trends of a marked decrease in σ_p or W_p with an increase in core spreading or d are retained and are useful in predicting crystal slip systems. Because d and b appear in the exponent in eq. (18), the relation suggests that the smallest b and largest d should correspond to the observed slip system, in good agreement with experiment when dislocation extension is not an important phenomenon. As an indication of the change of Peierls energy with slip system, the ratio of W_p for the closest packed plane slip system, $\langle 110\rangle$–$\{111\}$, to that of the next closest packed plane system, $\langle 110\rangle$–$\{100\}$, is 0.36 in fcc crystals.

While the empirical form of eq. (18) is useful, it has several deficiencies in that it does not include expected variations of W_p with temperature or with stress components other than the shear stress resolved on the appropriate glide system. DOBROMYSLOV *et al.*

References: p. 1872.

[1984] have obtained experimental evidence that the Peierls stress in Mo varies linearly with the normal stress acting on the glide plane, in accord with the latter expectation. At present, there are insufficient results from atomistic simulations to suggest empirical modifications to eq. (18) for these added effects.

A dislocation line containing *kinks* is shown in fig. 13. The configuration of a kink such as B is determined by a balance between line tension forces, which tend to make w in fig. 13 large and hence straighten the line, and the forces associated with the Peierls barrier, which tend to make the kink abrupt. In the simple line-tension model of eq. (14), this force balance gives an equilibrium kink width w and kink formation energy W_k given in terms of the total elastic energy W/L by

$$w = a\left(W/2W_p\right)^{1/2}, \qquad W_k = \left(2a/\pi L\right)\left(2W\,W_p\right)^{1/2}. \tag{19}$$

Typically, W increases successively for bcc metals, ionic crystals and covalent crystals with values $W_p \sim 10^{-4}$, 10^{-3} and 10^{-2}W, $W_k \sim 0.01$, 0.05 and 0.1 μb^3 and $w \approx 70$, 20 and $7a$, respectively, see DUESBERY [1983] and SUZUKI and SEEGER [1992]. For fcc and hcp metals W_p is much smaller, so that Peierls barrier effects are only important well below room temperature.

Kinks are of three types: *geometric kinks* such as B in fig. 13 are present by geometric necessity since the segment AE spans one Peierls hill. At thermal equilibrium, a dislocation line contains a concentration of *thermal kinks* of $\sim(1/b)\exp(-W_k/kT)$. Finally, since the motion of a dislocation produces an offset of b in the entire lattice, as illustrated in fig. 1, *intersection kinks* can be produced on each dislocation if two nonparallel dislocations intersect.

3.2. Core structure and energy

With the advent of fast computers, atomic calculations for the nonlinear core region have become prevalent. They often have the drawback of using atomic pair potentials which do not accurately represent real metals. However, they do approximate real metal behavior fairly well and they are most useful in delineating classes of core behavior for different crystals.

Such calculations have been performed using either lattice statics or lattice dynamics as reviewed by PULS [1981]. With the development of flexible boundary methods, in which a cylindrical atomic region concentric with the dislocation core is matched compatibly with a surrounding elastic continuum, the use of lattice dynamics in real space is very efficient according to Puls. The reliability of calculations of this type in

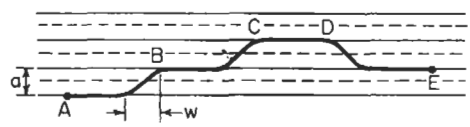

Fig. 13. Double kink CD and single kink B in a dislocation segment AE. Dashed and solid lines are maxima and minima in the varying lattice potential, respectively.

mimicking real materials has improved with the development of more accurate semi-empirical potentials beyond pair potentials (BASKES *et al.* [1992]; CARLSSON [1990]).

One important feature of these results is related to the volume of a dislocation. In the linear elastic approximation, the net volume change produced by a dislocation in a crystal is zero. The atomic calculations, both for metals and for ionic crystals, reveal that both edge and screw dislocations produce a volume expansion of about an atomic volume per close-packed atomic plane cut by a dislocation, i.e., the volume-equivalent of a row of interstitial atoms.

As also discussed by Puls, calculations of the core energy, while fewer, are of interest. In the reversible process of creating the edge dislocation, § 2.1, in addition to the elastic energy of eq. (8) stored between r_0 and R, elastic energy flows into the core and is stored there as core energy. The core energy can only be estimated by atomic calculations. Rather than adding a core term to all energies, it is convenient to retain the results of eqs. (6) to (8) and to incorporate the core energy by adjusting the value of r_0. In terms of a parameter α defined by $r_0 = b/\alpha$, estimates summarized in HIRTH and LOTHE [1982] indicate that $\alpha \approx 3$–5 for ionic crystals with screw values larger than those for edges, while $\alpha \approx 0.5$–2 for both partial and perfect dislocations in metals. Results for covalent crystals vary from about $\alpha = 1$ to 4, with the lower values for reconstructed cores and the higher values for unreconstructed cores (DUESBERY *et al.* [1991]; NANDEDKAR and NARAYAN [1990]).

One of the successes of atomic calculations has been in the understanding of the properties of screw dislocation cores in bcc metals, reviewed by VITEK [1974] and by SEEGER and WÜTHRICH [1976]. Figure 14 illustrates the result which indicates splitting of a $\frac{1}{2}[111]$ screw dislocation into a dislocation $q[111]$ at the origin and three dislocations $(\frac{1}{6}-\frac{1}{3}q)[111]$ at B, C, and D. Because the splitting is only over atomic dimensions and because of the variable nature of q, these are called *fractional* dislocations. For the glide sequence in fig. 14, the value of σ_p is large since the fractional dislocations must contract before motion can occur. Also, because of nascent extensions on {112} planes, also indicated in fig. 14, σ_p is asymmetric, being smaller in the so-called easy twinning direction than in the opposite direction, in agreement with experiments. The configuration of fig. 14a can exist in an alternate configuration rotated by π about the vertical in the page. The two configurations have opposite handedness, or polarity, and hence break the symmetry of the ⟨110⟩ direction along which the dislocation lies. A new localized type of defect, a flip, occurs where the configurations change from one to the other (SEEGER and WÜTHRICH [1976]). Because the fractional dislocations must at least partially constrict when the polarity changes, the flip can also be thought of as a type of constriction. Since kinks and flips can superpose, there is a wide variety of such defects, particularly in bcc metals where there are several low-index directions that are potential Peierls valleys in each glide plane. Computer simulations of metals indicate that the energies of flips are of the same order of magnitude as those of kinks (WÜTHRICH [1977]; DUESBERY [1983]). In diamond cubic crystals, simulations of partial dislocations show that core reconstruction can break symmetry, again leading to the possibility of flips (DUESBERY *et al.* [1991]). Concerning dislocation cores in intermetallic compounds see ch. 24, § 2.

References: p. 1872.

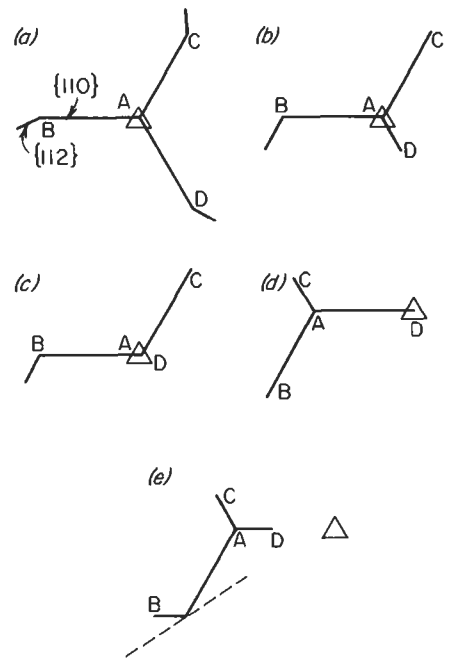

Fig. 14. (a) Core dissociation of screw dislocation; (b–e) Motion of screw under stress producing glide on the average on the dashed {112} plane shown in e.

3.3. Stacking faults and partial dislocations

In close-packed fcc and hcp crystals, stacking faults on {111} planes have relatively low energies and, consequently, perfect dislocations extend to form *partial dislocations* bounding a stacking fault. As an example, we consider the fcc case and the commonly observed intrinsic stacking fault, formed when a {111} plane is removed from the normal stacking sequence ABCABCABC and the crystal is collapsed together normally to form the fault ABCA:CABC (see discussion of fig. 17e). The notation of THOMPSON [1953] is useful. If one connects the atom centers of the four atoms near a corner of a unit cell, one forms the *Thompson tetrahedron*, fig. 15. The faces are the {111} glide planes and the edges are the $\frac{1}{2}\langle 110\rangle$ Burgers vectors (glide directions). Then AB, etc., denote Burgers vectors and (d) denotes glide plane.

Now consider the view of the glide plane in fig. 16. A perfect dislocation AB would shear the crystal and move an atom from 1 to 2. Clearly, in a central-force atom model, the path along the potential "valleys" (1)–(3)–(2) would be more favorable energetically. Yet, at the midpoint (3) the configuration is that of an *intrinsic stacking fault*. Hence, motion occurs first by the partial δB, creating the fault, followed by the partial Aδ, annihilating the fault. The actual configuration is shown in fig. 17a. The equilibrium spacing is achieved when the repulsive forces between the partials, eq. (11), just balance the attractive force γ of the fault. Here γ is the stacking fault energy (J/m^2), numerically

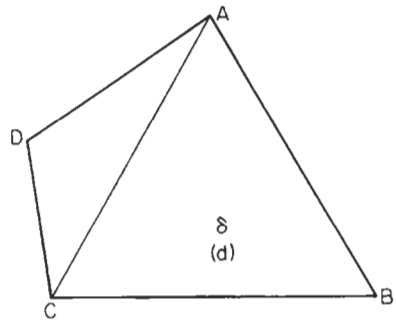

Fig. 15. Thompson tetrahedron.

equal to the surface tension (N/m) (see ch. 4, § 9.2).

The partial dislocations Aδ, etc., of the glide type, are also given on the Thompson tetrahedron, fig. 15, and are called *Shockley partials*. The correct sequence to form an intrinsic fault is established if: viewing the fault along positive ξ and viewing the plane as if one were outside the tetrahedron [as for (d) in fig. 17], place the Greek letter outside the fault. An example is given in fig. 17b for the dislocation AB bending from plane (d) to (c). Use of the continuity axiom of § 1.1 reveals that a *stair-rod partial* $\gamma\delta$ must exist at the bend. Stair-rods are sessile, since their glide would produce a very high energy fault.

Some other important arrays are also shown in fig. 17. Figure 17c shows a *Lomer–Cottrell barrier* (TEUTONICO [1964]) formed by the interaction of BA(d) and DB(a), the barrier strength being associated with the attractive interaction of Bδ and αB to form $\alpha\delta$. The symmetric array in fig. 17c is the original result. More detailed elastic calculations show that this is actually a rather flat saddle point with the true equilibrium configuration being asymmetric with relative extensions of the two arms in a ratio in the range 3 to 4 depending on the values of the elastic constants (KORNER *et al.* [1979]). The asymmetrical barrier has been found in computer simulations (GAO and BACON [1992]). However, the symmetrical configuration is often seen in experimental observations (e.g., ELKAJBAJI *et al.* [1988]), possibly because of the influence of nonlinear core–core repulsions. Other types of analogous barriers (HIRTH [1961]) are observed in the asymmetrical dissociated configuration (ELKAJBAJI *et al.* [1988]). Figure 17d is an

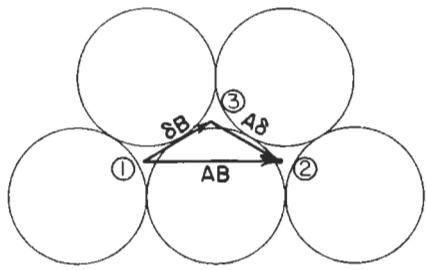

Fig. 16. Partial dislocation Burgers vectors in fcc crystals.

References: p. 1872.

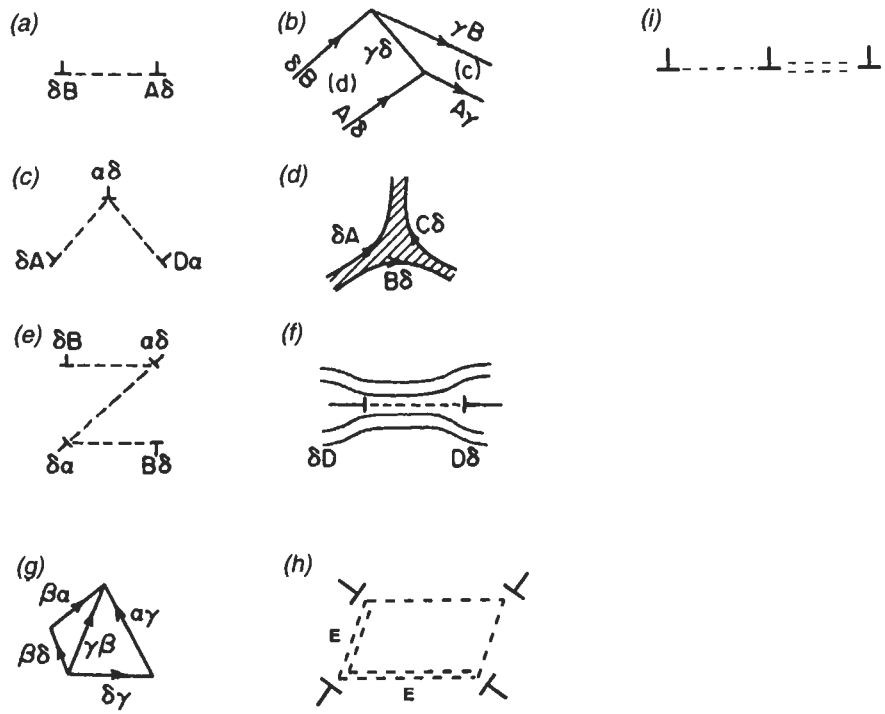

Fig. 17. Extended arrays in fcc. View is parallel to the {111} planes in a, b, e, and f, and perpendicular to it in d. Faults are intrinsic except for those labeled E which are extrinsic.

extended node, and 17e is an extended dipole. Figure 17f shows the removal of a plane of atoms by vacancy condensation to form a fault bounded by *Frank partials* of the type Dδ, the vector magnitude equalling the glide plane spacing. Frank partials are also sessile, but, as indicated by their formation process, they can climb by vacancy absorption or emission. Figure 17g is a stacking fault tetrahedron, formed from a Frank loop such as that in fig. 17f, with all faces corresponding to faults. Figure 17h is a stacking fault lozenge (KUMAR and HIRTH [1992]). Finally, fig. 17i represents the GALLAGHER [1970] fault. The parallel arrays of figs. 17a, c, e, h and i, for which interaction forces can be easily calculated in the anisotropic elastic case, are particularly suited for estimates of stacking fault energy on the basis of transmission electron microscopy observations. For example, a recent compilation for the case of GaAs is given by GERTHSEN and CARTER [1993].

Extrinsic faults, equivalent to insertion of a plane of atoms into the normal sequence, ABCABACABC have energies about equal to those of intrinsic faults (GALLAGHER [1970]) but are rarely observed. Extension to form this fault involves pairs of partials

bounding each side. The more complex movements to form these pairs probably hinder this type of extension, accounting for its rare appearance.

Analogous faults and partials form in hcp crystals, diamond cubic crystals, and in layer structure crystals such as mica and graphite (AMELINCKX [1979]). The fault energy is too large for meaningful extension to form a stacking fault in pure bcc metals, so extension into fractional dislocations occurs instead, as already discussed.

Among these other structures, there is great interest currently in diamond cubic and structurally related compounds for optoelectronic applications, so this structure serves as an example for more complex structures. A projection of the GaAs sphalerite structure is shown in fig. 18. Dislocations in principle can glide between the triply bonded {111} planes, the glide set, or the singly bonded planes, the shuffle set (HIRTH and LOTHE [1982]). In conformity with the now standard notation (AMELINCKX [1979]), the dislocations are identified by the atoms at the end of the inserted plane in edge orientation and the appropriate plane, glide (g) or shuffle (s). Hence, the four dislocations are Ga(s), As(g), As(s) and Ga(g). Since one often cannot determine between (s) or (g), the dislocations are also identified by the direction in which they move under stress, with α including Ga(s) and As(g) and β including As(g) and Ga(s).

Stacking faults analogous to those in fcc crystals occur in the glide set plane, and dissociation can occur directly for glide set dislocations. Shuffle set dislocations can dissociate into a glide set partial (and stacking fault) and a complex partial, zonal, because it extends over two planes. Glide in such structures is difficult to analyze because of the more complex core structure, the possibility of core reconstruction and the influence of electronic core states and electronic charge effects (HIRSCH [1981]). Recent discussions of such effects for the case of GaAs are given by YONENAGA and SUMINO [1992], MARKLUND and YONG-LIANG [1991] and ALEXANDER and TEICHLER [1991].

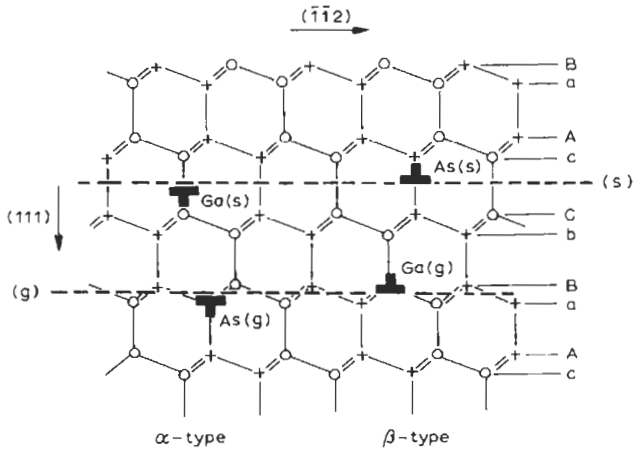

Fig. 18. GaAs lattice projected normal to [1$\bar{1}$0]. α represents atoms in the plane of the paper and β represents atoms in the plane below. [111] is perpendicular to the plane of the paper and appears as a horizontal trace. Planes with ABC contain Ga atoms, those with abc contain As atoms. Positions where inserted planes would terminate on dislocations if appropriate cuts were made are designated.

References: p. 1872.

Contrary to earlier assumptions, recent work indicates that dislocations slip on the glide set (LOUCHET and THIBAULT [1989]) although motion on both sets is suggested by some observations (CHIANG *et al.* [1980]). Because of the many types of dislocations in these structures, there is also a wide variety of partial dislocations as discussed for III–V compounds, for example, by DE COOMAN and CARTER [1989].

3.4. Ordered alloys

As an example of ordered alloys, we consider the $L1_2$ structure, with Ni_3Al as an illustration. Antiphase boundaries (APBs) occur where atom pairs across the interface have the correct atomic positions for the structure but the wrong chemical nature. Dislocations of the type **AB** (in the Thompson notation of fig. 15) that would be perfect dislocations in the disordered crystal become imperfect in the ordered crystal and must bound APBs. Perfect superdislocations are of the [110] type (**2AB**) and [100] type (**2AB/CD**). In the ordered lattice, the dissociation of **AB** into partials $\mathbf{A}\delta$ and $\delta\mathbf{B}$ creates a complex stacking fault, i.e., a fault structurally equivalent to an intrinsic stacking fault in fcc but with a superposed APB. Dissociation of **2AB** into $2\mathbf{A}\delta$ and $2\delta\mathbf{B}$ creates a superlattice intrinsic stacking fault (SISF).

A key to the understanding of deformation behavior and associated dislocation configurations in this structure is that the APB energy varies with orientation, being less for {100} than for {111} planes. Early regular solution models (FLYNN [1960] as modified by HIRTH and LOTHE [1982]) indicated a large difference in these energies. Values determined by correlation with transmission electron microscopy observations support the trend that the energy for {100} is less but show that the difference is much smaller, by about 20 to 60 percent (DIMIDUK *et al.* [1993]).

Some of the important dislocation arrays in the $L1_2$ structure are presented in fig. 19. A superdislocation dissociated in a planar manner into four partials is shown in fig. 19a. This configuration is convenient for the determination of fault energies (e.g., DIMIDUK *et al.* [1993]; BALUC *et al.* [1991]). Figures 19b and c show variations of the Kear–Wilsdorf lock, the important feature being the extension normal to the {111} planes. A superdislocation dissociated into superpartials and an SISF is shown in fig. 19d, while a further dissociation of one of these superpartials is depicted in fig. 19e (SUN *et al.* [1991a]). An APB tube, which can be formed by cross-slip, is presented in fig. 19f (VIDOZ and BROWN [1972]). Figure 19g shows a climb-dissociated loop (in perspective, unlike the other figures) which can be envisioned as a cross-slipped configuration for the screw portions of the loop but a climb-dissociated configuration for the edge and mixed portions (TAKASUGI and YOSHIDA [1993]). Figure 19h is the PAIDAR *et al.* (PPV) [1984] configuration, distinguished from the Kear–Wilsdorf lock by forming a cross-slipped segment only locally over a limited length of the dislocation. The climb dissociation in fig. 19i has been observed by DOUIN *et al.* [1988].

In addition to these defects, barriers and other reacted arrays analogous to those in fig. 17 can form. Of course, additional barriers, such as the double Lomer–Cottrell barrier (SUN *et al.* [1991b]), can exist because of the more numerous partials in dissociated superdislocations.

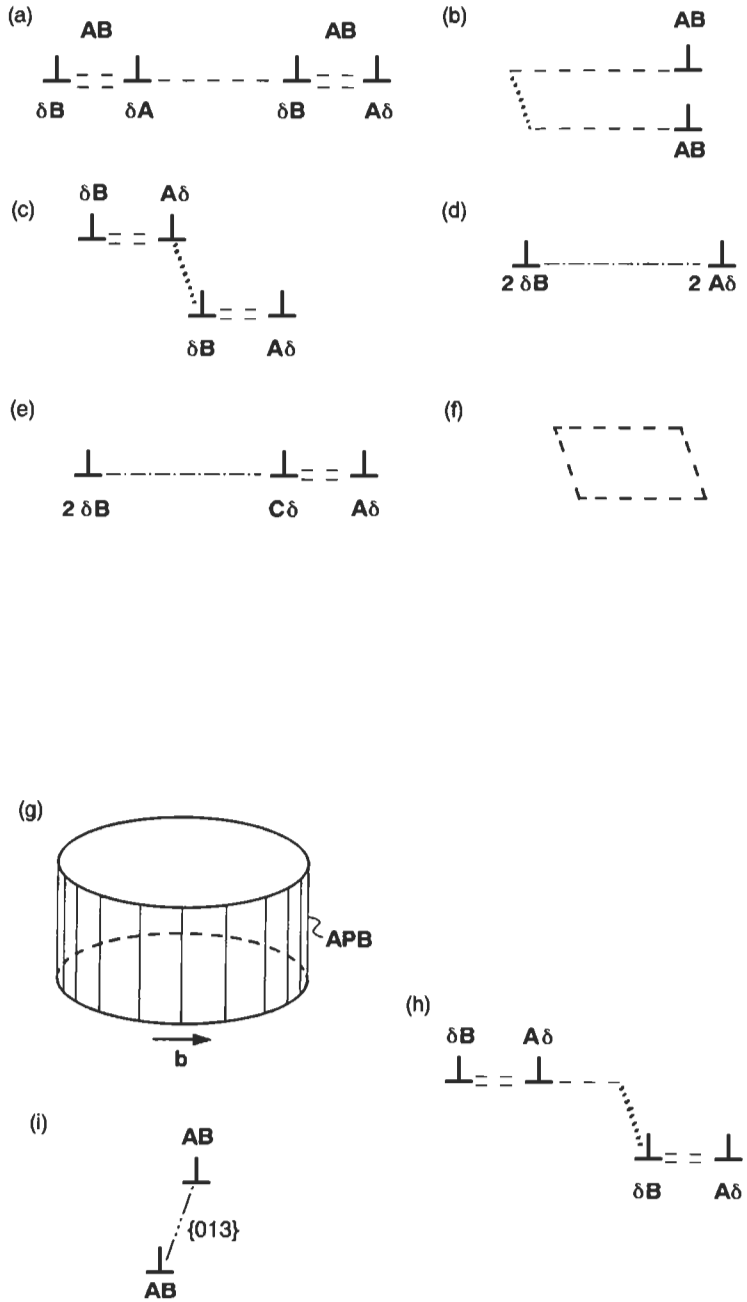

Fig. 19. Dislocation arrays in $L1_2$ structure. – – – represents {111} APB, === represents CSF, · · · · represents {100} APB, and –·–· represents SISF.

References: p. 1872.

3.5. Slip systems

Together, the concepts of Peierls energy and stacking faults are sufficient to explain most observed slip systems, with core structure and image effects having an influence in a few special cases. Equation (18), or its equivalent in a more exact model, predicts that the Peierls stress σ_p is least for the slip system with the smallest b and largest interplanar spacing d, that is, b along a low-index direction and d normal to a closed-packed plane. The value of σ_p increases rapidly with an increase in b or decrease in d, so the Peierls energy criterion would predict only a few low-index slip systems for a given crystal. A low stacking-fault energy is another factor favoring a given glide system, both because the extension of dislocations tends to restrict glide to the fault plane and because σ_p is less for Shockley-type partials.

The above ideas are borne out for observed slip systems as reviewed by HIRTH and LOTHE [1982]. $\langle 110\rangle$–$\{111\}$ is the predominant slip system in fcc crystals, fitting both criteria, while $\langle 110\rangle$–$\{100\}$ slip, on the second closest packed plane, appears occasionally. In hcp crystals with large c/a ratios, giving a relatively large d for the basal plane, which is also a low-fault energy plane, the $\langle 11\bar{2}0\rangle$–(0002) basal slip system is favored and is observed. With low c/a ratios, pyramidal slip or prismatic slip become favored and are observed.

In bcc crystals, the low-index $\langle 111\rangle$ direction is invariably the slip direction. This non-close-packed lattice has a smaller difference between the largest $\{110\}$ and next largest $\{112\}$ d spacing, and both slip planes are observed. As discussed in § 3.2, the pertinent glide plane for screw dislocations is determined by the behavior of fractional dislocations in the core. The situation for edge dislocations is unresolved, but there is some indication of fractional extension on $\{112\}$ planes at low temperatures.

Slip that is called anomalous because it does not occur on the slip system of a given type that experiences the maximum resolved shear stress is sometimes observed. For $\langle 111\rangle$ $\{112\}$ slip in bcc crystals,the core arrangement for motion in, say, a [111] direction differs from that in the $[\bar{1}\,\bar{1}\,\bar{1}]$ direction, so one expects the Peierls stress to differ as well, giving slip asymmetry. The fractional dislocations in fig. 14 reflect this expectation. FRANCIOSI [1983] has shown that in addition to effects of the Peierls stress, hardening associated with intersections with specific secondary forest dislocations influences this asymmetry. For Ta, anomalous $\langle 111\rangle$ $\{110\}$ slip is observed to be profuse at low strains at 77 K (WASSERBACH [1985]). The observation was explained by the mechanism proposed by LOUCHET and KUBIN [1975]: because of both elastic interaction and the formation of intersection jogs (see below) that pin the dislocations, screw/screw forest intersections should be particularly potent in providing hardening. If forest hardening is dominant, one then expects that the slip system with the lowest screw forest dislocation density to operate, and this criterion does explain the observations.

In fcc crystals, latent hardening of secondary slip systems varies for different systems, primarily at strains of 2 percent or less and most prominantly for crystals with low stacking fault energy (FRANCIOSI [1985]). This effect is also a form of slip asymmetry. The latent hardening is related to the intersection of systems that form intersection jogs, extended barriers and junctions.

Some ordered alloys, such as the widely studied case of Ni_3Al, exhibit anomalous behavior of slip in that the yield stress increases with increasing temperature (see the review by DIMIDUK [1991]). The effect had been associated with pins of the type in fig. 19h, which were postulated to form more easily with increasing temperature (PAIDAR *et al.* [1984]; GREENBERG *et al.* [1978]), although a role of the Peierls stress has also been suggested (CAILLARD *et al.* [1988]). However, a new view has appeared, stemming from observations of large kinks in screw dislocations that otherwise were locked in the Kear–Wilsdorf configuration in fig. 19b and c (SUN and HAZZLEDINE [1988]). This has led to further observations (COURET *et al.* [1993]), simulations (MILLS and CHRZAN [1992]) and other theories (DIMIDUK [1991]; HIRSCH [1992]; VEYSSIERRE [1989]) supporting the view of dislocation glide by a kink formation and lateral propagation mechanism. (See also ch. 23, 24.)

In thin crystals, where surface slip nucleation is important, unusual slip systems are observed in the sense that they do not have the maximum resolved shear stress (VESELY [1972]; LOHNE [1974]). These results are associated with image effects, either favoring glide by enhancing kink nucleation for screw dislocations oblique to the surface, or suppressing glide by pulling a dislocation more normal to the surface and creating jogs on it. The presence of surface steps that provide favorable sites for dislocation nucleation for dislocations with components of their Burgers vectors normal to the surface (DREGIA and HIRTH [1991]) can give rise to unusual slip. Nonlinear core effects also may have some influence on this phenomenon.

3.6. Jogs

An offset in a dislocation line which has a component normal to the glide plane is called a *jog*. A jog in a screw dislocation is simply a kink in the cross-slip plane and has properties as discussed in § 3.1. A jog in an edge dislocation is shown in fig. 20a. Rearrangement of the jog to a kink-like configuration would involve a very large misfit energy, so the jog remains sharp. Therefore, jogs have energies W_j of the order of the dislocation line energy multiplied by the jog height or $\sim \mu b^3$. These energies are 10–100 times larger than the formation energies for kinks, W_k. Consequently, the concentrations of thermal jogs are much less than those of thermal kinks at a given temperature. Intersection jogs and geometric jogs also exist, analogous to the equivalent kinks.

Climb occurs at jogs by vacancy formation or annihilation at jog sites. Self-interstitials could cause climb also, but their formation energy is so large in metals that they are

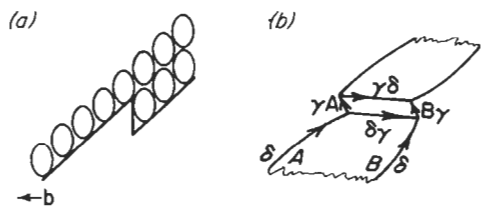

Fig. 20. Jogs in (a) a perfect edge dislocation and (b) an extended edge dislocation in fcc.

only important in the case of radiation damage. For a perfect dislocation, the only constraint to double jog nucleation or jog motion, the processes which produce climb in an analogous way to glide by kink processes as shown in fig. 13, is the formation of the pertinent defect, the double jog or vacancy.

An *extended jog* in a fcc crystal is depicted in fig. 20b. For a *superjog*, where the jog height is a multiple of the interplanar spacing, the extended jog is composed of partial dislocations and stacking faults, as shown. For a unit jog with height equal to a single interplanar spacing, the *stair-rod dipole* $\gamma\delta$–$\delta\gamma$ exists only over core dimensions. Rather than stair-rods and stacking faults, the jog is then better viewed as a jog-line, equivalent to a row of 1/3 vacancies for the present example (HIRSCH [1962]). Clarifying earlier puzzlement, work stemming from that of CARTER [1979] has shown that jogs of all heights, while constricted to some extent, exist in extended configurations: a high-resolution transmission electron micrograph is presented by SAKA *et al.* [1985] for the fcc case.

The extension of the jog evidently provides a constraint to both jog nucleation and motion. In early work, it was thought that the jog would have to constrict to a perfect dislocation to climb. However, as shown by BALLUFFI and GRANATO [1979] a vacancy itself can dissociate into the jog line and cause climb without constriction.

Observations by CHERNS *et al.* [1980] show that extended dislocations can also nucleate double jogs without constriction. Thus, the constraint to climb caused by extension, while present, is less than once expected. Direct climb by this mechanism has been observed, for example, for GaAs (CHERNS and FEUILLET [1985]) and Si (THIBAULT–DESSEAUX *et al.* [1989]).

4. *Dislocation behavior at low homologous temperatures*

4.1. Kink motion

In bcc metals at low temperatures, glide occurs by kink motion. For low stresses, kinks move and annihilate but nucleation easily replenishes them. The dislocation velocity v is the area swept per unit length per unit time or, fig. 13, the product of the equilibrium number of kinks of both geometric signs $2n_k$, the kink velocity v_k, and the distance between Peierls valleys $\sim b$. v_k is given by the kink mobility D_k/kT, where D_k is the kink diffusivity, and the driving force from eq. (9), σb^2,

$$v_k = \frac{2\sigma b^2 D_k}{kT} \exp\left(-\frac{W_k}{kT}\right). \tag{20}$$

For larger stresses, kinks are swept to the end of a segment of length L before they can be replenished, and double-kink nucleation is controlling. The formation energy $2W_k$ of a double-kink then enters the velocity expression, which becomes:

$$v_k = \frac{\sigma b L D_k}{kT} \exp\left(-\frac{2W_k}{kT}\right). \tag{21}$$

Further developments and detailed derivations are given by HIRTH and LOTHE [1982] and

by SEEGER [1981], who also notes that the phenomenon of soliton motion can be described by the same form of kinetics in the latter case.

The above relations were derived by LOTHE and HIRTH [1959] in the assumption that W_k is the formation energy of an isolated kink and this was revised by SEEGER and SCHILLER [1962] to include the stress dependence in W_k arising from kink–kink interaction energies. When eq. (20) holds, kink spacings are typically large, especially in ionic and covalent crystals (e.g., see PICHAUD *et al.* [1986]) and the stress dependent emendation is negligible. When eq. (21) holds, and especially for metals, the kink–kink interaction term is important (QUENET *et al.* [1987]).

Dislocation motion by this mechanism has received much recent attention in the case of semiconductors and compound semiconductors, where dislocation motion in nearly dislocation-free thin films can be observed directly by transmission electron microscopy. Results by HULL *et al.* [1991] for the Si–Ge system agree well with the above theoretical equations. In general, the above approach, when used to interpret both dislocation motion or plastic flow at low temperatures and low-temperature internal friction, see § 4.3, give self-consistent estimates of W_k, with values in rough agreement with the estimates in § 3.1 (recent examples include SUZUKI and SEEGER [1992] and BENOIT *et al.* [1987]). In some cases, the inclusion of the stress dependence arising from the kink–kink interaction energy is necessary (QUENET *et al.* [1987]).

All of the above discussion pertains to the case of kinks moving by diffusion under the control of phonon/electron damping. At very large stresses at low temperatures, underdamped, high-velocity kink motion is possible. In this case, as demonstrated by EYKHOLT *et al.* [1989], new phenomena are observed, such as the interpenetration of opposite-sign kinks instead of their mutual annihilation.

4.2. Point forces and bowout

For fcc and hcp metals or for bcc transition metals above about room temperature, $kT \gtrsim W_k$ and the effects of the Peierls barrier are removed by thermal fluctuation. In principle, dislocations under a driving force could then accelerate until their motion was controlled by damping produced by phonon scattering or radiation. However, except in shock-loading, dislocation motion becomes hindered by obstacles and breakaway from the obstacles becomes rate-controlling. A review of this subject is given by KOCKS *et al.* [1975].

Bowout at obstacles is illustrated in fig. 21. For small bowout, the force on a dislocation segment $\sigma b \lambda$ is transmitted to pinning points via line tension forces acting on

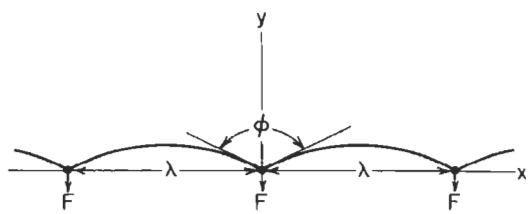

Fig. 21. Bowout from pinning points.

the pinning points. In the simple line tension case, eq. (14), the resultant force in the direction of bowout acting at the pinning point is $\mu b^2 \cos(\phi/2)$. The opposite stabilizing force F is the interaction force of the dislocation and a pinning point, often so localized that F can be considered a point force. At equilibrium, these forces are all equal and for a linear array of obstacles as in fig. 21.

$$\sigma = \frac{\mu b}{\lambda} \cos\left(\frac{\phi}{2}\right) = \frac{F}{b\lambda}. \tag{22}$$

For stresses $\sigma < \sigma_c$, the critical stress for breakaway, corresponding to $\phi > \phi_c$ and $F < F_c$, the bowout is stable. This case is relevant to the Granato–Lücke internal friction theory and to jog drag. For $\phi \geq \phi_c$, $F > F_c$; breakaway of dislocations from the pinning points occurs, relevant to solid-solution or precipitation-hardening and to dislocation–dislocation intersection. For obstacles so strong that $F < F_c$ when $\phi = 0$, complete bowout occurs at the particles, relevant to dispersion-hardening and the operation of dislocation sources. These several applications are now considered in succession.

4.3. Granato–Lücke internal friction theory

The vibration of a loop of length λ, such as that in fig. 21, produces energy dissipation and the GRANATO–LÜCKE [1956] internal friction peak. In discussing eq. (14), we mentioned the analogy of a dislocation of a stretched elastic string. The analogy is useful here and the vibrating loop under a driving shear stress σ is equivalent to a damped vibrating string segment. In this analogy, the dislocation has an effective mass per unit length $m = \mathcal{S}/C_t^2 = \mu b^2/2C_t^2$ with eq. (14) for the line tension and with C_t the transverse sound velocity. The damping force B is given by $\sigma b = Bv$, with v the dislocation velocity. As reviewed by ALSHITS and INDENBOM [1975], B is temperature dependent, but a rough value at room temperature for many materials is $B \cong 10^{-2}\, \mu b/C_t$.

With the above parameters, the equation of dynamic equilibrium for the vibrating loop in the coordinates of fig. 21 is

$$m\frac{\partial^2 y}{\partial t^2} + B\frac{\partial y}{\partial t} - \mathcal{S}\frac{\partial^2 y}{\partial x^2} = \sigma b. \tag{23}$$

The solution of eq. (23) is a standard problem in mechanics. The solution gives an internal friction (the relative energy loss per cycle $(\Delta W/W)$) for the fundamental mode of:

$$Q^{-1} = \frac{16\alpha^2 \mu \rho b^2}{\pi m \Omega_1} \frac{\omega\tau_1}{\left[1 - (\omega/\Omega_1)^2\right]^2 + (\omega\tau_1)^2}, \tag{24}$$

where ρ is the *active dislocation length per unit volume*, α is the *Schmid stress resolution factor*, Ω_1 is the *fundamental frequency*, $\Omega_1 = \pi^2 \mathcal{S}/m\lambda^2$, ω is the driving frequency and τ_1 is the relaxation time, $\tau_1 = B/m\Omega_1^2$. Inspection of eq. (24) shows that the internal friction peak, the maximum value of Q^{-1}, occurs near $\omega = \Omega_1$.

For large amplitudes, that is for large stresses, the pinning points can be dragged in either the x or y directions or breakaway from the pinning points can occur. In either

situation, the internal friction becomes amplitude dependent, increasing at large stresses.

The double-kink formation process discussed in § 4.1 also gives rise to internal friction phenomena, the so-called Bordoni and Niblett–Wilks peaks observed in bcc and fcc metals. These peaks are associated with the formation and lateral motion of double kinks. The characteristic relaxation time is that for kinks moving at a velocity given by eq. (20) or (21) to sweep over the relevant dislocation segment length or mean annihilation length. A review of these processes is presented by FANTOZZI *et al.* [1982]. Fine details of the kink energetics are discussed by INDENBOM *et al.* [1992] and by IUNIN *et al.* [1991]. As mentioned previously, the kink energies determined from internal friction studies, when compared to those deduced from dislocation velocity measurements, provide a key test of the selfconsistency of the double kink models.

4.4. Dislocation sources

Suppose that the segment λ in fig. 21 is a small portion of a larger loop. Then $\phi/2$ can be chosen near $\pi/2$ and the radius of curvature of the loop is $r=\lambda \tan(\phi/2) \cong \lambda/\cos(\phi/2)$. Then the simple line-tension expression of eq. (22) becomes

$$\sigma = \mu b/r. \tag{25}$$

Consider now the segment λ in fig. 22, pinned in its glide plane in such a way that the dislocation leaves the glide plane at the pinning points. As the stress increases the dislocation bows out further and r decreases. At position B, $r=\lambda/2$, the radius of curvature is a minimum, and the loop can grow spontaneously with an increase in r since eq. (25) can no longer be satisfied. When the loop reaches position D, the parts which touch one another are equal and opposite dislocations and annihilate one another (the dashed line in fig. 22). A complete loop is formed and the portion constrained by the pinning points can again bowout and repeat the process. The segment λ so operating is called a *Frank–Read dislocation source*. The source is important in dislocation multiplication since many dislocation loops can be produced from one segment.

If only one end of a segment is pinned, with the other end reaching a free surface, a single-ended source forms, with the dislocation winding into a spiral. Both types of

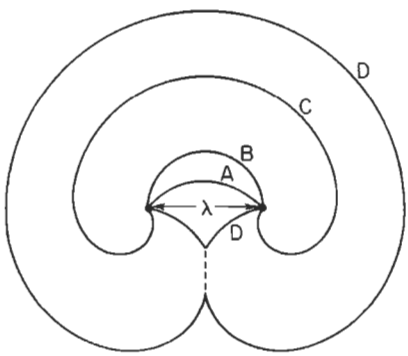

Fig. 22. Bowout of a segment λ to become a Frank–Read source.

References: p. 1872.

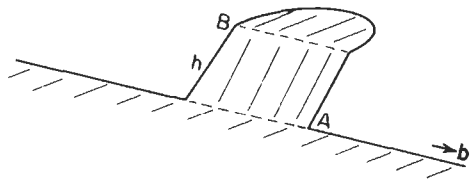

Fig. 23. Double cross-slip of a screw dislocation.

source can also operate in climb. They are then referred to as *Bardeen–Herring sources.*

There are other types of sources, but most of these can be thought of as variants of the above sources. Consider, for example, the double cross-slip of a screw dislocation in fig. 23. The screw dislocation can be imagined to cross-slip at A to avoid an obstacle and then to cross-slip back to the original glide plane at B. Provided that h is large enough that the Peach–Koehler force and the inertia of loop B can overcome its attractive interaction force with A (that is, if h is large enough, since the latter force $\propto 1/h$) the loop B can evidently act just like a Frank–Read source. The superjogs AB are sessile and pin the cross-slipped segment at its ends.

Surface nucleation of a half-loop at the site of a ledge on a free surface occurs in semiconductor thin films (reviewed by DREGIA and HIRTH [1991]). As demonstrated in a refined treatment by KAMAT and HIRTH [1990], the energy of the surface ledge that is removed when the loop is formed contributes to the ease of nucleation at such a surface site. Another important surface nucleation process occurs at atomistically sharp crack tips where dislocation formation, producing blunting, competes with crack propagation by bond decohesion (RICE and THOMSON [1974]). The problem involves both more complex image interactions than for planar surfaces and nonlinear core formation effects. Current approaches include effects of nearby lattice dislocations (HIRSCH and ROBERTS [1991]), Peierls barrier effects (SCHOECK and PÜSCHL [1991], RICE [1992]) and atomistic calculations (THOMSON *et al.* [1993]; HOAGLAND [1993]).

4.5. Dislocation pile-ups

Dislocations emanating from a source move until they encounter an obstacle. They then form an array called a *dislocation pile-up* as shown in fig. 24 for edges. At equilibrium the net force on each of the N edge dislocations is zero. Each dislocation is acted upon by the applied stress with a force σb. As shown for the second dislocation, this force is balanced by the summation of the repulsive interaction force for all but the lead dislocation. The lead dislocation only encounters the short-range stress field σ_0 of

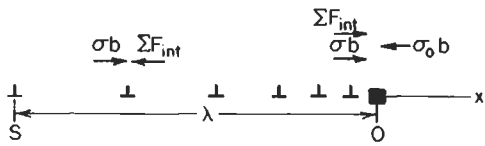

Fig. 24. View parallel to glide plane showing pile-up extending from source S to obstacle O.

the obstacle which gives a repulsive force $\sigma_0 b$, balanced by the *sum* of σb and the interaction forces.

A simple way to deduce the stress field of the pile-up is to imagine an infinitesimal increase in σ, which, since each dislocation is at equilibrium, to first-order produces the same virtual displacement δx of each dislocation. Since the entire array translates rigidly, the interaction forces, which sum to zero for the entire array, do no work. Moreover, the change in total free energy W is zero to first order since $\partial W/\partial x = 0$ defines equilibrium. Thus, the change in free energy $N\sigma b\delta x$ produced by the applied stress acting on all of the dislocations is balanced by the free energy change $\sigma_0 b\delta x$ produced by the leading dislocation moving against the stress field of the obstacle. Thus,

$$N\sigma = -\sigma_0 = \sigma_e. \tag{26}$$

The *effective stress* (or local stress) σ_e at the lead dislocation of the pile-up, composed of the applied stress and the sum of the stress fields of the other dislocations, is $N\sigma$. This is an enormous stress concentration since N typically ranges from ~20 to ~500.

The dislocation next to the tip encounters an apparent obstacle consisting of the first dislocation and its obstacle, so similar reasoning shows that the stress at this site is $(N-1)\sigma$. Thus, the stress decreases and the spacing increases with distance from the pile-up tip. An exact solution for the positions involves N equations in N unknowns, the positions of the dislocations, and can only be solved numerically as reviewed by CHOU and LI [1969] and HIRTH and LOTHE [1982]. As also discussed by those authors, an analytical integral solution can be obtained if the discrete dislocation array is replaced by a continuous distribution of infinitesimal dislocations with the same net Burgers vector Nb. The integral solution is precisely the continuum mechanics solution for a mode II shear crack. Thus, the infinitesimal dislocations make the connection between crystal plasticity and continuum plasticity.

Such solutions give the result for the number of dislocations in the pile-up $N = \pi(1-\nu)\lambda\sigma/\mu b$. Thus, the effective stress at the tip of the pile-up is:

$$\sigma_e = N\sigma = \pi(1-\nu)\lambda\sigma^2/\mu b. \tag{27}$$

This result is useful in explaining effects of microstructure on flow or fracture. A critical stress σ_e is required to propagate yield past an obstacle or to nucleate a crack there, with σ_e a material constant depending on surface energy, Frank–Read source size and the like. Then eq. (27) shows that the applied stress at yield or fracture varies as $\lambda^{-1/2}$. With the grain boundaries as barriers, the largest pile-ups have $\lambda = d/2$, with d the grain size, giving $\sigma \propto d^{-1/2}$, the form of the so-called *Hall–Petch relation.*

The stress field ahead of and near to the pile-up tip varies as $r^{-1/2}$, where r is the distance from the tip. The field of the infinitesimal dislocations gives, in fact, precisely the stress intensity $\sigma_e = K/(\pi r)^{1/2}$, identical to the continuum mechanics result. The far stress field ahead of a pile-up varies as Nb/r', where r' is the distance from a point 3/4 of the way from the source to the obstacle. Thus, the field is equivalent to that of a superdislocation with Burgers vector Nb at $r' = 0$. Even if cross-slip or climb should rearrange the dislocations at the tip, *blunting* the pile-up, the effects on the field would be short-range according to St. Venant's principle. Thus, the stress concentration remains that of a superdislocation except

References: p. 1872.

near the tip. The superdislocation analogy is useful in qualitative reasoning.

A little mentioned result is that a stack of edge dislocation pileups has a larger stress concentration at a given tip than does a single pileup while a stack of screw pileups has a smaller stress concentration than for a single pileup (SMITH [1968]). The effect arises because the screw dislocations in adjacent pileups repel one another, decreasing the dislocation density at the tip, while edges in adjacent pileups experience a short-range attraction (and only a long-range repulsion), producing the opposite effect on tip dislocation density. This interaction has obvious implications for the deformation of polycrystals and for the Hall–Petch relation.

A pileup of edge or screw dislocations is exactly equivalent to a mode II or III crack, respectively, in the approximation that the dislocations are smeared into a continuous distribution of infinitesimal dislocations. Hence, processes of dislocation emission from cracks, considered in the previous section, can be directly applied to the relaxation of pileup stresses by dislocation emission ahead of the tip of the pileup.

4.6. Pinning in alloys

In alloys, a variety of structural entities can pin dislocations. For solute atoms with strong binding energy (interaction energy) with dislocations, such as interstitials in bcc metals, either the model of fig. 21 or variants of it are applicable. The concentration of solute in the two planes through which the dislocation glides is $c = 2/\lambda^2 d$, with d the interplanar spacing and λ now the mean spacing of solute in the plane. Together with eq. (22) this result gives the FLEISCHER [1964] solid solution hardening law $\sigma \propto c^{1/2}$, valid for dilute solutions. Some modification of eq. (22) might be appropriate, as discussed in connection with fig. 25, but this would not influence the $c^{1/2}$ dependence. For concentrated solutions, core interactions and short-range ordering or clustering effects are more important giving $\sigma \propto c$. For weaker binding energy substitutional solutes or for intermediate concentrations with larger binding energies, a dislocation is more likely to bowout to break away from several solute pins simultaneously, giving a behavior $\sigma \propto c^{2/3}$. Such a dependence is predicted theoretically by LABUSCH [1972] and has very strong experimental support as discussed by HAASEN [1995] who elaborates on the theory of solid solution hardening.

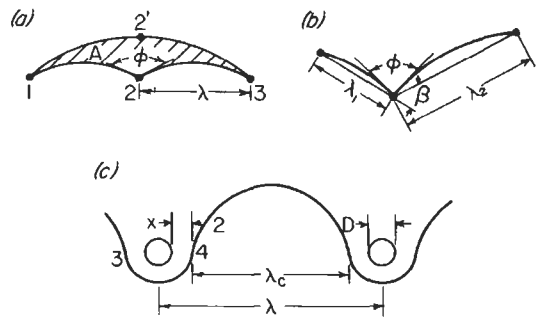

Fig. 25. (a, b) Bowout from pinning points; (c) bowout around particles.

For small coherent precipitates such as G–P zones in Al alloys, the obstacle strengths are such that the small-bowout eq. (22) should still be valid. The issue in this case is what produces the maximum resisting force F, although it is clear that dislocations cut the particles at breakaway. Possibilities are coherency strain interactions, the surface energy of the interface step formed when the particle is cut, incompatibility effects at the interface since the glide systems are not the same in the matrix and the precipitate, fault formation in the particle, or Peierls stress in the particle. Which of these is dominant is not yet known.

When the random distribution of pinning points in the glide plane, rather than the linear, regular array of fig. 21, is considered, modifications of eq. (22) appear. FRIEDEL [1956] supposed that at steady state the breaking of a pin at 2 in fig. 25a resulted in an area A being swept before the loop is repinned at 2′. In the small-bowout approximation and using eq. (25) he found for the area swept:

$$\frac{A}{\lambda^2} = \left(\frac{\mu b}{\sigma\lambda}\right)^2 \cos^3\left(\frac{\phi}{2}\right), \tag{28}$$

as can be verified readily for the geometry shown. If one associates $A \sim \lambda^2 \sim$ the mean area per pinning point in the plane, one can rearrange eq. (28) to give:

$$\sigma = \frac{\mu b}{\lambda} \cos^{3/2}\left(\frac{\phi}{2}\right) = h\,\frac{\mu b}{\lambda} \cos\left(\frac{\phi}{2}\right), \tag{29}$$

with $h = \cos^{1/2}(\phi/2)$ for the case shown. Except for the factor h, eq. (29) is identical to eq. (22).

More generally the critical bowout angle is expected to vary with length distribution λ_i, with pinning point strength distribution ϕ_i, and with the angle β_i as shown in fig. 25b. Equation (29) could then still be used but with $h = h(\phi_i, \lambda_i, \beta_i)$. For large bowouts a more complicated geometrical function would replace eq. (28). In computer simulations with random distributions of λ_i and β_i, and with the simple line-tension form, eq. (25), the simple result of eq. (29), with both the λ^{-1} and the $\cos^{3/2}(\phi/2)$ dependences, was found to hold for $\phi \gtrsim \pi/3$, see KOCKS *et al.* [1975] and ALTINTAS and MORRIS [1986]. Since $h < 1$ for this case, the resisting force is less than that for a regular array. This can be rationalized in terms of easy breaking points with large λ_i or large β_i (fig. 25b) within the statistical distribution. Whether the form of eq. (29) holds for real arrays and other than in the approximation of eq. (25) remains an open question. For any version of breakaway from point obstacles, where a constant line tension is assumed, the dependence $\sigma \propto \lambda^{-1}$ of eqs. (22) and (29) is retained.

For discrete obstacles, other effects appear as shown in fig. 25c. If the particles are harder than the matrix, the usual case, image repulsion leads to a repulsion distance x, which, together with the finite size of the obstacles D, reduces the effective spacing from λ to λ_e. In a refined line-tension model, the dimension λ replaces L in eq. (16) and this expression replaces that of eq. (15) in eq. (29). Further, when the interactions between adjacent loops are included, $\mathbb{S}$ would be lowered because of the attraction between opposite sign portions 1 and 2 in fig. 25, an effect that could be modeled by further

reducing the outer cutoff in eq. (16) to the dimension D (ASHBY [1964]). On the other hand, the harder particle would screen the interaction between segments 3 and 4 which would tend to partially offset the previous effect (HIRTH [1976]).

Including all of these effects, one finds, instead of eq. (29):

$$\sigma = \frac{h\mu b}{\lambda}\cos\left(\frac{\phi}{2}\right)\left[\ln\left(\frac{cD}{r_0}\right) + A\right]. \tag{30}$$

Here, $h = h(\phi_i, \lambda_i, \beta_i)$ as above, D is the nominal outer cutoff parameter, the factor $c > 1$ accounts for the elastic inhomogeneity between the particle and matrix, and A arises from long-range loop-loop interactions. The factor A introduces a (weak) dependence on λ. With all of these modifications, the simple $\sigma \propto \lambda^{-1}$ Orowan/Friedel relation is no longer valid. A few experiments support the form of eq. (30). MESSERSCHMIDT *et al.* [1985], in a study of loop bowout in MgO, found that bowing is easier than predicted by either eq. (30) or for a single bowed loop as calculated by the anisotropic, straight-line segment case (SCATTERGOOD and BACON [1975]), implying an effect of the factor A. Also, numerical calculations including loop–loop interactions (DUESBERY and SADANANDA [1991]) verify that the added λ dependence of σ arises from the factor A. Still, there are insufficient results of this type to predict a generally applicable constitutive relation of the type of eq. (30) so that the approximate form of eq. (29) is probably sufficient with the present state of understanding.

When the critical stress is exceeded for the case of fig. 25c, either the particles are cut or the loops bypass the particles, recombine, and leave a closed loop around each particle, in the Orowan process. Subsequent loops can form, giving rise to circular pile-ups (or their blunted versions) and attendant work-hardening in dispersion-hardened systems.

4.7. Work-hardening

In the absence of strong pinning points, work-hardening is dominated by dislocation–dislocation interactions. Early theories for work-hardening emphasized one single mechanism, but it now appears that a number of dislocation mechanisms can contribute. The loop length scaling of eq. (22) still applies for free segments, with dislocation interactions providing the pinning (see KUHLMANN–WILSDORF [1966]). Here, we briefly enumerate the hardening interactions.

For *forest* interactions of a dislocation with other dislocations threading its glide plane, the initial interaction is the elastic one of fig. 10, as verified by APPEL [1989]. In the process of intersection, energy must be supplied to form intersection jogs and kinks. The latter process is more important for extended dislocations, but the relative importance of the two contributions is unresolved for perfect dislocations. Continued pinning is provided by sessile jogs on screw dislocations.

Forest dislocations can be provided by glide on secondary slip systems or by several special mechanisms. One of these is dipole formation, which can be analyzed using fig. 23. If after cross-slip, h is less than the critical value to operate the new segment as a

source, the original dislocation and the new segment interact to form dislocation dipoles, pure edge in character. A dipole loop could also form by the condensation of vacancies into a disc which collapses. In materials of low stacking fault energy the latter process leads to the formation of stacking fault tetrahedra, fig. 17.

Another possibility in the process of intersection is the formation of *attractive junctions*, illustrated in fig. 26, which can form for either dissociated or undissociated dislocations (SAADA [1960]). The reacted part of fig. 26b is the Lomer–Cottrell barrier of fig. 17. Because W_{int} is negative between the reacting dislocations, energy must be supplied to remove the attractive junctions to complete the intersection process, and therefore their formation contributes to hardening.

Grain boundaries or Lomer–Cottrell barriers extensive in length are sufficiently strong barriers to sustain dislocation pile-ups (HIRTH [1972]; THOMPSON [1977]). These not only generate back stresses to stop the source producing the pile-up dislocations, but also generate long-range internal stresses, both effects leading to hardening.

The ideas discussed here provide the dislocation mechanisms to be considered in work-hardening. The integration of these models to provide a macroscopic work-hardening relation is discussed by ARGON [1995].

5. *Dislocation behavior at high homologous temperatures*

5.1. Osmotic climb forces

At temperatures greater than about $0.4T_m$, vacancy contributions become sufficient for dislocation climb to be important in deformation and recovery. In the absence of stress, the *equilibrium vacancy atom fraction* is:

$$c_0^0 = \exp(-G_f/kT), \tag{31}$$

where G_f is the formation energy of a vacancy. In the presence of external pressure P, the formation of a vacancy as in fig. 27a requires extra work $P\delta V$. Here δV is the volume change on vacancy formation, equal to the atomic volume v_a minus the relaxation volume $\delta v + \delta v'$ arising from the partial collapse of neighboring atoms into the vacant site. The term δv is the local volume change and $\delta v'$ is an image contraction of the

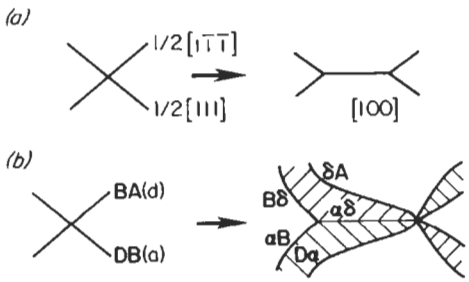

Fig. 26. Attractive junctions in (a) perfect bcc dislocations, (b) extended fcc dislocations.

References: p. 1872.

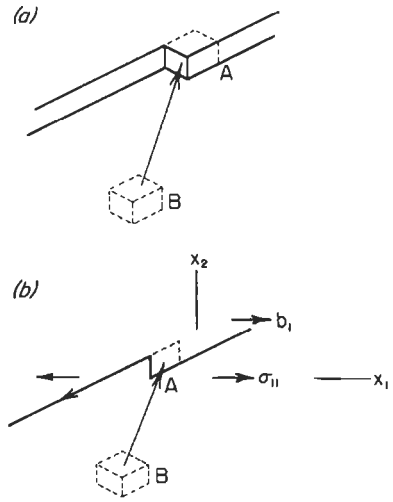

Fig. 27. Creation of a vacancy at B by depositing the atom from that site to (a) site A at a step on a free surface or (b) site A at a jog on an edge dislocation.

crystal associated with satisfying the free surface boundary condition. In the presence of an internal pressure p at site b there is extra work $p(\delta v + \delta v')$. Thus, the equilibrium atom fraction becomes

$$\begin{aligned} c &= \exp\left\{-\left[G_f + Pv_a - (P+p)(\delta v + \delta v')\right]/kT\right\} \\ &= c_0^0 \exp\left\{-\left[Pv_a - (P+p)(\delta v + \delta v')\right]/kT\right\} \\ &= c^0 \exp\left(-Pv_a/kT\right). \end{aligned} \tag{32}$$

It is convenient to include the image terms in c^0 and use this value as a reference concentration for dislocation problems so that first-order effects of stress can be separated from weak effects arising from internal pressure gradients (HIRTH and LOTHE [1982]).

For the creation of a vacancy by the process of fig. 27b, the net work is

$$\delta W = -\sigma_{11} b_1 a h + \overline{G}_v = -\sigma_{11} v_a + kT \ln\left(c/c^0\right). \tag{33}$$

Here $\sigma_{11} b_1$ is the Peach–Koehler force on the edge dislocation, eq. (9); a is the length and h the climb distance of an atomic unit of dislocation line, so that $b_1 a h = v_a$, $\overline{G}_v$ is the vacancy chemical potential referred to a reference state c^0, eq. (32), and c is the actual vacancy concentration. The net force in the x_2 climb direction per unit length is

$$\frac{F}{L} = \frac{1}{a}\frac{\partial W}{\partial x_2} = \frac{1}{ah}\delta W = -\sigma_{11} b_1 + \frac{kT b_1}{v_a} \ln\left(\frac{c}{c^0}\right) = \frac{F_{el}}{L} + \frac{F_{os}}{L}. \tag{34}$$

Here F_{el} and F_{os} are the elastic and osmotic climb force on the dislocation, respectively.

More generally, F_{el} would be the total Peach–Koehler force in the x_2 direction and could include forces on screw components of mixed dislocations, see § 2.2.

Let us consider some local equilibrium examples. At local equilibrium the total force $F/L=0$ and eq. (34) gives:

$$c = c^0 \exp(\sigma_{11} v_a / kT). \tag{35}$$

For a dislocation under uniform hydrostatic pressure P, $\sigma_{11}=-P$, eqs. (32) and (35) give the same local equilibrium value of c at the dislocation and at a free surface, and no vacancy diffusion or climb occurs. A dislocation under stress σ_{11} with local concentration c near a stress free surface with concentration c^0 experiences a vacancy concentration gradient and hence a tendency to climb. Often $\sigma_{11} v_a < kT$ at high temperatures and the gradient can be linearized, $c - c^0 \cong c^0 \sigma_{11} v_a / kT$.

If local equilibrium does not obtain, either F_{el} or F_{os} can give a net climb force. For example, a quenched-in concentration c of vacancies producing a supersaturation relative to c^0 at the final temperature gives an osmotic climb force given by eq. (34). For quenches from near T_m to $T_m/2$ or less, the osmotic forces are large, corresponding to stresses of $\sim\mu/10$ or greater, of the order of theoretical strengths of perfect crystals. Thus, there is little constraint to climb or to nucleation of vacancy discs which collapse to dislocation loops after quenches from near T_m. A special case is the development of a helical dislocation from a straight screw dislocation in which local equilibrium is established by a balance of the line-tension forces, tending to return the helix to a straight line, by the osmotic force on the edge component of the helical dislocation.

5.2. Jog drag

A climb-type process that can contribute to an overall glide process is the drag of jogs by screw dislocations. A jog on a screw is sessile, as seen in fig. 28, since the jog itself has edge character. Yet, whether it is a unit jog or a superjog, it can move along with the screw dislocation by vacancy absorption or emission. A steady-state configuration could be that of fig. 21 with the osmotic forces at the jogs balancing line-tension forces from the loops bowed out by the applied glide force. With opposite-sign jogs, the local equilibrium concentrations at the jogs would be given by eq. (35) but with opposite signs of the exponent. Thus, concentration gradients would exist and the rate of

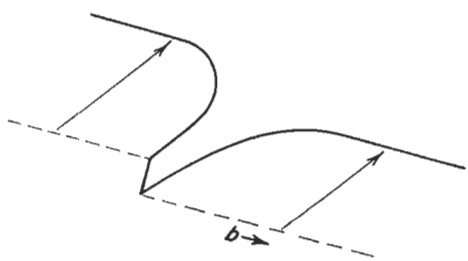

Fig. 28. Unstressed screw dislocation (dashed line) containing a jog, and glide of the dislocation under stress with pinning at the sessile jog.

climb would be controlled by vacancy diffusion from one sign jog to the other. Relevant to ch. 22, the concentration gradient in this case would involve a difference of exponentials, eq. (35), together giving a stress dependence $\sim 2 \sinh(\sigma_{11} v_a / kT)$.

For bowout forces giving point forces at the jog pinning points $F > F_{os}^{*} = G_f b_1 / v_a$, breakaway will occur in the sense that the dislocation will move rapidly in glide, athermally generating a string of vacancies (or interstitials) in the wake of the jogs. This can happen because the energy released on glide by a unit atomic distance exceeds the formation energy G_f of the appropriate point defect. The forces required for this process are modest when jog spacings are large and this process undoubtedly contributes to the large excess supersaturations of vacancies and interstitials produced in work hardening and detected in recovery measurements (see WOLLENBERGER [1995]).

5.3. Climb

In the absence of constraints, local equilibrium vacancy concentrations are maintained at jogs and the determination of the climb velocity of a dislocation becomes a diffusion boundary-value problem with the jogs as sources and sinks. Often the jog spacing is so small or the pipe diffusivity of vacancies along the core is so large that a dislocation acts as a perfect line source and sink and dislocation lines can be considered as the sources and sinks (BALLUFFI and GRANATO [1979]). The boundary-value solutions are beyond the scope of this work, but consideration of constraint is of interest.

In the presence of strong pinning, dislocations must climb to critical configurations as in fig. 22 to activate Bardeen–Herring sources. In the critical configuration, the sum of the elastic and osmotic forces, eq. (34), must balance the line tension forces ($\mu b / \lambda$).

For straight perfect dislocations, there are no indications of constraints preventing the attainment of local equilibrium vacancy concentrations. For extended dislocations, jog nucleation and jog motion are complex and could provide constraint (§ 3.6). However, experiments on the relatively low stacking fault energy metal gold show that the climb efficiency is greater than or equal to 0.1 (SEIDMAN and BALLUFFI [1966]). Here the climb efficiency was defined as the climb rate of a dislocation, under moderate to small osmotic forces produced by quenching, divided by the maximum climb rate under pure diffusion control. In general, constraint would be negligible when the relaxation time for diffusion from source to sink over a distance L, $\tau \sim L^2 / D_{vac}$ with D_{vac} the diffusivity of vacancies, is large compared to the time to nucleate and move jogs over a typical segment length λ. In most cases τ is expected to be large compared to the nucleation time in the gold quenching experiment. Thus, generally, one expects constraint to be absent so that it is a good approximation to treat climb as a pure diffusional boundary-value problem.

5.4. Solute drag

In analogy with the vacancy case already discussed, there is an interaction energy $p \delta v$ between a dislocation with internal pressure field p and a solute atom with a characteristic local volume change δv, equivalent to a ball inserted into a hole of different size in an elastic medium. A straight screw dislocation has no p field and thus no interaction.

For the edge dislocation of fig. 7, $p=-(\sigma_{rr}+\sigma_{\theta\theta}+\sigma_{zz})/3$. Hence, from eq. (5), the interaction energy is:

$$W_{\text{int}} = \frac{\mu b \delta v (1+\nu)\sin\theta}{3\pi(1-\nu)r}. \tag{36}$$

The solute concentration in local equilibrium in the presence of p, again analogous to § 5.1, is:

$$\frac{c}{1-c} = \frac{c_0}{1-c_0}\exp\left(-W_{\text{int}}/kT\right) = \frac{c_0}{1-c_0}\exp\left(-\frac{\beta\sin\theta}{r}\right). \tag{37}$$

where c_0 is the bulk equilibrium concentration and terms other than r and $\sin\theta$ in eq. (36) are included in β. Here it is important to use the Fermi–Dirac form, since for positive exponents $c \to 1$ as $r \to 0$, and the simpler Boltzmann form would artificially diverge. With δv positive, corresponding to a solute atom larger than the solvent atom, solute is depleted from the compressed region above the glide plane where $\sin\theta$ is positive, and attracted to the extended region (see fig. 2), as is physically reasonable. The solute of eq. (37) comprises the *Cottrell atmosphere*.

In addition, solute atoms are attracted to either screw or edge dislocation cores with a binding energy E_B for the appropriate case, forming a "core atmosphere". Also, interstitial atoms in bcc metals can form "Snoek atmospheres". These interstitials produce an asymmetric tetragonal strain in the octahedral or tetrahedral sites with the maximum principal strain aligned along ⟨100⟩ directions. A stress which produces extension along a [100] direction would then favor preferred occupation of that type of site with a corresponding negative interaction energy. All three atmospheres can produce dislocation drag and breakaway phenomena. As an example, the Cottrell atmosphere is considered here. The formation of the atmosphere is again a pure diffusion problem. For a discussion of the diffusion solutions, see BAIRD [1971]. (See also COTTRELL [1953]).

The atmosphere-drag problem involves a diffusion solution, in a moving reference frame, that is quite lengthy and complex. However, quite good approximate results can be found by use of a simpler dissipation theorem (HIRTH and LOTHE [1968]; HILLERT and SUNDMAN [1976]). The diffusion flux J in a volume element δV is related to the chemical potential gradient $\nabla\overline{G}$ by the Einstein relation:

$$\boldsymbol{J} = -\frac{D_c}{kT}\nabla\overline{G}. \tag{38}$$

The rate of dissipation of free energy in the element is:

$$-\boldsymbol{J}\cdot\nabla\overline{G}\,\delta V = \frac{\boldsymbol{J}\cdot\boldsymbol{J}kT}{D_c}\delta V, \tag{39}$$

with the use of eq. (38). However, for a problem where the driving force for diffusion is the Peach–Koehler force $\boldsymbol{F}$, the total work done on the system per unit time is $\boldsymbol{F}\cdot\boldsymbol{v}$ where $\boldsymbol{v}$ is the dislocation velocity. Thus, the total force is given by:

References: p. 1872.

$$\boldsymbol{F}\cdot\boldsymbol{v} = \frac{kT}{D}\int \frac{\boldsymbol{J}\cdot\boldsymbol{J}}{c}\mathrm{d}V. \tag{40}$$

Diffusion can occur in response to a concentration gradient ∇c or to a potential gradient ∇W. At steady state in the moving reference frame, the total flux is zero,

$$-D\nabla c - (Dc/kT)\nabla W - \boldsymbol{v}(c - c_0) = 0,$$

so the static frame flux $\boldsymbol{J}$ can be written

$$\boldsymbol{J} = -D\nabla c - (Dc/kT)\nabla W = \boldsymbol{v}(c - c_0). \tag{41}$$

The key to the use of the dissipation theorem is that, except for velocities so large that drag would be meaningless anyway, eq. (41) remains approximately valid with the *static* rest values substituted for $\boldsymbol{J}$.

Let us consider a dislocation-type problem with a driving force $\sigma\boldsymbol{b}$ in the x direction opposed by a drag force and with a dislocation velocity $\mathrm{d}x/\mathrm{d}t$. Equation (40) then reduces to

$$\frac{F}{L} = \sigma b = \frac{kT}{\boldsymbol{v}D}\int \frac{\boldsymbol{J}\cdot\boldsymbol{J}}{c}\,\mathrm{d}V. \tag{42}$$

As the dislocation moves through the solution, diffusion occurs to tend to establish the equilibrium concentration of eq. (37), producing the drag force of eq. (42). At low velocities, c is given by eq. (37) and the substitution of eq. (41) into (42) gives

$$\frac{F}{L} = \frac{kTv}{D}\int \frac{(c - c_0)^2}{c}\,\mathrm{d}V. \tag{43}$$

In this regime F/L increases with increasing v. At high velocities $c \approx c_0$, $\nabla c \approx 0$ and one must use the form $\boldsymbol{J} = (-Dc/kT)\,\nabla W$ giving:

$$\frac{F}{L} = \frac{D}{kTv}\int c_0(\nabla W)^2\,\mathrm{d}V. \tag{44}$$

In this regime F/L decreases with increasing v.

The form of the stress–velocity curve is thus that shown in fig. 29. The maximum value $\sigma_c b \cong 17\ c_0\beta$ occurs at a critical velocity $v_c \cong 4\,\mathrm{D}\,kT/\beta$, according to numerical

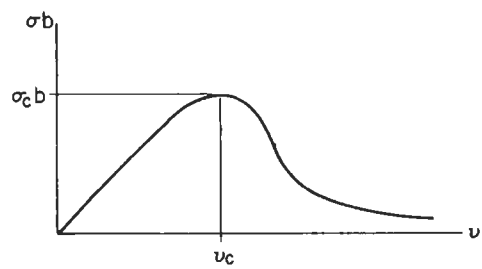

Fig. 29. Drag force–velocity relation for a dislocation with a Cottrell atmosphere of solute atoms.

solutions of several types (TAKEUCHI and ARGON [1979]; FUENTES–SAMANIEGO *et al.* [1984]). In the region of positive slope in fig. 28, stable flow occurs. Large stresses can push the dislocation past the peak to velocities in the negative-slope region where breakaway occurs, with the dislocation accelerating until some other mechanism such as phonon damping controls its motion. At about v_c, breakaway can occur, but if the dislocation should be slowed down, repinning can occur, and the behavior can oscillate from pinned to unpinned motion. There are two possible mechanisms for repinning: bulk diffusion to a temporarily slowed or arrested dislocation (VAN DEN BEUKEL [1975]) or pipe diffusion from a forest dislocation in contact with an arrested dislocation (MULFORD and KOCKS [1979]). As discussed by SCHLIPF [1993], the means of distinguishing between these models are subtle and both remain possible mechanisms on the basis of current analysis.

These phenomena relate to macroscopic flow behavior in tension through the Orowan relation:

$$\dot{\varepsilon} = m\rho b v, \tag{45}$$

where $\dot{\varepsilon}$ is the strain rate, m is a strain resolution factor and ρ is the average mobile dislocation density. At temperatures $T \gg T_c$, D is large and the slope $\mathrm{d}\sigma b/\mathrm{d}v$ is small, eq. (43). Thus, for a given $\dot{\varepsilon}$, a large v can be attained with a small σ to satisfy eq. (45) and ρ will tend to be small. For $T \ll T_c$, D is small, the slope is large, and even the maximum stress σ_c is insufficient to produce a sufficiently large v to satisfy eq. (45). Then breakaway to another high velocity region will occur and again ρ will tend to be small. For $T \approx T_c$, $\sigma \approx \sigma_c$, $v \approx v_c$ will be small compared to the other cases, ρ will tend to be large, and oscillating breakaway–repinning behavior will occur. The breakaway and repinning correspond to macroscopic yield point and serrated flow phenomena. These effects are associated with low ductility which would correlate with the expected larger values of ρ needed to satisfy eq. (45).

Actually, eq. (45) is a very rough approximation and should be replaced by a tensor relation (e.g., see HIRTH and LOTHE [1982], ch. 22) with sums of expressions like eq. (45) over segments of dislocations and the inclusion of segment–segment interaction energies. While simulations of such many-segment arrays are underway (KUBIN [1993]), there is not as yet sufficient data to give an explicit tensor form to replace the approximate eq. (45).

6. *Grain boundaries*

Grain boundaries represent a broad topic (see CHADWICK and SMITH [1976], POND [1989], and GLEITER [1995]), far beyond the scope of the present treatment. There are two aspects, however, that provide a connection between dislocations and other topics in this text. These are grain-boundary energy and grain-boundary dislocations. (See also ch. 9, § 2.2.5).

Consider the simple edge-dislocation tilt boundary in fig. 30. The geometry of fig. 30 shows that the number of incomplete planes terminating to form the length h of tilt boundary is $n = (2h/b)\sin(\theta/2)$. Hence the mean spacing between dislocations in the boundary is:

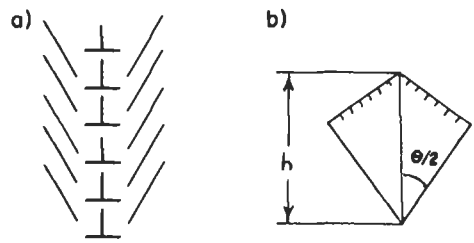

Fig. 30. A simple tilt boundary (a) and its representation in terms of planes ending at the boundary (b).

$$D = \frac{h}{n} = \frac{b}{2\sin(\theta/2)} \cong \frac{b}{\theta}, \tag{46}$$

with the approximate form holding for small angles θ. The tilt array of fig. 30a is a minimum-energy array because the tension and compression fields of adjacent dislocations overlap and tend to cancel out over distances of the order of D according to St. Venant's principle. The energy per dislocation is thus given by eq. (8) with $R \approx D \approx b/\theta$. Since there are $1/D = \theta/b$ dislocations per unit area of boundary, the strain-energy contribution to the boundary free energy per unit area (READ and SHOCKLEY [1950]) is:

$$\gamma = \frac{\mu b}{4\pi(1-\nu)}\theta(A - \ln\theta). \tag{47}$$

The term A contains the core energy, and while there are linear elastic estimates of A in terms of the core cutoff r_0, they are not expected to be very accurate for reasons discussed previously. Indeed, the measurement of A for small θ is a good way to estimate the core energy.

An equation with a similar θ-dependence holds for screw or mixed dislocation boundaries. Experiments by GJOSTEIN [1960] show that eq. (47) is valid up to $\theta \approx 5°$ for copper. Fits of the form of eq. (47) are possible for much larger angles, but the work of Gjostein shows that these do not properly match low-angle experimental data. Interestingly, WOLF [1990] has performed atomistic calculations of grain boundaries for a variety of materials and found that a version of eq. (47) with θ replaced by $\sin\theta$ empirically extends to values of θ much larger than expected (i.e., where a hyperbolic functional dependence is expected, HIRTH and LOTHE [1982]).

Many high-angle grain boundaries can be regarded formally as superposed arrays of dislocations spaced atomic distances apart. This description has little advantage over a purely atomic disregistry view as reflected, for example, by the polyhedral structural unit (ASHBY *et al.* [1978]; POND *et al.* [1978]). However, for high-angle grain boundaries near twin boundaries, the coincidence-lattice, DSC lattice model of BOLLMANN [1970] is appropriate. These are illustrated for a first-order {111}–⟨112⟩ twin in fcc in fig. 31a. The DSC is essentially the coarsest lattice containing all lattice sites from both constituent crystals of the twin. If a dislocation passes through the twin boundary, continuity of Burgers vector (§ 1) requires that a grain-boundary dislocation (GBD) is left in the

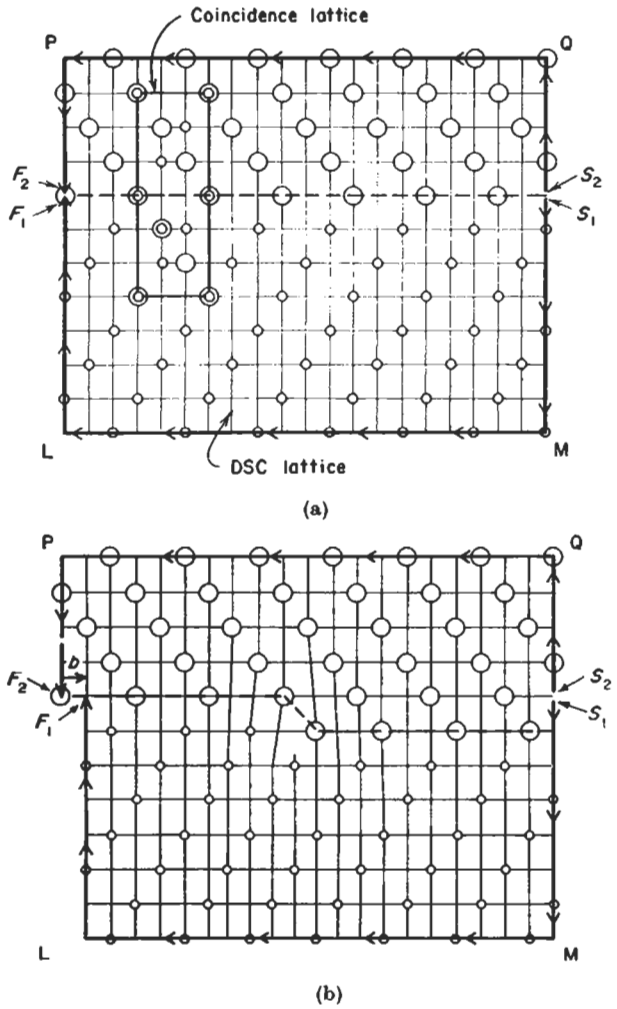

Fig. 31. View parallel to {111} of a first-order {111}–⟨112⟩ twin in fcc showing the coincidence lattice and the DSC lattice (a). This view provides a reference lattice for the Burgers circuit in (b) which also shows the GBD in the DSC lattice. For faulted crystals, the Burgers circuit must start and end on the fault plane.

boundary. As illustrated in fig. 31b, these GBDs have Burgers vectors corresponding to lattice vectors of the DSC lattice, small compared to those of perfect lattice dislocations.

While the DSC model is useful in some cases, in others, such as hcp twins, there is no applicable DSC lattice. In such cases, the symmetry theory of POND [1989], describing the two lattices that meet at the boundary as superposed to form a dichromatic complex, predicts and describes possible interface defects, including GBDs, in terms of perfect vectors of the dichromatic complex. Even for irrational boundaries or interfaces, a series of defects belonging to nearby orientations can be used to describe the boundary (POND and HIRTH [1994]).

References: p. 1872.

Twin boundaries of relatively low order are expected also to correspond to low-energy configurations or cusps on a grain-boundary energy-orientation plot (CHADWICK and SMITH [1976]). Near these cusp orientations small deviations are accomplished by the superposition of small-angle boundaries composed of GBDs. Thus, the percentage of boundaries with dislocation structure is greatly increased if one includes the GBDs. Extensive verifications by means of observations of such GBDs in grain boundaries have been made with the use of electron transmission microscopy, e.g., see LIU and BALLUFFI [1985].

References

ALEXANDER, H. and H. TEICHLER, 1991, in: Materials Science and Technology, vol. 4, Electronic Structure and Properties of Semiconductors, ed. W. Schroter (VCH, Weinheim) p. 248.

ALSHITS, V. I. and V. L. INDENBOM, 1975, Sov. Phys. Usp. **18**, 1.

ALTINTAS, S. and J. W. MORRIS, Jr., 1986, Acta Metall. **34**, 810, 809.

AMELINCKX, S., 1979, in: Dislocations in Solids, ed. F.R.N. Nabarro (North-Holland, Amsterdam) vol. 2, p. 67.

APPEL, F., 1989, Phys. Stat. Sol. **116a**, 153.

ARGON, A., 1995, ch. 21, this volume.

ASHBY, M. F., 1964, Z. Metallk. **55**, 5.

ASHBY, M. F., F. SPAEPEN and S. WILLIAMS, 1978, Acta Metall. **26**, 1647.

BAIRD, J. D., 1971, Met. Rev. **16**, 1.

BALLUFFI, R. W. and A. V. GRANATO, 1979, in: Dislocations in Solids, ed. F.R.N. Nabarro (North-Holland, Amsterdam) vol. 4, p. 102.

BALUC, N., H. P. KARNTHALER and M. J. MILLS, 1991, Phil. Mag. **64A**, 137.

BASINSKI, S. J. and Z. S. BASINSKI, 1979, in: Dislocations in Solids, ed. F.R.N. Nabarro (North Holland, Amsterdam) vol. 4, p. 261.

BASKES, M. I., R. G. HOAGLAND and A. NEEDLEMAN, 1992, Mater. Sci. Eng. **A159**, 1.

BENOIT, W., M. BUJARD and G. GREMAUD, 1987, Phys. Stat. Sol. **104a**, 427.

VAN DEN BEUKEL, A., 1975, Phys. Stat. Sol. **30a**, 197.

BOLLMANN, W., 1970, Crystal Defects and Crystalline Interfaces (Springer, Berlin).

BULLOUGH, R. and V. K. TEWARY, 1979, in: Dislocations in Solids, ed. F.R.N. Nabarro (North-Holland, Amsterdam) vol. 2, p. 1.

CAILLARD, D., N. CLEMENT, A. COURET, P. LOURS and A. COUJOU, 1988, Phil. Mag. Lett. **58**, 263.

CARLSSON, A. E., 1990, Solid State Phys. **43**, 1.

CARTER, C. B., 1979, Phys. Stat. Sol. **54a**, 395.

CHADWICK, G. A. and D. A. SMITH, 1976, Grain Boundary Structure and Properties (Academic, New York).

CHERNS, D., P. B. HIRSCH and H. SAKA, 1980, Proc. Roy. Soc. (London) **371A**, 213.

CHERNS, D. and G. FEUILLET, 1985, Phil. Mag. **51A**, 661.

CHIANG, S. W., C. B. CARTER and D. L. KOHLSTEDT, 1980, Scripta Metall. **14**, 803.

CHOU, Y. T. and J. C. M. LI, 1969, in: Mathematical Theory of Dislocations, ed. T. Mura (Am. Soc. Mech. Eng., New York) p. 116.

DE COOMAN, B. C. and C. B. CARTER, 1989, Acta Metall. **37**, 2765.

COTTRELL, A. H., 1953, Dislocations and Plastic Flow in Crystals (Clarendon Press, Oxford), p. 133.

COURET, A., Y. Q. SUN and P. B. HIRSCH, 1993, Phil. Mag. **67A**, 29.

DEVINCRE, B. and M. CONDAT, 1992, Acta Metall. Mater. **40**, 2629.

DIMIDUK, D. M., 1991, J. Phys. III, **1**, 1025.

DIMIDUK, D. M., A. W. THOMPSON and J. W. WILLIAMS, 1993, Phil. Mag. **67A**, 675.

DOBROMYSLOV, A. V., G. V. DOLGIKH and I. A. PERETURINA, 1984, Phys. Stat. Sol. **87a**, 559.

DOUIN, P., P. BEAUCHAMP and P. VEYSSIERE, 1988, Phil. Mag. **58A**, 923.

DREGIA, S. A. and J. P. HIRTH, 1991, J. Appl. Phys. **69**, 2169.

DUESBERY, M.S., 1983, Acta Metall. **31**, 1747, 1759.
DUESBERY, M.S., B. JOOS and D.J. MICHEL, 1991, Phys. Rev. **B43**, 5143.
DUESBERY, M.S. and K. SADANANDA, 1991, Phil. Mag. **63A**, 535.
DUESBERY, M. S., N.P. LOUAT and K. SADANANDA, 1992, Phil. Mag. **65A**, 311.
ELKAJBAJI, M., H.O.K. KIRCHNER and J. THIBAULT-DESSEAUX, 1988, Phil. Mag. **57A**, 631.
EMBURY, J.D., 1971, in: Strengthening Methods in Crystals, eds. A. Kelly and R.B. Nicholson, (Applied Science Publishers, London) p. 331.
ESHELBY, J.D., 1953, J. Appl. Phys. **24**, 176.
EYKHOLT, R., S.A. TRUGMAN and D.J. SROLOVITZ, 1989, J. Appl. Phys. **65**, 4198.
FANTOZZI, G., C. ESNOUF, W. BENOIT and I.G. RITCHIE, 1982, Prog. Mater. Sci. **27**, 311.
FILLIPOV, A.P., G. N. GAIDUKOV and S.K. MAKSIMOV, 1985, Phys. Stat. Sol. **90a**, 215.
FLEISCHER, R.L., 1964, in: Strengthening of Metals, ed. D. Peckner (Reinhold, New York) p. 93.
FLINN, P., 1960, Trans. TMS-AIME **218**, 145.
FRANCIOSI, P., 1983, Acta Metall. **31**, 1331.
FRANCIOSI, P., 1985, Acta Metall. **33**, 1601.
FRIEDEL, J., 1956, Les Dislocations (Gauthier-Villars, Paris) p. 123.
FUENTES-SAMANIEGO, R., R. GASCA-NERI and J.P. HIRTH, 1984, Phil. Mag. **49A**, 31.
GALLAGHER, P.C.J., 1970, Metallurg. Trans. **1**, 2429.
GAO, F. and D.J. BACON, 1992, Phil. Mag. **66A**, 839.
GERTHSEN, D. and C.B. CARTER, 1993, Phys. Stat. Sol. **136a**, 29.
GJOSTEIN, N.A., 1960, Acta Metall. **8**, 263.
GLEITER, H., 1995, ch. 9, this volume.
GRANATO, A.V. and K. LÜCKE, 1956, J. Appl. Phys. **27**, 583.
GREENBERG, B.A., M.A. IVANOV, Yu.N. GORNOSTYREV and L.E. KARKINA, 1978, Phys. Stat. Sol. **49a**, 517.
HAASEN, P., 1995, ch. 23, this volume.
HANSEN, N. and D. KUHLMANN-WILSDORF, 1986, Mater. Sci. Eng. **81**, 141.
HILLERT, M. and B. SUNDMAN, 1976, Acta Metall. **24**, 731.
HIRSCH, P.B., 1962, Phil. Mag. **7**, 67.
HIRSCH, P.B., 1992, Phil. Mag. **65A**, 569.
HIRSCH, P.B., 1981, in: Defects in Semiconductors, eds. J. Narayan and T.Y. Tan (North-Holland, Amsterdam) p. 257.
HIRSCH, P.B. and S.G. ROBERTS, 1991, Phil. Mag. **64A**, 55.
HIRTH, J.P., 1961, J. Appl. Phys. **31**, 700.
HIRTH, J.P., 1972, Metallurg. Trans. **3**, 3047.
HIRTH, J.P., 1976, Scripta Metall. **10**, 755.
HIRTH, J.P. and J. LOTHE, 1982, Theory of Dislocations, 2nd Ed. (Wiley, New York); 1992, Krieger (Melbourne, Florida).
HIRTH, J.P., T. JØSSANG and J. LOTHE, 1966, J. Appl. Phys. **37**, 110.
HOAGLAND, R.G., 1994, J. Mater. Res., **9**, 1805.
HULL, R., J.C. BEAN, D. BAHNCK, L.J. PETICOLAS, Jr., K.T. SHORT and F.C. UNTERWALD, 1991, J. Appl. Phys. **70**, 2052.
INDENBOM, V.L., B.V. PETUKHOV and J. LOTHE, 1992, in: Elastic Strain Fields and Dislocation Mobility, eds. V.L. Indenbom and J. Lothe (North-Holland, Amterdam) p. 489.
IUNIN, Yu.L., V.I. NIKITENKO, V.I. ORLOV and B.Ya. FARBER, 1991, Sov. Phys. JETP **73**, 1079.
KAMAT, S.V. and J.P. HIRTH, 1990, J. Appl. Phys. **67**, 6844.
KOCKS, U.F., A.S. ARGON and M.F. ASHBY, 1975, Prog. Mater. Sci. **19**, 1.
KORNER, A., H. SCHMID and F. PRINZ, 1979, Phys. Stat. Sol. **51a**, 613.
KUBIN, L.P., 1993, in: Materials Science and Technology, eds. R.W. Cahn, P. Haasen and E.J. Kramer (VCH, Weinheim) p. 137.
KUBIN, L.P., Y. ESTRIN and G. CANOVA, 1990, in: Patterns, Defects and Material Instabilities, eds. D. Walgraef and N. M. Ghoniem (Kluwer, Dordrecht) p. 277.
KUHLMANN-WILSDORF, D., 1966, in: Work Hardening, eds. J.P. Hirth and J. Weertman (Gordon and Breach, New York) p. 97.

KUHLMANN–WILSDORF, D., 1989, Mater. Sci. Eng. **A113**, 1.
KUMAR, A. M. and J. P. HIRTH, 1992, Phil. Mag. **65A**, 841.
LABUSCH, R., 1972, Acta Metall. **20**, 917.
LAVRENTEV, F. F., 1980, Mater. Sci. Eng. **46**, 191.
LIU, J. S. and R. W. BALLUFFI, Phil. Mag. **52A**, 713.
LOHNE, O., 1974, Phys. Stat. Sol. (a) **25**, 209.
LOTHE, J., 1967, Phys. Norvegica **2**, 153.
LOTHE, J. and J. P. HIRTH, 1959, Phys. Rev. **115**, 543.
LOUCHET, F. and L. P. KUBIN, 1975, Acta Metall. **23**, 17; Scripta Metall. **9**, 911.
LOUCHET, F. and J. THIBAULT, 1989, Struct. Prop. Dislocations in Semiconductors (Inst. Phys., London) p.47.
MARKLUND S. and W. YONG–LIANG, 1992, Solid State Comm. **82**, 137.
MESSERSCHMIDT, U., J. SHU and H. SCHMID, 1985, Phil. Mag. **A51**, 781.
MILLS, M. J. and D. C. CHRZAN, 1992, Acta Metall. Mater. **40**, 3051.
MOTT, N. F. and F. R. N. NABARRO, 1948, in: Report on Strength of Solids (Physical Society, London) p. 1.
MULFORD, R. A. and U. F. KOCKS, 1979, Acta Metall. **27**, 1125.
MUSKHELISHVILI, N. I., 1975, Mathematical Theory of Elasticity, ch. 19 (Nordhoff, Leyden).
NABARRO, F. R. N., 1947, Proc. Phys. Soc. (London) **59**, 256.
NABARRO, F. R. N., 1952, Adv. Phys. **1**, 269.
NABARRO, F. R. N., 1967, Theory of Crystal Dislocations (Oxford Univ. Press, Oxford).
NABARRO, F. R. N., 1986, in Strength of Metals and Alloys 7, eds. H. J. McQueen et al. (Pergamon, Oxford) p. 1667.
NANDEDKAR, A. S. and J. NARAYAN, 1990, Phil. Mag. **A61**, 873.
NEUHAUSER, H., 1990, in: Patterns, Defects and Material Instabilities, eds. D. Walgraef and N.M. Ghoniem (Kluwer, Dordrecht) p. 241.
OROWAN, E., 1934, Z. Phys. **89**, 605 and 634.
PAIDAR, V., D. P. POPE and V. VITEK, 1984, Acta Metall. **32**, 435.
PEACH, M. O. and J. S. KOEHLER, 1950, Phys. Rev. **80**, 436.
PEIERLS, R. E., 1940, Proc. Phys. Soc. (London) **52**, 23.
PICHAUD, B., P. JEAN and F. MINORI, 1986, Phil. Mag. **54A**, 54.
POLANYI, M., 1934, Z. Phys. **89**, 660.
POND, R. C., 1989, in: Dislocations in Solids, ed. F.R.N. Nabarro (Elsevier, Amsterdam) vol. 8, p. 1.
POND, R. C. and J. P. HIRTH, 1994, Solid State Phys. **47**, 287.
POND, R. C., D. A. SMITH and V. VITEK, 1978, Scripta Metall. **12**, 699.
PRINZ, F., A. KORNER and H. O. K. KIRCHNER, 1983, Phil. Mag. **47A**, 441.
PULS, M. P., 1981, in: Dislocation Modeling of Physical Systems, eds. M.F. Ashby et al. (Pergamon, Oxford) p. 249.
QUENET, B., G. GRENAUD, M. BUJAUD and W. BENOIT, 1987, J. Phys., Colloq. C8 **48**, 125.
READ, W. T. and W. SHOCKLEY, 1950, Phys. Rev. **78**, 275.
RICE, J. R., 1992, J. Mech. Phys. Sol. **40**, 239.
RICE, J. R. and R. THOMSON, 1974, Phil Mag. **29**, 73.
SAADA, G., 1960, Acta Metall. **8**, 841.
SAKA, H., S. SUGAWARA, T. IMURA and J. WATANABE, 1985, Phil. Mag. **52A**, L7.
SCATTERGOOD, R. O. and D. J. BACON, 1975, Phil. Mag. **31**, 179.
SCHLIPF, J., 1993, Scripta Metall. Mater. **29**, 287.
SCHMID, H. and H. O. K. KIRCHNER, 1988, Phil. Mag. **58A**, 905.
SCHOECK, G. and W. PUSCHL, 1991, Phil. Mag. **64A**, 931.
SEEGER, A., 1981, Z. Metall. **72**, 369.
SEEGER, A. and P. SCHILLER, 1962, Acta Met. **10**, 348.
SEEGER, A. and C. WÜTHRICH, 1976, Nuovo Cim. **33B**, 38.
SEIDMAN, D. N. and R. W. BALLUFFI, 1966, Phys. Stat. Sol. **17**, 531.
SHAIBANI, S. J. and P. M. HAZZLEDINE, 1981, Phil. Mag. **44A**, 657.
SMITH, E., 1968, Proc. Roy. Soc. (London) **A305**, 387.
SONDHI, S., R. G. HOAGLAND and J. P. HIRTH, 1992, Mater. Sci. Eng. **A152**, 103.

SUN, Y.Q. and P.M. HAZZLEDINE, 1988, Phil. Mag. **58A**, 683.
SUN, Y.Q., M.A. CRIMP and P.M. HAZZLEDINE, 1991a, Phil. Mag. **64A**, 223.
SUN, Y.Q., M.A. Crimp, P.M. HAZZLEDINE and A. COURET, 1991b, Phil. Mag. **64A**, 311.
SUZUKI, S. and A. SEEGER, 1992, Phys. Stat. Sol. **131a**, 727.
TAKASUGI, T. and M. YOSHIDA, 1993, Phil. Mag. **67A**, 447.
TAKEUCHI, S. and A.S. ARGON, 1979, Phil. Mag. **40**, 65.
TAYLOR, G.I., 1934, Proc. Roy. Soc. (London) **A145**, 362.
TEUTONICO, L.J., 1964, Phil. Mag. **10**, 401.
THIBAULT–DESSEAUX, J., H.O.K. KIRCHNER and J.L. PUTAUX, 1989, Phil. Mag. **60A**, 385.
THOMPSON, A.W., 1977, Work-Hardening in Tension and Fatigue (Met. Soc. AIME, Warrendale, PA).
THOMPSON, N., 1953, Proc. Phys. Soc. (London) **66B**, 481.
THOMSON, R., S.J. ZHOU, A.E. CARLSSON and V.K. TEWARY, 1993, Phys. Rev. **B47**, 7710.
TIMPE, A., 1905, Z. Math. Phys. **52**, 348.
VESELY, D., 1972, Scripta Metall. **6**, 753.
VEYSSIERE, P., 1989, in: High Temperature Ordered Intermetallic Alloys III, eds. C.C. Koch et al. (Materials Research Society Symposium Proceedings, Pittsburgh, PA) **133**, p. 175.
VIDOZ, A.E. and L.M. BROWN, 1972, Phil. Mag. **7**, 1167.
VITEK, V., 1974, Cryst. Latt. Defects **5**, 1.
VOLTERRA, V., 1907, Ann. Ecole Norm. Super. **24**, 400.
WASSERBACH, W., 1985, Phil. Mag. **51A**, 619.
WILKENS, M., 1969, Acta Metall. **17**, 1155.
DEWIT, G. and J.S. KOEHLER, 1959, Phys. Rev. **116**, 1113.
WOLF, D., 1990, Acta Metall. **38**, 781, 791.
WOLLENBERGER, H.J., 1995, this volume, ch. 18.
WÜTHRICH, C., 1977, Phil. Mag. **35**, 337.
YONENAGA, I. and K. SUMINO, 1992, J. Appl. Phys. **71**, 4249; 1993, **73**, 1681.

Further reading

Amelinckx, S., 1964, Solid State Physics, Suppl. 6.
Friedel, J., 1964, Dislocations (Addison-Wesley, Reading, MA).
Hirth, J.P., and J. Lothe, 1992, Theory of Dislocations (Krieger, Melbourne, FL).
Nabarro, F.R.N., ed., 1979, Dislocations in Solids, vols. 1–8 (North-Holland, Amsterdam).
Rabier, J., A. George, Y. Brechet and L. Kubin, 1993, Dislocations 93, vol. 35–36, Solid State Phenomena (Scitec, Zug, Switserland).
Read, W.T., Jr., 1960, Dislocations in Crystals (McGraw-Hill, NY).

CHAPTER 21

MECHANICAL PROPERTIES OF SINGLE-PHASE CRYSTALLINE MEDIA: DEFORMATION AT LOW TEMPERATURES

A. S. ARGON

Massachusetts Institute of Technology,
Department of Mechanical Engineering,
Cambridge, MA, U.S.A.

R. W. Cahn and P. Haasen†, eds.
Physical Metallurgy; fourth, revised and enhanced edition

1. Overview

In this chapter we discuss the deformation of single phase crystalline solids both from the point of view of actual mechanisms and to some extent from the point of view as continua. In the discussions of the precipitate particle resistance we will by necessity consider solids with a light concentration of heterogeneities. Outside of this natural excursion, however, we will not consider the broad subject of mechanical properties of composites. Moreover, our coverage will concentrate on mechanistic explanations of phenomena and will not develop any operational aspects in the form of deformation boundary value problems. References to such developments, however, will be given throughout the chapter wherever they are considered to be particularly relevant.

The subject of primary concern in this chapter and the closely allied chapter 22 is the modes of response of a crystalline solid to applied stresses. In the present chapter we develop the responses that occur in the absence of diffusion. The complementary discussion of deformation processes in the presence of diffusion where that controls either the recovery processes which govern the deformation rate, or enters directly in the production of strain by material transport is given in chapter 22. Deformation of amorphous solids will be considered only very briefly in section 11 where their mechanisms are contrasted with the mechanisms of strain production in crystalline solids.

We will use widely accepted terminology for phenomena of the different constituitive connections between strain, strain rate, temperature and stress. We call the time independent, completely reversible, linear connection between stress and strain components *elasticity*. All other forms of time and deformation rate dependent connections are collectively called *inelastic*. Among *inelastic*, however, we distinguish a number of different patterns of behavior. We call *anelastic* a linear but temperature and time dependent, completely reversible connection between stress and strain, arising from topologically isolated thermally activated shear relaxations in an elastic background structure. The formal theory of linear viscoelasticity, which we will not discuss, is a direct outcome of this connection. We call *visco-plastic* the temperature and moderately deformation-rate dependent, non-linear, and usually irreversible, connection between stress and strain. It is more meaningful to consider this as a constitutive connection giving the dependence of the deformation rate on temperature, stress and the defect microstructure. We will consider two limiting forms of this behavior: first the high temperature and low stress limit of linear, liquid-like, *viscous* flow, and second, the low temperature, high stress and nearly deformation rate independent form of *plastic* flow. The latter will be of primary interest. At elevated temperatures where the deformation-rate controlling defect microstructure can decompose by diffusion assisted processes, the visco-plastic connection becomes much more strongly deformation-rate dependent. This behavior we will refer to as *creep* and delay its discussion for chapter 22.

In the discussion of these phenomena we emphasize primarily the mechanistic aspects of the processes at a moderately advanced level but also show the operational forms in which these constitutive connections become useful in the solution of actual macro-scale technological problems.

2. *Kinematics of deformation*

2.1. Elasticity as an affine transformation

Hookean linear elasticity can be most generally characterized as a nearly instantaneous connection between any element of the symmetrical strain tensor and all elements of the symmetrical stress tensor, or vice-versa. In the first case of the strain-stress connection, the connecting tensor is known as the *compliance* tensor, while in the second case the connecting tensor is called the *elastic constant* tensor. These tensor connections are discussed in many excellent references (NYE [1957]; HIRTH and LOTHE [1982]).

For our purpose it is important to note that the source of the elastic response is at the atomic level and is a direct measure of the interatomic resistance to separation or shear. In a homogeneous crystal subjected to a homogeneous increment of stress, all atoms experience the same relative displacements, resulting in a homogenous increment of strain in the entire crystal, down to the scale of atoms. This can be viewed as an *affine transformation*, and the "material point" where the connection is considered can be taken down to the atomic scale where the material ceases to be a continuum. This property of elastic response is fundamentally different from all inelastic deformations which are inhomogenous over much coarser scales.

We note that the elastic response of a solid manifests itself in two physically distinct forms: *dilatation* and *shear*. In an isotropic idealization of the elastic connections the dilatation θ is proportional to the mean normal stress (negative pressure), σ_m, through the bulk modulus K, and the shear strain γ is proportional to the shear stress σ through the shear modulus μ, i.e.,

$$\theta = \frac{\sigma_m}{K} \tag{1}$$

$$\gamma = \frac{\sigma}{\mu} \tag{2}$$

where

$$\sigma_m = \tfrac{1}{3}\left(\sigma_{11} + \sigma_{22} + \sigma_{33}\right) = \tfrac{1}{3}\,Tr(\boldsymbol{\sigma}); \tag{3}$$

$$\sigma = \text{applied shear stress} \Rightarrow \left[\tfrac{1}{2}\,Tr\left(\boldsymbol{\sigma} - \sigma_m \boldsymbol{I}\right)^2\right]^{\frac{1}{2}}; \tag{4}$$

$$\theta = \varepsilon_{11} + \varepsilon_{22} + \varepsilon_{33} = Tr(\boldsymbol{\varepsilon}); \tag{5}$$

$$\gamma = \text{tangential shear strain} \Rightarrow \left[2\,Tr\left(\boldsymbol{\varepsilon} - \tfrac{1}{3}\,\theta \boldsymbol{I}\right)^2\right]^{\frac{1}{2}}, \tag{6}$$

where the $\Rightarrow$ indicates the 3-dimensional interpretation (see also sect. 9.1). In the above expressions $\boldsymbol{\sigma}$, $\boldsymbol{\varepsilon}$, and $\boldsymbol{I}$ are the stress tensor, the strain tensor, and the identity tensor respectively; σ_{11} etc., and ε_{11} etc., are the normal stress and strain components, and *Tr* stands for "trace". The RHS expressions in Eqns. (4) and (6) define the two invariants

of the stress and strain tensors respectively, which provide the basis of the physically distinct nature of the dilatational and shear responses of a solid.

The well-known Young's modulus E, and Poisson's ratio, ν, giving the uniaxial tensile stress/strain connection and the fractional lateral contraction, measure a combination of bulk (dilation) and shear responses. Therefore, they are less desirable forms of representation. For an isotropic solid they are related to the bulk modulus and shear modulus by the expressions:

$$E = \frac{9K}{1+\frac{3K}{\mu}} \therefore \quad \nu = \frac{1-\frac{2\mu}{3K}}{2+\frac{2\mu}{3K}}. \tag{7a, b}$$

The elastic connections introduced above are defined always at zero strain. As strains increase in magnitude, the connections become progressively non-linear and ultimately lead to volumetric decohesion or ideal shear. The self similar bulk decohesion obeys a remarkably simple scaling relationship arising from a Universal Binding Energy Relation that has been demonstrated by ROSE *et al.* [1983] which can be given for uniaxial tension simply as:

$$\sigma_{11} = E_0 \varepsilon_{11} \exp(-\alpha \varepsilon_{11}) \tag{8}$$

where E_0 is the uniaxial, zero strain, Young's modulus (or is $(1-\nu)E_0/(1+\nu)(1-2\nu)$ for the case of only uniaxial strain deformation), and α is the reciprocal of the ideal uniaxial decohesion strain. From here it is clear that the strain dependent decrease of the Young's modulus can be obtained readily as:

$$E(\varepsilon) = E_0(1 - \alpha \varepsilon_{11}) \exp(-\alpha \varepsilon_{11}). \tag{9}$$

The corresponding ideal shear response at large shear strains, is less well understood because of shear induced break-down of symmetry. It is a subject under active study.

The fundamental atomic level bases of the elastic connections and temperature dependence of the elastic constants have been widely discussed. While first principles connections are still rare, these are becoming better understood (see, e.g., NASTER and WILLAIME [1995]). Reliable experimental information on many pure solids and binary solid solutions for both single crystals and polycrystal averages are available in the literature (see, e.g., SIMMONS and WANG [1971]).

While dilatational and shear responses of an elastic solid are mechanistically distinct, they are not uncoupled. The presence of a pressure results in the stiffening of the shear response and the presence of a shear stress alters crystal symmetry, and, therefore, affects the bulk modulus. (For an operationally useful treatment see RICE *et al.* [1992]).

2.2. Kinematics of inelastic deformation

2.2.1. Plasticity resulting from transformations

Inelastic deformation cannot be exhibited by a perfect crystal. It requires for its local development a defective solid state which permits the various forms of local strain — producing configurations to take shape. In the broadest sense, all inelastic deformation

can be viewed as arising from a set of shear transformations, occurring in small volume elements, stimulated by the prevailing local stress state and emanating from the variety of crystal or structural defects. Thus, inelastic deformation is always inhomogenous on the mechanism scale and must be defined as an average over a volume element that must contain enough elementary transformations to result in an acceptably smooth process. The smallest such volume element above which the inelastic response can be considered smooth will be labeled as a *representative volume element* (RVE). It represents the scale of the so-called "material point" in any continuum field description of the process.

We consider first the kinematic aspects of inelastic deformation, separate from their energetic aspects, or the driving forces that cause them to develop. While such separation is instructive in clarifying the kinematics, it is not realistic in understanding the overall nature of the development of shear relaxations. Therefore, caution is necessary.

Consider, as shown in fig. 1a, a shear transformation in a small volume element Ω_f, occurring inside the large volume V. We define by ε^T the unconstrained transformation strain (tensor) as it would develop freely outside the body. When constrained by the elastic surroundings the transformation strain of the interior is only ε^c where all distant stresses are relaxed. If the volume element Ω_f is an ellipsoid and the exterior volume V is very large (infinite) the inner field is homogenous (ESHELBY [1957]). When the outer body is of finite size the effect of the transformed volume on the outside is to set up a compensating effective homogenous "image strain", in the same sense as the transformation strain inside Ω_f (ESHELBY [1954]). Thus, if a total volume fraction c of material has undergone the same transformation then the total volume average strain in the large body as a whole becomes (NABARRO [1940]),*

$$\varepsilon = c\varepsilon^T. \tag{10}$$

If there are m different types of transformations, as depicted in fig. 1, each producing separately unconstrained transformation strains ε_m^T and having volume fractions c_m, then collectively they produce an overall volume average strain,

$$\varepsilon = \sum_m c_m \varepsilon_m^T, \tag{10a}$$

provided that $\sum_m c_m$ remains relatively small so that mutual interactions between volume elements Ω_{fm} can be neglected, and all transformed volume elements have the same mechanical properties.

2.2.2. Plasticity resulting from dislocation glide

When the inelastic deformation is produced by a uniform shear $\delta\gamma$ in lenticular volume elements with principal planes, normal to a unit normal vector $\boldsymbol{n}$, and shear

* In this, and subsequent sections of this chapter the strains that are being referred to are all inelastic strains, or plastic strains. When they are experienced they occur in an elastically strained background. Thus, they should be conceived of as the residual strains that remain after the deformed body is unstressed.

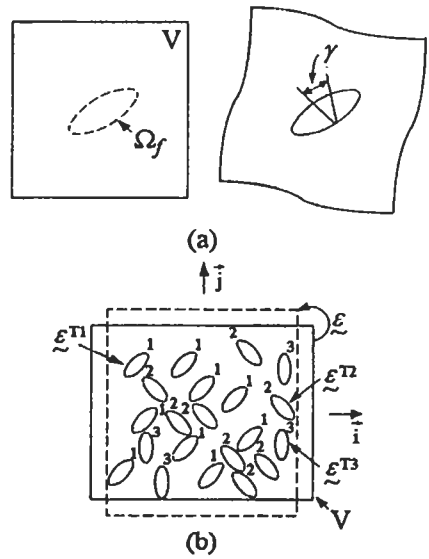

Fig. 1. Inelastic strain production: a) shear transformation producing a free standing transformation shear strain $\varepsilon^T = \gamma$ in a volume Ω_f of a large sample of volume V; b) average strain ε produced in a volume V as a result of three sets of transformations ε^{Tm} (m = 1,2,3).

direction parallel to $\boldsymbol{d}$, the average inelastic strain increment in the sample is still the volume average of all inelastic shears and is given by

$$\begin{aligned}\delta\varepsilon_{ij}^{P} &= \left(\frac{h\delta\gamma}{V}\right)\int_A \tfrac{1}{2}\left(d_i n_j + d_j n_i\right)dA \\ &= c\delta\gamma\,\tfrac{1}{2}\left(d_i n_j + d_j n_i\right)\end{aligned} \tag{11}$$

where h is the average thickness of the "lentils", d_i and n_j are the components of the unit vectors $\boldsymbol{d}$ and $\boldsymbol{n}$ in the direction of the macro axes i and j, the area integral is over the principal plane areas of the entire set of sheared lentils and c is the total volume fraction of sheared lentils.

Clearly, if the shear is produced by a set of m separate transformations having distinct plane normals $\boldsymbol{n}^m$, shear directions $\boldsymbol{d}^m$ and shear increments $\delta\gamma_m$, the overall increment of plastic strain in the macro sample is

$$\delta\varepsilon_{ij}^{P} = \sum_m c_m \delta\gamma_m \alpha_{ij}^m \tag{12a}$$

where

$$\alpha_{ij}^m = \tfrac{1}{2}\left(d_i^m n_j^m + d_j^m n_i^m\right) \tag{12b}$$

is the so-called *Schmid strain resolution tensor*. Finally, when the shears are due to individual translations of dislocation loops, or sweeping of dislocation segments of

portions of slip planes having unit normal vectors $\boldsymbol{n}$ with Burgers vectors in the direction $\boldsymbol{d}$ and having magnitudes b, the local shears degenerate into discontinuous translations and the strain increments, hereafter to be called *plastic*, of a set of m separate slip systems become, as a special case of eqs. (12a) and (12b),

$$\delta\varepsilon_{ij}^{P} = \sum_{m} b_m \frac{\alpha_{ij}^{m}\delta a_m}{V}. \tag{13}$$

Here α_{ij}^{m} is of the same form as given in eq. (12b) and the swept-out area δa_m is for the entire length of dislocation line of the specific set m under consideration.

Shear operations of this type, depicted in fig. 2, and resulting from relative translation of parts of the crystal over each other in the direction of the Burgers vector, are called *slip*.*

Often, single-slip systems are of interest in mechanistic considerations, for which eq. (13) simplifies to

$$\delta\varepsilon_{ij}^{P} = \left(\frac{b\delta a}{V}\right)\alpha_{ij} \tag{14}$$

where δa is again the entire area increment swept by mobile segments of dislocations on the slip planes oriented in relation to the external axes by α_{ij} as depicted in fig. 2. When this motion can be well characterized as an average displacement δx of a total segment length Λ of dislocations,

$$\delta\varepsilon_{ij}^{P} = \left(\frac{b\Lambda\delta x}{V}\right)\alpha_{ij} = b\rho_M \delta x \alpha_{ij} \tag{15}$$

where the final form ρ_M $(= \frac{\Lambda}{V})$ has been introduced as the mobile dislocation (segment) density, that is, the mobile line length per unit volume.

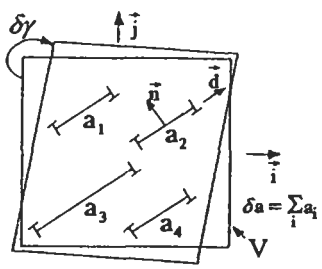

Fig. 2. A shear strain increment $\delta\gamma$ in a volume V resulting from a collection of translations (slip) over a total area δa with unit normal vectors parallel to $\boldsymbol{n}$ and in the direction $\boldsymbol{d}$ lying in the planes.

* We will use *slip* to refer to an accomplished translation and *glide* to refer to the conservative motion of dislocations.

Finally, whenever time enters into the motion of dislocations to establish a kinetic basis of the process, eq. (15) readily transforms into a rate expression as

$$\dot{\varepsilon}_{ij}^{P} = b\rho_M \dot{x}\alpha_{ij}. \tag{16}$$

Equation (16) relates the glide rate, based on the dislocation velocities $\dot{x}$ to the external strain rate, and constitutes a kinematic expression based on dislocation mobilities.

In certain instances the kinematics of the strain rate needs to be viewed differently where a characteristic incubation (activation) time t_a must elapse to form an *embryo*. This then produces an increment of volume fraction, δc, of the transformation ε^T, or results in an increment of area δa of translation of dislocation loops, within a time much shorter that t_a. This constitutes a nucleation controlled deformation process and gives rise to a plastic strain rate of

$$\dot{\varepsilon}^{P} = \frac{\delta c}{t_a}\varepsilon^{T} \tag{17a}$$

due to transformations, or

$$\dot{\varepsilon}_{ij}^{P} = b\frac{\delta a}{t_a}\frac{1}{V}\alpha_{ij}, \tag{17b}$$

due to slip.

It has applications to phenomena such as twinning, martensitic transformations, or in the case of dislocation glide to problems of thermally overcoming specific slip plane obstacles.

2.3. Lattice rotations accompanying slip

Slip results in lattice rotations that are instrumental in the development of deformation textures which we will discuss briefly in section 8.

The concepts are illustrated schematically in fig. 3. Figure 3a illustrates a reference

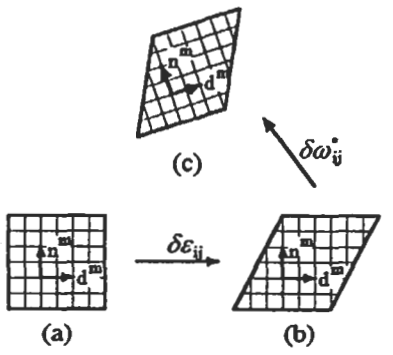

Fig. 3. Kinematics of the various components of crystallographic slip and rotation: a) initial undeformed lattice, b) plastically sheared lattice, c) plastically sheared and rigidly rotated lattice.

volume element along with the unit vectors $\boldsymbol{n}^m$ and $\boldsymbol{d}^m$ representing the slip plane normal and the slip direction of the system m. Without loss of generality, the instantaneous configuration can be taken as the external shape reference. At fixed lattice orientation an increment of crystallographic shear $\delta\gamma^m$ on the system m generates an increment of plastic strain $\delta\varepsilon_{ij}^p$ and an increment of lattice rotation $\delta\omega_{ij}^p$, provided by the mth system, is given by:

$$\delta\varepsilon_{ij}^p = \delta\gamma^m \alpha_{ij}^m \qquad \delta\omega_{ij}^p = \delta\gamma^m \beta_{ij}^m \tag{18a, b}$$

where

$$\beta_{ij}^m = \tfrac{1}{2}\left(d_i^m n_j^m - d_j^m n_i^m\right) \tag{19}$$

is the skew symmetric counterpart to the Schmid strain resolution tensor. The resulting intermediate deformed configuration of the body is depicted in fig. 3b. It must now be noted that the total crystallographic strain increment and plastic-strain induced rotation must be given by sums over all possible slip systems k as:

$$\delta\varepsilon_{ij}^p = \sum_{m=1}^{k} \delta\gamma^m \alpha_{ij}^m \;\therefore\; \delta\omega_{ij}^p = \sum_{m=1}^{k} \delta\gamma^m \beta_{ij}^m. \tag{20a, b}$$

Homogenous (or homogenized on the macroscale) slip processes alone, in general, alter lengths and orientations of fiducial lines and angles drawn on the element, but leave the lattice unchanged. Lastly, the intermediate configuration could be subject to a strain-free rigid body rotation increment $\delta\omega_{ij}^*$ which carries both material line elements and lattice vectors to their final orientations. This is shown as fig. 3c. This final stage of rigid body rotation is important in the operational analysis of deformation processing problems, but of no great interest to us here.

While all the kinematic relations discussed above have been derived on the basis of shears and translations of planes parallel to each other, they are applicable without change to dilatations as well. Thus, for example, if the areas in eq. (13) or eq. (14) were to be separated (or contracted) by a magnitude b, parallel to the unit normal vector $\boldsymbol{n}$, this would be reflected in the definition of the resolution factors α_{ij}; in this case of thickening or thinning of the area, $\boldsymbol{n} \| \boldsymbol{d}$. The type of dislocation motion which accomplishes this is called *climb*.

3. *The mechanical threshold of deformation*

3.1. The critical resolved shear stress for glide

It is intuitively clear that large strain distortions can only be accomplished by shear and that, as a result, the driving forces for it must involve shear stresses, or at least, a critical deviation from a state of pure mean normal stress (section 9). In that sense it is possible to conceive of a fundamental thought experiment carried out at 0 K, in which a nearly perfect crystal containing the necessary complement of microstructural or lattice defects is subjected to increasing levels of shear stress, while the shear strain rate, over

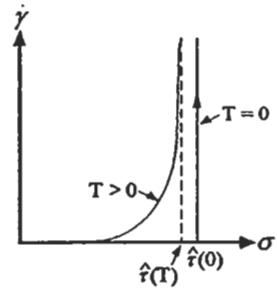

Fig. 4. Idealized threshold behavior: at $T = 0$ the deformation threshold is sharp, at $T > 0$ it is softened by thermally assisted processes, and $\hat{\tau}(T)$ is less than $\hat{\tau}(0)$.

and above the ubiquitous rate-independent elastic flexure, is monitored and plotted against the shear stress. Figure 4 shows the likely outcome, of no detectable shear strain rate, for shear stresses σ less than a definite value $\hat{\tau}(0)$. When $\sigma = \hat{\tau}(0)$ the shear strain rate should undergo an abrupt and, perhaps, only inertially limited increase through an apparent initiation of inelastic deformation by a specific mechanism. Clearly, in real materials with the usual internal variability of defect structure, the transition from no deformation to a high rate of deformation should be somewhat less abrupt but still exhibit a threshold behavior. We take this material property $\hat{\tau}(0)$ as the *mechanical threshold* to initiate deformation by a specific mechanism such as, e.g., an intrinsic lattice resistance to dislocation glide or resistance to such motion of a field of solute atoms, precipitate particles, and the like, associated with a specific level of defect structure. Thus, under this idealization we expect that

$$\dot{\gamma} = 0 \quad \text{for} \quad \sigma < \hat{\tau}(0) \tag{19a}$$

$$\dot{\gamma} > 0 \quad \text{(and large) for} \quad \sigma = \hat{\tau}(0) \tag{19b}$$

and that $\sigma > \hat{\tau}(0)$ should be unattainable under quasi-static conditions with a given initial defect structure.

At $T > 0$ the above behavior should be ameliorated in two important ways. Since the basic process governing $\hat{\tau}$ will usually be an elastic interaction on the atomic level, an increase in temperature should decrease $\hat{\tau}(T)$ ($< \hat{\tau}(0)$), to below the 0 K reference value, in proportion to the temperature dependence of the elastic constants. In this modified form we will refer to $\hat{\tau}(T)$ as the rate-independent reference mechanical threshold. Moreover, with increasing temperature the local energy barrier of the inelastic strain producing process can be overcome at lower resolved shear stresses with the help of thermal fluctuations. Thus, a finite inelastic strain rate should be observable even below the now reduced $\hat{\tau}(T)$. This should give rise to a typical softened behavior pattern as shown in fig. 4.

We note briefly here that the reference mechanical threshold can be increased with strain hardening, through the accumulation of immobile dislocations. Alternatively, at elevated temperatures in the range of half the melting point, and above, where self

diffusion becomes rapid, the reference mechanical threshold can be dismantled by recovery process resulting in steady state deformation at a substantially stationary defect structure. In addition, other purely diffusional transport processes can also be present which are capable of producing inelastic strain, and we will discuss these in chapter 22.

The hierarchy of deformation processes contributing to a net inelastic strain rate over the entire temperature range between 0 K and the melting point have been examined and catalogued for many metals and some alloys by FROST and ASHBY [1982] in the form of so-called *deformation mechanism maps*. Figure 5 shows such a mechanism map for vanadium. In this chapter we will be interested in the diffusionless processes.

4. *Elements of thermally activated deformation*

4.1. General principles

As stated earlier, inelastic deformation requires a defective crystal in which local shear relaxations are kinematically possible. Thus, we view as a general case a cluster Ω_f in a volume V, able to undergo a free-standing shear strain $\Delta\gamma^T$ which converts the unconstrained volume Ω_f from an unflexed state A to a flexed state B, as depicted in fig. 6a. When the shear transformation is completed inside the body, it results in a macroscopic shear strain increment of

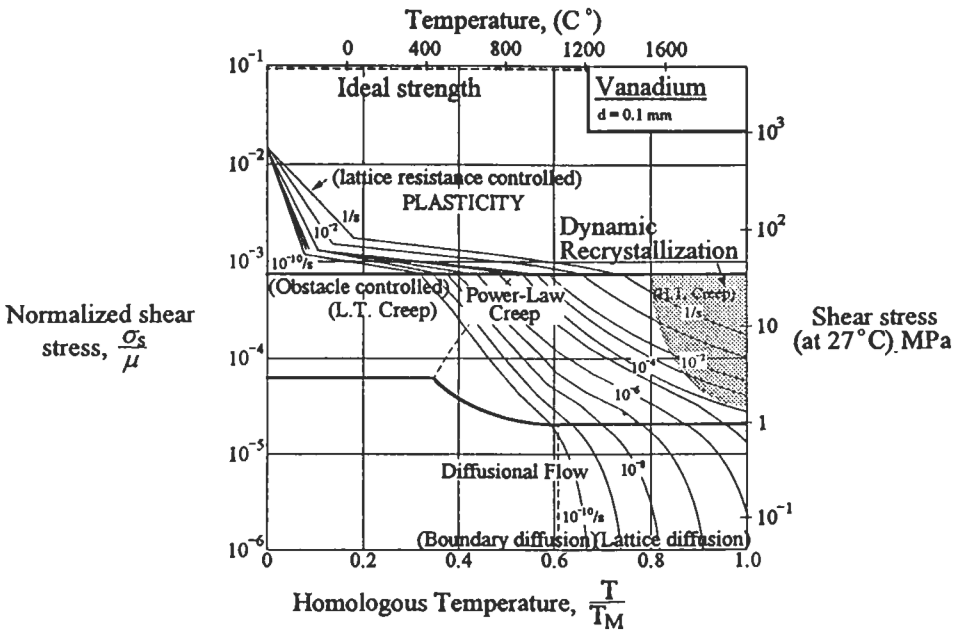

Fig. 5. Deformation mechanism map for vanadium (FROST and ASHBY [1982], Courtesy of Pergamon Press).

References: p. 1951.

$$\Delta\gamma_0 = \Delta\gamma^T \frac{\Omega f}{V}. \tag{20}$$

We consider a reversible thought experiment in which the overall system is flexed in small increments of strain $d\gamma$ from $\gamma = 0$ to $\gamma = \Delta\gamma_0$ in constrained equilibrium, and the resulting Helmholtz free energy ΔF of the system is monitored continuously. We expect that the resulting change in ΔF with increasing inelastic strain γ would look somewhat like what is shown in fig. 6b where we show $\Delta F_B > \Delta F_A$, indicating that, in this case, the final state is less stable than the initial one. We now define the associated deformation resistance τ for this process as

$$\tau \equiv \frac{1}{V}\frac{\partial \Delta F}{\partial \gamma} \tag{21}$$

and plot it in fig. 6c in line with ΔF as a function of γ. We take τ as a material property, and note that there is a maximum level of deformation resistance $\hat{\tau}$, reached where the slope of the ΔF vs. γ connection reaches a maximum value. Under an applied shear stress σ, incremented under quasi-static and constrained conditions, it should become possible to flex the system V reversibly up and down the configuration path from $\gamma = 0$ to $\gamma = \Delta\gamma_0$, and beyond.

We note that at any particular level of applied stress $\sigma = \hat{\tau}$ the stress is in equilibrium with the deformation resistance at two points of flexure s and u, for inelastic system strains γ_s and γ_u. If the system at this level of stress is given a virtual configurational variation $\Delta\gamma$, the external agency applying the stress would do an increment of work on the system given by

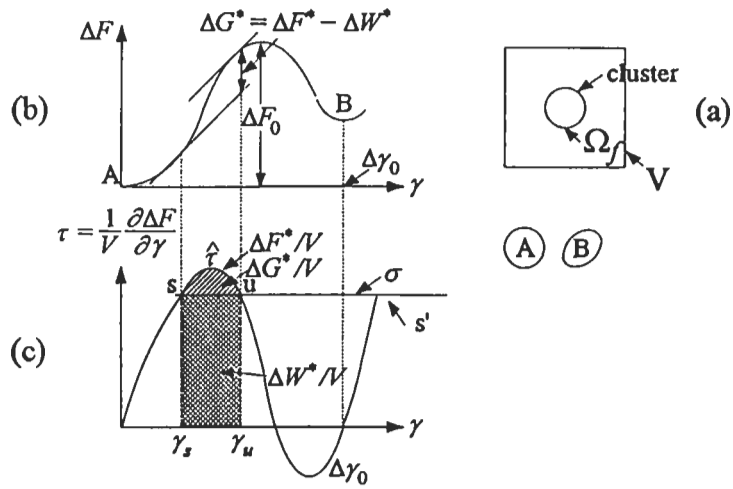

Fig. 6. Change of Helmholtz free energy and deformation resistance with strain during a reversible flexure of an activable cluster.

$$\Delta W = V\sigma\Delta\gamma. \tag{22}$$

On the ΔF diagram this can be shown as the sloping lines tangent to the diagram at points s and u where $\sigma = \tau$. We note that at s and u, the resulting changes in the Gibbs free energy

$$\Delta G_s = \Delta F_s - \Delta W_s > 0 \tag{23a}$$

$$\Delta G_u = \Delta F_u - \Delta W_u < 0 \tag{23b}$$

are of different sign, for both positive and negative flexure of the system. Clearly, the equilibrium at "s" is stable, while that at "u" is unstable. The difference in ΔF between the sloping lines on the ΔF diagram, and the singly cross-hatched area under the curve in the deformation resistance diagram represents a Gibbs free energy difference, or an energy barrier, ΔG^*, which we recognize as the required activation free energy that must be supplied by thermal fluctuations to permit the system to reach from the stable "s" to the unstable "u" (saddle point) configuration under the applied shear stress σ. Once the system is activated over the energy barrier, it can spontaneously flex into a new stable configuration shown by s' on the deformation resistance diagram, as it develops a total elemental strain increment $\Delta\gamma_0$. As is clearly delineated in figs. 6b and 6c, the activation free energy ΔG^* has two components: the Helmholtz free energy change ΔF^* and the external work increment ΔW^* during the activation

$$\Delta F^* = V\int_{\gamma_s}^{\gamma_u} \tau(\gamma) d\gamma \tag{24a}$$

$$\Delta W^* = V\int_{\gamma_s}^{\gamma_u} \sigma d\gamma = V\sigma(\gamma_u - \gamma_s). \tag{24b}$$

Here we note, in passing, that as indicated in fig. 6b, often during the strain-producing activated event the Helmholtz free energy will show an increase in the new flexed state. If this is a regular recurring feature, it is often useful to recognize that a certain component of the applied stress $\sigma = \tau_{\text{STOR}}$ must be reserved to provide this rate of free energy storage. Thus, the component of the stress that is available to assist the system over the thermally penetrable obstacle is $\sigma - \tau_{\text{STOR}}$ which is often called the effective stress. We will return to this in section 4.3.

The activation rate R of the inelastic process, in the direction of absorbing positive work, can then be given as:

$$R = \nu_G \exp\left(-\frac{\Delta G^*(\sigma, \hat{\tau})}{kT}\right) \tag{25a}$$

where ΔG^* is the activation free energy for the forward process and ν_G is a characteristic normal mode frequency of the cluster, or other configuration, along the activation path, where the "cluster" could be a dislocation line segment in front of an obstacle or a twin embryo, etc. The exponential or so-called *Boltzmann factor* gives the probability that a

thermal fluctuation of the required energy (or larger) can be supplied by the thermal reservoir, at temperature T. We note that ν_G, being a cluster frequency involving many atoms, will be much smaller than the usual Debye frequency of atoms, ν_D, to which it relates crudely as

$$\nu_G \approx \nu_D \left(\frac{\Omega}{\Omega_f} \right)^{\frac{1}{3}}, \tag{25b}$$

where Ω is the atomic volume, and the factor in parentheses is typically of the order of 10^{-2}–10^{-1}. Thus, the activation rate expression related to inelastic processes in its classical form holds valid well below the usual Debye temperature $\theta_D = h\nu_D/k$ where h and k are, respectively, Planck's constant and Boltzmann's constant.

Here we are interested in the net inelastic strain rate which is:

$$\dot{\gamma}_{net} = \dot{\gamma}_0 \left[\exp\left(-\frac{\Delta G^*}{kT} \right) - \exp\left(-\frac{\Delta G_r^*}{kT} \right) \right], \tag{26}$$

where the second term represents the reverse rate of deformation associated with a return of configuration B back to A, during which work needs to be done against the applied stress. For this, ΔG_r^* is the activation free energy for the reverse flexure reaction. The pre-exponential factor $\dot{\gamma}_0$ has the typical composition of

$$\dot{\gamma}_0 \cong c_f \Delta\gamma^T \nu_G \tag{27}$$

where c_f is the volume fraction of fertile material that can take part in the configurational transformation. When the applied stress $\sigma \ll \hat{\tau}$ it is possible to give a linearized form of ΔG^* and ΔG_r^* as

$$\Delta G^* \cong \Delta F_0^* - \sigma \Delta\gamma^T \Omega_f/2 \tag{28a}$$

$$\Delta G_r^* \cong \Delta F_0^* + \sigma \Delta\gamma^T \Omega_f/2. \tag{28b}$$

With these, eq. (26) can be simplified into a useful form for moderate stress levels,

$$\dot{\gamma}_{net} = 2\dot{\gamma}_0 \exp\left(-\frac{\Delta F_0^*}{kT} \right) \sinh\left(\frac{\sigma \Delta\gamma^T \Omega_f}{2kT} \right). \tag{29}$$

This gives $\dot{\gamma}_{net} \to 0$ when $\sigma \to 0$. For very low levels of stress all inelastic processes then have a linear form in stress,

$$\dot{\gamma}_{net} = \frac{\dot{\gamma}_0 \Delta\gamma^T \Omega_f \sigma}{kT} \exp\left(-\frac{\Delta F_0^*}{kT} \right). \tag{30}$$

For high stresses close to the mechanical threshold $\hat{\tau}$ (where $\Delta G_r^* \gg \Delta G^*$) however, the net strain rate is adequately given by

$$\dot{\gamma}_{net} = \dot{\gamma} = \dot{\gamma}_0 \exp\left(-\frac{\Delta G^*(\sigma, \hat{\tau})}{kT}\right), \tag{31}$$

the familiar Arrhenian expression.

4.2. Principal activation parameters for plasticity

Before considering specific processes of crystal plasticity, we develop a number of generally useful and instructive thermal activation parameters that characterize systems deforming close to their mechanical threshold.

In this range (see fig. 6c)

$$\Delta G^* = V\int_{\gamma_s}^{\gamma_u}(\tau(\gamma) - \sigma)d\gamma = V\int_{\sigma}^{\hat{\tau}} \Delta\gamma_a(\tau)d\tau = \int_{\sigma}^{\hat{\tau}} \Delta\gamma_{af}(\tau)\Omega_f d\tau \tag{32}$$

where $\Delta\gamma_a$ is the system activation strain, and $\Delta\gamma_{af}$ the cluster activation strain respectively, the two being related by eq. (20). For many, but not all, of the thermally activated local deformation processes, the energy barrier is governed by an elastic interaction mechanism which scales by some set of elastic constants, but usually by the shear modulus, μ, which has a known temperature dependence resulting from anharmonic effects. Thus, we can write

$$\Delta G^* = \Delta G_0 \frac{\mu(T)}{\mu_0} \tag{33}$$

where μ_0 and ΔG_0 refer to a reference state which as a first approximation can be taken at 0 K. Moreover, we recognize that

$$\Delta G^* = \Delta H^* - T\Delta S^* \tag{34}$$

and that

$$\Delta S^* = -\left(\frac{\partial \Delta G^*}{\partial T}\right)_{\sigma \cdot p} \therefore \left(\frac{\partial \Delta H^*}{\partial T} - T\frac{\partial \Delta S^*}{\partial T} = 0\right) \tag{35a}$$

so that

$$\Delta S^* = -\Delta G^*\left(\frac{1}{\mu}\frac{d\mu}{dT}\right). \tag{35b}$$

Two important and readily measurable properties of the activated process that convey important information about its nature are: (a) the shear activation volume Δv_σ^* and (b) the pressure activation volume Δv_p^* or the activation dilation. These we define as

$$\Delta v_\sigma^* \equiv -\left(\frac{\partial \Delta G^*}{\partial \sigma}\right)_{p \cdot T} = \Delta\gamma_{af}^*(\sigma)\Omega_f \tag{36}$$

$$\Delta v_p^* \equiv \left(\frac{\partial \Delta G^*}{\partial p}\right)_{\sigma,T}. \tag{37}$$

The determination of these two quantities and other activation parameters, by experimental means, is of great interest in probing the mechanism of the activated process. These additional quantities include ΔH^*, ΔS^*, ΔG^*.

The kinetic expression of the deformation experiment, eq. (31), is the principal vehicle for probing, through a number of so-called *jump experiments*, which in increasing complexity involve: the imposed strain rate (at constant temperature and pressure; T, p); the temperature (at constant stress and pressure; σ, p); and finally the pressure (at constant strain rate and temperature, $\dot{\gamma}$, T).

From such jump experiments we obtain

$$\Delta v_\sigma^* = kT\left[\left(\frac{\partial \ln \dot{\gamma}}{\partial \sigma}\right)_{p,T} - \left(\frac{\partial \ln \dot{\gamma}_0}{\partial \sigma}\right)_{p,T}\right] \cong kT\left(\frac{\partial \ln \dot{\gamma}}{\partial \sigma}\right)_{p,T} \tag{38a}$$

$$\Delta H_\sigma^* = kT^2\left[\left(\frac{\partial \ln \dot{\gamma}}{\partial T}\right)_{\sigma,p} - \left(\frac{\partial \ln \dot{\gamma}_0}{\partial T}\right)_{\sigma,p}\right] \cong kT^2\left(\frac{\partial \ln \dot{\gamma}}{\partial T}\right)_{\sigma,p} \tag{38b}$$

$$\begin{aligned}\Delta v_p^* &= -kT\left[\left(\frac{\partial \ln \dot{\gamma}}{\partial p}\right)_{\sigma,T} - \left(\frac{\partial \ln \dot{\gamma}_0}{\partial p}\right)_{\sigma,T}\right] \cong -kT\left(\frac{\partial \ln \dot{\gamma}}{\partial p}\right)_{\sigma,T} \\ &= kT\left(\frac{\partial \ln \dot{\gamma}}{\partial \sigma}\right)_{p,T}\left(\frac{\partial \sigma}{\partial p}\right)_{\dot{\gamma},T} = \Delta v_\sigma^*\left(\frac{\partial \sigma}{\partial p}\right)_{\dot{\gamma},T}\end{aligned} \tag{38c}$$

where $(\partial\sigma/\partial p)_{\dot{\gamma},T}$ reflects the important strength differential (SD) effect. To obtain the final form of the expressions we have noted that $\dot{\gamma}_0$ is given by eq. (27) in which the pressure and temperature dependence is negligible, and the stress dependence, usually coming through the stress dependence of mobilizable configurations $c_f(\sigma)$, is very much lower than the principal term when $\sigma < \hat{\tau}$ (see section 7.3.8). Through the principal temperature dependence of eq. (33), we arrive at (see also SUREK *et al.* [1973])

$$\Delta G^* = \frac{\Delta H^*}{\left(1 - \frac{T}{\mu}\frac{d\mu}{dT}\right)}, \tag{39}$$

$$\Delta S^* = \frac{\Delta H^*\left(\frac{1}{\mu}\frac{d\mu}{dT}\right)}{\left(1 - \frac{T}{\mu}\frac{d\mu}{dT}\right)}. \tag{40}$$

Since for the usually expected regular behavior of materials $d\mu/dT < 0$, between 0 K and T_m, ΔS^* will be positive. Of these so-called activation parameters ΔH^*, Δv_σ^* and Δv_p^* (the

activation dilation) are the most informative.

The forms of the activation parameters, presented above are cast in a very general way in which they are applicable to all inelastic relaxations regardless of mechanism. Since our primary interest in the rest of this chapter is crystalline solids we will note that when the mechanism of strain production is by dislocation glide the following specific forms apply (see fig. 7).

$$\Delta\gamma^T = \frac{b}{h} \tag{41a}$$

$$\Omega_f = \Delta a \cdot h \tag{41b}$$

$$\Delta\gamma_0 = \frac{b\Delta a}{V} \tag{41c}$$

$$\dot{\gamma}_0 = b\rho_M \Delta Y \nu_G \tag{41d}$$

$$c_f = N\left(\frac{\Delta a \cdot h}{V}\right) \tag{41e}$$

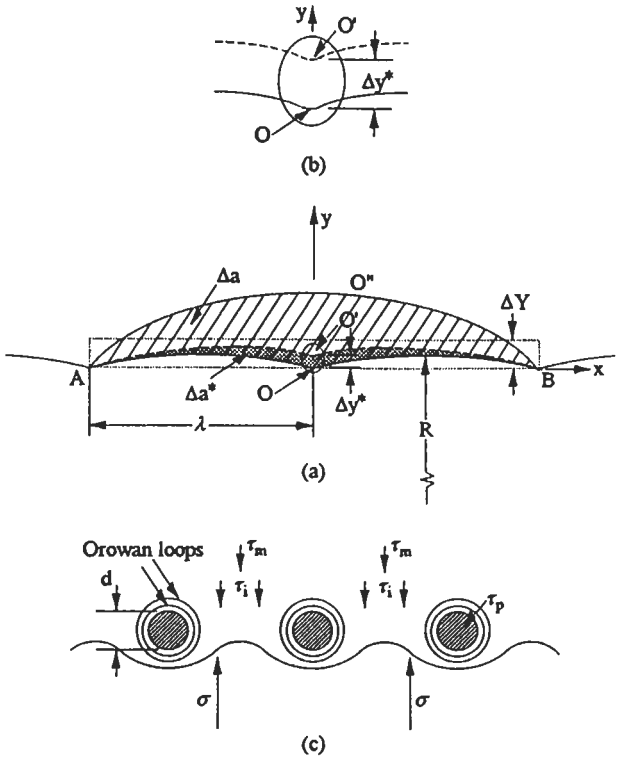

Fig. 7. A typical activation configuration in the thermal penetration of a dislocation segment $\overline{AB}$ through a local particle obstacle at 0.

$$\Delta v_\sigma^* = \Delta\gamma_a^*\Omega_f = b\Delta a^* = b\lambda\Delta y^* \tag{41f}$$

where h is the spacing between slips planes, ρ_M is the mobile dislocation density (= Nλ/V) i.e., N active segments of lengths λ in the given volume V, ΔY is the mean distance of advance of a segment ($=\Delta a/\lambda$), with λ, as the Friedel sampling length to be defined later, Δa^*, the activation area, Δy^*, the activation distance, and c_f, the volume fraction of mobilizable configurations transforms into the total slipped area of thickness h per unit volume.

4.3. Flow stress mechanisms

The plastic resistance at any given state of deformation can be controlled by a variety of mechanisms. In keeping with our projections in section 1 we consider the mechanisms in both pure substances and dilute alloys with light concentration of a second constituent either in solid solution or in the form of precipitate particles. In view of this perspective we divide the mechanisms into two basic groups as follows:

A. Intrinsic Mechanisms
   i) The lattice resistance
   ii) The dislocation resistance

B. Extrinsic Mechanisms
   i) Solute resistance
   ii) Precipitate (shearable) particle resistance
   iii) Dispersed, (non-shearable) particle resistance

Here we will merely introduce these mechanisms, explain their properties, and discuss how they individually and collectively govern the plastic resistance. Detailed discussion can be found elsewhere (see e.g. KOCKS *et al.* [1975]; REPPICH [1993]; chapter 23).

4.3.1. Intrinsic mechanisms

4.3.1.1 The lattice resistance. The atomic configurations and energies of cores of dislocations are sensitive to crystal structure and the orientation of the dislocation line in the lattice. Thus, in general at low temperatures, in the absence of other constraints, dislocation core energies can be expected to have a periodic variation on the scale of the spacing of lattice rows (PEIERLS [1940]; NABARRO [1947]) with a threshold resistance $\hat{\tau}$ of:

$$\hat{\tau} = \frac{\mu\pi\alpha}{b^2}\mathcal{E} \tag{42}$$

where $\alpha\mathcal{E}$ is the amplitude of the variation of the dislocation line energy $\mathcal{E}$ ($\cong \mu b^2/2$, in the constant line energy/line tension model), the coefficient α is typically of the order $(0.7-2.0)\times 10^{-2}$ for BCC transition metals, $(0.5-1.2)\times 10^{-3}$ for the NaCl structure (PULS [1981]), and approaching 10^{-1} for covalent compounds. At $T>0$, the dislocation line can advance in thermally activated steps by initiating double kinks into the neighboring lattice valley, followed by the propagation of the kinks along the dislocation line. An

approximate analysis (KOCKS *et al.* [1975]) of this activated configuration based on line notion of dislocations gives the following useful scaling relations for the activation free energy ΔG^* and the activation area Δa^* of the saddle point configuration,

$$\Delta G^* = \frac{\pi\sqrt{\alpha}}{2}\mu b^3\left(1-\frac{\sigma}{\hat{\tau}}\right)^2 \tag{43}$$

$$\Delta a^* = \frac{\pi b^2}{4\sqrt{\alpha}}\left(1-\frac{\sigma}{\hat{\tau}}\right). \tag{44}$$

While the above elementary consideration suffices for our overall view, it must be noted that the lattice resistance mechanism harbors unusual complexities since it may affect more strongly the edge or the screw dislocation and is sensitive to the actual atomic structure of the core, which cannot be treated by dislocation line notions. More advanced analyses of the thermally activated advance of dislocations against the lattice resistance can be found elsewhere, ranging from more elegant line analyses to fully atomistic forms (DORN and RAJNAK [1964]; GUYOT and DORN [1967]; KOIZUMI *et al.* [1993]; PULS [1981]).

4.3.1.2 The dislocation resistance. The interactions of dislocations with each other have different manifestations. We divide these interactions or resistances into two distinct parts: (a) the *interplane resistance* and (b) the *intra-plane resistance* (HIRSCH and HUMPHREYS [1970]). The first relates to the interaction of mobile dislocations on parallel slip planes with each other which is a characteristic of the "flow state" and is relatively unaffected by strain hardening. The second incorporates dislocation forest cutting resistances (cutting of glide dislocations through other less mobile dislocations penetrating through the glide plane), and longer range stress fields resulting from dislocation groups and deformation induced misfit. Of these, we will discuss the forest-cutting resistance together with the particle resistance, in section 4.3.2 as a pseudo-particle, and the discussion of the longer-range resistances we will delay to section 7 on strain hardening. Here we consider only the *interplane resistance* which governs the slip line spacing that we will consider in section 5 below.

During plastic deformation, dislocation fluxes (see also section 7.3.5) of positive and negative type have to flow through each other in opposite directions. This results in encounters between opposite edge, and opposite screw dislocations depicted in fig. 8. For planes of given spacing H the maximum interplane resistance τ for edge and screw dislocations are:

$$\tau_{ie} = \frac{\mu b}{8\pi(1-\nu)H}, \quad \tau_{is} = \frac{\mu b}{4\pi H}. \tag{45a, b}$$

If dislocation encounters occur at stress levels less than these resistances, they should trap each other in dipolar and multipolar arrangements if they are of edge nature. This is a primary source of strain hardening in Stage I of FCC and HCP crystals. If the encountering dislocations are of screw type they would, most likely, annihilate by cross-

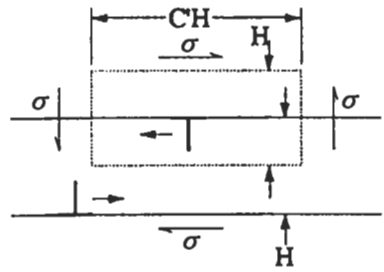

Fig. 8. Passing of two opposite types of edge dislocations on planes a distance H apart.

glide. The energetics of this mechanism of pairwise encounters are too unfavorable for the resistances to be subject to reduction by thermal activation.

4.3.2. Extrinsic mechanisms

4.3.2.1 The solute resistance. The resistance to dislocation motion by misfitting substitutional or interstitial solute atoms is one of the more powerful mechanisms of strengthening a pure metal, albeit mechanistically one of the most complex. The process has been considered first by MOTT and NABARRO [1940], followed by many refined considerations reaching the present day (for an earlier summary see KOCKS *et al.* [1975]). Much of the complexity arises from the collective and relatively weak interactions of misfitting solute atoms with dislocations which may tug the dislocation line in all directions but polarize against the direction of motion. Detailed considerations discussed by KOCKS *et al.* [1975] result in a threshold resistance $\hat{\tau}_{sol}$ given by:

$$\hat{\tau}_{sol} = \tfrac{2}{3}\left(\frac{\hat{K}}{2\mathcal{E}}\right)^{\frac{4}{3}} c^{\frac{2}{3}}\mu \tag{46}$$

where $\hat{K}/2\mathcal{E}$ is the peak resistive force of an individual solute atom against a dislocation, normalized by twice the line tension, (for reasons that will become apparent in the discussion of the precipitate particle resistance below), c is the volume fraction of the solute. This form of the resistance has been experimentally verified by TROJANOVA and HAASEN [1975] in dilute silver alloys, as fig. 9 shows.

The temperature and strain rate dependence of the resistance shows unusual complexity, some of these are discussed by HAASEN [1976]. A major complexity, however, arises because in many instances the solute atoms can be affected by and can migrate with the dislocation in the form of a solute atmosphere which forms dynamically polarizable clouds around the dislocation and from which the dislocation can be torn free with an attendant reduction of resistance, until the dislocation is again clogged up with solute, etc., resulting in serrated flow. Such behavior has been studied by a number of investigators. For a discussion of these see MULFORD and KOCKS [1979a]. For further discussions of the temperature dependence of solid solution strengthening see chapter 23 and also KOCKS [1985].

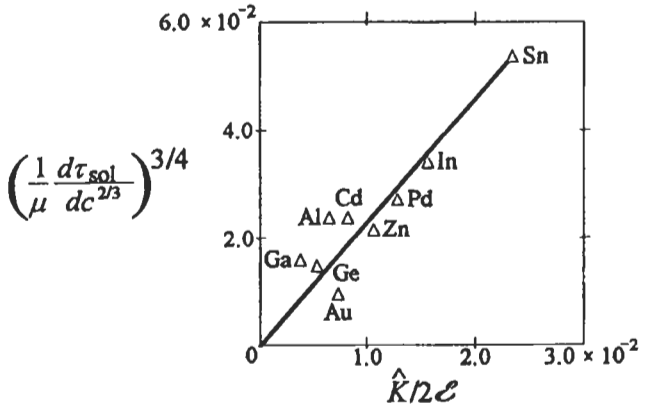

Fig. 9. The dependence of the solute resistance on the normalized peak resistive force (varying with solute concentration) in dilute alloys of silver (re-scaled from TROJANOVA and HAASEN [1975]).

4.3.2.2 Particle resistances. The resistance resulting from second-phase particles to dislocation motion is called *precipitate resistance* if the particles are potentially shearable, by the dislocation. If they are not shearable, the process is referred to as *dispersed-particle strengthening*. Here we will discuss both processes. There are a variety of mechanisms contributing to the precipitate particle resistance that have been identified. These can be divided into two groups: (a) *contact interactions*, and (b) *interactions at a distance*. The prominent mechanisms of the first category are depicted in fig. 10 and include: formation of an interface step by shear, generation of internal faults such as anti-phase boundaries in ordered coherent particles, interface loops around particles for which substantial differences between lattice parameters of the particles and the matrix exists, lattice resistance inside particles, and finally differences in core energy of dislocations lying inside vs. outside of the particles. The longer-range interactions between particles and dislocations are depicted in fig. 11, and include the size misfit interaction, and the modulus misfit interaction, for particles that respectively have a size difference between themselves and the matrix cavity they fill, or have important differences in elastic properties. In all instances it is assumed that the particle lattice is coherent with that of the matrix so that there are no kinematic restrictions to the entry of dislocations.

In all these cases the dislocation evokes a response within the particle along an effective interaction distance. Thus, the fundamental property of interest is the specific force-distance curve $K = K(y)$ for these various interactions. Each of these separate force-distance interactions exhibits a peak value $\hat{K}$ that is of interest in determining the plastic resistance of the crystal at 0 K. Establishment of the specific force-distance curves for any component mechanism of a particle requires considerable sophistication in analysis and cannot be discussed here. It must suffice to state that such interaction contours can be determined in principle for each component mechanism and that these must be combined to determine the overall interaction curve with its overall maximum resistance:

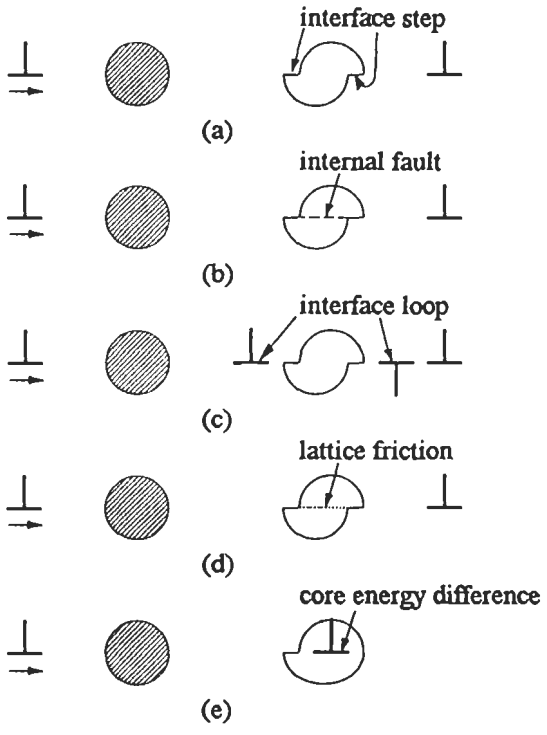

Fig. 10. Short-range, "contact", mechanisms resulting in resistive forces on dislocations: (a) interface step; (b) internal fault production; (c) interface loop production to preserve continuity of Burgers vector between inside and outside, (d) large internal lattice resistance; (e) difference of core energy between particle and matrix.

$$\hat{K} = \widehat{\sum_i K_i} \tag{47}$$

which determines the plastic resistance of the plane.

When a dislocation touches or otherwise interacts with a particle to test its strength, it does so by partly wrapping itself around the particle to exert increasingly larger components of the line tension force on the particle in the direction of advance as

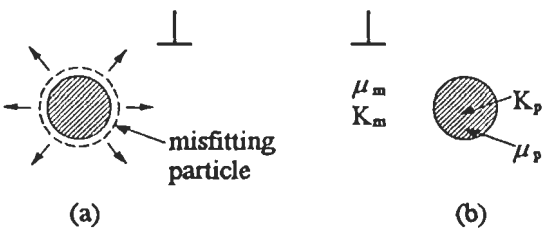

Fig. 11. Long-range mechanisms resulting in resistance to dislocations: (a) particle misfitting in either size or shape; (b) particle with different shear or bulk modulus.

depicted in fig. 7. Thus, the evoked particle resistance K in any instance is balanced by the components of line tension force of the cusped dislocation. The maximum force a dislocation can exert on a particle in this way is equal to twice the line tension $2\mathcal{E}$, which makes it useful to consider the resistance of particles in units of $2\mathcal{E}$. Hence, any particle with strength $\hat{K}/2\mathcal{E} > 1$ is impenetrable by dislocations. A dislocation can overcome such particles only by going around them. When $\hat{K}/2\mathcal{E} < 1$, the dislocation overcomes the particle by cutting it. Of these two limiting forms that for impenetrable obstacles results in *dispersed-particle strengthening*, and that for penetrable particles results in *precipitation strengthening*.

When impenetrable particles with $\hat{K}/2\mathcal{E} > 1$ are distributed randomly in a plane with mean center–center spacing l and having an overall volume fraction c, the flow stress is governed by bowing of dislocations through the gaps of average spacing l in semi-circular segment configurations. This gives rise to a threshold plastic resistance of

$$\hat{\tau} = \beta\left(\frac{2\mathcal{E}}{bl}\right) = \beta\left(\frac{2\mathcal{E}}{br_0}\right)\left(\frac{3c}{2\pi}\right)^{\frac{1}{2}}, \tag{48}$$

where r_0 ($\ll l$) is the actual particle radius and β (~ 0.85) is a statistical factor accounting for the variation in particle spacings in the plane, away from the mean, which the dislocation tests. Clearly, for a given particle size the maximum plastic resistance is

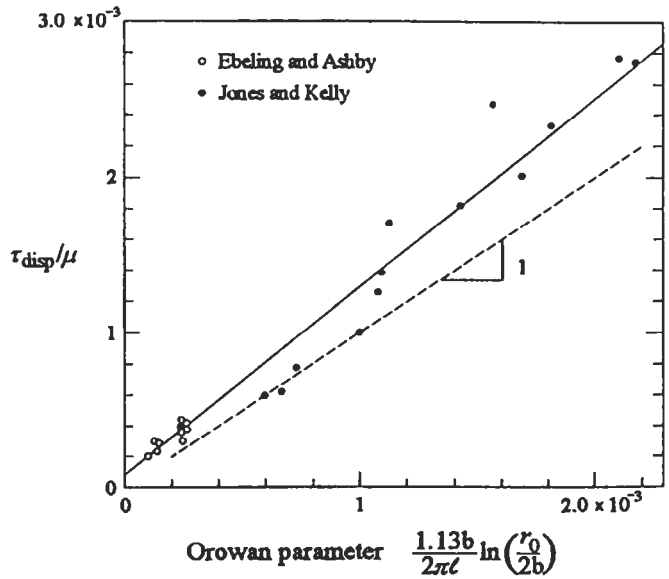

Fig. 12. Dependence of the dispersed particle resistance on geometrical particle field parameters (ASHBY [1969], Courtesy of MIT Press).

proportional to $c^{1/2}$, while for a given particle volume fraction, $\hat{\tau}$ depends on $1/r_0$ over the range in which $\hat{K}/2\mathcal{G} > 1$.

The form of eq. (48) with some second-order corrections has been experimentally well verified as fig. 12 shows (ASHBY [1969]). In this mechanism when dislocations circumvent the impenetrable particles they leave closed so-called Orowan loops (see OROWAN [1948]). Figure 13 shows a typical case of Orowan loops surrounding impenetrable particles (HIRSCH and HUMPHREYS [1969]). The consequence of such loops in producing a long range back stress (BROWN and STOBBS [1975]; ASARO [1975]) will be discussed in section 9.2.

When penetrable particles with $\hat{K}/2\mathcal{G} < 1$ are distributed randomly in a plane, dislocations sample them and penetrate them without the need to bow to semi-circular configurations. In fact, as the particle strength decreases, the mean distance between obstacles being sampled by the dislocation along its length gradually increases steadily above the mean spacing l. This mean distance, λ, known as the Friedel sampling length, is given by (for $\sigma = \hat{\tau}$)

$$\lambda = l\left(\frac{2\mathcal{G}}{\sigma b l}\right)^{\frac{1}{3}} = l\left(\frac{\hat{K}}{2\mathcal{G}}\right)^{-\frac{1}{2}}. \tag{49}$$

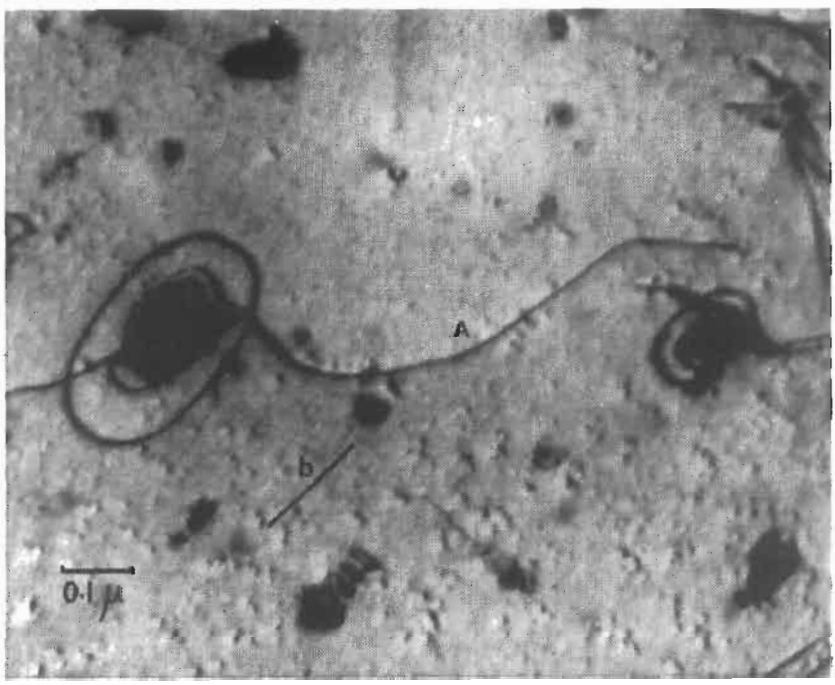

Fig. 13. Orowan loops left around impenetrable particles in Cu. (HIRSCH and HUMPHREYS [1969], Courtesy of MIT Press.)

An example of moving dislocations in MgO sampling iron oxide precipitates is shown in fig. 14. With this the threshold plastic resistance of the alloy with penetrable particles becomes

$$\hat{\tau} = \left(\frac{2\mathcal{G}}{bl}\right)\left(\frac{\hat{K}}{2\mathcal{G}}\right)^{\frac{3}{2}} = \left(\frac{2\mathcal{G}}{br_0}\right)\left(\frac{3c}{2\pi}\right)^{\frac{1}{2}}\left(\frac{\hat{K}}{2\mathcal{G}}\right)^{\frac{3}{2}}. \tag{50}$$

Comparison of eq. (50) with eq. (48) shows that it is modified primarily by the normalized obstacle strength $\hat{K}/2\mathcal{G}$ raised to the power $\frac{3}{2}$. Thus formally, as the particles become impenetrable the precipitate-governed particle resistance goes over smoothly into the expression given by eq. (48).

For many mechanisms the particle strength $\hat{K}/2\mathcal{G}$ depends on particle size. This dependence is often linear and introduces a technologically important possibility of maximizing the plastic resistance at constant volume fraction of particles by particle size control. Thus, in the range of precipitation strengthening, where $\hat{K}/2\mathcal{G} = K' r_0/2\mathcal{G}$, eq. (50) transforms into

$$\hat{\tau} = \left(\frac{K'}{b}\right)^{\frac{3}{2}}\left(\frac{3c}{2\pi}\right)^{\frac{1}{2}}\left(\frac{r_0 b}{2\mathcal{G}}\right)^{\frac{1}{2}}, \tag{51}$$

where $K'(= d\hat{K}/dr_0)$ is the coefficient of the particle size–strength connection. Equation (51) states that in the range $\hat{K}/2\mathcal{G} < 1$ the plastic resistance rises in proportion to $r_0^{1/2}$ for

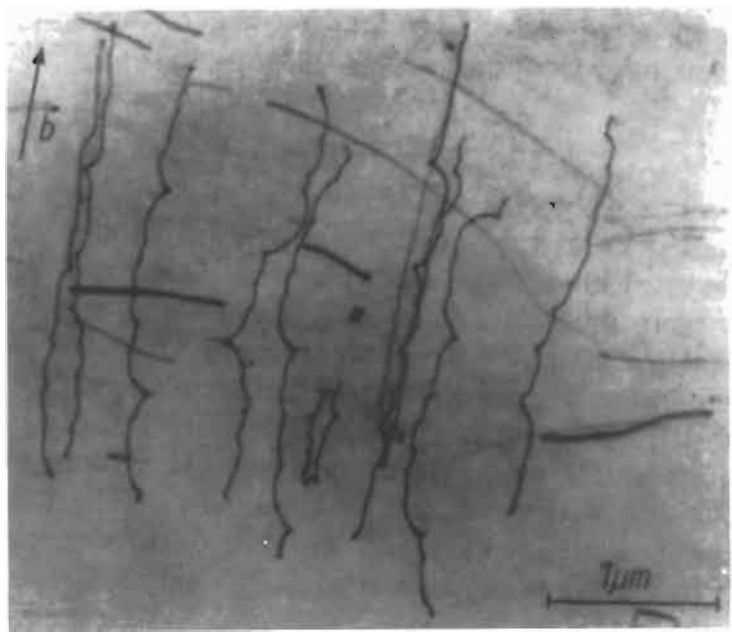

Fig. 14. Transmission electron micrograph of dislocations in a MgO crystal pressed against unresolvable iron oxide particles of approximate peak strength $\hat{K}/2\mathcal{G} = 0.5$ (A PPEL *et al.*, [1976], Courtesy of Phys. Stat. Sol.).

a constant volume fraction c of particles. The peak strength $(K'/b)(3c/2\pi)^{\frac{1}{2}}$ is then achieved at a particle size, $r_{peak} = 2\mathcal{G}/K'$ when the particles become just impenetrable.

This rise and fall of the precipitate resistance with increasing particle size, for a variety of alloys, shown in fig. 15, indicates that the form of the interaction is correct, but there is often a significant departure from the expected magnitudes (for a discussion see ARDELL [1985]).

The thermally assisted penetration of a field of shearable precipitate obstacles with a threshold plastic shear resistance $\hat{\tau}$, at a stress $\sigma < \hat{\tau}$ can be understood through the characteristic force-distance interactions $K = K(y)$, illustrated in the inset of fig. 7, of a particle being probed by a bowed out dislocation line. Thus, the free energy barrier ΔG^* is, in analogy with eq. (32)

$$\Delta G^* = \int_{y_s}^{y_u} \big(K(y) - \sigma b\lambda\big)dy = \int_{K=\sigma b\lambda}^{\hat{K}} \Delta y(K)dK = \Delta G^*\big(K, \hat{K}\big). \tag{52}$$

KOCKS *et al.* [1975] who have examined many typical force distance interactions related to particles have proposed a general form for the dependence of ΔG^* on K and $\hat{K}$ which gives the stress and threshold resistance dependence of ΔG^* as follows:

$$\Delta G_0 = \Delta F_0\left[1 - \left(\frac{\sigma}{\hat{\tau}}\right)^p\right]^q, \tag{53}$$

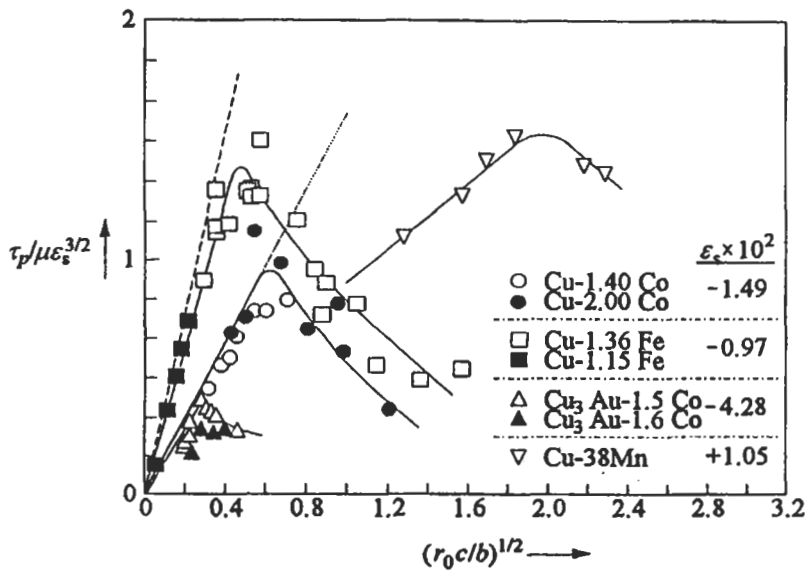

Fig. 15. Dependence of peak alloy strength on particle size for a collection of prominent particle-strengthened alloys. ε_s is the size misfit parameter (REPPICH [1993], Courtesy of VCH Publishing).

where ΔF_0 is the activation free energy at vanishingly small stress, and where use was made of the expressions:

$$K = 2\mathcal{G}\left(\frac{\sigma b l}{2\mathcal{G}}\right)^{\frac{2}{3}} \quad \therefore \quad \hat{K} = 2\mathcal{G}\left(\frac{\hat{\tau} b l}{2\mathcal{G}}\right)^{\frac{2}{3}}. \tag{54a, b}$$

The phenomenological exponents p and q are typically in the range

$$0 < p \leq 1.0 \tag{55a}$$

$$1.0 \leq q \leq 2.0. \tag{55b}$$

Substitution of the expression of eq. (53) into the basic kinetic law of eq. (31) gives, upon inversion,

$$\frac{\sigma}{\hat{\tau}}\left(1 - \left(\frac{T}{T_0}\right)^m\right)^n \tag{56}$$

with $m = 1/q$, $n = 1/p$, and

$$T_0 = \frac{\Delta F_o}{k \ln\left(\frac{\dot{\gamma}_0}{\dot{\gamma}}\right)}. \tag{57}$$

At $T > T_0$ the particle resistance is no longer present. We recall, from section 4.1, that there will be other resistances present that are not temperature sensitive. These superimpose directly on the particle resistance. Thus, for $T > T_0$ such mechanisms govern the flow stress. We note that T_0 is strain rate dependent and increases logarithmically with increasing strain rate. How the various shapes of the temperature dependence of σ given by eq. (56) relate to different force-distance profiles of obstacles has been discussed by KOCKS *et al.* [1975].

The strain-rate change experiment discussed in section 4.2 gives the shear activation volume,

$$\Delta v_\sigma^* = \tfrac{2}{3} b \Delta a^*(K) = \tfrac{2}{3} b \lambda \Delta y^*(K), \tag{58}$$

which together with eqs. (54a, b) and a knowledge of the mean obstacle spacing, l, in the plane makes experimental determination of force-distance curves possible.

The discussion above relates to dilute concentration of obstacle particles and is known as the *Friedel–Fleischer theory*. When the particle volume fraction increases, the way the dislocation samples the particles changes significantly. Such complexities have been dealt with by SCHWARZ and LABUSCH [1978]. For a discussion of the required modifications see REPPICH [1993] and ARDELL [1985].

4.3.2.3 Cutting of forest dislocations. Glide dislocations in a slip plane encounter many dislocations of other slip systems that thread through the plane. Such forest dislocations are cut in a number of different ways.

If both the glide dislocation and the forest dislocations are of edge nature, or if one

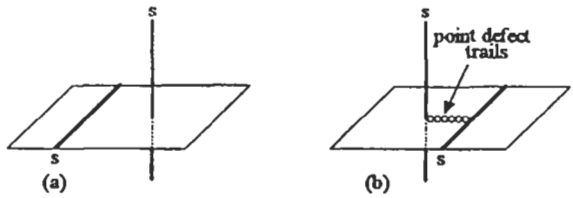

Fig. 16. Intersection of two edge dislocations producing a simple jog.

is an edge and the other a screw, the intersections can be accomplished without much complexity by forming simple steps, called *jogs*, on the dislocation lines at the points of intersections (see fig. 16). A typical simple jog has an energy of $\sim \mu b^3/10$ which has to be supplied by the cutting process over roughly the core width w. Hence the maximum resistive force $\hat{K}_j$ during an intersection process that produces simple jogs, should be of the order of

$$\hat{K}_j \approx \frac{\mu b^3}{10w}. \tag{59}$$

If the cutting dislocations are both screw and of the same type, namely, both are right hand screw or left hand screw, the intersection cannot be accomplished in one step but requires the formation of one interstitial atom per atom separation of the cutting dislocations. When the two screw dislocations are of opposite type, cutting requires the formation of one vacancy per atom separation of the two dislocations, as depicted in fig. 17. The maximum resistive force of the cutting operation $\hat{K}_s$ for screw dislocation intersections then should be

$$\hat{K}_s \approx \frac{\Delta F}{b} \tag{60}$$

where $\Delta F_v \approx \mu b^3/5$ for vacancies and $\Delta F_i \approx 2\mu b^3$ for interstitials.

In many instances the intersecting dislocations approach each other at angles other than right angles and have longer range interactions. Then, as the dislocations fuse before intersecting, reactions can occur that reduce considerably the line energy and set up reaction products such as the segment PP' depicted in fig. 18b. Because of their long range attractive nature, such forest junctions are called attractive, while the ones discussed above resulting in repulsive forces are called repulsive junctions.

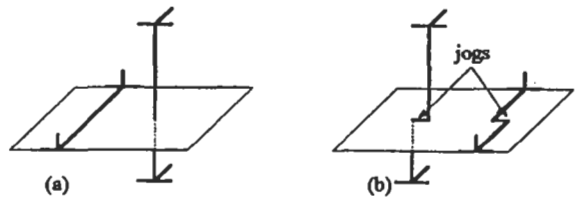

Fig. 17. Intersection of two screw dislocations producing a trail of point defects: interstitials or vacancies.

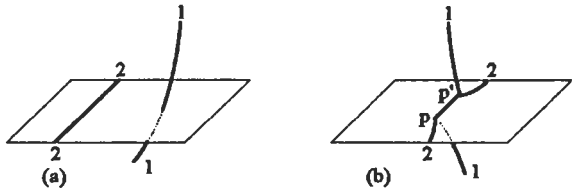

Fig. 18. Intersection of two dislocations resulting in the formation of a reaction product PP' that can act as an impenetrable obstacle.

The cutting of repulsive forest dislocation trees constitute the principal rate controlling mechanism in pure metals in the temperature range where the lattice resistance is no longer effective. The force-distance curves of repulsive forest dislocation obstacles have been determined in Cu by ARGON and EAST [1979]. A typical example, shown in fig. 19, indicates that the cutting widths w of the forest dislocations are of sub-atomic dimensions that can only be understood by atomistic considerations of interpenetrating cores of the intersecting dislocations. Measurements of activation areas and their stress dependence related to forest cutting have been reported by MULFORD and KOCKS [1979], and by MULFORD [1979] on pure Ni and some solid solution Ni alloys.

4.4. Superposition of resistances

For purposes of assessing the contributions of various mechanisms that contribute to the plastic resistance, it is necessary to determine how these mechanisms superpose. Different mechanisms are effective at different length scales. The lattice resistance and

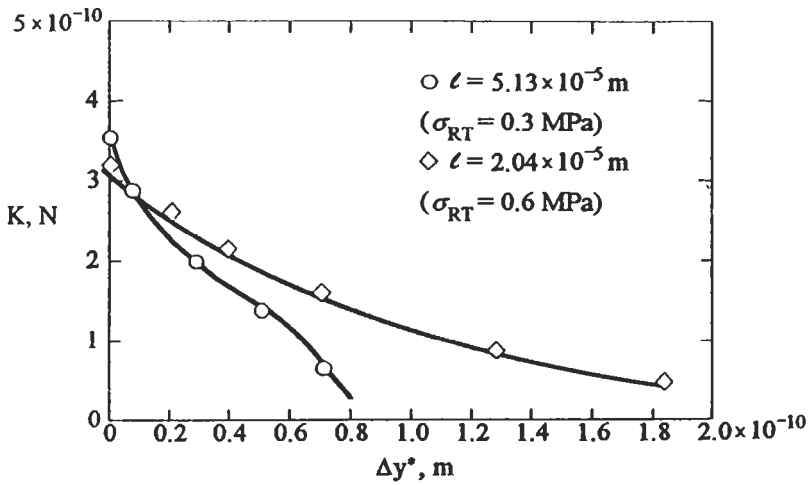

Fig. 19. The force-distance curve of a typical forest dislocation intersection in Cu (ARGON and EAST [1979], Courtesy of Pergamon Press).

the solid solution resistance act on the dislocation close to the atomic scale while the precipitate particle resistance is on a much coarser scale of the interparticle distance. The same is true for the forest dislocation resistance. The dislocation resistance, however, has other longer-range components that have even a coarser scale. Thus, in the superposition of such mechanisms the finer scale mechanisms can be considered smooth on the scale of the coarser mechanisms and are, therefore, directly additive. We ignore possible interactions such as solid-solution softening of the lattice resistance, etc.

The major complexity in superposition is on the scale of the precipitate particle resistance. As already noted in section 4.3.2, different mechanisms acting through the same precipitate, superpose through the direct additivity of their force-distance curves. When more than one type of particle is present their contribution to the slip resistance is more complex. Thus, if there are i different types of particles, each with a separate shear resistance $\tau_i(T)$ given by eq. (56), i.e.

$$\tau_i(T) = \hat{\tau}_i \beta_i \left(\frac{T}{T_{oi}} \right) \tag{61}$$

where

$$\beta_i \left(\frac{T}{T_{oi}} \right) = \left(1 - \left(\frac{T}{T_{oi}} \right)^{m_i} \right)^{n_i}, \tag{62}$$

then the total particle resistance is (ALTINTAŞ [1978]),

$$\tau_p(T) = \left(\sum_i \tau_i^2(T) \right)^{\frac{1}{2}}, \tag{63}$$

which includes the contribution of a population of dispersed (impenetrable) particles as well. Then, superposing all resistances gives a total resistance of

$$\tau_{\text{total}}(T) = \tau_l(T) + \tau_{ss}(T) + \tau_p(T) + \tau_{disl}(T) \tag{64}$$

where the different contributions include: lattice, solid solution, precipitate particle and dislocation resistances, respectively, the last being the only component affected in a major way by strain. Each of these contributions (with the exception of the dispersed particle resistance) will have a characteristic temperature dependence of the type given by eq. (62) with their characteristic cut-off, T_{oj}, dependent on strain rate as indicated in eq. (57). This form of temperature dependence with different T_{oj} is useful in decomposing the overall resistance into its individual components.

5. *Selection of slip systems in specific crystal structures*

While the crystallographic nature of plastic deformation in the form of slip bands had been known for a long time, the more specific identification of the latter with crystal

planes dates back to the early experiments on the plasticity of metal single crystals (SCHMID and BOAS [1935]).

Two basic and complementary criteria have been used to explain the selection of specific slip systems in crystals (ESHELBY [1949]).

The energy criterion for selection of slip planes notes that dislocation line energies are large and that, therefore, the crystal will contain only those dislocations with the minimum line energy, i.e., the ones with the smallest Burgers vectors and the smallest effective interplanar shear stiffness.

The complementary mobility criterion notes, in turn, that the dislocations that will dominate in plastic deformation are the ones that experience the lowest lattice resistance. Since the lattice resistance decreases exponentially with the ratio of the core width to the Burgers displacement, and the former scales with the interplanar spacing, as a first approximation dislocations on planes with the largest ratio of interplanar spacing to Burgers displacement should have the highest mobility, and should, therefore, be dominant in slip.

These criteria correctly predict that in BCC α-Fe the {110}<111> slip system should be the preferred one at low temperatures (ESHELBY [1949]). Moreover, the same system should be preferred in all other BCC transition metals, most of which, however, also show slip on the {112}<111> system.

In the application of these criteria to other systems such as FCC, HCP, diamond cubic, and ionic and covalent compounds, other considerations also play important roles. These include: a) reduction of line energy due to splitting of full dislocations into partial dislocations separated by stacking faults; b) strong directional bonding in the dislocation core; and c) charge neutrality.

In table 1 we list the prominent slip systems of some of the most common crystalline solids.

6. *Plastic deformation by shear transformations*

6.1. Types of transformations

Shear transformations in crystals constitute an alternative to slip for inelastic deformation. These transformations include deformation twinning, stress-induced martensitic transformations and kinking which we consider briefly below.

6.2. Deformation twinning

Most crystal structures can undergo deformation twinning in which the lattice inside a specific volume element of a characteristic lenticular shape undergoes a crystallographically specific, atomically homogeneous, simple shear strain γ^T $(=s/h)$ that transforms the interior lattice into a mirror image of the exterior, with respect to a so-called composition plane K_1 by shear in the η_1 direction as shown in fig. 20a. Figure 21 shows a collection of deformation twins in a Zn crystal. There are a number of important geometrical differences between twinning and slip. If each atomic plane a distance a apart, were to undergo slip by the passage of a single dislocation a homogeneous strain

Table 1
Glide Elements for Metals and Some Other Crystals[*]

Crystal Structure	Lattice Type	Slip Plane	Slip Direction	Ref.
Cu, Au, Ag, Ni, CuAu, α-CuZn, AlCu, AlZn	FCC	{111}	⟨110⟩	SEEGER [1958]
Al	FCC	{111} {100}	⟨110⟩ ⟨110⟩ (1)	SEEGER [1958]
α-Fe	BCC	{110} {112} {123}	⟨111⟩ ⟨111⟩ ⟨111⟩	SEEGER [1958]
Mo, Nb, Ta, W, Cr, V	BCC	{110} {112}	⟨111⟩ ⟨111⟩ (2)	SEEGER [1958]
Cd, Zn, ZnCd	HCP c/a ⟩ 1.85	(0001) (10$\bar{1}$0) (11$\bar{2}$2)	⟨2$\bar{1}\bar{1}$0⟩ [11$\bar{2}$0] (3) [$\bar{1}\bar{1}$23] (3)	SEEGER [1958]
Mg	HCP c/a = 1.623	(0001) {10$\bar{1}$1] {10$\bar{1}$0]	⟨2$\bar{1}\bar{1}$0⟩ (4) ⟨2$\bar{1}\bar{1}$0⟩ (4) ⟨2$\bar{1}$10⟩(5)	SEEGER [1958]
Be	HCP c/a = 1.568	(0001) {10$\bar{1}$0}	⟨2$\bar{1}\bar{1}$0⟩ ⟨2$\bar{1}\bar{1}$0⟩	SEEGER [1958]
Ti	HCP c/a = 1.587	{10$\bar{1}$0} {10$\bar{1}$1] (0001)	⟨2$\bar{1}\bar{1}$0⟩ (6) ⟨2$\bar{1}\bar{1}$0⟩ (6) ⟨2$\bar{1}\bar{1}$0⟩ (6)	SEEGER [1958]
Ge, Si, ZnS	Diamond cubic	{111}	⟨101⟩	SEEGER [1958]
As, Sb, Bi,	Rhombohedral	(111) (11$\bar{1}$)	[10$\bar{1}$] [101]	SCHMID and BOAS [1935]
NaCl, KCl, KBr, KI, AgCl, LiF	Rocksalt structure	{110} {001}	⟨110⟩ ⟨110⟩ (7)	SCHMID and BOAS [1935]
MgTl, LiTl, AuZn, AuCd, NH_4Cl, NH_4Br, CsI, CsBr, TlCl–TlBr, CsCl	Cesium chloride structure	{110}	⟨100⟩	SEEGER [1958] SPRACKLING [1976]

* arranged by KLASSEN–NEKLYUDOVA [1964]
(1) above 450°C
(2) secondary system at higher temp.
(3) above 250°C
(4) above 225°C
(5) at RT and below
(6) pyramidal and basal planes less active than prism planes
(7) secondary system at higher temp.

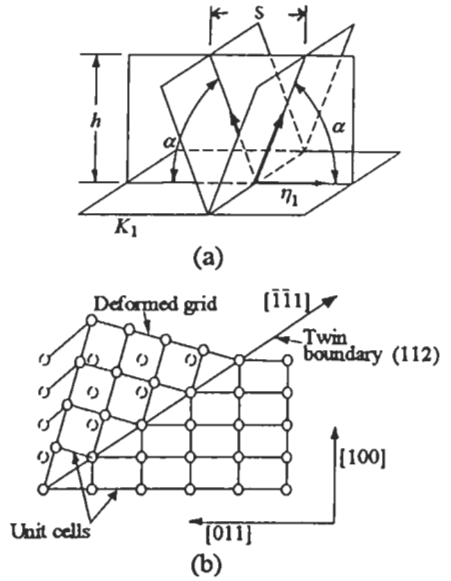

Fig. 20. (a) Crystallographic twinning elements, composition plane K_1, twinning direction η_1, twinning shear $\gamma^T = s/h$, (b) twinning in bcc accomplished by simple shear on {112} plane in <111> direction.

of $\gamma = b/a$ would result but the slipped volume would remain coherent and indistinguishable from the exterior. In the case of twinning, as shown in fig. 20b, for the case of a bcc metal, the lattice of the homogeneously sheared volume assumes a mirror relationship with respect to the exterior across the composition plane {112}. Twinning shear

Fig. 21. Twins in a Zn crystal.

strains, governed by the specific symmetry properties of the lattice are unidirectional and always less than the corresponding case of a homogeneous slip on every plane. The case of the homogeneous twinning shear shown in fig. 20b for the BCC lattice where a simple shear alone accomplishes the end result of relocating all atoms in their proper position is a special case. In many cases the twinning shear will only transform a sub lattice relative to the exterior, and relocating all other atoms properly inside the twinned region will require wholesale internal atom switches which are referred to as *shuffles*. (See detailed discussion by CHRISTIAN and MAHAJAN [1995].)

The conditions for the nucleation of twins, or the formation of martensite embryos, for that matter, have been discussed in great detail. Elementary considerations of homogeneous nucleation of twins under stress (OROWAN [1954]) involves the elastic strain energy of the constrained transformation (ESHELBY [1957]), the changes in the Helmholtz free energy of the partially stressed lattice, the interface energy, and the work done by the prevailing stress state. All such analyses show that, under the usual levels of the applied stresses, the activation free energy for homogeneous twin (or martensite) nucleation is unattainably large. This leads to the conclusion that twin (or martensite) nucleation requires high local stress concentrations, (20–50), pre-existing embryos and/or special heterogeneities such as so-called pole sources (COTTRELL and BILBY [1951]; VENABLES [1961]) that circumvent nucleation. As a result of these generally acknowledged difficulties, reported measurements of critical resolved shear stresses for twinning show very large scatter (VENABLES [1961]). Nevertheless, the validity of these conclusions have been well established, in that the occurrence of twinning increases: (a) with increasing levels of flow stress through strain hardening, and (b) with decreasing magnitudes of the twinning shear strain.

A collection of the twinning systems in some prominent metals and compounds are presented in table 2 (see also CHRISTIAN and MAHAJAN [1995]). An examination of the magnitudes of the twinning shear strains shows that they are all very substantial. This has important consequences. During the formation and early growth of a twin, the twin assumes a lenticular shape that minimizes the elastic strain energy of transformation (OROWAN [1954]; ESHELBY [1957]) which, however, severely concentrates shears at the tip, ahead of the twin. As a result, in crystals with high plastic slip resistance, under uniform levels of stress, twins propagate with near sonic velocity (BUNSHAH [1964]; TAKEUCHI [1966]), and under very non-uniform stresses, such as in surface indentations, they can spread quasistatically, and fully reverse when the stress is removed (CAHN [1954]). In crystals with moderate plastic slip resistance the very high stresses usually initiate local processes of plastic dissipation which level down the high stresses and remove the tendency of the twin to reverse. In the BCC lattice where the {112} composition plane and the <111> twinning direction are also the slip plane and the slip direction, the plastic dissipation is by emission of dislocations in the plane of the twin, (emissary dislocations, SLEESWYK [1963]), from its tip, thereby terminating the twinning process, but propagating and dissipating the concentrated shear. Since twins propagate very fast in materials with even moderate plastic slip resistance, it is not uncommon that stress relief occurs by local microcrack nucleation — particularly in crystals that can undergo cleavage.

In HCP metals and other systems with insufficient numbers of independent slip

Table 2
Mechanical twinning elements for metals (KLASSEN–NEKLYUDOVA [1964])

Metal	K_1	η_1	γ^T	Notes
		Face-centered cubic		
Cu	(111)	$[11\bar{2}]$	0.707	Only recrystallization twins (with these elements) occur in Ag, Al, Au, γ-Fe, and Co
		Body-centered cubic		
Cr, α-Fe, Mo, Na	(112) (441) (332)	$[11\bar{1}]$	0.707	
W	(112)	$[11\bar{1}]$	0.707	
		Diamond cubic		
Ge	(111)	$[11\bar{2}]$	0.707	
		Hexagonal Close Packed		
Be		$[\bar{1}011]$	0.199	c/a = 1.568
Cd		$[10\bar{1}\bar{1}]$	0.171	c/a = 1.886
Mg	$(10\bar{1}2)$	$[\bar{1}011]$	0.129	c/a = 1.624
Ti		$[\bar{1}011]$	0.189	c/a = 1.587
Zn		$[10\bar{1}\bar{1}]$	0.139	c/a = 1.856
Be	$(10\bar{1}1)$ $(10\bar{1}3)$			Additional Forms
Mg	$(10\bar{1}1)$	$[\bar{1}012]$	1.066	Ditto
	$(11\bar{2}1)$	$[\bar{1}\bar{1}26]$	0.638	,,
	$(11\bar{2}2)$	$[11\bar{2}3]$	0.957	,,
Ti	$(11\bar{2}3)$	$[\bar{1}\bar{1}22]$	1.194	,,
	$(11\bar{2}4)$	$[\bar{2}\bar{2}43]$	0.468	,,
	$\{30\bar{3}4\}$	$\langle 20\bar{2}3\rangle$	?	,,
				,,
				,,
	$\{10\bar{1}3\}$*	$\langle 30\bar{3}2\rangle$*	?	* 150 and 268°C
Bi	$(\bar{1}012)$	$[10\bar{1}1]$	0.118	
Hg	$(\bar{1}012)$	$[10\bar{1}1]$	0.447	
Sb	$(\bar{1}012)$	$[10\bar{1}1]$	0.146	
	$(10\bar{1}2)$	?	?	
α-Zr	$(11\bar{2}1)$	,,	,,	
	$(11\bar{2}2)$	,,	,,	
	$(11\bar{2}3)$	,,	,,	
		Tetragonal		
β-Sn	(301)	$[\bar{1}03]$	0.119	c/a = 0.541
In	(101)	$[10\bar{1}]$	0.150	c/a = 1.078
		Orthorhombic		
	$(1\bar{7}2)$	[312]	0.228	
	(112)	X[3$\bar{7}$2]	0.228	X = irrational twin
α-U	(121)	X[100]	0.329	
	(111)	$[12\bar{3}]$	0.214	
	(130)	$[3\bar{1}0]$	0.299	

References: p. 1951.

systems for unhindered deformation in polycrystals, twinning is an important supplementary form of plastic deformation (REED–HILL [1964]) that enhances formability.

6.3. Stress-induced martensitic transformations

In many crystal structures shear transformations exist, which upon completion, transform the sheared region into another crystal structure, such as the well known *martensite* transformation in carbon steels that converts FCC γ-Fe into a body centered tetragonal form, after which all such transformations have been named. Other similar and technologically important transformations include FCC to BCC in Fe–Ni (27–34% Ni) alloys; BCC to hexagonal in Ti; BCC to FC tetragonal in Cu–Zn (40% Zn) alloys, in metals, (KLASSEN–NEKLYUDOVA [1964]) tetragonal to monoclinic in ZrO_2, in ceramics, and orthorhombic to monoclinic, in polyethylene, with 6 different possible variants (BEVIS and CRELLIN [1971]). While the martensitic transformations are basically accomplished by shear, resulting in transformation shear strains of the order of 0.1–0.15 they are usually associated also with a substantial dilatational component of the order of 0.03–0.05. Moreover, the total transformation strain tensor depends on alloy content. The crystallography of martensitic transformations is usually complex and is made more so by the frequent occurrence of associated internal twinning in a number of variants. The early work has been summarized by KLASSEN–NEKLYUDOVA [1964], (including geometrical details of the transformation in many of the above listed cases) and the more recent work including assessment of mechanistic models by COHEN and WAYMAN [1981] and OLSON and COHEN [1986]. Many of the problems associated with the energetics of formation and propagation of twins also apply to martensitic transformations. Since stress-induced martensitic transformations can have very substantial and attractive benefits in toughening of ceramics and high strength steels, much recent research has been directed toward these effects (see OLSON *et al.* [1987]).

6.4. Kinking

Mineralogists have discovered in the past century (see MÜGGE [1898]) that certain minerals often deform plastically by undergoing organized simple shear by slip inside a narrow band in which the slip planes and the slip directions are perpendicular to the band boundaries as depicted in fig. 22. The role of this type of deformation in metal crystals with layered slip systems such as Zn was discussed by OROWAN [1942]. The formation of kink bands in Zn and Cd was investigated experimentally by GILMAN [1954] (see fig. 23), and the conditions for the growth of kink bands by a systematic process of punching of dislocation dipoles at the ends of the bands were investigated by FRANK and STROH [1952]. Kinking is ubiquitous when crystals with layered slip systems are subjected to compression parallel to the plane of the layers or extended normal to them. As pointed out by Orowan, in well accommodated kink bands the boundaries of the bands must bisect the lattice misorientation if the bands are to be free of long range stresses. This necessitates that the planes of the boundaries rotate at half the angular rate of the rate of increase of shear strain in the interior of the band. This is often not possible, resulting in the formation cleavage cracks in a variety of ways (GILMAN [1954]).

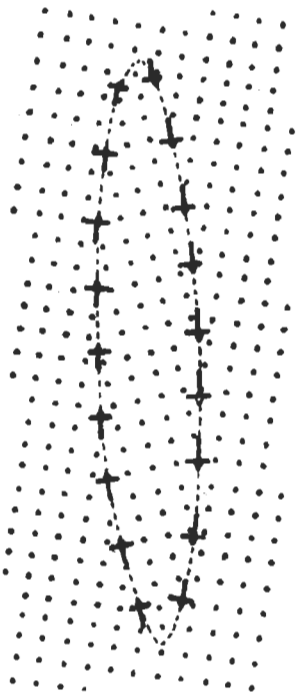

Fig. 22. A kink band formed by a stack of internal slip operations, and the resulting dislocation walls.

7. *Evolution of plastic resistance with strain: strain hardening*

7.1. General overview

In section 4 above, an intrinsic process of dislocation resistance was identified that results from the interaction of dislocations with each other during plastic deformation. Moreover, this resistance was ascribed to two separate parts: an *interplanar interaction* and an *intraplanar interaction* (HIRSCH and HUMPHREYS [1970]), where the former was identified to result from interaction of mobile dislocations and was, in itself, substantially independent of temperature, strain rate, and strain. How the interplane interaction couples to the intraplanar interaction will be discussed below in section 7.3.8. Here we discuss how the plastic resistance of slip planes increases with strain in single phase ductile metals which can undergo very large strains without deformation instabilities or fracture. Under certain conditions, which are discussed in section 10, deformation can localize in the form of a neck and the part undergoes rupture by thinning down to a pinpoint or knife edge. In compression the sample may undergo buckling. These are macroscopic features of plastic flow of no interest here. They can be circumvented by torsion experiments. Fracture, on the other hand, in a brittle or ductile form, can prematurely terminate deformation. In principle, at least, it can also be suppressed by a superposed pressure.

References: p. 1951.

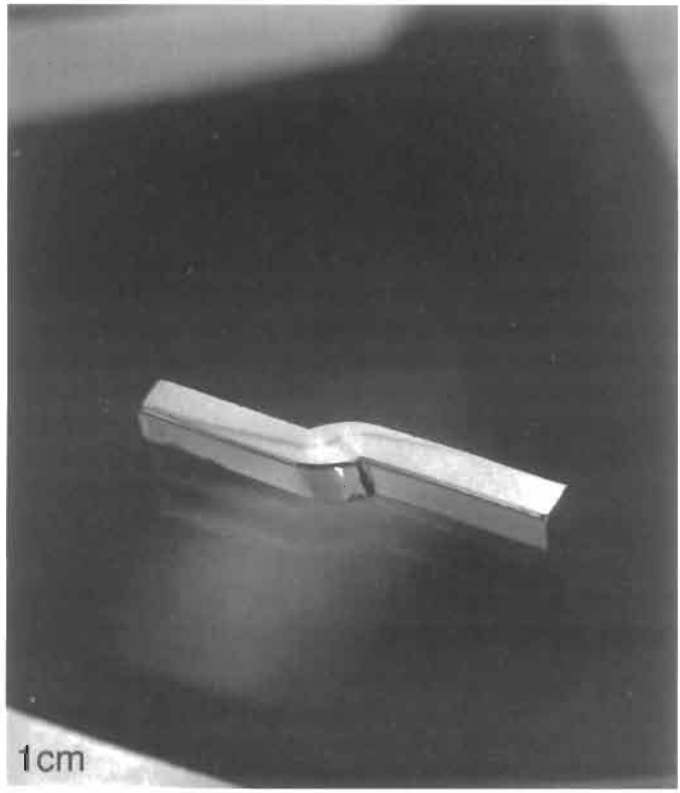

Fig. 23. A kinked Cd crystal. Shadow indicates trace of slip plane. (GILMAN [1961], Courtesy of McGraw-Hill).

Plastic resistance can be influenced by a strong lattice resistance at low temperatures or by various extrinsic processes related to second constituents that were discussed in section 4.3. The contribution of these can be separated by the superposition rules of section 4.4. When these precautions are taken, a remarkable degree of unity in the phenomena of strain hardening in all crystal classes appears — albeit some types may not exhibit all of the phenomena that crystals with an abundance of slip systems do. Thus, e.g., the strain hardening behavior of FCC, BCC, diamond cubic structures and ionic compounds such as NaCl, MgO, etc. are very similar at temperatures where the lattice resistance makes a negligible contribution. In HCP crystals and other layered materials where the characteristics of different slip systems can be very different, also when twinning is unavoidable, certain fundamental differences in the hardening behavior will be present.

We note that the *intraplane resistance* has a regular temperature dependent component that results from dislocation intersections. As was demonstrated by COTTRELL and STOKES [1955] and THORNTON *et al.* [1962], this component is usually a certain fraction of the total resistance, depending only on the mode of deformation. This so-called

Cottrell–Stokes law implies that during much of strain hardening the rate-controlling forest dislocation obstacles increase as a constant fraction of the total dislocation density. This temperature dependent behavior is fundamentally different from dynamic recovery which is present in a certain range of deformation and requires separate consideration.

The processes of strain hardening are extremely complex. In the initial stages of hardening they can be followed in some detail in single crystals of well chosen orientations, to shear strains of, perhaps up to 0.25 where meaningful attribution of strains to individual slip systems and resolution of stress on such systems is possible. At larger strains, however, differences in behavior between single crystals and polycrystals become less and less, as the accumulated dislocation configurations reduce in scale, and become of very much smaller dimensions than individual grain sizes. Thus, in subsequent sections we will consider the early stages of deformation primarily in FCC single crystals and the later stages in polycrystals. Moreover, these considerations are taken as generic and applicable to other crystal structures such as BCC, diamond cubic, NaCl, etc.

Finally in theoretical models we will follow the central processes, as much as possible, by dimensional analysis without delving into detail. For a more detailed review of the specific dislocation processes the reader is referred to NABARRO [1985].

7.2. Deformation features

7.2.1. The stress–strain curves

Figure 24 shows a family of resolved shear stress–strain curves, at room temperature, of Cu single crystals of a variety of orientations identified on the standard triangle on the left (DIEHL [1956]). A number of important points are apparent. Orientations C14, 18, 21, 25, 26, and 28 all maximize the resolved shear stress initially on only one slip system and therefore show very little initial hardening in a stage of deformation referred to variously as: *Stage I*, *Easy Glide*, or *laminar slip*. Here the reduced (with the shear modulus) strain hardening rate Θ_I/μ is typically in the range of $2–5\times 10^{-4}$. In compari-

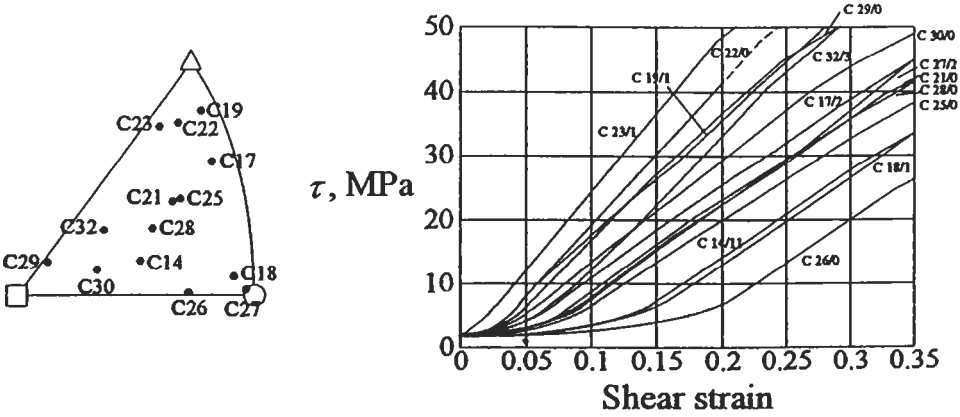

Fig. 24. The initial stages of strain hardening in FCC Cu single crystals at room temperature (DIEHL [1956], Courtesy of Z. Metallkunde).

son, crystals C19-22, 23, 29 are very close to high symmetry orientations where the resolved shear stress is large on several intersecting slip planes. As a result, crystals in these orientations show only a minimum of the Stage I behavior, but exhibit a high strain hardening behavior almost from the outset which the crystals of the first set only revert to after the Stage I behavior is exhausted. In this rapid hardening regime, labeled as *Stage II*, the reduced strain hardening rates Θ_{II}/μ are typically on the order of 10^{-2}. Polycrystals of high-melting-point pure FCC metals at room temperature exhibit only Stage II behavior from the very outset. This two mode behavior illustrates a fundamental aspect of all strain hardening by emphasizing that the rate of storage of dislocations, which is the fundamental basis of strain hardening, is governed by the presence of strong slip obstacles around which such storage can initiate and grow. In heterogeneous alloys with non-shearable particles these act as very effective sites for clustering of dislocations (ASHBY [1966]). In pure metals the obstacles have to be produced by intersecting slip itself. Crystals with an abundance of equivalent slip systems such as FCC, BCC, NaCl structure (ARGON *et al.* [1972]) etc., fall into this category while hcp crystals which deform primarily on the basal plane or on prism planes do not undergo intersecting slip until very late in their deformation. Therefore, their hardening behavior is dramatically different from the former group. This is demonstrated in fig. 25 (SCHMID and BOAS [1935]).

The stress–strain curves in fig. 24 show that all hardening curves in Stage II are substantially linear up to a point indicated on the curves where the hardening rate decreases. This non-linear behavior with progressively decreasing strain hardening rate is labeled *Stage III*. As stated earlier, for strains larger than roughly 0.25, or more precisely when the hardening behavior enters Stage III, no important differences remain between the behavior of single crystals and polycrystals. Therefore, for the later stages of strain hardening the polycrystal large strain torsion curves of Al and its various solid-solution and precipitation-strengthened alloys of fig. 26 can be considered as typical (ROLLETT [1988]). Stage II hardening behavior in these samples is severely contracted close to the stress axis on this scale of presentation. The figure shows clearly the

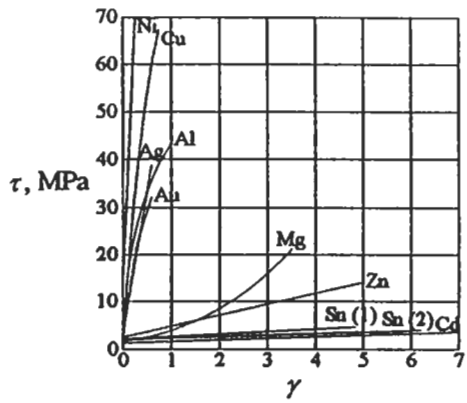

Fig. 25. Stress–strain curves of metal crystals. Those with intersecting slip show much higher hardening rates than those which do not (SCHMID and BOAS [1935]).

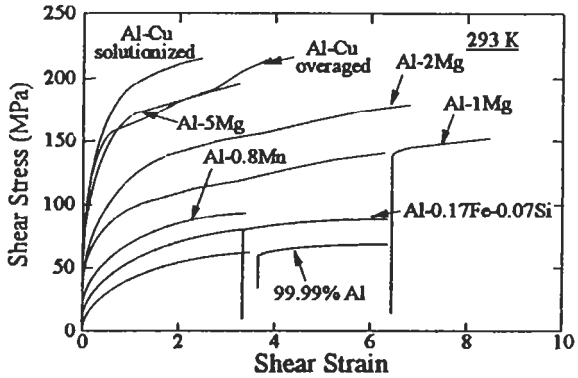

Fig. 26. Shear stress–shear strain curves of pure Al and dilute alloys obtained in torsion experiments at room temperature at $\dot{\gamma} = 6.9 \times 10^{-3}\ s^{-1}$ (ROLLETT [1988]).

parabolic Stage III hardening behavior terminating roughly at a shear strain of 1.0 beyond which there is a very long stage of low strain hardening, labeled as *Stage IV*, over strains reaching magnitudes of the order of 5–8, during which the reduced flow stresses τ/μ approach 0.01. The reduced strain-hardening rate in this stage, Θ_{IV}/μ, is of the order of that of Stage I, i.e., typically in the range of 5×10^{-4}. At very large strains Stage IV is terminated by a true saturation of hardening at *Stage V* (for an expanded discussion see ARGON and HAASEN [1993]). Apart from Stage I, all other stages of strain hardening have counterparts in BCC and in the diamond cubic structure. On the other hand, because of the relative rarity of intersecting slip, Stage I is dominant in HCP crystals, where it is called *Stage A*.

Of the five stages of strain hardening only Stage III and the terminal Stage V are temperature and strain rate dependent. Once reduced with the shear modulus, the hardening rates in Stages I, II, and IV are quite insensitive to temperature and strain rate. This effect is not very apparent in the stress–strain curves, but stands out clearly when the reduced strain hardening rates Θ/μ are plotted as a function of the reduced slip resistances τ/μ as shown in fig. 27 for Cu for five different levels of homologous temperatures — all comfortably in the range unaffected by diffusion (ALBERDI [1984]). The figure shows the strong temperature dependence in Stage III caused by dynamic recovery and the relative temperature independence of the hardening rate in Stage IV. Meanwhile, the basic temperature dependence of the plastic (slip) resistance remains relatively unaltered over the entire range of deformation as is demonstrated by the strain rate sensitivity of the reduced flow stress, indicated in fig. 28. At low temperatures there is no important discontinuity in the strain rate sensitivity at the transition between Stage III to Stage IV hardening (marked by an arrow in fig. 28), while at higher temperatures there is a small increase in the dependence at the point of the transition (ALBERDI [1984]). Similar results have been obtained for Al (ROLLETT [1988]) and Ni and its solid solution alloys (HUGHES and NIX [1989]).

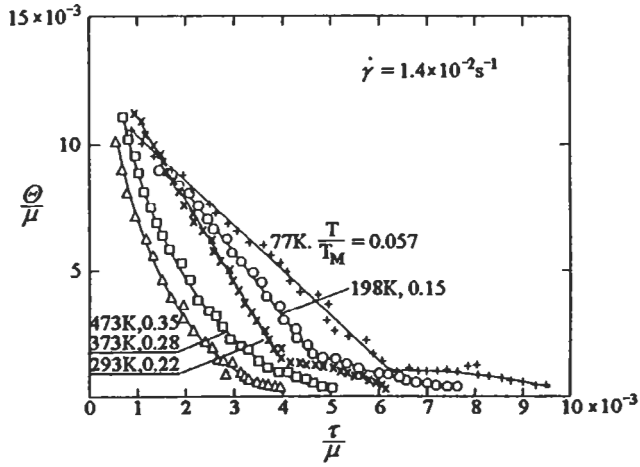

Fig. 27. Reduced strain hardening rate, Θ/μ, plotted against the reduced shear resistance, τ/μ, for polycrystalline Cu strained in torsion at low homologous temperatures (after ALBERDI [1984]).

7.2.2. Slip distribution and dislocation microstructures

Figure 29a shows the slip line distribution on a Cu crystal at the very end of Stage I at a total shear strain of 0.08. These slip lines are straight, remarkably uniformly distributed, on the average several mm long and very shallow (c.a. 2–3 nm deep). In Stage II the appearance of the slip lines are remarkably similar to those of Stage I but the new slip lines added in the course of further straining, are progressively shorter, and

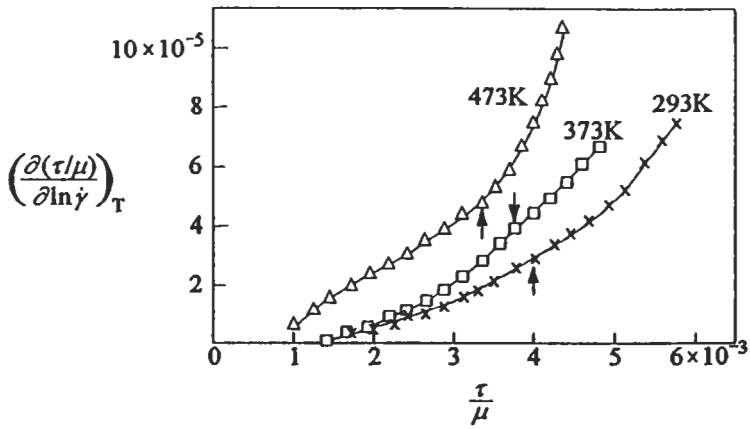

Fig. 28. Strain rate sensitivity of the reduced flow stress of Cu polycrystals strained in torsion, vs. reduced flow stress, obtained by a strain rate jump from 4×10^{-2} to 4×10^{-3}/s. Transition to Stage IV is shown by vertical arrows (ALBERDI [1984]).

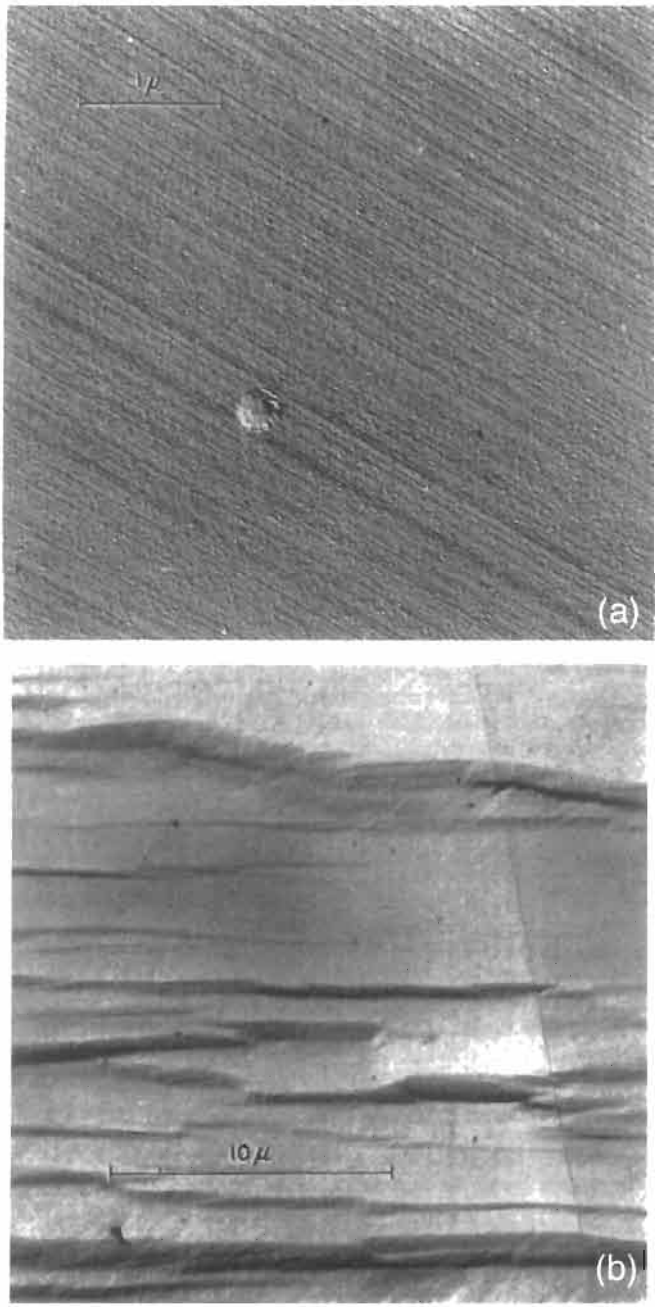

Fig. 29. Electron micrographs of a) slip lines at the end of Stage I ($\gamma = 0.08$) on a Cu single crystal (orientation C14 of fig. 24) deformed at room temperature; b) broken up coarse slip bands and traces of secondary slip in Stage III on Cu crystal (orientation C17). (SEEGER [1957], Courtesy of Wiley.)

References: p. 1951.

at the end of Stage II are only about 10 μm long. In Stage III where the hardening rate begins to decrease and becomes temperature dependent, the incremental additions of slip are in the form of broken-up coarse and deep slip bands as shown in fig. 29b (SEEGER [1957]). There is ample evidence of widespread cross slip. In Stage IV the incremental additions of slip bands resemble those of Stage II, as shown in fig. 30 (ROLLETT [1988]).

The forms of dislocation storage provide additional information on the hardening behavior. In Stage I dislocation storage is primarily in the form of well-screened multipolar groups or stacks of polygonized low angle walls as shown in the etch pit micrograph of fig. 31a for Cu (LIVINGSTON [1962]). Transmission electron microscopy (TEM) confirms that the stored dislocations are predominantly of edge character — with the screw components, apparently having been mutually annihilated by cross glide. In Stage II the predominant form of dislocation storage is in the form of open dislocation

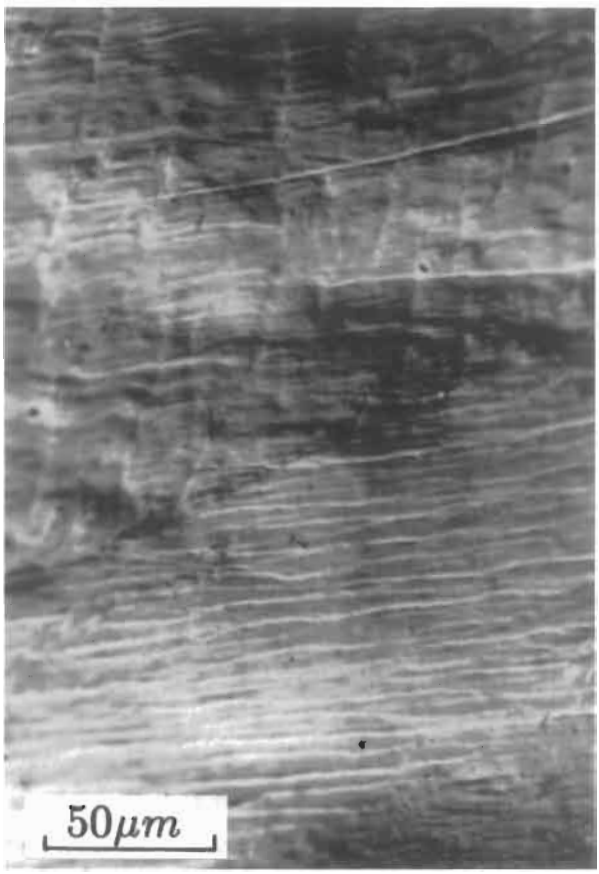

Fig. 30. Slip markings resulting from a strain increment of 0.09 on polycrystalline Al deformed in torsion in Stage IV up to a shear strain of 3.38 at room temperature. The slight wavyness of the slip markings are characteristic of Al which has a very high stacking fault energy (ROLLETT [1988]).

braids roughly perpendicular to the primary system Burgers vector, i.e., mostly of edge character as shown in fig. 31b (PRINZ and ARGON [1979]). Diffraction contrast analysis of the dislocation content of the braids shows a high concentration of short straight sessile dislocation segments parallel to <110> directions (Lomer–Cottrell segments) which form as a result of intersecting slip and apparently serve to anchor down the braids to the lattice. Toward the end of Stage II and all throughout Stage III these open

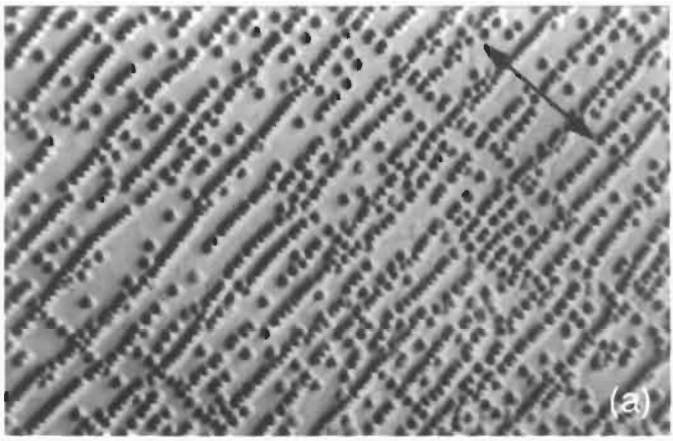

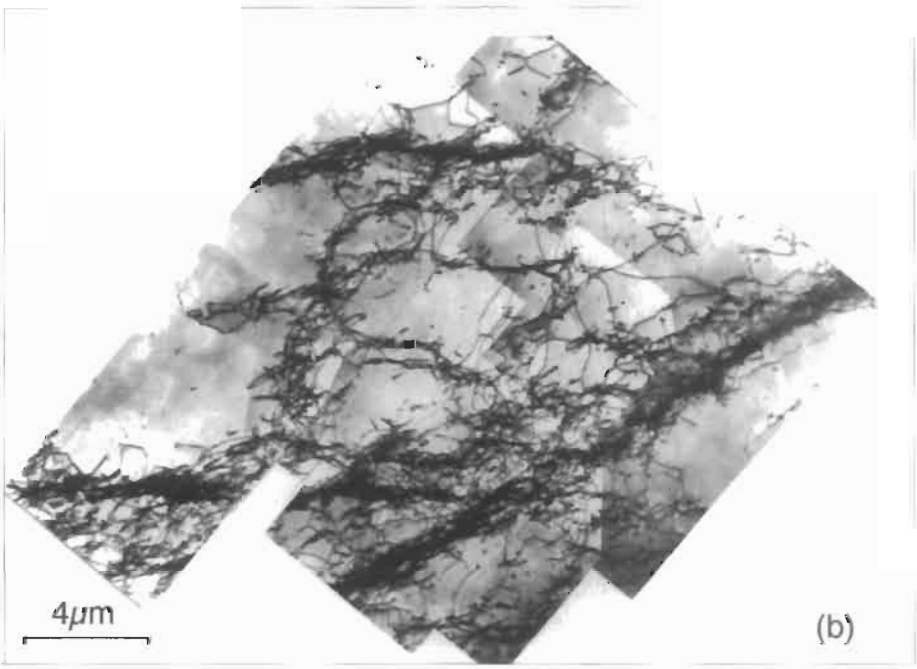

References: p. 1951.

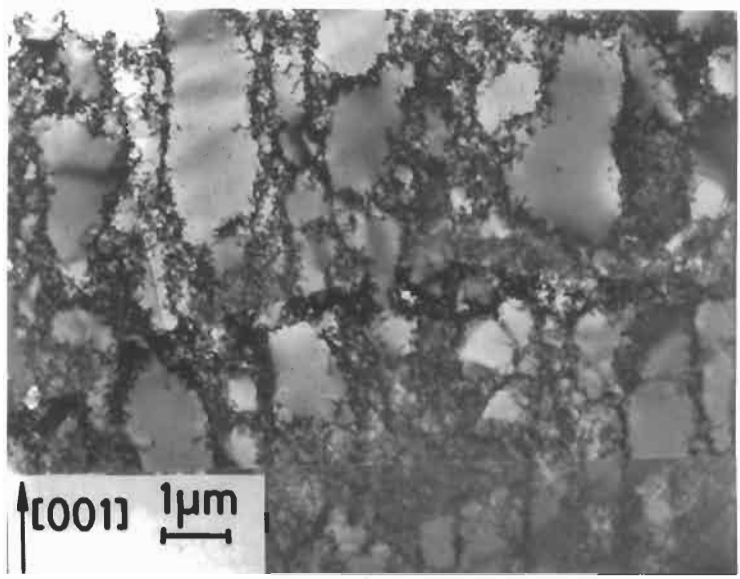

(c)

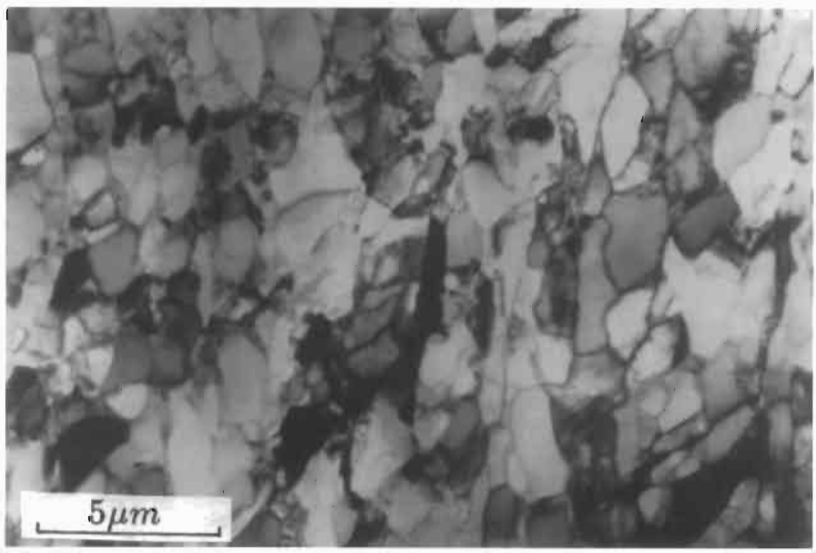

(d)

Fig. 31. Dislocation microstructures in various stages of strain hardening: a) etch pit pattern of multipolar dislocation structures in Stage I of Cu (LIVINGSTON [1962], courtesy Pergamon Press); b) dislocation braids in Cu crystal deformed at 77K to $\tau = 20$ MPa in Stage II viewed on primary plane slice (PRINZ and ARGON [1979], courtesy of Phys. Stat. Sol.); c) closed dislocation cells formed in Cu crystal deformed into Stage III at room temperature (MUGHRABI *et al.* [1986], courtesy of Taylor and Francis); d) cellular dislocation structure in pure Al polycrystal deformed to a strain of $\gamma = 3.46$ into Stage IV at room temperature (ROLLETT [1986]).

braids close up and form closed dislocation cells. With increasing flow stress in Stage III the cells refine in size in an apparently self similar form as shown in fig. 31c for Cu (MUGHRABI *et al.* [1986]). At the transition from Stage III to Stage IV the cell walls become sharply defined, and throughout Stage IV such well defined cells (often elongated in the direction of principal extensional strain), as shown in fig. 31d for Al (ROLLETT [1988]), continue to refine in scale.

A remarkable feature of this clustering process of dislocations being stored is its substantially self-similar nature. The principal braid spacing, and later the average cell diameter D, continues to relate to the plastic shear resistance τ by the general equation

$$D = K\left(\frac{\mu b}{\tau}\right) \tag{65}$$

where the constant of proportionality K is 5–10 (PRINZ and ARGON [1979]). While the mechanistic origin of this ubiquitous relationship remains obscure, its continued maintenance cannot be a result of motion of cell walls, which are too strongly anchored to the lattice by sessile defects, but is apparently accomplished by cell division (PRINZ and ARGON [1979]). It is usually referred to as the *principle of similitude* after KUHLMANN–WILSDORF [1968] who first drew attention to it. While corresponding information is sparse, the similitude applies also to the braid thickness or cell wall thickness w — with the ratio $f = w/D$ remaining roughly constant at a typical level of 0.1.

A further remarkable feature, indirectly associated with eq. (65), is the continued inverse proportionality between the average dislocation spacing l and the flow stress τ, or the square root of the total dislocation density ρ and the flow stress given by

$$\tau = \frac{\alpha\mu b}{\ell} = \alpha\mu b\sqrt{\rho} \tag{66}$$

where α is 0.2–0.3 (BASINSKI and BASINSKI [1979]). Below we will find it more meaningful to associate the plastic resistance τ with that of the cell walls τ_w and ρ with the dislocation density ρ_w in the cell walls — at least in the later stages of deformation.

Several additional observations on the mode of clustering are important. As figs. 31b, 31c and 31d show, in the relaxed state, the vast majority of the retained dislocations are tied to the braids or cell walls, and the cell interiors are substantially empty. While careful experiments of pinning dislocations by nuclear particle irradiation in the stressed state have indeed trapped dislocations inside cells, their density is some orders of magnitude lower than those retained in the walls (MUGHRABI [1975]). These must be identified as the mobile dislocations captured in transit.

Detailed measurements of lattice rotation by ROLLETT [1988] in pure Al, and some low concentration solid solution and precipitation strengthened alloys of Al, have shown a gradual increase of random misorientation between adjacent cells which reaches about 1° at the end of Stage III and continues to increase in Stage IV to reach 5–10° for very large shear strains in the range of 5–8.

7.2.3. Lattice elastic strains developing during deformation

There has been much evidence that, associated with the storage of dislocations in

braids and cell walls, there is a gradually increasing level of long range lattice elastic strain. Measurements of changes in magnetization in Ni with increasing plastic resistance by KRONMÜLLER [1967], measurement of the root mean square birefringence in NaCl single crystals deformed into Stage II by ARGON *et al.* [1972] have demonstrated that substantial levels of lattice elastic strains of relatively long-range build-up during plastic deformation and must play an important role in strain hardening. The most definitive measurements and unambiguous interpretation of the effect are based on the x-ray line broadening and peak shift measurements of MUGHRABI *et al.* [1986] and UNGAR *et al.* [1991] on Cu crystals deformed in the [001] orientation into Stage II and Stage III. These have demonstrated that in the unloaded state both the cell walls and the cell interiors are subjected to substantial uniaxial lattice elastic strains parallel to the principal direction of extension, and to a lesser extent in the transverse directions. The analysis of the measurements by MUGHRABI *et al.* [1986] have indicated that in the unloaded state the cell walls are in tension while the cell interiors are in compression. The direct internal stress measurement based on the organized birefringence in NaCl by ARGON *et al.* [1972] in Stage II have established that elongated cells normal to the active slip system are alternately in uniaxial tension or compression. While no direct measurements exist, it is most likely that such stresses increase in magnitude with increasing strain in Stages III and IV.

7.2.4. Dynamic recovery in Stage III

While the reduced strain hardening rates in Stages I, II, and IV are nearly constant and substantially independent of temperature and strain rate, the parabolic strain hardening behavior of Stage III is temperature and strain rate dependent. The slip distribution in Stage III has indicated that this dependence stems from dynamic recovery in the form of reduction of the dislocation storage rate due to concurrent enhanced annihilation of dislocations during glide made possible by thermally assisted cross slip of screw dislocations. These apparently trigger the removal of the less stable portions of dislocation clusters and reduce the strain hardening rate below what would be expected in Stage II. Since the transition from a constant hardening rate of Stage II to the progressively decreasing strain hardening rate, Θ, sets-in at a certain flow stress level τ that decreases with increasing temperature a convenient way of presenting the onset of cross slip controlled dynamic recovery is to plot $\tau\Theta$ as a function of τ for different temperatures of straining. Such a plot for Ag crystals is shown in fig. 32 (MECKING and KOCKS [1981]).

7.3. Theoretical models of strain hardening

7.3.1. The initial yield stress and strength differential effects

In pure FCC metals at room temperature the stress to move dislocations is immeasurably low. In very precise experiments TINDER and WASHBURN [1964] were unable to measure a threshold stress for the motion of dislocations in pure Cu crystals. The critical resolved shear stresses for initiation of plasticity measured in pure Cu single crystals by BRYDGES [1967] decreased continuously with decreasing forest dislocation density as shown in fig. 33. The straight line of the form

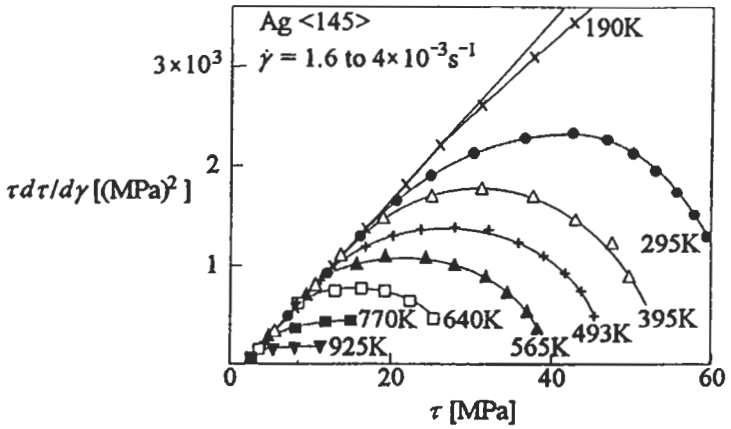

Fig. 32. Dynamic recovery in Ag single crystals deformed at different temperatures (MECKING and KOCKS [1981], courtesy of Pergamon Press).

$$\tau_y = \tau_{y_0} + \alpha\mu b\sqrt{\rho_f} \tag{67}$$

has a stress intercept at $\tau_{y_0} = 0.06$ MPa for vanishing forest density, ρ_f. While this intercept could be a result of experimental scatter it is also compatible with substitutional trace impurities at ppm concentrations (SUZUKI and ISHII [1969]). Of course, when the initial dislocation density in an FCC crystal is truly zero, the crystal becomes perfect and exhibits elastic behavior until the applied stress reaches levels close to the ideal shear strength as has been demonstrated in perfect Cu whisker crystals by BRENNER [1958]. Thus, barring the negligible effects of some trace impurities it must be concluded that the flow stress and the strain hardening in pure FCC metals is governed by dislocation interactions.

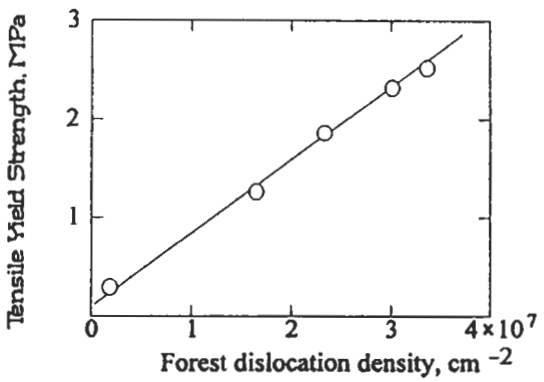

Fig. 33. Variation of the initial yield strength in shear of Cu single crystals as a function of their initial dislocation density (BRYDGES [1967], courtesy of Taylor and Francis).

References: p. 1951.

SCHMID and BOAS [1935], who initiated the systematic study of crystal plasticity stated that "a critical value of the resolved shear stress is required for the initiation of glide on a substantial scale". In this form the statement anticipates some of the interesting strength differential (SD) effects exhibited by BCC transition metals. In these materials the preponderance of slip activity on different possible slip planes is influenced by one or more forms of different core configurations of screw dislocations which make their motion on the {110} and {112} slip planes directionally anisotropic. Even in these instances while a predictive interpretation of the so-called Schmid law fails, when the conditions of glide on the actually observed slip systems are examined, the more conservative, (after the fact) interpretation of the law is found to be correct. The explanation of the SD effects in BCC metals based on the core structures of screw dislocations, which govern their directionally anisotropic mobility, is complex and beyond the scope of this treatment (see SUZUKI *et al.* [1991]).

7.3.2. Strain hardening rate in Stage I

In Stage I, where secondary slip activity is not present, strain hardening rate in pure FCC metals is governed by the unscreened ripple in the internal stress resulting from the rate of mutual trapping of edge dislocations into multipolar braids. Since the lattice resistance is negligible, however, the initiation of mutual trapping and the growth of multipoles requires a certain concentration of grown-in sessile dislocations not on glide planes. This is demonstrated in fig. 34 showing a two step etching experiment (ARGON and BRYDGES [1968]). The large etch pits are the grown-in dislocations while the small pits are due to the trapped dislocations following a small increment of plastic strain. The grown-in dislocations have not moved and the multipolar clusters resulting from the trapping of glide dislocations are forming around the grown-in dislocations acting as anchoring sites. Statistical models of such multipolar dislocation trapping developed by ARGON and EAST [1967] and ARGON [1969] give reasonable agreement with the observed low hardening rates in Stage I.

7.3.3. Strain hardening rate in Stage II

Elaborate models of strain hardening in Stage II based on interaction of glide dislocations with piled-up groups of dislocations have been developed by SEEGER [1956]. While these models introduced a number of important ideas such as the necessity of generating slip obstacles by intersecting slip and the role of long range lattice elastic strains, they have not had support from the observed dislocation structures in deformed crystals (MUGHRABI [1975]).

It is possible to capture the essence of Stage II hardening by rather elementary forms of dimensional analysis based on ideas put forth by KUHLMANN–WILSDORF [1962] and by KOCKS [1966]. In the model which we develop below we attribute the intra-plane hardening entirely to the interaction of the glide dislocations with the increasing density of forest dislocations as in the model developed by KOCKS [1966].

Thus, we consider the principal plastic resistance to arise from interaction of glide dislocations with both attractive and repulsive forest dislocation obstacles threading through the slip plane. Then, it is possible to define a penetrable, τ_p, and an im-

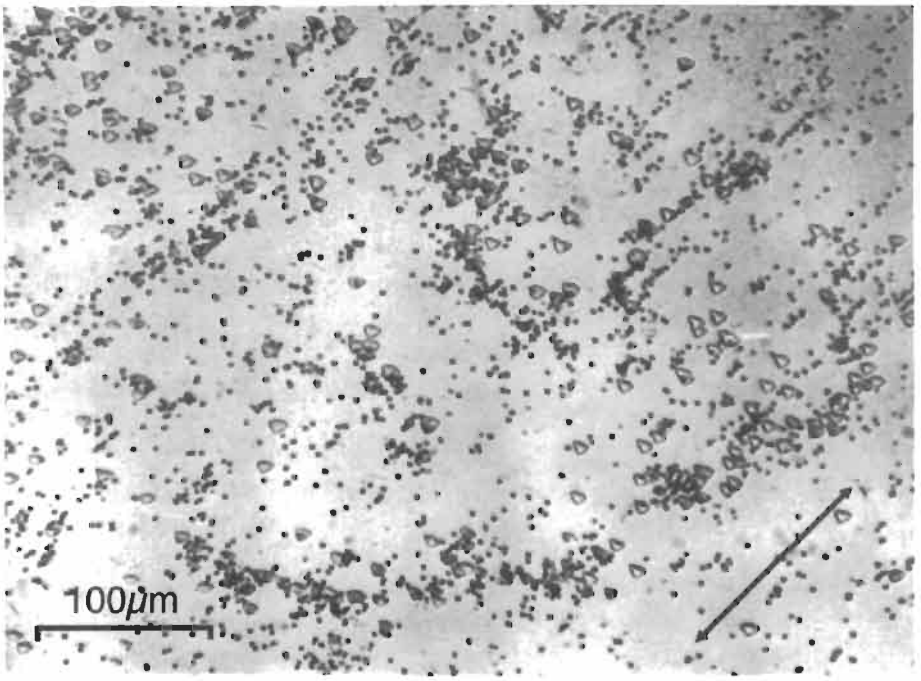

Fig. 34. Preferential formation of initial clusters by the trapping of glide dislocations (small pits), occurring in the neighborhood of grown-in sessile dislocations (large pits), revealed in a two-stage etching experiment (ARGON and BRYDGES [1968], courtesy of Taylor and Francis).

penetrable, τ_i, component of the slip resistance as:

$$\tau_p = \alpha_p \left(\frac{2\mathcal{E}}{bl_p}\right)\left(\frac{\hat{K}_p}{2\mathcal{E}}\right)^{\frac{3}{2}} \qquad \therefore \qquad \tau_i = \alpha_i \left(\frac{2\mathcal{E}}{bl_i}\right) \tag{68a, b}$$

where $\alpha_i = 0.85$ is a statistical factor, representing the effect of random distribution of local obstacles ($\alpha_p < \alpha_i$ is expected to be temperature dependent), l_p is the mean spacing between penetrable forest trees in the slip plane, l_i is the mean spacing of impenetrable trees, $\hat{K}_p$ the peak cutting force of penetrable "trees", and $\mathcal{E}$ is, as before, the line tension of the glide dislocations. According to the superposition law of slip plane resistances given by eq. (63), then the total plastic shear resistance τ is:

$$\tau = \sqrt{\tau_i^2 + \tau_p^2} \tag{63a}$$

$$\tau = \alpha' \left(\frac{2\mathcal{E}}{bl}\right) = \alpha' \mu b \sqrt{\rho} \tag{69}$$

$$l = \frac{l_p}{(1+\beta)^{\frac{1}{2}}} \quad \therefore \quad \beta = \left(\frac{\rho_i}{\rho_p}\right) = \left(\frac{l_p}{l_i}\right)^2 \tag{70a, b}$$

$$\alpha' = \sqrt{\frac{\left[\alpha_p^2\left(\frac{\hat{K}_p}{2\mathcal{G}}\right)^3 + \alpha_i^2\beta\right]}{1+\beta}}, \tag{71}$$

where l is the mean spacing of all forest obstacles in the plane, β the ratio of the density of the impenetrable to the penetrable forest dislocations; ρ_i, ρ_p, and ρ are respectively the impenetrable fraction, the penetrable fraction, and the total forest dislocation densities in the glide plane respectively, and all other terms are as defined previously.

Thus, on the basis of eq. (69), a change in the total shear resistance τ results from a strain induced change in the obstacle dislocation density ρ, i.e.,

$$d\tau = \left(\frac{\tau}{2}\right)\left(\frac{d\rho}{\sqrt{\rho}}\right). \tag{72}$$

The change in obstacle dislocation density results, however, from an increment of strain which has the following form:

$$d\gamma = \left(\frac{b}{V}\right)d\left(\sum_i \Delta a_i\right) = \left(\frac{b}{V}\right)d(L\Lambda_t) \tag{73}$$

where the sum on the Δa_i represents the entire area swept out by all glide dislocations during the strain increment, L is the mean free path of glide dislocations between sources and points of blockage and storage, and Λ_t is the total line length that has moved in a volume V of material. Thus, Λ_t/V is the total density of moved and subsequently blocked and stored dislocations during the increment of strain. Considering that the increment in the obstacle dislocation density must come from the increment of the density of blocked glide dislocations, it should follow that

$$d\gamma = bLd\rho \tag{74}$$

where it has been assumed that L is only slowly varying. If in addition, L is a multiple C_1 of the current mean obstacle spacing l in the plane, i.e.,

$$L = C_1 l, \tag{75}$$

then, the athermal strain hardening rate, $\Theta_{II} = d\tau/d\gamma$, must become

$$\Theta_{II} = \frac{\alpha'\mu}{2C_1}. \tag{76}$$

The statement in eq. (75) is another manifestation of the principle of similitude of eq. (65). It has been verified in computer simulations (KOCKS [1966]), where C_1 has been found to be in the range of roughly 15 for randomly placed obstacles. Since α is

typically 0.3 in the temperature range where penetrable forest dislocation obstacles are fully effective, and where some possible lateral motion of such dislocations is considered, a hardening rate of $\Theta_{II} = 10^{-2}\,\mu$ is found, which is close to the experimentally observed levels where dynamic recovery is absent.

7.3.4. Strain hardening rate in Stage III and dynamic recovery

The effect of dynamic recovery in reducing the strain hardening rate can be modeled in the same approach of dimensional analysis, as presented in section 7.3.3 for stage II (KOCKS [1976]).

We start by considering that the dynamic recovery steps are triggered by key cross-slip events of some screw dislocations where, e.g., a single glide dislocation or a small group initiates a cross slip annihilation event with some screw segments in an obstacle cluster. This then disturbs the equilibrium of some redundant dislocations in the cluster that had been held back by the eliminated segment, and results in a "glide collapse" process during which a certain decrease, $d\rho$, of total dislocation density occurs, nearly spontaneously, during the plastic strain increment $d\gamma$, which depends on the overall dislocation density itself. Thus, for the entire population

$$\left(\frac{d\rho}{d\gamma}\right)^{-} = -C_2\rho \tag{77}$$

where $C_2 = C_{02}P_{cs}$ and where P_{cs} is a probability of cross slip which under given local conditions of the annihilation encounter increases with increasing temperature. Since the total dislocation density is a measure of the plastic shear resistance as given by eq. (69), i.e.,

$$\tau = \alpha'\mu b\sqrt{\rho}, \tag{78}$$

incorporating the previously developed athermal strain hardening model

$$\left(\frac{d\tau}{d\gamma}\right)^{+} = \frac{\alpha'}{2C_1}\mu \tag{79}$$

gives a net strain hardening rate of

$$\left(\frac{d\tau}{d\gamma}\right)_{net} = \Theta_{III} = \frac{\alpha'(T)}{2C_1}\mu - \frac{C_2(T)}{2}\tau. \tag{80}$$

This can also be presented in reduced form as (MECKING and KOCKS [1981]),

$$\frac{1}{\mu}\Theta_{III} = \frac{\alpha'(T)}{2C_1} - \frac{C_2(T)}{2}\left(\frac{\tau}{\mu}\right), \tag{81}$$

or as,

$$\frac{\tau}{\mu}\left(\frac{\Theta_{III}}{\mu}\right) = \frac{\alpha'(T)}{2C_1}\left(\frac{\tau}{\mu}\right) - \frac{C_2(T)}{2}\left(\frac{\tau}{\mu}\right)^2 \tag{82}$$

where the form of eq. (81) gives the linear inverse dependence between the reduced strain hardening rate and the reduced flow stress shown in fig. 27, and the second form is exactly of the type shown in fig. 32, where the progressively earlier departures from linear behavior with increased temperature is influenced by the temperature dependence of $C_2(T)$.

7.3.5. Strain hardening rate in stage IV

While the strain hardening of Stages II and III are complex and are described best only in broad outline as we have done above, the mechanism of Stage IV hardening is, in comparison, much more amenable to a simple and specific explanation. This is a consequence of the relatively simple cellular dislocation microstructure that forms and refines throughout Stage III and enters Stage IV in a sharply defined form as shown in fig. 31d. The distinguishing features of hardening in Stage IV combine a low and temperature independent hardening rate with internal observations showing that nearly all the stored dislocations are found in the cell walls with a density close to or equal to that of saturation (ESSMANN and MUGHRABI [1979]), while the cell interiors are nearly fully devoid of dislocations. A number of investigators (PRINZ and ARGON [1984]; NIX *et al.* [1985], ZEHETBAUER [1993]) have developed two component composite models of strain hardening based on closely interacting processes of hardening and recovery in both the cell walls and the cell interiors. The model due to ARGON and HAASEN [1993] that we will present below also takes this point of view but makes important departures based on the following observations that: a) the hardening in the cell walls has reached saturation at a resistance τ_{ws} above the flow stress, τ_{III_s}, where the extrapolated Θ_{III} hardening rate vanishes, (see fig. 27); b) for $\tau > \tau_{III_s}$ the hardening rate of Θ_{IV} appears to be related directly and entirely to the substantial lattice elastic strains building-up in the interiors of the cells; c) during stage IV the cellular microstructure continues to refine with increasing flow stress in a self similar manner, obeying the principle of similitude, with $f = w/D$ remaining constant and d) the lattice misorientations ψ between cell interiors, which start at a level of about 1° at τ_{III_s}, continue to increase slowly in Stage IV.

Thus, for $\tau > \tau_{III_s}$ the overall plastic resistance becomes

$$\tau = f\tau_{ws} + (1 - f)\tau_c \tag{83}$$

where τ_{ws} $(=\alpha'\mu b\sqrt{\rho_{ws}})$ is the saturation plastic resistance of the cell wall material at a saturation dislocation density of ρ_{ws} and f their volume fraction, τ_c is the plastic resistance of the cell interiors devoid of any substantial dislocation population, being therefore, of an energy storing nature, related to the small but growing lattice misorientations between cells due to a storage in the walls of a subset of glide dislocations. It is conjectured that this storage is a result of random variations in the interpenetrating, cross flowing, dislocation fluxes producing the principal glide strain γ and that the lattice misorientation ψ increases as a function of $\gamma^{1/2}$ in the sense of random error accumulation, as

$$\psi = B\gamma^{\frac{1}{2}}. \tag{84}$$

Since the slip line lengths are always substantially larger than the cell sizes, D, it must be concluded that glide dislocations either directly, or virtually (by a relay race) cut through the cell walls. If this were to happen, the lattices of the cells would be alternately jacked-up or compressed elastically, which can be represented by a rate of build-up of a linear density N (with spacing h) of virtual sessile dislocations with Burgers vector ψb (normal to the glide plane), per unit length of cell wall (ARGON and HAASEN [1993]),

$$\frac{dN}{dt} = \frac{d}{dt}\left(\frac{1}{h}\right) = \phi \tag{85}$$

where ϕ is the total flux of glide dislocations ($= \bar{v}\rho_m$ with ρ_m being the mobile dislocation density and $\bar{v}$ their average velocity). Then, the rate of build-up of lattice elastic strains ε_c^e in the cell interiors with alternately + or − sign is

$$\left|\frac{d\varepsilon_c^e}{dt}\right| = \psi b \frac{dN}{dt} = b\psi\phi, \tag{86}$$

or on the basis of shear strain increment

$$\left|\frac{d\varepsilon_c^e}{d\gamma}\right| = \frac{1}{\dot{\gamma}}\left|\frac{d\varepsilon_c^e}{dt}\right| = \psi = B\gamma^{\frac{1}{2}}. \tag{87}$$

Considering that this build-up should commence early in Stage II (or with the beginning of deformation),

$$\left|\varepsilon_e^c\right| \cong \tfrac{2}{3} B\gamma^{\frac{3}{2}}. \tag{88}$$

Then the elastic strain energy of jacking-up the lattice per unit volume should be (ARGON and HAASEN [1993])

$$\Delta F = \tfrac{4}{9}\frac{B^2\gamma^3\mu}{(1-\nu)}. \tag{89}$$

Although this free energy storage occurs "orthogonally" to the active slip system it is energetically coupled to it and this results in the sought after rate independent plastic resistance τ_c of the cell interiors, i.e.,

$$\tau_c = \frac{d\Delta F}{d\gamma} = \tfrac{4}{3}\frac{B^2\gamma^2\mu}{(1-\nu)}. \tag{90}$$

Since, for $\tau > \tau_{IIIs}$, $d\tau_{ws}/d\gamma \cong 0$,

$$\frac{1}{\mu}\Theta_{IV} = \frac{1}{\mu}\frac{d\tau}{d\gamma} \approx \frac{(1-f)}{\mu}\frac{d\tau_c}{d\gamma} = \tfrac{8}{3}\frac{(1-f)}{(1-\nu)}B^2\gamma. \tag{91}$$

References: p. 1951.

Moreover, from eqs. (83) and (90)

$$\gamma = \sqrt{\tfrac{3}{4}\frac{(1-\nu)}{B^2}\left(\frac{\tau_c}{\mu}\right)} = \frac{g\left(\frac{\tau_{ws}}{\tau}\right)}{B}\sqrt{\tfrac{4}{3}\frac{(1-\nu)}{(1-f)}\left(\frac{\tau}{\mu}\right)} \tag{92}$$

with

$$g\left(\frac{\tau_{ws}}{\tau}\right) = \sqrt{1 - f\left(\frac{\tau_{ws}}{\tau}\right)} \approx 0(0.35), \left(\text{at } \tau \approx \tau_{IIIs}.\right) \tag{93}$$

which finally gives for the reduced strain hardening rate of Stage IV:

$$\frac{1}{\mu}\Theta_{IV} = \frac{4\sqrt{3}}{3} B\sqrt{\frac{1-f}{1-\nu}}\, g\left(\frac{\tau_w}{\tau}\right)\sqrt{\frac{\tau}{\mu}}. \tag{94}$$

For $B = 1.75 \times 10^{-2}$ ($\psi = 1°$ at $\gamma = 1.0$, (ROLLETT [1988])), $f \approx 0.1$, $\tau_{IIIs} \approx 4 \times 10^{-3}\,\mu$ at RT for Cu (see fig. 27), $\Theta_{IV}/\mu \approx 10^{-3}$, and is rising slightly with increasing $\sqrt{\tau/\mu}$ as the behavior depicted in fig. 27 suggests (ARGON and HAASEN [1993]). While this hardening rate is somewhat higher than the measured rates, it could be readily smaller if the jacking processes of the lattice are less efficient than they have been described. The hardening rate is strain rate and temperature independent and is qualitatively in agreement with the lattice elastic strains measured by MUGHRABI *et al.* [1986], and with the photoelastically measured lattice elastic strains of ARGON *et al.* [1972] in NaCl.

The rate-independent hardening process eventually saturates at Stage V, when the very substantial lattice elastic strains of eq. (88) become spontaneously relaxed by local secondary slip processes initiated from the cell walls (ARGON and HAASEN [1993]).

7.3.6. Latent hardening

In crystal structures having a number of equivalent slip systems, or even in those where different intrinsic resistances differentiate families of systems, once deformation is initiated in a given system the storage of dislocations of the active plane creates a rising density of slip obstacles for the other systems which may not have undergone much deformation. Thus, these systems will also harden with little or no glide strain occurring on them. This phenomenon of hardening of a slip system without expenditure of glide strain is called *latent hardening*. It has a number of important consequences. First, in crystals with high symmetry orientations when deformation is arranged to occur on more than one slip system, often only one system in a certain region is activated. For example in FCC crystals at or near the [110] orientation where four slip systems are equally stressed, and high rates of hardening might be expected, some of the longest stretches of Stage I and the lowest rates of hardening are observed (orientations C18, C26, C27 in fig. 24); in the NaCl structure, deformation in the [100] orientation where six slip systems are equally favored, often only one is found active and substantial ranges of Stage I deformation is observed (ARGON *et al.* [1972]). Moreover when, in a high-symmetry orientation, deformation actually occurs on more than one slip system, this

occurs in a patchy fashion with different systems dominating in different regions with little interpenetration of slips as is shown in fig. 35 for a Cu crystal deformed near the [110] orientation (SAIMOTO [1963]).

7.3.7. Transient creep at low temperatures

Another manifestation of the temperature and strain rate dependence of the plastic resistance at low temperatures where diffusion is not present is transient creep at constant stress. From the pioneering experiments of ANDRADE [1910] it has been established that at low temperatures, if a constant strain rate experiment is changed into a constant stress experiment at a given strain γ_0, the straining will continue for a while at a decreasing rate.

If the experiment is carried out on FCC metals of high melting temperature such as Cu, for moderate pre-strains γ_0, taking the deformation only into Stage II, the creep strain rate $\dot{\gamma}$ is found to decrease in inverse proportion with time. This leads to an increase in creep strain logarithmic in time, being appropriately referred to as *logarithmic creep*.

At somewhat higher temperatures, or more likely, also, with more substantial pre-strains (higher applied stresses) Andrade has found that the creep strain rate is larger than that at lower temperatures where logarithmic creep prevails, and that the new creep strain

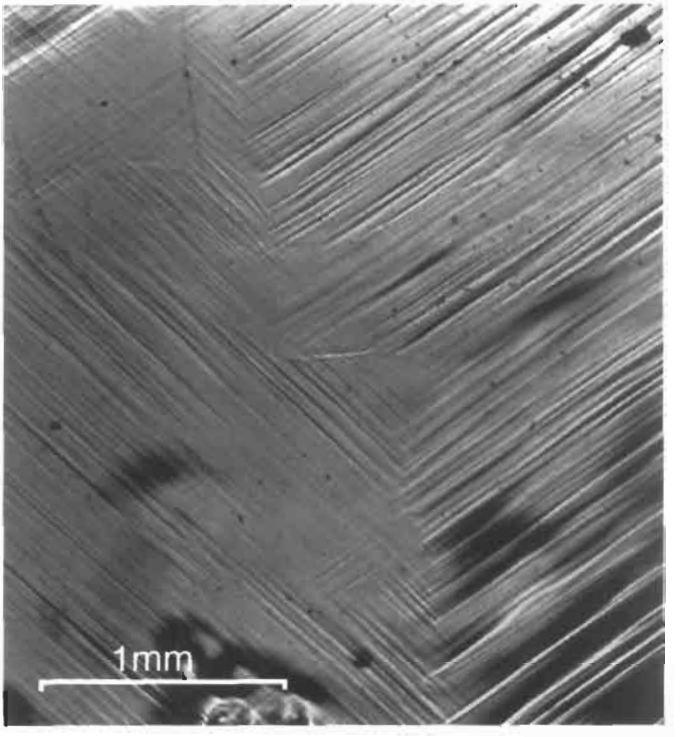

Fig. 35. Formation of patchy slip domains in a Cu crystal of [110] orientation, strained 10% (SAIMOTO [1963]).

rate is proportional to the reciprocal $\frac{2}{3}$ power of time, or that the time dependence of the creep strain is given by $t^{1/3}$ (WYATT [1953]). Moreover, the creep rate is more temperature dependent. This has been referred to as *Andrade creep*, and has been associated with some recovery processes (OROWAN [1952]) (for further discussion see VAN BUEREN [1960]).

While there have been many satisfactory explanations of logarithmic creep, there have been few satisfactory models for Andrade creep (see ARGON and BHATTACHARYA [1987] and COTTRELL [1995] for discussions). These two modes of non-diffusive creep response are a natural consequence of Stage II and Stage III hardening, and rate dependence of plastic resistance.

7.3.7.1 Logarithmic creep. The kinetic law of the plastic strain rate of eq. (31) is often given in a power law for operationally convenient application in a narrow range of stress and constant temperature as (see ARGON and BHATTACHARYA [1987])

$$\frac{d\gamma}{dt} = \dot{\gamma}_0(T)\left(\frac{\sigma}{\tau}\right)^m, \tag{95}$$

where σ is the applied shear stress, τ the current athermal deformation resistance, and $\dot{\gamma}_0(T)$ is a temperature dependent fitting factor accounting for all other specific dependencies of eq. (31). The exponent m, is typically in the range of 40 but decreases with increasing temperature. Consider a constant strain rate experiment with an initial shear strain rate of $\dot{\gamma}(0)$ converted into a constant stress experiment at a pre-strain of γ_0 in Stage II, whereupon the further strains are considered as creep strain. At the instant of conversion the current deformation resistance is τ_0 but continues to increase with strain as follows

$$\tau(\gamma) = \tau_0(\gamma_0) + \Theta_{II}(\gamma - \gamma_0). \tag{96}$$

Substitution of eq. (96) into (95), followed by integration and reference to the condition of initiation of the creep experiment gives

$$\gamma = \gamma_0 + \frac{\tau_0}{\Theta_{II}}\left[\left((m+1)\frac{\Theta_{II}}{\tau_0}\dot{\gamma}(0)t + 1\right)^{\frac{1}{m+1}} - 1\right]. \tag{97}$$

Re-differentiation of γ with time and examination gives,

$$\frac{d\gamma}{dt} = \dot{\gamma}(0)\left((m+1)\frac{\Theta_{II}}{\tau_0}\dot{\gamma}(0)t + 1\right)^{-\frac{m}{m+1}} \to \dot{\gamma}(0)\frac{1}{(m+1)\left(\frac{\Theta_{II}}{\tau_0}\right)\dot{\gamma}(0)t} \tag{98}$$

by virtue of the fact that $m/m+1 \to 1.0$ for large m, and $t > 0$.

This expression is a clear statement of logarithmic creep which can be presented in a more pleasing form through the use of eq. (95) once again as

$$\frac{d\gamma}{dt} = \frac{1}{m+1}\left(\frac{\sigma}{\Theta_{II}}\right)\left(\frac{\dot{\gamma}_0(T)}{\dot{\gamma}(0)}\right)^{\frac{1}{m}}\frac{1}{t} \tag{98a}$$

where explicit stress and temperature dependencies appear.

7.3.7.2 Andrade creep. For the case of Andrade creep we will start with an alternate statement of the creep law and demonstrate in reverse steps that it is fully consistent with dynamic recovery as stated in eq. (80). We start with

$$\frac{d\gamma}{dt} = \dot{\gamma}(0)\left(\frac{\gamma_0}{\gamma}\right)^2 \tag{99}$$

where all terms have their previously assigned meanings and strains are total strains. The expectation is that the pre-strain and the test temperature have taken the conditions of change-over into Stage III. Returning to eq. (95) we write it as

$$\frac{d\gamma}{dt} = \dot{\gamma}_0\left(\frac{\sigma}{\tau}\right)^m = \dot{\gamma}_0(0)\left(\frac{\tau_0}{\tau(\gamma)}\right)^m \tag{100}$$

where the second expression refers to the conditions where the experiment is converted into a constant stress experiment, with $\tau(\gamma)$ continuing to increase according to Stage III hardening. If the conditions of Andrade creep are to be consistent with expression (100), it is necessary that

$$\left(\frac{\gamma_0}{\gamma}\right)^2 = \left(\frac{\tau_0}{\tau}\right)^m, \tag{101}$$

from which certain implications of strain hardening appear. These can be deduced by obtaining the implied strain hardening rate Θ by differentiation as,

$$\Theta = \frac{2\tau_0}{m\gamma_0}\left(\frac{\tau_0}{\tau}\right)^{\frac{m-2}{2}} = \frac{m}{2}\Theta_0 - \left(\frac{m-2}{2}\right)\frac{\Theta_0}{\tau_0}\tau \tag{102}$$

with $2\tau_0/my_0 \equiv \Theta_0$, and where the last form is the result of a Taylor expansion of Θ at $\tau = \tau_0$. Clearly, if $m/2\,\Theta_0 = \Theta_{II}$ and $(m-2)/2\,(\Theta_0/\tau_0) = C_2(T)/2$ of eq. (80), the expected consistency is demonstrated. Using experimental values $\Theta_{II} = 10^{-2}\,\mu$, and $C_2(T)/2 = 3.3$ we obtain, with $m \gg 30$, $\tau_0/\mu = 3.0 \times 10^{-3}$ and $\gamma_0 = 0.3$. These are eminently acceptable values consistent with typical conditions of Stage III deformation, as is apparent from fig. 27.

In a very general and non-specific model Cottrell (1995) has demonstrated that the observed dependence of the creep strain rate on the inverse second power of creep strain in Andrade creep is consistent with the expected decrease of the volume of coherent shear relaxations with strain hardening.

7.3.8. Bauschinger effect

When monotonic plastic deformation is interrupted and reversed, the initial form of response is reverse elastic deformation as the concurrently elastically strained lattice

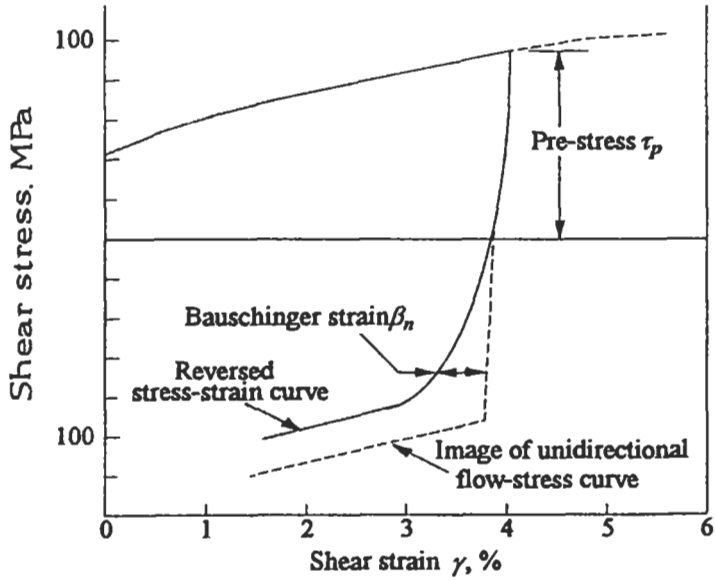

Fig. 36. Bauschinger effect in decarbonized polycrystalline steel in torsion (DEAK [1961]).

unloads. This effect, however, is soon followed by a departure from pure elastic response by reverse plastic straining that often begins well before the elastic unloading is completed. Continued reverse deformation will then show a very soft response on the way to large reverse plastic flow in the form of a rounded stress strain curve as depicted in fig. 36. This gradual and softened onset of reverse plastic flow is referred to as the *Bauschinger effect*, after its discoverer.

The general characteristics of the Bauschinger effect are that a) the Bauschinger strain β_n at any point in the reverse deformation half cycle increases with the initial flow stress level, and b) upon reaching the condition of reverse flow shows a permanent softening as illustrated in fig. 36. Moreover, these features of the reverse behavior are relatively resistant to removal by mild forms of heat treatment that do not produce major alterations in the total dislocation density.

The Bauschinger effect manifests itself most strongly in polycrystalline material. It is, however, present also in single slip. This has been investigated in basal slip in Zn single crystals by EDWARDS and WASHBURN [1954] who have probed the deformation resistance not only in the reverse direction but also in other directions in the base plane, between the forward and the fully reversed directions. They found that while there was early inelastic response in all directions the departures from elastic unloading was maximum in the fully reversed direction. A very prominent form of Bauschinger effect was reported by BROWN and STOBBS [1975] and ASARO [1975] in lightly dispersion strengthened Cu single crystals where the so-called Orowan loops of dislocations shown in fig. 13, and other polarized dislocation structures left around impenetrable dispersoids set up image stresses in the matrix which result in the observed soft initial reverse

response. These loops, however, are also responsible for the permanent softening effect when long range reverse deformation begins and the glide dislocations moving in the reverse direction remove some of the Orowan loops.

The fundamental cause of the Bauschinger effect is the inhomogeneous nature of plastic flow in which plastic strain increments, whether by slip or by shear transformations, occur in more intense form in separate volume elements, resulting in the continued development of residual back stresses in the elastic, or less intensely deformed background. Thus, upon reversal of strain, the residual stresses around the plastic inhomogeneities will hasten reverse deformation in the regions that have contributed to the deformation most recently. This process intensifies throughout strain hardening. In polycrystalline material where grain boundaries are natural barriers to long range slip the development of grain-scale residual stresses accentuate the Bauschinger effect (for complementary perspectives see OROWAN [1959] and VAN BUEREN [1960]).

7.3.9. Balance between the inter-plane and intra-plane resistances and the mobile dislocation density

In section 4.3.1 the notion was introduced that the dislocation resistance should be considered to be made up of an interplane and an intraplane resistance where the former is a result of the encounter of mobile dislocations with each other and the second denotes the resistance in the slip plane itself. For the latter, a number of prominent mechanisms were discussed in section 7.3.2–7.3.5. These two resistances are integrally coupled, as was pointed out by HIRSCH and HUMPHREYS [1970]. Referring to fig. 8 of two opposite type edge dislocations, each in a generic cell of size $C'H^2$ interacting, as a characteristic encounter of mobile dislocations of density $\rho_M = 1/C'H^2$, we consider the kinematic (and kinetic) equation of shear strain rate

$$\dot{\gamma} = b\bar{v}\rho_M \tag{103}$$

where

$$\bar{v} = v_0\left(\frac{\tau_{\text{intra}}}{\hat{\tau}}\right)^m \exp\left(\frac{-\Delta F_0}{kT}\right) \tag{104}$$

and where the forms of eqs. (103) and (104) together represent a phenomenological approximation to eq. (31) as we already used in eq. (95), v_0 being a geometrical pre-exponential term. Then, considering the interplane resistance, τ_1, of eq. 45b and the intraplane resistance or τ_2, with

$$\tau_1 = \frac{\mu b}{4\pi}\sqrt{C'\rho_M} \tag{105}$$

$$\sigma = \tau = \tau_1 + \tau_2, \quad \text{(at flow)} \tag{106}$$

with the abbreviations $bv_0 \cdot \exp(-\Delta F_0/kT) = B$ and $D = \mu b/4\pi\sqrt{C'}$,

$$\dot{\gamma} = B\rho_M\left(\frac{\sigma - D\rho_M^{\frac{1}{2}}}{\hat{\tau}}\right)^m. \tag{107}$$

References: p. 1951.

We note that $\dot{\gamma}$ is maximized when ρ_M reaches

$$\rho_{Mss} = \left(\frac{2}{2+m}\frac{\sigma}{D}\right)^2 = \frac{1}{C'}\left(\frac{8\pi}{2+m}\right)^2\left(\frac{\sigma}{\mu b}\right)^2. \tag{108}$$

This can be taken as the steady-state mobile dislocation density (ALEXANDER and HAASEN [1968]; ARGON [1970]). Considering that in low temperature plasticity $m \approx$ 30–40, and taking $C' \cong 10$ as reasonable, for a flow stress $\sigma/\mu = 10^{-3}$; typical of the mid range of Stages II or III,

$$\rho_{Mss} \approx 0\left(6 \times 10^7 \text{cm}^{-2}\right), \tag{109}$$

is obtained. This gives as an estimate of a typical interplane resistance to flow stress ratio of:

$$\frac{\tau_{\text{inter}}}{\sigma} = \left(\frac{2}{2+m}\right). \tag{110}$$

which for low temperature plasticity is typically 0.06, or generally negligible in comparison with the intraplane resistance as long as m is large. In more strain-rate sensitive materials with smaller m the effect of the interplane resistance, or the dependence of the behavior on the changes in mobile dislocation density can be more significant.

7.3.10. Yield phenomena

In many instances initiation of plastic deformation requires the application of an excess stress as shown, e.g., for the case of the initially aged α-Fe single crystal shown in fig. 37a (PAXTON and BEAR [1955]). Such behavior is referred to as a *yield phenomenon*. Figure 37b shows that for a complementary case of 1020 steel, unloading and immediate re-loading results in a barely perceptible elevation of flow stress for further deformation but that a 10 minute aging of the material at 100°C in the unloaded state results in the reappearance of a new pronounced yield phenomenon, and a fairly significant elevation of the flow stress upon re-loading after only 1 minute aging at 100° C. In the steel containing interstitial carbon, these phenomena are due to inactivation of mobile dislocations by carbon atoms. Thus, when the deformation is re-initiated there is initially a large deficiency of mobile dislocations below the steady state level suggested by eqs. (108) and (109) and generating the required concentration of new mobile dislocations requires the excess stress of the yield phenomenon. This behavior has been widely reported for many different initially "nearly perfect" crystals such as LiF (JOHNSTON and GILMAN [1959]); Si (ALEXANDER and HAASEN [1968]); GaAs (YONENAGA *et al.* [1987]); GaAsP (YONENAGA *et al.* [1989]); GaP (YONENAGA and SUMINO [1989]).

The theory of the development of such intrinsic yield phenomena has been proposed by JOHNSTON [1962], intended to explain the behavior of LiF crystals, but more broadly the behavior of all such initial glide transients. The principal ingredients are the strong stress dependence of the dislocation velocity given by an expression of the type of eq. (104), the kinematic expression for the plastic strain rate given by eq. (103), and the phenomenological observation of JOHNSTON and GILMAN [1959] that the mobile

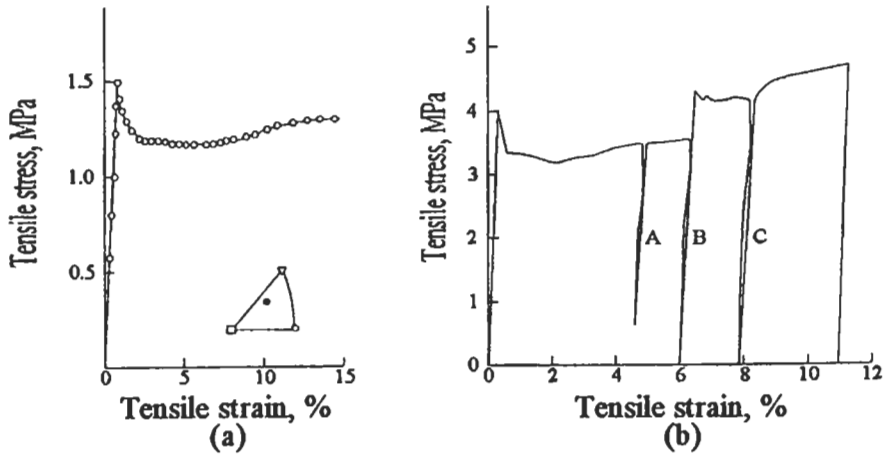

Fig. 37. (a) Yield phenomeon in a single crystal of α-Fe with 30 ppm of C, strained at 195 K at a rate of $\dot{\varepsilon} = 10^{-5}$ sec^{-1} (PAXTON and BEAR [1955]); (b) yield phenomenon in a normalized 1020 steel strained at a rate of 10^{-5} sec^{-1}. Path A represents unloading and immediate re-loading. Path B is for unloading with a 10 minute heat treatment at 100°C giving a new yield phenomenon. Even a 1 minute treatment (Path C) at 100° C brings back a yield phenomenon.

dislocation density initially increases in direct linear proportion with the total plastic shear strain, by kinematical processes of multiplication. These expressions, coupled with the statement that the condition imposed on the deformation process is one of constant total strain rate (i.e., the sum of the elastic stretching rate and the plastic strain rate), are sufficient to calculate by numerical methods the fundamental response of an initially dislocation deficient crystal. Johnston's calculated response of LiF crystals with different densities of initial mobile dislocations is shown in fig. 38a. These curves compare very well with the experimental stress strain curves of such crystals giving the effect of increasing amounts of pre-strain, which is to be construed as gradually increasing initial densities of mobile dislocations obtained by repeatedly straining through the upper yield points, unloading quickly and straining again.

As discussed in section 7.3.9, with increasing strain rate sensitivity of the flow stress, i.e., decreasing stress exponent m, the effects of transients in the mobile dislocations becomes more pronounced. This is clearly demonstrated in the behavior of Si and the various arsenides quoted above where m is of order 1–2 and the yield phenomena are very substantial indeed.

Such yield phenomena manifest themselves also in unloading and reloading when a sizable fraction of the mobile dislocation density can be demobilized in various ways. Such behavior has been studied by HAASEN and KELLY [1957] in Cu.

There exist other yield phenomena of fundamentally different nature due to strain softening. These occur in a partially strain hardened crystals when either the conditions or direction of deformation is changed by increasing the temperature or going, e.g., from tension to torsion. A pronounced form of this is the deformation of Al crystals, reported by COTTRELL and STOKES [1955] who deformed Al crystals in tension at 90 K and then

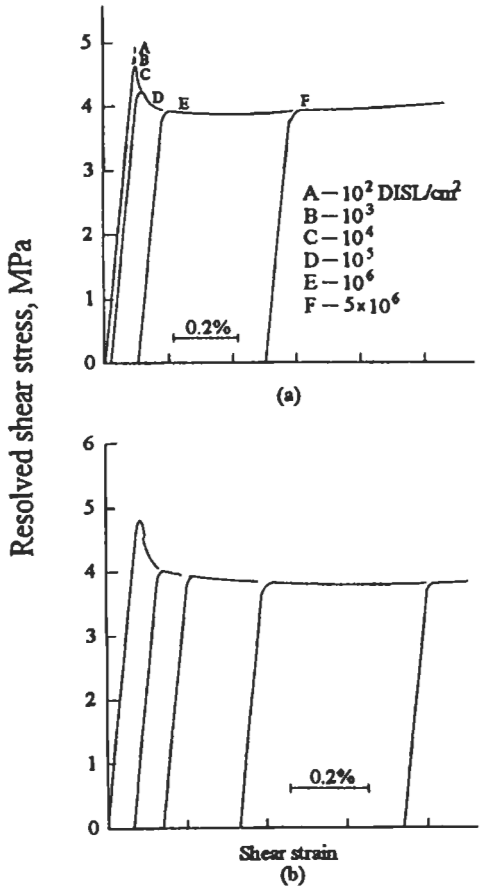

Fig. 38. (a) Calculated yield drops on the stress strain curves of LiF for different initial mobile dislocation densities; (b) experimental stress strain curves with unloading and re-loading at mobile dislocation density levels corresponding to the curves shown in part (a) (JOHNSTON [1962], courtesy of AIP).

continued the deformation at 196 K and 293 K and found not only an expected reduction of the plastic resistance but a substantial strain softening effect as shown in fig. 39, resulting from the instability of the low temperature deformed state to perturbations at more elevated temperatures — most likely due to the onset of some massive dynamic recovery.

8. *Deformation of polycrystalline solids*

8.1. Plastic resistance of polycrystals

While basic understanding of the mechanisms and kinetics of plastic flow is best obtained from the behavior of single crystals, with very few exceptions crystalline

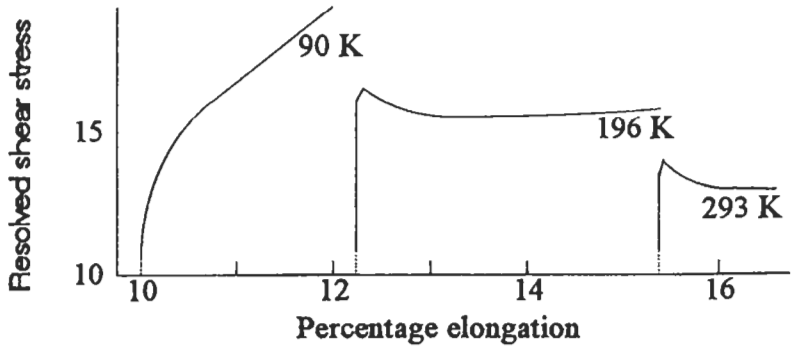

Fig. 39. Yield drops in Al observed at 196 K and 293 K after Stage II hardening at 90 K (COTTRELL and STOKES [1955], courtesy of Roy. Soc.).

materials of technological relevance are in relatively fine-grained polycrystalline form. Their plastic response has traditionally been dealt with by the phenomenological continuum theory of plasticity to which we will make brief reference in section 9 below. Here we will consider the mechanistic and crystallographic aspects of polycrystal plasticity, which not only relates the single crystal response to the homogenized response of aggregates of larger numbers of grains, but also develops the methodology on predicting, or at least rationalizing, the evolution of plastic anisotropy and deformation textures that develop as a consequence of large plastic strain encountered, e.g., in forging and plastic forming.

Here the first consideration has been the determination of the initial yield strength of polycrystalline aggregates, given the plastic shear resistances of various slip systems in single crystals. Since the actual solution of the response of polycrystalline aggregates is a formidable statistical exercise, from the beginning, consideration has been directed to obtaining bounds to the plastic resistance of the aggregate.

Thus, SACHS [1928] has considered the tensile response of a polycrystal as the orientation average of the least tensile resistance of individual grains deformed separately. Then, for a grain in which the most favorably oriented slip system has an orientation factor, m (reciprocal of the individual Schmid factor α of eq. (12b)), in relation to the tensile axis of the polycrystalline aggregate, the tensile resistance y of that particular grain should be

$$y = m\tau, \tag{111}$$

where τ is the plastic shear resistance of the slip plane. The overall tensile resistance Y of the aggregate should then be,

$$Y = \int m\tau\, N(m)dm \tag{112}$$

where $N(m)$ is the normalized orientation distribution of grains measured by their orientation factors. Thus, the connection between the tensile plastic resistance of the aggregate and the shear resistance of slip planes becomes simply

References: p. 1951.

$$\left(\frac{Y}{\tau}\right)_s = \overline{m}_s = \int mN(m)dm, \tag{113}$$

i.e., the population average of the orientation factors of the best slip planes in every grain. For FCC metals the Sachs average is $\overline{m}_s = 2.238$. Clearly, this approach satisfies neither local equilibrium nor compatibility, but merely a global average equilibrium. For this reason it is considered to give a lower bound to the estimate of the aggregate tensile yield strength. While it may give some idea on when local departure from elastic response occurs it falls quite short of predicting the yield strength of grain aggregates for the onset of fully plastic response.

Observing that the strains in individual grains of a polycrystal are often not too different from the overall strain that the aggregate suffers in deformation, and recognizing that compatibility of deformation in the entire aggregate must be satisfied, TAYLOR [1938] has developed another bounding approach based on homogeneous deformation inside grains. Taylor starts by recognizing that for a volume-preserving arbitrary plastic deformation, 5 independent slip systems need to be simultaneously active to achieve compatibility among the homogeneously deforming randomly misoriented grains. In FCC metals where 12 equivalent slip systems are present there is a substantial redundancy of sets of 5 systems for each grain. Considering, of the available sets only the ones with minimum internal dissipation, i.e., the ones for which

$$\tau \sum_i^5 d\gamma_i$$

is minimum, and invoking the principle of virtual work (equivalence of the external work increment and the internal dissipation increment),

$$Yd\varepsilon = \tau \left\langle \sum_i^5 d\gamma_i \right\rangle \tag{114}$$

must be obeyed, where the brackets indicate an average of the internal dissipation increment over all grains in the aggregate. Thus,

$$\left(\frac{Y}{\tau}\right)_T = \overline{m}_T = \frac{\left\langle \sum_i^5 d\gamma_i \right\rangle}{d\varepsilon}, \tag{115}$$

gives the so-called Taylor factor of $\overline{m}_T = 3.1$ for FCC crystal aggregates (for a more detailed discussion see COTTRELL [1953]).

The majority of considerations for the initial plastic response of polycrystals has been for FCC metals. It has been argued (KOCKS [1970]) that in BCC metals which deform primarily on the $\{110\}\langle 111\rangle$ slip systems, with additional slip possibilities on the $\{112\}\langle 111\rangle$ systems, there should be a direct application of the results of FCC metals — at least for the determination of the Taylor factor for initial deformation. As pointed out by GROVES and KELLY [1963], many crystal structures other than cubic, such as HCP, those with layered structures, many intermetallic compounds, and minerals, and even the

cubic NaCl structure, do not possess 5 equivalent independent slip systems at low temperatures. The HCP metals which include many technologically important examples where the second set of slip systems have often much higher slip resistances than the best set, have been analysed by HUTCHINSON [1977] who demonstrates that the plastic resistance of randomly oriented polycrystals then becomes governed by the systems with the highest resistance in the kinematically necessary set of systems for compatible deformation. Many such structures possess in addition to their insufficient set of easily shearable slip systems other sets of considerably higher resistance and a multiplicity of twinning systems. These, however, are relatively less effective in aiding the deformation of polycrystals, resulting in much higher Taylor factors. This difficulty often manifests itself in premature fracture. The deformation of such polycrystalline solids, which have many interesting properties is beginning to receive attention particularly from the point of view of texture development, as is discussed in the section below (SCHOENFELD *et al.* [1995]).

8.2. Evolution of deformation textures

As discussed in section 2.3 crystallographic slip results in lattice rotations relative to the external axes of a body. The lattice rotations due to simple glide strain in FCC single crystals were studied in considerable detail by SCHMID and BOAS [1935]. Their basic kinematical nature resulting from elementary rotations and their effect on the overall tensile stress strain curve were already well understood at that time.

In polycrystals these kinematical ideas find application on the grain scale to determine both the stress strain curve of the polycrystal as well as the evolving texture. They have been studied extensively in the context of the Taylor model which assumes an affine connection between the deformation gradient inside a grain and the global gradient, or that in a local representative volume element (RVE) containing many grains. An important element of the strain hardening of polycrystals is the requirement of compatibility of deformation among grains with as many as 5 different slip systems being active in intersecting slip. It was noted by KOCKS [1970] that, therefore, in polycrystals, well before the textural strengthening becomes significant, the stress–strain curve should exhibit enhanced hardening due to this enforced intersecting slip and that in this range there should be a good parallel between the polycrystal and single crystal curves of high symmetry, particularly the ⟨111⟩ orientation in FCC, which is texturally stable. Figures 40a and 40b show that this is true not only in FCC (KOCKS *et al.* [1968]) but also in BCC (KEH [1965]) where the agreement is even better.

The implementation of the texture development through the Taylor model has been carried out computationally by many investigators for various different deformation histories. These developments to which a large number of investigators have contributed, are discussed in broad outline and also in great detail by ASARO and NEEDLEMAN [1985]. An important element in the developments is the introduction of a rate dependent constitutive kinetic law of the type of eq. (95), for each slip system rather than a critical threshold stress. This has prevented problems of non-uniqueness in the selection of the most appropriate set of slip systems in each grain and their level of activity. The developments incorporate latent hardening relationships and some interaction between

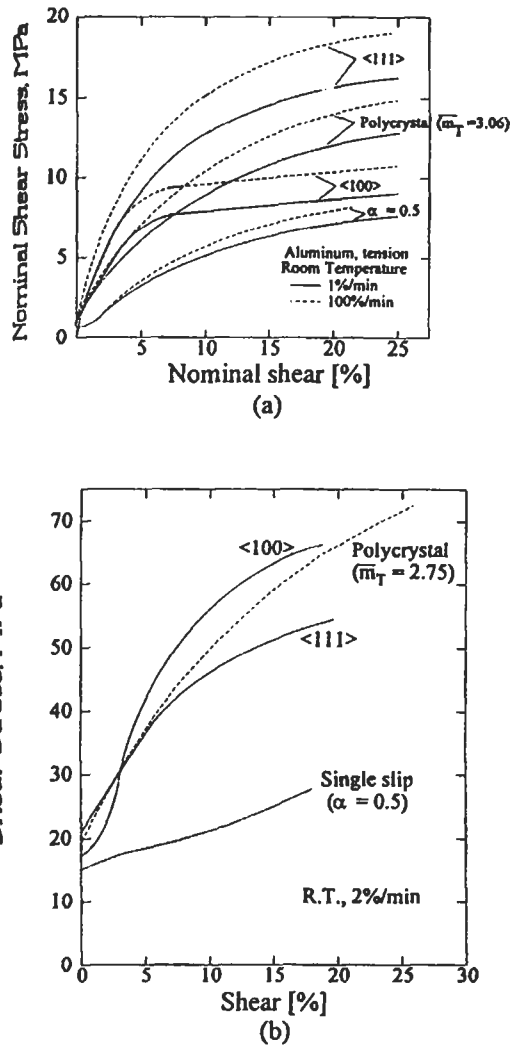

Fig. 40. Correspondence between the stress-strain curves of single crystals with high symmetry orientations and polycrystals in: (a) FCC (KOCKS *et al.* [1968]) and (b) BCC (KEH [1965]) structures.

slip systems. Moreover, the developments in their most recent applications in finite element programs, satisfy not only compatibility but equilibrium, at least over the RVEs in which they are applied. Extensive application of these development by BRONKHORST *et al.* [1992] to Cu have given excellent agreement between predictions and simultaneously pursued experimental observations of which a set, pertaining to simple shear, is shown in fig. 41 (BRONKHORST *et al.* [1992]). Thus, within the presently existing methodology the development of deformation textures can be followed in relatively complex in-

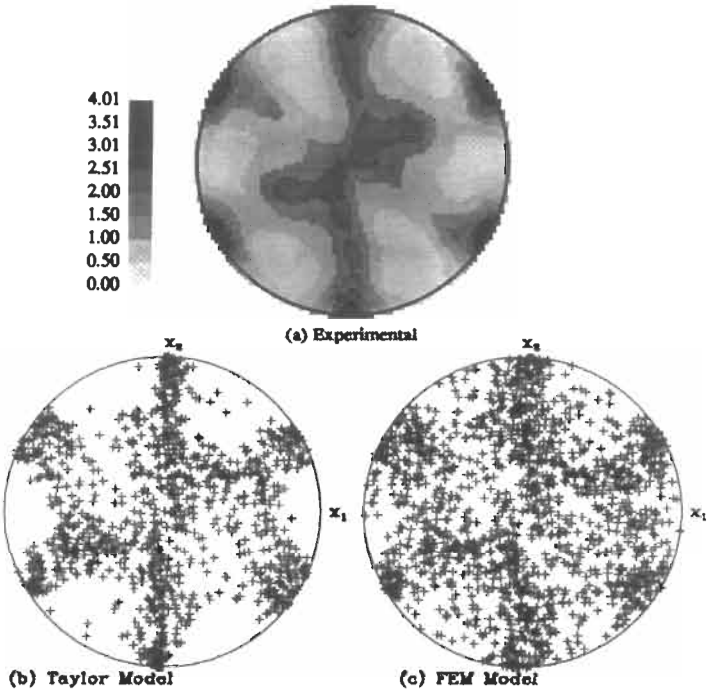

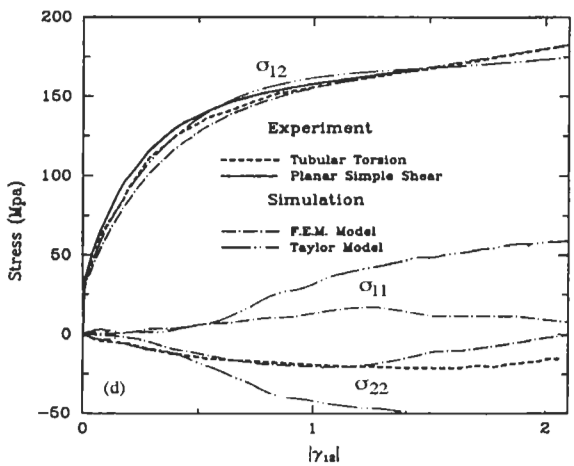

Fig. 41. Predictions and experimental measurements of the stress-strain response and texture development in simple shear of polycrystalline Cu {111} pole figures at a shear strain of $\gamma = 1.4$: (a) experimental; (b) Taylor model; (c) finite element model of a cluster aggregate, and (d) stress-strain curves showing σ_{12} as well as the spurious stresses σ_{11} and σ_{22} (BRONKHORST *et al.* [1992], courtesy Roy. Soc.).

homogeneous deformations by computational techniques. Moreover, the general level of excellent agreement indicates that the Taylor assumption of the affine connection between the individual grains and the polycrystalline aggregate or the local RVE is valid.

Such developments are now being applied more widely to complex crystal structures (SCHOENFELD *et al.* [1995]), and prospects of including even effects of deformation twinning appear promising (ANAND [1995]). Problem areas that remain include certain forms of deformation localization, recrystallization, and grain size effects.

9. *Phenomenological continuum plasticity*

9.1. Conditions of plastic flow in the mathematical theory of plasticity

As in the parallel case of the kinetic theory of gases dealing with motions of individual molecules and continuum mechanics of compressible fluids, dealing with the flow of dense gases, macroscopic problems of plastic flow on the technological level are best handled by the continuum theory plasticity and not by dislocation mechanics. Here we will merely motivate the connection between the crystal plasticity mechanisms and this formal theory of plasticity.

In its rate independent idealization the theory of plasticity takes its cue from crystal plasticity by starting with the assumptions that: a) a plastic continuum is incompressible and b) that deformation cannot be produced by a pure mean normal stress (pressure) but requires a critical deviation away from a state of pure pressure. Thus, it is taken at the outset that plastic work is produced by the stress deviators, s_{ij}, which are related to the full stresses, σ_{ij}, by subtraction of the mean normal stress:

$$S_{ij} = \sigma_{ij} - \delta_{ij}\sigma_m \tag{116}$$

where $\delta_{ij} = 1$ for $i = j$ and 0 for $i \neq j$ and σ_m is the mean normal stress (eq. 3)

$$\sigma_m = \tfrac{1}{3}\left(\sigma_{11} + \sigma_{22} + \sigma_{33}\right), \tag{117}$$

where σ_{11} etc. are the three normal stresses at a point. Then, in an initially isotropic solid, plastic flow in three dimensions is initiated when the equivalent stress in shear σ_e, defined by the deviatoric yield condition or the so-called *von Mises condition*, stated as

$$\sigma_e \equiv \sum_{i,j}^{3} \sqrt{\tfrac{1}{2} s_{ij} s_{ij}} \equiv k = \beta\tau \tag{118}$$

is satisfied. In eq. (118) τ is the individual critical slip plane resistance as discussed earlier, and β $(=\overline{m}_T/\sqrt{3})$ is the corresponding Taylor factor connecting the critical shear resistance τ of the plane to the macroscopic plastic resistance, k, in shear (where $k = Y/\sqrt{3}$, with Y being the polycrystalline plastic resistance in tension) (MCCLINTOCK and ARGON [1966]).

In its rate dependent form of the yield condition, τ is replaced with the temperature and strain rate dependent shear strength related to $\hat{\tau}$ by eq. (56) (KOCKS [1975]). This makes $k = k(T, \dot{\gamma})$ temperature and strain rate dependent.

The mathematical theory of plasticity deals with strain hardening by considering that

the fundamental polycrystalline stress/strain connection derived from a tension experiment giving $Y = Y(\varepsilon^p)$ where ε^p is the tensile plastic strain (or its shear counterpart $k = k(\gamma^p)$ where γ^p is the plastic shear strain) applies also in three dimensional deformation. For this, the tensile plastic strain must be generalized to a so-called work equivalent tensile strain ε_e^p (or its shear counterpart γ_e^p) defined in incremental form as

$$d\varepsilon_e^p \equiv \sum_{i,j}^{3} \sqrt{\tfrac{2}{3}\, de_{ij} de_{ij}} \equiv \frac{d\gamma_e^p}{\sqrt{3}} \tag{119}$$

where the so-called strain deviators de_{ij} are obtained by formally subtracting the dilatational increment (which in plastic deformation of fully dense solids should vanish)

$$d\theta \left(= \sum_i d\varepsilon_{ii} \right)$$

(eq. 5) from the strain increment, i.e.,

$$de_{ij} = d\varepsilon_{ij} - \delta_{ij} d\theta. \tag{120}$$

In this equivalent description of three dimensional behavior, the kinetic shear rate expression of eqs. (31) and (53) of the slip plane translate to the three dimensional polycrystalline form to result in an expression of the type

$$\dot{\gamma}_e^p = \dot{\gamma}_0 \exp\left\{ -\frac{\Delta F_0}{kT} \left(1 - \left(\frac{\sigma_e}{\beta \hat{\tau}} \right)^p \right)^q \right\} = \sqrt{3}\dot{\varepsilon}_e^p \tag{121}$$

with $\dot{\gamma}_\gamma$, ΔF_0, $\hat{\tau}$, and the exponents p and q, still relating to the slip plane properties.

How the solid strains plastically in three dimensions, once the generalized yield condition of eq. (118) is satisfied, and how the individual plastic strain increments are distributed according to the so-called associated flow rule, is beyond our scope and can be found in many references on continuum plasticity (see, e.g., McCLINTOCK and ARGON [1966]).

9.2. Transition from dislocation mechanics to continuum mechanics

In the analogous problem of gas flow, a transition from molecular flow (Knudsen flow) to compressible fluid mechanics is made when the mean free path length of gas molecules becomes very small on the scale of the system. Unfortunately, in the deformation of solids the conditions on the transition between crystal plasticity to continuum plasticity are not so simple. The effects of crystal plasticity can persist to quite a large scale. We demonstrate this here in the special case of the particle resistance mechanism where we consider initially shearable particles and progressively coarsen them until they become non-shearable, and quite large, to investigate at what scale the problem reverts to the well known rule of mixtures of continuum mechanics.

Consider a volume fraction c of initially shearable particles of diameter d, having an internal plastic shear resistance τ_p, embedded in a matrix of shear resistance τ_m, then, the overall (composite) shear resistance according to fig. 7,

$$\tau_c = (1 - c)\tau_m + \frac{\hat{K}}{b\lambda} \tag{122}$$

References: p. 1951.

where $\hat{K} = \tau_p bd$ is the peak particle shear force and λ is the Friedel sampling length, as defined by eq. (49). Then using eq. (49) we have (eq. 50)

$$\tau_c = \left(\frac{\hat{K}}{2\mathcal{E}}\right)^{\frac{3}{2}}\left(\frac{2\mathcal{E}}{bd}\right)\left(\frac{3c}{2\pi}\right)^{\frac{1}{2}} + (1-c)\tau_m. \tag{123}$$

The corresponding shear resistance, τ_{cc}, in the continuum model, by the rule of mixtures is

$$\tau_{cc} = c\tau_p + (1-c)\tau_m. \tag{124}$$

Eq. (123) can also be written as

$$\tau_c = \tau_p\left(\frac{\hat{K}}{2\mathcal{E}}\right)^{\frac{1}{2}}\left(\frac{3c}{2\pi}\right)^{\frac{1}{2}} + (1-c)\tau_m, \tag{123a}$$

where $\tau_c > \tau_{cc}$, because $\left(\frac{\hat{K}}{2\mathcal{E}}\right)^{\frac{1}{2}}\left(\frac{3c}{2\pi}\right)^{\frac{1}{2}} > c.$

This is a direct demonstration of the effectiveness of the non-local nature of precipitate strengthening in comparison with the continuum model. The difference between the non-local dislocation model and the continuum model increases further as $\hat{K}/2\mathcal{E} \to 1.0$ and the particles become impenetrable. When $\hat{K}/2\mathcal{E} > 1.0$ however, and the particle resistance decreases by overaging, a new resistance emerges in the form of the long range image stresses, τ_i, produced by the Orowan loops left around the particles of the type shown in fig. 7c. To a first approximation this image stress is

$$\tau_i = n\left(\frac{2\mathcal{E}}{bd}\right)c \tag{125}$$

where n is the number of Orowan loops left around the particles. When n becomes n_s, the steady state loop number, the particle is sheared, step by step, since presumably,

$$n_s \frac{2\mathcal{E}}{bd} = \tau_p. \tag{126}$$

Then in this regime of $\hat{K}/2\mathcal{E} > 1.0$ (of coherent particles) the composite resistance becomes

$$\tau_c = \tau_p c + \left(\frac{2\mathcal{E}}{bd}\right)\left(\frac{3c}{2\pi}\right)^{\frac{1}{2}} + (1-c)\tau_m, \tag{127}$$

i.e., it begins to approach the continuum form of eq. (124) but still contains the additional overaging component of resistance which only decays slowly with $1/d$. Thus, the continuum limit is approached only slowly as

$$d >> \frac{2b}{\sqrt{\pi c}}\left(\frac{\mu}{\tau_p}\right). \tag{128}$$

For a typical case of a 95% approach to the continuum limit for $c \approx 0.1$ and $\tau_p/\mu \approx 10^{-2}$, it is necessary that $d > 10^4 b$ or about 2.5 μm.

10. Deformation instabilities and strain localization

When uniaxial or bi-axial tensile deformation begins, the cross sectional area decreases because of plastic incompressibility, and the nominal applied stress rises. This should accelerate the plastic deformation rate locally where the initial cross sectional area is the smallest and could result in immediate local necking and plastic rupture were it not for strain hardening. Such a near ideal condition in a tungsten single crystal with a [110] orientation, where strain hardening is very small, is seen in fig. 42 (ARGON and MALOOF [1966]). This initial tendency to plastic instability is counteracted by strain hardening, and the strain rate sensitivity of the plastic resistance, but aided by a positive pressure dependence of the plastic resistance, and by adiabatic heating (ARGON [1973]). When these effects are considered, then the condition of the impending instability can be stated as (not including adiabatic heating),

$$\frac{1}{Y}\left(\frac{dY}{d\varepsilon}\right)_p = 1 - \left(\frac{\partial \ln Y}{\partial \ln p}\right) + \frac{1}{m} \tag{129}$$

where Y is the tensile plastic resistance, $dY/d\varepsilon$ the phenomenological tensile hardening rate, $\partial \ln Y/\partial \ln p$ the pressure dependence of the tensile plastic resistance (usually positive) and $m = (\partial \ln \dot{\varepsilon}_p/\partial \ln \sigma_{(T)})$, the phenomenological tensile stress exponent of the plastic extension rate (identical to that of the shear case considered above). In a near rate independent case, with $m \to \infty$, and negligible pressure dependence, the well-known Considère criterion of

$$\frac{1}{Y}\left(\frac{dY}{d\varepsilon}\right)_p = 1 \tag{129a}$$

is obtained for the onset of instability in uniaxial tensile deformation. Once the instability condition is reached, its development into a neck, and the rate of accentuation of the neck is affected by the non-uniform distributions of stress in the neck. Such problems for the case of uniaxial tension have been discussed in considerable detail by HUTCHINSON and OBRECHT [1977]. The onset and accentuation of necks or rupture zones, particularly in sheet material of anisotropic plastic properties have been topics of intense interest both from the point of view of fundamental kinematical mechanisms (see PEIRCE *et al.* [1982]) and commercial application (see KOISTINEN and WANG [1978]).

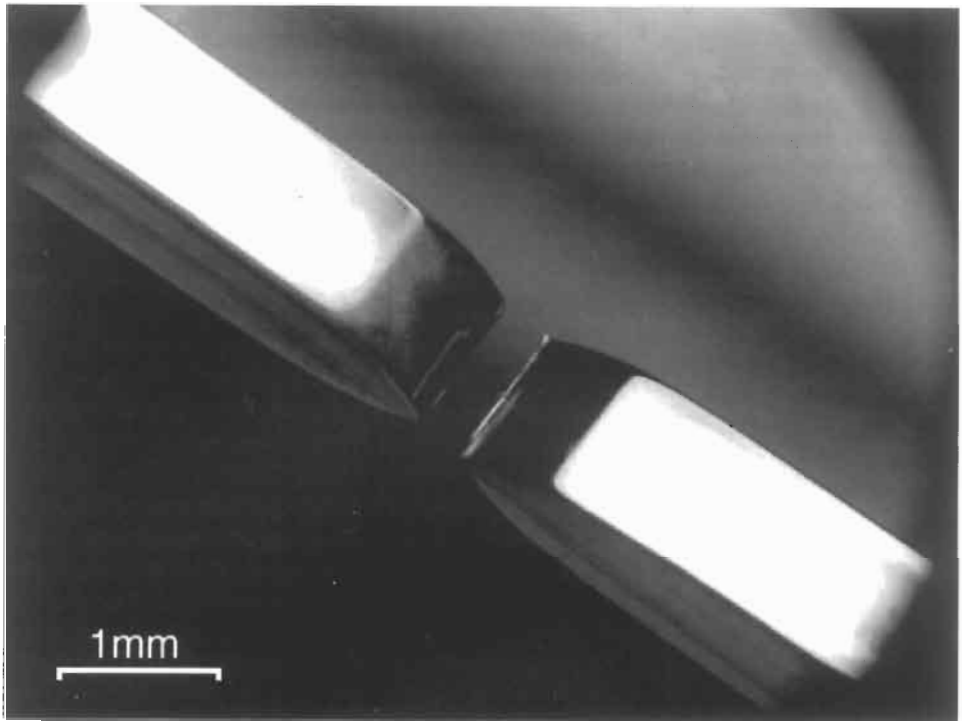

Fig. 42. Ideal rupture of a tungsten single crystal of a [110] orientation deformed in tension (ARGON and MALOOF [1966]).

11. Contrasting crystal plasticity with that in amorphous media

Many metallic alloys with two and more components can be obtained by rapid solidification in fully or partially amorphous form. The conditions of amorphization and the physical and mechanical properties of such materials have been of great interest both commercially and from the point of view of fundamental understanding of material structure. For an overview see DAVIS and HASEGAWA [1981]. In freshly prepared form, alloys with an amorphous structure with a high fictive temperature tend to be readily plastically deformable. Such deformation at low temperatures and high strain rates manifests itself in the form of very intense and thin shear bands having the appearance of slip bands in a crystalline metal. At elevated temperatures the deformation tends to be more diffuse and far less localized. For obvious reasons, the strain hardening in such materials is vanishingly small, and often negative, resulting in strain softening, consistent with the tendency for intense shear localization. The strain rate sensitivity of the flow stress is often quite comparable with that of crystalline alloys. The mechanistic interpret-

ation of the plasticity of amorphous metals has been controversial, with many attempts to invoke direct parallels to dislocation mechanisms (see GILMAN [1968]). The problem is difficult because of the amorphous nature of the material the local kinematical processes of strain production cannot be followed by the usual diffraction techniques of imaging specific structural faults. The most consistent models capable of explaining deformation phenomena have viewed the plasticity as resulting from local shear transformations in clusters on the atomic level (see ARGON [1993]). This view has been supported also by a large number of atomic level computer simulations which are referred to in the above reference.

Acknowledgment

The author is grateful to Professor L. Anand and D. M. Parks for carefully proofreading the manuscript to eliminate a number of misprints and awkward sentences.

References

ALEXANDER, H., and P. HAASEN, 1968, in "Solid State Physics", edited by F. Seitz, D. Turnbull, and H. Ehrenreich. (Academic Press, New York) vol. 22, p. 27.

ALBERDI, J. M. G., 1984, "Large Plastic Deformations in Polycrystalline Cu and Al at Low Temperatures", Ph.D. thesis, Univ. Navarra, Spain.

ALTINTAŞ, S., 1978, "Plastic Deformation of Crystals: Analytical and Computer Simulation Studies of Dislocation Glide", PhD Thesis, University of California, Berkeley.

ANAND, L., 1995, private communication.

ANDRADE, E. N. DA C., 1910, Proc. Roy. Soc. **A84**, 11.

APPEL, F., H. BETHGE, and U. MESSERSCHMIDT, 1976, Phys. Stat. Sol. **38**, 103.

ARDELL, A. J., 1985, Met. Trans. **16A**, 2131.

ARGON, A. S., 1969, in "Physics of Strength and Plasticity", edited by A.S. Argon (M.I.T.-Press, Cambridge, MA) p. 217.

ARGON, A. S., 1970, Scripta Metall. **4**, 1001.

ARGON, A. S., 1973, in "The Inhomogeneity of Plastic Deformation" (ASM, Metals Park, Ohio) p. 161.

ARGON, A. S., 1993, in "Materials Science and Technology", edited by R.W. Cahn, P. Haasen, and E.J. Kramer: vol. **6**, "Plastic Deformation and Fracture of Materials." edited by H. Mughrabi, (VCH, Weinheim) p. 461.

ARGON, A. S., and A. K. BHATTACHARYA, 1987, Acta Metall. **35**, 1499.

ARGON, A. S., and W. T. BRYDGES, 1968, Phil. Mag. **18**, 817.

ARGON, A. S., and G. H. EAST, 1967, Trans. Japan Inst. Metals (Supplement) **9**, 756.

ARGON, A. S., and G. H. EAST, 1979, in "Strength of Metals and Alloys", edited by P. Haasen, V. Gerold, and G. Kostorz, (Pergamon Press, Oxford) vol.**1**, p. 9.

ARGON, A. S., and P. HAASEN, 1993, Acta Metall. et Mater. **41**, 3289.

ARGON, A. S., and S. R. MALOOF, 1966, Acta Metall. **14**, 1449.

ARGON, A. S., A. K. NIGAM, and G. E. PADAWER, 1972, Phil. Mag. **25**, 1095.

ASARO, R. J., 1975, Acta Metall. **23**, 1255.

ASARO, R. J., and A. NEEDLEMAN, 1985, Acta Metall. **33**, 923.

ASHBY, M. F., 1966, Phil. Mag. **14**, 1157.

ASHBY, M. F., 1969, in "Physics of Strength and Plasticity", edited by A.S. Argon (M.I.T.-Press, Cambridge MA), p. 113.

ASHBY, M.F., 1971, in "Strengthening Methods in Crystals" edited by A. Kelly and R.B. Nicholson, (Halsted/Wiley, New York) p. 137.
BASINSKI, S.J., and Z.S. BASINSKI, 1979, in "Dislocations in Solids", edited by F.R.N. Nabarro, (North Holland, Amsterdam) vol. **4**, p. 261.
BEVIS, M., and E.B. CRELLIN, 1971, Polymer **12**, 666.
BRENNER, S.S., 1958, in "Growth and Perfection of Crystals", edited by R.H. Doremus, B.W. Roberts, and D. Turnbull, (Wiley, New York) p. 157.
BRONKHORST, C.A., S.R. KALIDINDI, and L. ANAND, 1992, Phil. Trans. Roy. Soc. **341**, 443.
BROWN L.M., and W.M. STOBBS, 1975, in "Constitutive Equations in Plasticity", edited by A.S. Argon, (M.I.T.-Press, Cambridge, MA) p. 387.
BRYDGES, W.T., 1967, Phil. Mag. **15**, 1079.
BUNSHAH, R.F., 1964, in "Deformation Twinning", edited by R.E. Reed–Hill, J.P. Hirth, and H.C. Rodgers (Gordon & Breach, New York) p. 390.
CAHN, R.W., 1954, Adv. Phys. **3**, 363.
CHRISTIAN, J.W., and S. MAHAJAN, 1995, Progr. Mat. Sci., in press.
COHEN, M., and C.W. WAYMAN, 1981, in "Metallurgical Treatises", edited by J.K. Tien and J.F. Elliott (The Metall. Soc. AIME, Warrendale, PA), p. 445.
COTTRELL, A.H., 1953, "Dislocations and Plastic Flow in Crystals", (Clarendon Press, Oxford).
COTTRELL, A.H., 1995, Mater. Sci. & Tech., in press.
COTTRELL, A.H., 1995, Phil. Mag. Letters, in press.
COTTRELL, A.H., and B.A. BILBY, 1951, Phil. Mag. **42**, 573.
COTTRELL, A.H., and R.J. STOKES, 1955, Proc. Roy. Soc. **A233**, 17.
DAVIS, L.A., and R. HASEGAWA, 1981, in "Metallurgical Treatises", edited by J.K. Tien, and J.F. Elliott, (The Metall. Soc. AIME, Warrendale, PA) p. 301.
DIEHL, J., 1956, Z. Metallkunde **47**, 331.
DORN, J.E., and S. RAJNAK, 1964, Trans. Met. Soc. AIME **230**, 1052.
EDWARDS, E.H., and J. WASHBURN, 1954, J. Metals **6**, 1239.
ESHELBY, J.D., 1949, Phil. Mag. (Ser. 7) **40**, 903.
ESHELBY, J.D., 1954, J. Appl. Phys. **25**, 255.
ESHELBY, J.D., 1957, Proc. Roy. Soc. **A241**, 376.
ESSMANN, U., and H. MUGHRABI, 1979, Phil. Mag. **40**, 731.
FRANK, F.C., and A.N. STROH, 1952, Proc. Phys. Soc. **B65**, 811.
FROST, H.J., and M.F. ASHBY, 1982, "Deformation Mechanism Maps", (Pergamon Press, Oxford).
GILMAN, J.J., 1954, J. Metals **6**, 621.
GILMAN, J.J., 1961, in "Mechanical Behavior at Elevated Temperatures", edited by J.E. Dorn, (McGraw Hill, New York) p. 132.
GILMAN, J.J., 1968, in "Dislocation Dynamics", edited by A.R. Rosenfield, G.T. Hahn, A.L. Bement, and R.T. Jaffee, (McGraw Hill, New York) p. 3.
GROVES, G.W., and A. KELLY, 1963, Phil. Mag. **8**, 877.
GUYOT, P., and J.E. DORN, 1967, Canad. J. Phys. **45**, 983.
HAASEN, P., 1979, in "Dislocations in Solids", edited by F.R.N. Nabarro, (North Holland, Amsterdam) vol. **4**, p. 155.
HAASEN, P., and A. KELLY, 1957, Acta Metall. **5**, 192.
HIRSCH, P.B., and F.J. HUMPHREYS, 1969, in "Physics of Strength and Plasticity", edited by A.S. Argon, (M.I.T.-Press, Cambridge MA), p. 189.
HIRSCH, P.B., and F.J. HUMPHREYS, 1970, Proc. Roy. Soc. **A318**, 45.
HIRTH, J.P., and J. LOTHE, 1982, "Theory of Dislocations", (Wiley/Interscience, New York), Chapter 2.
HUGHES, D.A., and W.D. NIX, 1989, Mater. Sci. Enging. **A122**, 153.
HUTCHINSON, J.W., 1977, Metall. Trans., **8A**, 1465.
HUTCHINSON, J.W., and H. OBRECHT, 1977, in "Fracture 1977", edited by D.M.R. Taplin, (Univ. Waterloo Press, Waterloo Canada). vol. **1**, p. 101.
JOHNSTON, W.G., 1962, J. Appl. Phys. **33**, 2716.
JOHNSTON, W.G., and J.J. GILMAN, 1959, J. Appl. Phys. **30**, 129.

KEH, A. S., 1965, Phil. Mag. **12**, 9.
KLASSEN–NEKLYUDOVA, M. V., 1964, "Mechanical Twinning of Crystals", (Consultants Bureau, New York).
KOCKS, U. F., 1966, Phil. Mag. **13**, 541.
KOCKS, U. F., 1970, Met. Trans. **1**, 1121.
KOCKS, U. F., 1975, in "Constitutive Equations in Plasticity", edited by A.S. Argon, (M.I.T.-Press, Cambridge MA), p. 81.
KOCKS, U. F., 1985, Met. Trans. **16A**, 2109.
KOCKS, U. F., H. S. CHEN, D. A. RIGNEY, and R. J. SCHAEFER, 1968, in "Work Hardening", edited by J.P. Hirth and J. Weertman, (Gordon and Breach, New York), p. 151.
KOCKS, U. F., A. S. ARGON, and M. F. ASHBY, 1975, "Thermodynamics and Kinetics of Slip", "Progress in Materials Science", edited by B. Chalmers, J.W. Christian, and T.B. Massalski, (Pergamon Press, Oxford) vol. **19**.
KOISTINEN, D. P., and N.-M. WANG (Eds.), 1978, "Mechanics of Sheet Metal Forming", (Plenum Press, New York).
KOIZUMI, H., H. O. K. KIRCHNER, and T. SUZUKI, 1993, Acta Metall. et. Mater. **41**, 3483.
KRONMÜLLER, H., 1967, Canad. J. Phys. **45**, 631.
KUHLMANN–WILSDORF, D., 1962, Trans. AIME **224**, 1047.
KUHLMANN–WILSDORF, D., 1968, in "Work Hardening", edited by J.P. Hirth and J. Weertman, (Gordon and Breach, New York), p. 97.
LIVINGSTON, J. D., 1962, Acta Metall. **10**, 229.
MCCLINTOCK, F. A., and A. S. ARGON, 1966, "Mechanical Behavior of Materials", (Addison Wesley, Reading, MA).
MECKING, H., and U. F. KOCKS, 1981, Acta Metall. **29**, 1865.
MOTT, N. F., and F. R. N. NABARRO, 1940, Proc. Phys. Soc. **52**, 86.
MUGHRABI, H., 1975, in "Constitutive Equations in Plasticity", edited by A.S. Argon, (M.I.T.-Press, Cambridge MA) p. 199.
MUGHRABI, H., T. UNGAR, W. KIENLE, and M. WILKENS, 1986, Phil. Mag. **53**, 793.
MULFORD, R. A., 1979, Acta Metall. **27**, 1115.
MULFORD, R. A., and U. F. KOCKS, 1979a, Acta Metall. **27**, 1125.
MULFORD, R. A., and U. F. KOCKS, 1979b, Scripta Metall. **13**, 729.
MÜGGE, O., 1898, Neues Jahrb. f. Miner. **1**, 71.
NABARRO, F. R. N., 1940, Proc. Roy. Soc. **A175**, 519.
NABARRO, F. R. N., 1947, Proc. Phys. Soc. **59**, 256.
NABARRO, F. R. N., 1985, in "Strength of Metals and Alloys", edited by H.J. McQueen, J.P. Bailon, J.I. Dikson, J.J. Jonas, and M.G. Akben, (Pergamon Press, Oxford), vol. **3**, p. 1667.
NASTER, M., and F. WILLAIME, 1995, Phs. Rev. B, in press.
NIX, W. D., J. C. GIBELING, and D. A. HUGHES, 1985, Met. Trans. **16A**, 2215.
NYE, J. F., 1957, "Physical Properties of Crystals", (Clarendon Press, Oxford).
OLSON, G. B., and M. COHEN, 1986, in "Dislocations in Solids", edited by F.R.N. Nabarro (Elsevier, Amsterdam) vol. **7**, p. 295.
OLSON, G. B., M. AZRIN, and E. S. WRIGHT (eds.), 1987, "Innovations in Ultra High Strength Steel Technology", (U.S. Army Laboratory Command, Watertown, MA). vol. **34**.
OROWAN, E., 1942, Nature **149**, 643.
OROWAN, E., 1948, in "Symposium on Internal Stresses in Metals and Alloys", (Institute of Metals, London) p. 451.
OROWAN, E., 1952, in "Proceedings of First Natl. Congr. Appl. Mech.", (ASME, New York) p. 453.
OROWAN, E., 1954, in "Dislocations in Metals", edited by M. Cohen, (AIME, New York), Monograph 103, p. 69.
OROWAN, E., 1959, in "Internal Stresses and Fatigue in Metals", edited by G.R. Rassweiler and W.L. Grube, (Elsevier, Amsterdam) p. 59.
PAXTON, H. W., and I. J. BEAR, 1955, J. Metals Trans. **7**, 989.
PEIERLS, R., 1940, Proc. Phys. Soc. **52**, 34.
PEIRCE, D., R. J. ASARO, and A. NEEDLEMAN, 1982, Acta Metall. **30**, 1087.

PRINZ, F., and A. S. ARGON, 1979, Phys. Stat. Sol. **57**, 741.
PRINZ, F., and A. S. ARGON, 1984, Acta Metall. **32**, 1021.
PULS, M. P., 1981, in "Dislocation Modeling of Physical Systems", edited by M.F. Ashby, R. Bullough, C.S. Hartley, and J.P. Hirth, (Pergamon Press, Oxford), p. 249.
REED–HILL, R. E., 1964, in "Deformation Twinning", edited by R.E. Reed–Hill, J.P. Hirth, and H.C. Rogers, (Gordon and Breach, New York) p. 295.
REPPICH, B., 1993, in "Materials Science and Technology", edited by R.W. Cahn, P. Haasen, and E.J. Kramer, "Plastic Deformation and Fracture of Materials" edited by H. Mughrabi (VCH, Weinheim) vol. **6**, p. 311.
RICE, J. R., G. E. BELTZ, and Y. SUN, 1992, in "Topics in Fracture and Fatigue", edited by A.S. Argon, (Springer, New York), p. 1.
ROSE, J. H., J. R. SMITH, and J. FERRENTE, 1983, Phys. Rev. B. **28**, 1835.
ROLLETT, A. D., 1988, "Strain Hardening at Large Strains in Aluminum Alloys", LA-11202-T, (Los Alamos Natl. Laboratory, Los Alamos, NM).
SACHS, G., 1928, Z. Ver. Deutsch. Ing. **72**, 734.
SAIMOTO, S., 1963, "Low Temperature Tensile Deformation of Copper Single Crystals Oriented for Multiple Slip", PhD Thesis (M.I.T., Cambridge, MA).
SCHMID, E., and W. BOAS, 1935, "Kristallplastizität", (Springer, Berlin).
SCHOENFELD, S. E., S. AHZI, and R. J. ASARO, 1995, J. Mech. Phys. Solids, in press.
SCHWARZ, R. B., and R. LABUSCH, 1978, J. Appl. Phys. **49**, 5174.
SEEGER, A., 1957, in "Dislocations and Mechanical Properties of Crystals", edited by J.C. Fisher, W.G. Johnston, R. Thomson, and T. Vreeland, Jr. (Wiley, New York), p. 243.
SEEGER, A., 1958, in "Encyclopedia of Physics", edited by S. Flügge (Springer, Berlin), vol. **7/2** (Crystal Physics II), p. 1.
SIMMONS, G., and H. WANG, 1971, "Single Crystal Elastic Constants and Calculated Aggregate Properties", Second Edition (M.I.T.-Press, Cambridge, MA).
SLEESWYK, A. W., 1962, Acta Metall. **10**, 705.
SPRACKLING, M. T., 1976, "The Plastic Deformation of Simple Ionic Crystals", (Academic Press, New York).
SUREK, T., M. J. LUTON, and J. J. JONAS, 1973, Phys. Stat. Sol. **57**, 647.
SUZUKI, T., and T. ISHII, 1969, in "Physics of Strength and Plasticity", edited by A.S. Argon, (M.I.T.-Press, Cambridge, MA) p. 159.
SUZUKI, T., S. TAKEUCHI, and H. YOSHINAGA, 1985, "Dislocation Dynamics and Plasticity", (Springer, New York).
TAKEUCHI, T., 1966, J. Phys. Soc. Japan **21**, 2616.
TAYLOR, G. I., 1938, J. Inst. Metals **62**, 307.
TINDER, R. F., and J. WASHBURN, 1964, Acta Metall. **12**, 129.
THORNTON, P. R., T. E. MITCHELL, and P. B. HIRSCH, 1962, Phil. Mag. **7**, 1349.
TROJANOVA, Z., and P. HAASEN, 1975, Z. Metallkunde **66**, 463.
UNGAR, T., H. MUGHRABI, M. WILKENS, and A. HILSCHER, 1991, Phil. Mag. **64**, 495.
VAN BUEREN, H. G., 1960, "Imperfections in Crystals", (North-Holland, Amsterdam).
VENABLES, J. A., 1964, in "Deformation Twinning", edited by R.E. Reed–Hill, J.P. Hirth, and H.C. Rogers, (Gordon and Breach, New York), p. 77.
WYATT, O. H., 1953, Proc. Phys. Soc. **B66**, 459.
YONENAGA, I., U. ONOSE, and K. SUMINO, 1987, J. Mater. Res. **2**, 252.
YONENAGA, I., and K. SUMINO, 1989, J. Mater. Res. **4**, 355.
YONENAGA, I., K. SUMINO, G. IZAWA, H. WATANABE, and J. MATSUI, 1989, J. Mater. Res. **4**, 361.
ZEHETBAUER, M., 1993, Acta Metall. et. Mater. **41**, 589.

Further reading

Argon, A. S., (editor) 1975, "Constitutive Equations in Plasticity", (M.I.T. Press, Cambridge, MA).
Kocks, U. F., A. S. Argon, and M. F. Ashby, 1975, "Thermodynamics and Kinetics of Slip", "Progress in Materials Science" edited by B. Chalmers, J. W. Christian, and T. B. Massalski, (Pergamon Press, Oxford).
Barrett, C. and T. B. Massalski, 1980, "Structure of Metals", Third revised edition (Pergamon Press, Oxford), vol. 19.

Frost, H. J. and M. F. Ashby, 1982, see references.

Mughrabi, H., (editor) 1993, "Plastic Deformation and Fracture of Materials", "Materials Science and Technology", edited by R. W. Cahn, P. Haasen, and E. J. Kramer, vol. 6, (VCH Publishers, Weinheim).

Nabarro, F. R. N., 1985, see references.

Suzuki, T., S. Takeuchi, and H. Yoshinaga, 1985, see references.

Reed–Hill, R. E., J. P. Hirth, and H. C. Rogers, (editors) 1964, "Deformation Twinning", (Gordon and Breach, New York).

CHAPTER 22

MECHANICAL PROPERTIES OF SINGLE-PHASE CRYSTALLINE MEDIA: DEFORMATION IN THE PRESENCE OF DIFFUSION

A. S. ARGON

Massachusetts Institute of Technology
Cambridge, MA 02139
USA

R. W. Cahn and P. Haasen†, eds.
Physical Metallurgy; fourth, revised and enhanced edition

1. Overview

Chapter 21 treated the inelastic deformation of crystalline solids at low homologous temperatures where diffusion plays no role and where the rate process of the deformation is governed by other considerations. A common characteristic of the processes discussed in chapter 21 was that nearly all were associated with continued evolution of a dislocation microstructure in which the deformation rate had to be associated with a prevailing state that itself changes with deformation.

The present chapter treats the complementary and often additional inelastic processes that are fundamentally affected by diffusion and permit alteration of the dislocation microstructure even in the absence of deformation, under static conditions. The new degrees of freedom permit the attainment of stationary states of microstructure and steady state deformation, that are possible through diffusion. It is primarily these diffusion-controlled deformation processes that are the subject of this chapter. These latter processes are often associated with the term *creep* because of the time dependence of the deformation. However, this is unsatisfactory since many forms of time-dependent inelastic response, ranging from thermally activated glide in a slowly evolving dislocation microstructure to deformation affected by dynamic recovery, also manifest themselves in phenomena called *logarithmic creep* or *Andrade creep*, and the like. As discussed in chapter 21, these latter creep processes at lower homologous temperatures are not affected by diffusion and are, therefore, not subjects for discussion here. The complexity of the present subject arises from the fact that the diffusion-controlled processes are often arrived at through transients that do not involve diffusion and that under changed conditions a purely diffusion-controlled deformation process can revert back to one in which diffusion is absent. Moreover, under service conditions of interest an engineering component or a deformation processing operation may straddle the ranges of operation that involve concurrent or sequential steps that are, or are not, fully diffusion controlled, but nevertheless, require some characterization. These operational requirements have given rise to much empiricism and confusion, reinforced by the fact that there is a lack of well documented experimental information for such mixed processes of response. In the present chapter we will discuss first the phenomenology and mechanisms of the diffusion-controlled deformation processes and some of their transients that are necessary for clarity. This we will follow with a discussion of some kinds of transitional behavior and more complex phenomena such as sliding of grain boundaries, reversion to thermally activated glide, dynamic recrystallization, superplasticity, etc.

The deformation processes and their interrelationships of primary concern here are well delineated in the *deformation mechanism maps* that have been developed by FROST and ASHBY [1982]. The map for polycrystalline nickel of a grain size of 0.1 mm, shown in fig. 1, is a typical example. In it the plastic resistance, normalized with the shear modulus, for different inelastic strain rates is plotted as a function of the homologous temperature. The ranges of the diffusion-controlled processes that can potentially give rise to steady state deformation in a stationary microstructure have been delineated clearly as: low-temperature and high-temperature dislocation creep (power-law creep) in the intermediate stress range extending from a homologous temperature of 0.3 to the melting

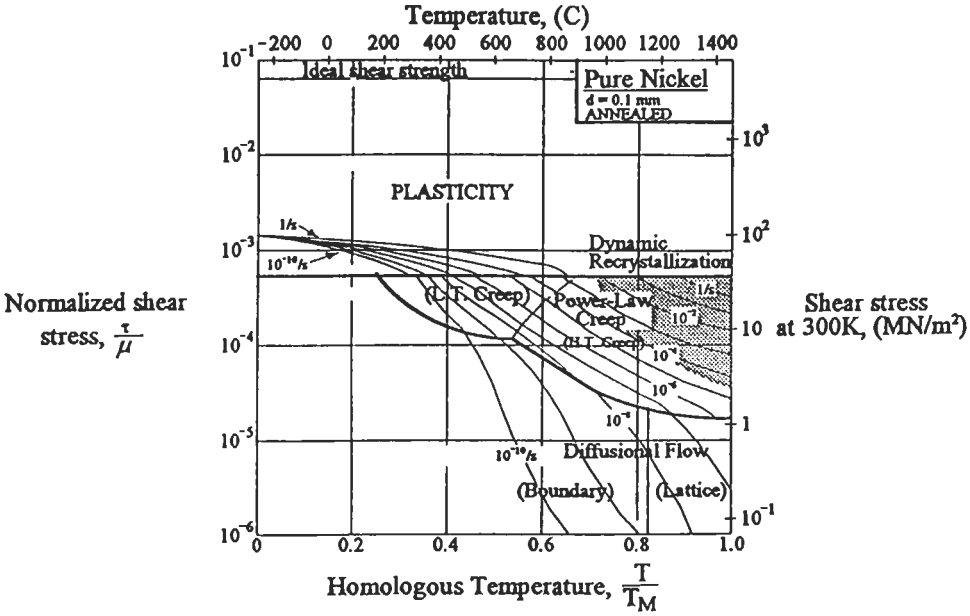

Fig. 1. A deformation mechanism map for polycrystalline nickel (FROST and ASHBY [1982], courtesy of Pergamon Press).

point and the boundary-diffusion and lattice-diffusion controlled processes of diffusional flow at low stresses and high temperatures. A shaded region at high stress and high temperature, but also characteristic of a high deformation rate, is identified as dynamic recrystallization in which the dislocation microstructure is quasi-periodically infused with recrystallized new grains of low deformation resistance that can undergo new spurts of rapid transient response. We discuss this complex process briefly in a later section.

In their graphical exercise of map production, FROST and ASHBY [1982] have had to deal with a multitude of complex phenomena of practical technological interest in a manner at least semi-quantitative, albeit usually inspired by mechanism. To gain an overall perspective of the high-temperature deformation phenomena the reader is advised to consult their work.

We note that much of the kinematical character of high temperature deformation is the same as that for low temperature. While point-defect transport associated with diffusion imparts to edge dislocations a new degree of freedom through climb motion, most of the strain in dislocation creep is still associated with the glide of dislocations. In a few exceptional cases where glide is geometrically not possible (EDELIN and POIRIER

References: p. 2004.

[1973a, b]) and in certain solid-solution alloys where edge dislocations can assume curvilinear paths through climb (TAKEUCHI and ARGON [1976a]) significant contribution to strain can indeed come from climb of dislocations. These cases, however, are rare. Certain forms of grain-boundary sliding can contribute additional strain to the glide-induced strain of dislocations, such sliding is kinematically very similar to dislocation glide. The new dimension in strain production occurs in diffusional flow where overall distortions result from the transport of point defects, through grains or along grain boundaries, from certain stressed incoherent boundaries or interfaces to others, without any distortion of the enclosed grains. This special kinematics of diffusional flow is discussed in section 7. As in chapter 21, attention will be limited to single-phase media only but will be broadened slightly to include the deformation of certain solid solution alloys and to make occasional observations related to precipitate particles where their presence significantly affects recovery or point defect transport.

We begin discussion of these phenomena with a brief account of the methods of measurement of creep response in the realm of high homologous temperatures.

2. *Phenomenology of power-law creep*

2.1. Measurement of creep strain

The time-dependent response of solids at elevated temperatures is generally probed in uniaxial creep experiments in tension, where most often a constant tensile load is applied to the sample at a given temperature and the total strain is recorded. Whenever the deformation process is multi-axial the formal connection between the one-dimensional behavior and the multi-axial behavior discussed in section 9.1 of chapter 21 applies. The initial elastic extension of the sample is usually ignored and only the time-dependent evolution of strain is considered.

Figure 2 shows a series of typical three-stage creep curves for copper at 270°C ($T/T_m = 0.4$) copper at 4 different stress levels. The curves show *primary creep* (P) with decreasing strain rate, leading to a *secondary* or *steady state* (*SS*) stage of creep, followed by a *tertiary* stage (*T*) of accelerating creep, all clearly delineated for the lowest stress creep curve at $\sigma = 50.13$ MPa (DYSON [1987]). This behavior is typical of many unalloyed, pure single-phase metals in the intermediate homologous temperature range associated with power-law creep. In distinction to these curves are the two primary creep curves in fig. 3. Of these the one for pure aluminum at 300°C ($T/T_m = 0.61$) is very similar to the primary portions of the curves for copper, showing a decreasing creep rate with increasing strain. The curve for the solid solution alloy of aluminum with 5 wt% magnesium, on the other hand, is qualitatively different with its inverted transient of accelerating creep with increasing strain. This latter creep response is characteristic of a broad class of solid solution alloys collectively labeled as Class I, which are discussed in section 3.

On rare occasions when the amount of material has been limited or has been of a nature making tensile creep experiments impractical, experiments have been carried out in compression, by means of high-temperature conventional hardness experiments

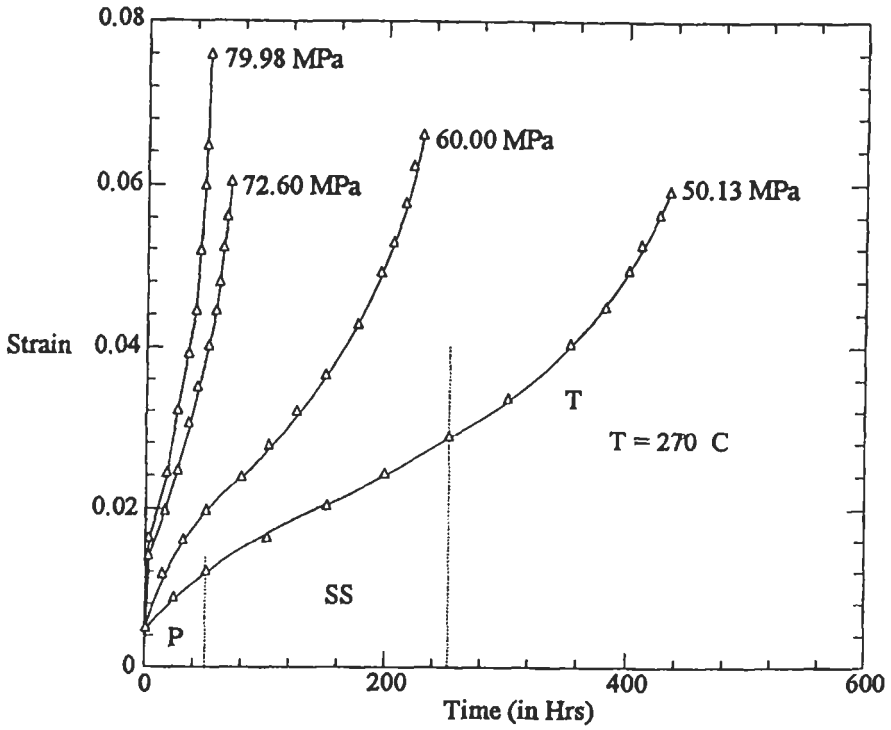

Fig. 2. Creep curves of pure polycrystalline copper at four stress levels (DYSON [1987], private communication).

(WESTBROOK [1953]) or in special so-called "impression creep" experiments involving the time dependent penetration of a flat punch under constant load into a half space (CHU and LI [1977]). In the latter case, the creep information is extracted from the impression rate by means of an associated computer model (YU and LI [1977]).

2.2. The functional forms of the creep relation

The shapes of creep curves, their various time laws, and the dependence of the strain rate on imposed external parameters have received much attention. The variety of empirical functional forms which have been proposed have been reviewed by TAKEUCHI and ARGON [1976b]. While some of these forms have been proposed purely for empirical operational convenience, others have been guided by underlying mechanisms. We will consider here only the latter.

In the usual three-stage creep behavior of pure metals and so-called Class II solid solution alloys, the time dependence of the primary creep response is found to obey the creep law discovered by ANDRADE [1911] in his pioneering experiments:

$$\varepsilon = \alpha t^{1/3}. \tag{1}$$

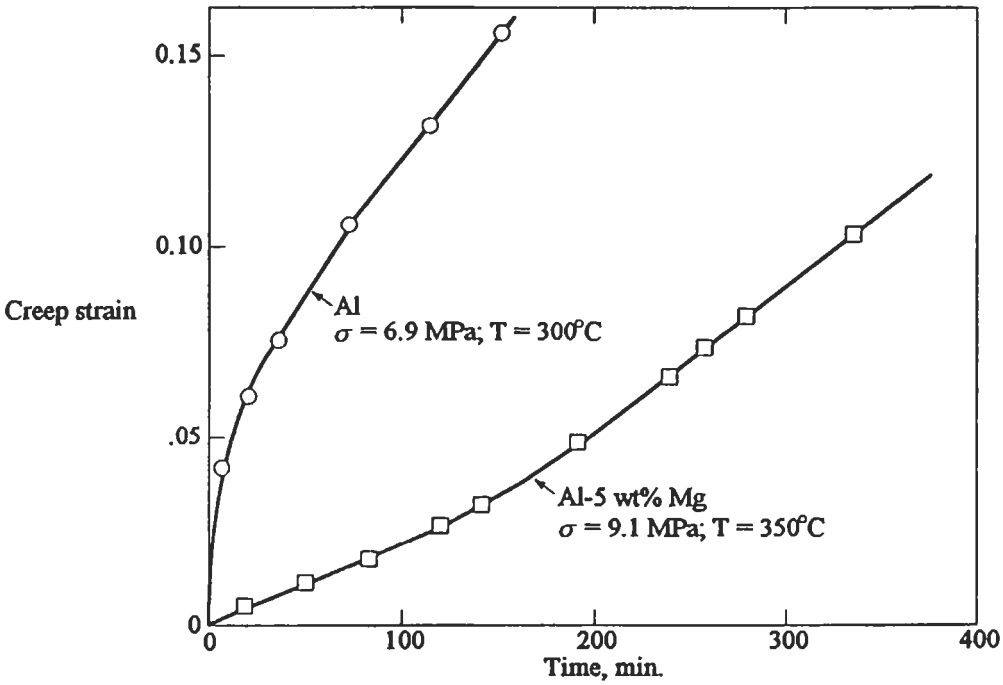

Fig. 3. Creep curves in aluminum and aluminum-magnesium (Class I) alloy (after TAKEUCHI and ARGON [1976b], courtesy of Chapman and Hall).

This is shown in figs. 4a and 4b for polycrystalline nickel where fig. 4a shows the initial primary creep response, and the form of a new transient resulting from a stress jump at the point in the initial curve where steady state creep appeared to set in (ARGON and BHATTACHARYA [1987]). Figure 4b gives the same information on logarithmic coordinates and shows that in the first experiment after an "initial instantaneous" plastic response is over (in the first minute of straining) the subsequent response follows the Andrade expression. In chapter 21 in section 7.3.7, it was demonstrated that at low temperatures, in the Stage III hardening regime, where dynamic recovery controls the rate of strain hardening, the transient creep response also obeys the Andrade creep behavior. It will be demonstrated below, in this section, that this remarkably universal time dependence is also compatible with diffusion-controlled recovery processes.

The portion of the creep curve of greatest interest is the steady-state part which is considered to have the potential to produce limitless strain at a constant structure under a constant applied stress. It is generally assumed that tertiary acceleration of creep in pure polycrystalline metals is an extension of the steady-state creep and results from a monotonic reduction of net cross sectional area due to either a change of external dimensions or the development of internal cavitation leading to eventual fracture. In engineering practice, where often creep information is collected in constant load

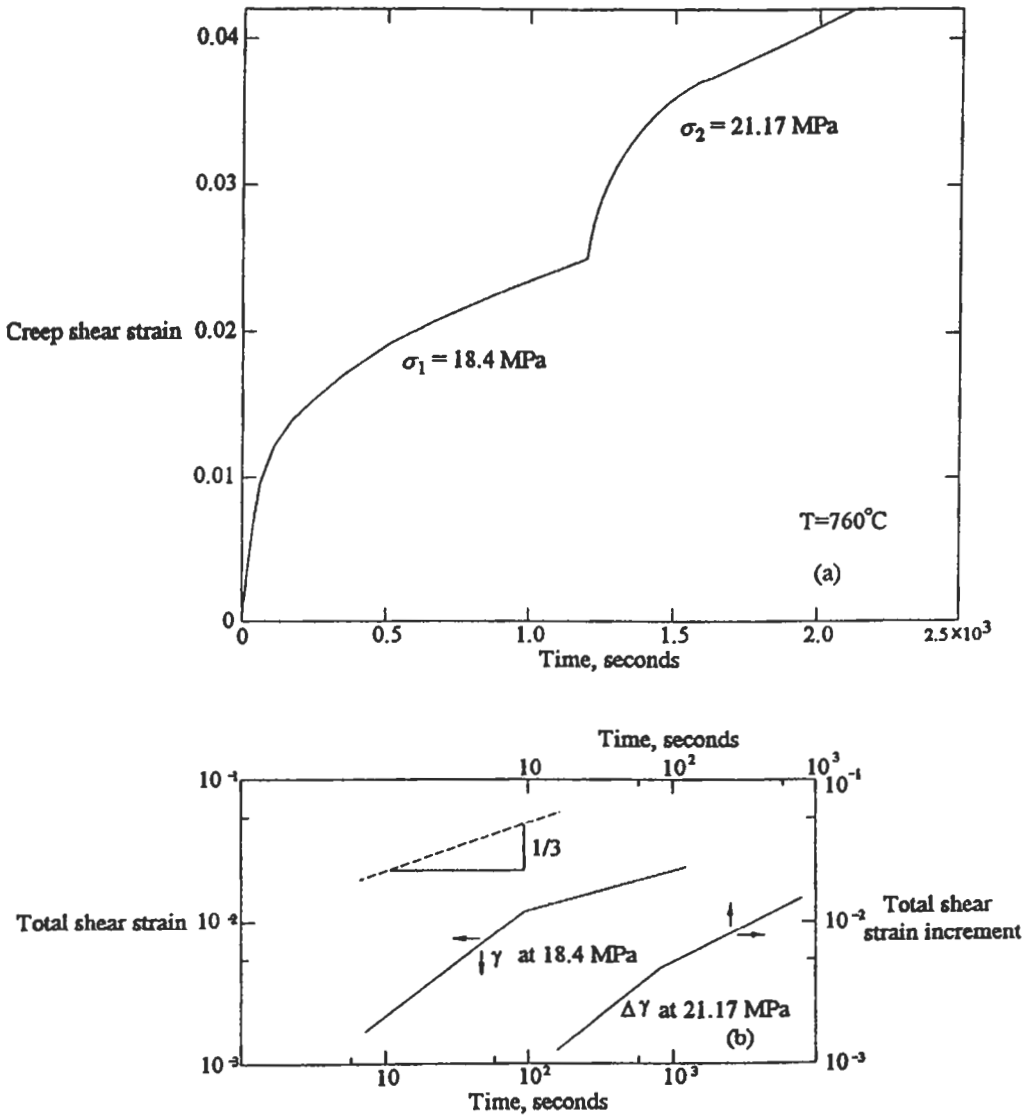

Fig. 4a,b. Two primary creep curves in pure polycrystalline nickel. (Measured tensile creep rates have been converted to shear strain rates by multiplying with $\sqrt{3}$ in accordance with the Mises formalism, see ch. 21). (ARGON and BHATTACHARYA [1987], courtesy of Pergamon Press).

experiments, the secondary stage often appears as an inflection between the end of primary creep and the beginning of tertiary creep. Therefore, this inflection is frequently taken as a representation of steady state creep, but is correctly referred to as the *minimum creep rate*.

As has been pointed out by OROWAN [1947], there is no assurance that this inflection behavior has much relation to steady state creep under constant stress. Nevertheless, the practice is widespread and is a contributing reason to why the stress exponents reported in the engineering literature derived from the minimum creep rate tend to be higher than those obtained from proper constant stress experiments.

A variety of functional forms have been proposed for the steady-state creep rate. These and their individual merits have been reviewed by TAKEUCHI and ARGON [1976b]. One that has received wide acceptance is that formulated by MCLEAN [1962] and by Dorn and co-workers (DORN and MOTE [1964], MUKHERJEE *et al.* [1969], and BIRD *et al.* [1969]), and amended by BARRETT and SHERBY [1965]:

$$\dot{\varepsilon}_{ss} = A_0 \nu_D \left(\frac{\chi}{\mu b}\right)^3 \left(\frac{\mu\Omega}{kT}\right) \left(\frac{\sigma}{\mu}\right)^m \exp\left(-\frac{Q_c}{kT}\right) \tag{2}$$

where Q_c is the activation energy of power-law creep, σ is the applied tensile stress, μ the shear modulus, Ω the atomic volume, χ the stacking fault energy, b the magnitude of the Burgers displacement, ν_D the atomic frequency, and m and A_0 material constants. Recognizing that the activation energy for creep is the same as that of self-diffusion, BIRD *et al.* [1969] proposed a more compact form:

$$\dot{\varepsilon}_{ss} = A_0' \nu_D \left(\frac{\chi}{\mu b}\right)^3 \left(\frac{\mu b D}{kT}\right) \left(\frac{\sigma}{\mu}\right)^m \tag{3}$$

where D is the self-diffusion constant which obeys

$$D = D_0 \exp\left(-\frac{Q_D}{kT}\right) = z b^2 \nu_D \exp\left(-\frac{Q_D}{kT}\right). \tag{4}$$

Eq. (3) is known as the *Dorn* equation. In eq. (4), z is a coordination number of atoms and ν_D the atomic frequency. Here Q_D can either be the activation energy for volume diffusion, Q_V, at high homologous temperatures or that of dislocation core diffusion, Q_{CD}, at lower homologous temperatures. The dependence of the steady-state creep rate on stacking fault energy, χ, has been demonstrated for FCC metals by MOHAMED and LANGDON [1974] as shown in fig. 5 and relates to a well developed mechanism to be discussed in section 6.4 below. While the magnitudes could differ from material to material, a convenient rule of thumb is that $Q_{CD} \approx 0.6 Q_V$. In a more condensed form, putting $A_0'(\chi/\mu b)^3 = A$, eq. (3) has a wide range of applicability to BCC and HCP metals and solid solution alloys of the so-called Class II type — albeit where A now ranges over 5 orders of magnitude. This broad correlation is shown in figs. 6a and 6b for FCC, BCC, HCP metals and solid-solution alloys (BIRD *et al.* [1969]).

The ranges of material parameters A and m relating to this representation are listed

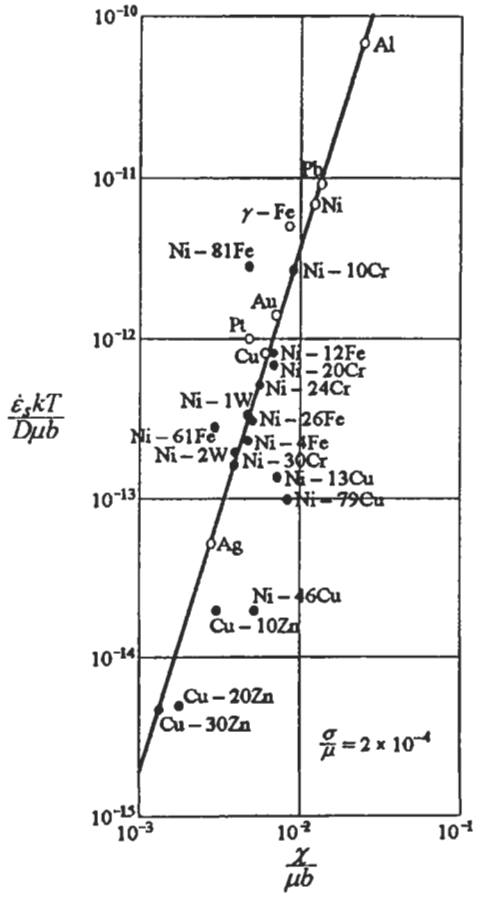

Fig. 5. Dependence of steady-state creep rate on stacking-fault energy in pure metals and dilute solid solution alloys for a given tensile stress level of $\sigma/\mu = 2 \times 10^{-4}$. (TAKEUCHI and ARGON [1976b], courtesy of Chapman and Hall).

in table 1, where the quantities in parentheses can be considered as mid-range values for the families of materials considered. Parenthetically, for the case of nickel presented in fig. 4, the values of A and m can be given as $.32 \times 10^5$ and 4.7 respectively ($A_0' = 1.06 \times 10^{12}$ of eq. (3), for $\chi/\mu b = 5 \times 10^{-2}$).

While the forms presented in eqs. (2) and (3) have a sound basis in statistical consistency for the pure metals in which m is of the order 5, they have been applied to other cases of alloys where the documentation has been less extensive and where m has ranged (on the basis mostly of minimum creep rate data) up to 8, with a consequence of a very wide range for the creep rate constant A. Based on this observation and with the goal of extending the steady state formalism back into the primary creep range where the microstructure is still evolving and strain hardening is dominating over recovery, BROWN

Table 1
Values of m and A related to eq. (3) for various metals by BIRD *et al.* [1969]. Typical values for each case are shown in parentheses

Material	n	A
FCC metals	4.4–5.3(5)	10^5–10^8(10^7)
BCC metals	4–7(5)	10^5–10^{15}(10^9)
HCP metals	4–6(5)	10^3–10^8(10^6)
Class II alloys	4.5–6(5)	10^5–10^9(10^6)
Class I alloys	3–4(3.3)	10^{-2}–10^4(10^1)

and ASHBY [1980] proposed a simpler expression which in connection with the well established Dorn form of eq. (3) would translate into

$$\dot{\varepsilon} = B\left(\frac{\mu b D}{kT}\right)\left(\frac{\chi}{\mu b}\right)^3\left(\frac{\sigma}{s}\right)^m, \tag{5}$$

where now s is the reference deformation resistance of the evolving microstructure which when reaching a stationary state gives the steady-state creep law, but has now the additional flexibility of providing a physically appealing mechanistic framework for primary creep where the deformation resistance s continues to evolve from some initial value to its steady state form s_{ss}. That this is indeed the case has been verified by ARGON and BHATTACHARYA [1987] in polycrystalline and single crystalline nickel by measuring both the Vickers micro-hardness and the increase in yield strength in reference experiments at room temperature at several points in the periodically interrupted primary

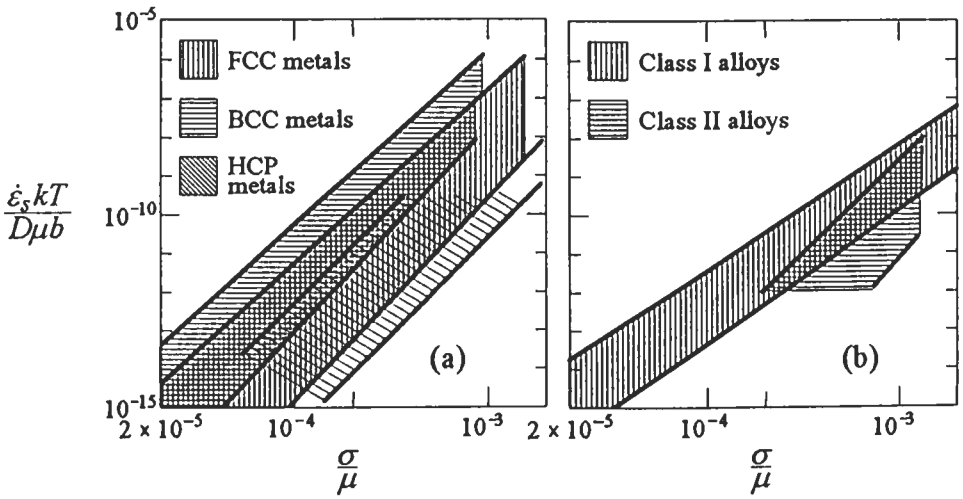

Fig. 6. Dependence of steady-state creep rate on stress: (a) in pure metals; (b) in dilute solid solution alloys (BIRD *et al.* [1969], courtesy Israel Univ. Press).

creep response. The measured results and the results of a theoretical model by Argon and Bhattacharya are shown in fig. 7. A side benefit of the creep law variant of eq. 5 is the smaller magnitudes of the creep constant B ($=3.69\times 10^{-3}$ for the nickel results of fig. 4).

It has been noted by a number of investigators that if the principal rate-controlling process is self-diffusion then more unity is achieved in the representation of the creep relations by a combined time–temperature variable (LUDEMANN *et al.* [1960]) defined as

$$\theta = t\exp\left(-\frac{Q_c}{kT}\right) \quad (\text{or } \theta' = \text{tD}) \tag{6a, b}$$

The relevance of this representation is reflected in the primary creep measurements in nickel at several different temperatures and two different stress levels, shown in figs. 8a and 8b. Figure 8a shows that the primary creep behavior of nickel at three different temperatures, but at two constant stress levels, can be very well represented by two master curves connecting primary creep into steady state creep smoothly, if the rate behavior is measured by the time-temperature parameter defined in eq. (6a) with $Q_c = 69$

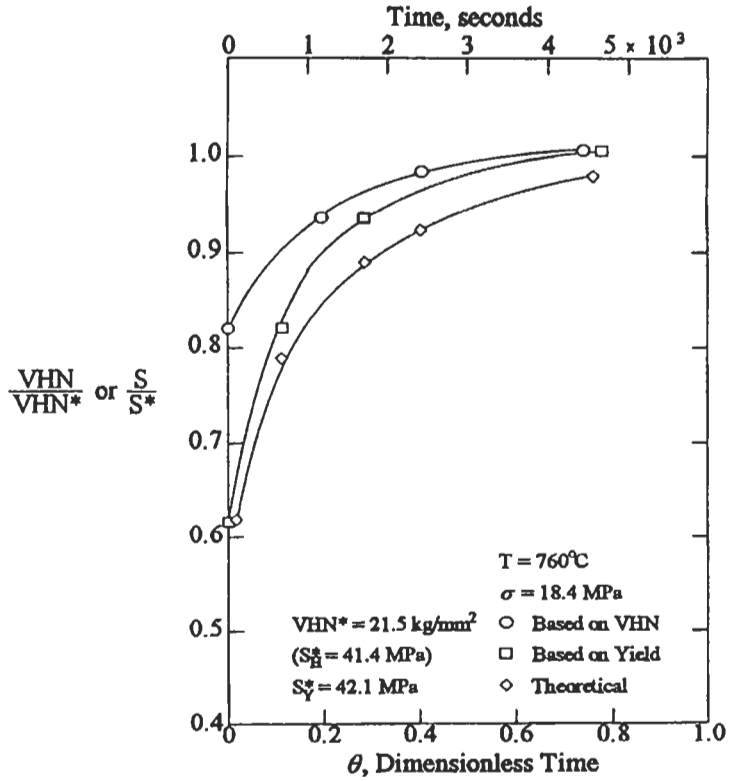

Fig. 7. The evolution of reference plastic resistance during primary creep in polycrystalline nickel (ARGON and BHATTACHARYA [1987], courtesy of Pergamon Press).

References: p. 2004.

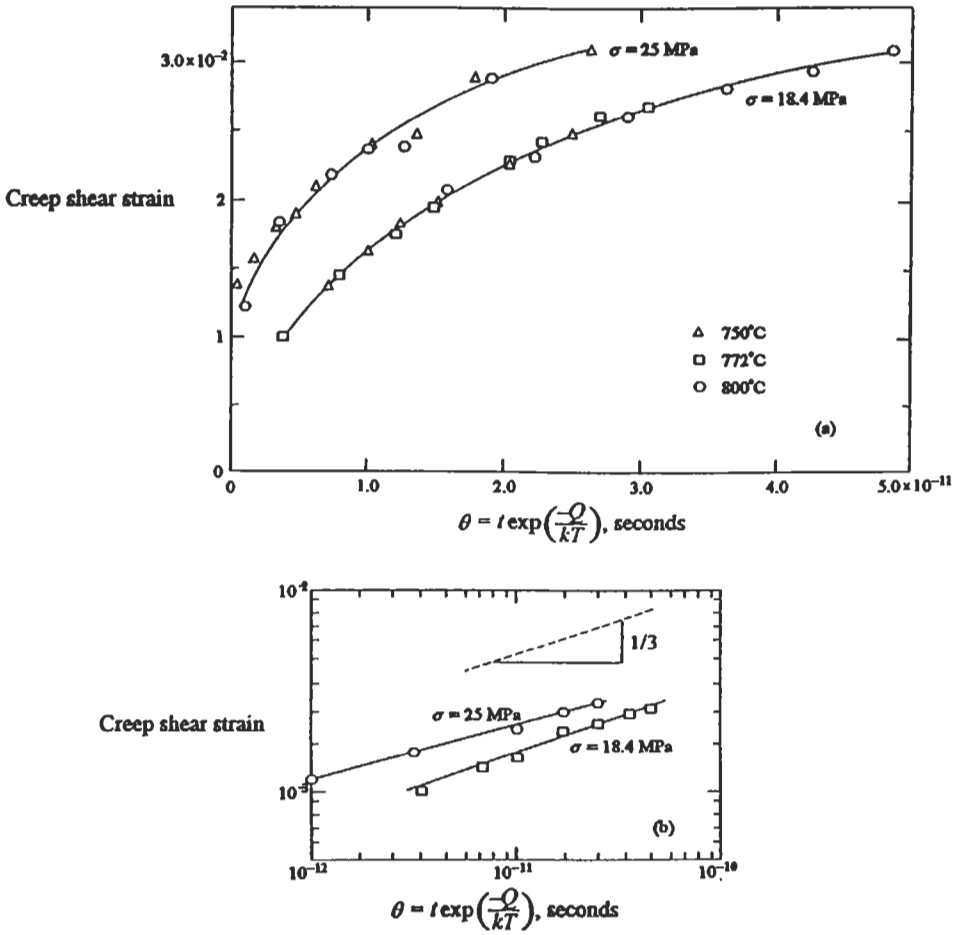

Fig. 8. Development of creep strain as a function of a time–temperature parameter at three different temperatures and two stress levels in polycrystalline nickel: (a) linear dependence, (b) logarithmic dependence. (ARGON and BHATTACHARYA [1987], courtesy of Pergamon Press).

kcal/mole, appropriate for nickel, at steady state. The same information is plotted in fig. 8b on logarithmic coordinates showing that the time law of the creep behavior is a power function with an exponent of 1/3 characteristic of the Andrade creep relation. Thus, this information demonstrates directly that the rate process which governs primary creep, after all but the first and nearly instantaneous plastic response, is the same as that which governs steady-state creep, namely diffusion-controlled static recovery. Thus, here too, as in the dynamic-recovery-controlled transient response of low homologous temperatures, the resulting time law of creep is the ubiquitous Andrade form (see also COTTRELL [1995]).

As stated in section 1, at high stress levels, progressively more strain rate is derived from thermally activated glide. Then the creep rate shows a smoothly increasing stress

dependence going from the characteristic exponents of $m = 4$–5 of power law creep to values characteristic of intermediate temperature glide-controlled processes of $m = 0(30)$. GAROFALO [1963] has found that this so-called *power-law breakdown range* of behavior can be well represented by a form

$$\dot{\varepsilon} = A_0''(\sinh c\sigma)^m \exp\left(-\frac{Q_c}{kT}\right) \tag{7}$$

which for low stress levels reverts to the Dorn expression of eq. (2). This transition from the steady-state deformation behavior of secondary creep to thermally activated glide can also be demonstrated by performing sudden stress jumps in steady-state creep followed by observing the corresponding instantaneous increase in the strain rate. This leads to substantially the same information as is obtainable from a conventional constant-strain-rate straining experiment in which a strain rate jump is imposed and the change in deformation resistance is noted. The resulting stress exponent, defined as

$$n = \left(\frac{d \ln \dot{\varepsilon}}{d \ln \sigma}\right)_T \tag{8}$$

is very nearly the same as that in thermally activated low temperature plasticity and nearly an order of magnitude larger than the steady-state creep exponent m. Table 2 gives the resulting response measured in such experiments with nickel at three different temperatures (ARGON and BHATTACHARYA [1987]).

In the following sections mechanistic interpretations and models are presented to explain the creep phenomenology discussed in this section.

3. *Creep in solid-solution alloys*

Creep in solid-solution alloys exhibits two separate forms. SHERBY and BURKE [1967] classified the creep behavior of such alloys into Class I and Class II, according to whether the stress exponent of the steady-state creep rate is given by 3 or 5. In a later paper MOHAMED and LANGDON [1974] revised this designation. Other designations referring to these two different patterns of solid solution behavior as Class A and B have also been proposed (YAVARI *et al.* [1981]) which has created some confusion in nomenclature. We adhere here to the original designation by Sherby and Burke. Class II

Table 2
Stress exponent $n = (d \ln \dot{\gamma}/d \ln \sigma)$ in jump experiments*

Temperature (°C)	Strain rate change	Stress jump
660	40	–
710	36.85 ± 1.68	30.4–42.6
800	27.78 ± 0.27	26–32

*ARGON and BHATTACHARYA [1987].

alloys, which tend to have lower concentrations of solute, exhibit an overall behavior of primary and steady-state creep which is very similar to that of pure metals outlined in section 2.0 above and to be discussed further in section 6.0 below. The creep behavior of concern here is that of the solid solution alloys known as Class I. These exhibit a minimal and inverted transient of the type shown in fig. 3 going almost immediately into steady state and show a third power stress dependence of the steady state strain rate. Moreover, dislocation arrangements observed by means of transmission electron microscopy (TEM) are unclustered showing essentially what appears to be viscous motion of individual dislocations of substantially edge character. A clue to the behavior of alloys at this type has been provided by COTTRELL [1947] and COTTRELL and JASWON [1949] who proposed that the rate of the deformation is governed by the rate that moving dislocations can carry along with them a solute atmosphere of misfitting atoms that are aggregated around edge dislocations, while screw dislocations are relatively free to move. In this model, a linear, velocity-dependent drag acts on the dislocation when the latter under an increasing applied stress becomes progressively displaced relative to the center of gravity of the solute atmosphere around it. Moreover, in the temperature regime where the phenomenon is observed, the climb resistance to edge dislocation motion is much less than the resistance offered by the solute atmosphere as this atmosphere is being dragged along by the dislocation. Therefore, edge dislocations are subjected to substantially uniform resistance to motion in all radial directions. In a direct lattice simulation of this atmosphere-dragging process, TAKEUCHI and ARGON [1979] have determined that while there is some anisotropy in the resistance to motion of the edge dislocations, for operational purposes this can be ignored in the stable range of motion of dislocations dragging along their solute environments. A detailed analysis by TAKEUCHI and ARGON [1976a] of the overall kinetics of motion of two typical opposite edge dislocations, under their mutual interaction and the applied stress, in the range where the solute drag resistance is far in excess of the climb resistance, shows that dislocations follow curvilinear paths between their initiation at sources and their mutual annihilation when they fall within the capture cross-sections of oncoming dislocations of opposite sign. The analysis gives that the average glide velocity of the typical dislocation over its life-time is:

$$\bar{v} = b\left(\frac{\tau}{\mu}\right)\left(\frac{D_{sol}}{b^2}\right)\left(\frac{kT}{\mu\Omega}\right)\frac{1}{8\,\epsilon^2\,c_0}, \tag{9}$$

where τ is the applied shear stress, ϵ is the size misfit parameter of the solute atom, c_0 is its average volume fraction in the background and D_{sol} is the diffusion constant of the solute in the solvent. From the associated analysis of the life-time of individual drifting dislocations, a time-averaged mobile dislocation density ρ_m is determined which is very close to

$$\rho_m = \frac{1}{b^2}\left(\frac{\tau}{\mu}\right)^2. \tag{10}$$

These two ingredients together define the steady-state creep rate of the Class I alloy as

$$\dot{\varepsilon}_{ss} = b\rho_m \bar{v} = \frac{1}{8\,\epsilon^2\, c_0}\left(\frac{kT}{\mu\Omega}\right)\left(\frac{D_{sol}}{b^2}\right)\left(\frac{\tau}{\mu}\right)^3. \tag{11}$$

The behavior of the alloy is stable for as long as the displaced solute environment can move along with the dislocation. Analysis shows that the dislocation should be torn away from the environment (COTTRELL [1953], HIRTH and LOTHE [1982]) when the velocity exceeds v_c, where

$$v_c \approx \frac{b}{\epsilon}\frac{\sqrt{2}}{4}\left(\frac{D_{sol}}{b^2}\right)\left(\frac{kT}{\mu\Omega}\right), \tag{12}$$

independent of solute concentration.

Figure 9 shows a comparison (TAKEUCHI and ARGON [1976a]) of the expression given in eq. (11) with experimental data for three solid-solution alloys having the apparent characteristics of Class I designation, based on the diffusion constants given by BIRD *et al.* [1969]. This agreement and the generally viscous motion of individual dislocations for a very similar aluminum 5.1% magnesium alloy shown in fig. 10, indicates that the model is on solid foundation. Further examination of the assumption that the solute-atmosphere resistance to glide far exceeds the climb resistance is not borne out in a number of alloys which otherwise satisfy the basic phenomenology (TAKEUCHI and ARGON [1976a]). Moreover, the examination of 28 different solid-solution alloys by MOHAMED and LANGDON [1974] for the dividing line behavior

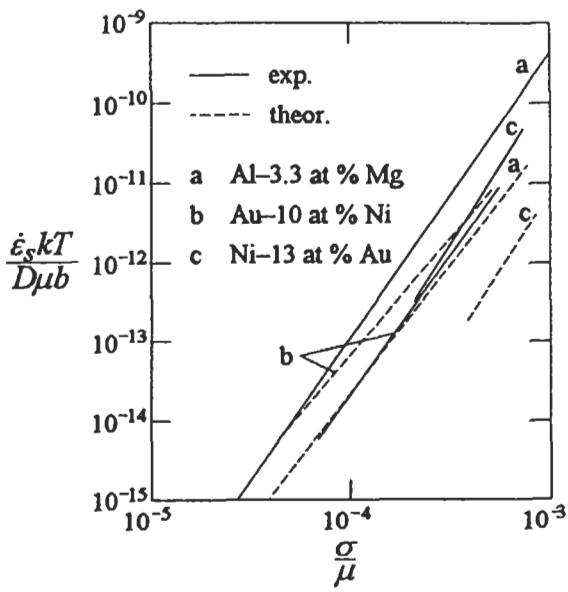

Fig. 9. Comparison between the observed creep rate and the theoretical model of Class I alloys, for three alloys (TAKEUCHI and ARGON [1976a], courtesy of Pergamon Press).

Fig. 10. The dislocation structure in a crept aluminum-5.1% magnesium Class I solid solution alloy at 359° C and 48 MPa and 0.05 creep strain. The bar is 1 μm (TAKEUCHI and ARGON [1976b], courtesy of Pergamon Press).

between Class I and Class II alloys, based on the above criterion has shown that a number of Class I alloys, including the aluminum-magnesium alloys, are difficult to separate on the basis of their dominance of drag resistance over climb resistance, while in phenomenology they obey the third power stress dependence of eq. (11). More recently, KOCKS and CHEN [1993] have found that aluminum-magnesium alloys with 2.3 and 5.2 atomic percent magnesium obey the basic phenomenology of eq. (11), but show an initial temperature dependence of the pre-exponential factor similar to that of the Class II alloys or pure metals of eqs. 2 or 3, and no dependence on solute concentration as given in eq. (11) indicating that the solute atmosphere around the dislocation may be of constant size and not in thermodynamic equilibrium (HIRTH [1993]).

An important feature of the Class I alloy behavior is that it represents what is considered a *rational creep law*, in which the dislocation velocity is a linear function of stress resulting from a simple drag model. Moreover, the mobile dislocation density, in quasi-straight form and in a state of viscous motion is in kinetic equilibrium, governed by a simple interplane resistance consideration presented in section 7.3.9 of chapter 21. As we will amplify in section 6 below, the behavior of pure metals and Class II alloys, which resemble the former, is radically different in both external phenomenology and in microstructure. This requires different and somewhat less satisfying models to explain their behavior.

4. *Harper–Dorn creep*

HARPER and DORN [1957] and HARPER *et al.* [1958] reported a linear viscous creep in aluminum at stress levels in the range of $5 \times 10^{-6}\,\mu$. The creep is relatively free of transients, shows no grain-size dependence and is at a level considerably in excess of what could be expected from diffusional flow. A similar response was reported by MOHAMED *et al.* [1975] in experiments on lead and tin, associated with observations of a very low and unchanging density of dislocations in the range of $10^8\ m^{-2}$. Additional observations were provided by YAVARI and LANGDON [1977] in the aluminum-magnesium Class I alloys at very low stress levels. The linear stress dependence of the creep rate and the absence of dependence of the dislocation density on stress level, reflects a viscous behavior of a relatively constant density of mobile dislocations. A rationalization of the mechanism of this type of creep relates it to the Class I type behavior discussed in section 3 above where, however, an unchanging dislocation density, giving a creep rate of

$$\dot{\varepsilon} = A_{HD}\left(\frac{\mu\Omega}{kT}\right)\left(\frac{D}{b^2}\right)\left(\frac{\sigma}{\mu}\right) \tag{13}$$

is assumed to be the case. In the above equation the creep constant A_{HD} ranges between 10^{-11} to 10^{-10} (YAVARI and LANGDON [1977]). The reports of Harper–Dorn creep behavior have been limited to the above cases, and more widespread observations in other pure metals is lacking. The behavior leaves many unanswered questions such as what governs the mobile dislocation density, how it is established and how it maintains itself in equilibrium.

5. *Static thermal recovery*

The critical element in the maintenance of steady-state creep at a constant structure is static thermal recovery that balances strain hardening. This long-standing point of view advocated by BAILEY [1926] and OROWAN [1947], recognizes that the rate process of steady-state creep must be controlled by the rate process of recovery. In spite of this, there has been considerable controversy on the nature of the rate-controlling process of steady-state creep. Views have ranged from various thermally activated steady-state glide configurations of dislocations such as jog-dragging screw dislocations (HIRSCH and WARRINGTON [1961], BARRETT and NIX [1965]) to extensions of dynamic recovery of Stage III hardening to high temperatures (KOCKS and MECKING [1979], MECKING and KOCKS [1981]). That steady state creep, at least in pure metals, is indeed a balance between concurrent strain-hardening and static thermal recovery has been demonstrated by MITRA and MCLEAN [1967] in a series of coupled incremental recovery and strain-hardening experiments with nickel and aluminum. The associated extensive demonstrations of DORN [1956] that the activation energy of steady-state creep is that of self diffusion is positive support to the proposition that the fundamental recovery process is indeed diffusion-controlled and must involve the systematic reduction of dislocation

density which is normally built-up in strain hardening. There have been many experimental studies involving observations of dislocation structures by TEM upon increments of recovery, followed by mechanical probing of such material in bulk to ascertain the effect of the recovery process. These have, however, not clarified the actual mechanisms and the kinetics of the process (see, e.g., HASEGAWA and KOCKS [1979]). Direct observations of creeping samples in the high-voltage electron microscope (HVEM) have shown a number of important details of the creep induced alterations of dislocation structures, but these have been adversely influenced by their proximity to free surfaces (for a discussion see MARTIN and ARGON [1986]). The most informative observations of the recovery mechanism and its underlying kinetics have come from *in situ* observations of the recovery process in the HVEM on previously deformed copper and nickel crystals by PRINZ *et al.* [1982]. A prevalent feature of the deformed and imperfectly recovered dislocation microstructure is the relatively equiaxed "woolly" dislocation cells containing a large number of redundant dislocations in the cell walls. The latter are pinned in place by a substantial density of barely resolvable small loops and short prismatic dipoles which often appear attached to the dislocations, apparently formed by local reactions. As the typical sequence of *in situ* observations of fig. 11 on nickel deformed at RT to 118 MPa and observed at 427°C (0.4 T_m) shows, the effect of recovery is a systematic reduction of dislocation density in the cell walls without any meaningful change in the cell size (see also ch. 28, § 2.4.1). The critical step of this dislocation reduction process was recorded in a number of sequences. These have established that the dislocation elimination process occurs in very jerky steps rather than involving quasi-viscous, climb-controlled, motions of dislocations. In such sequences, it was noted that during much of the time nothing happens. Then, sudden and almost spontaneous rearrangements and wholesale cancellations of considerable redundant dislocation length by glide occurs, triggered by the removal of some pinning points. A typical sequence in the removal of a pinning point and the ensuing rapid rearrangement of dislocations in copper, deformed previously to a flow stress of 70 MPa at RT and observed in the HVEM at 270°C (0.32 T_m) is shown in fig. 12. These observations have established that static recovery is basically a process of diffusion-controlled removal of pinning points, and that the major reduction of dislocation density occurs by glide-controlled spontaneous cancellations. Nevertheless, since the rate controlling process involves diffusion this is reflected in the measurements of the rate of reduction of the total dislocation density at around the recovery sites. Figure 13 shows such a measurement as a function of time at $T = 0.32\ T_m$ for copper crystals deformed to flow stresses of 40 and 70 MPa, including the final dislocation densities reached in bulk annealing treatments for 5.75×10^4 s at three homologous temperatures. The data of fig. 13 can be correlated well with dislocation core-diffusion-controlled-climb, presumably occurring around the pinning points. The activation energy of $Q = 1.09$ *eV*, derivable from the measurements, is in the range of activation energies listed for core diffusion in copper (PRINZ *et al.* [1981]). It can be expected that at higher temperatures, where volume diffusion becomes more effective the recovery should then be controlled by this process. As fig. 11d shows, after prolonged periods of recovery that eliminates the bulk of the redundant dislocations, the remaining dislocations in the cell walls (now referred to as *sub-grain boundaries*) reduce to the

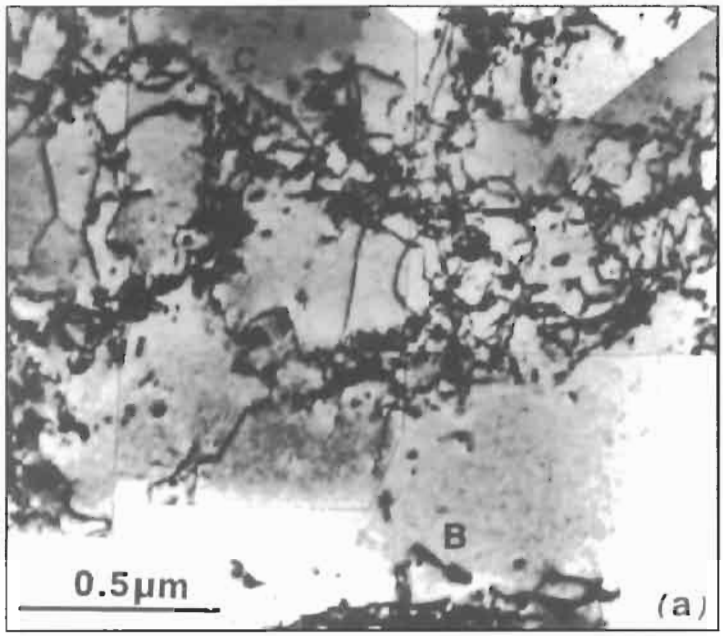

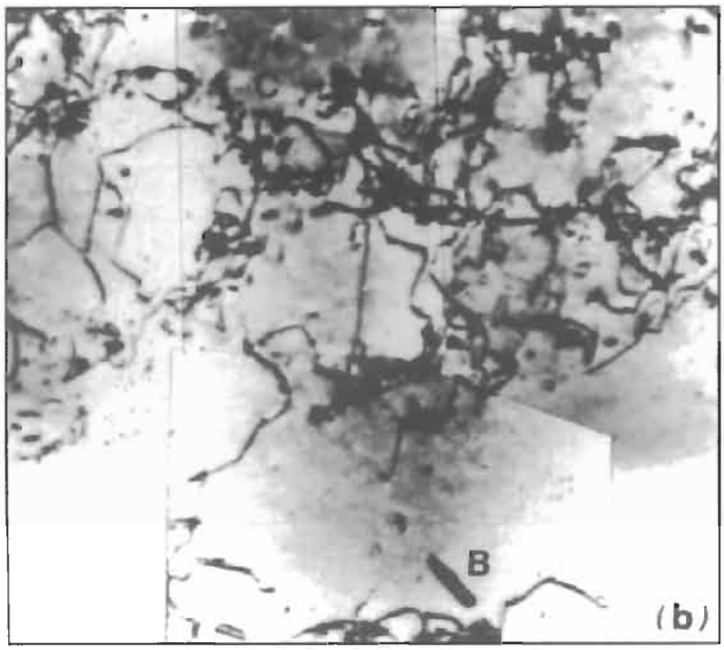

References: p. 2004.

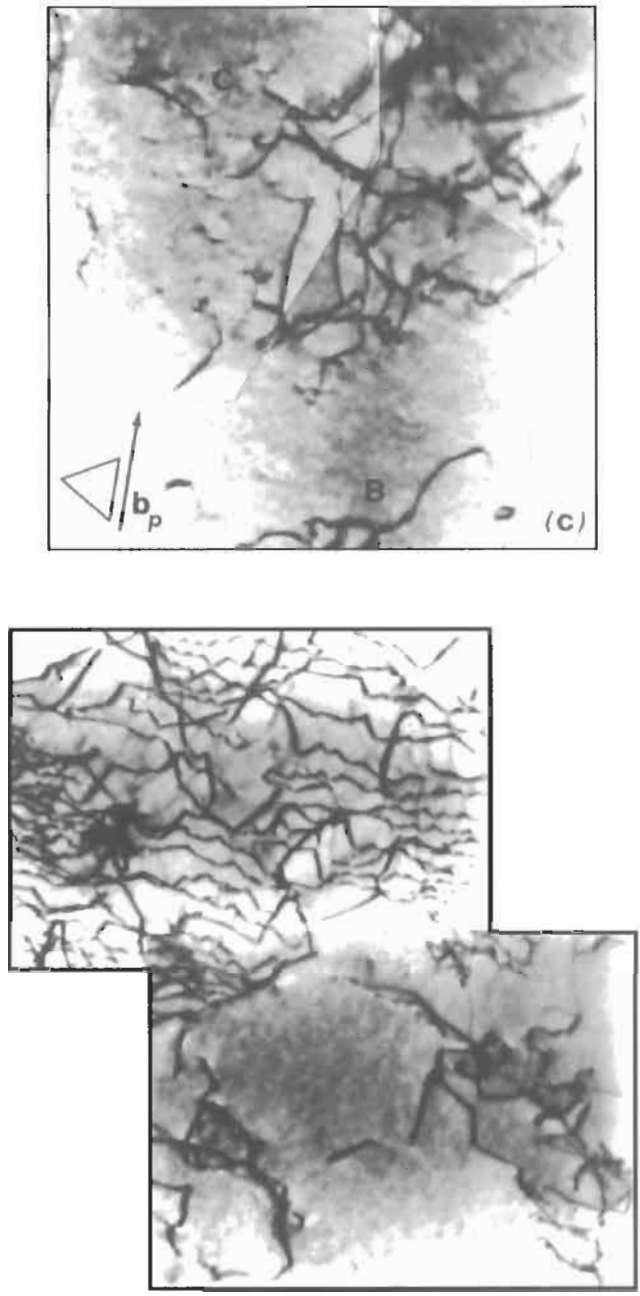

Fig. 11. Alterations in the dislocation structure with time in nickel predeformed at RT to 118 MPa, and observed in *in situ*, annealing in the TEM, at 543 K (0.32 T_m): (a) as deformed at RT, $t = 0$; (b) at $t = 700$s; (c) $t = 1900$s; (d) reacted network in a different area after annealing at 872 K for 1200 s. (PRINZ *et al.* [1982], courtesy of Pergamon

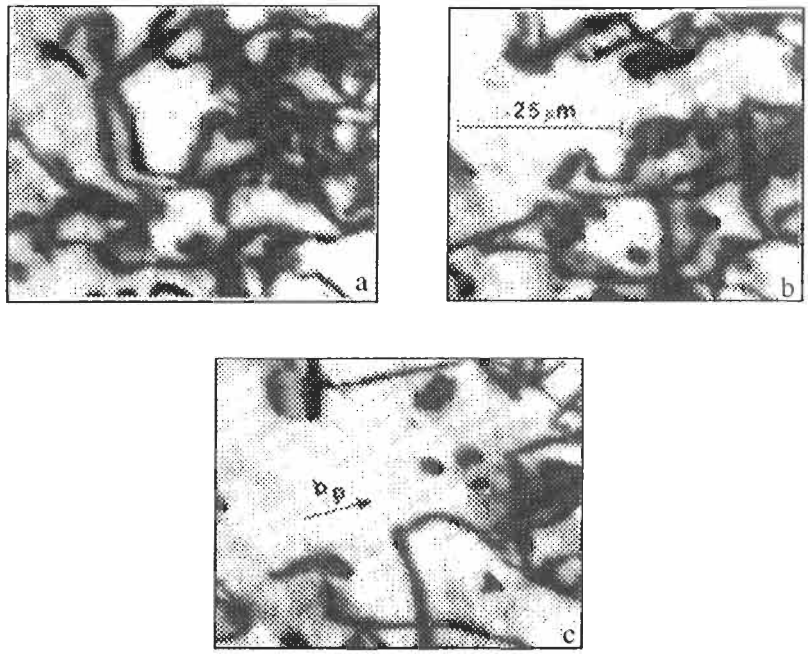

Fig. 12. A time sequence of diffusion-controlled removal of pinning points in a work hardened copper, resulting in "glide collapse" of redundant pinned dislocations (PRINZ *et al.* [1982], courtesy of Pergamon Press).

geometrically necessary set (see ch. 25, § 3.2.3), and eventually take forms of well-knitted dislocation nets like the one shown in fig. 14 (MIEKK-OJA and LINDROOS [1975]).

6. *Processes in steady-state creep in pure metals and class II solid-solution alloys*

6.1. Overview

As stated, earlier in sections 2 and 5 above, in the secondary creep stage of pure metals and Class II alloys a dynamic balance is reached between strain hardening and diffusion controlled thermal recovery associated with the establishment of a statistically stationary dislocation structure. Unlike the relatively simple set of processes established in the creep response of Class I solid solution alloys discussed in section 3, the processes that lead to steady state in pure metals and Class II alloys are complex and have resisted efforts to provide simple and straightforward models. In this section we take account of these processes and furnish some insights into possible mechanisms.

The principal distinguishing characteristic that differentiates the behavior of the pure metals and Class II alloys from Class I alloys is the establishment of well formed subgrains that take the part of the cells that form in the course of plastic deformation of these materials in the low temperature range. In fact, the similarity in the phenomenology

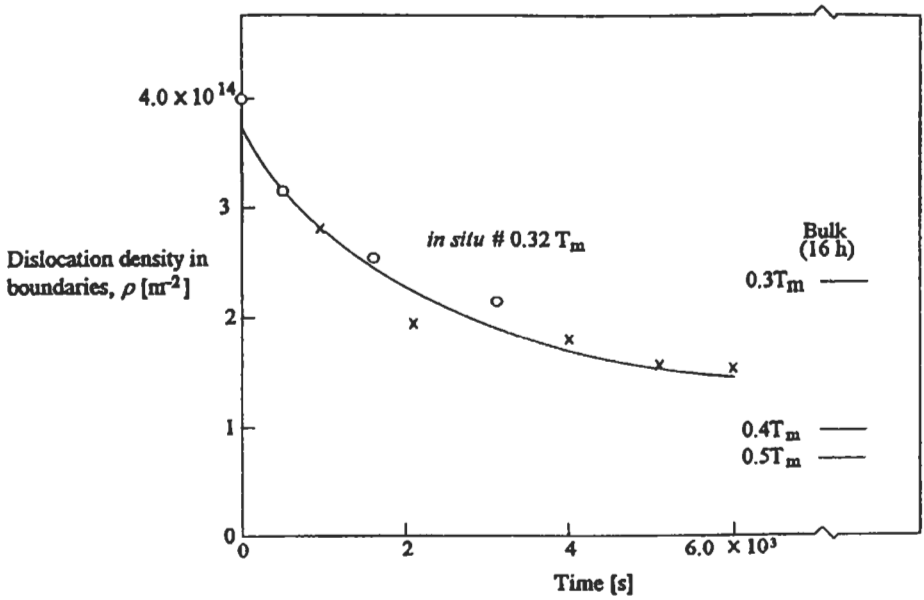

Fig. 13. Time-dependent reduction in dislocation density in *in situ* annealing at 0.32 T_m of a copper single crystal initially deformed to 70 (×) MPa, and 40 (○) MPa at RT (PRINZ *et al.* [1982], courtesy of Pergamon Press).

of evolving dislocation structures indicates that the processes of intersecting slip, production of slip obstacles, fluctuations in dislocation fluxes, etc., which are important in cell formation in Stage III and Stage IV deformation at low temperatures, continue to be active in creep. The presence of effective diffusional processes of obstacle removal as described in section 5, however, result in substantial modifications of the low-temperature processes of cell formation, giving rise to much better defined subgrains which have a far lower ratio of redundant to geometrically necessary dislocation density in their boundaries. In what follows, we describe the most prominent characteristics of the evolving dislocation microstructure associated with the creep deformation which were thoroughly reviewed by TAKEUCHI and ARGON [1976b], and by MARTIN and ARGON [1986].

6.2. Slip distribution and dislocation clustering into sub-boundaries

Well-defined slip bands which are a prominent feature of plastic deformation at low temperatures in the range where dynamic recovery is present, are absent in creep where dislocation motion is less channeled and spatially more dispersed. Dislocation aggregation, formation of kink bands, polygonization and clustering of dislocations into cells have been followed in detail in primary creep, leading to the gradual and progressive evolution of a set of increasingly better formed subgrains when steady state conditions are reached. Figure 15 gives a schematic rendering of the aggregation process, ending up with the subgrains of steady-state creep (TAKEUCHI and ARGON [1976b]). Figure 16 shows the appearance of subgrains in crept aluminum, as viewed in the SEM with the back

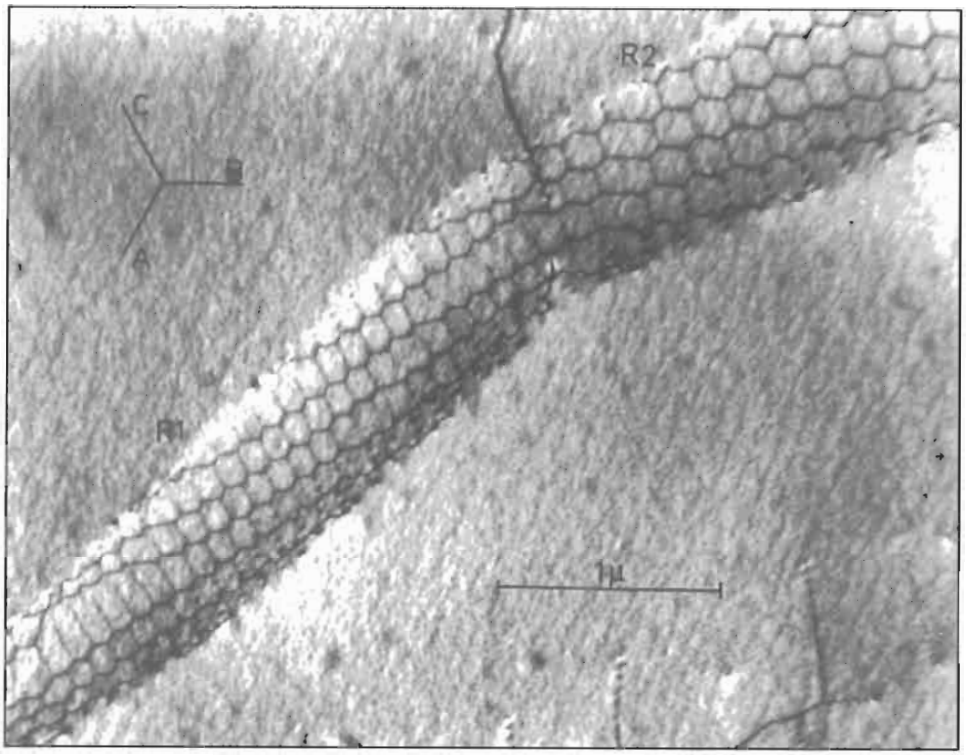

Fig. 14. A well-equilibrated hexagonal sub-grain boundary dislocation network in an aluminum–magnesium solid solution alloy (MIEKK-OJA and LINDROOS [1975], courtesy of M.I.T. Press).

scattered electron mode (CARRARD and MARTIN [1984]). A very important characteristic of the subgrain walls that distinguishes them from their low-temperature counterparts, the cell walls, is their mobility. EXELL and WARRINGTON [1972] have demonstrated that the subgrain boundaries are mobile and that for roughly every 0.05 increment of creep strain, they sweep over subgrain dimensions, to reinforce, annihilate, or modify neighboring subgrain boundaries that they encounter. In the process, individual subgrains can shrink, expand or break up. Thus, the self-similar appearance of subgrains during steady-state creep does not signify their unchanging nature, but that a dynamic steady state is present, keeping the subgrain modifications statistically stationary over the active population, while strong local alterations occur constantly. It is this ability to adjust to the current conditions of stress and temperature that makes the steady state response reversible when the stress or temperature are changed in steady state creep — albeit associated with a transient during which the new conditions are established. Figure 17 shows direct evidence for such subgrain boundary motions in aluminum creeping at 500°C during a creep strain increment of 1.5%. CAILLARD and MARTIN [1982a,b, 1983] have made a detailed study of the kinematics of subgrain boundary motion related to their specific

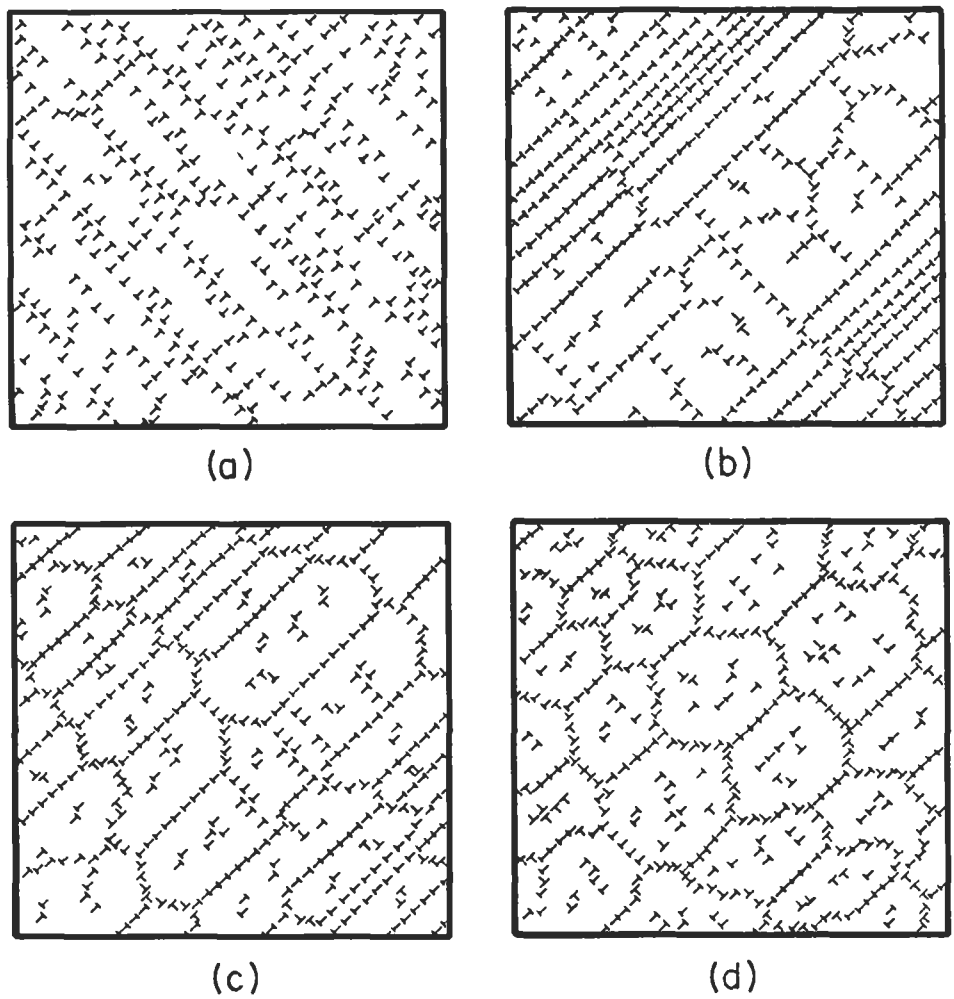

Fig. 15. Schematic representation of the gradual evolution of a subgrain structure in a pure metal during primary creep leading eventually to a steady state (TAKEUCHI and ARGON [1976b], courtesy of Chapman and Hall).

dislocation content and have established that, apart from pure twist boundaries which for fundamental reasons cannot be displaced by an applied stress, all other sub-boundaries contain at least one set of boundary dislocations which couple to the applied stress and can be displaced — albeit at times with considerable kinematically necessary internal rearrangements of these boundary dislocations. ARGON *et al.* [1981] have discussed in some detail how a given dynamic steady-state subgrain structure can maintain its statistically self similar character during steady state creep.

The angle of misorientation between subgrain interiors changes monotonically during

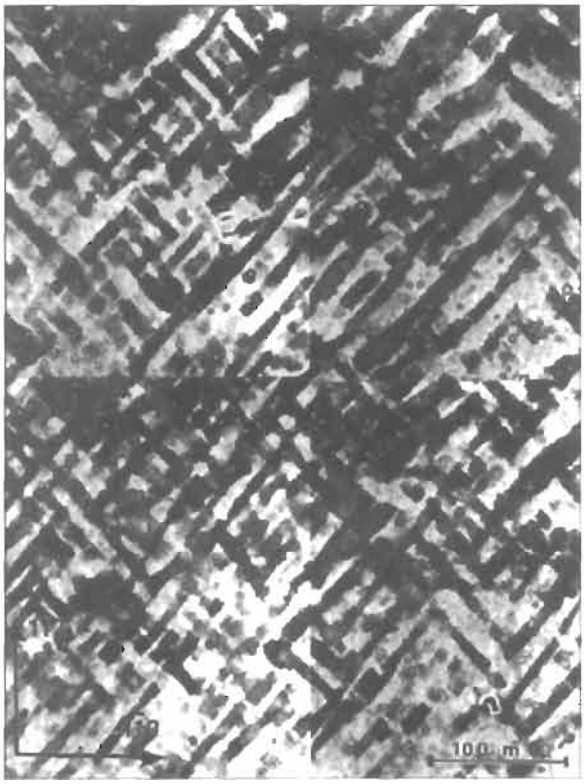

Fig.16. A typical subgrain structure formed in a crept aluminum <1 12> oriented single crystal to a shear strain of 0.34 at a shear stress of 6.5 MPa at 150° C as revealed by SEM in backscattered electron contrast (C ARRARD and MARTIN [1984], courtesy of Pineridge Press).

primary creep and reaches a definite steady state value around 1° at steady-state creep. The experimental measurements of ORLOVA *et al.* [1972a,b], shown in fig. 18a,b indicate that the angle of misorientation does not depend on stress, but increases monotonically with strain as it appears to do also in cell formation at low temperatures — possibly in response to random variations in the positive and negative dislocation fluxes flowing through each other that produce the creep strain (ARGON and HAASEN [1993]).

A remarkable characteristic of the subgrains of steady state creep is that their size d relates quite well to the reciprocal of the applied shear stress τ through a widely observed functional dependence of

$$d = K(\mu b/\tau) \tag{14}$$

which is also known to hold for cell size in low temperature deformation. This is another manifestation of a so-called *principle of similitude* that relates dislocation structures to the plastic resistance (or creep resistance) that they exert (or vice versa) (KUHLMANN–

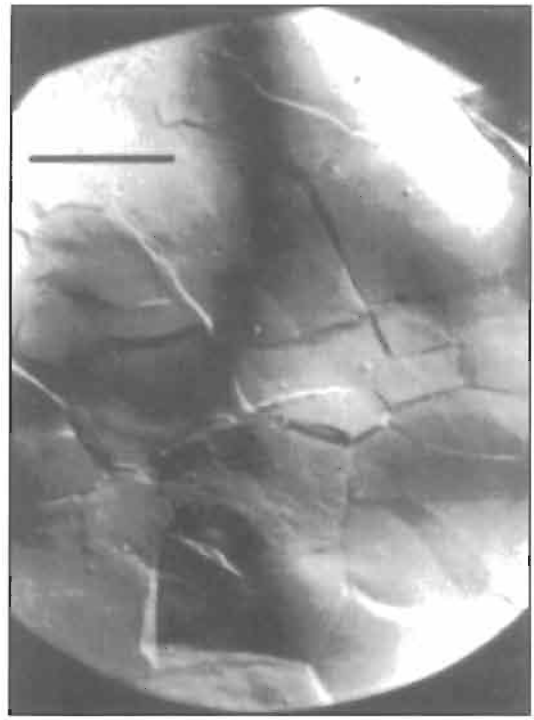

Fig. 17. Subgrain boundary migration during creep of aluminum under 1 MPa stress at 500° C, after a strain of 0.2. Motions relate to an incremental strain step of 0.015, bar is 200 μm (EXELL and WARRINGTON [1972], courtesy of Taylor and Francis).

WILSDORF [1968]). Figure 19 shows the actual dependence of d (normalized with respect to the Burgers vector) on τ for a variety of materials including FCC and BCC metals, ionic compounds and oxides (TAKEUCHI and ARGON [1976b]). The figure shows that while the dependence is close to that stated in eq. (14), the actual stress dependence of d is often less strong than is indicated in eq. (14) — relating to a stress exponent sometime as low 0.7. Nevertheless, the overall behavior band indicates that while for metals K tends to be close to 10, it is between 20–50 for compounds. The corresponding proportionality constant for cells at low temperatures is between 5–10 (PRINZ and ARGON [1980]). Figure 20 shows that during primary creep, as the dislocation segregation into subgrain boundaries is accomplished under a monotonically increasing dislocation density due to strain-hardening, the dislocation density inside the subgrains actually decreases. At steady state the dislocation density in the sub-boundaries is at least a factor of 20 above that remaining inside the subgrains. When compared with the corresponding behavior of cells and cell interiors for low-temperature deformation this ratio is far smaller than is encountered there, and is a direct demonstration of the effectiveness of the concurrent static recovery processes which keep the redundant dislocation density inside subgrain boundaries very low.

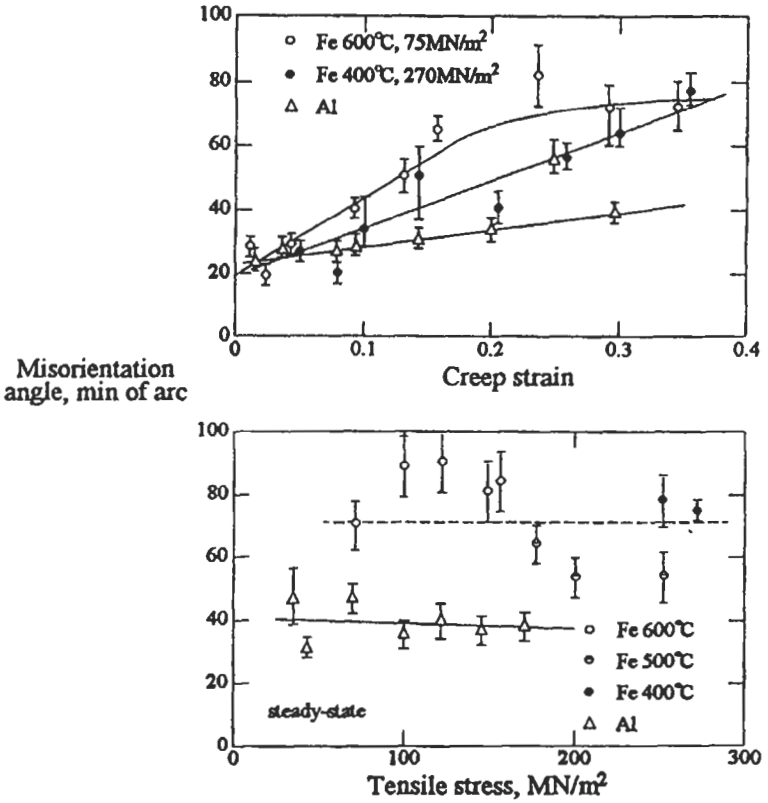

Fig. 18. Evolution of angle of misorientation with creep strain and its relative independence of stress (TAKEUCHI and ARGON [1976b], courtesy of Chapman and Hall).

The connection between the subgrain size d and the creep resistance τ given by eq. (14) has been the basis of certain practical processing practices to improve the creep resistance of commercial alloys. Several investigators have noted that in alloys with a small volume fraction of incoherent dispersoids, low temperature plastic deformation that results in cell formation where the dispersoids anchor the cell walls, actually results also in improved creep resistance at elevated temperatures. This is because the dispersoids effectively trap the redundant dislocation density and very markedly retard the recovery processes outlined in section 5 above (GRANT [1995]). Figure 21 which complements the information in figs. 19 and 20 shows that the steady-state creep resistance in shear, τ, is related to the overall dislocation density, ρ, by the well-known relation

$$\tau = \alpha\mu b\sqrt{\rho}. \tag{15}$$

Since most of the dislocation density resides in the sub-boundaries, it must be concluded that as in low-temperature deformation (PRINZ and ARGON [1984], ARGON and HAASEN

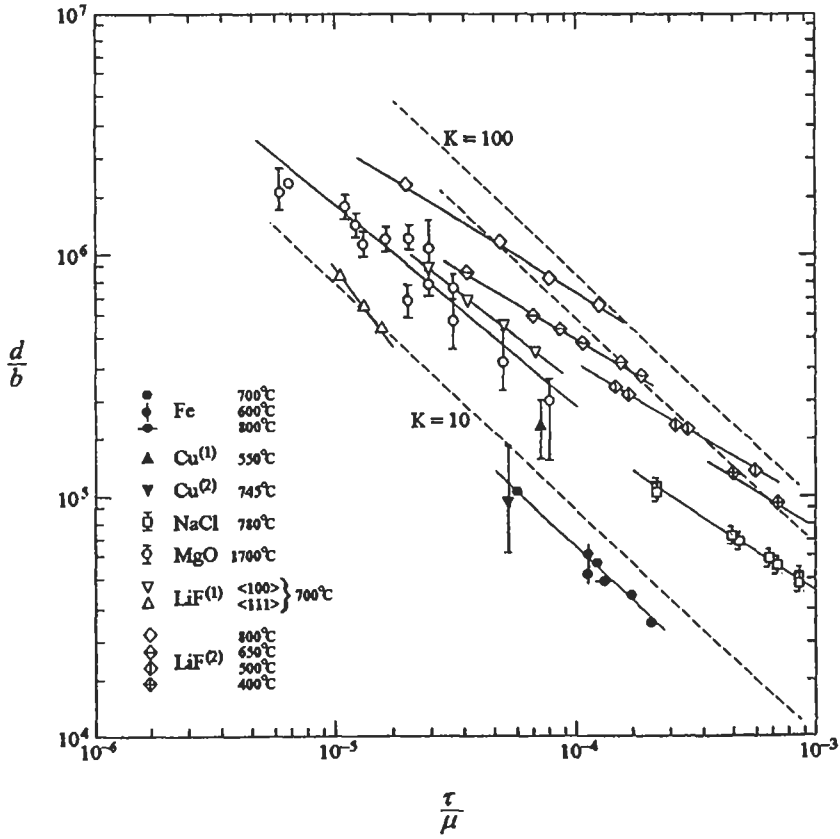

Fig. 19. Relation between the subgrain size and shear stress in steady-state creep in metals and some ionic compounds (TAKEUCHI and ARGON [1976b], courtesy of Chapman and Hall).

[1993]), the sub-boundaries and sub-grain interior make separate and distinct contributions to the overall creep resistance — albeit mechanistically in a possibly different manner. In section 2 above, results of primary creep experiments on nickel were presented which indicated that the rise in dislocation density during primary creep and the associated increase in reference plastic resistance does satisfy the creep rate expression of eq. (15) having the same temperature dependence as that of steady-state creep. The details given above are fully consistent with this picture.

6.3. Dynamic internal stresses

Another important characteristic of steady-state creep in subgrain-forming metals and alloys is that a significant part of the creep resistance is derived from dynamic internal stresses which have been measured by means of so-called *stress dip* experiments. In these experiments the applied stress is suddenly decreased by a certain amount. While small decrements of stress result in immediate decreases of creep rate, larger decrements give

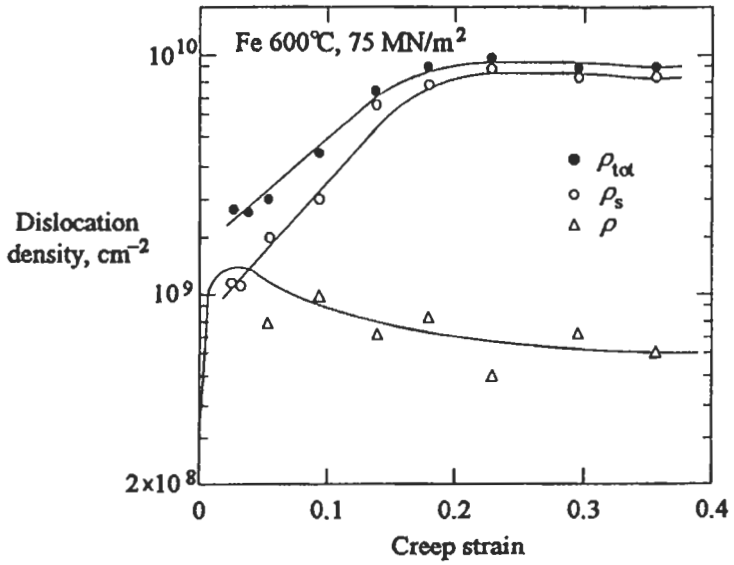

Fig. 20. Strain-dependent evolution of dislocation density in the subgrain boundaries and subgrain interiors in creep of iron at 75 MPa at 600° C (TAKEUCHI and ARGON [1976b], courtesy of Chapman and Hall).

rise to actual rates of reverse creep. In between, at a certain critical decrement, zero creep rate is observed for a certain time Δt followed by an eventual positive creep rate as shown in the top part of fig. 22. The corresponding response of a Class I alloy, where no subgrains are formed during creep, is shown in the lower part of fig. 22, indicating a near instantaneous response to stress change. It is then argued that in the subgrain-forming alloys at the critical stress decrement the applied shear stress τ exactly balances a dynamic internal back-stress, resulting in zero creep rate, until recovery processes lower the dynamic internal stress so that the now reduced applied stress can again produce a positive creep rate. While there has been considerable controversy associated with this interpretation (see TAKEUCHI and ARGON [1976b]); there is overwhelming evidence that some dynamic internal back-stresses do indeed develop as part of the subgrain structure and are not only responsible for an increased creep resistance, but also are associated with the higher creep stress exponent m above the so-called rational level of 3, discussed in section 3 above. Such internal stress-dip experiments have been made with a large number of sub-grain forming alloys. Most of the results are summarized in fig. 23, showing that, as might be expected, the internal stresses have a direct dependence on the actual level of plastic resistance. A quantitatively successful model for the dynamic internal stresses based on strain-induced bowing of the migrating subgrain boundaries during creep deformation has been advanced by GIBELING and NIX [1980] and ARGON and TAKEUCHI [1981], based on an earlier suggestion of ARGON [1977]. This model gives a dependence of the dynamic internal shear stress τ_i on the steady-state creep resistance τ, in shear, which is in power law form given by the expression

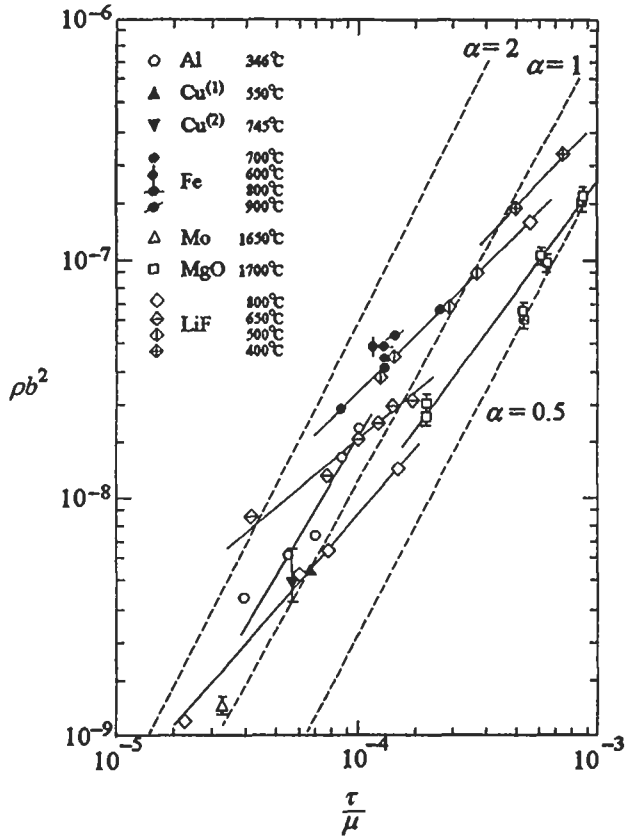

Fig. 21. Relationship between the overall dislocation density and shear stress during steady-state creep for single crystals of a variety of metals and ionic compounds (TAKEUCHI and ARGON [1976b], courtesy of Chapman and Hall).

$$\frac{\tau_i}{K\mu\theta} = \alpha\frac{(1-\nu)}{\pi}\left(\frac{\tau}{K\mu\theta}\right)^{2/3}, \tag{16}$$

where K is the proportionality constant in eq. (14), θ is the random misorientation angle between subgrains at steady state and α is a theoretical constant of magnitude 0.317. The form of this expression (for $K=30$) is shown in fig. 23 as the dashed curve labelled "Theory". ARGON and TAKEUCHI [1981] have also shown how such dynamic internal stress of random signs for which τ_i is the random error sum, can modulate a rational local creep rate response of a power-law stress dependence of 3 to show a considerably higher apparent stress exponent in the range between 4.5 and 6.

6.4. Effect of stacking-fault energy

The dependence of the creep rate on stacking-fault energy shown in fig. 5 and its incorporation into the creep-rate expression is usually treated as a reasonable empirical

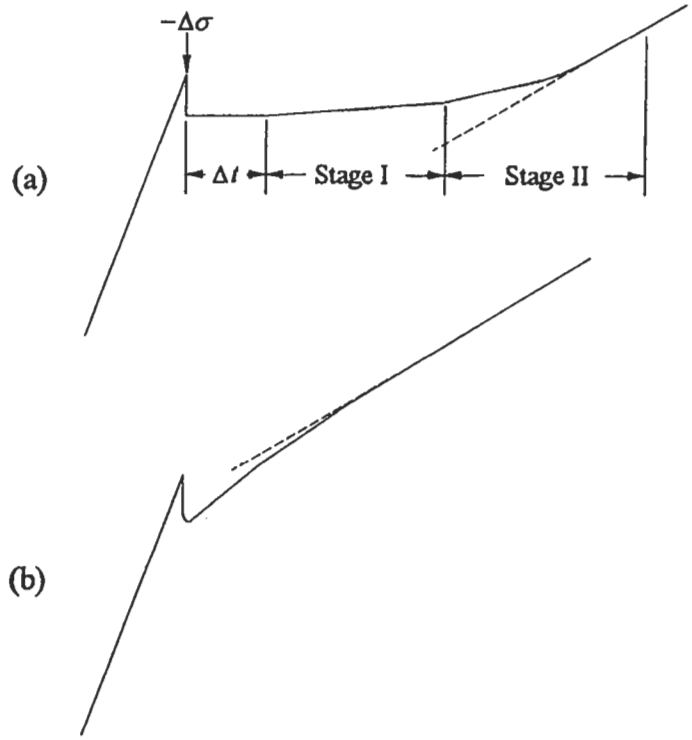

Fig. 22. Schematic representation of the transient behavior of creep after a stress drop in steady-state creep: (a) in pure metals and subgrain forming Class II alloys, and (b) in a Class I alloy (TAKEUCHI and ARGON [1976b], courtesy of Chapman and Hall).

finding and is justified by the argument that the climb of extended jogs (see ch. 20) along extended dislocations should experience more difficulty in climbing than contracted jogs. However, little is known about the structure of extended elemental jogs beyond the certainty that they cannot be contracted. A number of models for the climb of extended dislocations have been proposed which are based on formation partial vacancies in the core of the extended jog, followed by their chance coalescence into a full vacancy and its emission into the crystal (see HIRTH and LOTHE [1982]). In a specific consideration of such a model, ARGON and MOFFATT [1981] developed an expression for the climb velocity of an extended dislocation, based on the translation rate of extended jogs, as

$$v_c = \frac{A\sigma\Omega D}{bkT}\left(\frac{\chi}{\mu b}\right)^2 \tag{17}$$

where $A = 1050$ (for $\nu = 0.3$) is a numerical constant, σ is the tensile stress acting across the extra half plane of the dislocation, and D can be either the diffusion constant along the core of the extended dislocation or the volume diffusion constant. Moreover, ARGON and TAKEUCHI [1981] have demonstrated that the mobile dislocation density in creep can

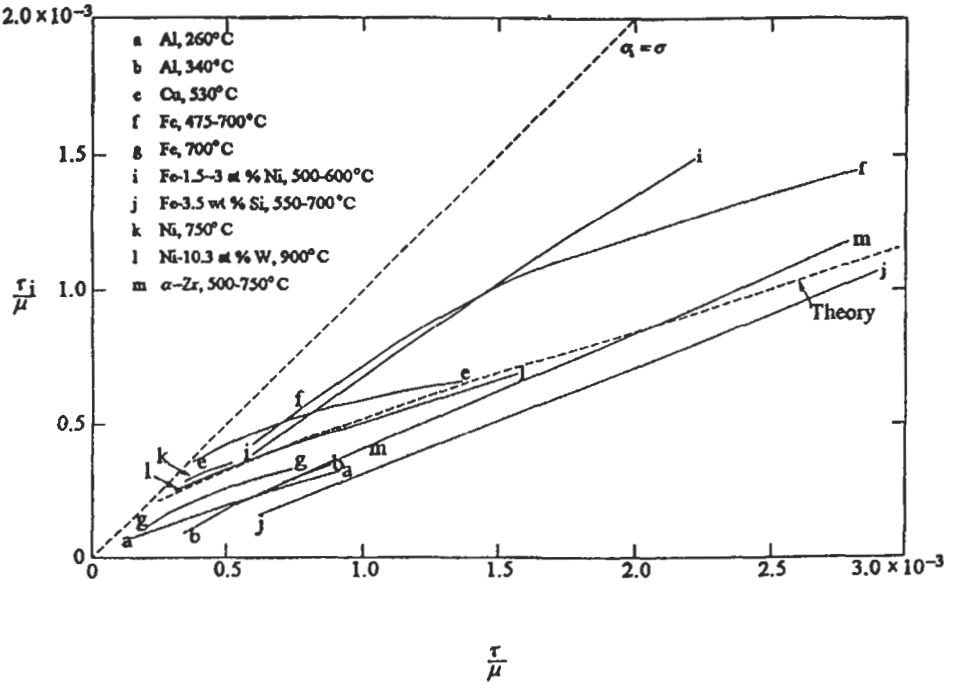

Fig. 23. Dependence of internal stress on the overall stress as measured in stress-dip experiments at steady-state creep, for a variety of subgrain forming metals and alloys, and the predictions of a theoretical model (ARGON and TAKEUCHI [1981], courtesy of Pergamon Press).

also be dependent on the stacking-fault factor ($\chi/\mu b$) linearly, giving together with the velocity expression of eq. (17) the third-power dependence of the creep rate on the stacking-fault factor of eqs. 2, 3, and 5.

7. *Diffusional flow*

At high homologous temperatures and low stresses where dislocation creep rates become very small, inelastic deformation is dominated by diffusional flow involving shape changes of polycrystalline samples purely by diffusional material transport. This deformation is of particular importance in ceramics and other substances in which very high lattice resistance to dislocation motion extends to very high homologous temperatures. The importance of the process was recognized in independent publications by NABARRO [1947] and HERRING [1950] who provided a mechanism for the deformation that relies on material transport by volume diffusion. In a later publication, COBLE [1963] noted that the process is dominated at lower temperatures and in fine grained material by grain-boundary diffusion fluxes rather than volume fluxes. Since the deformation does not

involve dislocations at all and is linked only to point-defect fluxes, it is perhaps the best understood inelastic deformation process. Some accumulating criticism of the mechanism of diffusional flow has been countered effectively by BURTON and REYNOLDS [1995].

Consider in a polycrystalline sample subjected to a shear stress σ a representative square shaped grain of size d, shown in fig. 24 with its edges normal to the pair of tensile (T) and compressive (C) stresses characteristic of a state of pure shear. These stresses enrich the local equilibrium atomic vacancy concentration adjacent to the grain boundary under tensile stress to c_T and lower it adjacent to the boundary under compressive stress to c_C given by

$$c_T = c_0 \exp \frac{\sigma\Omega}{kT} \quad \text{and} \quad c_C = c_0 \exp\left(-\frac{\sigma\Omega}{kT}\right) \tag{18a, b}$$

where

$$c_0 = \exp\left(-\frac{H_{fv}}{kT}\right) \tag{19}$$

is the equilibrium vacancy concentration at the given temperature in the absence of stress and where H_{fv} is the enthalpy of formation of a vacancy. The changed concentrations are established over very short periods of time of the order of $(\nu_D c_0)^{-1}$ where ν_D is the characteristic atomic frequency, and are made possible by the incoherent nature of the high-angle grain boundaries that can act as effective sources and sinks for vacancies. The changed vacancy concentrations along tensile and compressive grain boundaries act as a chemical potential and set up counter currents of vacancies from tensile to compressive boundaries and atom currents in the opposite directions, both through the volume of the grain and along the grain boundaries. A steady-state set of diffusional fluxes become established after a short transient period of the order of d^2/D_{eff} where D_{eff} is the effective diffusion constant defined in eq. (21) below, incorporating the weighted matter fluxes along both the volume paths and the grain boundaries, between the tension and compression boundaries, along which the concentration differences are maintained for as long as the stresses remain applied.

The material transport that is associated with these matter fluxes remove matter from the boundaries under compression and plate it on the boundaries under tension, thereby, producing a general elongation in the tension direction and a corresponding shrinkage in the compression direction, without producing any lattice distortion inside the grains. Elementary geometrical consideration lead to a final "homogenized" shear rate $\dot{\gamma}$ over a representative volume element incorporating a number of grains, which is

$$\dot{\gamma}_{DF} = A_{DF} \frac{\sigma\Omega D_{\text{eff}}}{d^2 kT} \tag{20}$$

where

$$D_{\text{eff}} = D_v + \frac{\pi\delta}{2d} D_B \tag{21}$$

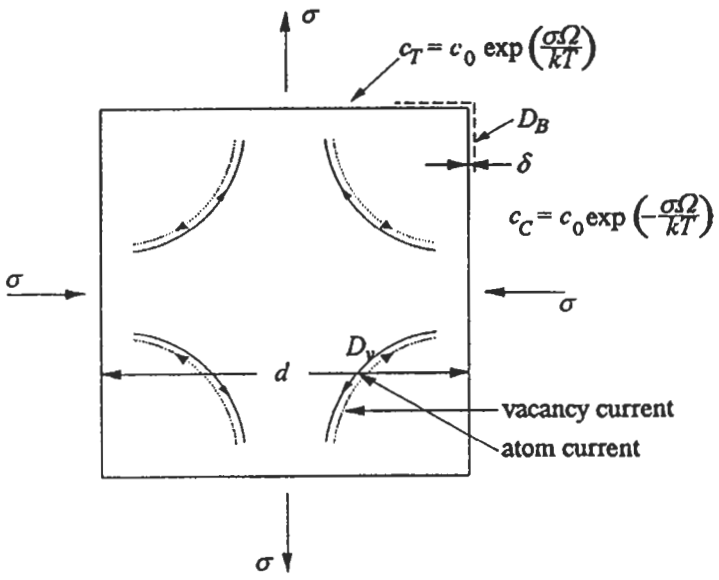

Fig. 24. The response of a square grain in diffusional flow under a state of pure shear.

is the effective diffusion constant and where A_{DF} the diffusional flow constant is of the order of 20 (HERRING [1950]). Both the volume diffusion constant, D_v, and the boundary diffusion constant, D_B, have a very similar constitution as:

$$D_v = D_0 \exp\left(-\frac{Q_B}{kT}\right) \therefore \quad D_B = D_0 \exp\left(-\frac{Q_v}{kT}\right) \tag{22a, b}$$

where once again the rule of thumb gives $Q_B \approx 0.6\, Q_v$ for close-packed metals.

For large grain sizes and high homologous temperatures where $(\pi\delta/2d)(D_B/D_v) < 1.0$, $D_{\text{eff}} \approx D_v$ and eq. (20) represents the response form of the phenomenon, the process is known as *Nabarro–Herring creep*. For small grain sizes, and lower homologous temperatures where the above ratio is much larger than unity the diffusional flow expression becomes

$$\dot{\gamma}_c = \frac{A_{DF}\pi}{2} \frac{\sigma\Omega\delta D_B}{d^3 kT} \tag{23}$$

and is known as *Coble creep* which has a stronger grain size dependence but a weaker temperature dependence.

The forms of the diffusional flow rate expressions in both the Nabarro–Herring limit and the Coble creep limit have been very well established with all the various dependencies. Figure 25 shows the creep rate data for relatively coarse grained beryllium, copper, magnesium and manganese-0.7% magnesium alloy compared with the prediction of the Nabarro–Herring theory (BURTON [1977]). The agreement in the low stress range is very good. In the high stress region the increase in the creep rate is due to the increasing

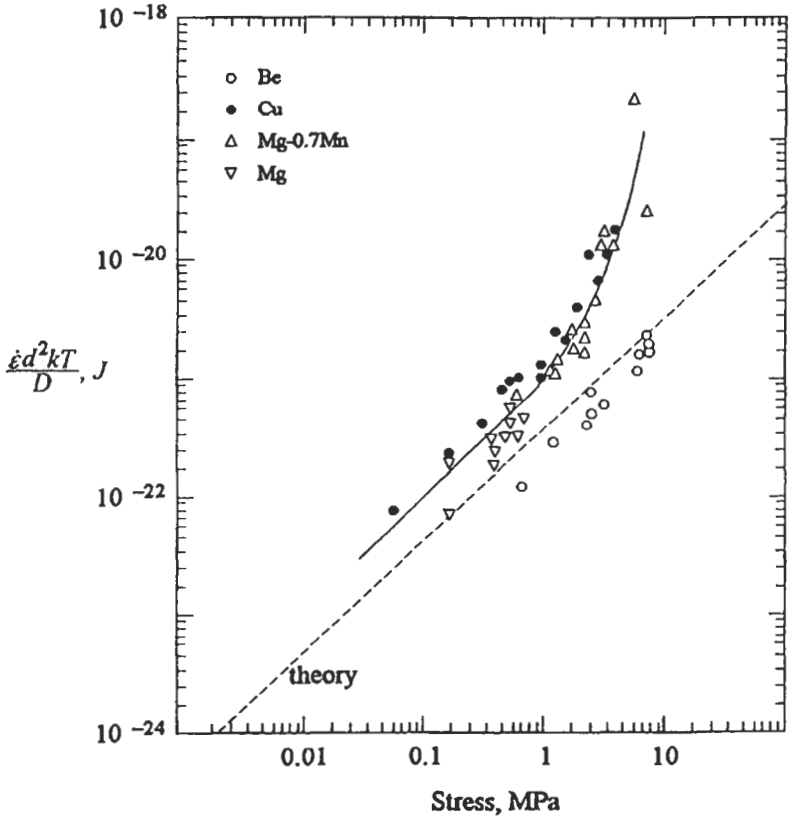

Fig. 25. The dependence of the diffusional flow strain rate on stress for three metals and one solid solution alloy (BURTON [1977], courtesy of Trans. Tech. Publ.).

contribution of dislocation creep which rapidly overwhelms diffusional flow. Figures 26a and 26b show the creep rates of copper and beryllium at a homologous temperature 0.82, and for copper at 0.61 and magnesium at 0.73 plotted respectively against grain size. Clearly, in the high temperature range, volume diffusion is dominant and the grain-size dependence of the creep rate is d^{-2} while in the low temperature range, grain-boundary diffusion is favored and the grain-size dependence is d^{-3} (BURTON [1977]). The transition from volume diffusion (lattice diffusion) to boundary diffusion with decreasing temperature in copper at two different grain sizes is shown in fig. 27 (BURTON [1977]). The transition is clear and sharp, showing a 46% decrease in the activation energy when the matter transport is dominated by boundary diffusion.

Deformation by diffusional flow has a number of important distinguishing characteristics that are worth emphasizing. First, the process is one of matter transport and produces no distortion in the individual grains. This is demonstrated dramatically in fig. 28 which shows grains in a magnesium-zirconium alloy crept to a strain of 0.42 at

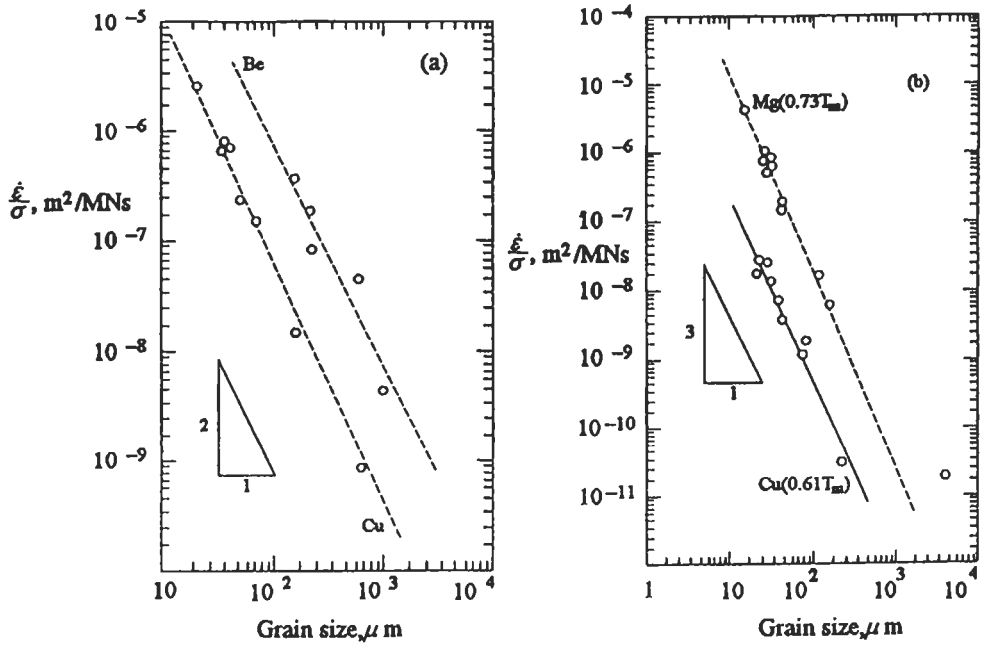

Fig. 26. The dependence of the diffusional flow strain rate on grain size: (a) in the range where Nabarro–Herring creep governs and (b) in the range where Coble creep governs (BURTON [1977], courtesy of Trans. Tech. Publ.).

400°C. The etched microstructure of the starting material is clearly visible. The white zones represent material that has been removed from the regions around grain boundaries under compression and has been "plated out" along the grain boundaries under tension (BURTON [1977]). Second, when individual grains are "eaten away" across the compression direction and "added to" across the tension direction, rigid displacements (and rotations as is clear from fig. 28) among grains become kinematically necessary. This results in a trivial, albeit essential, grain-boundary sliding that contributes nothing to the overall strains. This was recognized first by LIFSHITZ [1963], and is referred to as *Lifshitz sliding* to distinguish it from so-called *Rachinger sliding* (RACHINGER [1952]) which involves a form of grain boundary sliding that is linked compatibly with creep in the grain interior, as we will discuss further in section 7 below (MCLEAN [1951]). This emphasizes that observations related only to grain boundary sliding without knowledge of the mechanism of deformation of individual grains conveys little information and can be quite confusing (see SULLY [1956]). In support of the important distinction between the trivial (Lifshitz) and the non-trivial (Rachinger) sliding of grain boundaries are very dramatic observations of how diffusional flow can be completely stifled if the necessary Lifshitz sliding is suppressed by stable grain boundary precipitates (BURTON [1977]).

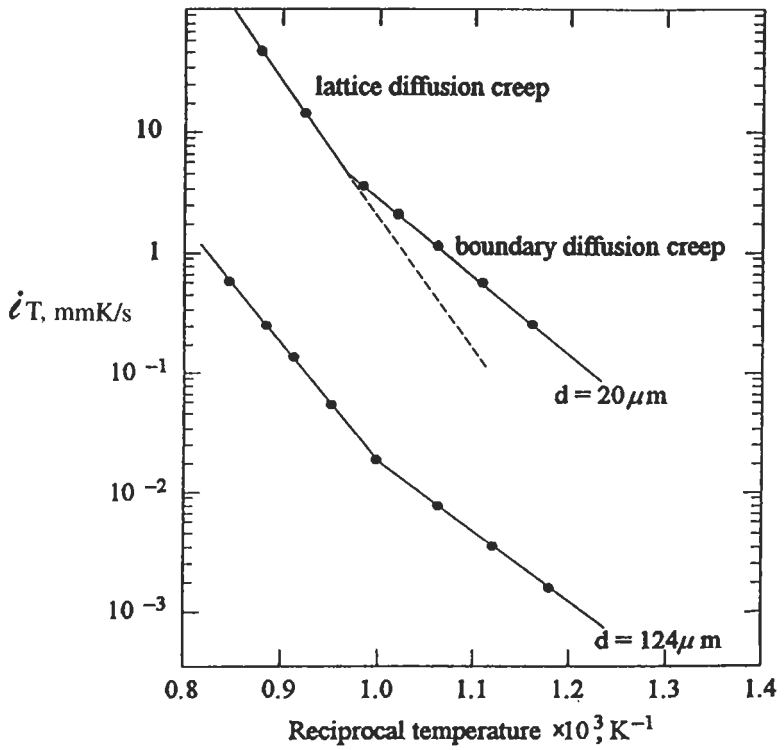

Fig. 27. Change in the rate controlling process of diffusional flow from Coble creep at low temperatures to Nabarro–Herring creep at high temperatures, in copper (BURTON [1977], courtesy of Trans. Tech. Publ.)

8. *Grain-boundary sliding during creep*

It has been observed by many investigators that during creep there are rigid-body sliding displacements of adjacent grains past each other, often accompanied by migration of these boundaries as well. That such sliding of grain boundaries could enhance creep rates was recognized early, followed by many measurements of such sliding to ascertain their contribution to the overall creep rate (see SULLY [1956] for an early review). These measurements led to contradictory conclusions that the contribution of grain-boundary sliding to the overall creep rate could range from a few percent only to nearly accounting for all the creep rate. Models of the effect of sliding on the overall deformation rate have been more informative. Many investigators considered the effect of complete shear relaxation across grain boundaries on the elastic moduli of polycrystalline elastic solids (ZENER [1941]; BUDIANSKY and O'CONNELL [1976]; GHAHREMANI [1980a]) and found that depending on somewhat different geometries and assumptions the ratio of the relaxed to the unrelaxed modulus ranges from 0.8–0.6, the lower value being more compatible with volume-filling grains. In the case when the material undergoes power-

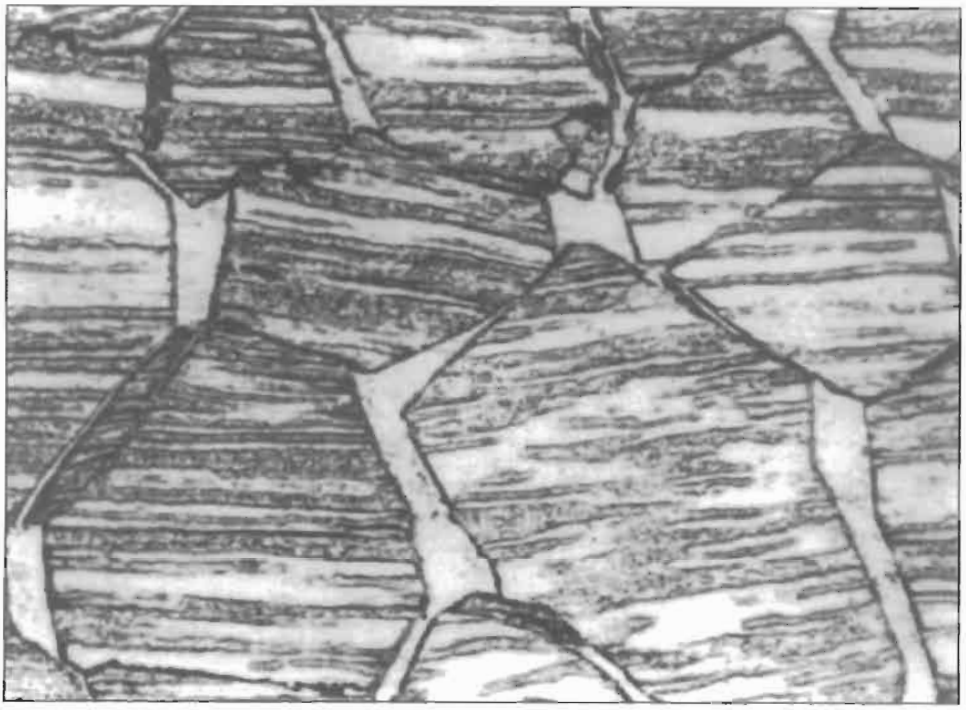

Fig. 28. A micrograph demonstrating graphically the nature of diffusional flow as a material transport process rather than local deformation process. Appearance of individual grains of a hydrided magnesium–zirconium alloy crept to a strain of 0.42 at 600° C (BURTON [1977], courtesy of Trans. Tech. Publ.).

law creep the effect of grain boundary relaxation is best viewed as a stress enhancement factor, f, affecting the power law creep rate. Such effective stress enhancements have also been determined by finite element methods (CROSSMAN and ASHBY [1975]; GHAHREMANI [1980b]; HSIA *et al.* [1991]) where they range from 1.16 to about 1.25 as the stress exponent m of creep ranges from 1 to ∞. Alternatively, the stress enhancement factor f has been determined by incrementally linear self-consistent method analyses (CHEN and ARGON [1979]) where they have been found to range from 1.33 to 1.5 for m increasing from 1 to ∞. Thus, the strain rate enhancement that would arise from the power law creep relation is in the form of

$$\dot{\varepsilon} = \dot{\varepsilon}_0(T)\left(f\sigma/\sigma_0\right)^m, \tag{24}$$

and can result in very substantial increases in creep rate with increasing m where the creep rate is expressed in its usually phenomenological approximation of $\dot{\varepsilon} = \dot{\varepsilon}_0(\sigma/\sigma_0)^m$.

Elementary considerations, equating the shear displacement rate across a grain by creep to the sliding velocity of a grain-boundary exhibiting a linear viscous response characterizable by a grain-boundary shear viscosity, η, gives a characteristic, grain-size dependent stress level

$$\sigma_c = \sigma_0 \left(\frac{\sigma_0}{\dot{\varepsilon}_0(T)} \frac{1}{3\eta} \frac{\delta}{d} \right)^{\frac{1}{m-1}} \tag{25}$$

which can be considered as a threshold for fully relaxed behavior of the polycrystal. Thus, at stress levels below σ_c, the boundary shear rate can be higher than the grain shear rate, so that in a polycrystalline assembly the grain boundaries transmit only normal stresses. Above σ_c, however, the opposite holds and the shear relaxation rate of grain boundaries becomes negligible, resulting in full transmission of all stresses by grain boundaries. This transition in overall creep response is depicted in fig. 29. It shows that both below and above σ_c the power law relations between stress and strain rate hold, even though the stress distribution is very inhomogeneous for $\sigma < \sigma_c$.

An important feature of grain-boundary sliding and its compatible relationship to the creep processes inside grains is that the apparent quasi-smooth external creep behavior is far from smooth on the grain level. Pioneering experiments carried out by CHANG and GRANT [1953], where in a coarse-grained aluminum sample the sliding rate of individual

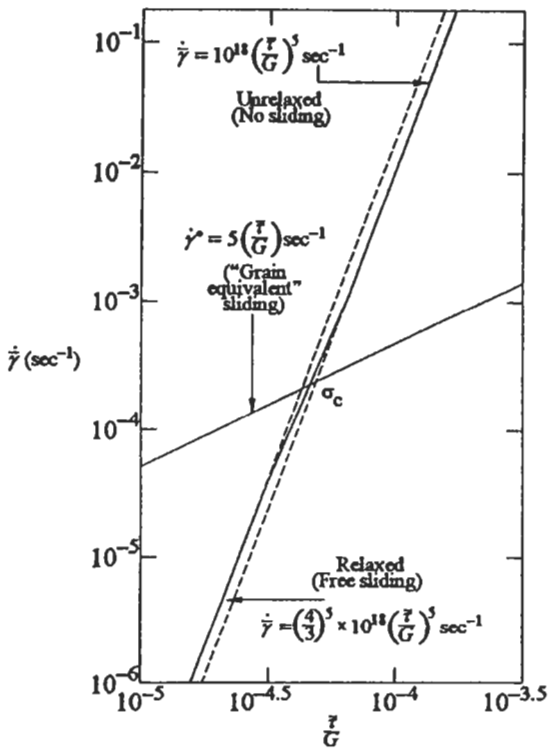

Fig. 29. Transition between relaxed and unrelaxed behavior of grain boundaries with increasing stress in a polycrystal where the grain matrix deforms by power-law creep with a stress exponent of 5 and grain boundaries have Newtonian viscous behavior (CHEN and ARGON [1979], courtesy of Pergamon Press).

grain boundaries was measured, this sliding was found to be made up of a series of transients as shown in fig. 30a and 30b. While the exact cause of these transients was not determinable, it is most likely that they are a result of rather jerky recovery processes in

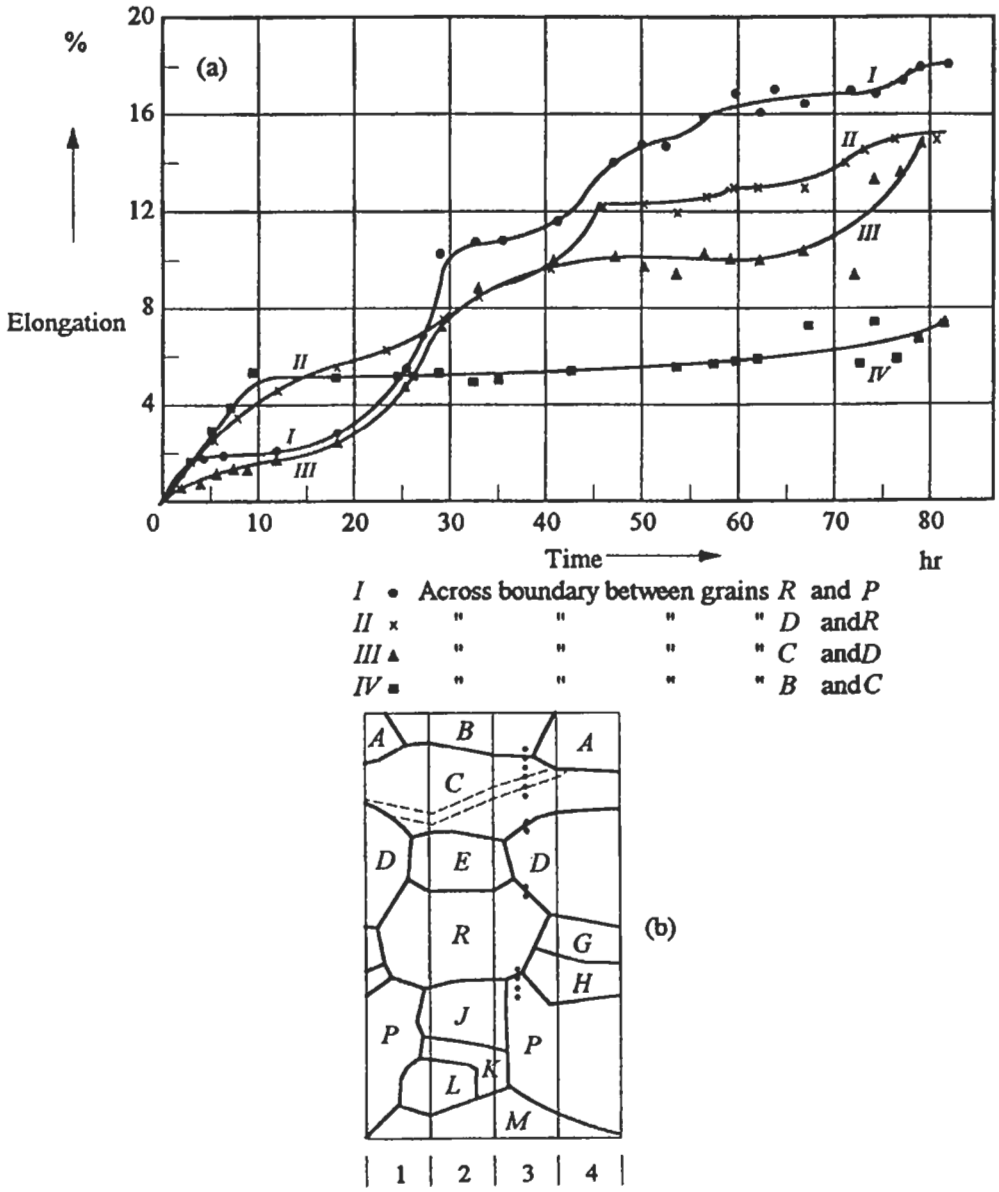

Fig. 30. Spurt-like sliding of grain boundaries in a creeping polycrystalline aluminum sample under a stress of 0.6 MPa at 370° C: (a) elongation vs time curves for sets of points across specific grain boundaries: (b) sketch of boundaries across which measurements were made (CHANG and GRANT [1953], courtesy of AIME).

the creeping grains on a scale much coarser than the jerky phenomena discussed in section 5.

Grain-boundary sliding and its attendant stress relaxation, including the transient effects shown in fig. 30 has very important consequences for the intergranular creep fracture of polycrystalline alloys at low stress levels (see ARGON [1982], RIEDEL [1987]).

9. *Superplasticity*

Many very fine-grained materials exhibit, at high temperatures and relatively low stresses in the diffusional flow response regime, a remarkable stable extensibility and avoidance of ductile or creep fracture resulting in extensionally large strains to failure — often by rupture, in the range of 10 or more. This behavior, quite characteristically, has been called *superplasticity*. In spite of the fact that it is quite slow in providing these large strains, it is nevertheless an industrially attractive means of forming complex parts of materials with usually limited deformability in the more conventional means of hot forming. The general requirements for superplastic behavior is a fine and stable grain size in the submicron range, a high, homologous temperature and deformation under a stress with a small mean normal component (low triaxiality). Under these conditions, the overall stress exponent, m, of the tensile strain rate is found to be close to but somewhat larger than unity. As has been discussed in section 10 of chapter 21 this is conducive to continued stable extensional deformation without localization and attendant rupture, both on the macroscopic scale as well as on the microscopic scale of cavities and pores which tend to harmlessly stretch out rather than expand in volume.

Examination of the microstructure of superplastically deforming fine-grained polycrystalline solids shows a number of remarkable characteristics. In spite of the very large accumulating strains, grains remain equiaxed. However, individual marked grains are found to show substantial rotations and move apart with other grains undergoing lateral displacements to fill the gaps, with the whole assembly of grains showing a mode of deformation resembling a collection of sand grains embedded in a viscous medium. Clearly, since such a medium does not exist the individual grains must undergo not only complex shape changes in squeezing past each other, but also large amounts of the trivial, but kinematically necessary Lifshitz type grain boundary sliding discussed in connection with diffusional flow in section 7 above. Thus, from the close phenomenological parallels, a strong and nearly inverse cube dependence of the strain rate of grain size, and a net activation energy of the deformation rate close to that of grain-boundary diffusion indicate that diffusional flow plays a prominent role in the deformation process. Careful examination, however, shows also considerable dislocation activity that manifests itself in the stress exponent of the strain rate being somewhat larger than unity.

There have been a number of models proposed to explain the mechanistic aspects of superplasticity. Of these the one that captures the basic essence of the complex processes is that the ASHBY and VERRALL [1973] which recognizes that the essential unit process in the flow of relatively equiaxed grains past each other is a grain switching exchange depicted in fig. 31. Here, the grains taking part in the switch are required to undergo a

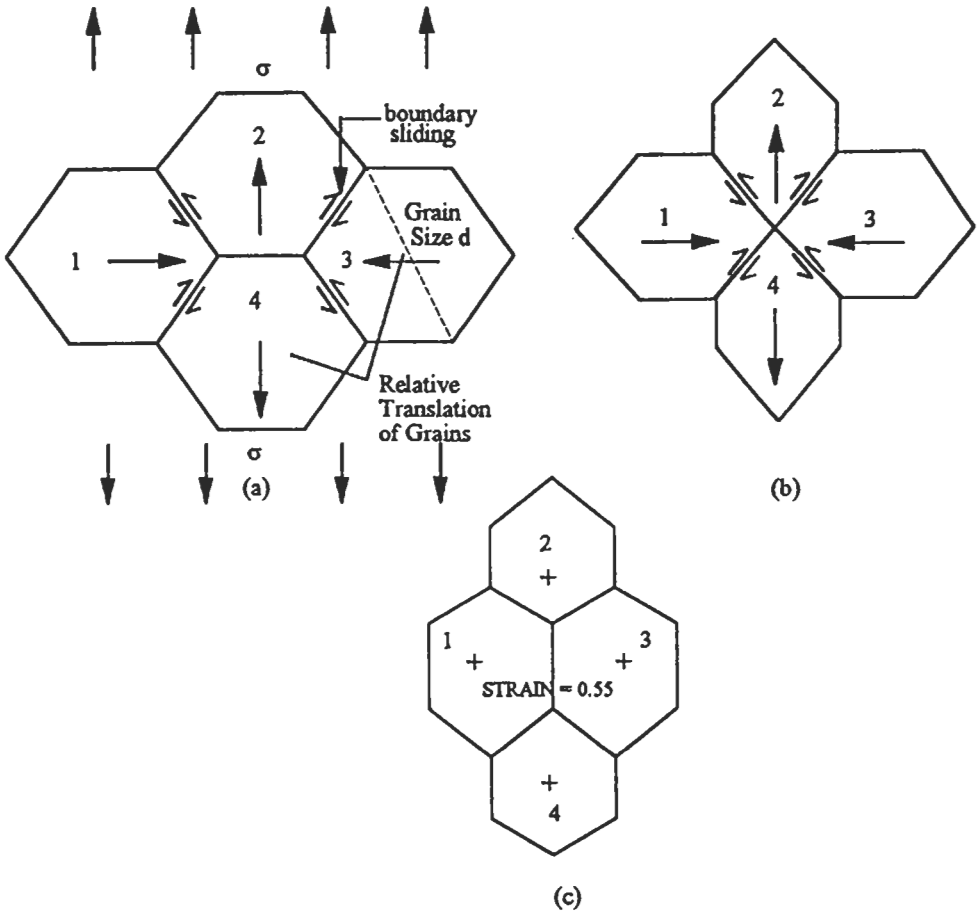

Fig. 31. The unit process of a grain switch among four hexagonal grains, observed in two dimensional flow of an oil emulsion, as an analog to a superplastic medium: (a) initial state, (b) intermediate state, (c) final state (ASHBY and VERRALL [1973]; courtesy of Pergamon Press).

recurring set of pulsating shape changes which are primarily accomplished by diffusional flow, with apparently a small amount of additional dislocation plasticity, and considerable amounts of trivial grain-boundary sliding. Thus, the overall superplastic tensile strain rate $\dot{\varepsilon}_{sp}$ is given primarily by the volume averaged transformation strain associated with the grain switch divided by the characteristic time constant of the required shape changes accomplished by local diffusional mater transport along grain boundaries. This strain rate, according to ASHBY and VERRALL [1973], is

$$\dot{\varepsilon}_{sp} = A\frac{\Omega D_v}{kTd^2}\left\{\sigma - \alpha\frac{\chi_B}{d}\right\}\left(1 + \beta\left(\frac{\delta}{d}\right)\frac{D_B}{D_v}\right) \tag{26}$$

where σ is the tensile stress, χ_B the grain-boundary energy d, the grain size, δ grain-boundary thickness. A, α and β are numerical constants with magnitudes of 100, 0.72 and 3.3, respectively, and all other quantities have their usual meaning. Detailed examination of the known facts in the light of the simple grain-switching model discussed above has revealed some discrepancies that have been dealt with through modifications of the model. These effects and much additional phenomenology associated with fracture avoidance and industrial applications of superplasticity have been discussed in considerable detail by MUKHERJEE [1993].

10. Other creep-related phenomena

As was discussed in section 2, when the stress is raised substantially during steady-state creep, where the thermal recovery processes that balance against the rise in plastic resistance due to strain-hardening, the deformation reverts to a Stage III type plasticity where the strain rate is controlled by thermally activated dislocation glide, and the strain hardening is ameliorated only by dynamic recovery. Under these conditions the changed behavior departing from power law creep into low temperature plasticity is usually referred to as *power-law breakdown*.

At high homologous temperatures in excess of 0.6, many pure metals exhibit a dynamic recrystallization phenomenon where the static thermal recovery is often superseded by waves of local recrystallization, particularly in regions of high strain rate concentration as around the triple junctions of grains etc. where high dynamic dislocation densities exist, as depicted in fig. 32 (FROST and ASHBY [1982]). The sudden loss of dislocation density and its attendant sharp decrease of local plastic resistance sets up a series of new spurts of local primary creep that results in large oscillations in overall strain rate of the order of 10 or more. While the process has been well investigated and catalogued in nickel, copper, lead and aluminum, notably by JONAS *et al.* [1969], comprehensive models of the process are lacking. The key missing information is on the conditions and the triggering mechanism for the formation of a new grain in the region of excess dislocation density. Most of these phenomena and the resulting growth rate of the newly formed grains into the quasi-smoothly creeping background are in principle well understood, but, collectively the complex phenomenon needs further consideration (for a brief overview of the conditions of stress and temperature where dynamic recrystallization is found see FROST and ASHBY [1982]). (This subject is further discussed in ch. 28, § 3.5).

11. Isomechanical scaling laws of inelastic behavior

ASHBY and FROST [1975] who have pioneered the assembly of the inelastic deformation rate behavior of solids between 0 K and the melting point into deformation mechanism maps on reduced stress and homologous temperature coordinates, have pointed out that the behavior patterns of solids of a given type such as FCC metals, BCC metals, etc., will outline relatively narrow bands. When solids with very different bonding and

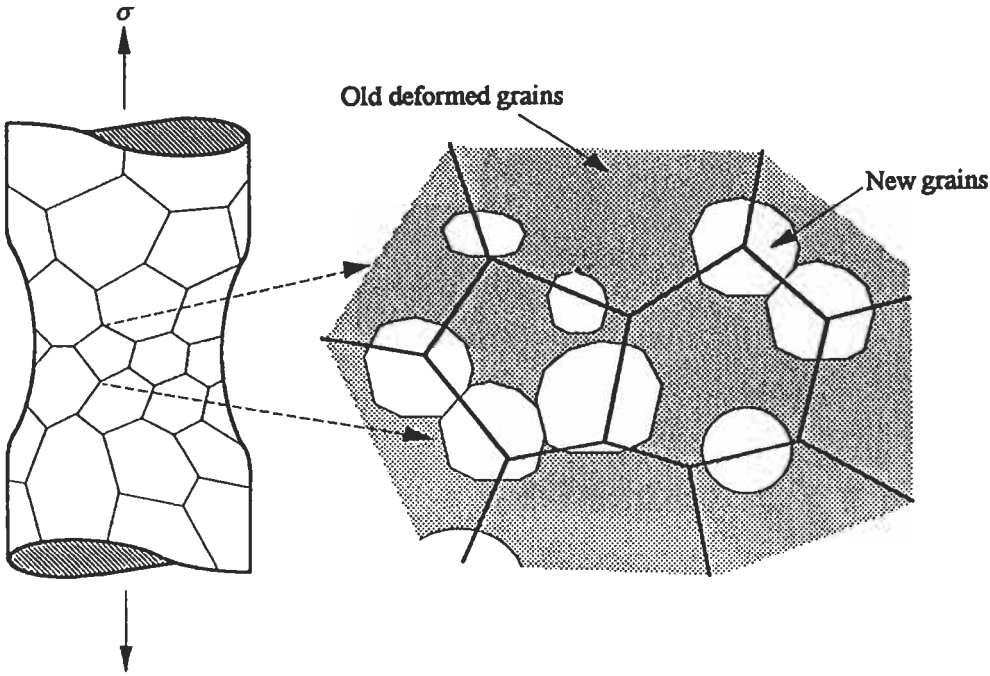

Fig. 32. Sketch of spacial distribution of dynamic recrystallization sites in a deforming polycrystal (after FROST and ASHBY [1982], courtesy of Pergamon Press).

crystal structure are all assembled on the same homologous temperature, reduced stress plane, their strain rate response will still fit into a reasonably narrow band at low temperatures where diffusion does not affect or control the deformation rate. However, the behavior band diverges over many orders of magnitude in deformation resistance in the high temperature region close to the melting-point, as fig. 33 shows. Since the low-temperature normalizations of behavior do not affect the diffusive processes another normalization condition becomes essential to capture the common features of all solids. ASHBY and FROST [1975] have proposed that this should be the diffusion constant of the particular solid at the melting point, i.e., D_{TM}. On the basis of this, they have normalized the strain rate with the diffusion constant of the material at its melting point (divided by $\Omega^{2/3}$) and have demonstrated that then the inelastic behavior of all solids, whether pure or in the form of compounds, will fall within a common and remarkably narrow behavior band between 0 K and the melting point. This is shown in fig. 34. It indicates that knowledge of the shear modulus, the melting point and the diffusion constant at the melting point of any solid permit a first order assessment of deformation resistance over the entire homologous temperature, reduced stress plane. This feature of deformation mechanism maps perhaps demonstrates their most dramatic educational value.

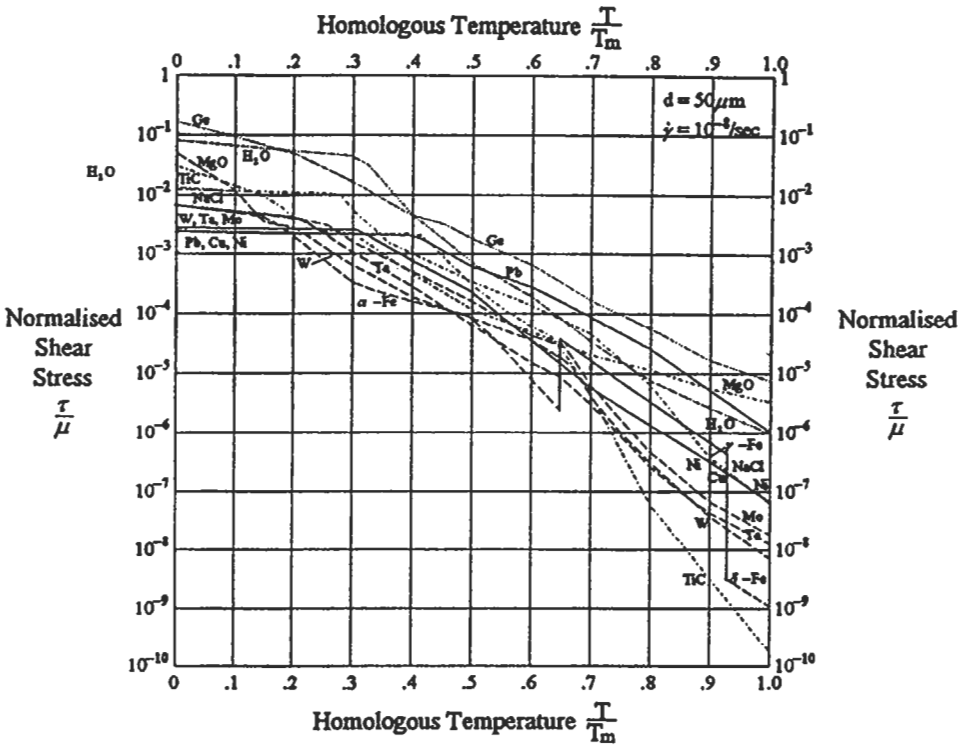

Fig. 33. Normalized stress and homologous temperature plots at a constant strain rate of inelastic behavior of a wide range of metals and compounds (ASHBY and FROST [1975], courtesy of MIT Press).

12. *Phenomenological descriptions of homogenized continuum deformation behavior*

12.1. The representative volume element

In chapter 21, in section 9, a connection was made between the usually one-dimensional shear response emphasizing the mechanistic processes and the conditions for three-dimensional continuum deformation. In the establishment of such conditions of three-dimensional deformation that can then be used in computational approaches to deformation processing in the high-temperature domain, several considerations have to be dealt with either explicitly or implicitly.

The first item of concern is on what scale the deformation in a particular material or microstructure could be considered as a continuum. This is arranged by introducing a *representative volume element* (RVE) as the volume of the smallest possible size over which the internal variations of the deformation process can be considered smoothed out. In low-temperature crystal plasticity, where the principal inhomogeneities are precipitate particles, or in the worst case are the cells of the cellular dislocation structure, the RVE

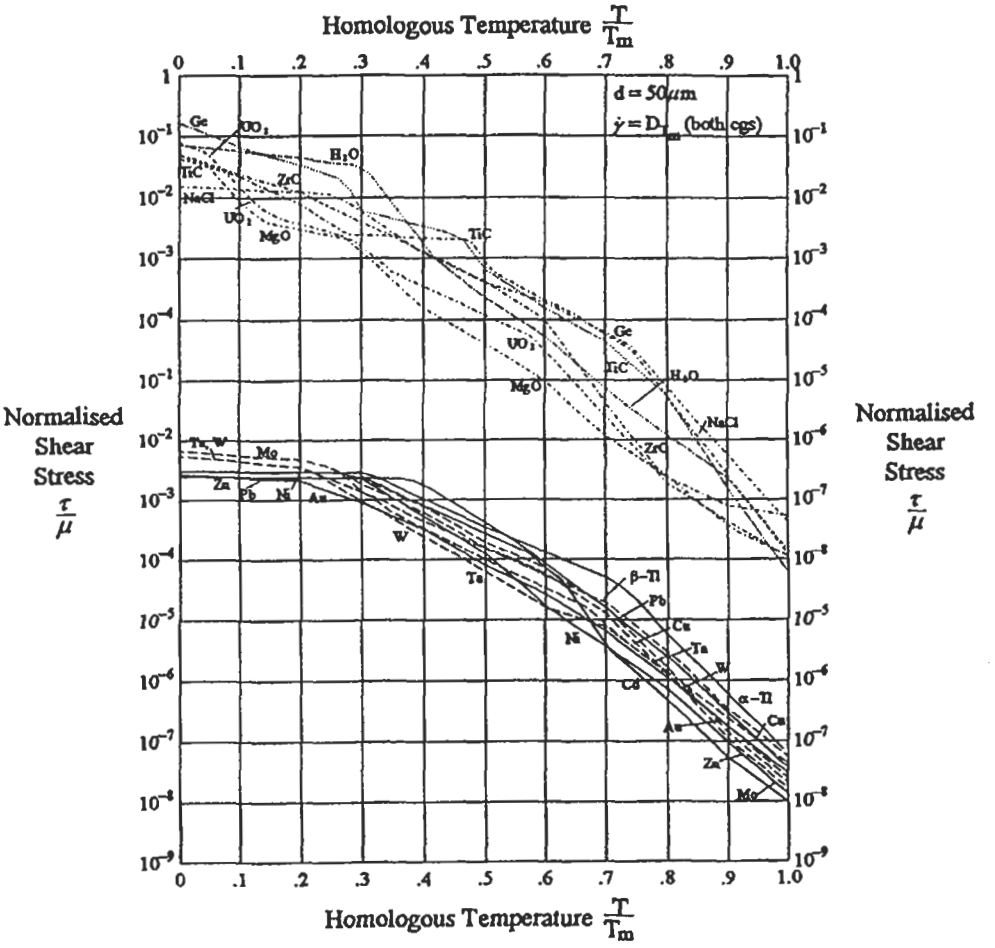

Fig. 34. Same information as that appearing in fig. 33, but with the strain rate normalized by the diffusion constant at the melting point. The behavior bands of metals and compounds have been separated, and shifted apart for clarity (ASHBY and FROST [1975], courtesy of MIT Press).

should be taken as a small multiple of the precipitate spacing or the cell size. In the high temperature realm of deformation as discussed in this chapter the jerky shear relaxation of grain boundaries shown in fig. 30 and the block-like deformations of diffusional flow shown in fig. 28 indicate that the RVE must be taken as a multiple of the grain size. Thus, when the developments of the present chapter are to be homogenized and applied as the constitutive property of a continuum, the scale of the so called material point will have to be taken considerably coarser and on the grain scale of a polycrystalline solid.

12.2. Evolution of deformation resistance

In continuum deformation it is customary to differentiate material properties such as

deformation resistances and external conditions affecting the deformation such as driving forces in the form of applied stresses and temperature. In the present chapter, where much emphasis was on the steady-state deformation processes, the applied stresses are in balance with the deformation resistances and are synonymous with the latter, making the distinction redundant. During deformation transients, however, as in primary creep such a distinction was made in connection with eq. (5) where σ was the applied tensile stress and s the tensile deformation resistance. Such a distinction becomes quite necessary in many of the so-called "hot working" deformation processes which, as was discussed in section 1 can exist primarily in the dynamic recovery range and exhibiting only minimal effects of static recovery. Nevertheless, if allowance is made for static thermal recovery it is customary to consider an evolution equation for the tensile deformation resistance s as responding to two competing effects of strain hardening rate h, and recovery rate r, in the rate form of

$$\dot{s} = h(\sigma, s, T)\dot{\varepsilon} - \dot{r}(s, T) \tag{27}$$

where it is recognized that the hardening is accomplished through straining and the time scale arises through the strain rate. Since dynamic recovery also occurs in the course of straining, it is incorporated into the hardening rate as was discussed in section 7 of chapter 21.

The evolution of deformation resistance during plastic deformation in the high-temperature realm, particularly its effect on, and its development during, transients of deformation have been discussed by many investigators (ANAND [1982], ARGON and BHATTACHARYA [1987], ARGON *et al.* [1987], BROWN *et al.* [1989], BLUM [1993]). Of these developments, the one by BROWN *et al.* [1989], which combines mechanism-inspired formalisms with extensive comparison with experimental results obtained under hot-working conditions is the most detailed one. It demonstrates how the considerations of strain hardening with dynamic recovery discussed in chapter 21 can be combined with static thermal recovery processes to describe how a flexible constitutive material response can be obtained.

12.3. Three-dimensional constitutive material response to deformation

In section 9 of chapter 21 it was discussed how the one-dimensional, mechanism-related description of deformation can be generalized into a framework of three dimensional deformation through the introduction of an equivalent or effective stress, σ_e, as defined by the von Mises expression given by eq. (118) of that chapter. Thus, in this framework the effective stress, σ_e, as a scalar quantity, prescribes the generalized three-dimensional driving force of deformation. Thus, together with the deformation resistance s (described as τ or $\hat{\tau}$ in chapter 21) and the prevailing temperature T, the effective stress σ_e, define an effective (scalar) strain rate, defined in chapter 21 by eq. (119), that can be given as

$$\dot{\varepsilon}_e = \dot{\varepsilon}_0 \exp\left\{-\frac{\Delta F_0}{kT}\left(1-\left(\frac{\sigma_e}{s}\right)^p\right)^q\right\} \tag{28}$$

for plasticity governed by thermally activated glide (eq. (121) chapter 21) and

$$\dot{\varepsilon}_e = B\frac{\mu b D}{kT}\left(\frac{\chi}{\mu b}\right)^3\left(\frac{\sigma}{s}\right)^m \tag{29}$$

for non-steady creep response (eq. (5)). In both cases it is to be assumed that the deformation resistance s may be evolving concurrent with the deformation through strain hardening and thermal recovery as stated in eq. (27) above.

In operational approaches it is, moreover, of interest that the equivalent strain rate has a well-defined decomposition into the individual tensor elements of strain rate according to the associated flow rule. These procedures, which are relatively straightforward for isotropic plastic response, are described in many treatments on continuum deformation (see, e.g., McCLINTOCK and ARGON [1966]). These are not of interest here and will not be pursued. For a discussion of how the one-dimensional mechanism based material response combining a kinetic law, and evolution of deformation resistance, into three-dimensional constitutive response statements, the reader is referred to BROWN *et al.* [1989] where it is also demonstrated how actual material response for a commercially pure aluminum and an iron-3% silicon alloy are translated into three-dimensional constitutive equations.

Acknowledgment

The author is grateful to Professor L. Anand for carefully proof-reading the chapter to catch a number of typographical errors and for suggesting the addition of section 12 to the chapter.

References

ANAND, L., 1982, J. Engrg. Mater. Techn. **104**, 12.

ANDRADE, E. N. DA C., 1911, Proc. Roy. Soc., **A84**, 1.

ARGON, A. S., 1977, unpublished developments on the creep law.

ARGON, A. S., 1982, in "Recent Advances in Creep and Fracture of Engineering Materials and Structures", edited by B. Wilshire and D.R.J. Owen. (Pineridge Press: Swansea, U.K.), p. 1.

ARGON, A. S., and A. K. BHATTACHARYA, 1987, Acta Metall., **35**, 1499.

ARGON, A. S., A. K. BHATTACHARYA and T. M. POLLOCK, 1987, in "Constitutive Relations and their Physical Basis", edited by S.I. Anderson, J.B. Bilde-Sorensen, N. Hansen, T. Leffers, H. Lilholt, O.B. Pedersen and B. Ralph, (Riso Natl Lab: Roskilde, Denmark), p. 39.

ARGON, A. S., and S. TAKEUCHI, 1981, Acta Metall., **29**, 1877.

ARGON, A. S. and W. C. MOFFATT, 1981, Acta Metall., **29**, 293.

ARGON, A. S., F. PRINZ, and W. C. MOFFATT, 1981, in "Creep and Fracture in Engineering Materials and Structures", edited by B. Wilshire and D.R.J. Owen, (Pineridge Press: Swansea, U.K.), p. 289.

ARGON, A. S., and P. HAASEN, 1993, Acta Metall. et Mater., **41**, 3289.
ASHBY, M. F., and R. A. VERRALL, 1973, Acta Metall., **21**, 149.
ASHBY, M. F. and H. J. FROST, 1975, in "Constitutive Equations in Plasticity", edited by A.S. Argon, (MIT Press: Cambridge, MA), p. 117.
BAILEY, R. W., 1926, J. Inst. Metals, **35**, 27.
BARRETT, C. R., and O. D. SHERBY, 1965, Trans. Met. Soc. AIME, **233**, 1116.
BARRETT, C. R. and W. D. NIX, 1965, Acta Metall., **13**, 1247.
BIRD, J. E., A. K. MUKHERJEE and J. E. DORN, 1969, in "Quantitative Relation Between Properties and Microstructure" edited by D.G. Brandon and A. Rosen, (Israel Univ. Press: Jerusalem), p. 255.
BLUM, W., 1993, in "Plastic Deformation and Fracture of Materials" edited by R. W. Cahn, P. Haasen, and E. J. Kramer, vol. 6 of "Materials Science and Technology", edited by H. Mughrabi, (VCH Publishers: Weinheim), p. 359.
BROWN, A. M. and M. F. ASHBY, 1980, Scripta Metall., **14**, 1297.
BROWN, S. B., K. H. KIM, and L. ANAND, 1989, Intern. J. Plasticity, **5**, 95.
BUDIANSKY, B. and R. J. O'CONNELL, 1976, Intern. J. Solids & Struct., **12**, 81.
BURTON, B., 1977, "Diffusional Creep of Polycrystalline Materials", Diffusion and Defect Monograph Series #5, edited by Y. Adda, A.D. LeClaire, L.M. Slifkin, and F.H. Wohlbier, (Trans. Tech. Publ.: Bay Village, Ohio).
BURTON, B. and G. L. REYNOLDS, 1995, Mater. Sci. Engng., **A 191**, 135.
CAILLARD, D., and J.-L. MARTIN, 1982a, Acta Metall., **30**, 791.
CAILLARD, D., and J.-L. MARTIN, 1982b, Acta Metall., **30**, 437.
CARRARD, M. and J.-L. MARTIN, 1984, in "Creep and Fracture in Engineering Materials and Structures", edited by B. Wilshire and D.R.J. Owen (Pineridge Press: Swansea, U.K.) p. 85.
CHANG, H. C., and N. J. GRANT, 1953, Trans. AIME, **197**, 1175.
CHEN, I.-W. and A. S. ARGON, 1979, Acta Metall., **27**, 749.
CHU, S. N. G. and J. C. M. LI, 1977, J. Mater. Sci., **12**, 2200.
COBLE, R. L., 1963, J. Appl. Phys., **34**, 1679.
COTTRELL, A. H., 1947, in "Report on the Strength of Solids", (Physical Society: London), p. 30.
COTTRELL, A. H., 1953, "Dislocations and Plastic Flow in Crystals", (Clarendon Press: Oxford).
COTTRELL, A. H., 1995, Phil. Mag. Letters, in press.
COTTRELL, A. H., and M. A. JASWON, 1949, Proc. Roy. Soc., **A199**, 104.
CROSSMAN, F. W., and M. F. ASHBY, 1975, Acta Metall., **23**, 425.
DORN, J. E., 1956 in "Creep and Fracture of Metals at High Temperatures", (National Phys. Lab.: London) p. 89.
DORN, J. E. and J. D. MOTE, 1964, in "High Temperature Structure and Materials", edited by A.M. Freudenthal, B.A. Boley, and H. Liebowitz, (Pergamon Press: Oxford), p. 95.
DYSON, B. F., 1987, private communication of creep data by Kandil and Dyson.
EDELIN, G., and J. P. POIRIER, 1973a, Phil. Mag., **28**, 1203.
EDELIN, G., and J. P. POIRIER, 1973b, Phil. Mag., **28**, 1211.
EXELL, S. F. and D. H. WARRINGTON, 1972, Phil. Mag., **26**, 1121.
FROST, H. J. and M. F. ASHBY, 1982, "Deformation Mechanism Maps", (Pergamon Press: Oxford).
GARAFALO, F., 1963, Trans. Met. Soc. AIME, **227**, 351.
GHAHREMANI, F., 1980a, Intern. J. Solids & Struct., **16**, 825.
GHAHREMANI, F., 1980b, Intern. J. Solids & Struct., **16**, 847.
GIBELING, J. C. and W. D. NIX, 1980, Acta Metall., 28, 1743.
GRANT, N. J. 1995, private communication.
HARPER, J. G., and J. E. DORN, 1957, Acta Metall., **5**, 654.
HARPER, J. G., L. A. SHEPARD and J. E. DORN, 1958, Acta Metall., **6**, 509.
HASEGAWA, T. and U. F. KOCKS, 1979, Acta Metall., **27**, 1705.
HERRING, C., 1950, J. Appl. Phys., **21**, 437.
HIRSCH, P. B. and D. H. WARRINGTON, 1961, Phil. Mag., **6**, 735.
HIRTH, J. P., 1993, private communication on creep in solid solution alloys.
HIRTH, J. P., and J. O. LOTHE, 1982, "Theory of Dislocations", (Wiley: New York), Second Edition.

HSIA, K. J., D. M. PARKS and A. S. ARGON, 1991, Mechanics of Materials, **11**, 43.
JONAS, J. J., C. M. SELLERS, and J. W. MCG. MCTEGART, 1969, Metall. Rev., **14**, 1.
KOCKS, U. F. and H. MECKING, 1979, in "Strength of Metals and Alloys", edited by P. Haasen, V. Gerold and G. Kostorz, (Pergamon: Oxford), Vol. 1, p. 345.
KOCKS, U. F., and S. R. CHEN, 1993 in "High Temperature Deformation and Fracture in Crystalline Materials", (Japan Inst. Metals: Tokyo).
KUHLMANN–WILSDORF, D., 1968 in "Work Hardening", edited by J. P. Hirth and J. Weertman, (Gordon and Breach: New York), p. 97.
LIFSHITZ, I. M., 1963, Soviet Phys. **17**, 909.
LUDEMANN, W. D., L. A. SHEPARD, and J. E. DORN, 1960, Trans. AIME, **218**, 923.
MARTIN, J.-L. and A. S. ARGON, 1986, Mater. Sci. Engng., **81**, 337.
MCLEAN, D., 1951, J. Inst. Metals, **80**, 507.
MCLEAN, D., 1962, Metal. Rev., **7**, 481.
MECKING, H. and U. F. KOCKS, 1981, Acta Metall., **29**, 1865.
MIEKK–OJA, H. M., and V. K. LINDROOS, 1975, in "Constitutive Equations in Plasticity", edited by A.S. Argon (M.I.T.Press: Cambridge, MA), p. 327.
MITRA, S. K., and D. MCLEAN, 1966, Proc. Roy. Soc., **295**, 288.
MOHAMED, F. A., K. L. MURTY and J. W. MORRIS, Jr., 1975, in "Rate Processes in Plastic Deformation of Materials", edited by J.C.M. Li and A.K. Mukherjee, (ASM: Metals Park, Ohio), p. 459.
MOHAMED, F. A. and T. G. LANGDON, 1974, Acta Metall., **22**, 779.
MUKHERJEE, A. K., 1993, in "Plastic Deformation and Fracture of Materials" edited by R.W. Cahn, P. Haasen, and E.J. Kramer, vol. 6 of "Materials Science and Technology", edited by H. Mughrabi, (VCH Publishers: Weinheim), p. 407.
MUKHERJEE, A. K., J. E. BIRD and J. E. DORN, 1969, Trans. ASM, **62**, 155.
NABARRO, F. R. N., 1947, in "Report of Conference on Strength of Solids", (Phys. Society: London), p. 47.
ORLOVA, A., M. PAHUTOVA and J. CADEK, 1972, Phil. Mag., **25**, 865.
ORLOVA, A., Z. TOBOLOVA and J. CADEK, 1972, Phil. Mag., **26**, 1263.
OROWAN, E., 1947, "The Creep of Metals", West of Scotland Iron and Steel Institute, p. 45.
PRINZ, F. and A. S. ARGON, 1980, Phys. Stat. Sol., **57**, 741.
PRINZ, F., A. S. ARGON and W. C. MOFFATT, 1982, Acta Metall., **30**, 821.
PRINZ, F., and A. S. ARGON, 1984, Acta Metall., **32**, 1021.
RACHINGER, W. A., 1952, J. Inst. Metals, **80**, 147.
RIEDEL, H., 1987, "Fracture at High Temperatures", (Springer: Berlin).
SULLY, A. H., 1956, in "Progress in Metal Physics", edited by B. Chalmers and R. King, (Pergamon: Oxford), vol. 6, p. 135.
TAKEUCHI, S., and A. S. ARGON, 1976a, Acta Metall., **24**, 883.
TAKEUCHI, S., and A. S. ARGON, 1976b, J. Mater. Sci., **11**, 1542.
TAKEUCHI, S,. and A. S. ARGON, 1979, Phil. Mag., **40**, 65.
WESTBROOK, J. H., 1953, Trans. ASM, **45**, 221.
YAVARI, P. and T. G. LANGDON, 1977, Scripta Metall., **11**, 863.
YAVARI, P., F. A. MOHAMED and T. G. LANGDON, 1981, Acta Metall., **24**, 883.
YU, H.-Y. and J. C. M. LI, 1977, J. Mater. Sci., **12**, 2214.
ZENER, C., 1941, Phys. Rev., **60**, 906.

Further reading

Argon, A. S., (editor) 1975, "Constitutive Equations in Plasticity," (M.I.T. Press, Cambridge, MA).
Blum, W., 1993, "High Temperature Deformation and Creep of Crystalline Solids" see references.
Brown, S. B., K. H. Kim and L. Anand, 1989, "An Internal Variable Constitutive Model for Hot Working of Metals", see references.
Burton, B., 1977, "Diffusional Creep of Polycrystalline Materials", see references.
Frost, H. J. and M. F. Ashby, 1982, "Deformation Mechanism Maps", see references.

Gittus, J., 1975, "Creep, Viscoelasticity and Creep Fracture in Solids", (Applied Science Publishers: London).

Nabarro, F. R. N. and H. L. de Villiers, 1995, "The Physics of Creep" (Taylor and Francis, London).

Mukherjee, A. K., 1993, "Superplasticity in Metals, Ceramics and Intermetallics", see references.

Poirier, J. P., 1976, "Plasticité a Haute Temperature des Solides Cristallins", (in French) (Edition Eyrolles: Paris).

Sully, A. H., 1956, "Recent Advances in Knowledge Concerning the Process of Creep in Metals", see references.

Takeuchi, S. and A. S. Argon, 1976b, "Steady-state creep of Single-Phase Crystalline Matter at High Temperature", see references.

CHAPTER 23

MECHANICAL PROPERTIES OF SOLID SOLUTIONS

P. HAASEN†

Institut für Metallphysik
Universität Göttingen
D-37073 Göttingen, FRG

R. W. Cahn and P. Haasen†, eds.
Physical Metallurgy; fourth, revised and enhanced edition

1. Introduction

This chapter deals with the influence of a second element on the mechanical properties of crystals, mainly metals. The foreign atom is assumed to substitute for an atom of the matrix. Interstitial solubility is in general limited and a second phase forms easily; the mechanical properties of this type of alloys are fully discussed in ch. 25. (See, however, also § 2.4.2.) The observations to be described here were obtained mainly on single crystals. They are thus best suited for interpretation by means of dislocation theory (as presented in ch. 20). In the discussion of the mechanical properties of terminal solid solutions the reader is assumed to be familiar with the mechanical properties of pure metals (chs. 21/22) and with the structure of solid solutions (described in ch. 3). Solute atoms in some alloys occupy preferentially one sublattice, i.e., there is (short range) order. Another kind of non-random distribution of the component atoms may lead to the formation of precipitates (ch. 15) which greatly harden the alloy. A truly random distribution is certainly rare because of differences in atomic size, charge etc., which lead to attractive or repulsive interactions between solute atoms, precipitation or order. The dislocation is influenced by such inhomogeneities on a rather fine scale, determined by its interaction force with a "cluster" and the dislocation line tension. It is known that a dislocation is bent by a force f on its atomic length b to a minimum radius $R = \mu b^3/f$ where μ is the elastic shear modulus. In typical hardened alloys $R = 100b$ is reached.

A special kind of alloying and subsequent hardening is that by self point defects of the material, introduced in non-equilibrium concentrations by *irradiation* with fast particles (e.g., electrons, neutrons) or by *quenching* from high temperatures. In the former case self-interstitial atoms and vacancies are produced and especially associates between them: Frenkel pairs, vacancy clusters transforming into dislocation loops, stacking-fault tetrahedra and voids, interstitial-solute pairs. In the latter case vacancies and their associates are formed (see ch. 18). All of these defects interact with dislocations and therefore harden the base metal similarly to solute atoms and precipitates treated extensively in this chapter. There is of course a tendency for the point defects to annihilate on heating, either among themselves or with dislocations and at (internal) surfaces. In this respect their hardening effect differs with increasing temperature from true alloy hardening. There is an extensive literature on irradiation- and quench hardening (also their technological aspects) which has been summarized by GITTUS [1978] and KIMURA and MADDIN [1971].

By mechanical properties we refer in the following mainly to the shear stress–shear strain (τ, ε) curve as measured at constant strain rate $\dot{\varepsilon}$ and temperature T: $\tau = \tau(\varepsilon, \dot{\varepsilon}, T)$. Supplementary information is obtained from creep experiments under constant stress and temperature: $\varepsilon = \varepsilon(t, T, \tau)$, where t = time of creep. Much progress in understanding the mechanical properties has been made by combining these measurements with surface observations of slip lines, particularly with the electron microscope. Also observations of dislocations in electron transmission, X-ray studies and atom probe measurements of the distribution of the component atoms and etch pit measurements of dislocation velocities have been used successfully in this connection. Other types of measurements may also be of great help, but are less direct in the interpretation of alloy hardening.

2. *Solid-solution hardening*

Consider first the hardening effect of a second element in a nearly ideal solution. Most of the discussion is confined to binary substitutional alloy crystals with fcc structure, but hcp, bcc, diamond cubic or NaCl structures are briefly mentioned. Reports by NEUHÄUSER and SCHWINK [1992], NABARRO [1985], KOCKS [1985], SUZUKI [1957], HAASEN [1977, 1979a] and SUZUKI [1979a] describe results on polycrystals or on the *yield* stress of single crystals. Following the theoretical analysis of the stress–strain curve of pure fcc single crystals by SEEGER [1957, 1958] it is interesting to discuss the effect of alloying on the different stages of this curve (see also HIRSCH [1975]). A first survey is presented in § 2.1. After a description of relevant slip line and etch pit observations and electron transmission work in § 2.2, the main theoretical ideas proposed for the explanation of solid solution hardening are presented in § 2.3. This enables the effect of solid solution alloying on different parts of the τ–ε-curve to be discussed in § 2.4. A discussion of similar effects in other structures follows in §§ 2.5–2.7. Creep of solid solutions is investigated in § 2.8, fatigue in § 2.9.

2.1. Survey of stress–strain curves of fcc alloy single crystals

Stress–strain curves of typical solid solution crystals with a stacking-fault energy (SFE) lower than that of the base metal are shown in fig. 1 (Ni–Co) as a function of composition. Depending on strain, the flow stress of the alloy may be higher or lower than that of the base metal. This does not, however, imply softening by alloying. The

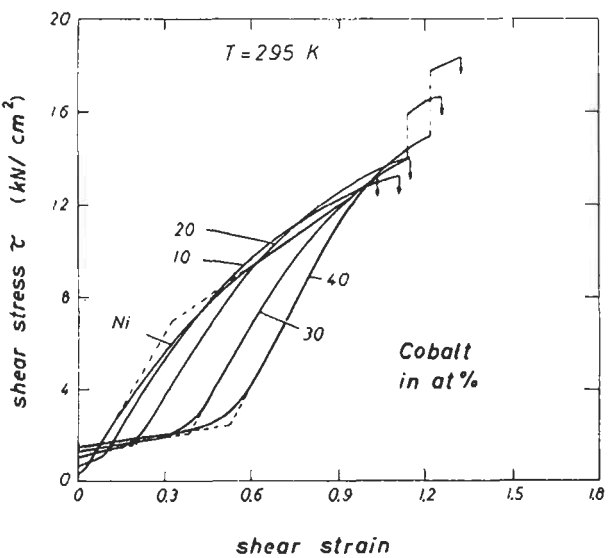

Fig. 1. Work-hardening of Ni–Co single crystals of various compositions (% Co indicated) (after MEISSNER [1959]).

References: p. 2066.

three first stages of the work-hardening curve of pure fcc crystals (cf. ch. 21) are still recognizable in the alloys, and thus the dislocation interactions leading to work-hardening must be much the same as in pure metals. But as the concentration of the solute is increased the critical shear stress increases, the easy glide range becomes longer, as does the stage II linear hardening range. Stage III, dynamic recovery, starts at higher stresses for the more concentrated alloys. The breaks in the Ni–Co curves indicate a delay in the usual change of slip system from primary to conjugate as a function of strain. As primary slip progresses, the orientation overshoots the side of the standard stereographic triangle as shown in fig. 31b (p. 2056) (which implies that an abnormally high stress is needed to activate the conjugate slip system). Horizontal serrated parts in the τ–ε-curves where the crystals are twinning are seen in Cu–Ga and Cu–Ge (HAASEN and KING [1960]). Qualitatively, alloying with elements which lower the SFE changes the work-hardening behaviour in a similar way as does a decrease in temperature, as illustrated for Ni–Co alloys in fig. 2.

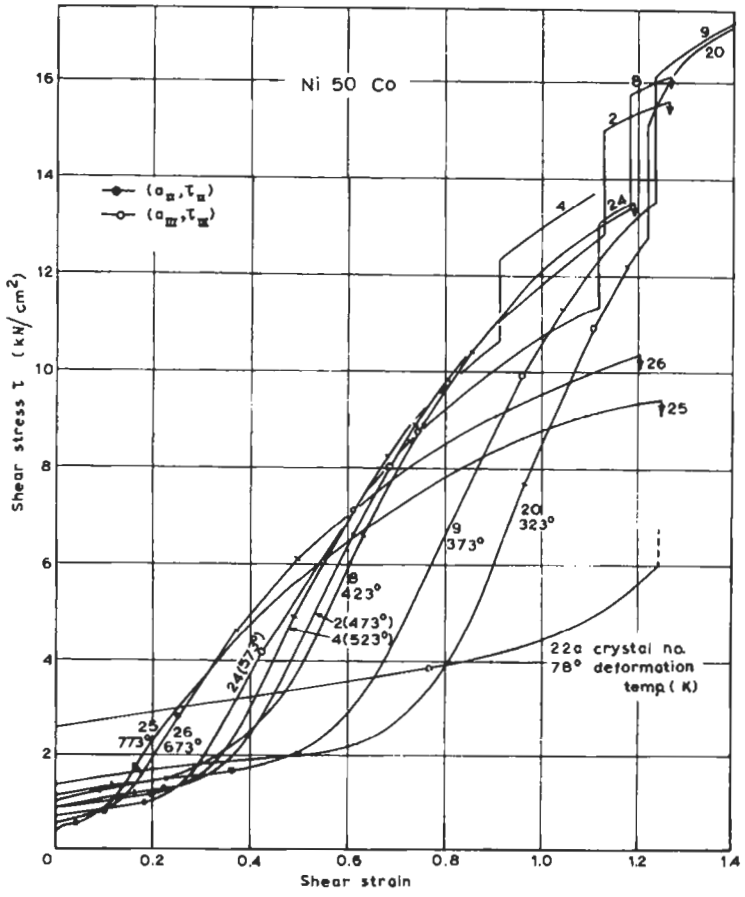

Fig. 2. Work-hardening curves of Ni–50 at% Co crystals as a function of temperature (after PFAFF [1962]).

If by alloying the SFE is not lowered, cross-slip starts already at the end of stage 1, thereby reducing work-hardening in the next stage, see WILLE *et al.* [1980] for Cu–Mn. Otherwise the stress–strain curves are quite similar (STEFFENS and SCHWINK [1983]).

2.2. Slip lines, etch pits, and electron transmission observations

Slip line measurements yield an authentic count of the number of (edge) dislocations that have left the crystal at a particular place. The intersection points of dislocations with the surface can frequently be detected by etch pits formed on them. By electron transmission micrography of thin foils cut from deformed crystals, dislocations left in the foil become visible. This powerful tool is particularly useful in alloy investigations.

2.2.1. Slip lines and etch pits

KUHLMANN–WILSDORF and WILSDORF [1953] have shown that slip lines on α-brass are more widely spaced and stronger than on pure metals (fig. 3). In between there is no fine slip. A strong line evidently does not correspond to a slip *band*, i.e., a packet of fine lines, but rather to a large single slip step on one atomic plane (WILSDORF and FOURIE [1956]). Deformed Ni–Co crystals, on the other hand, look more like pure metals in this respect although slip distribution is not quite as homogeneous in stage I (PFAFF [1962]). During easy glide the slip line density is found to remain constant, and steps grow. In stage II the density of lines increases and the new lines are shorter (inversely proportional to strain). Stage III is characterized as in pure metals by intimate cross-slip.

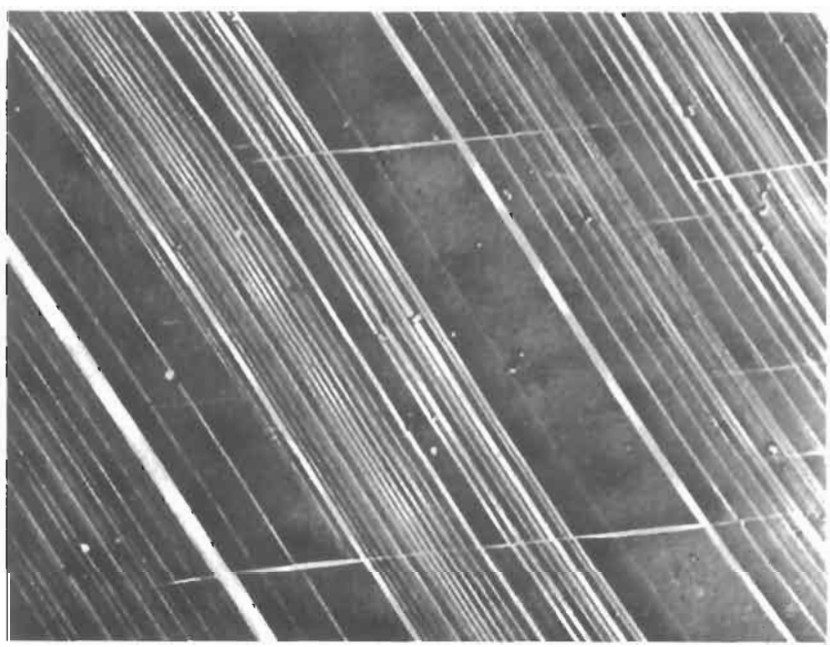

Fig. 3. Slip lines on Cu–30 at% Zn single crystal in stage I (from WILSDORF and FOURIE [1956]). 1000×.

α-Brass shows prominent steps on cross-slip planes even during stage I. At 300°C and above, "fanning" slip lines are seen in Ni–50 at% Co, corresponding to climb of edge dislocations.

MEAKIN and WILSDORF [1960] studied etch pits on α-brass after "decorating" dislocations by adding 0.7 at% Cd. Annealed specimens had a dislocation density $N \approx 10^6/\text{cm}^2$ similar to that in good pure metal crystals. During easy glide N rose to $\sim 10^8/\text{cm}^2$. Dislocations on the primary slip planes were arranged in discrete groups of about 20 dislocations of like sign. The distances within a group agreed with those calculated for a dislocation pile-up (ch. 20). KLEINTGES [1980] has studied the operation of dislocation sources in Cu–0.6% Al activated by stress pulses. The technique was also used, by KLEINTGES and HAASEN [1980], to measure dislocation velocities in dilute alloys. Typical values are 1 μm/s at the critical resolved shear stress (CRSS), but increasing with a very high power of the stress. TRAUB *et al.* [1977] and NEUHÄUSER and FLOR [1979] have obtained dislocation velocities of the same order of magnitude by microcinematography from the length-wise and in-depth growth of surface slip lines in concentrated solid solutions (see also NEUHÄUSER [1983]).

MITCHELL *et al.* [1967] have studied the dislocation structure of narrow discrete slip bands on Cu–6% Al single crystals by optical and electron-microscopic techniques, and also via etch-pitting (HOCKEY and MITCHELL [1972]). These authors conclude that deformation proceeds by big avalanches of dislocations running right across the slip plane at the beginning of deformation. The residual dislocation distribution consists of trains of edge-dislocations of opposite sign on closely spaced slip planes which have activated some secondary slip systems. These slip bands resemble in their dislocation structure those of stage II or III of pure copper and do not further contribute to deformation.

2.2.2. Electron transmission pictures of fcc alloys

Dislocations in fcc alloys observed in transmission look somewhat different from those in pure metals. Instead of tangles and three-dimensional network structures, a planar arrangement of dislocations predominates if more than about 4% solute is present. One reason for this change with alloying is probably the increasing difficulty of cross-slip (HONG and LAIRD [1990]). Also, in non-homogeneous alloys, preferential solute bonds are cut by the passage of the first dislocations and successive ones find an easier passage on the same slip plane (GEROLD and KARNTHALER [1989]). Dislocations in fcc crystals are split into partials. In between the partials there is a stacking fault. The width of the fault is proportional to $\mu b/\gamma$ where γ is the specific surface energy of the fault. WHELAN [1959] measured γ at extended dislocation nodes by transmission electron microscopy. γ decreases on alloying with an element of higher valency and cross-slip becomes more difficult (§ 2.4). Thus chances of retaining dislocation structures typical of bulk specimens during thinning to a foil are improved; see GALLAGHER [1970] for a review of measured SFEs and CARTER and RAY [1977] for weak beam measurements of the SFE of copper alloys.

The changes with strain of dislocation arrangement in Cu–10 at% Al, Cu–15 at% Al single crystals were studied by HOWIE [1960], PANDE and HAZZLEDINE [1971] and KARNTHALER *et al.* [1972, 1975]. During stage 1, "trains" of screw dislocations on

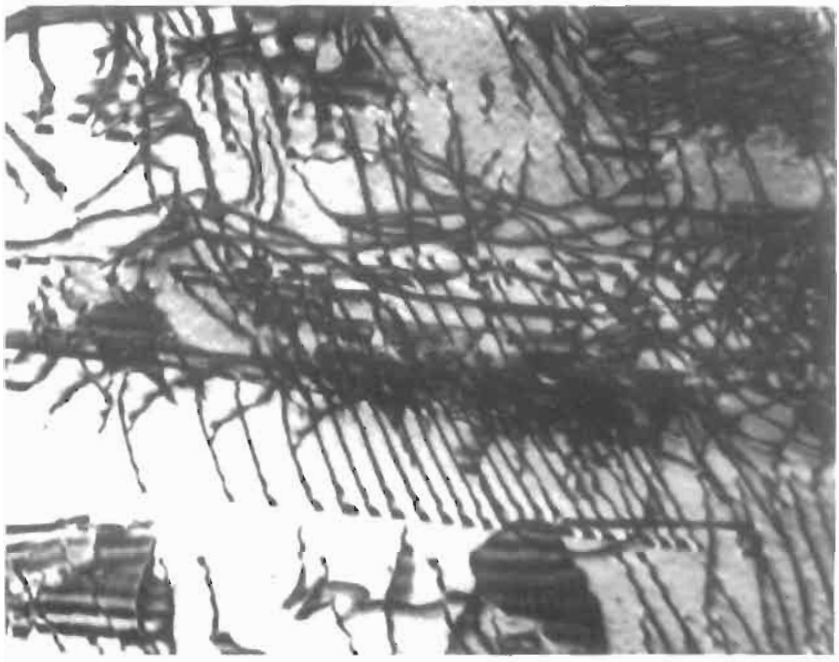

Fig. 4. Dislocations in Cu–10 at% Al single crystal foil deformed into stage II (from HOWIE [1960]). 23000×.

primary slip planes are seen. Dislocations in neighbouring trains frequently have opposite Burgers vectors. In stage II, interactions between trains and dislocations on other slip planes are observed (fig. 4), leading particularly to the formation of Lomer–Cottrell dislocations of ~ 1000 Å length. Large numbers of elongated loops are formed in the ⟨112⟩ direction. Howie has occasionally observed dislocation pile-ups on the primary slip plane. During stage III, faults widen and twins are formed. For comparison, in pure copper a ragged cell structure is observed during stage III.

Dislocations in Ni–Co single crystals have been studied as a function of deformation and γ by MADER *et al.* [1963] and MADER [1963]. These authors etched thin foils from bulk crystals parallel to the primary slip plane, which reduces interaction with the surface. The majority of the dislocations are found in edge orientation. Most of them are observed lying in dislocation "braids" parallel to ⟨112⟩. Overlapping dislocation pile-ups of opposite sign are rarely found, as are screw dislocations. Typical of stage II (except in pure Ni) is furthermore the formation of short Lomer–Cottrell dislocation segments. Little change of arrangement is observed with change of γ, although braids in pure nickel consist of short edge dislocation loops instead of groups of long dislocations of predominantly one sign. In stage I, most of the edge dislocations are paired with those of opposite sign and produce no long-range stress field. This dislocation arrangement is certainly more complex than envisaged by any of the present theories, although Seeger's comes quite close to describing the uniaxial dislocation distribution with groups of predominantly one sign observed in the alloys of low stacking-fault energy. In alloys

References: p. 2066.

with unchanged stacking fault energy (like Cu–Mn) similar dislocation structures are observed as in pure copper after comparable work-hardening (HEINRICH *et al.* [1992]).

2.3. Theories of solid-solution hardening

The last section shows that one reason for alloy-hardening is the change in the mechanism of work-hardening with alloying, i.e., the change in dislocation width, arrangement, density etc. The Hall–Petch relation for polycrystals describing the interaction of dislocations with grain boundaries is also changed in solid solutions (SUZUKI and NAKAMISHI [1975]). No great increase in grown-in dislocation density on addition of solute is observed although it could be expected for very dilute alloys (SEEGER [1957, 1958]). Most of the change of dislocation arrangement with alloying discussed so far can be explained in terms of a decrease in stacking-fault energy. Cross-slip then becomes more difficult. To form a jog in a widely split dislocation, a constriction must be produced. The formation and movement of jogs in extended dislocations in Cu–Al has been studied by CARTER [1980] by TEM. Twin nuclei are present in wide faults. In fact the stacking-fault energy would be expected to decrease in systems where alloying eventually produces a hexagonal phase (at low temperatures), as in the Hume–Rothery terminal solutions based on copper, silver, gold, and in Ni–Co. On the other hand, adding nickel to copper should raise γ_{Cu}.

In addition to the *change of dislocation structure* on alloying, there are in-situ observations of dislocation-solute interactions in specimens deformed in the TEM (KUBIN and MARTIN [1979]). Direct interactions between solute atoms and dislocations to be considered as mechanisms of solid-solution hardening can be subdivided into two groups:

a) *Dislocation locking:* Solute atoms collect on dislocations at rest.
b) *Dislocation friction:* Stationary solute atoms act on moving dislocations.

In the first case a pronounced yield point should be observed. Slip tends to concentrate by continuing where it has started. The effect of friction is simply to shift the whole stress–strain curve to higher stresses, although the friction may slowly decrease with increasing strain (if solute clusters are destroyed); a *gradual* yield point is then observed.

A few of the proposed elementary interactions between dislocations and solute will now be briefly described with respect to their overall dependence on solute concentration c and temperature of deformation T (not to be confused with the temperature T_e at which the alloy is in thermal equilibrium).

2.3.1. Dislocation locking mechanisms

a) Chemical locking (SUZUKI [1957]). The stacking fault in the fcc lattice can be considered as a hexagonal layer a few atoms thick. Solubility in this hexagonal "phase" may differ from that in the fcc matrix, and solute can thus segregate to the fault. This normally increases the width of the fault. (The opposite may also occur.) Edge dislocations and (to a lesser extent) screw dislocations thus become pinned. For a dislocation to break loose an extra stress $\Delta\tau_c$ must be applied which depends on concentration c.

$\Delta\tau_c(c)$ describes a flat-topped parabola, but is approximately linear in c for small c. This stress is independent of temperature T below that of incipient diffusion, since the solute-enriched fault is too large for a correlated thermal fluctuation to help a dislocation to escape, see however SUZUKI [1979], KOCKS [1985]. The magnitude of $\Delta\tau_c$ depends on the thermochemical parameters characteristic of the alloy, see FLINN [1958]. In typical cases $\Delta\tau_c \leq 10$ N/mm^2.

b) Elastic locking (SUZUKI [1979a]). Atoms of different size substituted in a crystal produce localized elastic strain fields which interact with those of dislocations. By compensation of their respective distortions, foreign atoms of different size find energetically favourable positions near dislocations. The elastic interaction energy between an edge dislocation and a substitutional atom may amount to several tenths of an eV. Since a screw dislocation has no hydrostatic stress field, its interaction with atoms of different size is much smaller. In the case of dissociated dislocations both partials will be locked separately, and since they in general will be of mixed character the strong locking difference between edges and screws disappears. Again a stress increment $\Delta\tau_c$ is needed to initiate dislocation movement from the solute cloud which depends on c in a manner similar to that for mechanism **a)** (SUZUKI [1957]). In this case $\Delta\tau_c$ is proportional to the *misfit parameter*,

$$\delta = \frac{1}{a}\frac{\mathrm{d}a}{\mathrm{d}c},$$

where a is the lattice constant of the alloy. Again, $\Delta\tau_c$ is independent of temperature for an extended atmosphere, except for the case when an "atmosphere" of foreign atoms "condenses" along the dislocation core. Then $\Delta\tau_c$ should decrease with increasing T as T^{-3} (HAASEN [1959]). Besides the above size misfit or *parelastic interaction* there is a modulus misfit or *dielastic interaction* (FLEISCHER [1961, 1963]). It is assumed that an individual solute atom interacts with a dislocation in the same way as a volume b^3 with a shear modulus differing from that of the matrix by $\Delta\mu$. Such elastically hard or soft spots in the matrix are felt by screw as well as edge dislocations. This interaction is called *dielastic*, as it is induced by the dislocation. It can be described by an "elastic polarizability" $\eta = 1/\mu(\mathrm{d}\mu/\mathrm{d}c)$ (KRÖNER [1964]).

c) Electrostatic locking (COTTRELL *et al.* [1953], FRIEDEL [1956]). The expanded dislocation core in metals is negatively charged and interacts with the extra charge located near a solute atom of different valency (for ionic crystals see § 2.7). Although screening by free electrons is quite effective, there must be an appreciable change in the electron energy levels at such defects. This problem has not yet been adequately treated. Thus the estimated order of magnitude for the electrostatic interaction energy between dislocation and solute atom (about 1/5 of the elastic interaction) may not be correct (see in particular the anomalously strong hardening of nickel by transition metal solutes, MISHIMA *et al.* [1986]). Apart from this, the considerations of the previous paragraph also apply to this type of interaction.

d) Stress-induced order-locking (SCHOECK and SEEGER [1959]). In the previously mentioned mechanisms a dislocation is locked when solute atoms collect on it. Even without this, a moving dislocation is impeded by the described interaction with the solute

atoms it passes (solute friction). As an additional pinning mechanism in a *homogeneous* alloy one has to consider that the directionality of forces exerted by the dislocation on its environment may produce local order in the alloy around it. The dislocation "digs itself in" energetically in this way and a yield point may result. The effect should depend quadratically on concentration in the case of substitutional alloys. Schoeck and Seeger calculate it to be independent of temperature below the temperature of rapid diffusion. The effect acts differently on edge and screw dislocations. Of course, any solute enrichment around the dislocation will enhance the order-locking. On the other hand, a moving dislocation will be impeded by cutting through ordered clusters (§ 2.3.2d).

2.3.2. Summation of solute forces acting on moving dislocations

In the case of *locking*, the solute atoms have the time to diffuse to positions of maximum interaction with a dislocation. In the other extreme, called *friction*, a stationary distribution of solute atoms, assumed to be a statistical distribution on both sides of the glide plane, interacts with a moving dislocation, and the question arises how many obstacles are in strong contact with the dislocation at any time. This is a summation problem. Its solution depends on geometrical parameters such as solute spacing, $l_s = b/\sqrt{c}$, and range w of interaction, as well as on the maximum elementary interaction force f_{max} in relation to the dislocation line tension $E_L = \frac{1}{2}\mu b^2$. LABUSCH [1970, 1972] defines a dimensionless range parameter,

$$\eta_0 = \frac{w}{b}\left(\frac{cE_L 2}{f_{max}}\right)^{1/2}, \tag{1}$$

which differentiates between two cases of hardening, i.e., of summation:

$\eta_0 \ll 1$ (Fleischer–Friedel) means hardening by dilute, strong obstacles.

$\eta_0 > 1$ (Mott–Labusch) implies concentrated, weak obstacles. Figure 5 shows various states of dispersion with respect to the radius of curvature of the dislocations at the given stress.

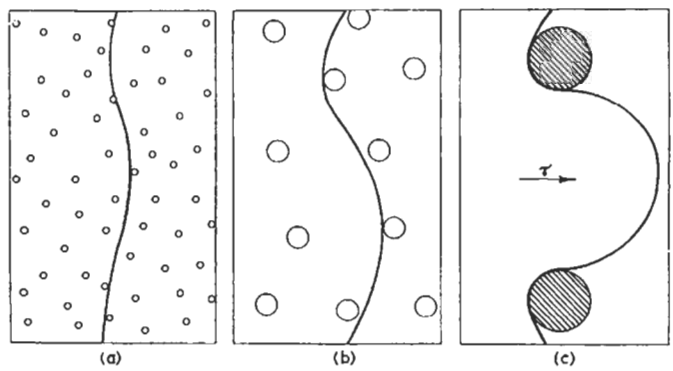

Fig. 5. Interaction between dislocation and foreign atoms in various states of dispersion.

a) Dilute solutions. The mean spacing L between two solute atoms touched by a dislocation under a stress τ_c is (according to FRIEDEL [1964]):

$$L = \left(2E_L b/\tau_c c\right)^{1/3}, \tag{1a}$$

where c is the solute concentration per atom. The force balance at breakthrough reads:

$$\tau_c bL = f_{max}. \tag{1b}$$

Therefore:

$$\tau_c b^2 = f_{max}^{3/2} c^{1/2} / \left(2E_L\right)^{1/2}. \tag{1c}$$

This *Fleischer–Friedel yield stress* of dilute solid solutions has been confirmed (except for a numerical factor near one) by extensive computer simulations (KOCKS [1966], FOREMAN and MAKIN [1966], HANSON and MORRIS [1975], SCHWARZ and LABUSCH [1978]). Characteristic of dilute hardening is that obstacles are touched by the dislocations at full interaction force or not at all. This is no longer possible at higher solute concentrations (in the sense of $\eta_0 > 1$ above).

b) Concentrated solutions. LABUSCH [1970, 1972] defines a distribution function $\rho(f)\mathrm{d}f = \rho(y)\mathrm{d}y$ for the number of interactions with solute atoms which a unit length of dislocation (along the x-direction) has with strengths between f and $f + \mathrm{d}f$ or at spacings y, $y + \mathrm{d}y$. The two quantities are uniquely related by the force–distance profile $f(y)$ of the obstacle (fig. 6). Then the force balance reads:

$$\tau_c b = \int \rho_c(y) f(y)\,\mathrm{d}y, \tag{2}$$

where "c" refers to the state at breakthrough. The distribution function is calculated to

$$\rho_c = \frac{c}{b^2}\left[1 + G(0)\cdot f'(y)\right] \quad \text{or} \quad \rho_c = 0 \tag{2a}$$

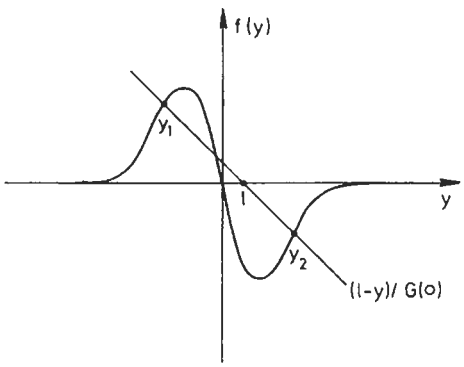

Fig. 6. Force–distance profile of elastic solute-dislocation interaction, showing instable interval (y_1, y_2) given by mean dislocation position at l and compliance $G(0)$, see text.

References: p. 2066.

for the intervals outside or inside (y_1, y_2) in fig. 6, respectively. Here $G(0)^{-1} = 2(\varphi E_L)^{1/2}$, where

$$\varphi = \int \rho_c(y) f'(y)\, dy \tag{2b}$$

is the average curvature of the obstacle potential. It is plausible that most interactions ($\rho_c = \max$) take place where the curvature of the interaction potential has its maximum. If the "one" in eq. (2a) is neglected, eq. (2) can be integrated with eq. (2b) to yield

$$\tau_c b^2 = f_{max}^{4/3} c^{2/3} w^{1/3} / 2(E_L b)^{1/3} (4I)^{1/3}, \tag{2c}$$

where

$$I = \int_0^1 \frac{\partial(f/f_{max})}{\partial(y/w)}\, d(f/f_{max})$$

is a pure number of order one. This is the *Labusch yield stress* for concentrated alloys ($\eta_0 > 1$). A rather similar result was obtained from completely different assumptions by RIDDHAGNI and ASIMOW [1968]. Computer simulations by SCHWARZ and LABUSCH [1978] have in the meantime confirmed the analytical solution for $\eta_0 > 1$, eq. (2c), and also allowed to interpolate between the Fleischer-(Friedel) ($\eta_0 \ll 1$) and (Mott)-Labusch ($\eta_0 > 1$) situations to give

$$\tau_c = \tau_c^{Fl} (1 + 2.5\eta_0)^{1/3}. \tag{2d}$$

Equation (2d) tends to τ_c^{Fl}, eq. (1c), for $\eta_0 \ll 1$ and to τ_c^{Lab}, eq. (2c), for $\eta_0 > 1$. Actually for fcc solid solutions $f_{max}/2E_L \approx \frac{1}{10}$ and $\eta_0 \geq 1$.

c) Effect of different obstacles on the same dislocation. One of the main advantages of Labusch's theory is that it allows one to *superimpose*, by various distributions ρ_{ci}, the effects of different obstacles on the same dislocation. These might be obstacles at different spacings from the slip plane (where it follows that only the ones adjacent to the slip plane are important). Also solute atoms above and below the slip plane interact differently with the compression and dilation zones of an edge dislocation as far as the size misfit (parelastic interaction) is concerned: $f_{max}^{p} = \mu b^2 |\delta|$. The dielastic component $f_{max}^{d} = \alpha \mu b^2 |\eta|$ is of the same sign for solute atoms above and below the slip plane. Labusch shows that both effects and positions add up to an effective interaction force (see also HAASEN and KRATOCHVÍL [1973]):

$$f_{max}^{eff} = \mu b^2 (\delta^2 + \alpha^2 \eta^2)^{1/2}. \tag{2e}$$

FLEISCHER [1963] in his theory had rather arbitrarily put:

$$f_{max}^{eff} = \mu b^2 |\delta - \alpha \eta'|, \qquad \text{with} \quad \eta' = \eta/(1 + |\eta|/2),$$

see also KOSTORZ and HAASEN [1969], SAXL [1964] and GYPEN *et al.* [1981].

d) Short-range order destruction. Another possible flow stress component for a dislocation stems from the destruction of any existing *short-range order* in the alloy by slip. This creates a diffuse antiphase boundary of specific energy Γ per cm^2 and leads to (FISHER [1954]):

$$\tau_c b = \Gamma = f_{max} w c_p / b^2, \tag{3}$$

where c_p is the fraction of solute pairs across the slip plane. c_p should depend on solute concentration as c^2 for small c (FLINN [1958]). This is an energy-storing interaction, not an elastic one. The computer simulation (SCHWARZ and LABUSCH [1978]) interpolates in this case as $\tau_c \approx \tau_c^{Fl}[(1+\eta_0)$. The elastic interaction of solute clusters of i atoms can be included in Labusch's theory by putting $c_i = c/i$ and $f_{max,i} = f_{max}\sqrt{i}$ without changing the overall result of eq. (2c).

e) Thermal activation. The above calculations all refer to $T=0$. Attempts have been made to include thermal activation into the theory of the friction stress due to elastic solute interactions (LABUSCH *et al.* [1975]). Labusch has described the motion of a dislocation in a field of obstacles under the action of random thermal forces, $b\tau_T$, by the equation

$$m\ddot{y} + B\dot{y} - E_L y'' = b\left[\tau_c + \tau_i(x - x_i, y - y_i) + \tau_T(x - x_n, t - t_K)\right]. \tag{4a}$$

Here m is the dislocation mass per unit length, B the phonon and electron drag coefficient, i numbers the solute atoms acting on the dislocation while the thermal forces (phonons) 'strike' at positions x_n, times t_K (there should be sums over all i, n, K). By clever scaling the equation can be written in new variables:

$$\xi = \frac{x}{b}\left(\frac{f_{max} c}{2E_L}\right)^{1/2}, \eta_1 = \frac{y}{b}\left(\frac{c 2E_L}{f_{max}}\right)^{1/2}, \theta = \frac{t}{b}\left(\frac{f_{max}}{2m} c\right)^{1/2},$$

$$S = \tau_c/\tau_c^{Fl}; g_i = \tau_i/\tau_c^{Fl}, \gamma = Bb\left(2 f_{max} mc\right)^{-1/2},$$

and with $g_{n,K} = \tau_T/\tau_C^{Fl}$ then becomes

$$\tfrac{1}{2}\frac{\partial^2 \eta_1}{\partial \theta^2} + \gamma \frac{\partial \eta_1}{\partial \theta} - \tfrac{1}{2}\frac{\partial^2 \eta_1}{\partial \xi^2} = S + g_i\left((\eta_1 - \eta_i)/\eta_0\right)\delta(\xi - \xi_i) + \Delta\theta \cdot g_{n,K}\delta(\xi - \xi_n)\delta(\theta - \theta_K). \tag{4b}$$

Solutions have been sought in three limiting cases:

1) Low temperatures ($T < 20$ K), no thermal activation, $\gamma \ll 1$, giving a lowering of the flow stress due to the dislocation inertial mass (especially in superconductors): GRANATO [1971], SCHWARZ and LABUSCH [1978], LABUSCH [1981].

2) Intermediate temperatures ($5T \ll T_{Debye}$), no inertial effects ($\gamma > 1$), giving athermal creep due to zero-point vibrations of the dislocation at the obstacles (NATSIK [1979], STARTSEV [1981]).

References: p. 2066.

3) Normal temperatures, $\gamma > 1$, thermally activated flow. The dislocation is excited to oscillations with random amplitudes and phases, the energy contained in each mode being kT, independent of γ. Then Labusch calculates:

$$\left\langle g_{n\cdot K}^2 \right\rangle = 2\gamma kT\left(2E_L c\right)^{1/2}/bf_{max}^{3/2}, \quad \left\langle g_{n,K} \right\rangle = 0.$$

This leads to a scaling of the temperature as

$$\vartheta = kT\left(2E_L c\right)^{1/2}/bf_{max}^{3/2} = \frac{kTc}{\tau_c^{Fl} b^3}, \tag{4b2}$$

while the yield stress at the temperature T scales with τ_c ($T=0$). This is called the *stress equivalence* of solution-hardening (BASINSKI *et al.* [1972], SCHWINK and WILLE [1980]). NABARRO [1982] has shown that stress equivalence follows naturally from Labusch's theory but should not be observed in the low-concentration range of the Friedel theory. LABUSCH [1992] has solved the eq. of motion (4b) numerically in a random array of obstacles, taking the thermal forces from a Gaussian distribution (see also ARSENAULT and LI [1989]). The average velocity was determined from the time it took the dislocation to proceed over a large part of the obstacle field at a given stress. Most of this time the dislocation spends in waiting in front of obstacles rather than travelling between them. The calculated velocity decreases exponentially with U_{eff}/kT where U_{eff} is several times the (stress-free) activation energy $U \approx \frac{1}{2} f_{max} \cdot w$ over single obstacles if the stress is small. This as well as the large (compared to c/b^2) activation volume $v = -(dU_{eff}/d\tau)$ is in agreement with experiments. As we will see below there is experimentally a "plateau" in $\tau_c(T)$ which is approximated but not truly realized in the computer simulation, see fig. 7. Here a dependence of (τ_c/τ_c^{Fl}) on η_0 is visible as one crosses from the Labusch limit ($\eta_0 > 1$) to the Friedel–Fleischer case ($\eta_0 < 1$). Stress equivalency is almost realized in the Labusch range as $(\tau_c(T) - \tau_c(0)/\tau_c(0)) = \text{const}$. Although the scaling of T is not quite correct – in terms of T_0 rather than ϑ (above). Comparing these predictions with experiments in the "plateau" range makes the exact choice of T unimportant. There should be a break in the concentration dependence of $\tau_c(T)$, however, as one moves down into the range $\eta_0 < 1$.

Often the cooperative overcoming of several obstacles at a time as demonstrated in Labusch's simulations is disregarded and a temperature dependence $\tau_c(T)$ is estimated from $U(\tau)$ as follows:

Assuming a parabolic top of the function $f(y)$ in fig. 6 one obtains generally, with an Arrhenius 'ansatz' for the strain rate $\dot{\varepsilon}$:

$$\tau_c(T, \dot{\varepsilon}) = \tau_{c0}\left[1 - \left(T/T_0\right)^{2/3}\right]^{3/2}, \tag{4c}$$

with $kT_0 = f_{max} w / \ln(\dot{\varepsilon}_0/\dot{\varepsilon})$.

The problem now is to establish the contribution of the various mechanisms to the measured critical shear stress and yield stress increment according to their respective temperature- and concentration dependence. Various investigators have also tried to judge different models of solute solution-hardening from the effect of varying the size misfit

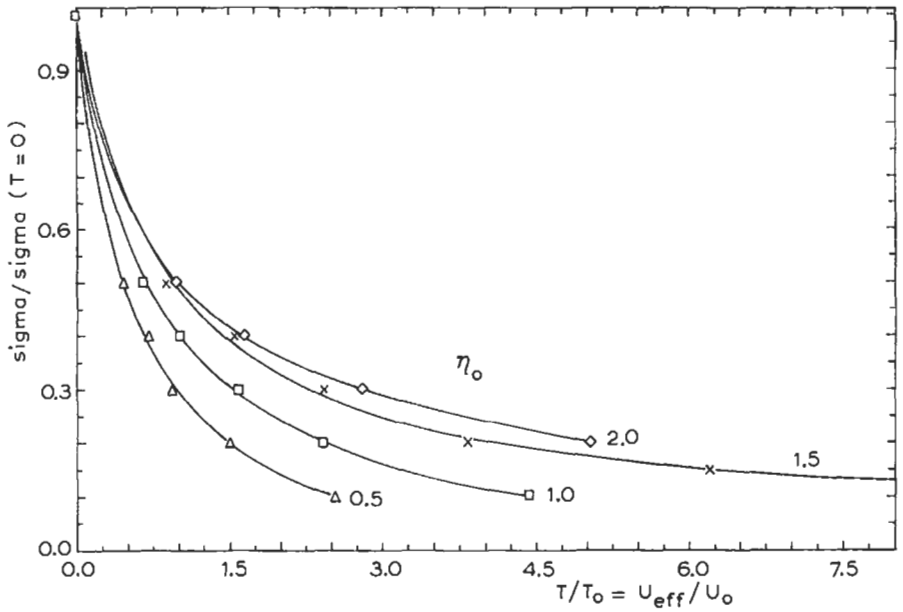

Fig. 7. Flow stress at a given dislocation velocity versus temperature for different values of η_0. The temperature is scaled by $T_0 = U_0/k\ln(\nu_0/\nu)$. The plot serves also to represent, as a function of applied stress, the activation energy in terms of that over a single solute atom (LABUSCH [1992]).

and valence. It is not always easy to define atomic "size" and "valency" in a solid solution (see ch. 3). A further difficulty arises in differentiating between locking and friction mechanisms: All models for dislocation locking might also lead to a friction drag if at high temperatures or low dislocation velocities solute enrichment moves with the moving dislocation (*microcreep* effect). Kocks has worked out a theory (unpublished) for the temperature-independent plateau in the CRSS assuming fast jumps of solute atoms in the case of moving dislocations; see also SCHWARZ [1979]. Furthermore, if the yield stress is attained successively in different parts of the specimen (by propagation of a *Piobert–Lüders band*, see HÄHNER [1992]) and work-hardening is rapid, a yield point maximum may not show and macroscopically the specimen will be characterized by a high friction stress. In both cases the stress–strain curve in the initial stages will appear serrated.

2.4. Solid-solution effect on fcc stress–strain curves

The different characteristic parameters describing a standard work-hardening curve of a fcc single crystal according to § 2.1 will be discussed in this section in the light of direct observations of deformed alloy crystals (§ 2.2) and of theoretical considerations (§ 2.3).

2.4.1. Critical shear stress τ_0 of fcc solid solutions

Without special treatment a yield point maximum is rarely observed at the beginning of plastic deformation in a tensile test at constant strain rate. Furthermore, the temperature dependence of the flow stress during easy glide as determined by temperature change on one crystal is found identical with that of the critical shear stress from a series of specimens (HAASEN and KING [1960], HENDRICKSON and FINE [1961b]). This implies that τ_0 is determined by a friction, rather than a locking mechanism. Typical examples for $\tau_0(T)$ are given in fig. 8. Below 300 K the critical shear stress increases more strongly with falling temperature in the alloy than in pure metals. Between 300 K and 500 K, $\tau_0(T)$ shows a nearly temperature-independent "plateau", the height of which increases rapidly for small concentrations. A second decline in $\tau_0(T)$ occurs at still higher temperatures, sometimes after a slight peak (ROGAUSCH, unpubl., see HAASEN [1964] and NEUHÄUSER *et al.* [1990]). Examples of the concentration-dependence of τ_0 are given in fig. 9. The curvature of $\tau_0(c)$ for fcc alloys is found to be negative at ~ 400 K with the exception of Al–Zn single crystals reverted after zone formation (DASH and FINE [1961]), which show a positive $d^2\tau_0/dc^2$ indicative of cluster hardening (see § 2.3.2d, also § 3 and fig. 22). At low temperatures, τ_0 for Ag–Al increases more nearly linearly with concentration. There is overwhelming evidence for many fcc alloys, particularly those based on Cu, Ag and Au, showing that the plateau stress τ_0 increases as the square root of the solute concentration, or as $c^{2/3}$, at least in the range $c \leq 0.1$ (HAASEN [1967a, 1968], see also NIXON and MITCHELL [1981]). Figure 10 shows a plot of measured plateau stresses of copper alloy single crystals vs concentration to the 2/3 power. A detailed analysis of $\tau_0(c, T, \dot{\varepsilon})$ of Cu–Mn and Cu–Ge single crystals has been presented by WILLE *et al.* [1987].

To understand *plateau hardening*, i.e., the room-temperature critical shear stress of the alloy, the forest intersection mechanism is of little help. Although the constriction energy will increase on alloying when γ decreases * and therefore dislocation intersection will become more difficult, the grown-in dislocation density does not change to the extent necessary to explain the strong decrease in activation volume observed for the alloys (see § 2.2). HENDRICKSON and FINE [1961b] observe, however, a refinement of the substructure of Ag crystals with increasing Al concentration. HAMMAR *et al.* [1968] have investigated by etch pits the contribution to solution-hardening from changes in either the dislocation density or the dislocation arrangement due to solute additions. They found this contribution to be of minor importance in Ag–In and Ag–Sn crystals. In the former, a $c^{2/3}$ or $c^{3/4}$ law was found to fit the $\tau_0(c)$ results better than $c^{1/2}$. KLOSKE and FINE [1969] analyzed τ_0 in the Au–Ag system in terms of a c^2-component of the friction stress in addition to the $c^{1/2}$ term. The former may be interpreted in terms of local order hardening (mechanism **d** in § 2.3.2). SVITAK and ASIMOW [1969] on the other hand found no effect of quenching on the CRSS of Ag–Au single crystals at 200 K except near the 75% Au composition. The plateau stress of all the investigated fcc alloys based on Cu, Ag, Au and Pb is, in its dependence on concentration and solute characteristics as well as in its absolute magnitude, fully explained by mechanism **b** (§ 2.3 2), eq. (2c), as fig.

* There are, also, alloys like Cu–Ni in which γ should increase with concentration of solute.

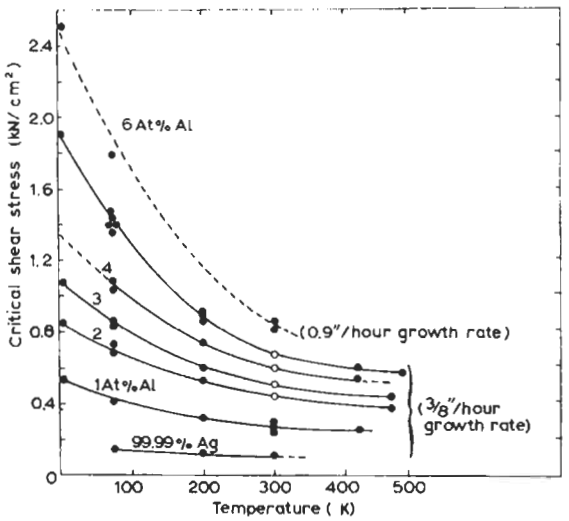

Fig. 8. Critical shear stress of Ag–Al single crystals (grown from the melt at two rates of solidification) versus temperature (after HENDRICKSON and FINE [1961b]).

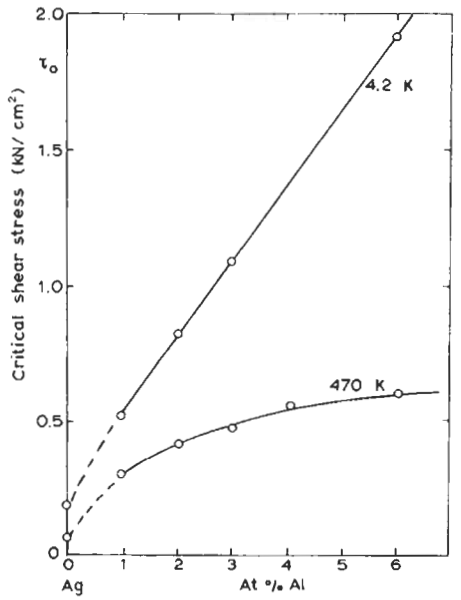

Fig. 9. Critical shear stress versus composition for Ag–Al single crystals at two temperatures (HENDRICKSON and FINE [1961b]).

References: p. 2066.

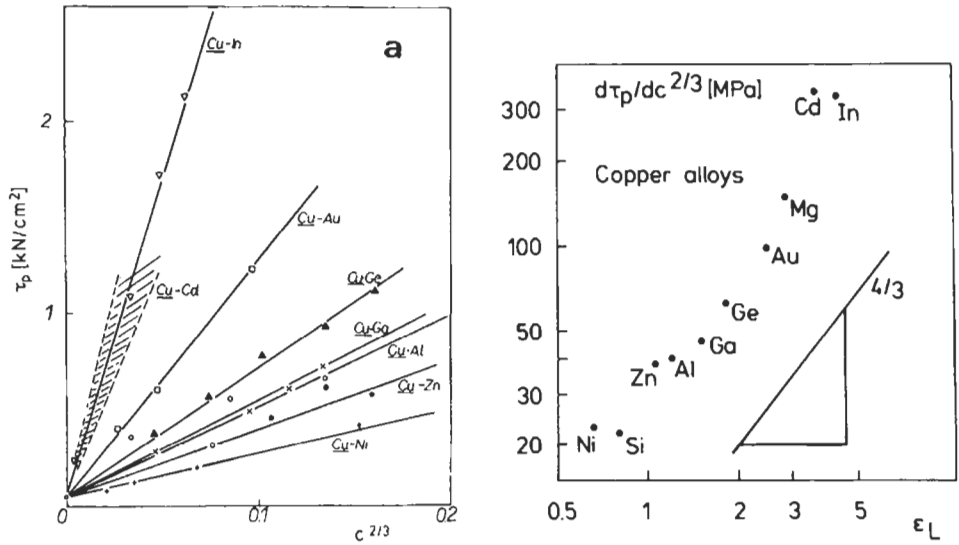

Fig. 10a, b. (a) Plateau stress of copper alloy single crystals versus solute concentration to power 2/3 (after KRATOCHVÍL and NERADOVA [1971]). (b) Slopes of straight lines of fig. 10a and of similar data by ČIZEK *et al.* [1974] versus the Labusch combined interaction parameter $\varepsilon_L = (\delta^2 + \eta^2\alpha^2)^{1/2}$.

10 proves for the case of copper alloys. In fig. 10b the slopes of the straight lines of fig. 10a are plotted to the power 3/4 versus the Labusch combined interaction parameter $\varepsilon_L = (\delta^2 + \eta^2\alpha^2)^{1/2}$ as required by eq. (2e). This plot includes the effect of a second order parelastic interaction as proposed by JAX *et al.* [1970] for dissociated dislocations, see also TAKEUCHI [1968] and GYPEN and DERUYTTÈRE [1981]. In particular, size misfit (δ) alone is not able to explain plateau hardening as evidenced especially by the Cu–Si and Cu–Ni results. $\alpha^{-1} = 16$ (for edge dislocations) on the whole gives a better fit than $\alpha^{-1} = 3$ (for screw dislocations). There are some alloy systems in which δ and η have the same sign, leading theoretically to partial compensation of dielastic and parelastic interactions if $\alpha > 0$. There is experimental evidence, however, that this does not happen in practice. Only the Labusch combination of parameters $(\delta^2 + \eta^2\alpha^2)^{1/2}$ is able to explain hardening in Ag–Al, Ag–Zn, Au–Zn within the frame-work of mechanism **b**. The dependence on the 4/3 power of ε_L in eq. (2c) fits the present experimental results better than a 3/2 power law. The cooperative obstacle mechanism, according to both theory and experiment, appears to be much more important in solution-hardening than the locking mechanisms (SUZUKI [1979]) at least for $c \leq 0.1$. In comparing the plateau stress with a friction theory there must be, however, despite its $c^{1/2}$ or $c^{2/3}$ dependence, a solute diffusion effect as evidenced by a $d\tau_c/dT > 0$ (KOCKS [1985]). Its concentration and characteristics solute dependence are not known yet. It is interesting to note that solution-hardening is in fact controlled by atomic concentration of solute rather than by electron concentration as has once been proposed (HUTCHISON and HONEYCOMBE [1967]). PEISSKER [1965a] showed this by the dependence of τ_0 on c (Ga–Ge) for ternary

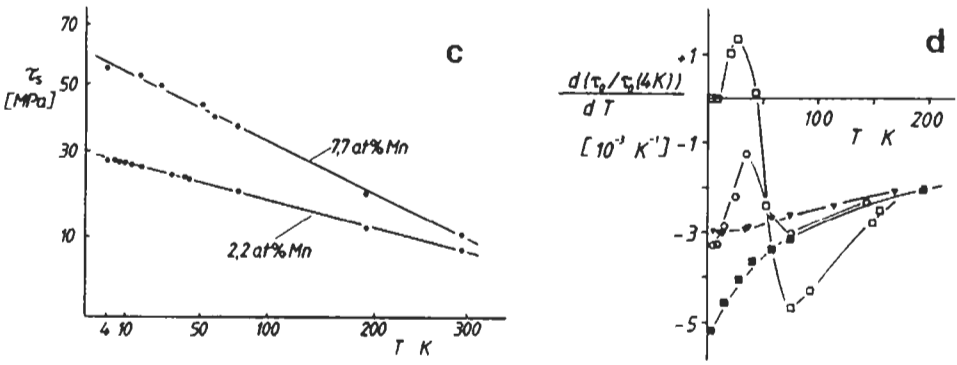

Fig. 10c, d. (c) Thermal CRSS component $\tau_s = \tau_c - \tau_\mu$ as $\tau_s^{2/3}$ versus $T^{2/3}$ for CuMn solid solutions ($\tau_\mu = \tau_{\mu 0}\mu(T)/\mu(0)$, μ = shear modulus, $\tau_{\mu 0} = 6$ MPa (for 2.2% Mn), $\tau_{\mu 0} = 15$ MPa for 7.7% Mn (after WILLE and SCHWINK [1980]). (d) Slopes of normalized CRSS of Cu–Mn alloys with respect to temperature. ■: 7,7%; ▾: 1,48%, ○:0.96%, □: 0,11% Mn. (After WILLE *et al.* [1982].)

Cu–Ga–Ge single crystals of constant electron concentration. Also the results in the Ag–Pd system (KRATOCHVÍL [1970]) do not correlate with electron concentration, while they do correlate with atom concentration. Ternary hardening was investigated in Cu–Si–Ge by FRIEDRICHS and HAASEN [1975]. As expected from Labusch's theory, the plateau stress τ_p follows from the binary hardening increments $\Delta\tau_{Ge}$ and $\Delta\tau_{Si}$ to the CRSS of pure Cu, τ_{Cu}, as

$$\left(\tau_p - \tau_{Cu}\right)^{3/2} = \Delta\tau_{Ge}^{3/2} + \Delta\tau_{Si}^{3/2}. \tag{4d}$$

A similar conclusion is reached by GYPEN and DERUYTTÈRE [1977]. The low-temperature increase in the CRSS of fcc alloys is well described by the formal eq. (4c), see fig. 10c. There is however a low-temperature anomaly at still smaller solute concentration, see fig. 10d (WILLE *et al.* [1982]). The CRSS goes through a maximum at 50 K, as expected from the theory of the inertial effect (GRANATO [1971] and SCHWARZ and LABUSCH [1978]). The activation energy obtained from the formal Arrhenius description, eq. (4c), often comes out rather high (0.5–1.5 eV), much higher than expected for the interaction of a dislocation with single solute atoms. This has been discussed above in relation to Labusch's computer simulation. It has been suggested (TRAUB *et al.* [1977], and KLEINTGES and HAASEN [1979]) that the dislocation on its way over the slip plane gets stuck in so-called hard configurations where it has to be thermally activated over *groups* of solute atoms. This would also explain the unexpectedly high stress exponents of the dislocation velocity (KLEINTGES and HAASEN [1979]). Furthermore, the stress equivalence of solution-hardening seems to get lost above about 2% solute concentration, perhaps as a consequence of clustering (SCHWINK and WILLE [1980] and WENDT and WAGNER [1982]). Another open question is that of strain-aging in the plateau range under conditions of dynamic deformation (GLEITER [1968], NEUHÄUSER and FLOR [1978], SCHWARZ [1982]), NEUHÄUSER *et al.* [1990], KOLK and SCHWINK [1992]).

References: p. 2066.

2.4.2. The yield phenomenon in fcc alloys

An initial maximum of the stress strain curve which can be recovered after deformation by heat treatment (strain-aging) has been found in carefully treated fcc solid solutions. This yield point has been studied in particular on single crystals of Cu–Zn (ARDLEY and COTTRELL [1953]), Cu–Al (KOPPENAAL and FINE [1961]) and Ag–Al (HENDRICKSON and FINE [1961a]). A typical series of yield-point observations on various Cu–Zn alloy crystals is shown in fig. 11. They fit the theoretical picture of pinning of dislocations by solute atoms described in § 2.3.1. A time t_a is necessary at a temperature T_e to permit solute atoms to diffuse to their energetically favourite positions at dislocations and thus establish a yield stress maximum. $\Delta\tau$ is the extra stress to free the dislocation from this interaction. t_a is surprisingly small in substitutional alloys after straining and depends exponentially on T_e with an activation energy E much smaller than expected for equilibrium solute diffusion. For Ag–6 at% Al, about 50% of $\Delta\tau_{max}$ is obtained after 2% straining and aging 1 min at 296 K, with $E \approx 0.55$ eV. Vacancies (and interstitials?) produced during deformation and/or moving in highly strained regions near dislocations could explain such rapid solute movement. If the aging is done under a stress approaching the flow stress it proceeds faster and reaches higher stresses $\Delta\tau_{max}$ (EVERS [1959]). This observation enables one to separate a strain-ageing yield point as described above from an unloading yield point often observed in pure metals (HAASEN and KELLY [1957]) and alloys (PFEIFFER and SEEGER [1962]). For Cu–Zn and Ag–Al, $\Delta\tau_{max}$ varies linearly with concentration for small c and more gradually for larger c. In Cu–Al on the other hand, $\Delta\tau(c)$ is a quadratic function as expected for order-locking, although numerically too small (§ 2.3.1d). In this alloy the yield drop is rather gradual and shows a minimum as a function of the annealing temperature before quenching. There is a slight decrease of $\Delta\tau$ for increasing deformation temperatures for this alloy as well as Ag–Al, while $\Delta\tau$ is found to be independent of T for Cu–Zn. This is to be

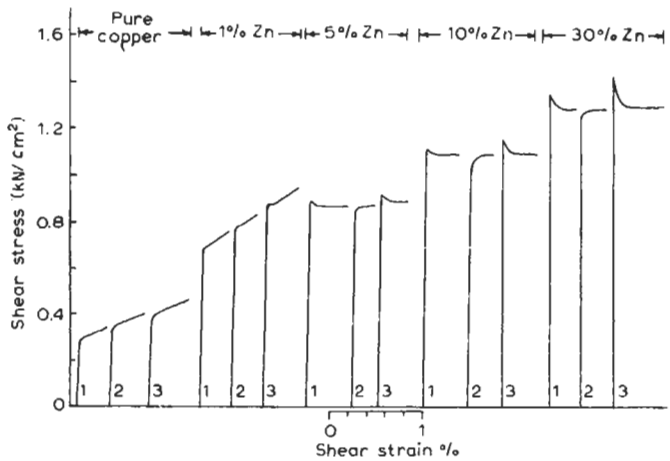

Fig. 11. Stress–strain curves of Cu and α-brass single crystals (1) first loading (2) immediately retested (3) after 2 h at 200°C (after ARDLEY and COTTRELL [1953]).

expected for chemical or order-locking, as well as for elastic locking in substitutional solid solutions. The latter is considered unlikely for Ag–Al because the size factor $\delta \approx 0$, and there are wide stacking faults. The hypothesis of chemical locking best fits the results for Ag–Al and Cu–Zn (see § 2.3.1a). FLEISCHER [1966] concludes that the binding energy W_m between dislocations and solute atoms, see FIORE and BAUER [1968], correlates well with the combined elastic interaction $\varepsilon_{Fl} = |\eta' - 3\delta|$, for Cu–Si, Cu–Ge, Cu–Sn. W_m is smaller than 0.4 eV for copper alloys.

2.4.3. Easy glide and overshoot in fcc alloys

There are two possible mechanisms of initial slow work-hardening (stage I, ch. 21, § 7.2.1) in alloy crystals: (a) *single slip* occurs, the mean free path of dislocations on the primary plane approaches the specimen width; (b) *inhomogeneous slip* by Piobert–Lüders band propagation may simulate "easy glide". HÄHNER [1992] describes Lüders band propagation in terms of non-linear dislocation dynamics leading to rapid dislocation multiplication, see ALEXANDER and HAASEN [1968]. In the first case, the work-hardening rate θ_I is finite and decreases with decreasing temperature and increasing concentration. θ_I depends strongly on orientation and is small for single-slip orientations only. The stress for onset of rapid hardening is $\tau_{II} \approx 2\tau_0$ (GARSTONE and HONEYCOMBE [1957]). The extent of easy glide a_{II} is therefore larger at low temperatures and for concentrated alloys. In the case of inhomogeneous slip, $\theta_I \approx 0$ and $\tau_{II} \approx \tau_0$. Here a_{II} is fairly independent of orientation and temperature and increases with concentration. Examples for case (a) are found in Ni–Co (PFEIFFER and SEEGER [1962], fig. 1) and Ag–Al (HENDRICKSON and FINE [1961b]), while α-brass is typical for case (b) (PIERCY *et al.* [1955]). In brass, yield propagation has been observed directly. The Cu–Ga and Cu–Ge alloys appear to change from (a) to (b) with increasing concentration, τ_{II}/τ_0 decreases from 2 to 1 and a_{II} shows a flat maximum at small concentrations (HAASEN and KING [1960], PEISSKER [1965a], see also STARTSEV *et al.* [1979], SCHWINK and WILLE [1980]).

To understand the pronounced true easy glide behaviour of alloys [case (a)] it must be realized that dislocations of secondary slip systems find it difficult to move when dislocations in the primary system are widely extended (SEEGER [1958]). An exception is the activity of dislocations in the cross-slip plane (having the same Burgers vector as the primary dislocations) observed in α-brass. The same argument leads to an explanation of the *overshoot* phenomenon typical for alloys of low γ (see § 2.1). Pinning of secondary slip dislocations on the other hand does not explain overshoot, as has been shown by a convincing experiment by PIERCY *et al.* [1955]. Overshooting is measured frequently by the ratio of the applied shear stresses $\varrho = \tau_{sec}/\tau_{prim}$ at the beginning of secondary (conjugate) slip ($\varrho = 1$ without overshoot, $\varrho > 1$ indicates overshoot). $\varrho = 1.28$ for Cu–30 at% Zn, independent of temperature and initial orientation of the crystal, while for Ni–Co ϱ is smaller at higher temperatures or unfavourable orientations (PFEIFFER and SEEGER [1962]).

2.4.4. Linear hardening

The work-hardening rate θ_{II} in stage II (ch. 21, § 7.2.1) of the stress–strain curve of fcc alloys is found to be remarkably independent of composition ($\theta_{II} \approx \mu/400$). This was predicted by SEEGER's [1957, 1958] theory of long-range elastic hardening which

describes θ_{II} as proportional to the square root of the ratio of slip distance to slip-line length. A more recent treatment of stage II has been given by HIRSCH [1975]. Higher and longer surface steps have been observed in α-brass than in copper. The ratio of height to length is constant and thus the back stress remains unchanged. As we have seen in § 2.2 the dislocation arrangement visualized by Seeger for stage II is realized best in alloy crystals of low γ.

2.4.5. Dynamic recovery

It was shown by slip-line observations by SEEGER [1958] and coworkers that the beginning of stage III (ch. 21) in pure metals coincides with the appearance of intimate cross-slip and fragmented slip bands. This stress-aided cross-slip is often described as dynamic *recovery* because it enables dislocations to circumvent obstacles. The same is true for Cu–Ga and Cu–Ge alloys (HAASEN and KING [1960]) and Ni–Co (PFEIFFER and SEEGER [1962]). A quantitative evaluation of the cross-slip process enabled HAASEN [1958] and SEEGER *et al.* [1959] to estimate stacking-fault energies γ from the stresses τ_{III} at the beginning of stage III as a function of temperature T and strain rate $\dot{\varepsilon}$:

$$\ln\left\{\tau_{III}(T,\dot{\varepsilon})/\tau_{III}^{0}\right\} = \left(\beta\gamma kT/\mu^2 b^4\right)\ln\left(\dot{\varepsilon}/\dot{\varepsilon}_0\right) \quad \text{for } 0.005 < \gamma/\mu b < 0.035. \tag{5}$$

Here τ_{III}^{0}, $\dot{\varepsilon}_0$ are constants to be evaluated from experiment and $\beta \approx 820$. (See SEEGER *et al.* [1959] for a more complete description and ESCAIG [1968] for an alternative theory; see also DUESBERRY *et al.* [1992] and PÜSCHL and SCHOECK [1993].) As expected, the temperature- and strain-rate sensitivity of τ_{III} becomes zero and τ_{III} increases as the concentration of Ga and Ge approaches that of the fcc–hcp phase boundary (fig. 12) and

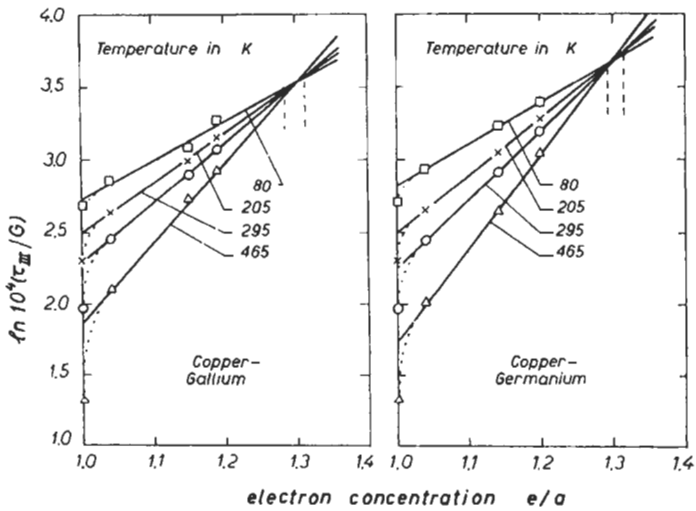

Fig. 12. Reduced stress at the beginning of stage III, logarithmically versus electron concentration $e/a = 1 + c(Z-1)$ for copper with gallium ($Z=3$) and germanium ($Z=4$) and various temperatures (after HAASEN and KING [1960]).

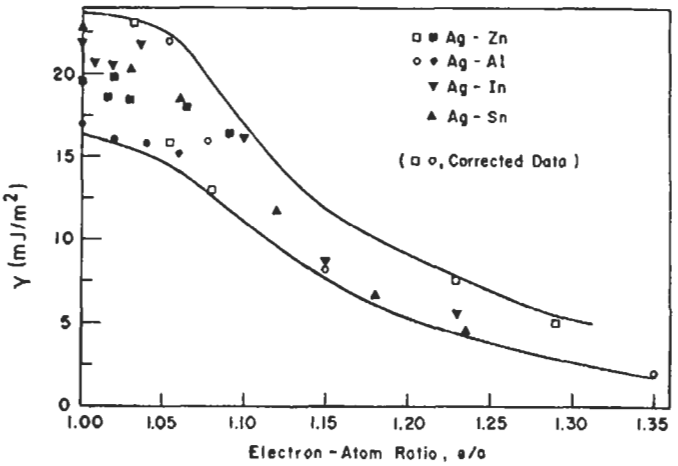

Fig. 13. Stacking-fault energy of copper alloys versus electron concentration, according to GALLAGHER [1970].

the stacking faults widen. Figure 13 shows γ estimated for Ag alloys by TEM on extended nodes (GALLAGHER [1968, 1970]) as a function of electron concentration. γ is a function of electron concentration only. While $\gamma(e/a)$ from τ_{III} appears to go through a maximum in Ag–Zn as well as in Cu alloys (ROGAUSCH [1967]) the node results indicate that γ does not change much with alloying, up to about $e/a = 1.05$ (cf. CARTER and RAY [1977]). In Ni–Co γ appears to decrease linearly towards the phase boundary (see PFAFF [1962]). Another theory to explain the increase of τ_{III} with concentration has been discussed by SEEGER [1958] for certain Al-base alloys with strong size factor δ. Here dislocations must straighten themselves out before cross-slip can occur. A second mechanism of dynamic recovery is observed above 600 K in Ni–50 at% Co crystals (PFAFF [1962]) and has been identified with dislocation climb. A theory of τ_{III}^{*} under these conditions is presented in § 2.8.

2.4.6. Deformation-twinning in fcc alloys

Owing to the crystallographic similarity between stacking faults and twins in the fcc lattice, which are both determined by an $a/6\langle 112\rangle\{111\}$ shear, the low-γ alloys can be expected to twin easily during deformation. This has been verified by X-rays and metallography for Cu–Ga, Cu–Ge at temperatures up to 500 K. The relation between twinning and $\gamma(e/a)$ in Cu–Ga–Ge has been studied by PEISSKER [1965b]. In α-brass and generally in alloys deformed at low temperature the characteristic drop in load at the nucleation of the first twin lamellae is often missing. Cu–Zn nevertheless twins on a very fine scale (VENABLES [1961, 1964], THORNTON and MITCHELL [1962]). In this case the propagation stress for the twin is thought to be higher than that for nucleation. Deformation-twinning in Ag–Au crystals has been studied by SUZUKI and BARRETT [1958]. Silver twins at 0°C while gold has to be deformed at 77 K to twin. Twinning occurs when a critical shear stress is reached; this is found to depend on composition. A

twinning-stress maximum at intermediate concentrations indicates a solute-hardening effect on twin propagation, in addition to the stress required to pull apart the partial dislocations bounding a stacking fault, which should vary with concentration linearly in $\gamma(c)$. For a review see MAHAJAN and WILLIAMS [1973], for experiments on Ag alloys see NARITA and TAKAMURA [1974], on Cu–Al VERGNOL and VILLAIN [1979], STARTSEV *et al.* [1979], TRANCHANT *et al.* [1988] and MORI and FUJITA [1980], on nickel alloys NARITA *et al.* [1978].

2.5. Solid-solution hardening in hcp crystals

Little has been known until recently about how a second element in solution influences plastic deformation in hcp crystals. Here, in addition to the features of the cubic close-packed structure (including stacking faults) the c/a axial ratio of hcp crystals is a variable with composition, and the contribution of non-basal slip may change with alloying. For $c/a > (c/a)_{ideal} = \sqrt{8/3}$ basal slip is favoured as in pure Zn and Cd, while for $c/a < \sqrt{8/3}$ slip often occurs also on prismatic planes or pyramidal planes. Mg is intermediate with a nearly ideal axial ratio. The slip direction in all cases is $\langle\bar{2}110\rangle$.

The axial ratio of Mg increases slightly on addition of Al atoms which are ~ 11 at% larger. The critical shear stress τ_0 increases strongly with concentration up to about 7 at% Al as does the work-hardening rate, contrary to the behaviour of non-hcp alloys (SCHMID and SELIGER [1932]). Since pure Mg recovers rapidly even at room temperature, the work-hardening results of Mg alloys are difficult to interpret, cf. LUKÁČ [1981]. The following discussion is therefore restricted to $\tau_0(c)$. The effect of alloying on the critical shear stress of Mg was investigated by LUKÁČ [1992]. Figure 14 shows results on

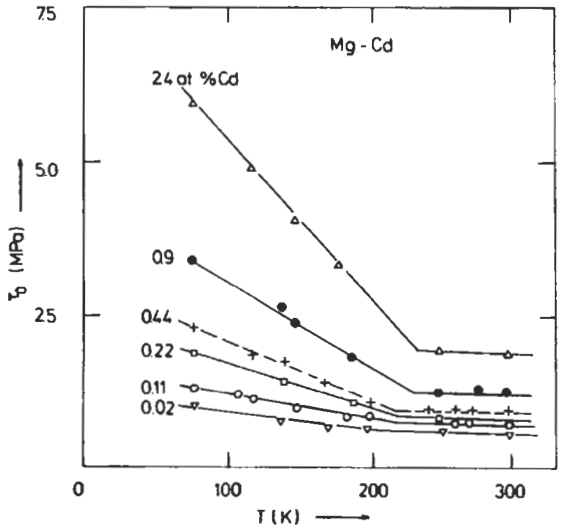

Fig. 14. Temperature variation of the critical resolved shear stress for Mg–Cd single crystals of various atomic concentrations (after LUKÁČ [1992]).

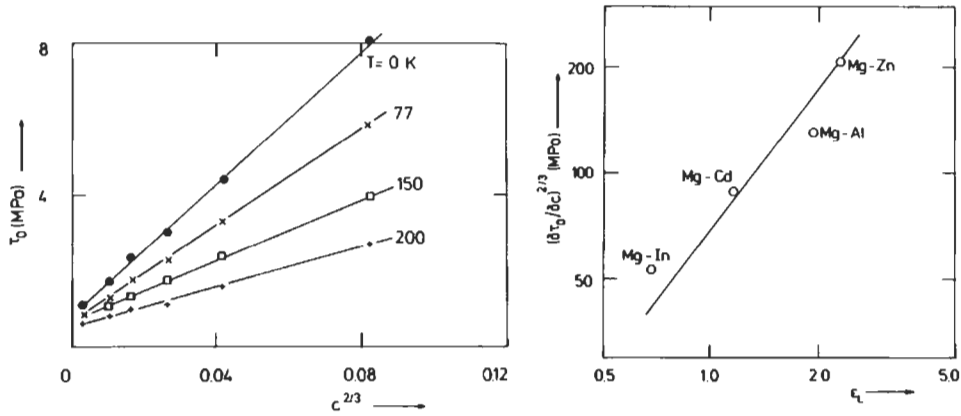

Fig. 15. (a) Concentration dependence of the critical resolved shear stress for Mg–Cd single crystals at different temperatures. (b) Specific strengthening $\partial\tau_0/\partial c^{2/3}$ at 0 K vs. Labusch parameter ε_L for various Mg-base systems (LUKÁČ [1992]).

various Mg–Cd single crystals oriented for basal slip and deformed at different temperatures. Figure 15a gives the concentration dependence of τ_0 according to Labusch's theory, eq. (2c), from which the proportionality to his combined parameter ε_L (eq. 2e) is derived for further Mg alloys (fig. 15b). In Mg–Cd η and δ have the same sign so that only $\varepsilon_L = (\delta^2 + \alpha^2\eta^2)^{1/2}$ gives a reasonable hardening, not Fleischer's combination $|\delta - \alpha\eta|$. Lithium markedly improves the ductility of Mg, as was observed in polycrystalline Mg–14.5 at% Li alloys by HAUSER *et al.* [1958]. Since the axial ratio decreases from 1.625 for pure Mg to 1.609 for this alloy it is likely that ductility is improved because additional prismatic slip can take place. Whereas pure Mg fails in a brittle manner below room temperature, it is ductile down to 78 K in the Mg–14.5 at% Li alloy.

It has been shown, however, that low-temperature prismatic slip becomes easier too when Mg is alloyed with Zn or Al, although c/a does not decrease or even increases in these systems (AKHTAR and TEGHTSOONIAN [1968]). The Peierls stress is supposed to control prismatic slip but not basal slip. Alloying always increases the flow stress for basal slip. A $c^{2/3}$ law fits these results better than $c^{1/2}$ at all temperatures from 1.5 K (NAVRATIL *et al.* [1983]) to the plateau range (LUKÁČ *et al.* [1979] and for Mg — as well as Zn — and Cd-based solid solutions.

GILMAN [1956] investigated the influence of temperature and strain rate on τ_0 for Zn–0.1 at% Cd single crystals. GILMAN finds prismatic slip to be less affected by the solute addition than basal slip. BOČEK *et al.* [1961] find for zinc single crystals with small additions of Cu, Pb, Cd etc. (of the order of 0.01 at%) that τ_0^2 is proportional to $A = \Sigma_i c_i \delta_i$, where c_i and δ_i are concentration and size factor, respectively, of the ith species of foreign atoms. According to a theory of TILLER [1958] the grown-in dislocation density N_0 should be proportional to A and thus $\tau_0 \propto \sqrt{N_0}$. Such an effect has been predicted by SEEGER [1957, 1958]. It plays no role, though, in Mg–Cd, Mg–Zn in the range investigated by AKHTAR and TEGHTSOONIAN [1968] and SCHARF *et al.* [1968]. It

is noteworthy in this connection that HAESSNER and SCHREIBER [1957] observed no change in the stress–strain curve of Al with additions of Ag ($\delta \approx 0$) up to 0.12 at%.

2.6. Solid-solution hardening in the bcc structure

Pure bcc metals deform on {110} or {112} planes in the ⟨111⟩ direction, depending on temperature and orientation. Below a critical temperature, screw dislocations are strongly bound to their Peierls valleys and the critical shear stress increases very strongly with decreasing temperature (ŠESTAK and SEEGER [1978], BRUNNER and DIEHL [1991]). Calculations show that the core of the screw is split on three {110} or {112} planes, so that two configurations exist of different "polarity" (VITEK [1985], SEEGER and WÜTHRICH [1976]), see fig. 16a. A constriction connects screw line elements of different polarity. A screw moves by the formation of kink pairs out of the $(1\bar{1}0)$ plane, fig. 16b, or together with polarity changes, fig. 16c. Thus cross-slip is natural quite at the beginning of bcc deformation and slip often follows the plane of maximum shear stress. Metals of bcc structure are hardened much more by interstitial than by substitutional solute atoms. Interstitial atoms distort the lattice tetragonally and thus interact strongly with edge *and screw* dislocations. Also the crystal tolerates larger shear strains (from these distortions) than dilatations (from the symmetrical substitutional defects). If the interstitial foreign atoms are in solution, like oxygen and nitrogen in the group V bcc metals, Nb and Ta, the hardening rate $d\tau_0/dc^{1/2}$ is well explained by a localized obstacle mechanism, see § 2.3.2 (FLEISCHER [1964]). The same applies to the hardening of the hcp metals, Ti, Zr and Hf, by interstitials such as O, N, C (TYSON [1968]). The group VI bcc metals Cr, Mo, W as well as α-iron have very low interstitial solubilities at room temperature (for

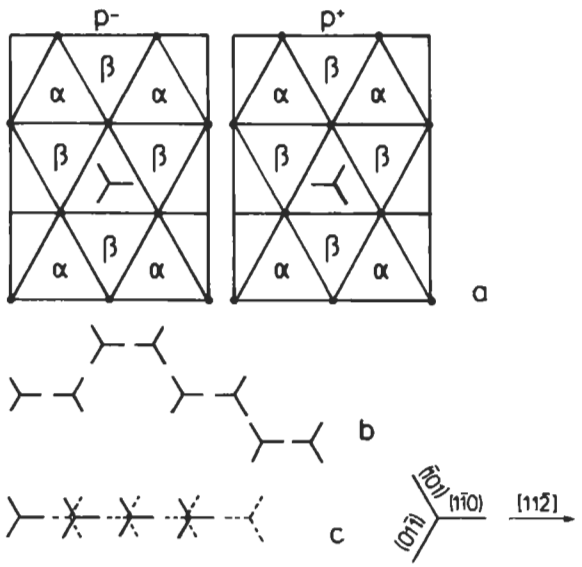

Fig. 16. Core-splitting of a screw dislocation in a bcc metal.

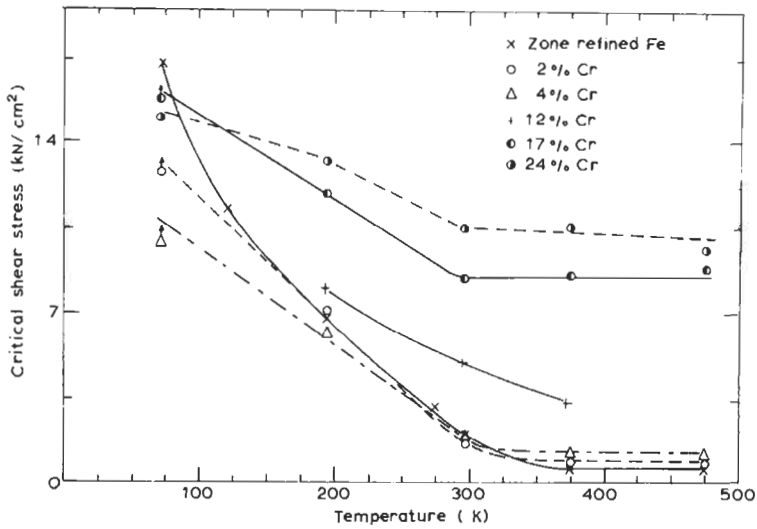

Fig. 17. Critical shear stress versus temperature for Fe–Cr single crystals (after HORNE *et al.* [1963]).

C in Fe, smaller than 10^{-7}). Small foreign atoms precipitation-harden these metals, as has been studied particularly in α-iron (see § 2.4.2 and ch. 17, § 5.5). Unfortunately interstitial and substitutional foreign atoms interact strongly, so their hardening effects are not additive (see ch. 17 and LÜTJERING and HORNBOGEN [1968], PINK *et al.* [1979]).

Fe–Cr single crystals have been studied by HORNE *et al.* [1963]. These authors observed a strong increase in the critical shear stress plateau (just above room temperature) with additions of chromium larger than 4 at% (fig. 17). The temperature dependence of τ_0 in the $\{112\}$, $\{110\}\langle 111\rangle$ systems below 300 K was actually reduced by the chromium addition. It is probable that chromium removed from solid solution some carbon which has been observed to influence the temperature-dependent part of the flow stress of α-iron + 0.003 at% C single crystals (MORDIKE and HAASEN [1962]). The size factor of Cr in Fe is very small. No stacking faults are expected in the alloy, although twins were observed to form. The almost quadratic increase of τ_0 (300 K) with concentration of chromium indicates friction due to cutting of favourable atom pairs by dislocations as discussed in § 2.3.2d. A miscibility gap has been reported below 550°C, $c < 12$ at%. The work-hardening rate of the crystals is quite small so that in the 24 at% Cr alloy at room temperature, necking started immediately after a pronounced yield point.

A solution-softening effect was also found at low temperatures in Ta-alloys, particularly in Ta–Re (fig. 18), by MITCHELL and RAFFO [1967]. It is doubtful whether in these alloys the scavenging effect of an interstitial-substitutional foreign atom interaction can be held responsible for this effect although scavenging can be shown to work in some alloys (GIBALA and MITCHELL [1973]). Three other explanations have been put forward: (1) anomalies in η(c) (HARRIS [1967]); (2) easier kink formation in the Peierls potential at substitutional atoms (ŠESTAK [1979], SUZUKI [1979b]; (3) formation of constrictions at misfitting solute atoms. A clear argument for model (3) comes from

References: p. 2066.

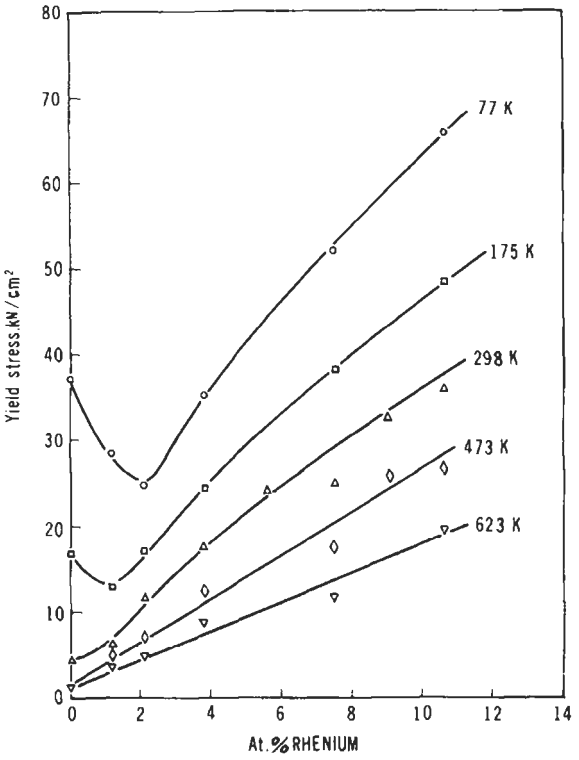

Fig. 18. Yield stress of tantalum–rhenium single crystals at various deformation temperatures (after MITCHELL and RAFFO [1967]).

recent experiments by BRUNNER and DIEHL [1993] on Fe single crystals with and without 330 ppm N. The pure crystals show three regimes in $\tau_0(T)$, fig. 19, which by comparison with theory can be uniquely attributed to kink pair formation on {110} planes (low temperatures), on {112} planes (high temperatures) and one where constrictions on {110} need to be formed as well (middle regime). It is only the latter that is facilitated by nitrogen and this leads to solution-softening. They interact more with solute atoms.

Assumption (2) has been disproved by SIETHOFF [1969] on Si–Ge alloys whose plasticity certainly is governed by the Peierls mechanism and which do not show solution-softening. Neither do the Nb alloys investigated by KOSTORZ [1968]. The plateau stresses of Nb–W, Nb–Ta and Nb–V measured in this work can be fully explained by eq. (1c), the localized elastic interaction mechanism, with $\varepsilon = |\eta' - 16\delta|$. Parelastic interaction alone would not explain the results on Nb–Ta ($\delta = 0$). The same conclusion is reached by MORDIKE *et al.* [1970] who investigated Ta–Os, Ta–Re, Ta–Mo and Ta–Nb. KOSTORZ [1968] finds a deviation from the $\tau_0 \sim c^{1/2}$ curve above 3% W in Nb, more like a linear concentration dependence (see also fig. 18). This is observed in many alloys now, see PINK and ARSENAULT [1979], and is explained by a theory of

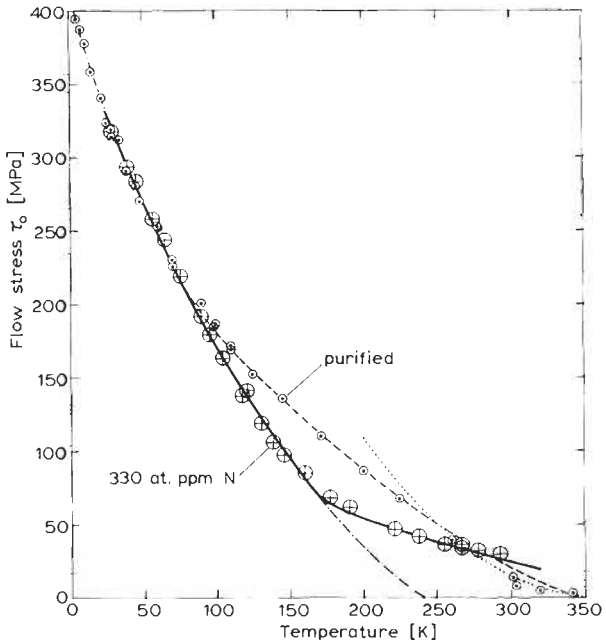

Fig. 19. Temperature dependence of the flow stress of α-iron single crystals, purified and with 330 ppm nitrogen. Lines give calculated curves in different regimes (BRUNNER and DIEHL [1993]).

Suzuki for kink motion along the Peierls valley overcoming solute atoms. (See also HATTENDORF and BÜCHNER [1992]). The interaction energy between kink and solute atom in iron substitutional solutions shows a linear superposition of size and modulus misfit parameters as was used by Fleischer, see § 2.3.2c) (BÜCHNER and WUNDERLICH [1993]).

LAWLEY and MADDIN [1962] studied single crystals of a solid solution of rhenium in molybdenium after polycrystalline studies had revealed the remarkable low-temperature ductility of these alloys. The solubility of Re in Mo is 42 at% at 2500°C. Deformation was by slip, except for the Mo–39 at% Re alloy which twinned extensively below 500 K. The critical shear stress on the $\{112\}\langle 111\rangle$ or $\{110\}\langle 111\rangle$ systems versus composition and temperature is shown in fig. 20. At room temperature and below, $\tau_0(c)$ rises with a positive curvature. The main temperature effect is present already in pure molybdenum. Above 30 at% Re, twinning becomes progressively easier (on $\{112\}\langle 111\rangle$) and is responsible for the fairly temperature-independent critical shear stress. A pronounced yield point (up to 8% drop in stress) was observed at the beginning of the tensile test and could be recovered by aging 2.5 h at 700°C, consistent with diffusion of C and N in Mo. The work-hardening rate is low (~ 70 kN/cm^2 average at 3% strain) and necking develops at 7% strain. The high ductility of the polycrystalline alloys with additions of Re is considered to be due both to the formation of a complex oxide (instead of MoO_2 in grain boundaries) and the promotion of twinning.

References: p. 2066.

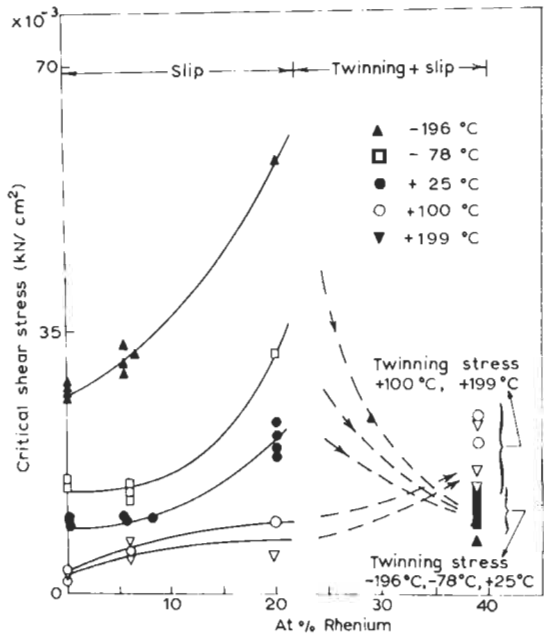

Fig. 20. Critical shear stress of Mo single crystals with additions of rhenium (after LAWLEY and MADDIN [1962]).

2.7. Hardening in the NaCl and diamond structures

From the classical work of Smekal and coworkers it is well known that divalent impurities, M^{++}, strongly harden NaCl crystals. In this case, a Na^+ vacancy has to be formed for every M^{++} introduced. Monovalent M^+ impurities have a much smaller effect on the yield stress. The dependence of the CRSS on temperature for doped *alkali halide* crystals and AgCl is shown schematically in fig. 21 (SKROTZKI and HAASEN [1981]). The upper curve is typical for, say, KCl with 70 ppm Sr^{++}, and the lower one for "pure" KCl, both in $\{110\}\langle 110\rangle$ slip. For $\{100\}\langle 011\rangle$ slip the curves look similar — only at 200 K higher temperatures. Four temperature regimes are visible. Regime I is controlled by the Peierls force and little influenced by doping. Regime II is that of Fleischer-hardening by the divalent foreign ion associated with a vacancy (dipole). It follows eqs. (1c) and (4c) and the maximum interaction force is of parelastic as well as electrostatic origin. The latter is particularly strong for edge dislocations on the $\{100\}$ slip planes. In regime III the CRSS depends linearly on doping and little on temperature as predicted by the Snoek interaction with the rotating dipoles (§ 2.3.1d). Finally, in regime IV dislocations are able to drag along the dipoles during their movement. Crystals with the *diamond cubic* structure like the semiconductors Si and Ge, but also those with partially ionic binding like the III–V and II–VI compounds become ductile only at elevated temperatures ($T > T_m/2$ for purely covalent bonding), while CdTe is ductile already at much lower

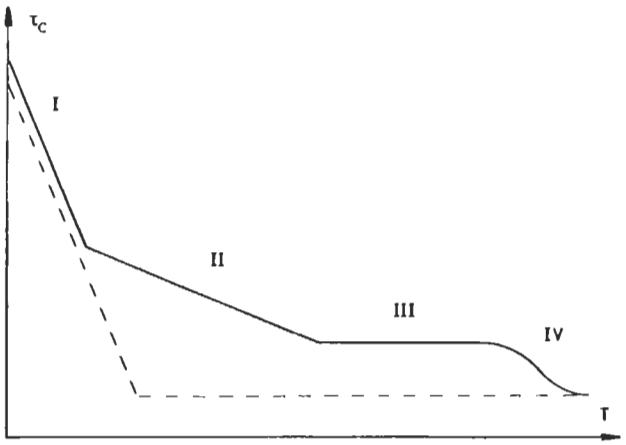

Fig. 21. Schematic regimes for the temperature dependence of CRSS of ionic crystals (dashed lines for pure, solid lines for doped crystals).

temperatures (ALEXANDER and HAASEN [1968], GUTMANAS and HAASEN [1981]). The plasticity of these semiconductors is clearly determined by the kinetics of formation and movement of kinks in the Peierls potential. This results in a viscous dislocation movement with a velocity $v \propto \tau_{\text{eff}}^{m} \cdot \exp(-Q/kT)$, $m \approx 1$ (ALEXANDER and HAASEN [1968]. For comparison, in Fe–6.5 at% Si, $m = 40$ (STEIN and LOW [1960])). A (stationary) creep rate can now be calculated from $\dot{\varepsilon} = Nbv$ as well as a (lower) yield point. The latter is decreased, the former strongly enhanced by $\geq 10^{19}$ cm^{-3} n-dopants (V-valent additions to the IV-valent matrix). This *Patel effect* is of electronic origin, not due to localized dislocation–solute interaction. It depends only on the position of the Fermi level for the particular temperature and doping relative to the occupation level of the neutral dislocation. If the two do not coincide, the dislocation becomes charged and accordingly unstable with respect to double-kink formation (HAASEN [1975]). This is an alloy-softening effect. On the other hand the charged dislocation interacts more strongly with charged point defects; this is the normal alloy-hardening (SIETHOFF [1969, 1970]).

2.8. Creep of solid solutions

A creep test under constant stress yields essentially the same information as the dynamic (prescribed strain-rate) experiment. The creep test is of particular value at higher temperatures. Only steady-state creep ($\dot{\varepsilon} = \text{const.}$) will be considered in the following and not transient creep (with decreasing rate). The reader is referred to reviews by SCHOECK [1980] and NIX and ILSCHNER [1979] and work by BIRD *et al.* [1969], WEERTMAN [1955, 1957] and ORLOVA and ČADEK [1986], SIETHOFF [1992a], OIKAWA and LANGDON [1969] for more detailed treatments. The results of Dorn and coworkers for the stationary creep rate $\dot{\varepsilon}(T, \tau)$ of metals and alloys are described by

$$\dot{\varepsilon} = f(\tau)\exp(-H_{\text{eff}}/kT)$$
$$f(\tau) = \begin{cases} C_1\tau^n & \text{for small } \tau \\ C_2 \sinh(B\tau) & \text{for large } \tau. \end{cases} \tag{6}$$

H_{eff} is determined by temperature change during creep and is found at high temperatures to approach H_d, the activation energy of diffusion of the material. For experimental reasons τ is chosen such that $\dot{\varepsilon}$ keeps within certain limits. H_{eff} is then found to be approximately proportional to temperature at low temperatures according to eq. (6). Relative to pure Al, the measured activation energies around 600 K are somewhat larger in Al–Cu alloys. WALTON *et al.* [1961] attribute this to a modification of the cross-slip process caused by solute atoms, see also SIETHOFF and AHLBORN [1991]. The region of strain-aging during creep will be discussed below (§ 2.8.2). In these class I alloys, creep is controlled by solute drag. Above 800 K, the Al–0.05 at% Cu alloy crystal showed distinct sub-grain formation. This is expected if the mechanism of high-temperature creep of metals and dilute alloys (called class II) is dislocation climb. The stationary creep of some Cu alloys does not fit in this scheme, however (SIETHOFF [1992b]).

2.8.1. Steady-state creep through dislocation climb *

WEERTMAN [1955] considers dislocations which have been stopped in their glide planes by various obstacles. The mean shear stress on each dislocation is zero, but the normal stress has an average value of σ_i. Under the influence of this normal stress the dislocations will start to climb over the obstacles. Some dislocations give off vacancies, some absorb them. The local concentration of vacancies near the dislocations is thus changed and an extra chemical potential introduced which tries to pull the dislocations back against σ_i. In equilibrium the rate of climb is determined by the flux of vacancies from one dislocation to another. The solution of this diffusion problem results in a creep rate

$$\dot{\varepsilon} = NAD/h\Lambda\left[\exp\left(\sigma_i b^3/kT\right) - 1\right], \tag{7}$$

where N is the density of dislocations per cm^2, Λ is the distance between obstacles touched by the dislocation, A the area of the slip plane the dislocation will cover after a successful climb, $D = D_0 \exp(-H_d/kT)$ is the self-diffusion coefficient of the material, and h is the height of the obstacle the dislocation has to climb over. Depending on the ratio $\sigma_i b^3/kT$ and on the way N, h (and A, Λ) change with stress, the experimental relation (6) can be interpreted now with the help of eq. (7). In particular, for $\sigma_i \ll kT/b^3$, eq. (7) becomes

$$\dot{\varepsilon} = \left(NAb^3/h\Lambda kT\right)\sigma_i D_0 \exp\left(-H_d/kT\right), \tag{8}$$

which is in agreement with most experimental data on creep rates of pure metals if the pre-exponential factor depends on stress as τ^n, $n \approx 4$–5 (see table 1). Concerning

* See also ch. 22, § 3.

Table 1
Stress-dependence of creep rate [a].

(Polycrystalline) Material	Temperature (°C)	Stress range (kN/cm²)	Stress exponent n of creep rate
Al	371–593	0.06–2	4.4
Al–0.94 at% Mg	260–482	0.2–2	3.0
Al–1.9 at% M8	260–482	0.2–2	3.0
Al–5.1 at% Mg	260–482	0.2–2	3.0
Al	480	0.03–0.3	3.9
Al–1.1 at% Mg	480	0.4–0.7	3.6
Al–2.1 at% Mg	480	0.2–0.7	3.4
Al–3.1 at% Mg	258–580	0.03–4	3.2
Al (coarse grain)	300	0.45–0.7	4.5
Al–2 at% Mg	250–380	0.5–3	4.0

[a] According to WEERTMAN [1955].

temperature dependence, SEEGER [1957, 1958] has discussed a possible contribution of H_j, the energy of jog-formation (and constriction of the stacking-fault), towards the measured activation energy H_{eff}, which would become noticeable when $H_j \approx H_d$ (particularly in alloys). Empirically $\dot{\varepsilon}$ is also found to be proportional to $(\gamma/Gb)^3$ (MOHAMED and LANGDON [1974], SIETHOFF [1992a]). For pure metals n can be explained by assuming $N \propto \tau^2/\mu^2$, i.e., the number of dislocations being determined by long-range elastic interaction. Further, $h \propto \mu b/\tau$ if the obstacle is a sessile dislocation and $\sigma_i \propto \tau$ as the mean internal stress in the crystal. An essential aspect of steady-state creep is the large fraction of the dislocations located in subgrain boundaries. The subgrain size is inversely proportional to stress. For class II alloys again $n \approx 4$–5. For high stresses the exponent $\sigma_i b^3/kT$ in eq. (7) is found experimentally to be independent of temperature, compare eq. (6), which is difficult to reconcile with theory (see also TAKEUCHI and ARGON [1976a]). An application of (the inverted) eq. (8) in a dynamic experiment gives the stress ($\tau^{\bullet}_{III}$) above which climb contributes noticeably to the prescribed strain rate $\dot{\varepsilon}$:

$$\tau^{\bullet}_{III} \propto \dot{\varepsilon}^{1/n} \exp(H_d/nkT). \tag{9}$$

This equation should be compared with high-temperature measurements on the dynamic recovery of low-γ alloys (see § 2.4.5).

2.8.2. Creep limited by dislocation drag (class I) and the Portevin–Le Chatelier effect

Besides climb there is another mechanism to explain high-temperature creep of solid solutions at small stresses, by considering the glide movement of dislocations which drag solute "atmospheres" with them in a viscous manner (COTTRELL [1953], BRION *et al.*

[1971], TAKEUCHI and ARGON [1976b] and WEERTMAN [1977]). If by one of the pinning mechanisms considered in § 2.3.1 a dislocation creates a dragging force F on a solute atom, the stationary microcreep rate is

$$\dot{\varepsilon} = Nbv, \text{ where } v = \left(D_s/kT\right)F \tag{10}$$

and D_s is the diffusion coefficient of the solute atoms. The dislocation attains a velocity v in dynamic equilibrium between the applied stress τ and the dragging force F, which is proportional to τ. $\dot{\varepsilon}$ is thus proportional to stress for constant N, and proportional to τ^3 after dislocation multiplication and interaction has increased $N \propto \tau^2$ as above (WEERTMAN [1957]). $n = 3$ as found for class I alloys (see table 1) could also been interpreted by eq. (8) if h is independent of stress, i.e., if the obstacles are provided by heterogeneities of the alloy. On increasing the stress the dislocation reaches a critical velocity v_c just too high for solute diffusion and breaks loose from its atmosphere (OIKAWA and LANGDON [1985]). Cottrell has pointed out that the velocity range near v_c is unstable since, by slightly accelerating, the dislocation will free itself completely and by slowing down somewhat it will be caught by the atmosphere. (The material strain-ages during creep.) This phenomenon will give rise to a serrated stress–strain curve (jerky flow, *Portevin–Le Chatelier* (PL) *effect*) or a sharp bend in the creep curve at a certain strain rate and temperature. A detailed discussion of the mechanism of the PL effect has been given recently by SCHWARZ [1982] in connection with the strain-rate sensitivity of the flow stress, see also KUBIN *et al.* [1988], HÄHNER [1992], VAN DEN BEUKEL and KOCKS [1982], KOLK and SCHWINK [1992], KUBIN and ESTRIN [1992], LING and MCCORMICK [1990], SCHLIPF [1992], ESTRIN *et al.* [1991]. This effect coincides with the high-temperature end of plateau-hardening if the plateau is due to the friction with single solute atoms (cf. § 2.4.1, fig. 12). In the calculation of the critical condition for the PL effect one has to consider enhancement of solute diffusion by vacancies produced during creep resulting in $\dot{\varepsilon} \approx \bar{c}_v \exp(-E_m/kT)$ at a critical strain. Here c_v is the excess vacancy concentration and E_m the activation energy of vacancy migration (MCCORMICK [1972] and VAN DEN BEUKEL [1980]).

2.8.3. Steady-state creep controlled by cross-slip

In semiconductors with diamond structure steady-state creep does not fit the climb model of sect. 2.8.1. Careful analysis by SIETHOFF [1992c] gives good agreement for Ge and GaAs of the observed activation energy of creep with the one calculated (from SFE γ) by ESCAIG's [1968] theory of cross-slip, see sect. 2.4.5. At the high deformation temperature and small values of $(\gamma/\mu b)$ in these materials, dynamical recovery of screws evidently is slower than that of edges. With strong doping (10^{19} to $10^{20}/\text{cm}^3$ corresponding to $c = 2 \cdot 10^{-4}$ to $2 \cdot 10^{-3}$) dragging of solute atmospheres and break-away from them is clearly observed in Si and Ge, as discussed for fcc material in sect. 2.8.2 (BRION *et al.* [1971]). The solute/dislocation interaction energy in semiconductors is mostly of electrostatic origin, therefore rather large compared to the parelastic one in fcc metals.

2.9. Fatigue of solid solutions *

The low-amplitude fatigue-strength of fcc metals does not increase with solute addition in proportion to their unidirectional fracture strength. While in pure metals the long-life "fatigue limit", τ_{10^6}, is about equal to the stress τ_{III} where thermally activated cross-slip starts (HAASEN [1965]), it becomes much smaller than τ_{III} in solid solutions (RUDOLPH *et al.* [1965]). τ_{10^6} for ordered Cu_3Au is only 20% higher than for disordered single crystals, despite an enormous increase in τ_{III}. NEUMANN [1967] has explained this disappointing behaviour in a model which relates fatigue-crack nucleation and propagation to the *coarseness of slip*. Slip is indeed coarser and more planar in solid solutions (and alloys with short-range order or coherent precipitates) than in pure metals, as is discussed in § 2.2.1 for unidirectional deformation.

During fatigue, cracks often nucleate at *persistent slip bands* (PSBs) named so because their coarse surface features cannot be removed by intermediate polishing (MUGHRABI [1979]). Finally PSBs may turn into "extrusions" of material as an extreme case of surface topography developed during fatigue. PSBs are soft lamellae in the cyclically hardened matrix in which voluminous arrays of dislocation multipoles are replaced by rather sharp dislocation walls, c.f. INNI *et al.* [1990]. In between those walls, to-and-fro glide of dislocations produces an easy steady-state deformation indicated by a plateau in the cyclic stress–strain curve (i.e., the asymptotic stress versus plastic strain-amplitude of cyclic deformation). Cross-slip evidently is instrumental in the transformation of the dislocation arrangements into those of PSBs. This has been treated quantitatively for Cu–4%Ti solid solutions by SINNING and HAASEN [1981]. In alloys of low SFE therefore no PSBs form but, instead, slip is concentrated and planar; this by itself produces a rather sharp surface topography at slip steps on which cracks can nucleate (as on PSBs).

During the plateau of the cyclic stress–strain curve PSBs spread over the whole specimen. This can occur in single as well as in polycrystals where stress concentrations at grain boundaries sometimes help in the transformation of the dislocation microstructure (SINNING and HAASEN [1981]). The effect of precipitation on fatigue properties again depends on how this changes slip localization. This in turn seems to be favoured by a large size misfit (SINNING [1982]).

3. *Precipitation-hardening*

The formation of a precipitate greatly strengthens an alloy. The increase in yield stress depends principally on the strength, structure, spacing, size, shape and distribution of the precipitate particles as well as on the degree of misfit or coherency with the matrix and on their relative orientation. To understand precipitation-hardening one must study in detail the way in which dislocations interact with precipitate particles. In addition to mechanical testing (mainly of *single* crystals) the problem is investigated by the classical method of small-angle X-ray diffraction (ch. 12, § 5.1), by magnetic measurements, and

* For details see ch. 27.

more recently by transmission electron microscopy and by field-ion microscopy. Very rarely, however, have different methods been compared in their application to one and the same specimen. This chapter is restricted to a review of some fundamental investigations of the dislocation-precipitate interaction in relative simple alloys as described in papers by REPPICH [1992], ARDELL *et al.* [1976, 1985], MELANDER and PERSSON [1978], HAASEN and LABUSCH [1979], GRÖHLICH *et al.* [1982], NEMBACH and NEITE [1985], and by GLEITER and HORNBOGEN [1968] rather than to discuss hardness versus aging time and X-ray diffraction results on alloys of technical importance. These studies are well documented in ch. 25 and in the reports of, e.g., BROWN and HAM [1971], BROWN [1979], KOCKS *et al.* [1975], GEROLD [1979] and KELLY and NICHOLSON [1963].

3.1. Interactions between dislocations and precipitate particles

A dislocation moving on its slip plane containing a distribution of precipitate particles may cut through the particles or avoid them by moving out of its slip plane or by bending between the particles, leaving a dislocation ring around each precipitate. For all of these processes energy must be expended. Which takes place, however, depends on the applied stress and the nature of the precipitate.

For a dislocation to *shear a particle*, sufficient energy must be supplied to break favourable bonds within the particle, thus increasing its "surface" area. The energy Γ (J/m^2) of the interface produced when a zone is sheared by one atomic distance is estimated from the heat of reversion for Al–Ag by KELLY and FINE [1957] to be about 0.1 J/m^2. In this case the precipitates are completely coherent with the matrix, there is little size misfit between Ag and Al. In the other extreme, if the particles are completely incoherent and of a quite different crystal structure, Γ will be of the order of the energy of a large-angle grain boundary, i.e., ≈ 1 J/m^2. The stress to force an essentially straight dislocation through a distribution of precipitate particles ("zones") of distance Λ, and radius r is:

$$\tau_c = (\Gamma/b)(r/\Lambda). \tag{11}$$

This is rather similar to eq. (3) for the short-range order (cluster) friction mechanism (§ 2.3.2d) except for the factor $r/\Lambda = f^{1/2}$ where f = volume fraction of the precipitate (KELLY [1958]). In this case the unfavourable bonds formed by deformation are concentrated in the interface of (spherical) zones instead of being statistically distributed over the slip plane. If the composition of the zones (concentration c' of solute, assumed $c' \approx 1$) is independent of that of the alloy c, then Γ = constant and $f = c - c''$, where $c'' \ll 1$ is the concentration of solute in solution in equilibrium with the zones. Thus $\tau_c \approx (c - c'')^{1/2}$ for zone hardening whereas $\tau_c \approx \Gamma \sim c^2$ for cluster (favourable atom pair) hardening. This has been verified approximately for Al–Zn (DASH and FINE [1961]) (figs. 22 and 23). Equation (11) is a special case of energy-storing obstacles in the concentrated, Labusch limit (see § 2.3.2). The corresponding equation in the Fleischer limit is obtained by putting $f_{max} = \Gamma r$ into eq. (1c) for particles of volume fraction $f = cr^2/b^2$, where r is the particle radius, yielding:

$$\tau_c b = f_{max}^{3/2} f^{1/2} / (2E_L)^{1/2} r = \Gamma^{3/2} (rf)^{1/2} / (2E_L)^{1/2}. \tag{1d}$$

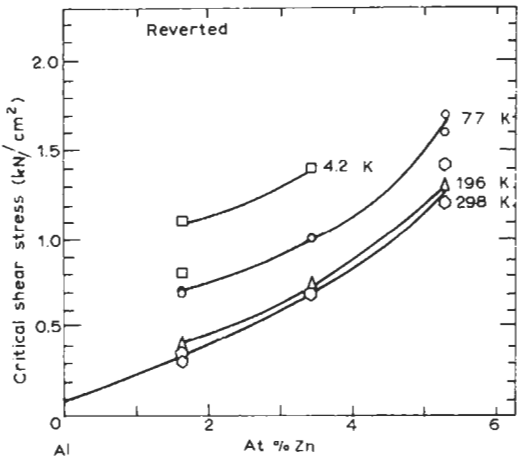

Fig. 22. Critical shear stresses of Al single crystals with various additions of zinc in solid solution at different temperatures (after DASH and FINE [1961]).

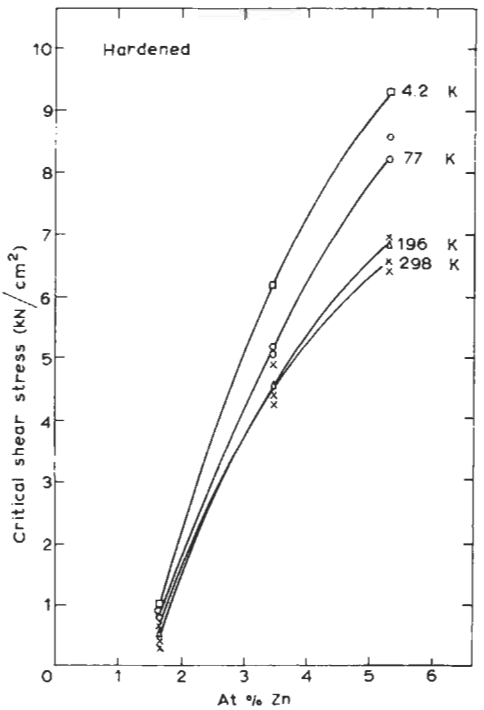

Fig. 23. As fig. 22, but for zone-hardened condition (quenched from 460°C and aged 24 h at 25°C).

References: p. 2066.

Another type of energy-storing obstacle is an ordered-phase particle which becomes disordered by the passage of a dislocation. If Γ_{APB} is the antiphase boundary energy (per m^2) then $f_{max} = \Gamma_{APB} \cdot r$ and eq. (1d) applies again.

The third case of an energy-storing interaction is that of a difference in stacking-fault energy $\Delta\gamma$ between particle and matrix (HIRSCH and KELLY [1965]). Here one calculates $f_{max} \approx 2r \cdot \Delta\gamma$. In addition to this chemical hardening effect there may be a (short-range) elastic one if the zones are surrounded by local coherency strains or have an elastic modulus different from that of the matrix, as in Al–Cu ($\delta = -12\%$), factors to be overcome by a cutting dislocation. Temperature may assist in the shearing process if the dimensions of the zones are sufficiently small. In the parelastic case $f_{max} = \mu b \delta \cdot r$ and depending on the Labusch or Fleischer limits one obtains $\tau_c \sim f^{2/3} r^{1/3}$ or $\tau_c \sim f^{1/2} r^{1/2}$, respectively. In the dielastic case it is more complicated to calculate f_{max} (see WENDT and WAGNER [1982]), but it looks as if the modulus difference between particle and matrix does not determine the flow stress in any of the investigated alloys.

A dislocation can *avoid a particle* by climbing (§ 2.8) or cross-slipping (§ 2.4.5) around it. The minimum stress for this decreases strongly with increasing temperature; the slip lines are wavy as will be seen below. For a large enough particle spacing the dislocation may pass between two particles (fig. 5c) at an *Orowan* stress

$$\tau_m = \alpha \mu b / \Lambda, \tag{12}$$

where α is a constant of order of magnitude one (cf. ch. 20). This leaves dislocation rings around the particles which work-harden the crystal. τ_m depends on temperature through μ only. Comparing eqs. (11) and (12) one finds the largest size of particles to be sheared to be

$$r_{max} = \alpha b (\mu b / \Gamma), \tag{13}$$

where Γ is any of the above surface energies, or $\mu b |\delta|$ in the parelastic case. For a "critical dispersion", r_{max} is ~ 25 Å for $\Gamma = 1$ J/m^2, ~ 250 Å for $\Gamma = 0.1$ J/m^2.

A more detailed calculation of the Orowan stress, eq. (12) also has been made by ASHBY [1966], considering the orientation-dependence of the line tension, the dissociation into partials, and the interaction between the two dislocation segments on both sides of one particle (fig. 5c). If the particle is incoherent with the matrix, localized plastic flow may be nucleated at the particle-matrix interface by the approaching dislocation. The stress necessary for this is of the order of one hundredth of the shear modulus of the matrix and decreases with increasing particle size (ASHBY [1968]). Thus the Orowan process, eq. (12) and fig. 5c, truly arises only with large coherent particles.

A special problem arises in the interaction of dislocations with particles of a certain degree of internal order but with $\delta = 0$ (γ'-Ni_3Al precipitated from Ni–Cr,Al, GLEITER and HORNBOGEN [1965]). In this case dislocations move in pairs as superdislocations (§ 4.1) because single dislocations are partials of the ordered structure, see fig. 25. The equilibrium shapes of these dislocations and the flow stress τ_p in these alloys have been calculated by NEMBACH and NEITE [1985]. At the point of breakthrough of the first dislocation D_1, strongly bowing between γ' particles at spacing L_1, the straight second

dislocation D_2 pushes it by the stress τ_R (while it is pulled by D_1) touching its obstacles at spacing L_2. So the force balance reads

$$\begin{aligned} \tau_p b L_1 + \tau_r b L_1 - \Gamma_{APB}\, d_1 &= 0 \\ \tau_p b L_2 + \tau_r b L_2 + \Gamma_{APB}\, d_2 &= 0 \end{aligned} \tag{14a}$$

where the length d_i of D_2 lies in γ' ($d_1 \approx 2r$). Combining these equations with the Friedel length L_1 (eq. 1a) and introducing the vol. fraction $f = d_2/L_2$, Nembach and Neite arrive at

$$\tau_p = \frac{\Gamma_{APB}}{2b}\left[A_1\left(\Gamma_{APB}\frac{rf}{E_L}\right)^{1/2} - A_2 f\right]. \tag{14b}$$

The A_i are numbers of order one. The result is in good agreement with their measurements on PE-16 single crystals, supported by TEM data on r and f. A dynamic theory of hardening by ordered particles was published by COPLEY and KEAR [1967].

SCHWARZ and LABUSCH [1978] have computer-simulated the movement of a dislocation in a dense array of energy-storing (or elastically interacting) obstacles, see also FUCHS and RÖNNPAGEL [1993]. HAASEN and LABUSCH [1979] have compared the theory with experiments of ARDELL *et al.* [1976] on Ni–Ni_3Al. New experiments on this alloy have been compared with the Labusch–Schwarz theory by GRÖHLICH *et al.* [1982]. They make use of the superposition of order and parelastic hardening calculated by MELANDER and PERSSON [1978].

3.2. Direct observation of precipitate-dislocation interactions

The change in slip-line pattern of Al alloys due to the presence of various precipitates has often been studied (e.g., THOMAS *et al.* [1957], GREETHAM and HONEYCOMBE [1961]). In Al–2 at% Cu containing GP zones, slip lines are found to be wavy, indicating that dislocations cross-slip. In the presence of GP II and θ' precipitates, well defined slip bands do not form and slip lines appear very "indistinct". Overaged alloys with coarse θ precipitates show very fine multiple slip. At high resolution slip lines appear to bend around θ precipitate particles at room temperature, whereas at heavy deformations partially coherent θ' plates are distorted by slip bands passing through them. Electron transmission observations on thin films of deformed precipitation-hardened Al alloys confirm that some dislocations do in fact pass through partially coherent precipitates, while others are held up, forming cusps. Large non-coherent θ precipitates are free of dislocations (NICHOLSON *et al.* [1960]). SWANN [1963] finds that dislocation walls connect large precipitates in deformed Al–2.3 at% Cu alloys. JAN [1955] and KELLY and SATO [1961] showed by small-angle scattering of X-rays that spherical precipitates in Al–Ag and Al–Zn alloys became elliptical by plastic deformation, as would be expected if slip were homogeneous within a volume of (40 Å)^3. The same conclusion was reached by LIVINGSTON and BECKER [1958] for precipitation-hardened Cu–2 at% Co alloys from the measurement of magnetic anisotropy. This is definitely not in agreement with the heterogeneous distribution of slip indicated by slip-line observations. It is possible that

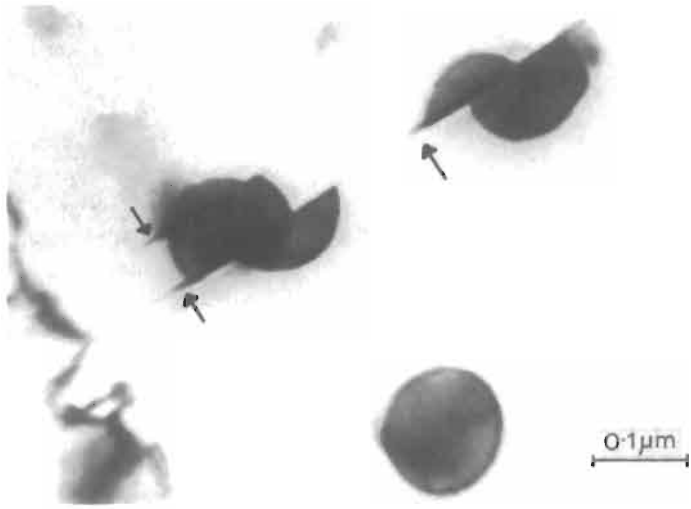

Fig. 24. Sheared γ'-zones in Ni–19% Cr–6% Al aged 540 h at 750°C and deformed 2% (from GLEITER and HORNBOGEN [1965]).

dislocations cross-slip in front of the particle to various parallel slip planes. This cross-slip may lead to the dislocation circumventing the particle. In agreement with this it was found that the precipitates were deformed somewhat less than the specimen as a whole.

GLEITER [1967b] has computed the formation of prismatic dislocation loops by cross-slip near large coherent particles. He also observed (fig. 24) that large γ'-zones in Ni–Cr–Al are cut by dislocations on a few slip planes only, in agreement with slip-line

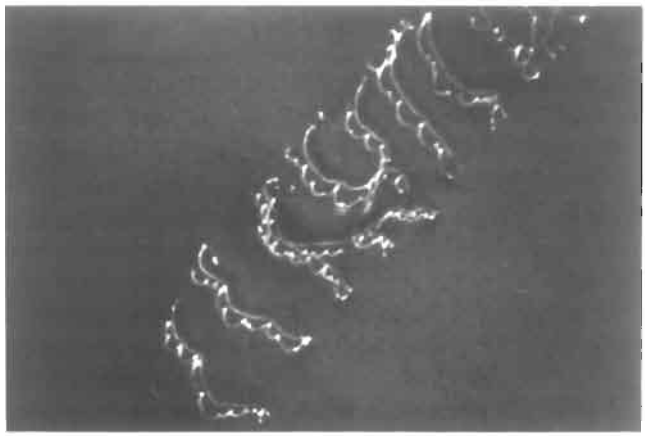

Fig. 25. Weak-beam electron micrograph of single crystal Nimonic PE 16 foil ($Ni_{42}Fe_{33}Cr_{18}Mo_2Al_1Ti_2$). Dispersion of γ'-particles with $r = 8$ nm (invisible), $f = 0.09$, glide plane (111), tensile axis [$\bar{1}$23] (NEMBACH and NEITE [1985]). 45000×.

observations (GLEITER and HORNBOGEN [1965]). Figure 25 shows the interaction of superdislocations with peak-aged γ' (Ni_3Al, Ti) precipitates in the alloy PE 16 (under load) (NEMBACH and NEITE [1985]). Notice that the second dislocation of each pair is much straighter than the first.

3.3. Mechanical properties of precipitation-hardened Al alloys

As an alloy ages, a coarser and more stable precipitate is formed. The character of the stress–strain curve is then changed completely. After 2 h ageing at 190°C the precipitates in Al–1.6 at% Cu crystals are predominantly GP II; after 40 h some θ' has formed and after 300 h θ' only is present (ch. 19, § 5.1). For GP II alloys the critical shear stress is large and the rate of work-hardening low, but after 300 h ageing just the opposite is observed. The variations in τ_0 and $d\tau/d\varepsilon$ (at $\varepsilon = 2\%$) are shown in figs. 26 and 27, respectively, according to Kelly and Bonar, cf. KELLY and NICHOLSON [1963]. Between 30 and 100 h the mode of deformation changes from single slip, during which

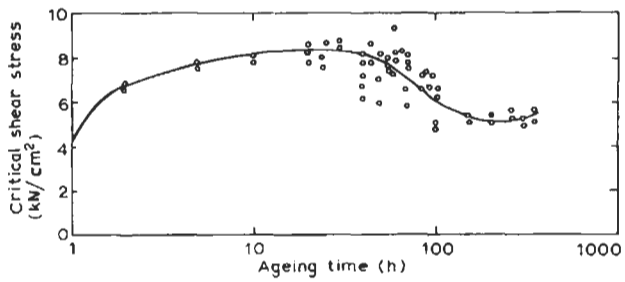

Fig. 26. Critical shear stress of Al–1.6 at% Cu crystals at room temperature after solution treatment, water quenching, and ageing at 190°C for various times. $\dot{\varepsilon} = 3 \times 10^{-4}\ s^{-1}$ (after KELLY and BONAR, cf. KELLY and NICHOLSON [1963]).

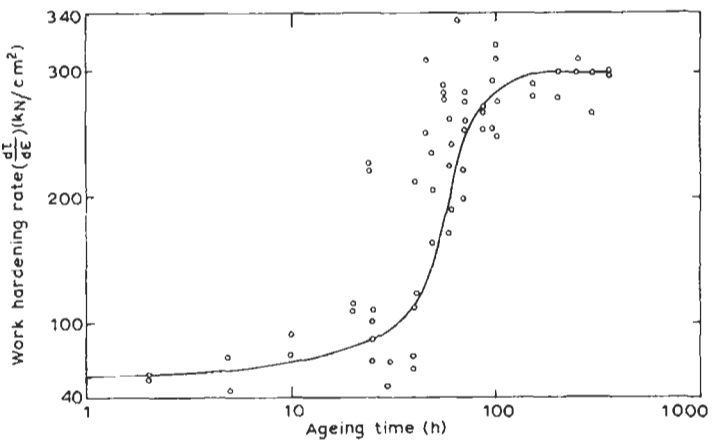

Fig. 27. Work-hardening rate (at 2% strain) of a crystal as in fig. 26 versus ageing time at 190°C.

References: p. 2066.

the specimen axis rotates towards the slip direction, to multislip showing extensive asterism without change in specimen axis orientation and external specimen shape.

3.3.1. Overaged alloys

After 300 h the minimum particle spacing in Al–1.6 at% Cu is about 2400 Å and appears to be controlling the initial flow stress. A critical shear stress of ≈ 3 kN/cm^2 calculated from eq. (12) is of the same order of magnitude as the observed values (fig. 26). Similar conclusions were reached by DEW-HUGHES and ROBERTSON [1960] for Al–1.3 to 2.1 at% Cu overaged to precipitate the θ phase in various dispersions. Figure 28 shows a plot of the Orowan relation [eq. (12)] which is quite satisfactory for the 1.7 at% alloy except for a group of specimens which contained very coarse plate-shaped particles. For these, Orowan's particle distance may vary considerably with orientation. An uncertainty in the choice of Λ also arises for semi-coherent particles where coherency strain might produce a radius of influence larger than the particle radius. The high work-hardening rate of overaged alloys, about $\mu/10$, apparently is a consequence of multiple slip enforced by non-deforming particles and of the high dislocation density due to loops around particles. The work-hardening of overaged alloys depends strongly on deformation temperature (BYRNE *et al.* [1961]). This would not be expected from the theory by FISHER *et al.* [1953] who explained work-hardening in terms of the back-stress of planar bundles of loops around particles. ASHBY [1968] analyzes the dislocation density as a function of strain in deformed dispersion-hardened alloys and concludes that the flow stress is best described by a "forest intersection" model (ch. 21, § 7.3). According to this, diffuse dislocation walls connecting particles form by reaction between prismatic

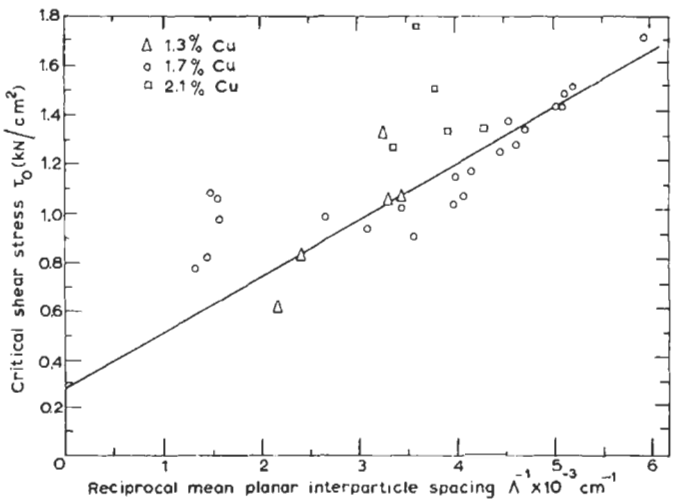

Fig. 28. Critical shear stress τ_0 of Al–Cu single crystals of various compositions aged to precipitate θ particles of different mean planar spacing Λ (data from DEW-HUGHES and ROBERTSON [1960]). For the solid solution $\tau_0 = 0.3$ kN/cm^2.

loops around particles in several slip systems. The stress necessary for glide dislocations to cut these walls with the help of thermal fluctuations is calculated to be

$$\tau(\varepsilon) \approx \mu\left(\frac{fb}{r}\cdot\varepsilon\right)^{1/2}\alpha(T,\dot{\varepsilon}), \tag{15}$$

where the factor α decreases with temperature T and increases with strain rate $\dot{\varepsilon}$ similarly to the thermally activated flow-stress contribution τ_s for pure metals (SEEGER [1957]). The theory is in good agreement with experiments described by EBELING and ASHBY [1966], DEW-HUGHES and ROBERTSON [1960], JONES and KELLY [1968], and ASHBY [1964].

3.3.2. Zone-hardened alloys

In zone-hardened alloys the precipitates are too closely spaced for dislocations to pass between them at the observed critical shear stresses [cf. eq. (13)]. These particles must be sheared during deformation in agreement with direct observations of the dislocation-precipitate interaction (§ 3.2). For aging times up to the peak value the yield stress then is determined by the work done in forcing the dislocations through the precipitates, and the rate of work-hardening is similar to that of the matrix material ($\sim\mu/250$ for Al alloys). The parelastic interaction cannot in general explain the critical shear stress of zone-hardened alloys. This is because no coherency strains are observed around silver-rich zones in Al–Ag and yet there is appreciable zone-hardening. The stacking-fault hardening mechanism described above seems to work here. In Al–Li alloys ordered particles offer resistance to shear by dislocations, cf. § 3.1. In the case of Al–Cu the interfacial strengthening mechanism is estimated to dominate hardening. For Al–1.7 at% Cu, the critical shear stress in the reverted and the GP I condition is strongly temperature-dependent below 200 K contrary to the behaviour of either pure Al or the alloys with larger precipitates (BYRNE *et al.* [1961]). In the reverted state, small Cu clusters are expected to be present. The answer to the question which kind of precipitate provides strongest hardening thus depends on temperature. In Al–Ag τ_0 is very little temperature-dependent, as would be expected for spherical zones larger than a few Ångström units. There is an anomaly in the CRSS of Al–1% Ag single crystals as a function of particle radius r or ageing time (RABE and HAASEN [1988]): τ_0 increases non-monotonically with $\sqrt{r}$, perhaps due to the presence of two sorts (ε and η) of precipitates already in the as-quenched crystals. In the case of Al–Cu, on the other hand, the mono-atomic platelets of GP I can be cut with the help of thermal fluctuations. Much about the atomic mechanism of zone-hardening can thus be learned from a "*thermal activation analysis*" of the flow stress of alloy single crystals (BYRNE *et al.* [1961], KELLY and NICHOLSON [1963]).

3.4. Precipitation-hardening in other alloy systems

3.4.1. Copper–cobalt

In addition to the aluminium alloys, aged Cu–1 to 3 at% Co alloys have been the subject of some fundamental mechanical studies, which are of particular interest to us

here. In this system it is possible to determine independently the volume fraction f of precipitate and the size and shape of the precipitated particles, e.g., from the magnetic properties (LIVINGSTON and BECKER [1958], LIVINGSTON [1959]). It was found that during the first 1000 min at 600°C the yield stress at 300 K increased at apparently constant f, while the precipitate was coarsening, see eq. (1d). A broad maximum of the yield stress was reached at a particle radius of about 70 Å or a particle spacing of 500–1000 Å. This maximum stress is approximately proportional to $f^{1/2} = r/\Lambda$ as would be expected from eq. (11) describing the "chemical" shear strength of the particles. The constant of proportionality, Γ, is about 0.12 J/m^2. This can be interpreted as being caused by the parelastic mechanism (GEROLD and HABERKORN [1966]). The movement of a flexible dislocation over a statistical array of misfitting particles has recently been computer-simulated by FUCHS and RÖNNPAGEL [1992]. The results are in quantitative agreement with eq. (1d) for the case of coherency stress interaction with a complete dislocation. FUSENIG and NEMBACH [1993] have discovered inertial dislocation effects in Cu(1–2)% Co aged to particle sizes of $r \approx 3$ nm. The CRSS rises with increasing T below 200 K similarly to Cu–Mn solid solutions, fig. 10d, but only if no further solutes are present besides the Co particles. The phonon damping of the dislocations is estimated according to eq. (4b) as $\gamma \approx 0.1$ to 0.5, low enough for dislocations to intertially overcome the Co particles at a 20% lower stress than for $\gamma > 1$, at higher T. Magnetic anisotropy measurements do in fact show the particles to be sheared during deformation (§ 3.2). The decrease of strength beyond the hardness peak can probably be explained by Orowan's mechanism although the observed particle spacing is somewhat too small for dislocations to pass between at the measured flow stresses. LIVINGSTON [1959] ascribes the decrease in strength above a critical particle diameter of 140 Å to a loss of complete coherency of the precipitate and the formation of interface dislocations. At a precipitate-matrix mismatch of $\delta = 1.6\%$ the interface dislocations should have a spacing about equal to the critical particle diameter. Electron transmission observations of *deformed* Cu–Co foils indicate, however, that particles maintain full coherency to several times the diameter corresponding to peak hardness (PHILLIPS [1964]). This is in agreement with KELLY and NICHOLSON [1963] who have pointed out that the hardening peak cannot in general be explained in terms of coherency strain (or particle size) in preference to particle spacing, since coherency strains are only rarely observed in Al–1.6 at% Cu on both sides of the peak.

3.4.2. Iron–carbon

Interstitial carbon in α-iron will always be in excess of its solubility limit at room temperature. It will precipitate as carbide along dislocations and in the volume of the matrix, especially if grain boundaries are absent. This gives rise to a pronounced yield point as well as an increase in the flow stress, both of which depend on heat treatment (KÖSTER *et al.* [1932]). As an alternative process, carbon atoms can form a more or less condensed solute atmosphere around dislocations, as considered by COTTRELL [1953] and coworkers. This would also explain a sharp yield point which in detail differs from the precipitate yield point. The Cottrell yield stress should be strongly temperature-dependent, as has been calculated by a number of workers; one calculation is by HAASEN

[1959], who used the assumption that the dislocation line energy is not increased significantly in the yield process. On the other hand thermal fluctuations would not help much to free a dislocation from a row of precipitates. A precipitate yield point can be overaged but not the Cottrell yield maximum. Finally, the magnitude of the precipitate yield maximum depends on the curvature the dislocation has attained by ageing under load, i.e., on the line tension, contrary to the behaviour of a Cottrell-locked dislocation (HAASEN [1959]). Carefully aged iron–carbon specimens have been studied by thin film electron transmission (HALE and MCLEAN [1961], LESLIE [1961]). Figure 29 shows a transmission photograph of an Fe–0.05 wt% C specimen thinned after water-quenching from 690°C and ageing one month at room temperature. Lines of precipitates are seen along the dislocations as well as some carbide particles in the matrix. Leslie finds the precipitate formed in the matrix of Fe–0.014 wt% C on ageing below 60°C to be a voluminous, deformable carbide (probably $Fe_{16}C_2$), not the (brittle) ε-carbide. On overageing, Hale and McLean see loops around carbide particles after deformation.

EVERS [1961] studied the pronounced yield point of Fe–0.005 wt% C single crystals and found the difference between upper and lower yield stress to depend very little on temperature and strain rate, whereas the lower yield stress itself or the flow stress does

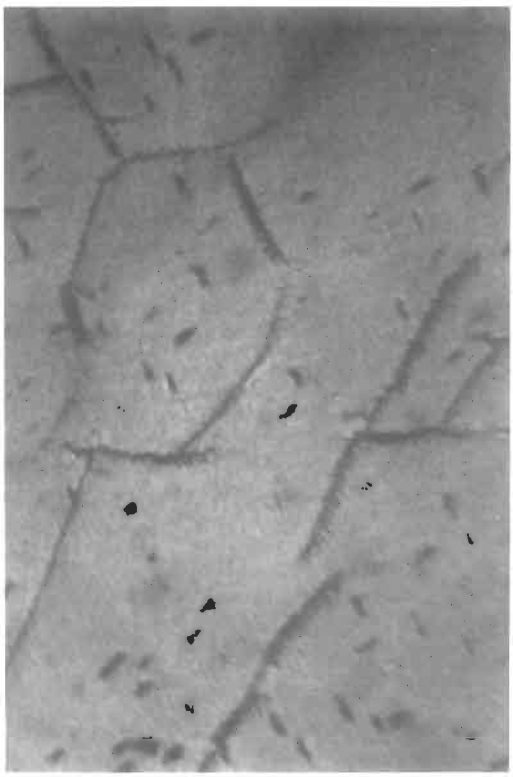

Fig. 29. Carbide precipitates in Fe–0.005 wt% C, water-quenched from 690°C and aged one month at room temperature (from HALE and MCLEAN, unpublished).

References: p. 2066.

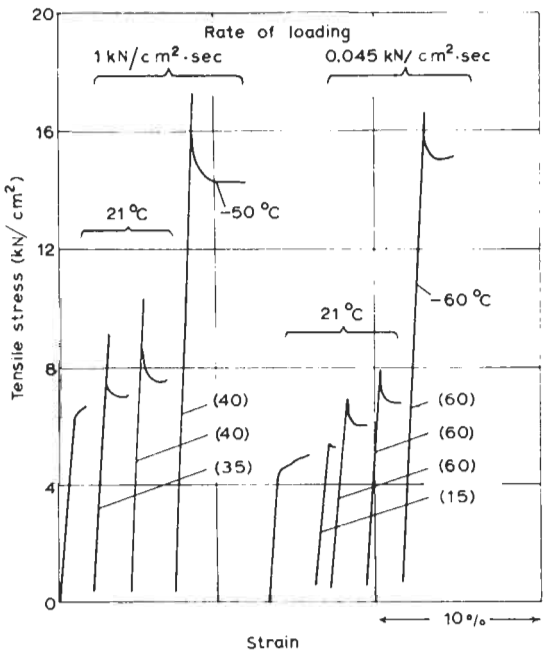

Fig. 30. Stress–strain curves for Fe–0.005 wt% C single crystals deformed at different rates and temperatures with intermediate ageing treatments at 21°C (times in ageing minutes given in brackets) (after EVERS [1961]).

so very strongly (fig. 30). The constant in the Petch analysis of the dependence of yield stress on grain size should be proportional to the dislocation/carbon unlocking stress according to the theory of COTTRELL [1958] and yet in most materials is found to be independent of the temperature of deformation (HESLOP and PETCH [1956]). All this points towards a precipitate-locking yield point. The same conclusion was reached by MIGAUD [1960] in a study of mechanical properties and residual electric resistivity of zone-refined iron. Migaud finds that the yield stress decreases on overageing. The dependence of the yield stress on ageing stress (EVERS [1961]) also suggests precipitate- and not atmosphere-locked dislocations.

MORDIKE and HAASEN [1962] have investigated the flow stress of α-iron–0.003 wt% C single crystals by temperature- and strain rate changes between room temperature and –72°C. They measured a stress-free activation energy U_0 of 0.55 eV and a very small activation volume v (corresponding to a distance between obstacles $v/b^2 \approx 7 \times 10^{-6}$ cm) which is sensitive to heat treatment. The authors identify the obstacles overcome by dislocations with thermal help as small carbide precipitates. CONRAD [1960] found that the temperature dependence of the lower yield stress τ_{ly} of polycrystalline iron depended on its purity, increasing particulary with the total carbon plus nitrogen content. HESLOP and PETCH [1956] have shown, on the other hand, that τ_{ly} (T) for iron with 0.16 wt% $(C+N)$ does not depend on the amount *in solution*. The work-hardening rate $d\tau/d\varepsilon$ of Mordike and Haasen's single crystals showed a maximum of 30 kN/cm^2 at 350 K. A

similar behaviour is observed for hardenable Al-alloys (§ 3.3). At low temperature $d\tau/d\varepsilon$ was the same as in stage III of nickel single crystals (~ 10 kN/cm^2 at 200 K). On the whole, α-iron–carbon in its mechanical properties between 200 and 300 K closely resembles an age-hardened alloy (see also ŠESTAK and SEEGER [1978]). For some further comments on the mechanical properties of α-iron see ch. 17, § 4.1, but also sect. 2.6 here.

3.4.3. Spinodally decomposed Cu–Ti alloys

WAGNER [1979] and KRATOCHVÍL and HAASEN [1982] have studied the mechanical properties of alloys which have undergone spinodal decomposition and have developed modulated microstructures (Cu solid solution + Cu_4Ti) of various wavelengths and perfections. The CRSS shows a double-peak behaviour as a function of ageing (or a plateau-plus-peak curve). This is interpreted by the formation of a regular array of ordered particles at first which then by Ostwald ripening turns into a more statistical particle array. Similar effects were found in polycrystalline Cu_9Ni_3Sn by KRATOCHVÍL *et al.* [1984]. Spinodal hardening is modelled by KATO *et al.* [1980] in terms of coherency stresses acting on 60°-dislocations and found in good agreement with single-crystal yield stresses vs. composition amplitude measured on $Cu_{11}Ni_3Sn$ (KATO *et al.* [1986]).

4. *Order-hardening*

Some solid-solution crystals develop long-range order in superlattice structures described in ch. 3. Of these, the fcc structures Cu_3Au, Ni_3Mn, fc tetr. CuAu (I) and bcc β'-CuZn, and Fe_3Al are considered here with respect to the influence of crystallographic order on the mechanical properties. Above the critical temperature for ordering, T_c, these properties can be influenced by short-range order (cf. § 2.3.2d). For a detailed review of this topic the reader is referred to ch. 24 and to surveys by YAMAGUCHI *et al.* [1990], VEYSSIÈRE [1992], WESTBROOK [1977], SAUTHOFF [1995], FLEISCHER *et al.* [1989], STOLOFF and DAVIES [1966] and STOLOFF [1971] as well as MARCINKOWSKI [1974].

The difference in stress–strain behaviour between the ordered and disordered state of a Cu_3Au crystal was demonstrated as early as 1931 by SACHS and WEERTS (fig. 31). The disordered and quenched crystal behaves like the random solid solutions discussed in § 2.4. It has a high critical shear stress, long "easy glide" with little work-hardening, strong overshoot and shows coarse slip lines on the surface as does α-brass (TAOKA and SAKATA [1957]). The well annealed and long-range ordered specimen on the other hand is similar in its stress–strain curve to a pure metal with a low stacking-fault energy. It shows strong linear hardening like pure copper, and a rather high τ_{III} while its critical shear stress is intermediate between pure copper and the quenched crystal. There is little overshoot and fine slip is observed for the ordered crystal.

Stress–strain behaviour of Ni_3Mn single crystals (VICTORIA and VIDOZ [1968]) was found to differ considerably from that described above for Cu_3Au. The reason for that is the much smaller typical domain size of the ordered structure in the former (5×10^{-7} cm, compared with 10^{-5} cm in Cu_3Au). The critical shear stress of ordered Ni_3Mn is higher than that of disordered, the work-hardening rate lower for single slip orientations.

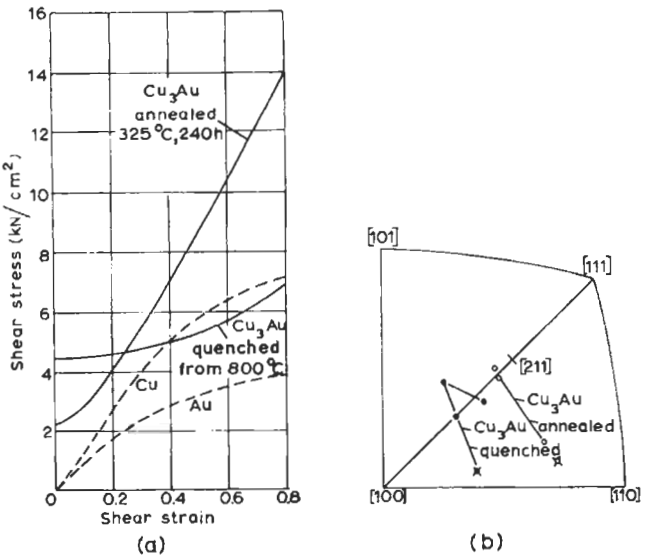

Fig. 31. (a) Stress–strain curves of disordered (quenched) and ordered (annealed) Cu_3Au single crystals at room temperature (after SACHS and WEERTS [1931]). Also curves for Cu and Au single crystals for comparison. (b) Change of orientation with strain of crystals (a).

Polyslip orientations work-harden very strongly though in ordered Ni_3Mn. This behaviour is explained by VIDOZ [1968] by the formation of so-called antiphase-boundary tubes during intersecting slip. Jogs in super-dislocations will in general not be aligned, and disordered regions will thus be formed, leading to an extra flow stress component. HIRSCH and CRAWFORD [1979] and more recently HAZZLEDINE and SUN [1992] have discussed work-hardening of ordered alloys.

4.1. The superdislocation

In order to understand the mechanical properties of ordered structures, one has to realize that a moving glide dislocation ($b=\frac{1}{2}a\langle 110\rangle$) in the fcc lattice creates disorder across its slip plane, leaving an *anti-phase boundary* (APB) behind. Order is restored, however, by a second identical dislocation following on the same plane. Thus in an ordered structure dislocation pairs or *superdislocations* are to be expected, bound together by an APB whose width is determined by the equilibrium between the order fault energy Γ and the elastic repulsion between the bordering dislocations of like sign (cf. ch. 20): fig. 32. The superdislocation is extended similarly to and independently of the stacking-fault splitting. This explains the difficulty of complete cross-slip and the high τ_{III}. In stage III slip then occurs by ordinary dislocations. Except for that, a superdislocation moving through a fully ordered crystal feels no solid-solution hardening (to a first approximation) in agreement with experiment. KEAR [1964] noted that since APBs in the Cu_3Au structure have lowest energies on {100} planes, one partial of the superdislocation trailing the order

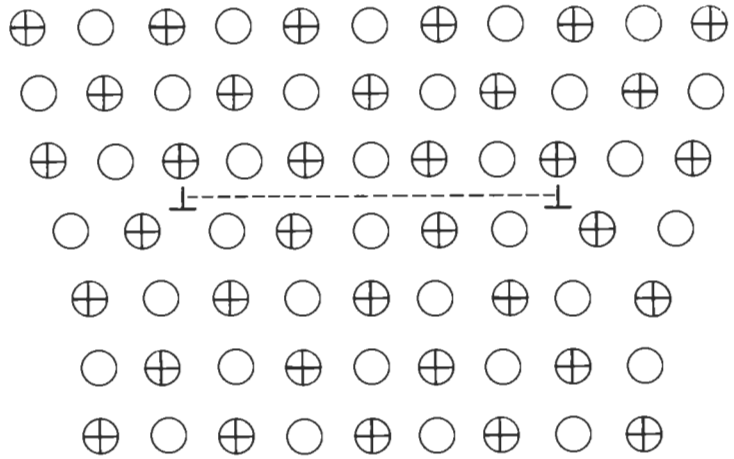

Fig. 32. Atomic arrangement in a cross-section through a superdislocation of edge orientation in a cubic primitive AB lattice, dashed line = APB (from BROWN [1960]).

fault would cross-slip spontaneously onto this secondary type of slip plane. This explains the ⟨110⟩ alignment of dislocations seen in electron transmission in these ordered alloys as well as the increase in work-hardening rate, particularly in Cu_3Au, with temperature between 77 K and 373 K because spontaneous cross-slip becomes easier (STOLOFF and DAVIES [1966]). The flow stress of a Ni_3Al-based alloy goes over a peak at 800 K, beyond which *cubic slip* is found to become prevalent (LALL *et al.* [1979]). VIDOZ [1968] is, however, able to explain $\theta_{II}(T)$ also by the formation of APB tubes as secondary slip becomes activated with increasing temperature. The extended superdislocation has been observed directly in electron transmission by MARCINKOWSKI *et al.* [1961] in Cu_3Au (fig. 33) and Ni_3Mn (but not in CuZn, Fe_3Al or NiAl). These authors calculated the widths of

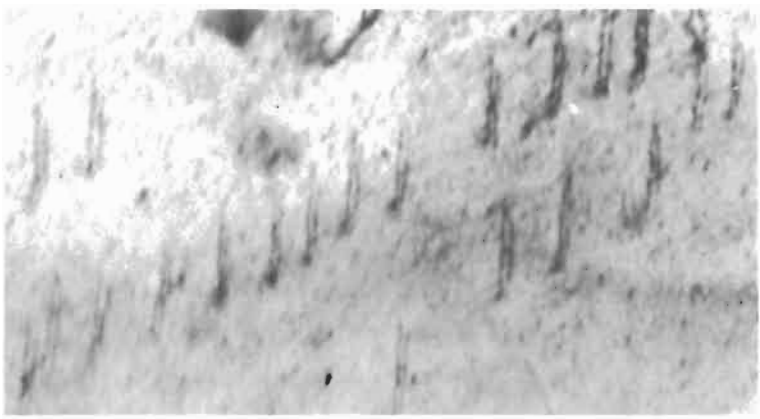

Fig. 33. Superdislocations in fully ordered Cu_3Au (from MARCINKOWSKI *et al.* [1961]).

References: p. 2066.

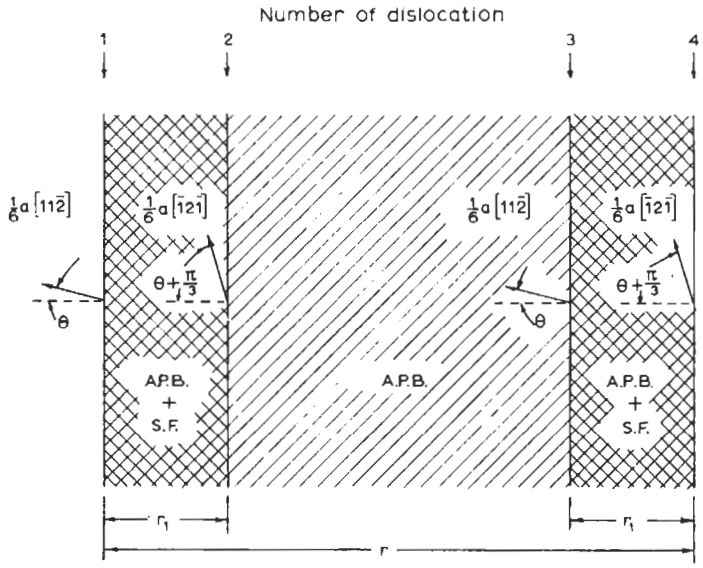

Fig. 34. Extended [011] superdislocation in its slip plane in Cu_3Au (from MARCINKOWSKI *et al.* [1961]).

the superdislocations in these structures by a quasichemical, nearest- (NN) and next-nearest (NNN) neighbour bond approach, see also MARCINKOWSKI [1974]. In Cu_3Au and Ni_3Mn the combination of stacking- (SF) and order-faults (APB) creates an extended superdislocation as shown in fig. 34. The widths r and r_1 are given by:

$$\left.\begin{aligned} r_1 &= \frac{\mu b^2}{2\pi\left(\gamma + \frac{1}{2}S^2\Gamma\right)} f_1(\theta) \\ r - r_1 &= \frac{\mu b^2}{2\pi\Gamma S^2} f(\theta) \end{aligned}\right\} r_1 \ll (r - r_1), \tag{16}$$

where S is the long-range order parameter, $0 \le S \le 1$, f, f_1 are functions, of the order of magnitude one, of the angle θ as defined in fig. 34 (θ is $-30°$ and $60°$ for edge and screw dislocations, respectively). For the edge dislocation in Cu_3Au and for $S = 1$ these authors estimate $r = 102$ Å, $r_1 = 17$ Å from $\Gamma = 92$ mJ/m^2 and assuming $\gamma = 40$ mJ/m^2. A more recent estimate (SASTRY and RAMASWAMI [1976]) is $\Gamma = 39$ mJ/m^2 and γ (ordered) $= 13$, γ (disord.) $= 21$ mJ/m^2. Experimentally $r = 95$–130 Å (θ unknown). For Ni_3Mn they estimate $\gamma = 20$ mJ/m^2 and $\Gamma = 75$ mJ/m^2 and calculate, for $S = 1$, $\theta = -30°$, a width $r_1 = 35$ Å, $r \approx 176$ Å. Measurement gives $r = 110$–170 Å. In the case of β'-CuZn there should be no stacking, only an order-fault which according to HERMAN and BROWN [1956] has a width too small to be observed, $r = 30b/S^2$, for accessible values of S. SAKA *et al.* [1984] estimate $\Gamma_{110} = 50$, $\Gamma_{112} = 37$ mJ/m^2. For Fe_3Al the superdislocation in the DO_3 ordered structure must consist of *four* $1/2a\langle 111\rangle$ (normal) dislocations in order to leave correct NN and NNN after slip. In this case Γ is small (77 mJ/m^2 for NN, 85 mJ/m^2 for NNN according to CRAWFORD *et al.* [1973]) and the width so large ($r \approx 1200$ Å

for an edge dislocation) that only single (incomplete) dislocations are expected and in fact observed. The slip lines are wavy, the dislocations in electron transmission leave cross-slip trails. In CuAu(I) there are two nonequivalent types of dislocations in a (111) plane because of the tetragonal distortion of the fcc lattice. According to MARCINKOWSKI *et al.* [1961] the one type forms no superdislocation and the other an asymmetrical one.

As S decreases, the widths r and r_1 in Ni_3Mn increase in agreement with observation (MARCINKOWSKI and MILLER [1961]). r_1 is determined by an effective stacking-fault energy $\gamma_{eff} = \gamma + 1/2S^2\Gamma$. In the disordered specimens quenched from above T_c ($S=0$) dislocations are observed to be single in Ni_3Mn (MARCINKOWSKI and MILLER [1961]). Increasing the equilibrium order temperature from $T=0$ to T_c, i.e., decreasing S to zero, generally results in the critical shear stress passing through a maximum: fig. 35 (ARDLEY and COTTRELL [1953], BROWN [1959a]). The low-temperature rise of τ_0 for CuZn is thought to be due to a phase transformation. A second, high-temperature peak of $\tau_0(T)$ for Cu_3Au has been ascribed by ARDLEY [1955] to strain-ageing during deformation.

4.2. Theoretical dependence of the yield stress on the degree of order

It is qualitatively evident that there will be a yield stress maximum at an intermediate

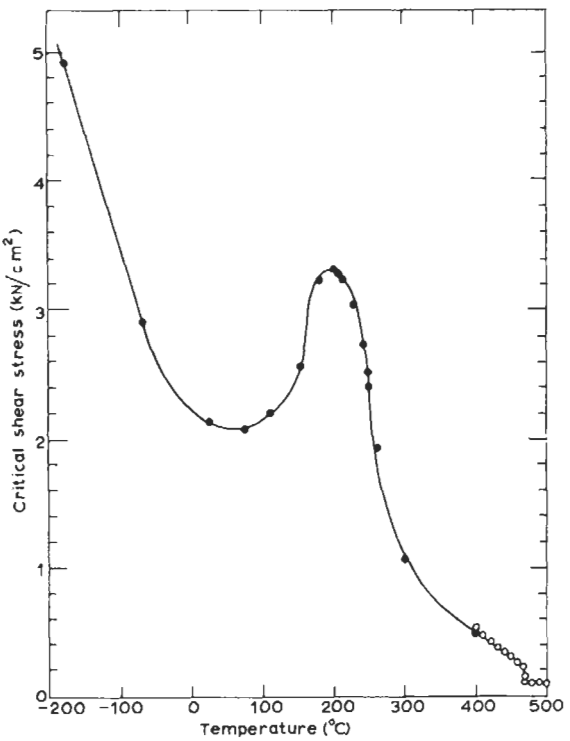

Fig. 35. Critical shear stress of β-brass, CuZn single crystals versus temperature (after ARDLEY and COTTRELL [1953] and BROWN [1959a]).

References: p. 2066.

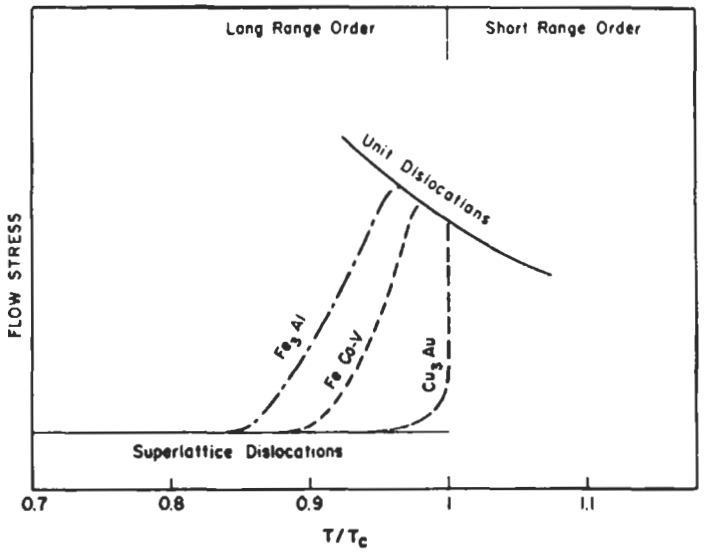

Fig. 34a. CRSS versus reduced temperature for several ordered alloys with quenched-in order (from STOLOFF [1971]).

degree of long-range order: Both the superdislocation in a completely ordered crystal and the single dislocation in a completely disordered structure will feel less friction than either of them at an intermediate S, see fig. 34a. Several mechanisms have been proposed to account for the order-hardening peak (e.g. BROWN [1960], LAWLEY *et al.* [1961], STOLOFF [1971], YAMAGUCHI and UMAKOSHI [1990], SCHRÖER *et al.* [1991], CAILLARD *et al.* [1993]).

4.2.1. Distortion of a partially ordered structure

When the ordered phase has a distorted structure relative to the disordered one, as in AuCu (fc tetr. versus fcc) internal stresses are produced in fitting the two structures together. This should impede dislocations particularly at an intermediate degree of order (or temperature, if at low temperatures complete order is reached without misfit).

4.2.2. Change of lattice parameter with order

Even without changing the crystal structure long-range order will decrease the lattice parameter. This again can lead to misfit-hardening in a partially ordered structure. If only one phase exists at any time ordering may still appear near dislocations where atom distances are changed locally: At points where the dislocation strain is compressional, atom distances are decreased and the order increased and *vice versa* (SUMINO [1958]; see also § 2.3.1d). The theory predicts a locking effect mainly for edge dislocations with a maximum near T_c.

4.2.3. Anti-phase domains of finite size

When a (super-)dislocation moves through an order domain structure it will increase the domain boundary area. COTTRELL [1954] has calculated the stress τ_c necessary for this as a function of domain diameter l.

$$\tau_c = (\Gamma/l)\,[1-\alpha(d/l)], \tag{17}$$

where d is the thickness of the domain boundary and α a geometrical factor of ≈ 6. $\tau_c(l)$ passes through a maximum of $\tau_c(l_{max}) = \Gamma/4\alpha d$ for a diameter $l_{max} = 2\alpha d$. At smaller l the alloy is already disordered before slip and at larger l there are few boundaries for the dislocation to create disorder at: In both cases the alloy is softer than for l_{max}. A hardness maximum has in fact been observed by BIGGS and BROOM [1954] in Cu_3Au at $l_{max} = 50$ Å, giving $d = 2b$ and about the observed magnitude of τ_c from eq. (17). See also LOGIE [1957]. If order changes crystal symmetry (to non-cubic as in CuPt, IRANI and CAHN [1973]) then large internal stresses will develop in a microstructure of random small domains and contribute to order-hardening.

4.2.4. Thickness of anti-phase boundary

BROWN [1959a] has drawn attention to the fact that the profile of order across an APB in a superdislocation must be different when this dislocation is in thermal equilibrium or in rapid movement. As the dislocation is pulled away from the equilibrium profile of its APB a *yield phenomenon* should be observed depending on the degree of order, i.e., on temperature. The calculated unlocking stress for CuZn has a maximum at $0.7T_c$ which has been related by Brown to the maximum observed for the *critical shear stress* of this material at about the same temperature (fig. 35). The agreement is good although this comparison needs justification.

4.2.5. Cross-slip and climb of superdislocations

The stacking-fault splitting is on {111} while the APB of low energy is on {100}. Thus, the superdislocation tends to lock itself by cross-slip out of the low-temperature {111} slip plane ("Kear–Wilsdorf lock", see KEAR and WILSDORF [1962]). According to FLINN [1960] the minimum energy configuration of two dislocations connected by a strip of APB and forming a superdislocation may not be such that their common plane is the slip plane. If the temperature is high enough for some diffusion to occur, dislocations will climb to reach a lower-energy position (fig. 36a). They are then difficult to move unless the temperature is increased further so that diffusion becomes very rapid, possibly with the help of deformation-produced vacancies (fig. 36b). Thus again a maximum of the yield stress is expected at intermediate temperatures.

4.2.6. Short-range order hardening

This concept, due to FISHER [1954], has already been discussed in § 2.3.2. ARDLEY [1955] has pointed out that a superdislocation moving through an *almost* perfect *super*-lattice is restrained by the unfavourable bonds it creates during glide in just the same way as a *simple* dislocation moving through a *short-range* ordered lattice. The flow stress will increase in the first case as *disorder* increases, in the second as short range *order*

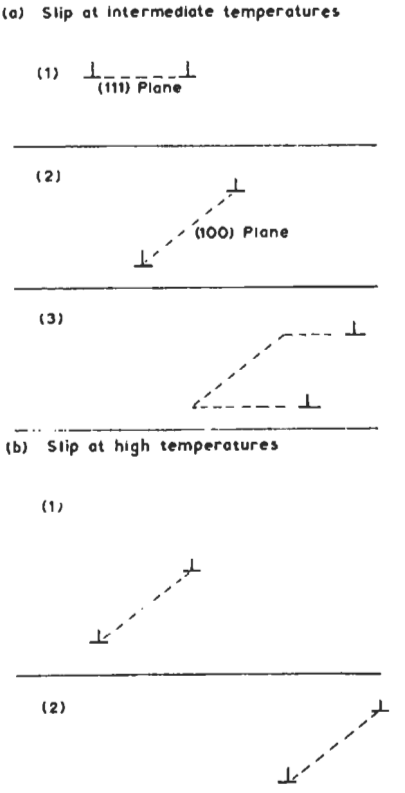

Fig. 36. Movement of a superdislocation at elevated temperatures (from FLINN [1960]).

increases. The maximum should appear for an intermediate degree of long-range and short-range order. RUDMAN [1962a] calculates $T = T_c$ for the position of the maximum.

4.2.7. Quench-hardening

If the order–disorder reaction is sluggish, the strength after quenching will depend on the degree of order at the quenching temperature. On the other hand vacancies may be trapped during the quench, leading to a faster rate of ordering than obtained by slow cooling. Dislocations may combine during the ordering process to form superdislocations of an equilibrium width corresponding to $S(T)$ [eq. (16)]. Such dislocation movement is expected to produce jogs and vacancies by intersection and climb. Both kinds of defects will harden the alloy (ch. 21). RUDMAN [1962b] has pointed out that ordering due to excess vacancies will be inhomogeneous in the crystal since quenched-in vacancies decay more rapidly near dislocations. Thus dislocations will be locked by an order gradient in partially ordered crystals, and a yield point is to be expected.

In conclusion, several mechanisms have been proposed to account for the hardness

peak at intermediate degrees of order and at temperatures of a certain fraction of T_c. Comparatively little experimental evidence is available so far to substantiate these theories.

4.3. Temperature dependence of the flow stress of ordered alloys

The initial flow stress of most of the ordered alloys considered here shows a maximum very near to the critical temperature, e.g., Cu_3Au, Ni_3Mn (MARCINKOWSKI and MILLER [1961]), and Fe_3Al (LAWLEY *et al.* [1961]). The degree of long-range order at the peak temperature is smaller than 0.7–0.4. An exception is CuZn (fig. 35) which shows a flow stress peak well below T_c, at $S > 0.9$. By "initial flow stress" is meant the critical shear stress in the case of single crystals (Cu_3Au, CuZn) and the stress to produce a small defined strain for polycrystals. In addition, for a number of alloys under various conditions, small pronounced yield points have been observed at the beginning of deformation. The dislocation-locking models of Sumino (§ 4.2.2), Brown (§ 4.2.4) and Rudman (§ 4.2.7) are well suited to explain them although some of the other mechanisms discussed above might also contribute. To explain the critical shear stress maximum of these three A_3B alloys the *local order–disorder* friction mechanism (§ 4.2.6) appears to be most suitable if a number of complicating factors can be eliminated. There should be no change in structure or lattice parameter with order and the domains should be larger than 50 Å. It is further assumed for the present discussion that the temperature is not high enough for extensive dislocation climb, and that the strength is measured at this temperature and not after quenching, which itself may produce hardening. The formation of Kear–Wilsdorf locks (sect. 4.2.5) by cross-slip is at present favoured for the explanation of the yield stress peak in Ni_3Al but this depends on quite essential and so far unproven assumptions (CAILLARD *et al.* [1993], YAMAGUCHI and UMAKOSHI [1990], HIRSCH [1992]). (See also ch. 24, § 3). Under these conditions the short-range order-disorder mechanism is used to explain the T_c flow stress peak in Cu_3Au by Ardley, Ni_3Mn by Marcinkowski *et al.* and in Fe_3Al by Lawley *et al.* The latter authors also see evidence for the Sumino locking mechanism for $T \leq T_c$, at the low-temperature flank of the peak in Fe_3Al. The same mechanism is invoked by BROWN [1959a] to explain the small step in τ_0 at T_c for CuZn (fig. 35). (The low-temperature peak in CuZn has already been considered in § 4.2.4. For a discussion of the possible contribution of an unlocking stress to the flow stress see § 2.3.) In fig. 37, due to RUDMAN [1962a], the temperature dependence of the yield stress based on the short-range order, Sumino and Brown mechanisms is shown for the β' CuZn structure. On the basis of the available data no quantitative comparison between theory and experiment is attempted here.

Frequently the flow stress of ordered alloys is measured at room temperature after quenching from various temperatures T_Q near T_c. In as far as the degree of order at T_q is retained during quenching the yield stress should then correspond to that measured at temperature since the order-strengthening mechanisms of § 4.2 depend little on temperature of deformation (with the exception of Flinn's climb mechanism which works only at elevated temperatures). In studies of order-hardening after quenching a possible contribution of quench-hardening must be considered. The latter can be investigated

References: p. 2066.

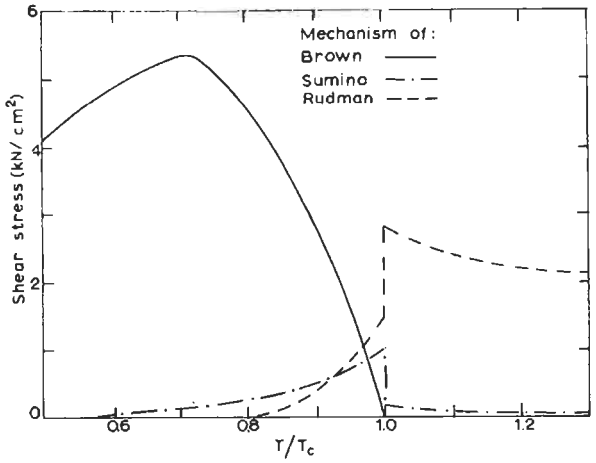

Fig. 37. Temperature dependence of the yield stress of CuZn as calculated by BROWN (§ 4.2.4), SUMINO (§ 4.2.2) and RUDMAN (§ 4.2.6) (after RUDMAN [1962a]).

separately in CuZn which orders too rapidly for any disorder ever to be quenched in. BROWN [1959b] has shown that the yield stress of CuZn exhibits a maximum as a function of quenching temperature. The position of the maximum depends on the rate of quenching and coincides with a maximum in the density of vacancies retained after quenching. The yield stress after the quench anneals out rapidly with an activation energy of 64.5 kJ/mole.

4.4. Creep in ordered alloys

At high temperatures superdislocations in ordered alloys probably move by climb (§ 4.2.5, SAUTHOFF [1995]). WEERTMAN [1956] and HONG and WEERTMAN [1986] have analyzed creep results of HERMAN and BROWN [1956] on CuZn as a function of temperature and stress within the framework of the theory presented in § 2.8.1. The activation energy according to eqs. (6) and (8) in the ordered state is 160.5 kJ/mole, close to, although somewhat higher than, that for the diffusion of zinc in β'-CuZn. The stress exponent is $n = 3.2$ in agreement with theory. The creep rate in the disordered state extrapolated to T_c is higher by a factor of 26 than in the ordered state. This could be due to additional glide movements by single dislocations in the disordered state.

FLINN [1960] has investigated creep in an alloy based on the Ni_3Al structure (20 at% Al, 10 at% Fe, 70 at% Ni) which is ordered up to the melting point. He attributes a peak at 600°C in the initial flow stress of this alloy to the difficulty in moving superdislocations whose APB does not lie in their slip plane, illustrated in fig. 36a. At high temperatures, diffusive movement of the APB may control the creep rate by a microcreep mechanism as described in § 2.8.2. The APB is dragged by its bounding dislocations which glide on their regular slip planes (fig. 36b). The creep rate (according to § 2.8.2)

depends on stress and temperature in much the same way as in the climb theory, in agreement with the measurements. Flinn finds $n = 3.2$ and an activation energy of 327 kJ/mole close to the expected values. LAWLEY *et al.* [1960] observed anomalies in the creep behaviour of Fe–Al solid solutions near the composition Fe_3Al. The apparent activation energy for creep near T_c rises to about twice that of iron diffusion which controls creep in the disordered state [eq. (10)]. This is probably due to a rapid change of order parameter with temperature in this range. The authors also found that recovery periods during creep *hardened* the alloy while continuing creep *softened* it near T_c. Both of these creep anomalies could possibly be interpreted along the lines of § 4.2.6 as due to the interaction of simple dislocations with short-range order. Sometimes anomalous *primary* creep is found which accelerates with time as in Ni_3Al, not decelerates as usual (HEMKER *et al.* [1991]). This has to do with the different stresses to activate octahedral and cube slip (SCHNEIBEL *et al.* [1992]) and with the initial shortage of mobile dislocations (ALEXANDER and HAASEN [1968]).

4.5. Twinning of ordered alloys

According to a classical prediction by LAVES [1952], an ordered cubic alloy should find it difficult to twin mechanically. The twin shear would leave a certain fraction of the atoms in wrong places in the scheme of order (fig. 38). Diffusive movements are in general impossible at the low temperatures where twinning occurs. An alloy with partial long-range order will lose some of its favourable bonds during twinning. Below a critical degree of order S_c the applied stress will just be able to move the twinning dislocations against the friction resistance from the destruction of order. These predictions have been

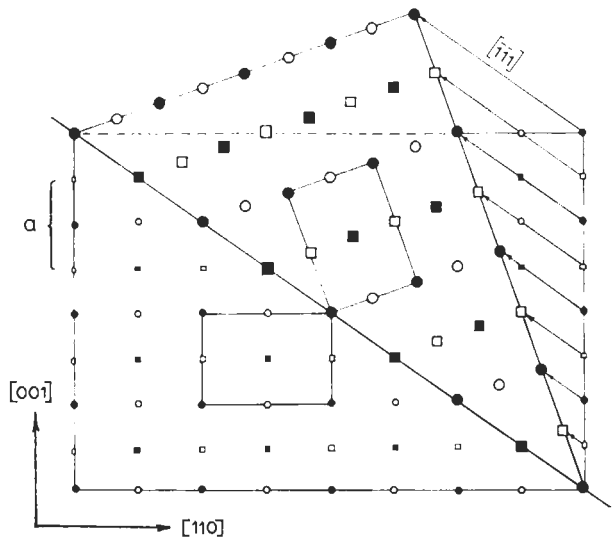

Fig. 38. Atomic movements during twinning of β' CuZn. Black symbols represent atoms in plane of projection, open symbols those on adjacent planes. Circles = Cu atoms, squares = Zn atoms. The cross-section of a unit cell is outlined. (From CAHN and COLL [1961].)

References: p. 2066.

confirmed by BARRETT [1954] for β'-CuZn and by CAHN and COLL [1961] in the case of Fe_3Al. The latter authors determined $S_c \approx 0.5$ corresponding to 5–10% of favourable nearest-neighbour bonds being destroyed during twinning. It has been shown more recently that certain non-cubic superlattices can be mechanically twinned without destruction of favourable bonds. For further discussion see VANDERSHAEVE and SARRAZIN [1977], VANDERSHAEVE and ESCAIG [1983], YAMAGUCHI *et al.* [1987], CHRISTIAN and LAUGHLIN [1988], YOO [1989], JIN and BIELER [1993], SAUTHOFF [1995] and an overview by CHRISTIAN and MAHAJAN [1995].

Acknowledgement

The author would like to thank Profs. H. Neuhäuser, P. Kratochvíl and P. Lukáč, as well as Drs. G. Sauthoff and H. Siethoff, for their comments on the fourth edition of this chapter.

References

AKHTAR, A., and E. TEGHTSOONIAN, 1968, Proc. Int. Conf. Strength of Metals and Alloys, Tokyo, Trans. Japan. Inst. Met. Suppl. **9**, 692.

ALEXANDER, H. and P. HAASEN, 1968, Solid State Physics, F. Seitz and D. Turnbull eds., vol. 22, 28.

ARDELL, A.J., V. MUNJAL and D.J. CHELLMAN, 1976, Metallurg. Trans. **7A**, 1263.

ARDELL, A.J., 1985, Metal. Trans. **16A**, 2131.

ARDLEY, G.W., 1955, Acta Metall. **3**, 525.

ARDLEY, G.W., and A.H. COTTRELL, 1953, Proc. Roy. Soc. **A219**, 328.

ARSENAULT, R.J. and S. LI, 1989, Met. Trans. **20A**, 1429.

ASHBY, M.F., 1964, Z. Metalik. **55**, 5.

ASHBY, M.F., 1966, Acta Metall. **14**, 679.

ASHBY, M.F., 1968, in: Strengthening Mechanisms in Solids, eds. A. Kelly and R.B. Nicholson (Elsevier, Amsterdam).

BARRETT, C.S., 1954, Trans. AIME **200**, 1003.

BASINSKI, Z.S., R.A. FOXALL and R. PASCUAL, 1972, Scripta Metall. **6**, 807.

BIGGS, W.D., and T. BROOM, 1954, Phil. Mag. **45**, 246.

BIRD, J.E., A.K. MUKHERJEE and J.E. DORN, 1969, in Quantitative Relations of Properties and Microstructures, ed. D. Brandon *et al.*, Israel Univ. Press, Jerusalem, p. 255.

BOČEK, M., P. KRATOCHVÍL and P. LUKÁČ, 1961, Czech. J. Phys. B11, 674.

BRION, H.G., P. HAASEN and H. SIETHOFF, 1971, Acta Metall. **19**, 283.

BROWN, L.M., 1979, in: Strength of Metals and Alloys, eds P. Haasen et al. (Pergamon Press, Oxford) vol. 3, 1551.

BROWN, L.M., and R.K. HAM, 1971, in: Strengthening Methods in Crystals, eds. A. Kelly et al. (Elsevier, Amsterdam) p. 10.

BROWN, N., 1959a, Phil. Mag. **4**, 693.

BROWN, N., 1959b, Acta Metall. **7**, 210.

BROWN, N., 1960, in: Mechanical Properties of Intermetallic Compounds, ed. J. Westbrook (Wiley, New York) p. 177.

BRUNNER, D. and J. DIEHL, 1991, Phys. Stat. Sol. (a) **125**, 203.

BRUNNER, D. and J. DIEHL, 1993, Mat. Sci. Eng., **164**, 350.

BÜCHNER, A.R. and W. WUNDERLICH, 1993, Phys. Stat. Sol. (a) **135**, 391.

BYRNE, J.G., M.E. FINE and A. KELLY, 1961, Phil. Mag. **6**, 1119.
CAHN, R.W., and J.A. COLL, 1961, Acta Metall. **9**, 138.
CAILLARD, D., A. COURET and G. MOLENAT, 1993, Mat. Sci. Eng., A, **A164**, 68.
CARTER, C.B., 1980, Phil. Mag. **A41**, 619.
CARTER, C.B., and J.L.F. RAY, 1977, Phil. Mag. **35**, 189.
CHRISTIAN, J.W. and D.E. LAUGHLIN, 1988, Acta Met. **36**, 1617.
CHRISTIAN, J.M. and S. MAHAJAN, 1995, Progr. Mater. Sci. **39**, 1.
ČIŽEK, L., P. KRATOCHVÍL and B. SMOLA, 1974, J. Mat. Sci. **9**, 1517.
CONRAD, H., 1960, Phil. Mag. **5**, 745.
COPLEY, S.M., and B.H. KEAR, 1967, Trans. AIME **239**, 984.
COTTRELL, A.H., 1953, Dislocations and Plastic Flow in Crystals (Oxford, Clarendon Press).
COTTRELL, A.H., 1954, in: Relations of Properties to Microstructure (ASM, Ohio).
COTTRELL, A.H., 1958, Trans. AIME **212**, 192.
COTTRELL, A.H., C.S. HUNTER and F.R.N. NABARRO, 1953, Phil. Mag. **44**, 1064.
CRAWFORD, R.C., I.F.L. RAY and D.J.H. COCKAYNE, 1973, Phil. Mag. **27**, 1.
DASH, J., and M.E. FINE, 1961, Acta Metall. **9**, 149.
DEW-HUGHES, D., and W.D. ROBERTSON, 1960, Acta Metall. **8**, 147 and 156.
DUESBERRY, M.S., N.P. LOUAT and K. SADANANDA, 1992, Acta Met. **40**, 149.
EBELING, R., and M.F. ASHBY, 1966, Phil. Mag. **13**, 805.
ESCAIG, B., 1968, in: Dislocation Dynamics, eds. A. Rosenfield *et al.* (McGraw-Hill, New York) p. 655.
ESTRIN, Y., C.P. LING and P. MCCORMICK, 1991, Acta Met. **39**, 2943.
EVERS, M., 1959, Z. Metallk. **50**, 638.
EVERS, M., 1961, Z. Metallk. **52**, 359.
FIORE, N.F., and C.L. BAUER, 1968, Prog. Mater. Sci. **13**, 85.
FISHER, J.C., 1954, Acta Metall. **2**, 9.
FISHER, J.C., E.W. HART and R.H. PRY, 1953, Acta Metall. **1**, 336.
FLINN, P.A., 1958, Acta Metall. **6**, 631.
FLINN, P.A., 1960, Trans. AIME **218**, 145.
FLEISCHER, R.L., 1961, Acta Metall. **9**, 996.
FLEISCHER, R.L., 1963, Acta Metall. **11**, 203.
FLEISCHER, R.L., 1966, Acta Metall. **14**, 1867.
FLEISCHER, R.L., D.M. DIMIDUK and H.A. LIPSITT, 1989, Ann. Rev. Mater. Sci. **19**, 231.
FOREMAN, A.J.E., and M.J. MAKIN, 1966, Phil. Mag. **14**, 131.
FRIEDRICHS, J., and P. HAASEN, 1975, Phil. Mag. **31**, 863.
FUCHS, A. and D. RÖNNPAGEL, 1993, Mat. Sci. Eng., **A164**, 340.
FUSENIG, K.D. and E. NEMBACH, 1993, Acta Met., in press.
GALLAGHER, P.C.J., 1968, J. Appl. Phys. **39**, 160.
GALLAGHER, P.C.J., 1970, Trans. AIME **1**, 2429.
GARSTONE, J., and R.W.K. HONEYCOMBE, 1957, in: Dislocations and Mechanical Properties of Crystals, eds. J.C. Fisher et al. (Wiley, New York) p. 391.
GEROLD, V., 1979, in: Dislocations in Solids, ed. F.R.N. Nabarro (North-Holland, Amsterdam) vol. 4, p. 215.
GEROLD, V. and H. HABERKORN, 1966, Phys. Stat. Sol. (a) **16**, 675.
GEROLD, V. and H.P. KARNTHALER, 1989, Acta Met. **37**, 2177.
GIBALA, R., and T.E. MITCHELL, 1973, Scripta Metall. **7**, 1143.
GILMAN, J.J., 1956, Trans. AIME **206**, 1326.
GITTUS, J., 1978, Irradiation Effects in Crystalline Solids (Appl. Sci. Publ., London).
GLEITER, H., 1968, Acta Metall. **16**, 455.
GLEITER, H., 1967b, Acta Metall. **15**, 1213.
GLEITER, H., and E. HORNBOGEN, 1965, Phys. Stat. Sol. **12**, 235.
GLEITER, H., and E. HORNBOGEN, 1968, Mater. Sci. Eng. **2**, 285.
GRANATO, A.V., 1971 Phys. Rev. Lett. **27**, 660; Phys. Rev. **B4**, 2196.
GREETHAM, G., and R.W.K. HONEYCOMBE, 1961, J. Inst. Met. **89**, 13.
GRÖHLICH, M., P. HAASEN and G. FROMMEYER, 1982, Scripta Metall. **16**, 367.

GUTMANAS, E. Yu., and P. HAASEN, 1981, Phys. Stat. Sol. (a) **63**, 193.
GYPEN, L. A., and A. DERRUYTTÈRE, 1981, Scripta Metall. **15**, 815.
GYPEN, L. A., and A. DERRUYTTÈRE, 1977, J. Mater. Sci. **12**, 1028, and 1034.
HAASEN, P., 1958, Phil. Mag. **3**, 384.
HAASEN, P., 1959, in: Internal Stresses and Fatigue in Metals, eds. G.M. Rassweiler and W.L. Grube (Elsevier, Amsterdam) p. 205.
HAASEN, P., 1964, Z. Metallk. **55**, 55.
HAASEN, P., 1965, in: Alloying Effects in Concentrated Solid Solutions, ed. T.B. Massalski (Gordon and Breach, New York) p. 270.
HAASEN, P., 1967, Krist. u. Techn. **2**, 251.
HAASEN, P., 1968, Proc. Int. Conf. on Strength of Metals and Alloys, Tokyo, Trans. Japan. Inst. Met. Suppl. **9**, XL.
HAASEN, P., 1975, Phys. Stat. Sol. (a) **28**, 145.
HAASEN, P., 1977, in: Fundamental Aspects of Structural Alloy Design, eds. R.J. Jaffee et al. (Plenum, New York) p. 3.
HAASEN, P., and A. KELLY, 1957, Acta Metall. **5**, 192.
HAASEN, P., and A. H. KING, 1960, Z. Metallk. **51**, 722.
HAASEN, P., and P. KRATOCHVÍL, 1973, Proc. Int. Reinststoff-Symp., Dresden (Akad. d. W., Berlin) p. 383.
HAASEN, P., and R. LABUSCH, 1979, in: Strength of Metals and Alloys, eds. P. Haasen *et al.* (Pergamon Press, Oxford) vol. 1, p. 639.
HAESSNER, F., and D. SCHREIBER, 1957, Z. Metallk. **48**, 263.
HÄHNER, P., 1992, thesis Univ. Stuttgart; 1993, Mat. Sci. Eng. **A164**, 23.
HALE, K. F., and D. MCLEAN, 1961, private communication; see also: Proc. Europ. Reg: Conf. Electron Microscopy, Delft, 1960, p. 425.
HAMMAR, R. H., W. C. T. YEH, T. G. OAKWOOD and A. A. HENDRICKSON, 1967, Trans. AIME **239**, 1692.
HANSON, K., and J. W. MORRIS, Jr., 1975, J. Appl. Phys. **46**, 2378.
HARRIS, B., 1967, J. Less-Common Met. **12**, 247.
HATTENDORF, H. and A. R. BÜCHNER, 1992, Z. Metallk. **83**, 690.
HAUSER, F. E., P. R. LANDON and J. E. DORN, 1958, Trans. ASM **50**, 856.
HAZZLEDINE, P. M. and Y. Q. SUN, 1992, Mater. Sci. Engg. A **152**, 189.
HEINRICH, H., R. NEUHAUS and Ch. SCHWINK, 1992, Phys. Stat. Sol. (a) **131**, 299.
HEMKER, K. J., M. J. MILLS and W. D. NIX, 1991, Acta Met. **39**, 1901.
HENDRICKSON, A. A., and M. E. FINE, 1961a, Trans. AIME **221**, 103.
HENDRICKSON, A. A., and M. E. FINE, 1961b, Trans. AIME **221**, 967.
HERMAN, M., and N. BROWN, 1956, Trans. AIME **206**, 604.
HESLOP, J., and N. J. PETCH, 1956, Phil. Mag. **1**, 866.
HIRSCH, P. B., 1975, in: The Physics of Metals, vol. 2, Defects (Cambridge Univ. Press) p. 189.
HIRSCH, P. B., 1992, Progr. Mater. Sci. **36**, 63.
HIRSCH, P. B., and R. C. CRAWFORD, 1979, in: Strength of Metals and Alloys, eds. P. Haasen et al. (Pergamon Press, Oxford) vol. 1, p. 89.
HIRSCH, P. B., and A. Kelly, 1965, Phil. Mag. **12**, 881.
HOCKEY, B. J., and J. W. MITCHELL, 1972, Phil. Mag. **26**, 409.
HONG, S. H. and J. WEERTMAN, 1986, Acta Met. **34**, 743.
HONG, S. I. and C. LAIRD, 1990, Acta Met. **38**, 1581.
HORNE, G. T., R. B. ROY and H. W. PAXTON, 1963, J. Iron Steel Inst. **201**, 161.
HOWIE, A., 1960, Thesis Cambridge; cf. Proc. Europ. Reg. Conf. on Electronic Microscopy Delft, p. 383.
HUTCHISON, M. M., and R. W. K. HONEYCOMBE, 1967, Met. Sci. J. **1**, 70.
INNI, H., S. I. HONG and C. LAIRD, 1990, Acta Met. **38**, 2261.
IRANI, R. S., and R. W. CAHN, 1973, Acta Metall. **21**, 575.
JAN, J. P., 1955, J. Appl. Phys. **26**, 1291.
JAX, P., P. KRATOCHVÍL and P. HAASEN, 1970, Acta Metall. **18**, 237.
JIN, Z. and R. BIELER, 1993, Mat. Res. Soc. Symp. **288**, 775.

JONES, R. L., and A. KELLY, 1968, Proc. **2nd** Bolton Landing Conf. on Oxide Dispersion Strengthening (Gordon and Breach, New York).
KARNTHALER, H. P., P. M. HAZZLEDINE and M. S. SPRING, 1972, Acta Metall. **20**, 459.
KARNTHALER, H. P., F. PRINZ and G. HASLINGER, 1975, Acta Metall. **23**, 155.
KATO, M., T. MORI and L. H. SCHWARTZ, 1980, Acta Met. **28**, 285.
KATO, M., S. KATSUTA, S. OKAMINE and A. SATO, 1986, Mat. Sci. Engg. **77**, 95.
KEAR, B. H., 1964, Acta Metall. **12**, 555.
KEAR, B. H. and H. G. F. WILSDORF, 1962, Trans. TMS-AIME, **224**, 382.
KELLY, A., 1958, Phil. Mag. **3**, 1472.
KELLY, A., and M. E. FINE, 1957, Acta Metall. **5**, 365.
KELLY, A., and R. B. NICHOLSON, 1963, Prog. Mater. Sci. **10**, 1.
KELLY, A., and S. SATO, 1961, Acta Metall. **9**, 59.
KIMURA, H., and R. MADDIN, 1971, Quench-Hardening in Metals (North-Holland, Amsterdam).
KLEINTGES, M., 1980, Scripta Metall. **14**, 993.
KLEINTGES, M., and P. HAASEN, 1980, Scripta Metall. **14**, 999.
KLOSKE, R. A., and M. E. FINE, 1969, Trans. AIME **245**, 217.
KOCKS, U. F., 1966, Phil. Mag. **13**, 541.
KOCKS, U. F., 1985, Met. Trans. A **116**, 2109.
KOCKS, U. F., A. S. ARGON and M. F. ASHBY, 1975, Prog. Mater. Sci. **19**, 1.
KOLK, A. and Ch. SCHWINK, 1992, Acta Met. **172**, 133.
KOPPENAAL, T. J., and M. E. FINE, 1961, Trans. AIME **221**, 1178.
KÖSTER, W., H. v. KÖCKRITZ and E. H. SCHULZ, 1932, Arch. Eisenhüttenw. **6**, 55.
KOSTORZ, G., 1968, thesis Göttingen; Z. Metallk. **59**, 941.
KOSTORZ, G., and P. HAASEN, 1969, Z. Metallk. **60**, 26.
KRATOCHVÍL, P., 1970, Scripta Metall. **4**, 333.
KRATOCHVÍL, P., and P. HAASEN, 1982, Scripta Metall. **16**, 197.
KRATOCHVÍL, P., J. MENCL, J. PESICKA and S. M. KOMAIK, 1984, Acta Met. **32**, 1493.
KRATOCHVÍL, P., and E. NERADOVA, 1971, Czech. J. Phys. B21, 1273.
KRÖNER, E., 1964, Phys. Kondens. Materie **2**, 262.
KUBIN, L. P., and J. L. MARTIN, 1979, in: Strength of Metals and Alloys, eds. P. Haasen et al. (Pergamon Press, Oxford) vol. 3, 1639.
KUBIN, L. P. and Y. ESTRIN, 1992, Phys. Stat. Sol. (b) **172**, 173.
KUBIN, L. P., K. CHIHAB and Y. ESTRIN, 1988, Acta Met. **36**, 2707.
KUHLMANN–WILSDORF, D., and H. G. WILSDORF, 1953, Acta Metall. **1**, 394.
LABUSCH, R., 1970, Phys. Stat. Sol **41**, 659.
LABUSCH, R., 1972, Acta Metall. **20**, 917.
LABUSCH, R., 1981, Czech. J. Phys. **B31**, 165.
LABUSCH, R., 1991, Proc. ICSMA 9, ed. D. G. Brandon, R. Chaim, and A. Rosen, (Freund Publishing House, Haifa).
LABUSCH, R., G. GRANGE, J. AHEARN and P. HAASEN, 1975, in: Rate Processes in Plastic Deformation of Materials (ASM, Metals Park, OH) p. 26.
LALL, C., S. CHIN and D. P. POPE, 1979, Metallurg, Trans. **10A**, 1323.
LAVES, F., 1952, Naturwiss. **39**, 546.
LAWLEY, A., and R. MADDIN, 1962, Trans. AIME, **224**, 573.
LAWLEY, A., J. A. COLL and R. W. CAHN, 1960, Trans. AIME **218**, 166.
LAWLEY, A., A. E. VIDOZ and R. W. CAHN, 1961, Acta Metall. **9**, 287.
LESLIE, W. C., 1961, Acta Metall. **9**, 1004.
LING, C. P. and P. MCCORMICK, 1990, Acta Met. **38**, 2631.
LIVINGSTON, J. D., 1959, Trans. AIME **215**, 566.
LIVINGSTON, J. D., and J. J. BECKER, 1958, Trans. AIME **212**, 316.
LOGIE, H. J., 1957, Acta Metall. **5**, 106.
LUKÁČ, P., 1981, Cz. Jl. Phys. **B31**, 135.
LUKÁČ, P., 1992, phys. stat. sol. (a) **131**, 377.

LUKÁČ, P. and Z. TROJANOVÁ, 1979, in Strength of Metals and Alloys, ed. P. Haasen *et al.*, Pergamon, Oxford, p. 1061.
LÜTJERING, G., and E. HORNBOGEN, 1968, Z. Metallk. **59**, 29.
MADER, S., 1963, in: Electron Microscopy and Strength of Crystals (Interscience, New York) p. 183.
MADER, S., A. SEEGER and H. M. THIERINGER, 1963, J. Appl. Phys. **34**, 3376.
MAHAJAN, S., and D. F. WILLIAMS, 1973, Int. Met. Rev. **18**, 43.
MARCINKOWSKI, M. J., 1974, in: Order–Disorder Transformations in Solids, ed. H. Warlimont (Springer, Berlin, 1974) p. 365.
MARCINKOWSKI, M. J., and D. S. MILLER, 1961, Phil. Mag. **6**, 871.
MARCINKOWSKI, M. J., N. BROWN and R. M. FISHER, 1961, Acta Metall. **9**, 129.
MCCORMICK, P. G., 1972, Acta Metall. **20**, 351.
MEAKIN, J. D., and H. G. WILSDORF, 1960, Trans. AIME **218**, 737.
MEISSNER, J., 1959, Z. Metallk. **50**, 207.
MELANDER, A., and P. A. PERSSON, 1978, Met. Sci. J. **12**, 391.
MIGAUD, B., 1960, Thèse, Université de Paris.
MISHIMA, Y., S. OCHIAI, N. HAMAO, M. YODOGAWA and T. SUZUKI, 1986, Trans. JIM **27**, 656.
MITCHELL, T. E., and P. L. RAFFO, 1967, Can. J. Phys. **45**, 1047.
MITCHELL, J. W., J. AHEARN, B. J. HOCKEY, J. P. MONAGHAN and R. K. WILD, 1968, Proc. Int. Conf. on Strength of Metals and Alloys, Tokyo, Trans. Japan. Inst. Met. Suppl. **9**, 769.
MOHAMED, F. A. and T. G. LANGDON, 1974, Acta Met. **22**, 779.
MORDIKE, B. L., and P. HAASEN, 1962, Phil. Mag. **7**, 459.
MORDIKE, B. L., A. A. BRAITHWAITE and K. D. ROGAUSCH, 1970, Met. Sci. J. **4**, 37.
MORI, T., and H. FUJITA, 1980, Acta Metall. **28**, 771.
MUGHRABI, H., 1979, in: Strength of Metals and Alloys, eds. P. Haasen et al. (Pergamon Press, Oxford) vol. 3, p. 1615.
NABARRO, F. R. N., 1982, Proc. Roy. Soc. **A381**, 285.
NARITA, N., and J. TAKAMURA, 1974, Phil. Mag. **29**, 1001.
NARITA, N., A. HATANO, J. TAKAMURA, M. YOSHIDA and H. SAKAMOTO, 1978, J. Japan Inst. Metals **42**, 533.
NATSIK, V. D., 1979, Fiz. Nizkikh Temp. 5, 400.
NAVRATIL, V., M. HAMERSKY, P. LUKÁČ, V. P. SOLDATOV and V. I. STARTSEV, 1983, Phys. Stat. Sol. (a) **78**, 633.
NEMBACH, E., and G. NEITE, 1985, Progr. Mater. Sci. **29**, 177.
NEUHÄUSER, H., 1983, in "Dislocations in Solids", vol. 6, **319**, ed. F. R. N. Nabarro, Amsterdam, North-Holland.
NEUHÄUSER, H., J. PLESSING and M. SCHÜLKE, 1990, J. Mech. Beh. Met. **2**, 231.
NEUHÄUSER, H., and H. FLOR, 1978, Scripta Metall. **12**, 443.
NEUHÄUSER, H., and H. FLOR, 1979, Scripta Metall. **13**, 147.
NEUMANN, P., 1967, Z. Metallk. **58**, 780.
NICHOLSON, R. B., G. THOMAS and J. NUTTING, 1960, Acta Metall. **8**, 172.
NIX, W. D., and B. ILSCHNER, 1979, in: Strength of Metals and Alloys, eds. P. Haasen et al. (Pergamon Press, Oxford) vol. 3, p. 1503.
NIXON, W. E. and J. W. MITCHELL, 1981, Proc. Roy. Soc. **A376**, 343.
OIKAWA, H. and T. G. LANGDON, 1985, in: Creep Behaviour of Crystalline Solids, ed. B. Wilshire *et al.*, Pineridge Press, Swansea.
ORLOVA, A. and J. ČADEK, 1986, Mat. Sci. Eng. **77**, 1.
PANDE, C. S., and P. M. HAZZLEDINE, 1971, Phil. Mag. **24**, 1039 and 1393.
PEISSKER, E., 1965a, Acta Metall. **13**, 419.
PEISSKER, E., 1965b, Z. Metallk. **56**, 155.
PFAFF, F., 1962, Z. Metallk. **53**, 411 and 466.
PFEIFFER, W., and A. SEEGER, 1962, Phys. Stat. Sol. **2**, 668.
PHILLIPS, V. A., 1964, Trans. AIME **230**, 967.
PIERCY, G. R., R. W. CAHN and A. H. COTTRELL, 1955, Acta Metall. **3**, 331.
PINK, E. and R. J. ARSENAULT, 1979, Progr. Mater. Sci. **24**, 1.
PÜSCHL, W. and G. SCHOECK, 1993, Proc. LEDS **3**.

RABE, F. and P. HAASEN, 1988, Strength of Metals and Alloys, ed. Kettunen *et al.* (Pergamon Press, Oxford) p. 561.
RIDDHAGNI, B.R., and R.M. ASIMOW, 1968, J. Appl. Phys. **39**, 4144 and 5169.
ROGAUSCH, K.D., 1967, Z. Metalik, **58**, 50.
RUDMAN, P.S., 1962a, Acta Metall, **10**, 253.
RUDMAN, P.S., 1962b, Acta Metall. **10**, 195.
RUDOLPH, G., P. HAASEN, B.L. MORDIKE and P. NEUMANN, 1965, Proc. Ist Intern. Conf. on Fracture, Sendai, ed. T. Yokobori (Japan. Inst. of Metals, Sendai) p. 501.
SACHS, G., and J. WEERTS, 1931, Z. Phys. **67**, 507.
SAKA, H., M. KAWASE, A. NOHARA and T. IMURA, 1984, Phil. Mag. **A50**, 65.
SASTRY, S.M.L. and B. RAMASWAMI, 1976, Phil. Mag. **33**, 375.
SAUTHOFF, G., 1995, in: Intermetallic Compounds, eds. J.H. Westbrook and R.L. Fleischer (J. Wiley, New York), p. 911.
SAXL, J., 1964, Czech, J. Phys. B14, 381.
SCHLIPF, J., 1992, Acta Met. **40**, 2095.
SCHMID, E. and H. SELIGER, 1932, Metallwirtsch. **11**, 421.
SCHNEIBEL, J.H. and P.M. HAZZLEDINE, 1992, in: Ordered Intermetallics, eds. C.T. Liu *et al.* (Kluwer Publ., Dordrecht), p. 565.
SCHOECK, G., 1980, in: Dislocations in Solids, ed. F.R.N. (?) Nabarro (North Holland, Amsterdam) vol. 3, p. 63.
SCHOECK, G., and A. SEEGER, 1959, Acta Metall. **7**, 469.
SCHRÖER, W., H. MECKING and C. HARTIG, 1991, in: Proc. Int. Sympos. Intermet. Comp., ed. O. Izumi (Jap. Inst. Met., Sendai), p. 567.
SCHWARZ, R.B., 1979, in: Strength of Metals and Alloys, eds. P. Haasen *et al.* (Pergamon Press, Oxford) vol. 1, p. 953.
SCHWARZ, R.B., 1982, Scripta Metall. **16**, 385.
SCHWARZ, R.B., and R. LABUSCH, 1978, J. Appl. Phys. **49**, 5147.
SCHWINK, Ch., and Th. WILLE, 1980, Scripta Metall. **14**, 1093.
SEEGER, A., R. BERNER and H. WOLF, 1959, Z. Physik **155**, 247.
SEEGER, A. and C. WÜTHRICH, 1976, Nuov. Cimen. **33B**, 38.
ŠESTAK, B., 1979, in: Strength of Metals and Alloys, eds. P. Haasen *et al.* (Pergamon Press, Oxford) vol. 3, 1461.
ŠESTAK, B., and A. SEEGER, 1978, Z. Metallk. **69**, 195, 355 and 425.
SIETHOFF, H., 1969, Thesis Göttingen.
SIETHOFF, H., 1969, Mater. Sci. Eng. **4**, 155.
SIETHOFF, H., 1970, Phys. Stat. Sol. **40**, 153.
SIETHOFF, H., 1992a, Scripta Met. **27**, 7.
SIETHOFF, H., 1992b, Phys. Stat. Sol. (a) **131**, 309.
SIETHOFF, H., 1992c, Semicond. and Semimet. **37**, 143.
SIETHOFF, H. and K. AHLBORN, 1991, Phys. Stat. Sol. (a) **128**, 397.
SINNING, H.R., 1982, Acta Metall. **30**, 1019.
SINNING, H.R. and P. HAASEN, 1981, Z. Metalik. **72**, 807.
SKROTZKI, W., and P. HAASEN, 1981, J. Physique **42**, C3–119.
STARTSEV, V.I., 1981, Czech. J. Phys. B31, 115.
STARTSEV, V.I., V.V. DEMIRSKI and S.N. KOMNIK, 1979, in: Strength of Metals and Alloys, eds. P. Haasen er al. (Pergamon Press, Oxford) vol. 2, p. 1043.
STEFFENS, T. and Ch. SCHWINK, 1983, Acta Met. **31**, 2013.
STOLOFF, N.S., 1971, in: Strengthening Methods in Crystals, eds. A. Kelly and R.B. Nicholson (Elsevier, Amsterdam) p. 193.
STOLOFF, N.S., and R.G. DAVIES, 1966, Prog. Mater. Sci. **13**, 1.
SUMINO, K., 1958, Sci. Rep. RITU, **A10**, 283.
SUZUKI, H., 1979a, in: Strength of Metals and Alloys, eds. P. Haasen *et al.* (Pergamon Press, Oxford) vol. 3, 1595.

SUZUKI, H., and C.S. BARRETT, 1958, Acta Metall. **6**, 156.
SUZUKI, H., and K. NAKAMISHI, 1975, Trans. Japan. Inst. Met. **16**, 17.
SVITAK, J.J., and R.M. ASIMOW, 1969, Trans. AIME **245**, 209.
SWANN, P.R., 1963, in: Electron Microscopy and Strength of Crystals (Interscience, New York) p. 131.
TAKEUCHI, S., 1968, Scripta Metall. **2**, 481.
TAKEUCHI, S., and A.S. ARGON, 1976a, J. Mat. Sci. **11**, 1542.
TAKEUCHI, S., and A.S. ARGON, 1976b, Acta Metall. **24**, 861 and 883.
TAOKA, T., and S. SAKATA, 1957, Acta Metall. **5**, 61.
THIERINGER, H.M., 1962, Thesis Stuttgart; cf. MADER [1963].
THOMAS, G., J. NUTTING and P.B. HIRSCH, 1957, J. Inst. Met. **86**, 7.
THORNTON, P.R., and T.E. MITCHELL, 1962, Phil. Mag. **7**, 361.
TILLER, W.A., 1958, J. Appl. Phys. **29**, 611.
TRANCHANT, F., J. VERGNOL and J. GRILHÉ, 1988, Proc. ICSMA **8**, ed. P.O. Kettunen, T.K. Lepiste and M. E. Lehtonen (Pergamon Press, Oxford), p. 167.
TRAUB, H., H. NEUHÄUSER and Ch. SCHWINK, 1977, Acta Metall. **25**, 437 and 1289.
TYSON, W.R., 1968, Can. Met. Quart. **6**, 301.
VAN DEN BEUKEL, A., 1980, Acta Metall. **28**, 965.
VAN DEN BEUKEL, A. and U.F. KOCKS, 1982, Acta Met. **30**, 1027.
VANDERSHAEVE, G., and T. SARRAZIN, 1977, phys. stat. sol. (a) **43**, 459.
VANDERSHAEVE, G., and B. ESCAIG, 1983, Phil. Mag. **48**, 265.
VENABLES, J.A., 1961, Phil. Mag. **6**, 379.
VERGNOL, J., and J.P. VILLAIN, 1979, in: Strength of Metals and Alloys, eds. P. Haasen et al. (Pergamon Press, Oxford) vol. 3, p. 121.
VEYSSIÈRE, P., 1992, in: Ordered Intermetallics, eds. C.T. Liu *et al.* (Kluwer Publ., Dordrecht) p. 165.
VICTORIA, M.P., and A.E. VIDOZ, 1968, Phys. Stat. Sol. **28**, 131.
VIDOZ, A.E., 1968, Phys. Stat. Sol. **28**, 145.
VITEK, V., 1985, Dislocations and Properties of Real Materials (Inst. of Metals, London), p. 30.
WAGNER, R., 1979, in: Strength of Metals and Alloys, eds. P. Haasen *et al.* (Pergamon Press, Oxford) vol. 1, p. 645.
WALTON, D., L. SHEPARD and J.E. DORN, 1961, Trans. AIME **221**, 458.
WEERTMAN, J., 1955, J. Appl. Phys. **26**, 1213.
WEERTMAN, J., 1956, Trans. AIME **206**, 1409.
WEERTMAN, J., 1957, J. Appl. Phys. **28**, 1185.
WEERTMAN, J., 1977, Acta Metall. **25**, 1393.
WENDT, H., and R. WAGNER, 1982, Acta Metall. **30**, 1561.
WESTBROOK, J.H., 1977, Met. Trans. **A8**, 1327.
WHELAN, M.J., 1959, Proc. Roy. Soc. **A249**, 114.
WILLE, Th., and Ch. SCHWINK, 1980, Scripta Metall. **14**, 923.
WILLE, Th., B. WIELKE and Ch. SCHWINK, 1982, Scripta Metall. **16**, 561.
WILLE, Th., W. GIESECKE and Ch. SCHWINK, 1987, Acta Met. **35**, 2679.
WILSDORF, H.G., and J.T. FOURIE, 1956, Acta Metall. **4**, 271.
WOOD, D.L., and J.H. WESTBROOK, 1962, Trans. AIME **224**, 1024.
YAMAGUCHI, M., Y. UMAKOSHI and T. YAMANE, 1987, Phil. Mag. **55A**, 301.
YAMAGUCHI, M. and Y. UMAKOSHI, 1990, Progr. Mat. Sci, **34**, 1.
YOO, M.H., 1989, J. Mater. Res. **4**, 50.

Further reading

Blum, W., 1992, in: Mater. Sci. Techn., eds. R.W. Cahn *et al.* (VCH, Weinheim), vol. 6, p. 359.
Cottrell, A.H., Dislocations and Plastic Flow in Crystals (Clarendon, Oxford, 1953).
Escaig, B., in: Dislocation Dynamics, eds. A. Rosenfield et al. (McGraw–Hill, New York, 1968) p. 655.
Fleischer, R.L., in: The Strengthening of Metals, ed. D. Peckner (Reinhold, New York, 1964) p. 93.

Friedel, J., Les Dislocations (Gauthier–Villars, Paris, 1956) Engl. Transl.: Dislocations (Pergamon, Oxford, 1964).
Gerold, V., in: Dislocations in Solids, ed. F. R. N. Nabarro (North-Holland, Amsterdam, 1979) vol. 4, 215.
Gittus, J., Irradiation Effects in Crystalline Solids (Applied Sci. Publ., London, 1978).
Haasen, P., Physical Metallurgy (Springer Verlag/CUP Cambridge, 1974, 1978).
Haasen, P., in: Dislocations in Solids, ed. F. R. N. Nabarro (North-Holland, Amsterdam, 1979a) vol. 4, p. 155.
Kelly, A., in: Electron Microscopy and Strength of Crystals (Interscience New York, 1963) p. 947.
Kelly, A., and R. B. Nicholson, Prog. Mater. Sci. 10 (1963) 151.
Kimura, H., and R. Maddin, Quench-Hardening in Metals (North-Holland, Amsterdam, 1971).
Kocks, U. F., A. S. Argon and M. F. Ashby, Prog. Mater. Sci. 19 (1975) 1.
Marcinkowski, M. J., in: Order–Disorder Transformations in Solids, ed. H. Warlimont (Springer, Berlin, 1974) p. 365.
McLean, D., Met. Rev. 7 (1962) 481.
Nabarro, F. R. N., 1985, in Disloc. and Propert. Real Mater. (Inst. of Met., London), p. 152.
Nadgornyi, E., 1989, Progr. Mater. Sci. 31, 1.
Nembach, E. and G. Neite, 1985, Progr. Mater. Sci. 29, 177.
Neuhäuser, H. and C. Schwink, 1992, in: Mater. Sci. Techn., eds. R. W. Cahn *et al.* (VCH, Weinheim), vol. 6, p. 191.
Reppich, B., 1992, in: Mater. Sci. & Techn., eds. R. W. Cahn *et al.* (VCH, Weinheim), vol. 6, (ed. H. Mughrabi), p. 311.
Seeger, A., in: Dislocations and Mechanical Properties of Crystals, eds. J. C. Fisher et al. (Wiley, New York, 1957) p. 243.
Seeger, A., in: Encyclopedia of Physics, VII/2 (Springer, Berlin–Göttingen–Heidelberg, 1958) p. 1.
Suzuki, H., in: Dislocations and Mechanical Properties of Crystals, eds. J. C. Fisher et al. (Wiley, New York, 1957) p. 361; unpublished data.
Suzuki, H., in: Dislocations in Solids, ed. F. R. N. Nabarro (North Holland, Amsterdam, 1979b) vol. 4, p. 191.
Venables, J. A., in: Deformation Twinning, eds. R. E. Reed–Hill *et al.* (Gordon and Breach, New York, 1964) p. 77.

CHAPTER 24

MECHANICAL PROPERTIES OF INTERMETALLIC COMPOUNDS

DAVID P. POPE

University of Pennsylvania
Department of Materials Science & Engineering
Philadelphia, PA 19104–6272

R. W. Cahn and P. Haasen†, eds.
Physical Metallurgy; fourth, revised and enhanced edition

1. Introduction

Intermetallic compounds have been used over the millennia for various structural applications — see WESTBROOK [1993] for an excellent historical perspective on the subject — but it was the development of Ni-base superalloys for gas turbine applications that showed their true potential, especially for high temperature use. Ni-base superalloys are microstructurally very simple, even though they can be compositionally complex, consisting of a large volume fraction, up to 70%, of submicron-sized precipitates based on Ni_3Al, surrounded by a Ni-base solid solution as shown in fig. 1. These alloys are used at temperatures as high as 0.9 T_m (T_m = melting temperature), a remarkably high temperature compared to disordered metals (see ANTON [1995] for more information).

When it was realized that Ni_3Al (in alloyed form) is largely responsible for the excellent high-temperature properties of Ni-base superalloys, a search for other alloys began with great activity in the 1960s and again in the 1980s (see WESTBROOK [1993]). To see why this effort took place it is useful to compare the strength and plastic deformability of pure metals, intermetallic compounds, ceramics, and covalently bonded materials, as a function of homologous temperature, as shown in fig. 2 for Ni, NiAl,

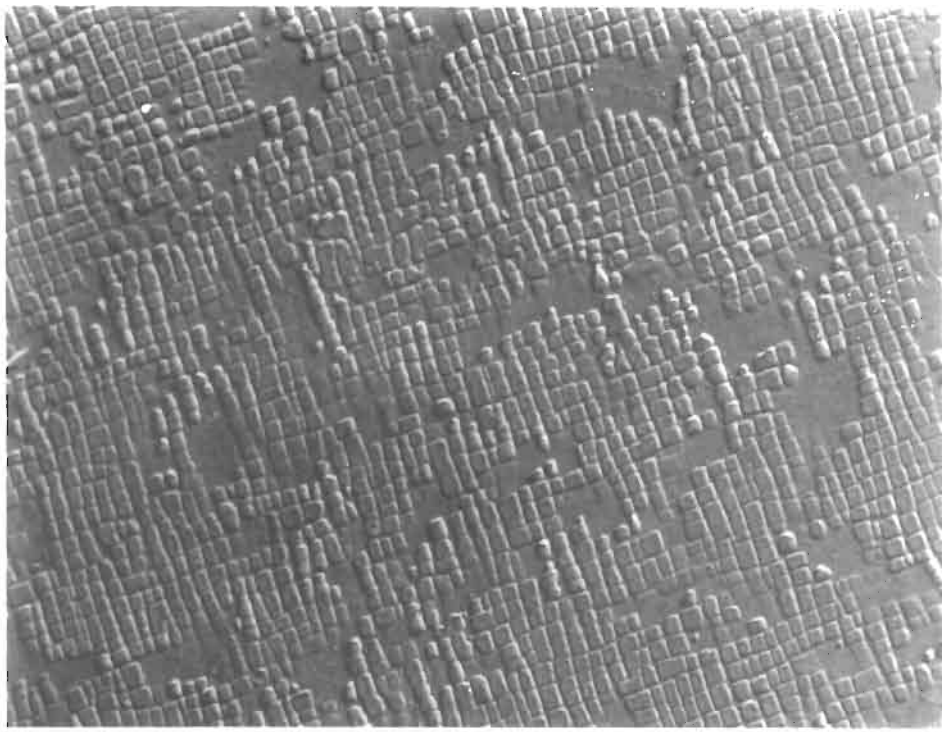

Fig. 1. Microstructure of MAR-M200, typical nickel-base superalloy containing a high volume fraction of γ', photographed from a replica (Courtesy Dr. D. M. Shah, Pratt and Whitney Aircraft Corp.)

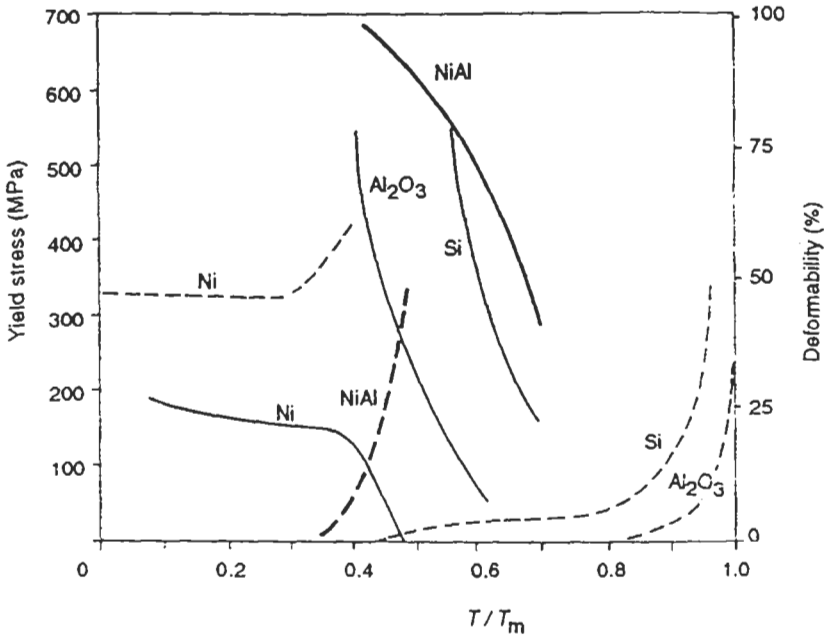

Fig. 2. Yield stress (——) and deformability (– – –) for various materials as a function of homologous temperature T/T_m (T_m = melting temperature) (from WESTBROOK [1965]).

Al_2O_3 and Si. Note that NiAl is significantly stronger than Al_2O_3, Si and Ni and that it softens and shows significant ductility at temperatures above approximately 0.5 T_m whereas Si and Al_2O_3 soften in a similar temperature range but show significant ductility only above about 0.8 T_m. Thus, intermetallic compounds have mechanical properties that are, in many ways, intermediate between those of disordered metals, on the one hand, and ceramics and covalently bonded materials, on the other. They tend to have higher strengths than metals but, at the same time, they also tend to have much lower ductilities. However, they are less brittle than ceramics. Problems associated with low ductility and/or fracture toughness have limited the applications of these alloys for structural uses.

Intermetallic compounds have a number of properties in addition to strength that make them intrinsically more appealing than disordered alloys for high-temperature use. First, and perhaps most important, as stated above, intermetallic compounds tend to be intrinsically very strong (high yield or fracture stress) and the strength tends to be maintained up to high temperatures. For example, the yield strength of NiAl at 0.5 T_m is dramatically above that of pure Ni, as shown in fig. 2. Other intermetallic compounds, many with the $L1_2$ structure, actually show an increasing yield strength with increasing temperature, e.g., Ni_3Al (FLINN [1960]). Not only is the strength of intermetallic compounds maintained to high temperatures, the modulus also tends to be high and tends to decrease more slowly with increasing temperature than does that of disordered alloys. For example, Ray *et al.* [1983] have compared the temperature dependence of Young's

modulus of an alloy based on Fe_3Al with that of an alloy based on a disordered Fe-base solid solution and shown that the modulus of the Fe_3Al-based alloy is the larger, by a substantial margin, between room temperature and about 800°C. Since stiffness is the controlling property for many applications, e.g., in systems subjected to vibrations, a high modulus is an important benefit.

In addition to having high strength and high stiffness, those compounds based on light elements, such as TiAl, can have extremely low densities. The low density combined with the high strength and modulus give rise to very attractive *specific* properties (property divided by density), which are especially important for rotating machinery and aerospace applications.

Because of the ordered structure, intermetallic compounds tend to have much lower self-diffusion coefficient than do disordered alloys. This can be demonstrated most clearly in those systems which show an order–disorder transition at a critical temperature, T_c, e.g., CuZn, which has the bcc-based B2 structure (GIRIFALCO [1973]). The slope of the log D vs. 1/T plot for both Cu and Zn shows a discontinuous increase as the temperature is reduced below T_c, see fig. 3, indicating that the activation energies for self-diffusion are much higher for the ordered than for the disordered alloy. As a result, the self-diffusion coefficients of an ordered alloy can be several orders of magnitude smaller than that of the disordered alloy at a given temperature. (This is most notably so in phases in which all nearest neighbors are unlike, such as CuZn). Slow rates of diffusion bring with them the attendant advantages of improved microstructural stability at elevated temperatures and, since the creep rate is proportional to the diffusion coefficient, improved creep strength. This was shown very dramatically by HERMAN and BROWN [1956] on β-brass where they showed that there is a discontinuous ten-fold drop in the creep rate when the material is cooled through T_c, see fig. 4.

Of course, the advantages of improved strength, modulus, density, microstructural stability and creep rate offered by intermetallic compounds do not come without attendant disadvantages. The single largest disadvantage is low ductility and/or toughness — most intermetallic compounds tend to be quite brittle, especially at low temperatures. For example, the NiAl referred to above as having a high strength up to 0.5 T_m is also relatively brittle up to that temperature and the ductility begins to increase only in the temperature range where the strength is rapidly decreasing. Also, the tensile ductility of Fe–Al alloys at room temperature goes almost to zero as the aluminum content is increased to 25 at.%, producing Fe_3Al (MARCINKOWSKI *et al.*, [1975]). In fact, a loss of ductility is commonly the first indication of the occurrence of significant volume fractions of an intermetallic compound in an alloy. For example, prior to the widespread availability of crystal growing facilities, small single crystals of Ni_3Al were produced by several investigators simply by cooling a large-grained polycrystalline sample to a low temperature, then breaking the sample along the grain boundaries with a sharp blow.

Most disordered alloys used for structural applications have either the fcc or bcc structure and only a very few have the hcp or other structures. In fact it is generally found that metals having the fcc and bcc structure are more ductile than those with more complex structures. So by analogy, it is perhaps not surprising that similar results have been found for intermetallic compounds. As a result, most studies have been performed

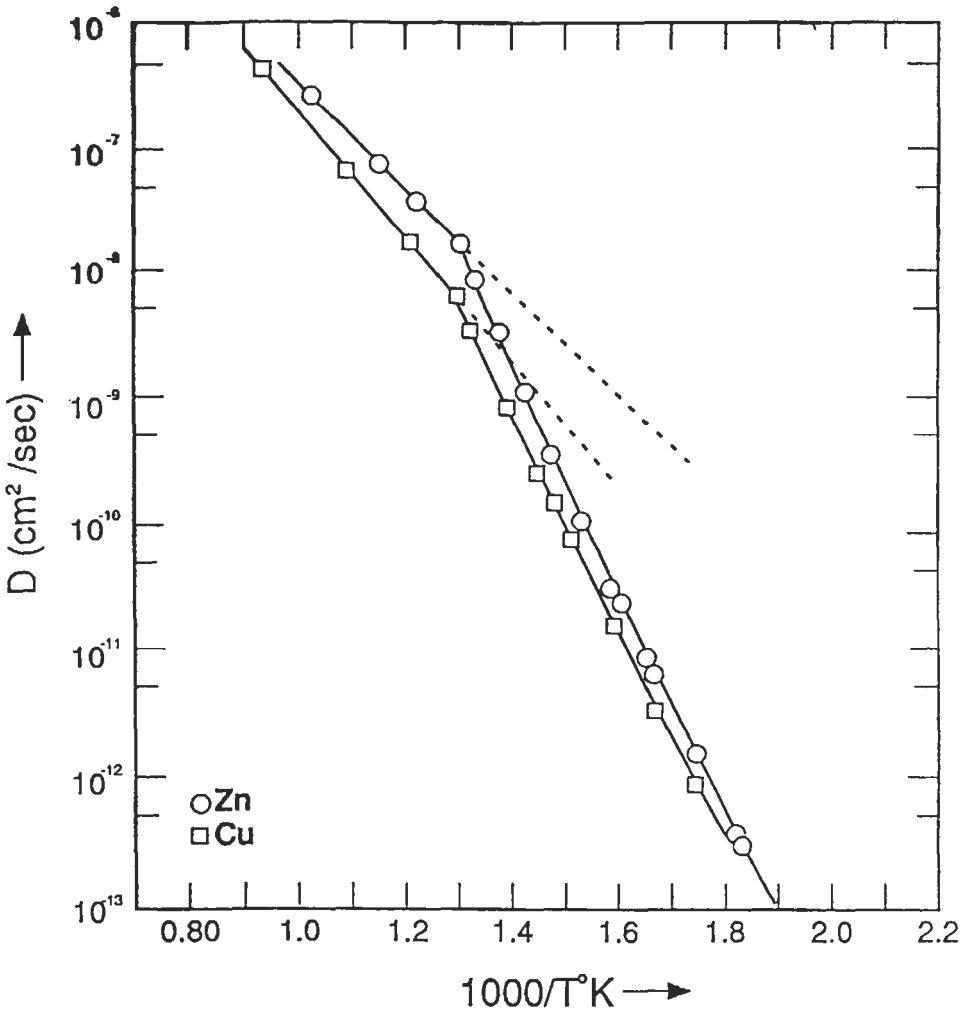

Fig. 3. Diffusion rates in ordered vs. disordered states of CuZn. KUPER *et al.* [1956].

on intermetallic compounds having fcc- or bcc-derivative structures. By far the most widely studied are those having the fcc derivative $L1_2$ structure with composition A_3B, in which A atoms occupy the face centers and B occupy the corners, fig. 5. Examples are Ni_3Al and Cu_3Au. The next most widely studied intermetallic compounds are those having the bcc-derivative B2 structure with composition AB, e.g., NiAl. A great deal is known about the mechanical properties of $L1_2$ and B2 alloys.

The amount of research devoted to intermetallic compounds having structures other than $L1_2$ and B2 is much smaller. For example, the work on hcp-derivative DO_{19} intermetallics (the composition is A_3B) is largely devoted to Ti_3Al and Mn_3Sn. If one

References: p. 2102.

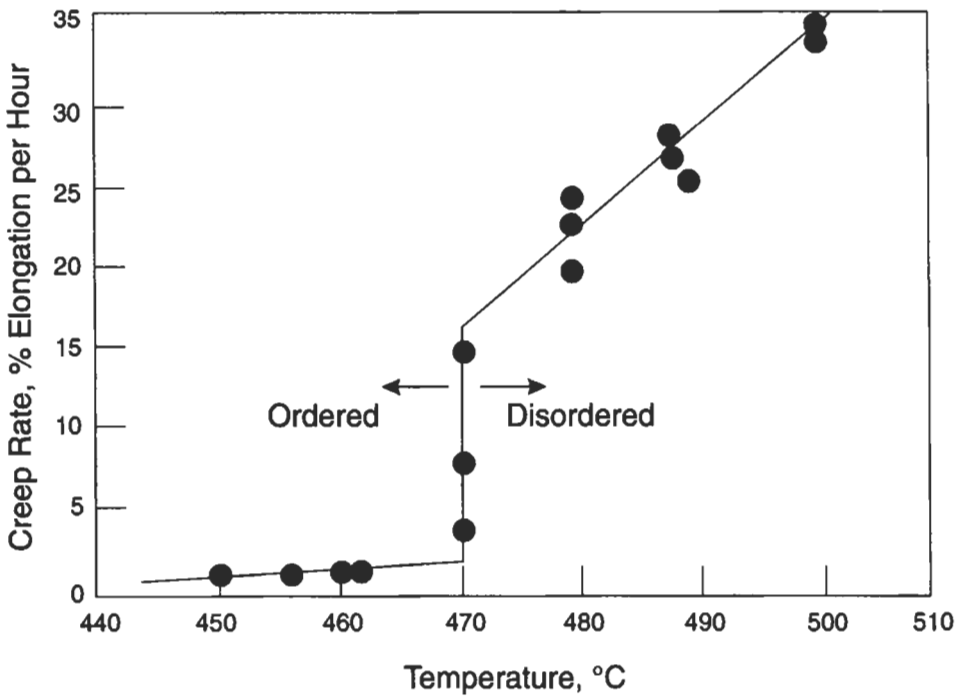

Fig. 4. Creep rate vs. temperature for β-brass. HERMAN and BROWN [1956].

now excludes all intermetallics with fcc-, bcc-, and hcp-derivative structures, the number of studies becomes relatively small. Two compounds in this category that have been widely studied are DO_{22} Al_3Ti and $L1_0$ TiAl. In this chapter, attention will be focused on three compounds: a material with the fcc-derivative $L1_2$ structure, Ni_3Al; the bcc-derivative B2 structure, NiAl; and the tetragonal $L1_0$ structure, TiAl. All are shown in fig. 5. A complete review of the mechanical properties of intermetallic compounds would fill an entire volume (has indeed filled several volumes, see "Further reading"), and therefore the scope of this chapter must be limited for lack of space. A full treatment would include a discussion of plasticity and deformation mechanisms, dislocation structure, alternative deformation modes, creep properties, toughness, fracture, environmental effects, and the relation between mechanical properties and microstructure, among others. Since plasticity is the basic property that links all these properties together, the focus of this chapter will be on dislocation plasticity, with emphasis on the relationship between dislocation core structures and plastic properties. The plastic behavior of Ni_3Al, NiAl and TiAl are discussed and the macroscopic flow behavior is related to the nature of the dislocation dissociation observed in these materials, on both the macroscopic and the atomistic level.

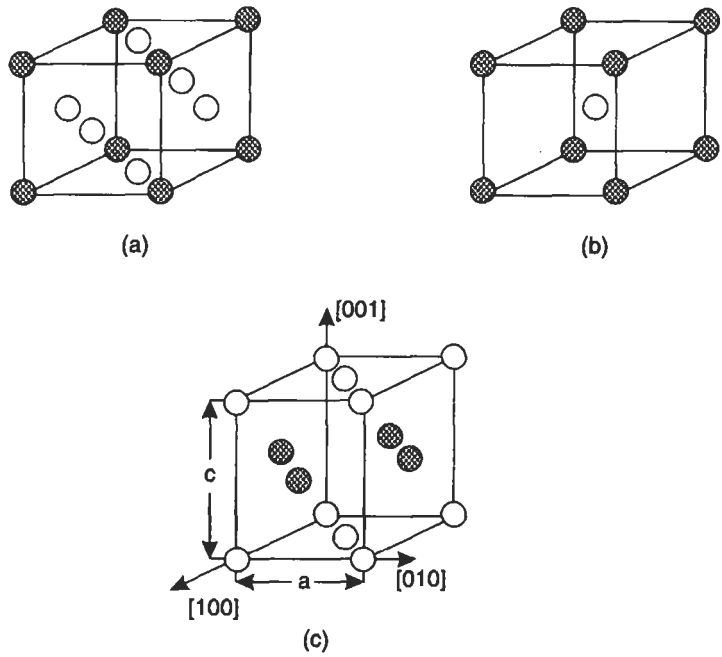

Fig. 5. Unit cells of (a) L12, (b) B2, and (c) $L1_0$ structures. The species are distinguished by shading.

2. *The superdislocation and planar faults*

The ordered structure of intermetallic compounds gives rise to the fact that the Burgers vector of a dislocation in such a compound can be quite long compared to that in disordered materials because the Burgers vector is, in general, not a nearest neighbor interatomic distance in intermetallic compounds. For example, in fcc materials it is 1/2[110], but in $L1_2$ materials it is [110], i.e., it is twice as long in $L1_2$ materials. Since the total elastic energy of a dislocation is proportional to the square of the total Burgers vector, the elastic energy is reduced if the dislocation dissociates into one or more partial dislocations separated by planar faults. The total dislocation in the superlattice is commonly referred to as a *superdislocation* because of the long Burgers vector, and the resulting partial dislocations are also commonly called *superpartials* or *partials*, depending on the magnitude of their Burgers vectors relative to that in the disordered alloy. The equilibrium dissociation is then determined by a balance between the reduction in elastic energy resulting from the dissociation and the increase in energy due to the creation of the faults. An example of such a dissociation is shown in fig. 6, where the fault is an *antiphase boundary* (APB) separating the two partial dislocations. It is called an antiphase boundary (or *antiphase domain boundary*) because the nearest neighbors are out of phase across the boundary, i.e., there are A–A and B–B bonds across the fault; but note that when the total dislocation glides, either to the right or left, the leading

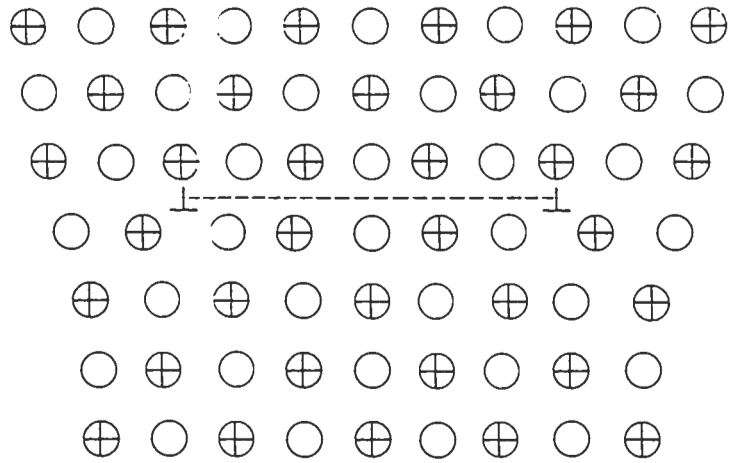

Fig. 6. Atomic arrangement in a cross-section through a superdislocation of edge orientation in a cubic primitive AB lattice. The dashed line represents an antiphase domain boundary (after BROWN [1960]).

superpartial creates such a fault while the trailing partial annihilates it.

These dissociations can be quite complex, as will be discussed later in this chapter, but consider the case of a $b=[01\bar{1}]$ dislocation on the (111) plane of an $L1_2$ material, e.g., Ni_3Al or Cu_3Au. As shown in fig. 7, this superdislocation can dissociate into two $b=\frac{1}{2}[01\bar{1}]$ partial dislocations separated by an APB. The partial dislocations can further dissociate into $\frac{1}{6}[112]$ and $\frac{1}{6}[121]$ Shockley partial dislocations separated by a fault similar to a stacking fault, but which also contains incorrect nearest neighbors, i.e., a "complex" stacking fault.

The extended superdislocation was first observed directly by transmission electron microscopy by Marcinkowski *et al.* [1961] in Cu_3Au (fig. 7) and Ni_3Mn. These authors

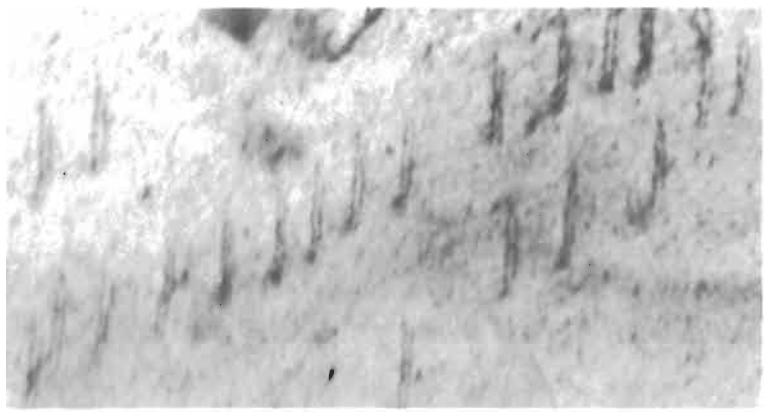

Fig. 7. Superdislocations in fully ordered Cu_3Au (from MARCINKOWSKI *et al.* [1961]).

calculated the widths of the superdislocations in these structures by a quasichemical, nearest- and next-nearest neighbor bond approach. Each superpartial dislocation is itself dissociated into Shockley partial dislocations separated by stacking faults. The widths r and r_1 (see fig. 8) are given by:

$$\left.\begin{aligned} r_1 &= \frac{\mu b^2}{2\pi\left(\gamma + \frac{1}{2}S^2\Gamma\right)} f_1(\theta) \\ r - r_1 &= \frac{\mu b^2}{2\pi\Gamma S^2} f(\theta) \end{aligned}\right\} \; r_1 \ll (r - r_1) \qquad (1)$$

where S is the long-range order parameter, $0 \leq S \leq 1$, Γ is the complex stacking fault energy and γ the antiphase boundary energy, f, f_1 are functions, of order of magnitude unity, of the angle θ where θ is –30° and 60° for edge and screw dislocations, respectively. For the edge dislocation in Cu_3Au and for $S = 1$, Marcinkowski *et al.* estimate r = 102 Å, $r_1 = 17$ Å from $\Gamma = 93$ mJ/m^2 and assuming $\gamma = 40$ mJ/m^2. From their observations, r = 95–130 Å (θ unknown).

The increased length of the Burgers vector in intermetallic compounds gives rise to two additional effects: (1) Complex dissociations of the total dislocation into several partial dislocations can occur, each separated from the other by a fault, such as an antiphase boundary (APB), superlattice intrinsic stacking fault (SISF), or a complex stacking fault (CSF) — as indeed is exemplified in fig. 8. (These concepts are discussed in detail in section 3.1 below). These faults will have low energies on only certain planes, and hence the number of slip systems may be limited, especially at low temperatures, resulting in brittleness at low temperatures. In addition, anisotropy of fault energies

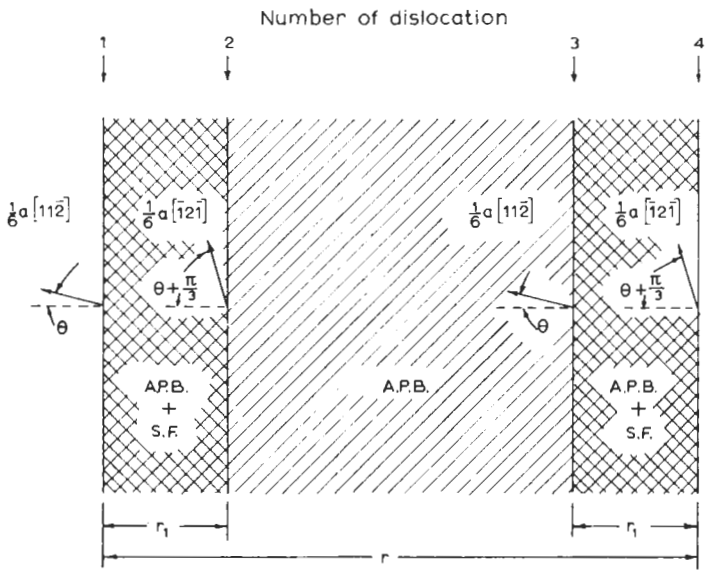

Fig. 8. Extended [011] superdislocation in its slip plane in Cu_3Au (from MARCINKOWSKI *et al.* [1961]).

References: p. 2102.

can give rise to complex cross-slip or dislocation core transformation phenomena, as is observed in Ni_3Al and (probably) in CuZn. In addition, these complex dissociations may also mean that the dislocation core is non-planar and hence lies on no one slip plane. When this occurs, the Peierls force (ch. 20, § 3.1) is high and dislocations can move only when the temperature is sufficiently high to provide the necessary thermal energy to nucleate double kinks on the dislocation (VITEK [1968]). As a result, the strength will be high (and commonly the ductility will be low) at low temperatures.

The planarity (or nonplanarity) of dislocation cores is an important factor in determining the Peierls force. If a $\frac{1}{2}[01\bar{1}]$ dislocation in an fcc material dissociates into two Shockley partial dislocations separated by a planar stacking fault on the (111) plane, then it is well known that such a dislocation is highly mobile. If one of the Shockley partials climbs out of the original glide plane, producing a non-planar dissociation, then the pair becomes sessile on the (111) plane, because the leading and trailing dislocations both create stacking fault as they move on the (111) plane. Computer simulations of dislocation motion using a variety of interatomic potentials to describe the bonding (e.g., VITEK [1975]) have shown that similar effects apply even when the partials are overlapping, i.e., the cores are not clearly separated and no clearly-defined fault is formed. In such cases, as shown by calculating the applied force necessary to move the dislocation at absolute zero, it is found that planar cores (dissociations in the slip plane) result in very low Peierls stresses, while nonplanar cores (dissociation out of the slip plane) result in high Peierls stresses. Thus, the planarity of dislocation cores in intermetallic compounds is an extremely important factor in determining the plastic behavior of intermetallic compounds, especially at low temperatures. Dissociations can occur in high-symmetry crystals in which the lowest energy dislocation configuration has a nonplanar core and therefore these dislocations will require a high resolved shear stress in order to move at low temperatures.

Perhaps the best known example of an intermetallic compound whose strength is apparently controlled by dislocation core transformations is Ni_3Al (POPE and EZZ [1984]) which is discussed in detail in section 3. In this material the APB energy on (111) planes (first-neighbor violations) is expected to be higher than on (010) planes (no first-neighbor violations). This difference in APB energy causes $\frac{1}{2}[101]$ screw dislocations to cross-slip from (111) planes, where they are mobile, to (010) planes where they are sessile. Since this process is thermally driven, the flow stress increases with increasing temperature, as was first observed by FLINN [1960], fig. 9. Since the rate of cross-slip is also affected by different components of the stress tensor, the critical resolved shear stress (CRSS) for $(111)[\bar{1}01]$ slip depends on the orientation *and sense* of the applied uniaxial stress, i.e., Schmid's law does not hold (PAIDAR, POPE and VITEK [1984]). A qualitatively similar orientation and temperature dependence of the CRSS for $(110)[\bar{1}11]$ slip is also observed in CuZn (UMAKOSHI *et al.*, [1976]), although no detailed analysis of this process has been performed for B2 materials.

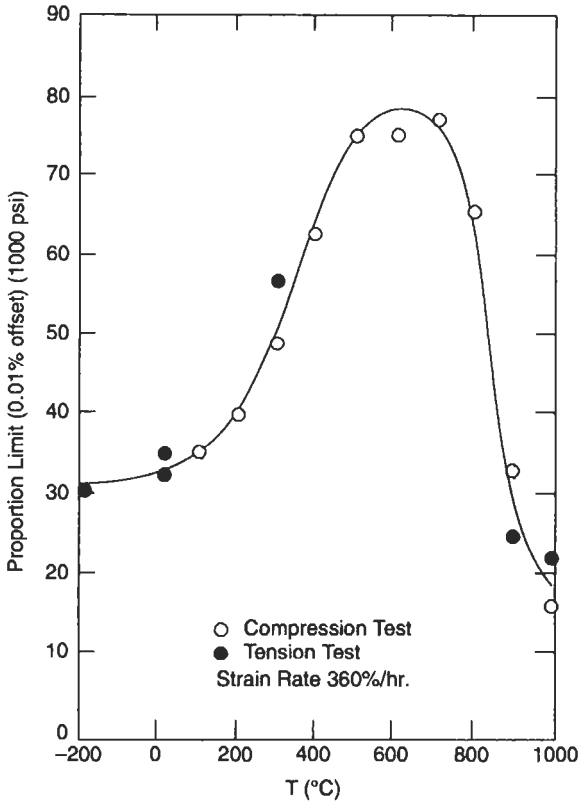

Fig. 9. Flow stress of polycrystalline Ni_3Al as function of temperature (FLINN [1960]).

3. *Plastic deformation of $L1_2$ materials: Ni_3Al*

In this section, we concentrate on the so-called *anomalous flow behavior* observed in Ni_3Al and in a number of other intermetallic compounds. However, since the behavior of Ni_3Al is very well documented compared to other materials, the examples will be chosen from Ni_3Al. (This subject has been recently discussed in much greater detail by VITEK *et al.* [1995]). The signature of the anomalous behavior is the increasing flow strength observed with increasing temperature, as shown in fig. 9. This behavior is *not* the result of a change in long-range order with temperature since the (Bragg) long-range order parameter, S, is almost constant in Ni_3Al up to 1000°C (POPE and GARIN [1977]).

There are situations where S does change substantially with temperature, leading to a change in flow strength, e.g., Cu_3Au. In this case, S decreases continuously from near 1 at low temperatures to about 0.8 at 390°C (where it then drops to zero), and the CRSS for $\{111\}\langle 101\rangle$ dislocation motion increases over the same temperature range (POPE [1973]). This behavior was modelled as solid-solution strengthening, where the matrix is

ordered Cu_3Au and the "solute" is disordered Cu and Au atom pairs which comprise the disorder. The moving dislocations are impeded by the "solute" through a modulus-type interaction, based on the fact that the shear modulus is a strong function of the long-range order parameter. Using these assumptions, the increase in the flow stress over the value at low temperatures should change with the "solute" concentration (i.e., the level of disorder) raised to some power, around ½–⅔, (ch. 23, § 2.4). The measured exponent is 0.61, giving quite good agreement with the model. These ideas also explain why the flow stress at room temperature of quenched, disordered Cu_3Au is higher, by a substantial margin, than that of ordered Cu_3Au.

Returning now to Ni_3Al, the important characteristics of the anomalous flow behavior in this material are:

1. The flow stress increases with temperature, reaches a maximum value at the "peak temperature", then decreases, see fig. 9.
2. The flow stress depends only on temperature, except for a small amount of work-hardening which occurs with each test (DAVIES and STOLOFF [1965]).
3. Slip occurs on the $\{111\}\langle 101\rangle$ system below the peak temperature and on the $\{001\}\langle 101\rangle$ system above the peak (STATON, BEVAN and RAWLINGS, [1975a,b]), except for [001]-oriented samples which continue to deform on $\{111\}\langle 101\rangle$ above the peak (UMAKOSHI *et al.*, [1984]).
4. The dislocation structure in samples deformed below the peak consists predominantly of long, straight screw dislocations with $b=\langle 101\rangle$, which are usually immobilized by Kear–Wilsdorf locks (KEAR and WILSDORF [1962]) due to cross-slip from $\{111\}$ to $\{010\}$ planes.
5. In the anomalous temperature regime, Schmid's Law does not apply, meaning that "non-glide" components of the stress tensor are involved. This is seen by a dependence of the CRSS for $\{111\}\langle 101\rangle$ slip on the orientation and sense of the applied stress (LALL *et al.* [1979]; EZZ *et al.* [1982]; UMAKOSHI *et al.*, [1984]), fig. 10.
6. The magnitude of the anomaly depends on the offset yield strain used in the experiment. It is fully developed at a plastic offset strain of 10^{-3}, but disappears at 10^{-6} to 10^{-5} (THORNTON *et al.* [1970]; MULFORD and POPE [1973]; EZZ and HIRSCH [1995]).
7. The strain-rate sensitivity is small (and positive) in the anomalous region and large (and positive) above the peak (e.g., UMAKOSHI *et al.* [1984]).
8. Most of these properties are also seen in Ni-base superalloys containing a high volume fraction of Ni_3Al.

We can conclude from #2 that work-hardening is not the cause of the anomaly because it is thermally reversible and, from #7, that diffusive mechanisms are not involved (since the strain-rate sensitivity is low). There is now near-universal agreement that the anomaly results from the special properties of screw dislocation cores and the anisotropy in APB energies in Ni_3Al (although there are still deep differences of opinion about the details of the interpretations, e.g., see VEYSSIÈRE and SAADA [1995]).

3.1. APBs, faults and dislocation cores in $L1_2$ materials

The stacking arrangement of (111) planes on the $L1_2$ structure is the same as that in

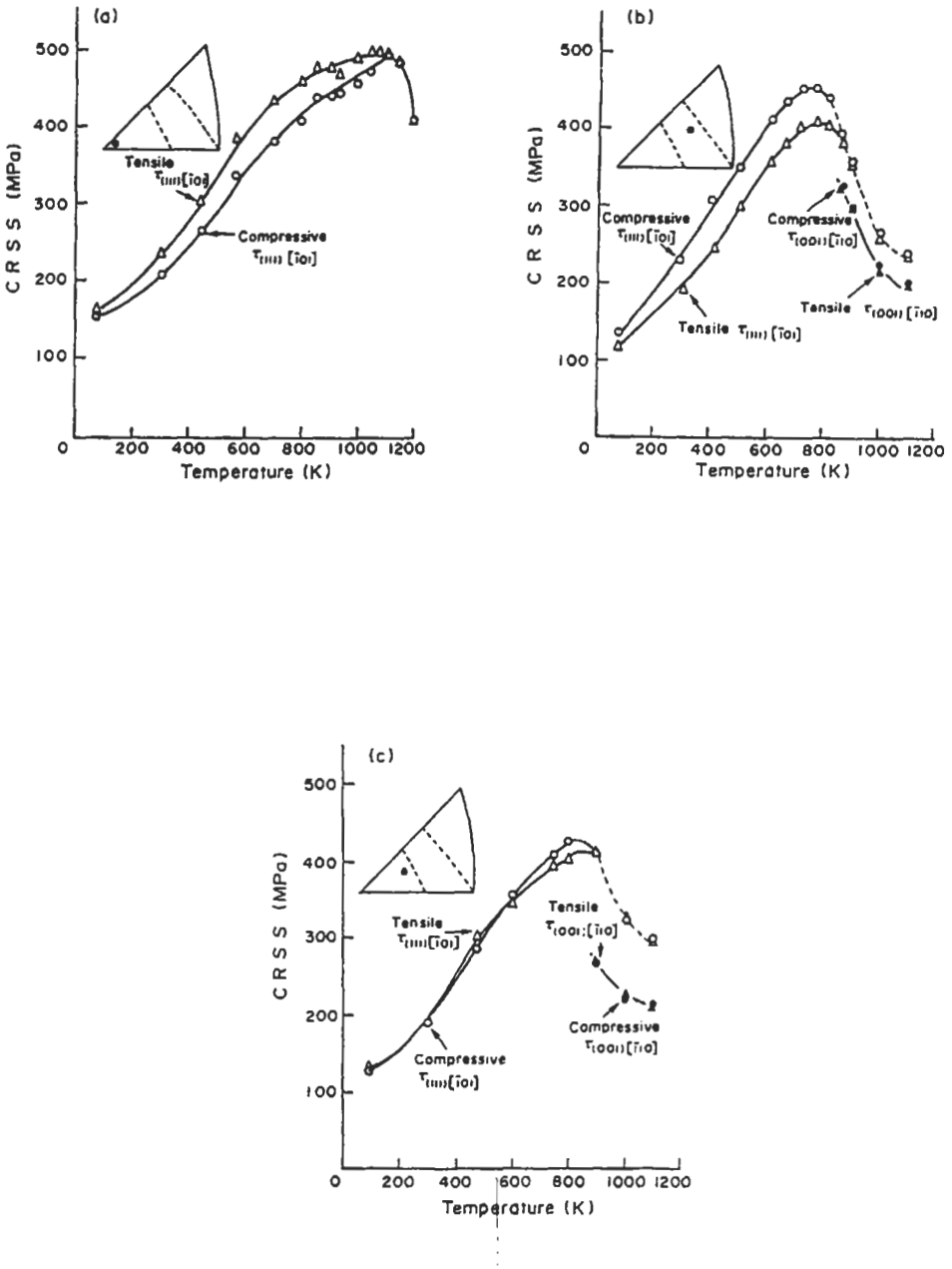

Fig. 10. (a)–(c) The temperature dependence of the CRSS for the (111)[$\bar{1}$10] slip measured in tension and compression at a strain rate of 6.5×10^{-3}/s (UMAKOSHI *et al.* [1984]).

References: p. 2102.

the fcc (abc, abc...) except for the fact that $L1_2$ contains two atomic species. This arrangement is shown in fig. 11 in which the size of the circles represent the layer and filled or unfilled circles represent the minority and majority species, respectively. (Note that all 12 nearest neighbors of the minority atoms are majority atoms.) Using this figure it is easily seen that there are three distinct faults that are formed by changing the stacking sequence: APB (b_A and b'_A); SISF, *superlattice intrinsic stacking faults* (b_s and b'_s); and CSF, *complex stacking fault* (b_c and b'_c). Faults with arbitrary fault vectors can be constructed by shifting one layer relative to its neighbor by an arbitrary amount.

The energies of these various faults have been calculated using the concept of the so-called γ-surface (VITEK [1968]). A fault with a given displacement vector is created, the energy of the fault is calculated on the basis of a set of interatomic potentials, and the energy is then plotted as a function of fault vector (see, for instance, YAMAGUCHI *et al.* [1981a,b]). Maxima correspond to unstable faults and minima correspond to metastable faults. It has been found, on the basis of the results of the calculations and crystal symmetry arguments, that the SISF is always metastable, but the stability (and precise fault vector) for the APB and CSF depend upon the details of the interatomic potentials employed. For some potentials the APB can be metastable while the CSF is not, or they can both be unstable, e.g., TICHY, VITEK and POPE [1986]; VITEK *et al.* [1991]. The possibilities for faults on {010} planes are much more limited. Only APBs with fault vectors of $\frac{1}{2}\langle 101\rangle$ are metastable on {010}. All others are unstable.

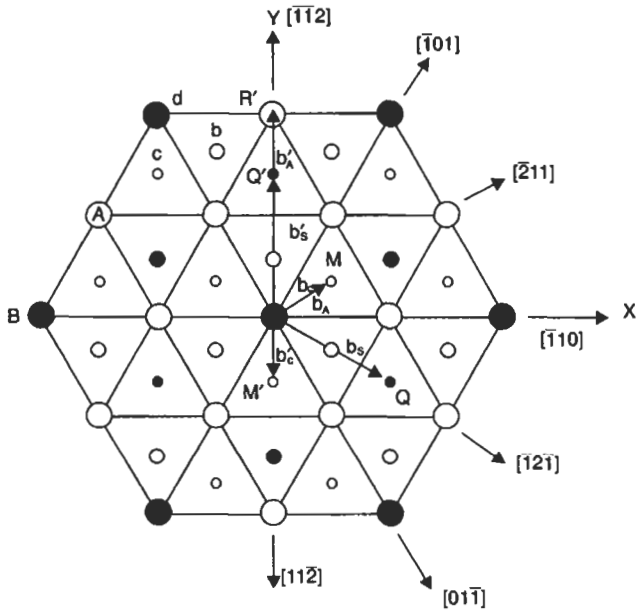

Fig. 11. The atomic arrangement on the (111) plane in an A_3B compound with the $L1_2$ structure. The a, b, and c layers are stacked in the sequence abcabc... representing an $L1_2$ lattice.

Given the fact that the SISF with fault vector $\frac{1}{3}[\bar{1}\,\bar{1}2]$ is always metastable, a dissociation on (111) planes with SISF according to

$$[\bar{1}01] \rightarrow \tfrac{1}{3}[\bar{2}11] + \tfrac{1}{3}[\bar{1}\,\bar{1}2] \tag{2}$$

is always possible. This will occur if the APB on (111) planes has a very high energy (or is unstable). If the APB energy is not too high, then a dissociation with APB according to

$$[\bar{1}01] \rightarrow \tfrac{1}{2}[\bar{1}01] + \tfrac{1}{2}[\bar{1}01] \tag{3}$$

is possible and, furthermore, the individual $\frac{1}{2}[101]$ partials can dissociate into Shockley partials, $\frac{1}{6}[\bar{1}\,\bar{1}2] + \frac{1}{6}[\bar{2}11]$, separated by CSF. On {010} planes only the dissociation according to equation (3) is possible.

Dislocation core configurations have been modelled using both central force and many-body potentials, as with the calculations of the γ-surfaces. The differences between the core structures, based on the two kinds of potentials, are fairly small. Two limiting cases are of interest: (1) The APB and the CSF are both metastable on the (111) plane and (2) the APB is metastable, but has high energy, and the CSF is unstable.

In case 1 the $\frac{1}{2}[\bar{1}01]$ dislocations dissociate as shown in figs. 12a and b, i.e., a planar or non-planar core is possible for dissociation on (111) planes, but a non-planar core is always seen for dissociation on (010) planes, figs. 12c and d. Thus, the screw dislocation has at least one glissile configuration on (111) *but it is always sessile on* (010). For case 2, dissociation occurs according to equation (2), that is, with SISF separating the superpartials. In this case, the cores of the $\frac{1}{3}\langle 112\rangle$ dislocation are always highly nonplanar and therefore motion is difficult at low temperatures.

From these simulations, it is concluded that dislocations dissociated according to equation (3) can be glissile when dissociated on (111) planes, fig. 12a, but they can reduce their energy by dissociating on (010) planes (figs. 12c and d) and then become sessile. Thus, the glissile configuration on (111) planes is metastable relative to the sessile configuration on (010) planes, and *this difference is the essence of the so-called core dissociation or cross-slip models of the yield anomaly.*

4. *The yield anomaly: models*

In both the TAKEUCHI and KURAMOTO [1973] model and the later PAIDAR, POPE and VITEK [1984] model (PPV), it is assumed that the transition from the configuration of fig. 12a to that of 12c or 12d is a thermally and stress-activated process that occurs *locally*, creating short sessile segments on the otherwise glissile dislocation. Thus, as the temperature increases, the probability of producing pinning points by local cross-slip increases (higher density of cross-slipped segments) and therefore the CRSS for $\langle 101\rangle\{111\}$ slip increases. Furthermore, any components of the stress tensor that drive the transformation (for example, by pushing the dislocation onto the (010) plane, or by easing the transition by contracting the core on the (111) plane or expanding it on the $(1\bar{1}1)$ plane) are expected to increase the cross-slip pinning rate. Note that this rate is a

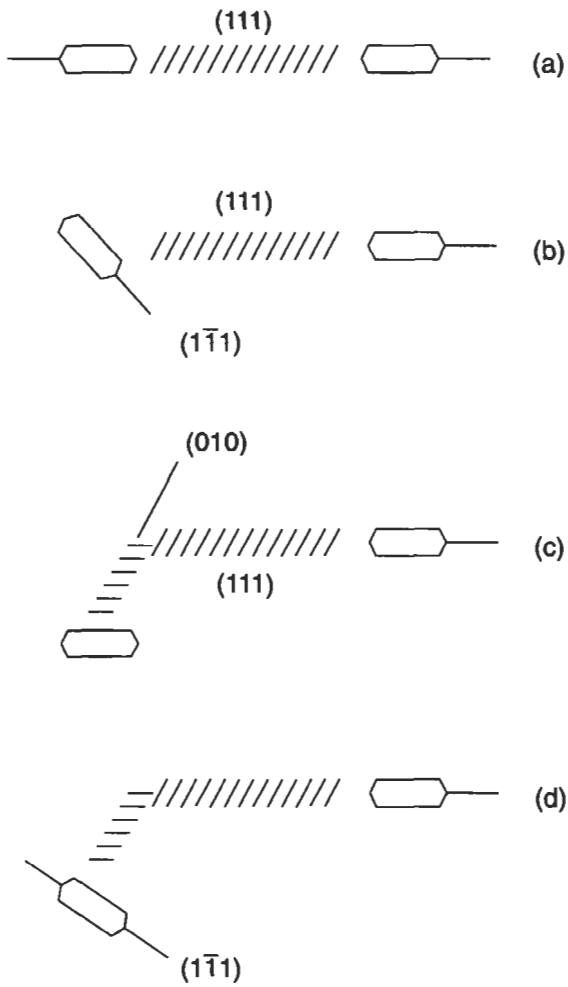

Fig. 12. Partial dislocation cores in the $L1_2$ structure represented schematically by pill-boxes, indicating that the cores have a planar dissociation, but the total dislocation may or may not be planar, depending on the situation. (a,b) A pair of $\frac{1}{2}[\bar{1}01]$ screw superpartials with planar cores separated by APB on (111). (c) The configuration in (a) after cross-slip of the leading partial onto (010) and redissociation on (111). (d) As (b), but with redissociation on $(\bar{1}11)$. Thus, the total dissociation in (a) is planar and glissile, but the others are nonplanar and are therefore sessile.

function only of the temperature and the stress state. (The details of the models are described and compared by VITEK *et al.* [1995].

The model predicts that the CRSS for $(111)[\bar{1}01]$ slip should increase as the tensile or compressive axis moves away from [001] in the standard unit triangle and that there should be a distinct difference between the tensile and compressive CRSS, depending upon orientation. The tensile value should exceed the compressive near [001] and the

opposite should arise on the other side of the unit triangle, the two being equal at some intermediate orientation. This has been observed in a number of studies, e.g., EZZ *et al.* [1982]; UMAKOSHI *et al.* [1984] (see fig. 10).

There have been numerous recent additions and improvements to the models, (e.g., VITEK *et al.* [1995]), but the essence of the model remains unchanged, viz.: the core structure of the dislocations determine the stress- and temperature-response, including the anomalies in the flow behavior. Finally, it should again be noted that there is not yet unanimity about the details of this process: see VEYSSIÈRE and SAADA [1995] for an opposing point of view, even though there is unanimity that core structure plays the dominant role.

5. *Plasticity of NiAl*

NiAl, which is light and very oxidation-resistant, has become one of the most promising candidates for application in the hot sections of gas turbine engines (e.g., see MIRACLE and DAROLIA [1995] and DAROLIA [1993]), and is currently the subject of active alloy development at the General Electric Corporation for use in precipitation-hardened single-crystalline form.

The crystal structure of NiAl is the bcc-derivative B2 structure (fig. 5b) for which the most likely slip vectors are ⟨100⟩, ⟨110⟩ or ⟨111⟩. The predominant slip modes are ⟨001⟩{100} and ⟨001⟩{110}, but ⟨110⟩ and ⟨111⟩ slip are also observed, depending on the orientation and temperature. This material shows a very low ductility at low temperatures which appears to be related to an intrinsically low dislocation mobility. Since the dominant slip vector is ⟨001⟩ and this slip vector is not activated by a uniaxial stress applied along ⟨001⟩, this (cube) orientation is called the "hard" orientation and others are called "soft". It is the hard orientation that is being considered for technological use and this orientation also shows the lowest tensile ductility.

Soft orientation crystals show a CRSS vs. temperature plot as shown in fig. 13(a) where the CRSS for ⟨100⟩ slip is plotted and the slip plane is the {001} or {110} plane with the highest RSS. ({110} is the most common slip plane, but {100} slip planes are observed for certain orientations and temperatures). Note the dramatic increase in CRSS at low temperature, which indicates a very high Peierls stress and therefore a nonplanar core. Note also that, unlike the case for Ni_3Al, there is considerable scatter in the reported values of the CRSS, which probably relates to slight compositional differences.

Hard-orientation crystals show a CRSS-temperature dependence as shown in fig. 13b. Two slip systems are observed: ⟨111⟩{112} below about 600 K and ⟨110⟩{110} above 600 K. The stress required for deformation is much higher than for the soft-oriented crystals, and the tensile ductility is very low, typically near zero at temperatures below 600 K, but it increases rapidly with increasing temperature.

Given the potential utility of NiAl, a great deal of effort has gone into attempting to understand why the observed slip systems operate and how ⟨111⟩ slip might be induced more readily so that the ductility at low temperatures might be increased. Two important factors are involved in this: (1), as in the case of Ni_3Al, core structure is important, but

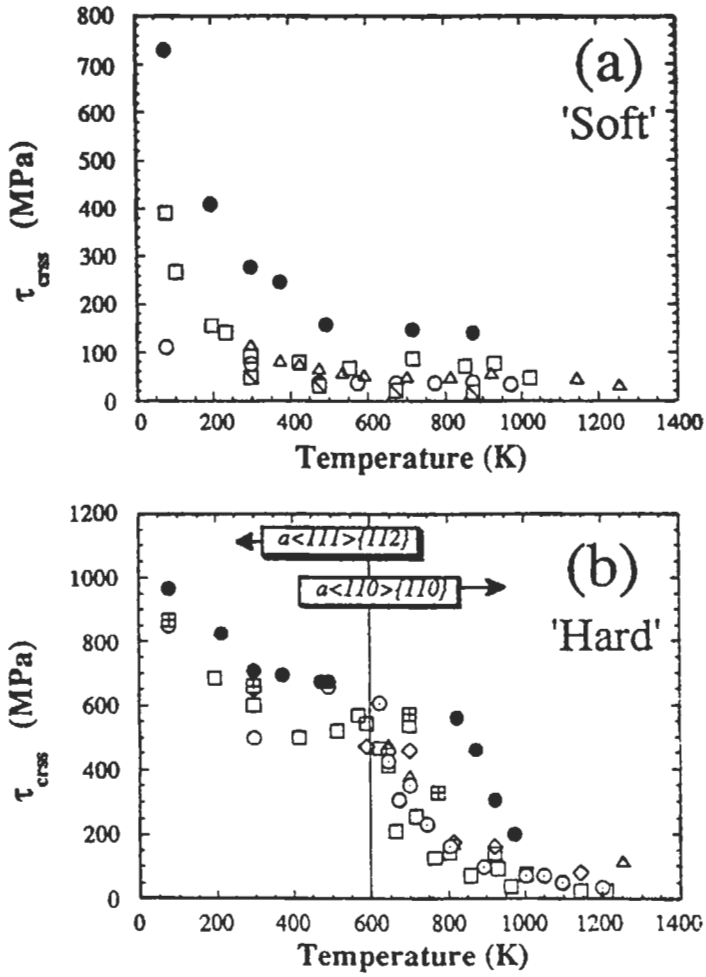

Fig. 13. NiAl: the critical resolved shear stress for (a) a<100> slip in "soft" crystals, (b) a<111>{112} and a⟨110⟩{110} slip in "hard" crystals. Plot from MIRACLE [1993].

since NiAl is elastically highly anisotropic, (2), the (line) energy of dislocations as a function of orientation is also very important. Considering line energy first, it is found that [100] dislocations always have a lower energy than [110] or [111] dislocations (e.g., MIRACLE [1993]) and edge dislocation always have lower energies than screw dislocations. (Since screw dislocations are probably elastically unstable, models that relate to the special properties of screw dislocations must be viewed with caution).

Given the high relative energy of undissociated ⟨111⟩ dislocations, a great deal of attention has been focused on reducing the APB energy on {111} and {112} planes so that dissociation might occur and slip be initiated at a lower CRSS. As discussed by

MIRACLE [1993], many calculations have been performed using a variety of techniques and interatomic potentials. The values obtained vary widely, from 240 to 900 mJ/m^2, and some calculations suggest that the APB energy can be reduced by alloying, most significantly by chromium (HONG and FREEMAN [1991]). Unfortunately, the amounts of chromium required far exceed the solid solubility in NiAl, and thus, little or no increase in ⟨111⟩ slip results from chromium or any other addition.

Calculations of dislocation core structures have shown that behavior inferred from these core structures does coincide with the observed experimental results. Recent calculations by a number of investigators MILLS *et al.* [1993]; PARTHASARATHY *et al.* [1993]; XIE *et al.* [1993]; and PASIANOT *et al.* [1994]) using embedded atom potentials have shown that ⟨100⟩ screw dislocations are spread on {110} planes, which is the observed preferred slip plane. However, as discussed above, screw dislocations are probably elastically unstable and therefore the cores of edge dislocations are probably the most important. Edge dislocations with ⟨001⟩ slip vectors on {110} planes were found to have planar cores while those on {100} planes were found to be nonplanar — the cores are spread on two (110} planes. This is in qualitative agreement with experiment, i.e., {110} slip is preferred over {100}. Atomistic calculations of ⟨001⟩ dislocation motion on {110} and {100} are in agreement with these observations (PARTHASARATHY *et al.* [1993]). These authors also showed that ⟨110⟩ dislocations are nonplanar and have a Peierls stress considerably higher than that for ⟨001⟩ dislocations, again consistent with experimental results.

In summary, plastic deformation is much more difficult to achieve in NiAl than in Ni_3Al and there is much less complexity in the flow behavior or NiAl. Attempts to increase the amounts of ⟨111⟩ slip have been largely unsuccessful, and it is believed that this is due to the high energy of $\frac{1}{2}$⟨111⟩ APBs on {110} planes. Nonetheless, dislocation core structure calculations have been an important part of our attempts to understand this important material.

6. *TiAl*

There have been relatively few studies of materials having the $L1_0$ structure (for reviews see YAMAGUCHI [1990], HUANG and CHESTNUTT [1995], YAMAGUCHI and INUI [1993]). However, it has been receiving much more attention in recent years because TiAl has this structure, and it is a very attractive material for lightweight structural applications at elevated temperature owing to its low density and good oxidation resistance. In the following discussion, the unit cell, shown in fig. 5, the *c*-axis being the tetragonal axis, will be used. Owing to the tetragonality of the $L1_0$ structure, the crystals can deform by glide of either ordinary or super-dislocations. A representative (111) plane of the $L1_0$ structure is shown in fig. 14 to illustrate this point. For this plane, slip along $[1\bar{0}1]$ or $[0\bar{1}1]$ requires super-dislocations but slip along [110] requires only ordinary dislocations.

KAWABATA *et al.* [1985, 1988] prepared single crystals of Ti–56 at% Al and measured the CRSS as a function of temperature and crystallographic orientation. They

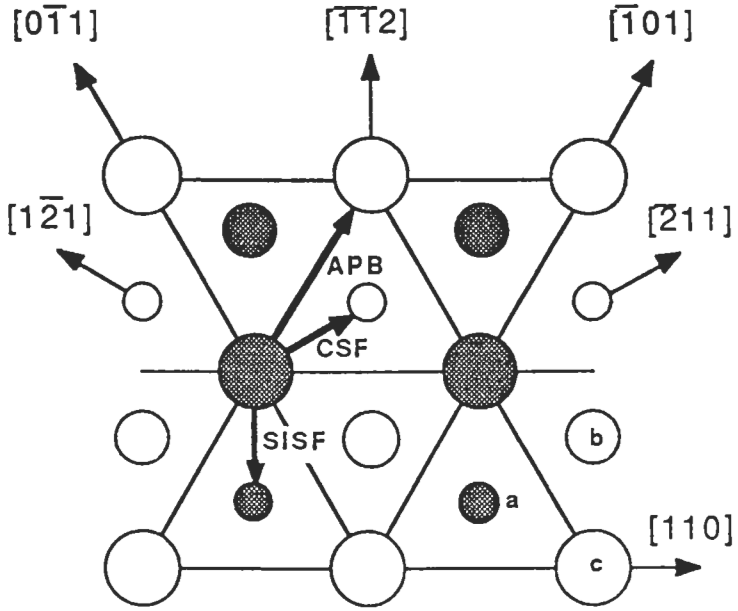

Fig. 14. The atomic arrangement on the (111) and fault vectors of the APB, CSF and SISF in the $L1_0$ structure. The species are distinguished by shading and the layers labelled a, b and c (and distinguished by the size of the circles) define the abcabc... stacking of the (111) planes.

found that, similarly as in Ni_3Al, the flow stress increases with increasing temperature, attains a peak, and then rapidly drops at higher temperatures for both $a/2\langle 110]$ (ordinary dislocations) and $a\langle 011]$ (super-dislocations) slip. It has been suggested that the origin of this behavior lies in the special features of the cores of screw dislocations, similarly as in the case of the $L1_2$ compounds (KAWABATA *et al.* [1991]). However, work by STUCKE *et al.* [1993] has cast doubt on the interpretation that this effect has an origin similar to that observed for Ni_3Al, since the flow stress anomaly is *not* thermally reversible, that is, the flow stress is not just a function of temperature, but also depends on the test sequence. For example, if the flow stress is measured sequentially on one sample at a low, then high, then low temperature, the values obtained at the two low temperatures are very different. Mechanical twinning has not been observed in macroscopic single crystals at low temperatures, but it has recently been seen in specially prepared, low-Al single crystals, see below.

6.1. Two-phase $L1_0/DO_{19}$ material: Ti-rich TiAl

In this section the plastic behavior of two-phase $TiAl/Ti_3Al$ alloys is discussed. (Ti_3Al is a hcp-derived phase with the DO_{19} structure). These alloys exhibit some remarkable properties which are unlike those of either constituent. For example, both phases separately show an anomalous temperature dependence of the CRSS for certain

slip systems, yet no anomalous flow behavior has yet been observed in polycrystalline two-phase alloys. Also, both phases are quite brittle, but the lamellar two-phase alloy can be quite tough, a fact that is probably related to interfacial processes in the lamellar microstructure. Furthermore, single-phase TiAl deforms plastically by dislocation motion yet TiAl in the $TiAl/Ti_3Al$ composite deforms mostly by twinning.

Practical application of TiAl has been hampered by low toughness and/or ductility, difficulties recognized at the time of the earliest reported systematic studies of Ti–Al alloys (SASTRY *et al.* [1977]; SHECHTMAN *et al.* [1974]; LIPSITT *et al.* 1975]). Recent studies of Ti–Al alloys of different compositions subjected to different heat-treatments have been more encouraging.

6.2. Crystal structure and phase equilibria

The currently-accepted TiAl phase diagram for alloys with compositions near TiAl is shown in fig. 15 (MCCULLOUGH *et al.* [1989]). The details of the phase transformations which occur during cooling or isothermal aging of different alloys have been discussed in detail by KIM [1989] and KIM and FROES [1990]. The following is a very brief summary. Binary alloys with approximately 52 at% Al, or more, can be produced as

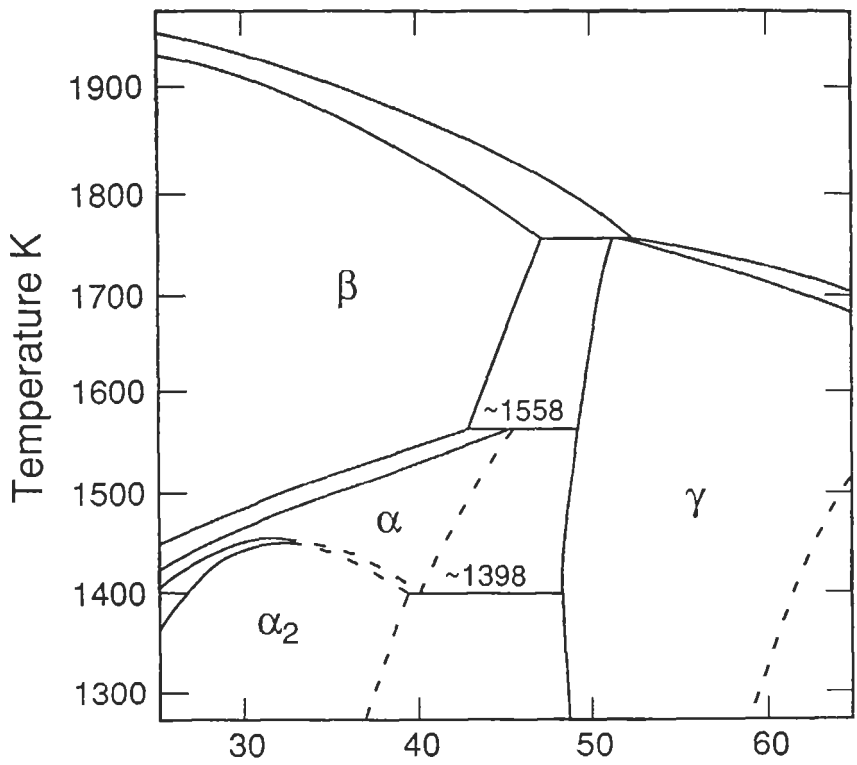

Fig. 15. The TiAl phase diagram (MCCULLOUGH *et al.* [1989]).

References: p. 2102.

single-phase TiAl but single crystals have been produced only with at least 54 at% Al. TiAl has the $L1_0$ crystal structure shown in fig. 5c which consists of layers of Al and Ti atoms on alternate (001) planes. (In this discussion the c-axis of TiAl will always be the [001] direction.) The c/a ratio is 1.02 at the stoichiometric composition and increases to 1.03 at Al-rich compositions [BUMPS *et al.* [1952]); DUWEZ and TAYLOR [1952]); HUANG *et al.* [1987]). Thus the structure can be considered to be an fcc-derivative structure with a nearly-cubic unit cell.

Alloys containing less than approximately 52 at% Al tend to have lamellar microstructures in the as-cast form, consisting of layers of Ti_3Al and layers of twin-related TiAl. The interfacial relationship between the two phases is: $(111)\gamma//(0001)\alpha_2$ and $[110]\gamma//\langle 11\bar{2}0\rangle\alpha_2$. (The Miller indices of the DO_{19} phase are referred to the underlying hcp lattice for simplicity). In the following, γ is the TiAl with the L_0 structure, α is disordered Ti_3Al with the hcp structure and α_2 is Ti_3Al with the DO_{19} structure. This lamellar structure forms as a result of the peritectoid reaction at approximately 1558°C and the subsequent $\alpha \rightarrow \gamma$ transformation which occurs during cooling. The twin-related layers of TiAl form, it is believed, as a result of the $\alpha \rightarrow \gamma$ transformation. The (0001) plane of α_2 has three crystallographically equivalent $\langle 11\bar{2}0\rangle$ directions which are coincident with three different $\langle 110]$ or $\langle 101]$ directions of the matching $\{111\}$ plane of TiAl. (Here, the symbol $\langle 101]$ refers to [101] and [011], but *not* [110] with negatives, and similarly for the planes.) The dissolution of an α_2 layer between two γ layers, induced by cooling into the single-phase field, can produce six different kinds of γ/γ interfaces (see YAMADA *et al.* [1990] and YAMAGUCHI [1990] for a complete discussion of this point). Thus the final microstructure consists of alternate layers of α_2 and γ, but the γ layers also have different orientations relative to each other. Of the six different orientation possibilities, one is a true ordered twin.

6.3. Ti-rich single crystals

If a polycrystalline bar of Ti-rich TiAl is directionally zone-melted and solidified, a lamellar "single crystal" is produced in which all the lamellae are parallel to each other, but not necessarily parallel to the growth direction (FUJIWARA *et al.* [1990]). These "crystals" which actually contain two parallel plate-like phases, $(\alpha_2+\gamma)$, along with multiply oriented (but parallel) γ plates, have been termed by Yamaguchi *polysynthetically twinned* (PST) crystals, adopting terminology borrowed from mineralogy.

The deformation of these crystals occurs by several different processes. The "easy mode" of deformation at room temperature occurs mostly by twinning in the γ platelets on (111) planes parallel to the α_2/γ interface, along with some $(111)\langle\bar{1}10]$ slip, i.e., by glide of ordinary dislocations on the same planes. Such deformation occurs in crystals in which the α_2/γ interface is inclined to the uniaxial stress axis and in which there is, therefore, a resolved shear stress (RSS) on the interfacial planes. When the interface is either parallel or perpendicular to the uniaxial stress axis, the RSS on these planes is zero and therefore other deformation modes are required, modes which require transfer of slip across the α_2/γ interface. A plot of the uniaxial flow stress of a PST crystal as a function of orientation is shown in fig. 16. In this figure, ϕ is the angle between the

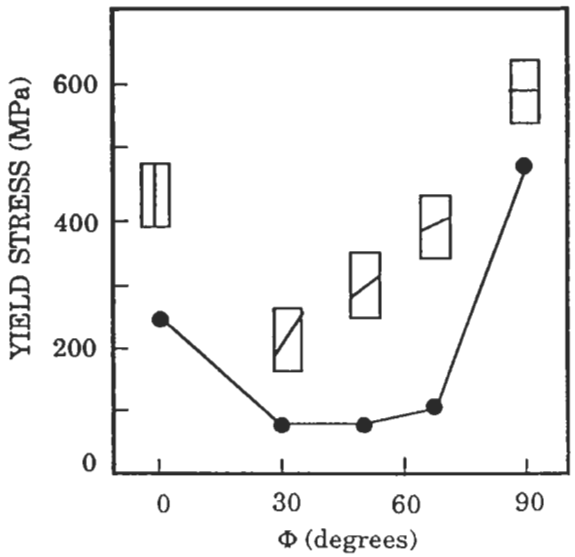

Fig. 16. Yield stress of TiAl PST crystals as a function of angle between compression axis and the lamellar interfaces (FUJIWARA *et al.* [1990]).

compressive axis and the interfacial plane. Note that the uniaxial flow stress is low for intermediate values of ϕ but higher for ϕ near 0 or 90°; it is a maximum for $\phi = 90°$. Also the flow stress for intermediate values of ϕ is substantially lower than that for Al-rich single crystals (comparing both at room temperature and for easy slip). This suggests that twinning in the Ti-rich alloys occurs at a lower CRSS than slip in the Al-rich alloys.

When ϕ is near 0 or 90°, fig. 16, slip must cross the α_2/γ interface, thereby requiring twinning of the γ on planes which are not parallel to the interface *and* slip in the α_2 phase (for other orientations the α_2 does not deform in PST crystals). These crystals tend to be not only strong, but also quite brittle, with a cleavage-like failure parallel to the α_2/γ interfaces occurring at or near yield (YAMAGUCHI and INUI [1993]). It is not yet known whether the failure occurs at the interfaces, but on the basis of indirect results this appears unlikely. Crystals of intermediate orientations can be deformed by as much as 20% in tension before failure, but the final fracture mode is the same as that for $\phi = 0$ and 90°. Furthermore, even after such large plastic deformations the final failure is sudden and macroscopically brittle, without local necking or large local plastic flow in the vicinity of the failure.

The flow properties of the PST crystals are different for $\phi = 0$ and 90° because of the different slip systems required in the α_2 phase. For $\phi = 90°$ slip must occur on a pyramidal system, whereas for $\phi = 0°$, slip can occur on the prismatic system (UMAGUCHI *et al.* [1992]). Recent results on the flow properties of single crystalline Ti_3Al show that prismatic slip by $\langle 11\bar{2}0\rangle$ dislocations occurs at a much lower CRSS than does pyramidal slip on the $(11\bar{2}1)$ $\langle\bar{1}\,\bar{1}26\rangle$ system (MINONISHI and YOO [1990]; MINONISHI *et al.* [1991];

UMAKOSHI *et al.* [1991]). Thus, deformation occurs by twinning and slip in the γ phase for all ϕ, but only for ϕ near 0° and 90° does deformation occur in the α_2 phase, on the prismatic system for ϕ near 0° and on the pyramidal for ϕ near 90°.

In summary, the deformation properties of the PST and single-phase structures are substantially different. At room temperature, the main deformation mode in PST crystals is twinning on {111} planes along the ⟨112] direction. Slip by ordinary 1/2⟨110] dislocations on {111} planes is the complementary deformation mode while ⟨101] superdislocations are usually not observed at this temperature (INUI *et al.* [1992a, 1992b]; FARENC *et al.* [1993]). At high temperatures twinning is still active, but its propensity decreases, and slip is accommodated by both ordinary dislocations and superdislocations. In contrast, single-phase aluminum-rich TiAl deforms at room temperature by the glide of ⟨101] superdislocations. However, twinning becomes active at temperatures around 800°C; this is an unusual phenomenon since twinning is commonly a low-temperature deformation mode. At the same time, at high temperatures the slip is dominated by ordinary 1/2⟨110] dislocations while superdislocations are not observed. A pronounced yield stress anomaly is also observed in this material.

The reasons for the differences in plastic behavior between PST and single-phase TiAl were investigated by MAHAPATRA *et al.* [1995] using an unusual experimental technique, combined with dislocation core simulations. (Since the deformation modes most commonly seen in the PST crystals are parallel to the lamellar interfaces, it was concluded that microstructure is probably not the major reason for the differences in behavior). To produce single-phase TiAl of near-stoichiometric composition, a single-crystalline sample of TiAl containing 56 at% Al was placed in intimate contact with a sample of Ti_3Al and held for a long time at 1265°C to produce, by diffusion, a layer of near-stoichiometric single-phase TiAl at the interface which grows in thickness with increasing time at temperature. As long as some of both initial phases still exist, the composition of the TiAl layer remains fixed. A single-crystalline $Ti_{49}Al_{51}$ layer 150 μm thick resulted. The composite sample was then deformed along the [001] tetragonal axis of the single-crystalline TiAl, producing deformation traces on the $Ti_{49}Al_{51}$. Since both twinning and slip occur on (111) planes these two deformation modes cannot be distinguished by slip markings alone; however the two modes can be differentiated by the use of the electron backscattering patterns (EBSP) obtained in a scanning electron microscope. The electron beam was scanned across the sample while recording the changes in the electron backscattering pattern. It was found that the pattern changes from the matrix orientation to the twin orientation and back again as the beam is scanned across the (111) traces, indicating the presence of twins. Thus the deformation of near-stoichiometric TiAl occurs primarily by twinning. Unfortunately, this experiment does not say whether dislocation slip is totally absent and it is possible that some slip does occur. Compression tests were also performed on an [001]-oriented $Ti_{46}Al_{54}$ single phase single crystal. Using both EBSP and slip trace analysis of a deformed sample, the deformation was found to occur via slip only. The exact nature of the dislocations involved in this slip has not been determined, but it is presumed that they are superdislocations, on the basis of the work of Yamaguchi and co-workers (YAMAGUCHI and INUI [1993]; YAMAGUCHI *et al.* [1995]).

The results reported here demonstrate that deformation in $Ti_{49}Al_{51}$ single-phase single

crystals occurs primarily by order-twinning, the same mode as is observed in PST single crystals. However, an increase in the Al content to only 54 at% results in deformation primarily by slip. Since both the single-phase 51 at% Al crystal and the single-phase 54 at% Al crystal have the same microstructure and only the compositions are different, it can be concluded that the compositional difference determines the deformation mode.

7. *Atomistic studies of dislocation cores in TiAl*

Atomistic simulations of the dislocation cores have been made for three types of screw dislocations, ordinary $1/2[1\bar{1}0]$ and $1/2[11\bar{2}]$ dislocations and a $[10\bar{1}]$ superdislocation. In these calculations the atomic interactions were described by Finnis–Sinclair type empirical central-force potentials (FINNIS and SINCLAIR [1984]) which were fitted to reproduce, as well as possible, the equilibrium tetragonal lattice parameters, the cohesive energy and six elastic moduli; for more details see (GIRSCHICK and VITEK [1995]). The lattice parameters and the c/a ratio are reproduced excellently and the agreement with most of the elastic moduli is reasonable, but C_{44} differs by a factor of two when compared with the ab initio calculated value. The reason is that one of the Cauchy pressures, C_{13}–C_{44}, is negative and Finnis–Sinclair potentials always yield a positive Cauchy pressure. This is a limitation of these potentials and the negative Cauchy pressure suggests that the non-central character of interatomic forces may be of importance in this material (PETTIFOR *et al.* [1995]).

Two alternate core structures of the ordinary $1/2[1\bar{1}0]$ dislocation were found: one core is planar, spread into the (111) plane, while the other core is non-planar, spread in both the (111) and $(11\bar{1})$ planes and thus it is sessile. The sessile core is energetically favored since, when a shear stress is applied in the (111) plane parallel to the $[1\bar{1}0]$ direction, the planar core transforms into the non-planar one. However, in a similar simulation of $1/2[1\bar{1}0]$ dislocations (SIMMONS *et al.* [1995]) found only the planar core configuration.

For the $[10\bar{1}]$ superdislocation, two possible configurations of the core were found. They correspond to two alternate splittings of this dislocation and are shown schematically in figs. 17a and b. The first is planar and corresponds to the splitting $[10\bar{1}] = 1/6[11\bar{2}] + \text{SISF} + 1/6[2\bar{1}\bar{1}] + \text{APB} + 1/2[10\bar{1}]$ in the (111) plane (fig. 17a) and the second is non-planar and corresponds to the splitting $[10\bar{1}] = 1/6[11\bar{2}] + 1/3[20\bar{1}] + 1/6[1\bar{1}\bar{2}]$ simultaneously into the (111) and $(\bar{1}1\bar{1})$ planes, forming ribbons of SISF in these planes. The partial dislocation with the Burgers vector $1/3[20\bar{1}]$, which lies at the intersection of the two {111} planes, is entirely immobile. The latter configuration is always favored when the energy of the SISF is low. However, the glissile configuration does not transform spontaneously into the sessile one upon the application of external loading but glides in the (111) plane at a relatively low stress. A dissociation similar to the sessile one found here has recently been observed by high-resolution electron microscopy but it involves a superlattice extrinsic stacking fault (SESF) on one of the {111} planes (HEMKER *et al.* [1993]). This alternative splitting can be expected to have the same influence on deformation properties as that found in this study.

References: p. 2102.

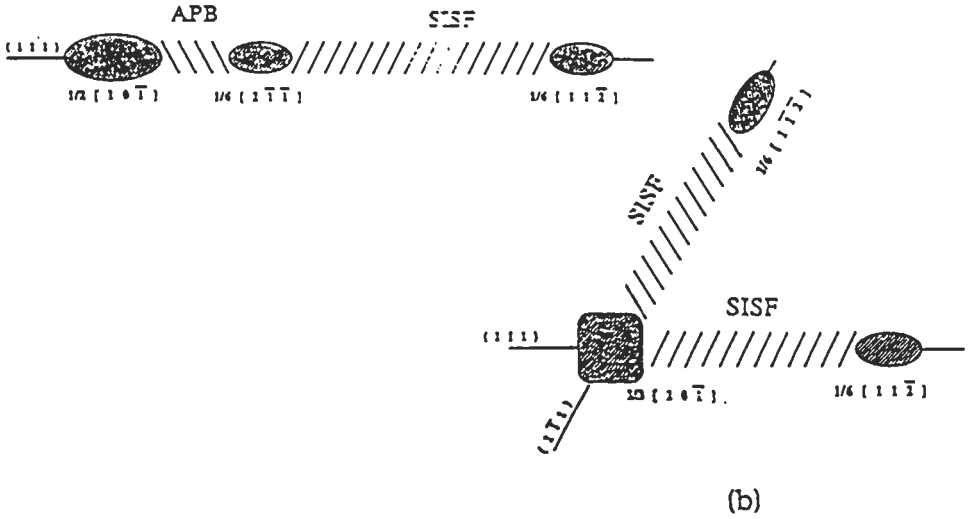

Fig. 17. Schematic core structure of a 1/2 [1$\bar{1}$0] screw dislocation in the $L1_0$ structure. (a) Planar core spread in the (111) plane; (b) non-planar core spread into the (111) and (11$\bar{1}$) planes. The oblate-shaped cores are dissociated in the plane of the long axis, while the square-shaped core is dissociated both in the (111) and the (1$\bar{1}$1) planes.

The core structure of the 1/2[11$\bar{2}$] dislocation is spread into two adjacent (111) planes and SESF is formed within the core. Such faults have, indeed, been observed by electron microscopy (HUG *et al.* [1986]). This fault represents a microtwin two atomic layers wide which may serve as a nucleus for twinning. Application of the corresponding external shear stress, indeed, showed that at high enough stresses, growth of the twin in the [111] direction started to take place. A similar core configuration was found in studies of dislocations in the tetragonal DO_{22} structure which deforms almost exclusively by twinning (KHANTHA, VITEK and POPE [1992]).

Results of these calculations may provide a basis for our understanding of the plastic behavior of both single-phase and PST TiAl, assuming that the energies of the SISF and coherent twin boundary are much lower for near-stoichiometric material. First, on the basis of the results of the simulations, it is seen that ordinary 1/2[1$\bar{1}$0] dislocations always have non-planar cores and require, therefore, substantial thermal activation to attain significant mobility. Assuming that in PST crystals the SISF energy is low, the sessile form of the superdislocations, shown in fig. 17b, will be strongly favored over the planar splitting. Hence, both ordinary dislocations and superdislocations will be sessile. At the same time, since the SISF energy is low, the twin boundary energy will also be low and thus twinning may be the easiest deformation process. Nuclei for twinning are readily available at 1/2[11$\bar{2}$] dislocations which are widely split on (111) planes. At high temperatures both the ordinary and superdislocations with non-planar cores become more mobile owing to the help of thermal activations.

If the SISF energy is high as assumed for the single phase TiAl, the twin-boundary energy will also be high and thus twinning will be more difficult than in PST crystals. Furthermore, the energy difference between planar and non-planar core configurations of the superdislocations will not be large when the SISF energy is high. Hence, even if the sessile form is preferred, the superdislocations may possess metastable planar cores when gliding at room temperature. However, as the temperature increases superdislocations may be transforming into energetically more favorable sessile configurations, involving SISF on both (111) and $(\bar{1}1\bar{1})$ planes. Ordinary dislocations will then dominate the slip but since their glide will still be more difficult than glide of superdislocations at low temperatures, twinning may occur as an alternative yielding mechanism. This also explains the anomalous increase of the yield stress with increasing temperature.

The above explanation of the different deformation modes in the single-phase and PST TiAl crystals is based purely on the assumption that the SISF energy is very different in the two cases. The reason for this difference is not related to the microstructure, so it is reasonable to assume that this energy strongly depends on aluminum content. In particular, if the SISF energy is a strongly increasing function of aluminum concentration it will be much lower in near-stoichiometric PST crystals than in Al-rich single phase $L1_0$ crystals. This dependence cannot be investigated in the framework of empirical potentials and more fundamental quantum mechanics-based studies of the alloying effects on SISF energy are needed.

However, if it is the aluminum content which controls the deformation modes via the energy of the SISF, this implies that the same deformation mode should occur at room temperature in both PST and near-stoichiometric single crystals, namely, twinning. This is, indeed, what has been observed in the experimental studies reported in this chapter. The deformation mode in $Ti_{49}Al_{51}$ single-phase single crystals, prepared employing solid state diffusion to reduce the Al content, is primarily twinning, just as it is in PST crystals. The reason for the change from twinning to slip at room temperature as the aluminum content is increased over 50 at% is most probably related to increases in SISF energy as the composition deviates from stoichiometric. Hence, both the experimental and theoretical results presented in this paper support the suggestion that it is the aluminum content rather than the microstructure which determines the deformation mode of TiAl based compounds.

8. *Closing remarks*

These examples, drawn from a diverse range of intermetallic compounds, show that the flow properties of these alloys are very complex. The details of the flow properties, e.g., which slip systems are active, whether twinning occurs, the presence of flow anomalies, and the presence of a high Peierls stress, are closely linked to the dislocation core structure.

References: p. 2102.

Acknowledgments

The author's work in this area has been supported from a number of sources, but primarily through the National Science Foundation through Grant No. DMR92-19089. Support from the NEDO Foundation of Japan is also gratefully acknowledged.

References

ANTON, D. L., 1995, in: "Intermetallic Compounds-Principles and Practice" Edited by J. H. Westbrook and R. L. Fleischer (John Wiley & Sons, Chichester, New York) vol. 2, p. 3.

BUMPS, E. S., H. D. KESSLER, and M. HANSEN, 1952 Trans. TMS-AIME **194**, 609.

DAVIS, R. G and N. S. STOLOFF, 1965, Trans. AIME **233**, 712.

DAROLIA, R., 1993, in: Structural Intermetallics, Edited by R. Darolia, J. J. Lewandowsik, C. T. Liu, P. L. Martin, D. B. Miracle and M. V. Nathal, Proceedings of the First International Symposium On Structural Intermetallics (TMS), p. 495.

DUESBERY, M. S. and G. Y. RICHARDSON, 1991 CRC Critical Reviews in Solid State and Materials Science **17**, 1.

DUWEZ, P. and J. L. TAYLOR, 1952, J. Metals **70**.

EZZ, S. S., and P. B. HIRSCH, 1995, High-Temperature Ordered Intermetalllic Alloys (VI), Edited by J. Horton, S. Hanada, I. Baker, R. D. Noebe and D. Schwartz, (Pittsburgh: Materials Research Society), p. 35.

EZZ, S. S., D. P. POPE, and V. PAIDAR, 1982, Acta Metall. **30**, 921.

FARENC, S., A. COUJOU, and A. COURET, 1993, Mat. Sci. Eng. **A164**, 438.

FINNIS, M. W. and J. E. SINCLAIR, 1984, Phil. Mag. **A50**, 45.

FLINN, P. A., 1960, Trans TMS-AIME **218**, 145.

FUJIWARA, T., A. NAKAMURA, M. HOSOMI, S. R. NISHITANI, Y. SHIRAI, and M. YAMAGUCHI, 1990, Phil. Mag. **60**, 34.

GIRIFALCO, L. A., 1973, Diffusion, ASM, Metals Park, Ohio, p. 185.

GIRSCHICK, A. and V. VITEK, 1995, High-Temperature Ordered Intermetallic Alloys VI (edited by J. Horton, I. Baker, S. Hanada, R. D. Noebe and D. Schwartz), Materials Research Society: Pittsburgh, Vol. 364, p. 145.

HEMKER, K. J., B. VIGUIER, and M. J. MILLS, 1993, Mat. Sci. Eng. **A164**, 391.

HEREDIA, F. E., and D. P. POPE, 1986, Acta Metall. **34**, 279.

HERMAN, M., and N. BROWN, 1956, Trans. AIME **206**, 604.

HIRTH, J. P. and J. LOTHE, 1982, Theory of Dislocations, Wiley-Interscience: New York.

HONG, T., and A. J. FREEMAN, 1991, Phys. Rev. **B43**, 6446.

HUANG, S. C. and J. C. CHESTNUTT, 1995, in: "Intermetallic Compounds-Principles and Practice" Edited by J. H. Westbrook and R. L. Fleischer (John Wiley & Sons, Chichester, New York) vol. 2, 73.

HUANG, S. C., E. L. HALL, and M. F. X. GIGLIOTTI, 1987, High Temperature Ordered Intermetallic Alloys II (edited by N. S. Stoloff, C. C. Koch, C. T. Liu and O. Izumi), Materials Research Society: Pittsburgh, Vol. 81, p. 481.

HUG, G., A. LOISEAU, and A. LASALMONIE, 1986, Phil. Mag. **A54**, 47.

INUI, H., A. NAKAMURA, M. H. OH, and M. YAMAGUCHI, 1992a, Phil. Mag. **A66**, 557.

INUI, H., M. H. OH, A. NAKAMURA, and M. YAMAGUCHI, 1992b, Acta Metall. Mater. **40**, 3095.

KAWABATA, T., T. KANAI, O. and IZUMI, 1985, Acta Metall. **33**, 1355.

KAWABATA, T., T. KANAI, and O. IZUMI, 1991, High-Temperature Ordered Intermetallic Alloys IV (edited by L. A. Johnson, D. P. Pope and J. O. Stiegler), Materials Research Society: Pittsburgh, Vol. 213, p. 279.

KAWABATA, T., Y. TAKEZONO, T. KANAI, and O. IZUMI, 1988, Acta Metall. **36**, 963.

KEAR, B. H., and H. G. F. WILSDORF, 1962, Trans. TMS-AIME **224**, 382.

KHANTHA, M., V. VITEK, and D. P. POPE, 1992, Mat. Sci. Eng. **A152**, 89.

KIM, Y.-W., 1989, J. Metals **41/7**, 24.

KIM, Y.-W. and F. H. FROES, 1990, High Temperature Aluminides and Intermetallics (edited by S. H. Whang, C. T. Liu, D. P. Pope and J. O. Stiegler), TMS: Warrendale, Pennsylvania, p. 465.
KUPER, A. B., D. LAZARUS, J. R. MANNING, and C. T. TOMIZUKA, 1956, Phys. Rev. **104**, 1536.
LALL, C., S. CHIN, and D. P. POPE, 1979, Metall. Trans. **A10**, 1323.
LIPSITT, H. A., D. SHECHTMAN, and R. E. SCHAFRIK, 1975, Metall. Trans. **A6**, 1991.
LIU. C. T., 1984, Int. Met. Rev. **29**, 168.
MAHAPATRA, R., A. GIRSHICK, D. P. POPE, and V. VITEK, 1995, Scripta Metall. et Mater. **33**, in press.
MARCINKOWSKI, M. J., and D. S. MILLER, 1961, Phil. Mag. **6**, 871.
MARCINKOWSKI, M. J., N. BROWN, and P. M. FISHER, 1961, Acta Metall. **9**, 129.
MARCINKOWSKI, M. J., M. E. TAYLOR, and F. X. KAYSER, 1975, J. Mat. Sci. **10**, 406.
MCCULLOUGH, C., J. J. VALENCIA, C. G. LEVI, and R. MEHRABIAN, 1989, Acta Metall. **37**, 1321.
MILLS, M. J., and D. B. MIRACLE, 1993, Acta Metall. Mater. **41**, 85.
MINONISHI, Y., M. OTSUKA, and K. TANAKA, 1991, International Symposium on Intermetallic Compounds Structure and Mechanical Properties — (edited by O. Izumi), The Japan Institute of Metals: Sendai, Japan, p. 543.
MINONISHI, Y. and M. H. YOO, 1990, Phil. Mag. Lett. **61**, 203.
MIRACLE, D. B, 1993, Acta Metall. **41**, 649.
MIRACLE, D. B., and R. DAROLIA, 1995, in "Intermetallic Compounds-Principles and Practice" Edited by J. H. Westbrook and R. L. Fleischer (John Wiley & Sons, Chichester, New York) vol. 2, p. 53.
MULFORD, R. A., and D. P. POPE, 1973, Acta Metall. **21**, 1375.
NABARRO, F. R. N., 1967, Theory of Crystal Dislocations, Clarendon Press: Oxford.
PAIDAR, V., D. P. POPE, and V. VITEK, 1984, Acta Metall. **32**, 435.
PARTHASARATHY, T. A., S. I. RAO, and D. M. DIMIDUK, 1993, Phil. Mag. **A67**, 643.
PASIANOT, R., Z. XIE, D. FARKAS, and E. J. SAVINO, 1994, Modelling and Simulation in Mat. Sci. Eng. **2**, 383.
PETTIFOR, D. G., M. AOKI, P. GUMBSCH, A. P. HORSFIELD, D. N. MANH, and V. VITEK, 1995, Mat. Sci. Eng. **A192/193**, 24.
POPE, D. P., 1973, Phil. Mag. **25**, 917.
POPE, D. P. and S. S. EZZ, 1984, Int. Met. Rev. **29**, 136.
POPE, D. P., and J. L. GARIN, 1977, J. Appl. Cryst. **10**, 16.
RAY, R., V. PANCHANATHAN, and S. ISSEROW, 1983, J. of Metals **35(6)**, 30.
SASTRY, S. M. L. and H. A. LIPSITT, 1977, Metall. Trans. **A8**, 299.
SHECHTMAN, D., M. J. BLACKBURN, and H. A. LIPSITT, 1974, Metall. Trans. **A5**, 1373.
SIMMONS, J. P., M. J. MILLS, and S. I. RAO, 1995, High-Temperature Ordered Intermetallic Alloys VI (edited by J. Horton, I. Baker, S. Hanada, R. D. Noebe and D. Schwartz), Materials Research Society: Pittsburgh, vol. 364, p. 137.
STATON-BEVAN, A. E. and R. D. RAWLINGS, 1975a, Phys. Stat. Sol. (A), **29**, 613; 1975b, Phil. Mag. **32**, 787.
STUCKE, M. A., D. M. DIMIDUK, and P. M. HAZZLEDINE, 1993, High-Temperature Ordered Intermetallic Alloys V (edited by I. Baker, R. Darolia, J. D. Whittenberger and M. H. Yoo), Materials Research Society: Pittsburgh, vol. 288, p. 471.
TAKEUCH, S., and E. KURAMOTO, 1973, Acta Metall. **21**, 415.
TICHY, G., V. VITEK, and D. P. POPE, 1986a, Phil. Mag. **A53**, 467; 1986b, Philos. Mag. **A53**, 485.
THORNTON, P. H., R. G. DAVIES, and T. L. JOHNSTON, 1970, Metall. Trans. **A1**, 207.
UMAKOSHI, Y., D. P. POPE, and V. VITEK, 1984, Acta Metall. **32**, 449.
UMAKOSHI, Y., T. NAKANO, and T. YAMANE, 1992, Mat. Sci. Eng. **A152**, 81.
UMAKOSHI, Y., M. TAKENAKA, and T. YAMANE, 1991, Proc. Tokyo Meeting of Japan Inst. Metals (The Japan Institute of Metals: Sendai), p. 1932.
UMAKOSHI, Y., M. YAMAGUCHI, Y. NAMBA, and K. MURAKAMI, 1976, Acta Metall. **24**, 89.
VEYSSIÈRE, P., and G. SAADA, 1995, will appear in Dislocations in Solids, Vol. 10 (Plasticity of Gamma Alloys), Edited by F. R. N. Nabarro and M. S. Duesbery (Elsevier Science Publishers).
VITEK, V., 1968, Phil. Mag., **A18**, 773.
VITEK, V., 1975, Crystal Lattice Defects **5**, 1.
VITEK, V., M. KHANTHA, J. CSERTI, and Y. SODANI, 1991b, Int. Symp. on Intermetallic Compounds, Edited by O. Izumi (Sendai: The Japan Institute of Metals), p. 3.

VITEK, V., D. P. POPE, and J. L. BASSANI, 1995, will appear in Dislocations in Solids, Vol. 10 (Plasticity of Gamma Alloys), Edited by F. R. N. Nabarro and M. S. Duesbery (Elsevier Science Publishers).

VITEK, V., Y. SODANI, and J. CSERTI, 1991c, High-Temperature Ordered Intermetallic Alloy (IV), Edited by L. A. Johnson, D. P. Pope, and J. O. Stiegler, Materials Research Society Symposium Proceedings, (Pittsburgh: Materials Research Society) vol. 213, p. 195.

XIE, Z. Y., C. VAILHE, and D. FARKAS, 1993, Mat. Sci. Eng. **A170**, 59.

YAMADA, Y., K. SUGAWARA, and M. KIKUCHI, 1990, Proc. Tokyo Meeting Japan Inst. of Metals (The Japan Institute of Metals: Sendai) Vol. ?, p. 409.

YAMAGUCHI, M., 1990, Metals and Technology **60**, 34.

YAMAGUCHI, M. and INUI, H., 1993, in: Structural Intermetallics (edited by R. Darolia, J. J. Lewandowski, C. T. Liu, P. L. Martin, D. B. Miracle and M. V. Nathal), TMS: Metals Park, Ohio, p. 127.

YAMAGUCHI, M., H. INUI, K. KISHIDA, M. MATSUMORO, and Y. SHIRAI, 1995, High-Temperature Ordered Intermetallic Alloys VI (edited by J. Horton, I. Baker, S. Hanada, R. D. Noebe and D. Schwartz), Materials Research Society: Pittsburgh, Vol. 364, p. 3.

YAMAGUCHI, M. and Y. UMAKOSHI, 1990, Prog. Mater. Sci. **34**, 1.

YAMAGUCHI, M., V. VITEK, and D. P. POPE, 1981a, Phil. Mag. **A43**, 1027.

YAMAGUCHI, M., V. VITEK, D. P. POPE, and Y. UMAKOSHI, 1981b, Phil. Mag. **A43**, 1265.

WESTBROOK, J. H., 1993, in: Structural Intermetallics, Edited by R. Darolia, J. J. Lewandowski, C. T. Liu, P. L. Martin, D. B. Miracle and M. V. Nathal, Proceedings of the First International Symposium On Structural Intermetallics (TMS), p. 1.

Further reading

Special issue on 'Ordered Alloys'. International Metals Reviews. **29** (1984) 123–248.

Yamaguchi, M. and Y. Umakoshi, the Deformation Behaviour of Intermetallic Superlattice Compounds, Progress in Materials Science **34** (1990) 1–148.

Liu, C. T., R. W. Cahn and G. Sauthoff (editors), Ordered Intermetallics — Physical Metallurgy and Mechanical Behaviour. NATO ASI Series, (E, Appl. Sci., Volume 213), Kluwer Academic Publishers, Dordrecht/ Boston/London (1992). (701).

Darolia, R., J. J. Lewandowski, C. T. Liu, P. L. Martin, D. B. Miracle and M. V. Nathal (editors), Structural Intermetallics, TMS, Warrendale, PA, 1993. (900 pages).

George, E. P., M. Yamaguchi, K. S. Kumar and C. T. Liu, Ordered Intermetallics, Annu. Rev. Mat. Sci. **24** (1994) 409–451.

Westbrook, J. H. and R. L. Fleischer (editors), Intermetallic Compounds: Principles and Practice. Wiley, Chichester/New York, etc. (1995). (2 volumes, 1126 [Principles] + 752 [Practice]).

CHAPTER 25

MECHANICAL PROPERTIES OF MULTIPHASE ALLOYS

Jean-Loup STRUDEL

Centre des Matériaux
École Nationale Supérieure des Mines de Paris
91003 Evry, France

R. W. Cahn and P. Haasen†, eds.
Physical Metallurgy; fourth, revised and enhanced edition

1. Introduction

A large majority of alloys used in everyday life are and have been for years or even centuries, knowingly or not, multicomponent materials. Except for pure noble metals such as platinum, gold, silver and copper which have been devoted to the manufacture of ornamental pieces since early periods of antiquity, high mechanical and thermal resistance have been expected from man-made metallic objects or engineering structures — blades, weapons, stoves, burners, piston- and jet-engine parts, nuclear reactors, etc. Strengthening a plastically deformable material can be achieved in a number of ways: reducing the grain size, solid-solution hardening of the matrix, strain-hardening, precipitate-, particle- or fiber-hardening. Each of these methods has its domain of stress, temperature, feasibility and cost where it is best suited but one must always keep in mind that grain-boundary resistance has to match the improved mechanical performance of the matrix.

This chapter will be devoted to polyphase alloys in which one phase, called the *matrix,* entirely surrounds on all sides the second phase, called *particle* or *precipitate.* This definition excludes dual-phase alloys such as certain types of steels which are examined in ch. 16, and titanium-base alloys. Fiber-composite materials are not considered either, although some of the theoretical tools developed in § 3 can easily be extended to encompass this field of newly developed materials (ch. 30). Consequently the hardening obstacles considered in this chapter will be implicitly of polygonal convex shape, often described simply by spheres or roughly spheroidal objects with sizes ranging from a few nanometers to a few microns (10–20 μm at the most).

Macroscopic properties of materials are revealed to the metallurgist by experimental data such as stress–strain curves, fatigue, relaxation, or creep curves which depend on external parameters (temperature, strain rate or loading rate) and on the internal structure of the material. These basic manifestations of the alloy's response to various mechanical and thermal solicitations remain the ultimate framework of reference for the practical engineer on one hand, and for the theoretical metallurgist on the other hand. In the course of the last twenty years, innumerable transmission electron microscopy (TEM) observations have brought deep insights into microscopic mechanisms taking place during deformation. Complex dislocation interactions have enabled the metallurgist to develop microscopic models with a mass of geometric details which must be abandoned when an attempt is made to derive macroscopic flow rates or observed recovery kinetics. But the importance of these observations is of a qualitative nature — the halting of a dislocation in the glide plane in front of a particle, various alternatives for circumventing the obstacle, such as by-passing, cross-slipping, climbing, cutting, etc.

On the other hand, macroscopic models based on continuum mechanics effectively provide the modern engineer, surrounded by high-speed computers, with sophisticated equations capable of yielding precise quantitative answers in a good number of well-defined loading schemes: yield strength, fatigue curves, creep rates, hardening rates are well described, responses to abrupt thermal or stress transients and creep–fatigue interactions still need some improvements. Much too often these models are faced with the necessity of introducing numerical parameters whose physical significance is either obscure or often nonexistent. In the course of this chapter, only a few of these models

are briefly described, and they have been chosen on the basis of the physical interpretation they can provide.

The first part of the chapter is concerned mostly with non-shearable particles such as oxides or carbides. The unusually high strength of multiphase materials is related to the origin and the structure of their internal stress pattern. Several approaches to the concept of *internal stress* are also presented in this section. (See also ch. 22, § 6.3.)

The second part is devoted to the behavior of alloys containing shearable precipitates. Nickel-base superalloys provide a large range of complex deformation processes also observed in other alloy systems. With origins ranging from powder-metallurgy manufacture to single-crystal growth, they tend to encompass all possible grain sizes and shapes and a large variety of precipitate diameters.

Recrystallization can either be stimulated or inhibited by the presence of a second phase in a plastically deformed matrix. This leads to patterns of recrystallization that are quite specific to multiphase materials and are described in a later section. At the end of the chapter a few examples are given of complex multiphase alloys or multiplex structures of importance in recent industrial developments of high-performance materials. A short review of grain-size effects in multiphase alloys is presented in the last section.

2. *Description and microstructure of dispersed-phase alloys*

The main goal achieved in two-phase alloys is to provide means of raising the yield stress in crystals above the value due to the lattice friction stress: either the Peierls–Nabarro stress alone, as in pure solids, or solid-solution hardening associated with solute atoms of odd sizes in the crystal lattice. In industrial alloys, both strengthening mechanisms are usually operating.

Hard particles such as carbides cannot be sheared by gliding dislocations and remain stable in size and distribution up to the highest service temperatures. In order to avoid the complications inherent in industrial alloys, model materials have been designed and abundantly studied. *Oxide-dispersion-strengthened* (ODS) alloys belong to this category and provide a good basis for the understanding of more complexe alloys.

The first-born among the synthetic alloys made of a metal oxide dispersed into a ductile metallic matrix seems to have been SAP (*sintered aluminium powder*) alloys obtained by LENEL *et al.* [1957] who fabricated bars by extrusion of a mixture of 1–10 vol% of Al_2O_3 powder in pure Al powders: ANSELL and WEERTMAN [1959], ANSELL and LENEL [1961] and later GUYOT [1962] and GUYOT and DEBEIR [1966] were intrigued by the internal structure of these alloys which exhibited interesting creep resistance. Observations by TEM (fig. 1) reveal a wide distribution of sizes (10 nm to 1 μm) and a lack of coherency with the matrix.

Several types of crystallographic relationships between the lattice of the particle and that of the matrix can be met:

Coherency: either strict if both lattice parameters are equal and equivalent lattice directions are aligned, or quasi-coherency as described by fig. 2a if lattice parameters differ slightly. The lattice misfit is then described by the relative parameter difference

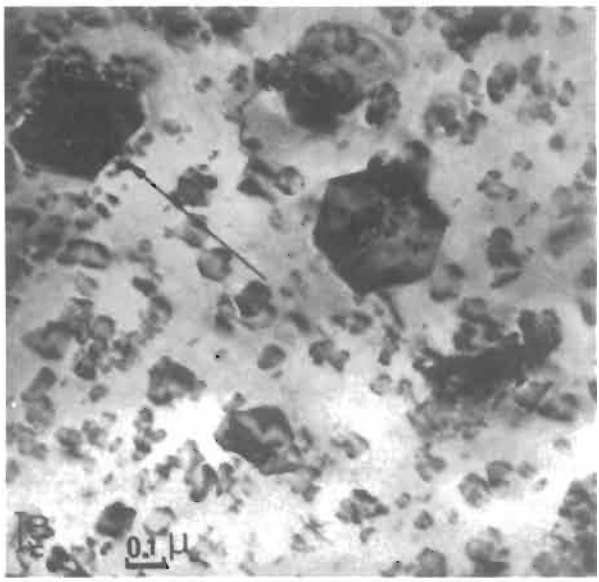

Fig. 1. Structure of Al–Al_2O_3 SAP alloy observed by TEM (after GUYOT and RUEDL [1967]).

$$\delta = 2\frac{a_p - a_M}{a_p + a_M}, \tag{1}$$

where a_p and a_M are the precipitate and matrix parameters respectively. In fig. 2a the misfit parameter δ is positive. This situation is usually the result of precipitation from supersaturated solid solution, e.g., γ' precipitates in nickel-base alloys.

Semi-coherent precipitates (fig. 2b): the precipitate and the matrix lattices coincide along one set of crystallographic directions and the parameters are closely similar, but along another direction dislocations are needed in order to accommodate the large differences in lattice parameters. In aluminium-base alloys (Al–Cu), the θ' phase illustrates this situation.

Incoherent particles (fig. 2c): the lattice of the particle (Al_2O_3, SiO_2) has nothing in common with the lattice of the matrix (Al, Cu, Ni). Overaging of the θ' phase in Al–Cu stimulates the formation of θ particles which become incoherent with the matrix.

The average size of the population of dispersed particles plays a major role in the mechanical and metallurgical properties of dispersed-phase alloys, which retain a dense network of subgrain boundaries even after long-term annealing treatments. There are several distinct situations:

Small particles (1–100 nm): they have the strongest effect on the yield strength and tend to assume approximately spherical shapes due to surface tensions. They are usually generated inside the matrix by internal oxidation techniques. A solid solution of Si, Al or Be in copper, for instance, is exposed to oxidizing conditions in the appropriate temperature range. Oxygen diffuses into the alloy and SiO_2, Al_2O_3 or BeO particles are

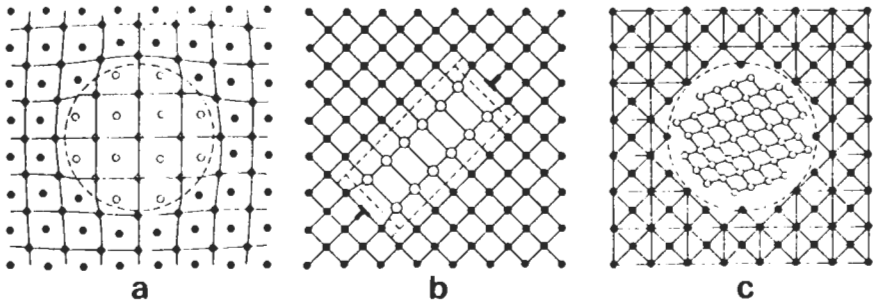

Fig. 2. Coherency of a precipitate: (a) quasi-coherent or coherent with positive misfit; (b) semi-coherent; (c) non-coherent. (From MARTIN [1980]).

formed inside the base metal. Single crystals containing fine dispersions of oxide particles can be produced and constitute an ideal model material for basic studies. Very low initial dislocation densities can easily be obtained in materials annealed before the oxidizing treatment.

Mechanical alloying consists in blending and grinding together oxide and metal powders in a vertical ball mill in which a rapidly rotating impeller agitates the steel balls. The initial oxide particles break into very fine debris and are cold-welded into the ductile matrix. The metal-oxide pellets thus formed (fig. 3) are then consolidated by hot extrusion, rolling and high-temperature annealing. Thoria-disperse nickel (TD-Nickel) and TD-nichrome have been successfully produced and the technique has been generalized by BENJAMIN and BROMFORD [1977] to manufacture complex ODS nickel-base superalloys and aluminium-base alloys. The end-result is a homogeneous distribution of finely dispersed small particles (fig. 4).

Secondary carbides (M_7C_3, $M_{23}C_6$) can precipitate in stainless steels after prolonged

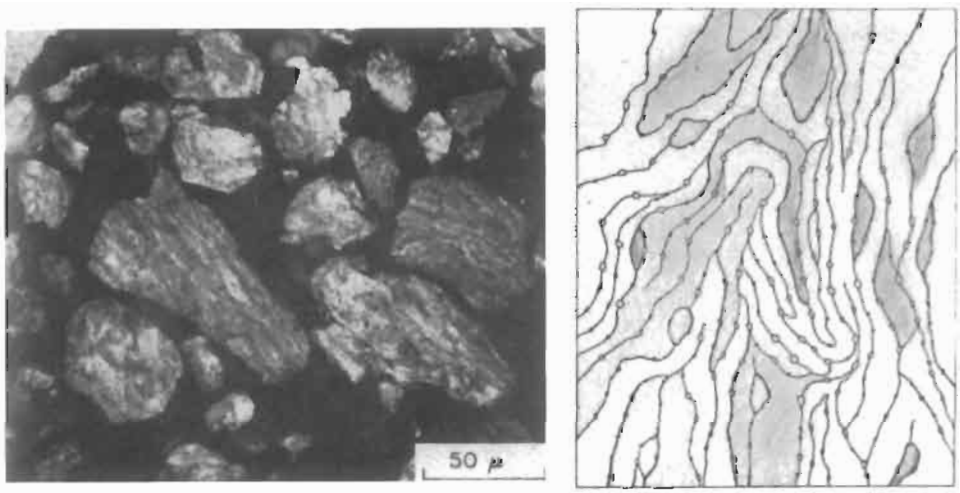

Fig. 3. Metal oxide pellets obtained by mechanical alloying (from BENJAMIN [1977]).

References: p. 2174.

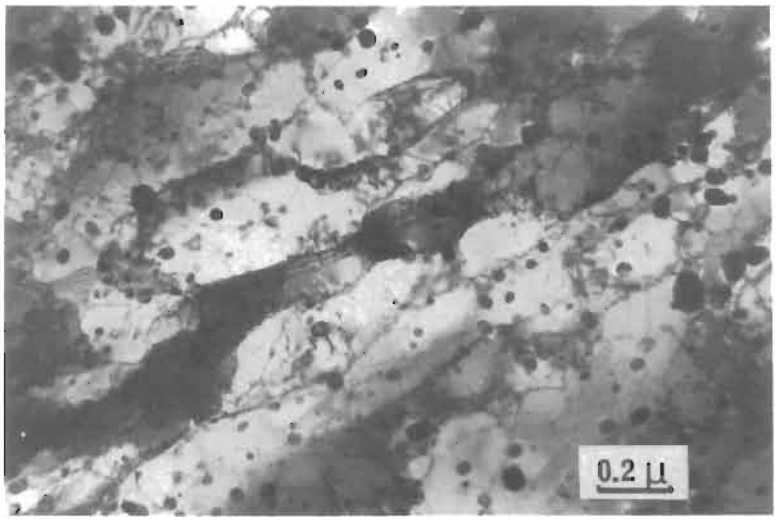

Fig. 4. Subgrain structure and particle dispersion in TD-nickel after 100 h anneal at 1200°C.

exposure at service temperature (fig. 5) and generate a finely dispersed colony of hardening particles which significantly alter the mechanical strength of the as-quenched material (DELEURY *et al.* [1981]). Since the nucleation of a misfitting precipate is facilitated by the presence of a stress field they nucleate on dislocations.

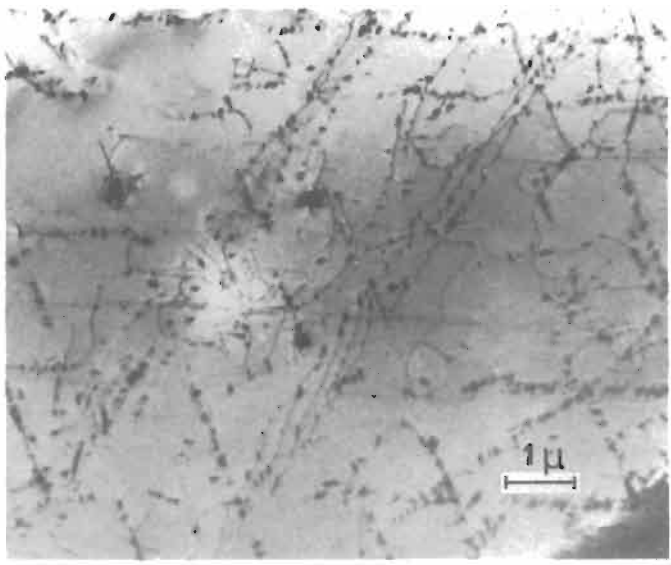

Fig. 5. Heterogeneous precipitation of $Cr_{23}C_6$ carbides in stainless steel after 5000 h at 600°C (from DELEURY *et al.* [1981]).

Medium-size dispersoids (0.1–1 μm): this type of obstacle has a strong inhibiting effect on recrystallization and grain growth (§ 8). It appears as a losely dispersed population in aluminium-base alloys containing Cr, Zr or Mn additions.

More densely distributed, their strengthening influence is not so much felt on the low-temperature yield strength as on the high-temperature creep resistance. They also have a tendency to induce cavitation on their tensile side during deformation.

Coarse inclusions (5–50 μm): because of their large size, they create problems of compatibility of deformation, and intense stress gradients are generated in their vicinity. They are widely recognized as the potential sources of weakness in commercial alloys. In steel and nickel-base alloys they are byproducts of deoxidation processes or may come from accidental slag bursts or debris of refractory materials used for casting the liquid melt.

Some of them are rather ductile, e.g., MnS inclusions in steels, or iron and silicon-rich inclusions in aluminium alloys. Because of their lack of cohesion with the surrounding matrix they are always preferential sites for crack initiation and failure.

3. *Tensile properties of two-phase alloys*

In engineering practice, the most basic criterion for a mechanical evaluation of a material still remains the yield strength and its decay with increasing temperature. The two striking features of multiphase materials are: (1) their rather high limit of elasticity at relatively low temperature (up to $\sim 0.2T_m$); (2) their tendency to preserve fairly high flow stresses up to temperatures close to their melting point (0.90–$0.95T_m$). Let us successively examine each of these aspects in the following sections.

3.1. Experimental results in macroscopic tests

A clean case of oxide dispersion strengthening is that of copper and copper–zinc single crystals containing alumina particles, as HIRSCH and HUMPHREYS extensively reported in 1969 and 1970.

Stress–strain curves obtained at various temperatures between that of liquid nitrogen and 200°C appear in fig. 6a for copper single crystals with 0.11% volume fraction (f) of alumina particles with average diameter $\bar{d}_s \approx 40$ nm and interparticle spacing $\bar{D}_s \approx 0.8$ μm and in fig. 6b for crystals with a higher volume fraction $f = 0.88\%$, $\bar{d}_s \approx 80$ nm and $\bar{D}_s \approx 0.5$ μm. Obviously the mechanical strength of these crystals (20–40 MPa) is one order of magnitude larger than that of pure copper (1–4 MPa).

The effect of the matrix composition was also examined by straining Cu–Zn single crystals with various solute concentrations (fig. 7). Solid-solution strengthening is superimposed on two-phase hardening.

3.1.1. Initial yield stress

Although not very sensitive to strain rate, the initial yield stress appears to be the sum of two contributions, the yield stress of the matrix, τ_m, which decreases with increasing temperature, and the particle by-passing stress, τ_p, which appears to be temperature-independent at least up to 500 K (HIRSCH and HUMPHREYS [1970]; JONES [1969] in

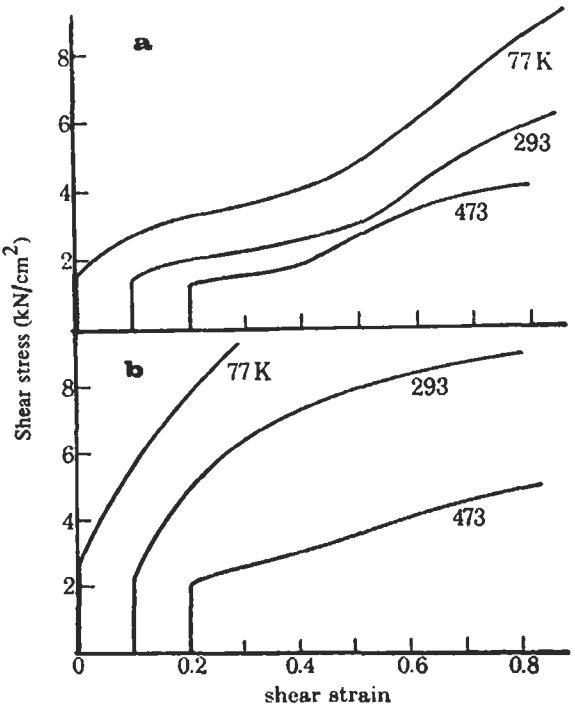

Fig. 6. Stress–strain curves at several temperatures of Cu–Al_2O_3 single crystals containing: (a) 0.11 vol% Al_2O_3; (b) 0.88 vol% Al_2O_3. (After HIRSCH and HUMPHREYS [1970].)

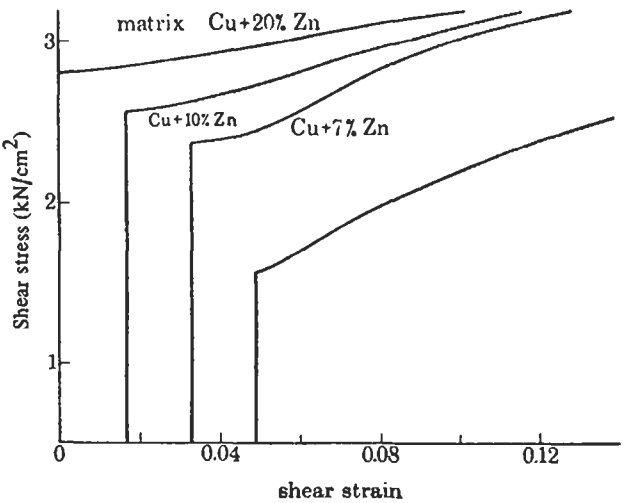

Fig. 7. Stress–strain curves at 293 K of Cu–Zn single crystals with 0.22 vol% Al_2O_3 (after HIRSCH and HUMPHREYS [1970]).

Cu–BeO):

$$\tau_{ys} = \tau_m + \tau_p. \tag{2}$$

The friction stress due to solid-solution hardening is included in the first term, its variation with solute concentration and temperature in single-phase alloys is described in ch. 23.

3.1.2. Stress–strain curves

All stress–strain curves are composed of three stages at room temperature, as in the case of single-phase crystals.

Stage I is characterized by an initial region ($\lesssim 1\%$) of low and quasi-linear hardening rate, followed by a short regime of rapidly increasing rate of hardening ($1\% \lesssim \varepsilon \lesssim 3\%$) which merges into a long domain ($3\% \lesssim \varepsilon \lesssim$ 15–20%) reputed for its parabolic hardening law. All the microscopic models presented in the literature are aimed at explaining each of these regions of the first stage.

It is more developed at room temperature than at 77 K where it tends to disappear into stage II or even directly stage III to form an apparent single-stage hardening (fig. 6b). Orientations of slip lines, shape changes and crystal rotations examined by HIRSCH and HUMPHREYS [1970] and HUMPHREYS and MARTIN [1967] indicate that primary dislocations are responsible for the deformation. Solute additions tend to expand that stage, diminish its work-hardening rate (fig. 7) and drastically lower its temperature sensitivity (fig. 22, below), this latter effect being related to recovery of the microstructure.

Stage II is a domain of 10–20% extension in strain characterized by a linear rate of work-hardening. Lower temperatures and higher volume fractions of dispersed phase tend to make it vanish into stage I and the spreading stage III (fig. 6).

Stage III is parabolic with decreasing strain-hardening rates as in single-phase metals. It tends to overtake the whole curve when f is increased and T is low.

3.1.3. Bauschinger effect

After tensile deformation, if the stress is reversed to compression, reverse straining in two-phase alloys seems to start even before the externally applied stress reaches zero. This very strong *Bauschinger effect* typical of two-phase alloys can best be characterized by plotting the opposite of the compressive stress value versus cumulative strain (fig. 8) as suggested by ATKINSON *et al.* (1974). Notice in this figure that:

- the apparent reverse yield stress is negative (points A, A′);
- it is followed by a stage of 2% strain extension with a very high strain-hardening rate (zone B) as opposed to the forward loading curve;
- finally a "permanent softening" $\Delta\sigma_p$ appears in C where the reverse curve takes on nearly the shape of the forward curve.

When making several fatigue loops, the Bauschinger effect seems to decrease in amplitude. As reported by ATKINSON *et al.* [1974], Cu–SiO_2 crystals tested at 77 K show a lack of fatigue-hardening in the forward direction and progressive hardening in the reverse direction, so that the entire stress–strain loop tends to be more symmetrical with respect to the strain axis as the cumulative strain increases. See also ch. 21, § 7.3.8.

References: p. 2174.

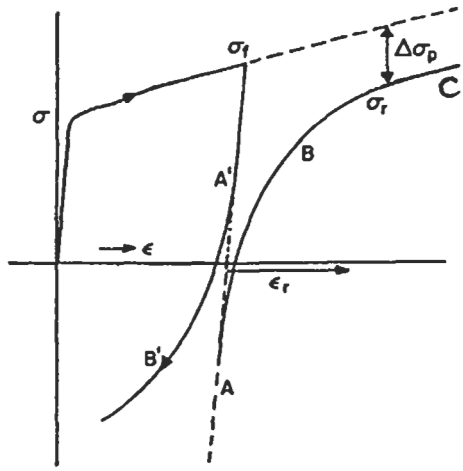

Fig. 8. Schematic stress–strain curve of an ODS material showing strong Bauschinger effect. The reverse loading curve ABC has been inverted to show the apparent softening $\Delta\sigma_p$. (After ATKINSON *et al.* [1974].)

3.2. Microscopic mechanisms and models

An extensive description of dislocation mechanisms is outside the scope of this chapter and will be found mainly in the original papers published by the Cambridge and Oxford groups referred to in the text. A comprehensive review of micromechanisms in deformation and fracture processes of two-phase alloys has been published by MARTIN [1980]. Only the most striking features of this intricate problem of dislocation configurations in connection with the deformation of a mechanically heterogeneous medium will be presented.

3.2.1. Initial yield stress

An important contribution to the theory of yield stress of alloys containing non-shearable particles was made by OROWAN [1948] when he suggested that particles could be by-passed by the mechanism depicted in fig. 9, at a stress of the order of

$$\tau_p = \alpha \frac{Gb}{D_s}. \tag{3}$$

A more precise evaluation of the by-passing stress was obtained by taking into account the influence of the dislocation character (edge or screw) on the equilibrium shape of the loop and the interaction of the two arms of the dislocation on opposite sides of the particle (ASHBY [1968]), as well as the statistical nature of the effective spacing D_s between particles (KOCKS [1966] and FOREMAN and MAKIN [1966]). An excellent fit of experimental results is obtained with the expression:

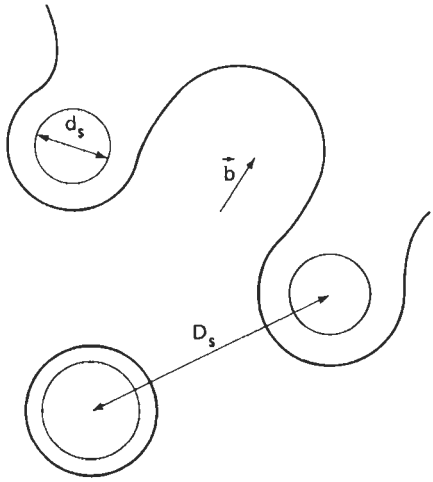

Fig. 9. Edge dislocation by-passing particles by the Orowan mechanism.

$$\tau_p = K \frac{G_K b}{2\pi(D_s - d_s)} \ln \frac{d_s}{r_0}, \tag{4}$$

where K is a statistical factor and G_K is an average shear modulus combining both screw and edge contributions to the dislocation line tension.

When a dislocation is held up by point obstacles it bows out between them as described in ch. 20, § 2.5. The force exerted by the dislocation line on the anchoring point is transmitted by the line tension. Strong obstacles, such as particles larger than 20 nm, do not release the dislocation before an Orowan loop is formed. Other, weaker, obstacles such as solute atoms, may release the dislocation at a larger angle ϕ (see fig. 25, ch. 20 for the definition of ϕ). The behavior of edge and screw dislocations encountering a statistical distribution of obstacles of various strengths has been studied by several authors. BROWN and HAM [1971], using the assumption of constant line tension, show that the forward penetration of a dislocation following a path of easy movement is more pronounced in the case of strong obstacles ($0 < \phi < \pi/2$, fig. 10) than in the case of weak obstacles ($\pi/2 < \phi < \pi$, fig. 11) where it tends to sweep across the slip plane in a more rigid manner. The macroscopic effect of an array of randomly distributed obstacles is to lower the flow stress by a factor of 0.84 (KOCKS [1969]) with respect to a regular arrangement of similar obstacles. When particles tend to form clusters the mechanical properties are adversely affected further, as shown in fig. 12.

3.2.2. Work-hardening at low temperature in alloys with small particles

One of the earliest model was imagined by FISHER, HART and PRY in 1953. They imagined that Orowan loops would pile up around particles, thereby creating such a

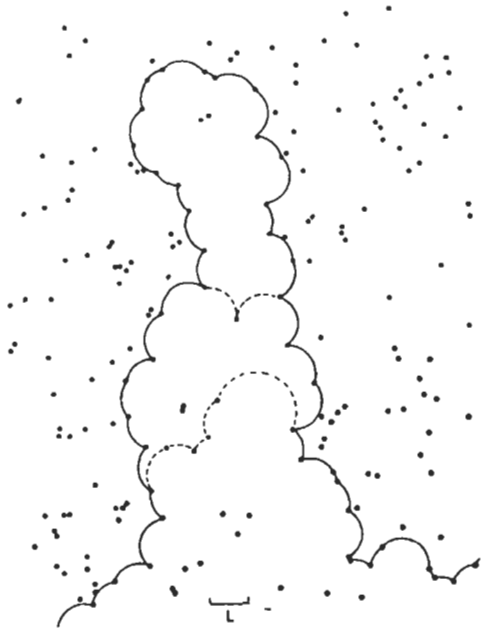

Fig. 10. Dislocation penetrating an array of strong obstacles ($0<\varphi<\pi/2$) (from BROWN and HAM [1971]).

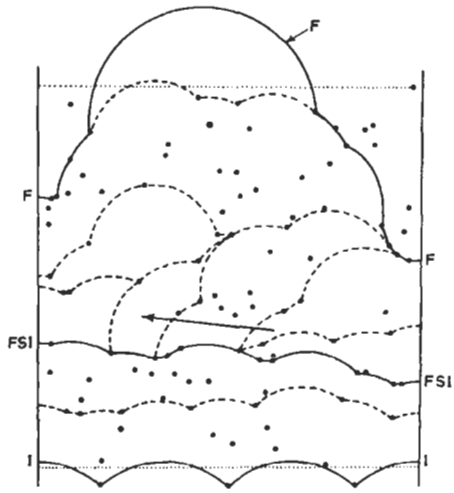

Fig. 11. Dislocation cutting through a population of weak obstacles ($\pi/2<\varphi<\pi$) (from BROWN and HAM [1971]).

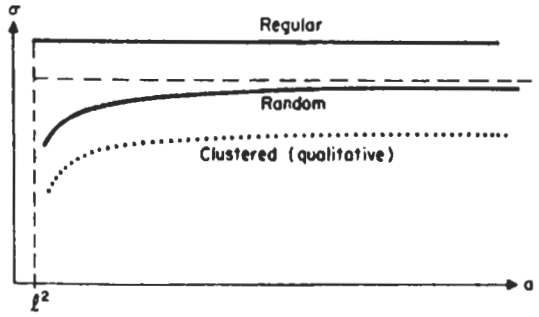

Fig. 12. Applied stress σ versus mean free slip area a of one dislocation for strong obstacles of area density $1/l^2$ as a function of obstacle distribution (from KOCKS [1969]).

back-stress in the matrix that the active dislocation sources would stop operating. The stress–strain curve then was found to be linear with strain:

$$\sigma = \sigma_0 + 6Gf^{3/2}\varepsilon, \tag{5}$$

where f is the volume fraction of the particles. This model cannot explain the observed stage II of the work-hardening curves (fig. 6) where the dislocation density is extremely high, but may be relevant to the initial region of stage I at low temperature.

HART [1972] later refined the model and clearly stated that the friction stress of the pure matrix should be considered as an additional term to the general flow stress of the alloy rather than as an alternative strengthening mechanism: the very large Bauschinger effect of these alloys was even somewhat overestimated in this improved version, but the hardening rate was proportional to $\varepsilon^{1/2}$, as found experimentally in the major part of stage I.

The retention of Orowan loops is simply a statement of the fact that the region within the loop has not undergone the plastic shear displacement of the rest of the surrounding material. One wonders then, how stable such a situation can be, especially when several loops are formed or when the initially applied stress is relaxed. HIRSCH and HUMPHREYS [1969,1970] reported from TEM observations of the early stages of plastic deformation (fig. 13) that Orowan loops may well be transformed into prismatic loops by cross-slip mechanisms such as those schematically drawn in fig. 14, and generalizing the mechanism originally proposed by HIRSCH [1957]. Screw segments can move in the cross-slip plane of the dislocation and recombine, thus leaving behind one or two loops with Burgers vector normal to their habit plane (prismatic loops). This event can be repeated a number of times and creates rows of prismatic loops (fig. 15) or be combined with further Orowan bowing of new dislocations as in figs. 14 or 15. The actual stability of coplanar stacks of Orowan loops in Cu–Al_2O_3 was studied in detail by HAZZLEDINE and HIRSCH [1974], who concluded that no more than four or five loops can be present around a particle at room temperature and that a hybrid model, in which both shear loops and prismatic loops are included, is necessary in order to account for the observed data: (1) the Bauschinger effect is entirely due to Orowan loops; (2) the low work-hardening rate

References: p. 2174.

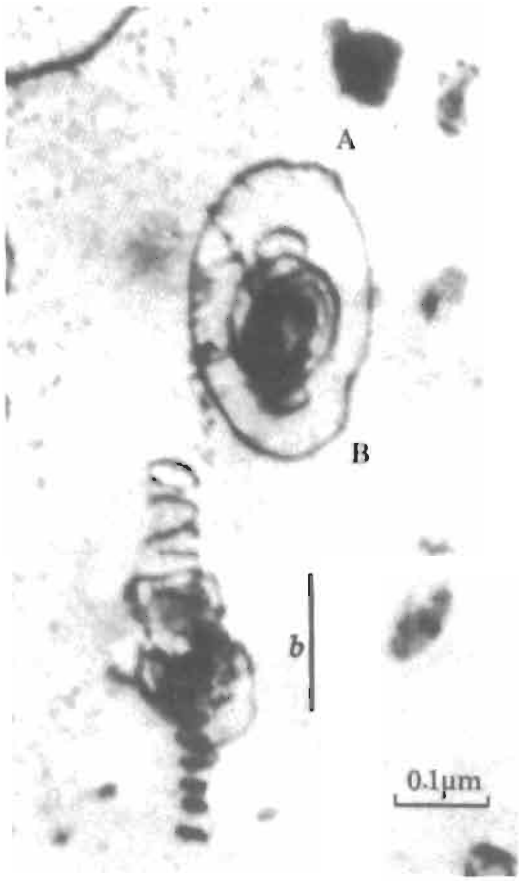

Fig. 13. Prismatic loop formation due to the cross-slip of inner Orowan loops. Segment AB is starting to cross-slip on the outer loop. Cu–30% Zn + 0.22% Al_2O_3. (From HUMPHREYS and HIRSCH [1970].)

of the initial region of stage I originates from the accumulation of Orowan loops, and the increasing proportion of prismatic loops progressively dominates the rest of the domain.

BROWN and STOBBS's model [1971] (also STOBBS [1973]) is based on ESHELBY's [1961] technique of treating the mechanical problem of the stress and strain distributions around an inclusion in a deformed matrix. They considered a local plastic shear strain around each particle, of amplitude

$$\varepsilon_p = \frac{nb}{4r_0}, \tag{6}$$

in a matrix containing a volume fraction f of spherical inclusions of radius r_0 separated by an average distance L. The particles are assumed to be non-shearable but to have the same elastic constants as the matrix. They are surrounded by n shear loops of Burgers

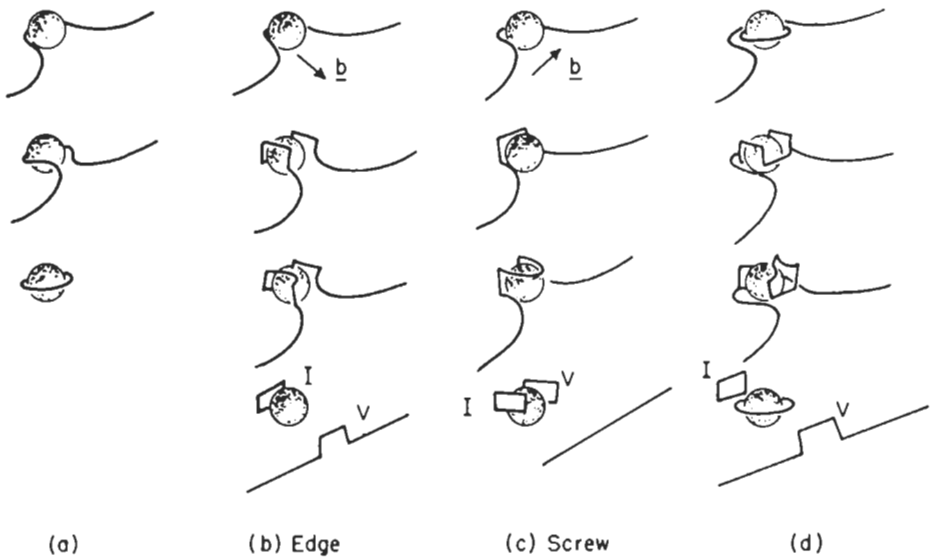

Fig. 14. By-passing of a hard particle: (a) a simple Orowan mechanism; (b) edge dislocation forming prismatic loops by double cross-slip; (c) screw dislocation; (d) multiple Orowan mechanism and cross-slip. (After ASHBY [1969].)

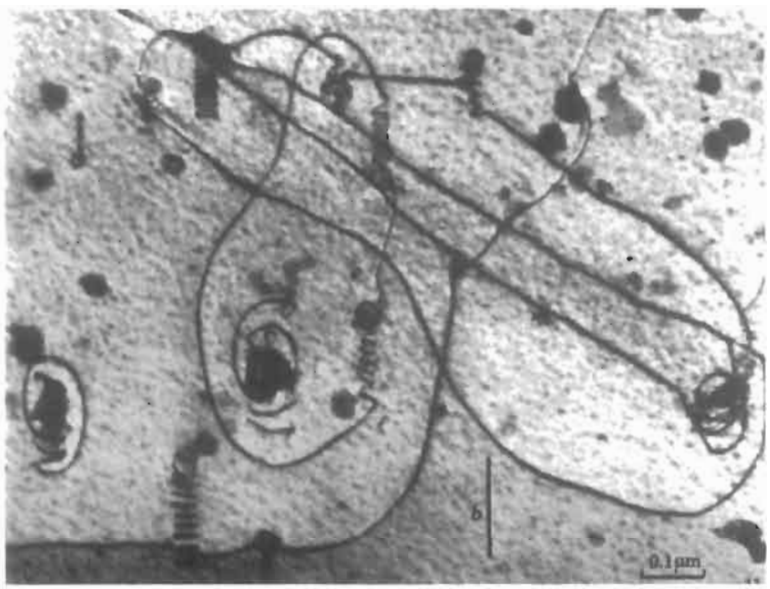

Fig. 15. Rows of prismatic loops, Orowan loops and glide dislocations interacting with the prismatic loops to form helices (same conditions as in fig. 13) (from HUMPHREYS and HIRSCH [1970]).

References: p. 2174.

vector $\boldsymbol{b}$ which are smeared around the inclusion into infinitesimal dislocations with infinitesimal Burgers vectors, in the usual fashion required by the use of continuum mechanics.

It is interesting to note a general form of the solutions found for this model. The various components of the stress tensor at a point located at a distance r from the particle surface ($r > r_0$) look like:

$$\sigma = G\varepsilon_p r_0^3 \left(\frac{A}{r^3} + \frac{B}{r^5} \right). \tag{7}$$

The term in r^{-5} describes the *local stresses* prevailing in the immediate vicinity of the particles, to which the first Orowan loops are directly exposed. The term falling off as r^{-3} is related to the *source-shortening stress* which describes the increase in the by-passing stress above the initial Orowan stress. It is a fluctuating component of the internal stress with essentially zero mean value. The bowing dislocations will experience it in their random movements across their glide plane as an effective reduction of the interparticle spacing. ATKINSON *et al.* [1974] gave the following simple estimate for it:

$$\sigma_{ss} = Gb \frac{f}{r_0} \left[\left(\frac{4r_0\varepsilon_p}{b} \right)^{\frac{1}{2}} - 1 \right]. \tag{8}$$

The concept of the source-shortening stress σ_{ss} also appears in the work-hardening of fiber composite materials made of a copper matrix traversed by tungsten wires (BROWN and CLARICE [1977] and LILHOLT [1977]).

On the other hand, the stresses within the particle ($r < r_0$) are not fluctuating but uniform and take on the value

$$\sigma(r < r_0) = 2G\nu'\varepsilon_p, \tag{9}$$

where ν' is a numerical factor related to Poisson's ratio. When considering a finite body with no externally applied stress, these stresses alone generate a uniform stress throughout the matrix, with a magnitude:

$$\langle \sigma \rangle_M = -2G\nu'\varepsilon_p, \tag{10}$$

where the subscript M implies averaging over the matrix containing a volume fraction f of particles. This is also called the *mean matrix stress* or *image stress;* it is the main contribution to the internal stress in two-phase alloys and has so far been treated generally as a scalar quantity rather than as a tensor.

Now the description of the stress–strain curves appears as:

$$\sigma = \sigma_0 + \alpha G f \varepsilon_p + \frac{Gb}{r_0} f \left(\frac{4r_0\varepsilon_p}{b} \right)^{1/2}, \tag{11}$$

where the first term describes the initial yield under the Orowan stress $\sigma_0 = Gb/D$ [eq. (3)], the second term gives the short linear hardening domain of stage I and the third term yields the correct representation of the parabolic strain rate prevailing in the remain-

der of the stage. Notice also that the strengthening rate is proportional to f as expected from experimental results and not to $f^{\beta/2}$ as incorrectly found in earlier models [eq. (5)].

However, the relevance of a model cannot be established by comparison with the forward hardening curve alone, it has to be equally successful in its interpretation of related phenomena such as the reverse straining curve or the stress-relaxation curves. Considering the permanent softening effect denoted by $\Delta\sigma_p$ in fig. 8 as characteristic of the Bauschinger effect, one is interested in comparing it with twice the mean matrix stress:

$$\langle\sigma\rangle_M = \Delta\sigma_p/2, \tag{12}$$

since $\langle\sigma\rangle_M$ opposes flow in the forward direction and is additional to it in the reverse direction. ATKINSON *et al.* (1974) found excellent agreement between this expression and experimental results in a number of oxide-dispersion-hardened alloys.

Despite the obvious success of this model in describing stress–strain curves obtained at very low temperature (77 K) in Cu–SiO_2 for instance, it tends to grossly overestimate the hardening behavior around room temperature and above. Relaxation effects become essential at these temperatures; they lower the work-hardening rate and reduce the reversible part of the plastic flow taking place when unloading.

Another type of dislocation arrangement has been observed in Cu–Zn–SiO_2 alloys by HUMPHREYS and STEWART [1972]. They found very clear evidence of *secondary loops* of *prismatic* character (fig. 16) and interpreted it with the wire model shown in fig. 17. Shear loops in the primary glide plane are accompanied by primary prismatic loops with identical Burgers vectors. Outside the primary slip system, several sets of secondary dislocation loops are developed along ⟨100⟩ directions with non-primary Burgers vectors. A void tends to form on the dark side of the particle (fig. 17). The origin of this type of stress relief mechanism is best appreciated from the scheme originally drawn by ASHBY [1966] (fig. 18). The action of the tensile stress is to create a shear stress in the primary slip plane at the same time as it tends to separate the particle from the matrix along the tensile direction, thus generating a cavity. In the direction normal to the tensile axis, an excess of material does appear under the form of *prismatic punched loops* of interstitial character. Notice that the exact geometry of a particular crystallographic system (fcc, bcc, etc.) is not considered in this scheme and will complicate the final picture.

Several types of dislocation arrangements have now been mentioned. They are best summarized by the two-dimensional representation proposed by BROWN and STOBBS [1971b] and shown in fig. 19.

Mechanism A describes the cross-slip of Orowan loops around small particles (< 300 nm) as suggested by HIRSCH's model [1957] (see also fig. 14), leading to the formation of prismatic loops having the Burgers vector of the primary slip system.

Mechanism B appears around somewhat larger particles (> 300 nm) and has been observed by CHAPMAN and STOBBS [1969] and reviewed by BROWN and STOBBS [1971b]. This involves Burgers vectors belonging to the cross-slip plane and shows very characteristic small rotations in the immediate surroundings of the particle with respect to the matrix. This can be easily deduced from the presence of two orthogonal sets of similar screw dislocations on the two facets of the particle contained in the projection plane in fig. 19.

Mechanism C is purely formal and has never been observed. Its particularity consists

References: p. 2174.

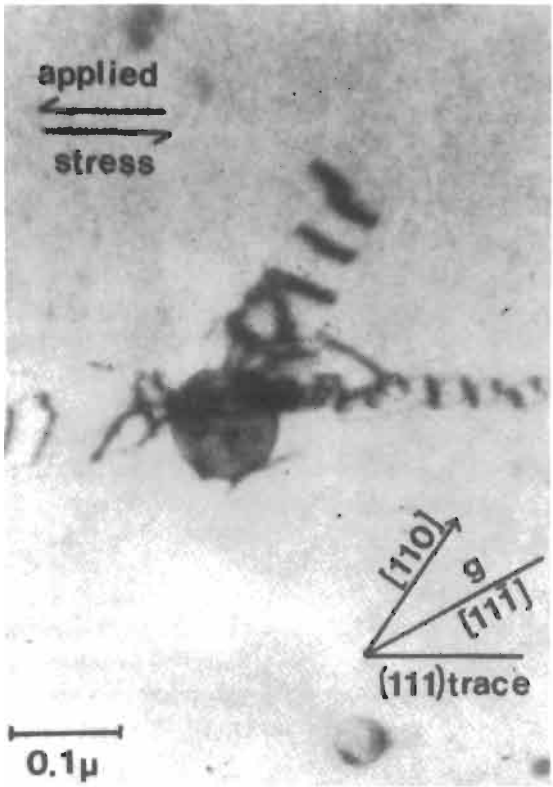

Fig. 16. Primary and secondary prismatic loops in α-brass + SiO_2 deformed at 25°C in simple glide (after HUMPHREYS and STEWART [1972]).

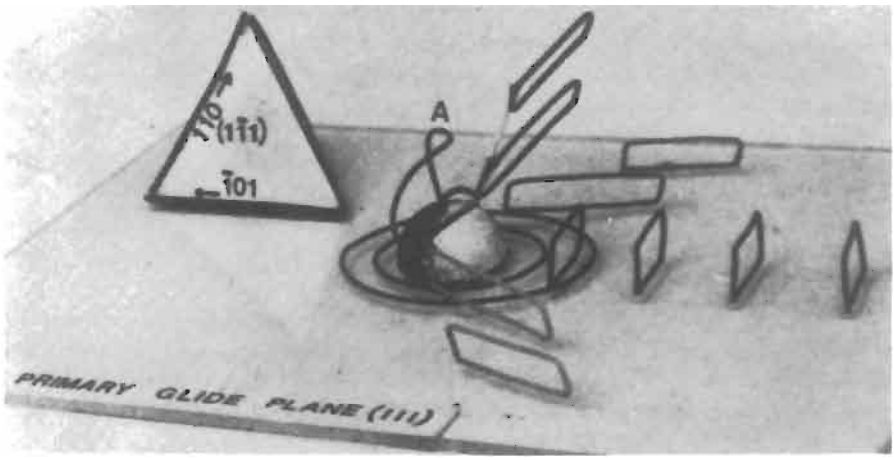

Fig. 17. A wire model describing prismatic loop formation along three systems and void formation on the dark side of the particle (after HUMPHREYS and STEWART [1972]).

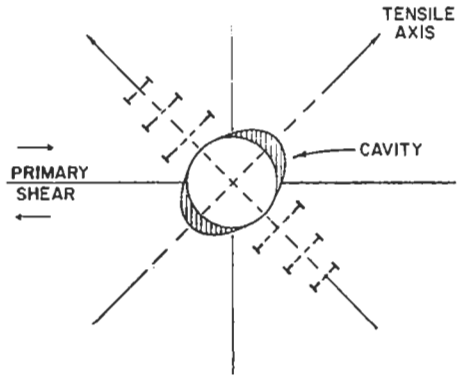

Fig. 18. Interstitial prismatic loops and void formation under tensile stress (after ASHBY [1966]).

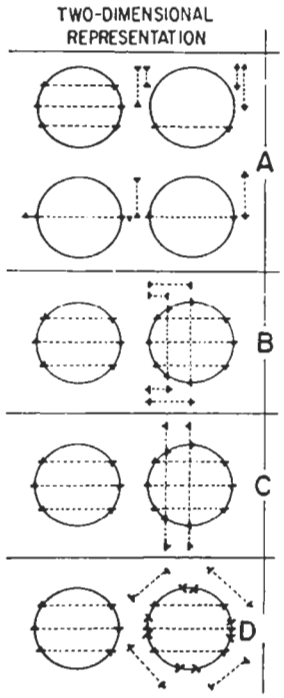

Fig. 19. Two-dimensional summary of the various modes of plastic relaxation: (A) formation of Orowan loops and cross-slip by Hirsch mechanism (small particles $\lesssim 300$ nm); (B) activation of several slip systems, Orowan and prismatic loop formation, screw segments form twist boundaries, particle rotates (sizes $\gtrsim 300$ nm); (C) association of shear loops without rotation (not observed experimentally); (D) accumulation of prismatic loops and/or punched loops as in Asby's model (fig. 18). (From BROWN and STOBBS [1971b].)

References: p. 2174.

in containing only shear loops and no prismatic loops but it does not yield the correct compatibility of deformation.

Mechanism D is that of HUMPHREYS and STEWART [1972] and involves both primary and secondary prismatic loops of interstitial and vacancy characters, the latter type being able to condense on the particle–matrix interface and create a void along the tensile direction when the cohesive forces between the oxide and the metallic matrix are not very strong.

Before going further into the mechanisms of stress relaxation and recovery, let us look into more macroscopic models which are more relevant for the deformation of alloys with larger particles.

3.2.3. Heterogeneous deformation of alloys containing large particles

Instead of looking at detailed dislocation mechanisms in the immediate vicinity of the particle, one can envisage a more general approach to the deformation process of two-phase alloys and ask the question: how do crystals develop resistance to deformation? Of course, the density of forest dislocations in the path of gliding dislocations and the subsequent reduction of the mean link-length between dislocation nodes provide the correct answer. Following this approach, ASHBY [1971] draws a parallel between pure metals having a density of statistically stored dislocations, ρ^S, with a corresponding average slip distance λ^S, and two-phase materials where the multiplication of dislocations is greatly enhanced by the presence of the second phase. In the latter case, large strain gradients are induced in the matrix and *geometrically necessary dislocations* are created in order to accommodate these gradients and thus allow the two phases to deform in a compatible way. Their density ρ^G is definitely higher than in pure metals and its proposed value is given by the expression

$$\rho^G = \frac{f}{r}\frac{4\gamma}{b}, \tag{13}$$

where γ is the shear strain. The average geometric slip distance, λ^G, for a volume fraction f of particles with radius r can be written as:

$$\lambda^G = \frac{r}{f} = \frac{1}{nr^2}, \tag{14}$$

where n is the number of particles per unit volume. ρ^G takes on the form:

$$\rho^G = \frac{1}{\lambda^G}\frac{4\gamma}{b}, \tag{15}$$

similar to the expression

$$\Delta\rho^S = \frac{1}{\lambda^S}\frac{4\Delta\gamma}{b} \tag{16}$$

in pure metals obtained by writing that the dislocation loops emitted by an active source stop expanding when they reach a diameter equal to λ^S.

When straining a two-phase crystal, the actual shear resistance is given by an expression similar to that of single-phase materials:

$$\tau = \tau_0 + \beta G b \sqrt{\rho^G}, \tag{17}$$

where τ_0 is the friction stress. This yields:

$$\tau = \tau_0 + \beta G \left(\frac{f}{2r} b\gamma \right)^{1/2} \tag{18}$$

which gives the correct parabolic dependence of the strain-hardening rate on both strain and volume fraction.

Another macroscopic continuum approach was followed by HUMPHREYS [1979] in trying to describe the deformation features produced at high strains (10–50%) in the neighborhood of micron-sized particles. A detailed account of dislocation arrangements can no longer be given, nevertheless a small volume of matrix containing a particle will tend to deform by a shearing mechanism involving several intersecting slip systems, the primary system being dominant (fig. 20a). If the particles were shearable as in fig. 20b no rotation would appear: this is the case in nickel-base alloys with excessively small γ' particles (see § 6.2). If, on the contrary, the particles are large and unshearable, the dense network of dislocations which develops in the volume adjacent to the particle will rearrange into subgrain boundaries. Each subgrain is slightly rotated with respect to its neighbor and the progressive misorientations will add up to the final rotation of the deformed zone of radius R (fig. 20c). The angle of rotation of a simple arrangement of similar dislocations separated by equal distances h is:

$$\tan\theta \approx b/h \approx \gamma. \tag{19}$$

Calling ρ^R the average dislocation density in the deformed zone, a more general expression applicable in the case where several types of dislocations are present in the deformation zone reads:

$$\tan\theta \approx \rho^R b R \approx \gamma. \tag{20}$$

This is a good approximation at small strains. Local lattice rotations can be estimated by X-ray techniques or by selected-area electron diffraction. This latter method was used by HUMPHREYS [1977] who examined an Al–Cu solid solution containing silicon particles of several μm size. Local misorientations of adjacent subgrains were measured and the cumulative misorientation was plotted as a function of the distance from the particle (fig.

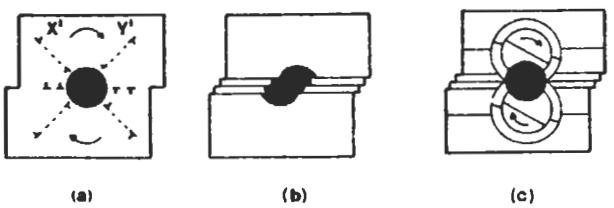

Fig. 20. The origin of a deformation zone at a particle: (a) Orowan loops on multiple slip systems; (b) when precipitates are sheared, as in γ'-hardened alloys, no rotation takes place; (c) continuum model of the rotation around a particle. (After HUMPHREYS [1977].)

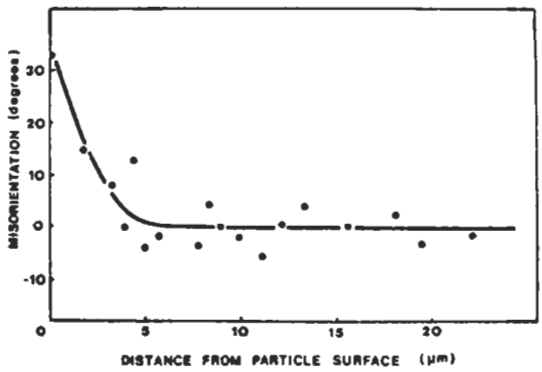

Fig. 21. Cumulative misorientation of the matrix in the vicinity of a 4 μm-size particle in cold-rolled aluminium (from HUMPHREYS [1977]).

21). We see that the cumulative rotation can attain 30° in a deformation zone of the order of the size of the initial particles. One can expect these regions of the material to be extremely active when recovery or recrystallization events start operating (see § 8).

3.3. Stress relaxation and recovery effects

All strengthening mechanisms described so far rest quite naturally on high densities of dislocations being developed in the matrix and particularly in the vicinity of the particles. If such structures are expected to be rather stable at low temperature (77 K for instance), one wonders what will happen to them at room temperature and above. Experimentally, the strain-hardening coefficient of two-phase alloys is found to drop drastically in the temperature range 200–400 K and the rate of recovery exhibits a maximum in the same domain as shown in fig. 22, taken from the work of HIRSCH and HUMPHREYS [1970]. Note that higher strain rates tend to shift the drop to higher temperatures, as expected. Note also that the Cu–Zn solid solution is less affected by temperature (dashed curve, upper graph) than the pure matrix.

Turning to the point of micromechanisms responsible for recovery effects at about room temperature, the original value of about 1.1 eV (125 kJ/mole) measured by HIRSCH and HUMPHREYS [1970] most likely pertains to the local and limited rearrangement of dislocations by cross-slip and pipe-diffusion-aided climb. All mechanisms summarized in fig. 19 will benefit from limited climb by pipe diffusion and thus realize the equilibrium plastic relaxation state described by BROWN and STOBBS [1976]. Its main character however is of glissile nature. At still higher temperatures (550 K and above) diffusional relaxation starts playing a dominant role in the behavior of the material and most authors agree upon an apparent activation energy of 1.5–1.7 eV (140–160 kJ/mole). GOULD *et al.* [1974] consider that climb is controlled by jog nucleation on the dislocations trying to by-pass the particles and interpret the rather high values of the activation energy as the sum of two terms: pipe-diffusion for copper plus twice the formation energy for a jog: $U_p + 2U_j \approx 0.9 + 2 \times 0.4 \approx 1.7$ eV. Experiments carried out on Cu–SiO_2 single crystals by LLOYD and

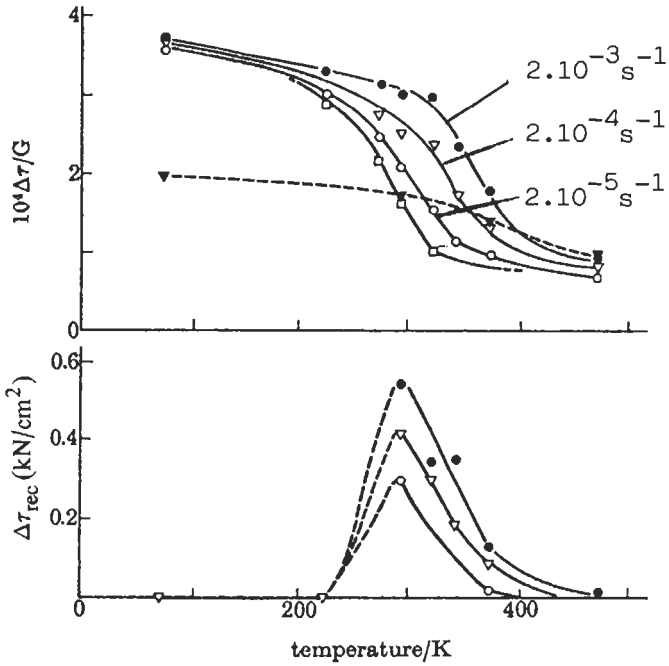

Fig. 22. The effect of temperature and strain rate on the work-hardening rate (top) and the extent of recovery (bottom) in Cu + 0.22% Al_2O_3. The Cu + 10% Zn + 0.22% Al_2O_3 crystals (dashed curve) are less sensitive to temperature.

MARTIN [1978] provide strong support for this model in the temperature range 470–1010 K. The interested reader will find an extensive discussion of creep recovery in original articles by LLOYD and MCELROY [1975, 1976] dealing with anelasticity. Anelastic strains are time-dependent recoverable components of deformation which accompany reduction or removal of stress during high temperature deformation.

Not only does the strain-hardening coefficient fall off rapidly around room temperature (HIRSCH and HUMPHREYS [1970]) and the initial yield stress in the temperature range of 400–500°C (LLOYD and MARTIN [1978]) but also the final dislocation structure is less disorganized as mentioned by HAUSSELT and NIX [1977] who observed by TEM the high temperature deformation of Ni–20Cr–2Tho_2. They also found that the final dislocation density is proportional to $\sigma^{1.6}$ rather than σ^2 as found in pure metals at low temperature. The threshold stress for by-passing of particles is significantly lowered ($\sim 0.43\sigma_0$, LLOYD and MARTIN [1978]) or even tends to vanish: the thermal fluctuations assist the dislocation in by-passing the particle by climb before the critical configuration for Orowan looping is reached (HOLBROOK and NIX [1974]). This effect is quantitatively considered in the model of SHEWFELT and BROWN [1973]. It becomes the key phenomenon in precipitation-hardened alloys at high temperature.

References: p. 2174.

3.4. A continuum-mechanics approach to the internal stress

The problem of correctly describing the plastically deformed state of a single- or two-phase material is far from trivial. Metallurgists have been looking for a hardness state variable (HART [1970]) with the uneasy feeling that entrusting the effect of complex dislocation arrangements to a single scalar variable is far from satisfactory. Although on a microscopic scale ($< 1\ \mu$m) the tensorial nature of dislocation stress fields (LI [1963]) and of strain gradients around particles (ESHELBY [1961] and BROWN and STOBBS [1971]) is duly acknowledged, this sophistication is lost in the equations describing stress–strain curves, creep curves or strain hardening rates.

On the other hand, the macroscopic approach of continuum mechanics has developed general constitutive equations for viscoelastic and viscoplastic behavior of isotropic and anisotropic materials, but seems to ignore the crystallographic nature of slip and dislocation mechanisms. Readers unfamiliar with basic descriptions of elasto–plastic flow equations will find them in McClintock and Argon's [1966] book (see *Further reading*).

Understanding and describing the behavior of crystalline solids under alternative loading (tension, compression, fatigue) and multiaxial stress conditions (tension–torsion) is forcing the mechanical and the metallurgical approaches towards a necessary point of convergence.

Since transient regimes are usually the most revealing tests for a model, let us look at what happens to the creep curve when the applied stress σ_a is suddenly lowered slightly by $\Delta\sigma$ during the steady-state regime characterized by a strain rate $\dot{\varepsilon}_1$. This so-called *strain transient dip test* was first proposed by SOLOMON and NIX [1970] in order to obtain an estimate of the internal stress σ_i. The various alternatives are schematically represented in fig. 23: for small stress reductions, forward creep continues with a reduced rate $\dot{\varepsilon}_2 < \dot{\varepsilon}_1$. For larger stress decrements the flow rate of the specimen is stopped for a period of time Δt which increases with $\Delta\sigma$. This has been called the *incubation period* by PARKER and WILSHIRE [1975], who observed it in Cu–Co and nickel-base superalloys (WILLIAMS and WILSHIRE [1973]). For still larger stress reductions, the instantaneous creep rate, just after the stress transient, is negative: macroscopic strain recovery is taking place. This effect in creep is the high-temperature equivalent of the Bauschinger effect in tensile tests. Reversing the stress is not necessary in order to reverse the flow: negative strain rates appear already after partial unloading.

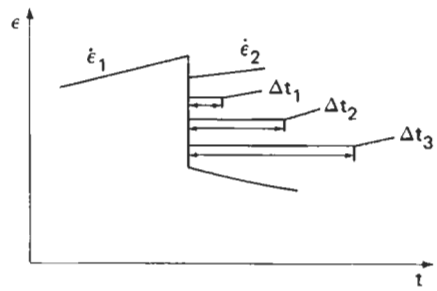

Fig. 23. Various possible alternative responses to a stress drop $\Delta\sigma$ during a creep test.

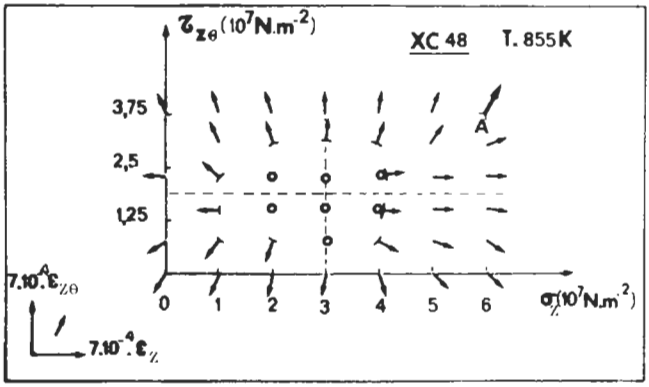

Fig. 24. Tension–torsion test. Steady-state stress with vectors indicating flow direction. Evolution of the plastic flow vector after various load decrements in tension and/or torque. (After OYTANA *et al.* [1979b].)

In a more general fashion, if creep tests are carried out under multiaxial loading such as hollow cylinders tested in tension-torsion, experimental results such a those reported by OYTANA *et al.* [1979] and presented in fig. 24 confront us with the evidence that the material has developed an internal structure with an anisotropic character related to the temporal and spatial features of the applied stress. These experiments have been performed on α-brass and on XC48 mild steel. The tensile stress σ is plotted along the horizontal axis and the torsion stress $\tau_{z\theta}$ along the vertical axis so that each point fully describes a complex shear- and tensile stress state to which the specimen is submitted until a stationary creep rate is reached: the flow rate is represented in intensity and direction by the arrow attached to each point: the $\dot{\varepsilon}_z$ component lies along the horizontal axis and $\dot{\varepsilon}_{z\theta}$ along the vertical axis. Stress reductions affecting either the tensile load or the torque have been carried out as well as combined reductions, and the corresponding flow rates are indicated by arrows in fig. 24 for each new stress state. It is clear, here also, that a domain of zero creep rate does exist which is not centered around the origin of the diagram. The crystal is not hardened isotropically around the origin as a result of the strain it has undergone. There is, however, a region of *isotropic hardening* centered around the point defined by the vector $\boldsymbol{K}$ (fig. 25), and the stress shift $\boldsymbol{K}$ is called the *kinematical hardening* according to the suggestion first made by PRAGER [1955] who pioneered this new method of analyzing stress and strains in plastically work-hardening solids. Strain memory effects are adequately handled by this model. In the schematic two-dimensional representation (fig. 25), separating the shear and tensile components of the stress state, one would expect well-behaved materials to work-harden isotropically as shown by the dashed circle around the origin, but we find that most alloys and especially two-phase alloys develop strong kinematical hardening characteristics (large $\boldsymbol{K}$) combined with rather weak isotropic hardening (small R).

In order to develop a general formulation of the constitutive equations for plastic flow under complex stress states it is necessary to consider the referential coordinate system of the principal axis for the stress tensor and look at it in projection along the direction

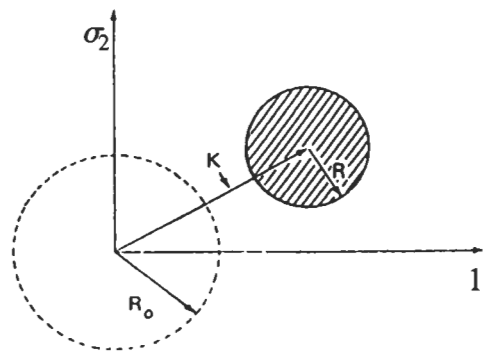

Fig. 25. Schematic representation in two-dimensional diagram of simple isotropic hardening R_0 and of kinematical + isotropic hardening $K+R$.

of the isostatic stress $\sigma = \frac{1}{3}(\sigma_1+\sigma_2+\sigma_3)$ where the usual yield criteria (TRESCA, VON MISES), are easily represented (fig. 26). Isotropic strain-hardening (dashed curves) leads to the absence of a Bauschinger effect, as shown schematically in fig. 26b. R_0 is the initial field strength of the material and $R(p)$ is the yield stress of the material after it has been hardened by the effect of the cumulative plastic strain identified by $p=|\varepsilon_{ij}|$ and defined as the time integral over the strain path of:

$$\dot{p} = \tfrac{1}{2}\sqrt{2}\left[\left(\dot{\varepsilon}_1 - \dot{\varepsilon}_2\right)^2 + \left(\dot{\varepsilon}_2 - \dot{\varepsilon}_3\right)^3 + \left(\dot{\varepsilon}_3 - \dot{\varepsilon}_1\right)^2\right]^{1/2}, \tag{21}$$

which can be understood by analogy with eq. (22), below.

The yield criteria proposed by VON MISES (see McClintock and Argon's [1966] book, *Further reading*) simply expresses the fact that the second invariant of the strain deviator, the scalar quantity $J(\sigma)$, is the radius of a circle in the σ_1, σ_2, σ_3 plane (dotted circle in fig. 26):

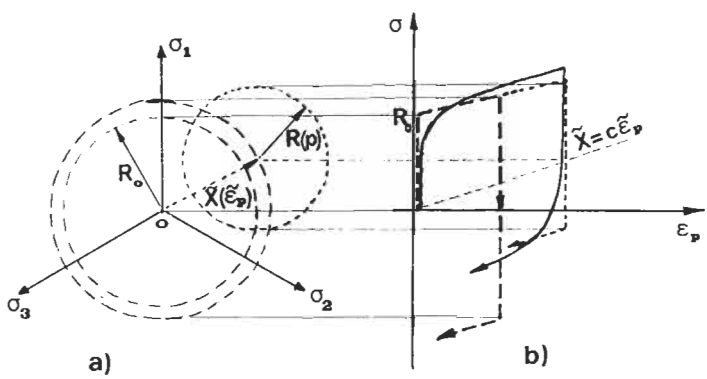

Fig. 26. Schematic representation of isotropic (dashed) and linear kinematical (dotted) yield criteria with associated stress–strain curve and reverse loading curve.

$$J(\sigma) = \tfrac{1}{2}\sqrt{2}\left[(\sigma_1 - \sigma_2)^2 + (\sigma_2 - \sigma_3)^2 + (\sigma_3 - \sigma_1)^2\right]^{1/2}. \tag{22}$$

Now introducing a kinematical stress variable $\boldsymbol{X}$ of tensorial nature as suggested by PRAGER [1956] simply changes the last expression into a similar relation which can be written symbolically:

$$J(\boldsymbol{\sigma} - \boldsymbol{X}) = \tfrac{1}{2}\sqrt{2}\left[(\sigma'_{ij} - X'_{ij})(\sigma'_{ij} - X'_{ij})\right]^{1/2}, \tag{23}$$

where σ' and $\boldsymbol{X}'$ are the applied and kinematic stress deviators. The linear kinematic yield criterion reads:

$$\begin{cases} f(p) = J(\boldsymbol{\sigma} - \boldsymbol{X}) - R(p) \le 0, & (24) \\ \boldsymbol{X} = c\boldsymbol{\epsilon}_p, & (25) \end{cases}$$

where the internal stress tensor $\boldsymbol{X}$ is proportional to the plastic strain tensor. Now the stress–strain curve (fig. 26b) exhibits a Bauschinger effect which the isotropic strain hardening model could not account for. But the experimental curve (solid line in the figure) is not yet correctly represented by this elementary model because linear hardening is too crude an approximation. Confronted by the nonlinear strain-hardening behavior and the elasto-plastic memory effects of γ'-hardened nickel-base superalloys (IN 753 and Nimonic 80A) when tested in fatigue, ASARO [1975] already suggested the introduction of a kinematical hardening model with several successive linear regions. CHABOCHE [1977] has introduced the concept of nonlinear kinematical hardening by changing eq. (25) into

$$\dot{\boldsymbol{X}} = ac\dot{\boldsymbol{\epsilon}}_p - c\boldsymbol{X}\dot{p} \tag{26}$$

and taking a general yield criterion with a set of convex hypersurfaces in $\sigma_1, \sigma_2, \sigma_3$ space (the dot symbolizes the time derivative). The general equation of an equidissipative surface can be written as:

$$\Omega\left[\boldsymbol{\sigma} - \boldsymbol{X}, R(p,T)\right] = K(p,T), \tag{27}$$

where R and K increase with the cumulative strain p and decrease with temperature T. The plastic flow rate $\dot{\varepsilon}_p$ is found by writing that it is taking place in the direction normal to the equidissipative surfaces described above (fig. 27). So finally the constitutive equations for nonlinear kinematic hardening can be written formally as:

$$\begin{cases} \dot{\boldsymbol{\epsilon}} = \dfrac{\partial \Omega}{\partial \sigma}, & (28) \\ \mathrm{d}\boldsymbol{X} = ac\,\mathrm{d}\boldsymbol{\epsilon}_p - c\boldsymbol{X}\,\mathrm{d}p - h\boldsymbol{X}\mathrm{d}t, & (29) \\ \sigma = \boldsymbol{X}(\boldsymbol{\epsilon}_p) \pm R(p,T) \pm K(p,T)\left|\dot{\boldsymbol{\epsilon}}_p\right|. & (30) \end{cases}$$

Equation (29) is a more sophisticated version of eq. (26), now including two recovery

References: p. 2174.

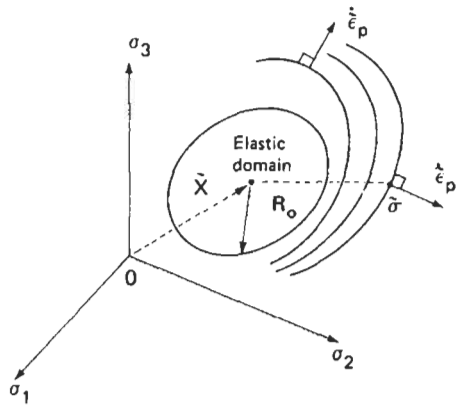

Fig. 27. Representation of successive yield surfaces and of the plastic flow rate which is perpendicular to them.

terms. The first one, $-cX\mathrm{d}p$, is related to cumulative strain and will tend to cancel kinematical hardening after repeated stress reversals so that a stabilized fatigue loop can be reached as experimentally observed in fatigue tests. The second one, $-hX\mathrm{d}t$, describes the time-dependent recovery effects taking place during relaxation tests, for instance, and previously referred to as *anelasticity*.

Finally, eq. (30) can closely describe experimental stress–strain curves with stress reversals such as in fig. 28: R_0 is the initial yield stress which can be a threshold stress

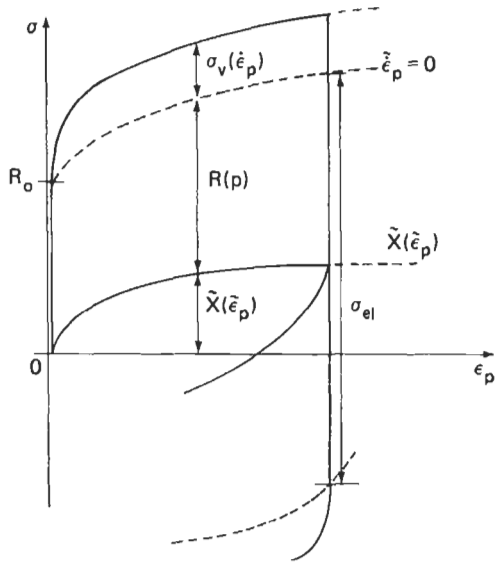

Fig. 28. Nonlinear kinematical hardening and strain-rate sensitivity of the stress–strain curve (after CHABOCHE [19771).

as in the Orowan by-passing process; $R(p)$ is the isotropic strain hardening component of the material's resistance, the *latent hardening* produced by straining a crystal in one direction prior to deforming it by slip on a second slip system is an effect of this nature, it is also called *forest hardening* in dislocation theory; $\boldsymbol{X}(\boldsymbol{\varepsilon}_p)$ on the other hand is of tensorial nature and describes the stress tensor associated with the *internal stress* field generated inside the material by the specific dislocation configuration associated with the strain $\boldsymbol{\varepsilon}_p$; and the last term $K(p, T)|\dot{\boldsymbol{\varepsilon}}|$ describes the strain-rate effects encountered in tensile tests. The elastic domain or zero-creep-rate domain after a stress reduction has a diameter equal to $2R(p)$ (see fig. 24, for instance).

Looking at equations (28)–(30), we can see that several numerical constants have been introduced. With the help of modern computers, they can be rapidly adjusted to obtain the closest possible fit with the various experimental curves, but such an approach does not provide any serious insight into the physical processes underlying the described mechanical behaviour. This model has been refined enough by CAILLETAUD and CHABOCHE [1979] to enable the authors to describe the macroscopic effects of microstructural changes induced by varying the temperature in a series of cyclic tests performed on a γ'-hardened nickel base superalloy, namely IN-100. More recently, CULIE *et al.* [1982] have made an interesting attempt to correlate microstructural changes observed by TEM in this alloy after various temperature and stress cycles with the parameters involved in the macroscopic equations describing the flow rate of the material. Dislocation rearrangements and γ'-coarsening during high-temperature anneals followed by the precipitation of fine γ' particles during rapid cooling, are correctly handled by this model. This successful attempt to bridge the gap between microscopic phenomena and the macroscopic equations describing the behavior of a two-phase industrial material under complex loading and thermal history needs to be developed further. Refinements in the description of elementary mechanisms at the scale of grains and subgrains in polycrystalline materials need to be introduced. Since the tensorial nature of the internal stress is given due attention, this quantitative approach can be used with confidence in polyphase materials which are known for their anisotropic response to stress, even at high temperature.

4. *High-temperature behavior of dispersed-phase alloys*

At temperatures low enough to keep climb processes down to a level where their contribution to the deformation rate is negligible, dislocations can only glide and possibly cross-slip when stress levels and orientations are favorable. At higher temperatures, however, ($T \gtrsim 0.5T_m$ or even $T > 0.4T_m$ under high local stresses) climb events start having a high enough frequency to contribute significantly to the material's efforts to relax local stress concentrations or even long-range stresses. High dislocation densities introduced during swaging, extrusion or cold work have raised the yield strength of the material to very high levels and the presence of the finely dispersed oxide particles has stabilized these disorganized tangles of dislocations. When the material is then heated up to temperatures where diffusion is operating, recovery can take place by climb-assisted

References: p. 2174.

glide. A new degree of freedom is thus introduced for dislocations which can now climb over small particles, recombine and annihilate or, at least, associate with each other to form better organized configurations or networks which are more energetically stable under local stress conditions.

4.1. High-temperature subgrains in polycrystalline oxide-dispersion-strengthened alloys

The various aspects of recovery in ODS alloys have been best explored by GREWAL *et al.* [1975] in a study of BeO-dispersed polycrystalline nickel. Samples were cold-worked by swaging at room temperature down to 70% reduction in area and then annealed for 1 h at various temperatures between 400 and 982°C. The resulting creep stress for 100 h rupture life at 982°C is plotted as a function of the intermediate anneal temperature in fig. 29. These authors report that unorganized and extremely dense tangles of dislocations formed during swaging at room temperature transform into small elongated subgrains 0.2–0.5 μm in width during intermediate anneals and appear by TEM to be best organized for a 1 h treatment at 815°C, which corresponds to the highest creep resistance. At higher temperature the rearrangement of dislocations is too far advanced to preserve a good resistance of the material, and its stress rupture life drops again.

One can conclude that recovery in cold-deformed ODS alloys is a very active process as soon as temperatures are high enough to allow climb and rearrangement of dislocations into well organized subgrain boundaries (fig. 30). It is so active that recrystal-

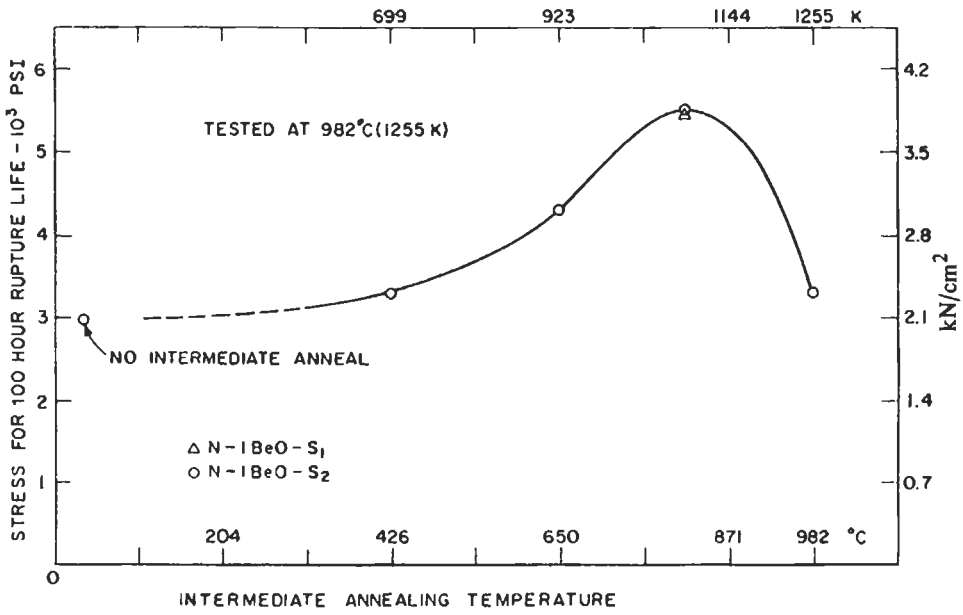

Fig. 29. Stress for 100 h rupture life at 982°C as a function of intermediate anneal temperature after swaging at 25°C of nickel-BeO (after GREWAL *et al.* [1975]).

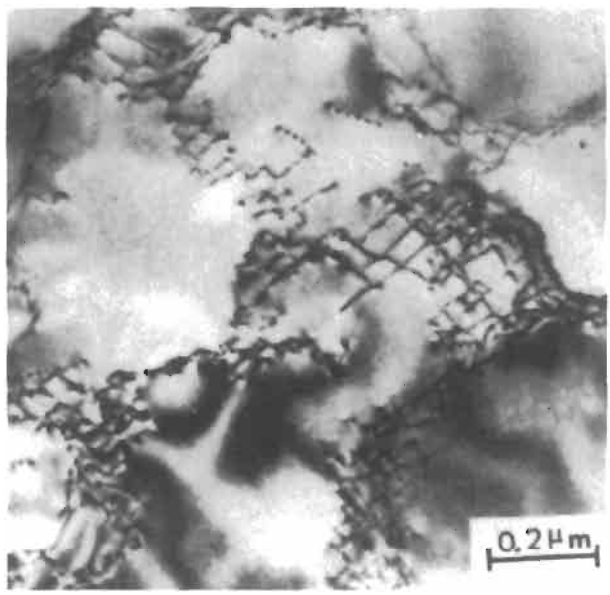

Fig. 30. Effect of 1 h recovery at 815°C in nickel–BeO after 60% reduction by swaging (from GREWAL *et al.* [1975]).

lization cannot take place even after large amounts of cold work. Rearrangements take place on a small scale (0.1–1 μm) owing to the stabilizing effect of the dispersed phase, and the formation of large-angle mobile boundaries is prevented. Existing grain boundaries on the other hand are also efficiently pinned by the particles and cannot absorb large amounts of dislocations by moving into deformed grains. Hence, recovery is extremely intense in these alloys until all necessary local rearrangements have taken place. Then again the structure appears frozen if no change in external conditions $(\sigma, T, \dot{\varepsilon})$ takes place. If the material is exposed to stresses at high temperature, dynamic dislocation patterns will develop which look less stable than static arrangements (fig. 31). The average size of the dynamically stable subgrains is inversely proportional to the applied stress,

$$d = 4\frac{Gb}{\sigma_a}, \tag{31}$$

as suggested by the observations of LASALMONIE and STRUDEL [1975a] in nickel and AHLQUIST and NIX [1971] in aluminum.

4.2. Apparent and effective creep parameters

Ever since the oxide-dispersion-strengthened alloys appeared on the market in the late fifties, scientists have been astonished and fascinated by the unusually high values of their apparent creep parameters (ANSELL and WEERTMAN [1959]). Experimentally measured

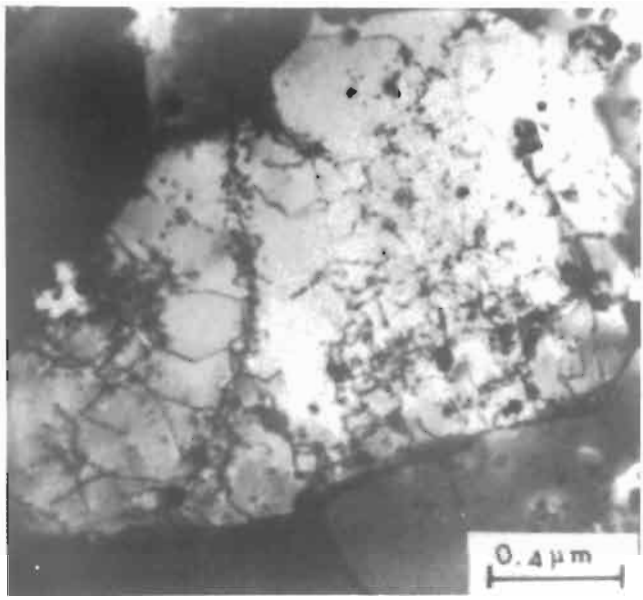

Fig. 31. Dislocation structure of the same material as in fig. 30 after 2 h creep at 982°C under 21 MPa (from GREWAL *et al.* [1975]).

activation energies for creep range from 400 to 800 kJ/mole and the apparent stress-sensitivity exponent can be as high as 10 and even 30 or 40 (WILCOX and CLAUER [1966]).

Another striking aspect of this type of material concerns its exceptionally high flow stress: at 600°C pure nickel will flow under a stress of about 20 MPa, whereas TD-nickel will strictly resist deformation up to an applied stress of 200 MPa. One is naturally led to inquire about the origin of such an unusual resistance: is there a stress inside the material itself which opposes the applied stress and thereby prevents individual dislocations from being exposed more or less directly to it? We are now aware of the fact that any kind of plastically deformable crystalline material develops particular dislocation arrangements whenever it undergoes deformation; it work-hardens in such a way as to oppose further straining in the same direction. In the case of monotonic uniaxial loading, a simple approach using scalar functions to deal with average values of stresses, the *internal stress* can be introduced as:

$$\sigma_a = \sigma_i + \sigma_e. \tag{32}$$

Here the applied stress, σ_a, is balanced by the internal stress, σ_i, plus the stress experienced by each individual dislocation, σ_e. This is of course a very direct and dramatic way of going from the macroscopic scale (σ_a) to the level of the individual dislocation (σ_e) and it is probably much too coarse a model to give a precise description of the actual situation, except perhaps in single crystals.

Creep models using internal stresses are many in the literature and numerous controversies have given this potent concept a rather confusing image. We shall

voluntarily restrict ourselves to one particular model which has developed enough self-consistency to be sketched rapidly.

If we accept eq. (32), despite its ambiguity, as a first approach to a definition of the internal stress, we can then ask: what variables does σ_i depend upon? Temperature, applied stress, internal structure of the material, strain, metallurgical history of the sample are probably some of them. Early models did not consider the internal stress to be temperature-dependent; most of them even used to call it the *athermal stress* as if it were an intrinsic property of a particular alloy.

The creep rate in the steady state is generally written as a function of applied stress σ_a and of temperature T as:

$$\dot{\varepsilon}_s = A\sigma_a^{n_a} \exp(-Q_a/kT), \tag{33}$$

where the pre-exponential factor A includes entropy terms plus structural and metallurgical factors.

The *apparent creep parameters* are defined by the following expressions:

$$n_a = \left(\frac{\partial \ln \dot{\varepsilon}_s}{\partial \ln \sigma_a}\right)_T, \quad Q_a = -kT^2\left(\frac{\partial \ln \dot{\varepsilon}_s}{\partial(1/T)}\right)_{\sigma_a}. \tag{34}$$

Similarly, *effective creep parameters* can be introduced by reference to the effective stress:

$$n_e = \left(\frac{\partial \ln \dot{\varepsilon}_s}{\partial \ln \sigma_e}\right)_T, \quad Q_e = -kT^2\left(\frac{\partial \ln \dot{\varepsilon}_s}{\partial(1/T)}\right)_{\sigma_e}. \tag{35}$$

These should relate directly to elementary mechanisms and thus be more easily interpreted physically. The creep equation can now be written as:

$$\dot{\varepsilon}_s = B\left(\frac{\sigma_a - \sigma_i}{E}\right)^{n_c} \exp\left(-\frac{Q_e}{kT}\right), \tag{36}$$

but eqs. (33) and (36) are just two different ways of describing the same phenomenon, namely the steady-state creep rate. Apparent and effective creep parameters must therefore be related, as SAXL and KROUPA [1972] pointed out. Assuming that the internal stress is a function of applied stress σ_a and temperature only, $\sigma_i(\sigma_a, T)$, two partial derivatives must be introduced:

$$\sigma_i' = \left(\frac{\partial \sigma_i}{\partial \sigma_a}\right)_T, \quad \sigma_i^* = \left(\frac{\partial \sigma_i}{\partial T}\right)_{\sigma_a}. \tag{37}$$

They describe how the internal structure of the material is altered by changes in external conditions.

A complete derivation can be found in the original article (LASALMONIE and STRUDEL [1980]); it leads to the following relations:

References: p. 2174.

$$n_a = n_e \frac{\sigma_a}{\sigma_a - \sigma_i}\left(1 - \sigma_i'\right), \tag{38}$$

$$Q_a = Q_e - n_e kT^2 \frac{dE}{EdT} - n_a kT^2 \frac{\dot{\sigma}_i}{1 - \sigma_i'}, \tag{39}$$

which clearly indicates that the *apparent* creep parameters can be drastically different from their *effective* counterparts in particle-hardened alloys. Note that the temperature dependence of the elastic modulus is introduced by the second term of eq. (39).

4.3. Average internal stresses in dispersed-phase alloys

Some of the experimental data which have stimulated the development of the scalar but quantitative representation of the internal stress will now be examined.

In a **single-phase alloy** where no threshold stress is present, hardening can be described as a function of the applied stress by $\sigma_i = \alpha\sigma_a$, and eqs. (38) and (39) reduce to:

$$n_a = n_e, \quad Q_a = Q_e - n_a kT^2 \frac{dE}{EdT}, \tag{40}$$

where the corrective term for the activation energy comes from the decrease of Young's modulus with temperature alone. It is a significant correction, as pointed out by LUND and NIX [1975]. For instance, pure nickel at 900°C has a stress exponent of 4, $Q_e = Q_D \approx$ 350 kJ/mole and the corrective term is about 42 kJ/mole, so that the measured activation energy for creep is about 390 kJ/mole.

In **dispersion-strengthened** alloys the situation is different since most authors seem to consider that one component of the back-stress is the threshold stress, either associated with the Orowan stress for by-passing the particles (LUND and NIX [1976]), or indirectly with the stress necessary for a dislocation to break away from well knitted networks of immobile dislocations (HAUSSELT and NIX [1977] and LASALMONIE and STRUDEL [1975a, 1980]).

Considering the case of TD-nickel, for instance, the activation energy for plastic flow varies with temperature as shown in fig. 32. Similar results have been reported by GUYOT and RUEDL [1967] for Al–Al_2O_3 alloys. Several ranges of temperatures must be considered; in each of them a different dislocation mechanism is controlling the flow stress.

At *low temperatures* ($T < 100$°C) the activation energy is very low, ~ 0.4 eV, which is about twice the energy for the formation of a jog on a dislocation. At such low temperatures flow stresses are very high and decrease rapidly until a plateau is reached where the formation of jogs between repulsive dislocations can take place by thermal activation. The model for the formation of jogs on moving dislocations cutting repulsive trees of the forest dislocations is outlined in ch. 21, p.1904 (see also ch. 20, § 3.6).

At *intermediate temperatures* (100°C $\lesssim T \lesssim$ 700°C) activation energies are clearly in the range of the energy for self-diffusion in nickel (320–360 kJ/mole) but the stress exponents can become very large. The applied stresses are of the order of the threshold

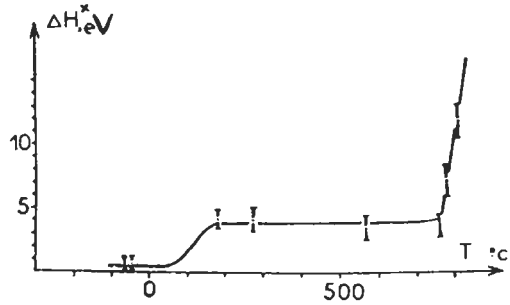

Fig. 32. Variation of the activation energy for plastic flow with temperature in TD-nickel (from LASALMONIE and SINDZINGRE [1971]).

stress σ_0 and do not significantly modify the inner dislocation density of the material; they simply assist and bias the climb events into producing a strain in a given direction. Hence in eqs. (38) and (39), $\sigma_i \approx \sigma_0$ and σ_i' and σ_i^* are negligible:

$$n_a = n_e \frac{\sigma_a}{\sigma_a - \sigma_0}, \quad Q_a = Q_e. \tag{41}$$

This can be best observed in creep tests where σ_a is just above σ_0 and n_a takes on strikingly high values (10–40).

At *high temperatures* ($T \gtrsim 700°C$) and for stresses above 180 MPa (LASALMONIE and STRUDEL [1980] the situation is more complex especially when the applied stress is larger than the threshold stress. This is clearly described by fig. 33, suggested by the work of LUND and NIX [1976] on single crystals of TD-nichrome. The total back-stress appears as the sum of the threshold stress (taken here as the Orowan stress) present in TD-nichrome and the strain-hardening stress as measured in the pure Ni–20% Cr matrix without ThO_2 particles. If we assume that a simple additive rule applies, then

$$\sigma_i = \sigma_0 + \alpha\sigma_a. \tag{42}$$

Now $\sigma_i' = \alpha$ as for pure metals and

$$n_a = n_e \frac{(1-\alpha)\sigma_a}{(1-\alpha)\sigma_a - \sigma_0}. \tag{43}$$

Since $\alpha \approx 0.1$–0.2, the denominator can be much smaller than the numerator. For applied stresses just above the threshold stress, the apparent exponent reaches high values such as 10 or 40 and tends to infinity as the applied stress approaches the threshold stress. In fig. 33, n_a is simply the tangent to the line through the experimental points.

The other limiting case is achieved at high stress ($\sigma_a \gg \sigma_0$); equations (38) and (39) then become

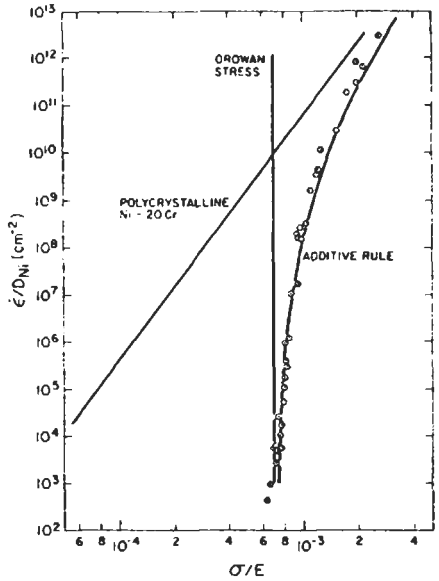

Fig. 33. Creep rates for polycrystalline single-phase Ni–20 Cr and TD-nichrome tested between 650°C and 1200°C (after LUND and NIX [1976]).

$$n_a = n_e, \quad Q_a = Q_e - n_e k T^2 \left(\frac{dE}{E dt} + \frac{\sigma_i^*}{1 - \sigma_i'} \right), \tag{44}$$

which describes the situation in either tensile tests or short creep tests. The stress exponent is nearly that of the pure matrix (fig. 33) but the activation energy becomes very large (fig. 32): the dynamical dislocation arrangements which form inside the material are very sensitive to the high-stress regime ($\sigma_i' \approx 0.3$–0.6) and the dependence on temperature σ_i^* also becomes large since recovery is very effective and increases rapidly with a rise in temperature. In magnesium hardened by MgO particles, the apparent activation energy varies from 230 kJ/mol (CROSSLAND and JONES [1972]) to 420 kJ/mol (VICKERS and GREENFIELD [1968]) depending on experimental parameters, as compared to the 135 kJ/mol energy for volume self-diffusion. Similarly in TD-nickel, values of 800 kJ/mol (WILCOX and CLAUER [1966]) and ranging from 400 to 1100 kJ/mol (LASALMONIE and SINDZINGRE [1971]) are to be compared with the 295 kJ/mol of the energy for self-diffusion. Activation energies for creep in pure aluminium and in SAP exhibit the same kind of distortion (GUYOT and RUEDL [1967] and GITTUS [1975]).

5. *Composition and microstructure of precipitation-hardened alloys**

When the hardening phase is obtained by precipitation of an intermetallic compound dispersed inside the matrix and often at grain boundaries too, the particles are called precipitates. They are usually shearable although their crystallographic system may be entirely different from that of the matrix. As reviewed in detail by MARTIN [1980], the strengthening effects may come from one or several of the following sources:

Coherency hardening: coherency stresses developed in the matrix by misfitting particles interact with moving dislocations. This effect is very strong in Cu–Co alloys (THREADGILL and WILSHIRE [1974]) where it raises the yield stress at low temperature but does not bring any appreciable contribution to creep resistance.

Chemical hardening arises from the energy associated with the additional precipitate-matrix surface generated in the shear plane of the cutting dislocation. This term is only significant at low temperature or during rapid and repeated cyclic loading.

Order-hardening is related to the possible creation of a surface of antiphase boundary (APB) when a dislocation of the disordered matrix cuts across the precipitate.

Stacking-fault (SF) hardening is another example of a strengthening mechanism connected with the creation of a high-energy surface. These last two processes are very effective at high stresses at intermediate temperatures (0.5–0.7 T_m).

Modulus hardening originates from the difference of elastic moduli between matrix and precipitates.

Steel hardened by ferrite particles and various carbides and aluminium-base alloys hardened by GP zones or θ, θ' and θ'' precipitates have been examined in other chapters. Most of the examples presented in this chapter will be taken from modern nickel-base superalloys which are widely used in aircraft, marine and industrial gas turbines for their mechanical strength as well as in nuclear reactors, submarines or petrochemical equipment for their high resistance to corrosion and oxidation. The interested reader will find more specialized information in a book edited by Sims and Hagel (see *Further reading*).

The nickel atom has the striking property of being able to engage in bonds with a large number of elements and form solid solutions, intermetallic phases or chemical compounds of all sorts. This basic affinity for other elements stems from the partially filled 3d shell of nickel ($3d^8, 4s^2$). This structure distinguishes it radically from its immediate neighbor, copper ($3d^{10}4s^1$), which is more limited in its ways of forming bonds despite having one more electron.

The simplest way to start looking into the various ordered intermetallic compounds of type A_3B that nickel can form with Al, Ti, Nb and similar elements, is to consider the structure of the densely packed planes in the fcc crystal which is the basic crystallographic system for nickel. Two configurations are possible: in the first one the threefold symmetry is preserved (fig. 34a), in the second one a tetragonal symmetry appears (fig. 34b). Notice that each plane has the Ni_3M composition, with M atoms avoiding the nearest neighbor M–M configuration. In the dense packing of these planes

* See also ch. 23, § 3.1.

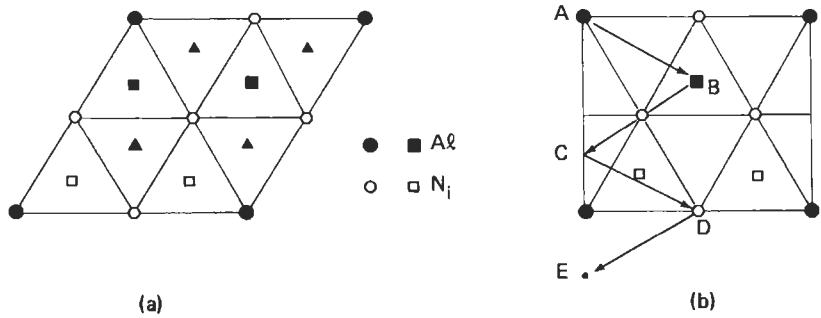

Fig. 34. Structure of the close-packed planes in A_3B ordered phases: (a) threefold symmetry of Ni_3Al, Ni_3Ti; (b) tetragonal or orthorhombic structures of Ni_3Nb, Ni_3Ta.

in the third dimension, creating M–M bounds means generating an antiphase boundary. With the triangular scheme (fig. 34a), packing as indicated by ▲ atoms will respect this rule and the sequence of planes can be called AB as in the fcc structure. If the third plane is located in such a way that M atoms are in ■ sites, an ABC stacking is obtained and can be repeated: this is the $L1_2$ structure (Strukturbericht notation) of Cu_3Au and Ni_3Al, which belong to the simple cubic system (Pm3m). When the stacking follows the simple ABABAB sequence, a hexagonal structure, $D0_{19}$, is created: it is that of $MgCd_3$ and only appears as locally faulted crystals in nickel-base intermetallic compounds. However, when the stacking sequence reads ABAC ABAC it belongs to the $P6_3/mmc$ symmetry group as the ABAB stacking and it is the familiar arrangements of the η-phase, Ni_3Ti, with $D0_{24}$ structure. Finally with the rectangular pattern (fig. 34b) two basic types of stacking are possible: (1) ABAB when the ● and ■ positions of M atoms are alternately repeated. This is the body-centered tetragonal lattice, $D0_{22}$ of the γ'' phase represented by Ni_3Nb or Ni_3Ta. (2) A long sequence of six planes, ABCDEF, with orthorhombic structure, $D0_a$, in which Ni_3Nb and Ni_3Ta can also crystallize.

Optimal mechanical properties are obtained by combining precipitation-hardening with solid-solution hardening. In table 1 the major matrix elements appear in the first three columns (Fe, Ni, Co), next to the elements which tend to expand the matrix lattice and thereby increase the flow stress of the alloy. Large amounts of Cr are required to change the lattice parameter appreciably, whereas little Mo and/or W is needed and this latter element also hardens the γ' phase. On the other hand, Ti is a very efficient strengthening factor when it remains in solid solution, as it does at very high temperature. At low temperature its solubility in the matrix is very low. The influence of several solutes on solid-solution hardening in nickel is shown in fig. 35.

For instance, Alloy 800, an iron-base alloy (table 1), is used, besides its excellent resistance to corrosive environments, in heat exchangers for nuclear power plants for its good creep resistance between 500 and 700°C. Chromium and iron provide the solid-solution strengthening, whereas the minute quantities of Al and Ti left in the alloy after the deoxidizing process are able to generate a very fine population (5–50 nm) of γ' precipitates. Their presence after 100 h at 500°C can be detected by hardness tests or

Table 1
Chemical composition of some alloys.

Trade name	Composition (wt%)									
	Fe	Ni	Co	Cr	Mo	W	Al	Ti	Nb	Ta
Alloy 800	44	34	–	21	–	–	0.3	0.4	–	–
INCO 718	7	53	–	18.5	3.1	–	0.4	2.5	–	–
Nimonic 80A	–	75	1	19	–	–	1.3	2.5	–	–
Waspaloy	–	58	13	19	4.5	–	1.3	3	–	–
Astroloy	–	55	17	15	5.3	–	4	3.5	–	–
INI00	–	60	15	10	3	–	5.5	4.5	–	–
MAR-M 200	–	60	10	9	–	12	5	2	1	–
CM SX2	–	65	5	8	0.5	8	5.5	1	–	6

relaxation tests. The γ' phase is fully precipitated after 1000 h at the same temperature and reaches about 2–3% volume fraction.

The volume fraction of the hardening precipitates is generally greater than 15%. Table 1 gives the composition of four typical wrought alloys, starting with INCONEL 718 which is hardened by γ' and γ'' simultaneously at a low volume fraction, and ending with Astroloy (or Udimet 700) containing 40–45% volume fraction. In the last three alloys of table 1, the volume fraction reaches 55–70%, the alloy can no longer be solutionized, even at temperatures close to the melting point of the alloy. These alloys cannot be forged and are used to cast highly critical engine parts such as turbine blades.

In most nickel-base superalloys the γ' phase is stabilized by the higher atomic proportion of Al atoms. Precipitation from the supersaturated solid solution is almost instantaneous. A recent investigation by electron diffraction and TEM of early stages of

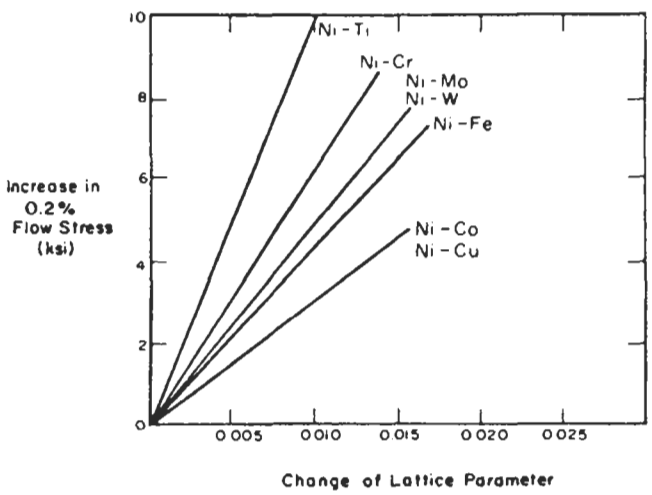

Fig. 35. Solid-solution hardening in nickel; 1 Ksi ≈ 15.2 kPa. (After PELLOUX and GRANT [1960]).

References: p. 2174.

nucleation in a Ni–Ti alloy showed that formation of the ordered phase can result from a spinodal decomposition of the solid solution (LAUGHLIN [1976]). Even in the case where γ' precipitates may form by a nucleation and growth process, overcoming the low γ–γ' interfacial energy is easy and the growth rate is controlled by lattice diffusion during the aging treatment. The expected growth rate of spherical precipitates of radius r, in this case, should obey an equation of the form:

$$r = A(Dt)^{1/2} \tag{45}$$

as a function of time t and diffusion coefficient D as described by MARTIN and DOHERTY [1976] in a recent review. During the course of prolongued aging, the growth rate due to Ostwald ripening is slower:

$$r = B(Dt)^{1/3}, \tag{46}$$

as given in the LSW model (see ch. 9, § 4.2.2 and ch. 15, § 2.4.2).

Loss of coherency

After an extensive TEM study of several semi-coherent precipitates, WEATHERLY and NICHOLSON [1968] established that θ precipitates in Al–Cu alloys lose coherency by the nucleation of dislocation loops within the precipitate, probably from collapsing point-defect clusters followed by climb of the loops into the particle-matrix interface.

On the other hand, γ' and β' (Al–Mg–Si) precipitates lose coherency by attraction of matrix dislocations initially stored in subgrain boundaries and pulled to the particle–matrix interface. They may move large distances by glide and reach their final equilibrium position by climb and interaction with other dislocations. LASALMONIE and STRUDEL [1975b] later described a three-dimensional model with all six $a/2$ ⟨110⟩ edge dislocations combined to form closed loops around each particle (fig. 36).

The dislocation spacing in the interface can be estimated by BROOKS's [1952] formula,

$$d = \frac{b}{|\delta|} \tag{47}$$

where b is the Burgers vector and δ the misfit parameter defined by eq. (1).

A more accurate description of the problem of misfit dislocations in matrix particle interfaces takes into account the differences in elastic constant between matrix and precipitate and the crystallographic anisotropy of each phase (see BONNET [1980] and DUPEUX and BONNET [1980]).

6. *Tensile properties of precipitation-hardened alloys — behavior under high stress*

Precipitation-hardened alloys are best appreciated at high temperature. While the 0.2% yield stress of pure nickel declines from about 20 down to 10 MN/m^2 between

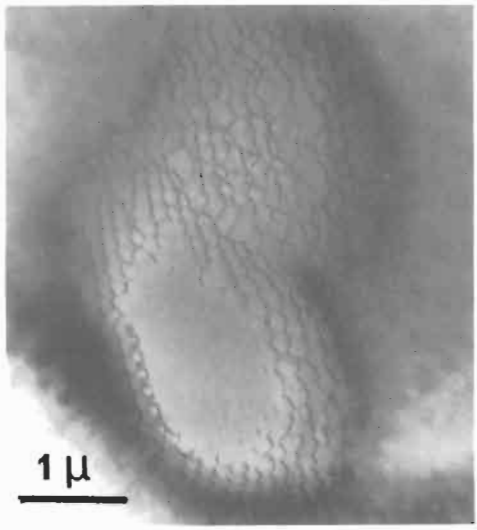

Fig. 36. Three-dimensional network of misfit dislocations around a γ' precipitate with $\delta = 0.3\%$ (from LASALMONIE and STRUDEL [1975b].

room temperature and 600°C and that of TD-nickel is fairly stable and of the order of 200 MN/m^2, it reaches 1000 MN/m^2 and more in most nickel-base superalloys in the same temperature range but decreases rapidly above 900°C.

6.1. Macroscopic properties

The stress–strain curves for polycrystalline materials depend strongly on temperature:

At low temperatures, below 650°C, the first-stage hardening is parabolic (up to 1–2% strain) and followed by a linear second stage which can extend from 5% for heavily hardened alloys to 20–30% for softer varieties. The hardening coefficient of stage II is of the order of 3000–4000 MN/m^2. Work-softening, constriction and rupture take place in stage III.

At intermediate temperatures (650–850°C) the linear stage is reduced at the expense of the parabolic stage at one end and the recovery stage at the other end.

At high temperatures (850°C and above) the initial yield stress is followed by a very short stage-I hardening before general decrease appears which extends until rupture (fig. 37). This mechanical instability at high temperature is also observed in single crystals tested in compression (LAW and GIAMEI [1976]) and has been attributed by CARRY and STRUDEL [1978] to the onset of massive dynamic recovery after the burst of gliding dislocations initially stored and locked in subgrain boundaries.

In single-crystal specimens, several different curves can be observed, depending on orientation:

For cube-oriented crystals the general features are similar to those of polycrystalline samples.

References: p. 2174.

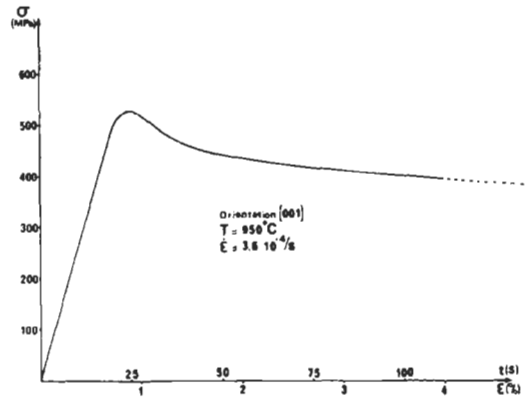

Fig. 37. Stress–strain curve of a cube-oriented nickel alloy single crystal showing mechanical instability at high temperature beyond the threshold stress (from CARRY and STRUDEL [1978]).

In crystals oriented for single slip, the stress–strain curve hardly rises above the initial yield strength; the crystal is progressively filled by slip bands which are channelled by the closely spaced precipitates until slip concentrates in one section of the specimen and induces terminal tearing of the material.

In ⟨111⟩ oriented crystals the yield strength is about 60% higher than in cube-oriented crystals at all temperatures. The elastic modulus is maximal in this direction and the Schmid factor for all slip systems is minimal.

A detailed account of orientation and temperature effects on stress–strain curves of MAR M-200 single crystals will be found in the original publications of KEAR and PIEARCEY [1967] and COPLEY *et al.* [1972].

The influence of the volume fraction of γ' precipitates on the 0.2% flow stress of a series of Ni–Cr–Al alloys has been summarized by BEARDMORE *et al.* [1969] as shown in fig. 38. At first glance, it can already be seen that the strength of the γ' phase is not simply added to the strength of the γ matrix but it does become increasingly dominant at higher volume fractions, 60 and 80%. Since the γ' phase remains ordered up to temperatures close to its melting point (1100–1200°C) (COPLEY and KEAR [1967]) the prominent peak in the γ' flow stress around 800°C can only be attributed to slip mechanisms in the γ' phase itself. As suggested by MULFORD and POPE [1973] the anomalous temperature dependence of the yield stress is caused by the thermally activated formation of sessile dislocation segments which form by the cross-slip of screw dislocations from (111) slip planes on the (010) cube planes. Edge dislocations, on the other hand, retain high mobility (KURAMOTO and POPE [1978]). A ductility minimum of 3–5% elongation to rupture in tensile test and sometimes less than 1% rupture strain in creep adversely affects most nickel-base superalloys in the temperature range 750–800°C corresponding to the peak hardness of the γ' phase.

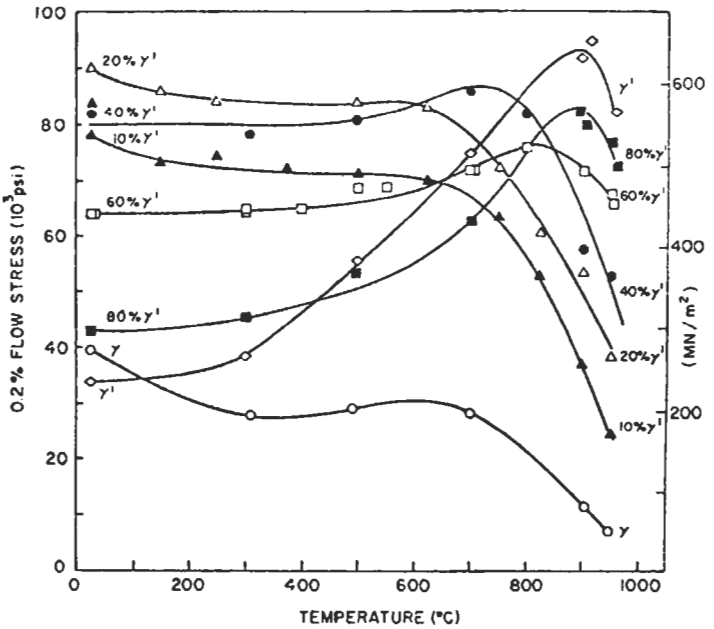

Fig. 38. Temperature dependence of flow stress in Ni–Cr–Al alloys with various volume fractions of γ' precipitates (from BEARDMORE *et al.* [1969]).

6.2. Deformation modes and hardening mechanisms

As seen in ch. 23, § 4, ordered structures belonging to the Cu_3Au system ($L1_2$) can be sheared by matrix dislocations travelling in pairs, thus forming a total Burgers vector $2\times(a/2)[110]$ twice as long as in fcc crystals. The APB energy pulling the two similar dislocations together is of the order of 164 mJ/m^2 (COPLEY and KEAR [1967]) or may be less if due account is taken of the decrease in APB energy with aging time. In complex alloys the final composition of the γ' phase varies as the matrix precipitates out other components. SHIMANUKI's recent investigations [1981] indicate 130 mJ/m^2.

The change in yield strength with particle size has been evaluated by GLEITER and HORNBOGEN [1965, 1968] to be of the order of

$$\tau_c = \alpha\gamma_{APB}^{3/2} f^{1/3} r^{1/2}, \tag{48}$$

which has been successfully applied to a variety of austenitic alloys.

The parabolic $r^{1/2}$ dependence seems to indicate that larger precipitates will increase the critical stress. This is true until another mechanism requiring less energy becomes possible. Since the critical stress for Orowan by-passing by single dislocations falls off as $1/r$, the two curves meet (fig. 39) and the Orowan mechanism takes over for large γ' particles. The same kind of transition has been observed by REPPICH [1975] in iron-doped MgO where magnesia-ferrite particles precipitate in stress-free coherent octahedra inside the MgO matrix. In complex Al–Li alloys quasi-coherent ordered particles δ' (Al_3Li)

References: p. 2174.

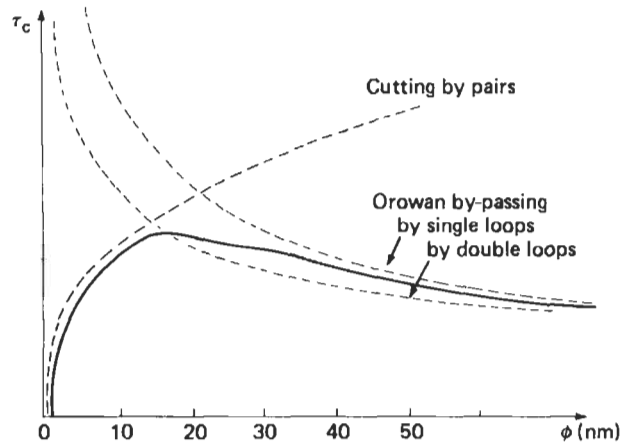

Fig. 39. Schematic representation of the transition from cutting to by-passing of ordered precipitates as a function of particle diameter ø. The solid line is a schematic experimental curve. (After STOLOFF [1972].)

with $L1_2$ structure precipitate in the solid-solution hardened Al matrix. The microstructure of these alloys observed by TEM is strikingly similar to that of nickel-base superalloys. The transition from cutting by pairs of dislocations to by-passing is also observed (STARKE *et al.* [1981]) and can be related to changes in the ductility of the material (SANDERS and STARKE [1982]). In actual crystals intermediate configurations can occur (fig. 40) where the first dislocation by-passes the γ' precipitate which is now surrounded by a shear loop of Orowan type. When a second dislocation sweeps across the same plane, shearing by pairs can take place under the increased stress of the combined dislocations: eventually the first Orowan loop is removed. This type of mechanism combined with the statistical size distribution of the γ' precipitates in the slip plane accounts for the flattened top of the schematic experimental curve in fig. 39 (BERGMAN [1975]; LAGNEBORG and BERGMAN [1976]).

The transition from cutting by pairs to Orowan by-passing actually depends on obstacle strength and volume fraction of the hardening phase. Although early models (GLEITER and HORNBOGEN [1965]; GUYOT [1971]) took these factors into account, they all assumed that obstacles remained rather far apart as compared to particle size, i.e., $f \leq 10\%$. For large volume fractions of the γ' phase, i.e., 20% to 60%, experimental data show major deviations from calculated curves (REPPICH *et al.* [1982]) unless the LABUSCH and SCHWARZ model [1978] is used. In this model the elastic interaction between the moving dislocation and the misfitting particle is represented by a particular profile, and the energy storing effect while the dislocation is approaching and cutting the particle is taken into account. HAASEN and LABUSCH [1979] have shown that the behavior of alloys with large γ' volume fractions can be rationalized well with this approach. REPPICH [1982], distinguishing between weakly coupled and strongly coupled dislocation pairs, has drawn theoretical strength vs particle diameter curves which give a close fit to experimental results. REPPICH *et al.* [1982] report an optimum particle size for strength above 650°C

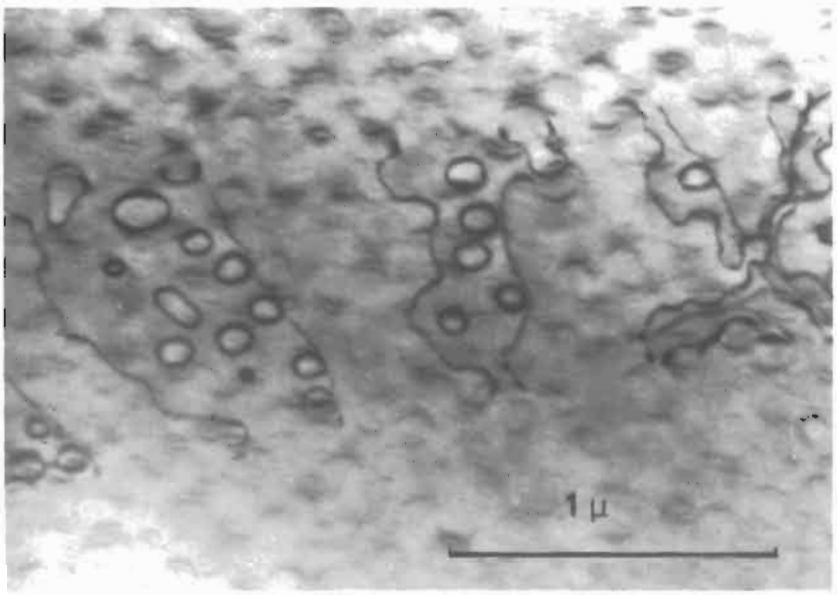

Fig. 40. Combined Orowan by-passing and cutting by pairs of dislocation in Waspaloy deformed at 750°C (from GUIMIER and STRUDEL [1970]).

of about 30 to 40 nm for volume fractions up to 20% and of 80–160 nm for volume fractions of about 50%.

6.2.1. Superlattice stacking faults

In the temperature range 700–800°C, a two-phase alloy containing ordered coherent particles can deform by viscous shear under creep conditions, i.e., high stresses and/or slow dislocation motion enabling local atomic rearrangements.

The partial dislocation arrangement observed commonly in the Cu_3Au system (ch. 23, § 3) creates high-energy surfaces connected either with complex faults (stacking fault + APB) or with APB. As first suggested by KEAR *et al.* [1968], simply adding an extra Shockley partial dislocation to the fcc scheme,

$$BA \rightarrow \delta A + B\delta, \tag{49}$$

yields, in the ordered phase, a *superlattice partial dislocation* (fig. 41):

$$2B\delta \rightarrow \delta A + B\delta + \delta C \tag{50}$$

and leads to the creation of a *superlattice intrinsic stacking fault* (S-ISF), a low-energy surface in the ordered phase of structure $L1_2$ since it is simply equivalent to four layers, ABAB, of the $D0_{19}$ hexagonal structure (see § 5).

Taking the $2B\delta$ configuration as a superlattice Shockley partial dislocation, paired dislocation arrangements can be decomposed as:

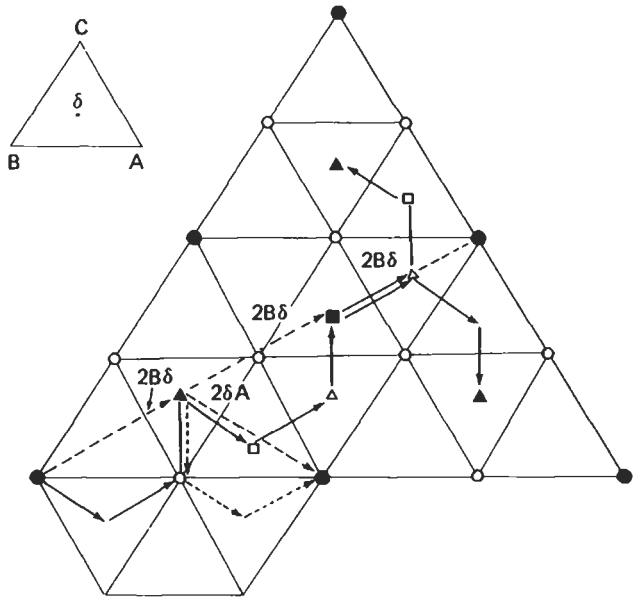

Fig. 41. Schematic directions of slip between dense planes in Ni_3Al ordered crystal, showing Shockley partial superdislocations 2Bδ and also δ shears associated with the formation of S-ISF/S-ESF pairs.

$$2\mathrm{BA} \rightarrow 2\delta A + 2B\delta = (C\delta + \delta A + B\delta) + (\delta A + B\delta + \delta C), \tag{51}$$

a decomposition which appears as dotted and dashed vectors in fig. 41. This scheme would describe a shearing mechanism taking place along a ⟨110⟩ direction and result in the creation of a S-ISF strip bounded by two superlattice partial dislocations. What is actually observed in nickel-base superalloys is much more complex and results in a general shear direction oriented along the ⟨112⟩ axis as described in detail by KEAR *et al.* [1970]. It is very similar to the intrinsic-extrinsic fault pairs observed by GALLAGHER [1970] in an fcc structure with low stacking-fault energy at the dissociated junction of two repulsive dislocations. If the dissociation described by eq. (49) takes place one more time on the plane just above (fig. 42a) two layers of S-ISF are superimposed, thus creating a *superlattice extrinsic stacking fault* (S-ESF) equivalent to seven layers, ABACABA, of the $D0_{24}$ structure, i.e., the crystal structure of Ni_3Ti. Finally a partial dislocation with a formal Burgers vector 2Bδ must bound the end of the S-ESF. The real atomic movements again take place in two successive planes and have actual Burgers vectors 2δA and 2δC:

$$2\overline{\mathrm{B}\delta}\begin{cases} 2\delta\mathrm{A} = \mathrm{C}\delta + \delta\mathrm{A} + \mathrm{B}\delta, \\ 2\delta\mathrm{C} = \mathrm{B}\delta + \delta\mathrm{C} + \mathrm{A}\delta. \end{cases} \tag{52}$$

Another possible decomposition of this superlattice stacking-fault pair leading to the same shear amplitude of 6Bδ is shown in fig. 42b: Shockley partials of the fcc lattice are

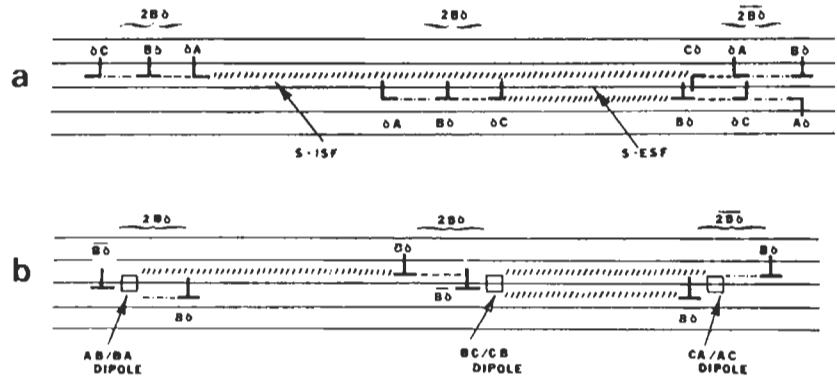

Fig. 42. Two possible configurations for superlattice intrinsic–extrinsic stacking-fault pairs with $6B\delta = a\langle 211\rangle$ net Burgers vector: (a) pure slip representation; (b) viscous slip including dipoles (After KEAR *et al.* [1970].)

coupled with dislocation dipoles, simply describing local lattice rearrangements (KEAR *et al.* [1969]). Such complex dislocation structures are mobile during creep at 750°C; their viscous glide motion requires short-range diffusion and is thermally activated.

In two-phase alloys the complex γ' dislocation arrangements must be compatible with matrix shear vectors, i.e., the sum of all Burgers vectors in the matrix must be equal to the sum of the Burgers vectors in the precipitate. The combination of partial dislocations may be different in each phase. The correspondence

$$\begin{array}{lcl} 2BA + 2BC & \rightarrow & 6B\delta \\ \text{in the matrix} & & \text{in the precipitates} \end{array} \qquad (53)$$

is explicitly drawn in fig. 43 and brings a correct interpretation of the widely observed stacking fault features in nickel-base alloys tested in creep under high stress (fig. 44). Simultaneous shearing on several successive planes or *synchro-shear* is known to take place in other ordered structures and also in corundum and spinels (ESCAIG [1974]).

6.2.2. Mechanical twinning of the ordered phase

As in fcc crystals, stacking-fault formation is associated with twinning for larger deformations. This is exemplified in Waspaloy (fig. 45) where the volume fraction of twinned increases with strain and also with temperature, isolated S-ISF being observed alone at 600°C and below. At higher temperatures, stacking faults first initiated in the γ' precipitates progressively invade the matrix lengthwise and then sideways by lateral thickening as deformation proceeds (fig. 46). Electron diffraction patterns reveal (GUIMIER and STRUDEL [1970]) that the twinned γ' phase remains ordered. The shear amplitude associated with twinning by single Shockley partial dislocations gliding in consecutive planes, as in fcc crystals, is very large: $(a/6\langle 112\rangle)/(a/3\langle 111\rangle) = \sqrt{2}/2 \approx 71\%$. In the $L1_2$ structure, repeated shearing by $2B\delta$ partials would double this value. It is therefore concluded that order is restored in the twinned γ' phase by local atomic rearrangements: hence the thermal dependence of its domain of occurrence (fig. 45). Mechanical twinning is also frequently observed

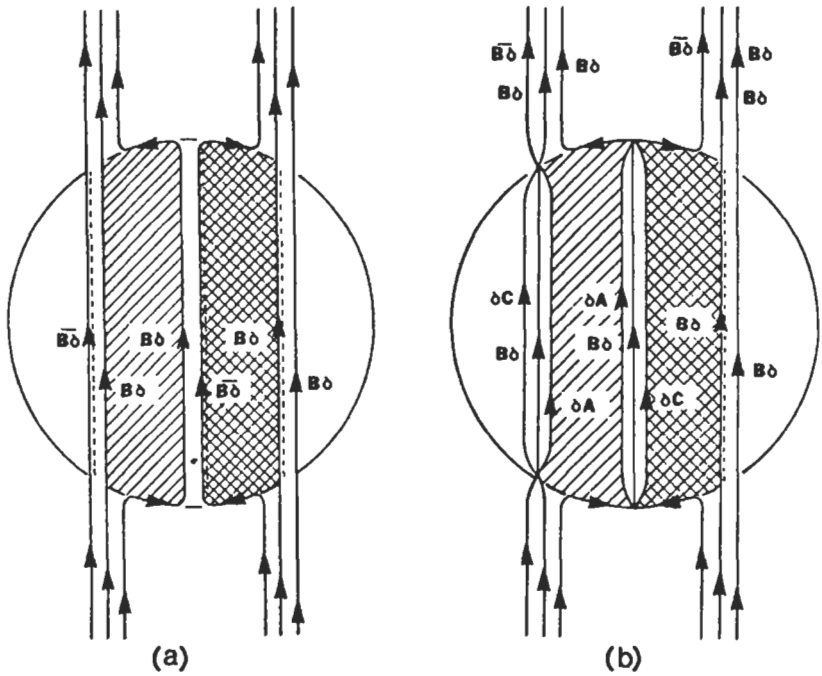

Fig. 43. Rearrangement of partial dislocations between matrix and γ' precipitate: (a) and (b) correspond to figs. 42b and 42a, respectively. (After KEAR *et al.* [1970].)

in high-temperature fatigue tests (CLAVEL *et al.* [1980] and CLAVEL and PINEAU [1982]) and in forged powder-metallurgy alloys (MENON and REIMAN [1975]) (see also ch.23, § 4.5).

Mechanical twining of fcc alloys at temperatures above 600°C and as high as 1080°C (DERMARKAR and STRUDEL [1979]) may seem incongruous since pure fcc metals resort to this deformation mechanism only at low temperature. Actually the general principle, that twinning only occurs when no other mechanism of lesser energy is available for plastic deformation, still holds in this case. Dislocations are too few at the start of the deformation, they are immobilized by the dense population of γ' precipitates, hence they cannot multiply. By-passing by climb requires low strain rates and time for recovery events to take place. The threshold stress for the Orowan by-passing mechanism is of the order of the critical stress for twin formation. The S-ISF energy of the γ' phase being lower than the SF energy of the matrix, twinning often originates in the ordered phase and spreads to the matrix.

7. *High-temperature creep of precipitation-hardened alloys*

At high temperature and low stresses, the threshold stress associated with Orowan looping is never exceeded. Deformation processes are strongly climb-assisted although glide is not excluded but only restricted drastically.

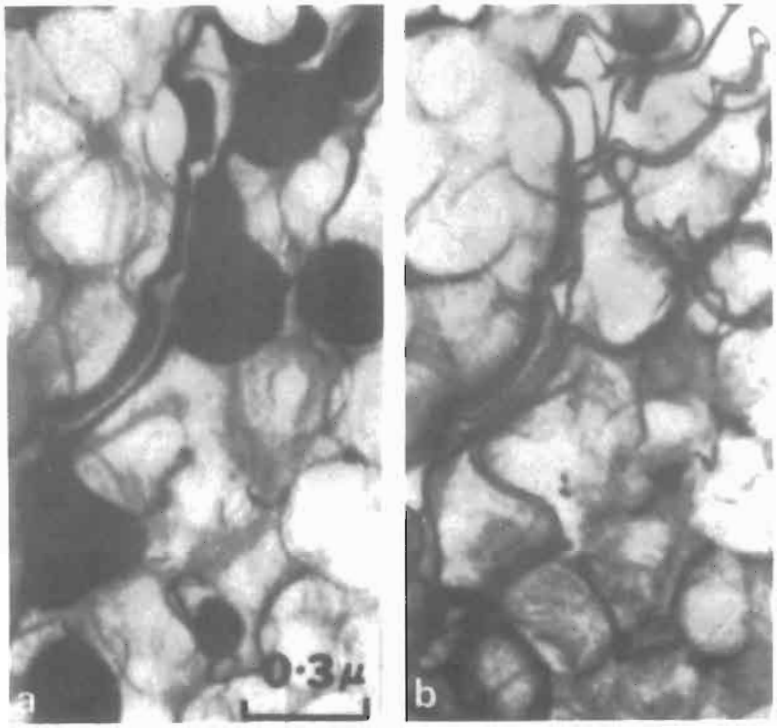

Fig. 44. Detail TEM observations of S-ISF/S-ESF pairs and associated partial dislocations in Mar-M 200 single crystals deformed at 760°C: (a) bright-field, (b) dark-field observation. (From KEAR and OBLAK [1974].)

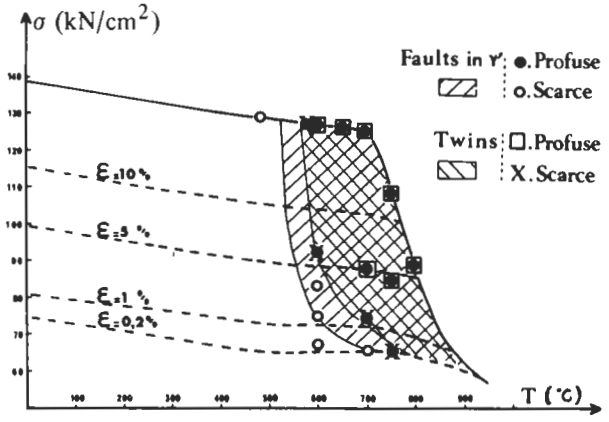

Fig. 45. Density of stacking faults and twins in deformed Waspaloy as a function of temperature and strain (after GUIMIER and STRUDEL [1970]).

References: p. 2174.

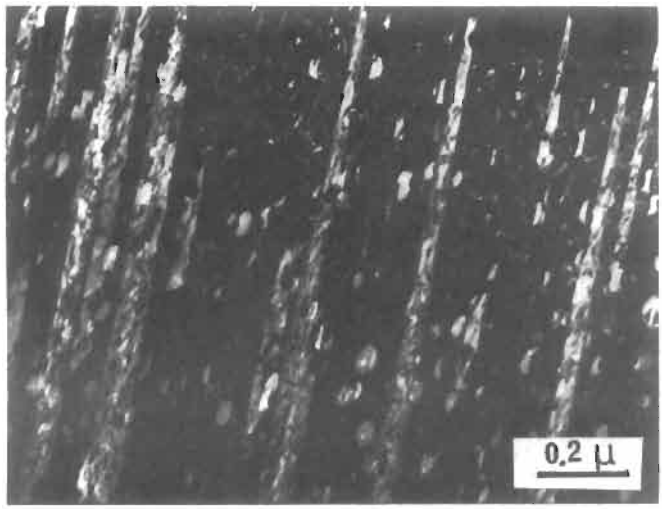

Fig. 46. Dark-field TEM observation of stacking faults and twins in Waspaloy deformed at 800°C.

7.1. Creep curves

The general aspect of high-temperature creep curves is radically different from that of the matrix alone (fig. 47). Primary creep is replaced either by a short sigmoidal stage at 850°C or by an incubation period (LEVERANT *et al.* [1973]). The steady-state creep stage

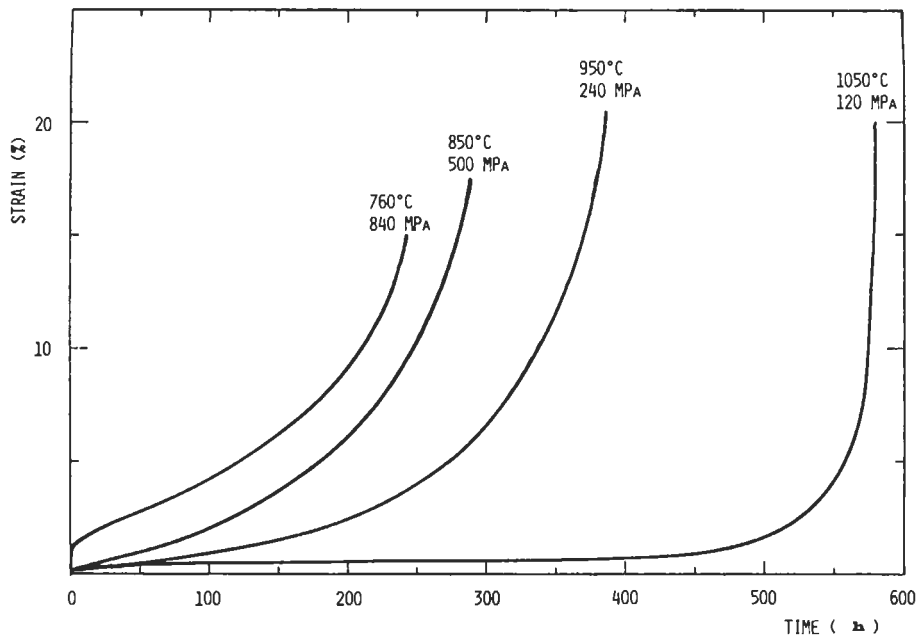

Fig. 47. High-temperature creep curves of cube-oriented single crystals of the alloy CM SX2.

is short compared with an overwhelming third stage which either starts very early in the lower part of the temperature domain (850–1000°C) or contains most of the creep strain at higher temperature (1000–1100°C) and is soon followed by rupture. Comparing the forms of tensile (fig. 37) and creep (fig. 47) curves strongly points to the conclusion that two-phase alloys hardened by soluble quasi-coherent precipitates are mechanically unstable structures. The lack of initially mobile dislocations is the corner-stone of their mechanical resistance. The onset of dislocation movement, especially when it is dominated by climb, is the beginning of their degradation.

7.2. Deformation modes

In the lower part of the temperature domain (870°C), steady-state creep under high stresses can occur by viscous shearing of the γ' phase as evidenced by LEVERANT *et al.* [1973]. At higher temperature and lower applied stress, the hardening phase is no longer traversed by dislocations which remain confined to either:

- thermally activated glide in the matrix
- diffusion controlled climb in the γ–γ' interfaces.

Under conditions of low strain rate in single crystals oriented either for single slip or for multiple slip in the vicinity of the (001) pole, the dominant slip system in the fcc matrix is of type $(110)\,a/2\,[1\bar{1}0]$ as also observed by LE HAZIF *et al.* [1973] in work-hardened pure fcc metals at intermediate temperatures.

Dense arrays of edge dislocation dipoles are stored in the γ–γ' interfaces (fig. 48) and climb by stress-assisted pipe-diffusion (CARRY and STRUDEL [1978]). As they reach the edge of the γ' cuboids by climb, segments of opposite signs can glide toward one another and finally annihilate. A constant dislocation density is preserved by the glide of screw segments generating new edge dipoles in regions where the local internal stress has been lowered by intense recovery and the balance in the dislocation population as well as in the stress distribution is restored.

7.3. Internal stress

High-temperature creep in precipitation-hardened alloys takes place under stresses as low as 20–50% of the experimentally determined threshold stress or the calculated Orowan stress. It can only take place by a diffusion-controlled climb process around the unsheared particles as suggested by HOLBROOK and NIX [1974].

The tensorial structure of the internal stress field created inside the matrix by the closely spaced edge-dislocation dipoles (fig. 49) can be evaluated by summation of the stress fields of individual dislocations (CARRY *et al.* [1979]). In a cube-oriented single crystal tested in tension along the y axis, the σ_{yy} component of the stress tensor is the only component which exhibits a strong negative value in the matrix. All other components vary in sign and so does σ_{yy} in the γ' region. A substantial compression stress ($\sigma_{yy} < 0$) is created inside the matrix by the dislocations generated during deformation and it opposes a large fraction of the applied stress. This kinematical hardening (§ 3.4) is the foundation on which the mechanical resistance rests at high temperature. It is anisotropic in nature and its degradation will accelerate the ruin of the crystal under unidirectional stress.

References: p. 2174.

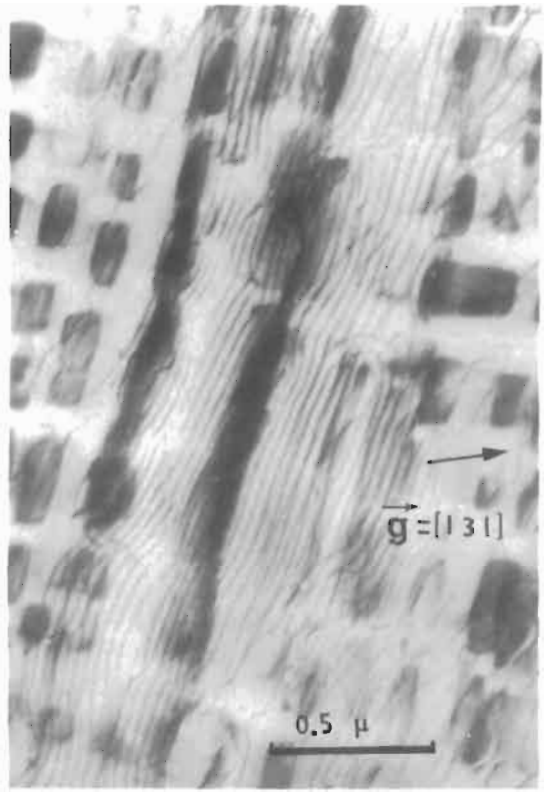

Fig. 48. Formation of edge-dislocation dipoles in the γ–γ' interfaces by activated glide of screw segments bowing out between precipitates (after CARRY and STRUDEL [1975]).

In order to write the simpler scalar equations for the flow rates, an average value of σ_{yy} is considered, usually in the form of an internal stress component $\sigma_i(\sigma_a, T)$ (§ 4.2). The apparent creep parameters are unusually high:

$$Q_a \simeq 400\text{–}700\ \text{kJ/mol}, \quad n_a \simeq 6\text{–}12 \tag{53a}$$

according to most authors (KEAR and PIEARCEY [1967], PARKER and WILSHIRE [1975], CARRY and STRUDEL [1978] and STEVENS and FLEWITT [1981b]). But the temperature and stress dependence of σ_i can be experimentally measured. These introduce large corrective terms in eqs. (38) and (39). The effective creep parameters estimated from these equations are in the range of $Q_e \approx 250$ kJ/mole and $n_e \approx 1$–2. These values suggest that the elementary mechanism is effectively controlled by climb. In accord with the early predictions of Nabarro and Herring (ch. 22, § 7), high-temperature creep of single crystals takes place by an intense climb process. The massive flux of atoms is not taking place in volume, however. It is channeled by the climbing arrays of dislocations held up in the γ–γ' interfaces. Similar conclusions drawn from a study of precipitation-hardened Al + 0.5% Fe alloys led

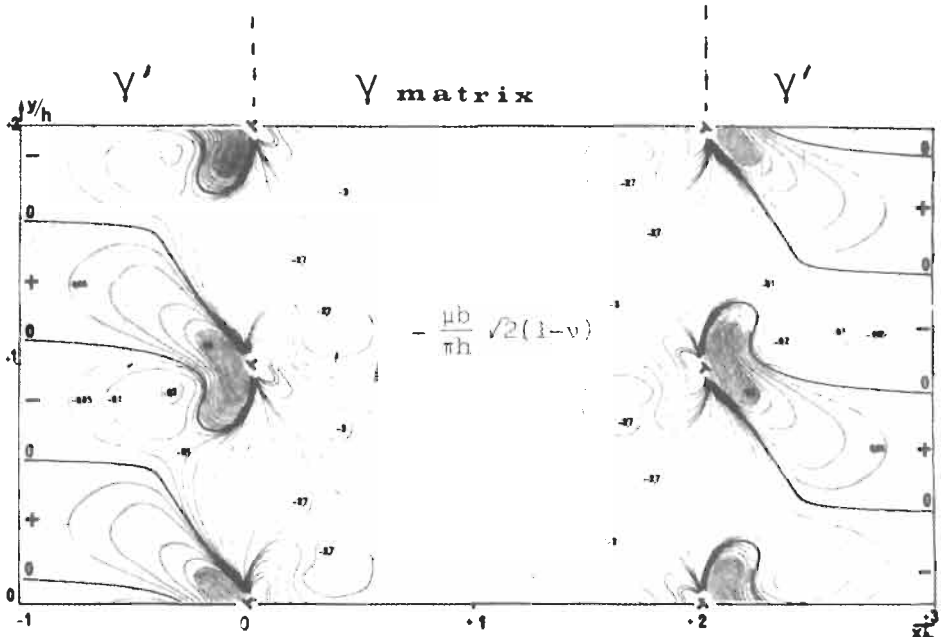

Fig. 49. Arrays of edge-dislocation dipoles generating a compression stress σ_{yy} along the tensile axis (after CARRY *et al.* [1979]).

BARRETT *et al.* [1972] to elaborate on the original creep model proposed by Nabarro and Herring.

A phenomenological approach to the internal stress problem has been taken by WHILSHIRE and co-workers (THREADGILL and WILSHIRE [1974] and PARKER and WILSHIRE [1975]), where the creep equations for precipitation-hardened alloys take on the form:

$$\dot{\varepsilon}_s = C_0(\sigma_a - \sigma_0)^4 \exp\left(-\frac{Q_c}{kT}\right) \tag{54}$$

similar to the flow equations for pure metals,

$$\dot{\varepsilon}_s = C\sigma_a^4 \exp -\frac{Q_a}{kT}. \tag{55}$$

This type of analysis is found to be quite fruitful in interpreting the unusual creep behavior of two-phase alloys. The friction stress σ_0 in this approach is connected with the internal stress distribution in the *relaxed state* after some amount of recovery has taken place, rather than with the instantaneous value of the internal stress as in the former approach.

7.4. Oriented coalescence of the hardening phase under strain

Several authors (TIEN and COPLEY [1971], CARRY and STRUDEL [1976], MIYAZAKI *et al.* [1979]) have observed that annealing of nickel-base alloys under stress can produce

significant changes in the morphology of the γ' phase in relation to creep strain (CARRY and STRUDELL [1978]).

If the crystals are deformed in tensile creep along the (001) axis several slip systems are operating and two orthogonal sets of platelets appear along the cube planes parallel to the tensile axis when the γ–γ' misfit parameter δ is negative (fig. 50). When the stress is oriented along a direction of lower symmetry, (103) for instance, only one slip system is activated and γ' rafters form only along one plane. Similarly, if either the tensile stress is changed into a compression stress along the (001) direction, or the sign of δ is changed from negative to positive, γ' platelets extend in the direction normal to the stress (TIEN and COPLEY [1971]). The critical role of the lattice misfit is explained by fig. 51 (CARRY and STRUDEL [1976]): the matrix dislocations produced by the tensile stress aggravate the γ–γ' misfit along the vertical facets of the γ' cuboids when $\delta < 0$ and tend to compensate δ on the horizontal facets. Climb by pipe-diffusion along the dislocation line will follow the stress gradient and growth of horizontal facets will be favored (CARRY *et al.* [1981]). In order to restrain this deteriorating effect which destabilizes the strengthening configuration, δ must be minimized for the service temperature, and appropriate thermal treatment of the alloy can promote optimal resistance (STEVENS and FLEWITT [1981a]). The basic mechanism, however, can only be slowed down, not suppressed.

8. *Recrystallization*

Basic concepts concerning the recrystallization of alloys containing a second phase are set out in ch. 28, § 3.8. We shall simply emphasize and illustrate the main features of recrystallization phenomena specific to the materials with which we are here concerned. Three parameters play a major role in these alloys: *particle size*, *interparticle distances* and *degree of deformation*.

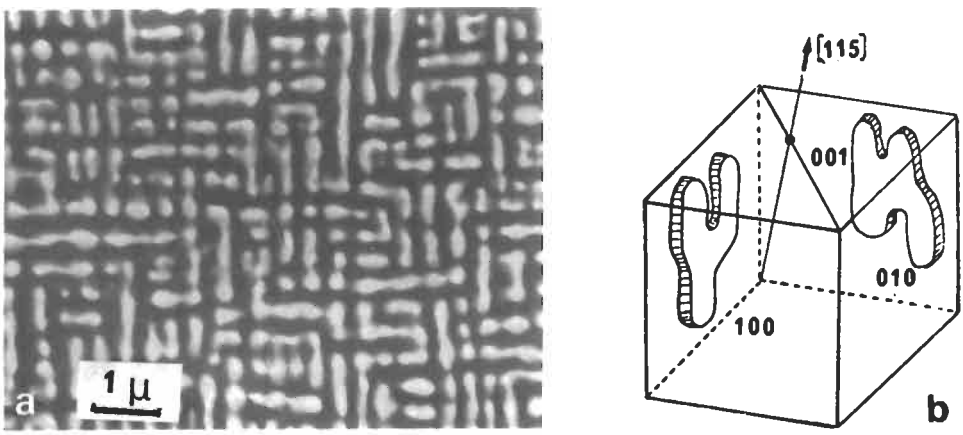

Fig. 50. Strain-induced coalescence (now termed *rafting*) of the hardening phase during creep at 950°C (a). Two orthogonal sets of rafters (b) are formed when several slip systems are operating.

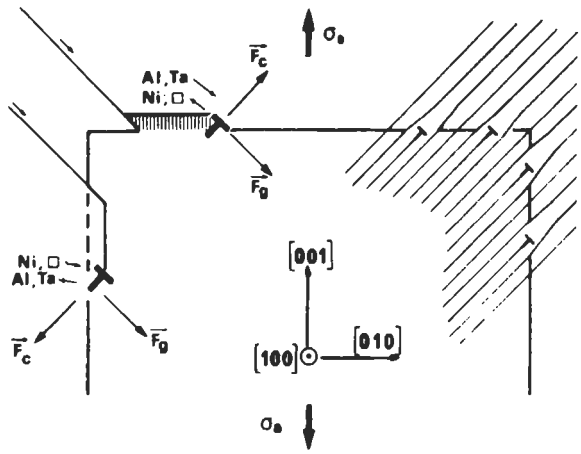

Fig. 51. Dislocation climb in the γ–γ' interface with $\delta < 0$ (bold symbols: matrix dislocations; light symbols: misfit dislocations). (From CARRY *et al.* [1981].)

8.1. Particle size and amount of strain

Second-phase particles of radius r exert a retarding force F_Z, also called *Zener force*, on a migrating boundary as illustrated by HANSEN and JONES [1981] in the case of low-angle boundaries and subgrains (fig. 52). A rough estimate of this force was first proposed by ZENER [1948] as a function of volume fraction, f, and interfacial energy, γ_s, of the particles [see also eq. (8), ch. 28]:

$$F_z = \tfrac{3}{2}\frac{f}{r}\gamma_s. \tag{56}$$

Thus a high volume fraction of small particles can retard or even completely inhibit recrystallization. This is the case with TD-nickel which can retain its elongated grain structure (fig. 53) inherited from wire-drawing even after annealing at 1400°C.

JONES *et al.* [1979] and JONES and HANSEN [1980] have summarized the various physical causes for the inhibiting effect of small particles on the recrystallization process:

A fine dispersion of small particles homogenizes plastic deformation. Dislocations are more uniformly distributed in the matrix and subgrain boundary formation is more difficult. Local lattice rotations due to strain concentration are less frequent than in the absence of small particles, and the critical radius for recrystallization is thereby increased.

When subgrain boundaries do form, they are efficiently stabilized by the second phase. A good example is given by TD-nickel seen by TEM (fig. 4, above). Rearrangement and coalescence of subgrains, leading to nucleation of recrystallized nuclei, is impeded.

As a consequence, nucleation of recrystallization embryos is more frequent at grain boundaries than inside the matrix.

These various aspects of the inhibiting effects of second-phase particles point to the

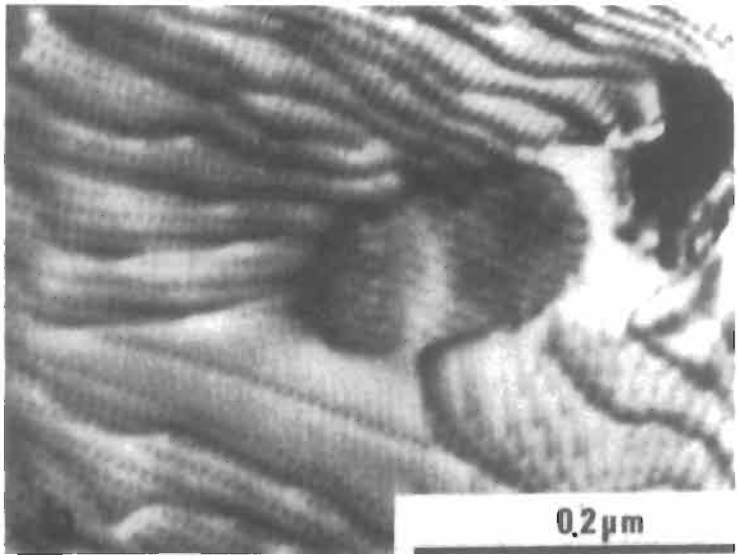

Fig. 52. Low-angle boundary pinning in an Al–Al_2O_3 alloy (after HANSEN and JONES [1981]).

excessive simplicity of Zener's approach whose expression tends to underestimate the retarding force experienced by each individual boundary or subgrain boundary developing inside the deformed matrix.

On the other hand, large second-phase particles tend to stimulate nucleation of recrystallization nuclei in their immmediate vicinity (see fig. 45a, ch. 28). The critical

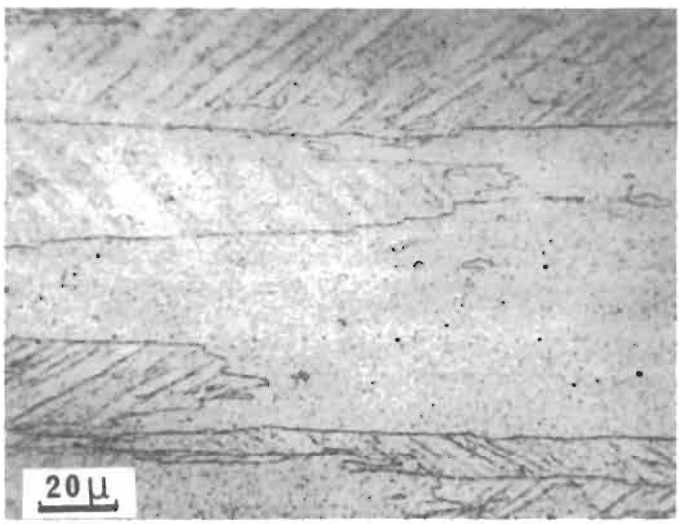

Fig. 53. TD-nickel wire-drawn and annealed 3 h at 1400°C (after LASALMONIE and SINDZINGRE [1971]).

size for nucleation enhancement depends directly on the amount of strain the alloy has been subjected to: let us call it $d(\varepsilon)$. HUMPHREYS [1979b] gives a graphic representation of a $d(\varepsilon)$ function established experimentally in the case of Al–Si alloys. It is clear that in this material, particles less than 2 μm in diameter inhibit recrystallization whereas those of 4 μm and above act as strong nucleation sites. This effect of course is justified by the strain accumulation and large lattice rotations observed around larger particles as described in §§ 3.2 and 3.3, above.

8.2. Interparticle spacing

Kinetics of recrystallization are affected not only by particle size but also by interparticle spacing when their size is larger than the critical diameter $d(\varepsilon)$. DOHERTY and MARTIN [1962] pointed out that both the growth rate (represented by the time for 50% recrystallization) (fig. 54a) and the nucleation rate (fig. 54b) are strongly dependent on interparticle spacing. They used an aluminium-base alloy hardened by various distributions of $CuAl_2$ precipitates obtained by a sequence of heat-treatments. A distance of at least 1 μm between precipitates is needed for the recrystallization process to overcome the inhibiting effects and to become stimulated by the presence of precipitates.

MOULD and COTTERILL [1967] developed an elementary theory to describe similar results obtained in cold-drawn and annealed wires of an aluminium-base alloy hardened by Al_3Fe precipitates. The critical interparticle spacing they found (fig. 55) was of the order of 2–4 μm.

Finally, retardation and acceleration effects are best summarized by the two schematics of fig. 56 first suggested by NES [1976] and later elaborated on by HORNBOGEN and KÖSTER [1978]. For a given deformation and various particle sizes the time for 50% recrystallization is plotted as a function of interparticle distance (fig. 56a) and for a given particle size one obtains a similar description when the amount of strain applied to the material is varied (fig. 56b).

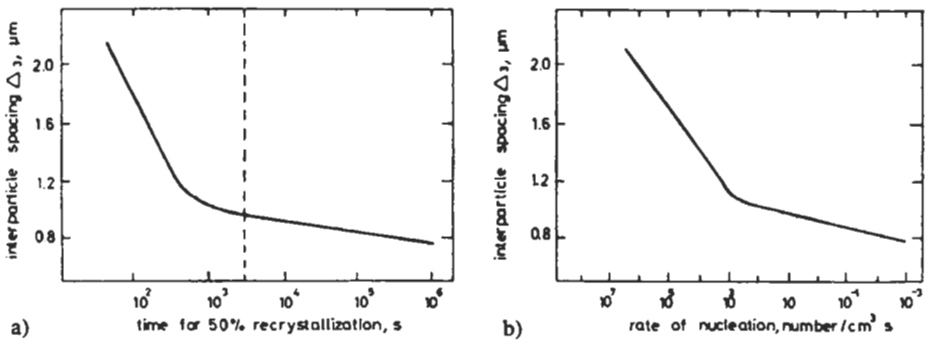

Fig. 54. Relation between interparticle spacing and: (a) time for 50% recrystallization (time for single-phase alloy shown by dashed line); (b) rate of nucleation. (After DOHERTY and MARTIN [1962].)

References: p. 2174.

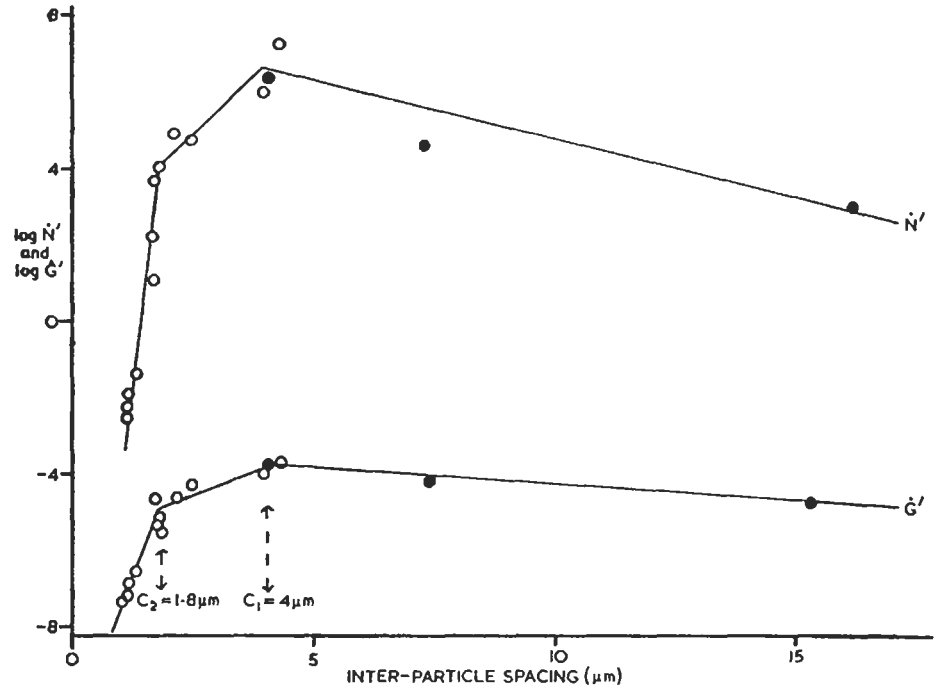

Fig. 55. Apparent nucleation rate ($\dot{N}$) and apparent growth rate ($\dot{G}$) as a function of interparticle spacing for Al–Cu alloys (after MOULD and COTTERILL [1967]).

8.3. Effect of temperature

Since recrystallization is basically a thermally activated process, temperature has a strong effect on its kinetics even in two-phase alloys. JONES and HANSEN [1980] studied the variation of the recrystallization temperature in Al–Al_2O_3 alloys containing various

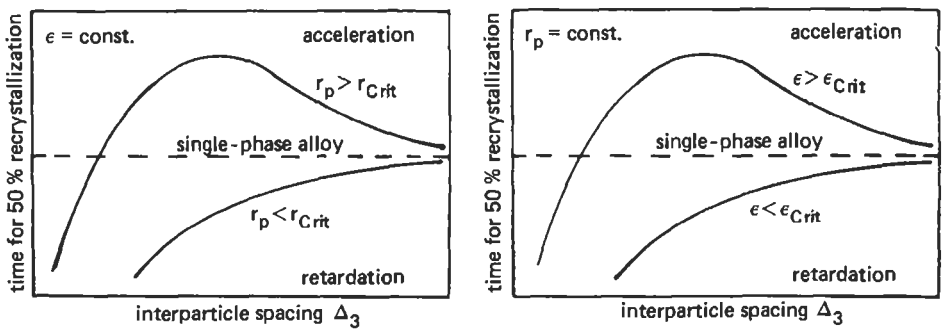

Fig. 56. Schematic diagram of the influence of dispersed particles on recrystallization: (a) acceleration of recrystallization occurs only if the particle size is large enough to give rise to local lattice curvature ($r_p > r_{crit}$); (b) for a given particle size, a critical strain is necessary for particle-simulated nucleation ($\varepsilon > \varepsilon_c$). (After HORNBOGEN and KÖSTER [1978].)

volume fractions of small particles (0.1 μm). They observed that the recrystallization temperature was low and independent of interparticle spacing when this latter parameter was larger than 8 μm (fig. 57), but was slowly increasing when particles came as close as 8–2 μm apart and finally increased drastically for interparticle spacings in the submicron range.

8.4. Micromechanisms

Micromechanisms have been observed in great detail by HUMPHREYS [1979a] who characterizes the immediate vicinity of a large particle as highly rotated with respect to the surrounding matrix and heavily deformed. Subgrain coalescence will therefore take place within a fraction of a micron from the particle. It will be followed by a rapid growth of the recrystallization nucleus into the deformed zone extending a few microns around the undeformed particle. Finally the recrystallization front will have grown rapidly through the more heavily strained region around the particle where the density of dislocations is much lower and the driving force much weaker: the growth rate therefore slows down considerably.

These three stages have been described more quantitatively in a recent model developed by SANDSTRÖM [1980b], which can be sketched as follows.

In stage I, associated with the coalescence of very small subgrains of average radii $\bar{R}$, the radius R of the growing subgrain increases by a coalescence mechanism:

$$\left(\frac{dR}{dt}\right)_I = \alpha m \tau \left(\frac{1}{\bar{R}} - \frac{1}{R}\right), \tag{57}$$

where m is the mobility of dislocations and τ their line tension.

In stage II, the growth rate in the deformed zone can be written as proportional to the

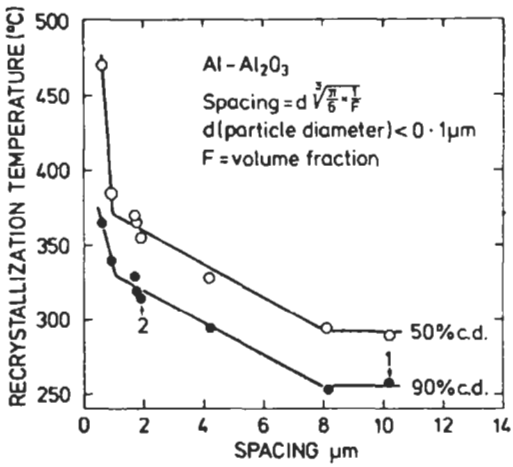

Fig. 57. Recrystallization temperatures of 50 and 90% cold-drawn (c.d.) Al–Al_2O_3 alloys as a function of particle spacing (after JONES and HANSEN [1980]).

References: p. 2174.

difference between the energy associated with the high dislocation density in the deformed zone, ρ_{dz}, and that of the curved boundary:

$$\left(\frac{dR}{dt}\right)_{II} = \beta M\left(\tau\rho_{dz} - \frac{2\gamma_s}{R}\right), \tag{58}$$

where M is the mobility of the growing interface and γ_s the surface energy per unit area.

In stage III, growth outside the deformation zone can be described by the same equation as in stage II where ρ_{dz} is now replaced by ρ_M, the actual dislocation density in the matrix, which is much lower than in the deformed zone, and the growth rate drops drastically:

$$\left(\frac{dR}{dt}\right)_{III} = \beta' M\left(\tau\rho_M - \frac{2\gamma_s}{R}\right). \tag{59}$$

These three stages appear in fig. 58 where theoretical curves fit quite closely experimental points obtained in an Al–Al_2O_3 alloy. Extrapolating stage III growth rates backwards toward the origin may lead to apparently negative incubation periods. In practical terms, this means that the first two stages could take place so rapidly during a forging sequence at high temperature, that they may not be observed. This is the case in nickel-base superalloys, for instance, during forging sequences above 1000°C. Static recrystallization cannot take place when the material is water-quenched just after forging and yet micron-size recrystallized grains are observed in thin foils by TEM. If these grains would result from dynamic recrystallization, some of them would show traces of deformation such as dislocation bundles. Since these new grains are free of dislocations,

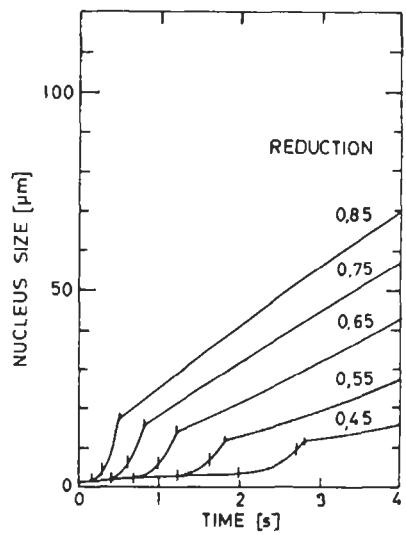

Fig. 58. Three-stage recrystallization process in forged nickel-base superalloys where metadynamic recrystallization is frequently observed (after SANDSTRÖM [1980a]).

DERMARKAR and STRUDEL [1980] suggest that they are the landmarks of a *metadynamic recrystallization* process as described by the above equations.

9. *Duplex structures and multiphase alloys*

At higher temperatures, little or no strain-hardening is available. On the other hand, plastic strain damages materials and tends to destabilize structures obtained by precipitation or thermomechanical treatments. As a consequence, engineers must imagine and implement ingenious stratagems to circumvent or retard the rapid mechanical and chemical degradation processes operating at high service temperatures.

9.1. Duplex structures

In nickel-base superalloys, the size of the γ' precipitates and to some extent the locations of the nucleation sites can be controlled by appropriate heat treatment: γ' precipitates will nucleate preferentially in grain boundaries and grow to large size if the first stage of an annealing treatment is carried out under conditions of low supersaturation, i.e., 20 K below the γ' solvus temperature, for instance. The alloy can now be forged at that temperature since the volume fraction of the precipitates remains small. Cooling it rapidly will preserve the deformed structure, and subsequent aging at 100–200 K below the γ' solvus temperature will induce: (1) the precipitation of a dense population of 100 nm size γ' particles; (2) the recrystallization of the alloy. Owing to the stimulating effect of the large γ' particles, recrystallization nuclei will form near grain boundaries (fig. 59). Growth of these new grains will be inhibited by the dense population of submicronic γ' precipitates and recrystallization will only be of a very limited extent. A *duplex or necklace structure* is thus created (MENON and REIMAN [1975]). It is made of a necklace-like arrangement of 1–5 μm recrystallized grains located in the original grain boundaries of the material (fig. 60). The inside of each grain is partially recovered and contains a high density of small subgrains (0.1–0.5 μm) providing excellent tensile and creep resistance to the complex structure. The detailed microstructure has been studied by BEE *et al.* [1980] and STRUDEL [1980]. The low-cycle fatigue properties of this duplex structure are higher than those of the heat-treated or conventionally forged material (MENON and REIMAN [1975] and SHAMBLEN *et al.* [1975]). The ductility is improved and the fatigue-crack growth rate is reduced owing to the multiple branching effect of the small grain size on the propagating crack tip as clearly shown by PEDRON and PINEAU [1982] for INCO-718 alloy at 650°C.

9.2. Multiphase precipitation-hardening

Nickel-rich austenites can not only precipitate γ' particles but also primary and secondary carbides (see the book by Sims and Hagel in *Further reading*). Deformed under high stresses, γ'-hardened alloys have a strong tendency to form twins (§ 6.2) which extend across the matrix grain and impinge upon the grain boundaries. Compatibility of deformation between grains cannot be maintained when only a small number

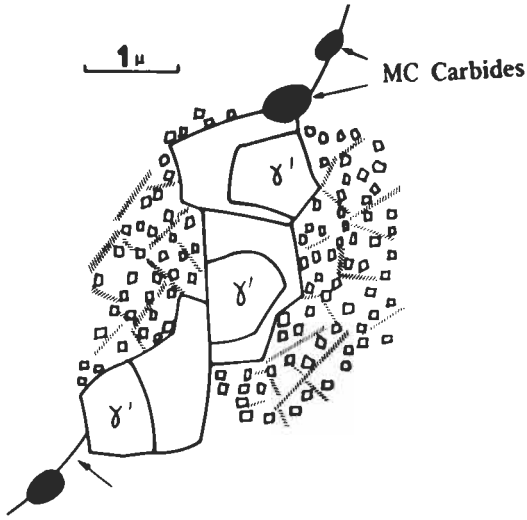

Fig. 59. Stimulated nucleation at large particles and inhibition of grain growth by small precipitates (after DERMARKAR and STRUDEL [1980]).

of slip systems is activated, and cracks are therefore nucleated at the point where the mechanical twins meet grain boundaries. This mechanism is responsible for the very poor tensile ductility of most nickel-base alloys in the temperature range (750–800°C) where the strength of the γ' phase is maximum. The situation can be remedied however, not by inhibiting twinning which is not intrinsically detrimental to mechanical strength, but on the contrary by stimulating it. This can be implemented by adding 0.5–1% Hf to Waspaloy for instance (see table 1). Hafnium's avidity for carbon leads to the formation

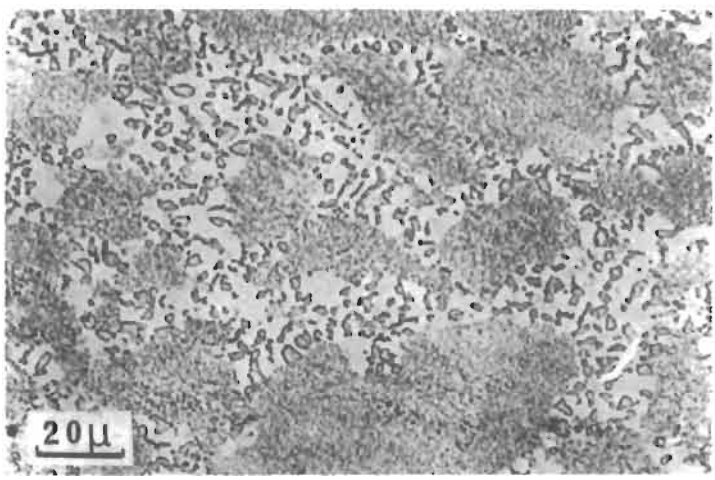

Fig. 60. Duplex-grain size in a PM superalloy deformed 22% at 1060°C and partially annealed.

of micron-size primary HfC carbide particles with equiaxed morphology (STRUDEL [1978]). This undeformable phase acts as a strong dispersoid: it limits grain growth during aging treatments and stimulates the nucleation of numerous small twins on the primary as well as on secondary slip systems (fig. 61). The homogeneity of plastic deformation is restored on the scale of the metallurgical grain because of the slip dispersion effect triggered by the HfC particles, and ductility is enhanced without loss of mechanical strength.

9.3. Mechanical alloying of complex alloys

Encouraged by the unequalled mechanical properties of ODS nickel and nickel–chromium alloys, BENJAMIN [1970] extended mechanical alloying to more complex matrices which could, in turn, provide precipitation-hardening. This development was prompted by the rather poor mechanical performance of TD-nickel and TD-nichrome alloys in the temperature range 500–1000°C when compared with basic nickel-base superalloys such as Nimonic 80A (fig. 62). Alloy IN-853 (77 Ni–19 Cr–1.2 Al–2.4 Ti + 2.25 vol% Y_2O_3) combines the low-temperature yield strength and stress-rupture life of a precipitation-hardened alloy, with the high-temperature creep performance of an ODS alloy. The thermal stability of this ingenious mixture of materials can be characterized by its temperature of recrystallization: 1230°C (CAIRNS [1974]). The grain size of the material is in the micron range and the internal substructure starts recovering above 1100°C.

This sophisticated combination of metals and oxyde cannot be achieved by melting and the appropriate blending of minute oxyde particles cannot be manufactured by conventional powder metallurgy.

Recent progress has also been made in the development of aluminium-base alloys which combine solid-solution strengthening by Mg and OD and Al_4C_3 strengthening

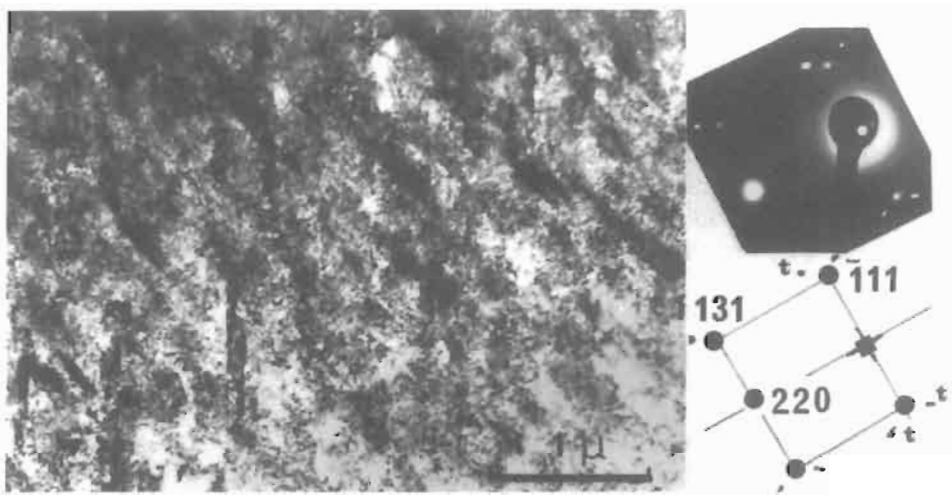

Fig. 61. Enhanced nucleation of twins on several systems. The slip dispersion effect is due to HfC particles finely distributed in the matrix of Waspaloy + 1% Hf. (After STRUDEL [1978].)

References: p. 2174.

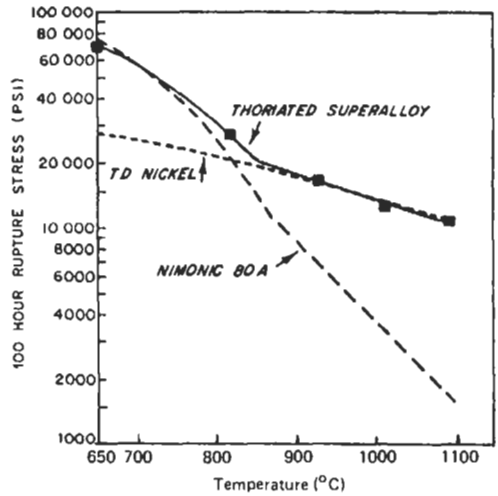

Fig. 62. Combined precipitation-hardening and OD strengthening in mechanically alloyed nickel-base superalloy IN-853 (1 psi ≈ 6.9 kPa) (after BENJAMIN [1970]).

(BENJAMIN and SCHELLEN [1981]). Avoiding precipitation-strengthening improves the corrosion resistance of the material. The thermal stability of the fine-grained structure up to several hours at 350°C makes the forging and extrusion processes much easier.

9.4. Grain-size effects in multiphase alloys

The effect of grain size on the mechanical properties of single-phase materials is treated in ch. 17, § 5.1 and also in ch. 20, § 4.5. Recent aspects of the Hall-Petch relation between yield strength or flow stress and grain size or substructure size in single-phase metals and alloys have been reviewed by ARMSTRONG [1983].

Whatever the material, grain size effects are very sensitive to temperature and of course to strain rate. The case of manganese austenitic steels has been extensively documented experimentally by KUTUMBA RAO *et al.* [1975] and then discussed further by MCLEAN (1976). Grain size has opposite effects on the flow stress at high and low temperatures; the finer the grain size, the higher the flow stress at low temperature and the lower the flow stress at high temperature (fig. 63). Therefore a *cross-over temperature* T_c can be defined where the effect is reversed. It lies in the temperature range 750–800°C in austenitic steels for a strain rate of 3.6/h and in the range 450–500°C for $\dot{\varepsilon} = 3.6 \times 10^{-3}$/h when taking an activation energy for plastic flow and recovery of the order of 300 kJ/mole.

At *low temperature*, crystallographic slip in neighboring grains leads to strain incompatibilities in the vicinity of grain boundaries and generates internal stresses that can be released only partially by the activation of secondary slip systems in that region

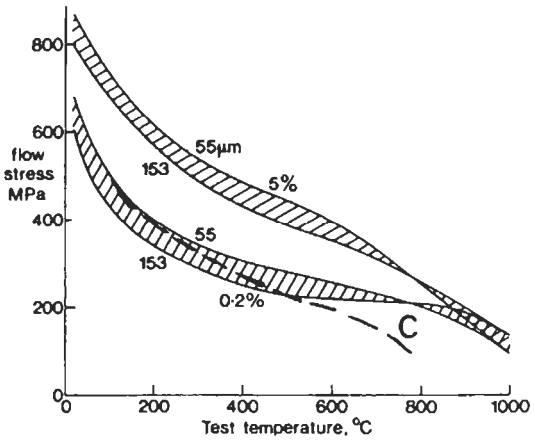

Fig. 63. Influence of a grain size from 55–153 μm on flow stress at 0.2% and 5% strain over a range of temperature straddling the crossover point C. Dashed curve corresponds to lower strain rate. (After McLEAN [1976].)

(ASHBY [1970]). The theory conforms qualitatively to the experimental observation that the dislocation density increases with decrease in grain size. The yield strength of the material follows a Hall–Petch law,

$$\sigma_y = \sigma_0 + kl^{-1/2}, \tag{60}$$

where σ_0 is a friction or threshold stress and $k \simeq 0.16\sqrt{b}$ is the hardening coefficient. (l is used here for grain diameter, whereas d is used in ch. 19.)

At *high temperature*, or low strain rates, i.e., for $T > T_c$, stress concentrations near grain boundaries are removed by diffusion creep either in the grain boundary itself or by climb-controlled dislocation motion in its vicinity. The grain boundaries cease to act as barriers to deformation as they do at lower temperature; on the contrary, rapid grain-boundary transport accelerates the recovery of dislocation substructures and tends to create a softer zone in its immediate neighborhood as first suggested by McLEAN (fig. 64). A coarser subgrain structure near grain boundaries has been observed by ROBERT *et al.* [1981] in 316-type stainless steels after creep at 650°C. Hence the difficulty for single-phase materials of small grain size to retain a stable subgrain structure under creep conditions and also the absence of any dislocation substructure in materials having a grain size small enough to exhibit superplastic behavior (ch. 22, § 9).

The role of grain size and grain elongation in strengthening of ODS alloys has been well documented by the work of WILCOX and CLAUER [1972] who compared mechanical properties of various microstructures in pure nickel and nickel alloys hardened as solid solutions Ni–20 Cr and Ni–20 Cr–10 W with those of TD nickel, TD nichrome and Ni–20 Cr–10 W–2 ThO_2.

At *room temperature* all these materials follow a Hall–Petch relationship [eq. (60)]

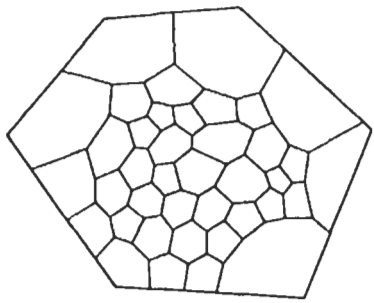

Fig. 64. Large dislocation meshes at grain boundaries caused by rapid grain-boundary diffusion — diagrammatic (from McLean [1976]).

with somewhat lower k values for ODS alloys (fig. 65). The convergence of the lines in this figure indicates that the linear additivity rule for the various strengthening mechanisms (i.e., solid solution, particle, grain and subgrain refinement hardening) suggested by Hansen and Lilholt [1971] and implicitly assumed in the earlier parts of this chapter, is probably incorrect. Looking at linear distances between obstacles (i.e., oxide particles on one hand, grain or subgrain boundaries on the other hand), this plot indicates that boundaries are more than six times as potent in raising the room-temperature yield strength than are oxide particles, but of course this feature is not retained at high temperature.

At *elevated temperature* the yield strength of ODS alloys does not seem to correlate with $l^{1/2}$ in the Hall–Petch manner but rather well with *grain aspect ratio* (GAR), L/l, as suggested by Wilcox and Clauer [1972]. This parameter is defined schematically in fig. 66b. A close fit of both tensile and creep properties at 1093°C of these materials and microstructures is obtained when L/l is used (fig. 66). Considering these results, the authors suggest a dependence of the flow stress of the form:

$$\sigma = \sigma_e + K\left(\frac{L}{l} - 1\right), \tag{61}$$

where σ_e is the strength for equiaxed grains ($L/l = 1$) and K a hardening coefficient which increases with solid-solution hardening (fig. 65). The physical interpretation for the prominent role of this parameter in most materials designed for elevated temperature resistance rests on the important contribution of grain-boundary sliding in high-temperature yielding and strain accommodation (whenever a material is tested above the cross-over temperature T_c). A highly elongated microstructure tends to align grain boundaries along the main stress axis and thereby minimize the resolved shear and tensile stresses acting on them. These effects have been exploited in engineering applications where improved high-temperature ductility and creep rupture life are required: ODS tungsten filaments for lamps and electron guns, directionally solidified nickel-base superalloys for turbine blades, and thoriated platinum wire and strips for the chemical industry. Appropriate thermomechanical treatments can usually lead to strongly anisotropic mechanical properties based on large GAR values (5–20).

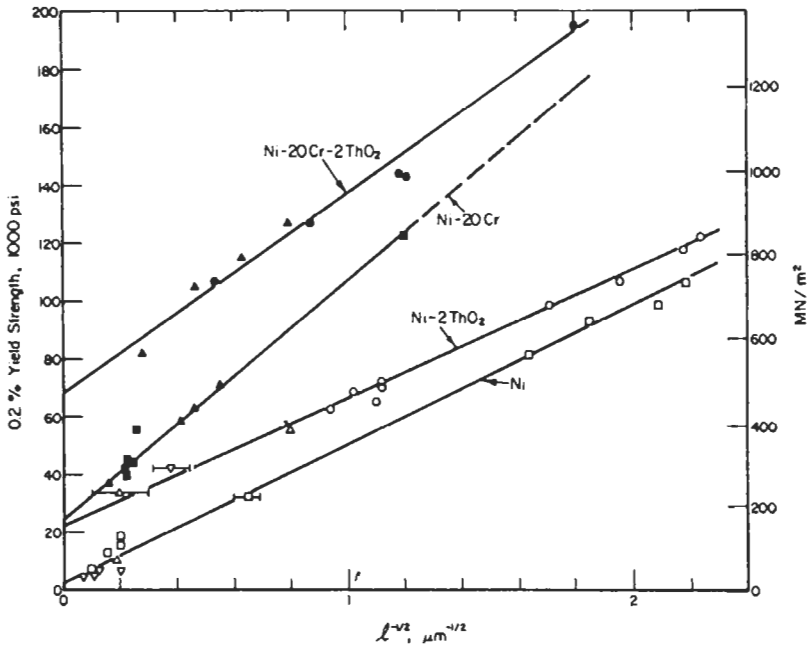

Fig. 65. Dependence of room-temperature yield strength (0.2% offset) of Ni, Ni–2ThO_2, Ni–20Cr and Ni–20Cr–2ThO_2 on grain size and cell size produced by drawing (from WILCOX and CLAUER [1972]).

GRANT [1983] has recently reported comparative creep studies on single-phase type 316 stainless steel, tested at 650°C, and the same steel strengthened with a fine dispersion of TiC. The single-phase alloy resists creep much better with a 65 μm grain size

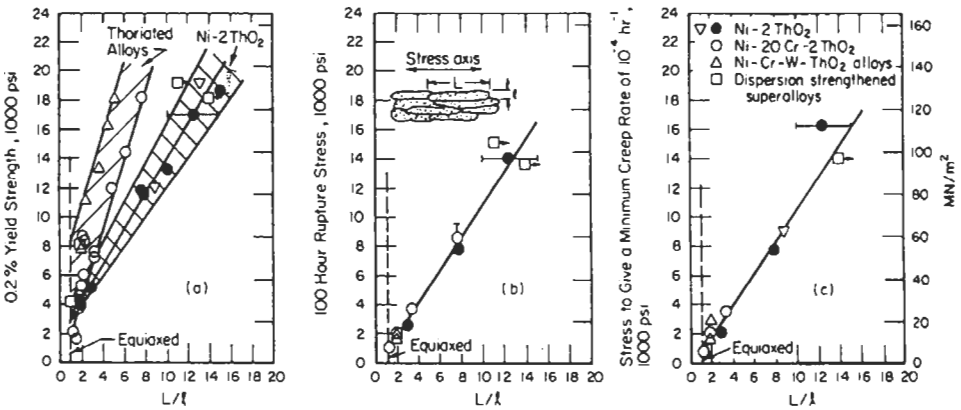

Fig. 66. The effect of grain aspect ratio, L/l, in dispersion-strengthened nickel alloys on strength properties at 1093°C: (a) 0.2% offset yield strength; (b) 100-hr rupture stress; (c) stress to give a minimum creep rate of 10^{-4}/h. Open points are recrystallized, closed points are non-recrystallized. (From WILCOX and CLAUER [1972].)

References: p. 2174.

(ingot processed) than with a 5 μm grain size (rapid solidification processed), whereas the dispersion-strenghtened alloy is actually somewhat more creep-resistant with 5 μm grains. This behavior suggests that the cross-over temperature is probably lower for the single-phase material ($T_c < 650°C$) than it is for the TiC-strengthened steel. The basic reason for the shift of T_c to slightly higher temperatures in the two-phase material is probably to be related to the retardation of all recovery phenomena in the presence of a dispersed phase.

In precipitation-hardened alloys such as γ'-strengthened nickel, changes in mechanical properties are drastic from one side of the cross-over temperature T_c to the other. Increasing the γ' volume fraction enhances this tendency further as evidenced by the steeper slopes of the curves in fig. 67 as the γ' content of the alloy is increased.

Since the cross-over temperature is usually estimated to lie in the temperature range 650–700°C in nickel-base alloys, grain refinement by powder metallurgy or thermo-mechanical treatments is actively pursued only for jet engine parts such as turbine disks which require high strength and fatigue resistance up to 650°C (DAVIDSON and AUBIN [1982]). For parts exposed to temperatures above T_c, casting techniques are common practice and larger grain sizes yield longer creep rupture life in IN-100 (MOSKOWITZ *et al.* [1972]) as well as in IN 939 for instance (fig. 68).

From the many above examples, one would be tempted to conclude that the mechanical properties of ODS and precipitation-hardened alloys do not correlate with grain size in a simple manner. This difficulty often originates from the use of inappropriate parameters for characterizing the microstructure of the material. The significant structural

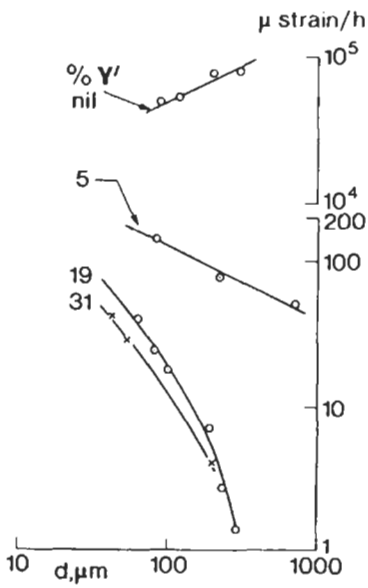

Fig. 67. Strain rate versus grain size for various γ' volume fractions in a nickel-base alloy tested at 750°C under 154 MN/m^2 (after GIBBONS and HOPKINS [1971]).

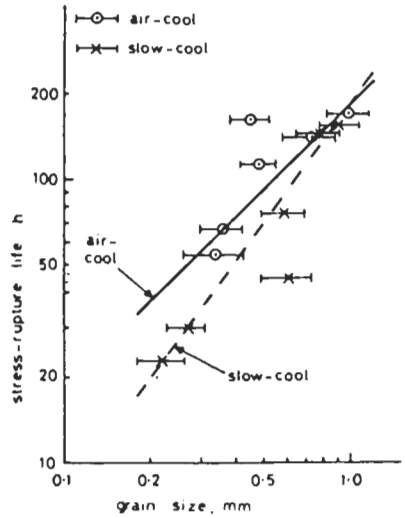

Fig. 68. Creep life versus grain size in IN939 for two different cooling rates from solution temperature, 1160°C. Creep test: 278 MN/m^2 at 870°C. (After CUTLER and SHAW [1979].)

distance is more likely to be the cell size or the subgrain size, which is directly related to the dislocation mean free path or the average dislocation link length. Subgrain boundaries in these materials are associated with strong local misorientations (as evidenced by electron diffraction in fig. 4, above); therefore the distinction between grain boundaries and large-angle subgrain boundaries tends to disappear, especially when cumulative misorientations are examined over several subgrains. This situation normally leads to continuous recrystallization during annealing (MONTHEILLET [1981]) but this

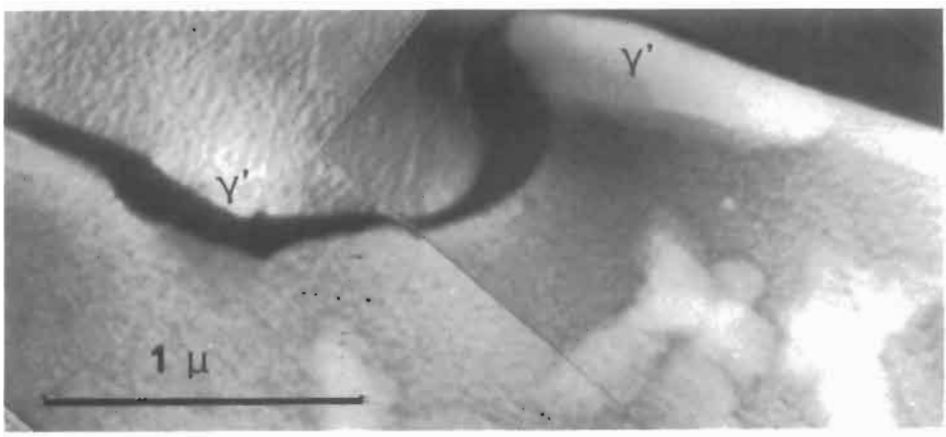

Fig. 69. An adequate cooling rate through the γ' solvus temperature yields wavy grain boundaries anchored by large γ' precipitates in a PM superalloy. Higher creep and fatigue ductility is achieved.

References: p. 2174.

process is strongly inhibited by precipitates and particles in multiphase alloys.

One further reason why grain boundaries often play a minor role in tensile tests as well as in creep in these composite materials is their wavy aspect, resulting from the pinning effect of the hardening particles (figs. 52, 53). In precipitation-hardened materials, an appropriate sequence of thermomechanical treatments can favor the development of interpenetrating grains (fig. 69) which provide the alloy with improved ductility and fatigue resistance (RUNKLE and PELLOUX [1979]). Hence both grains and subgrains are strongly pinned and distorted from the fairly straight polyhedral shape they would assume under the sole effect of interfacial tension. Their strength relies more on their morphology and on the anchoring effect of the hardening phases than on the absence of segregated elements or on their intrinsic structure.

References

AHLQUIST, C.N., and W.D. NIX, 1971, Acta Metall. **19**, 373.

ANSELL, G.S., and F.V. LENEL, 1961, Trans AIME **221**, 452.

ANSELL, G.S., and J. WEERTMAN, 1959, Trans. Met. Soc. AIME **215**, 838.

ARMSTRONG, R.W., 1983, in: Yield, Flow and Fracture of Polycrystals, ed. T.N. Baker (Appl. Science Publ., Barking, Essex, UK) in press.

ASARO, R.J., 1975, Acta Metall. **23**, 1255.

ASHBY, M.F., 1966, Phil. Mag. **14**, 1157.

ASHBY, M.F., 1968, in: Proc. 2nd Bolton Landing Conf. on Oxide Dispersion Strengthening (Gordon and Breach, New York) p. 143.

ASHBY, M.F., 1969, in: Physics of Strength and Plasticity, ed. A.S. Argon (MIT Press, Cambridge, MA) p. 113.

ASHBY, M.F., 1970, Phil. Mag. **21**, 399.

ASHBY, M.F., 1971, in: Strengthening Methods in Crystals, eds. A. Kelly and R.B. Nicholson (Elsevier, New York) p. 137.

ATKINSON, J.D., L.M. BROWN and W.M. STOBBS, 1974, Phil. Mag. **30**, 1247.

BARRETT, C.R., E.C. MUEHLEISEN and W.D. NIX, 1972, Mater. Sci. Eng. **10**, 33.

BEARDMORE, P., R.G. DAVIES and T.L. JOHNSTON, 1969, Trans. Met. Soc. AIME **245**, 1537.

BEE, J.V., A.R. JONES and P.R. HOWELL, 1980, J. Mater. Sci. **15**, 337.

BENJAMIN, J.S., 1970, Metallurg. Trans. **1**, 2943.

BENJAMIN, J.S., 1977, Scientific American **234**, 40.

BENIAMIN, J.S., and M.J. BROMFORD, 1977, Metallurg. Trans. **8A**, 1301.

BENJAMIN, J.S., and G.R. SCHELLEN, 1981, Metallurg. Trans. **12A**, 1827.

BERGMAN, B., 1975, Scand. J. Metall. **4**, 97.

BONNET, R., 1980, Ann. Chim. Franç. **5**, 203.

BROOKS, H., 1952, in: Metal Interfaces (ASM, Metals Park, OH) p. 20.

BROWN, L.M., and D.R. CLARKE, 1977, Acta Metall. **25**, 563.

BROWN, L.M., and R.K. HAM, 1971, in: Strenghtening Methods in Crystals, eds. A. Kelly and R.B. Nicholson (Elsevier, New York), p. 9.

BROWN, L.M., and W.M. STOBBS, 1971a, Phil. Mag. **23**, 1185.

BROWN, L.M., and W.M. STOBBS, 1971b, Phil. Mag. **23**, 1201.

BROWN, L.M., and W.M. STOBBS, 1976, Phil. Mag. **34**, 351.

CAILLETAUD, G., and J.L. CHABOCHE, 1979, 3rd Int. Conf. on Mechanical Behavior of Materials (Cambridge Univ. Press).

CAIRNS, R.L., 1974, Metallurg. Trans. **5**, 1677.

CARRY, C., and J.L. STRUDEL, 1975, Scripta Metall. **9**, 731.

CARRY, C., and J.L. STRUDEL, 1976, in: Proc. 4th Int. Conf. on Strength of Metals and Alloys, Nancy (INPL, Nancy) p. 324.
CARRY, C., and J.L. STRUDEL, 1977, Acta Metall. **25**, 767.
CARRY, C., and J.L. STRUDEL, 1978, Acta Metall. **26**, 859.
CARRY, C., S. DERMARKAR, J.L. STRUDEL and B.C. WONSIEWICZ, 1979, Metallurg. Trans. **10A**, 855.
CARRY, C., C. Houls and J.L. STRUDEL, 1981, Mem. Sci. Rev. Metallurg. **78**, 139.
CHAHOCHE, J.L., 1977, Bull. Acad. Polon. Sci. **25**, 33.
CHAPMAN, P.F., and W.M. STOBBS, 1969, Phil. Mag. **19**, 1015.
CLAVEL, M., and A. PINEAU, 1982, Mater. Sci. Eng. **55**, 157.
CLAVEL, M., C. LEVAILLANT and A. PINEAU, 1980, in: Proc. Conf. on Creep-Fatigue Environment Interaction, eds. R.M. Pelloux and N.S. Stoloff (AIME, Warrendale, PA) p. 24.
COPLEY, S.M., and B.H. KEAR, 1967, Trans. Met. Soc. AIME **239**, 977.
COPLEY, S.M., B.H. KEAR and G.M. ROWE, 1972, Mater. Sci. Eng. **10**, 87.
CROSSLAND, I.G., and R.B. JONES, 1972, Met. Sci. J. **6**, 162.
CULIE, J.P., G. CAILLETAUD and A. LASALMONIE, 1982, La Recherche Aerospatiale **2**, 51.
CUTLER, C.P., and S.W.K. SHAW, 1979, in: Proc. 5th Int. Conf. on Strength of Metals and Alloys, Aachen, eds. P. Haasen, V. Gerold and G. Kostorz (Pergamon Press, Oxford) p. 1357.
DAVIDSON, J.H., and C. AUBIN, 1982, in: High Temperature Alloys for Gas Turbines, eds. R. Brunetaud *et al.* (D. Reidel, Dordrecht, Holland) p. 853.
DELEURY, M.J., J.R. DONATI and J.L. STRUDEL, 1981, Ann. Chim. Franç. **6**, 59.
DERMARKAR, S., and J.L. STRUDEL, 1979, Proc. Int. Conf. on Strength of Metals and Alloys, Aachen, eds. P. Haasen, V. Gerold and G. Kostorz (Pergamon Press, Oxford)) p. 705.
DERMARKAR, S., and J.L. STRUDEL, 1980, in: Recrystallization and Grain Growth in Multiphase and Particle-Containing Alloys, eds. N. Hansen *et al.* (Risø National Laboratory, Roskilde, Denmark) p. 139.
DOHERTY, R.D., and J.W. MARTIN, 1962, J. Inst Metals, **91**, 332.
DUPEUX, M., and R. BONNET, 1980, Acta Metall. **28**, 721.
ESCAIG, B., 1974, J. Physique **35**, C7-151.
ESHELBY, J.D., 1954, J. Appl. Phys. **25**, 255.
ESHELBY, J.D., 1961, Prog. Solid Mech. **2**, 89.
FISHER, J.C., E.W. HART and R.H. PRY, 1953, Acta Metall. **1**, 336.
FOREMAN, A.S.E., and M.J. MAKIN, 1966, Phil. Mag. **14**, 911.
GALLAGHER, P.C.J., 1970, Metallurg. Trans. **1**, 2429.
GIBBONS, T.B., and B.E. HOPKINS, 1971, Met. Sci. J. **5**, 233.
GITTUS, J.H., 1975, Proc. Roy. Soc. (London) **A342**, 279.
GLEITER, H., and E. HORNBOGEN, 1965, Phys. Stat. Sol. **12**, 251.
GLEITER, H., and E. HORNBOGEN, 1968, Mater. Sci. Eng. **2**, 285.
GOULD, D., P.B. HIRSCH and F.J. HUMPHREYS, 1974, Phil. Mag. **30**, 1353.
GRANT, N.J., 1983, J. Metals **35**, 20.
GREWAL, M.S., S.A. SASTRI and N.J. GRANT, 1975, Metallurg. Trans. **6A**, 1393.
GUIMIER, A., and J.L. STRUDEL, 1970, Proc. 2nd Int. Conf. on Strength of Metals and Alloys, Asilomar (USA) (ASM, Metals Park, OH) p. 1145.
GUYOT, P., 1962, Acta Metall. **12**, 665.
GUYOT, P., 1971, Phil. Mag. **24**, 987.
GUYOT, P., and R. DEBEIR, 1966, Acta Metall. **14**, 43.
GUYOT, P., and E. RUEDL, 1967, J. Mater. Sci. **2**, 221.
HAASEN, P., and R. LABUSCH, 1979, Proc. 5th Int. Conf. on Strength of Metals and Alloys, Aachen, eds. P. Haasen, V. Gerold and G. Kostorz (Pergamon Press, Oxford) p. 639.
HANSEN, N., and A.R. JONES, 1981, in: Les Traitements Thermiques, 24e Colloque de Metallurgie de Saclay (CEN-Saclay, France), p. 95.
HANSEN, N., and H. LILHOLT, 1971, in: Modern Developments in Powder Metallurgy, ed. H.H. Hausner (Plenum, New York) vol. 5, p. 339.
HART, E.W., 1970, Acta Metall. **18**, 599.
HART, E.W., 1972, Acta Metall. **20**, 275.

HAUSSELT, J. H., and W. D. NIX, 1977, Acta Metall. **25**, 595.
HAZZLEDINE, P. M., 1974, Phil. Mag. **30**, 1327.
HAZZLEDINE, P. M., and P. B. HIRSCH, 1974, Phil. Mag. **30**, 1331.
HIRSCH, P. B., 1957, J. Inst. Metals, **20**, 275.
HIRSCH, P. B., and F. J. HUMPHREYS, 1969, in: Physics of Strength and Plasticity, ed. A.S. Argon (MIT Press, Cambridge, MA) p. 189.
HIRSCH, P. B., and F. J. HUMPHREYS, 1970, Proc. Roy. Soc. (London) **A318**, 45.
HOLBROOK, J. H., and W. D. NIX, 1974, Metallurg. Trans. **5**, 1033.
HORNBOGEN, E., and U. KOSTER, 1978, in: Recrystallization of Metallic Materials, ed. F. Haessner (Dr. Riederer Verlag, Stuttgart) p. 159.
HUMPHREYS, F. J., 1977, Acta Metall. **25**, 1323.
HUMPHREYS, F. J., 1979a, Acta Metall. **27**, 180.
HUMPHREYS, F. J., 1979b, Met. Sci. **13**, 136.
HUMPHREYS, F. J., 1980, in: Recrystallization and Grain Growth of Multiphase and Particle-Containing Materials, eds. N. Hansen *et al.* (Risø National Laboratory, Roskilde, Denmark) p. 35.
HUMPHREYS, F. J., and P. B. HIRSCH, 1970, Proc. Roy. Soc. (London) **A318**, 73.
HUMPHREYS, F. J., and J. W. MARTIN, 1967, Phil. Mag. **16**, 927.
HUMPHREYS, F. J., and A. T. STEWART, 1972, Surf. Sci. **31**, 389.
JONES, A. R., and N. HANSEN, 1980, in: Recrystallization and Grain Growth of Multiphase and Particle-Containing Alloys, eds. N. Hansen *et al.* (Risø National Laboratory, Roskilde, Denmark) p. 13.
JONES, A. R., B. RALPH and N. HANSEN, 1979, Met. Sci. **13**, 140.
JONES, R. L., 1969, Acta Metall. **17**, 229.
KEAR, B. H., and J. M. OBLAK, 1974, J. Physique **35**, Colloque C7, 35.
KEAR, B. H., and B. J. PIEARCEY, 1967, Metallurg. Trans. **239**, 1209.
KEAR, B. H., A. F. GIAMEI, J. M. SILCOCK and R. K. HAM, 1968, Scripta Metall. **2**, 287.
KEAR, B. H., A. F. GIAMEI, G. R. LEVERANT and J. M. OBLAK, 1969a, Scripta Metall. **3**, 455.
KEAR, B. H., G. R. LEVERANT and J. M. OBLAK, 1969b, Trans. ASM **62**, 639.
KEAR, B. H., J. M. OBLAK and A. F. GIAMEI, 1970, Metallurg. Trans. **1**, 2477.
KOCKS, U. F., 1966, Phil. Mag. **14**, 1629.
KOCKS, U. F., 1969, in: Physics of Strength and Plasticity, ed. A.S. Argon (MIT Press, Cambridge, MA) p. 133.
KURAMOTO, E., and D. P. POPE, 1978, Acta Metall. **26**, 207.
KUTUMBA RAO, V., D. M. R. TAPLIN and P. R. RAO, 1975, Metallurg. Trans. **6A**, 77.
LAGNEBORG, R., 1969, Met. Sci. J. **3**, 161.
LAGNEBORG, R., 1972, Int. Metall. Rev. **17**, 130.
LAGNEBORG, R., and B. BERGMAN, 1976, Met. Sci. **10**, 20.
LASALMONIE, A., and M. SINDZINGRE, 1971, Acta Metall. **19**, 57.
LASALMONIE, A., and J. L. STRUDEL, 1975a, Phil. Mag. **31**, 115.
LASALMONIE, A., and J. L. STRUDEL, 1975b, Phil. Mag. **32**, 937.
LASALMONIE, A., and J. L. STRUDEL, 1980, Ann. Chim. Franç. **5**, 19.
LAUGHLIN, D. E., 1976, Acta Metall. **24**, 53.
LAW, C. C., and A. F. GIAMEI, 1976, Metallurg. Trans. **7A**, 5.
LE HAZIF, R., P. DORIZZI and J. P. POIRIER, 1973, Acta Metall. **21**, 903.
LENEL, F. V., G. S. ANSELL and E. C. NELSON, 1957, Trans. AIME **209**, 117.
LEVERANT, G. R., B. H. KEAR and J. M. OBLAK, 1973, Metallurg. Trans. **4**, 355.
LI, J. C. M., 1963, in: Electron Microscopy and Strength of Crystals, eds. G. Thomas and J. Washburn (Interscience, New York) p. 713.
LILHOLT, H., 1977, Acta Metall. **25**, 571 and 587.
LLOYD, G. J., and J. W. MARTIN, 1978, Scripta Metall. **12**, 217.
LLOYD, G. J., and R. J. MCELROY, 1975, Phil. Mag. **32**, 231.
LLOYD, G. J., and R. J. MCELROY, 1976, Acta Metall. **24**, 11.
LUND, R. W., and W. D. NIX, 1975, Metallurg. Trans. **6A**, 1329.
LUND, R. W., and W. D. NIX, 1976, Acta Metall. **24**, 469.
MARTIN, J. W., 1980, Micromechanisms in Particle-Hardened Alloys (Cambridge University Press).

MARTIN, J.W., and R.D. DOHERTY, 1976, Stability of Microstructure in Metallic Systems (Cambridge University Press).
MCLEAN, D., 1962, in: Mechanical Properties of Metals (Wiley, New York; new edition 1977, Krieger, New York).
MCLEAN, D., 1966, Rep. Prog. Phys. **29**, 1.
MCLEAN, D., 1976, in: Proc. 4th Int. Conf. on Strength of Metals and Alloys (INPL, Nancy, France) p. 958.
MENON, M.N., and W.H. REIMAN, 1975, Metallurg. Trans. **6A**, 1075.
MIYAZAKI, T., R. NAKAMURA and H. MORI, 1979, J. Mater. Sci. **14**, 1927.
MONTHEILLET, F., 1981, in: Les Traitements Thermiques, 24e Colloque de Metallurgie de Saclay (CEN-Saclay, France) p. 57.
MOSKOWITZ, L.N., R.M. PELLOUX and N.J. GRANT, 1972, quoted by: DAVIDSON, J.H., and C. AUBIN, in: High Temperature Alloys for Gas Turbines, eds. R. Brunetaud *et al.* (D. Reidel, Dordrecht, Holland) p. 853.
MOULD, P.R., and P. COTTERILL, 1967, J. Mater. Sci. **2**, 241.
MULFORD, R.A., and D.P. POPE, 1973, Acta Metall. **21**, 1375.
NES, E., 1976, Acta Metall. **25**, 1323.
OROWAN, E., 1948, in: Symp. on Internal Stresses in Metals and Alloys, London (The Institute of Metals, London) p. 451.
OYTANA, C., P. DELOBELLE and A. MERMET, 1979a, J. Mater. Sci. **14**, 549.
OYTANA, C., MERMET, A. and P. DELOBELLE, 1979b, Proc. 3rd Int. Conf. on Strength of Metals and Alloys, Cambridge (The Institute of Metals, London) p. 203.
PARKER, J.D., and B. WILSHIRE, 1975, Met. Sci. J. **9**, 248.
PEDRON, J.P., and A. PINEAU, 1982, Mater. Sci. Eng. **56**, 143.
PELLOUX, R.M.N, and N.J. GRANT, 1960, Trans. Met. Soc. AIME **218**, 232.
PRAGER, W., 1955, Proc. Inst. Mech. Engrs **169**, 41.
REPPICH, B., 1975, Acta Metall. **23**, 1055.
REPPICH, B., 1982, Acta Metall. **30**, 87.
REPPICH, B., P. SCHEPP and G. WEHNER, 1982, Acta Metall. **30**, 95.
ROBERT, G., J. DESSUS and M.F. FELSEN, 1981, Ann. Chim. Franç. **6**, 209.
RUNKLE, J.C., and R.M. PELLOUX, 1979, Amer. Soc. Testing Mater. Spec. Tech. Publ. **675**, 501.
SANDSTROM, R., 1980a, Z. Metallk **71**, 681.
SANDSTROM, R, 1980b, in: Recrystallization and Grain Growth of Multiphase and Particle-Containing Materials, eds. N. Hansen *et al.* (Risø National Laboratory, Roskilde, Denmark) p. 45.
SAXL, I., and F. KROUPA, 1972, Phys. Stat. Sol. All, 167.
SHAMBLEN, C.E., R.E. ALLEN and F.E. WALKER, 1975, Metallurg. Trans. **6A**, 2073.
SHEWFELT, R.S.W., and L.M. BROWN, 1973, Proc. 3rd Int. Conf. on Strength of Metals and Alloys, Cambridge (The Institute of Metals, London) p. 311.
SHIMANUKI, Y., 1981, Trans. Japan Inst. Met. **22**, 17.
SOLOMON, A.A., and W.D. NIX, 1970, Acta Metall. **18**, 863.
STARKE, Jr., E.A., T.H. SANDERS and I.G. PALMER, 1981, J. Metals **32**, 24.
STEVENS, R.A., and P.E. FLEWITT, 1981a, Acta Metall. **29**, 867.
STEVENS, R.A. and P.E. FLEWITT, 1981b, in: Creep and Fracture of Engineering Materials and Structures, eds. B. Wilshire and D.R.J. Owen (Pineridge Press, Swansea) p. 187.
STOBBS, W.M., 1973, Phil. Mag. **27**, 1073.
STOLOFF, N.S., 1972, in: The Superalloys, eds. C.T. Sims and W.C. Hagel (Wiley, New York) p. 79.
STRUDEL, J.L., 1978, J. Microsc. Spectrosc. Electron. **3**, 337.
STRUDEL, J.L., 1980, in: Les Traitements Thermomecaniques, 24e Colloque de Metallurgie de Saclay (CEN-Saclay, France) p. 81.
THREADGILL, P.L., and B. WILSHIRE, 1974, Met. Sci. J. **8**, 117.
TIEN, J.K., and S.M. COPLEY, 1971, Metallurg. Trans. **2**, 543.
VICKERS, W., and D.P. GREENFIELD, 1968, J. Nucl. Mater. **27**, 73.
WEATHERLY, G.C., and R.B. NICHOLSON, 1968, Phil. Mag. **17**, 801.
WILCOX, B.A., and A.H. CLAUER, 1966, Trans. Met. Soc. AIME **236**, 570.

WILCOX, B. A., and A. H. CLAUER, 1972, Acta Metall. **20**, 743.
WILLIAMS, K. R., and B. WILSHIRE, 1973, Met. Sci. J. **7**, 176.
ZENER, C., quoted by: C. S. SMITH, 1948, Trans. AIME **175**, 47.

Further reading

Argon, A.S., 1975, Constitutive Equations in Plasticity (MIT Press, Cambridge, MA).
Balakrishna Bhat, T., and V.S. Arunachalam, Strengthening Mechanisms in Alloys, in: Alloy Design, eds. S. Ranganathan *et al.*, Proc. Indian Acad. Sci. (Eng. Sci.) 3 (1980) 275.
Gittus, J., 1975, Creep, Viscoelasticity and Creep Fracture in Solids (Appl. Science Publ., London).
Hansen, N., A.R. Jones and T. Leffers, eds., 1980, Recrystallization and grain growth of Multiphase and Particle-Containing Materials (Risø National Laboratory, Roskilde, Denmark).
Hansen, N., A. Horwell, T. Leffers and H. Lilholt, 1981. Deformation of polycrystals: Mechanisms and Microstructures (Risø National Laboratory, Roskilde, Denmark).
Kelly, A., and R.B. Nicholson, 1971, Strengthening methods in crystals (Elsevier, Amsterdam).
Martin, J.W., 1980, Micromechanisms in Particle-Hardened Alloys (Cambridge University Press).
McClintock, F.A., and A.S. Argon, 1966, Mechanical behavior of materials (Addison-Wesley, Reading, MA).
Poirier, J.P., 1976, Plasticité a Haute Temperature des Solides Cristallines (Edit. Eyrolles, Paris).
Sims, C.T., and W.C. Hagel, 1972, The superalloys (Wiley, New York).
Wilshire, B., and D.R.J. Owen, 1981, Creep and Fracture of Engineering Materials and Structures (Pineridge Press, Swansea, UK).

Addendum

A1. Introduction

The development of alloys combining high mechanical strength at room temperature as well as at elevated temperature with reasonable ductility, good resistance to oxidation and/or corrosion, acceptable fracture toughness and safe fatigue crack growth rates has been, during the last fifty years, the main motivation of many engineers and scientists. A large number of metallic alloys were already known and commonly used in industry, but their main features were far from being optimized. High-strength steels; high-performance nickel-base alloys and aluminum-base alloys, hardened by carefully controlled distributions of various precipitates and protected by the formation of oxide films, natural or artificial; titanium-base alloys combining high strength with low density... each new alloy was developed to its optimal performance and became progressively more specific, often to the point where it could only be used for one specific part of an engineering device: an example is the development of alloys for hollow single-crystal turbine blades which demanded the full attention of hundreds of investigators and required a large financial input.

Also during the past 50 years, extensive electron microscope (SEM and TEM) examinations of high-performance alloys confronted theoreticians with a body of experimental observations that revealed the existence and crucial importance of numerous elementary mechanisms previously regarded as incidental details. An example: complex dislocation core structures controlling the movement of dislocations and hence the ductility of most crystalline materials, and in turn determining dislocation/impurity atom interactions that contribute to the viscoplastic strength of most industrial alloys but also create anomalous mechanical effects such as Portevin–Le Chatelier instabilities and strain localization. With regard to most high-strength materials, the naive yet inescapably complex picture, of perfect dislocations multiplying and interacting with one another, had to be abandoned in order to take into account the large variety of mobile defects observed in crystalline materials: paired dislocations, pileups, partial dislocations resulting from either climb- or glide-induced dissociations, dipoles, stacking-fault ribbons, antiphase boundaries, whole dislocation networks or subgrain boundaries and grain boundaries participating actively in the plasticity or even superplasticity of materials.

This Addendum is not intended to be a comprehensive review of recent progress in understanding all possible strengthening phenomena, but rather to provide a limited number of illustrative examples of modern engineering materials whose outstanding performance relies on fairly well understood strengthening mechanisms.

A2. Stress relaxation and the measurement of activation parameters

Dispersion- and precipitation-strengthened materials oppose to the smooth path of dislocations on their glide planes a large variety of obstacles which can be more or less stable with respect to temperature changes. The apparent sizes and mutual separation of these obstacles, the degree of their ability to be sheared by dislocations or to either repel

References: p. 2204.

or retain them, can be characterised statistically by macroscopic measurements made during tensile, creep and stress relaxation tests. At low temperatures ($T<0.3T_m$), obstacles can be bypassed by gliding dislocations if local stress conditions permit it, and since thermal activation plays no part in the process this stage is commonly referred to as the *athermal stage*, characterized by an athermal stress, almost constant over a range of temperatures. When the material is exposed to stresses at temperatures between $0.3T_m$ and $0.8T_m$, its flow stress decreases with increasing temperature since the moving dislocations are now assisted by thermal activation in their attempt to circumvent or overcome the obstacles. The concepts of *activation volume*, V, and *activation enthalpy*, ΔH_0, generally used in connection with plastic flow equations of the type

$$\dot{\varepsilon}_p = \dot{\varepsilon}_0 \exp - \frac{\Delta G}{kT} = \rho_m b \nu \bar{L} \exp \frac{\Delta S}{k} \exp - \frac{\Delta H_0 - \sigma V}{kT} \tag{A1}$$

are very helpful in characterizing the strength of obstacles (CONRAD [1964]). The overall energy level of an obstacle is proportional to ΔH_0 and the spatial extent of the obstacle is characterized by the activation volume $V=bA$, where b is the Burgers vector of the dislocation and A is the *activation area*, i.e., the area swept by the dislocation during the activation event. (See also ch. 21, § 4.2)

Furthermore, in eq. (A1) the preexponential term $\sigma_m b \nu \bar{L}$ includes at least two terms characterizing the microstructure of the material: the density of mobile dislocations, ρ_m, which may not remain constant when the applied stress is varied, the Burgers vector, b, which is constant only for a specific glide mechanism, a frequency factor, ν, associated with vibrational modes of the dislocation and the mean free path, $\bar{L}$, of a dislocation when moving from one obstacle to the next. This last term depends strongly either on the density of "trees" (i.e., immobile dislocations) or of precipitates which are both constituent elements of the landscape of obstacles met by the dislocations. These problems in correlating macroscopically measured values of activation volume with elementary dislocation/obstacle interactions have been considered at length in several recent publications (e.g, SPÄTIG *et al.* [1995].

Simple stress relaxation tests may yield only *apparent* activation volumes. In order to take into account the internal stress of the material, its plastic strain-hardening coefficient, K, must be introduced and technique of repeated relaxation has been proposed by KUBIN [1974] and by SPÄTIG *et al.* [1993] who suggested periodic reloading to the initial stress level. The apparent and *effective* (true) activation volumes are related by the expression

$$V_a = V_{eff}\left(1 + \frac{K}{M}\right) \tag{A2}$$

where M is the elastic modulus of the specimen–machine assembly. The measurement of true activation volumes allows identification of the microscopic deformation mechanisms, which may be quite different during the initial stages of plasticity and later stages, for larger strains.

In precipitation-hardened nickel-base alloys, when tested in relaxation mode at intermediate temperatures (500–700°C), three stages have been observed by SAINT-ANTONIN *et al.* [1990] in Astroloy and similar results have been reported (PROVENDIER–

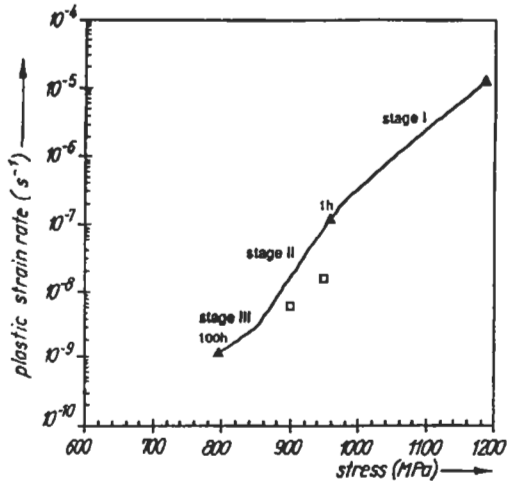

Fig. A1. Relaxation curve of a nickel-base superalloy, after loading to a plastic strain of 1.4% at a strain rate of 10^{-5}/s. □ data for creep tests. (After PROVENDIER–AUBOURG and STRUDEL [1995].)

AUBOURG and STRUDEL [1995]) in alloy N–18, a recently developed, damage-tolerant powder-metallurgy alloy (fig. A1). In N–18, the γ' precipitates occupy a volume fraction of 65%, hence the matrix dislocations must either pair up to shear the ordered γ' phase, as they do during loading and in the first stage of relaxation, or they must bow out between narrowly spaced γ' precipitates by assuming very small radii of curvature in order to infiltrate the narrow matrix corridors (20 nm or less), in the second stage. Finally, during the third stage, when the remnant applied stress has dropped to 0.8–0.7 of the initial value, perfect dislocations can no longer bow between the γ' precipitates, but since they tend to dissociate into their Shockley partials, the latter can become coupled on two adjacent (111) slip planes and shear both γ and γ' phases, leaving behind large ribbons of stacking-faults cutting across both phases. The signatures of all these mechanisms are simultaneously present in thin foils extracted from a fully relaxed sample. The first stages, which correspond to microplasticity, are associated with the motions of a small density of fairly mobile perfect or paired dislocations and hence with very large activation volumes (1500 Å^3 and higher) as SPÄTIG *et al.* [1993] also reported in their work on the pure ordered phase Ni_3 (Al, Hf). The viscoplasticity in the last stage, on the other hand, rests on the activation of more subtle phenomena, and more sluggish ones also, which require local atomic rearrangements. The activation volume in this stage can decrease to values of 150–200 Å^3, which characterize rate-controlling processes more complex than simple volume diffusion. This latter point is also confirmed by the values of activation energies which currently reach 500–600 kJ/mole as reported by DUPEUX *et al.* [1987] for single crystals of CMSX-2 oriented along the [001] direction, which favors octahedral slip on several glide systems. Similar values were measured in polycrystalline Astroloy by SAINT–ANTONIN *et al.* [1990] and by PROVENDIER-AUBOURG and STRUDEL [1995] in alloy N–18, thus clearly suggesting that strong though not insurmountable obstacles in the path of dislocations effectively control the viscoplastic behavior of highly

strengthened materials and are responsible for unusually high values of activation parameters at $0.4–0.6T_m$. These values are considerably larger than those commonly reported for creep in pure metals since the latter correlate closely with volume self-diffusion data.

A3. Continuum mechanics approach to multiphase materials

Efforts to develop tools capable of handling and explaining the elastic behavior, the instantaneous plastic behavior and the viscoelastic behavior of multiphase materials have been concentrated around several distinct lines of action, which can be schematically reduced to three:

(1) local micromechanical descriptions of two-phase materials, making use of finite element methods;
(2) the development of two-dimensional or three-dimensional constitutive equations describing the macroscopic behavior of materials containing inclusions, fibers and heterogeneous phases in general;
(3) phenomenological methods using scalar equations and including microstructural and metallurgical aspects of materials.

A3.1. Local micromechanical models

Modern nickel-base superalloys contain impressive volume fractions of the γ' (hardening) phase, ranging from 50 to 65%, the ordered (Ni_3Al) precipitates having a lattice parameter generally smaller than that of the matrix by 0.2–0.3%. Elastic interactions between precipitates and matrix and mutual interactions between closely spaced precipitates must be taken into account, first in the absence of an externally applied stress and then in the presence of a uniaxial stress usually applied along a simple crystal direction characterized by a high degree of symmetry, such as [001]. SOCRATE and PARKS [1993] investigated the origin of the driving force for the coalescence, or "rafting", of the γ' cuboids during creep at high temperature by use of a purely elastic model, using finite element techniques. POLLOCK and ARGON [1992], in an effort to interpret microstructural observations of γ' rafting phenomena during creep of single crystals of CMSX3 alloy, resorted to similar calculations but also considered the role of the many dislocations that progressively collect at the γ/γ' interfaces in the course of plastic deformation. A similar approach had been used earlier by FELLER–KNIEPMEIER *et al.* [1989] and by GLATZEL *et al.* [1989].

A3.2. Macroscopic behavior of particle-hardened materials

Understanding the behavior of composite materials, whether the second phase actually consists of fibers, spherical or elliptical inclusions, usually relies on analysis of the nature of the inclusion/matrix interaction, often including terms of anisotropy, and assumes that an elementary sphere is embedded in a *homogeneous equivalent medium* having averaged uniform properties. HERVÉ and ZAOUI [1990] have extended such self-consistent models to the effective non-linear behavior of two- and three-phase materials, formally extending

it to n-layered inclusions (HERVÉ and ZAOUI [1993]), thus both including the local specific behavior of interfaces and improving the representation of the actual spatial distribution of components in such materials. Extensions of the model to include situations where different kinds of particles are dispersed with different coexisting morphologies are in progress. LEE and MEAR [1992] have considered the case of solids containing rigid inclusions, represented as elliptical inhomogeneities, and exhibiting power-law behavior. They were able to establish accurate constitutive relations for dilute concentrations of inclusions over a wide range of matrix-hardening exponents and inclusion aspect ratios. Approximate relations were derived for non-dilute concentrations by use of a differential self-consistent scheme primarily concerned with randomly oriented inclusions; the authors also suggested solutions for aligned inclusions such as are often observed in nickel-base superalloys with high γ' volume fractions.

Most of the recent models describing the deformation behavior of two-phase materials containing coarse rigid particles in a ductile, plastically deforming matrix undergoing strain-hardening (TANDON and WENG [1988], RAVICHANDRAN [1994]) have only so far considered the instantaneous plastic behavior of such materials. WENG [1990], in a similar scheme, has examined the case of two phases with different stiffnesses, each capable of undergoing plastic flow simultaneously.

A3.3. Phenomenological approach

A less rigorous but simpler approach, using scalar equations at the macroscopic scale but including physical parameters usually observed and measured at the microscopic scale, has been repeatedly followed by many physicists, metallurgists and engineers.

In their model describing the role of interfaces during creep in fiber-reinforced materials, GOTO and MCLEAN [1991] considered a random array of aligned, non-creeping but elastically deforming, fibers embedded in a matrix undergoing power-law creep. They included the specific behavior of interfaces that differed from those between the two main phases. Their conclusions tend to indicate that weak reinforcement/matrix interfaces have little or no effect on the creep performance of fiber-composite materials. These conclusions are less encouraging than those of ARZT *et al.* [1989] concerning dispersed-phase alloys (see § A4.2); he found a positive contribution of a weak interface between matrix and particle. But microstructural observations of fracture surfaces underline the high sensitivity of creep behavior to the characteristics of the interfaces, the aspect ratio of the fibers or grains and to the volume fraction of the reinforcing constituent.

Also making use of modified power-law creep equations, the so-called "θ projection method" developed by EVANS and WILSHIRE [1985] (see *Further reading*, at end) rests on the view that normal creep curves can be envisaged as the sum of a decaying primary component and an accelerating tertiary contribution to the instantaneous viscoplastic strain, $\varepsilon_{(t)}$. They suggest writing the equation that relates creep strain to time t as

$$\varepsilon_{(t)} = \varepsilon_t - \varepsilon_0 = \theta_1\left(1 - \exp\left[-\theta_2 t\right]\right) + \theta_3\left(\exp\left[\theta_4\right] - 1\right) \tag{A3}$$

where ε_0 is the initial strain on loading and ε, the total strain at time t. θ_1 and θ_3 act as scaling parameters defining the extent, respectively, of the primary and tertiary stages

with respect to strain, and θ_2 and θ_4 are rate parameters which characterize the curvatures of the primary and tertiary stages of the creep curve, respectively. Considering thermally activated elementary processes, the authors rationalize the previously introduced coefficient by writing equations such as

$$\theta_1 = G_1 \exp\left[H_1\left(\sigma/\sigma_y\right)\right] \tag{A4}$$

and

$$\theta_2 = G_2 \exp\left[\left(Q_2 - H_2\sigma\right)/kT\right] \tag{A5}$$

where G_1, H_1, G_2 and H_2 are material constants. These restrictive assumptions preclude changes in activation volume and hence in creep mechanisms with applied stress, yet they have been successfully used to describe the viscoplastic behavior of multiphase materials, as shown in a recent study of creep and creep fracture of an oxide-dispersion-strengthened (ODS) ferritic steel (EVANS *et al.* [1993]).

A4. Oxide-dispersion-strengthened (ODS) materials and their resistance to high-temperature viscoplastic flow

Among the processes recently developed to generate novel, high-performance alloys, *mechanical alloying* techniques offer an unmatched ability to incorporate a large variety of constituents, thus additively combining the contributions of several hardening mechanisms in a single material. Invented by Benjamin at INCO Alloys in the 1970s as a method for processing alloys dispersion-strengthened by hard particles, for use at high temperatures, this technology probably culminated in the 1980s with the development of Inconel MA 6000, which combines precipitation-hardening by γ' (via 4.5 Al + 2.5 Ti + 2 Ta in wt.%), solid-solution-strengthening (via 2 Mo + 4 W) and oxide-dispersion-strengthening by means of 2.2 vol.% Y_2O_3–Al_2O_3.

As shown in fig. A2, even the best conventional nickel-base superalloys (columnar-grain DS Mar-M 200 + Hf or single-crystal CMSX-2, for instance) are limited at high temperature by the resolutionizing of the γ' phase and of the refractory carbides on which they depend for strength. On the one hand, thoria-disperse (TD) nickel or even TD–Ni,Cr are potentially superior to γ'-strengthened alloys only above 1100°C, whereas MA 6000 is already comparable with nickel superalloys at 800°C and keeps its superior behavior up to 1150°C. Ferritic alloys such as MA 956 provide a significant improvement over conventional alloys and at a lower cost than the austenitic alloys. Their good corrosion and oxidation resistance is the result of their optimised chromium and aluminum content (20 Cr + 4.5 Al, in wt.%), in addition to ≈ 1 vol.% Y_2O_3. It should be noted (fig. A3) that both materials need to be recrystallized with coarse grains and a high grain aspect ratio (5–30) in order to achieve the expected improvement in creep resistance at very high temperatures. The contribution of intense grain-boundary diffusion to viscoplastic flow of the alloy is clearly demonstrated by these results, which show a 6–8 orders of magnitude factor of difference in the creep regimes at a given stress, as the grain size is varied.

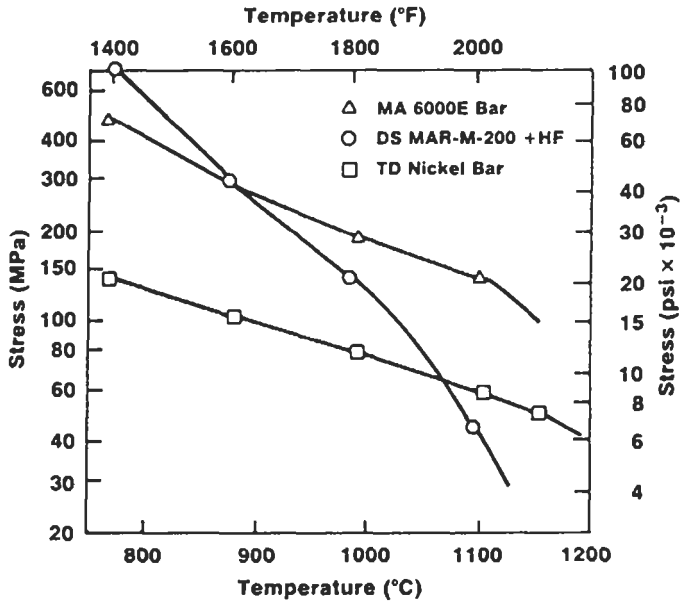

Fig. A2. Stress for 1000-hour life for Inconel alloy MA 6000, TD (thoria-disperse) nickel and MAR-M-200 + Hf. (After BENJAMIN [1989].)

A4.1. The threshold stress

The presence of second-phase particles introduces a yield strength which can be associated with their mean mutual separation, $\bar{l}$, through the Orowan expression

$$\sigma_{or} = \frac{0.84 m_T}{2\pi(1-\nu)} \frac{Gb}{\bar{l}} \ln\left(\frac{r}{b}\right) \tag{A6}$$

where m_T is the Taylor factor (the reciprocal of the Schmid factor in single crystals), G is the shear modulus, $\nu = 0.3$ is the torsion ratio and b, the Burgers vector.

At low temperature no glide can take place at a resolved stress below τ_{or} (σ_{or} corrected by the Taylor factor). Therefore it is reasonable to consider it as a true *threshold stress*. BROWN and HAM [1971], later LUND and NIX [1976] have extended the original concept to high temperature, and indeed it is found experimentally that at high temperature, ODS materials exhibit barely detectable plastic flow rates below a specific stress level, depending on the alloy, which is denoted σ_{th} in fig. A3. As the applied stress level approaches this value, the apparent stress exponent, n_a, takes on values of 30–60.

While at low temperature or at high strain rates, the yield stress of ODS materials corresponds quite closely to the value estimated by the Orowan equation, as has been confirmed by REPPICH *et al.* [1990] for Pt–ZrO_2 as well as for engineering ODS materials such as MA 754 (REPPICH *et al.* [1986]); nevertheless at higher temperatures the observed threshold stress is only loosely related to the Orowan stress. As pointed out

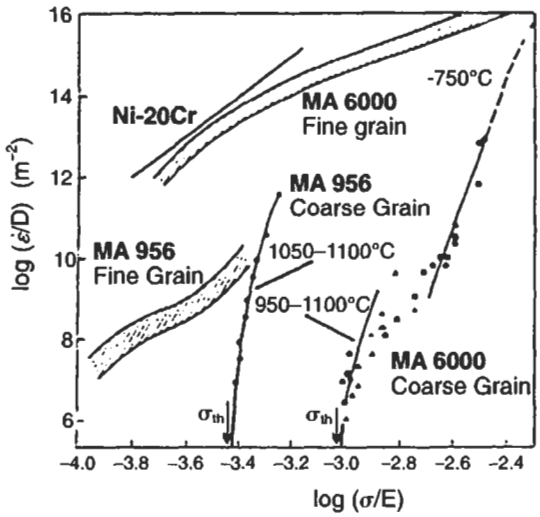

Fig. A3. Diffusion-compensated creep rates as a function of modulus-compensated applied stress for Inconel alloy MA 6000 and Inconel alloy MA 9056. (After SINGER and ARZT [1985].)

by ARZT [1990], the ratio σ_{th}/σ_{or} decreases with rising temperature from ≈ 0.7 to ≈ 0.3 for most ODS materials (fig. A4). Since the various materials examined have absolute threshold values which differ by more than one order of magnitude, the Orowan stress, σ_{or}, appears to be a useful normalization parameter. However, the fact that at high temperature, viscoplastic flow can take place under stresses significantly below σ_{or} remains to be explained by elementary dislocation movements radically distinct from the Orowan bypassing mechanism.

A4.2. Dislocation climb models

At elevated temperature, dislocation motion is no longer limited to the glide plane. With the help of point defects whose migration is accelerated in the vicinity of the dislocation core, dislocations can climb over obstacles and finally surmount the particles. BLUM and REPPICH [1985] provided a simple derivation of a threshold stress which added two terms to the previous models: they took into account not only the glide force applied to the dislocation but also the normal force contributing to its climb, and finally a term specifying the elastic interaction between the segments of dislocations located in the immediate vicinity of the particle, but they assumed the dislocation line tension, T_L, to be constant along the dislocation and independent of temperature.

The important parameter introduced by ARZT and ASHBY [1982] is called the *climb resistance*, R:

$$R = \left(\mathrm{d}l/\mathrm{d}y\right)_{max} \tag{A7}$$

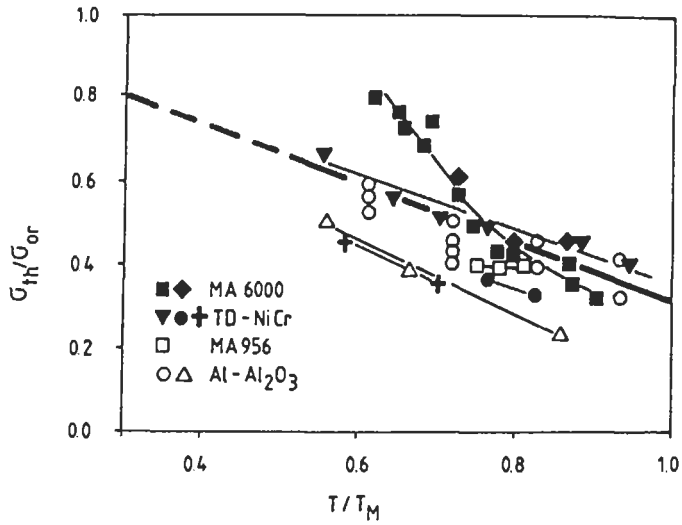

Fig. A4. Plot of experimental "threshold stresses", normalized with respect to the calculated Orowan stress, as a function of homologous temperature, for coarse-grained or single-crystal materials. (After ARZT [1990].)

where l is the free length of dislocation between two particles, and R describes the rate of increase in line length as the dislocation segment climbs over the particle in the Z direction and the rest of it climbs over a distance dy in the slip plane.

Local climb models correspond to rather low values of R (≤ 1); for small and widely spaced particles, climb occurs in the particle/matrix interface (fig. A5a) and the model of STEVENS and FLEWITT [1981] offers a satisfactory description of the plastic behavior. The critical stress for climb, τ_c, is now given by the expression

$$\tau_c = \left(\frac{2T_L}{b\bar{L}}\right)\left(\frac{R}{2}\right)^{\alpha} \tag{A8}$$

with $\alpha = 1$ when $\bar{l}$ is approximated by the mean planar square partial spacing $\bar{L} = r(2M/3f)^{1/2}$ for a particle of radius r and a volume fraction of particles f, and $\alpha = 3/2$ in the Fleischer–Friedel model of random isolated monodisperse particles acting as individual point-like obstacles of identical strength.

Pointing out the striking feature of the rapid fall in creep resistance with temperature of most alloys hardened by a second phase, even in ODS alloys (fig. A2), LAGNEBORG [1972] was the first to suggest that the dislocation segment that undergoes climb, when a dislocation is surmounting an unshearable particle (fig. A5b), extends to regions FA and BD on either side of the particle and is not limited to AB, the precipitate/matrix interface. This model of *general climb* was applied to ODS materials in connection with the concept of *reduced line tension* of the dislocation segment localized near the particle. The parameter k introduced by ARZT and WILKINSON [1986] can be thought of as a *relaxation factor*, having value 1 in the absence of interaction between the dislocation

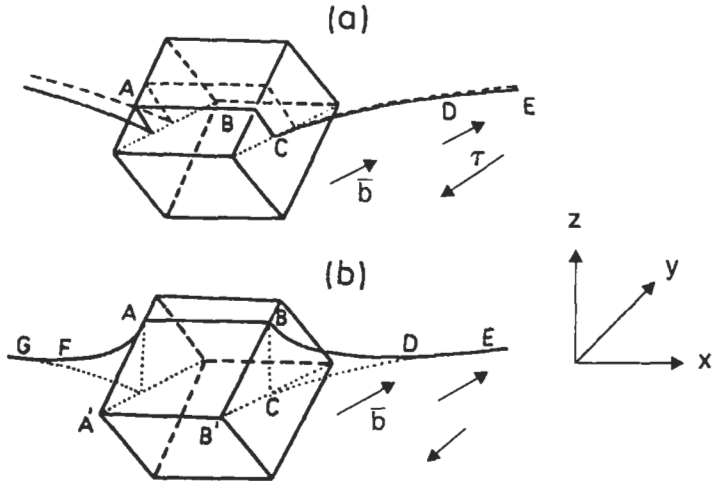

Fig. A5. Two modes of interaction between an unshearable particle and a dislocation.

and the particle and 0 for the formal case of complete relaxation. The *climb threshold*, σ_c, is obtained to a good approximation by the expression (ARZT and WILKINSON [1986])

$$\sigma_C(k) = 0.32k\, m_T \frac{Gb}{2\bar{L}}. \tag{A9}$$

At low values of k, i.e., in the case of strong attractive interaction, R will fall to values below 0.2 and even to zero.

A different viewpoint advanced by SROLOVITZ *et al.* [1984] considered the possible *attractive interaction* between the dislocation and the particle, especially in the case of an incoherent interface which is free to shear. The authors suggested that, in many cases, the assumption of a particle/matrix interface loose enough to experience shear, as in fiber-composite materials, is more realistic than that of a strongly adherent particle, as is generally assumed in metallurgical models. SCHRÖDER and ARZT [1985] did confirm by TEM that dislocations in γ'-ODS alloys such as MA 6000 were actually pinned on the *back side* of the particle (fig. A6). Hence the dislocation is retained by the particle which it has already surmounted by a complex combined movement of glide, cross-slip and climb. Now a second threshold becomes more important: the *threshold for detachment* of the dislocation from the dispersoid, σ_d, which is given by

$$\sigma_d = m_T \frac{Gb}{2\bar{L}} \sqrt{1 - k^2}. \tag{A10}$$

The overall threshold stress for the dislocation bypass is simply the larger of the two stresses given by eqs. A9 and A10. Thus σ_d will be the rate-controlling threshold at low k values, i.e., for strong attractive interaction, and σ_c will only dominate in the case of weak dispersoid-dislocation interaction.

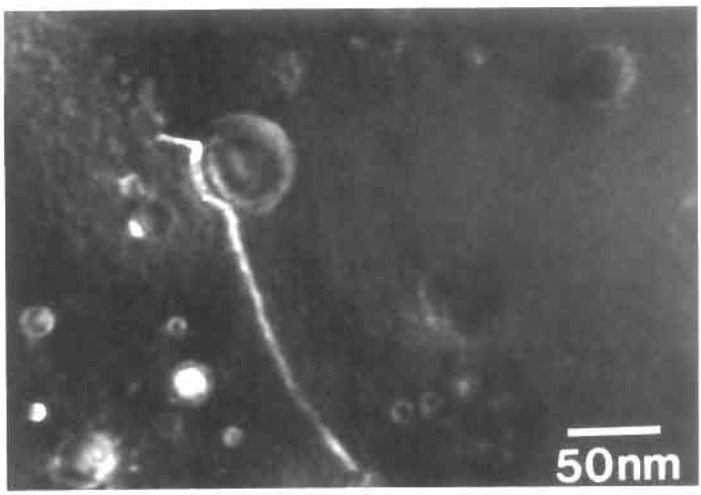

Fig. A6. Weak-beam TEM image of dislocations held back by oxide dispersion particles of different size. (After SCHRÖDER and ARZT [1985].)

A kinetic model which combines general dislocation climb with an allowance for the effects of an attractive interaction between dislocations and particles has been developed by ARZT and RÖSLER [1988] and the resulting creep rate for detachment-controlled plasticity is

$$\dot{\varepsilon} = \dot{\varepsilon}_0 \exp\left(-\frac{Gb^2 r}{kT}(1-k)^{3/2}\left(1-\sigma/\sigma_d\right)^{3/2} \right) \tag{A11}$$

where σ_d is given by eq. A10. This model offers an appropriate interpretation of experimental results when thermally activated detachment of dislocations from particles is assumed, provided that the preexponential term $\dot{\varepsilon}_0 = 3D\rho\bar{L}/b$ is strongly stress-dependent. Hence a strong variation of the dislocation density, ρ, with both applied stress and test temperature is required. This latter aspect of the model has been criticized by ORLOVÁ and CADEK [1992] who suggested an alternative procedure which actually reduced this unrealistically strong dependence but led to an increased stress dependence of the detachment stress σ_d given by eq. A10. The role of grain boundaries which are also strongly pinned by the particles is not yet explicitly considered in these models and will need to be clarified. An extensive discussion of the various models and associated constitutive equations proposed for creep of dispersion- and precipitation-strengthened materials can be found in a review article by ARZT [1990].

A4.3. High-temperature fatigue properties of ODS alloys

The attractive engineering properties of mechanically alloyed materials have recently been extensively explored in the domain of low-cycle fatigue (LCF) behavior, fatigue-

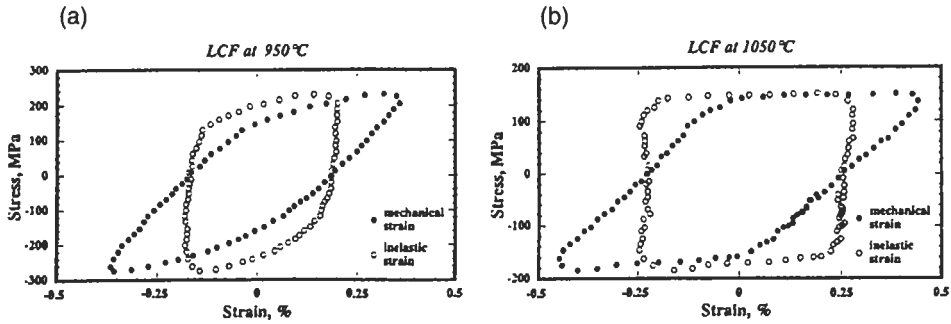

Fig. A7. Stabilised stress-strain response of MA 760, (a) at 950°C, (b) at 1050°C. (After VASSEUR and REMY [1994].)

crack initiation and growth rates and finally in thermomechanical fatigue tests (TMF), which combine simultaneous variations of stress and temperature according to cycles typifying the type of conditions met by specific parts during their service life (VASSEUR and REMY [1994]).

While MA 760 still strain-hardens detectably at 950°C at a strain-rate of 10^{-3}/s (fig. A7a), it has lost this ability at 1050°C (fig. A7b) where the alloy can be identified as elastic/perfectly plastic with a yield strength hardly superior to the *threshold stress* of 130 MPa deduced from creep tests in the same temperature range.

The cyclic hardening curves, whether in stress-control or strain-control tests (ch. 27, § 2), reveal no strain-hardening (figs. A8a and b) and deconsolidation is hardly detectable, although the stabilized cyclic stress level decreases significantly with increasing temperature.

The fatigue life of MA 760 reveals a dependence on strain rate and on frequency. This behavior results from an interaction between instantaneous plasticity and time-dependent processes such as creep, oxidation and microstructural changes such as rafting. Crack nucleation is generally localized at grain boundaries and propagation is transgran-

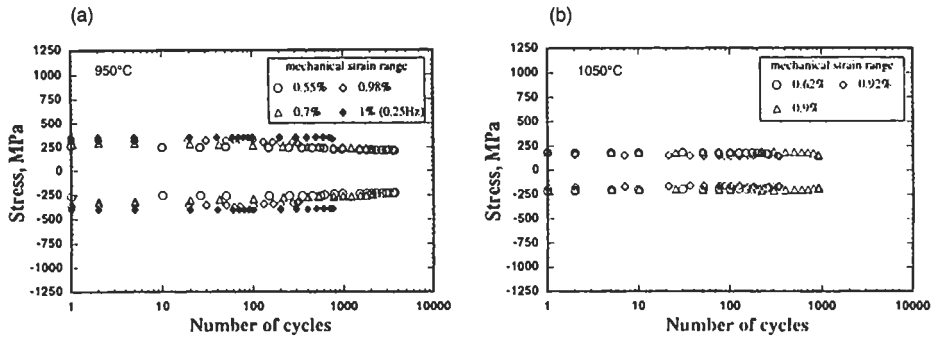

Fig. A8. Cyclic hardening, under controlled strain, of MA 760: (a) 950°C, (b) 1050°C. (After VASSEUR and REMY [1994].)

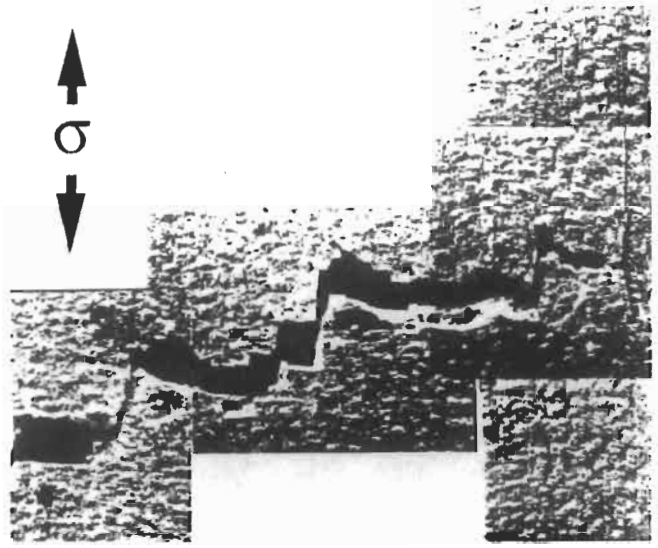

Fig. A9. Fatigue crack in MA 760 tested in thermomechanical fatigue tests. The main crack is normal to the applied stress. (After VASSEUR and REMY [1994].)

ular, perpendicular to the applied stress (fig. A9). This SEM micrograph also reveals delamination along longitudinal grain boundaries. The performance of alloy MA 760, when tested in LCF and in TMF at high temperature, is impeded by grain-boundary weaknesses probably resulting from inadequate control of recrystallization, according to VASSEUR and REMY [1994].

The low cycle fatigue properties of iron-base ODS alloys and the effect of grain structure have recently been reviewed by BANHARDT *et al.* [1995].

A5. Micromechanisms of plasticity in nickel-base alloys

Among precipitation-hardened alloys, nickel-base superalloys have received much attention from the scientific community since they are widely used industrially, hence are commercially successful and with their rather simple microstructure constitute, despite their complex chemical compositions, the archetype for many other alloys. For instance, Al–Li alloys, hardened by the ordered intermetallic phase Al_3Li, are very similar to superalloys in crystallographic structure (both Ni_3Al and Al_3Li, precipitate in the simple cubic $L1_2$ structure in epitaxy with the surrounding fcc matrix) and in morphology as well, with finely dispersed spherical or cuboidal of a few nm to a few hundred nm, depending on heat-treatment.

As mentioned in the main text (§ 5, above), the main origins of all strengthening mechanisms due to the presence of particles or precipitates can be summarized as follows:

References: p. 2204.

- *modulus-hardening*, resulting from differences in elastic constants between matrix and precipitates;
- *chemical hardening*, arising from compositional differences;
- *stacking-fault hardening*, when partial dislocations become the most mobile defects in the alloy;
- *atomic-order hardening*, which will appear if a perfect dislocation from the disordered matrix is pushed alone (i.e., unpaired) into the ordered crystalline structure of an A_3B precipitate, for instance, thus creating an antiphase boundary (APB); and
- *coherency-hardening*, which is the result of stresses induced in the matrix of parameter a_M by a precipitate growing in epitaxy with the matrix, but having a different lattice parameter a_P, resulting in a misfit usually characterized by a parameter $\delta = 2(a_P - a_M)/(a_P + a_M)$. Incoherent particles may also induce similar stress fields when temperature changes take place if their thermal expansion coefficient differs from that of the surrounding matrix.

A comprehensive review of the various theoretical models which have attempted to evaluate quantitatively the contribution of each of these mechanisms to the strengthening of idealized alloys has been published recently by REPPICH [1993] (see *Further reading*, at end). One further consideration which appears as a necessary concept when trying to describe the hardening landscape felt by a dislocation which moves inside a matrix hardened by a second phase, is the distribution and the effective size of the hardening phase. This can be alternatively described by

- a regular square array of point-like obstacles — the simplest model and also the one most remote from reality;
- a random array of monodisperse particles in an isotropic medium, as described by the models of FLEISCHER and HIBBARD [1963] and FRIEDEL [1964]. The motion of a dislocation in such a distribution of point-like obstacles has been computer-simulated by FOREMAN and MAKIN [1966] (§ 3.2.1, in the main text);
- a random distribution of particles having a finite effective size Y, a maximum interaction force with a dislocation F_M, and separated from each other by an average distance L. SCHWARZ and LABUSCH [1978] analysed the motion of a dislocation of line tension T_L in such an array of obstacles and showed that the previous theory of Friedel and Fleischer could only be applied if the "normalized obstacle depth", η_{SL}, describing the extent of the particle's interaction with the dislocation (the suffix "SL" denotes Schwarz–Labusch) is fairly small, i.e.,

$$\eta_{SL} = \frac{\gamma_{SL}}{\bar{L}} \left(\frac{F_m}{2T_L} \right)^{-1/2} \ll 1 \qquad \text{(A12)}$$

NEMBACH and NEITE [1985] examined the local situation of a straight edge dislocation approaching an isolated spherical γ' precipitate of diameter $20b$ intersecting its glide plane. The spatial localisation of the various interactions and their strength profiles are represented in fig. A10, where γ_{SL} is made explicit. Note that the elastic repulsion, F_e, resulting from the lattice misfit, if repulsive on the approaching side, appears attractive on the emerging side, thereby reminding us that quasi-coherent particles do not neces-

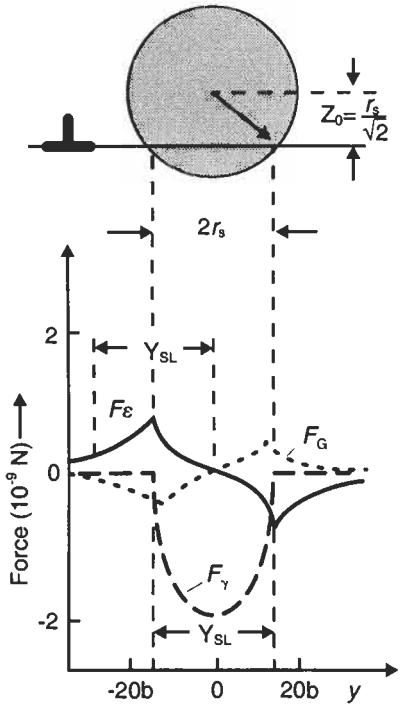

Fig. A10. Interaction–force profiles between a straight undissociated edge dislocation and a γ' particle of radius $r = 20b$ embedded in a fcc γ-matrix. The material is Nimonic PE 16, a nickel-based superalloy. (After NEMBACH and NEITE [1985].)

sarily repel dislocations. The dielastic interaction force, F_G, due to the differences in elastic moduli, also extends considerably beyond the actual precipitate periphery and peaks at the precipitate/matrix interface, just as F_ε does. The two forces tend to compensate each other in the case of γ' precipitates in the PE16 alloy examined by Nembach and Neite. Finally, the force F_γ represents the energy storage interaction necessary for the dislocation to generate an APB across the γ' precipitate as it traverses it. The APB is confined to the interior of the precipitate.

The macroscopic mechanical response of such a material at intermediate temperatures, in relation to its microstructure, has been examined in detail by REPPICH [1982] and by REPPICH *et al.* [1982].

When the resolved critical shear stress of the material is plotted as a function of particle diameter, the experimental data cannot be interpreted in terms of the schematic model of Gleiter and Hornbogen based on parabolic hardening by pair-cutting for small radii followed by a decrease of hyperbolic form resulting from Orowan looping as precipitates are overaged (see § 6.2, in main text). The stress level associated with peak-hardening is lower than that predicted by the simple theory and the stress decrement after the peak has a different shape. Thin-foil TEM examinations of various alloys revealed

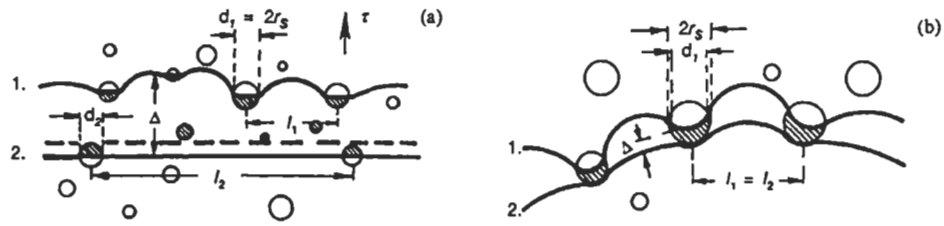

Fig. A11. A pair of dislocations shearing coherent ordered particles. Schematic illustration of the modelled dislocation configuration in the case of (a) weak pair-coupling, and (b) strong pair-coupling.

that an intermediary mechanism is then operating. As shown earlier (fig. 40, above) the first dislocation of the pair bypasses the precipitates by bowing around and leaving behind a loop, which can then be removed by the second dislocation of the pair following behind. Finally, two different situations arise that have been schematically represented by REPPICH [1993] (see *Further reading*): *weak-pair coupling* for small precipitate sizes causes increased hardening as particle size and volume fraction increase (fig. A11a), while *strong-pair coupling* is associated with a weakening mechanical resistance as precipitate sizes become larger (fig. A11b) until the Orowan process for isolated perfect dislocations takes over. The same general strengthening scheme is observed in alloys with different composition and larger γ' volume fractions, such as Nimonic 105. In highly strengthened single crystals with a γ' volume fraction around 65%, a strong coupling of the matrix dislocations is observed (fig. A12) when elevated strain rates are imposed on the material. The high value of the APB energy (125–240 mJ/m^2) and the large precipitate size (0.2–0.4 μm) compared with the relatively narrow matrix "corridors" (10–40 nm) are compelling conditions for the dislocation pair to move in a constricted configuration.

A5.1. Single crystals hardened by a shearable phase

A different approach to understanding plasticity in nickel-base superalloys involves taking into account the fact that they are constituted by two different but epitaxially related phases: the deformation mode of each phase can be examined separately and this should shed some light on the mechanical behavior of the two-phase material. Single crystals of each phase, γ and γ' of various compositions were grown and stressed along various crystal directions: [001], which favors multiple slip on close-packed {111} planes (octahedral glide); [111], which favors multiple slip on {100} planes (cube glide); [110] and [123], and other directions of low symmetry, which favor single glide (which can facilitate the direct observation by TEM of elementary mechanisms).

As mentioned earlier (fig. 38, above), the temperature dependence of the flow stress of $L1_2$ (Ni, Cr, Al) alloys exhibits anomalous peaks at intermediate temperatures (650–850°C) which are clearly related to the behavior of the pure γ' phase itself: the flow stress profiles of the two-phase alloys progressively resemble more closely that of the pure γ' phase as the volume fraction of γ' (Ni_3Al) in the alloy is augmented.

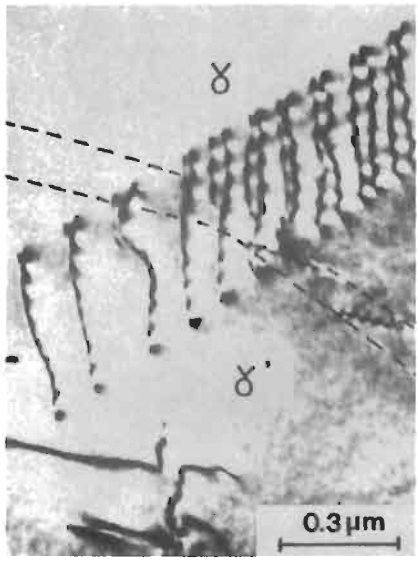

Fig. A12. Head of a pileup of screw dislocations, moving on a (111) plane in CMSX2 superalloy. This alloy, deformed by impact at room temperature, contains coalesced γ' precipitates. The matrix $1/2\langle 011\rangle$ dislocations react at the interface with $\langle 011\rangle$ dislocations of the γ' phase. The matrix dislocations become paired at the γ/γ' interface, indicated by dashed lines. (After BONNET and ATI [1989].)

A5.1.1. Plasticity of the γ' phase

The plasticity of the γ' phase is characterized by:

- an anomalous increase in the flow stress and of the strain-hardening rate as the temperature is raised — the *flow stress anomaly*;
- a tension-compression asymmetry;
- a breakdown of Schmid's Law.

These unusual features have been firmly established by many mechanical tests on oriented single crystals carried out at various temperatures. The flow stress anomaly was first reported by Westbrook in 1957 and the tension-compression asymmetry was first examined in detail by EZZ *et al.* [1982]. The nature and interpretation of these phenomena form the principal subject-matter of chapter 24 (§§ 3 and 4).

In order to offer an interpretation not only for the flow-stress anomaly but also for the tension-compression asymmetry, PAIDAR *et al.* [1984] proposed a model, now widely accepted, based on the assumption that the activation enthalpy for cross-slip of screw $a/2\langle 110\rangle$ dislocations from the octahedral to the cube plane is principally controlled by the following phenomena:

- the anisotropy of the APB energy, which is lower on the cube plane than on the octahedral plane in all known intermetallics based on Ni_3Al;
- the resolved shear stress on the cube plane;
- the difference in energy of the superpartial pair of dislocations associated with a stress-induced constriction or widening of the superpartial before a jump, and an equilibrium splitting afterwards;

References: p. 2204.

- the nature of the dislocation core splitting before and after a cross-slip event. Chapter 24 should be consulted for further details.

A recent investigation of polycrystalline Ni_3Al by RONG *et al.* [1995] showed:

- an inverse temperature dependence of the *creep resistance*, as evidenced in fig. A13a where the alloy creep rate is smaller at 580°C than at 380°C under the same applied stress. This is the creep aspect of the flow stress anomaly;
- logarithmic creep at high temperature under a low stress (580°C/250 MPa) characterizing a progressive exhaustion of the mobile defects in the material (fig. A13b). However, under higher stresses (400 MPa) the exhaustion mechanism does not entirely control the plasticity, and the creep rate is seen to increase again (fig. A13b), a phenomenon called *inverse creep* by HEMKER *et al.* [1991] who first observed it by deforming Ni_3Al (Hf, Ta) single crystals. It is attributed to the development of a large number of elementary kinks and macroscopic kinks which accumulate along the long screw dislocations and gather together during the first stage of creep.

This interpretation rests on the convincing "post-mortem" TEM micrographs (fig. A13c) which show a large majority of orthogonal dislocations lying alternatively either in the pure screw orientation, immobilized by Kear–Wilsdorf locks (see ch. 24), or in the pure edge orientation, either forming microkinks or slowly moving by climb if they have undergone a climb dissociation.

A5.1.2. Plasticity of the γ matrix

The γ matrix of modern nickel-base superalloys is a chemically complex solid solution basically of nickel and chromium with varying amounts of solid-solution-hardening elements such as aluminum, titanium, tantalum and niobium. For a given alloy, the matrix composition varies with the service temperature.

Aware of the fact that the mechanical behavior of concentrated nickel-chromium alloys (Cr concentration > 10wt%) does not fit any of the dislocation models for solid-solution hardening (FLEISCHER [1961], LABUSCH [1970]) or thermally activated mechanisms such as dislocation intersection or cross-slip, CLÉMENT *et al.* [1984] investigated the possible presence of short-range order and its role in phenomena such as strain bursts (on the microscopic level) and strain localization. Their work combined conventional straining tests and *in-situ* TEM straining experiments between room temperature and 300°C, with concentrated binary Ni–Cr alloys (with 20 and 30 wt.% Cr). More recently, a similar investigation in a wider temperature range was carried out in the same laboratory (BENYOUCEF *et al.* [1995]) with more complex alloy compositions simulating the γ matrix of CMSX2 or AM1 alloys. The main conclusions were:

- the critical resolved shear stress in the close-packed planes is higher than usually expected (52 MPa at 850°C instead of 20 MPa);
- at room temperature and up to ≈ 500°C, dislocation pileups containing up to ≈ 100 dislocations propagate in planar groups (fig. A14) headed by 4–6 dislocations coupled in pairs, thus revealing the presence of short-range order which is locally destroyed behind them;
- the average size of the short-range order domains can be estimated at ≈ 2–4 nm and confirms the direct observations made on the same γ matrix composition by DUVAL *et al.* [1994] with a tomographic atom probe.

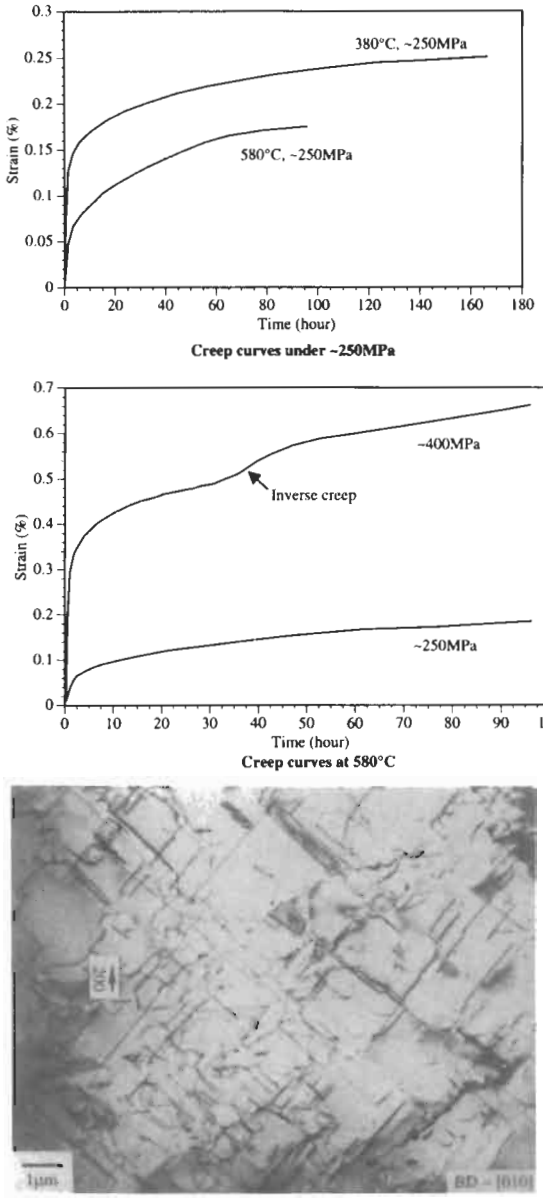

Fig. A13. Creep of polycrystalline Ni_3Al: (a) Creep curves at 380°C and 580°C under the same stress, 250 MPa. Anomalous dependence of creep resistance is exhibited. There is no inverse creep at either temperature. (b) Creep curves at 580°C at two stresses, ≈ 250 and 400 MPa. (c) TEM micrograph of a specimen crept at 580°C and ≈ 400 MPa for 196 hours, showing ⟨110⟩{001} slip. The dislocations consist of nearly pure edge and screw segments. (After RONG *et al.* [1995].)

References: p. 2204.

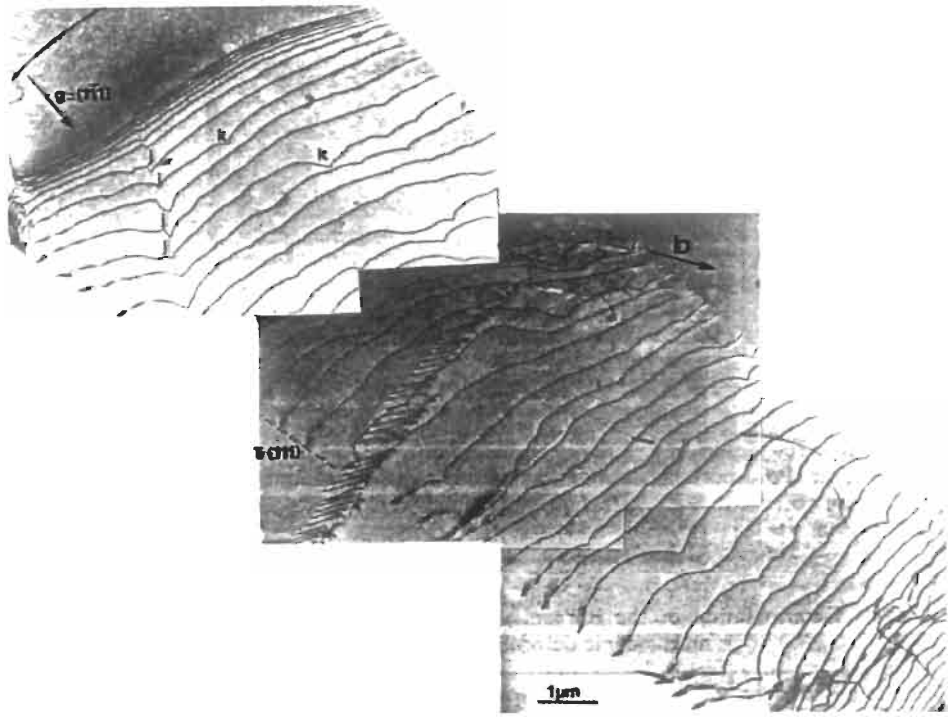

Fig. A14. A pileup of ≈ 50 near-edge dislocations in an oriented nickel-base superalloy single crystal. Three pairs of dislocations can be seen at the front of the pileup (top). (After BENYOUCEF *et al.* [1995].)

A5.1.3. Plasticity of oriented nickel-base single crystals at intermediate temperatures

Since nickel-base superalloys are used in a large temperature domain extending from 400°C in polycrystalline turbine discs to 1150°C in single-crystal turbine blades, the temperature range from 400°C to 700°C, corresponding to the ascending side of the flow stress anomaly, is usually referred to as the *domain of intermediate temperatures*.

In that domain, service conditions impose upon the material fairly high stresses in the range 800–1000 MPa, i.e., of the order of the 0.2% proof stress or engineering yield strength. Hence, from the standpoint of engineering practice as well as from the scientific standpoint, it appears quite relevant to examine the instantaneous plastic behavior and the viscoplastic flow of these materials in relation to the precipitates and dislocation microstructures created by the deformation.

The stress–strain curves for crystal orientations (fig. A15) corresponding to the three corners of the standard stereographic triangle clearly reveal the mechanical anisotropy of the material, with [001] as the strongest orientation and [011] as the weakest. While the yield strength is of the order of 1000 MPa, the rupture strength in creep is only 100–150 MPa at 650°C and a marked tendency to strain-softening is already detectable at 750°C. Maps depicting the mechanical "worth" of oriented crystals of superalloys have been drawn in the standard triangle (fig. A16) for various alloy compositions and several temperatures.

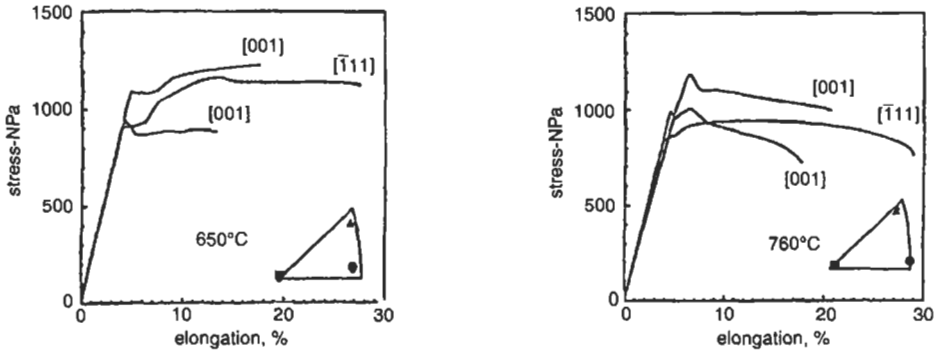

Fig. A15. Stress-strain curves for CMSX2 alloy. (After CARON and KHAN [1987].)

When one turns to micromechanisms of plasticity, the first stages seem to be characterized by the motion of perfect dislocations in the narrow γ matrix channels for strain rates above 10^{-4}/s. These dislocations find their origin in the numerous subgrain boundaries present in single crystals and also in the grain boundaries of polycrystals. The leading segments lie in pure screw orientation and bow out between the γ' cuboids, but instead of following a straight line along a $\langle 110 \rangle$ direction, they tend to cross-slip repeatedly as they reach the edges of the γ' cuboids (fig. A17) and are thus channeled into a general $\langle 100 \rangle$ direction (AYRAULT *et al.* [1987a]). Similar observations have been reported after laser shock-loading experiments carried out at room temperature on AM1 single crystals (AYRAULT *et al.* [1987b]), i.e., at strain rates in the neighborhood of 10^6/s and dislocation velocities approaching the speed of sound. Similar configurations have also been observed by POLLOCK and ARGON [1992] during the incubation period preceding creep at 850°C under 450 MPa in CMSX3 (fig. A18).

Dislocation pairs in the γ matrix are made up of two similar, perfect dislocations ($b_p = a/2\langle 110 \rangle$) which repel each other, but they are forced together inside the ordered γ' phase by the APB energy in order to form superdislocations, $b_{SD} = a\langle 110 \rangle$, which seem

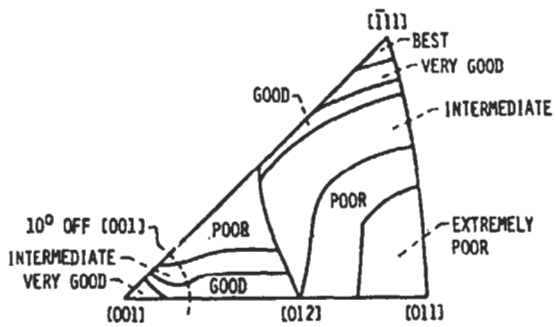

Fig. A16. Suggested regimes of stress-rupture lives for MAR-M247 and MAR-M200 single crystals at about 760°C. (After MACKAY and MAIER [1982].)

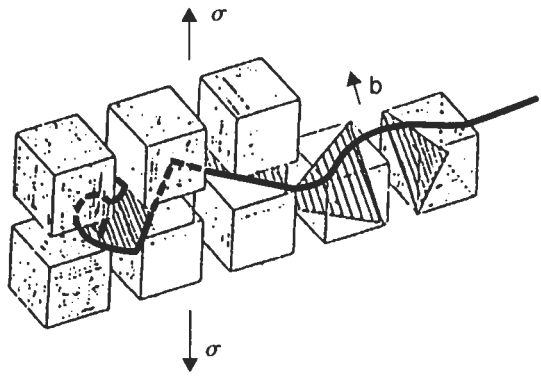

Fig. A17. Repeated cross-slip of perfect screw dislocations moving in matrix corridors along ⟨100⟩ directions. (After AYRAULT *et al.* [1987b].)

to be barely dissociated. In polycrystalline materials containing large primary γ' precipitates, the matrix dislocations must pair up and recombine at the γ/γ' interfaces in order to penetrate the γ' cuboids.

Another simple and "clever" way the perfect matrix dislocations have found to penetrate the γ' precipitates is to transform into super-Shockley partials, according to the scheme:

$$\begin{aligned} &\mathrm{BA} + \delta\mathrm{C} \rightarrow 2\mathrm{B}\delta \\ &\tfrac{1}{2}[1\bar{1}0] + \tfrac{1}{6}[11\bar{2}] \rightarrow \tfrac{1}{3}[2\bar{1}\bar{1}] \end{aligned} \qquad \text{(A13)}$$

as first proposed by GUIMIER [1972] who observed it after straining Waspaloy by 2% at ≈ 700°C, and also by CONDAT and DECAMPS [1987] in AM1 at 760°C. As the perfect dislocation BA (fig. A19) penetrates the edge of the γ' precipitate, a Shockley partial

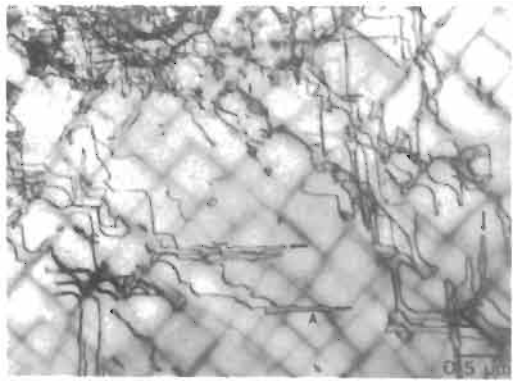

Fig. A18. Long, narrow dislocation loops spreading through the matrix of a superalloy during the incubation period. These dislocations originated from the network in the upper left corner. (After POLLOCK and ARGON [1992].)

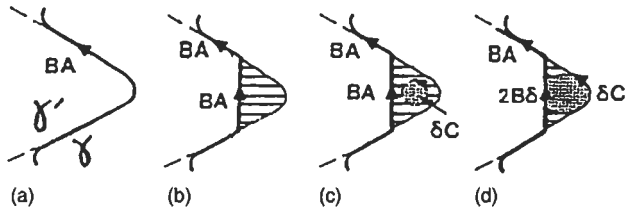

Fig. A19. First stage of γ' shearing. (After CARON *et al.* [1989].)

dislocation δC is nucleated. It sweeps out the small antiphase boundary surface that may have been created inside the ordered precipitate by the intruding partial (fig. A19c) and replaces it by a much less energetic superlattice intrinsic stacking-fault surface and stops at the γ/γ' interface where no further driving force for its motion remains (fig. A19d). As CARON *et al.* [1989] pointed out, this mechanism is frequently observed in CMSX2 at 760°C at the beginning of the straining process, when perfect dislocations have propagated and multiplied extensively in the γ matrix channels and must now intrude into the elastically sheared γ' cuboids as these begin to experience plastic deformation.

As plastic deformation proceeds, the "landscape" of defects, involving perfect dislocations, superdislocations, stacking-fault ribbons and their bounding Shockley partials or super-partials becomes very dense and difficult to analyse in detail. But no matter how complex the population of defects and their mutual interaction may be, they seem to provide these alloys with a harmonious diversity of means to respond adequately to the most demanding mechanical and thermal requirements ever imposed on a load-bearing material. Similar levels of performance and ductility are not yet approached by single-phase intermetallic compounds which present other attractive properties.

A5.1.4. Rafting phenomena at high temperature

The microstructure of γ' cuboids imperfectly aligned along the three cube directions (fig. A20) can be idealized by a three-dimensional periodic distribution of regular cubes of equal size. When a rather small tensile stress is applied to a single crystal of AM1 along the [001] axis taken as vertical, at temperatures ranging from 800°C (at 600 MPa) to 1150°C (at $\approx$ 100 MPa) the γ' cuboids seem to coalesce into horizontal rafters oriented perpendicular to the applied tensile stress. The matrix is rapidly expelled from the vertical corridors (FREDHOLM and STRUDEL [1984]). Already after 1 h at 120–140 MPa at 1050°C, many vertical matrix partitions have already disappeared (see insert to fig. A21); later (main picture) all have disappeared. Loading in a purely elastic domain however does not result in rafting, as evidenced in fig. A20. The type of rafting seen in fig. A21 is often referred to a *type N* since the rafts are *normal* to the applied stress and the γ/γ' misfit parameter, as in most modern superalloys for turbine blades, is *negative*. The most obvious physical parameters responsible for this phenomenon can be listed as:

- direction and sense of the applied stress: orientation of these with respect to the crystallographic directions of the crystal;
- sign and amplitude of the γ/γ' misfit parameter $\delta = 2\{(a_{\gamma'} - a_\gamma)/(a_{\gamma'} + a_\gamma)\}$;
- the differences in elastic moduli between the two phases, characterized by E_p/E_m

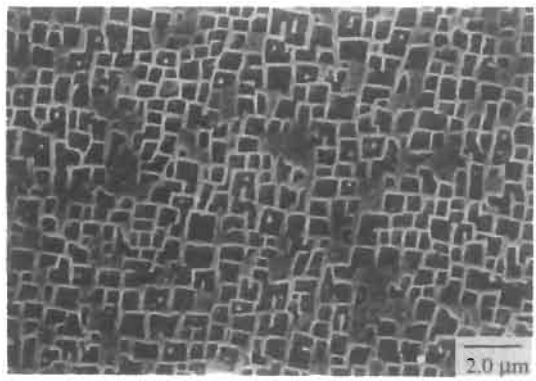

Fig. A20. γ' cuboids in a superalloy after elastic loading under 95 MPa at 850–950°C. The microstructure has not been altered by this loading. (After POLLOCK and ARGON [1994].)

smaller or larger than unity, or by $m = E_p - E_m$ positive or negative.

The kinetics of the phenomenon depend on the temperature and on the chemical composition of the phases.

The phenomenon of *rafting* has attracted much attention during the past 10 years. As long as twenty years ago, PINEAU [1976], using a two-dimensional, purely elastic model based on Eshelby's treatment of an isolated misfitting inclusion in a continuous isotropic matrix, had predicted several possible precipitate configurations (plates, needles or spheres). Much more recently, NABARRO [1995], using Eshelby's energy/momentum tensor to provide an analytical expression for the driving force for rafting, extended the model to a three-dimensional array of regular γ' cubes separated by thin sheets of γ matrix.

From computer simulation, using a finite-elements method, of the micromechanical configuration of a γ' cuboid assembly with different elastic moduli inserted in a

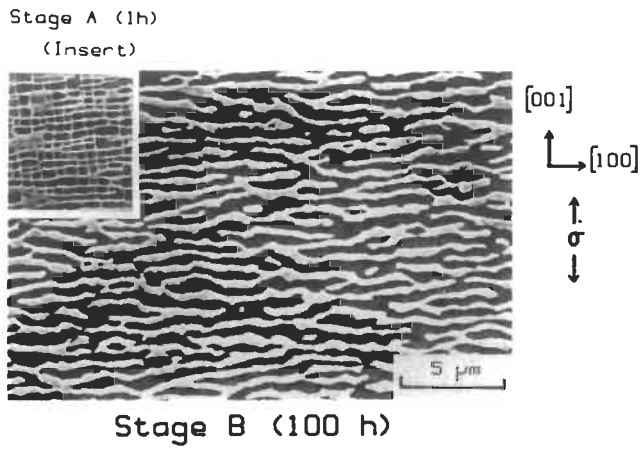

Fig. A21. Rafting in AM1 alloy after creep at 1050°C/140 MPa. (After FREDHOLM and STRUDEL [1984].)

misfitting manner into a γ matrix, it can be seen that the cuboids are only lightly stressed and that only near their edges, whereas the matrix corridors experience substantial levels of stress resulting from a misfit of $\approx -2 \times 10^{-3}$. The first models of this kind were purely elastic (FELLER–KNIEPMEIER *et al.* [1989]).

During high-temperature plasticity, the matrix dislocations originating from the numerous subgrain boundaries ingrown in the single crystals, explore the various γ channels where the effective stress is pushing them; when several systems have been activated they tend to form regular networks in the γ/γ' interfaces, as observed by FREDHOLM and STRUDEL [1984] and AYRAULT *et al.* [1989b] in AM1 and by POLLOCK and ARGON [1992] in CMSX3. The stresses are not sufficient to force the gliding dislocations to take shortcuts across the γ' phase, but climb and pipe diffusion are very intense and assist the dislocations in regaining mobility in the γ/γ' interfaces. For instance, in tension creep in AM1, four Burgers vectors are activated and the dislocations criss-cross the horizontal channels where they leave mixed dislocation dipoles which later rearrange themselves by climb into pure edge orientation, in an ideal situation to best compensate the γ/γ' misfit at the horizontal interfaces. In a rafted structure, the crystalline misfit is distorted by the topographic arrangement of the phases and by the presence of the dislocations in the γ/γ' interfaces. Hence its value, and even its sign, can vary not only with temperature but also the direction in which it is measured (fig. A22). Recently it has been measured *in situ,* both by high-resolution x-ray diffraction and by high-resolution neutron diffraction.

Much effort is still required to introduce dislocations and viscoplastic flow into theoretical models of rafting and to understand the influence of the rafted morphology on the mechanical properties of nickel-base superalloys, as for instance in the work of NATHAL *et al.* [1989].

A6. Recrystallization of ODS alloys

Owing to the Zener force (ch. 28, § 3.8) exerted by the fine particles on the pinned grain boundaries, recrystallization processes are very sluggish in most ODS alloys. They are also difficult to control industrially since they only take place at unusually high temperatures, 1300°C and above.

Fabricated usually by mechanical alloying techniques, the powder pellets are transformed into dense materials by hot extrusion at intermediate temperatures (900–1000°C) which result in ultrafine-grained microstructures (2–5 μm). A common practice is to stabilize the grain size by an isothermal treatment at high temperature which leads to the formation of markedly elongated grains in the direction of rolling or extrusion.

In an effort to elucidate the mechanism of recrystallization and the process parameters relevant to the microstructural evolution, BALOCH and BHADESHIA [1990] studied the directional recrystallization process which stimulates the highly anisotropic grains in alloy MA 6000. They confirm that the material undergoes continuous dynamic primary recrystallization during the transformation process and they consider that during zone-annealing across a temperature gradient, only secondary recrystallization phenomena are

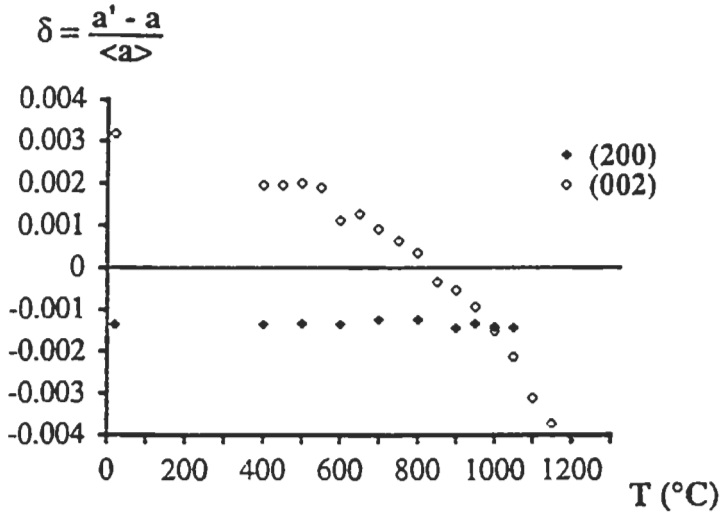

Fig. A22. Temperature dependence of the lattice mismatch measured in the [200] and [002] directions in a crept sample of the alloy AM1. The stress was parallel to [001]. (After ROYER *et al.* [1984].)

taking place. Directional recrystallization was found to occur only when the rate of passage through the thermal gradient remained compatible with the migration rates of the grain boundaries; otherwise, equiaxed grain microstructures are formed (see also KIM and HANADA [1994] and GODFREY and MARTIN [1995]).

More complex still is the case of ferritic-type ODS alloys such as MA 956 where the role of texture becomes predominant under certain circumstances. In a recent study of the role of various fabrication processes on the recrystallization behavior of this alloy, REGLE and ALAMO [1994] clearly identified the role of textures in the determination of the final grain size. When annealing in the temperature range 1300–1325°C, a population of large elongated grains is formed with a fiber-type [110] texture. Equiaxed recrystallization and fine grains only start appearing at higher temperatures when the mobilities of all grain boundaries become similar, as is strictly the case at about 1470°C. Between 1350°C and 1450°C, the presence of grain boundaries with low mobility, such as "special" or low-angle boundaries induced by the pronounced deformation texture, is responsible either for inhibition of grain growth or for the triggering of abnormal grain growth (secondary recrystallization) when only a few isolated general grain boundaries are able to move in an otherwise inhibited population, leading to the formation of large, elongated grains.

References for Addendum

ARZT, E., 1990, Res Mechanica **31**, 399.

ARZT, E., 1989, in: New Materials by Mechanical Alloying Techniques, eds. E. Arzt and L. Schultz (Deutsche Gesellschaft für Metallkunde, Oberursel), p. 185.

ARZT, E., and M. F. ASHBY, 1982, Scripta Metall. **34**, 1893.

ARZT, E., M. F. ASHBY and R. A. VERRALL, 1989, Acta Metall. **31**, 1977.
ARZT, E., and J. RÖSLER, 1988, Acta Metall. **36**, 1043.
ARZT, E., and D. S. WILKINSON, 1986, Acta Metall. **34**, 1893.
AYRAULT, D., R. FABBRO, J. FOURNIER and J. L. STRUDEL, 1987a, C.R. Acad, Sci. Paris 305, Serie 2, 353.
AYRAULT, D., A. FREDHOLM and J. L. STRUDEL, 1987b, Proc. Amer. Soc. Materials Europe Tech. Conf, ed. T. Khan and A. Lasalmonie, (ASM International, Ohio), p. 71.
BALOCH, M. M., and H. K. D. H. BHADESHIA, 1990, Mat. Sci. and Techn. **6**, 1236.
BANHARDT, V., M. NADER and E. ARZT, 1995, Metall. Trans. **26A**, 1067.
BLUM, W., and B. REPPICH, 1985, in: Progress in Creep and Fracture, eds. B. Wilshire and R.W. Evans (Pineridge Press, Swansea), vol. 3, p. 83.
BENJAMIN, J. S., 1976, Sci. Amer. **234** (May), 40.
BENJAMIN, J. S., 1989, in: New Materials by Mechanical Alloying Techniques, eds. E. Arzt and L. Schultz (Deutsche Gesellschaft für Metallkunde, Oberursel), p. 3.
BENYOUCEF, M., B. DECAMPS, A. COUJOU and N. CLÉMENT, 1995, Phil. Mag. **A71**, 907.
BONNET, R., and ATI, A., 1989, Acta Metall. **37**, 2153.
BROWN, L. M. and HAM, R. K., 1971, in: Strengthening Methods in Crystals, eds. A. Kelly and R.B. Nicholson (Elsevier, New York), p. 9.
CARON, P., and KHAN, T., 1987, Symposium on Advanced Materials and Processing Techniques for Structural Applications, Paris, eds. T. Khan and A. Lasalmonie (ONERA, Chantillon, France).
CARON, P., KHAN, T. and VEYSSIÈRE, P., 1989, Phil. Mag. **A60**, 267.
CLÉMENT, N., D. CAILLARD and J. L. MARTIN, 1984, Acta Metall. **32**, 961.
CONDAT, M., and B. DECAMPS, 1987, Scripta Metall. **21**, 7.
CONRAD, H., 1964, J. Metals **16**, 582.
DUPEUX, M., J. HENRIET and M. IGNAT, 1987, Acta Metall. **35**, 2203.
DUVAL, S., S. CHAMBRELAND, P. CARON and D. BLAVETTE, 1994, Acta Metall. Mater. **42**, 185.
EVANS, R. W., J. A. PRESTON, B. WILSHIRE and E. A. LITTLE, 1993, Mat. Sci. & Eng. **A167**, 65.
EZZ, S., D. P. POPE and V. PAIDAR, 1982, Acta Metall. **30**, 921.
FELLER–KNIEPMEIER, M., and T. LINK, 1989, Metall. Trans. **20A**, 1233.
FLEISCHER, R. L., 1961, Acta Metall. **9**, 996.
FLEISCHER, R. L., and W. R. HIBBARD, 1963, in: Symposium on the Relation between the Structure and Mechanical Properties of Metals, Nat. Phys. Lab., (London, H.M. Stationery Office) p. 261.
FOREMAN, A. J. E. and H. J. MAKIN, 1966, Phil. Mag. **14**, 911.
FREDHOLM, A., and J. L. STRUDEL, 1984, in: Superalloys 1984, The Met. Soc. of AIME, Philadelphia, p. 211.
FRIEDEL, J., 1964, Dislocations (Pergamon Press, Oxford).
GLATZEL, U. and M. FELLER–KNIEPMEIER, 1989a, Scripta Metall. **23**, 1839.
GLATZEL, U. and M. FELLER–KNIEPMEIER, 1989b, Proc. EUROMAT '89, eds. D. Driver and H. Mughrabi, (DGM Informationsgesellschaft, Oberursel) p. 475.
GODFREY, A. W., and J. W. MARTIN, 1995, Phil. Mag. **A72**, 737.
GOTO, S., and M. MCLEAN, 1991, Acta Metall. et Mater. **39**, 153, 165.
GUIMIER, A., 1972, Doctoral Thesis, University of Nancy, France, p. 34.
HEMKER, K. J., M. J. MILLS and W,D. NIX, 1991, Acta Metall. et Mater. **39**, 1909.
HERVÉ, E. and A. ZAOUI, 1990, Eur. J. Mech. of Solids **9**, 505.
HERVÉ, E. and A. ZAOUI, 1993, Internat. J. Engn. Sci. **31**, 1.
KIM, S. S., and S. HANADA, 1994, Mat Sci. & Eng. **A184**, 45.
LABUSCH, R., 1970, Phys. Stat. Sol. **41**, 659.
LAGNEBORG, R., 1972, Internat. Metall. Rev. **17**, 130.
LEE, B. J. and M. E. MEAR, 1992, Mechanics of Materials **13**, 313, 336.
LUND, R. W. and W. D. NIX, 1976, Acta Metall. **24**, 469.
MACKAY, R. A., and R. D. MAIER, 1982, Metall. Trans. **13A**, 1747.
NABARRO, F. R. N., 1995, Acta Metall. et Mater. **43**, in press.
NATHAL, H. V., R. A. MCKAY and R. V. MINER, 1989, Metall. Trans. **20A**, 133.
NEMBACH, E., and G. NEITE, 1985, in: *Progress in Materials Science*, Vol. 29, p. 177.
ORLOVÁ, A., and J. ČADEK, 1992, Acta Metall. et Mater. **40**,. 1865.
PAIDAR, V., D. P. POPE and V. VITEK, 1984, Acta Metall. **32**, 435.
PINEAU, A., 1976, Acta Metall. **24**, 559.
POLLOCK, T. M., and A. S. ARGON, 1992, Acta Metall. et Mater. **40**, 1.

POLLOCK, T. M., and A. S. ARGON, 1994, Acta Metall. et Mater. **42**, 1859.
PROVENDIER–AUBOURG, V., and J. L. STRUDEL, 1995, Phys. Stat. Sol. (a), **149**, 355.
RAVICHANDRAN, K. S., 1994, Acta Metall. et Mater. **42**, 1113.
REGLE, H., and A. ALAMO, 1995, Proc. Powder Met. World Congress (PM '94) (Les Editions de Physique, Paris).
REPPICH, B., 1982, Acta Metall. **30**, 87.
REPPICH, B., P. SCHEPP and G. WEHNER, 1982, Acta Metall. **30**, 95.
REPPICH, B., W. LISTL and T. MEYER, 1986, in: Proc. Conf. High Temperature Alloys for Gas Turbines and Other Applications, eds. Betz *et al.* (Reidel, Dordrecht), p. 1023.
REPPICH, B., F. BRUNGS, G. HÜMMER and H. SCHMIDT, 1990, in: Proc. 4th Int. Conf. Creep and Fracture of English Mater. and Structures, eds. B. Wilshire and R. W. Evans (Inst. of Metals, London), p. 141.
RONG, T. S., I. P. JONES and R. E. SMALLMAN, 1995, Acta Metall. et Mater. **43**, 1385.
RÖSLER, J. and E. ARZT, 1988, Acta Metall. **36**, 1053.
ROYER, A., P. BASTIE, D. BELLET and J. L. STRUDEL, 1995, Phil. Mag. **A72**, 669.
SAINT–ANTONIN, F., and J. L. STRUDEL, 1990, in: Creep and Fracture of Engineering Materials (The Institute of Metals, London), p. 303.
SCHRÖDER, J. H. and E. ARZT, 1985, Scripta Metall. **19**, 1129.
SCHWARZ, R. B. and R. LABUSCH, 1978, J. Appl. Phys. **49**, 5174.
SINGER, R. F. and E. ARZT, 1986, in: High-Temperature Alloys for Gas Turbines and Other Applications, eds. W. Betz et al. (Reidel, Dordrecht), vol. 1, p. 97.
SOCRATE, S. and D. M. PARKS, 1993, Acta Metall. et Mater. **41**, 2185.
SPÄTIG, P., J. BONNEVILLE and J. L. MARTIN, 1993, Mat. Sci. & Eng. **A167**, 73.
SPÄTIG, P., J. BONNEVILLE and J. L. MARTIN, 1995, Mat. Res. Soc. Symp. Proc. **364**, 713.
SROLOVITZ, D. J., M. P. ANDERSON, G. S. GREST and P. S. SAHNI, 1984, Acta Metall. **32**, 1429.
STEVENS, R. A., and P. E. FLEWITT, 1981, Acta Metall. **29**, 867.
SUZUKI, T., S. TAKEUCHI and H. YOSHINAGA, 1991, in: Dislocation Dynamics and Plasticity. Springer Series in Materials Science, vol. 12, p.131.
TANDONG, G. P. and G. J. WENG, 1988, J. Appl. Mech. **55**, 126.
VASSEUR, E. and L. REMY, 1994, Mat. Sci. & Eng. **A184**, 1.
VEYSSIÈRE, P. and G. SAADA, 1995, Microscopy and Plasticity of the $L1_2$ γ' Phase, in: Dislocations in Solids, vol. 10, ed. F. R. N. Nabarro and M. S. Duesberg (North-Holland, Amsterdam), in press.
WENG, G. J., 1990, J. Mech. Phys. Solids **38**, 419.

Further reading

Ardell, A. J., 1995, "Intermetallics as precipitates and dispensoids in high-strength alloys," in: Intermetallic Compounds: Principles and Practice, ed. J. H. Westbrook and R. L. Fleischer (Wiley, Chichester), Vol. 2, p. 257.
Arzt, E. and L. Schultz, 1989, "New Materials by Mechanical Alloying Techniques" (Deutsche Gesellschaft für Metallkunde, Oberursel).
Bressers, J., 1981, "Creep and Fatigue of High Temperature Alloys" (Applied Science Publishers, London).
Cadek, J., 1988, "Creep in Metallic Materials", Elsevier Materials Science Monographs, vol. 48. (Elsevier, Amsterdam).
Castaing, J., J.L. Strudel and A. Zaoui, 1988, "Mechanisms and Mechanics of Plasticity", Revue de Physique Appliquée, April.
Evans, R. W. and B. Wilshire, 1985, "Creep of Metals and Alloys" (The Institute of Metals, London).
Gerold, V., 1981, "Precipitation Hardening" in: vol 4, chap. 5 of "Dislocations in Solids", ed. by F.R.N. Nabarro (North-Holland, Amsterdam).
Mura, T., 1987 "Micromechanics of Defects in Solids", 2nd edition (Martinus-Nijhoff, Boston).
Reppich, B., "Particle strengthening", 1993, in: "Plastic Deformation and Fracture of Materials", ed. H. Mughrabi, vol. 6 of "Materials Science and Technology", ed. R.W. Cahn, P. Haasen and E.J. Kramer (VCH, Weinheim).
Schöck G., 1980, "Thermodynamics and Thermal Activation of Dislocations", in: vol. 3, chap. 10 of "Dislocations in Solids", ed. F. R. N. Nabarro (North-Holland, Amsterdam).
Sims, C. T., W. C. Hagel and N. S. Stoloff, 1987, Superalloys II (Wiley, New York).
Suzuki T., S. Takeuchi and H. Yoshinaga 1991, "Dislocation Dynamics and Plasticity", 1991, Springer Series in Materials Science, vol. 12 (Springer, Heidelberg).

CHAPTER 26

FRACTURE

R. M. THOMSON

Materials Science and Engineering Laboratory
National Institute for Standards and Technology
Gaithersburg, MD 20899, USA

R. W. Cahn and P. Haasen†, eds.
Physical Metallurgy; fourth, revised and enhanced edition

1. Introduction and fracture overview

In this chapter, a fundamental approach to fracture will be followed in order to develop a few central ideas about why any given material is ductile or brittle, and how the basic lattice defects of the material cooperate to give rise to these two general classes of behavior. The analytical discussion will tend to focus on relatively brittle phenomena, partly because any idealization of fracture-leads one first to the consideration of *brittle fracture*, and partly because the analysis for brittle fracture is better understood, and therefore more accessible. Nevertheless, the more ductile aspects of fracture, though more difficult to analyze quantitatively, will be kept in view throughout, because of the inherently ductile tendencies of most metals.

There are two extreme poles of material failure under stress. In the first, fig. 1, the material *necks down* under tension like taffy (single crystals of pure copper are an example) in a continuous plastic manner, until the last atoms in the narrowing neck come apart and the material splits into two pieces. This type of failure is usually termed *ductile rupture*. In the other case (fig. 2), the material suddenly and catastrophically fractures with no discernible plastic flow either preceding or during the failure event. Examples of the latter are glass and silicon at low temperature. These two poles are useful to keep in mind, because they illustrate how two crystal or lattice defects — dislocations and atomically sharp cleavage cracks — are responsible, ultimately, for the mechanical failure of crystalline materials. In the first instance, only dislocations are involved, while in the second only a sharp crack participates in the failure event. Materials scientists are not accustomed to thinking of brittle cracks (fig. 3) as one of the fundamental crystal defects which have proven so useful as constructs for understanding the structure-sensitive material properties. However, in this chapter, we will put such cracks on the same conceptual footing as dislocations because, like dislocations, they answer one of the two most fundamental questions in the mechanical behavior of materials. Dislocations were postulated to explain why the yield strength of a solid can be much lower than the theoretical shear strength of the atomic bonds of the solid. Likewise, cracks provide the answer to why fracture occurs in materials at average stress levels well below the theoretical tensile strength of the atomic bonds of the material. The reason is that a pre-

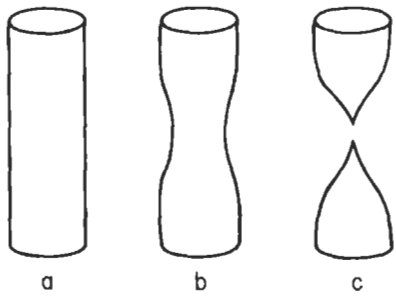

Fig. 1. A rod of ideally ductile material when pulled develops a region of plastic instability which finally thins uniformly down to a sharp point.

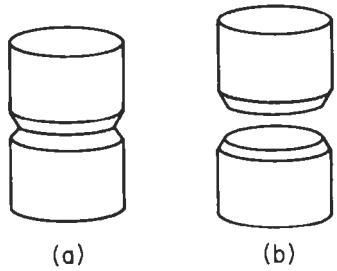

Fig. 2. An ideally brittle material when pulled separates suddenly by cleavage with no prior or simultaneous deformation. A notch is shown which localizes the plane of fracture.

existing crack in the material magnifies or concentrates the low applied stress to a value at the tip of the crack which may be many orders of magnitude higher. When this magnified stress at the tip reaches the maximum atomic bond strength, the crack will propagate through the solid and fracture it. From this chapter, we hope the reader will find that the otherwise very confusing subject of mechanical failure is best understood by viewing it as an interplay between, and sometimes a competition between dislocations and cracks.

The *stress concentration* referred to around a slit crack is shown in fig. 4 where the analogy of the magnetic lines of force around a similar slit in a magnet is striking. Physically, the crack must act as a stress concentrator, because every horizontal plane (line in two dimensions) in the figure must carry the total force imposed on the two external surfaces. Since the cut line representing the crack means there is less material on the cleavage plane defined by the cut to carry the applied force, the force per unit area (or stress) on this plane outside the crack must be higher. The stress is especially concentrated near the source of the "force transmission difficulty" at the crack tips, and

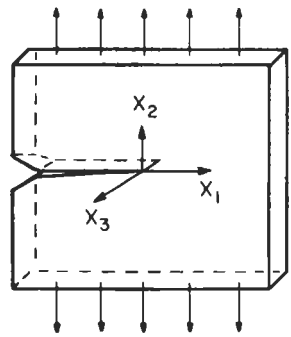

Fig. 3. A brittle crack in a material is viewed as a mathematical cut in the medium across which the atom bonds have been cut. For mathematical simplicity the crack line will be assumed to be straight and to lie along the x_3 axis. The cleavage plane is the negative x_3x_1 plane. External stresses are also exerted on the external surfaces of the material in an arbitrary manner in order to hold the crack open.

References: p. 2287.

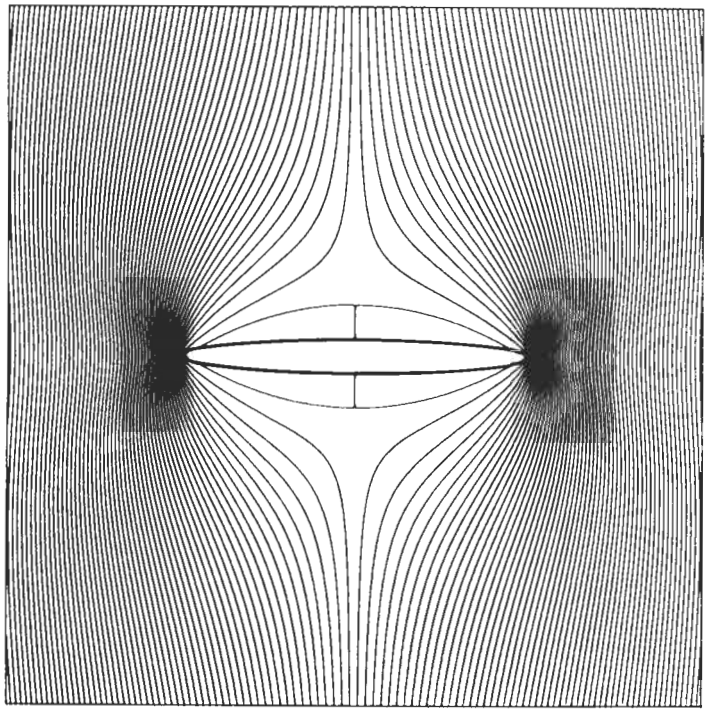

Fig. 4. Stresses are concentrated near the tip of a crack in a way suggestive of magnetic lines of force around a slit. In this diagram, the lines are computer-generated to simulate crack stress lines quantitatively (Courtesy Prof. P. NEUMANN.)

indeed we will show that for a mathematically sharp cut, the stresses become singular at a tip. If the tip is rounded, the maximum stress is finite, and if the tip has a radius of atomic size, the maximum average stress which can be sustained in the material is that which begins to break the bonds at the tip in a progressive fashion as alluded to above (fig. 5).

An interesting contrast between dislocations and cracks follows from the fact that, unlike a dislocation, a crack cannot exist in a material without the presence of "external" stresses. This is easily seen from fig. 5, where the atomic bonds across the cleavage plane will close up the slit unless a counteracting set of external forces is applied. This "external" stress may of course be supplied by misfitting grains, precipitates, etc. in the solid, as well as by actual external forces applied to the surface of the specimen.

Although the atomically sharp brittle crack will play the dominant conceptual role in this chapter, other kinds of cracks also exist in materials. In particular, we will find in the next section that in ductile materials, a sharp crack will open up under appropriate conditions into a wedge shape, with a finite opening angle at its tip. However, it is the sharp crack which possesses the well known dynamical properties of cleavage, while the

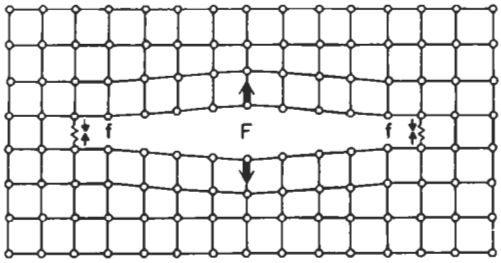

Fig. 5. Diagram of a crack in a two-dimensional square lattice with external forces exerted at the center of the crack. Bonds at the two crack tips are nonlinear. The nonlinear attractive forces at the tip are labeled f, and the external applied forces at the center of the crack are labeled F.

wedge-shaped crack and its derivatives are associated with a complex form of ductile failure. Thus, the sharp crack is the only one which we shall elevate to the status of fundamental crystal defect.

Cracks are formed in materials in a variety of ways by any mechanism which causes a sufficiently high stress, locally. Examples are high-density dislocation structures formed near surfaces during fatigue, stress concentrations in brittle particles due to the strain incompatibility at the interface between the particle and the deforming metal matrix, grain-boundary triple points, etc. In their early stages these cracks in many cases are sharp.

The materials scientist will find in studying this chapter that the problem of fracture deeply involves several other disciplines, and that this fact is both the cause of stimulation because of the breadth of ideas involved, and also daunting because these ideas often involve unfamiliar subjects. In particular, fracture has from the first involved continuum fracture mechanics on a deep level. The fundamental reason why the mechanics of the problem cannot be ignored is that a crack cannot exist in a material without an external stress, and the way in which this stress is transmitted to the crack tip is the subject of *continuum mechanics*. The necessity of the external force is related to the long-ranged $1/\sqrt{r}$ stress field surrounding the crack, which means that the crack is not a localized defect in the same sense as a vacancy or even a dislocation is. Fortunately, for long cracks, the atomic configuration around the tip depends only on a quantity termed the *stress intensity*, K, and not on other mechanical and geometric details, but the way the plastic zone interfaces to the immediate region around the crack tip is both a materials problem and a mechanics problem. Likewise, fracture deeply involves surface physics and chemistry, because the tip region of the crack is an incipient surface, and reactions at the tip with external environments involve ideas and processes which are brought over from those fields. The concept of *fracture mechanics* is defined in § 9.1.

Finally, the question of the structure of the crack tip, which determines such fundamental properties as whether dislocations can be emitted from it, or how it interacts with external chemical species, depends upon the kind of atomic bonding involved in the material. In spite of the large amount of work and substantial progress which has gone into understanding the metallic bond, we still are not in possession of bonding laws or

References: p. 2287.

"force laws" which are adequate for the fracture problem in some of the materials of most interest. Part of the problem is that we do not have adequate assurance that the empirical force laws which have been used so successfully in recent years are fully capable of describing the very highly distorted and restructured bonds which exist in the tip region. A second part of the problem is that bonding at metal/ceramic interfaces is only recently being seriously addressed. Finally, some of the metal systems in the middle of the transition series are not amenable to current EAM techniques. Thus, fracture is a subject which depends for its progress on the contributions from several adjacent fields, and the materials scientist cannot ignore these connections.

For other treatments of fracture on approximately the level observed here, the reader is referred to the books by BROEK [1985, 1989], THOMASON [1990], and LAWN [1993]. The older books by KNOTT [1973] and KELLY [1966], and the chapter by Smith on "Dislocations and Cracks" in the Nabarro series all still provide rewarding insights — especially the first, because it is not easy to find modern treatments at this level written from the materials point of view. For an excellent qualitative statement of the general status of fracture mechanics and its application in design and service, which is still current, see the 1979 Discussion of the Royal Society, FORD *et al.* [1981]. A very practical guide to the practicing metallurgist will be found in the book by CAMPBELL *et al.* [1982]. More advanced treatments will be found in the book by KANNINEN and POPELAR [1985], and in the older articles in volumes 1 and 2 of the "Fracture" series edited by LIEBOWITZ [1968]. Review volumes have been edited by DIENES and THOMSON [1987] and by LATANISION [1982] on fracture fundamentals and by KNAUSS and ROSAKIS [1990] on fracture mechanics. Dislocations will be found treated in HIRTH and LOTHE [1981].

2. *Qualitative and observational aspects of fracture*

Before digging into the quantitative discussions of later sections, a selection of fractographs and other material will be presented here to provide the reader with an observational basis for further discussion.

2.1. Fracture modes

We begin with a definition of terms which describe the macroscopic stress state of the fracture in terms of the three primary modes of fracture. A crack is defined by a two-step process. First, as in fig. 3, a cut is made in the medium, which becomes the *cleavage plane*, and then forces are exerted on the external surfaces of the specimen which define the particular fracture mode depicted in fig. 6. In *mode* I, the stress is a *tensile* stress with the principal stress axis normal to the cleavage plane. Mode I is the only mode leading to physical fracture, because unless the external stress physically separates the two surfaces on the cleavage plane, rewelding would occur even after the stress is applied. In *mode* II, the stress is a *shear* parallel to the cut in the x_1*-direction.* (We retain in future the coordinate system of fig. 3.) In *mode* III, the stress is a *shear* parallel to the cut in the *antiplane* or x_3-direction. Mode III is important because antiplane strain is associated with a particularly simple analysis. We shall thus make

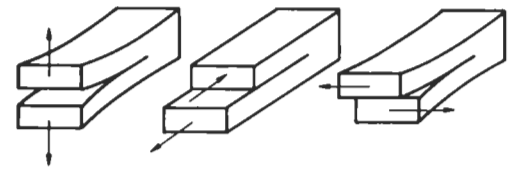

Fig. 6. The three prototype modes of fracture. In each case, the crack is formed by making a planar slit in the material, with the crack line along the edge of the cut. In mode I, the opening mode, the force is exerted normal to the cleavage plane. In mode II, the force is in the plane of the crack normal to the crack line. In mode III, or antiplane strain, the force is in the plane along the crack line. Modes II and III are shear cracks.

extensive use of this analysis to describe results for cracks in a generic sense. Of course, most actual cracks are not pure cases; the fracture surfaces are not flat, and the crack fronts are not straight. Thus, a crack may be produced which is primarily mode II or III, but with enough mode I present to separate the cleavage plane. Needless to say, curved cracks possessing nonplanar fracture surfaces are much more difficult and often impossible to handle mathematically, at least analytically, so that the pure modes listed above will be featured almost exclusively in this discussion.

2.2. Fractographic observations

A desirable steel exhibits high *toughness*, which means that it requires a large energy to pull it apart in fracture. Such a steel has a fracture surface which exhibits a non-crystallographic "fibrous" quality on a microscopic scale as shown in fig. 7 The surface is composed of microdimples, which are the result of holes forming ahead of the main

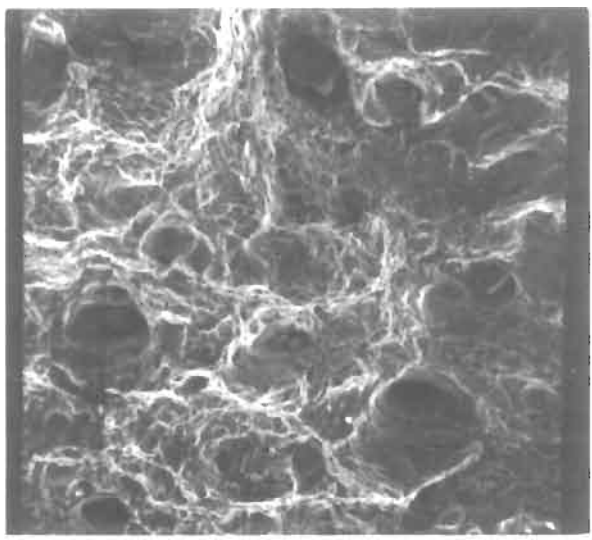

Fig. 7. Ductile fracture surface, showing the final dimpled structure of hole growth. Precipitate particles are visible in some of the dimples which served as nucleation sites for the holes. (Courtesy C. INTERRANTE.)

References: p. 2287.

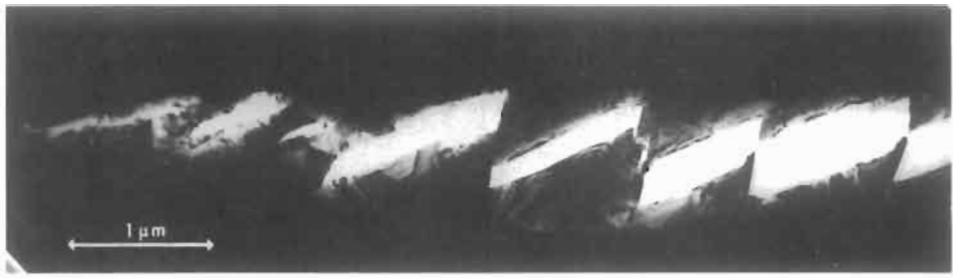

Fig. 8. Side view of a growing fracture in a thin film of gold. Holes are shown nucleating ahead of the crack; see LYLES and WILSDORF [1975]. (Courtesy H. G. F. WILDORF).

crack as shown in fig. 8. These holes are thought to initiate in practical alloy steels primarily at the site of precipitate particles in the matrix as illustrated in fig. 7. Often the large voids in the medium are connected by bands of intense shear, as shown in fig. 9. Within these shear bands, void formation also occurs, but typically at a much smaller average size than in the case of the larger precipitates. The initiating sites of the smaller voids are at the time of writing still a matter of controversy. In some cases, they are associated with precipitates — but in this case particles of very small size (100–1000 Å) (GARRISON and HANDERHAN [1989]). However, holes have been observed by GARDNER *et al.* [1977] to nucleate in very pure metals without the help of precipitates, and the small voids in impure steels may be produced homogeneously also. Figure 10 illustrates two forms of relatively brittle fracture in a high-strength steel under embrittling condi-

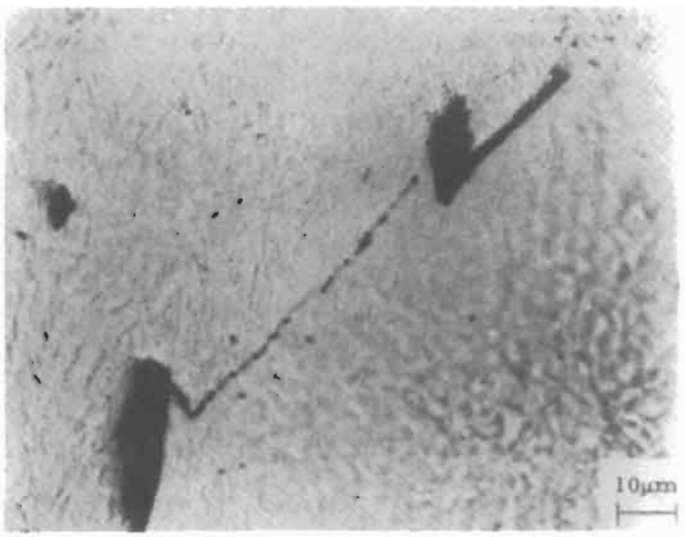

Fig. 9. Hole growth at precipitates in ductile fracture. Between the large holes, shear bands develop consisting of large numbers of much smaller holes. (After COX and LOW [1974]).

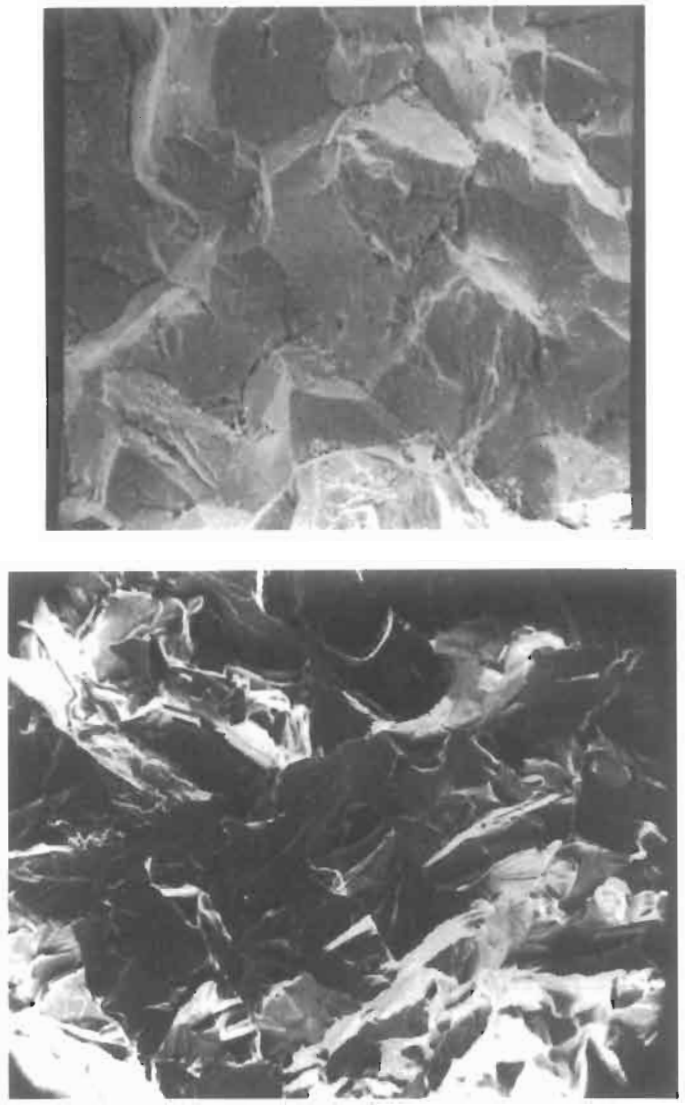

Fig. 10. Appearance of relatively brittle fracture in steel. Top: the fracture is along the grain boundaries (intergranular). Bottom: the fracture is transgranular. (Courtesy C. INTERRANTE.)

tions. In one case, the fracture path follows the grain boundaries of the steel, while in the other, the cleavage path is transgranular.

In the next set of observations, phenomena characteristic of more ideal conditions are illustrated. Figure 11a shows results for completely brittle cracks by LAWN *et al.* [1980] in Si single crystals. The crack was injected at room temperature, where dislocations are

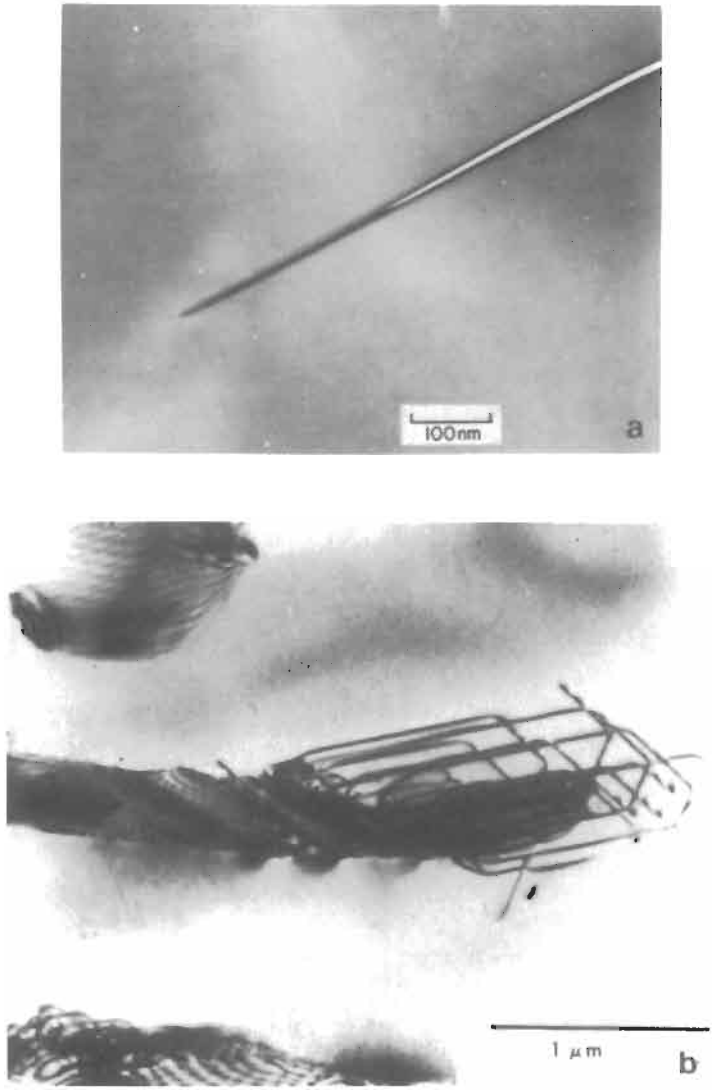

Fig. 11. (a) An electron microscope picture of a fully brittle crack in Si. In the photo, the crack is seen edge on. (b) Cracks formed in Si at 500°C are associated with dislocations as shown (see LAWN *et al.* [1980]). (Photos courtesy B. HOCKEY.)

immobile, by an indentation technique. In the figure, the crack is shown in cross-section. No dislocations whatsoever are present, proving that completely brittle atomically sharp cracks are possible. If cracks are injected into the same material at a temperature of 500°C, where the dislocations are mobile, then considerable dislocation activity is evident (fig. 11b).

This behavior is a particularly simple example of a type of brittle/ductile transition

which intrinsically brittle materials can undergo at elevated temperatures. By intrinsically brittle, we mean a material which can sustain a sharp crack and is cleavable at low temperatures. Here, we see that at higher temperatures, the crack itself becomes a source of dislocations, which inhibit the crack mobility by their elastic shielding. The material becomes much tougher when the dislocations are present. There is uncertainty about whether the dislocations are created spontaneously out of the straight crack line (ZHOU and THOMSON [1991]), or whether the source is at some kind of inhomogeneity on the crack line. However, once the sources begin to act, and the loading strain rate is not so fast as to de-pin the crack from its dislocations, then the material becomes ductile. The brittle/ductile transition in this simplest case has been worked on by a number of authors in recent years, and we refer the reader to recent papers on the subject by the principal authors, BREDE [1993], HIRSCH and ROBERTS [1991], and GEORGE and MICHOT [1993].

In fig. 12, photographs by VEHOFF *et al.* [1981] in Fe(+Si) show a wedge-shaped crack, and "propagation" of this crack takes place by dislocation emission on the two complementary slip planes which intersect at the tip. When the crack is loaded at a strain rate above a critical amount, the crack breaks away from its dislocation zone, and cleaves. Also, when the cracked sample is in an atmosphere of hydrogen gas, the crack again begins to cleave. In this case, the angle of the wedge becomes a function of the hydrogen partial pressure for a given strain rate. The mechanism of just how the hydrogen induces brittleness is a hotly contested controversy in the research community at this time (see § 10.5). The brittleness could be caused by a lowering of the bond strength at the crack tip, or by increasing the dislocation mobility.

The fact that Fe can be cleaved by modestly raising the strain rate in the experiments of VEHOFF *et al.* [1981] shows that Fe is capable of inherent cleavability. That is, the material will support an atomically sharp crack at its tip, without shear breakdown and dislocation emission. But, as in the case of Si, when the loading rate is sufficiently slow for the crack not to outrun the dislocations, then the material becomes ductile. In the case of the Fe, the wedge shape is consistent with an emission mechanism at the crack tip shown in fig. 12c, because the angle of the opening wedge in fig. 12b is exactly that determined by the intersection of the two slip planes at the crack tip. But in the case of Fe, and especially in other even more ductile metals, there is also dislocation generation in the medium beyond the crack tip, and in cases where this external dislocation generation is high, the absorption of the externally generated dislocations may modify the shape of the crack to a more rounded shape. (The precise shape would depend upon the details of the source mechanism, but there are many cases of rounded crack shapes in hole growth fracture, and these shapes are indicative of the randomly distributed dislocation sources in the medium.) Thus, apparently Fe is again, like Si, a material which can cleave, but can be made to behave in a ductile fashion because of the elastic shielding action of the dislocations produced in its vicinity. As we have seen, however, the intrinsic cleavability of Fe makes it a material which is susceptible to a transition to brittle behavior if the dislocation mobility is not sufficient. Actually, there is some indication (to be discussed in § 7) that Fe is a borderline case between the highly cleavable materials such as Si and the truly ductile materials like gold.

Figure 13 shows results KOBAYASHI and OHR [1981] in foils of Cu (similar results

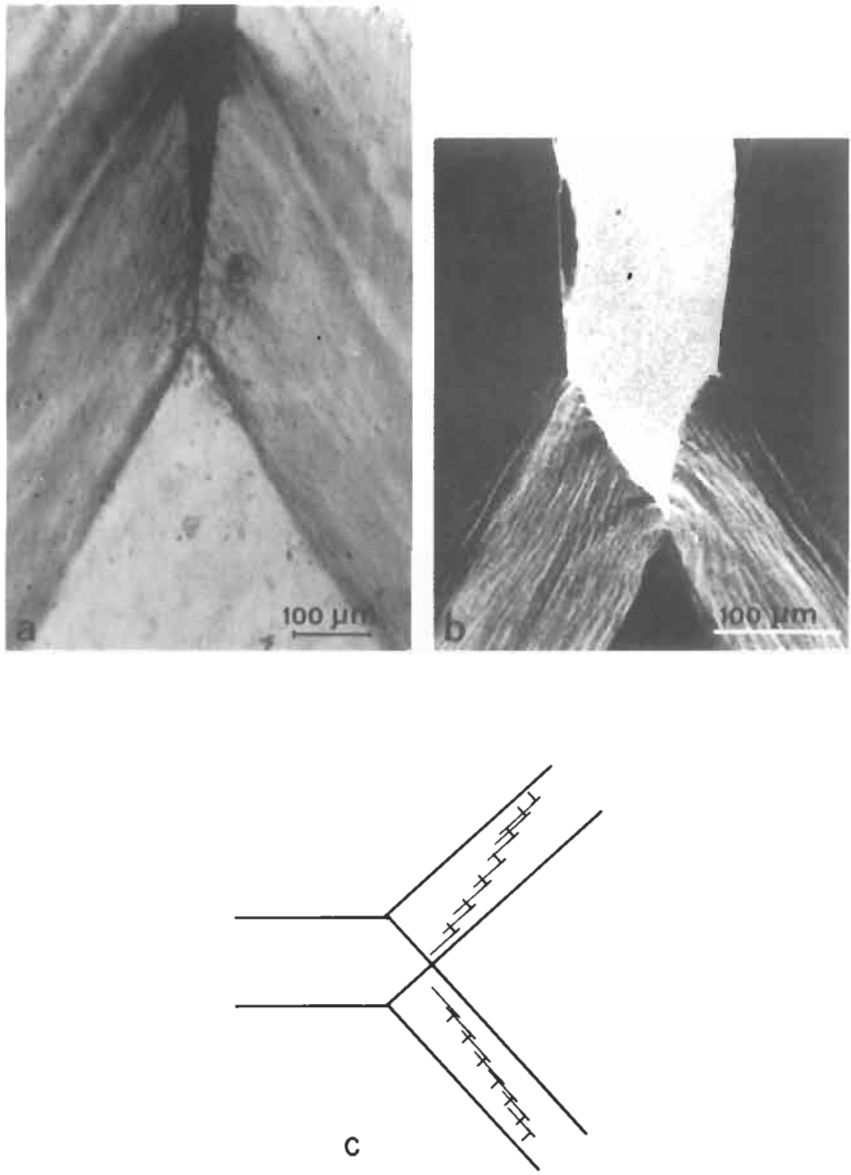

Fig. 12. In (a) sharp cracks are formed in a hydrogen atmosphere in Fe (+Si). In (b) the crack opens entirely by dislocation slide-off at the crack tip. In both cases, dislocations are emitted from the crack tip, and form slip bands. In (a), cleavage must also be present. The angle of the wedge opening in (b) is defined by the intersection angle of the two slip planes with the crack plane. In (c) the dislocation configuration generating the crack is illustrated in terms of alternate emission of dislocations on the two complementary slip planes. (After VEHOFF and NEUMANN [1980], courtesy P. NEUMANN.)

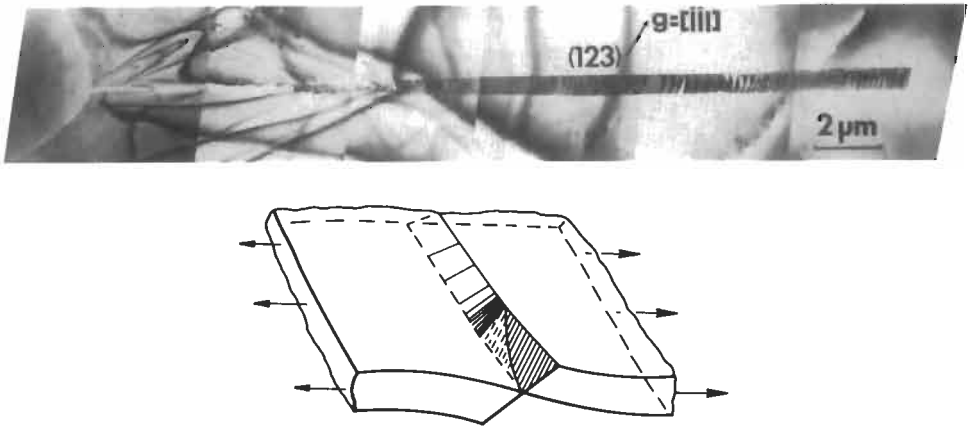

Fig. 13. (a) Dislocations emitted from the tip of a crack in a foil of copper. The crack has grown from the left. Immediately ahead of the crack is a region free of dislocations. The pile-up of dislocations is seen extending on the cleavage-slip plane to the right. In b) the crack-dislocation geometrical configuration is illustrated. (After KOBAYASHI and OHR [1981], courtesy S. M. OHR.)

are obtained for Ni and steel). In this case, the foil "slides off" on its slip plane which is at an oblique angle to the plane of the foil. When the foil locally shears completely through its thickness, a cracklike artifact is generated (a mode III crack of zero length) which grows by dislocation emission and translation. This figure illustrates that the crack has a substantial region near its tip (termed an elastic enclave, or a dislocation-free zone) where no dislocations are present.

2.3. The basis for fracture science

The illustrations selected above exemplify the major experimental findings to be used as a basss for a science of fracture. The reader is referred to vol. 9 of "The Metals Handbook" (SHUBAT [1974]) and to vol. I of the "Fracture" series (LIEBOWITZ [1958]) for a compendium and atlas of fractographic examples which go far beyond what we can display here. The illustrations demonstrate clearly enough, however, that fracture in materials is most often a very complex phenomenon which depends upon a large number of material and external variables, and that the task of sorting out the fundamental phenomena which are critical to the fracture event is not an easy nor straightforward one. However, primarily on the basis of these observations, we shall state a number of qualitative conclusions as a point of departure for the sections which follow:

(a) In practice, cracks are most often flaws of very complex structure which only approximate the three idealized two-dimensional modes of fig. 6. However, because of the necessity of using models which can be analyzed and described in accessible mathematics, we are led to the study of these idealized modes.

(b) The two major poles, of brittle and ductile fracture, are discernible in the fractography of metals (figs. 7 and 10).

(c) The ubiquitous presence of dislocation sources in metals assures that copious dislocations are generated to accompany the fracture process in all cases, even when the material is intrinsically brittle. Only in such exceptional (nonmetallic) cases as Si at low temperatures, where dislocation sources in the medium are nonexistent, are ideally brittle fractures found (fig. 11). Thus, even for metals which can cleave, ductile behavior is possible because of the elastic interactions with the dislocations. This ductility will be highly dependent on the dislocation mobility and source density (and thus on the microstructure of the material), and the material will exhibit an unstable tendency for transition between the ductile and brittle forms. In contrast to the kind of ductility which is controlled by the atomic bonding character of the crack tip, which we have termed intrinsic ductility, this latter form of ductility will be termed extrinsic ductility, because it depends on the material microstructure, as well as load rate and temperature.

(d) Although the extreme pole of ductile failure is the macroscopic rupture by necking depicted in fig. 1, a more localized form of ductile failure is also possible which has the macroscopic appearance of a fracture. Pure forms of such ductile fracture occur when dislocation emission at the crack tip generates a mode I wedge-shaped crack (fig. 12) or a mode III shear crack (fig. 13), or a sharp crack is rounded by the action of a ductile matrix. In all these cases again, the dislocation interactions with the underlying "crack" should be a key to the overall behavior. However, the criterion for dislocation emission, in the form of a local "fracture criterion" at the crack tip, will involve different physical ideas from the fracture criterion for a sharp cleavage crack as envisioned in the last paragraph. Such a treatment of ductile fracture has been developed for the mode III shear crack, and will be presented in the following sections, but the wedge case has not yet been analyzed in these terms.

(e) In practice, however, ductile fracture is characterized by void nucleation and growth as discrete events ahead of the main crack (figs. 7–9). The larger voids are initiated first at precipitates in practical alloys. Shear bands of intense localized shear associated and coincident with sheets of very small voids then connect the large voids. Final failure occurs by purely plastic rupture processes operating between the voids and the main crack. Clearly, this (mixed) form of failure is very complex, and we shall only be able to address it in a qualitative way, and only after development of ideas conforming to the simpler pure forms of brittle and ductile fracture.

(f) A given material can be influenced to respond over a range of the ductile-brittle axis by varying the external environment (fig. 12), the strain rate, or the temperature. Internal metallurgical variables also have the same effect. Thus, we shall be very sensitive in the following sections to the features in the models to be developed, which may lead to the breakdown of either the brittle or ductile poles in favor of the opposite pole of behavior.

3. *Elastic analysis of cracks*

3.1. Stress analysis

In this section we derive some of the principal results of elasticity as applied to slit cracks. We will derive some results for the antiplane strain (mode III), and quote results

for mode I and II as appropriate. The analysis of mode III is much simpler than for the other two cases, and since many of the results which are possible to obtain quite easily in mode III can be taken over with obvious modifications to modes I and II, we shall restrict our formal analysis to this case. The difference between mode III and mode I cracks is analogous to the difference between screw dislocations (antiplane strain) and edge dislocations.

In antiplane strain, the displacement, $\boldsymbol{u}$, is totally in the x_3 direction, and is a function of both x_1 and x_2, but not of x_3. In this case, the only nonzero stress components are σ_{32} and σ_{31} (and their symmetrical components σ_{23} and σ_{13}), and likewise for strain ε_{32} and ε_{31}. Hooke's Law is written as

$$\sigma_{3j} = \mu u_{3,j}, \quad j = 1,2, \tag{1}$$

where μ is the shear modulus (see also the table of symbols at the end of the chapter). In this and the following equations we shall define the comma in eq. (1) as $u_{3,j} \equiv \partial u_3 / \partial x_j$, and shall also use the "summation convention" wherein repeated indices in a product are summed over: $u_i u_i \equiv \Sigma_i u_i u_i$. Two-dimensional problems lend themselves to complex variable notation, and our expressions will be simplified by its use. Thus, writing $x_1 + ix_2 = z$, the stress tensor is written as a complex "vector":

$$\sigma(z) = \sigma_{32}(x_1, x_2) + i\sigma_{31}(x_1, x_2). \tag{2}$$

Since $\boldsymbol{u}$ has only a single component, it is convenient to introduce a somewhat redundant complex function, $w(z)$, related to $\boldsymbol{u}$ by the definition

$$\mathrm{Im}[w(z)] = u_3(x_1, x_2). \tag{3}$$

Here "Im" means "the imaginary part of". Similarly, "Re" will mean "the real part of". In this notation, Hooke's Law is written:

$$\sigma(z) = \mu \frac{\mathrm{d}w}{\mathrm{d}z}. \tag{4}$$

The *strain energy density function*, W, takes the simple form

$$W = |\sigma^2| / 2\mu. \tag{5}$$

The equations of elastic equilibrium become the simple Laplace equation

$$\nabla^2 u_3 = \frac{\partial^2 u_3}{\partial x_1^2} + \frac{\partial^2 u_3}{\partial x_2^2} \equiv u_{3,ii} = 0. \tag{6}$$

In the theory of complex functions, when eq. (6) is satisfied, it is known that a general solution is any regular complex function of z. It is then only necessary to choose from among these functions one which satisfies the appropriate boundary conditions of the particular problem. In the case at hand, a function which is finite at infinity is sought, which satisfies the boundary condition of elasticity at a free surface. This boundary condition states that no force is transmitted across the surface,

References: p. 2287.

$$\sigma_{ij} n_j = 0, \tag{7}$$

for a surface, S, with normal components n_j. If the crack is an infinite cut along the negative x_1 axis, with the tip of the crack at the origin (see fig. 3), then in complex notation

$$\mathrm{Re}\,\sigma = 0, \qquad x_1 < 0, \qquad x_2 = 0. \tag{8}$$

Square root functions are known to have special properties along the negative χ_1 axis, and indeed a stress function proportional either to $\sqrt{z}$ or $1/\sqrt{z}$ would satisfy eq. (8). If we also require that σ be finite at infinity, then we choose

$$\sigma = \frac{K}{(2\pi z)^{1/2}} = \frac{K}{(2\pi r)^{1/2}} e^{-i\theta/2} \tag{9}$$

for the crack solution. That eq. (9) satisfies eq. (8) is easily verified. The alternative polar form of eq. (9) is often useful. K is a constant of proportionality, which is a measure of the magnitude of the stress-singularity at the crack tip, and is called the *stress intensity factor*. The displacement field, w, related to σ by eq. (4) is:

$$w = \frac{K}{\mu}\left(\frac{2z}{\pi}\right)^{1/2}. \tag{10}$$

The expression (9) demonstrates the basic result for cracks that they possess a stress concentration singularity of the form $1/\sqrt{z}$. The reader will note that the strain-energy density function, eq. (5), integrated over all space is linearly divergent at infinity, showing that the crack is not a localizable defect. The non-localizability is related to the fact that the crack must be associated with a long-range stress, such as finite constant stress at infinity. Unfortunately, this long-range stress is not explicit in eq. (9), and the reason is that the cleavage plane of the crack is infinite in extent. To explore this further, it is necessary to discuss the case of a finite crack, explicitly.

Consider a finite cut on the x_1-axis from $x_1 = -a$ to $x_1 = +a$. Then we seek a complex function, w, which has the limiting form $(z-a)^{1/2}$ as $z \to a$ and $(z+a)^{1/2}$ as $z \to a$. A simple complex function which has this property is the product of these two limiting forms,

$$w \propto \left(z^2 - a^2\right)^{1/2}. \tag{11}$$

Taking the derivative of eq. (11) to find the stress,

$$\sigma \propto \frac{z}{\left(z^2 - a^2\right)^{1/2}}. \tag{12}$$

The reader can verify directly that the boundary condition $\mathrm{Re}(\sigma) = 0$ is satisfied on the cut from $-a$ to $+a$. We make the connection to eq. (9) by requiring σ to take the form $\sigma(z) \to K/[2\pi(z-a)]^{1/2}$ near $z = a$ and write eq. (12) in terms of K:

$$\sigma = \frac{K}{(\pi a)^{1/2}} \frac{z}{\left(z^2 - a^2\right)^{1/2}}. \tag{13}$$

In the limit, the solution (13) has the desired finite uniform stress at $z \to \infty$, and the stress at infinity has the form

$$\sigma_\infty = \frac{K}{(\pi a)^{1/2}}. \tag{14}$$

Since in the limit for $z \to \infty$, σ is real, $\sigma_\infty = \sigma_{32}(\infty)$. Equation (14) yields the desired relation between the externally applied stress and the stress-intensity factor. This relation involves the crack length in a characteristic way.

The solutions (11)–(14) represent a particular choice of complex functions which satisfy the boundary conditions on the crack, and which follow from the assumption of a particular form of externally applied stress. Other choices are possible; for example, the external stress may be applied at the midpoint of the crack itself, or at some other arbitrary place on the surface of the medium. In all cases, the stress at the crack tip is characterized by a $1/\sqrt{z}$ field with a stress intensity factor, K. By solving the elasticity problem, K can be related to the external force, resulting in some kind of relation such as eq. (14) which depends upon the geometry of the crack, the geometry of the external surfaces of the sample, and the distribution of the applied force. The case of eq. (14) represents a particularly simple choice for these geometry-dependent factors. Elastic calculations of K for a variety of special cases have been tabulated by TADA *et al.* [1973].

One other interesting fact is implicit in eq. (13). Although there is a $1/\sqrt{z}$ singularity at $\pm a$, the total stress field is not of the form $1/\sqrt{z}$, and from the standpoint of function theory should be represented as a power series expanded at, say $z = +a$, with $1/(z-a)^{1/2}$ as the first term in the expansion. This is a general result, and is forced by the fact that the stress must not only generate a singularity at the crack tip, but also describe the external loading arrangements at large distance from the crack tip, which vary from case to case.

Having derived elastic results for mode III, we summarize below the corresponding elastic equations for all modes. In these equations, the complex function format is dropped, and this set of equations, (15), reverts to the traditional real variables, x, y, and z or, correspondingly, r, θ and z.

Equations for Mode I:

$$\left.\begin{matrix}\sigma_{xx}\\ \sigma_{yy}\\ \sigma_{xy}\end{matrix}\right\} = \frac{K_I}{(2\pi r)^{1/2}} \cdot \begin{cases}(\cos\theta/2)\left[1 - \sin(\theta/2)\sin(3\theta/2)\right]\\ (\cos\theta/2)\left[1 + \sin(\theta/2)\sin(3\theta/2)\right];\\ \sin(\theta/2)\cos(\theta/2)\cos(3\theta/2)\end{cases}$$

References: p. 2287.

$$\left.\begin{matrix}\sigma_{rr}\\ \sigma_{\theta\theta}\\ \sigma_{r\theta}\end{matrix}\right\} = \frac{K_I}{(2\pi r)^{1/2}} \cdot \begin{cases}(\cos\theta/2)\left[1+\sin^2(\theta/2)\right]\\ \cos^3(\theta/2)\\ \sin(\theta/2)\cos^2(\theta/2)\end{cases};$$

$$\sigma_{zz} = \nu'\left(\sigma_{xx}+\sigma_{yy}\right) = \nu'\left(\sigma_{rr}+\sigma_{\theta\theta}\right),$$

$$\sigma_{xz} = \sigma_{yz} = \sigma_{rz} = \sigma_{\theta z} = 0;$$

$$u_z = -\left(\nu''z/E\right)\left(\sigma_{xx}+\sigma_{yy}\right) - \left(\nu''z/E\right)\left(\sigma_{rr}+\sigma_{\theta\theta}\right);$$

$$\left.\begin{matrix}u_x\\ u_y\end{matrix}\right\} = \frac{K_I}{2E}\left(\frac{r}{2\pi}\right)^{1/2} \cdot \begin{cases}(1+\nu)\left[(2\kappa-1)\cos(\theta/2) - \cos(3\theta/2)\right]\\ (1+\nu)\left[(2\kappa+1)\sin(\theta/2) - \sin(3\theta/2)\right]\end{cases};$$

$$\left.\begin{matrix}u_r\\ u_\theta\end{matrix}\right\} = \frac{K_I}{2E}\left(\frac{r}{2\pi}\right)^{1/2} \cdot \begin{cases}(1+\nu)\left[(2\kappa-1)\cos(\theta/2) - \cos(3\theta/2)\right]\\ (1+\nu)\left[-(2\kappa+1)\sin(\theta/2) + \sin(3\theta/2)\right]\end{cases} \tag{15a}$$

Equations for Mode II:

$$\left.\begin{matrix}\sigma_{xx}\\ \sigma_{yy}\\ \sigma_{xy}\end{matrix}\right\} = \frac{K_{II}}{(2\pi r)^{1/2}} \cdot \begin{cases}-(\sin\theta/2)\left[2+\cos(\theta/2)\cos(3\theta/2)\right]\\ \sin(\theta/2)\cos(\theta/2)\cos(3\theta/2)\\ (\cos\theta/2)\left[1-\sin(\theta/2)\sin(3\theta/2)\right]\end{cases};$$

$$\left.\begin{matrix}\sigma_{rr}\\ \sigma_{\theta\theta}\\ \sigma_{r\theta}\end{matrix}\right\} = \frac{K_{II}}{(2\pi r)^{1/2}} \cdot \begin{cases}(\sin\theta/2)\left[1-3\sin^2(\theta/2)\right]\\ -3\sin(\theta/2)\cos^2(\theta/2)\\ (\cos\theta/2)\left[1-3\sin^2(\theta/2)\right]\end{cases};$$

$$\sigma_{zz} = \nu'\left(\sigma_{xx}+\sigma_{yy}\right) = \nu'\left(\sigma_{rr}+\sigma_{\theta\theta}\right),$$

$$\sigma_{xz} = \sigma_{yz} = \sigma_{rz} = \sigma_{\theta z} = 0;$$

$$u_z = -\left(\nu''z/E\right)\left(\sigma_{xx}+\sigma_{yy}\right) = -\left(\nu''z/E\right)\left(\sigma_{rr}+\sigma_{\theta\theta}\right). \tag{15b}$$

$$\left.\begin{matrix}u_x\\ u_y\end{matrix}\right\} = \frac{K_{II}}{2E}\left(\frac{r}{2\pi}\right)^{1/2} \cdot \begin{cases}(1+\nu)\left[(2\kappa+3)\sin(\theta/2) + \sin(3\theta/2)\right]\\ -(1+\nu)\left[(2\kappa-3)\cos(\theta/2) + \cos(3\theta/2)\right]\end{cases};$$

$$\left.\begin{matrix} u_r \\ u_\theta \end{matrix}\right\} = \frac{K_{II}}{2E}\left(\frac{r}{2\pi}\right)^{1/2} \cdot \begin{Bmatrix} (1+\nu)\left[-(2\kappa-1)\sin(\theta/2) + 3\sin(3\theta/2)\right] \\ (1+\nu)\left[-(2\kappa+1)\cos(\theta/2) + 3\cos(3\theta/2)\right] \end{Bmatrix};$$

Equations for Mode III:

$$\sigma_{xx} = \sigma_{yy} = \sigma_{rr} = \sigma_{\theta\theta} = \sigma_{zz} = 0, \qquad \sigma_{xy} = \sigma_{r\theta} = 0;$$

$$\left.\begin{matrix} \sigma_{xz} \\ \sigma_{yz} \end{matrix}\right\} = \frac{K_{III}}{(2\pi r)^{1/2}} \cdot \begin{Bmatrix} -\sin(\theta/2) \\ \cos(\theta/2) \end{Bmatrix};$$

$$\left.\begin{matrix} \sigma_{rz} \\ \sigma_{\theta z} \end{matrix}\right\} = \frac{K_{III}}{(2\pi r)^{1/2}} \cdot \begin{Bmatrix} \sin(\theta/2) \\ \cos(\theta/2) \end{Bmatrix};$$

$$u_z = (K_{III}/2E)(r/2\pi)^{1/2}\left[2(1+\nu)\sin(\theta/2)\right];$$
$$u_x = u_y = u_r = u_\theta = 0.$$

For all modes:

$$\begin{aligned} &\kappa = (3-\nu)/(1+\nu), \quad \nu' = 0 \quad \nu'' = \nu \quad \text{(for plane } \textit{stress}\text{)}; \\ &\kappa = (3-4\nu), \quad \nu' = \nu \quad \nu'' = 0 \quad \text{(for plane } \textit{strain}\text{)}. \end{aligned} \tag{15c}$$

3.2. Eshelby's theorem and the J-integral

In addition to the stress-distribution problem, one other essential quantity in the elastic description of a crack is the force on the crack. By this is meant the analogous concept to the Peach–Koehler force on the dislocation (ch. 18, § 2.2), or the driving force which moves the crack forward or backward on its cleavage plane. In the fracture mechanics literature, this quantity is referred to as the *crack extension force* or the *crack energy release rate*, and is often written by $\mathcal{G}$. It is also equal to the *J-integral* of RICE [1968]. For the material scientist, however, it is more appropriate to simply call it the "force" on the crack, and derive its value in a way which shows its close kinship to analogous dislocation concepts. We shall thus follow the development first given by ESHELBY [1956] in his discussion of the force on a general elastic singularity.

To derive the Eshelby theorem, imagine a finite body (fig. 14), on whose external surfaces an external stress is distributed. This discussion is fully general, so the full 3-d tensor notation will be used. The body will contain sources of self-stress, such as dislocations, cracks, etc., which will be stress-singularities in the medium. A strain-energy density function is assumed to exist, and since, except at the singularities, the medium is elastic, this function is given by:

References: p. 2287.

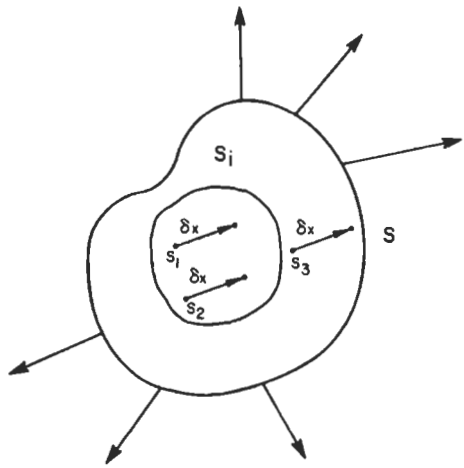

Fig. 14. Figure for deriving Eshelby's theorem. A body is contained within an external surface, S, and is subject to external stresses. Strain singularities exist at s_1, s_2, s_3..., which are translated by δx to new positions. S_i is an inner surface enclosing singularities s_1 and s_2.

$$W = \tfrac{1}{2}\sigma_{ij}u_{i,j}. \tag{16}$$

If all the singularities move a constant distance δx from their initial positions x_ρ to $x_\rho + \delta x$, the energy change is calculated in three stages.

In stage 1, the energy change, $\delta U^{(1)}$, arises from integrating the strain-energy density function over the solid. In this stage, when the sources translate, the stresses and displacements constituting the elastic solution are assumed to move rigidly with them in space. Thus, after the displacements occur, the new value of the strain energy function is

$$W^{(1)}(x) = W^{(0)}(x) - \frac{\partial W}{\partial x_i}\delta x_i. \tag{17}$$

The total energy change, integrated over the body is thus

$$\delta U^{(1)} = -\int \frac{\partial W^{(0)}}{\partial x_i}\delta x_i \, dV = -\int W \, dS_i \delta x_i. \tag{18}$$

In the second stage, the boundary condition on the surface of the body when the sources translate is considered. In stage 1, just above, when the elastic solutions translate rigidly with the sources, the stresses at the boundary translate in the same way. However, although the stress originally on the boundary satisfied the required boundary condition,

$$\sigma_{ij}n_j = 0 \tag{19}$$

on the boundary, where $\boldsymbol{n}$ is the normal to the boundary, after the rigid translation of the elastic solution the new stresses and displacements on the boundary no longer satisfy eq.

(19). In stage 2, an additional surface stress is generated, such that when it is added to the translated stress, the total stress satisfies the required condition, eq. (19), on the surface. The added stress, $\Delta\sigma_{ij}$, generates a new set of displacements at the surface *after the translation has taken place*. Thus, if $u^{(0)}$ is the initial displacement before the sources are displaced, the changes generated in displacements during stage 2 are:

$$\Delta u_i = u_i^{\text{final}} - \left(u_i^{(0)} - \frac{\partial u_i^{(0)}}{\partial x_j} \delta x_j \right). \tag{20}$$

The work done on the body by the total stress acting over (Δu_i) is then, to first order $(\sigma + \Delta\sigma \sim \sigma)$,

$$\begin{aligned} \delta U^{(2)} &\simeq \int \sigma_{ij}^{(0)} \Delta u_i \, \mathrm{d}S_j \\ &= \int \sigma_{ij}^{(0)} \left(u_i^{\text{final}} - u_i^{(0)} + \frac{\partial u_i}{\partial x_k} \delta x_k \right) \mathrm{d}S_j . \end{aligned} \tag{21}$$

The third contribution is the energy change in the external loading machinery caused by the total change in displacement at the surface, $u^{\text{final}} - u^{(0)}$. This is the total change in displacement from that before the source translates to that after the end of stage 2, when the boundary conditions are satisfied:

$$\delta U^{(3)} = -\int \sigma_{ij}^{(0)} \left(u_i^{\text{final}} - u_i^{(0)} \right) \mathrm{d}S_i . \tag{22}$$

Addition of eqs. (18), (21) and (22) gives the final result:

$$f_m = -\frac{\delta U}{\delta x_m} = \int \left(W \delta_{im} - \sigma_{ij} u_{j,m} \right) \mathrm{d}S_i . \tag{23}$$

f_m is the force on the singularity because it represents the negative of an energy derivative.

A subtlety arises when applying eq. (23) to a crack. The slit comprising the cleavage plane of the crack is, of course, a part of the external surface of the body. However, since on the free surface of the slit eq. (19) is satisfied, the second term in eq. (23) is zero. Also, by symmetry, W on the lower surface is equal to W on the upper. Because of the change in sign of $\mathrm{d}S_i$ when comparing the upper to the lower surface, the contribution of the first term is thus zero also. Hence, in making a contour around a crack, the contour may end on the crack cleavage surface.

The integration in eq. (23) is over the actual external surface of the body, and may enclose a number of singularities. The force in this case represents the total force on the entire set of singularities. If instead, the force on a single singularity, or subset of the original group, is desired, the following strategem can be adopted. An inner boundary, S_i, is drawn surrounding the singularities in question (fig. 14), and the remainder of the body then serves as an "external driving system" on the inner surface. In carrying out stage 2 of the argument, however, a subtle point must be observed. The boundary conditions are established on the *real* surfaces of the body, and the Δu_i as calculated in

References: p. 2287.

eq. (20) are the Δu_i on the inner integration path S_i which are induced by satisfying the boundary conditions on the external surface, S. The rest of the argument then follows as before. In this case of course, the force on the singularities within S_i is not only a function of the external driving stresses, but also of the remaining singularities outside S_i. Equation (23) is quite general. In antiplane strain, a great simplification occurs. Using the complex variable notation, and Hooke's Law, eq. (3.4), the simple result follows by direct substitution:

$$f^* = \frac{1}{i}\oint \frac{\sigma^2}{2\mu}\,dz. \tag{24}$$

In the complex plane $z = x_1 + ix_2$ the surface integral becomes the line integral of fig. 15. f^* is the complex conjugate of f. f is a complex number whose real part is the x_1-component of the force, and whose negative imaginary part is the x_2-component.

Equation (24) has a familiar form in the theory of complex functions. Cauchy's residue theorem states that any such closed integral is zero unless there are singularities in the integrand of the form $1/z$. Then it has a finite value given by

$$f^* = \frac{\pi}{\mu}\sum_a \Re_a(\sigma^2), \qquad \Re(\sigma^2) = \lim_{z\to a}\big((z-a)\sigma^2(z)\big), \tag{25}$$

where $\Re$ is the coefficient of the $1/(z-a)$ term in the Laurent expansion of σ^2 about the point $z = a$.

Equation (25) is a remarkable result. If we focus on a single singularity, it says that the force on that singularity is specified by the form of the stress as it goes to infinity at the singularity. For a screw dislocation, $\sigma \simeq 1/z$, so there is *no* self-force on the dislocation, because $\sigma^2 \simeq 1/z^2$, and σ^2 has no inverse linear term. If there is an external stress on the dislocation, then $\sigma^2 = (\sigma_0 + \mu b/2\pi z)^2 = \sigma_0^2 + \mu b\sigma_0/\pi z + \mu^2 b^2/4\pi^2 z^2$. Now there is a force $f^* = b\sigma_0$, as predicted by the Peach–Koehler result. If the singularity is a crack, then the force from eq. (14) is

$$f^* = \mathcal{G} = \frac{K^2}{2\mu}. \tag{26}$$

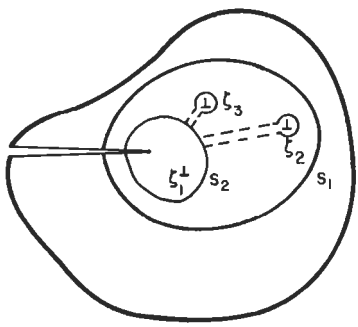

Fig. 15. Contours for Eshelby's theorem in two dimensions, in a body containing a crack and dislocations at $\zeta_1, \zeta_2, \zeta_3$. The inner surface, S_i, of fig. 14 becomes S_1. As S_1 shrinks to S_2, it passes ζ_2 and ζ_3. f^* is invariant if circles are left as shown, but not if S_2 encloses only ζ_1 and the crack.

This form of the force on a bare crack (mode III) was originally obtained by IRWIN [1957] by a different route, and in the fracture-mechanics community is called the crack extension force, or the *strain-energy release rate*, $\mathcal{G}$.

The corresponding equation for the force in the x_1-direction on a mode I or mode II crack is

$$f = \mathcal{G} = (1-\nu)\frac{K_I^2 + K_{II}^2}{2\mu} + \frac{K_{III}^2}{2\mu}, \tag{27}$$

where ν is Poisson's ratio and μ is the shear modulus. K_I refers to the mode I crack, etc. Equation (27) is calculated by a direct application of eq. (23) and the expressions for the appropriate stresses and displacements.

Equation (23) has been derived independently by RICE [1968], who called the integral quantity on the right-hand side (rhs) of eq. (23) the *J-integral*. J has been used extensively in the fracture-mechanics field for the analysis of fracture problems in plastic materials. The approach is to assume that the medium obeys a nonlinear stress-strain law which is a single-valued function of position. Then the strain-energy function can be defined everywhere, and J can be calculated from eq. (23). Such a stress-strain law adequately describes the loading history of a plastic material, and J, so calculated, can be used to characterize the stress condition of the material.

A further property of eq. (23) is that the integral on the rhs is to some degree path-independent. This result must be true if eq. (23) is indeed the force, because since any surface, S_i, can be used to calculate f, the force should not be a function of the surface of integration. Analytically, this result follows immediately from eq. (24), since from the Cauchy residue theorem, the integral is specified by the number and type of singularities enclosed in the path and not by its size or shape. If the path of the integral is thus deformed in such a way that it does not pass over one of the singularities, then, indeed, its value is unchanged. However, when the path is shrunk over one or more singularities so that it encloses fewer singularities than before, then the value of f is changed by the amount of the residue it bypasses during shrinking (fig. 15).

The quantity J, on the other hand, has a different meaning for a crack with a surrounding deformation field than does f. Since in J, the deformation field is not represented by dislocations, but by a continuous nonsingular nonlinear stress-strain function, no singularities are bypassed when the path is shrunk. Thus, J is completely independent of path throughout the deformation zone, and has the same value whether calculated within the deformation zone or outside it.

The complete path-independence of J gives it a great interpretive power for engineering purposes. The reason is that the critical value of K for which the material fails, known as K_{IC}, is an important engineering parameter for any material. However, sometimes K cannot be defined, but J can be. For example, in many cracked materials, the plastic region is confined to a small region near the crack tip (fig. 16). In these cases, the stresss in the elastic region is given by the simple result (Mode III):

References: p. 2287.

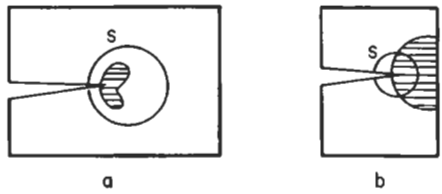

Fig. 16. The path for calculating J in (a) can be shrunk from a position where the crack and the shaded deformation zone are fully enclosed to any arbitrary size. In (b) there is no position of S enclosing the crack, which runs entirely through elastic material.

$$\sigma = \frac{K}{(2\pi z)^{1/2}}, \tag{28}$$

with the stress field centered at an effective crack tip position. In this case,

$$J = \frac{K^2}{2\mu}. \tag{29}$$

However, in a very tough material, and especially in "small" specimens, often the entire specimen undergoes plastic deformation, or a portion of the plastic zone overlaps an external surface. In this case, the stress is quite complicated, not given by eq. (28), and of course cannot be characterized by K. Nevertheless, even in these cases, J can be calculated by eq. (23). Because of its invariance properties, intuitively, the conditions near the crack tip which determine whether the crack grows or not should not depend strongly on the details of external specimen shape. The critical value of J when cracking occurs should still be a material property. Furthermore, J_{IC} should be equal to that calculated through eq. (29) for the large specimens.

Thus, much materials testing effort has been expended on developing techniques for measurement of critical values of J, and establishing the limits of application for these measurements. Various publications of the ASTM are referred to for further details, e.q. BEGLEY and LANDES [1972] and RICE [1976].

A major conceptual problem with J, however, is that plastic materials when unloaded do not follow the same stress-strain law as when loaded. Thus, W is not a unique point function of position, and the J-integral theory breaks down. Nevertheless, if the crack is not allowed to move, and the stress is not reversed, the J can be used to characterize the not-yet-moving crack, and on this basis the engineering use of J as described above is well founded. Another difficulty with using J to discuss the materials fundamentals of fracture is that it cannot easily describe the dislocation phenomena which ultimately control the actual response of a crack to external stress. For these two reasons, in this chapter, we shall often be more concerned with f^* than J.

The elastic theory presented here treats the crack as an independent entity from the dislocation, and this approach is confirmed by the fact that the crack stress field goes as $1/\sqrt{z}$ and the dislocation as $1/z$. Nevertheless, there is a fundamental sense in which the distinction disappears. For example, by eq. (15a) in the mode I crack shown in fig. 17,

Fig. 17. Near the tip of an elastic crack, the opening is parabolic (see eq. 15). This opening can be made equivalent to the displacement of a distribution of prismatic dislocations as shown. The stress and displacement outside the crack is then given by a distribution of "crack dislocations".

the displacement on the negative x-axis cleavage plane is given by:

$$\Delta u_y \sim K\sqrt{z}. \tag{30}$$

If the space between the two opposite sides of the cut were filled with a continuous density of Burgers vector, which just fills the empty space with matter, then the external stress could be released, and the material around the crack would possess exactly the same elastic displacement, stress and strain as before. Thus a prismatic "pile-up" of dislocations is equivalent to the crack. This equivalence has been used to obtain analytic results for crack problems by using dislocation theory, and forms the basis for the elastic theory of cracks presented by BILBY and ESHELBY [1968] and others. For the materials scientist who is more familiar with dislocations than with cracks, the equivalence is often an intuitive help.

4. *Elastic dislocation–crack interactions*

The elastic interactions between cracks and dislocations can be derived from eqs. (24) and (25). General results are possible, but lead to very complicated expressions. Thus our treatment will address the simple dislocation–crack configuration illustrated in fig. 18 in mode III.

The first step is to find the stress for a dislocation in the presence of a crack. There

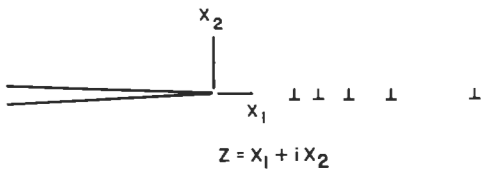

Fig. 18. For calculations of dislocation–crack configurations, the dislocations are all assumed to lie on the x_1-axis ahead of the crack tip. In this case, z and ζ are real.

References: p. 2287.

are several techniques for doing this. One is to use a Green's function or source function for the elastic field (THOMSON and SINCLAIR [1982]) and another is to use the known solution for a dislocation in the presence of a plane surface and use complex function techniques to transform the plane surface into a slit surface (MAJUMDAR and BURNS [1981]).

Intuitively, however, we may obtain the solution by building on the known solution for a screw dislocation,

$$\sigma(z) = \frac{\mu b}{2\pi(z-\zeta)}, \tag{31}$$

and modifying it to conform to the requirements of the crack. Here b is the Burgers vector of the dislocation, ζ the (complex) position of the dislocation, and z the point where the stress is measured. The origin is at the crack tip (fig. 18). The necessary modification is made by considering the form of the solution in the immediate neighborhood of the crack tip in a region where $z \ll \zeta$. If there is no external stress (and the cut is not allowed to heal) then the stress field of the dislocation will develop the characteristic crack stress-concentration around the crack tip just as an external stress would. That is, near the crack tip, the stress from the dislocation field must vary as $1/\sqrt{z}$. However, in a region near the dislocation, the stress field must look like eq. (31). Thus, if we multiply eq. (31) by the factor $(\zeta/z)^{1/2}$ the total stress field has these required characteristics:

$$\sigma = \frac{\mu b}{2\pi(z-\zeta)}\left(\frac{\zeta}{z}\right)^{1/2} \tag{32}$$

The stress must also satisfy the boundary conditions, eq. (19), on the crack slit, and a direct check of eq. (32) shows that eq. (19) is indeed satisfied on the negative x_1 axis. Equation (32) corresponds to the dislocation–crack field without the presence of an external stress. If we add an external stress (i.e., a K field) to the dislocation field, and add other dislocations at positions ζ_j, then the final result for the stress *of symmetric distributions* is

$$\sigma(z) = \frac{K}{(2\pi z)^{1/2}} + \sum_j \frac{\mu b_j}{2\pi(z-\zeta_j)}\left(\frac{\zeta_j}{z}\right)^{1/2}. \tag{33}$$

The Burgers vector convention used in these expressions is that consistent with a positive sign in eq. (33). A geometric interpretation will be made later in terms of the absorption of dislocations by the crack surface.

In a calculation of f from eq. (25), it is only necessary to square eq. (33), and identify the $1/z$ singularities. Singularities in σ^2 appear at the crack tip and at each dislocation. Taking only those singularities of order (–1) at the cack tip, we find for the force on the crack, f_c:

$$f_c = \frac{k^2}{2\mu}, \qquad k = K - \sum_j \frac{\mu b_j}{(2\pi\zeta_j)^{1/2}}. \tag{34}$$

Thus, the force on the crack corresponds to a new K-field at the crack which we label k, and call the *local k*. Equation (34) means that the externally applied field is *shielded* from the crack tip by the presence of dislocations, and the contribution of each dislocation is in the amount $\mu b/(2\pi\zeta)^{1/2}$. It is important to note that the dislocation contribution is algebraic in b; that is, positive Burgers vectors shield the crack, while negative Burgers vectors enhance the external field. Thus, we speak of "shielding" dislocations and "antishielding" dislocations. Although eq. (34) has only been derived for the configuration of fig. 18, it is valid as it stands for an arbitrary symmetric distribution of screw dislocations around the crack; i.e., if there is a dislocation at ζ, there is also one at ζ^*.

The force on one of the dislocations, f_d, is equally straightforward. In the expression σ^2, there are terms which are of the form $1/(z-\zeta)$. These terms contribute to the residue, and after carrying out the necessary algebra, the result is

$$f_d^* = \frac{Kb}{(2\pi\zeta)^{1/2}} - \frac{\mu b^2}{4\pi\zeta} + \sum_j \frac{\mu b_j b}{2\pi} \frac{1}{\zeta - \zeta_j} \left(\frac{\zeta_j}{\zeta}\right)^{1/2}. \tag{35}$$

In this expression, the reference dislocation is unlabeled, but all other dislocations in the distribution are labeled by the index j. Thus the sum does *not* include the reference dislocation, b, at ζ. Again all b's are algebraic. The three terms in eq. (35) can be interpreted as follows:

The first term is the contribution from the direct crack stress field. Note that the appropriate K is the unshielded value.

The second term is an image term as if the crack were a vertical surface through its tip. Qualitatively, such an image term is expected because, after all, the cleavage plane of the crack is an open surface, and dislocations of both signs are attracted to surfaces as if by an image. The simplicity of the result and its equality to the image of a simple vertical surface is the only surprise.

The third term in eq. (35) is the dislocation–dislocation interaction, as modified by the crack. The $(\zeta_j/\zeta)^{1/2}$ factor must be present because, as explained earlier, a dislocation generates its own $(1/z)^{1/2}$ singularity at the crack tip, and a second dislocation used as a probe will experience the stress as a singular force near the crack tip. On the other hand, near the dislocation, the $(\zeta_j/\zeta)^{1/2}$ factor does not affect the normal dislocation-dislocation interactions. A final curiosity, however, results from an investigation of eq. (35) when $\zeta \gg \zeta_j$. In this case, the crack shields the dislocations! The reason is that the dislocation is near the open surface of the crack, and its stress field is partially cancelled by its image in the crack, though the cancellation is more complex than a simple image term.

Equation (35) is a simplification of the actual force on a dislocation at an arbitrary position off the crack plane. If the dislocation is not on the crack plane, additional image terms are present which lead to complex expressions for nonsymmetric distributions.

Equations (34) and (35) correspond to contours in the sense explained in fig. 15, drawn around each individual defect in question. If the contour is drawn around the entire distribution, then the force is that to translate the entire configuration rigidly. The residue is then composed of a sum of all the terms, eqs. (34) and (35), and the result is then simply

References: p. 2287.

$$f^*_{\text{total}} = f_c + \sum_j f^*_d(j) = \frac{k^2}{2\mu} + \sum_j f^*_d(j) = \frac{K^2}{2\mu}. \tag{36}$$

f^*_{total} has the same value as the force on a bare crack sustaining a total external K-field value of K. f^*_{total} also has the same value as the J-integral defined in the last section for the crack with its deformation field eq. (29).

The discussions of crack–dislocation interactions do not yet reflect the important fact that the total dislocation Burgers vector is a conserved quantity. Suppose a configuration consisting of a crack and its associated screening dislocations is considered to be generated from an initially perfect crystal. The crack is constructed by making a cut in the presence of an external stress as explained in the introduction. The dislocations, however, will be assumed to be formed from dislocation sources in the neighborhood of the crack on the crystallographic slip planes specified by the crystal geometry. Although these multiplication processes in real materials are highly chaotic, for our two-dimensional purposes we may consider them to be formed in pairs of opposite Burgers vectors (fig. 19). The one with shielding Burgers vector will be repelled from the crack, and the other, with antishielding Burgers vector, will be attracted to the crack. The dislocations will move under the elastic forces calculated in eq. (35) until they come into equilibrium with lattice friction forces (see the following section). Many of the antishielding dislocations will be attracted toward and be absorbed and annihilated by the open cleavage surface, producing steps on these surfaces, of height equal to the total absorbed Burgers vector. Of course, many of the antishielding dislocations are oriented to pile-up in the region ahead of the crack tip, and exert a force on the crack, forcing it to the right (fig. 18). The net result of these processes is to produce a crack with a new cloud of shielding dislocations (fig. 19), and a *crack opening displacement* (COD) equal to the antishielding dislocations which were absorbed by the cleavage plane. Figure 19 shows edge dislocations interacting with a mode I crack, whereas the analysis has been entirely in terms of screw dislocations in mode III. The qualitative similitude of the anaysis between the two cases allows us to do this. The crack opening displacement is quantitatively given by

$$\sum b_j = \text{COD} = Nb_c, \tag{37}$$

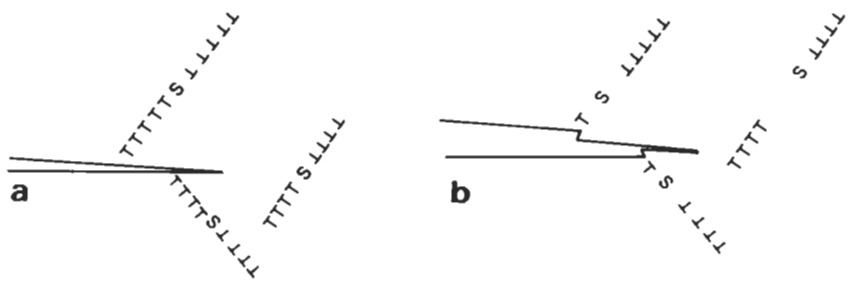

Fig. 19. Dislocation sources operate external to a crack and cause a crack-opening displacement as shown.

where b_c is the component of the Burgers vector normal to the crack plane. N is the net remaining number of screening dislocations in the shielding configuration. Because many, and in fact most, of the antishielding dislocations created in the deformation zone around the crack do not find their way to the cleavage surface where they can be annihilated, the deformation zone is composed of dislocation networks whose Burgers vectors nearly cancel. Only the residual, or net Burgers vector of the distribution contributes to the screening effect.

As shown in fig. 19, those antiscreening dislocations whose slip planes pass in front of the crack are trapped in the vicinity ahead of the crack in a region of dislocation stagnation. Since the crack is attracted toward them, if sufficient pile-up takes place, the crack will be pulled ahead until absorption can occur on the cleavage surface. This effect has indeed been observed in NaCl by WIEDERHORN *et al.* [1970]. In metals, this stagnation region is also the region of hole formation.

For an extension of these ideas to the general case of mixed Mode I, II, III, see LIN and THOMSON [1986]. Also, the detailed interaction of an external source interacting with a moving crack has been explored by ZHOU and THOMSON [1992]. These latter authors show that the initial effect of an external source in the medium which creates a dislocation pair in response to the presence of a crack is antishielding, but that the overall response, as the crack moves past the source, is shielding. Thus, transient effects in the shielding field may be antishielding in character, but the final effect is always positive shielding, as one would expect on the grounds of energy conservation.

5. *Equilibrium configurations*

In this section, we will bring together the ideas of the last two sections, and address the problem of the brittle crack interacting with a surrounding screen of dislocations. In § 2, we pointed out the possibility that in metals, where sources external to the crack tip can create dislocations which shield the crack, a ductile regime is possible, but that this regime is subject to perhaps sudden transitions back to the brittle state. We wish to deal quantitatively with this case. At least, we wish to use the highly ideal Mode III elastic theory of the past two sections to build a physical picture of toughness for such cracks, by setting up the conditions of equilibrium between an underlying brittle crack and its surrounding dislocation screen.

Actually, the physical picture will have a somewhat wider applicability. The elastic theory has been built for sharp cracks, and is thus not applicable to the problem of dislocations interacting with a wedge-shaped crack or a rounded crack. But there are cases where dislocations can be emitted on the cleavage plane, wherein the crack tip is not blunted, and there are also cases where the crack tip may be a source of dislocations, but for some reason, the crack tip is not a copious source. We will suppose the crack still retains the ability to cleave, so that the effective "wedge" angle is very narrow, and the crack can still be considered sharp. The theory to be developed can also be applied to these two latter cases.

Although the analysis we shall be able to use will be qualitative in nature, it will

nevertheless serve to highlight the physical ideas, and lay the basis for a more adequate, but far more sophisticated, theory which is now accessible. See HUANG and GERBERICH [1994].

5.1. The Griffith crack

In terms of dislocation shielding, the fracture problem comes down to finding the equilibrium configuration of dislocations and cracks under a given external load. The force represented by f^* is the elastic force exerted on a defect, and these elastic forces which are partly interaction forces between the defects, and partly due to externally generated stresses, are balanced by other forces induced by the material. For the configuration to be in static equilibrium each defect must experience a total net zero force.

The simplest crack configuration, of course is an isolated crack, without dislocation screen. The force balance condition for the isolated brittle crack was first studied by GRIFFITH [1920], who suggested that the elastic force is balanced by the surface tension of the two cleavage surfaces joined at the crack tip. That is, when the crack is opened, additional surface energy is created, and this energy residing in the surface exerts a surface tension force on the crack tip tending to close it. If γ_s is the surface tension, the equilibrium for mixed load from eq. (27) is

$$\mathcal{G}_C = (1-\nu)\frac{K_I^2 + K_{II}^2}{2\mu} + \frac{K_{III}^2}{2\mu} = 2\gamma_s. \tag{38}$$

γ_s is also the surface free energy per unit area. In the simpler Mode I loading, then

$$\mathcal{G}_{IC} = \frac{(1-\nu)K_{IC}^2}{2\mu} = 2\gamma_s. \tag{39}$$

In these equations, the subscript C relates to the critical value for fracture. That is, for values greater than the critical values, cleavage will occur. K_{IC} and $\mathcal{G}_C$ are also called *fracture toughness parameters*, because they relate to the onset of fracture in a material, and are material properties.

As an equation expressing force balance between elastic and lattice forces, eq. (38) is flawed, because it does not also express the requirement that the loaded crack is held open against the atomic bonding forces at its tip which tend to close the crack. That is, a criterion for full crack stability in the lattice is not specified. The problem is simply that some critical amount of opening Mode I is necessary, because without the tensile stress, the crack will simply close on itself. This stability criterion will be brought up again, and dealt with in § 7.

The mechanical equilibrium expressed by eq. (39) is an unstable equilibrium in the usual case where the load is constant tensile stress at infinity, σ_∞. This unstability can be seen from the expression for the energy of the system as a function of crack length,

$$U = 2\int_0^a \left(-f^* + 2\gamma\right) \mathrm{d}l. \tag{40}$$

In this equation, we use a finite crack configuration in which the crack extends from $x=-a$ to $x=+a$. The total crack length is $2a$. Using $f^* = K^2/2\mu$ and the relation (14) relating K to crack length for mode III, we get:

$$U = 4\gamma_a - \frac{\pi\sigma_\infty^2 a^2}{2\mu}. \tag{41}$$

This curve is an inverted parabola, with its maximum at the point of unstable static equilibrium. Thus if K is increased slightly above K_c, catastrophic crack growth occurs, as observed in such brittle materials as glass. The crack healing predicted for $K < K_c$ has been observed by LAWN *et al.* [1980] in very careful experiments, but requires the material to come back together in exact atomic registry, which is often difficult to ensure. Also, in practice, the cleavage surfaces are usually coated by oxides and other films, which makes crack growth an irreversible process.

Another useful relation for the "Griffith criterion" of eq. (39) is obtained by combining eq. (14) with eq. (38):

$$\sigma_C = \left(\frac{4\gamma\mu}{\pi a}\right)^{1/2}. \tag{42}$$

In this equation, σ_∞ given in eq. (14) (the externally applied stress) is renamed as the *critical Griffith stress*, σ_C.

Equations (41) and (42) have different forms when the loading geometry is changed and $K(a)$ is then different from the functional form, eq. (14), used in the derivation (see TADA *et al.* [1973]). The constant coefficients are also somewhat different in modes I or II, given the same crack geometry, and involve other elastic constants. In mode I plane strain, the Griffith relation corresponding to eq. (5.5) is:

$$\begin{aligned} \sigma_C &= \left(2\gamma E/\pi a\right)^{1/2} \quad \text{for plane } \textit{strain}, \\ \sigma_C &= \left[2\gamma E/\pi a\left(1-\nu^2\right)\right]^{1/2} \quad \text{for plane } \textit{stress}. \end{aligned} \tag{43}$$

The fracture criterion, or fracture toughness given in eqs. (38) and (39) for the pure brittle case describes only a few actual materials. Glass, silicon at room temperature, and mica are some examples. Historically, fracture mechanics as developed by Griffith in the 1920s thus had little applicability until Orowan and Irwin in the 1930s independently began the process of generalization to ductile materials when they realized that γ in eqs. (38) and (39) should be thought of as an *effective* surface energy which includes the plastic work done during fracture (see BROEK [1986]).

5.2. Shielding by one dislocation

After the isolated crack, the next simplest configuration is a crack plus one dislocation on the x-axis, for which the equilibrium equations become:

$$f_c = 2\gamma = \frac{k^2}{2\mu} = \left(K - \frac{B\mu}{(2\pi x)^{1/2}}\right)^2 \frac{1}{2\mu}, \tag{44}$$

$$f_d = \frac{KB}{(2\pi x)^{1/2}} - \frac{\mu B^2}{4\pi x} = B\sigma_f. \tag{45}$$

In eqs. (44) and (45), x is the distance along the crack plane, and all quantities are real. $B\sigma_f$ is the lattice resistance to dislocation motion expressed in terms of an effective friction stress, σ_f. B is the Burgers vector, written as a capital to note the possibility that the "dislocation" may be a superdislocation composed of many elementary crystal dislocations. If the external stress as specified through K and the distance, x, are independent variables, the solution is immediate. After eliminating x from eqs. (44) and (45),

$$K_C = \left(2B\mu\sigma_f + k^2\right)^{1/2} = \left(2B\mu\sigma_f + 4\mu\gamma\right)^{1/2}. \tag{46}$$

The local force balance on the core crack is satisfied by the Griffith relation as given in eq. (38), $k^2 = 4\mu\gamma$.

Toughness in a material is an engineering concept developed from the impact testing of specimens, and relates to the energy absorbed on fracture. It is thus also a measure of the resistance to fracture in the sense that a material requiring a high stress to fracture it is also a tough material. To be more precise, K_C is a standard measure of toughness, and thus eq. (46) is a very simple or prototype toughness relation for a material. From the way it was derived, it is also true that high toughness is correlated with high dislocation shielding, and thus to the shielding "charge", B. Since B is also equal to the COD because of eq. (37), the COD is another alternative measure of toughness. Thus a second form of the toughness relation is

$$B = \mathrm{COD} = \frac{K_C^2 - k^2}{2\mu\sigma_f} = \frac{K_C^2 - 4\mu\gamma}{2\mu\sigma_f}. \tag{47}$$

5.3. General shielding and the extrinsic toughness of materials

Although eq. (46) illustrates the basic physics of the fracture toughness problem in a very transparent way, it does not address what the size of the shielding charge is — i.e., what is the size of the superdislocation Burgers vector, B. For this, a more complex theory is required which allows the dislocation distribution to arrange itself in a self-consistent fashion in the presence of sources in the material.

The general statement of the equilibrium problem for an arbitrary configuration of crack plus shielding dislocations is the generalization of eqs. (44) and (45) for an arbitrary number of dislocations:

$$f_c^* = 2\gamma, \quad f_d^*(j) = b_j\sigma_f(\zeta_j), \tag{48}$$

where f_c^* and f_d^* are given by the general relations (35) and (34), respectively. This prescription for solving the problem is intractable except by numerical methods for any but the simplest configurations. To make further progress, assume again that the dislocations are distributed along the x-axis as in fig. 18, so that the dislocation distribution is one-dimensional. The actual discrete distribution is also approximated by a continuous dislocation density.

Concentrating for the moment on the second equation of (48), from eq. (35) the force on the dislocation of Burgers vector b at x is

$$f_d = \frac{Kb}{(2\pi x)^{1/2}} - \frac{\mu b^2}{4\pi x} + \sum_{b_j} \frac{\mu b b_j}{2\pi} \left(\frac{x_j}{x}\right)^{1/2} \frac{1}{x - x_j}. \tag{49}$$

If the Burgers vector is a distributed quantity, then $db = \beta(x)dx$ and the sum becomes an integral:

$$\frac{1}{\beta}\frac{df_d}{dx} = \frac{K}{(2\pi x)^{1/2}} - \frac{\mu\beta dx}{4\pi x} + \frac{\mu}{2\pi}\int_c^d \sqrt{\frac{x'}{x}}\,\frac{\beta(x')}{x - x'}\,dx' \tag{50}$$

where c and d are the points at the beginning and end of the assumed dislocation distribution (fig. 20). The second term on the right is infinitesimal compared to the other terms, and should be dropped. The resulting equation is an integral equation for the unknown function β of a type which has been studied by HEAD and LOUAT [1955] in connection with dislocation pile-up theory.

A special case of eq. (50) has been studied for cracks in mode I by BILBY, COTTRELL, and SWINDEN [1963] (in what is called the BCS model) in which c is set equal to zero. The general equation was solved first by CHANG and OHR [1981] and in modified form by MAJUMDAR and BURNS [1983], and WEERTMAN *et al.* [1983]. In the approximation where $d > c$, very simple relations can be obtained:

$$\frac{k}{K} = \frac{3}{2\pi}\left(\frac{c}{d}\right)^{1/2}\left(\ln\frac{4d}{c} + \frac{4}{3}\right); \tag{51}$$

$$K = 2(2/\pi)^{1/2}\sigma_f\sqrt{d}; \tag{52}$$

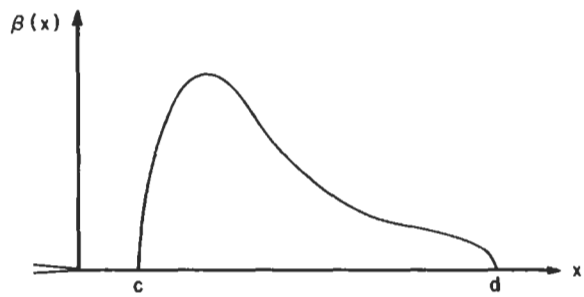

Fig. 20. Solution of eq. (50) for the continuous dislocation distribution, $\beta(x)$. The crack tip is at the origin, and the distribution begins at c and drops to zero at d. There is a strong maximum near c.

References: p. 2287.

$$B = \int_c^d \beta(x)\,\mathrm{d}x = \frac{2K}{\mu}\left(\frac{d}{2\pi}\right)^{1/2}. \tag{53}$$

These equations relate the external K to the local k, to the total dislocation screening charge, B, and to σ_f. The distribution β is a combination of elliptic integral functions, and is sketched in fig. 20. There is a strong maximum near the tip just ahead of the cut-off, c. As $c \to 0$, in the BCS limit, this maximum in fact diverges. It is important to note that as $c \to 0$ the crack becomes completely screened, and $k \to 0$. This latter result is an alternative expression of an important theorem by RICE [1965], that in a continuum treatment of the plastic field surrounding the crack, as the crack expands under an externally applied load, all the energy is absorbed by the plastic field, and none is absorbed by the crack itself. In such a theory, the crack is thus disconnected from the problem entirely. On the other hand, since dislocation densities in materials are almost never high enough to overlap the central nonlinear core region of the defect, there will be a region around the crack tip sufficient in size to establish its elastic identity, and under these conditions, a local k field at the crack tip can be defined. The distance c is the parameter which measures the average distance to the nearest dislocation in the configuration, and constitutes a lower cut-off for the application of continuum deformation theory. The relations (52) and (53) are relatively simple, and do not depend on c. If the field far from the crack and the dislocation screen is characterized by the K-field, then the stress is given there by $\sigma = \mathrm{K}/(2\pi\mathrm{x})^{1/2}$. Where $x = d$, σ should be given by the yield stress, σ_f, on the slip plane at the far end of the dislocation screen. Hence, $\sigma_f \cong \mathrm{K}/(2\pi\mathrm{d})^{1/2}$, which is a good approximation to eq. (52), and is a generally valid result for the size of the plastic zone for any shape of the plastic zone, and for all modes.

Equation (53) gives the total offset plastic displacement at the crack tip generated by the dislocations. In mode I, where a similar relation holds, this is the crack opening displacement known simple as the COD. Combining eqs. (52) and (53) then:

$$\mathrm{COD} = \frac{K^2}{2\mu\sigma_f}, \tag{54}$$

which is the same as eq. (47) for $K_C^2 \gg k^2$. The corresponding result for mode I is:

$$\mathrm{COD}_I = \frac{2K_I^2}{E\sigma_f}, \tag{55}$$

where E is Young's Modulus.

Expressions such as eqs. (47) and (54) have been derived in the literature in numerous ways, and have been widely used in applications of fracture mechanics. In particular, the COD which can be inferred experimentally is a popular measure of toughness, which is then related to K_C through eq. (54). In addition, attempts to correlate the critical COD with a critical strain in front of the crack have been made.

In the equations (51)–(53) however, the total number of dislocations is not determined. This question involves one of the major problems of dislocation theory, yet largely unsolved in a fundamental way, and we shall adopt one of the traditional heuristic

approaches. Namely, a *constitutive relation* is introduced between stress and strain: in this case, between the number of dislocations produced, B, and the local stress. Remembering that σ_f is the negative of the elastic stress on the slip plane, because each dislocation experiences zero net force, such a constitutive relation can be written:

$$\sigma_f = \sigma_0 (B/b)^m. \tag{56}$$

This relation exhibits *work-hardening*, because a larger σ_f is required to achieve a larger B. m is the work-hardening power law parameter, and in such a law σ_0 is the *yield stress*, because it is the value of σ_f for the first dislocation, $B = b$.

As a constitutive relation, however, eq. (56) is very limited, because in an adequate description σ_f should be a function of the *local* density of Burgers vector, not the total integrated value, B. Because the basic integral equations cannot be integrated for such a law however, eq. (56) is the best we can do for analytic results.

Using the constitutive relation, eqs. (51)–(53) can be combined to obtain a second approximation to a toughness relation:

$$K_C = \left(\frac{k^2}{c}\right)^{(1+m)/4m} \eta, \qquad \eta = \frac{\pi^3}{18} \frac{(2\mu)^{1/2}}{\sigma_0^{1/2m} (\ln 4d/c + 4/3)}. \tag{57}$$

This relation is much improved over the primitive relation (46). Since the logarithm term in η is slowly varying, we may simply take η as a collection of material parameters. Then the only parameter in eq. (57) which cannot be determined from macroscopic measurements on materials is the distance c, the average distance from the crack tip to the closest shielding dislocation.

Another interesting relation can be obtained by eliminating K from eq. (51) and (52):

$$k = 3\left(\frac{2}{\pi^3}\right)^{1/2} \sigma_f \sqrt{c} (\ln 4d/c + 4/3). \tag{58}$$

Except for numerical factors, this equation is approximately $k \sim \sigma_f \sqrt{c}$, which says that the stress at the radius of the dislocation-free zone is the local yield stress. This equation was in fact used by THOMSON [1978] and WEERTMAN [1978] as a cut-off in the standard plasticity solution for a crack embedded in a plastic zone, but with an elastic enclave around the core crack. In this work it was possible to incorporate work-hardening in the plastic zone in a more satisfactory manner than eq. (57), with the result given by THOMSON [1978]:

$$K^2 = 2\pi \left(\frac{2\gamma\mu}{\pi}\right)^{(1+m)/2m} / \left(c\sigma_y^2\right)^{(1-m)/2m}, \qquad \sigma = \sigma_y (\varepsilon/\varepsilon_y)^m, \tag{59}$$

where σ_y is the initial yield stress, and m is the work hardening power coefficient. When the dislocation constitutive relations are included in the self-consistent solution of the total equilibrium configuration, as in eqs. (57) and (59), the toughness relations are seen to depend upon the intrinsic surface energy, γ, in an essential way. [Crudely, γ is simply the energy to break the bonds as the fracture is formed; see eq. (38).] The reason is that γ governs the local equilibrium of the core crack, and the required equilibrium between

References: p. 2287.

core crack and dislocation cloud thus involves γ in the expression of the overall toughness of the material. On the other hand, when $K^2 \gg k^2$ in (47) it would appear that γ could be ignored, as has often been claimed in the fracture literature. However, in the simple relation (46), and in the more complex equations (51)–(53), B (and σ_t) depend on γ in an implicit way because of the required overall equilibrium. Hence, it is in general an error to ignore the effect of γ on toughness even for tough materials.

We conclude this attempt to relate the toughness of a material to its fundamental properties by noting the most recent attempt along these lines by HUANG and GERBERICH [1994] who modified earlier models by the same authors. The detailed modeling was shown to be consistent with experimental work by others in the same group, e.g., MARSH and GERBERICH [1994]. The models were numerical extensions of the ideas proposed in this section, in which the loading is Mode I, with the slip plane making a finite angle to the cleavage plane. However, in addition to the complexity introduced into the analysis by the Mode I emission configuration (emission slip plane not on the cleavage plane), the authors found it necessary to invoke a full anisotropic shielding analysis. The toughness relation obtained was of the form,

$$K_{IC} = \frac{1}{\beta} \exp\left(\frac{k_{IG}^2}{\alpha \sigma_y} \right), \tag{60}$$

where K_{IC} and k_{IG} are the external critical stress intensity for fracture, and the Griffith relation, respectively. σ_y is the yield strength of the material, and α and β are parameters. This law has applied to Fe/Si, Mo and to the intermetallics, successfully. It is particularly satisfying to learn from this extensive shielding modeling, and the very careful interpretation of the concomitant experiments, that toughness is actually amenable to fundamental calculation under at least some conditions.

One of the interesting findings of these authors is that the emission condition at the crack tip apparently was not a constant, as would be true if it were controlled by the local stress intensity factor at the crack tip, k_{IC}. This deviation may be due to a non-local effect which has been discussed by SHASTRY *et al.* [1994], caused by a finite sized crack/dislocation core.

5.4. The HRR crack tip field

Although a fundamental understanding of fracture must be built up from the type of dislocation/crack equilibrium analysis of the last paragraphs, wherein a dislocation free zone, and local k_{IC} at the crack tip are featured, there are many cases where totally smeared dislocation distributions can be useful descriptions of the deformation zone. A great deal of continuum mechanical modeling of such models has been done on this basis, much of it using finite element numerical techniques. (See BROEK [1989].) In such contexts, it is often exceedingly useful to have an analytic asymptotic result for the stress fields in the near tip region, known as the HRR field, after HUTCHINSON [1968] and RICE and ROSENGREN [1968]. The relation follows from the assumption that the material follows power law hardening,

$$\varepsilon^p \propto \sigma^n, \tag{61}$$

where ε^p is some plastic strain invariant, and σ is some similarly defined stress invariant. It can be proved (HUTCHINSON [1968]) that the stress and strain can be factored into r-dependent and angular-dependent functions. If it is assumed that the energy contained in a finite element circle centered at the crack tip is finite, and that the stress is singular there, then the quantity, $(r\varepsilon^p\sigma)$, is finite, and thus that $n(p+1)=-1$. Thus, at the crack tip, the stress, and from eq. (5.1), the strain, must have the asymptotic forms,

$$\begin{aligned} \sigma_{ij} &= \frac{K}{r^{1/(n+1)}} f_{ij}(\theta) \\ \varepsilon^p &= \alpha \frac{K^n}{r^{n/(n+1)}} g_{ij}(\theta), \end{aligned} \tag{62}$$

where θ is the angle at the crack tip, and α is a constant derived from the power law, Eqn. (61). K is a constant — not to be confused with the stress intensity factor. (It is unfortunate two different K's are introduced at this stage, but we have followed the standard practice.)

This asymptotic relation is very useful in engineering studies of plastic fracture. For example, the constant, K, is directly related to the J, and hence to the fracture condition. Further discussion of these points will be found in the books by BROEK [1986] and KANNINEN and POPELAR [1985].

5.5. Summary

In summary, the burden of this section has been to show that on a fundamental level, if a crack exists in a material, the material will fracture at a very low value of toughness unless the material can respond plastically to the high stress-concentration immediately surrounding the crack tip. If dislocations can be generated in this region, then the effect of these dislocations is to shield the crack from the external stress field after a portion of the antishielding dislocation population has been absorbed by the cleavage surface. The degree of shielding, or the level of toughness achievable, is then determined by the yield stress, work-hardening characteristics of the medium, and the size of the inner elastic enclave. It also, of course, depends upon the local critical k of the crack, which we have suggested is determined by the true surface energy of the solid, but may in fact be more complex for reasons discussed in the section.

The descriptions and Mode III models used have, of course, been very simple, so the relations derived cannot be expected to describe in detail the complex fracture phenomena observed in a polycrystalline multiphase material such as a practical steel. Their major purpose, of course, is to demonstrate the materials science principles which underlie fracture toughness, and in particular the role of dislocations in multiplying the intrinsic lattice toughness of a crack by many orders of magnitude. Specifically, a typical value of k is of order 2×10^5 Pa$\sqrt{\text{m}}$, whereas, from eq. (59) one infers toughness values of order $K=50$ MPa$\sqrt{\text{m}}$ for a high-strength steel.

There are several fundamental limitations of the model used which must be kept in

mind, and which will suggest to the materials scientist further elaborations which may be used to achieve more satisfactory descriptions of cracks in materials:

a. It has always been assumed here that the fracture processes depend on the external shape of the sample and other macroscopic quantities, such as crack length, only through the stress intensity factor, K. The dependence of K on shape of sample, crack length, and the geometry of the stress application all lie in the domain of macroscopic stress analysis, and our approximation amounts to what is termed the two-dimensional small-scale yielding case, where the crack length is small compared to distances to all external surfaces in x_1 and x_2 directions, and the deformation zone is in turn small compared to the crack length. On the other hand, macrostructural inhomogeneities such as precipitates and grain boundaries are also assumed to be absent, and this is a much more serious assumption. To some degree, one can incorporate these effects in the dislocation constitutive law parameters, but we have already expressed reservations about the adequacy of the constitutive-law approach to deformation theory, especially in the region nearest the crack tip. A second difficulty concerns the interaction of the crack itself with microstructural inhomogeneities. By using interfacial surface energy ideas, one can make some progress in this direction by generalizing the Griffith argument for grain boundaries. However, the three-dimensional effects of cracks moving along faceted grain boundaries and precipitate interfaces, and the pinning effects of precipitates to cracks, introduce mathematical complexities which have not yet been worked out for cracks. In short, our understanding of three-dimensional crack interactions is very primitive when compared with the status of similar dislocation pinning theories. One promising approach would be to use the crack–dislocation analogue for these three dimensional crack configurations.

b. We have relied primarily on mode III in the analysis. This approach is analogous to studying dislocation theory by restricting oneself to screw dislocations. Nevertheless, the obvious geometrical generalizations are easy to make to modes I and II, and the analytic results are expected to be correct in a qualitative sense. The success of Gerberich and his group (see HUANG and GERBERICH [1994]) demonstrates the general correctness of these physical ideas and suggests that quantitative predictions in realistic cases may ultimately be expected. For example, the general applicability of eq. (60) is not yet demonstrated, but looks plausible.

c. The analysis leading up to the relations for f_c^* assumed the crack was sharp, and yet the requirement for COD $\neq 0$ is an essential aspect of a shielded crack as shown in eq. (37). Certainly, there is no difficulty so long as the COD is small, and the crack-opening angle is near zero. However, as the COD is increased, the changed geometry of the crack surface behind the tip will lower the stress on the atom bonds at the crack tip. Indeed, if the material is sufficiently soft, plastically, then the stress at the crack tip may never be able to achieve a value sufficient to break the atomic bonds — in our terminology k_{critical} cannot be achieved because of progressively greater combined blunting and shielding and the crack will never cleave. Only continued plastic blunting of the crack

can occur. This process is, of course, precisely what happens during fully plastic failure. During fibrous fracture by hole growth, small cracks open ahead of the main crack and are progressively blunted out as soon as they are formed. In addition, the dramatic transition from relatively brittle fracture to ductile fracture observed when the temperature is varied in some steels and many other materials is also to be understood on these grounds (see § 10.4).

d. In fig. 19, antishielding dislocations are absorbed at the crack. Generally, of course, only a small fraction of the total dislocations formed in the dislocation screen will be absorbed. That is, the majority of dislocations in the screen cancel each other out, leaving only a small fraction of the total population (sometimes termed the geometric dislocation component) to perform the shielding function. Thus, in the analysis, sums over dislocations and Burgers vectors are in effect sums over the local *net* Burgers vector. The nonshielding dislocations are important, however, because they provide the essential work-hardening interactions which ultimately limit the total shielding dislocation density. They are also important, because as a crack moves through the material, the large tangled mass of nonshielding dislocations is left behind as a wake. Thus the energy required to form this wake, most of which is immediately converted into heat during the formation of the dislocation tangles, must be supplied by the crack and its effective screening charge of geometric dislocations as they move through the material. The rate of doing this work is the effective surface energy postulated by IRWIN [1948] and OROWAN [1948], and is given by the relation

$$\frac{K_C^2}{2\mu} = 2\gamma_{\text{eff}}. \tag{63}$$

6. *Atomic structure of cracks: theory*

In the next three sections, we leave the realm of continuum elasticity in order to deal with the fundamental atomic bonding considerations which determine the Griffith relation, and which also determine the criterion for dislocation emission.

6.1. Methodology

Atomic modeling of cracks is not, in principle, different from modeling of other defects in solids, but cracks are much more difficult to treat than other defects for two reasons.

First, a crack tip is a highly distorted region of incipient surface, where bonds are being completely broken. This type of distortion is thus much more severe than that of a vacancy or even a dislocation core, and it is more severe than the perfect surface, in part, because the highly inhomogeneous strain field destroys the 2D symmetry of the true surface. Thus the force laws used in the modeling must be robust, and appropriate to the crack application.

A second reason why the crack is difficult to model is that the strain field is long

ranged. In the case of the crack, the strains fall off with distance as $1/\sqrt{r}$, which is longer ranged than any other lattice defect, and this fact makes modeling the core very sensitive to total system size. There are two general ways of modeling such systems. In one method, the defect is embedded in a lattice of finite size, with a true bounding surface (surface boundary conditions). In the second, the defect is embedded in a "super cell" which is repeated, periodically, in all directions (periodic boundary conditions). In either case, unless the super cell or system size is very large, the distortions in the crack tip will be modified by the repeating cracks in neighboring cells, or by the image terms in the surface. For a 2D model of a crack, in practice, the crack must be of order 100 atom spacings so that short crack corrections are not necessary, and the cell size must be at least an order of magnitude greater than the crack length to make image terms negligible. Thus, in 2D, the system or super cell must contain of order 10^6 lattice points for adequate detailed atomic scale modeling of the crack tip energetics and other phenomena. This is a very severe requirement, and makes first principles approaches to crack tip phenomena impossible, because the quantum mechanical problem becomes intractable for more than a few hundred atoms.

Nevertheless, atomic modeling of cracks has a respectable history, beginning with GOODIER (and Kanninen) [1966]. This work dealt with a very simple model of a 2D cubic lattice with nonlinear springs attached across the cleavage plane. Subsequently, Kanninen and coworkers at Battelle addressed the iron lattice with the "Johnson potential". See the review by MARKWORTH, KANNINEN and GEHLEN [1973]. This latter work constitutes the serious beginning of crack modeling, because the authors put a crack of respectable length into a realistic crystal with a model force law. The rather inadequate methodology used at the time was subsequently developed by these authors into one of the successful techniques still used to model cracks, which we will term the enclave method. In this method, a relatively small number of atoms is embedded within a larger continuum region. At the boundary between the atomic and continuum regions, forces must be applied between the two regions, which are obtained from the asymptotic continuum solutions. See HOAGLAND and LIU [1994] for a modern incarnation of this technique, and references to earlier work.

Modern methods used for studying the crack can conveniently be divided into static and dynamic techniques. In the first, an equilibrium static structure or configuration is found, the enclave method described above being an excellent example. Although apparently severely limited by the static requirement, the method can be, and is, used to find saddle points, and to calculate activation energies, from which kinetic descriptions can be built on the basis of reaction rate theory. A variation on the enclave method has been developed by KOHLHOFF, GUMBSCH and FISCHMEISTER [1991], in which the inner discrete atomic region is connected to an outer region modeled by the finite element approach. A spring network model, another static method, has been used by a number of authors to study failure in random networks. In this case, usually the application is not to an atomic scale lattice, but each lattice point represents a microstructural element with random failure criteria, in order to simulate the failure of a material at the microstructural level. See CURTIN [1993], BEALE and SROLOVITZ [1988], and LI and DUXBURY [1988].

The most popular method for modeling defects, in general, is the molecular dynamics

technique, wherein the computer simply solves the classical mechanics problem of many atoms interacting by specified force laws. In this case, the problem is time dependent and dynamic, and atomic motion as well as system dynamic response can be studied. Molecular dynamics approaches to the study of cracks were first used by Dienes, Paskin, Sieradzki and their coworkers. Specifically, 2D models of simple lattices with pair force laws were used to explore the generic behavior of cracks in lattices. See the review article by DIENES and PASKIN [1987]. Typically, most recent modeling in molecular dynamics has been with the EAM force laws to be discussed below.

The problem of "force laws" is a serious one for the fracture problem because of the difficulty we have alluded to above regarding the high distortions in the incipient surface and high deformation characteristic of the crack tip region. Also, because of the current impossibility of modeling the crack tip with first principles quantum mechanics, already mentioned, all force laws in computer simulations must be a variety of empirical or semi-empirical force law. Recent progress in the development of the semi-empirical force laws, especially those for many body interactions has been rapid, and crack modeling has profited considerably. But because these force laws must usually be fitted to parameters which are not very closely related to the crack problem, it is probably fair to say that we do not have a picture of the crack structure which is truly reliable for any actual material. This is an unfortunate consequence of the fact that the distorted incipient surface character of the crack tip represents a very severe case. It is thus necessary to "make do" with semi-empirical force laws like the widely used *embedded atom method* (EAM). (See DAW [1989].) In spite of this difficulty, however, current computer modeling can yield much generic information about the atomic properties of the crack. See DAW *et al.* [1986] and HOAGLAND and LIU [1994]. Also see de CELLIS *et al.* [1983] and CHEUNG and YIP [1990] for a treatment of the ductility of fcc copper and bcc iron and for references to other papers on the general ductility question.

The author and coworkers have taken a different approach to the problem, using a static technique based on lattice Green's functions. In their work, the goal is to study the generic behavior of cracks in simple lattices with simple force laws, so that the limits of the elastic picture of cracks can be critically examined. Their method features a very large number of atoms in the super cell (typically 4×10^6 atoms), with a finite crack of 100–200 atoms length, and a nonlinear region containing dislocations interacting with the crack which extend over 10–40 atoms in front of, or to the side of the crack. In the method, the crack and its attendant dislocations are embedded in a lattice whose distortions are assumed to be restricted to the linear regime of the force laws. Then the nonlinear portions of the cores of the defects are treated numerically. The method is rigorous, and it is fast, because in any problem with a small number of defects present, the number of nonlinear bonds is small enough to allow very fast numerical computation — typically of the order of a minute for a fully converged solution. The reader will find a description of the method for the general defect (including the interface) in THOMSON *et al.* [1992], and some of the applications of the method will be discussed in subsequent sections.

References: p. 2287.

6.2. Lattice trapping and slow crack growth

The simplest lattice property of a crack, its trapping by the lattice analogous to the Peierls trapping of the dislocation, will be presented here to illustrate in a rather elegant way the characteristic features of a crack in a lattice. This trapping will then be correlated with certain features of the response of a crack to chemical attack.

The argument will proceed in a series of steps. 1) Consider an infinite 2D lattice of atoms interconnected by springs. For the moment these springs will be considered to be true linear springs. 2) A finite crack is constructed in the lattice by cutting all the bonds crossing the chosen cleavage plane in the lattice between the two ends of the crack. See fig. 5. The length of the crack will be $2L+1$ lattice spacings. For definiteness, the simple cubic lattice of fig. 5 will be considered, but the analysis is generally applicable to any lattice structure. 3) Load the lattice, so the crack faces are pulled out of range of the atoms opposing one another across the cleavage plane. The load may be exerted on the upper and lower cleavage plane as shown in fig. 5, or it may be exerted on the far boundaries of the lattice. The load is obviously important, however, because the bonds of the crystal will close the crack unless the load is sufficient to keep the crack open against the atomic bonds in the tip region, and we return to this subtle issue later.

The construction to this point relates entirely to a linear lattice, and cutting bonds in the original linear lattice still leaves a linear system. Thus, a graph of the displacement response at a lattice site anywhere in the system to a load exerted anywhere else in the system is a simple linear line. Specifically, the displacement at the center of the crack in fig. 5 where the load is applied is graphed in fig. 21, for a variety of crack lengths. Since the compliance of the total system is greater as more bonds are snipped in the system (the crack grows in length), the slope of the displacement curve in the figure decreases

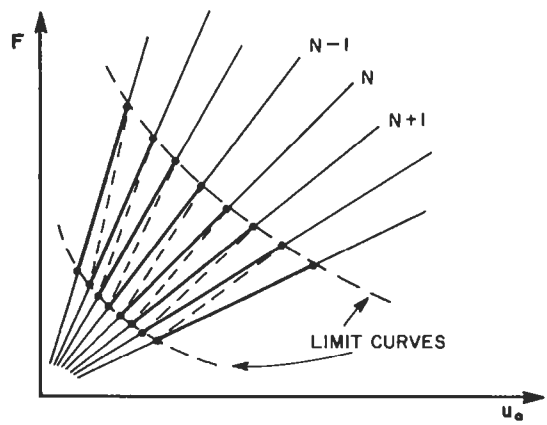

Fig. 21. Solution of eq. (61). A family of compliance curves is generated for various values of crack length, N. The curves are limited at a maximum displacement by the bond strength at the tip, and at a minimum displacement by reconnection of the first broken bond at the tip. At the maximum displacement for N, the solution snaps back to $N+1$ at the minimum, as shown by the dotted lines, provided F can be varied at the same time.

as the crack length increases. Thus, for different crack lengths, there results a family of linear displacement curves, as shown.

In the next step, (4), a "force law" is assumed, such that the bond is a linear spring up to some critical displacement in the spring, where the force drops discontinuously to zero, as shown in fig. 22. Further, the load is adjusted such that the first connected bond at the tip, $(n=\pm(L+1))$, is within the linear portion of the force law, but the last snipped bond, $(n=\pm L)$, has a displacement larger than the critical value. Now, if the crack length is finite, there exists a range of loads above which the first connected bond breaks, and below which the last snipped bond will reconnect to its neighbor across the cleavage plane. Beyond these limiting values for a given value of L, no solution exits. Thus, the family of response curves in fig. 21 has two limit curves, $F_{max}(L)$ and $F_{min}(L)$, as shown.

Figure 21 demonstrates the phenomenon of lattice trapping, because for each length of crack, there exists a range of loads over which the crack is mechanically stable at the given crack length. Further, if the load is raised above the upper critical value where the first connected bond at the tip snaps (see fig. 21), the crack will grow by one lattice spacing to the next stable solution. Likewise, as the load is decreased below the lower critical value, the crack will heal by one lattice spacing. The full lines in fig. 21 correspond to fully stable positions. But there also exist a set of unstable positions, shown by the dotted lines, which connect the upper limiting point on the curve for crack length, L, and the lower limiting point for crack length $L+1$. These solutions correspond to finding an intermediate load between F_{max} and F_{min} where the first broken bond is just exactly connected. A moment's thought will convince the reader that such a solution is unstable. Now we assume that a force law like that in fig. 22b acts between the atoms. Then the response curve becomes rounded, like that shown in fig. 23, drawn for two lengths of crack.

Suppose, now, that an intermediate load is applied somewhere in the middle of the trapping range for a given crack length, so the crack is stable. If the system were embedded in a thermal bath, local fluctuations in the forces in the bonds at the crack tip would permit the crack to grow or heal, even when the crack is mechanically stable under the externally applied load. To find the rate for this thermally induced growth, an energy description is needed so the energy of surmounting the barrier can be calculated. For this purpose, let F_0 be the externally imposed force at the middle of the crack of fig. 5. The activation energy to carry the crack over the barrier can be calculated by increasing the external force to the upper critical value, and then decreasing the force,

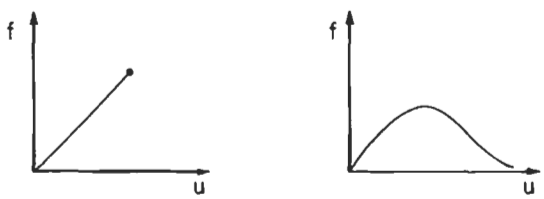

Fig. 22. Bond forces, f. A variety of bond forces are discussed. In the left-hand part, the force is a snapping spring. In the right-hand part, a more realistic nonlinear force is shown.

References: p. 2287.

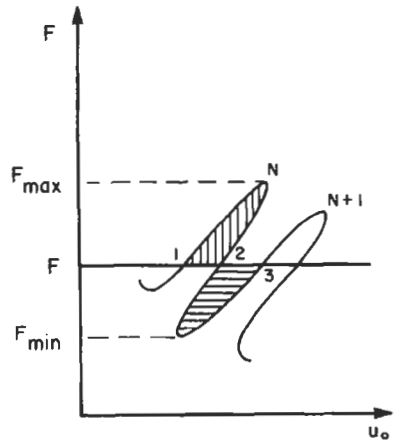

Fig. 23. Crack solution for nonlinear forces for N and $N+1$. For a given F, several discrete solutions are possible. Positions 1 and 3 are stable. Position 2 is unstable. The cross-hatched areas correspond to trapping barriers. That from 1 to 2 is a forward barrier and that from 3 to 2 is a reverse barrier.

with the system responding along the unstable portion of the response diagram — the dotted line in fig. 21, and the reverse part of the line in fig. 23. When F is decreased back to its initial value, F_0, on the unstable line, an amount of work has been done on the system given by the integral, $\int_1^2 F\,du(0)$, where $u(0)$ is the relative displacement of the pair of atoms facing each other across the cleavage plane at the point of application of the force. The integral is taken over the excursion of the system in following the line enclosing the vertically hatched region. In the energy bookkeeping, one must include the energy change in the loading system in order to calculate the total energy of the complete system when a thermal fluctuation takes place. This additional work is simply given by the change in potential energy of the load system during the fluctuation, $F\Delta u_0$, and this change is negative. Thus, the energy change in the total system including the loading system is given by the area enclosed by the vertically hatched region above the horizontal line at F, and is given by the equation

$$\Delta U = \int_1^2 F\big(u(0)\big)\,du(0) - F_0\Delta u(0). \tag{64}$$

This equation gives the energy to go from the stable point, 1, to the unstable point, 2. Being an unstable point, the state at 2 must be an energy maximum, and ΔU must be the energy barrier for motion of the crack through the lattice at the load, F_0. The activation energy is thus given by the vertically hatched region in fig. 23.

The reader will recall that the theory here applies to the 2D crack, and may be concerned that the physical 3D crack might be different. Indeed, in 3D the fluctuations involve the nucleation of 3D kink pairs on the crack, just as a thermally fluctuating dislocation moves by the nucleation and growth of 3D kink pairs on the 2D dislocation line. (See THOMSON *et al.* [1987].) Beyond noting the added complexity needed to complete

the theory of crack growth by considering kinks, we continue here with the 2D picture.

With these caveats, the very simple argument presented shows the fundamental differences between the continuum crack and the lattice description.

Just as in the similar lattice theory of dislocations due to Peierls, the lattice trapping barriers for cracks must depend on the shape of the force law. Simulations of actual lattices with reasonable force laws have shown that the lattice barriers are actually small in all cases which have been investigated, with the possible exception of Si and its relatives. In fact, the existence of significant barriers has been associated with the shape, and specifically of the slope, of the back side of the force law for the material. (See THOMSON *et al.* [1987].) In the normal case, where the slope of the force law on its back side is considerably less than on its front, the barriers are negligible. However, in certain types of chemical reactions, it is possible for the system to jump rather suddenly from one electronic configuration to another. In such cases, the "slope" will be high, and it is possible for the barriers to be significant, and observable. It has been proposed that precisely this mechanism is responsible for the phenomenon of slow crack growth in silica glass. (See THOMSON and FULLER [1982].)

Figure 24 from WIEDERHORN *et al.* [1980] shows slow crack growth in silica glass in the presence of varying partial pressures of water vapor. The crack velocity is shown to be a strong function of the applied stress. This stress dependence of the velocity follows directly from eq. (64), because as the load is increased, the energy barrier is decreased, roughly linearly with the stress. (This dependence is seen from fig. 23, when the value

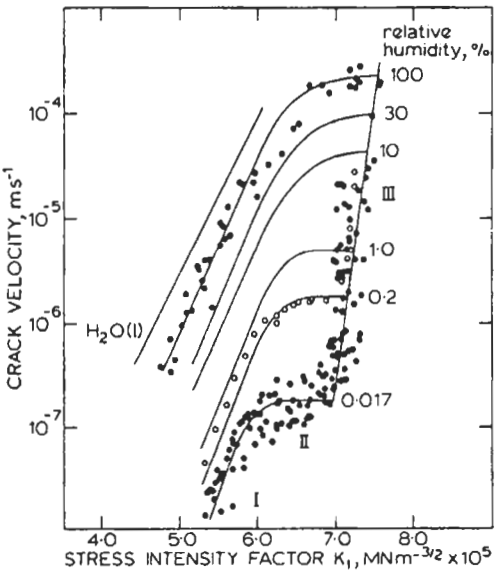

Fig. 24. Slow crack growth of glass in water. Three regions are observed. Region I corresponds to the chemically enhanced growth theory displayed here. In Region II, the external environment is outrun by the crack. Region III is the intrinsic growth region. (After WIEDERHORN *et al.* [1980], courtesy S. WIEDERHORN).

References: p. 2287.

of F_0 is increased, the vertically hatched area decreases roughly linearly with the increase in applied load.) A better check of the theory would be a measurement of the temperature dependence of the velocity, and one report of the temperature dependence does not agree with eq. (6.1), suggesting a different interpretation, FISK and MICHALSKE [1985]. However, in the opinion of the author, additional experiments on this phenomenon are desireable before a conclusion should be drawn regarding the controlling mechanism.

MICHALSKE and FREIMAN [1983] have shown that slow crack growth is a rather general phenomenon in a variety of materials, with a range of chemical agents. The chemically assisted slow crack growth is very chemically specific, however, in that different environments affect different materials in quite different ways. The reader is referred to the excellent review by White for guidance on the subject of chemical effects in ceramics, WHITE [1994].

6.3. The Griffith condition

In fig. 23, to go from the unstable point, 2, to the next stable point at 3, the system must go through the excursion from 2 through the lower minimum point for F_{min} to the point 3. In order to climb up from the stable point, 1, to the unstable point, 2, the work done on the system is greater than the energy absorbed by the loading system, so the energy change is positive. In going from 2 to 3, however, by the same argument, the energy change is negative. This negative energy is given by the horizontally hatched area in fig. 23. If, however, the system is initially at 3, then to reverse the path from 3 to 2 requires a positive energy given by the integral,

$$\Delta U_{3,2} = \int_3^2 F\big(u(0)\big), \mathrm{d}u(0) - \Delta F_0 4(0). \tag{65}$$

The first process described by eq. (64) represents positive crack growth, while the second, in eq. (65), represents negative crack growth, or crack healing. At any given crack position in the lattice, thermal fluctuations will test both the positive and the negative barriers, and net crack growth will be due to the difference between them. This difference is also the difference in the areas of the horizontally and vertically shaded regions of fig. 23. If $\Delta U_+ = \int_1^2 F(u(0))$, $\mathrm{d}u(0)$ and $\Delta U_- = \int_3^2 F(u(0))$, $\mathrm{d}u(0)$, then the net velocity of the fluctuating crack is given by

$$v = v_0 \exp - \big(\Delta U_\pm \Delta_-\big)/kT. \tag{66}$$

Here, v_0 is an entropy factor which would typically be computed in reaction rate theory and T is the temperature. When the forward and reverse energy barriers are equal, the crack is quiescent in the lattice, and the crack is at its thermal equilibrium length. This condition for the cracked lattice is, therefore, just the thermodynamic Griffith condition for the lattice. (A small point of rigor might be mentioned here: The v_0 for forward and backward motion is not exactly the same, because the entropy for the forward motion is not the same as for the backward one, but except for this very minor point, eq. (66) is the Griffith condition for the crack in the lattice.)

This Griffith condition, however, is quite different in its form from the Griffith

condition, eq. (60), expressed in terms of the stress intensity factor and the intrinsic surface energy. This difference is due to the fundamentally different ideas involved in the continuum and lattice descriptions of the crack. In the continuum, crack theory is a theory of singularities in the elastic field, and in particular, the stress intensity factor is a measure of the strength of the crack singularity. In the lattice theory, on the other hand, all singularities disappear, and so do their descriptors such as the stress intensity factor. However, energy is a valid concept in both theories, and through it, a correspondence between the two can be reached.

The energy of the finite crack in the continuum is given by eq. (41), and is graphed as the dotted parabola in fig. 25 with the Griffith point for the continuum at the maximum in the curve. According to the lattice theory, for a particular crack length, and a given load, there is only one solution. But for the given load, there are a finite number of solutions for different crack lengths. These are given as the points at the local minima in the "dinosaur back" function shown in fig. 25. If we choose some parameter in the lattice for a "reaction coordinate", and if this reaction coordinate is analogous to, and reduces to, the crack length in the continuum theory, then we can draw the energy of the lattice in fig. 25 as the solid "dinosaur back" curve through the points of mechanical equilibrium. The local energy minima are separated from one another by the energy barriers of eqs. (64) and (65). The thermodynamic lattice Griffith point can be shown to correspond to the global maximum in the dinosaur back function, THOMSON [1980], and at that point, the total system energy is stationary. That is, the elastic energy change in the system including the load mechanism, is balanced by the surface tension. This lattice Griffith condition thus has precisely the same properties as the continuum theory Griffith condition. When the crack is long, the Griffith condition occurs in both theories at the same crack length, and under these circumstances, the correspondence between the two is demonstrated. As noted above, the concept of stress intensity factor is not used to prove the correspondence theorem, but if the stress intensity factor is expressed in terms

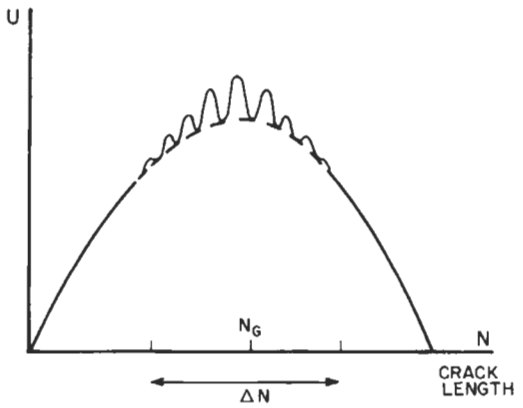

Fig. 25. Modified Griffith energy function. The smooth parabolic curve corresponding to eq. (41) (dashed), becomes a "dinosaur back" function. The trapping occurs over the range ΔN about the central maximum at N_G.

References: p. 2287.

of the load and crack length through relations such as eq. (14), then when the crack is long compared to a lattice spacing, the stress intensity factor can be converted into a valid lattice concept.

The thermodynamic Griffith condition for the lattice is defined as the quiescent state for the crack. As the load deviates above the Griffith value, the crack will advance over the barriers. As it grows in length, the barriers decrease in value, and the crack accelerates until dynamic crack advance occurs when the lattice barriers disappear. Similarly, below the Griffith value the crack will heal by thermal processes until the lattice trapping disappears. Because it is difficult to achieve the experimental conditions for fully reversible crack healing (the surfaces must heal exactly with no defects), crack healing is normally not observed. LAWN *et al.* [1980], however, do report healing results in careful experiments designed to observe it.

7. *Atomic structure of cracks: dislocation emission*

For metals, the most important aspect of the atomic structure of the crack is the stability of the crack against shear breakdown at the tip and the consequent emission of a dislocation. As discussed in § 2, the shear stability of the crack is associated with what is called the intrinsic ductility of the material. In this section, we will first demonstrate the connection between the ductility of the material and the emission of dislocations, review results for the emission criterion, and then return to a more general discussion of material ductility and of ductile/brittle transitions in the light of these results. The section will end with a discussion of the overall stability of a crack in the lattice.

KELLY *et al.* [1967] first noted that an atomically sharp crack, if it is in equilibrium with its atomic forces at the tip, must have tensile stresses there of the order of the theoretical tensile strength of the solid, and that this implies that the tip region must also be near its shear strength, as well. RICE and THOMSON [1974] then pointed out that if shear breakdown occurs, a dislocation is emitted from the crack tip, and that if this emission takes place at an angle to the crack tip, the crack is blunted. See fig. 26.

When the crack is blunted, the stress singularity at the crack tip is altered, because it is no longer a sharp slit, and the crack at its tip is no longer describable as a "K-field". If this is true, the Eshelby theorem says that the elastic force on the crack disappears.

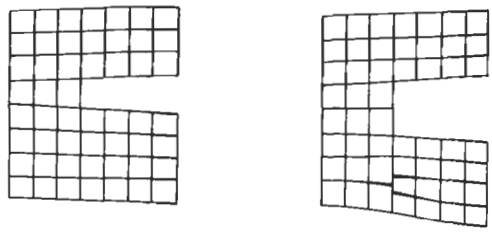

Fig. 26. Crack tip breakdown in shear by dislocation emission.

The physical reason for this is that the blunted crack cannot be translated rigidly in the lattice unless it creates a series of dislocations to propagate the blunted shape. This dislocation production violates the elastic assumptions of the theory. The result is that the crack is no longer mobile, unless a new sharp cleavage crack is nucleated from the blunted region. Thus the blunted crack is "ductile" in the sense that its cleavability has been destroyed. Under increasing stress, it simply continues to blunt itself, and emit more dislocations. Thus, the intrinsic ability of the bonds of the tip region to stabilize in a cleavage configuration is a fundamental property which separates materials which can cleave from those which cannot. Clearly, this is a property of the bonding of the material. (Later, we will see how other considerations besides the bonding enter, as well.)

7.1. Dislocation emission criteria

In the original treatment of Rice and Thomson, the authors considered the fate of a dislocation as it emerges from a crack tip. According to eq. (35), as the dislocation emerges, because of the different distance dependence of the image and K-field terms, the dislocation first experiences a net attractive force and beyond a critical distance, a net repulsive force from the crack tip. But a dislocation can only experience an elastic force if it is at a distance from the crack tip greater than its core size. That is, for the emerging dislocation, the dislocation must be "well formed", before elastic equations can be applied. Thus, if the core of the dislocation is larger than the critical distance, where the force is attractive, then the dislocation will always experience a repulsive force from the crack tip, and the crack is mechanically unstable against emission of the dislocation. If the core of the dislocation is less than the critical distance, then the crack tip is stable against the emission.

These words can be converted into equations by writing down from eq. (35) the critical stress intensity, K_{Ie}, for which the net force on the dislocation is zero at the dislocation core size, r_0

$$K_{Ie} = \frac{\mu b}{(1-\nu)}\sqrt{\frac{Y(\theta)}{8\pi r_0}}. \tag{67}$$

A factor, Y, is introduced to account for geometric corrections when the dislocation is emitted at angle θ to the cleavage plane, and the factor, $1-\nu$, to generalize eq. (35) to the Mode I case.

By comparing the critical condition for emission with the critical condition for emission, the material is determined to be intrinsically brittle or ductile. That is, if $K_{Ic} < K_{Ie}$, the material is intrinsically brittle, and vice versa. In terms of their associated crack extension forces, a brittle/ductile crossover parameter, $\mathscr{D}$, is defined from $\mathscr{G}$ by the relation

$$\mathscr{D} = \frac{\mathscr{G}_{Ie}}{\mathscr{G}_{Ic}} = Y\frac{b}{32\pi(1-\nu)r_0}\frac{\mu b}{\gamma_s}, \tag{68}$$

When $\mathscr{D} < 1$, the material is ductile, and vice versa. With typical values of the parameters, it turns out that $\mu b/\gamma_s \simeq 10$ is the critical crossover point. Note this is a universal

relation, which can be compared for different types of materials. RICE and THOMSON [1974] predicted that using this criterion, and taking account of the variation of the core size with type of material, that the fcc metals should be ductile, and the bcc metals (except for the alkalis), the ionic crystals and the diamond cubic materials should be brittle. On this criterion, Fe is a borderline material between ductile and brittle behavior.

Since that paper, there have been a number of alternative treatments and improvements. Notably, WEERTMAN [1981] pointed out that if a dislocation pair is nucleated in the high shear stress region near the core, one dislocation will be captured by the crack (experience a negative force) and the other will be repelled from it under the same conditions, essentially, as in the Rice–Thomson criterion. SCHOECK [1991] discussed the criterion with the force balance on a Peierls-type distributed core model of the emitting dislocation, with a result which was again similar to the Rice–Thomson criterion, except that the core size was specified in terms of the Peierls model of the dislocation.

HOAGLAND and HEINISCH [1992] have carried out a particularly interesting study of the emission criterion from a very different point of view from other authors. They studied the fcc lattice with the Al EAM potential in two different configurations, one of which is ductile and the other brittle. They showed that the elastic parameter, M, can be interpreted in terms of a blunting configuration force. The details are beyond the discussion here, but briefly, M is defined from the Eshelby equation, eq. (23),

$$\begin{aligned} f_m &= \int P_{ij} dS_j \\ M &= \int x_i P_{ij} dS_j \\ &= 2\gamma_s R + \mathbf{v}\mathbf{F}. \end{aligned} \tag{69}$$

In this equation, the second line is a definition, and the third line represents a theorem by Rice that M depends upon the origin of coordinates for the crack, with $\mathbf{v}$ equal to the radius vector from the crack tip to the origin. $\mathbf{F}$ is then a configurational force on the crack tip, and the first term is valid for an integral over a circular radius of value R centered at the crack tip. When the crack is blunted, HOAGLAND *et al.* [1992] show that $\mathbf{v}$ is the blunting distance, and $\mathbf{F}$ becomes a nonzero blunting force acting at the crack tip in the lattice calculations. Unfortunately, no elastically based predictions are available for the magnitude of this force, and no prescriptions are available for using it to predict a brittle/ductile crossover criterion. For further details, the reader is referred to the paper by HOAGLAND and HEINISCH [1992].

Finally, RICE [1992] returned to the problem with a significant variation of the Rice/Thomson analysis, which we shall discuss in detail. Consider a crack with an emerging dislocation on the cleavage plane under pure Mode II load. That is, the dislocations have the same relation to the crack tip as shown in fig. 18. Rice adopts the Peierls view of the emerging (distributed) dislocation core, and notes that the lattice resistance stress exerted on an element, db, of the dislocation distribution is given by the Peierls misfit stress, σ_{12}^{mf}, shown in fig. 27. If the dislocation element at dx on the axis is given by $db = \beta(x)dx$, then the total misfit force in the x-direction exerted on the total emerging dislocation core can be written as

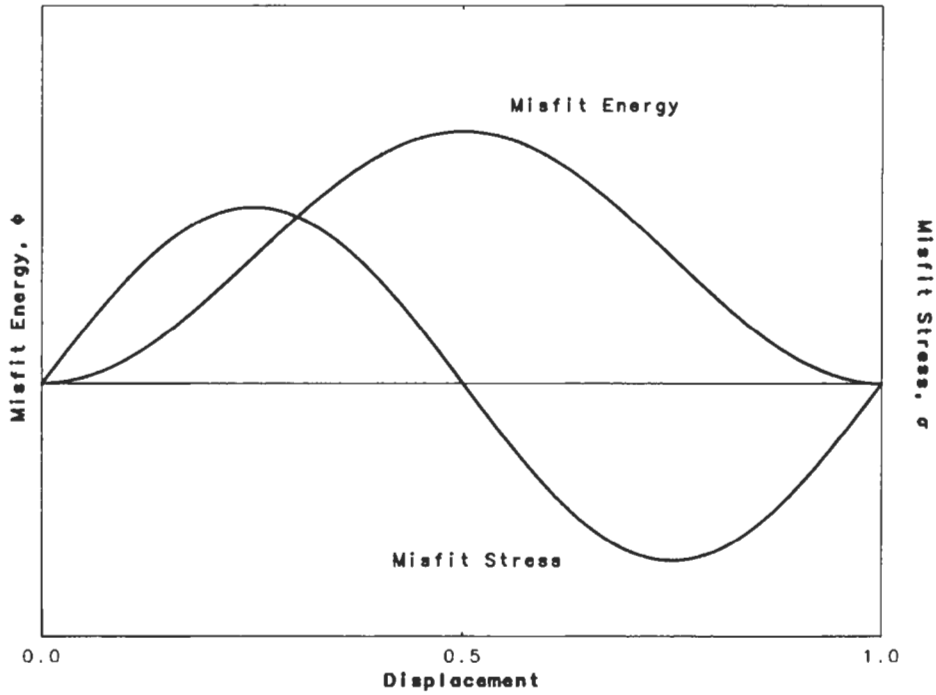

Fig. 27. Graph of the misfit stress, σ, and misfit energy, Φ, as functions of the shear displacement of two block lattices past one another.

$$f_d^{(mf)} = \int_{tip}^{\infty} \beta(x)\sigma_{12}^{(mf)}\,dx = \int_{tip}^{\infty} \sigma_{12}^{(mf)} \frac{d\delta_x}{dx}\,dx = \Phi_{tip}. \tag{70}$$

Here we have used the fact that the local dislocation density is equivalent to the local strain, $d\delta_x/dx$, where δ_x is the relative shear displacement across the slip plane, also called the crack opening displacement (in shear). The second integral on the right is just the total strain energy per atom pair of the lattice, due to the misfit stress, at the crack tip graphed as Φ in fig. 27. Rice notes that since there is no dislocation free zone at the crack tip as the dislocation emerges, the stress there must be finite, and thus there can be no local stress intensity, $k_{II}=0$. That is, the shielding of the emerging dislocation just exactly cancels the applied load, K_{II}. (See the discussion surrounding eqs. (51)–(53).) In this case, from eq. (27), the externally applied driving force on the entire system, $(1-\nu)K_I^2/2\mu$, is exactly cancelled by the lattice misfit stress,

$$f_{total} = 0 = \frac{(1-\nu)K_{II}^2}{2\mu} - f_d^{mf}. \tag{71}$$

When the misfit energy function, Φ_{tip} in fig. 27 reaches its maximum, the system can no longer sustain an equilibrium of forces, and the dislocation is emitted. Thus, at emission, the Burgers vector is $b/2$, and

References: p. 2287.

$$\mathcal{G}_{II} = \left[\Phi_{tip}\right]_{\max} = \gamma_{us}. \tag{72}$$

In this derivation, some sublety revolves around the role of the image force, but this can be shown to be cancelled by the dislocation-dislocation forces, and eq. (72) is rigorous.

The derivation of the Rice result in eq. (72) assumes that the dislocations are emitted on the cleavage plane in front of the crack, in what we will call the Mode II configuration. The more important case is that where the dislocations are on an inclined plane, so the crack can be blunted by the emission, as in fig. 18. When the emission is at an angle to the cleavage plane, and blunts the crack, we will call it the Mode I emission configuration. In that case, the derivation breaks down, and a rigorous analysis has not been carried out to date. Rice has suggested that an aproximate way to calculate it is to introduce again the geometric factor, $Y = 8/(1+\cos\theta)\sin\theta$. The reader is warned that this suggestion is not a rigorous proof, and is only an educated guess of how to convert eq. (72) into a blunting configuration criterion. Thus, for a crack loaded in pure move I, and able to emit and blunt on a plane inclined to the cleavage plane, the Rice criterion is

$$\mathcal{G}_I = Y\gamma_{us}. \tag{73}$$

With this expression, the ductility crossover criterion becomes

$$\mathcal{D} = \frac{Y\gamma_{us}}{2\gamma_s} \tag{74}$$

The Rice criterion has been checked for the special case of a simple hexagonal lattice (which is isotropic in the continuum elastic limit) for the Mode II configuration by ZHOU *et al.* [1993], and found to be highly accurate. However, in the Mode I emission configuration, the same authors [1994] (hereafter referred to as ZCT) have shown that the presence of the ledge means that the emission of the dislocation involves surface formation as well as shear misfit, and the emission criterion in eq. (73) is incomplete. They note that the lattice misfit construction in fig. 27 corresponds to a homogeneous lattice, while the dislocation emission occurs at the open surface of a crack tip, and the ledge which is formed corresponds to an edge correction to the homogeneous lattice misfit construction.

ZCT show that when the end correction is included in the misfit energy, and plugged into the crack tip analysis, that (for a simple hexagonal lattice) a new misfit force term in eq. (71) arises, given by

$$\left(f_d^{mf}\right)_{\max} \simeq 8\pi \frac{\gamma_{us}\gamma_s}{\mu b}. \tag{75}$$

In terms of the crossover parameter, $\mathcal{D} = \mathcal{G}_{Ie}/\mathcal{G}_{Ic}$, and

$$\mathcal{D} = \frac{\gamma_{us}}{\mu b} \simeq 0.014. \tag{76}$$

Equation (76) is a startling result, because it states that the boundary between brittle and ductile solids does not depend upon the intrinsic surface energy, because surface

energy is required in both the cleavage and the emission process. Numerical studies by ZCT for the simple hexagonal lattice with a variety of pair forces confirms this result in that special case. In their studies, the crossover is determined quite accurately by eq. (76), and not by eq. (74). See fig. 28.

The new criterion is very simple. Except for geometric factors relating to the lattice cleavage and slip planes, the criterion states that materials having a $\gamma_{us}/\mu b$ below a roughly universal value are ductile, and those above this value are brittle. There is a direct connection between the dislocation Peierls energy and γ_{us}, so the ductility criterion for fracture can also be stated in terms of a critical value for the dislocation width, or the Peierls energy, in the material. In this sense, the prediction is not unreasonable, because the ductile fcc metals are also materials whose dislocation Peierls energy is very low.

The new criterion shares with the earlier Rice and Rice/Thomson criteria the feature that the ductility is controlled, at least primarily, by a quantity which, except for the geometric factor, M, is a fundamental property of the bonding of the material, and not a function of subtle details of the core structure of the crack. Although the ductility criterion has not been tested yet in a sufficiently wide range of crystal types and classes of force laws, it is enormously useful to have such a simple criterion, because guidance on making predictions about the ductile/brittle criterion is easily done for wide classes of materials simply from the bonding characteristics of the material.

In order to evaluate the ZCT criterion relative to what is known about intrinsically brittle/ductile materials, one needs good estimates of the unstable stacking fault. There exist at present four quantum mechanically based calculations of γ_{us}; two (EAM) for fcc materials (Al and Ni) RICE *et al.* [1993] and one (EAM) for bcc (Fe) CHEUNG *et al.* [1991], and one (density functional/local density approximation) for Si JUAN and KAXIRAS [1993]. Using the partial dislocation Burgers vector in the case of the fcc and Si lattices, the normalized relaxed values for $\gamma_{us}/\mu b$ are 0.022 (Al), 0.023 (Ni), 0.038 (Fe) and 0.142 (Si). Since in the fcc calculations for the ductile materials, the Burgers vector is not the full b, but the ZCT criterion is couched in terms of the full b, the hexagonal lattice prediction must be considered excellent, especially, since there should be additional lattice corrections, as described above for the fcc and bcc cases. On this evidence, the value for Fe (a full Burgers vector) is high enough to be considered brittle on our simple modeling, but is intermediate between the fcc metals, and the truly brittle Si. (In this discussion, we have used the partial dislocation Burgers vector, because if the dislocation is split, first one partial will be emitted, and then the second, thus lowering the critical emission condition. Thus, a rough guess of the emission criterion should use the Burgers vector for the partial dislocation, even though the actual process will be considerably more complex than before.)

One of the very surprising features of the new criterion is the fact that chemical embrittlement is usually thought to take place because of its effect on the intrinsic surface energy, γ_s, not on the shear strength of the material, γ_{us}. We will delay a discussion of this point till § 9.2, since many forms of embrittlement take place on boundaries because embrittling chemical species often segregate there.

References: p. 2287.

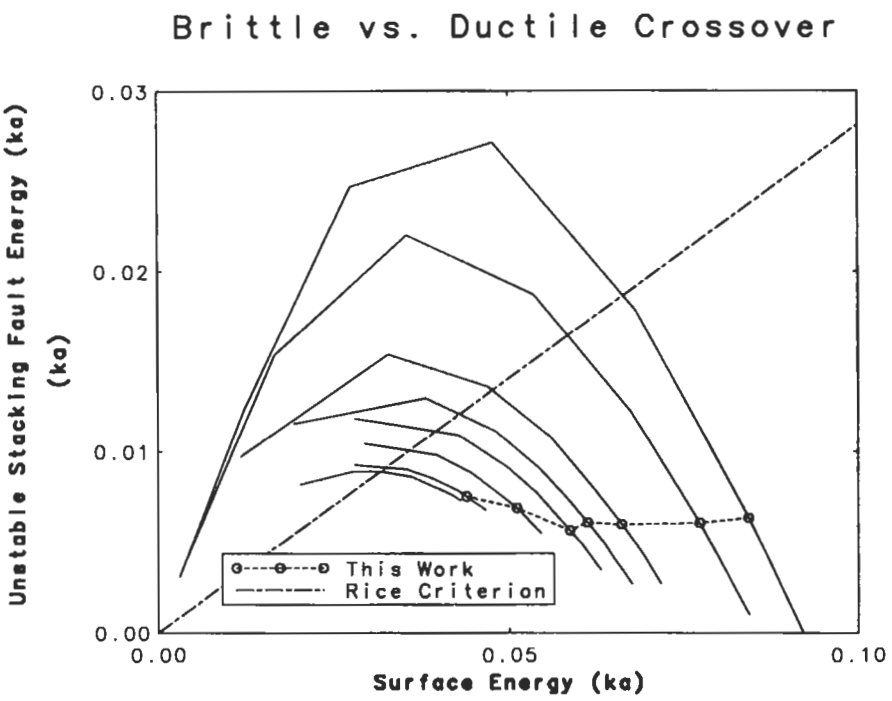

Fig. 28. Emission criterion as a function of surface energy, γ_s. The Rice prediction is the straight line. The points are the cross-over between ductile to brittle behavior for a series of force law functions. The space above the points is brittle, that below, ductile.

7.2. Summary of ductility criteria

In this section, we compare the three different ductility criteria and tabulate them for a variety of crystals and classes in order to achieve a general overview. See table 1. In this, we extend and update a similar attempt by RICE *et al.* [1993].

The three ductility criteria derived in the previous subsection appear to reflect quite different physical basics, and they result in quite different expressions. However, they are not as different as they seem. For example, consider Rice's version of ductility. In the misfit function of fig. 27, a simple guess of the theoretical misfit stress response between the two materials is a sinusoidal function with slope given by the shear modulus of the material. (See FRENKEL [1926].) On this basis, the unstable stacking fault energy is given by $\gamma_{us} = \mu/2\pi^2$ for a simple cubic, with corresponding corrections for other lattices. In the table, we also include the correction for the Burgers vector for the fcc and diamond cubic materials. On this basis, for a given crystal class, the ratio, $\gamma_{us}/\mu b^*$, where b^* is the partial dislocation Burgers vector, is a constant. RICE *et al.* [1993] point out that the Frenkel estimate of the γ_{us} is about 1.8 times the values for γ_{us} obtained for the three metals for which EAM calculations have been made (see previous section). Thus, they suggest that a corrected Frenkel value makes a reasonable estimate for the fcc and bcc

Table 1.
Material ductility

Solid	γ_s J/m^2	μ_{slip} GPa	b^* nm	$\gamma_{us}(F)$ J/m^2	$\gamma_s/\gamma_{us}(EAM)$
fcc					
Ag	1.34	25.6	0.166	0.15	16.1
Al	1.2	25.1	0.165	0.15	14.6
Au	1.56	23.7	0.166	0.14	20.1
Cu	1.79	40.8	0.147	0.22	15.1
Ir	2.95	198.	0.156	1.1	4.8
Ni	2.27	74.6	0.144	0.39	10.7
Pb	0.61	7.27	0.201	0.053	21.1
Pt	2.59	57.5	0.16	0.33	14.3
bcc					
Cr	2.32	131.	0.250	2.	2.1
Fe	2.37	69.3	0.248	1.1	4.1
K	0.13	1.15	0.453	0.032	7.4
Li	0.53	3.9	.302	0.073	13.2
Mo	2.28	131.	0.273	2.2	1.9
Na	0.24	2.43	0.366	0.055	7.9
Nb	2.57	46.9	0.286	0.83	5.6
Ta	2.9	62.8	0.286	1.1	4.7
V	2.28	50.5	0.262	0.82	5.1
W	3.07	160.	0.274	2.7	2.1
Diamond					
C	5.79	509.	0.145	2.7	4.0
Ge	1.2	49.2	0.231	0.41	5.4
Si	1.56	60.5	0.195	0.42	11.0†

† Si values calculated for $\gamma_{us}=0.142\,J/m^2$. JUAN and KAXIRAS [1993].

metals. This corrected value is used in the table. This procedure, however, shows that an empirical relation exists between γ_{us} and μ, which brings us precisely back to the old criterion, eq. (68) of Rice and Thomson.

The new relation of ZCT is different from the earlier two, because it does not contain the surface energy. If the surface energy scales with the unstable stacking fault energy, then the Rice ductility criterion would be equivalent to the ZCT criterion. Indeed, intuitively, one might expect that the surface energy and unstable stacking fault energy would scale together for the simple monovalent metals. For example, if we take the simplest view of bonding in which the bond strength (surface energy) scales with Young's modulus (Orowan's hypothesis, OROWAN [1949]), and that the unstable stacking fault scales with the shear modulus (Frenkel's hypothesis above), since the shear modulus and Young's modulus usually scale more or less together, this expectation does follow.

References: p. 2287.

However, the reader is warned that inverse relations between the surface energy and unstable stacking fault energy are possible, and the simple Frenkel/Orowan scaling is not always satisfied. The reader is referred to ZCT for such examples in the case of the UBER force law. Certainly, when covalent bonding is important, the Frenkel/Orowan scaling would not be expected, because the tensile and shear strengths in the bond are controlled by different parts of the force law.

In table 1, we show the known material parameters for a variety of materials and crystal classes. The values are drawn from RICE *et al.* [1993], except for γ_{us} for Si, which is from JUAN and KAXIRAS [1993]. Because the table gives the normalized Frenkel value of γ_{us}, the Rice and Rice/Thomson criteria are equivalent. Those authors have also carefully evaluated the various geometric factors we have glossed over, and suggest the following ductility criterion

$$\frac{\gamma_s}{\gamma_{us}} > 2.9\ (fcc)\ or\ 2.4\ (bcc). \tag{77}$$

According to the table, the predictions track the known results well. Among the fcc metals, iridium is the one brittle case, while in the bcc, the alkali metals have ratios of γ_s/γ_{us} well into the ductile region. Nb, V, Ta and Fe are borderline cases where ductility should be inducible under mixed mode loading. Cr, Mo and Tungsten should be fully brittle.

On the ZCT criterion, using the Frenkel normalized value for γ_{us} does not distinguish between any members of a given crystal class, and, in particular, cannot separate the alkalis from tungsten! On the other hand, the alkali metals are highly malleable, and must have very low Peierls energies, while Tungsten is not. On this basis, then, the Frenkel approximation must be badly wrong, and until we have more reliable estimates of the actual γ_{us}, rather little can be said. On the basis of the known calculations of γ_{us}, as noted in the last section, however, the ZCT criterion is not violated.

The reader is referred to the exhaustive attempts of RICE *et al.* [1993] to extract meaningful trends from the known and calculated ductility criteria on the basis of the Rice model. The ZCT model has not yet been adequately explored to see just how far its validity extends for various crystal types and force laws.

The fifth column of the table is the Frenkel value of γ_{us}. Except for Si, the last column is calculated with the normalized Frenkel γ_{us}, where $\gamma_{us}(EAM) = 0.54\gamma_{us}(F)$ as explained in the text.

7.3. Crack stability and mixed mode effects

With the derivation of dislocation emission criteria, it is important to come back to the Griffith condition, and ask what are the general conditions under which the crack is stable in the lattice? From the uncritical mechanical point of view, the crack is supposed to be in equilibrium when the Griffith condition is satisfied. This would seem to follow from the discussion of § 5.1. From the previous paragraphs, however, one also knows that the crack cannot sustain an unlimited amount of shear at the crack tip, because the lattice will ultimately break down and create a dislocation.

Thus, under the combined requirements that the lattice not be loaded at its tip with stresses which neither break it down in either tension or in shear, a region in the space of stress intensity factors K_I/K_{II} can be drawn, within which both of these requirements are satisfied. Since we know that lattice trapping always exists to some degree for a crack in any lattice, the stability region is not a line, but a region. Figure 29 depicts such a region of stability. On the K_I axis, lattice trapping is rather small, but with addition of Mode II, the trapping region grows. Ultimately, as Mode II is increased, the crack breaks down in shear with dislocation emission. This figure does not include possible Mode I emission, which would additionally complicate it. But the reader should remember that the stability diagram should include dislocation emission on all possible slip planes, in order to be complete. The figure is consistent with lattice modeling in the hexagonal lattice. (See ANDERSON and THOMSON [1994].)

In the figure, along the K_I axis to the right of the stability limit, the crack grows. To the left, along the K_I axis, the crack recedes. Exceeding crack stability in the K_{II} direction corresponds to dislocation emission, in either direction. The stability region will be symmetric about the K_I axis if the lattice itself has that symmetry, meaning that positive and negative dislocation emission is equally possible.

The reader will note that the circle representing the line of combined ModeI/ModeII elastic driving force on the crack from eq. (27), $\mathcal{G} \propto (K_I^2 + K_{II}^2)$, is roughly at the center

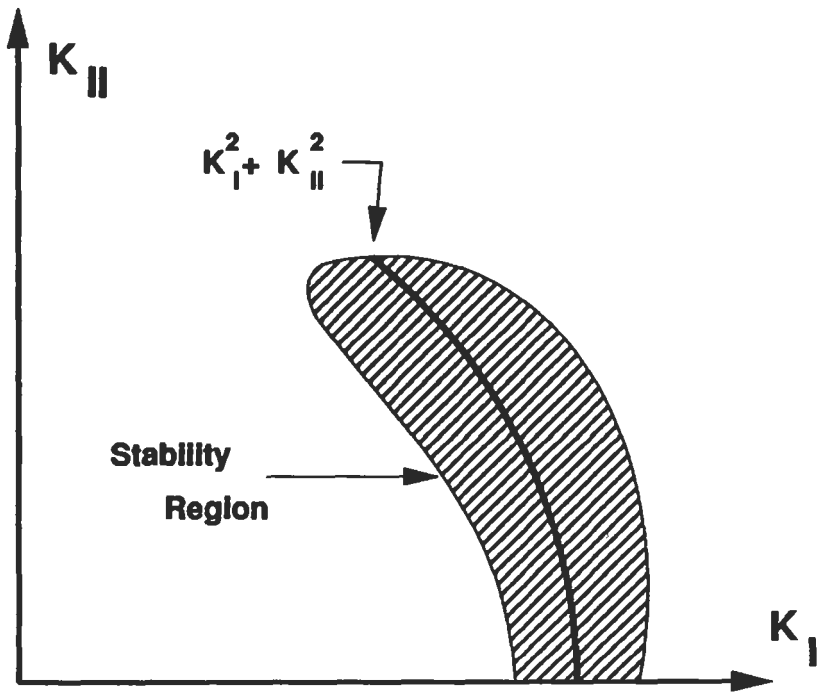

Fig. 29. Stability construction for the lattice. The hatched region is the region in k_I/k_{II}-space where the crack is stable in the lattice under the specified loads.

References: p. 2287.

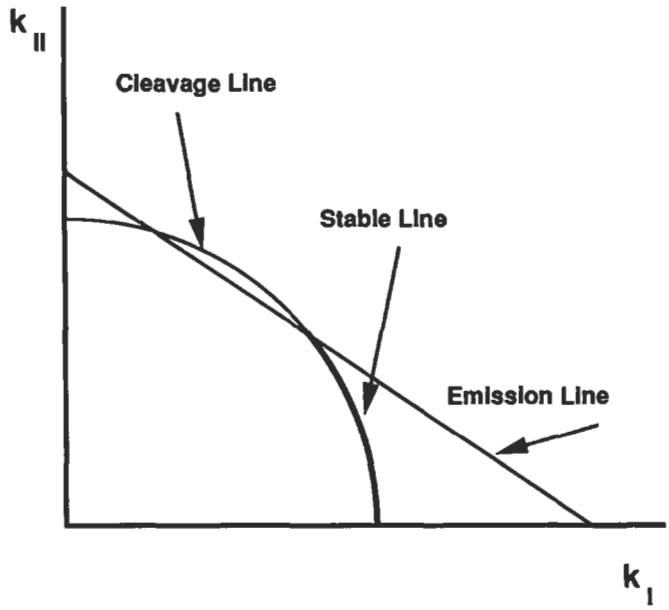

Fig. 30. Stability construction for the continuum. The Griffith cleavage line is a circle in k_I/k_{II}-space, and the emission line is a straight line which intersects the two axes. The portion of the cleavage line below the intersection with the emission line is the stable line for the continuum crack.

of the stability region. As an exercise it can be demonstrated that unless the $\mathscr{G}$ circle is enclosed within the stability region, then as the crack grows or retracts, energy is not conserved between the loading system and the material, including any heat which might be generated in the material.

It was noted in the presentation of fig. 29 that emission on blunting planes would complicate the stability diagram because of the additional emission, and that in general, all emission possibilities must be included in any such diagram. LIN and THOMSON [1986] have discussed the generalization of the original Rice/Thomson emission criterion to the mixed mode case. Unfortunately, we do not have a picture yet of the effect of mixed modes on the new ZCT emission criterion, except to expect that the criterion will surely depend upon K_{II}, as well as on K_I. Lacking this insight, however, we will briefly report the Lin and Thomson results. According to those authors, the emission criterion is linear in the loading. That is, the emission criterion is given by

$$
\begin{aligned}
&b_s k_{IIIe} f_3(\theta) + b_e\left[k_{Ie} f_1(\theta) + k_{IIe} f_2(\theta)\right] = \frac{\mu}{2\sqrt{2\pi r_0}}\left(b_s^2 + \frac{b_e^2}{1-\nu}\right) \\
&f_1(\theta) = \tfrac{1}{2}\sin\theta\cos\theta/2 \\
&f_2(\theta) = \cos(3\theta/2) + \tfrac{1}{2}\sin\theta\sin(\theta/2) \\
&f_3(\theta) = \cos(\theta/2).
\end{aligned}
\tag{78}
$$

In this (continuum) case, the crack stability lies along the Griffith line, and the emission condition is another line in k_I/k_{II}-space, which intersects the k_I and k_{II} axes, and also intersects the emission line at a point. In the continuum description, the intersection of the emission and cleavage lines represents the point of instability where the equilibrium crack breaks down in shear, with emission. Now, it appears that when the crack is stable in, say, pure Mode I (the Griffith point on the k_I axis lies below the intersection of the emission line with the same axis), that adding Mode II load will carry the crack up along the Griffith line to the point of intersection between the emission line and the Griffith line. That is, we have achieved a shear breakdown in the lattice simply by adding Mode II. (The same might be true by the addition of Mode III.)

The reader now sees how the stability construction in fig. 29 would depend upon blunting emission. The emission surfaces, which are expected to depend upon the load, in some yet unknown manner, in a ZCT theory will again interrupt the Griffith-trapped stability at some point, where the lattice emits a blunting dislocation, and the stability of the sharp crack is truncated. The stability diagram will thus be generalized in a straightforward manner.

8. *Interfacial cracks and chemical effects*

Perhaps the most important fracture events in materials involve either cracking on interfaces or cracking in the presence of external or internal environments which alter the failure process from that which would occur in the "nominal" bulk of the solid. Often these effects go together in the sense that interfacial fracture is modified in some way by chemical effects. For the reason that chemistry and interfacial effects so often go hand in hand it is therefore useful to consider them under the same heading.

Grain boundaries and other interfaces in materials are preferred paths for fracture in materials, because they are generally regions of weak bonding. Also, such interfaces are sites where embrittling chemical species congregate, which often adds dramatically to the propensity for brittle fracture at boundaries.

Unfortunately, the elastic analysis of interfacial cracks is difficult and subtle. We shall therefore not enter into a detailed discussion of the subject, but will simply quote the results, and discuss them. Then we will report the modifications of the elastic analysis which are required by lattice studies. Finally, we will return to a discussion of the problems associated with characterizing interfacial embrittlement.

8.1. Elasticity of interfacial cracks

We begin this section on the mechanics of cracks on interfaces by referring the reader to an excellent review of the mechanics by HUTCHINSON and SUO [1991]. In that article, the authors go well beyond our limited treatment here, with a very readable account of the important applications to materials, and in particular to criteria for when the crack stays on or branches off the interface.

The interfacial crack was first studied by WILLIAMS [1959]. A particularly beautiful treatment is given by ENGLAND [1965]. The striking feature of the elastic solution, noted

in Williams' first paper on the subject, is that closure oscillations are predicted at the crack tip. These are seen from the analytic prediction for the stress and displacments for the region ahead and behind the crack tip on the cleavage plane. On this plane, the x-axis, the tensile and shear stress can be written as a complex vector, $\sigma = \sigma_{22} + i\sigma_{12}$, with

$$\begin{aligned} \sigma(x) &= \frac{K}{\sqrt{2\pi x}} e^{i\psi} \\ \psi &= \varepsilon \ln \frac{x}{L} \\ \varepsilon &= \frac{1}{2\pi} \ln \frac{\kappa_1\mu_2 + \mu}{\kappa_2\mu_1 + \mu 2} \\ K &= K_I + iK_{II} \end{aligned} \tag{79}$$

κ is defined in eq. (15c). Similarly, the relative displacement, $\delta(-x) = \delta_y + i\delta_x$, across the cleavage plane behind the crack is given by the expression

$$\delta(-x) = \frac{1-\nu}{2\mu(1+2i\varepsilon)\cosh(\pi\varepsilon)} K \sqrt{\frac{-x}{2\pi}} e^{-i\psi}. \tag{80}$$

In these expressions, the phase angle, ψ, is a logarithmic function of the distance from the crack tip, and the constant, ε, depends on the elastic mismatch between the two media. The reader will find the elastic solutions often quoted in terms of two parameters originally introduced by DUNDERS [1968], which completely determine the elastic mismatch between two bodies. They are defined as

$$\begin{aligned} \alpha &= \frac{\mu_1(\kappa_2 + 1) - \mu_2(\kappa_1 + 1)}{\mu_1(\kappa_2 + 1) + \mu_2(\kappa_1 + 1)} \\ \beta &= \frac{\mu_1(\kappa_2 - 1) - \mu_2(\kappa_1 - 1)}{\mu_1(\kappa_2 + 1) + \mu_2(\kappa_1 + 1)} \\ \varepsilon &= \frac{1}{2\pi} \ln \frac{1-\beta}{1+\beta}, \end{aligned} \tag{81}$$

where the third equation quotes the expression for ε, in terms of the second Dundurs parameter. Tables of these quanitities are given in the review article by HUTCHINSON and SUO [1991]. This equation shows that interfaces of finite mismatch, but with $\beta = 0$ are possible, in principle, wherein the oscillations disappear.

When $\varepsilon \neq 0$, the stresses and opening displacements near the crack tip are similar to their counterparts in the homogeneous case (see eq. (15)), but with an additional factor, $\exp(i\psi)$. This factor mixes the stresses at the tip in the sense that if the crack is loaded in pure Mode I, then the stresses at the tip become mixed Mode I and Mode II. In addition, the mixing increases as the tip is approached, in a logarithmically singular manner. That is, the mode mixity increases faster and faster as the tip is approached. The same is true of the displacement. If the crack is loaded in pure Mode I, then shear displacements are generated at the crack tip. Further, because of the sinusoidal nature of

the exponential function, the stresses and displacements **change sign** as well as mode mix. Thus, there are regions near the tip where the crack **closes** as well as opens. These closures are oscillatory, and have caused much puzzlement since the solution was first found.

The physical reason for this strange behavior is quite easy to understand. Consider a Mode I crack in a homogeneous material. According to the standard elastic solution, eq. (15), in pure Mode I, there is a u_x displacement at the crack tip, which is a kind of "Poisson ratio" contraction at the tip in response to the tensile load. (It is not exactly a Poisson ratio effect, because it is still present even when $\nu = 0$.) When the material is homogeneous, this shear displacement is equal above and below the crack cleavage plane. But in the case where the materials on top and bottom are different, these displacements differ, and give rise to shear strains and stresses at the crack tip which are not present in the homogeneous case. Thus the mixing of stresses is necessary in the interface case (except for the special case where $\varepsilon = 0$). The actual negative excursions in stress and displacement are merely an overshoot caused by the mathematics of the elastic solution.

The mechanics community has basically taken two approaches to this problem. The first (see RICE [1988] and HUTCHINSON and SUO [1991]) is to note that the crack must be very long before the oscillations can be observable, even at atomic distances from the crack tip. Thus, for reasonable mismatch, $\mu_1/\mu_2 = 2$, and if $\nu_1 = \nu_2 = 0.3$, then $\varepsilon = 3.0 \times 10^{-2}$, which means that if $\psi = \pi$, for the first oscillation, the crack must be of order 10^{45} atom spacings long in order that the first atom at the tip be in closure. Such numbers vary greatly with the elastic mismatch, but they are always very large. It is thus tempting to simply say that the unphysical predictions are ignorable.

A second approach has been to explore what happens when the closure actually takes place, and repulsive forces come into play where the oscillations close the cracks COMNINU [1977]. Then, the crack closure can be controlled, with local changes in the K-field solutions, but the far fields are not significantly altered. But even if the point of view is adopted that the cracks are never long enough for anything but atomic effects to occur, one is left in a serious quandary, because the Griffith condition and the dislocation emission conditions are expressed in terms of the local stress intensity factor at the crack tip. When the stress phase is itself not defined at the crack tip, then we are in serious trouble. In one respect, the difficulty is less than one might guess, because it turns out that the total driving force on the crack is independent of the mode mixing at the tip.

$$\mathcal{G} = \frac{1-\nu}{2\mu}\left(K_I^2 + K_{II}^2\right) = \frac{1-\nu}{2\mu} K\overline{K}. \tag{82}$$

Thus, if there is a load, K, the driving force is still given by eq. (27), and only depends on the magnitude of the complex vector, $K_I + iK_{II}$, not its phase. But the stability region of the crack most certainly does depend on the phase at the tip, because unless there is a critical amount of K_I at the tip, the crack is not stable. "Stability" is thus not defined unless the local K, including its phase, can be defined.

References: p. 2287.

8.2. Lattice description of the interfacial crack

The way out of this difficulty is to realize that the physics of the crack, i.e., its cleavage and emission criteria, are determined by the core structure of the crack. Thus, the phase singularity at the crack tip must be cut off at some distance from the crack tip defined by its core size. That is, in the lattice, we expect the elastic solutions to be valid at distances from the crack tip large compared to the core size, but certainly not less than the core size. Consequently, we define a local stress intensity, k, which characterizes the phase of the stresses at the core, and we expect that the physical criteria should be expressible in terms of this core k. Thus,

$$\begin{aligned} k_{core} &= Ke^{-i\psi_0} \\ \psi_0 &= \varepsilon \ln x/r_0, \end{aligned} \tag{83}$$

where r_0 is the core size. Further, there should be a region in the space of the local k_I/k_{II} axes where the crack is stable, similar to the same construction in the homogeneous lattice. See fig. 29. Relative to the **load** stress intensity factor K_I/K_{II} axes, the stability region depends on the crack length. In the space of the core stress intensity factors, this region is an invariant. This state of affairs is shown in fig. 31, where the same stability

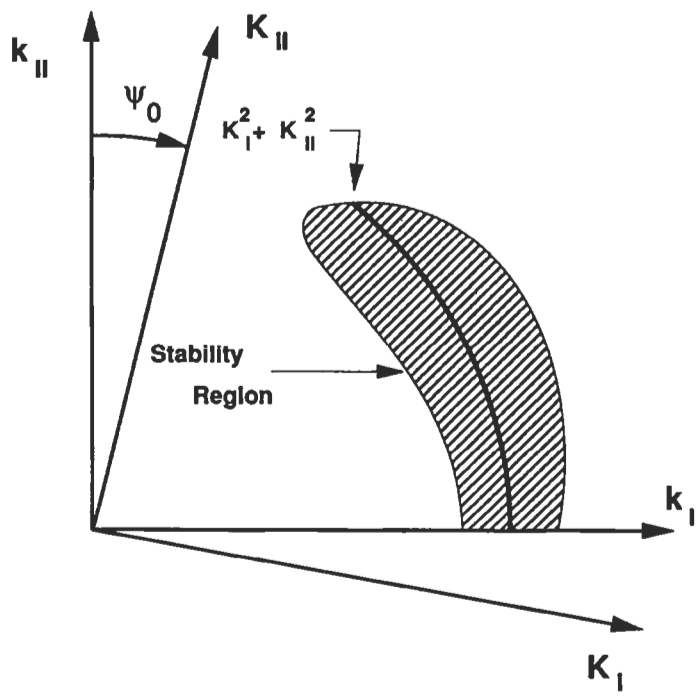

Fig. 31. Stability diagram for the interface. The two kinds of stress intensity factors, K and k are shown phase shifted by the angle, ψ_0. The standard stability region graphed on the local core stress intensity axes, k.

diagram from fig. 29 has been drawn with the two sets of axes, $k_{(core)}$, and the load K.

Lattice studies of a crack on the interface between two hexagonal lattices of different force laws, connected together at the interface, show that the picture described above is correct (THOMSON and ZHOU [1994]). The only surprise is that the core size is nearly an order of magnitude smaller than the actual size of the nonlinear region in the computer solution. The physical reason for this seems to be that the nonlinear region in the core causes larger phase shifts than the linear lattice predicts, because the nonlinear lattice has less resistance than the linear medium to the stresses. The fact that the effective core size is so small means that cracks of even modest lengths can show significant mode mixing, and the effects of the phase shifts at the crack tip are more important than uncritical application of the elastic theory would suggest.

But more important, the lattice model shows that no crack can ever exhibit the unphysical closure effects for the following reason. Suppose we start with a short crack loaded in Mode I such that the stresses in the core are primarily Mode I in character. As the crack is allowed to grow, the phase angle at the tip builds up, and the shear stresses in the core increase until the lattice breaks down in shear. At that point, a dislocation is emitted on the cleavage plane ahead of the crack, and shields the tip so that it reverts back to more nearly Mode I. As the crack continues to grow in length, dislocation emission continues to occur, always keeping the crack tip within the stability region, where no closure can occur.

8.3. Ductility at interfaces

The discussion to this point, though useful in gaining a physical picture of the crack, does not address why the interface is a favorable path for fracture. On the basis of the Rice and Rice/Thomson ductility criteria discussed in § 7, the explanation is straight forward and simple: The weak bonds on the interface correspond to lower γ_s, and the ductility criterion shifts in the brittle direction. To make this statement quantitative, the Griffith condition for the interfacial crack is given by the condition that the driving force on the crack is balanced by the net surface tension at the crack tip,

$$k^2_{Ic(core)} = \frac{2\mu}{(1-\nu)}\left(2\gamma_s - \gamma_{\text{int}}\right), \tag{84}$$

where γ_{int} is the interfacial boundary energy. Here, the work done in creating the two surfaces energies is lowered by the work stored in the interface structure.

It is important to put eq. (84) into its proper thermodynamic framework. It has already been discussed in § 7 how the Griffith relation is actually a thermodynamic condition, which reflects the kinetic equilibrium between forward and backward fluctuations at the crack tip. Hence, the two γ's in eq. (84) are actually free energies for the surface and interface. Since segregation will occur on an interface, which reflects the lowered energy at the interface, relative to the bulk, and the same type of segregation will occur at the free surface, the γ's reflect the equilibrium segregation at both surface and interface. But a fracture event may take place sufficiently fast that the impurities do not have time to come to their equilibrium concentrations on the surface, but are

"quenched" to their interfacial values. This situation can be expressed in eq. (84) by using "constrained" values for γ_s. Thus there are two cases: 1) where fracture is so slow that equilibrium is attained during the fracture processes at the atomic level. Then true equilibrium free energy values must be used. 2) Fracture is sufficiently fast that the segregation on the interface is frozen into the surface, as well. This situation was first pointed out by HIRTH and RICE [1980], and has been pursued, experimentally by Wang and collaborators. (See RICE *et al.* [1989] and WANG [1995] and WANG and VEHOFF [1991].) Detailed analysis of interfacial fracture, either experimental or theoretical, must specify which thermodynamic assumption describes the particular situation.

Because of the lowered Griffith criterion for cracking on the interface, other things being equal, the interface is favored over the bulk as a fracture path. In particular, for a favorably oriented flat boundary, a crack will grow on the boundary before a crack of equal length will grow in the bulk. But in a polycrystal, most of the boundaries will not line up approximately normal to the tensile axis, where the crack stability is favored. An interface oriented off the normal to the axis of the tensile load will generate a mixed mode crack on that interface and the stability of the crack on the interface would have to conform to the stability criteria discussed in § 8.1. Thus, in a polycrystal, there will be a competition for a mixed mode crack lying on a boundary at an acute angle to the load axis, and a more direct crack path through the crystal bulk with a higher surface energy. As the crack approaches each node of a complex polycrystal, given a particular grain boundary structure, the crack may branch in the new interface direction, if it can satisfy all the crack branching and stability requirements on the new boundary direction, or it may branch away from the boundary onto a more direct path through the bulk. This is a complicated problem, clearly. In the first place, no analytic stress analysis is possible for a complicated 3D intergranular crack path, so numerical analysis is necessary. In the second place, generally, there will be plastic zone contributions to the toughness for both paths, but the intergranular path will have less plastic work than the bulk because of the lower Griffith criterion on the boundary. (We discussed the relation between the surface energy and toughness in § 5.3.) Nevertheless, there have been attempts to analyze this competition, with some success by EBRAHIMI [1991], who showed that intergranular cracking is not always preferred in any given material. This competition also becomes visible in normally ductile fracture in steels, where the crack surface usually exhibits regions of intergranular brittle cracks along with hole growth fibrous fracture. In the vicinity of a ductile-to-brittle transition, the ratio of brittle intergranular cracking shifts to a larger fraction of brittle events as the transition is approached from the ductile side. See § 10.

The explanation of embrittlement on the basis of the Rice and Rice/Thomson models of ductility is very simply and intuitively due to the lowering of the surface energy, and the increased ease of cleavage. On that model, one generally assumes that the dislocation emission criterion does not change, at least to first order. But this intuitively obvious approach breaks down completely on the newer ZCT criterion, where the ductile/brittle crossover does not depend on the surface energy. We must acknowledge to the reader that considerable additional study of the ductility crossover is indicated, and that further study may lead to restrictions and qualifications of the ZCT criterion which are not

appreciated at the time of writing. Indeed, in essentially qualitative modeling of the crossover using simple quasi-continuum dislocation models, THOMSON and CARLSSON [1994] have suggested that there may be a transition between a surface independent $\mathcal{D}$ and a region where the traditional Rice dependence shown in eq. (73) is valid, for small values of γ_s. That is, if an embrittling species can lower the γ_s sufficiently, then the ductility criterion begins to depend on the γ_s. Thus, until more detailed studies can be made, the embrittlement problem is one where predictions cannot be made with any confidence.

In view of these circumstances, our discussion of chemical embrittlement must be provisional. But because of the previous inclination to identify embrittlement with decreased bonding at the interface, considerable effort has been expended on theoretical calculations of the bonding at interfaces and the effect of segregated impurities, and on experimental studies of the effect of segregation on the ductility. We will thus report on some of this work (discussion of the experimental situation must await § 10), with the proviso that the theoretical situation contains important unanswered questions.

BRIANT [1990] and HARRISON *et al.* [1990] have written extensive analyses clarifying the important role that simple chemical bond configuration considerations plays in the grain-boundary bonding. They also provide updates on the experimental situation regarding segregation. For example, Briant demonstrates how chemical valence bonding familiar from inorganic chemistry can play crucial roles through the types of molecular configurations which the impurities can take in grain boundaries, and suggests that this kind of thinking can explain the fact that B has a ductilizing effect in disordered alloys, and in Ni_3Al, but leaves Ni_3Si brittle. According to Briant, the difference lies in the valence charge transfer electronegativity considerations which apply to the grain boundary configurations, and the proposition that strong boundaries correspond to high charge densities in the boundary. With similar ideas in mind, HARRISON *et al.* [1990] have shown that a ninefold coordination structure with metalloids taking the position at the center of a trigonal prism are characteristic of iron systems, and that these structures are similar to the metal-rich molecular compounds such as Fe_3P.

Beyond these rather qualitative cluster considerations, detailed first principles calculations have been carried out in a number of systems. For example, in iron, WU *et al.* [1993, 1994] have reported grain-boundary calculations for the $\Sigma 3[1\bar{1}0](111)$ system with P, which confirm the embrittling influence of that segregant. Given that the structure of the grain boundary itself is still a subject of considerable difficulty and controversy and that Fe is a magnetic system, these calculations must be considered perhaps the best example of the current state-of-the-art. The authors find that relaxations occur in the boundary to form an ω phase, and that these relaxations are decisive in determining the segregation and fracture work. The results were that P segregation to the boundary was weaker than to the free surface, in good agreement with experimental measurements of the work of fracture. Further, the authors were surprised to find that the Fe/P bond is of a relatively simple metallic embedding type, rather than polar/covalent, and this result makes future extensions to other metalloid systems relatively easy to accomplish. Previous, less accurate calculations, by KRASKO and OLSON [1990, 1994] on the work of fracture on the same boundary in Fe showed that C and B enhance bonding,

References: p. 2287.

while P and S weaken the bonding, and that H drastically weakens it. In the quite different Al system, GOODWIN *et al.* have shown that Ge and As increased the (111) "cleavage" energy of Al.

In a quite different type of system, HONG *et al.* [1993, 1994] have studied impurity segregation effects on the adhesion of the heterophase interface $Mo/MoSi_2$. Again, charge transfer effects are important in this system, and make necessary a full first principles approach. In the $Mo/MoSi_2$ system, the authors showed that the impurities simply increased the interface separation distance, thereby lowering the interfacial work of separation. S had the strongest embrittling effect, and lowered the work of separation by about a factor of 2. These same authors have begun studies of the metal/ceramic interface problem and have reported results for the MgO/Ag and MgO/Al systems, HONG *et al.* [1994]. They report that the bond at the interface has a mixed covalent/metallic/ionic character, but that a fit to the universal bonding curve form also works reasonably well. Aside from this finding, there appear to be no simplifying characteristics to the bonding.

It is unfortunate in view of this beautiful and extensive work on adhesion and interfacial energy, that one cannot apply it immediately to the problem of interfacial fracture, until further work clarifying the emission criterion in the presence of segregated impurities on an interface is performed. However, a couple of points stand out. The first is that when bonding across the interface is lowered, the bonding lateral to the interface may be increased by rehybridization of the bonding electrons, and such strengthening within the interface will probably make it more difficult to emit a blunting dislocation. This tendancy, if present, would act in the same direction as the earlier prediction that weakened boundaries will be brittle boundaries. But the principle conclusion from the ZCT criterion is that the subtleties in the bonding, both across the boundary, as well as within it will be important in the final result. One is left with the impression that the problem of chemical embrittlement may always require a complete treatment of the crack tip environment, and that the determination of bulk parameters such as surface or interface energy (or even unstable stacking fault energy) will not be adequate to determine the criteria for ductile or brittle behavior in these cases. And finally, we note the possibility that for low interfacial bonding, the traditional interfacial energy relationship for ductility may be restored, as noted earlier (see also ch. 13).

9. *Summary of basic ideas*

After the discussion of the fundamental ideas underlying fracture in the previous sections, and before going on to some of their applications, it will be useful to summarize here the general conceptual structure as it has been developed.

a. The material is intrinsically brittle if it can sustain an atomically sharp crack in the material without shear breakdown and dislocation emission. The material is intrinsically ductile if it cannot.

b. In the highly constrained configuration space of the crack tip, a full scale fundamental theory of the crack will undoubtedly never be fully worked out. However,

surface, interface and unstable stacking fault energies, which are parameters in fracture theory, can be addressed from first principles theory, and such calculations have been, and will continue to be, important to an overall understanding of fracture. But for atomic level studies of the crack tip, itself, semi-empirical chemical theories, such as the EAM and tight binding schemes, constructed with guidance from first principles quantum-mechanical theory have been very useful, and will certainly continue to be the methods of choice when modeling the atomic processes in the crack tip region.

c. If the crack is sharp at the tip, then there is a local k-field, and the quiescent point for the crack is governed by the macroscopic thermodynamic Griffith relation. In general, and especially in the case of chemically enhanced fracture, lattice effects and chemical reactions at the crack tip will lead to thermally activated stress-dependent slow crack growth. Fracture in vacuum is a unimolecular decomposition of the lattice, while chemically enhanced fracture is a bimolecular (or higher order) process.

d. If the sharp crack is stable, then all metals, and many other materials as well, possess dislocation sources close enough to the crack to create a dislocation screen which shields the crack from the external stress field, and leads to *extrinsic* ductility. For a static crack in equilibrium, detailed balance applies: the local core crack is in equilibrium with its local fracture criterion (its simplest form is the Griffith relation). Each dislocation in the cloud also takes an equilibrium position in which the overall configuration depends on the dislocation friction stress (or local yield stress), and the elastic interactions with the other dislocations in the plastic region surrounding the crack tip. If the entire configuration is in motion, the same considerations apply, except that k and σ_f are velocity-dependent. Even though a screening cloud of dislocations accompanying a sharp crack may contribute significant toughness to the system, the fact that a brittle crack exists at the heart of the total configuration means that the situation is basically unstable against ultimate brittle failure when temperature or load rates make it impossible for the dislocation cloud to keep up with the underlying crack. Such a system will be susceptible to a "brittle transition", which causes great concern in practical systems designed to take advantage of the high strength which can be attained in these cases.

e. On the other hand, if the sharp crack is not stable in the lattice, as in the soft fcc metals, then the lattice breaks down under stress with continuous dislocation emission. Ultimately, the crack opens into a notch of finite angle equal to the angle between the active slip planes (fig. 12). If the crack is loaded in pure mode III, then the notch angle is zero, and the emitted dislocations form a dislocation screen. The simple screening analysis developed in § 5 applies. If the notch angle is finite, however, although some numerical shielding analysis has been done, a complete picture has not yet been attempted. In ductile materials, however, external sources of dislocations are always important, and the overall morphology becomes modified into that characteristic of hole growth, or fibrous fracture. In such cases, not only do the external dislocations round out the shape of the notch, but the process is dominated by nucleation and growth of holes (or cracks) ahead of the main crack. The overall fracture morphology then becomes complicated by the coalescence of the newly formed holes and cracks. This kind of behavior should not be described as a cracking process, because it is so dominated by the ductile response of the matrix. True cracking may not be taking place at all, except to the

References: p. 2287.

extent that the hole nucleation process may involve a fast growing crack nucleus which becomes arrested by microstructural barriers. Such a ductile failure is one of the goals of all materials designers, because it is so forgiving, and is characterized by very high toughness. Problems arise when some chemical or other event intervenes to modify the basic emission processes at the crack tip. Problems also arise when designers become dissatisfied with the low strength associated with true ductile fracture, and try to harden the material, thereby introducing possibilities for brittle cracking. It goes without saying that an analytic description of such a complex phenomenon as hole growth fracture is not possible, because of the difficulties of describing adequately what is taking place in the "process zone". The best one can do is to average over the actual material complexity with a "constitutive law" based continuum description.

f. But the most interesting situations are those where one is somewhere between the pure brittle and the pure ductile cases — with both atomic scale cleavage and atomic scale emission occurring. The reader will remember that in a material balanced precariously between intrinsic ductility and intrinsic brittleness, the mode of loading at the crack tip can tip the balance to one side or the other. However, most practical materials are mixtures of phases, some of which are brittle, and some which are ductile, and with brittle interfaces either between grains of a phase or between different phases. It is important to realize that material structural complexity is not usually an accident; it is more often a part of the design, as in the case of a high strength steel or a composite. In part, the complexity is desireable, because high strength requires barriers to restrict the mobility of dislocations (but not to stop them entirely!). Of course, what happens is that the barriers to the dislocations are usually excellent sources for microcracks. Thus, in most cases, the material designer "lives dangerously" in the sense that complexity is necessary to gain high strength, but sufficient ductility must be built into the system, so that cracks are arrested before they can become disastrous. A fatigue-prone material is, thus, often the result, caused by the slow accumulation of "damage" in the material. See the chapter on Fatigue in this series.

g. From the point of view of fundamental materials science, it is clear that at the core of fracture science is a major problem of atomic bonding at the crack tip. Beyond that, toughness in the material is a much more complex phenomenon which is very difficult to model. But probably the most important challenges arise in understanding the criteria which govern the transitions which occur from ductile to brittle behavior. Such transitions are usually the cause of the great surprise material failures, as when bridges or pipe lines fail. Needless to say, they are not easy to describe adequately at the fundamental level.

10. Some practical implications and problems

In this chapter, a very fundamental approach to fracture has been followed in order to develop a few central ideas regarding the interactions between cracks and dislocations. We have mostly focussed on sharp cracks and relatively brittle behavior, whereas engineering materials are deliberately designed to fall more in the middle of the brittle-

ductile spectrum in order to optimize both high strength and high toughness. Consequently, engineering materials will show a much more complex mechanical response than can ever be quantitatively described by means of the fundamental properties of simple dislocations and cracks. Nevertheless, the fundamental ideas are useful as thinking tools when one is faced with the more complex systems, and in this short section, we shall tour briefly several areas of practical interest with these tools in hand. At the time of writing, this attempt will be more a promise and challenge for the future than a demonstration of current capability, however. This state of affairs exists partly because the fundamentals are presently in a state of intense investigation, with new insights still in the wings, and partly because the application of these ideas to practical problems is still in a rudimentary and often controversial state.

Because the discussion in this section is more practically oriented than the previous sections, we list, again, some general references which will be particularly relevant to this section. First, the two texts of BROEK [1986, 1989] are useful for their complete but more elementary level. But the review series organized by KNAUSS and ROSAKIS [1990] provide up-to-date reviews of most of fracture mechanics and many of its applications. The more materials aspects are less complete, but fracture in high strength steels is richly covered in the 1987 Sagamore Conference, OLSON, AZRIN and WRIGHT [1987], and hydrogen embrittlement in the 1987 hydrogen conference, MOODY and THOMPSON [1989]. We continue to list the older book of KNOTT, [1973], because its coverage of materials aspects, though somewhat out of date, is still good. Other specific references appear as they become relevant.

10.1. Implications for final materials reliability

In the widest sense, fracture science and technology is a part of the overall concern for the reliability of a material in its ultimate use. This problem has been important to mankind since he first used tools of any sort, and is certain to remain with him as new materials are developed for new uses in new environments. Early engineering approaches to materials reliability made heavy use of safety factors and relatively ductile materials. More recently, the need for high materials performance and the heavy penalty paid for large safety factors in such areas as aerospace have driven the development of materials technology relentlessly, resulting in ever greater sophistication in materials engineering practice. One of the penalties paid for higher materials performance, unfortunately, is a greater exposure to the possibility of brittle failure, and the sudden catastrophe that often results from it, because of the rough correlation which exists between higher strength and lower toughness. Although there are ways to mitigate this tendency, it arises simply because when dislocation activity is constrained in order to obtain high strength, the ability of the material to shield its cracks diminishes as well.

The current approach to materials reliability is along two related paths. The straightforward first path is simply to optimize the strength-toughness durability through materials development. Some approaches to this goal are: (i) Control of grain structure and second-phase morphology, usually by increasing uniformity and decreasing grain and precipitate size; the Hall–Petch relation [eq. (10.2)] is relevant here. (ii) Design the

References: p. 2287.

material as a composite, making use of the properties of matrix and fiber to optimize overall results. (iii) Attention to embrittlement factors such as external chemistry, temperature, etc.

The alternate, or second, path is loosely called the fracture mechanics approach and works from the critical flaw concept. This concept connects the macroscopic stress in a part to the critical-sized crack which can be sustained, by means of eq. (14), and to the critical stress intensity, K_C, or critical J_C, which a crack in the material can sustain before it advances. The relation for the former can be expressed from eq. (14) as

$$\sigma_\infty = \frac{K_C}{\sqrt{\pi a}}, \tag{85}$$

where K_C is the same materials toughness parameter modeled in § 5. It, and more frequently, J_C, is determined empirically by standardized measurements under appropriate conditions specified by the ASTM.

In critical applications, the generalization of eq. (85) is derived from a computed stress-distribution in the part, so that a critical-sized flaw can be inferred for any portion of the structure or part for the assumed design maximum load on the structure. The material toughness for the given service conditions must be known, of course. It then becomes a quality assurance problem during manufacture or construction to ensure that no flaws larger than the critical size are present, and a maintenance problem to ensure that the flaws do not grow to the critical size during service. Since cracks can grow owing to fatigue during service, the in-service inspection problem is often the most critical one. The technology for finding and evaluating flaws in materials is termed *non destructive evaluation* (NDE) or *non destructive testing* (NDT). Thus *materials reliability assurance* is a three-cornered technology involving materials technology through materials toughness considerations, mechanics through stress analysis, and NDE.

The materials technology "input" to materials reliability assurance in terms of the critical toughness parameter is decidedly complex. First, the flaws in materials are never the idealized cracks visualized in earlier sections, but voids and odd shapes associated typically with other inhomogeneities in the material. Hence the critical K_C or J_C for a given material must include a judgmental factor regarding how "flaws" relate to the idealized cracks studied in standardized measurements. Aside from this, however, all the materials science and technology already referred to are relevant to determining and enhancing toughness. Over and above all, however, ride concerns for a change of mode from ductile to brittle under conceivable service conditions.

In spite of all the complexity and implied uncertainty apparent to the reader, the use of the fracture mechanics approach to materials design and reliability assurance has been a great boon to designers in situations where reliability and performance must be optimized. It promises even more success for the future, as the materials aspects of fracture become better understood, and the NDE technology becomes better developed. For further perspective on the subject of materials reliability in general, the reader is referred to the excellent and mainly qualitative monograph covering the Royal Society Discussion of the subject, FORD *et al.* [1981].

10.2. Brittle crack initiation

Logically the next topic in this section should address the problem of how cracks are formed in a material in the first place. Generally speaking, of course, they exist in any material of technological interest as processing artefacts. But even when care is taken to reduce pre-existing cracks, they can be initiated by a variety of mechanisms associated with dislocations and twins. For example, when dislocations pile up against any obstacle such as a grain boundary, it has been proposed by STROH [1957] that the edge dislocations at the head of a sufficiently intense pile-up coalesce into a superdislocation with the lattice below the extra half-planes opening into a mode I crack (SMITH [1979]).

A review of the complicated subject of crack initiation in steels in general will be found in KNOTT [1977]. For the important special case of the initiation of transgranular brittle cleavage, it is found that the brittle carbide precipitate particles in the steel first crack because of the strain-incompatibility due to the brittle particle in the deforming matrix, or in other words, because of the pile-up of dislocations at the particle. This process is similar to the initial stage depicted for ductile hole growth in fig. 7. The initial size of the crack is then given by the size of the brittle particle, and the crucial question is whether the cleavage crack can then propagate through the ferrite matrix by means of the local effective stress on the crack. Provided the crack can propagate through the first ferrite grain, it can then generally propagate through the entire steel sample.

SMITH [1966] has published a successful, but qualitative model of the stress to nucleate and propagate a crack under these conditions which depends both on the size of the carbide particle and the effective shear stress caused by a dislocation pile-up. An important feature of this theory is the grain-size dependence of the fracture stress. Since the stress to form and propagate the crack depends on the effective shear stress, σ_{eff} in the grain as given by the Hall–Petch relation (ch. 19, § 8),

$$\sigma_{eff}^2 = \lambda d. \tag{86}$$

The fracture stress should also obey this relation. Here λ is a constant and d is the grain size. A striking verification of the same grain-size dependence of fracture and deformation is shown in fig. 32, after early work by LOW [1955]. Later work and the comparison with the theory by Smith has been reviewed by KNOTT [1977].

10.3. Ductile fracture, hole growth and the R curve

For an excellent discussion of all aspects of ductile fracture, the reader is referred to GARRISON and MOODY [1987] and GARRISON and HANDERHAN [1989]. If a sharp crack is injected into a ductile specimen by some means such as that of § 10.2, when a stress is applied, the crack first blunts plastically into a cigar-shaped cross-section with a significantly increased COD. This stage of the specimen compliance is termed the stretch zone, Continuum plastic studies have shown that such a cigar-shaped crack has maximum stress not at the surface of the tip, but at a point in the material in front of the crack, a distance about one COD from the tip, RICE and JOHNSON [1970].

There also exists a maximum negative pressure in the same region. As the stress is

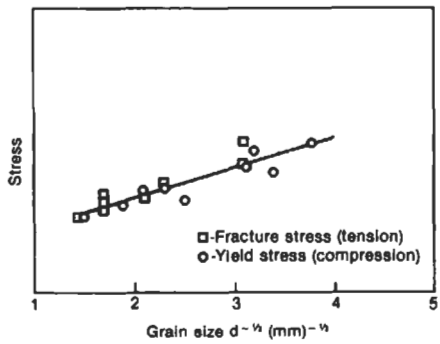

Fig. 32. Comparison of yield stress and fracture stress of steel at 77 K (after LOW [1955]).

increased into the stretch zone, holes form in the region of maximum negative pressure, which grow under continued strain, and eventually connect to one another and to the main crack (see fig. 8). Further straining simply continues this process. Most studies of this phenomenon (see GARRISON and MOODY [1987]) are made in multicomponent metals, in particular steel, and the holes are found to form at the sites of the minor-phase particles (fig. 7). Sometimes the particle interface is the origin of a hole. In other cases where the interface is strong, the particles themselves first crack in brittle fashion as discussed in § 10.2, and this crack then blunts as it runs into the matrix. Even in pure metals containing no particles, such holes still form, apparently by nucleation of vacancy clusters in the dislocation cell walls (GARDNER *et al.* [1977]).

One of the striking features of the hole growth fracture process is the development of bands of localized intense shear between the larger holes, within which large numbers of small holes are formed on small particles, as shown by COX and LOW [1974]. These shear instabilities are widespread phenomena, and their origins and general properties are still being sorted out (see GARRISON and MOODY [1987].) Clusters of impurities on the finest scale, well below 1 μm in size, do not form holes or shear bands, but do affect the yield strength of the matrix, and thus the rate of blunting of the crack tip.

The overall toughness of the material is determined, then by a combination of the large voids initiated at the large segregants in the metal, the spacing and interfacial strengths of the small segregants where the unstable shear bands form, and the dispersion of the smallest impurity clusters, which determine the yield strength (GARRISON and HANDERHAN [1989]).

We conclude this subsection with a discussion of the R-curve, and the analysis associated with it. If eq. (14) is combined with the expression for $\mathscr{G}$ in eq. (27) and the Griffith relation in eq. (38), then we get the following expression for $\mathscr{G}$, the driving force on the crack in Mode I,

$$\mathscr{G} = \frac{2\pi(1-\nu)\sigma_\infty a}{\mu}. \tag{87}$$

At equilibrium, $\mathscr{G}$ is balanced by the resistance the material exerts against growth of the crack, which will be called R. For a brittle crack, $R = 2\gamma_s$, the Griffith result. But in this

case, we wish to include all other forms of global resistance to the crack plus its deformation cloud, so R is much greater than the Griffith value.

For the case of a crack which has been formed in the material by some external agent, such as cutting the bonds on the crack plane in a mathematical construction, or by some actual physical process such as a spark cutter, or by some processing accident which leaves a flaw, then the crack or flaw may have no deformation zone associated with it. As the sample is loaded, however, assuming a ductile material, then the crack tip becomes a concentrator of stress, deformation begins around the crack tip, and the tip begins to blunt. The crack "grows" by blunting, and contributes a far-field displacement, characteristic of a crack displaced from its original sharp tip position. Because of the increasing deformation surrounding the crack, R increases, in a curve which rises sharply at first and then more slowly, as shown in fig. 33. The graph in fig. 33 has two ordinates, $\mathcal{G}$, and R, and one absissa, the crack length. The graph of $\mathcal{G}$ in fig. 33 is a straight line, according to eq. (87). The point were $\mathcal{G}$ meets R corresponds to the equilibrium crack. But as the external load exerted on the far boundaries of the material increases, there comes a point where $\mathcal{G}$ becomes tangent to R, above which, the crack is not in equilibrium, and grows unstably. Since the material is responding in a highly ductile fashion, presumably the unstable crack growth is by means of hole growth, but a brittle crack embedded in a ductile medium would also behave in the same way.

The description so far has been heuristic, and nothing about the process is claimed to

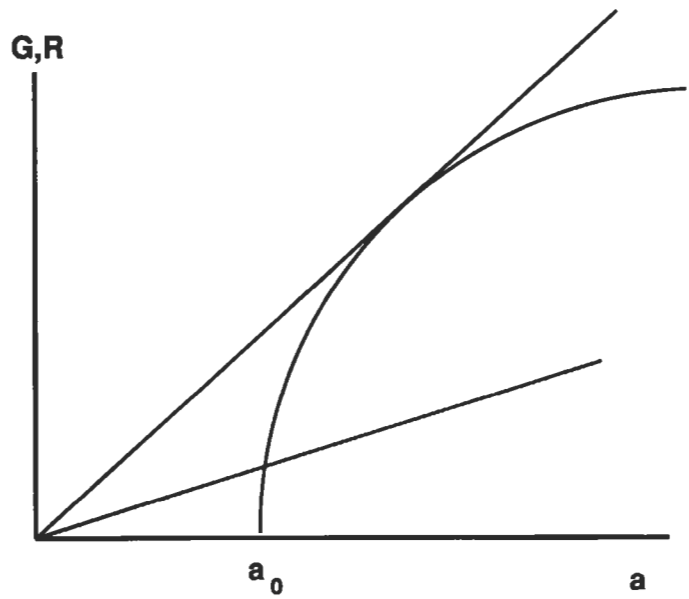

Fig. 33. R-curve construction. The resistance (R) for a crack of initial length, a_0 is graphed as the steeply rising curve, as a function of the crack length. The theoretical driving force, $\mathcal{G}$, according to eq. (87), is graphed as a straight line. Below the critical stress, σ_{cr}, the crack is stable, and above the tangent curve, the crack is unstable.

References: p. 2287.

be universal. However, empirically, it is found that the R-curve is more or less crack-length independent. Thus, R is found to be a material parameter (see BROEK [1986]), and thus of considerable use to materials engineers. In practice, the R-curve is valid only if the crack is already long compared to the deformation zone of the fully developed crack, and the specimen size is large compared to this zone (small scale yielding). "Short" cracks require special treatment (see HARLIN and WILLIS, [1990]).

10.4. Ductile-brittle transitions — temperature and rate effects

As implied at various points in the chapter, aside from fatigue to which a whole chapter is devoted in this book, perhaps the most serious concern of the materials engineer when it comes to practical fracture control is the worry that a material may undergo a transition from its normal toughness to a much lower and dangerous value because of some unforeseen change of conditions, either in the material or in the way it is used. In general, the materials parameters which control toughness once the material has been fabricated are temperature, strain rate, and external chemical environment. The first two are usually linked effects in materials science for general reasons, so will be discussed together here, and discussion of chemical embrittlement will follow separately.

Much of the early study of fracture control in metals focussed on the transition which mild steels undergo between their ductile high-temperature and brittle low-temperature regimes, and the dramatic nature of this transition is perhaps best shown by a schematic example of these early tests (fig. 34). In this figure, the energy necessary to fracture a notched specimen is measured by a Charpy apparatus. In this measurement, a standard specimen is struck by a hammer pendulum, and the height of fall of the pendulum when the complete fracture occurs is converted to the energy plotted. In more sophisticated real time measurements, the time dependent response of the system can be plotted in what is called an instrumented Charpy test. The lower portion of the curve (the so-called lower shelf) corresponds to K_{IC} or J_{IC}, or dynamic versions of them, rather straightforwardly. Above a rather indeterminant point, say near halfway in the rise to the

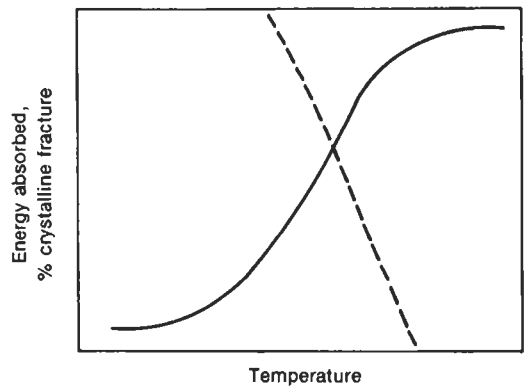

Fig. 34. Typical transition curve for mild steel. The solid curve gives energy absorption; the dashed curve shows "percent crystalline fracture" as estimated from surface appearance.

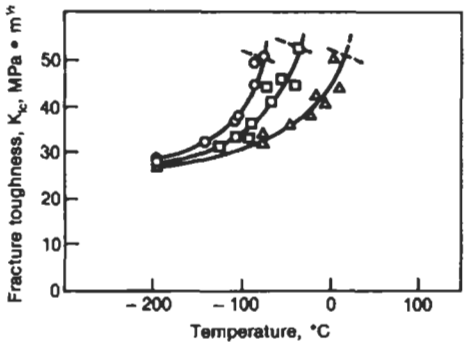

Fig. 35. Effect of strain rate on fracture toughness of ASTM A36 steel as a function of temperature. The curves are for strain rates of $10\,s^{-1}$ (triangles), $10^{-3}\,s^{-1}$ (squares) and $10^{-5}\,s^{-1}$ (circles). (After BARSOM [1979].)

upper shelf, the material exceeds its yield point through most of the specimen, and the K is no longer well defined. Nevertheless, the entire curve gives a good qualitative picture of material toughness, and the Charpy measurement is still used in many materials selection applications. As the diagram shows, the transition is also associated with a change in appearance of the fracture surface from a hole growth to a cleavage mode.

The temperature range of the ductile–brittle transition is a function of the strain rate as shown in fig. 35, and a function of microstructural variables, as shown in figs. 36 and 37.

The toughness and ductility of high strength materials are functions of the strain rate, especially for temperatures in the general vicinity of the brittle transition temperature. The rate effects are associated both with the crack tip (assumed sharp), and with the mobility of the dislocations in the plastic zone. The crack exhibits a rate dependent critical stress intensity factor in a generalized dynamic Griffith relation, which deviates from the static value at velocities in the vicinity of a sound speed. In this relativity-like

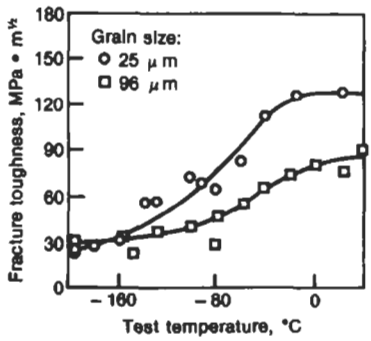

Fig. 36. (left). Effect of grain size on fracture toughness. Material is St37-3 steel in grain sizes shown. (After DAHL and KRETZCHMANN [1977].)

References: p. 2287.

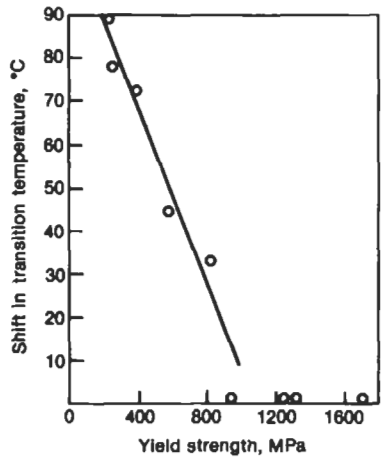

Fig. 37. (right). Effect of yield strength on shift in transition temperature between impact and slow-bend test loading rates. (After BARSOM [1979].)

effect, the moving crack requires a higher external load to move the crack to high speeds because energy must be radiated from the tip in order to generate the correct moving crack field. Thus, energy input is required to create both the dynamic radiation field and the free surface, as well. Dislocation mobilities, especially in the bcc metals, are limited by the Peierls barriers, so in these materials the deformation zone cannot follow the crack at high strain rates, and the overall response becomes brittle. The reader will find a complete discussion of this problem in the book of FREUND [1990].

Another important factor in the brittle-ductile transition problem in plates is the effect of plate thickness. This effect is, strictly speaking, not a materials problem, but a mechanics effect associated with the size of the deformation zone around a crack in comparison with the plate thickness. Nevertheless, it is important to the materials engineer, and is due to the change in stress state associated with the change from "plane strain" to "plane stress" (KNOTT [1973]) when the deformation zone decreases to the size of the plate thickness. Thus, the entire transition curve becomes a function of plate thickness. For thin plates, the transition temperature shifts to the left in fig. 34, relative to thick plates. That is, thick plates are in a sense more brittle than thin ones.

This mixed bag of temperature, metallurgical variables, strain rate and specimen thickness leads to a very complex engineering problem in practice, which in critical applications is the subject of extensive data collection and code formulation efforts. A good introduction to the subject will be found in KNOTT [1973] and, beyond that, in the excellent and practical book by CAMPBELL *et al.* [1982] and the various publications of the ASTM.

10.5. Chemical effects — hydrogen embrittlement

Fundamental aspects of the chemical effects on fracture were presented in § 8. In the present section, some of the ways external chemical attack and internal minority chemical

impurities and phases embrittle materials will be presented in more practical terms. In metals, chemical effects manifest themselves, generally, in two quite different ways: as effects on the local crack tip chemistry, and effects on the dislocation mobility. Because of this duality in mechanism, sorting out the fundamental processes can be difficult. In § 8, chemical effects were associated with interfacial cracking, and in practice, observed chemical effects are usually, indeed, associated with intergranular (or interphase) cracking.

Conceptually, the simplest form of chemical embrittlement is that where a crack grows directly exposed to an external chemical environment. In this case, the external environment should form an adsorbed surface layer on the solid, and interact molecularly with the stretched bonds at the tip. This is the way water vapor has been proposed to interact with cracks in silica (WIEDERHORN *et al.* [1980]), and gaseous hydrogen with iron (ORIANI and JOSEHPHC [1974]). Liquid metal embrittlement is also thought to be a rather straightforward crack tip chemical effect (NICHOLAS and OLD [1979]). We will thus discuss these subjects before addressing the case of internal chemical segregation effects on grain boundaries in the following section. Stress corrosion is also a form of chemical embrittlement, but because corrosion involves much more surface electrochemistry than we can afford to discuss here, it will not be included.

From a practical standpoint, hydrogen embrittlement is the most important form of embrittlement, in part because hydrogen is present in some form in most metals, and is a common by product of corrosive products on the metal surface. But in large part, hydrogen is important because it can participate in so many different embrittlement mechanisms. The reason is that hydrogen is not only highly chemically active in a metal matrix, but it is also enormously mobile. In iron, it can difuse 10 μm in one second at room temperature. Thus, it never "stays put", but continues to be a factor, kinetically, in the metal at even low temperatures, where it interacts with other chemical segregants, forming hydride phases as well as smaller aggregates in the matrix and in the boundaries. But hydrogen also interacts with dislocations in unique ways, because it can move with the dislocations, and can have either a hardening or a softening influence on the dislocation mobility, depending on the temperature. And finally, hydrogen alters the bond strength of the matrix metal when it is stretched at the crack tip. It comes as a surprise that hydrogen can be so important, when its solubility in the matrix of bcc metals is usually very small. (In Fe, the solubility at ambient conditions is only 3×10^{-8} atom fraction.) But much larger amounts can be stored in hidden ways as part of other segregants, or in other traps. So its effects are much more pronounced than one would otherwise suspect.

There are two older reviews on the subject which are still excellent, HIRTH [1980] and ORIANI [1978], but for more modern material, the reader is referred to the most recent conference on hydrogen, MOODY and THOMPSON [1989]. Also see the Sagamore Conference proceedings on high strength steels, OLSON, AZRIN and WRIGHT [1987].

Embrittlement in high-strength steels is much more drastic than in low-strength steels. In high-strength 4340 steels, with a toughness value of 60 MPa$\sqrt{m}$, one atmosphere of hydrogen lowers the toughness to about 15 MPa$\sqrt{m}$, according to experiments by ORIANI and JOSEPHIC [1974]. The pressure dependence of embrittlement over a pressure

References: p. 2287.

range of 0.1 to 1000 Torr can be fitted to a law $K \propto \ln P$, which is what one would expect if the primary effect is the change in the surface energy via the Gibbs adsorption equation. In these experiments, the hole-growth ductile fracture of the initial steel converts to a cleavage fracture on the prior austenite grain boundaries. Under these conditions, it is possible to model the toughness entirely in terms of the change in γ, or as ORIANI and JOSEPHIC [1974] have called it, by decohesion of the bonds at the crack tip. However, it is not possible to rule out the possibility of diffusion of hydrogen into the local region in front of the crack where discontinuous cracking might occur (see GERBERICH *et al.* [1975]). In either case, i.e., if the crack proceeds by hydrogen attack at the tip of the main crack or is nucleated at a small distance ahead of it, changes in surface energies or in interfacial energies are the crucial events.

But most of the cases of hydrogen embrittlement involve hydrogen already trapped in the matrix, and for this type of embrittlement, there is much controversy about what the mechanisms might be. According to BIRNBAUM [1989], there are two clearly evident mechanisms, the formation of brittle hydrides in those systems where they are formed (no hydrides are formed in the steels, incidentally), and enhanced shear instability in ductilizing the matrix. This latter mechanism is odd in the sense that making the matrix more ductile is proposed as a mechanism for making the macroscopic behavior more brittle! This mechanism will be discussed further in § 10.7. According to BIRNBAUM [1989], the direct bond weakening at the crack tip is also possible. However, MCMAHON [1989] proposes that the effect in steels is mainly an effect whereby the hydrogen present near the grain boundaries is concentrated at the crack tip by the dilatation of the crack stress field (which increases the solubility of the hydrogen), thereby allowing molecular attack at the stretched bonds at the tip to occur. Since hydrogen embrittlement in steels is an intergranular event, hydrogen effects are in some manner facilitated by the boundaries, and apparently by the segregants present on them (see MCMAHON [1989]).

In the author's opinion, it is pretty clearly demonstrated that hydrogen lowers the decohesion at the crack tip, perhaps most convincingly, because of the theoretical calculations already reported in § 8 by KRASKO and OLSON [1994] for the boundary energy of Fe. In themselves, such interfacial energy calculations are incomplete in demonstrating debonding effects at the crack tip, but HOAGLAND and HEINISCH [1992] have also explored details of the crack tip, itself, for the case of Ni with the EAM potentials of DAW *et al.* [1986], and shown how interactions at the crack tip actually modify the dislocation emission.

Part of the difficulty in sorting out the hydrogen embrittlement problem is the complexity of the effect of hydrogen on the dislocation mobility, as already mentioned. The direct effect of hydrogen on a dislocation in pure iron is to lower the Peierls energy and thus soften the material (HIRTH [1980]). In impure iron, however, addition of hydrogen hardens the material, presumably because of chemical interactions between hydrogen and oxygen, carbon, etc., impurities. In addition, the dislocations can carry hydrogen atoms with them through the lattice, thereby concentrating hydrogen in regions of high dislocation density. Thus, the complex behavior of the dislocations in the presence of hydrogen contributes in no small way to the difficulty of sorting out the hydrogen embrittlement problem.

In cases of low strength steels, LEE *et al.* [1979] have shown that, macroscopically, the cracking occurs at the surface when dynamic hydrogen charging takes place, but it is usually believed that in lower-strength steels, diffusion of the hydrogen into the critical regions of high triaxial stress in front of a blunted crack is important. In low-strength steels, the action of the hydrogen has also been shown to enhance hole formation at precipitate particles (LEE *et al.* [1979]), presumably by lowering the interfacial energy. Moreover, an enhancement of plastic instability is also observed by the same authors, which is not yet understood. These effects can be engendered either by introducing hydrogen as an external gas, or by prior charging of the specimen to very high supersaturations of internally bound hydrogen.

Hydrogen also embrittles other metals besides iron. In bcc cases where, like iron, the solubility is low, similar effects as those in irons are observed, and similar mechanisms proposed. In numerous other systems, hydrogen is relatively soluble, and forms a stable hydride phase. In these metals, the hydride formation is generally aided by the stress in the vicinity of the crack. Since the hydrides are all found to be extremely brittle, the formation of the brittle phase at the crack tip drastically embrittles the material, presumably by inhibiting the formation of dislocations near the crack. These systems have been intensively studied and the embrittlement model verified by BIRNBAUM [1979, 1989].

10.6. Temper embrittlement and intergranular segregation

Here, we very briefly present a few of the more practical aspects of embrittlement due interfacial segregation, whose fundamentals were discussed in § 8. Because segregation to boundaries in the material is temperature dependent, interfacial segregation embrittlement will be a function of temperature and history. That is, heat treatments and other microstructure altering processes also change the degree of embrittlement which occurs. For this reason, embrittlement due to boundary segregation is also known as temper embrittlement.

For a general reference on segregation induced intergranular fracture, the reader is referred to MCMAHON *et al.* [1980]. For the special case of steels, the excellent fairly recent Sagamore Conference report is the relevant reference. See OLSON *et al.* [1987].

As a region of crystal where accumulation of impurities occurs, the greater concentration on boundaries also accelerates *cosegregation* of individual impurities into new compounds, with important embrittlement implications. For example, Sn, Sb, P, and Si have attractive interactions with Ni in steels. But, the effect of such interactions may increase or decrease embrittlement, depending on whether cosegregation occurs on the boundaries. Mo in steels, for example, interacts strongly with P. But the Mo remains in solution, and prevents the embrittling segregation of the other elements on the boundaries (see also ch. 13, § 6.3). There is also evidence that hydrogen embrittlement may in some, or even most, cases be enhanced by interactions with other impurities on the prior austenite boundaries in steels (TAKEDA and MCMAHON [1982]).

Clearly, cosegregation is not only an important effect from the practical point of view with respect to alloy design, but it also makes the study of embrittlement much more

References: p. 2287.

difficult, because the detailed chemical changes taking place at the boundary must be probed before the facts can be properly determined. Experimental techniques which can give this type of information, such as Auger analysis, are widely used and very important.

Finally, on a more fundamental level, we note that where segregation to boundaries lowers the interfacial "γ", it thus enhances interfacial fracture. But the dislocation emission criterion is more complex, and lowering γ does not necessarily lower the ductility parameter, $\mathscr{D}$. That is, if the matrix is ductile, one cannot a-priori say that the lower fracture energy on the boundary will ensure brittle fracture there. According to the discussion in § 8, the ductility parameter will be sensitive to the magnitude of the drop in fracture energy, and to the more subtle details of the bonding within and transverse to the interface plane.

10.7. Liquid-metal embrittlement

Perhaps the most dramatic chemical effect on fracture in metals is caused by certain liquid metals. For example, simply painting a polycrystalline ductile fcc metal like Al with gallium changes the normally ductile metal into an easily fractured highly brittle material. This effect has a complicated temperature dependence, usually leads to intergranular fracture, and requires an external stress sufficient to cause some microyield. The effect is most dramatic with liquid metals, but vapors of the appropriate metallic agent also may be effective. The former (and perhaps still valid) explanation of this embrittlement is that γ is drastically lowered by the embrittling metal, so that dislocation emission cannot occur. The reader is referred to the review by NICHOLAS and OLD [1979] for details.

In this chapter, we have proposed that intrinisic ductility of a material is associated with the stability of the lattice at the crack tip against breakdown in shear. In direct contradiction to these ideas, in liquid-metal embrittlement experiments by LYNCH [1981], and in hydrogen embrittlement studies in Ni by both LYNCH [1979] and BIRNBAUM [1979, 1989], these authors have claimed that the embrittlement process corresponds rather to an enhancement of dislocation emission at the crack tip. According to these authors, the overall effect is to localize the shear ahead of the crack on the crack plane. The fact that enhanced dislocation emission can be invoked to explain diametrically opposite observations illustrates the difficulty of correctly interpreting the more complex aspects of mechanical properties of materials!

10.8. Transformation-toughening

As the final application topic, a fundamentally different physical mechanism for crack shielding will be mentioned. When a local region of a material undergoes a phase transformation, the new phase, because it has a lattice with unit cell of different size and shape from the old, in general will generate compressive and shear stresses in both the old and the new lattice. By means of these stresses, transformed particles will interact with any cracks present for precisely the same reason that dislocations do. Also, just as a crack may generate a shielding plastic deformation in its vicinity, so a crack may

induce phase transformations because of the shift in transformation free energy driving force caused by the k field of the crack. The transformation will take place in an orientation such that its reaction back on the crack is in a shielding configuration. There is not space here to develop fully the shielding theory for transformation analogous to that in § 5 for dislocations. The straightforward way to do this, however, would be to assign a force multipole to each transformed particle, with a dilatation center to represent the net change in volume induced by the transformation, and a shear multipole to represent the shear component. The magnitude of the multipole is proportional to the local stress field with a constant of proportionality to be worked out on the basis of the transformation thermodynamics. The shielding theory then follows point-by-point that developed for dislocations in § 5.

Toughening transformations are observed in the ceramic, zirconia (see MCMEEKING and EVANS [1981]) and in steels, where the so-called TRIP (TRansformation-Induced Plasticity) steels demonstrated a remarkably high toughness from room temperature to liquid nitrogen temperatures. In a TRIP steel, the relevant transformation is that from metastable quenched austenite to martensite, where the free energy of the transformation indeed depends on the local stress, and can thus be triggered by the presence of a crack. Thus the toughening potential due to this mechanism will be limited roughly to the temperature regime over which the martensite transformation can be stress-induced in the steel. This will, of course, depend on carbon content and other metallurgical variables. Estimates of the degree of toughening achievable by the transformation suggest that the energy absorbed by the transformation can be as much as five times as large as that contributed by deformation in a particular TRIP steel. (The increase in K_{IC} due to transformation-toughening is roughly a factor of two.) The reader is referred to GERBERICH *et al.* [1969, 1971], and to ANTOLOVICH and SINGH [1970] for further details.

References

ANDERSON, P., and R. THOMSON, 1994, J. Appl. Phys., J. Appl. Phys. **76,** 843.

ANTOLOVICH, S., and B. SINGH, 1971, Metallurg. Trans. **2**, 2135.

BARSOM, J., 1979, Dynamic Fracture Toughness, ed. M. Davies (The Welding Institute, Abingdon Hall, Cambridge).

BEGLEY, J., and J. LANDES, 1972, Fracture Toughness (Am. Soc. Testing Mater., Spec. Tech. Pub. 560) p. 187; see other articles in this publication.

BEALE, P.D. and D.J. SROLOVITZ, 1988, Phys. Rev. **B37**, 5500.

BILBY, B.A., and J. ESHELBY, 1968, Fracture, vol. 1, ed. H. Liebowitz (Academic, New York) p. 99.

BILBY, B.A., A.H. COTTRELL and K. SWINDEN, 1963, Proc. Roy. Soc. (London) 272, 304.

BIRNBAUM, H., 1979, in: Environmentally Sensitive Fracture of Engineering Materials, Proc. AIME Conference, ed. Z. Fourlis (Met. Soc. AIME, Warrendale, PA).

BIRNBAUM, H., 1989, in International Conference on the Effect of Hydrogin on the Behavior of Materials, ed. N. R. Moody and A. W. Thompson, The Minerals, Metals and Materials Society, Warrendale, PA.

BREDE, M., 1993, Acta Met. **41**, 211.

BRIANT, C.L., 1990, Met. Trans. A., 1990 **21A**, 2339

BROEK, D., 1986, "Elementary Engineering Fracture Mechanics", Martinus Nijhoff, Dordrecht

BROEK, D., 1989, "The Practical Use of Fracture Mechanics", Kluwer Academic Publishers, Dordrecht.

CAMPBELL, J., W. GERBERICH and J. UNDERWOOD, 1982, Application of Fracture Mechanics for Selection of Metallic Structural Materials (ASM, Metals Park. OH).
DE CELLIS, B., S. YIP, and A. ARGON, 1983, J. Appl. Phys. **54**, 4864.
CHANG, S., and S. OHR, 1981, J. Appl. Phys. **52**, 7174.
CHEUNG, K. and S. YIP, 1990, Phys. Rev. Lett. **65**, 2804.
CHEUNG, K., S. YIP, and A. ARGON, 1991, J. Appl. Phys. **69**, 2088.
COMNINOU, M., 1977, J. Appl Mech. **44**, 780.
COX, T. and T. LOW, 1974, Metallurg. Trans. **5**, 1457.
CURTIN, W., 1993, J. Mech. Phys. Sol. **41**, 35.
CURTIN, W. 1993, Compostites **24**, 98.
DAHL, W., and W. KRETZCHMANN, 1977, in: Fracture 1977, vol. 2a, ed. D. Taplin (Pergamon Press, New York) p. 17.
DAW, M., M.I. BASKES, C.L. BISSON, and W.G. WOLFER, 1986 in Modeling Environmental Effects on Crack Growth Processes, ed. R. H. Jones and W. Gerberich (The Metallurgical Society, Warrendale PA)
DAW, M., 1989, Phys. Rev. **B 39B**, 7441.
DIENES, G.J., and A. PASKIN, 1987, J. Phys. Chem. Sol. **48**, 1015.
DIENES, G.J., and R. THOMSON, 1987, eds. J. Phys. Chem. Sols. **48**, 965–1155.
DUNDERS, J., 1968, Mathematical Theory of Dislocations, ASME, New York.
EBRAHIMI, F., 1991, Scr. Met. **25**, 1737.
ENGLAND, A.H., 1965, J. Appl. Mech. **32**, 400.
ESHELBY, J.D., 1956, Solid State Physics vol. 3, eds. F. Seitz and D. Turnbull (Academic, New York) p. 79.
FISK, G.A., and T.A. MICHALSKE, 1985, J. Appl. Phys. **58**, 2736.
FORD, H., P.H. HIRSCH, J.F. KNOTT, A. WELLS and J. WILLIAMS, 1981, Fracture Mechanics in Design and Service, A Royal Society Discussion (Royal Soc. London); also in Phil. Trans. Roy. Soc., 1981, A299, 3–239.
FRENKEL, J., 1926, Z. Phys. **37**, 572.
FREUND, L.B., 1990, Dynamic Fracture Mechanics, Cambridge U. Press, New York.
GARDNER, R., T. POLLACK and H.G.F. WILSDORF, 1977 Mater. Sci. Eng. **29**, 169.
GARRISON, W.M. and N.R. MOODY, 1987, J. Phys. Chem. Sol. **48**, 1035.
GARRISON, W. M., and K.J. HANDERHAN, 1989, Innovations in Ultrahigh-strength Steels, ed. G. Olson and M. Azrin, p. 443, Us Army Materials Techn. Lab., Watertown, MA.
GEORGE, A., and G. MICHOT, 1993, Matls. Sc. Eng. **A164**, 118.
GERBERICH, W., P. HEMMING, V.F. ZACKAY and E.R. PARKER, 1969, Fracture 1969, ed. P.L. Pratt (Chapman & Hall, London) p. 288.
GERBERICH, W., P. HEMMING and V.F. ZACKAY, 1971, Metallurg. Trans. **2**, 2243.
GERBERICH, W., Y. CHEN and W. St. JOHN, 1975, Metallurg. Trans. **6A**, 1485.
GOODIER, J.N., 1968, Fracture Vol. 2, p. 1, Ed. H. Libowitz, Academic Press, New York.
GOODWIN, L., R.J. NEEDS, V. HEINE, 1988, Phys. Rev. Lett. **60**, 2050.
GRIFFITH, A.A., 1920, Phil. Trans. Roy. Soc. (London) **A221**, 163.
HARLIN, G., and J.R. WILLIS, 1990, Int. J. Fract. **42**, 341.
HARRISON, R.J., F. SPAEPEN, A.F. VOTER, and S.P. CHEN, 1990, Innovations in Ultrahigh Strength Steel Technology, ed. G. B. Olson, M. Azrin and E. S. Wright, Sagamore Army Materials Research Conference Proceedings: 34th, p. 651.
HEAD, A., and N. LOUAT, 1955, Austr. J. Phys. **8**, 1.
HIRSCH, P.B., and S.G. ROBERTS, 1991, Phil. Mag. **A64**, 55.
HIRTH, J.P. and J.R. RICE, 1980, Met. Trans. **11A**, 1502.
HIRTH, J.P., 1980, Metallurg. Trans. **11A**, 861.
HIRTH, J.P., and J. LOTHE, 1981, Theory of Dislocations (McGraw–Hill, New York). Second edition, 1992 (Krieger, Melbourne, Florida).
HIRTH, J.P., and J. RICE, 1980, Metallurg. Trans. **11A**, 1501.
HOAGLAND, R.G. and H.L. HEINISCH, 1992, J. Matls. Rsh. **7**, 2080.
HOAGLAND, R. and Y. LIU, 1994 to be published (Yamata Conf. Proceedings.)
HONG, T., J.R. SMITH, and D.J. SROLOVITZ, 1993, Phys. Rev. Lett. **70**, 615.

HONG, T., J.R. SMITH, and D.J. SROLOVITZ, 1994, Acta Metall. Mater. **43**, 2721.
HUANG, H., and W.W. GERBERICH, 1994, Acta Met., in press.
HUTCHINSON, J.W., 1968, J. Mech. and Phys. Sol. **16**, 13.
HUTCHINSON, J.W. and Z. SUO, 1991, Adv. Appl. Mech. **29**.
IRWIN, G.R., 1948, Fracturing of Metals, American Society for Metals, Cleveland, p 147.
IRWIN, G., 1957, J. Mech. **24**, 361.
JUAN, Y.M. and KAXIRAS, 1993, J. Comp. Aided Matls. Des. **1**, 55.
KANNINEN, M.L. and C.H. POPELAR, 1985, Advanced Fracture Mechanics, Oxford Univ. Press, New York.
KELLY, A., 1966, Strong Solids (Oxford Univ. Press).
KELLY, A., A.H. COTTRELL and W. TYSON, 1967, Phil Mag. **29**, 73.
KNAUSS, W.G., and A.J. ROSAKIS, editors, 1990, Int. J. Fract. **42**, 1–404.
KNOTT, J.F., 1973, Fundamentals of Fracture Mechanics (Butterworths, London).
KNOTT, J.F., Fracture 1977, Proc. Fourth Int. Conf. on Fracture (Waterloo Univ. Press, 1977) vol. 1, p. 61.
KOBAYASHI, S., and S.M. OHR, 1981, Scripta Metall. **15**, 343.
KOHLHOFF, S., P. GUMBSCH, and H.F. FISCHMEISTER, Phil. Mag. **64**, 851 (1991).
KRASKO, G.L. and G.B. OLSON, 1990, Solid State Comm. **76**, 247.
KRASKO, G.L. and G.B. OLSON, 1994, Solid State Comm., in press.
LATANISION, R., ed., 1982, Atomistics of Fracture. Proc. NATO Advanced Study Institute (Plenum, New York).
LAWN, B.R., 1993, Fracture of Brittle Solids (Cambridge Univ. Press).
LAWN, B.R., B. HOCKEY and S. WIEDERHORN, 1980, J. Mater. Sci. **15**, 1207.
LEE, T., T. GOLDENBURG and J. HIRTH, 1979, Metallurg. Trans. **10A**, 199.
LI, Y.S. and P.M. DUXBURY, 1988, Phys. Rev. **B 38**, 9257.
LIEBOWITZ, H., 1968, Fracture, Vols. 1, 2 (Academic, New York).
LIN, I.H. and R. THOMSON, 1986, Acta Met. **47**, 187.
LOW, J.R., 1955, Proc. Conf. Intern. Union. Theor. & Appl. Mech., Madrid, 60.
LYLES, R., and H. WILSDORF, 1975, Acta Metall. **23**, 269.
LYNCH, S., 1979, Scripta Metall. **13**, 1051.
LYNCH, S., 1981, Acta Metall. **29**, 325.
MARKWORTH, A.J., M.F. KANNINEN and P.C. GEHLEN, 1973, Proc. Int. Conf. Stress Corrosion Cracking , France June 12.
MAJUMDAR, B., and S. BURNS, 1981, Acta Metall. **29**, 579.
MAJUMDAR, B., and S. BURNS, 1983, Int. J. Fract. Mech. **21**, 229.
MARSH, P.G. and W.W. GERBERICH, 1994, Acta Met., in press.
MCMAHON, C., V. VITEK and J. KAMEDA, 1980, in: Developments in Fracture Mechanics, ed. G. Chell (Appl. Sci. Publ., Barking, Essex, UK), 193.
MCMAHON, C.J., 1989, in International Conference on the Effect of Hydrogin on the Behavior of Materials, ed. N. R. Moody and A. W. Thompson, p. 587, The Minerals, Metals and Materials Society, Warrendale, PA
MCMEEKING, J., and A. EANS, 1981, J. Amer. Cer. Soc. **65**, 242.
MICHALSKE, T.A. and S.W. FREIMAN, 1983, J. Am. Ceram. Soc. **66**, 284.
MOODY, N.R. and A.W. THOMPSON, editors, 1989, International Conference on the Effect of Hydrogen on the Behavior of Materials. The Minerals, Metals and Materials Society, Warrendale, PA.
NICHOLAS, M., and C. OLD, 1979, J. Mater. Sci. **14**, 1.
OLSON, G.B., M. AZRIN, and E.S. WRIGHT, 1987, editors, Innovations In Ultrahigh-Strength Steel Technology, Us Army Materials Technology Laboratory, Watertown, MA.
ORIANI, R.A., and P. JOSEPHIC, 1974, Acta Metall. **22**, 1065; 1977, Acta Metall. **25**, 979.
ORIANI, R.A., 1978, Ann. Rev. Mater. Sci. **8**, 327.
OROWAN, E., 1948, Rpts. Prog. Phys. **XII**, 185.
OROWAN, E., 1949, Prog. Phys. **12**, 185.
RICE, J., 1965, Proc. Int. Conf. on Fracture, eds. T. Yokohari et al. (Japan. Soc. Strength & Fracture, Sendai) vol. I, 309.
RICE, J., 1968, J. Appl. Mech. **35**, 13.
RICE, J.R., and G.F. ROSENGREN, 1968, J. Mech. and Phys. Sol. **16**, 1

RICE, J.R., and M.A. JOHNSON, 1970, Inelastic Behavior of Solids, ed. M. Kanninen, W. Adler, W. Rosenfield and R. Jaffee, Mc Graw–Hill, New York, p 641.
RICE, J., and R.M. THOMSON, 1974, Phil. Mag. **29**, 73.
RICE, J., 1976, The Mechanics of Fracture, ADM vol. 19 (ASME, New York) p. 23.
RICE, J.R., 1988, J. Appl. Mech **55**, 98.
RICE, J.R., Z. SUO, and J.-S. WANG, 1989, Proceedings of Conference on Metal-Ceramic Interfaces, Santa Barbara, CA, Pergamon, New York, ed. M. Ruhle, A. Evans, M. Ashby, and J. Hirth, p 269.
RICE, J.R., 1992, J. Mech. Phys. Solids **40**, 239.
RICE, J.R., G.E. BELTZ, and Y. SUN, 1993, Topics in Fracture and Fatigue, ed A. S. Argon, Springer.
SHASTRY, V., P. ANDERSON, and R.M. THOMSON, 1994, J. Matls. Rsh. **9**, 812.
SCHOECK, G., 1992, Philos. Mag. **63**, 111.
SHUBAT, G., et al. eds., 1974, Metals Handbook, vol. 9 (ASM, Metals Park, OH).
SMITH, E., 1966, Proc. Conf. Physical Basis of Yield and Fracture (Inst. of Phys. and Phys. Soc.) p. 36.
SMITH, E., 1979, in: Dislocations in Solids, vol. 4, ed. F.R.N. Nabarro (North-Holland, Amsterdam) p. 363.
STROH, A.N., 1957, Adv. Phys. 6, p. 418.
TADA, H., P. PARIS and G. IRWIN, 1973, The Stress Analysis of Cracks Handbook (Del. Rsch. Corp., Hillertown, PA).
TAKEDA, Y., and C. MCMAHON, 1981, Metallurg. Trns. **12A**, 1255.
THOMASON, P.F., 1990, Ductile Fracture of Metals, Pergamon, New York.
THOMSON, R.M., 1980, J. Mater. Sci. **15**, 1027.
THOMSON, R.M., and E. FULLER, 1982, in: Fracture Mechanics of Ceramics, eds. R. Bradt et al. (Plenum, New York).
THOMSON, R.M., and J. SINCLAIR, 1982, Acta Metall. **30**, 1325.
THOMSON, R., V.K. TEWARY, and K. MASUDA–JINDO, 1987, J. Matls. Res. **2**, 619.
THOMSON, R., S.J. ZHOU, A.E. CARLSSON, V.K. TEWARY, 1992, Phys. Rev. **B46**, 10613.
THOMSON, R., and S.J. ZHOU, 1994, Phys. Rev. **49**, 44.
THOMSON, R., and A.E. CARLSSON, 1994, Philos. Mag. **70**, 893.
VEHOFF, H., and P. NEUMANN, 1980, Acta Metall. **28**, 265.
VEHOFF, H., W. ROTHE and P. NEUMANN, 1981, Advances in Fracture Research **1**, 275; see also
WANG, J.S. and H. VEHOFF, 1991, Scr. Met. **25**, 1339.
WANG, J.S., 1995, Mech. of Matls. **20**, 251.
WILLIAMS, M.L., 1959, Bull. Seismol. Soc. Amer. **49**, 199.
WU, R., A.J. FREEMAN, G.B. OLSON, 1992, J. Matls. Rsh. **7**, 2403.
WU, R., A.J. FREEMAN, and G.B. OLSON, 1994, Phys. Rev. B **B50**, 75
WEERTMAN, J., 1978, Acta Met. **26**, 1731.
WEERTMAN, J., 1981, Phil. Mag. **A43**, 1103.
WEERTMAN J., I. LIN and R.M. THOMSON, 1983, Acta Metall. **31**, 473.
WHITE, G.S., 1996, Environmental Effects on Crack Growth of Ceramics, ed. D. Cranmer and D. Richardson (Marcel Decker, New York).
WIEDERHORN, S., R. MOSES and B. BEAN, 1970, J. Am. Ceram. Soc. **53**, 18.
WIEDERHORN, S., E. FULLER and R.M. THOMSON, 1980, Met. Sci. **14**, 450.
ZHOU, S. and R. THOMSON, 1991, J. Mater. Res. **6**, 639.
ZHOU, S., A.E. CARLSSON, and R. THOMSON, 1993, Phys. Rev. **47**, 7710.
ZHOU, S., A.E. CARLSSON, and R. THOMSON, 1994, Phys. Rev. Ltr., **72**, 852.

Further reading

1. Fracture Mechanics in Design and Service, A Royal Society Discussion, organized by H. Ford, P. Hirsch, J., F. Knott, A. Wells and J.Williams (Royal Society, London, 1981); also in Phil. Trans. Roy. Soc. A299 (1981) 3–239.
2. Elementary Engineering Fracture Mechanics, D. Broek, Marinus Nijhoff, Dordrecht. 1986.
3. Advanced Fracture Mechanics, M.L. Kanninen and C.H. Popelar, Oxford Univ. Press, New York, 1985.

4. Fracture of Brittle Solids, B.R. Lawn (Cambridge Univ. Press, London, 1993).
5. Strong Solids, A. Kelly (Oxford Univ. Press, 1966).
6. Fundamentals of Fracture Mechanics, J. Knott (Butterworths, London, 1973).
7. W.G. Knauss and A.J. Rosakis, editors, Int. J. Fract., 42 p. 1–404, 1990.
8. Applications of Fracture Mechanics for Selection of Metallic Structural Materials, eds. J. Campbell et al. (ASM, Metals Park, OH, 1982)
9. Atomistics of Fracture, eds. R.M. Latanision and J.R. Pickens (Plenum, New York. 1982).
See comments on these and other sources in the Introduction.

Appendix A. Table of symbols

σ	stress tensor
μ	shear modulus
u	displacement vector
$u_{ij}=\partial u_i/\partial x_i$	partial derivatives of displacement vector
x_1, x_2, x_3	rectangular coordinates
$z=x_1+ix_2$	complex variable
W	strain energy function
w	u_3 displacement
a, N	half crack length
K	macroscopic stress intensity factor
k	local stress intensity
E	Young's modulus
$K_c, K_k,$	etc. critical stress intensity for onset of fracture
b, B	Burgers vector, total Burgers vector
COD	crack opening displacement
c	core crack enclave radius
d	outer extent of plastic zone
P	dislocation density
σ_f	dislocation friction stress
m	work hardening parameter
$\mathcal{D}$	ductility parameter
F	external force exerted on a lattice point
U	total energy of system plux external loading system surface free energy
f	interatomic force
ν	Poisson's ratio
f^*	complex vector force on an elastic singularity
$\mathcal{G}$	crack extension force, elastic energy release rate
J	Rice "J integral"

CHAPTER 27

FATIGUE

Campbell LAIRD

Department of Materials Science and Engineering
University of Pennsylvania
Philadelphia, PA 19104–6272, USA

R. W. Cahn and P. Haasen†, eds.
Physical Metallurgy; fourth, revised and enhanced edition

1. *Introduction — History, fatigue design and nomenclature*

The classes of stresses to which engineering materials and structures are commonly subjected in service are static or steady stresses, repeated stresses, impact stresses and combinations of these three; for examples, it is possible to have repeated impact stresses or repeated stresses in combination with a steady stress. Documented efforts to understand and control the resistance of materials to fracture by repeated or cyclic stresses have been on-going for 166 years with ever-increasing intensity. In 1983, Battelle Laboratory under contract to US Government agencies performed detailed economic analyses of the costs of fractures in materials such as metals, wood and glass, and efforts to prevent it. These costs to US industry amounted to $119 billion/year, that is, a significant percentage of the GNP. It is unlikely that the percentage is much different today. By far the largest fraction of the fractures in metals is associated with cyclic stresses. The enormous literature on fatigue which has been driven by the severity of the problem has been documented by MANN [1970, 1978] up to 1960.

Service-related cyclic stresses may vary from zero to a positive extremum, from a positive or negative extremum to another positive or negative extremum, or from a negative extremum to a positive extremum. The nature of the stress range is conventionally indicated by R, the ratio of the minimum to maximum stress. That is, when the negative and positive stresses are numerically equal, an alternating stress would be designated $R=-1$. Failure from repeated nominally negative stresses (i.e., compression) is known to occur although it is unlikely in such circumstances that the material actually sees only negative stresses. The majority of experimental efforts to understand mechanisms of failure under cyclic stress have employed alternating stress with $R \approx -1$.

The term "fatigue" has been applied to the phenomenon of fracture under repeated stresses, dating from the latter half of the 19th Century. While it is admittedly not a proper descriptive term, it has become so thoroughly established in the literature that no worker has had the temerity or the energy to discard it. The term "progressive failure" is more precisely descriptive of the action of cyclic stresses on a member or material. The stresses needed to produce failure in fatigue lie well below the ultimate tensile strength and for commercial materials, below the yield stress as well. In pure metals and alloys, cyclic stressing can cause hardening and the stresses required to cause failure in experimentally-accessible numbers of cycles are usually greater than the yield strength of the annealed metal.

The earliest reported tests on fatigue appear to be those of ALBERT [1838] made in Germany on welded chain used in mine hoists. The British were very active in the early days in association with the development of railroads and bridges, being represented by such well-known personalities as Rankine, Hodgkinson, and Fairbairn. Wöhler justly receives credit for the concept of the *S–N curve* and the *fatigue limit*, by which is meant that unit cyclic stress which may be applied to a given material for an indefinitely large number of cycles without producing rupture. Wöhler may have been slow in publishing. Although, like the other early workers, he was ingenious in designing machines for stressing his specimens, he was forced to run his machines at slow speeds and the highest speed he had available to him appears to have been 72 rpm in his rotating

bending machine. Thus it took many years to accumulate measurements at long lives (for example, a test of 10^8 cycles would take about three years). It is interesting that MOORE and KOMMERS [1927], who wrote one of the first books on fatigue, dedicated it to ..."the many distinguished British investigators, who have been foremost in forwarding our knowledge of the fatigue phenomena of metals, ..." but, with American even-handedness, in the frontispiece, showed a portrait of Wöhler. In more recent decades, it is apparent that now, as then, the nationality of those interested in fatigue has followed the center of gravity of the global economy, just as to be expected from a critically fatal phenomenon associated with mechanical systems.

Bauschinger, whom we remember best for reversing the stress once (see ch. 21, § 7.3.8 for a discussion of the Bauschinger effect), also carried out experiments in which he reversed the stress many times [1886]. He essentially discovered *cyclic strain-hardening* and *cyclic-softening*, by which last term we understand the softening produced by cyclic stresses of hardening previously introduced into a metal by monotonic straining. EWING and HUMPHREY [1902] initiated a different approach to fatigue by microscopically studying slip band behavior when specimens were subjected to reversed stress. With increase in the numbers of cycles of stress, additional slip lines appeared which had not been visible before, and the first ones to have formed showed a tendency to broaden. Ultimately cracks were observed to form in the broadened bands. They thus discovered the phenomenon of *Persistent Slip Bands* (PSBs) although the slip bands were not thus termed until decades later when THOMPSON and WADSWORTH [1958] discovered that they reappeared in the same location after the test had been interrupted, the surface repolished, and the test restarted.

Before the first World War, a Royal Commission summoned by the British addressed the problem of fatigue and offered a statement of the understanding of their time, which is surprisingly modern. For example, they debunked the celebrated "crystallization" theory of fatigue. Erroneous scientific ideas seem to die hard, especially in the public mind. Many years later T.E. Lawrence described in the "Seven Pillars of Wisdom" an incident during a skirmish with the Turks when one of their vehicles lost a leaf spring (after hard usage in the desert). T.E. explained the fracture as having "crystallized through."

The stress-based approach to fatigue design rooted in the S–N curve dominated the technology of fatigue up to the time of World War II and later. However, in the 1950s, MANSON [1953] and COFFIN [1956]; COFFIN and READ [1956]; COFFIN and TAVERNELLI [1958] reported test results in which strain rather than stress was used as the control mode of the test. These investigations not only gave rise to the well-known strain-life correlation named after the investigators (the *Coffin–Manson Law*), but also permitted *cyclic stress–strain response* to be explored. If a test is conducted at constant cyclic strain, the stress necessary to enforce that strain repeatedly can be measured. Usually, but not always depending on material, the specimen ultimately attains a constant stress, termed the *saturation stress*. A plot of the saturation stress as a function of the applied strain amplitude (total or plastic strain) defines the *cyclic stress strain curve*, analogous to the monotonic stress–strain curve. This analogy gave rise to the definition of fatigue properties similar to monotonic mechanical properties and by the 1970s, industries were

References: p. 2391.

formulating specifications in terms of these properties. Up to then, published fatigue properties were expressed primarily in terms of the *fatigue or endurance limit* and no other. An elaborate "strain-based" approach to fatigue design has been developed and is now widely used (Fatigue Design Handbook, Society of Automotive Engineers). The study of cyclic deformation also provided a different route to the understanding of fatigue mechanisms.

Although it had long been recognized that fatigue life was dominated by the initiation and propagation of cracks, there were essentially no measurements of crack growth kinetics up to the early 1960s. At that time Paris and co-workers (PARIS, GOMEZ and ANDERSON [1961]; PARIS and ERDOGAN [1963]) suggested that the rate of fatigue crack growth should be characterized in terms of *linear elastic fracture mechanics* and based on the range of the *stress intensity factor*. This approach circumvented the difficult problem of defining the elastic-plastic behavior at the crack tip and permitted the correlation of measurements obtained in different specimens and loading systems. It produced an explosion of effort on the measurement of crack growth in a wide variety of metals and alloys, which has dominated fatigue research in the last 25 years and has defined yet more fatigue properties, such as the *threshold stress intensity* for fatigue crack propagation, and the exponent of the so called *Paris curve*, a plot of crack growth rate versus the stress intensity.

The emphasis on fatigue crack propagation produced yet another approach to fatigue design based on the tolerance of the structure to an existing crack or flaw. This approach is connected to the "*fail-safe*" philosophy of design, meaning that no single member of the structure is "critical" for its survival, and that there is sufficient redundancy in the structure that the failure of one part can be sustained by the others until the partial failure is detected during inspection. The crack propagation approach, which is economically applicable to expensive and safety-critical structures like aircraft, calls for costly methods of non-destructive testing which have to be applied in order to detect fatigue cracks, often when they are quite small, such as 0.15 mm deep for engine components, or 0.80 mm for airframes. The high cost of inspections drives efforts to improve the predictability of fatigue crack propagation and the residual strength of a cracked structure. The older stress-based and strain-based fatigue methodologies and fracture mechanics are both required at the present day in fatigue design, the former for predicting the durability of a structure or component, the latter for controlling its safety.

Reliable prediction of fatigue failure can be obtained only by a thorough understanding of the physical mechanisms involved. For commercial materials, with their complicated microstructures, we are far removed from a quantitative theory which relates elementary processes to the observable life under fatigue loading, although so much experimental data exist for crack propagation kinetics that reasonable estimates of residual life can be obtained if the geometry of the pre-existing flaw is known. Understanding of cracking mechanisms, rooted in the early work of Gough and co-workers (GOUGH [1933]) who initiated work on single crystals, has benefited from the modern approach of using single crystals in conjunction with tools such as transmission electron microscopy and scanning microscopy, for research into mechanisms and into dislocation behavior. The present chapter does not deal with engineering aspects of fatigue except

for the brief summary given above and performance indicators, but focuses on the basic phenomena of fatigue and their mechanisms in metals and alloys.

If the structure or specimen is "smooth", meaning that it does not contain a flaw which can immediately develop into a growing fatigue crack under the action of the applied cyclic stresses, then the phenomena of fatigue are complex. At the start of life, the material undergoes *cyclic hardening* which conditions the material to form cracks. Such conditioning usually causes the strain to localise, with considerable local enhancement of the plastic strain that stimulates both crack initiation and growth. Usually the localisation will be emphasized by a stress concentrator, either in the member (e.g., a weld or re-entrant) or in the material (non-metallic inclusion or other microstructural feature), but localisation can occur by dislocation mechanisms in simple specimens of pure metals. No clear position has emerged to distinguish fatigue-produced surface roughness from a defined, growing crack. However, a crack is usually regarded as a "proper" crack, engaged in propagation, if it is 3–5 μm in depth. The slow development of such small cracks is described by the study of "short" cracks which refers to cracks which are: 1) physically small, 2) small in relation to the size of the localized plastic zone which has favored their development or 3) small in relation to a significant microstructural feature, such as a grain. After the crack has grown to the depth of many microns, the behavior of the plastic zone at the crack tip controls the crack growth rate, and the size of the plastic zone becomes small in relation to the size of the crack ("long crack growth"). These various fatigue phenomena, and their mechanisms, are treated in detail in what follows.

2. *Fatigue testing*

In order to obtain repeatable results in tension testing, especially for elongation to monotonic fracture, the tension test is standardized with respect to the shape of the specimen. Fatigue behavior and properties are so complex that no generally acceptable testing standards apply to fatigue except that fracture mechanics specimens are frequently used for measuring crack propagation in fatigue. Fatigue tests have been conducted in many different ways, and minor differences in testing can produce significant differences in behavior. Scatter of the results is therefore endemic to fatigue studies as much from testing reasons as from variability between specimens. The most popular testing methods are as follows:

2.1. Constant amplitude stress tests

In commercial materials where both yield and ultimate tensile strengths are high, fatigue can occur at long life at stresses that are relatively low. Consequently both the elastic and plastic strain are small. Such materials can be subjected to the full stress amplitude at the first cycle, and the test can be run truly at constant stress amplitude until the specimen fails. Complete fracture of the specimen is normally taken to define failure.

If the material is in the annealed condition, the strain amplitude produced by a typical value of the stress amplitude will be largest in the first cycle, but such straining will

References: p. 2391.

cyclically harden the specimen and the strain will continuously decrease during the initial period of cycling and finally reach a saturation value after some 100s or 1000s of cycles depending on the material and the stress amplitude.

A wide variety of waveforms and frequencies have been used for fatigue testing but those preferred for fatigue research are usually kept simple, such as sinusoidal or sawtooth forms.

In work conducted on older machines which often operated on a resonance principle, a specimen might undergo a complex series of work-up cyclings before the desired "constant" stress amplitude was attained. Such machines continue to be widely used. However, since the mid-1960s, electrohydraulic, closed-loop systems have been employed. The specimen is stressed by means of a hydraulic cylinder in which the high pressure fluid is controlled by a servo-valve actuated by an electrical input, often subject to a computer. Such a testing mode offers very flexible control and sophistication in testing, so that a constant amplitude test can be truly carried out from the onset of cycling. The ability to obtain a wide range of loads from very large down to a few Newtons by selection of the appropriate size of hydraulic cylinder enables electro-hydraulic test methods to be applied to a wide range of specimen sizes and configurations, from macro-structures to mini-specimens.

2.2. Increasing stress amplitude tests

In soft commercial metals and alloys, or in model materials used in research, such as single crystals, the stress needed to cause fatigue fracture at long life may be high enough to strain the material to an unacceptably high level if applied to the full level at the first cycle. The specimen might become destructively deformed, for example. In order to avoid this very large initial strain, the stress amplitude must be worked up gradually, say in 30 to 100 cycles, to the desired final stress amplitude, which may then be kept constant for the remainder of the experiment. These relatively high initial strain amplitudes may well affect the fatigue behavior of the specimen.

In order to avoid such a history effect on the life behavior, or for other reasons, an experimenter may choose to ramp up the alternating stress over a much longer interval, say 20,000 cycles, to the desired final stress amplitude, at a controlled constant rate of stress increase.

2.3. Constant plastic strain amplitude tests

Although most structures are subject to load cycling, suggesting that constant stress amplitude tests would be most representative of service fatigue, in practice fatigue cracks tend to occur in regions of stress concentration. In such regions the straining behavior is constrained and the stress–strain response is more complicated than under simple stress control, which thus represents an extreme of behavior. As LANDGRAF [1977] amongst others has pointed out, the normally used test conditions represent extremes of completely unconstrained (or stress-cycling conditions) and completely constrained (or strain-cycling conditions). In actual engineering structures, stress–strain gradients do exist, and there is usually a certain degree of structural constraint of the material at critical

locations. Such a condition tends to be similar to strain control. Therefore, this type of test has become increasingly favored in the last 30 years, for both low strain and high strain fatigue testing. Furthermore, tests at high stress under stress control are difficult to conduct because the specimen creeps uncontrollably, even at room temperature, by "cyclic creep". *Cyclic creep* is that deformation produced by an alternating stress superimposed on a mean stress (for reviews, see KENNEDY [1962]; LORENZO [1983]).

Accordingly, for well-behaved tests conducted at high strains, tests in strain control are necessary. It is also necessary to choose between control in *total* strain amplitude, or *plastic* strain amplitude. In tests under total strain control, cyclic hardening causes the elastic component of the strain to increase at the expense of the plastic strain. However, since hardening usually saturates rapidly, tests in total strain control do end up to amounting to tests in plastic strain control. With the advent of sophisticated electronic control of electrohydraulic testing equipment, it is now more readily possible to control the plastic strain amplitude to be constant from the onset of cycling, a control mode which is widely practiced.

It is generally accepted that plastic strains are necessary for the development of fatigue in spite of the fact that, in long-life fatigue, the plastic strain amplitude is a small fraction of the total strain amplitude, and may be so small as to be difficult to measure. Because of the fundamental importance of plastic strain in fatigue, some workers choose to use plastic strain controlled tests even at long life (plastic strain amplitude 5×10^{-5} to 5×10^{-4}), but at the cost of much greater effort because of the great resolution needed to measure the strain. Tests conducted at strain amplitudes in the range 5×10^{-4} to 10^{-2} would be considered high strain fatigue tests, in which the lives would typically be less than 100,000 cycles to failure. Reports of fatigue tests at strains $> 10^{-2}$ are rare.

The relative sizes of the elastic and plastic components of the fatigue strain are used to define formally the distinction between low and high strain fatigue. The dividing point is that total strain amplitude for which the elastic and plastic components of the strain are equal. The life associated with this point is termed the *transition life*, N_t. If the plastic strain is greater than the elastic strain, the fatigue is defined as *high-strain fatigue*, and *low-strain fatigue* for vice versa.

2.4. Variable amplitude tests

In order to simulate more realistically the loading history of the components of actual structures, tests are also performed with highly complicated loading sequences. In such tests, it becomes difficult to define a stress cycle, and reversals of the stress tend to be counted instead. Special techniques have been developed to characterize such loading histories (WETZEL [1971]). The physics of load interaction in fatigue under variable amplitudes are poorly understood and extremely complicated; they are not treated here (see MA and LAIRD [1989a]).

Test frequency is an important variable both for research purposes and in practical matters. For example, long tests are more economical if they can be run at high frequencies. For high strain fatigue tests, frequencies in the range from 0.1 Hz to a few Hz are convenient. Long-life tests can be run with frequencies up to 100 Hz.

References: p. 2391.

One of the limitations of electrohydraulic equipment is the difficulty of controlling tests at high frequencies, and such tests are generally conducted at frequencies less than 20 Hz. With special resonance machines, frequencies up to 500 Hz can be reached. Using ultrasonic resonance techniques with horn-shaped specimens or appropriately-gripped cylindrical specimens, fatigue experiments can also be performed with frequencies in the range of some 20 kHz (TSCHEGG and STANZL [1981]). Such testing is valuable for obtaining results at long life but specimen heating due to the high rate of heat generation is a problem and requires special techniques for avoiding it.

3. *Performance parameters of fatigue*

The monotonic tensile properties of materials are described by such well-known parameters as the yield or flow stress (often evaluated at 0.2% strain), the ultimate tensile strength, the percent reduction in area, the true fracture stress (defined as the final load divided by the final area of the neck), and the true fracture ductility ($= \ln (A_o/A_f)$, where A_o is the initial cross-sectional area of the specimen, and A_f the final area at the point of fracture). Properties parallel to these have been defined for the fatigue behavior of materials, dealing with both stress–strain response and fracture behavior. (For a detailed review of this subject, see MITCHELL [1979]).

3.1. Cyclic stress–strain behavior

Since metals are metastable under the application of cyclic loads, their *stress–strain response* can be drastically altered when subjected to cyclic strains. Depending on the initial state of the metal (whether it has been hardened by some metallurgical process, or softened by annealing) and its test condition, the specimen may: a) *cyclically harden,* b) *cyclically soften*, c) maintain its flow stress, when it is said to be *cyclically stable*, or a) show mixed behavior (soften or harden, depending on strain amplitude, or both harden and soften, as life progresses). Examples of some of these types of behavior are shown in fig. 1: a) if the stress required to enforce the strain increases as life unfolds, the metal undergoes hardening. This behavior is typical of annealed metals and alloys, and the softer steels and aluminum alloys. b) If the stress required to enforce the strain decreases with successive cycles, the phenomenon is called cyclic softening. Cold-worked metals and steels which have inherited dense dislocation structures from their processing history tend to behave in this way. The stress-time plots shown in figs. 1a and b are *cyclic strain-hardening* and *softening curves* respectively (see also ch. 28, § 2.3). Some metals (rare) are cyclically stable, in which case their monotonic stress–strain behavior adequately describes their cyclic response. Whatever the nature of the material, cycled under control of the strain amplitude, it will eventually attain (almost always) a steady-state stress response. To construct a *cyclic stress–strain curve*, one connects the tips of the stabilized hysteresis loops from comparison specimen tests at several controlled strain amplitudes (see fig. 2).

The cyclic stress–strain curve can be compared directly to the monotonic stress–strain curve to quantitatively assess cyclically induced changes in mechanical behavior. Typical

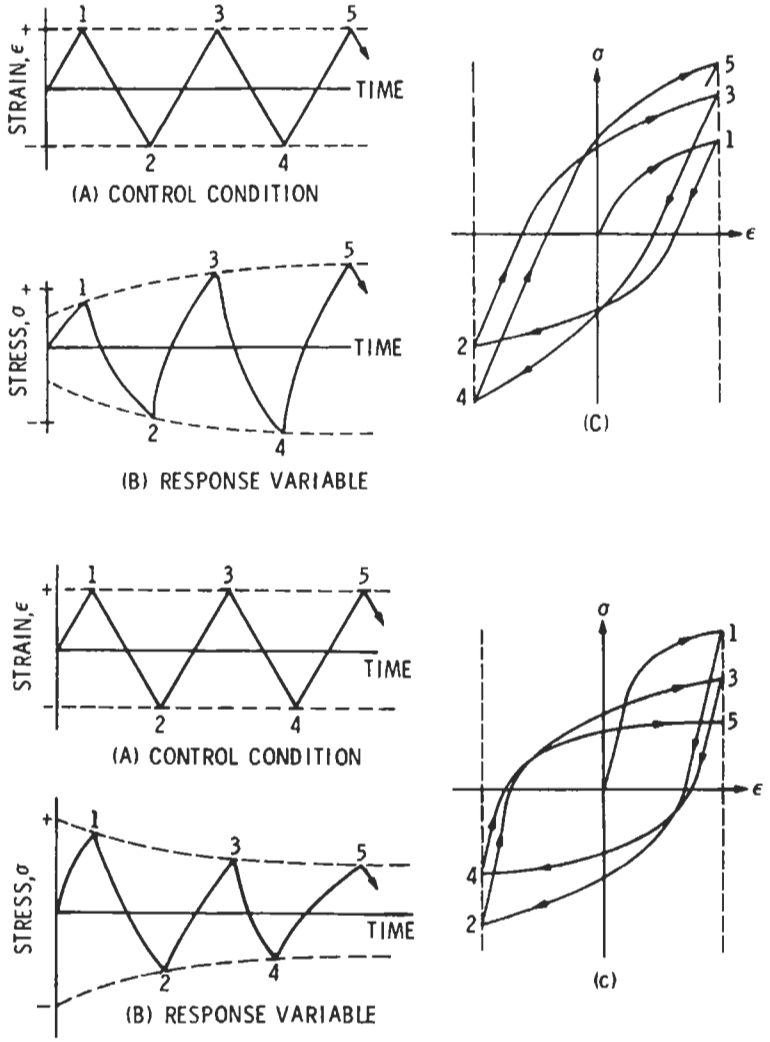

Fig. 1. Cyclic response under controlled-strain-amplitude cycling showing the control condition, the response of the stress to the cycling and hysteresis loops associated with the accumulating cycles for (a) cyclic hardening, (b) cyclic softening. Courtesy of M. R. Mitchell and ASM International.

examples taken from MITCHELL [1979] are shown in fig. 3; materials which cyclically harden and others which soften are shown. Note that, for extreme examples, meaning materials containing metallurgical structures well removed from equilibrium, softening can be considerable. Thus the "cyclic yield stress", defined at some elapsed strain, just as for monotonic deformation, can be a mere 50% of the monotonic yield strength.

If the cyclic stress–strain curve is represented by a power-law function, such as:

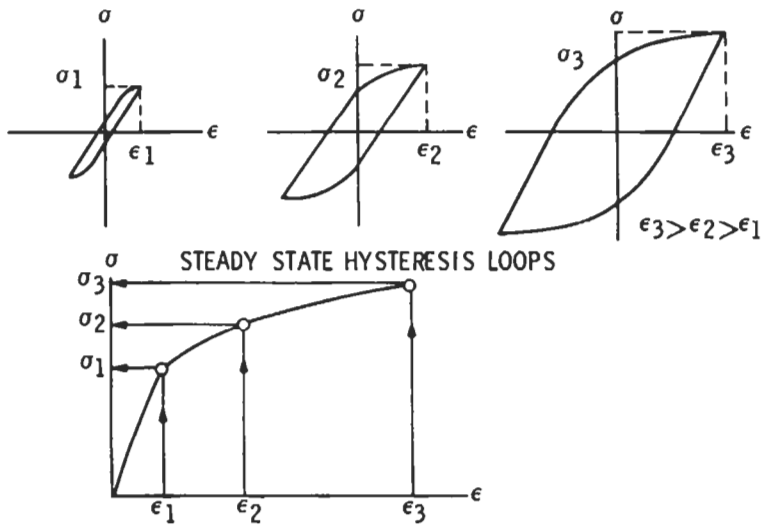

Fig. 2. Construction of cyclic stress–strain curve by joining tips of stabilized hysteresis loops. In the cyclic stress–strain curve, the total strain has been used for the abscissa. If the loop half-width at zero stress had been used, the CSSC would be plotted for the plastic strain. Courtesy of M. R. Mitchell and ASM International.

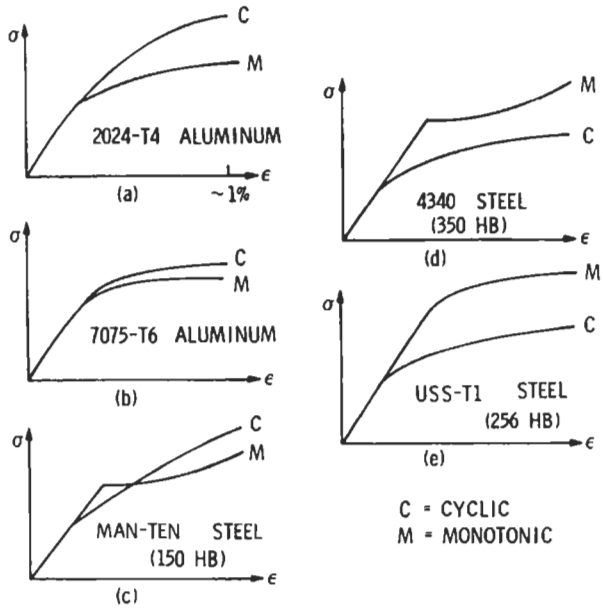

Fig. 3. Cyclic stress–strain response, curve C, compared with monotonic behavior, stress–strain curve M, for typical commercial metals. If the C curve lies above the M curve, cyclic hardening has occurred; cyclic softening has occurred for vice versa. The Brinell hardnesses of the steels are indicated. Soft steels generally harden, quenched and tempered steels generally soften. Courtesy of M. R. Mitchell and ASM International.

$$\sigma_a = K(\varepsilon_p)^n \tag{1}$$

where σ_a is the *steady-state* (saturation) stress amplitude, ε_p is the plastic strain amplitude, then the parameters K and n can be used to describe the cyclic stress–strain response. K is termed the *cyclic-strength coefficient* and n the *cyclic strain hardening exponent*. In cyclically softening materials, where completion of softening may be doubtful, σ_a is conventionally defined at 50% of life. Some materials may show such large stress variations during life that the cyclic stress strain curve may be undefinable. The value of n usually varies between 0.10 and 0.20.

3.2. Fatigue life behavior

Because of the old-fashioned emphasis on the S_a–N_f curve, where S_a is the stress-amplitude and N_f is cycles to failure, fatigue life data are generally most available in this form. For a compilation of such data, see FORREST's book [1962]. Around the turn of the century, Basquin showed that the S_a–N_f plot could be linearized with full log coordinates, and thereby established the exponential description of fatigue life:

$$S_a = \sigma_f(N_f)^b \tag{2}$$

where σ_f is the *fatigue strength coefficient* and b is the *fatigue strength exponent*, often called after Basquin; these parameters are fatigue properties of the metal.

Recalling the Coffin–Manson finding that plastic strain-life data may also be linearized with log-log coordinates, we have the well-known, so-called *Coffin–Manson law*:

$$\varepsilon_p = \varepsilon_f(N_f)^c \tag{3}$$

where ε_p is the plastic strain amplitude, ε_f is the *fatigue ductility coefficient*, and c the *fatigue ductility exponent*. ε_f correlates very well with the true strain to fracture in a monotonic test, and c varies between approximately –0.5 and –0.7 for most metals. The fatigue ductility exponent can approach –1 or –2 if the strain localization shown by the material is especially marked.

Fatigue life behavior is now usually displayed in a plot of log strain versus log cycles (or reversals $= 2N_f$) to failure, and such a plot is shown in fig. 4, along with the fatigue strength and ductility properties from the four fatigue parameters which have been introduced: fatigue strength coefficient σ_f and exponent b, and fatigue ductility coefficient ε_f and exponent c. For those materials which are expected to possess a fatigue limit, this parameter is added to the four as another defining index of performance. In fact, all materials which require plasticity for their fatigue failure mechanism possess a fatigue limit corresponding to the threshold for PSB formation (LAIRD [1976]) or, more generally, for strain localization. The evidence indicates that metals last indefinitely if strain localisation does not occur, but this fact does not show itself so readily in the S–N curves of fcc metals as in those for bcc metals, and realization of the behavior has been slow in coming. Yet another parameter defining fatigue behavior, the *transition life*, N_t,

References: p. 2391.

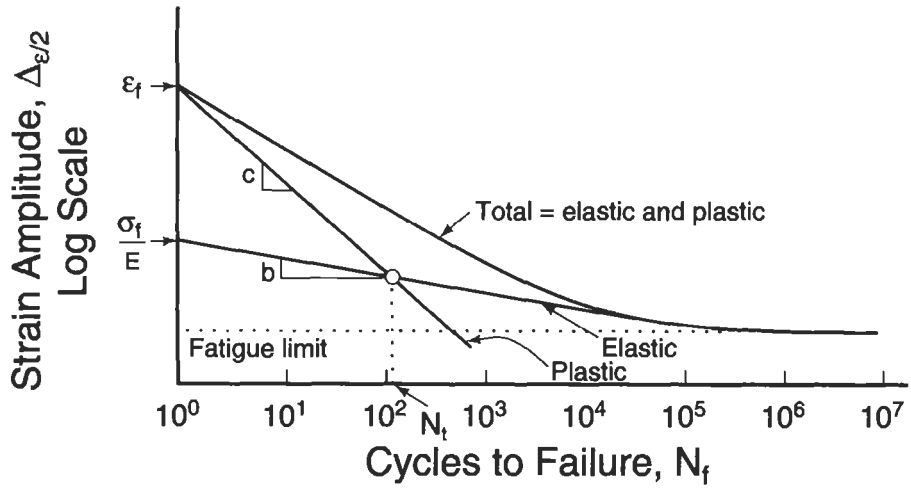

Fig. 4. Log plots of plastic strain, elastic strain and total strain against cycles to failure, showing the "fatigue ductility and strength" parameters indicating performance, as well as the fatigue limit and the transition life, N_t.

is shown on fig. 4, and, as already remarked, it marks the formal distinction between high and low strain fatigue, for the particular material. In the (hypothetical) example shown, N_t is low but not unusually so, and is typical of a brittle metal. N_t is nearer 100,000 cycles for ductile metals.

4. *Cyclic deformation*

Cyclic deformation is usually studied in fatigue by tests conducted in total or plastic strain control. Since fatigue strains are generally low in relation to those employed in monotonic deformation, the stress is also low at the start of cycling if the material is soft or annealed. However, the specimen typically hardens rapidly giving rise to the phenomenon classified as *rapid hardening*. With continued cycling the hardening rate declines and eventually falls to zero, at which point the specimen is termed as being *in saturation*. The dislocation mechanisms during rapid hardening and the dislocation behavior by which a specimen carries plastic strain in saturation without hardening further are usually different. These aspects of cyclic deformation are therefore treated separately. Often, as mentioned in the Introduction, *strain localisation* occurs during cyclic deformation, and it is this phenomenon which is particularly destructive in promoting fatigue cracking. It has received much attention in fatigue studies and is accordingly emphasized here.

The fundamental aspects of cyclic deformation and fatigue cracking have repeatedly been reviewed (LAIRD [1977, 1979, 1981, 1983]; MUGHRABI [1980, 1983, 1985]; LAIRD *et al.* [1986]; GEROLD and MEIER [1987]; BASINSKI and BASINSKI [1992]). However, fatigue research continues actively and there have been new results on the cyclic deformation and fatigue of both wavy and planar slip alloys, which have provided

additional insights into the mechanisms of fatigue. For reviews of early work, the reader is referred to THOMPSON and WADSWORTH [1958]; GROSSKREUTZ [1971]; and GROSSKREUTZ and MUGHRABI [1975]; for engineering aspects of cyclic deformation, see MITCHELL [1979].

4.1. Phenomenological behavior and dislocation structures

Rapid hardening ends when the *saturation stress* is reached. This saturation stress, when plotted against the applied plastic (or total) strain amplitude, defines the cyclic stress–strain curve (CSSC) as identified in § 3. That for copper single crystals deforming in single slip is shown in fig. 5. This curve, which is typical of fcc pure metals and most of their substitutional alloys, is seen to consist of a three stage curve centered around a prominent *plateau* (which lies at a stress amplitude of 28 MPa). This curve differs in its form in minor ways for the different fcc metals for reasons which are still not well understood, although the *plateau stress* normalized by the shear modulus has the constant value of $\sim 6.6 \times 10^{-4}$ (MUGHRABI [1980]). Since copper is by far the most studied metal of all metals, let alone fcc metals (of the approximately three dozen references concerning cyclic deformation cited by LAIRD in his early review [1983], about half dealt with copper, and the preponderance continues to this day) the examples cited here will mainly be taken from copper, but the understanding claimed for this metal can be taken as broadly applicable to all of the class.

The saturated dislocation structures differ for the various regions of the CSSC: A, below the plateau; B, in the plateau; C, above the plateau. It is to be anticipated therefore that the rapid hardening behavior will reflect these differences. One method of showing

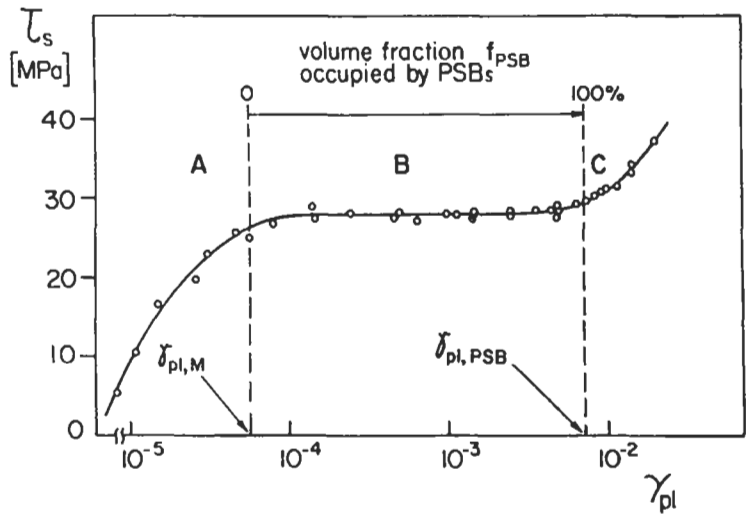

Fig. 5. The cyclic stress–strain curve for copper single crystals oriented for single slip showing the plateau, and the three stage nature of the curve. (The refined data of Mughrabi taken from LAIRD *et al.* [1986]).

these differences is by plotting and comparing the "cyclic hardening curves", i.e., those obtained by plotting the peak stress per cycle conducted in constant strain amplitude against the number of cycles or *cumulative plastic strain*. This frequently used quantity, which is specific for fatigue, is defined as the plastic strain which occurred in all previous cycles summed without regard to sign. For constant strain cycling, the cumulative plastic strain is the product of four times the plastic strain amplitude and the number of cycles. The behavior which corresponds to regions A and B and applies to single slip orientations appears to be understood best. Under these conditions, the dislocation structures produced during rapid hardening consist of dense and irregular *loop patches* strung out in the orientations of edge dislocations. Loop patches are made up of edge

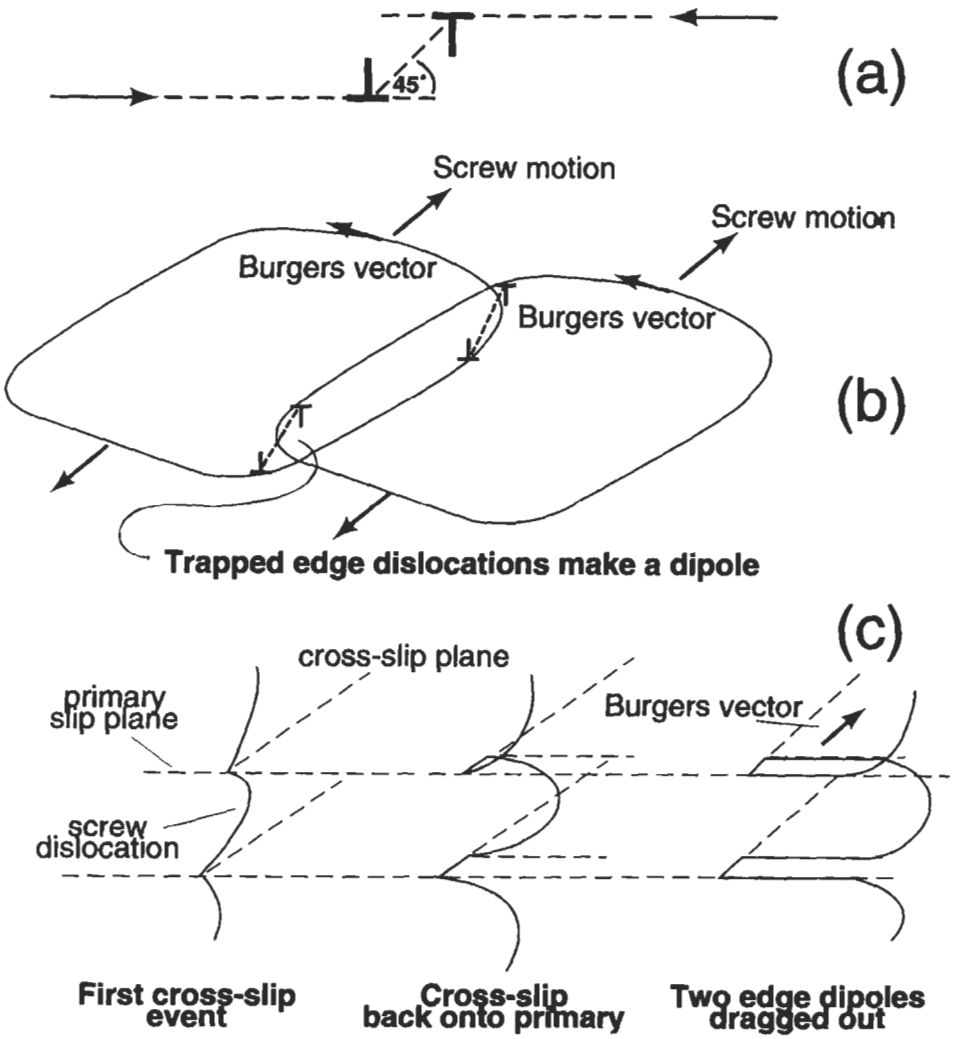

Fig. 6. The formation of dislocation dipoles by (a) and (b) mutual trapping of edge dislocations, and (c) a double cross-slip mechanism. (d) The clumping of these dipoles forms loop patches seen in a three dimensional view corresponding to region A of the CSSC (plastic shear strain amplitude, 2.6×10^{-5}, shear stress = 19.8 MPa) from the unpublished work of Ackermann and Mughrabi via LAIRD *et al.* [1986].

dislocation dipoles in which the positive and negative dislocations of the pair typically end up being separated by about 100 Å. They are formed most likely by a variety of mechanisms: mutual trapping of positive and negative edge dislocations travelling on different atomistic slip planes in different directions (fig. 6a), screw dislocation pairs gliding on different atomistic planes and drawing out an edge dislocation dipole between them, fig. 6b, and/or by a double cross-slip mechanism, fig. 6c. The trapped edge

References: p. 2391.

dislocations position themselves at their 45° equilibrium position (fig. 6a) and can flip-flop past one another as the stress is cycled. They act as barriers to other dislocations and can be swept up into clumps — the loop patches. Because the stress is cycled in fatigue many times, positive and negative dislocations have many opportunities of encountering and trapping each other, and loop patches rarely show excess dislocations of one sign. Continued trapping events gradually refine the dipoles to smaller and smaller separations. The typical appearance of these structures is shown in fig. 6d. At the low magnification used to record fig. 6d, the individual loops cannot be seen, just the patches of them. Under normal viewing of the transmission electron microscope, close to the Bragg condition, the dislocation images can be as wide as the separation of the positive and negative edge dislocations in the dipole and it may be difficult even to resolve an isolated dipole. They can of course be resolved separately using the weak-beam technique (ANTONOPOULOS *et al.* [1976]), even when the dipoles are clumped in a loop patch. The three dimensional view shown in fig. 6d suggests the vein-like structure by which the loop patches are often called. The nomenclature is not well-defined in the literature: the term "loop patches" seems most appropriate to the dense clusters of dislocation dipoles, "veins" may be best reserved for loop patches joined up into semi-continuous clouds of dipoles separated by channels.

Typical cyclic hardening curves for low and moderate strain amplitudes are shown in fig. 7. It is interesting that the saturation stress and thus the shape of the CSSC appears to be quite insensitive to crystal orientation (CHENG and LAIRD [1981]) here indicated by the orientation parameter Q, defined as the ratio of the Schmid factor* for the second most highly stressed slip system to that of the primary system. If $Q < 90\%$, the slip tends to be dominantly single; for $Q > 90\%$, secondary slip becomes more evident but remains dominated by the primary slip (CHENG and LAIRD [1981]). The rapid hardening rate is not affected by orientation for a wide range of crystal orientations provided the amplitude is low (fig. 7a). However, if the amplitude increases, the rate of hardening increases as the Q parameter increases (fig. 7b). Under these circumstances the loop patches can acquire significant populations of secondary dislocation dipoles.

The conclusion that the CSSC and rapid hardening behavior are fairly constant for most orientations within the standard triangle needs careful qualification. The behavior will almost certainly be different for orientations on the great circle connecting the 011 and 111 poles where two slip systems on the primary plane are simultaneously excited and produce network dislocation structures different from loop patches (JIN and WINTER [1984]). Behavior is still more complex for multi-slip orientations, in which hardening can develop to high levels (LEPISTO [1984]; LEPISTO *et al.* [1986]). The cyclic hardening curve for a $[\bar{1}11]$ oriented crystal is shown in fig. 8 in comparison to the behavior of a single slip crystal. Note that for the multi-slip crystal the maximum attained stress is double that of the single slip crystal which saturates at the regular level of ~ 28 MPa (after a small peak) whereas the multi slip crystal, which hardens in fewer cycles (by an

* The Schmid factor is defined as the ratio of the shear stress, resolved on the plane and in the direction of the relevant slip system, to the normal applied stress.

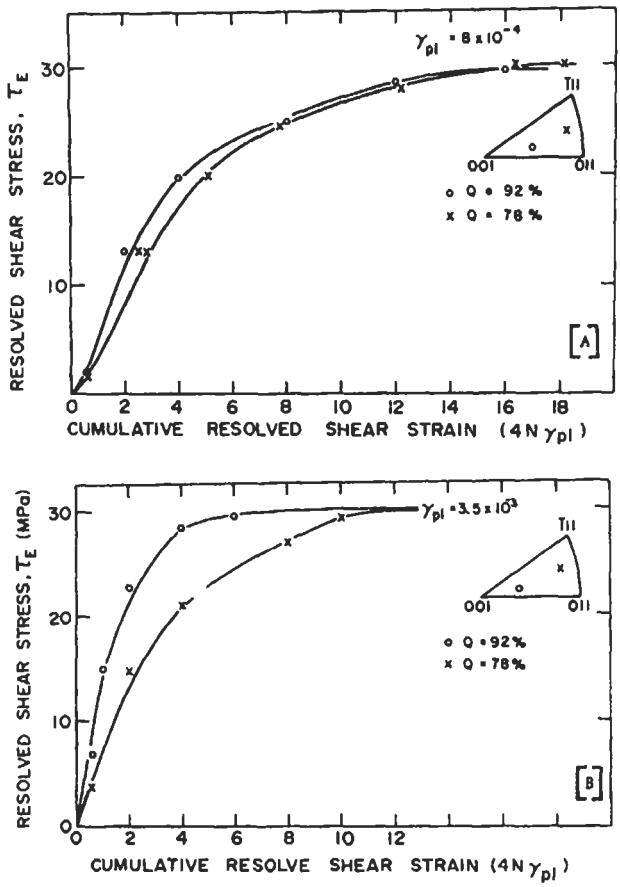

Fig. 7. Cyclic hardening curves for single crystals of different orientations specified by the orientation parameter Q: (a) at low strain amplitude; (b) at higher strain amplitude. Note the much higher hardening rate for the more multi slip condition (nearer 001) when the strain amplitude is high. (Taken from CHENG and LAIRD [1981a]).

order of magnitude), shows no saturation but the resolved shear stress decreases continuously until fracture of the specimen. The reduction of the stress might well be caused by cracking, the kinetics of which are very high because the stress is high. The dislocation structure of this specimen consisted of walls normal to the $[\bar{1}11]$ direction and cellular shear bands oriented at ~45° to the axis. These types of structure may well apply to rapid hardening in the C region of the CSSC. A related behavior seems possible for crystals of axis orientations near [001], where very rapid hardening and a saturation stress of 44 MPa have been reported (JIN and WINTER [1984]).

For the majority of crystal orientations in which the cyclic deformation is dominated by single slip, the results of TEM show that rapid hardening at low strain amplitudes is

References: p. 2391.

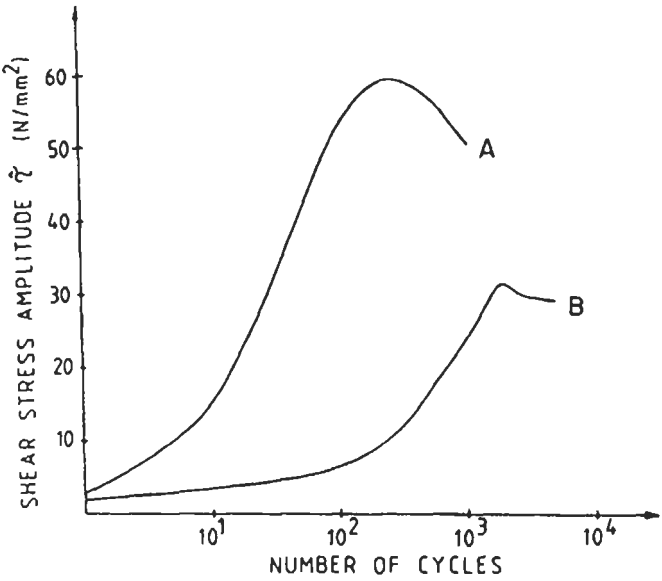

Fig. 8. Cyclic hardening curves of copper single crystals: curve A, multi-slip orientation, curve B, single slip orientation. Plastic strain amplitude 1.5×10^{-3}. Courtesy of LEPISTÖ *et al.* and Elsevier [1986].

primarily caused by the accumulation of dislocations of the primary slip system (for reviews of early work, see LAIRD [1977, 1979 and 1983]; MUGHRABI [1983]). With increasing strain amplitude, and particularly for amplitudes greater than 2×10^{-3}, the increasing rate is associated with increasing amounts of secondary slip. There is much evidence for this behavior; the dependence of rapid hardening rate on orientation shown in fig. 7 is one form of it. Mughrabi reviewed bulk measurements of magnetic properties in fatigued nickel single crystals (MUGHRABI [1980]). Deviations in the magnetic measurements from the symmetry characteristics of crystals containing primary dislocations occur with increasing cycles at strain amplitudes corresponding to the upper half of the plateau, and these reflect the growing contribution of secondary dislocations. More recently, ACKERMANN *et al.* [1984] showed that the strain amplitude of 2×10^{-3} which lies near the low strain end of the plateau in the CSSC (6×10^{-5} to 7.5×10^{-3}), represents a threshold. Below this amplitude, TEM showed the loop patches to be dominated by primary dislocations. Above this amplitude, the density of secondary dislocations increased significantly as the amplitude increased. The role of secondary dislocations, in bundling with the primaries and to some extent controlling the vein morphology, can be seen in the early work of HANCOCK and GROSSKREUTZ [1969]. The amplitude chosen for their study lay at the top end of the plateau.

Thus, early in rapid hardening, and especially at low amplitudes, the dislocation structures consist almost entirely of primary dislocation dipoles. The dipolar nature of the structures is obvious from TEM micrographs which show no change in background contrast across the loop patches. The dipoles collect initially as "*unit loop patches*", i.e.,

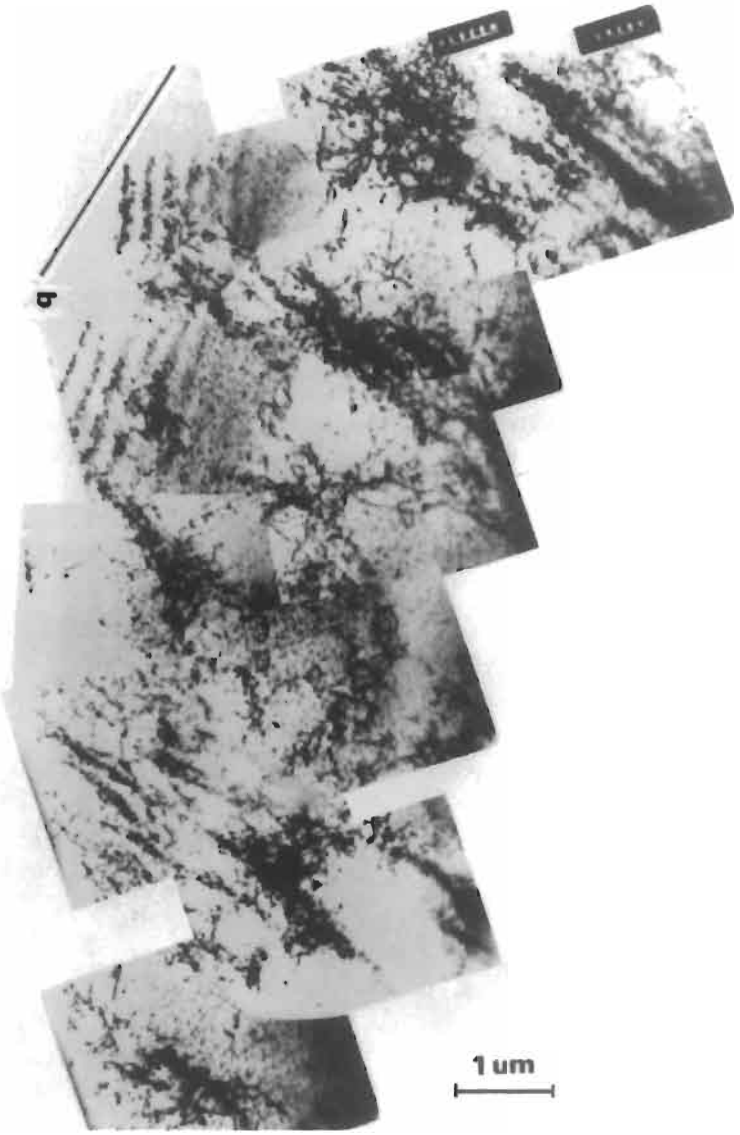

Fig. 9. Unit loop patches consisting almost exclusively of primary dislocations, seen on the primary glide plane for a stress of about 8 MPa. The direction of the primary Burgers vector, *b*, is indicated. This montage of micrographs was taken from a thin area of the foil as can be seen from the thickness fringes on the left side — the foil is wedge shaped and is tapering to a hole out of sight to the left. (Taken from BUCHINGER *et al.* [1986]).

juvenile loop patches shown in fig. 9. The unit loop patches are well-matched in the sense of dipoles but are rather ragged and have a low volume fraction. Again, because of the low magnification used for fig. 9, the individual dipoles cannot be resolved. At higher stresses the volume fraction of loop patches increases, apparently by dipoles

References: p. 2391.

occupying the space between closely situated unit loop patches (BUCHINGER *et al.* [1984]) and the structure gradually becomes similar to that seen in fig. 6d, which applies to ~ 20 MPa. By the time the regular plateau stress is reached, the volume fraction of loop patches is about 50%; the channels between the loop patches become more sinuous while remaining inter-connected.

During the accumulation of loop patches, the slip lines observed on the surface of the specimen are long, straight and uniformly distributed, indicating homogeneous shear. These observations indicate that the loop patches and channels are deforming cooperatively, by edge dislocation motion in the loop patches and by screw dislocations gliding in the channels (LAIRD [1983]; KUHLMANN–WILSDORF and LAIRD [1977, 1980]). This widely accepted model (KUHLMANN–WILSDORF and LAIRD [1977]; MUGHRABI and WANG [1982]) for the dislocation behavior is schematically indicated in fig. 10.

The effect of the secondary dislocations on the extent of hardening in crystals oriented mainly for single slip does not appear to be large. This can be gaged from results of ramp-loading tests. Neumann reported early on the occurrence of strain bursts [1968] if copper single crystals are fatigued under ramp loading conditions where the controlled load amplitude is gradually increased from zero to a maximum of 32 MPa (the stress at which PSBs initiate). The nature of the strain bursts is shown in fig. 11, that is,

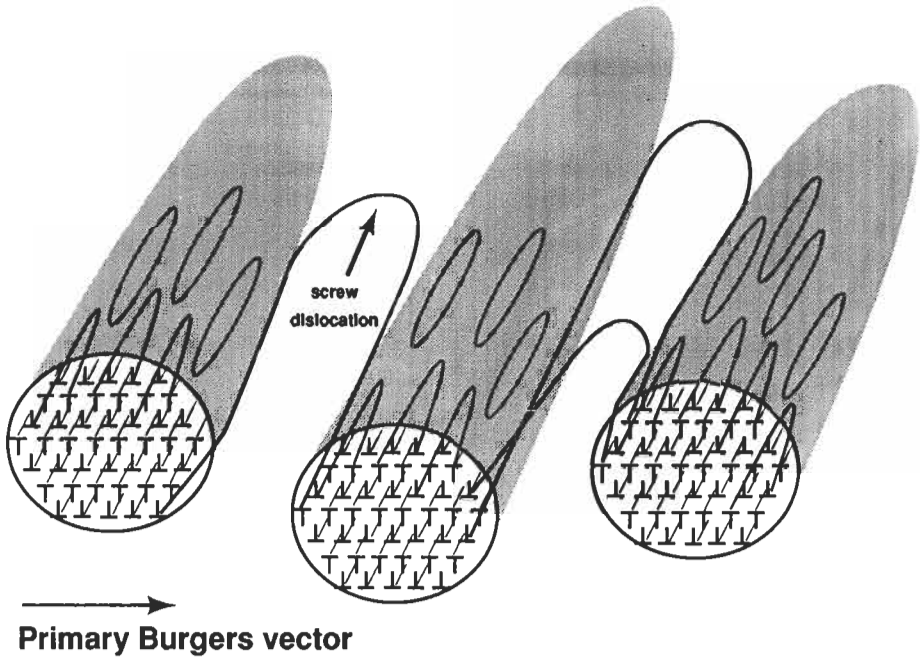

Fig. 10. Model of deformation in the loop patches — edge motion in the dipolar patches coupled with screw dislocations gliding in the channels. Note the Taylor lattice in the loop patches; the existence of loops can be seen on the upper surfaces of the patches.

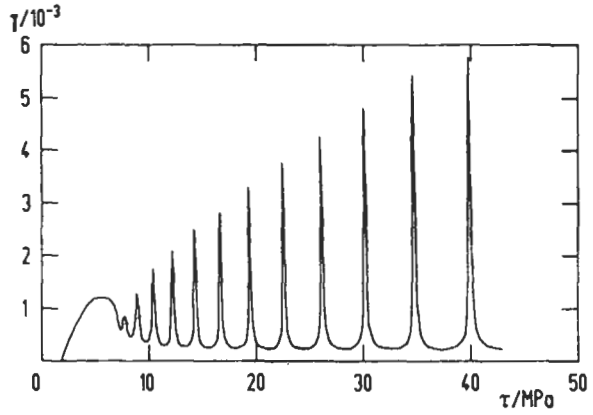

Fig. 11. Strain bursts in a copper crystal fatigued with a stress amplitude which increased linearly with the number of cycles at a rate of 7.1 kPa/cycle. Since the temperature of testing was 90 K — the plateau stress was higher than the 32 MPa value observed at room temperature and loop patches were still the appropriate structure at 40 MPa, still undergoing bursts. The plateau stress at 90 K will be about 49 MPa (BASINSKI, KORBEL and BASINSKI [1980]). Taken from previous edition, Chapter 24; courtesy of P. Neumann.

there are periodic episodes of high strain lasting for a number of cycles with intervening periods of low strain. It is known that the dislocation structures produced by ramp loading consist of regular loop patches (YAN *et al.* [1986]); however, they contain a much higher, and more uniform, density of secondary dislocations than the loop patches produced by regular tests under strain control. The strain bursts indicate instabilities in the developing structure of the loop patches, which change discontinuously, burst by burst, to more stable arrangements, depending on the level of the applied stress. Almost certainly the change consists in a refinement of the loop patches, involving a decrease in the dipole width so that the passing stress for the edge dislocations increases, and brings the structure into stability with the load increase.

After ramp-loading to 32 MPa, persistent slip bands (PSBs), the agent by which saturation is obtained, normally develop at a rate which depends on the frequency of cycling, a low frequency, e.g., 2 Hz, encouraging PSB formation (YAN *et al.* [1986]). This compares with a stress of 28 MPa which is required to produce PSBs in a regular test in strain control. The ~ 10% increment in flow stress produced by ramp loading is significant and can be attributed both to the secondary dislocation content of the loop patches and their uniformity.

4.2. Models of rapid hardening behavior: loop patches, persistent slip bands and channels

Interpretation of the dislocation behavior during rapid hardening has been of interest for many years. Early models used to explain the behavior have previously been reviewed (LAIRD [1983]). More recently, interpretation has been made via analysis of the friction stress and back stress acting on the dislocations (KUHLMANN-WILSDORF and

LAIRD [1977, 1979]; KUHLMANN–WILSDORF [1979a and b]). The friction stress acting on the dislocations, being dependent on point defect hardening, Peierls forces and jog-dragging, is independent of straining direction, but the back stress changes sign during each half cycle. The back stress reaches its maximum value at maximum applied strain, thus acting to lower the yield stress in the reversed direction. As it is of elastic nature due to dislocation interactions, it soon decreases on straining in the direction favored by it, and then reverses again so as to oppose the imposed strains. Measurements of the friction stress and back stress have been made by analysing hysteresis loops by the *Cottrell method* (KUHLMANN–WILSDORF and LAIRD [1979]). The results show that the friction stress and back stress (the sum of which equal the applied stress) increase during rapid hardening in parallel, the friction stress leading by 1–2 MPa. From this analysis the friction stress is separated into two parts, one equal in magnitude to the back stress (and presumed to have the same physical cause) and the other, smaller, part due primarily to jog dragging by the screw dislocations shuttling in the channels between the loop patches (KUHLMANN–WILSDORF and LAIRD [1979]).

Further analysis of the behavior of these stresses suggests that the loop patches fully participate in the cyclic deformation via coordinated loop flipping in the manner illustrated in fig. 12 (KUHLMANN–WILSDORF [1979a and b]). That is, the loop patches are idealized as *Taylor lattices*, in which the dislocations are regarded as being infinitely long rather than consisting of dipolar loops as they actually do (see fig. 10), and they are

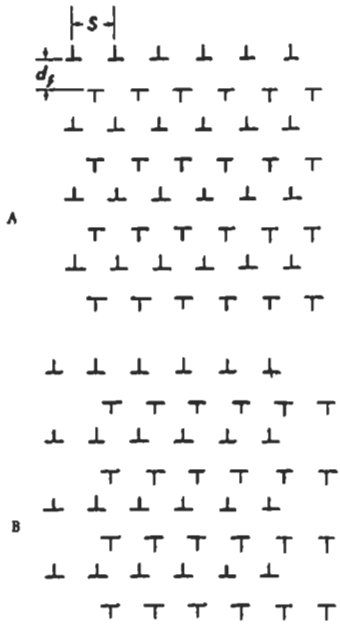

Fig. 12. The Taylor dislocation lattice corresponding to an idealized description of the structure in the loop patches (a) before shearing the top of the lattice to the left with respect to the bottom and (b) afterwards. Courtesy of Kuhlmann–Wilsdorf and Elsevier (27).

conceived to deform by slipping rows of oppositely signed dislocations past each other (compare figs. 12a and b). In practice the Taylor lattices are not ideal, the density of loops being greater on the outsides of the patches than on the insides, the loops being of finite length, and the lattices may not be uniform enough everywhere to prevent individual loop flipping, in coordination with synchronized flipping.

A detailed theory of the Taylor lattice behavior and interpretation of the friction and back stresses has been proposed by KUHLMANN–WILSDORF [1979a and b]. The physical essence of the theory is that, at the strain limits of the cycles, the bulk of the stress is supported by the loop patches, so that the back stress roughly equals one half of the stress at which the loop patches would deform in the absence of friction since they occupy only half the volume. The part of the friction stress which is equal to the back stress comes about because the dislocation motions within the loop patches are irreversible (in the mechanical sense) for every dislocation as soon as it flips with its neighbors of opposite sign. Thus this component of the friction stress, along with the back stress, is given by the flipping stress of the Taylor lattice (KUHLMANN–WILSDORF [1979a and b]). Many aspects of rapid hardening have been worked out, including anelastic effects and the shapes of hysteresis loops (KUHLMANN–WILSDORF [1979a and b]). One of the interesting behavioral effects of the loop patches is that anelastic motion of the sub-lattices of the Taylor lattice produce an apparent reduction of the shear modules when stresses are applied lower than the flipping stress. There is a problem, however, as WILKENS *et al.* [1980] have pointed out, with the quantity of the reduction of shear modulus resulting from the elastic polarisation of the dislocation dipoles, which Kuhlmann–Wilsdorf calculates as too large compared to the shear modulus effect, measured on fatigued copper by internal friction technique. This is because loop patches do not contain the infinitely long dislocations of an ideal Taylor lattice. In reality the areas swept out by the displacements of the dipole dislocations are reduced by the requirement that the segments must bow out between the dipole ends, the dipoles exhibiting a wide range of lengths.

It is necessary to set this model in the proper context of rapid hardening. As mentioned above, hardening takes place by multiplication of primary dislocations, of which many become trapped as edge dislocation dipoles (see ch. 20, § 3.3). Patches of dipoles then act as obstacles to the motion of the primary glide dislocations. At this early stage of hardening, the screw dislocations glide over long distances in the channels between loop patches and the Taylor sub-lattices flip relative to each other several times the interloop spacing. In this slip, the passing stress controls the hardening (KUHLMANN–WILSDORF and LAIRD [1977]; KUHLMANN–WILSDORF [1979a]). Later in rapid hardening, when the volume fraction of loop patches has built up considerably, the channel screw dislocations glide over shorter distances and the loops may not accomplish a single flip but merely oscillate about their equilibrium positions. If the specimen is called upon to strain more than the channels and loop patches can accommodate at this point, persistent slip bands occur by strain localisation. A model for the mechanism of this transition, which is stimulated by secondary dislocations, has been provided by KUHLMANN–WILSDORF and LAIRD [1980].

Figure 13 shows schematically the model for the transition from loop patches to

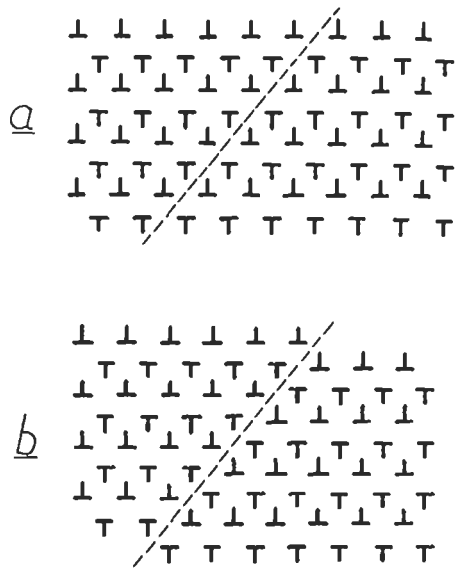

Fig. 13. The mechanism by which the dislocations in the interiors of loop patches are annihilated, via slip on a secondary system (a) before secondary slip, plane indicated by dotted line; (b) after secondary slip, positive and negative Taylor sub-lattices aligned for annihilation. Taken from KUHLMANN–WILSDORF and LAIRD [1980].

PSBs, which is considered to take place by clearing the dislocations from the interiors of the loop patches, and allowing the outer skin to become the PSB walls. That is, the loop patches are converted into a series of quite uniformly-separated, densely-packed dipolar, dislocation walls which, observed in elevation (e.g., by a $(\bar{1}2\bar{1})$ TEM section perpendicular to the primary slip plane), look very like a ladder structure. Secondary slip, stimulated by the self stresses of the primary dislocations (KUHLMANN–WILSDORF and LAIRD [1980]), occurring along the dotted trace shown in fig. 13 acts to translate the sub-lattices of the oppositely-signed dislocations into positions favorable for them to annihilate by glide. Residual loops and debris are then swept up into the walls to form the well-known ladder structure of the PSBs. In this type of model, then, the loop patches decompose from the inside, a process which might take a number of cycles. By another point of view, PSBs have been considered to form from outside the loop patches, by a process creating a shear band penetrating many patches. This type of process may well occur if the crystal is suddenly called upon to bear a heavier strain than its current PSBs are experiencing (by a sudden increase in amplitude). The "cords" reported by MECKE [1973] and others (WANG and LAIRD [1989]) may well be incipient PSBs created by external penetration of the loop patches.

There is a great deal of available evidence showing that secondary slip stimulates

PSB formation. For example, in polycrystals, PSBs are frequently found to nucleate adjacent to twins, often parallel to them when the grain adjoining the twin has its primary system parallel to the twin boundary (LLANES *et al.* [1992]). In such a situation the stress concentration of the twin acts to raise the stresses of the secondary system (PERALTA *et al.* [1994]). An example of a PSB lying adjacent to a twin boundary is shown in fig. 14a. Figure 14b shows an example of PSB walls having been nucleated adjacent to steps at a twin boundary, again presumably because of their stress concentrations, and their local effect in increasing the stress on secondary slip systems.

It is interesting that the stress necessary to nucleate PSBs decreases at higher amplitudes within the plateau of the CSSC (MUGHRABI [1981]; MECKE *et al.* [1982]; BLOCHWITZ and KAHLE [1980]) because the higher density of secondary dislocations and irregular structures which prevail at higher amplitude make the transition easier. Loop patches produced by ramp-loading are unable to transform so easily, in spite of their secondary dislocation content, because they are harder and more uniform.

The cumulative strain (transition point) at which loops in the patches cease to slip during rapid hardening has been treated semi-quantitatively by CHENG and LAIRD [1981]; this treatment amounts to an adjustment of Kuhlmann–Wilsdorf's theory and describes the variation of the transition point with strain amplitude, and also the dependence of the friction stress and back stress on strain amplitude and crystal orientation. The initial model of Kuhlmann–Wilsdorf assumed constancy of the friction and back-stresses throughout the plateau of the CSSC, and this assumption is invalid.

Neumann has modeled loop patch geometry by computer techniques [1986] and has confirmed the Taylor lattice morphology. His results agree in general terms with those of Kuhlmann–Wilsdorf, but again there are some minor differences, for example, Neumann computes a different network configuration for the Taylor lattice. In a regular Taylor lattice, the dislocation cores (viewed in the x–y plane, the z axis corresponding to the dislocation lines) form a two dimensional centered rectangular lattice. As shown in fig. 12, the lattice has an aspect ratio of about 2, which is the preferred aspect ratio and slightly different from the aspect ratio selected by KUHLMANN–WILSDORF [1979b] in her treatment of loop patch structure. In addition, Neumann discovered that finitely-sized loop patches are not always stable (Taylor lattices are formally considered to be infinite), and there are some shapes of the Taylor lattice which decompose spontaneously at zero applied stress. It will be noted that the shapes observed for the loop patches in fig. 6d can be regarded as assemblies of the diamond shape, one of these stable configurations.

It is of interest to explore whether the shapes predicted by the computer calculations can be observed in simple form. The outlines of loop patches can best be observed in $[1\bar{2}1]$ sections, i.e.. normal to both the primary Burgers vector $[\bar{1}01]$, and the slip plane normal, [111]. A typical example is shown in fig. 15. The shapes turn out to be irregular but have facets that roughly conform to the quadrupole stability requirement. It will be seen also that the loop patches are quite uniformly separated and clear channels exist between them at angles of about 20° and 35° with respect to the primary slip plane. These channels suggest a possible role of secondary dislocations in loop patch morphology. The structure shown in fig. 15 was obtained after long cyclic exposures obtained

References: p. 2391.

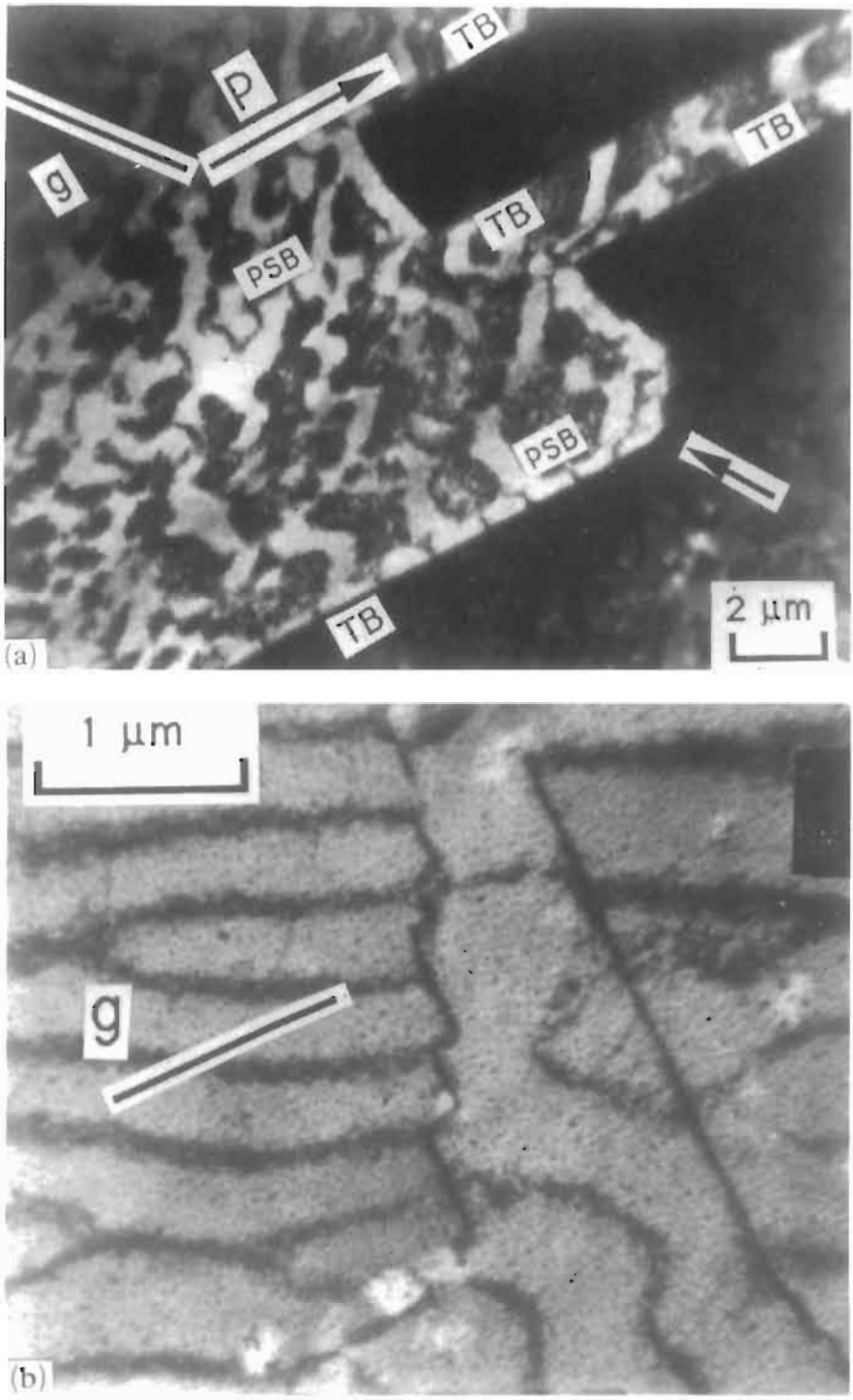

Fig. 14. Dipolar wall formation stimulated by stress concentrations from twin boundaries (TB) in copper: (a) PSBs parallel and adjacent to TBs; (b) walls emanating from steps in a TB. The twinned regions are near the Bragg condition in (a) and so appear dark but contain loop patches. Taken from LLANES and LAIRD [1992].

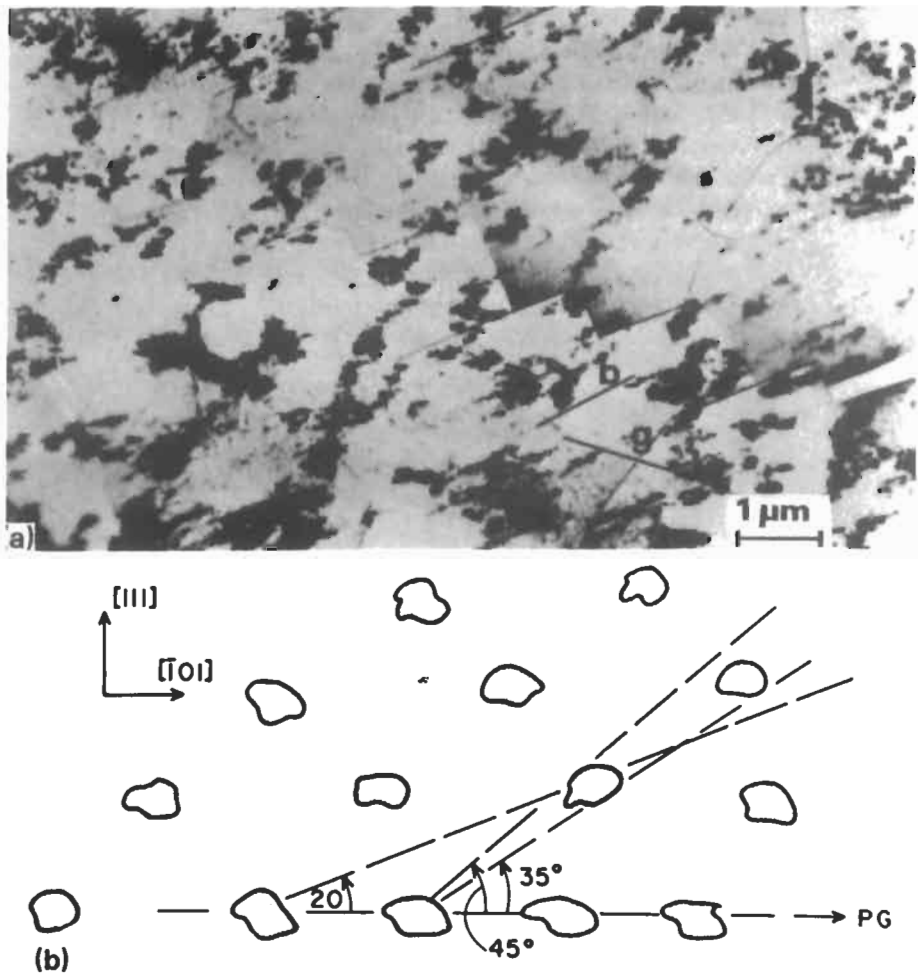

Fig. 15. The outlines of loop patches and the structure of the channels separating them in monocrystalline copper viewed along the [1$\bar{2}$1] direction: (a) actual structure, (b) loop patch alignment indicated schematically (Taken from BUCHINGER *et al.* [1984]).

with a high frequency machine, when secondary dislocations were customarily observed by TEM (BUCHINGER *et al.* [1984]). Also, even for low frequencies, MA and LAIRD [1988] have found secondary dislocations to appear in loop patches at amplitudes equal to, or lower than, the threshold reported by ACKERMANN *et al.* [1984] if cycling is extended long enough. The presence of these secondary dipoles exerts a stabilizing influence on the loop patches and causes deviations from the simple morphologies.

Since secondary dislocations are well-known to exist in loop patches, models of their behavior which deal only with primary dislocations must be simplistic. DICKSON *et al.* (DICKSON, HANDFIELD and L'ESPERANCE [1986]; DICKSON, BANDE and L'ESPERANCE

[1988]; TURENNE, L'ESPERANCE and DICKSON [1988]), taking secondaries into account, developed a model to explain the specific crystallographic directions adopted by the borders of loop patches and dislocation dipolar walls. If more than one slip system is involved in developing a dislocation structure (and two systems seem to operate in many fatigue conditions even at fairly low amplitudes), the structure consists of appropriate stacking of the dipoles from the contributing systems. The modes in which this can be done are illustrated schematically in fig. 16. If the loops with the Burgers vector b_1 are extended in the direction n_1, and those with Burgers vector b_2 in the direction n_2, then the dislocation dipoles can be stacked in walls (or loop patch borders) in the three directions: $a = n_1 + n_2$, $c = n_1 - n_2$, and $b = a \times c$, i.e., the walls or borders adopt a direction which "averages" the dipolar configurations. DICKSON *et al.* [1986 and 1988] have had considerable success in explaining irrational crystallographic orientations taken up by walls and veins. Very pronounced orientations can be produced in loop patches if a crystal is first cycled at high amplitudes to introduce a cell structure based on several Burgers vectors, and the crystal is subsequently cycled at low amplitudes to convert the cells into well faceted loop patches, which inherit the secondary dislocations (MA and LAIRD [1988]).

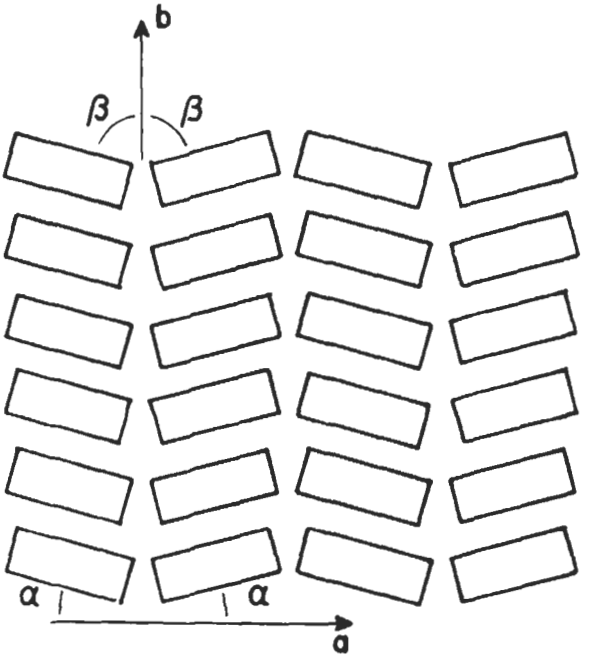

Fig. 16. Schematic two-dimensional drawing of possible three-dimensional stacking arrangements which can be constructed from dipolar loops having two different Burgers vectors. The long segments of the loops correspond to the two systems, as seen in the plane containing both orientations of long segments. There are other ways to stack these loops, in addition to the plane shown, which has its stacking direction normal to the paper; the other two stacking directions are parallel to the directions indicated *a* and *b*. Courtesy of TURENNE *et al.* [1988].

MUGHRABI [1981] had modeled cyclic plasticity in loop patches by a composite model, in which he regards the loop patches and channels as hard and soft phases respectively. He then considers the compatible shear deformation in the direction of the primary Burgers vector under the condition of uniform total strain γ_{tot}. Mughrabi points out that this is the basic idea underlying Masing's model of polycrystal plasticity, where the different grains are considered as a large number of components which have different flow stresses. When the two-phase structure produced by rapid hardening is exposed to stress, the softer channel elements (#2) will yield plastically when $\gamma_{tot} = \tau_2/G$, τ_2 being the yield stress of the channels and G the shear modulus. After yielding of the channel elements, the applied stress will increase further with an apparent shear modulus f_1 G (f_1 being the volume fraction of the loop patches) until the harder loop patches flow plastically at $\gamma_{tot} = \tau_1/G$ (τ_1 is the yield stress of the loop patches). At that point the channels will already have undergone a plastic shear strain $\gamma_{pl} = (\tau_1 - \tau_2)/G$. Subsequently the shear stress, τ, remains constant and is now equal to the macroscopic flow stress of the composite, given by $\tau = f_1\tau_1 + f_2\tau_2$, f_2 being the volume fraction of the channels. To apply this model, MUGHRABI [1981] employed dislocation mechanisms for calculating τ_1 and τ_2. These mechanisms were: 1) screw dislocation bowing in the clear channels between the loop patches and 2) loop flipping in the loop patches. To judge from the many previous opinions expressed about these mechanisms (BASINSKI *et al.* [1969]; KUHLMANN–WILSDORF and LAIRD [1977, 1979] and BROWN [1980]), there seems to be a strong consensus about dislocation behavior in the loop patches produced by rapid hardening.

4.3. Saturation behavior and strain localization

The cyclic stress–strain curve (CSSC) for copper single crystals is shown in fig. 5, divided in three regions A, B and C. A is the region in which the slip is uniformly dispersed, the slip lines long and even, and the dislocation microstructures consist of loop patches. In this region, the slip is carried uniformly by the loop patches and channels, by Taylor lattice flipping and by screw dislocation motion, respectively. Since the strain is small, the dislocation microstructures are stable and the deformation mechanically reversible. The stress reaches saturation.

Within region B, the plateau of the CSSC, PSBs form and carry the strain at the expense of the loop patch matrix structure. A threshold plastic shear strain of 6×10^{-5} is required to initiate PSB formation (MUGHRABI [1978]) and at this low strain a single PSB alone is needed to carry the strain. As the strain amplitude is increased within the plateau region, the volume fraction of PSBs increases. Since a constant stress is required to strain the PSBs, the stress is constant and defines the plateau stress. At the high strain end of the plateau, 7.5×10^{-3} plastic shear strain, the whole gauge section of the specimen becomes filled with PSBs. At intermediate strain amplitudes, the volume fraction of PSBs varies linearly with the applied strain (WINTER [1974]; FINNEY and LAIRD [1975]). The value of the strain at the high end of the plateau, about 1%, is commonly viewed as representing the *average* local strain in the PSBs, while the value of the plastic strain at the low end of the plateau is taken to be that of the matrix. Within

the plateau, then, the applied strain is related to the PSB and matrix strain, and their respective volume fractions, by the rule of mixtures (WINTER [1974]; MUGHRABI [1980]). The properties of PSBs have been studied by many workers, mainly in copper (for reviews, see LAIRD [1977]; MUGHRABI [1980]; LAIRD [1983]; MUGHRABI [1985a]; BASINSKI and BASINSKI [1991]).

Since, within the plateau regime, nearly all the applied strain is carried by the PSBs, they completely traverse the specimen as lamellae parallel to the primary glide plane, and thus they determine bulk deformation behavior. Although it can be inferred from the CSSC and the plateau that there is a constant local strain in the PSBs, the deformation in the PSBs is not constant and varies widely, in several different ways. The evidence for such behavior comes from interferometric technique (FINNEY and LAIRD [1975]; LAIRD, FINNEY and KUHLMANN–WILSDORF [1981]; CHENG and LAIRD [1981]; and MA and LAIRD [1989]). After cycling a single crystal to saturation, these workers would interrupt a test, repolish the surfaces of the crystal on which the PSBs were evident, subject the crystal to a quarter cycle of strain and then study the slip off-sets of the PSBs by two-beam interferometry. Since the dislocation structure of the PSBs is known by etch-pitting studies (WINTER [1974]; BASINSKI, KORBEL and BASINSKI [1980]) to extend virtually unchanged through the bulk of the crystal, the slip offsets observed must reflect the bulk behavior. Typical "well-behaved" PSBs, observed by interferometry, are shown in fig. 17a. These PSBs show a reasonably uniform concentration of strain (~ 1%) within micro-PSBs of which five are visible in the field of view. PSBs often occur as macro-bands, just visible to the naked eye, but they are composed of smaller bands, often separated by matrix structure, termed micro-PSBs, sometimes very narrow and appearing as a single step of coarse slip, but mostly in wider packets such as those shown in fig. 17a. The more familiar appearance of PSBs is shown in fig. 17c, taken with an SEM at the rounded corner of a square-sectioned crystal. This view of the PSBs is as they appear after thousands of cycles and their detailed morphology is very complex because of the accumulated effect of much localized slip. Also, they have protruded from the surface as commonly happens. The PSBs shown in fig. 17a and b were polished off so as to allow the observation of slip during a single reversal (or a few).

Examples of micro-PSBs where large steps formed in very narrow bands are shown in fig. 17b. The crystal shown in this figure had been cycled 2763 3/4 cycles (i.e., interrupted from compression), repolished and then subjected to 1 1/4 cycles, thus being returned to the state of zero stress and zero strain, but with a net 1/4 tensile strain from the point of repolishing. It will be noted that the steps do not all have the same sign and thus some of the steps were formed in the previous compression stroke; they were thus wholly or partially reversed. In light of the height of the offset and the narrowness of the bands, the investigators (LAIRD, FINNEY and KUHLMANN–WILSDORF [1981]) opined that the plastic strain concentration factor for these micro-PSBs would be about 1000. These values of strain localization are much greater than the widely-accepted average value of 1%.

Figure 17a shows another interesting feature of PSB behavior — the strain within the PSB is not uniform but tends to be further localized near the matrix-PSB boundary. Note that the slip offsets are highest in such regions. This observation explains the tendency

of PSBs to initiate cracks at the PSB-matrix interface, because the damage mechanism responds to the magnitude of the local strain.

CHENG and LAIRD [1982] found not only that the plastic strain is not uniform, even at the upper end of the plateau, where the gauge length of the crystal is essentially a single large PSB, but also that the magnitude of the localized strain in the PSB that produced the fatal crack, increases with increase of applied strain. Therefore, the fatigue lives of the crystals decreased as the strain increased, so that normal Coffin–Manson life

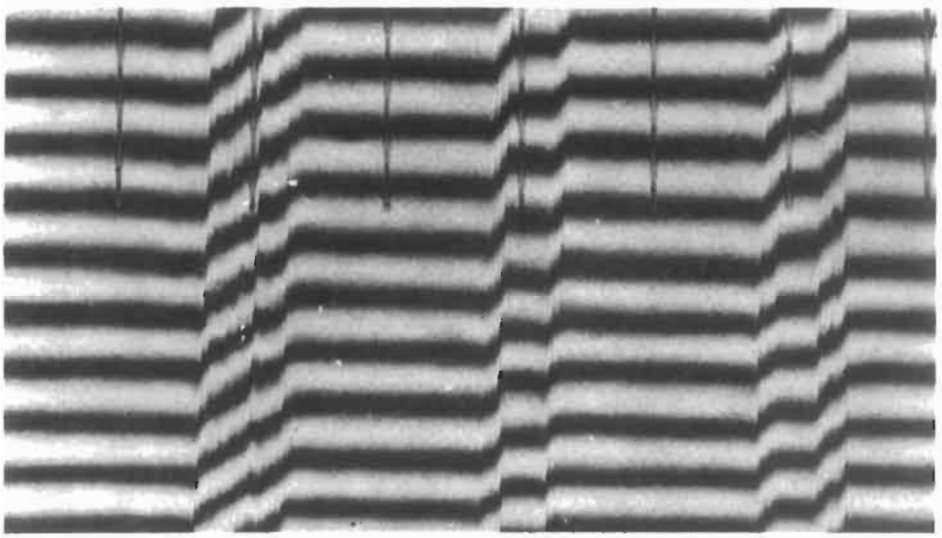

(a)

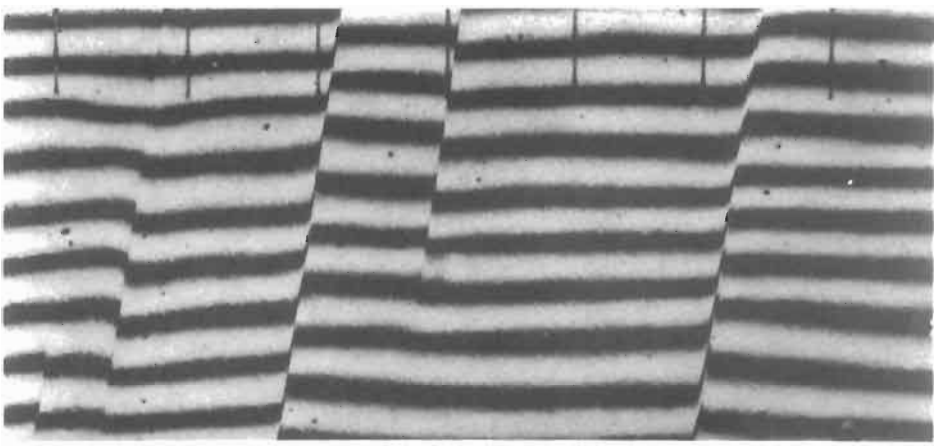

(b)

References: p. 2391.

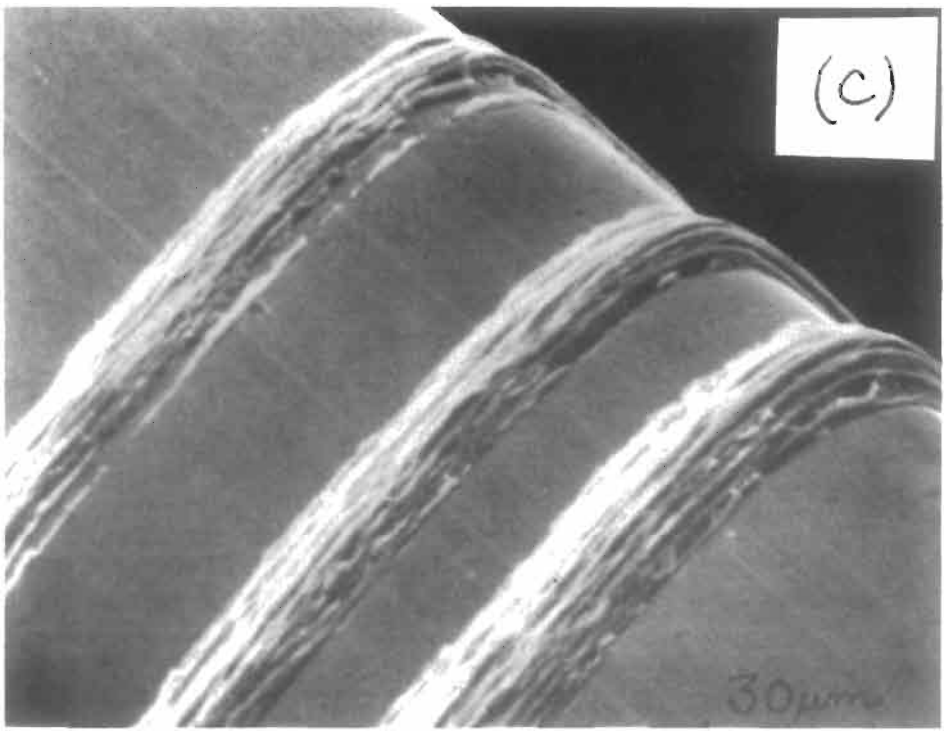

Fig. 17. Interferograms of copper single crystals after repolishing and straining for part cycles, showing strain concentrations at micro-PSBs: (a) plastic shear strain amplitude of ± 0.00125 for 30,000 cycles, repolished, strained in tension; (b) plastic shear strain of ± 0.0025. History given in text. Note that the shear strain is not uniform along the individual lines. Fiducial marks distant 100 μm apart. Taken from LAIRD, FINNEY and KUHLMANN–WILSDORF [1981]. (c) Actual appearance of PSBs after much accumulated strain (30,000 cs at $\pm 2 \times 10^{-3}$ strain) showing protrusion and complex PSB morphology. Taken from MA and LAIRD [1986].

behavior was observed with a fairly steep slope, ~ –0.78 (CHENG and LAIRD [1981b]). It is important to note that Cheng and Laird cycled in constant plastic strain control. The life behavior, therefore, was different from that observed by HUNSCHE and NEUMANN [1986], who employed the gradual ramping approach of testing their specimens. The crystals were therefore conditioned with structures similar to those which apply at the low strain end of the plateau. Therefore, when Hunsche and Neumann subsequently converted their test control to plastic strain, the PSBs behaved more uniformly and the crystal lives, although showing large scatter, tended to be constant. History effects are well-known to be important in controlling fatigue lives.

As previously noted, secondary slip becomes increasingly active in the upper regime of the plateau. At strains higher than 7.5×10^{-3}, the top end, significant amounts of slip begin to occur on systems other than the primary, and the wall structure of the PSBs is broken down into a more complex structure of cells, involving multiple Burgers vectors.

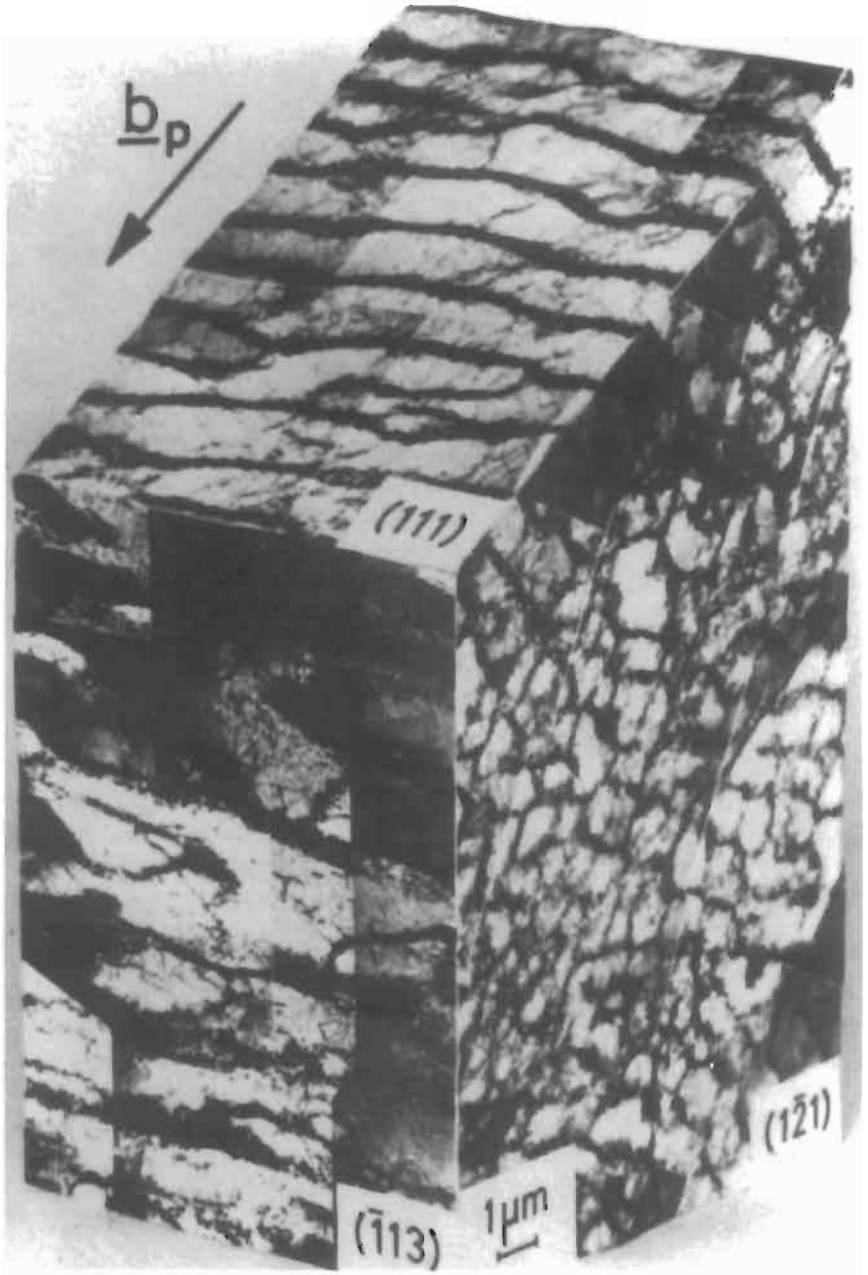

Fig. 18. Cell structures observed in three dimensions in a copper single crystal saturated at a plastic shear strain amplitude of 1.45×10^{-2}. (Region C, dislocation structures neutron pinned in the unloaded state). Unpublished work of Ackermann and Mughrabi, taken from LAIRD, CHARSLEY and MUGHRABI [1986].

References: p. 2391.

The stress saturates as the cell size saturates and the strain distribution is more uniform than at lower applied strains. Figure 18 shows a three dimensional view of the dislocation structures observed in a copper single crystal cycled in the C region of the CSSC.

4.4. Models of dislocation behavior in persistent slip bands

Our understanding of how the localized deformation is accomplished in PSBs by dislocation mechanisms is based mainly on observations of dislocation structures by TEM. Seen from a direction normal to the Burgers vector of the primary slip system on which the PSB has formed, the appearance of typical narrow PSBs is shown in fig. 19. The PSBs are the ladder like structures embedded in the matrix of loop patches. The rungs of the ladder, the PSB walls, consist of primary edge dislocation dipoles which gather together to form some type of multipole viewed, perhaps rather idealistically, as dipolar walls. The dipolar nature can be seen because the background contrast of the electron micrograph does not vary from side to side of the walls. The average separation of the walls is about 1.4μm and their spacing is not precisely uniform.

The relation of the PSBs to the matrix structure of loop patches, and how it varies with applied strain, is shown schematically in fig. 20. At low strain amplitudes, the PSBs occupy a relatively small volume fraction of the crystal. With increase of strain amplitude, the rungs of the PSBs extend until the whole structure comprises dislocation dipolar walls. Figure 18 shows in actuality what is represented schematically in fig. 20b.

How the dislocations glide in the PSBs to carry the localized strain has been the object of much study. There appear to be two different, but overlapping, viewpoints. According to one viewpoint (FINNEY and LAIRD [1975]; MUGHRABI, ACKERMANN and HERZ [1979]) dislocations are considered to bow out from free links in the dipolar PSB walls and glide across the channel to the adjacent walls, where they become trapped and partially annihilated by interacting with dislocations of opposite sign. The screw dislocations at either side of these bowing loops are then liberated to glide down the channels until they encounter oppositely-signed screw dislocations which can mutually annihilate by cross-slip. Thus an equilibrium between dislocation multiplication and annihilation is considered to exist in the PSBs, and the wall structure is maintained stable.

The bulk of the PSB strain is carried by screw dislocations, and the value of the strain is limited by the maximum density of screw dislocations arranged in groups of the same sign. There is a problem with this link-bowing mechanism, however: If the channel screw dislocations are all continually annihilated, then the walls would build up by acquisition of edge dislocations from the bowing. Mughrabi and coworkers overcome this objection by requiring the dipoles of smallest spacing (the near-miss entrapments of oppositely signed dislocations) to spontaneously dissolve by point defect emission, thereby also explaining the high point defect content of the PSBs. This self-annihilation by climb maintains the stable structure of the walls.

According to the other viewpoint, the role of the screw dislocations in the PSB channels is emphasized at the expense of the edge bowing mechanism (KUHLMANN–WILSDORF and LAIRD [1977]; LAIRD, FINNEY and KUHLMANN–WILSDORF [1981]). The

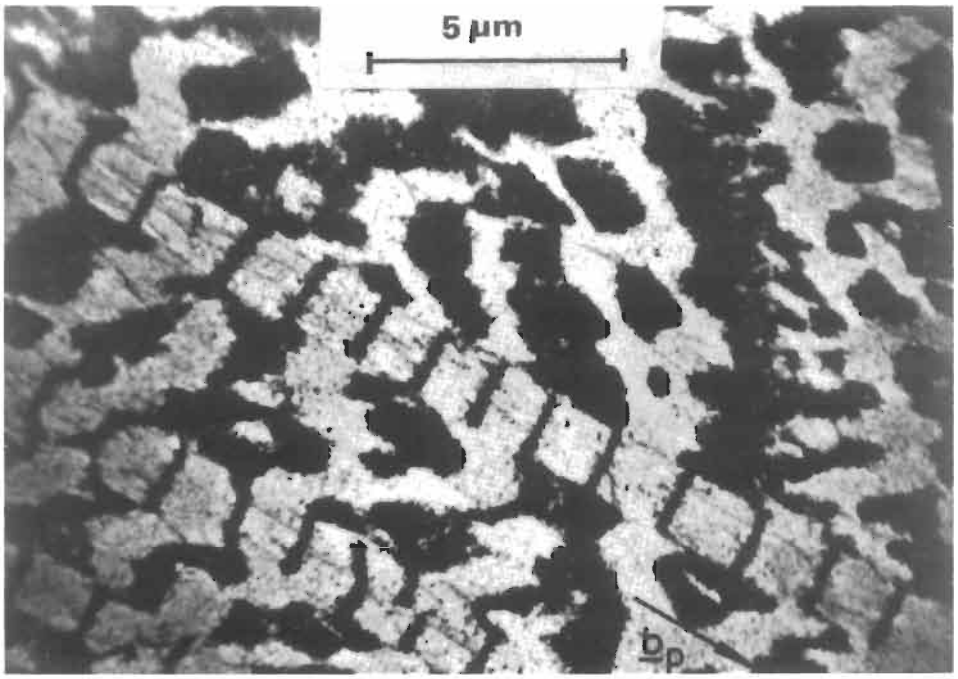

Fig. 19. The ladder structure of PSBs in a copper crystal cycled at a strain amplitude in the plateau (crystal neutron pinned in the unloaded state; [1$\bar{2}$1] slice, primary slip plane (111)). Taken from LAIRD, CHARSLEY and MUGHRABI [1986], from an earlier series by Mughrabi.

dipolar structure of the walls accounts for the prominence of screw dislocation motion in the channels by a theory of *low energy dislocations* (LEDS). These screw dislocations, gliding in groups of the same sign, move in coordination between PSB walls, so as to lay

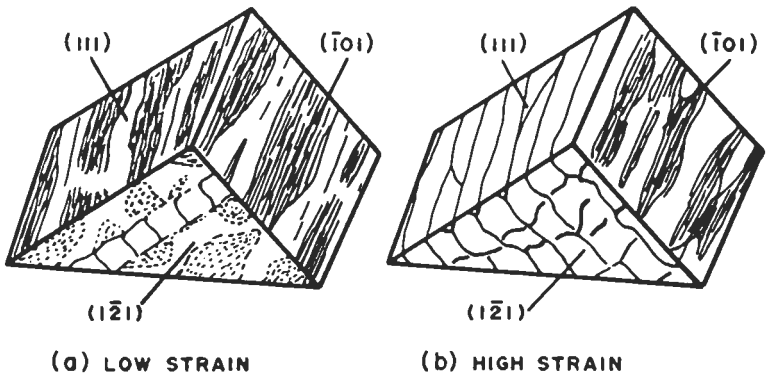

Fig. 20. Three dimensional configuration of dislocations in copper single crystals strain cycled to saturation. (a) a single narrow PSB contained in the matrix structure of loop patches, (b) the whole crystal is a PSB. Courtesy of FINNEY [1974].

References: p. 2391.

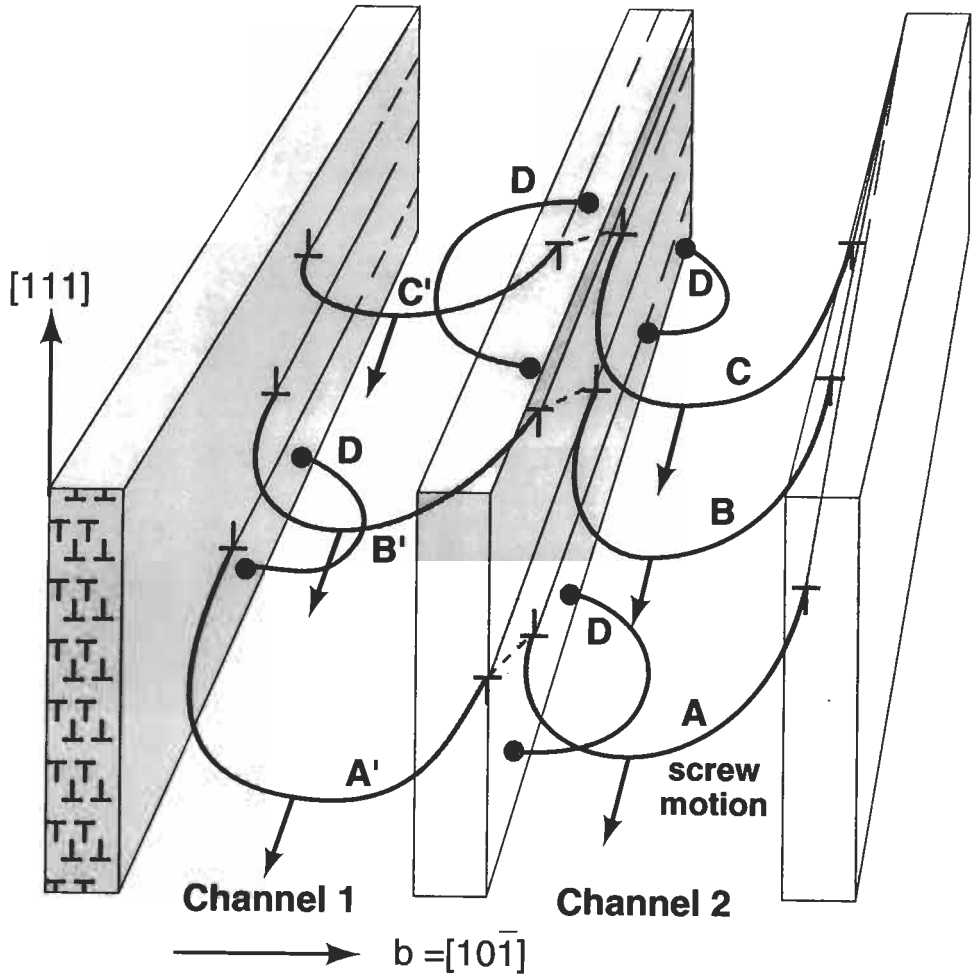

Fig. 21. Models of dislocation behavior in PSBs, showing both the link bowing mechanism, D, and the coordinated motions of screw dislocations A, B, C and A′, B′ and C′ across the walls. It is understood that A′, B′ and C′ are positioned lower than A, B and C so that their edge dislocations match as dipoles across the center wall, (connected by dotted line). The dipolar wall structure shown in the left wall applies to the others as well.

down simultaneously edge dislocations of opposite sign in dipolar configuration at the walls. The detailed manner in which this could be done is shown in fig. 21, a schematic representation of three adjacent dislocation walls. Only the left hand wall is shown with its dipolar structure; the other two walls are left blank, the better to show the coordinated behavior of the screw dislocations. The screw dislocations A, B, C in channel 2 are laying down edge dislocations at the walls, and the coordinated motions of A′, B′, C′ are doing likewise in channel 1, but their atomistic glide planes are stepped with respect to

those in channel 2. Thus considering the center wall, the negative edge dislocation deposited by C^1 is being matched as a dipole by the positive edge dislocation of C. The matching pairs in the dipoles are joined by dotted lines to show their "connection" across the wall thickness. Under the action of the applied strain, the screw dislocations are gliding toward the reader, with their bowing likewise directed. As the strain is cycled, the screw dislocations reverse their directions of travel, picking up edge dislocations or laying them down, in coordination. The particular possibility of the structure shown is considered a likely one, on LEDS principle, because these coordinated screw dislocations maintain the dipolar balance of the wall structure and thus the lowest energy configuration of the dislocations. No annihilation by point defect action is necessary. The dislocation structure is maintained purely by a glide process.

The most reasonable position seems to be that both the coordinated screw dislocation mechanism and the dislocation link bowing mechanism both occur, but to different degrees (LAIRD, FINNEY and KUHLMANN–WILSDORF [1981]). For good measure, then, fig. 21 shows both mechanisms, and the experimental evidence seems to indicate both. In this connection, it is difficult to use regular TEM for assessing this point because the screw dislocations escape from the foil during specimen preparation. However, Mughrabi and his coworkers (MUGHRABI, ACKERMAN and HERZ [1979]; MUGHRABI [1981]) irradiated specimens retained under load so as to keep the screw dislocations in place during TEM specimen preparation. Representative photographs taken parallel to the slip plane are shown in fig. 22. Figure 22a shows a region in which link bowing is clearly dominant, and fig. 22b shows regions where screw dislocations, bowed under stress, are grouped with the same sign as can be seen by the similarity of their bowing, and they are coordinated across the channel walls.

Models have been offered to explain the flow stress of the plateau (i.e., PSB deformation) on the basis of the dislocation models described above (KUHLMANN–WILSDORF and LAIRD [1977]; MUGHRABI [1981]). These models have a great deal in common; however, the composite approach employed by Mughrabi has the virtue of simplicity and is described as follows:

Consider a PSB at saturation with the applied stress/strain at zero. As the stress is applied, the crystal first deforms elastically and then begins to yield, initially in the channels because of their lower dislocation density and their large Frank–Read bowing distance, i.e., the width of the channel. As the stress builds up, the walls will begin to yield, but by this time the channels will already have experienced a plastic strain given by the difference of the flow stresses of the walls and channels divided by the shear modulus. The large local strains perceived as easily measurable slip offsets at the surface imply that the plastic strain is ultimately continuous through the wall/channel structure of the PSBs, and this result supports the assumption that the *total* strain is the same in the walls and channels. This means that the edge dislocations laid down at the walls infiltrate them, dipoles flip within the walls and new dislocations bow out of the walls. On the assumption of continuity of total strain, Mughrabi expresses the applied stress τ_a as:

$$\tau_a = f_w \tau_w + f_c \tau_c \tag{4}$$

References: p. 2391.

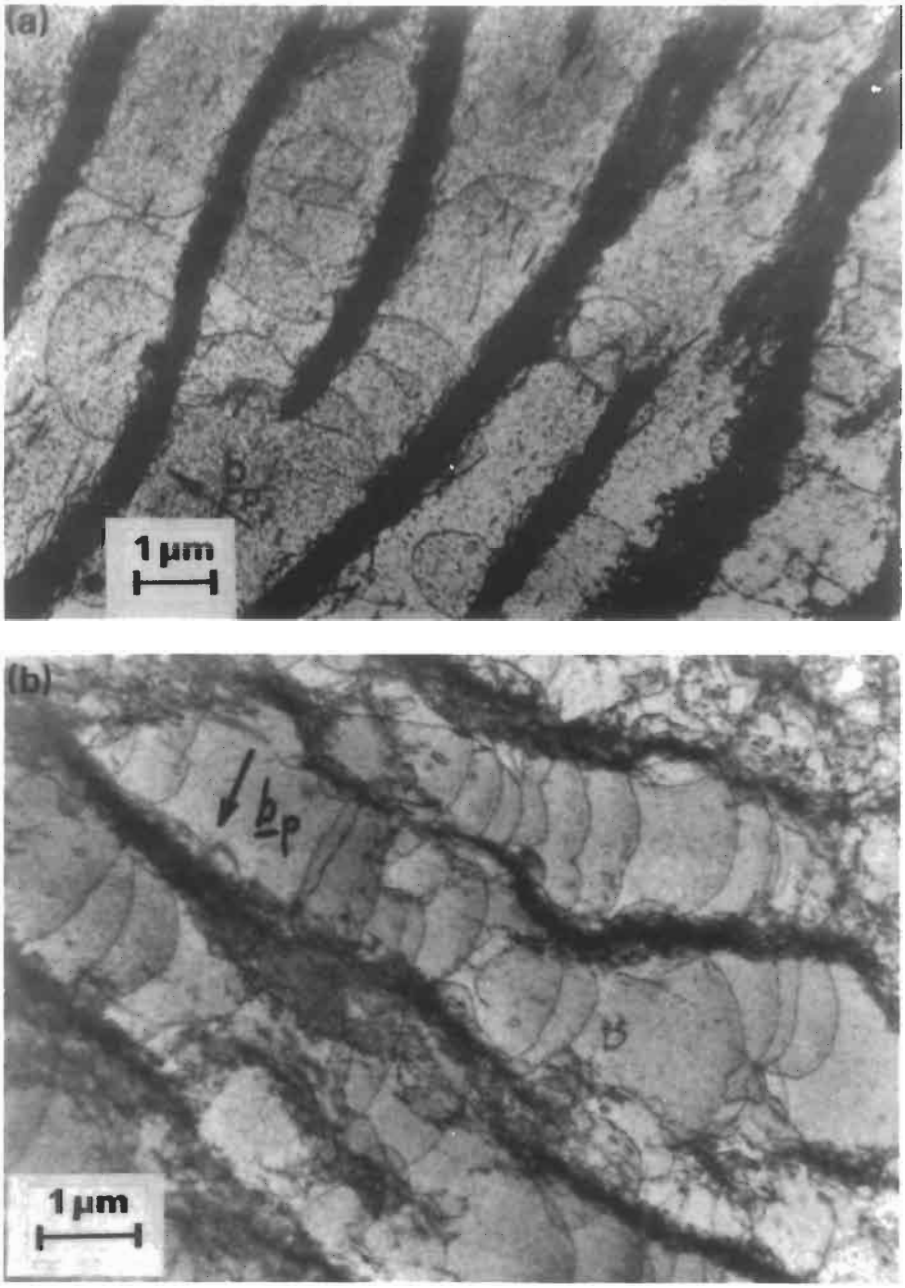

Fig. 22. Dislocation arrangements in a PSB from a fatigued copper single crystal (neutron irradiated in the stress-applied state: section parallel to the primary glide plane). Taken from LAIRD, CHARSLEY and MUGHRABI [1986], originating in work by Mughrabi and co-workers.

where f_w and f_c are the volume fractions of walls and channels respectively, and τ_w and τ_c the flow stresses of the walls and channels. That is, the rule of mixtures applies.

There is a slight difference in the *plastic* strain of the walls and channels because the flow stress in the walls is higher, so that their elastic strain is greater. KUHLMANN–WILSDORF and LAIRD [1977] expressed the flow stress of the walls in terms of the local stresses adjacent to dipolar walls. Mughrabi measured the flow stresses in the walls and channels by examining the curvatures of dislocations pinned in each of the regions by neutron irradiation and TEM examination. He found $\tau_w = 90$ MPa and the average $\tau_c \approx 15$ MPa, i.e., in close approximation to the Frank–Read stress. Since the volume fractions of walls and channels are typically 20 and 80% respectively in the section analyzed by him (e.g., fig. 22b), the rule of mixtures correctly predicts the plateau stress as ~ 28 MPa. The volume fractions observed in [1$\bar{2}$1] sections taken perpendicular to the walls (the "ladder" structures) generally show somewhat lower values, e.g., 10 and 90%, but the volumes affected by elastic stresses extend beyond the volumes actually occupied by dislocations.

It was noted above that spontaneous dissolution of edge dipoles by point-defect emission allowed PSB walls to remain stable and also produced high densities of point defects. In addition, since much of cyclic deformation is produced by screw dislocations, which will be dragging jogs and emitting point defects, point defect concentrations can be expected to be high in fatigue (KUHLMANN–WILSDORF and LAIRD [1979]). This high production of point defects has been verified by measurements of the electrical resistivity (POLAK [1970]; CHARSLEY [1981]) and is also reflected in a large temperature dependence of fatigue hardening (BROOM and HAM [1959]).

There are other implications of heavy point defect production. For example, the formation of PSB protrusions like those shown in fig. 17c is taken to be connected with enhanced point defect production in PSBs. This point has been discussed and developed into a detailed model by ESSMANN *et al.* [1981] and ESSMANN [1982], who argue that vacancy production dominates the point defect formation, thereby causing the protrusion. However, there is other evidence to indicate that interstitials can produce significant effects in other situations. For example, LEE *et al.* [1981] cycled Al–15% Ag alloy aged so as to contain GP zones at 77 K and found that γ' precipitates had nucleated and grown during a fatigue life (at high strain) lasting only the order of ten minutes. The only mechanism which could explain these surprising precipitate-growth kinetics was point defect enhancement of the interdiffusivity (the precipitates which formed were silver-rich); short circuit diffusion mechanisms were not adequate without enhanced volume diffusivity. Since it is unlikely that vacancies would be mobile at such low temperature, interstitials seem the likely cause for the behavior. A full discussion of point defect behavior was given by Neumann in the third edition of this work.

The dipolar wall structures of the PSBs follow from the dominance of primary dislocations in them. At the upper end of the plateau, where multi-slip begins to occur, and especially in polycrystals, more complex wall structures are observed. Space restrictions do not permit a full description of their varieties. However, as an example, consider the particularly interesting *maze* structure which has been observed frequently

in polycrystals, particularly for grains with [001] or [011] axes (RAJAN *et al.* [1975]; PAGE and WEERTMAN [1981]; CHARSLEY [1981]; KUHLMANN–WILSDORF and CHARSLEY [1981]), and occasionally in single crystals (ACKERMAN *et al.* [1984]). A beautiful example of a maze structure is shown in fig. 23. KUHLMANN–WILSDORF and CHARSLEY [1981] have interpreted wall patterns composed of these mutually perpendicular walls as dipolar walls with different Burgers vectors, mutually perpendicular. For example, it was known from TEM observations that dislocations with two different Burgers vectors were present. This is a bi-wall variant of PSB walls (KUHLMANN–WILSDORF and LAIRD [1977]). By the well-known LEDs principle, groups of similarly signed edge dislocations can reduce their energy if they arrange themselves as a tilt wall. Such a wall can further reduce the energy of the system by pairing with a similar wall, but of oppositely signed dislocations (i.e., a dipolar wall). But even dipolar walls have remnant stresses, that may be reduced by other dislocations, where they end. Thus where a dipolar wall ends, it will attract another dipolar wall oriented at 90° to its plane, as schematically illustrated in fig. 24. Possible L and T wall intersections and the dislocation configurations within them are shown in this figure. Note that the dislocations are pairwise in equilibrium not only within each wall, but from wall to wall along the diagonal lines indicated. Note also in fig. 23 that the intersecting walls have free ends, L-bends and T intersections, and no

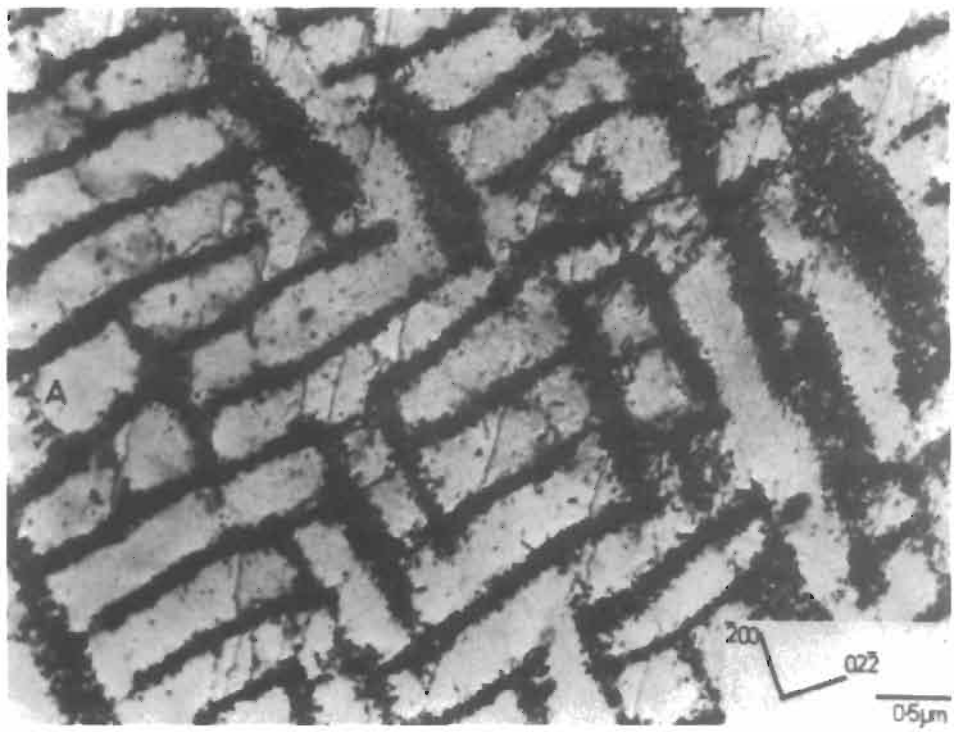

Fig. 23. "Maze" structure in commercial Cu–Ni alloy fatigued to saturation, showing wall structure on {100} planes. Courtesy of CHARSLEY [1981].

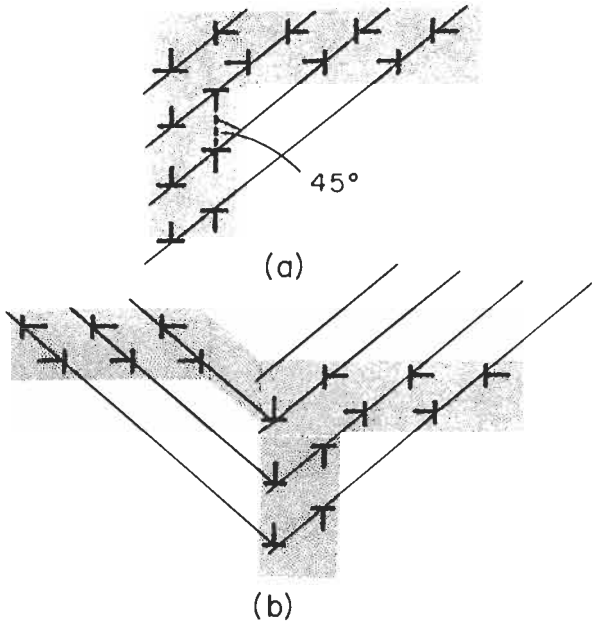

Fig. 24. Possible configurations of intersecting, perpendicular dipolar walls and the arrangement of dislocations within them to permit pairwise equilibrium: (a) the preferred L shape and (b) the popular, skewed T. Courtesy of KUHLMANN–WILSDORF and CHARSLEY [1981].

other kinds of intersections. In the T-intersection, there is repulsion between the opposed horizontal walls (fig. 24) of the T, thus leading to a skew configuration. On the basis of such considerations, Kuhlmann–Wilsdorf and Charsley are able to understand the frequency of occurrence of the various intersections and other properties of the dislocation structure. The agreement of these predictions with the observations of dislocation morphology lends support to the model.

4.5. Cyclic hardening in metals other than fcc

The cyclic deformation of metals with crystal structures other than fcc has not received nearly as much attention as that for fcc. However, the basic studies have been conducted and reviewed from time to time (LAIRD [1977]; MUGHRABI [1980] and MUGHRABI *et al.* [1979]). Most investigations pertain to bcc metals.

The factors of temperature, strain rate and small amounts of impurities, especially of interstitials, play large roles in the cyclic deformation of bcc metals, but are not so important for fcc metals. For example, the cyclic response of copper containing several percent of substitutional alloying element differs very little from that of pure copper (WOODS [1973]). Under slow strain rates, bcc metals can behave similarly to fcc metals, but under other conditions their behavior is quite different from that of fcc metals. The details for bcc metals, many of which have been elucidated by Mughrabi and his co-

workers (MUGHRABI, ACKERMANN and HERZ [1979]; MUGHRABI and WÜTHRICH [1976]; and MUGHRABI, HERZ and STARK [1976]) are as follows:

For *pure* single crystals of bcc metals cycled at low temperatures and at a high strain rate ($> 10^{-4}$ s^{-1}), the cyclic stress strain curve is typical of that of iron shown in fig. 25. Unlike copper, a PSB plateau does not occur. Instead for cyclic plastic strain range $\Delta\varepsilon_{pl} \lesssim 5 \times 10^{-4}$, cyclic hardening and microstructural changes are negligible (MUGHRABI *et al.* [1979]). The dislocation arrangement is dominated by screw dislocations in low density and has been explained by assuming that only edge dislocations move to-and-fro as the strain is reversed in a non-hardening, mechanically reversible manner (MUGHRABI, ACKERMANN and HERZ [1979]; MUGHRABI and WÜTHRICH [1976]; and MUGHRABI, HERZ and STARK [1976]). It will be recalled that the thermally activated glide of the screw dislocations is strongly impeded at ambient temperature and below, giving rise to a behavior reflecting typical features of the low temperature mode of unidirectional deformation of bcc metals. At higher strain amplitudes, cyclic hardening is pronounced and is associated with the formation of equiaxed cells. The slip traces are generally diffuse and in single crystals oriented for single slip do not follow the trace of the primary plane. MUGHRABI and his co-workers [1979] claim that, at high strain rates, the effective stress component characteristic of thermally activated dislocation glide dominates the contribution of the athermal component to the total flow stress, i.e., that due to the elastic interaction of the dislocations.

One of the most interesting observations is that cyclically deformed bcc crystals undergo shape changes (MUGHRABI, ACKERMANN and HERZ [1979]; MUGHRABI and

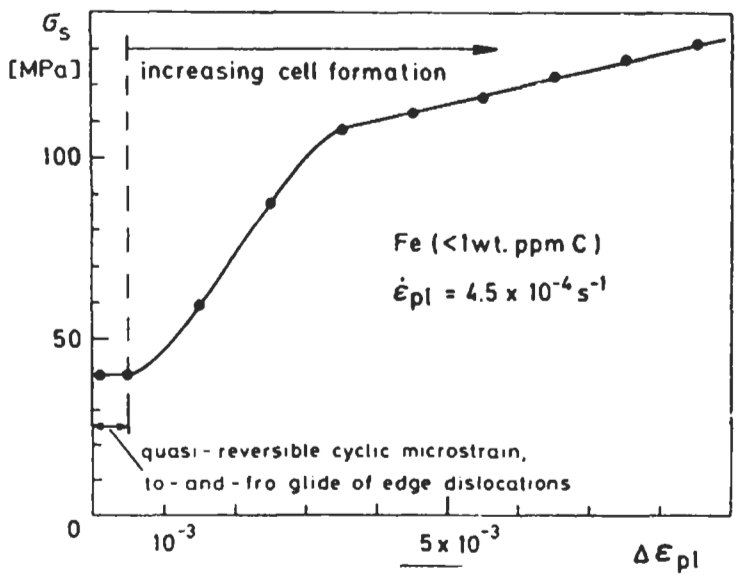

Fig. 25. Cyclic stress–strain curve of pure α-iron single crystals at 295K. (Courtesy of MUGHRABI and co-workers [1979]).

WÜTHRICH [1976]; and MUGHRABI, HERZ and STARK [1976]; NINE [1970, 1972]; NEUMANN [1975]) which are related to the asymmetric slip of screw dislocations with respect to tension and compression. They are brought about by mass displacements in unconstrained directions. Rather high applied strains are required to produce shape changes, so as to force the screw dislocations to glide. Typically, for crystals with single slip orientations, and having primary dislocations of Burgers vector a/2 [111], asymmetric slip can develop through the glide of screw dislocation segments on slip planes belonging to the $\bar{1}01$ zone in tension and the $\bar{2}11$ zone in compression (MUGHRABI and WÜTHRICH [1976]). The shape changes which occur are impressive, being easily visible to the naked eye. The cross-section of a cylindrical single crystal cycled in push-pull will change from circular to elliptical and because of the constraints of the grips, additional couples are applied to the specimen which can give it an "S" shape. More complicated shape changes have been reported on α-iron crystals of orientations other than that of single slip (IKEDA [1980]).

Slip plane asymmetry can be overcome by cycling at higher temperatures, at lower strain rates ($\sim 10^{-5}$ s^{-1}), and with interstitial impurities present. Investigations conducted under these conditions have been made (MUGHRABI *et al.* [1979]). For a strain rate of 2.5×10^{-5} s^{-1} and an α-iron crystal containing 30 wt ppm carbon, the cyclic stress strain curve is shown in fig. 26. In distinction to specimens tested at higher strain rates, considerable cyclic hardening was observed down to a plastic strain range of 10^{-4}. Shape changes were much less pronounced and the contribution of the athermal component of the flow stress, i.e., that due to the elastic interaction of the dislocations, dominated the

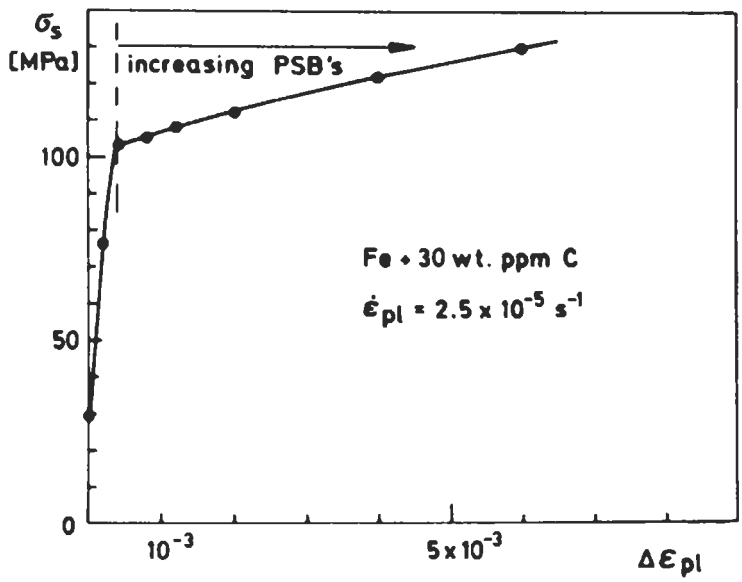

Fig. 26. Cyclic stress–strain curve of impure α-iron single crystals tested step-wise with respect to amplitude and at slow strain rate. Note the difference from that of fig. 25. (Courtesy of MUGHRABI and co-workers [1979]).

References: p. 2391.

effective stress component at all strain amplitudes (MUGHRABI, ACKERMANN and HERZ [1979]). Mughrabi and his co-workers observed slip lines paralled to the trace of the primary slip plane, and sometimes these were intense enough to be labelled PSBs. Moreover, their density increased with increasing strain amplitude. Congruent with their appearance, the slope of the cyclic stress–strain curve flattened to a gently sloping plateau. Mughrabi *et al.* were not convinced they had evidence of localized deformation in the PSBs (MUGHRABI, ACKERMANN and HERZ [1979]) but it is almost certain that strain localization does occur because of the widespread observation of PSBs in polycrystalline bcc metals in early work. Thus the overall behavior is seen to be similar in some respects to that of cyclically deformed fcc crystals.

A few investigations of the cyclic deformation of hcp single crystals have been made (STEVENSON and VAN DER SANDE [1974]; KWADJO and BROWN [1978]). Kwadjo and Brown working with magnesium have shown that PSBs form at suitable strain amplitudes and the properties of the PSBs are quite similar to those of fcc metals. However, at high strains, twinning is extensive and significantly affects the hardening; in this respect, the behavior of hcp metals is dissimilar. It is surprising that titanium has been neglected until quite recently (GU *et al.* [1994]) but investigations are now being reported about orientation effects and the dislocation structures of this important metal (TAN, GU, ZHANG and LAIRD [1995]).

4.6. Differences and similarities between monotonic and cyclic deformation

Monotonic and cyclic hardening behavior have been compared from time to time (FELTNER and LAIRD [1967]; KUHLMANN–WILSDORF [1975]; LAIRD and BUCHINGER [1985]); similarities and differences have been noted, depending on the manner in which the phenomena are viewed. For example, it is possible to consider cyclic hardening with respect to cycles. A copper single crystal cycled at a low plastic shear strain amplitude, say 3×10^{-5}, may take thousands of cycles to reach saturation, during which time it would typically increase its flow stress by about 19 MPa. If this hardening is viewed in terms of cumulative plastic strain, i.e., summed without respect to sign, it then represents an average hardening rate of G (the shear modulus) divided by several thousand. This average hardening rate is not constant — it is higher initially, similar to hardening rates observed in monotonic deformation, and then falls to very low values as saturation is approached. Viewed against such hardening rates, fatigue hardening thus would seem extraordinarily gentle, as compared to monotonic behavior.

With increase in amplitude, the flow stress increases considerably. As another example of hardening rate, consider the behavior of a copper single crystal cycled at a plastic shear strain amplitude (γ_p) of 2×10^{-3}. This crystal would reach saturation in about 2000 cycles and would increase its flow stress typically by 27 to 28 MPa, for an average hardening rate of $28 \div$ (number of cycles to reach saturation $\times 4\gamma_p$) $\sim G/25{,}000$ still a very low rate. Thus, while the average hardening rate is not strongly dependent on strain amplitude for $\gamma_p \sim$ few $\times 10^{-3}$ and lower, the *initial* hardening rate quite strongly increases with increasing amplitude. Hysteresis loops and rapid hardening data can be found in many publications (see, e.g., MUGHRABI [1978]; KUHLMANN–WILSDORF and LAIRD

[1979]; LAIRD [1981]). Also, see the paper of KETTUNEN and TIAINEN [1981] who have presented measurements of cyclic strain-hardening rates as a function of flow stress in both single crystals and polycrystals, and compared the behavior with that in monotonic hardening.

If fatigue-hardening is viewed in terms of saturation behavior, a different conclusion about hardening rates appears to hold. Saturation is conventionally defined in terms of the CSSC (fig. 5). It will be noted that the strain of 3×10^{-5} cited above applies to the straining region below the plateau (regime A) while the other strain cited above, 2×10^{-3}, corresponds to the mid-region of the plateau. Consider the hardening rates in terms of saturation behavior; at low strains the rate is simply enormous, i.e., $\Delta\tau/\Delta\gamma \simeq 20$ MPa/$10^{-4} \sim 4G$. This astonishing value corresponds to dislocation structures consisting of loop patches, and thus the hardening mechanism is analogous to that which occurs in Stage I monotonic deformation in which the hardening rate is barely noticeable. This difference is one of the largest between monotonic and cyclic deformations, and is associated with the very much higher dislocation densities which apply in fatigue after saturation is atttained. At strains above the plateau, the hardening rate is about $G/100$.

Now consider the plateau, which is customarily drawn with zero slope. Note that results from different observers are quite scattered. A case could be made for an actual negative slope of the plateau. It is possible to imagine that a test which started with large amplitudes could actually produce a flow stress less than 28 MPa, the plateau stress, in the upper reaches of the plateau. However, the most likely situation is that the flow stress increases by about 1 MPa (which is much less than the scatter in the measurements). The hardening rate associated with this stress increment is $1/7\times 10^{-3}$ MPa or $G/350$. It is important to note that this rate is about the same as the typical Stage II hardening rate, $\sim G/300$, in the monotonic deformation of a single crystal. Thus the lowest rate observable in fatigue deduced from the CSSC is equal to the *highest* rate observed in monotonic deformation. Again, the reason for this behavior is that dislocation densities produced in fatigue are much greater than typically observed in monotonic deformation (except at the highest levels); also strain increments in fatigue are minute. The CSSC plateau is thus seen as an important episode of decreased hardening rate between regions in which the rate is gigantic; the emphasis is, however, that the conclusion applies to saturation.

Comparisons between the cyclic and monotonic hardening behavior of alloys with low stacking fault energy/planar slip mode can be found in FELTNER and LAIRD [1967] and LAIRD and BUCHINGER [1985].

Comparisons of the dislocation structures which occur in monotonic and cyclic deformation can be made on the basis of the numerous TEM reports which are available about both. Certainly, in specimens cycled at low strain amplitudes, the very dense loop patches have their counterpart in the braids of primary edge dislocations and edge dislocation dipoles characteristic of Stage I monotonic deformation. Specimens fatigued at higher strain amplitudes exhibit dipolar walls, which are the counterpart of the polygonisation structures reported to result from the reorganisation of braids in unidirectional strain (KUHLMANN–WILSDORF [1975]). The same connection appears to exist between the loop patches and the "ladder" walls in PSBs. The major difference between

References: p. 2391.

the Stage II polygonisation structures and PSB dipolar walls is the lack of any relative misorientation in the ladder walls while polygonisation structures contribute to asterism. In the often-repeated to- and fro-motion of fatigue, the net Burgers vector vanishes to a good approximation.

At the highest cyclic strains, provided there is adequate three-dimensional dislocation mobility, then fatigue cells are formed. Three dimensional mobility occurs in wavy slip material, even in PSBs after very long cycling, and more easily in polycrystals. These fatigue cells are the equivalent of the cells which are characteristic of Stages II and III in monotonic deformation. KUHLMANN–WILSDORF [1975] has discussed the subtle misorientations which can develop in fatigue cell structures, between groups of cells. These misorientations occur by rotations normal to the active slip plane and with alternating sense of rotation, from one group of cells to another. More disorderly misorientations occur between cells in monotonic deformation.

4.7. Cyclic deformation of polycrystalline metals

The understanding of cyclic deformation in polycrystalline metals has lagged that of single crystals because it is much more complicated and, for a given type of behavior, the plastic strains are lower in polycrystals than in single crystals. Experimental demands are therefore more severe. Early work (e.g., FELTNER and LAIRD [1967]) therefore tended to focus on high-strain fatigue behavior (for review see LAIRD [1983]). LUKÁŠ and KLESNIL [1973] showed the way in greatly improving strain resolution and increasing the fatigue lives for which studies of cyclic deformation could be made. Their results encouraged other workers to run tests in plastic strain control at very small amplitudes, 10^{-5} to 10^{-3}. Strain resolution in cyclic deformation has usually lagged that in monotonic deformation because the guage length must be kept small in fatigue to avoid buckling during compression reversals. The arrival of electrohydraulic test methods brought significant improvements in extensometers and the electronics needed to excite them and record from them. In addition, studies of polycrystalline deformation received impetus from results on single crystals and there now exists a large body of results on polycrystals and greatly improved understanding.

The suggestion that the connection between the cyclic response of mono- and polycrystalline material might be much simpler than that in monotonic deformation was first made when hardening mechanisms in stages I and II/III were identified with low and high strain fatigue respectively (FELTNER and LAIRD [1967]) as noted above. BHAT and LAIRD [1978] extended the connection when they claimed, on the basis of LUKÁŠ and KLESNIL's [1973] data, that the cyclic stress–strain curve of polycrystalline copper contained a plateau at low strain amplitudes and that the plateau levels in the two kinds of material could be related by the Taylor factor. These views were initially difficult to sustain because, as new results were gathered at low strain amplitudes, the cyclic stress–strain curves of copper showed great variation.

One kind of result for the CSSC of copper is shown in fig. 27. It is apparent that, for this copper, in strain control, there is no plateau, but a tendency to one is shown over the range of strains to be expected from the cyclic stress–strain curve of copper single

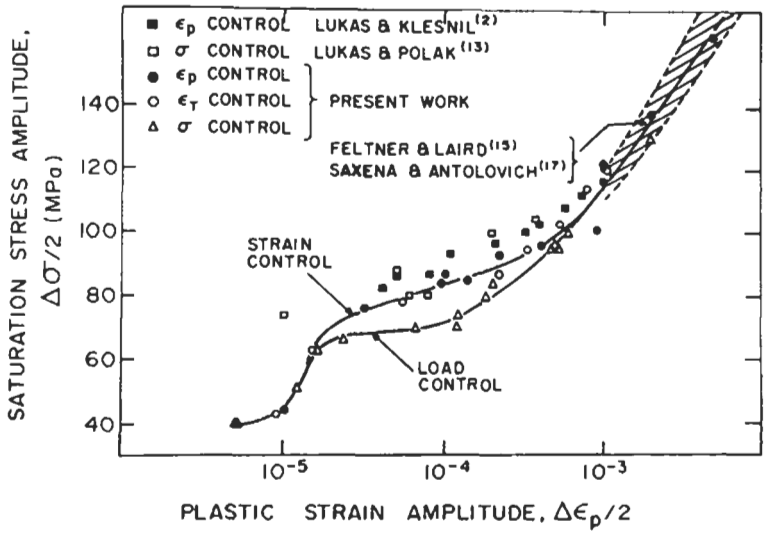

Fig. 27. The cyclic stress–strain curve of polycrystalline copper at low strains for tests under various forms of control, compared to earlier results of LUKÁŠ and KLESNIL [1973] at low strain and of other workers at high strain. Taken from FIGUEROA *et al.* [1981].

crystals. MUGHRABI and WANG [1981] found similar behavior and also noted that the first PSB to be observed at the specimen surface occurred at the plateau stress divided by the optimum Schmid factor, indicating that, at low levels of strain, individual grains were behaving much like isolated crystals. RASMUSSEN and PEDERSEN [1980], on the other hand, claimed a plateau for their polycrystals. As shown in fig. 27, a plateau occurs in load control in circumstances where the strains early in life are permitted to be large. Such large strains create cell structures within which there are ample mobile dislocations to carry the strain when saturation is reached. Otherwise, in strain control, the dislocation structures are rather similar to those observed in single crystals except perhaps for a somewhat greater density of secondary dislocations. That is: loop patches are observed at low strains, a mixture of loop patches and dipolar walls are found at intermediate strains and cell structures occur at higher strains, $>5\times10^{-4}$ (FIGUEROA *et al.* [1981]). The ladder structure of real PSBs has repeatedly been observed in polycrystals, both at the surface in fcc material (LUKAS *et al.* [1966]) and in the bulk (WINTER *et al.* [1981]; WANG and LAIRD [1988]; LLANES and LAIRD [1992]; MORRISON and CHOPRA [1994]) and in impure bcc polycrystals (POHL *et al.* [1980]) both at the surface and in the bulk.

With the passage of time and further investigations, the cyclic response of polycrystals seems to be even more complicated. A convincing plateau in the CSSC of polycrystalline nickel has been reported by MORRISON and CHOPRA [1994]. WANG and LAIRD [1988] were able to induce a plateau in the CSSC of polycrystalline copper if they ramp-treated their specimens first, thereby producing a more uniform distribution of loop patches from grain to grain, and so enhancing PSB formation when the stress/strain were high enough to require their production, but LLANES, ROLLETT, BASSANI and LAIRD

References: p. 2391.

[1993] were unable to reproduce this CSSC with another batch of copper although it was supposedly treated in similar fashion with regard to annealing and grain size. A very prominent plateau was found in the CSSC of polycrystalline Al–4% Cu alloy containing shearable precipitates, which correlated well with that for single crystals containing the same kind of precipitate (see fig. 28) but in this alloy the localized strains are extremely high (LEE and LAIRD [1983]).

The explanation for the wide range of polycrystalline response observed by the different workers in different metals and even the same metal originated in systematic efforts to study grain size effects (LLANES, ROLLETT, BASSANI and LAIRD [1993]). Llanes and co-workers found the CSSC curve of large-grained copper to lie at *higher* stresses (by 20 MPa) than that for smaller-grained copper. They attributed this behavior to the occurrence of a strong ⟨111⟩ cum ⟨100⟩ texture induced in the copper by the high annealing temperatures needed to obtain the large grain size. These multi-slip orientations caused enhanced cyclic hardening in the large grain specimens as compared to that in the smaller grain specimens in which the texture was not so pronounced. This interpretation was supported by critical experiments in which such a texture was formed in a slab of copper large enough to permit specimens to be cut in different directions, so as to vary the "texture" without otherwise varying the metal (PERALTA, LLANES, CZAPKA and LAIRD [1995]). For choices of specimen directions in which single slip orientations were favored, the stresses fell considerably and the normally expected hierarchy with respect to the flow stress of differently grain-sized specimens was re-established. Typical results are shown in fig. 29. Rather similar conclusions can be found in Morrison's work on polycrystalline nickel [1995], in which the texture details vary in a different fashion with respect to grain size.

Since twin boundaries seem to stimulate PSB formation and secondary slip (fig. 14),

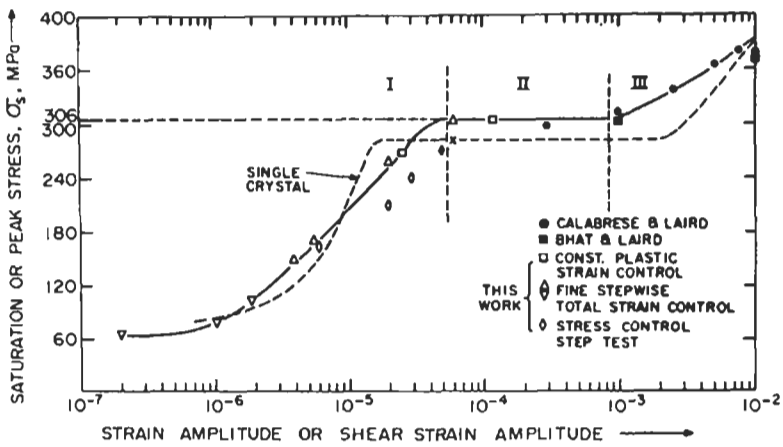

Fig. 28. The cyclic stress–strain curve for polycrystalline Al–4% Cu alloy containing shearable precipitates (θ'') compared with that for the same alloy in monocrystalline form. Note that the ordinate scale should be divided by three to apply to the shear stress of the monocrystal; the abscissa applies to both forms of material. Courtesy of LEE [1980].

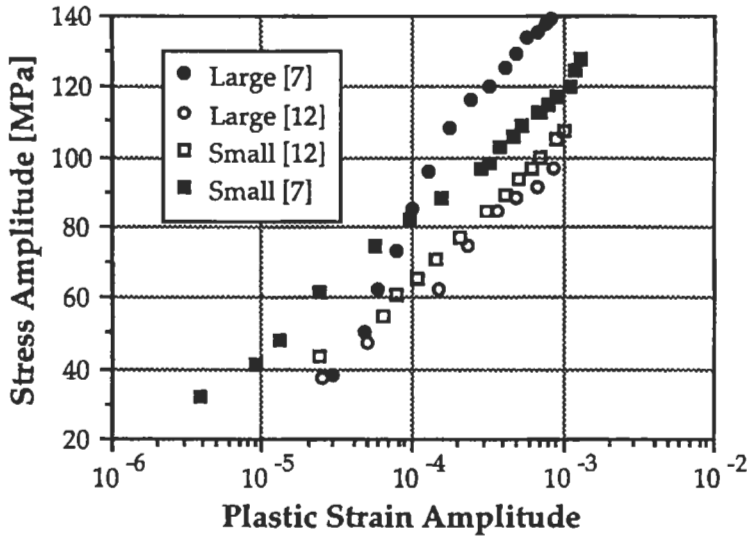

Fig. 29. Cyclic stress–strain curves (obtained by step-testing) for large and small grained copper, one set (filled points) (LLANES, ROLLETT, BASSANI and LAIRD [1993]) having a variously pronounced ⟨111⟩–⟨100⟩ texture and the other, referring to PERALTA *et al.* [1995], having a more random texture (open points). Taken from the latter reference.

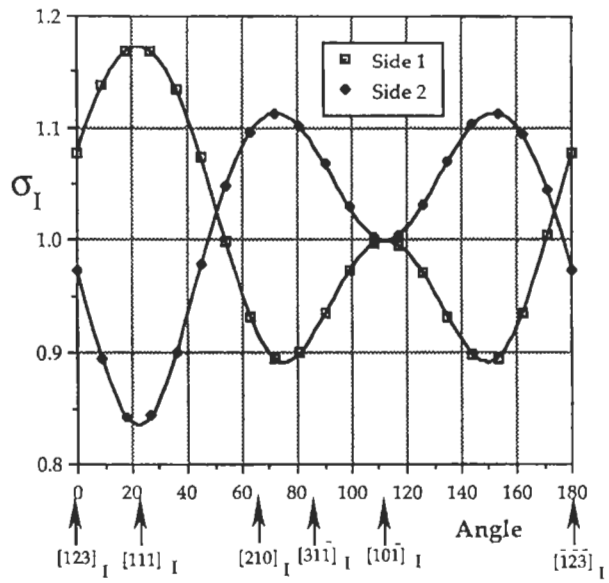

Fig. 30. Maximum principal stress at both sides of a twin boundary as a function of the crystallographic direction of the tensile axis. The crystal has been rotated through 180° from a single slip orientation, [123], to its opposite pole, about a rotation axis which was selected to orient the other poles shown in sequence. Taken from PERALTA *et al.* [1994].

References: p. 2391.

the study of the stress interaction at twin boundaries as a function of crystallographic orientation appeared interesting. PERALTA and co-workers [1994] developed a simple model to account for the increase of the stresses adjacent to a twin boundary due to compatibility requirements in copper. One of the main results, which is shown in fig. 30 and which shows the effect of grain orientation on the compatibility stresses next to a twin boundary, indicates that the stress-concentrating effects of a twin reach a maximum when the tensile axis is parallel to a ⟨111⟩ direction. That is, the effect of the twin depends on the crystallographic orientation of the grain in which the twin is embedded and, therefore, is a function of texture. Thus the ⟨111⟩ textures which produce enhanced cyclic hardening in polycrystals are reinforced in their effect by the presence of twins in metals with medium and low stacking fault energy.

PERALTA, LI *et al.* [1995] have shown that this conclusion can be extrapolated to other types of boundaries as well. In an example taken from the work of PERALTA, SCHOBER and LAIRD [1993], they cite a bicrystal containing a twist boundary about the [$\bar{1}$49] direction, a boundary that could be expected (say) in an FCC polycrystal containing a texture related to single slip orientations, and another bicrystal with a [110] asymmetrical tilt boundary, consonant with a multi-slip type of texture. The crystallography of these boundaries is shown in fig. 31. Their results showed that the stresses at the latter can be about four times higher than those in the former case. The additional stresses found at grain boundaries can in part be responsible for: 1) the presence of more "advanced" dislocation structures adjacent to them, meaning that cell structures will occur at grain boundary regions if dipolar walls are the operating structure in the center of grains (FIGUEROA and LAIRD [1981]; LLANES [1992] — see fig. 32); and 2) the observation of enhanced cross-slip in polycrystalline metals with low stacking fault energy (LI and LAIRD [1994]).

Given that local stresses can be very important in fatigue, mostly at low values of the plastic strain (long life fatigue), the correlation between texture, grain size, and the type of grain boundary/misorientation in polycrystals (studied by several authors from a

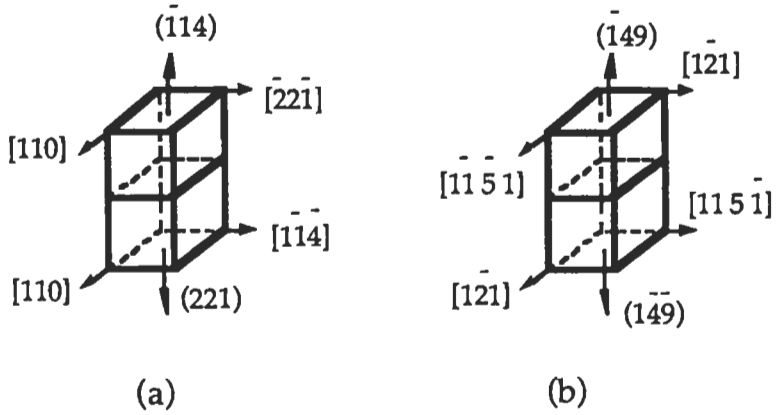

Fig. 31. The bicrystal misorientations, "large", used in the elastic calculations of PERALTA, SCHOBER and LAIRD [1993]: (a) [110] asymmetrical tilt boundary, and (b) [$\bar{1}$49] twist boundary.

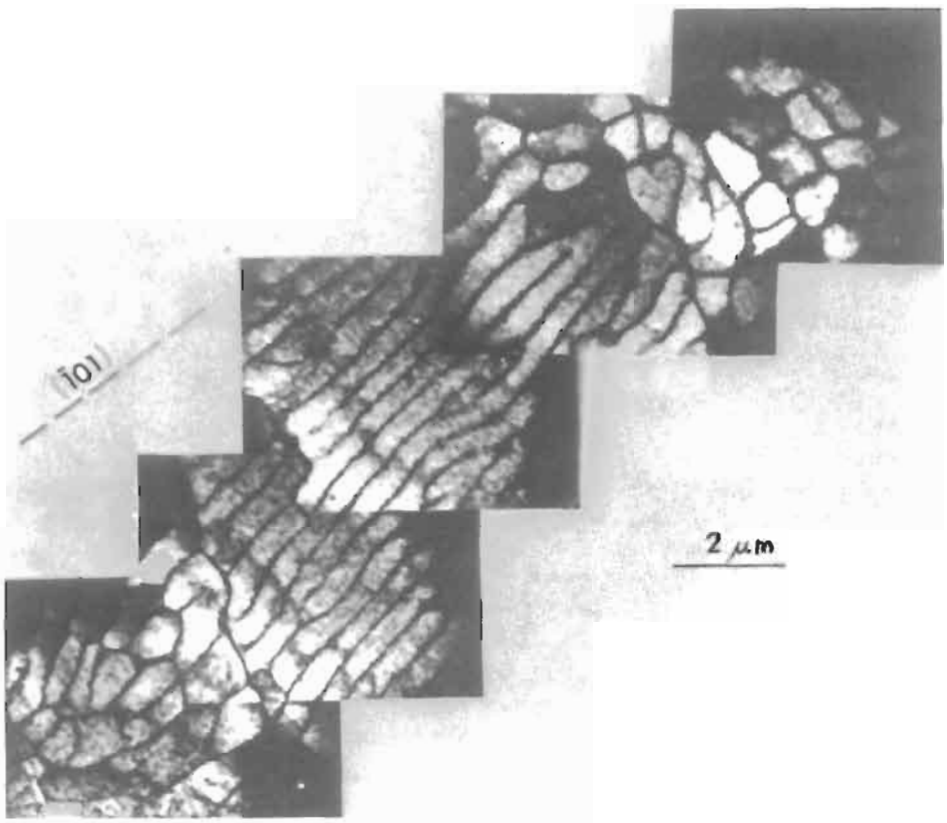

Fig. 32. Dislocation structure of copper tested under a "strain decremental step test", meaning: alternating bouts of cycles to saturation between a high strain (2×10^{-3}) and a progressively lower strain. Specimen removed for TEM examination after final cycling at a plastic strain amplitude of 5×10^{-5}. Dipolar walls from the primary system in the grain center — the alternating cycling at high amplitude has emphasized the cellular structures near the grain boundaries. Taken from FIGUEROA and LAIRD [1981].

"geometrical" point of view, PAN and ADAMS [1994]; GARBACZ *et al.* [1995]) must be fully taken into account if a reasonable model of polycrystalline behavior is to be developed.

Another factor which could play a significant role in polycrystalline deformation is the elastic anisotropy of the metal. KITAGAWA *et al.* [1986] showed, using finite element methods, that the compatibility stresses that appear at grain boundaries for a given misorientation depend on the anisotropy. PERALTA and his coworkers [1993, 1994, 1995] attempted to estimate [1995] the stresses around the boundaries of bicrystals for several fcc-metals as a function of their *anisotropy factor* (A.F.), defined as follows:

$$A.F. = \frac{S_{44}}{2(S_{11} - S_{12})} \tag{5}$$

References: p. 2391.

Table 1
Anisotropy factors and stacking fault energies for representative fcc metals and copper alloys of wavy and planar slip mode, respectively.

Material	A.F.	S.F.E. [mJ/M^2]
Al	1.2231	250.0
Ni	2.4077	150.0
Au	2.8523	50.00
Ag	3.0207	20.00
Cu	3.2726	42.00
Cu–5 at% Al	3.3891	24.00
Cu–10 at% Al	3.5118	12.00
Cu–23 at% Zn	3.7925	15.00

where S_{ij} are the components of the compliance tensor. The values of A.F. for typical fcc metals and alloys are shown in table 1. It will be noted from these values and the associated values of stacking fault energy that the anisotropy of the metals and the slip mode are coupled, because there is a tendency for metals with a high A.F. to have a low S.F.E. This is interesting since, as noted above, cross slip has been observed to be enhanced in near boundary regions of polycrystalline metals with low stacking fault energy (LI and LAIRD [1994]).

To investigate the role of anisotropy in polycrystalline cyclic stress–strain response, PERALTA *et al.* [1995] chose the maximum principal stress in the plane parallel to the boundary as the parameter to characterize the strength of the elastic interactions. The results expressed as a function of the A.F. and for the pair of archetypal tilt and twist boundaries shown in fig. 31, are given in fig. 33. The maximum principal stress at the two interfaces increases with the degree of the A.F., as expected, but the behavior is different for the two types of boundaries. The stress for the twist boundary is low and increases monotonically with the A.F., whereas the stress for the tilt boundary is larger and shows oscillations. The twist boundary is associated with a high index direction, and thus the property contributions of the principal directions become averaged. The tilt boundary is associated with a low index axis and this can make the stresses more sensitive to changes in stiffness with respect to orientation. These results show that the interactions between adjacent grains not only depend on the structure and crystallography of the boundary, but also on the basic elastic properties of the material.

It was noted above that the most convincing plateaus observed in the CSSCs of polycrystals have been found for aluminum (alloy) and nickel (MORRISON and CHOPRA [1994]). It is tempting to speculate that the lower elastic interactions in the polycrystalline structures of these metals (0.06 for Al and 0.28 for Ni versus 0.42 in Cu — see the normalized in-plane principal stress shown in fig. 33) favor the presence of plateaus in their CSSCs, whereas the high anisotropy of copper works against localization of deformation.

Given all the complex interactions that influence the cyclic response of polycrystals, it is not surprising that our understanding of the behavior is rather modest; in particular,

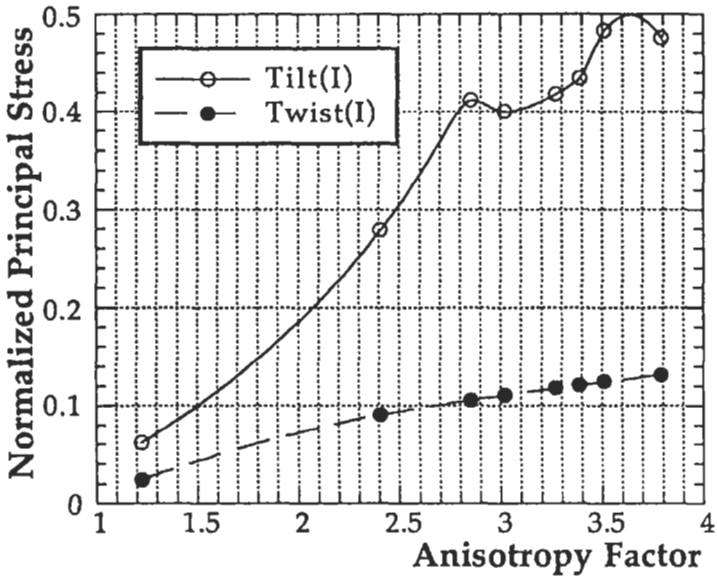

Fig. 33. The maximum "in-plane" principal stress for the two boundaries shown in fig. 31, for the various fcc metals and solid solution alloys listed in table 1 and represented here through the specific values of their A.F. Taken from PERALTA *et al.* [1995].

a good model to extrapolate the cyclic behavior of polycrystals from that of a single crystal seems to be still out of reach. Some of the models used for monotonic behavior have been applied to fatigue with a certain degree of success by LUKÁŠ and KUNZ [1994], mostly on the conversion of S–N data of fcc polycrystals and the CSSC of pure iron. The basic principle behind these models is the idea of finding a conversion factor between the resolved shear stress τ and the resolved shear strain γ of individual grains and the stress σ and the axial plastic strain ε of the polycrystal, according to the following formulas:

$$\tau = \frac{\sigma}{\overline{M}} \quad \text{and} \quad \gamma = \varepsilon \overline{M} . \tag{6}$$

The conversion factor $\overline{M}$ lies between 2.24 (Sachs) and 3.06 (Taylor) for polycrystals with randomly oriented grains (KOCKS [1970]).

On the Taylor model the strain in every grain is assumed to be the same and equal to the macroscopic strain, and each grain is supposed to deform by the activation of the 5 slip systems that minimize the product of the resolved shear stress on each system and its corresponding shear strain (KOCKS [1970]). As a consequence of the anisotropy of the grains, both plastic and elastic, Taylor assumptions violate equilibrium and the estimations obtained by using it represent an upper bound of the real behavior. Sachs, on the other hand, assumed that grains deform in single slip, and that they act as individual entities subjected to an axial stress. These conditions violate compatibility, and thus the

Sachs factor gives a lower bound of polycrystalline behavior.

Given the implicit assumptions in the two models, it is obvious that the Taylor model should apply better to situations where multiple slip is involved, and Sachs to those where single slip is dominant. High-cycle fatigue is a typical situation where the plastic strains are low and polycrystals deform by single slip processes for a significant range of plastic deformations (LAIRD [1983]), therefore, Sachs should apply in this case. Nevertheless, experimental evidence seems to indicate that the Taylor model offers a better approximation to the behavior of polycrystals (WANG and LAIRD [1988]; LUKÁŠ and KUNZ [1994]). It is surprising, though, that many fatigue workers apply these models without taking into account some of the basic assumptions on which they are based. For example, the use of a Taylor factor of 3.06 is only valid when the polycrystal is *completely random*. When the sample has some crystallographic texture, the average Taylor factor changes, and it can change by a significant amount depending on the nature and sharpness of the induced texture. It is also necessary to remember that the Taylor model represents an *upper bound* to the expected behavior. Therefore, features that seem to correlate exactly with the random Taylor factor should be checked to account for the effects of texture and other microstructural variables.

Taylor's model is unable, by its very nature, to account for one of the basic features of fatigue (KOCKS [1970]): localization of strain in PSBs and *Persistent Lüders Bands* (PLBs) which develop in planar slip metals. Besides this, the evolution of plastic deformation predicted by Taylor's model implies the development of a deformation texture, which is not the case in fatigue, since the back and forth motion of dislocations is very effective in eliminating any residual Burger vectors, i.e., the misorientation due to dislocation structures like fatigue cells is minimal compared to that of similar structures developed during monotonic deformation, as remarked in the preceding section.

4.8. Cyclic deformation in alloys

As noted from the sections above, a wide range of phenomena in the fatigue of fcc metals is now understood, at least qualitatively. Studies of substitutional alloy behavior which involve single crystals have been rarer but reports of sustained attempts to understand such alloys are now available. For substitutional alloys of low concentration (WOODS [1973]; WILHELM and EVERWIN [1980]), the behavior has been found rather similar to that of pure metals, even to such details as the value of the plateau stress in the cyclic stress–strain curve (CSSC), and the nature of the dislocation structures.

When the solute concentration is significantly greater, so that the alloy behaves with a planar slip mode (for discrimination of wavy and planar slip modes, see HONG and LAIRD [1990a]), the dislocation structure of the alloy is considerably different from that of wavy metal (YOUSSEF [1970]; LUKÁŠ and KLESNIL [1970, 1971]; BUCHINGER *et al.* [1986]). The typical ladder structure and loop patches which are produced in the cyclic deformation of pure metals have never been observed in planar slip metals at room temperature.

One of the controversies concerning the cyclic deformation behavior of planar slip

alloys was whether or not strain localization exists. YAN *et al.* [1986], employing the same interferometric method as previously used on copper, observed strain localization, contrary to previous reports (YOUSSEF [1970]; LUKÁS and KLESNIL [1970, 1971]); they also observed the existence of a plateau in the cyclic stress–strain response. However, the Cu–16 at% Al alloy used by them hardens very sluggishly, exhibits burst phenomena, and shows strain-aging behavior to a marked degree. It is possible that saturation was not attained. Interferometric methods involve tests interruptions and are very time-consuming because the specimen preparation technique is demanding. The strain-aging phenomena which occurred during such lengthy delays could and probably did affect the subsequent straining behavior when attempts were made to measure localized strain. The interactions of all these complex phenomena have since been understood through more extensive investigations (ABEL *et al.* [1979]; HONG and LAIRD [1990b,c,d, 1991a,b]; INUI *et al.* [1990]; HONG, INUI and LAIRD [1992]) and a fairly clear picture of the behavior has emerged:

In a typical planar-slip alloy, such as Cu–16 at% Al, studied by Hong and his coworkers, the friction stress acting on the dislocations by reason of the alloy content is very high and the application of a stress of about 20 MPa is needed simply to produce yielding (HONG and LAIRD [1990b]). The slip is confined to bands and persists in them for a while, as the metal gradually hardens. This hardening causes the localized strain to peter out, and new slip bands appear elsewhere, generally accompanied by a strain burst. These bursts can readily be seen in the shapes of the hysteresis loops and in load-cycle recordings for which the specimen is cycled in strain control. The typical cyclic stress–strain response during hardening, while burst behavior is occurring, is shown in fig. 34. Note that, at low amplitudes, the hardening rate is extremely small and bursts are few and far between. Slip is localized in the active bands for a long time. As the amplitude increases, the bursts become more numerous and the hardening rate increases — note that a gradient in the load-cycle plot becomes more evident in fig. 34 (c) to (e). At the highest amplitude, the bursts are so numerous that they are no longer distinguishable. Thus the slip gradually percolates throughout the gauge length until the whole crystal becomes occupied by bands. This temporary persistence of the slip gave rise to the term "*Persistent Lüders Bands*" (PLBs) to describe the regions of currently active slip (BUCHINGER *et al.* [1986]). Bands which were previously active and had become quiescent can be reactivated if the other volumes of the specimen have undergone slipping, temporary persistence, gradual hardening, and subsequent quiescence.

The appearance of the stress–strain hysteresis loops during hardening is shown in fig. 35. The shapes fluctuate between round-topped and sharply pointed, the latter occurring while the PLBs are settled, the former after a burst has occurred. This behavior is connected with solute effects and its segregation. In freshly deformed areas, dislocations can be pinned during the quiet moments of a cycle. Once they break free, their reduced friction stress allows them to run with limited resistance by back stresses until the limit of the strain cycle causes them to stop. After hardening and dislocation accumulation has developed in an active band, the back stresses reassert their values and the pointed loop shape returns.

It is interesting to find that, in single crystals of Cu–16 at% Al alloy, saturation

References: p. 2391.

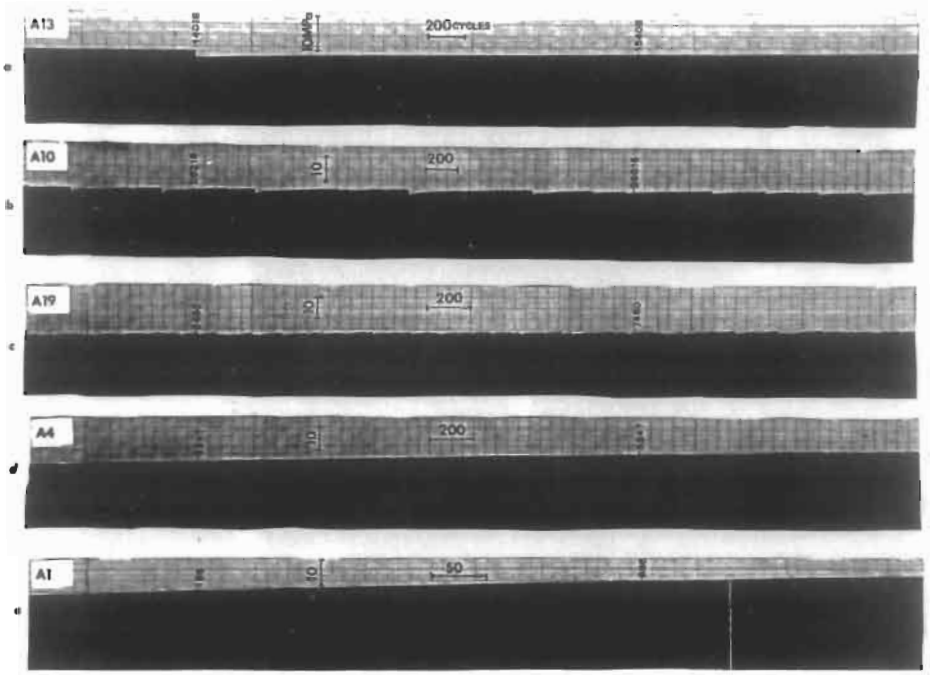

Fig. 34. The cyclic stress–strain response of Cu–16 at% Al single crystals, cycled under strain control at various shear strain amplitudes, perceived in load-cycle actual recordings. The chart is moving so slowly (note the abscissa scale, cycles indicated) that the pen traces out a solid ink band. When bursts occur, a step appears in the record band. (a) $\gamma_t - 1.47 \times 10^{-3}$; (b) 3.2×10^{-3}; (c) 4.94×10^{-3}; (d) 8.8×10^{-3}; (e) 2.15×10^{-2}. The specimen number is indicated in the upper left hand corner of each recording. Taken from HONG and LAIRD [1990b].

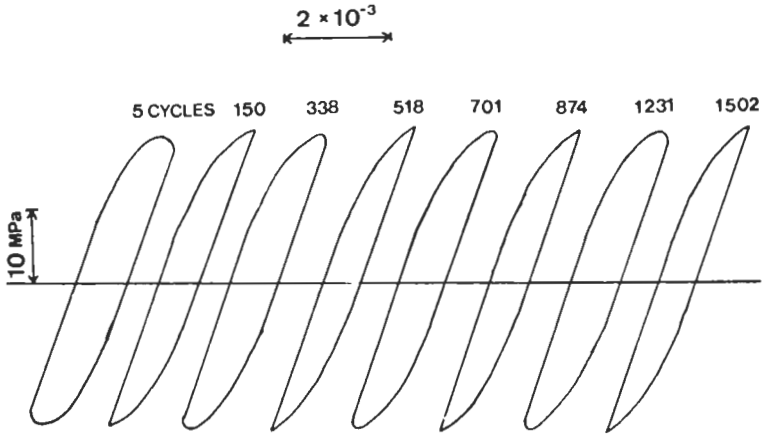

Fig. 35. Periodic fluctuations in the shapes of hysteresis loops with cycles in Cu–16 at% Al alloy single crystals. The pointed loop shape occurs between and before bursts, the round-topped loops just after bursts. Taken from HONG and LAIRD [1990b].

behavior is not observed and earlier claims to a cyclic stress–strain curve, containing a plateau, must be attributed to over-optimism on the part of the investigators that hardening had been exhausted. The hardening behavior is therefore presented in the form of cyclic hardening curves — see fig. 36. At low amplitudes, the tests were interrupted without reaching saturation or failure. At higher amplitudes, hardening also never seemed to stop but cracks formed and grew instead (the final "drop-offs" in the curves were caused by crack propagation). Note in fig. 36 that the initial flow stress, representing the solute friction contribution, has been subtracted off so that actually the stresses are much higher (except at low amplitudes) than those observed in copper (see HONG and LAIRD [1990c] for a treatment of the friction and back stress behavior in Cu–16 at% Al alloy). Consequently cracks grow very rapidly as soon as they form.

The dislocation structures associated with this hardening behavior are shown in figs. 37 and 38, INUI *et al.* [1990]. Rafts of dipoles and multipoles are formed both from perfect dislocations and from partial dislocations (see BUCHINGER *et al.* [1986], for examples). These rafts are organized as well-defined two-dimensional bands at low stresses (fig. 38a) with well-paired dislocations. As hardening proceeds, the intervening volumes are gradually filled up and the dislocation density progressively increases (figs. 38b and c). Primary slip is dominant by far and the residual dislocations observed by TEM (without neutron irradiation) are almost all edge dislocations. However, secondary slip is active from early in cycling and becomes progressively more so as hardening proceeds. In the later stages of hardening, the back stress begins to increase abruptly, presumably because Lomer–Cottrell lock formation accelerates and there is increasing evidence of the formation of small circular prismatic loops probably associated with

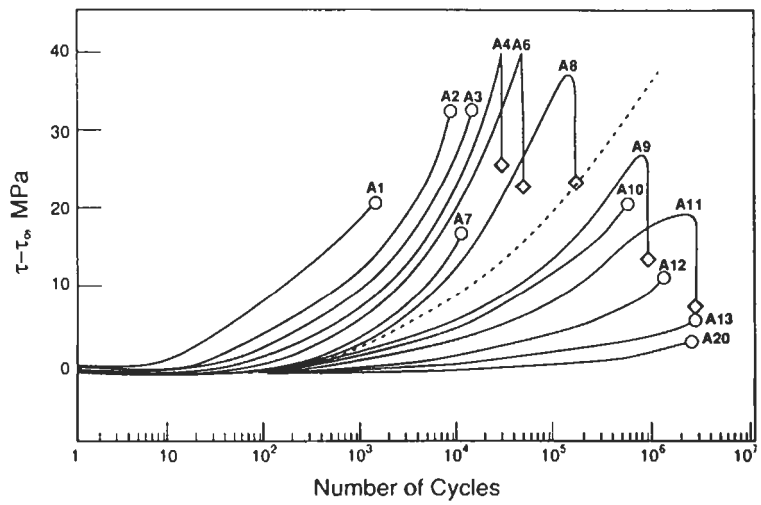

Fig. 36. Cyclic hardening behavior of Cu–16 at% Al single crystals, oriented for single slip, cycled under strain control at various strain amplitudes. Here, τ is the shear stress and $\tau_0 = 19$ MPa is the critical resolved shear stress. Plots are smoothened from the effects of strain bursts to represent average hardening behavior. Taken from HONG and LAIRD [1990c].

References: p. 2391.

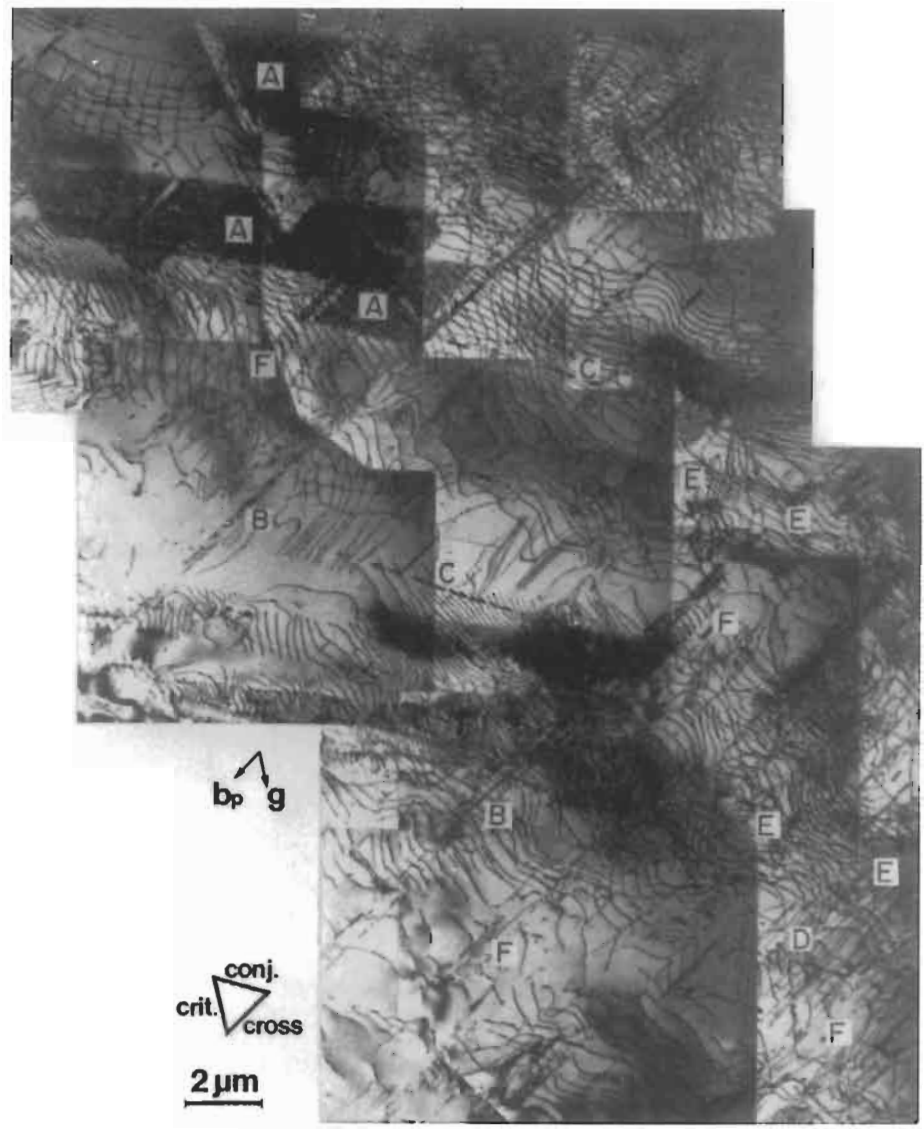

Fig. 37. Dislocations structure observed in the primary slip plane after fatigue of a Cu–16 at% Al single crystal to a stress of 34 MPa with a total shear strain amplitude of 3.2×10^{-3}. Rafts of well-matched primary edge multipoles are present along with traces of slip on the cross and conjugate slip planes. Taken from INUI *et al.* [1990].

point defects produced by intersecting slip. The structures formed in these planar slip alloys of low stacking fault energy amount to large, irregular Taylor lattices, in which there are large variations in the extent of localized strain, both spatially and temporarily. Because of the planar slip nature of the alloy and the difficulty of cross-slip, the

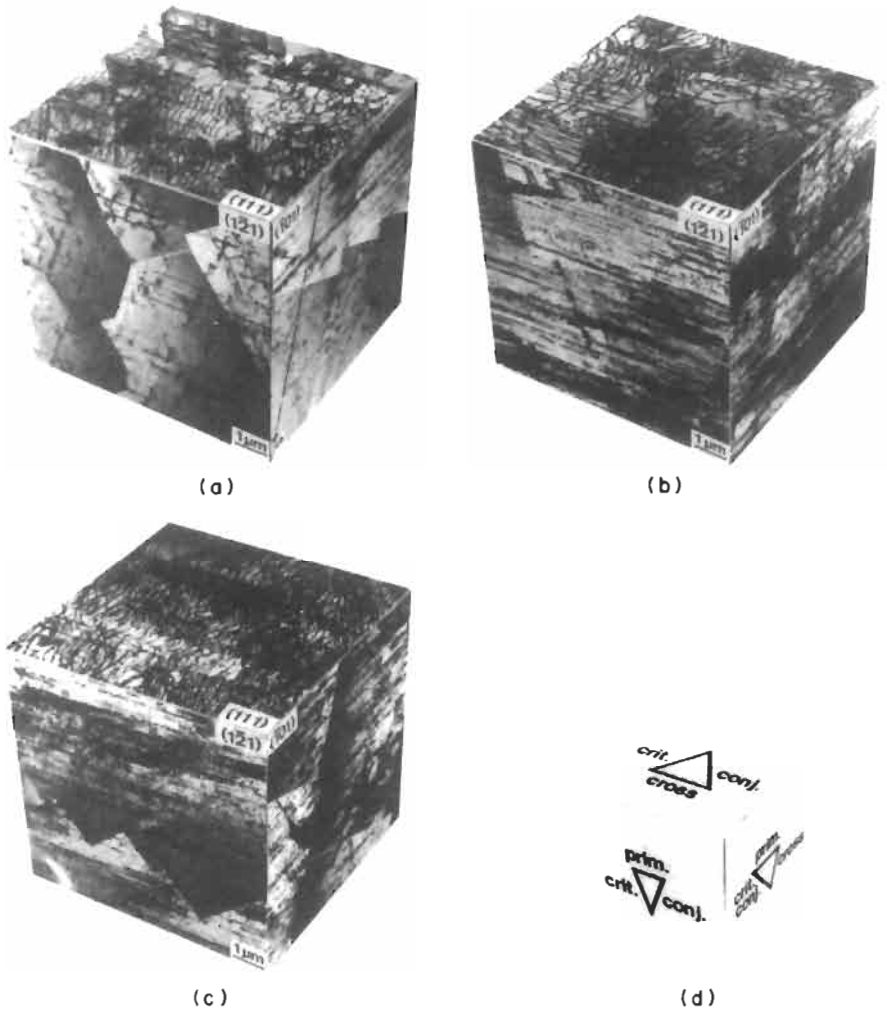

Fig. 38. Three-dimensional views of dislocation structures in a planar slip, Cu–16 at% Al single crystal cyclically hardened to: (a) 28 MPa, (b) 34 MPa and (c) 41 MPa. The TEM section planes are indexed and in (d) the traces of the {111} planes are indicated. Taken from INUI *et al.* [1990].

dislocation agglomeration which occurs in wavy metals cannot occur. The Taylor lattice is therefore extended in three dimensions.

Since the dislocation structures consist of Taylor lattices, the flow stress can be explained by the passing stress of the oppositely signed edge dislocations in the multipoles:

$$\tau_p = \frac{Gb}{8\pi(1-\nu)d} \tag{7}$$

References: p. 2391.

where G is the shear modulus, ν is Poisson's ratio and d is the separation of the slip planes. Hardening is accomplished by the gradual reduction in d as shown in fig. 38. In wavy-slip metals the friction stress and back stress are coupled via the behavior of the loop patches (KUHLMANN–WILSDORF [1979a and b]). In Cu–16 at% Al, the friction stress, dominated by solute effects, remains fairly constant and hardening is mainly accomplished by an increase in the back stress which is to be expected in multipolar structures (HONG and LAIRD [1990b]). The question as to why the friction stress does not increase with cycling in spite of the multipoles is answered by assuming that the geometry of dipoles in the multipole can be modeled as shown in fig. 39a. That is, the dipoles are kinked, in the sense that the relative orientation of the dislocations is changed at some inter-multipole point. The slipping stress (and thus the friction stress) would be greatly reduced for a dipole with the kinked configuration, and the zipping–unzipping of the dipole seems a more appropriate term in describing the motion of the dipole. Also, zipping would be much easier than flipping of the whole dipole. With application of

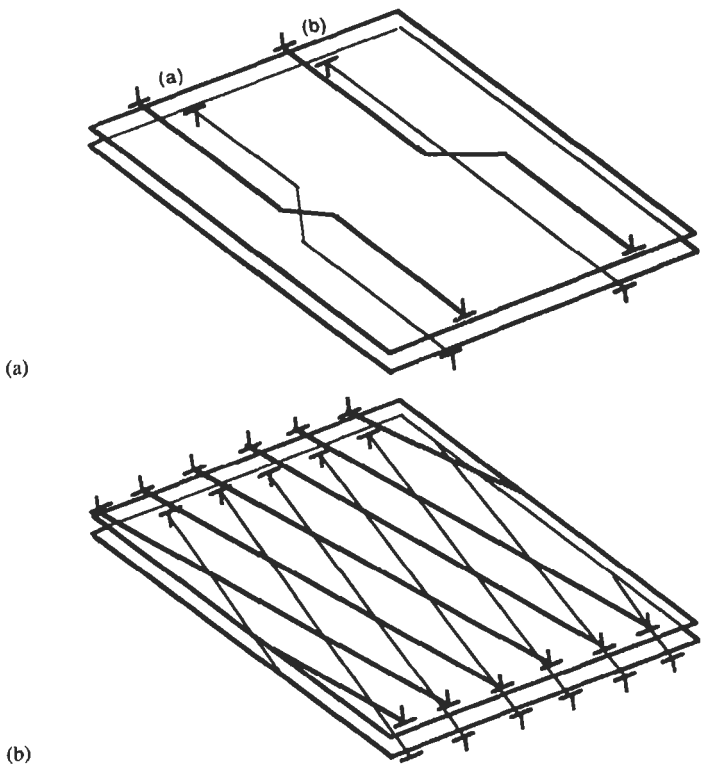

Fig. 39. Schematic representations of dislocation structures observed in the multipoles of planar slip alloys: (a) kinked dipoles, (b) cross-grid-like multipoles. These kinds of structures are on primary plane sections. Taken from HONG and LAIRD [1990c].

stress which is smaller than that needed to separate the dipole, the cross-over point will move to-and-fro depending on the sign of the applied stress.

Copper cannot behave in such a fashion. If the dipolar partners in a loop patch of pure copper were kinked as in fig. 39, cross-slip would easily occur at the cross-over point because of the high stacking fault energy and the small spacing between the partners. Thus the dipole would become sub-divided and the kinks would not be stable. In copper, therefore, the equality between the back stress and the friction stress holds for the deformation of the Taylor lattice.

Another common type of structure observed in planar slip alloy is the cross-grid type of multipole shown in fig. 39b. Although this type of multipole is less stable than the normal (unkinked) multipole, it has the advantage of easily accommodating large cyclic strain, and they are more frequently observed in the heavily-deformed areas (HONG and LAIRD [1990c]). In less heavily deformed areas, such a multipole could be decomposed with the application of a stress large enough to overcome the sum of the friction stress due to the solute and the friction stress for zipping–unzipping. As such it would not contribute much to the hardening, unless it were constrained by obstacles such as Lomer–Cottrell locks or other dislocation structures. Under such circumstances they could contribute to the hardening by their elastic interaction (the back stress) which is unaffected by the cross-grid geometry. For a more detailed discussion of the hardening in such alloys, see HONG and LAIRD [1990c].

Single crystals of AISI 316L stainless steel, also fcc in structure, and also planar in its slip mode in spite of having a higher stacking fault energy than Cu–16 at% Al alloy (20 ergs/cm^2 vs <5 ergs/cm^2), behave rather similarly in their cyclic response (LI and LAIRD [1994]) except that stainless steel manages to saturate its hardening and, on prolonged cycling, transforms its dislocation structure gradually from planars arrays into ragged loop patches quite like those observed in copper. Such transformation occurs more rapidly in polycrystals (LI and LAIRD [1994]).

Just as studies of planar slip single crystals lagged behind those of wavy slip pure metals, so also much less is known about polycrystalline planar slip behavior, and the effects of grain size and texture. Clearly there is a strong tendency for single crystals and polycrystals to show common dislocation structures and mechanisms, and the results may be briefly summarized as follows:

In early work, THOMPSON and BACKOFEN [1971] studied the fatigue behavior of polycrystalline 70–30 brass as a function of grain size, presenting their results in terms of fatigue life, which limited the information about cyclic hardening and saturation behavior that could be extracted from them. They found that the fatigue life of brass depended on grain size within a certain range, below which the cycles to failure were insensitive to grain size. This was interpreted as a result of the planarity of slip and the effect that the longer slip length of large grains has on the stress concentrations at grain boundaries. Such an interpretation involves "pile-ups" which are not favored in cyclic deformation where dislocation pairing limits long range stress fields. Moreover, LI and LAIRD [1994] have found wavy type dislocation structures in near-boundary regions of stainless steel. LAIRD and coworkers [1986] and FELTNER and LAIRD [1967] studied polycrystalline Cu–16 at% Al, and LUKÁŠ and KLESNIL [1973] worked on Cu–Zn. LI and

References: p. 2391.

LAIRD [1994] and POLÁK *et al.* [1994] studied polycrystalline 316L stainless steel, but all these studies, with the exception of the last one, were limited to one grain size and even though texture was sometimes mentioned in their analyses, it was not properly characterized as to derive proper conclusions about its effect in this kind of material. The works of LI and LAIRD [1994] and POLÁK *et al.* [1994] show yet another contradiction in the results related to strain localization, since the former workers did not find a plateau in their polycrystalline samples, even though they used ramp loading, whereas the latter group found a plateau for the two grain sizes they used, also without any previous mechanical treatment. Furthermore, the strain range of the plateau they found seemed to depend on grain size. Typical CSSCs obtained by these groups of workers are shown in fig. 40. A texture effect could be, in principle, responsible for the absence of the plateau in the curves reported by Li and Laird.

These results indicate however, that saturation does occur in polycrystals, that hardening occurs more rapidly than in single crystals (although unevenly as well, because of strain bursts, LAIRD *et al.* [1986]; YAN *et al.* [1986]), probably because of multislip effects stimulated by adjacent grains, and that strain localization also occurs. Thus PLBs do eventually become transformed to PSBs. More research focused to determine the effects and interactions of texture and grain size in planar slip alloys is definitely needed. It is likely that a similar synergism between the variables will be present in these materials, and perhaps to a stronger degree than in wavy slip metals.

A class of alloy containing high solute concentration which shows particularly interesting behavior is the ordered alloys (see the chapter by Pope in this volume), which are characterized by tension-compression asymmetry, very high stresses, extreme slip localization and a high degree of planarity of slip. Their cyclic hardening behavior is complex and, because of the tension-compression asymmetry, single crystal behavior is much more orientation dependent than in any other metals (BONDA *et al.* [1987]) except for hcp. Also, because of their unusual localized cross-slipping behavior, which tends to immobilize the screw dislocations, their background dislocation structures are more homogeneous and more dominated by screw dislocations than is usually observed. The PSBs are extremely complex and difficult to examine by TEM because the dislocation density is so high.

Aged alloys containing small precipitates which are so dense and closely spaced that they must be sheared by mobile dislocations, are very susceptible to localized deformation in PSBs, although the PSBs are structurally different from those in pure metals. The typical hardening behavior for this class of alloy is shown in fig. 41. Rapid hardening is considerable, the flow stress reaches a peak, and softening then sets in. Since saturation does not occur, there is no generally accepted definition of flow stress for the cyclic stress–strain curve. LEE and LAIRD [1982] chose to define the cyclic stress–strain curve in terms of the peak stress, and it is this curve which is shown in fig. 28 for the same type of specimens illustrated in fig. 41. Since the peak marks the onset of strain localization and the first appearance of PSBs, it is not surprising that a plateau is observed in the cyclic stress–strain curve. However, for this system, the onset of the plateau occurs at 1.8×10^{-5}, and the high strain end occurs at $\sim 2 \times 10^{-3}$. Both of these strains are much lower than those of pure metals, because the localized strains in the PSBs are greater.

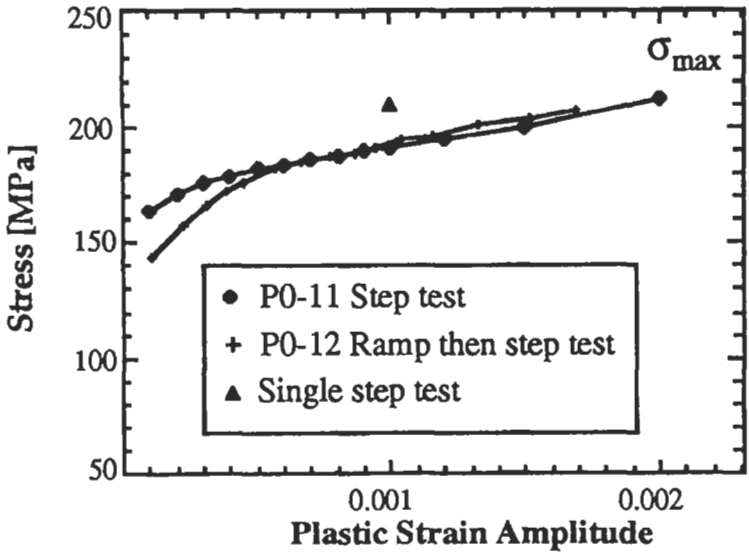

(a)

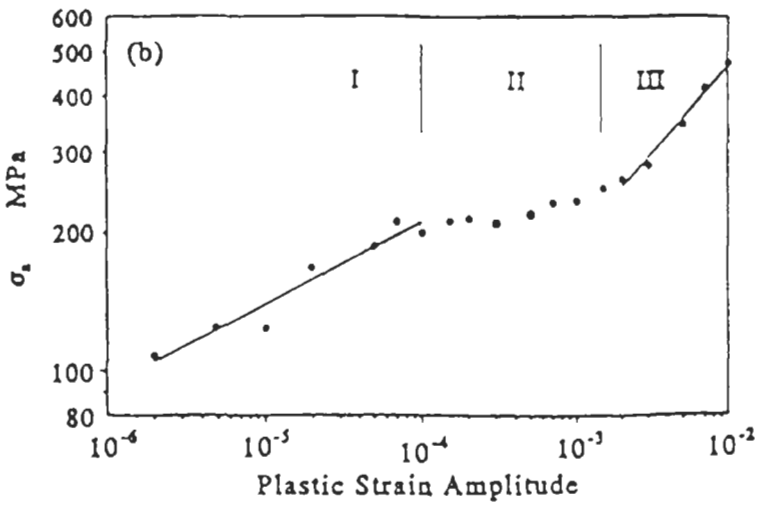

(b)

Fig. 40. Cyclic stress strain curves of polycrystalline 316L stainless steel, as observed by different workers: (a) LI and LAIRD [1994], no plateau is observed, and (b) POLÁK *et al.* [1994], a plateau appears. Note that the stresses for this stainless steel are greater than those of Li and Laird. There may be differences of interstitial content.

During rapid hardening, the slip was observed to be fine and homogeneous (LEE and LAIRD [1983]). For strains below those of the plateau, saturation behavior occurred and softening was not observed; rather the slip remained homogeneous for hundreds and thousands of cycles and a fatigue limit was defined by the lower end of the plateau. As

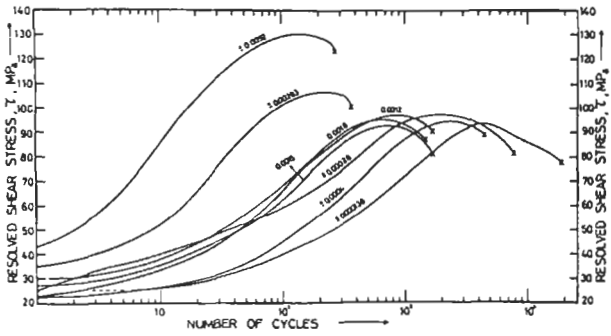

Fig. 41. Cyclic hardening curves of Al–Cu alloy single crystals containing shearable θ'' precipitates cycled in constant plastic shear strain control, indicated. Measurements for specimens of various single slip orientations. Hardening occurs first, followed by softening, and is not strongly dependent on orientation.

usual, PSBs occurred for strains corresponding to the plateau. Interferometric techniques were used to measure the heights of slip offsets at the PSBs and thus to measure the localized strain (LEE and LAIRD [1983]). It was found to be very large, varying from 0.3 to 0.6. As softening developed, the strain became more localized. Initially the most numerous PSB offsets were about 30 nm high with a few groups of micro-PSBs being closely clumped and showing a combined height of ~ 300 nm. With continued cycling the extremes of the PSB offsets did not change, but the distribution of offsets became more uniform (LEE [1980]) and progressed towards higher values. TEM observations indicated that the PSBs are quite narrow, typically 0.25 μm thick, and densely occupied by dislocations and precipitates. The softening occurred only after the PSBs formed and was attributed to degradation of the precipitates by a disordering mechanism. "Disordering" can occur by a number of mechanisms. Since the shearable θ'' precipitates in Al–Cu alloy are ordered, the scrambling of the crystals by repeated cutting events could eliminate the component of the order hardening, consistent with the kinetics of softening (LEE *et al.* [1981]). Also, the roughening of the precipitate-matrix interface could reduce the chemical hardening contribution to the overall flow stress. Also, it is likely that some of the precipitates were chopped up to the point of dissolution and, locally, the material reverted to the solutionized condition.

It is interesting that the volume fractions of PSBs are always very low in the Al–Cu alloy within the plateau. At strains greater than those of the plateau, deformation continues to be localized in PSBs but they develop on more than one slip system (LEE and LAIRD [1982]). Intense kink bands were also observed. The PSBs really constitute micro-PSBs, and like those of pure metals, they are limited in length — typically 400 μm. Nevertheless the PSBs pass right through the crystal as a string of overlapping short segments (LEE [1980]).

The dislocations in the PSBs have roughly equal densities of edge and screw dislocations (LEE and LAIRD [1982]). In Al–Cu they tend to be somewhat denser at the interface between the PSB and matrix because the PSBs are slightly misoriented with respect to the matrix. There is a slight tendency to clumping of the dislocations,

sometimes observed, but more often they are uniformly arranged. Apparently the highly localized strains can be accommodated by motion of many of the dislocations and by a balance between their multiplication and annihilation.

Because of the large values of the strains in the PSBs, the lives of Al–Cu single crystals (LEE [1980]) are two orders of magnitude smaller than those of copper single crystals (CHENG and LAIRD [1981b]). Also, the slope of the Coffin–Manson plot is greater in Al–Cu alloy than in pure copper for the same reason.

Although the broad aspects of cyclic deformation are similar in different alloys containing shearable precipitates, the details are often quite dissimilar. For example, Gerold, Wilhelm and their co-workers (WILHELM and EVERWIN [1980]; VOGEL *et al.* [1980, 1982]; WILHELM [1981]; WILHELM *et al.* [1979]) have carried out an elegant study of Al–Zn–Mg alloy containing shearable precipitates, η', and find many aspects of mechanical response similar to those described above. However, in the PSBs of Al–Zn–Mg, the precipitates dissolve and leave the cleared channel supersaturated in alloy elements, explaining the softening which occurs on extended cycling. Even within a single alloy system, a wide variety of behavior can be observed. For example, in Al–Ag of high solute concentration and activity, Al–15% Ag, a structure initially containing GP zones, which one would expect to be cut up and dissolved, did not behave in such a manner. Rather the alloy underwent cyclic strain-induced formation of more stable precipitates, γ' and γ, which cause enhanced strengthening rather than softening (LEE, BHAT *et al.* [1981]; LAIRD and LANGELO *et al.* [1978]). Thus, tests conducted at lower strains (and which therefore lasted longer, and provided more opportunity for precipitate nucleation and growth) produced more hardening than at higher strains and a reduction in strain localization. This behavior caused the cyclic stress–strain curve to have a negative slope over part of its range (LAIRD and LANGELO *et al.* [1978]). On the other hand, GEROLD *et al.* [1987], who studied an Al–5% Ag alloy of much lower solute activity, found that PSBs formed and the GP zones were dissolved in them in association with cyclic softening. A good example of PSBs containing dissolved particles is shown in fig. 42. For precipitate behavior in a wider range of alloys hardened with shearable precipitates, see the work of Gerold and his co-workers (GEROLD and STEINER [1982]; STEINER *et al.* [1983]; LERCH and GEROLD [1985]).

When the precipitates are large, the cyclic hardening behavior is entirely different. A typical example of such an alloy is Al–4% Cu alloy containing θ' precipitates. Such precipitates consist of plates on {001} habit planes, roughly 1 μm in diameter and the three families of plates serve to divide up the material into small cubical volumes separated by reasonably dislocation-impermeable particles. In such a case, the cyclic deformation is homogeneous, slip lines are hardly visible, hardening is rapid, saturation is extremely stable and softening does not occur (BHAT and LAIRD [1979]; HORIBE and LAIRD [1983, 1985a and b]). Since PSBs are not possible, the cyclic stress–strain curve does not contain a plateau — typical CSSCs for monocrystals containing θ' precipitates are shown in fig. 43a.

The CSSCs shown were obtained by an incremental step-test starting at low amplitude and ascending by small steps in plastic strain control (s-test), and it is interesting that the crystal of multiple slip orientation has lower stresses than that for single slip

References: p. 2391.

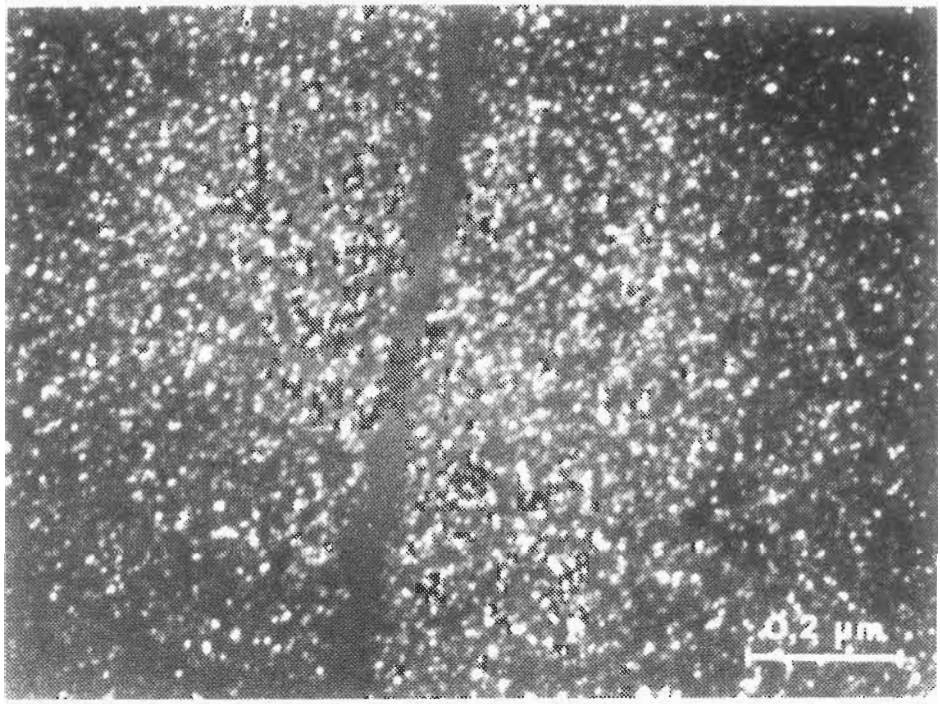

Fig. 42. A narrow PSB in Al–Zn–Mg alloy single crystal, cycled 5200 cycles at a plastic strain range of 2.5×10^{-3}, showing dissolution of precipitates revealed by dark field contrast. Courtesy of VOGEL *et al.* [1982].

(HORIBE and LAIRD [1983]). Note that the crystal orientations are shown in the inset stereographic projection. This behavior was not a fluke resulting from the step method of testing, as can be seen from the cyclic hardening curves shown in fig. 43b for tests in constant amplitude (c-test). The multi-slip crystal hardens to a greater extent in the first application of strain, familiar from behavior in monotonic deformation but then hardens less as cycles accumulate.

The cyclic hardening and saturation behaviors of metals containing impenetrable (somewhat) precipitates have been interpreted in a variety of ways, in early work in terms of *geometrically-necessary dislocations* (CALABRESE and LAIRD [1974]). The idea here is that the dislocations are confined to the matrix between the particles which resist deformation and cannot be cut by dislocations (actually the situation is more complex; at high strains the particles do become cut, as can be seen by APDBs left behind in the ordered θ' particles (HORIBE and LAIRD [1983]). Accordingly, the dislocations in the matrix are arrayed at the interfaces of the particles to accommodate the curvatures introduced by the incompatible deformation of the two phases. The increase in the flow stress is associated with the increase of the dislocation density. In crystals oriented for single slip, the dislocations will be dominated by primary dislocations, and they can

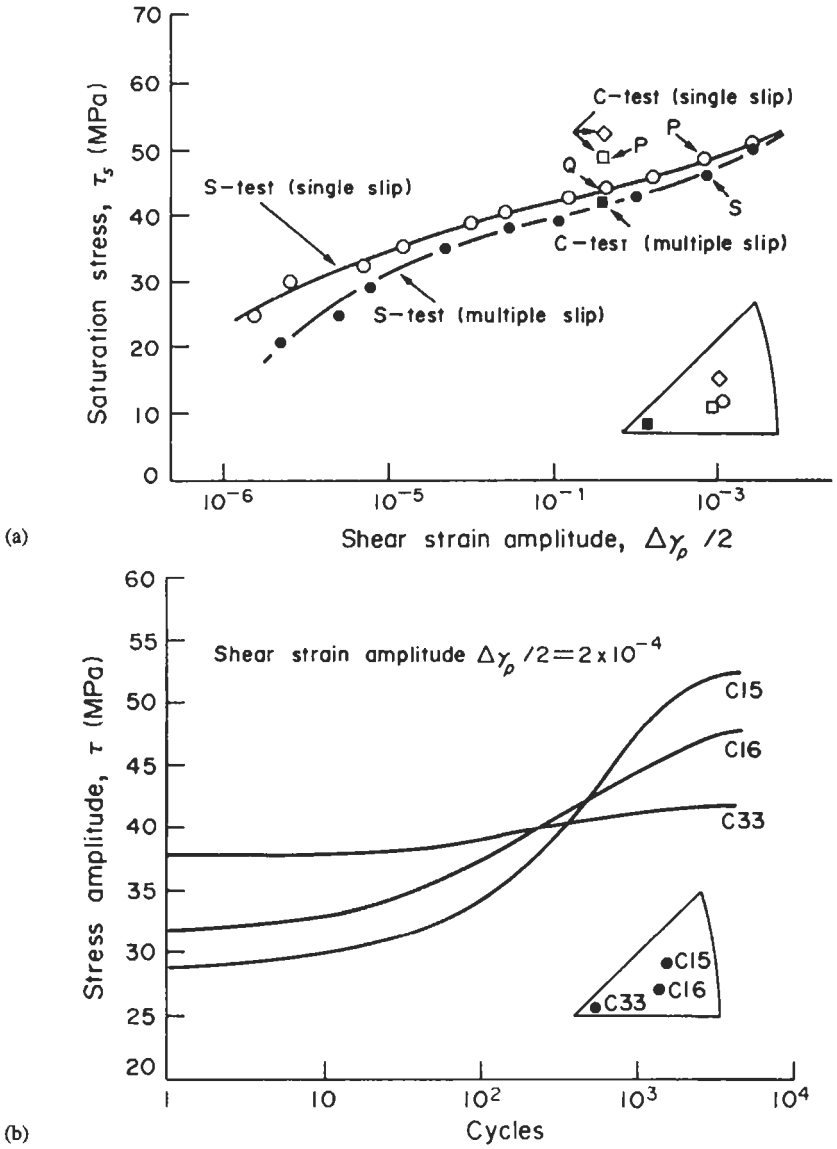

Fig. 43. (a) Cyclic stress strain curves for single- and multi-slip single crystals for Al–4% Cu aged to contain θ' precipitates. CSSCs obtained by a step ascending test and crystal orientations given in the inset. Saturation stresses for specimens tested in constant amplitude are also shown. (b) Cyclic hardening curves for three Al–4% Cu single crystals containing θ' precipitates of the orientations shown in the inset standard triangle, and all cycled at the same constant strain amplitude. Each curve is coded with the crystal serial number to indicate the specimen orientations.

References: p. 2391.

provide strong back stresses through tilt wall arrangements at the θ' interfaces. A principle of LED theory is that multiple slip permits more complete pairing of oppositely signed dislocations as well as energy reductions between dislocation arrangements of different Burgers vectors. This approach can explain the reduced flow stress of the multi-slip crystals as compared to that of single-slip crystals. HORIBE and LAIRD [1983], report seeing the equivalent of "Labyrinth" structure at the θ' interfaces.

An alternative approach to understanding dislocation behavior is that of *non-linear dynamics*, an approach to dealing with dislocation populations as a whole in conditions far-from-equilibrium, which corresponds to those of cyclic straining. GLAZOV and LAIRD [1995], have shown that in the relatively small volumes of matrix accessible to dislocations between impenetrable precipitates, the self-organization of the dislocations acts to arrange them at the extremities of their glide space, i.e., at the particle interfaces, provided the particles are approximately 1 μm apart. If the cutting-resistant particles are arranged more densely (and therefore with decreased separations), so as to limit further the glide volume (or distance — GLAZOV and LAIRD reported a one-dimensional problem [1995]), then the available dislocation populations can carry the applied strain without a tendency to rearrange or to clump together. This behavior applies, for example, to T–D (thoria-dispersed) nickel in which a dislocation population is inherited from the processing and the thoria particles are both dense and resistant to cutting. This analysis explains the observations of BHAT and LAIRD [1979b], who found the starting dislocation structures in T–D nickel extremely stable to cyclic deformation at both room and elevated temperatures.

Commercial alloys based on the simple systems treated above, and other fcc systems, show many differences in detail, depending on the specifics of their microstructures. For example, commercial aluminum alloys typically contain three levels of precipitates: constituent particles, the largest; dispersoids, of intermediate size; and G–P zones, the smallest and most responsible for the superior hardness of the alloys. The fatigue behavior is determined by a compromise between the effects of the different microstructural components: the constituent particles and dispersoids act to homogenise the strain during cyclic deformation, while the G–P zones encourage PSB formation, slip localization and zone dissolution. The complexities of the behavior are still not well-understood (STARKE and LÜTJERING [1979]; LAIRD [1977]), but the larger particles seem to be effective in limiting cyclic softening.

Commercial alloys based on ordered, intermetallic compounds tend to show different kinds of behavior. For example, unlike the commercial aluminum alloys which show rapid hardening, Waspaloy does not show rapid hardening associated with general fine slip, but all the plastic strain is localized in PSBs from the start of cycling (STOLTZ and PINEAU [1978]). The kinetics of the hardening and softening processes that govern the cyclic deformation were observed to be the same in each slip band regardless of plastic strain because, in order to accommodate the higher strains, the number of slip bands increased linearly with applied strain (STOLTZ and PINEAU [1978]). In this regard, the behavior is similar to that of PSBs in pure metal single crystals. However, since it contains shearable precipitates, Waspaloy shows hardening to a peak and then softening, similar to the behavior observed in model Al–Cu alloy, but no plateau was found in the

cyclic stress–strain curve. Low cycle fatigue of oxide-dispersion-hardened alloys is discussed in the Addendum to ch. 25, § A4.4.

4.9. Dislocation patterning in cyclic deformation

Reference to the treatment of cyclic deformation by non-linear dynamics in the previous section calls for comments on the application of such techniques to fatigue. While it is tempting to devote space to such matter, it does not seem justifiable at present, partly because Kubin has just published an excellent review [1993] covering classical models of dislocation patterning such as those of HOLT [1970] and KOCKS [1985], the reaction-plus-diffusion approach and the approach by numerical simulations, and partly because the application to fatigue is still in its infancy. Aside from Kubin, many of those possessing the necessary mathematical erudition to apply the method are unfamiliar with the physics of fatigue problems, distributed through a vast literature, and dissipate energy on minor problems. Even when KUBIN and ESTRIN [1992] treated the Portevin–Le Chatelier effect, considering several experimental systems: Cu–Mn, Al–Mg, Cu–Zn and Au–Cu, and obtained a good description of the experimental data, based on a well justified physical model, the mathematics were oversimplified. As GLAZOV has pointed out [1995], the model did not satisfy the important requirement of stability of non-linear stress serrations with respect to small perturbations in the initial conditions. It will take some time to debug the method.

So far, the reaction-plus-diffusion approach to dislocation patterning in cyclic deformation has been pioneered by Walgraef and Aifantis (WALGRAEF and AIFANTIS [1985]; AIFANTIS [1986]), and has been complemented by numerical simulations of the solutions of the model equations (SCHILLER and WALGRAEF [1988]). The set of non-linear governing equations proposed has no *direct* connection to dislocation behavior, but must be interpreted liberally with respect to the overall population behavior.

For the investigation of fatigue patterning, two populations of dislocations are considered: the mobile and immobile dislocation densities. The latter, which may of course be just temporarily immobile, are supposed to be those in loop patches, dipolar walls or other typical fatigue structures. Mobilities of widely differing values are ascribed to these two populations and the equations contain dislocation trapping and strain-dependent mobilization terms which govern the solutions of the system. Through appropriate choice of the dislocation mobilities (by trial and error), very realistic descriptions of PSB wall formation have been reported by SCHILLER and WALGRAEF [1988]. GLAZOV and LAIRD [1995a], by using different initial conditions, have displayed yet other properties of PSB walls and the effects of dimensional limits, noted in the previous section. In the opinion of the present writer, the method offers much promise. It is ideal for handling instabilities such as Neumann bursts, treated by SCHILLER [1989] and complex problems involving many factors such as commonly encountered in fatigue. GLAZOV [1995] has recently applied the method to Lorenzo–Laird bursts in cyclic creep, and Yan–Hong–Laird strain avalanches which show up within a single cycle. His model successfully reproduces stress serrations in terms of the underlying dislocation mechanisms and thus establishes a fundamental link between the micro- and macromechanics of cyclic deformation.

References: p. 2391.

5. *Fatigue crack initiation in ductile metals*

The initiation of fatigue cracks is defined by the determination of the investigator, and the precision and resolution of the technique used to find them. A mechanical engineer may either regard them as an inevitable development of the manufacturing process consisting of flaws which simply grow during subsequent service, or view them at the scale of ~ 1 mm on the basis of performance in non-destructive evaluation. A materials scientist defines them in terms of a failure mechanism associated with a microstructural feature, such as a PSB, a grain boundary, non-metallic inclusion or other kind of stress concentrator or strain localiser. Even in smooth specimens, it is widely accepted that fatigue cracks initiate early in the fatigue life, earlier in pure metals than in commercial metals; however, the earliest point of crack detection seems to depend strongly on the skill of the investigator. The pennant in this respect seems to be shared by M. Henry of GE (private communication) and Fine and his co-workers (KIM, CHUNG and FINE [1987]; KWON, WEERTMAN and FINE [1987]).

As noted in the introduction, where design philosophies were outlined, the emphasis on fatigue crack initiation varies widely. Our understanding, in quantitative terms, of fatigue crack initiation remains poor partly because investigative techniques and ideas are limited.

The present section deals with models for fatigue crack initiation and their dependence on dislocation structure (and thus strain amplitude) and microstructure, on the assumption that the specimen contains no gross strain concentrator, and the initiation mechanisms arise purely from the deformation processes of the metal. In actual structures, the hope is to keep fatigue stresses at low levels generally, and this usually causes fatigue to occur (if it does) at stress concentrators. In principle, there is no reason why crack initiation at a stress concentration should be different from that on a smooth specimen cycled at a stress equivalent to that in the stress concentration.

5.1. Fatigue crack initiation and surface roughness: the phenomena

In order for fatigue cracks to nucleate at all, the applied stress or strain in a fatigued specimen must be above the fatigue limit, or at some time in its life have been above. When these conditions are satisfied, PSBs form and intensify. Cracks ultimately form at the surface both in the PSBs and at other regions, such as twin or grain boundaries, on which the PSBs impinge. Usually, the cracks are associated with localized strain and its interaction with the microstructure. In the absence of a sub-surface flaw which can provide a site for crack initiation, the free surface is the preferred site for crack initiation.

Cracks will initiate in PSBs or other regions of localized strain (say a narrow twin which has a more favorable Schmid factor than its host grain, and essentially becomes a PSB in itself) as long as the straining conditions satisfy the conditions for localized strain, namely, corresponding to the plateau region of the cyclic stress–strain curve for single crystals, or the deformation equivalent for polycrystals. If the stress or strain is high enough to homogenise the deformation in which case the dislocation structure will consist of cells, either locally near grain boundaries or more generally throughout the

structure, then cracks initiate at the grain boundaries instead. These comments particularly refer to metals of wavy slip character. In single phase alloys of planar slip mode, PSBs (or their planar equivalents, PLBs), are the preferred sites of crack nucleation both at low and high amplitudes (LAIRD and FELTNER [1967]). The mechanisms of crack initiation have been repeatedly reviewed (THOMPSON and WADSWORTH [1958]; LAIRD and DUQUETTE [1972]; BROWN [1977]; KOCANDA [1978]; FINE and RITCHIE [1979]; KLESNIL and LUKÁŠ [1980]; SURESH [1991]).

The phenomena associated with crack initiation in PSBs are as follows:

1) PSBs initiate, localise the strain within them and start to protrude. This happens early in life, and the typical appearance of the PSBs at this stage is shown in fig. 17c. A *protrusion* is a surface uplift, several micrometers in height, usually occupying the width of a micro-PSB, like those in fig. 17c, and distinct from an *extrusion* which is narrower, more pointed and deserves more detailed treatment. Often, a wide PSB and its associated protrusion may contain several *intrusions* and extrusions, but these features generally occur somewhat later in life. An example of a macro-PSB in this condition is shown in fig. 44. Note that the crystal had been given 120,000 cycles when the SEM photograph was recorded, a large fraction of life.

2) After 5 to 10% of life has been expended, numerous small cracks (fissures) can be found within the PSBs, and the cracks can be considered to have initiated. Typical evidence for this behavior is shown in fig. 45, comprising an SEM photograph of a

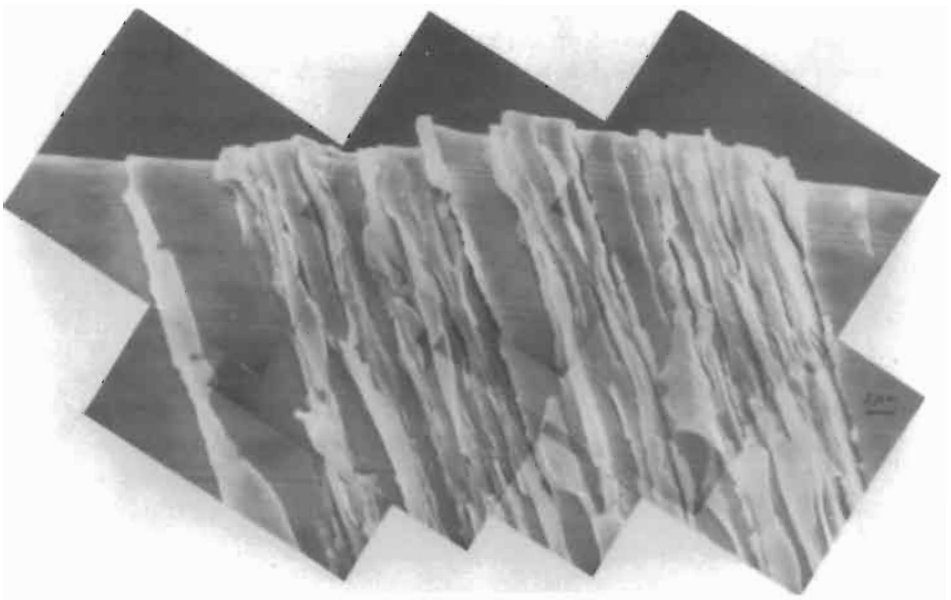

Fig. 44. A macro-PSB in a copper single crystal, oriented for single slip, fatigued at room temperature for 120,000 cycles at a plastic shear strain amplitude of 2×10^{-3}. The macro-PSB consists of many micro-PSBs, separated by regions of matrix structure (loop patches.) There are numerous extrusions and intrusions superimposed on an overall protrusion. Taken from MA and LAIRD [1989b].

References: p. 2391.

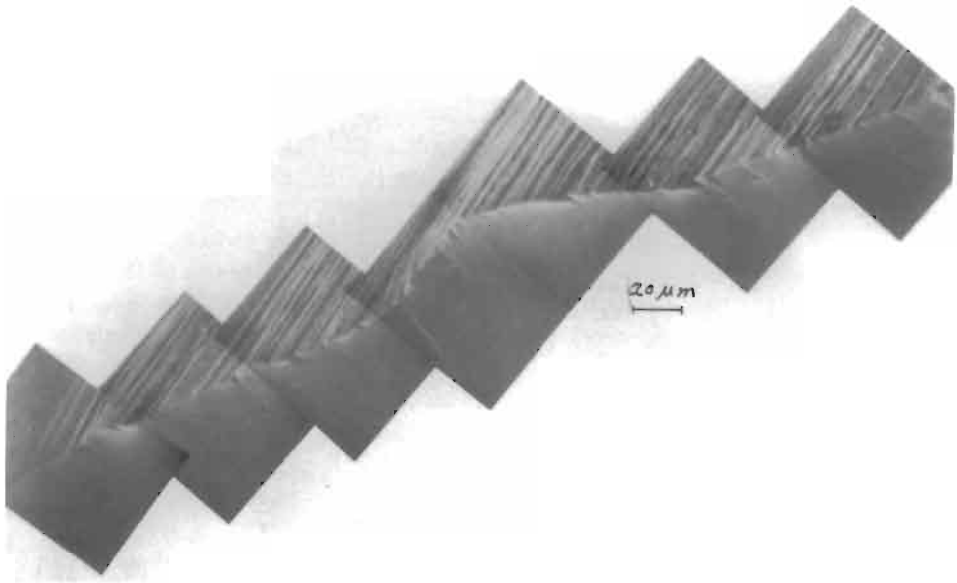

Fig. 45. Numerous Stage I cracks visible in a "sharp-corner" section. Copper single crystal cycled at a shear strain amplitude of 2×10^{-3} for 30,000 cycles. Courtesy of MA [1987].

single crystal prepared by the "sharp corner" technique. This technique is employed on specimens of square cross-section, in which the cracks tend to initiate preferentially along the corners of the gauge section. After cycling, the surface appearance is as shown in fig. 44. Since the extrusions fold over the surface, they hide the cracks and it is not possible to observe how deep the cracks are. The cracks can be revealed and their depths measured by carefully removing a thin layer from the side surface of the specimen and polishing that surface without affecting the cracks, a difficult art which reveals the cracks in a 90° section. In early work, a *taper section* might be employed to "magnify" the cracks geometrically, but given the high resolution of the SEM, taper sections seem obsolete, except perhaps for special purposes. The sharp corner technique was developed by BASINSKI and BASINSKI [1984] and a description of it can be found in MA [1988].

3) The morphology of extrusions is shown in fig. 46. Some workers, including the present writer, view them as thin tongues of metal, schematically indicated in fig. 46a. Others, such as SURESH [1991] report them as having a triangular cross-section (base width ≈ 1–2 μm, height 2–3 μm); no doubt, a great variety of shapes and sizes has been observed (see LAIRD and DUQUETTE [1972]). Extrusions grow at high rates, 1–10 nm/cycle, whereas the growth rate of the kind of protrusions shown in fig. 17c is an order of magnitude slower. The overall protrusion visible in the macro-PSB shown in fig. 44 is connected, at least in part, with shearing of micro-PSBs and the "sliding" of the matrix slabs between. The kinetics of such behavior are rather "stochastic", and the overall protrusion height tends to scale with the width of the PSB. It is necessary to have a different nomenclature for this type of protrusion, to distinguish it from that shown in

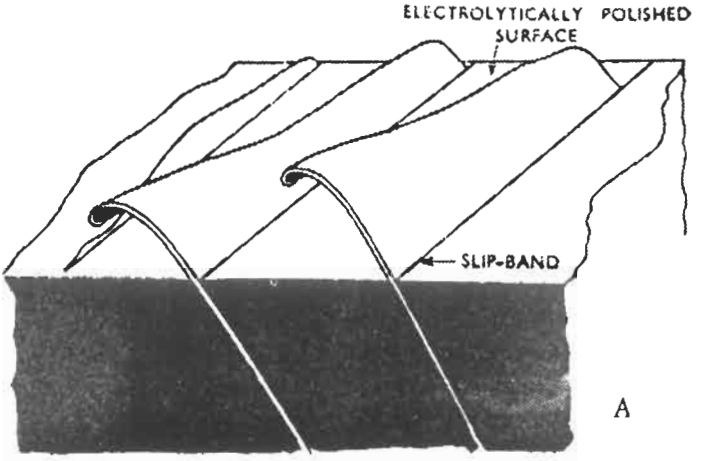

(a)

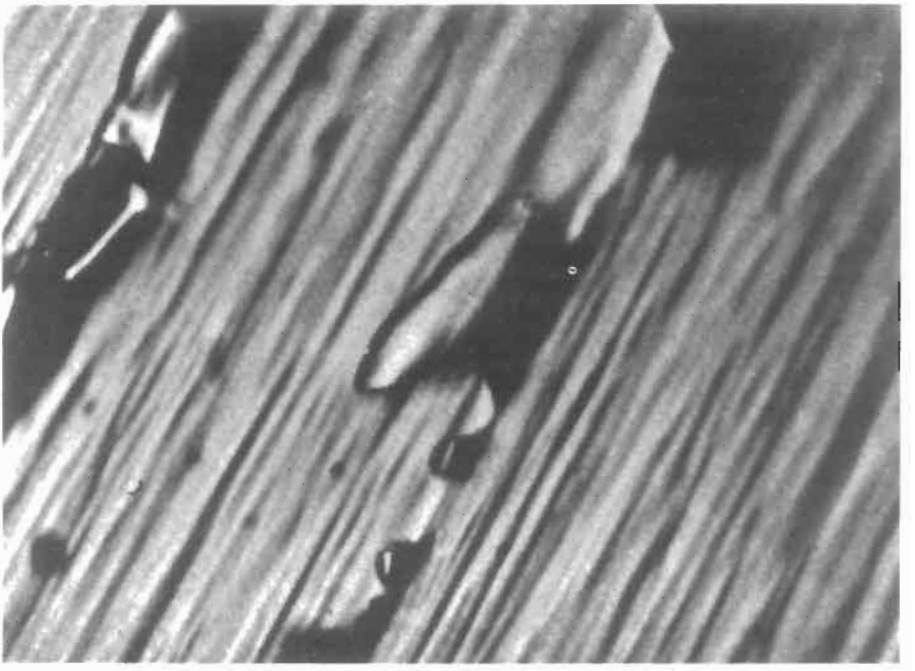

(b)

Fig. 46. (a) Schematic representation of a slip-band, or micro-PSB, extrusion. (b) Actual PSB extrusions in aged Al–Cu alloy fatigued at low strain. The magnification can be gauged from the height of the largest extrusion, about 10 μm. Courtesy of FORSYTH [1956].

fig. 17c, for which "protrusion" should be retained, but the archival literature contains no such distinction. The writer offers: "*bulging*". Such bulging would be associated with a

net inward displacement on the opposite side of the single crystal. The term "*encroachment*" has been employed by MA and LAIRD [1989b] to label such a phenomenon.

4) The strain localized within groups of PSBs is macroscopically reversible, in that the local strain at the tensile maximum is identical to that at the compressive maximum, at least within the time interval of several cycles or even hundreds of cycles. Clearly it cannot be reversible all the time, or bulging and encroachments would not occur. Moreover, the local strain within a micro-PSB appears to increase linearly with the overall strain (FINNEY and LAIRD [1975]) during a typical straining excursion, and reverses with the cycling of the strain, again for most of the time. The evidence shown in fig. 17b indicates that micro-PSBs do not deform wholly reversibly all of the time. There is an interplay and re-division of strain between the micro-PSBs. At the finest distribution of slip within a PSB, the deformation is definitely not strictly reversible. Good evidence for this behavior can be seen in fig. 47, where a slight roughening is associated with the action of several cycles, although the slip offsets continue to be mechanically reversible over a whole PSB.

This roughening evidence indicates that lamellae defined by the atomistic slip within the PSBs undergo constrained slip in the direction of the primary Burgers vector, and produce notch-peak topology by the micro-irreversibility of the slip. This roughness will be superimposed on the protrusion and the initial stages of it can be seen in fig. 17c.

5) As noted in the previous chapter, optical interferometry indicates that a greater than average local strain develops at (or near) the PSB-matrix interface. This "double" localization of slip increases the kinetics of crack initiation at the PSB-matrix interface. Counts of crack nuclei reported by NEUMANN and TÖNNESSEN [1987] indicate that cracks located at the PSB-matrix interfaces outnumber all the others by about 6:1. Bear in mind that this result applies to copper crystals in which the ramp-loading method of starting the test had been used, and the results could be skewed by the test method. However, even in crystals cycled in constant amplitude, cracks occur frequently at the PSB-matrix interfaces. A typical example of such behavior can be seen in the "sharp corner" section shown in fig. 48. Note the protrusion containing minor cracks, a leading crack on the acute angle side of the PSB and a lesser crack on the obtuse angle side. These cracks are parallel to the primary slip plane and as such belong to a class of short cracks termed *Stage I cracks* because they propagate at 45° to the tensile axis and are strongly influenced by the shear stress, as found decades ago by GOUGH [1933].

6) The fatigue crack initiation behavior in planar slip metals, which form PLBs rather than PSBs, is different from that in wavy slip metals. Since the localized strain does not persist, but moves around the guage section, the fatigue life increases, at least in Cu–16 at% Al (HONG and LAIRD [1991a]), as compared to that in copper. In association with the uniform slip distribution, a very uniform hill and valley surface morphology develops on Cu–Al crystals with continued cycling. This morphology, which is shown in fig. 49, is related to strain burst behavior (HONG and LAIRD [1990c]), because it develops when bursts are active. The hill and valley morphology is seen in fig. 49 side-on in a square sectioned specimen so that the profile can be observed directly. The crystal was oriented with the primary Burgers vector parallel to the side facing the photographer in fig. 49, and the morphology forms on the face at which the slip steps emerge. The wavelength

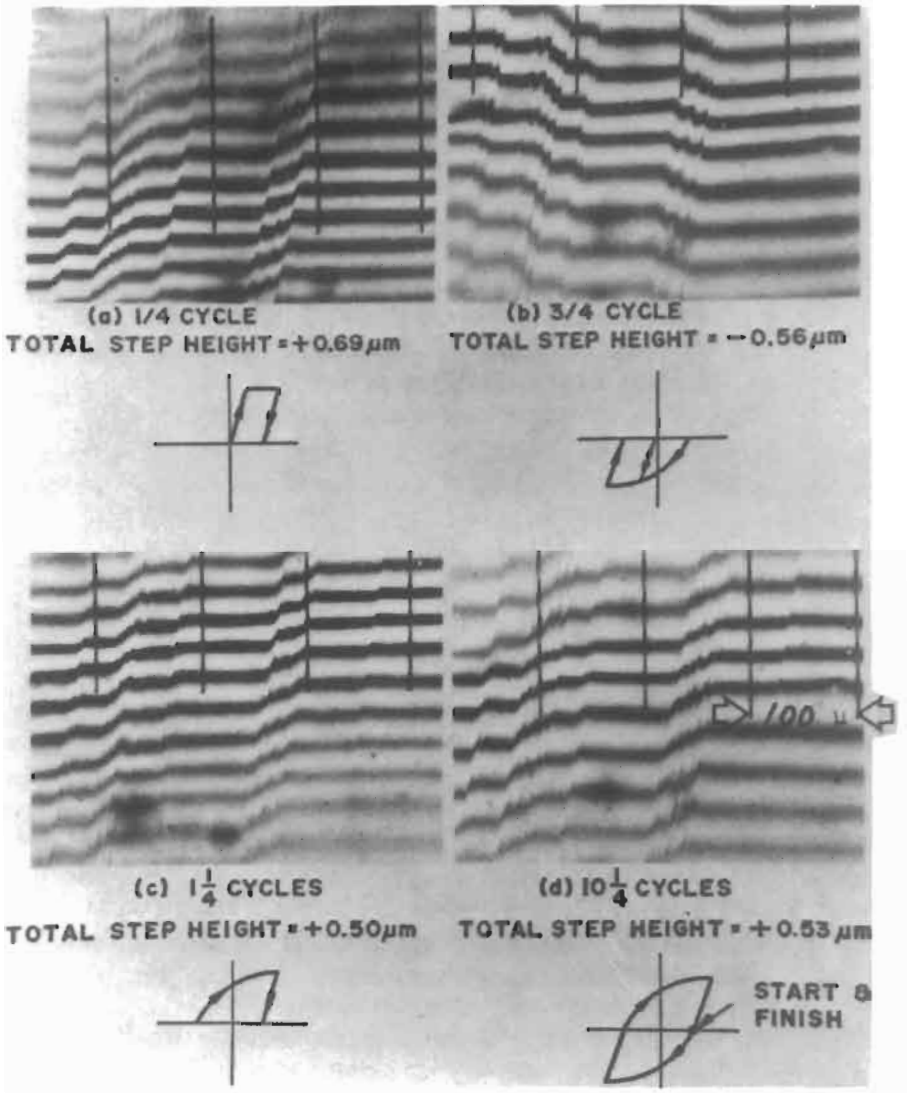

Fig. 47. Straining behavior of micro-PSBs revealed by interferograms, in a copper single crystal cycled at a plastic shear strain amplitude of 0.0025 for 2750 cycles, repolished, and subjected to the strain increments shown in the schematic segments of hysteresis loops. Note from the offsets that the strain is consistently reversible from tension to compression and cycle to cycle through a whole micro-PSB, but roughening occurs from the atomistic slip within a PSB. Taken from FINNEY and LAIRD [1975].

of the morphology increases with strain amplitude because the strain bursts are larger in the early stages of life (HONG and LAIRD [1990c]). When the bursts die out, as they do later in life, the morphology stabilizes (compare (a) and (b) in fig. 49). The development of the protrusions observed in copper does not occur in Cu–16 at% Al single crystals but

References: p. 2391.

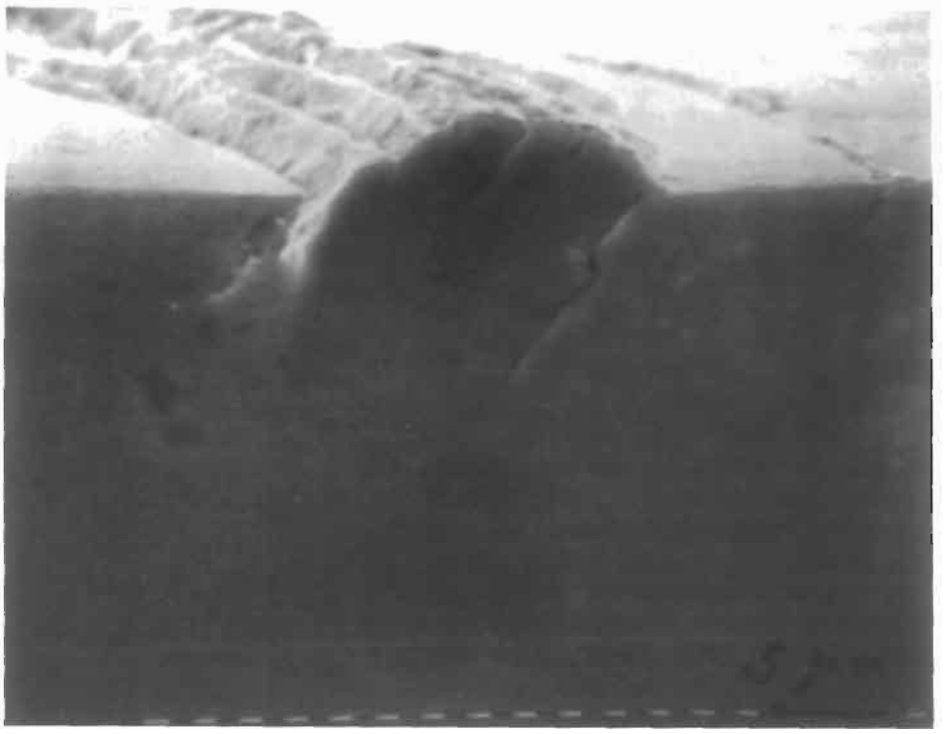

Fig. 48. Fatigue crack initiation in PSB for a copper single crystal fatigued for 60,000 cycles at a plastic shear strain amplitude of 2×10^{-3} at room temperature, showing preferred initiation at the PSB matrix interfaces. Taken from MA and LAIRD [1989b].

(a)

(b)

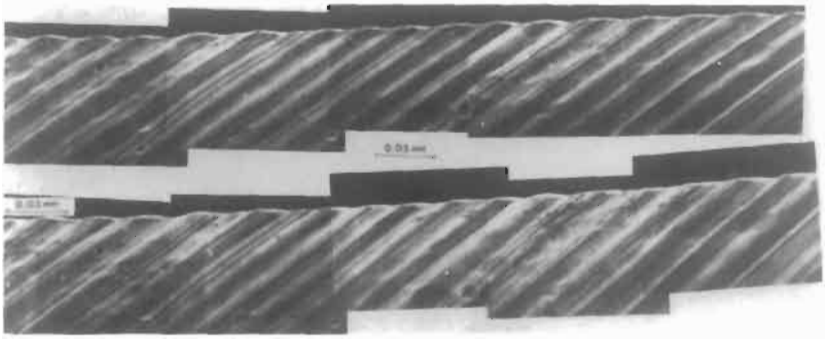

Fig. 49. The uniform hill and valley surface morphology observed on Cu–Al single crystals oriented for single slip, fatigued at room temperature. Subject crystal cycled at an (average) plastic shear strain amplitude of 4.9×10^{-3} for (a) 16,500 cycles; (b) 37,200 cycles. No significant changes occurred between (a) and (b). Taken from HONG and LAIRD [1990c].

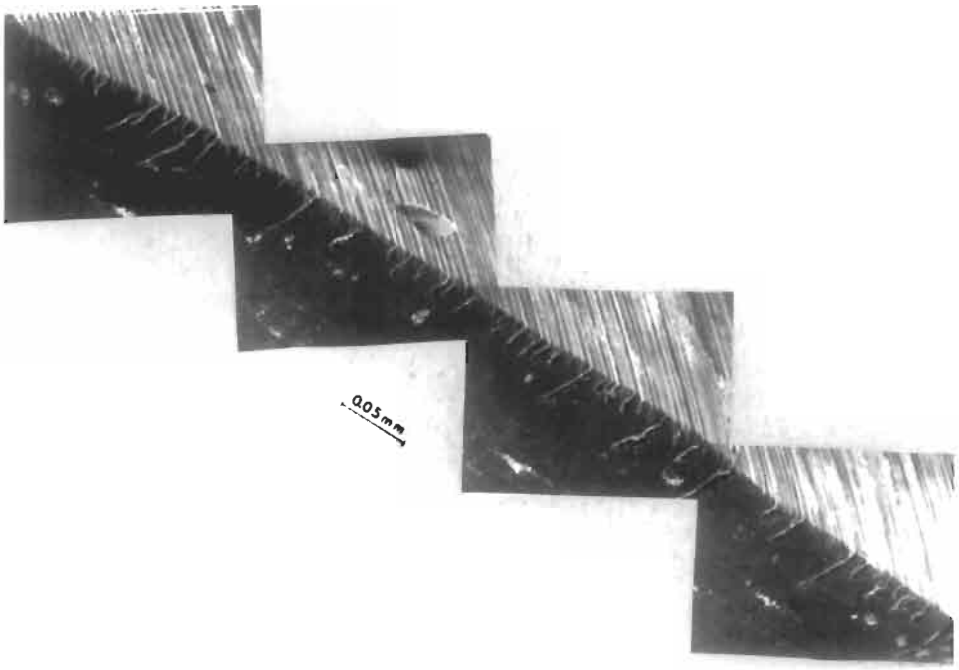

Fig. 50. Typical view of Stage I cracks in a single crystal of Cu–16 at% Al alloy, prepared by the sharp corner technique, cycled for 500 K cycles at a plastic shear strain amplitude of 1.4×10^{-3}. Courtesy of HONG [1989].

extrusions are seen in polycrystals. In the closing stages of life, numerous cracks initiate in the valleys of the surface morphology (see fig. 50) and propagate rapidly because the stress amplitude is high, on account of the long-drawn-out and pronounced cyclic hardening, HONG and LAIRD [1991a].

5.2. Fatigue crack initiation in persistent slip bands — mechanisms

The origin of fatigue cracks in metals and alloys of high purity is often rationalized by mechanisms of the type championed by WOOD [1958]. The basic premise of the mechanism is that repeated cycling of the material leads to different amounts of net slip on different atomistic glide planes, of the type shown in the interferograms of fig. 47. The irreversibility of shear displacements along the slip bands then results in roughening of the surface of the material and the gradual development of the roughening into notch-peak morphology. The valleys in the morphology function as micro-notches and the effect of stress concentration at the root of the valleys promotes additional slip. This step is likely to be more intense in tension than in compression because the micro-notches can close in compression and defocus the stress concentration, further enhancing slip irreversibility. Thus fatigue cracks initiate. In 1972, the bulk of the evidence favored this mechanism (LAIRD and DUQUETTE [1972]) and, in the opinion of the present writer, it does so today.

References: p. 2391.

A quantitative statistical model for random slip leading to the formation of hills and valleys on the surfaces of fatigued metals was published by MAY [1960a,b]. May initially offered the model to explain the Coffin–Manson law, with the implicit assumption that the model applied to high strain fatigue, which it does not, because cracks form by a different mechanism at grain boundaries. ROSENBLOOM and LAIRD [1993], who studied slip irreversibility in single crystals very early in life with special respect to crack initiation, have applied May's model to PSB behavior and find it to give reasonable predictions of the cycles required to initiate cracks in PSBs of copper. The observations of these authors also cast doubt on some of the details of the surface roughening model of ESSMANN *et al.* [1981], who base their model on dislocation irreversibility judged from intra-bulk behavior of PSBs, not of PSBs where they intersect the surface (MUGHRABI, WANG, DIFFERT and ESSMANN [1983]).

The mechanisms of crack initiation by slip irreversibility, as they relate to the variations in localized strain from one PSB to another, have been explored by CHENG and LAIRD [1981c]. By repolishing, re-straining and interferometric observations on one side of a fatigued single crystal, and observations of cracking in the same PSBs on the opposite (unpolished) side of the crystal, these authors have documented the properties of the PSBs in which the crack nucleates. As noted in the previous chapter, for copper single crystals subject to an applied strain in the plateau of the cyclic stress–strain curve, there will be a certain distribution of strains localized in the PSBs, and not a constant strain equivalent to that of the upper end of the plateau. The crack nucleates in the "fatal band" which contains the highest localized strain (CHENG and LAIRD [1981c]). It is found that the length of the slip offset in a fatal band (nb, i.e., n Burgers vectors) and the applied plastic shear strain amplitude, γ_p, are related as $\gamma_p = C(nb)^{0.78}$, where C is a constant (CHENG and LAIRD [1981c]). The orientation of the crystal is found to affect only the step height, the volume fraction of the PSBs only slightly, and the slip offsets not at all within some scatter. It is the magnitude of the slip offset which controls the crack nucleation behavior if the cyclic stress is uniaxial, and thus there is no effect of orientation on the cycles to nucleate a crack, assuming of course the wide range of orientation within the standard triangle over which the slip remains single. Multi-slip orientations have not been explored in this connection.

There are many competing models for crack initiation. When the thin type of extrusion was first reported in the 1950s (FORSYTH [1953]), it caused great excitement in the context of initiation. It was soon discovered to exist in all sorts of ductile materials including silver chloride (FORSYTH [1957]), and in all kinds of metals and microstructural features, including twin boundaries and grain boundaries (see LAIRD and DUQUETTE [1972], for details), which should have given a useful hint for the mechanism of extrusion formation. Most significantly, the formation of an intrusion-extrusion pair (meaning an extrusion was observed in conjunction with a small crack) was identified by FORSYTH and STUBBINGTON [1955] and by COTTRELL and HULL [1957]. Many distinguished investigators have offered ingenious explanations for the formation of extrusions and of extrusion-intrusion pairs in terms of dislocation behavior. But it turns out that the thin extrusion has been something of a red herring. DICKSON, BAÏLON, XIA and BUREAU [1993] have presented the most convincing argument that extrusions come after the fact

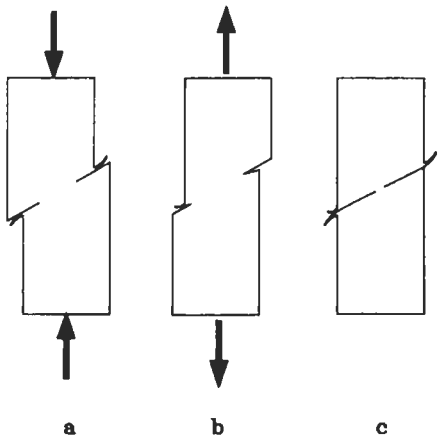

Fig. 51. The mechanism of extrusion formation offered by DICKSON, BAILON, XIA and BUREAU [1993]: the extrusion is formed by a rubbing-cum-burring process at the mouth of a pre-existing small crack. Courtesy of the authors.

of initiation rather than before. Their mechanism for the formation of intrusions in the presence of a small crack is shown schematically for a single crystal in fig. 51. Consider that a specimen contains a small stage I crack. During the compression portion of the cycle, fig. 51a, the extrusion is produced by a rubbing/burring process on the crack face which subtends an obtuse angle with the specimen surface. The fracture surface rubbing also tends to push the extrusions away from the crack. During the tensile part of the cycle (or possibly the load-increasing part), an extrusion can form on the other face, if there is sufficient local closure to produce the required fracture surface rubbing (fig. 51b). The net effect is that more numerous and larger extrusions are formed on the crack faces subtending an obtuse angle with the surface. This mechanism appears to explain all the facts of extrusions known to the present writer, for example, the rapidity of their formation, their ability to form in conjunction with grain boundary cracks, their formation at soldered joints oriented at 45° to the stress axis, and their formation under a wide variety of testing conditions. In the context of crack initiation, let us bury the extrusion with honour.

Another group of mechanisms consists of vacancy-dipole models. There is no evidence known to the writer in which point defects directly contribute to crack initiation at low temperatures, including room temperature. It does appear reasonable however, to suppose that vacancy clusters produced by cyclic deformation are responsible for the swelling of the material which produces protrusions, and which can therefore contribute to roughness (see SURESH [1991] for more details on vacancy models).

Micromechanical models have been proposed to describe intrusion and extrusion formation due to glide on parallel planes, but with more systematic selection of slip in tension and compression than applies to random slip models (LIN and ITO [1969]; LIU and LIN [1979]). In bcc systems, where slip in tension and compression can occur on different types of slip plane, it is possible that this type of model, suitably modified, may

operate. Other models that have been proposed, e.g., those by TANAKA and MURA [1981] or by VENKATARAMAN *et al.* [1990], depend on some kind of storage of elastic energy to initiate cracks. These models violate the LEDS or SODS (*self-organized dislocation structures*, GLAZOV and LAIRD [1995b]) principles of cyclic deformation. Fatigue processes are well known to reduce the elastic energy level, not increase it.

In commercial metals, many of the considerations described above apply to the crack initiation behavior. For example, in aluminum alloys containing shearable precipitates, PSBs may well occur and behave similarly in principle to PSBs in pure copper. If the microstructure is such that the strain is homogenized, e.g., when the precipitates are large and impenetrable, then most likely grain boundary initiation will occur. In hard metals containing non-metallic inclusions, cracks initiate at the inclusions either from a stress concentration effect or from a property of the inclusion or its interface with the matrix (see STARKE and LÜTJERING [1979]), either of which may crack.

5.3. Grain-boundary crack initiation

At strain amplitudes greater than those needed to produce PSBs, dislocation dipolar walls or more complex cell structures are general throughout a specimen and the deformation is broadly homogeneous. Only in planar slip materials is the deformation sufficiently confined to bands to give rise to slip band cracking, as noted above. More usually, notches develop at grain boundaries and cracks form in them. The mechanisms of this cracking were explored by interferometric observations of cracking morphology at grain boundaries in conjunction with efforts to study the nature of the boundaries which acted as nucleation sites (KIM and LAIRD [1978a,c]). In fig. 52, white light interference fringes show the development of a grain boundary step. At the beginning of life a small step is formed in tension but it is cancelled by the compression stroke. With continued cycling, the amplitude of the boundary step increases and resists complete cancellation in compression. Eventually a step 1.5 μm high, having a sharp root radius, develops and the crack grows along the grain boundary into the material from this step (KIM and LAIRD [1978b,c]). A step can have nearly as high a stress concentration as a crack. However, a crack would need to start growing from the step to be considered initiated. Only a relatively small fraction of grain boundaries were observed to be susceptible to this mechanism of failure. The "vulnerable" boundaries were identified as those separating highly misoriented grains, the dominant slip systems of which were directed over large distances at the intersection of the boundary with the surface, as schematically shown in fig. 53. The ratcheting mechanism by which the step develops was attributed to cross-slip resulting from the presence of a boundary-induced stress gradient.

The grain boundary step mechanism of crack nucleation and the associated crystallographic requirements are not specific to pure metals, and thus the mechanism may be a general one, subject of course to modifications in complex commercial materials (STARKE and LÜTJERING [1979]; HODGSON [1968]; COFFIN and MCMAHON [1970]). The asymmetric slip of screw dislocations in tension and compression can lead to severe shape changes of bcc single crystals in fatigue as described above. Such changes will act to aggravate the formation of boundary steps and cracking. It has been shown on fatigued polycrystalline α-iron

specimens (MUGHRABI [1975, 1977]) that near surface grains do suffer shape changes similar to those in single crystals and cause surface roughness leading to crack nucleation.

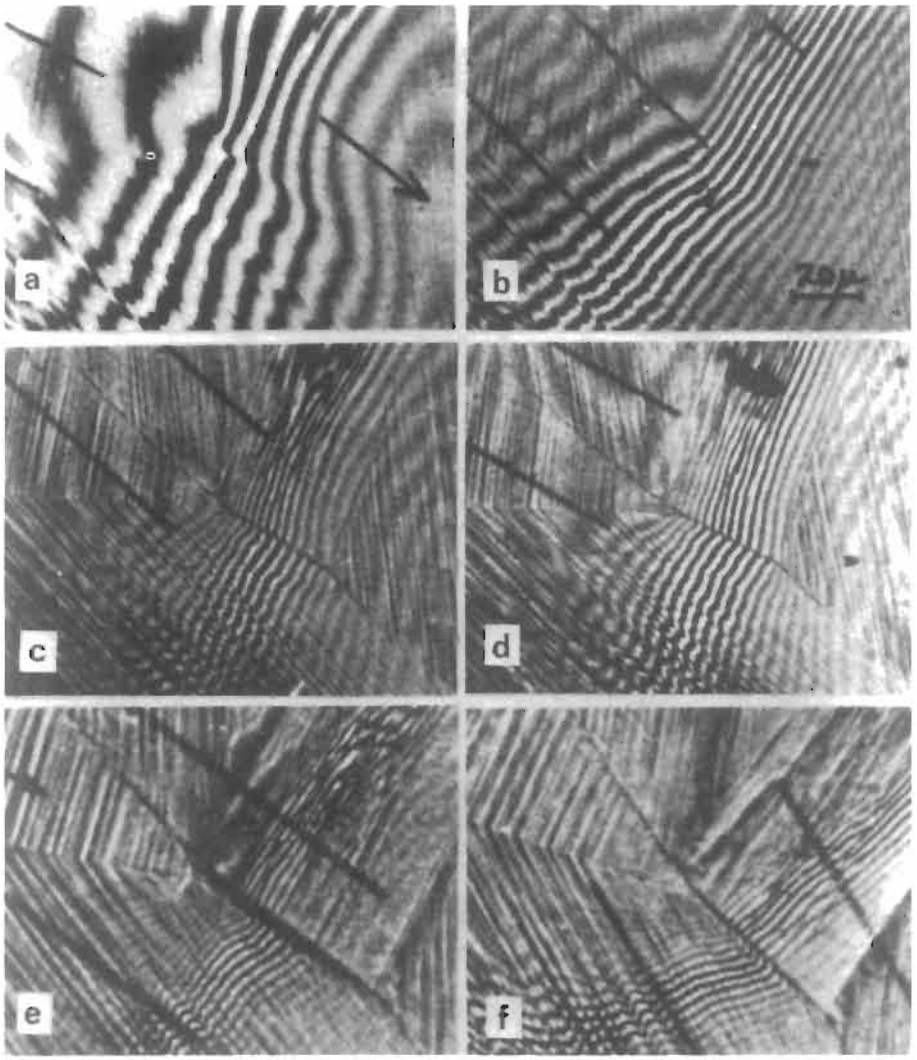

Fig. 52. White light interferograms all from the same area of the polycrystal specimen, showing grain boundary step growth in copper, cycled at a plastic strain of ± 0.0076. Fringes shifted from left to right indicate depressions: (a) 10 cycles, tension; a small step of 0.1 μm is observed; (b) 10 cycles, compression, this step is canceled. (c) 30 cycles, tension, step height ~0.4 μm; (d) 30 cycles, compression, step partly canceled, 0.15 μm. (e) 60 cycles, tension, step height ~0.9 μm; (f) 60 cycles, compression, step partly canceled. Taken from KIM and LAIRD [1978b].

References: p. 2391.

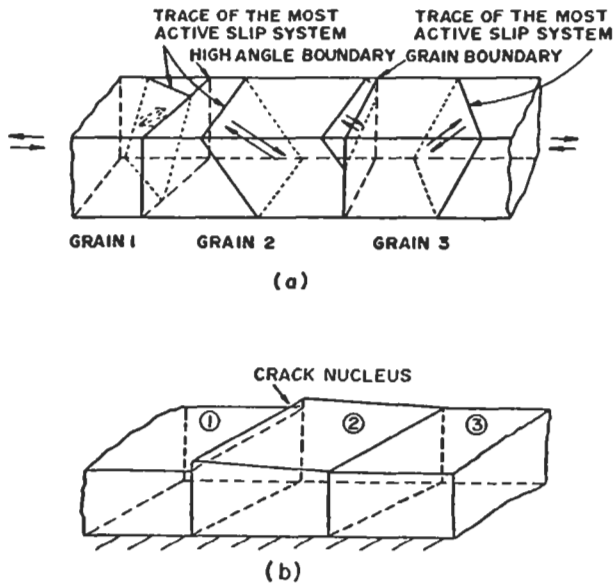

Fig. 53. Schematic representation of the crack nucleation process in high strain fatigue. (a) The active slip systems in either grains 1 or 2, or in both of them, are directed at their boundary. (b) After cycling, a step forms at the boundary between grains 1 and 2, but not 2 and 3. Courtesy of KIM and LAIRD [1978c].

5.4. Environmental effects on crack initiation

It is well known that low-strain fatigue lives can be prolonged by an order of magnitude by fatiguing *in vacuo* or in an inert environment (GOUGH and SOPWITH [1932]; THOMPSON, WADSWORTH and LOUAT [1956]). The increase of fatigue life which occurs at low temperatures arises partly from the increase of strength associated with the temperature change and partly from the immersion in liquid nitrogen or helium used to obtain the low temperature (LAIRD and KRAUSE [1968]), which confers some environmental protection. The formation of PSBs, surface roughening and fatigue crack initiation can occur at low temperatures down to 4.2K (MCCAMMON and ROSENBERG [1957]), and many of the usual features, such as intrusions-extrusions, occur at low temperatures also (COTTRELL and HULL [1957]). The absence of water vapor and oxygen seems to be the important factor, and the effect of water vapor varies with the metal, probably depending on its sensitivity to hydrogen arising from the interaction between water vapor, hydrogen and oxygen.

The discussion here is mainly focused on gaseous environments because there is insufficient space to deal with the widely complex phenomena associated with liquid environments. However, if the electrochemical reactions are controlled to be benign for aqueous environments, e.g., a cathodic bias for copper in a weak acid, or neutral solution, then the aqueous environment is no more damaging than common laboratory air

(LI *et al.* [1993]; ORTNER *et al.* [1987]; YAN *et al.* [1985]. See MAGNIN [1993] for a review of corrosion fatigue.

At really high strains, aggressive gaseous environments have little effect on fatigue life or on crack initiation and propagation (LAIRD and SMITH [1963]) because the associated deformation events are too gross to be much affected by the environment. A really aggressive liquid environment will have an effect, even at short lives (LAIRD [1962]). As the lives lengthen with reduction of applied stress or strain, the effect of the environment in prolonging life becomes more pronounced, but this probably involves a more marked effect on propagation kinetics than on crack initiation.

When lives are strongly prolonged in long life fatigue by testing *in vacuo*, the effect of the environment on crack initiation is not really clear. There definitely is a large effect in delaying the growth kinetics of short Stage I cracks, and the early workers (e.g., THOMPSON, WADSWORTH and LOUAT [1956]) ascribed life prolongation to retardation of crack propagation. Since it is difficult anyway to discriminate crack initiation developing from roughness and the propagation of the small cracks growing from the fissures, determining the role of the environment in initiation is going to be difficult. WITMER *et al.* [1987a,b] made a very careful comparison of PSB morphology, using interferometry and SEM observations, in copper single crystals cycled in air and in vacuo, and could find no significant differences in the early stages of life.

The role of the environment in initiation must be connected with the surface roughening behavior. The localized strain in the PSBs produces slip steps, and their extent can be diminished by reverse slip during compressive loading (see fig. 17 and ROSENBLOOM [1990]). Irrespective of the environment, surface roughening during fatigue occurs primarily by a random slip mechanism. If an aggressive environment is present, chemisorption of the aggressive species (or the formation of an oxide film) on the freshly formed slip step makes reverse slip more difficult on the same slip plane upon load reversal. Thus the presence of an aggressive environment provides a mechanism of enhanced surface roughening as well as transport of the aggressive species into the near-surface volumes of the PSBs, thereby facilitating crack initiation. This mechanism is illustrated schematically in fig. 54.

Actually, there are more subtle effects of the environment on PSB behavior. If Stage I cracking in the PSBs is delayed by testing in vacuo, the PSBs have the opportunity to accumulate much more elapsed strain than in normal air-fatigue. WANG and MUGHRABI [1984] have shown that such PSBs undergo *secondary hardening*, meaning that their flow stress increases by a few MPa, and their dipolar walls change into dislocation cells. WITMER, FARRINGTON and LAIRD [1987], have shown by interferometric technique that these changes are associated with changes in the degree of localized strain: "old" PSBs carry only 3×10^{-3} instead of the higher strain they carried in their youth. If a test is conducted in strain control, this change calls for the creation of new PSBs to take up the difference. In order to develop more fatigue damage, the new PSBs must mature, initiate new cracks and then propagate them. This gradual percolation of localized strain causes an increase of life, and provides another reason why periodic removals of surface layers during life produce prolonged lives: they give the PSBs an opportunity to age.

References: p. 2391.

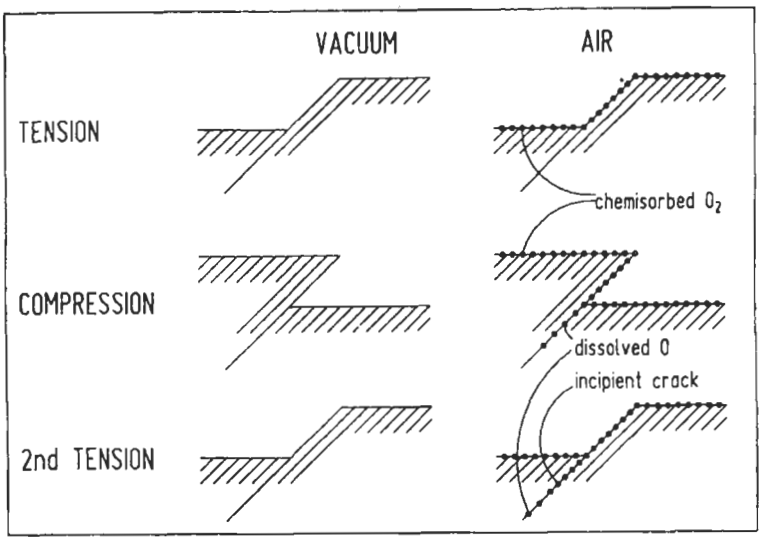

Fig. 54. The interaction of an aggressive species with freshly formed slip steps in fatigue, making reverse slip more difficult, entrapping the species in the material and hastening crack initiation and Stage I growth. (After THOMPSON, WADSWORTH and LOUAT [1956]; and NEUMANN [1983], Third Edition).

6. *Fatigue crack propagation*

6.1. Macroscopic behavior of fatigue crack propagation

The great bulk of research into crack propagation in the last thirty years (dating from the application of linear *elastic* fracture mechanics, LEFM, to crack propagation, which provided a rational basis for growth measurements) has been empirical with the aim of defining crack propagation rate as a function of the stress intensity. Propagation for long cracks, under variable loading, after overloads, in different environments, and for different modes of stressing has been explored in great detail. Studies of long crack growth (crack length greater than a few mm) often permit a direct comparison between the behaviors of large structures and small laboratory specimens via the elastic stress intensity factor, $\Delta K = Y\Delta\sigma\sqrt{\pi c}$, where c is the crack length, $\Delta\sigma$ the stress range and Y a crack length dependent parameter which also depends on the specimen configuration and stress state, provided the ΔK terms are the same in both cases. This similitude can only apply when the plastic region at the crack tip is small in relation to the length of the crack and the size of the structure. Generally, the small extent of the plasticity does not significantly perturb the elastic crack tip stress field in the laboratory specimen, thereby allowing direct use of laboratory results for predicting the behavior of large engineering structures, containing bigger defects, but where the stress intensity is similar because the operating stresses are lower. There are handbooks available providing LEFM solutions for a wide variety of structure and specimen geometries and stressing modes (e.g., Stress Intensity Factors Handbook, Two Volumes, Ed., Y. Murakami, Pergamon, Oxford

[1987]). It is not the purpose here to review the theoretical basis of this approach (see SURESH [1991]), or the great body of works in which it has been applied, nor the theories of crack propagation which have been spawned by its results (for example, the sustained investigations of WEERTMAN [1979], and subsequently), in spite of all their usefulness. The reader interested in such matters is referred to the many excellent publications of the American Society for Testing and Materials, the review of MILLER [1987], and the book by SURESH [1991], to cite a few. Rather the focus here will be on the basic phenomena and those aspects which give insight directly into the mechanism.

Fatigue crack propagation could not be covered entirely by the long crack approach however. Crack growth rates were sometimes recorded as being faster than LEFM analyses would predict, especially in the last ten to fifteen years when attempts were made to measure the growth kinetics of small cracks. Such cracks are typical of fatigue in smooth specimens and their growth behavior is life determining. The reasons for cracks growing faster or slower than LEFM would predict are manifold, but (chemical effects aside) generally are connected with a loss of similitude (DAVIDSON and LANKFORD [1984]) which occurs when stress levels are too high and general yielding occurs or when cracks are so small as to be affected strongly by small scale plasticity effects, such as PSBs, or by microstructural features. Consequently it is necessary to consider the behavior of short cracks.

A common method of presenting kinetic data on the crack propagation of long cracks is to plot the fatigue crack propagation rate, dc/dN, versus the stress intensity range, ΔK, on a log-log basis, as shown in fig. 55. Such a curve has become as familiar in the last two decades as the S–N curve. Three regimes of dc/dN are widely recognized: I) The

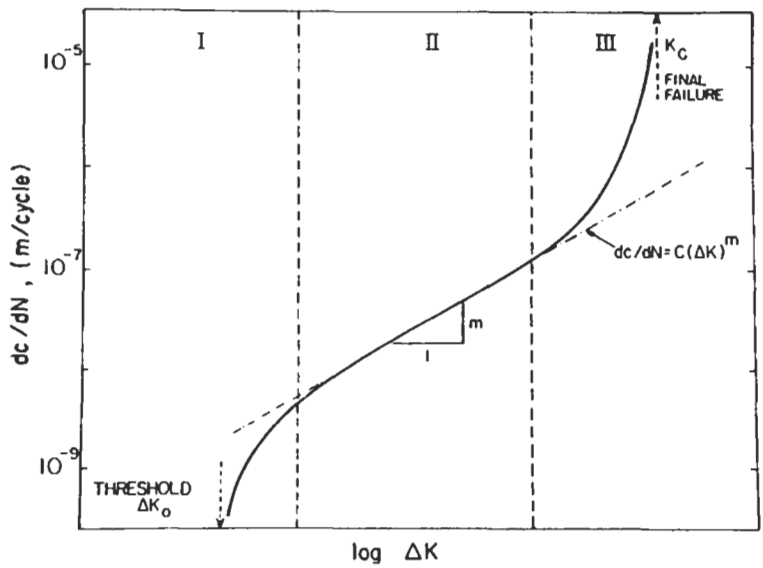

Fig. 55. Schematic plot of fatigue crack propagation rate dc/dn, versus stress intensity range, ΔK, depicting three regimes of crack propagation, I, II and III. (Courtesy of FINE [1980]).

References: p. 2391.

threshold region where the propagation rate is of the order of an atomic spacing per cycle or less. At low enough stress intensities (the "threshold") the crack can be considered immobile. II) A mid-region where the Paris equation $dc/dN = C(\Delta K)^m$, C and m being constants, is considered to hold. III) A high rate region in which the mechanisms of failure are of the static type and the maximum stress intensity approaches the critical stress for static failure. This region is one in which general yielding may occur, and the residual strength of a cracked member is of concern. Since it involves static failure mechanisms, it will not be treated here.

In regime I, where the stress intensity is low, a crack may typically develop along an active slip plane, like a stage I crack in a copper single crystal, and may involve PSB formation ahead of the crack. In this case the PSB is short compared to the length of the crack. Since the PSBs are formed on the most highly stressed slip plane (having the most favorable Schmid factor), the orientation of this crack is usually near 45° to the stress axis. To obtain a Stage I crack, the stress intensity must be low and such propagation is associated with regime I described above. However, it is noteworthy that many materials, including steels, do not propagate in the Stage I, 45° manner, and even cracks in copper, which normally propagate by Stage I in air, can be induced to propagate normal to the direction of stressing by enclosing the specimen in a vacuum (NEUMANN, VEHOFF and FUHLROTT [1977]). Note that the crack may stop growing altogether if the stress intensity is too low, and thus the threshold stress intensity, ΔK_o or ΔK_{th}, shown in fig. 55, is defined.

When a Stage I crack is propagating in a copper single crystal, the PSB hosting it may well go right through the crystal. Under these conditions LEFM will not apply and the plasticity of the specimen, for purposes of analyzing growth, must be taken into account by *elasto-plastic fracture mechanics* (*EPFM*). Such a crack may be considered a short crack, especially since the great part of the fatigue life of the crystal is taken up with the crack growing physically as a short crack (MA and LAIRD [1989b]).

In regime II, cracks usually propagate by a mechanism of plastic deformation which leaves characteristic fatigue striations on the fracture surface, provided the metal is a well-behaved ductile deformer and does not introduce another mechanism of failure such as intergranular fracture or a progressive brittle fracture. Fracture surface striations can, in some circumstances, be suppressed by testing in vacuum (LAIRD [1979]), but at high stresses, a ductile metal will form regular striations even in a good vacuum (LAIRD and SMITH [1963]).

KITAGAWA and TAKAHASHI [1976] compared high stress and low stress fatigue fracture behavior on a diagram similar to fig. 56a. The line given by ΔK_{th} represents the low-stress threshold condition below which a crack should not grow if LEFM assumptions are valid. They will be invalid of course, if the plastic zone at the crack tip is no longer small in relation to the size of the crack, and this occurs to an increasing extent when the term $\Delta\sigma$ increases above about two-thirds of the cyclic yield stress, or exceeds the threshold for PSB formation in a polycrystal, in a push-pull test, if that is the factor which determines the fatigue limit (it may not, the fatigue limit may be higher for some reason). The reader is aware that fatigue limits lie generally below the monotonic yield stress of commercial materials, but in a pure copper polycrystal, the fatigue limit may be

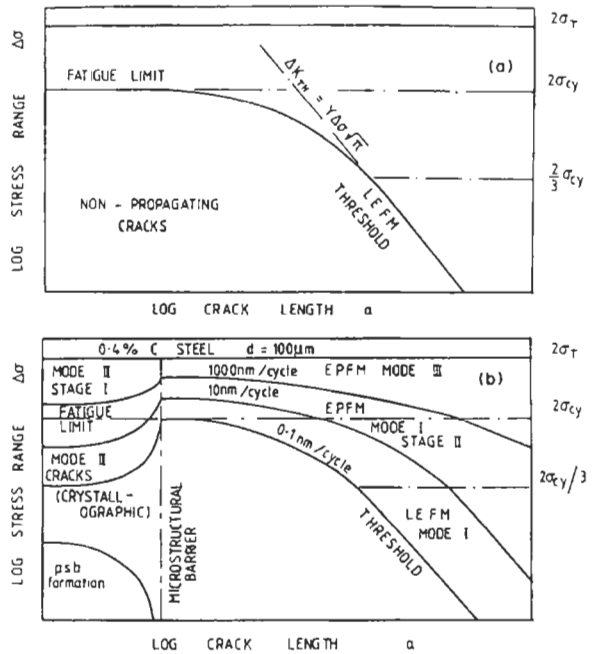

Fig. 56. Fatigue failure boundary maps: (a) the KITAGAWA–TAKAHASHI [1976] diagram and (b) the BROWN [1986] diagram with crack speed contours. Both plot the stress range versus the crack length. Courtesy of MILLER [1987].

several times the monotonic 0.2% flow-stress of a well-annealed copper. A second line of the Kitagawa–Takahashi plot is the fatigue limit itself, approximated to the cyclic yield stress range (MILLER [1987]). The lines for the fatigue limit, and the threshold stress intensity are then joined up by "rounding off the corner", to create a curve separating regions of stress-crack length space in which cracks do and do not propagate. The corner is rounded off because nature abhors corners, as any fatigue practitioner will agree.

Figure 56a was subsequently reanalyzed and extended by BROWN [1986] to the form shown in fig. 56b, to include contours of crack speed and fatigue fracture modes (Stages I and II). The *Modes* I to III shown on the diagram correspond not to the fatigue modes but to the fracture stressing modes shown in fig. 57. In many situations these modes may well operate in combination. For example, a thumb-nail Stage I crack growing in a PSB under push-pull stress will be subjected to Mode I by the uniaxial stress, Mode II in the direction of the primary Burgers vector at the front of the crack and by Mode III at the sides of the "nail". It is customary, in complex situations, to describe the mode according to the dominant one of the three. For example, the Stage I crack growing in a PSB would be described under Mode II.

Brown associated in fig. 56b the fatigue limit and the ΔK_{th} lines of fig. 56a with the

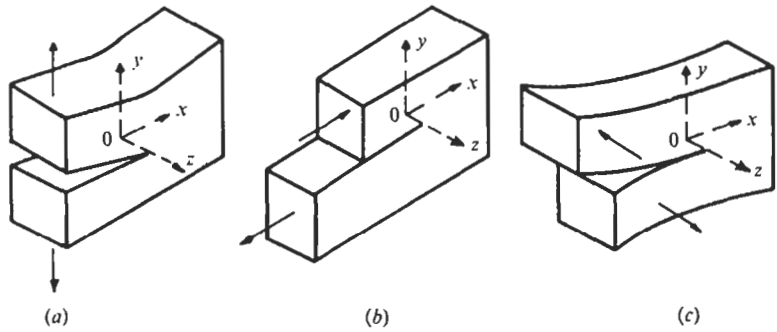

Fig. 57. The three basic modes of stressing a crack: (a) Tensile opening (Mode I); (b) in-plane sliding (Mode II) and (c) anti-plane shear (Mode III).

contour of ≈ zero crack growth rate. It will be noted, on the left of the diagram, that short cracks can initiate and grow at stresses greater than two-thirds of the cyclic yield stress. However, if a microstructural feature, such as a grain boundary or a patch of a second phase, provides a large barrier to growth, then the crack may stop growing, giving rise to the phenomenon of *non-propagating cracks*. Even at stresses above the fatigue limit, a short crack growing in a single grain can be retarded by a microstructural barrier but it will accelerate again once the barrier is overcome. On the other hand, it is evident from the Brown map, as MILLER [1987] points out, that cracks growing under conditions of LEFM only increase in speed as the crack length increases, assuming of course that the applied stress range is constant and the expression for ΔK given in fig. 56a applies. Variations in crack growth can come about for geometrical reasons — for example, a crack which has nucleated and grown in a stress-concentration may grow out of it and, entering a region where LEFM applies, become a non-propagating crack.

Typical results obtained under conditions of LEFM are shown in fig. 58, for the near-threshold region. Note that the threshold decreases as the tempering temperature decreases, i.e., as the monotonic yield and ultimate tensile stresses increase. It often happens in fracture, that a failure property improves as the toughness improves or as the ultimate tensile strength decreases, and this is another case in point. The behavior at high growth rates is also affected but not as severely as the threshold stress. The opposite kind of result has been observed by SUZUKI and MCEVILY [1979], who investigated specimens containing either martensite islands in a ferrite matrix or vice versa. The latter structure exhibited a significantly larger threshold stress intensity range, accompanied by a higher, and not a lower, yield stress, different from the behavior observed by RITCHIE [1977]. However, the strength levels of the two sets of steels were considerably different, and Ritchie's high strength steels are much more environmentally sensitive than the other steel. The complex interaction of many factors determines the threshold stress.

The above overview serves to establish the context of scientific interest in Stage I and II crack propagation. The phenomena and mechanisms of these fatigue fracture modes are described as follows:

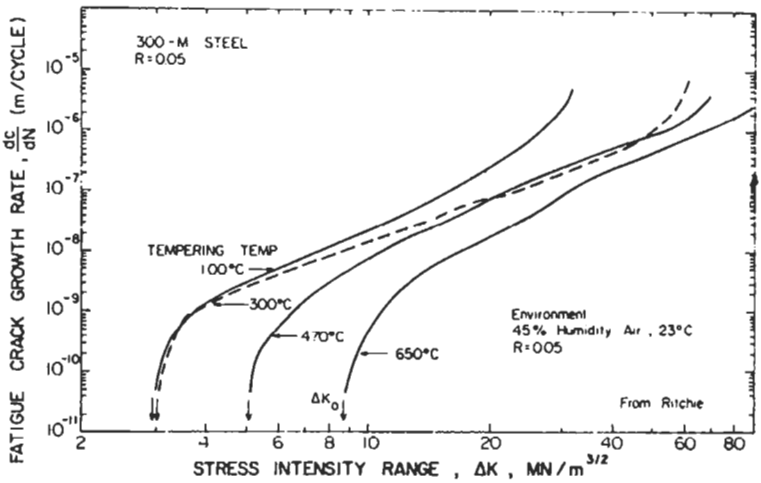

Fig. 58. Near threshold crack growth in 300-M steel (a Si-modified 4340 steel) tempered at various temperatures from 100 to 650°C, showing an increase in the threshold stress with decrease in monotonic strength. From RITCHIE [1977], via FINE [1980]. Courtesy of both authors.

6.2. Short crack growth — Stage I growth

Interest in research on short crack growth has grown enormously in the preceding ten years and there have been many investigations of growth behavior in both commercial and single metals (see RITCHIE and LANKFORD [1986]; MILLER and DE LOS RIOS [1986]; and the proceedings of the Triannual Fatigue conferences). Space does not allow treatment of the many interesting interactions that can occur between small cracks and microstructural features in complex materials. The focus here will be on simple metals in which the behavior is well-defined.

By delicate techniques of specimen preparation, TEM studies have been conducted on short Stage I cracks in pre-existing PSBs in copper (KATAGIRI, OMURA *et al.* [1977]). These studies show that cracks can penetrate to depths many times the inter-wall spacing of the PSBs without altering their dislocation structure significantly. Observations of this kind are not confined to pure metals but age-hardened alloys have been shown to propagate in this way (VOGEL, WILHELM and GEROLD [1980, 1981]; WILHELM, NAGESWARARAO and MEYER [1979]). Thus, a propagating Stage I crack conditions the metal in the PSB ahead of it and follows its path.

The implication of results of this type is that the PSB deformation processes, which act first to form notch-peak topography containing the crack embryo, now can lead to Stage I propagation. As noted in section 4, screw dislocations are the main agent for carrying strain in the PSBs of copper and they are distributed with roughly equal probability on all the slip planes within the PSB. A notch, i.e., a crack embryo, serves to concentrate slip in tension along a narrow group of slip planes at the base of the notch. That is, a stress concentration attracts the screw dislocations into the planes at the tip of

the notch, the dislocations cross-slipping from their regular planes to meet the notch. In compression, the notch closes, the stress concentration is not sensed, and the PSB screw dislocations return to the other end of their channel more equally distributed on the planes in the PSB. Repetition of such deformation causes crack intrusion, Stage I growth; the mechanism is illustrated schematically in fig. 59. The mechanism shown in fig. 59 was offered (LAIRD [1979]) before it was understood that (and why) narrow extrusions develop after the crack has formed, but this mechanism shows that extrusion formation accompanies the process of crack growth. It represents therefore a current mechanism of extrusion formation in terms of dislocation behavior.

MUGHRABI [1980] has offered helpful suggestions for explaining the absence of (or reduced tendency to) Stage I cracking in steels, and perhaps in other bcc metals. He cites the work on α-iron of KATAGIRI, AWATANI *et al.* [1979] who have observed dislocation cell structures at the tips of young cracks formed in a 45° mode, and points out that, in typical fatigue conditions, where the strain rates are quite fast, bcc transition metals do not usually deform by PSBs, since they deform by the low temperature mode of deformation. Clearly, a capacity for conventional Stage I growth is tied very closely with

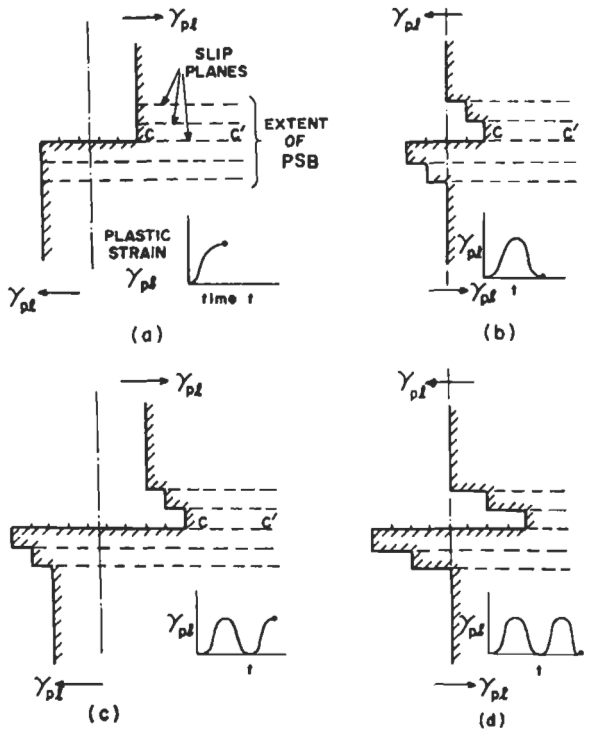

Fig. 59. Schematic representation of Stage I propagation in a PSB, via the deformation produced in a surface normal to the primary Burgers vector. A notch, omitted for clarity from (a), serves to concentrate the strain during tension in or near slip plane C–C′. During compression, (b) and (d), the strain is more evenly distributed on the atomistic slip planes, shown as dotted lines. The inserted γ_{pl} ν time plot indicates the loading sequence corresponding to the slip behavior. Taken from LAIRD [1979].

PSB formation. Also, the role of the environment, in limiting the reversibility of slip at the crack tip by a mechanism similar to that shown in fig. 54, will have important effects on the crack growth kinetics.

Because of the environmental problem, few workers have been bold enough to advance theories for Stage I growth. Of course, insofar as the mechanisms of Stage I and Stage II are common, any theory for Stage II growth which emphasizes plasticity mechanisms for growth should frequently apply to Stage I. PURUSHOTHAMAN and TIEN [1978] and TIEN and PURUSHOTHAMAN [1978] have treated Stage I growth by an interesting discontinuous growth mechanism analogous to ledge growth in phase transformations. There is experimental support for such a mechanism: STANZL [1980] investigated near-threshold growth for variously oriented copper single crystals and observed large variations in growth kinetics. She also observed that the fracture surfaces were not planar on a macroscopic scale and that the crack propagation direction changed frequently. Furthermore, SEM examination showed that the crack propagated along at least two planes. These effects in combination with step changes in growth kinetics (often observed as "scatter") are the hallmarks of a ledge mechanism. The interaction of Stage I cracks with multi-slip systems is still an unsolved problem in fatigue, even for wavy slip metals. The morphologies of Stage I faceted fracture surfaces for Cu–16 at% Al alloy single crystals have been reported by HONG and LAIRD [1991c]. Even in this planar slip metal, there are interesting effects of multi-slip on the fracture surface morphology.

The phenomena of Stage I growth in copper single crystals are now much better understood through application of the sharp corner technique (BASINSKI and BASINSKI [1984]; MA and LAIRD [1989b]) or its equivalent, precision sectioning through crystals containing Stage I cracks (NEUMANN and TÖNNESSEN [1987]; HUNSCHE and NEUMANN [1986]). The sharp corner technique has the unique advantage of permitting the population of Stage I cracks, or any one of them, to be studied during the whole fatigue life, whereas precision sectioning sacrifices the crystal, and growth behavior can then be treated only statistically.

The growth behavior goes much as follows: the cracks initiate fairly early in life, and a sizable population of them is established by 10,000 cycles, but they are still small at this stage. MA and LAIRD [1986] have documented the distributions of small crack sizes in fatigued copper single crystals and treated the statistical aspects of their competitive growth. Typical results for constant strain amplitude testing, for amplitudes embraced by the plateau of the cyclic stress strain curve, are shown in fig. 60 (MA and LAIRD [1989b]). Both crack lengths and growth rates are shown as a function of numbers of cycles applied. The growth kinetics of these cracks can be expected to vary with specimen history — for example, by ramp loading at the start in the Neumann manner. However, for the constant amplitude testing method used and for the results shown here, the average growth rate for *much* of Stage I life does not differ very much for crystals cycled at different amplitudes (fig. 60a). Such behavior reflects the average localized strain of the PSBs. However, the maximum growth rate for each specimen, reflecting the highest level of the local strain (figs. 60b, c), increases as the strain increases. Note that the rates diminish slightly as cycling proceeds. It is not clear why such behavior occurs

References: p. 2391.

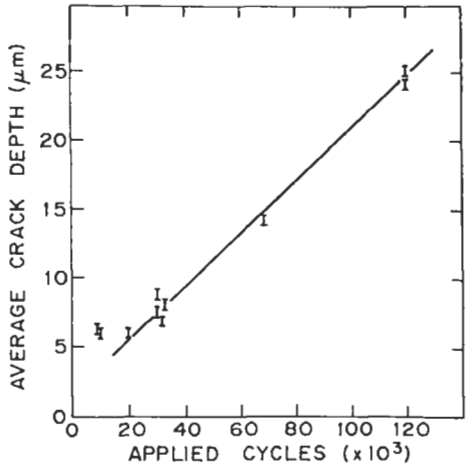

(a)

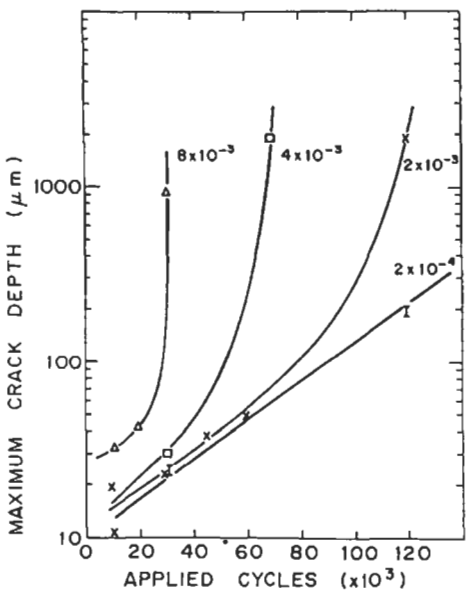

(b)

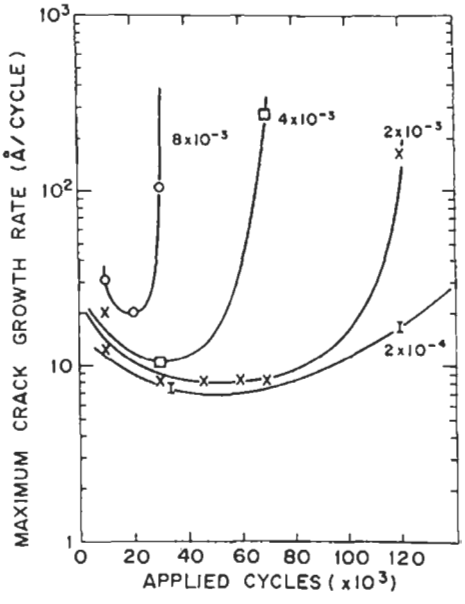

(c)

Fig. 60. Crack growth behavior of Stage I cracks (in PSBs) in copper single crystals cycled at constant strain amplitudes within the plateau: (a) Correlation between *average* crack depth and cycles for the crystals shown in (b). (b) Correlation between *maximum* crack depths and applied cycles for crystals cycled at the indicated plastic shear strain amplitudes. (c) Correlation between *maximum* crack growth *rates* and applied cycles for the same specimens as shown in (b).

but the most likely explanation at present is that the population of PSBs is not actually constant during life and it takes a good fraction of life to become established. Later arriving PSBs act to deprive older PSBs (which contain the cracks) of some of the localized strain they carried at earlier stages of life. This deprivation operates in an average sense, not by nearest neighbor interactions.

After slow Stage I crack growth has occurred, with an average rate of about 0.1 nm/cycle, crack acceleration takes place, the earlier the higher the amplitude, giving rise to shorter lives at higher amplitudes. According to regular LEFM such an acceleration would be surprising because, under strain control, the stress intensity does not vary with crack length. The reason for the acceleration is connected with the localized strain of the PSBs and how it interacts with the growing cracks. It turns out, MA and LAIRD [1989b], that there is little effect of crack growth on the local strain behavior until the cracks become so numerous that their stress shadows fall on each other. There is a critical spacing of about 10 μm within which the effect becomes strong. Since the PSB volume fraction increases with applied strain amplitude, the crack population also increases proportionately. Therefore, the higher the strain amplitude, the sooner the cracks start to compete with each other for localized strain, and the quicker failure ensues. Naturally the longest cracks survive this process and rob their lesser neighbors of the strain they formerly carried.

Evidence for such behavior is shown in fig. 61 in the form of both sharp corner observations (a) and PSB slip behavior on that surface of the specimen for which the primary Burgers vector is most normally oriented (b). Figure 61a shows a series of Stage I cracks and the longer ones have robbed the smaller crack of strain. In this experiment, a sharp corner section was prepared for observation and then the crystal was returned to the machine for further cycling. Reactivation of the PSBs produced slip markings once again on the polished face of the "sharp corner". Note how the slip markings connected with the PSB of the shortest crack have stopped short of the crack, quenching its growth. The cracks are now close enough for the acceleration phase to begin. Figure 61b gives a different view of localized strain deprivation. Here the top face was repolished (slightly) but without eliminating the cracks. On restarting the test, elliptical shadows free of slip markings are cast around the larger members of the crack population, indicating the extent of the shadowed volume. On average, the larger cracks grow a few hundred μm in depth before the acceleration process takes over, and complete failure develops rapidly. As the Stage I crack propagates, multi-slip conditions develop in the remainder of the cross-section, and the crack turns normal to the tensile stress axis.

Naturally, if a Stage I crack is propagating under LEFM, meaning that the PSBs at the crack tip are small in relation to the crack size then the detailed kinetics will be different from those described above which apply to single crystals. An attempt at analyzing monocrystalline Stage I growth by EPFM has been made by MA and LAIRD [1989b].

6.3. Long crack growth — Stage II

How deep a Stage I crack grows in a smooth specimen depends on the applied stress. In low strain fatigue, a Stage I crack can penetrate to the depth of several grain

References: p. 2391.

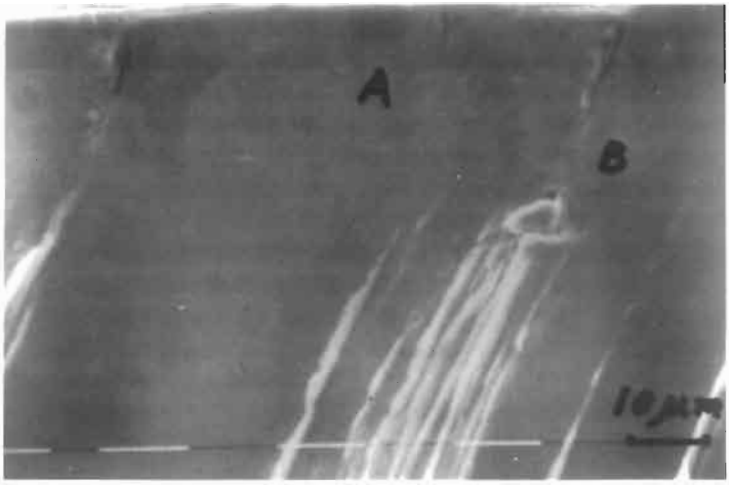

(a)

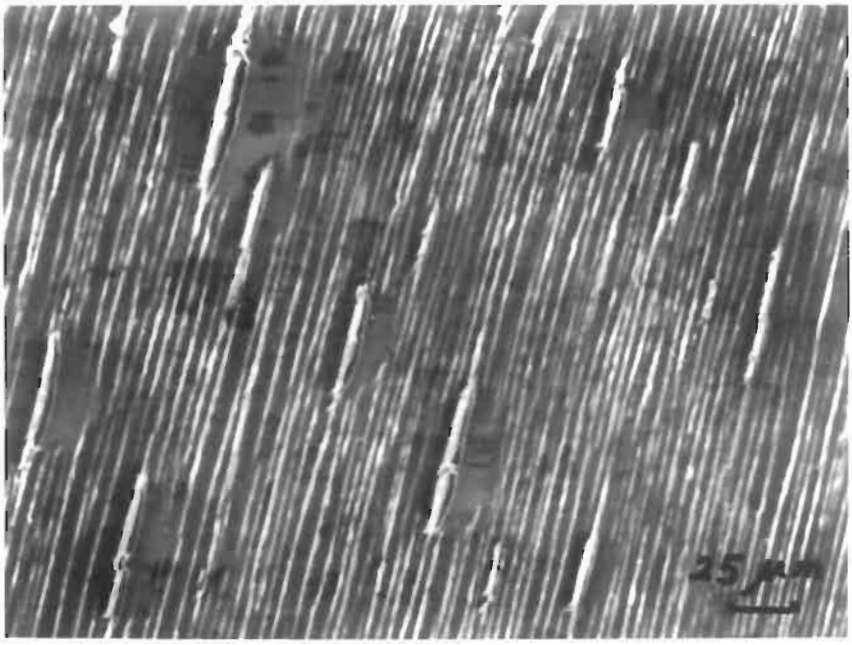

(b)

Fig. 61. Competition for plastic strain between growing Stage I cracks in a copper single crystal and adjacent PSBs: (a) Sharp corner technique. Crack A finally fell within the strain relaxation region caused by crack B, and stopped growing. The PSB immediately ahead of its tip became inactive. (b) Stress shadows causing PSB inactivity around more significant Stage I cracks. Crystal originally cycled at 2×10^{-3} and then at 8×10^{-3}, next repolished, and finally cycled at 24 MPa for 341 K cycles. Courtesy of MA [1987].

diameters before the increase of the stress intensity with the crack length promotes slip on systems other than the primary one in any grain. A dislocation cell structure normally forms at the crack tip under these conditions as frequently observed (WILKINS and SMITH [1970]), and the PSB structure is broken down. Since slip is no longer confined to planes at 45° to the stress axis, the crack begins to propagate normal to the stress axis, and is then in Stage II growth by definition. In high strain fatigue the stress intensity is so large at a crack nucleus that the crack will almost immediately propagate by the Stage II process (LAIRD and SMITH [1962, 1963]; KIM and LAIRD [1978]).

The transition from Stage I to II has been of concern for many years. CHENG and LAIRD [1983] explored this transition in copper single crystals, both theoretically and experimentally. They have taken as the criterion for the transition the situation in which the plastic zone at the crack tip in the PSB (the crack has grown quite long and therefore now does interfere with the regular PSB structure) raises the shear stress on the second most highly stressed, non-primary plane, to that of the plateau in the cyclic stress–strain curve. They chose the plateau stress because they had no information concerning latent hardening in fatigue. Latent hardening was later studied in sufficient detail by WANG, ROMANOW and LAIRD [1989], to show that the model needs only minor modification for the actual flow stress on slip planes intersecting the primary. When the transition criterion is satisfied, a slip band can emanate from the crack tip at a large angle to the primary slip plane, and the duplex slip at the crack tip changes the plane of the crack from 45° to the stress axis to one approximately normal to it (CHENG and LAIRD [1983]).

As mentioned above, Stage II fracture surfaces are recognized by the observation of fatigue striations on them provided the propagation rate is large enough for the striations to be resolved. Striations occur in two morphological types, "ductile" striations, by far the most common, and "brittle" striations which occur in strongly hardened metals, or metals prone to brittle fracture mechanisms. Typical striations of the ductile variety are shown in fig. 62. These striations were produced under conditions of variable loading and therefore vary in width (LAIRD and DE LA VEAUX [1977]). Observations of this type were first used to prove that each striation was associated with one load cycle (FORSYTH and RYDER [1961]). The morphology of the striation can vary considerably in any material and in some materials have such a distorted morphology as to be unrecognizable. The variations in striation morphology and their dependence on the details of the slip processes have been repeatedly discussed (LAIRD [1967, 1979]). It has also long been understood that cycling in vacuo at low or intermediate stress intensities suppresses the appearance of the striations while lowering the crack propagation rate by an order of magnitude or more. Welding at the crack tip during the compression strokes of the cycle and/or an influence of the absence of the environment on slip localization at the crack tip may provide the explanation for such behavior (See also BOWLES and SHIJVE [1983]).

The regular ductile striation has a profile consisting of a more or less flat region (actually curved when the striation spacing is small) bounded by a trench (fig. 62). Both the morphology of the striation and its one-to-one connection with each load cycle were major clues to unraveling the mechanism of Stage II growth. Furthermore, the trench is formed on the side of the striation in the direction of crack propagation (fig. 62). By making sections through cracks in specimens unloaded from different parts of the

References: p. 2391.

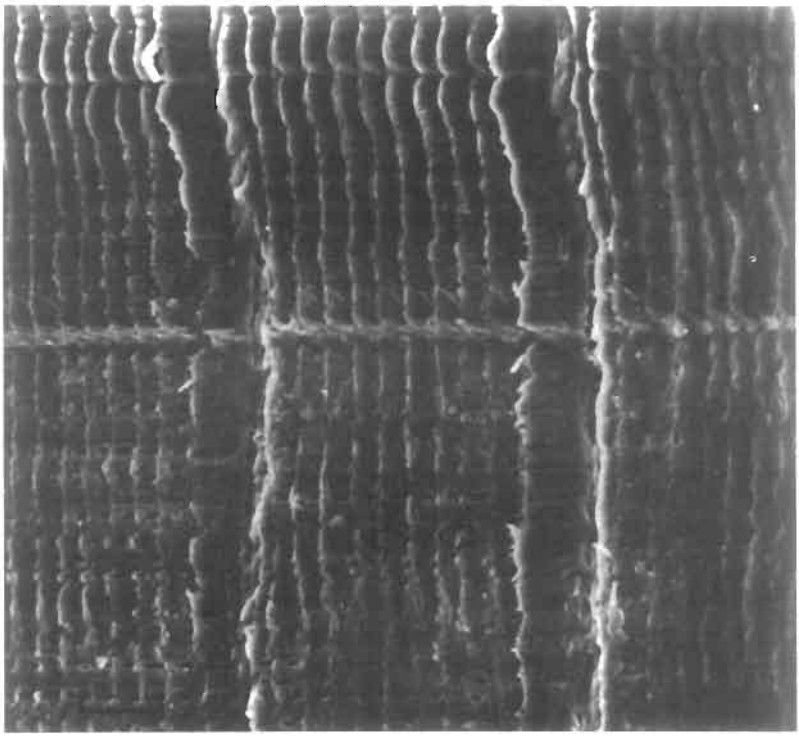

Fig. 62. Typical ductile fatigue striations. Note that each striation, indicated by a double headed arrow, consists of a flat region and trench. These striations were produced by a push-pull load sequence of 10 cycles at ± 0.0025 and 1 cycle at ± 0.005 plastic strain. Direction of crack advance from left to right. Taken from LAIRD and DE LA VEAUX [1977].

straining cycle, LAIRD and SMITH [1962] provided direct evidence for the purely ductile model of crack propagation. This evidence was refined and led to the model for crack growth shown in fig. 63, termed the "plastic blunting process" (LAIRD [1967]). Although this model was proposed some time ago, the author believes it is an accurate representation of the ductile fatigue crack growth mechanism, as follows:

The initially unloaded crack tip is shown in fig. 63a. As tensile loading is applied, slip is concentrated in sharp bands at the double notch of the tip. Depending on the detailed morphology of the striation, the crack tip can also be singly pointed (LAIRD [1967, 1979]). With continued tensile deformation, the crack progresses a distance proportional to the sliding off. This model has been directly supported by in situ observations in single crystals (NEUMANN *et al.* [1977]). On reversing the loading direction, the slip in the zones is reversed, the crack faces close, and the new crack surface just created is folded by buckling of material at the crack tip, producing the double notch (i.e., a trench on each fracture face) and unit of crack advance shown in fig. 63. Depending on the planarity and coarseness of slip, the details of this process can

vary considerably. For example, it is frequently observed that a trench on one face of the fracture matches with a ridge on the other (LAIRD [1967]).

The basic similarity between the mechanisms of Stage I and Stage II growth will be noted, in that both involve crack advance by a "slipping-off" process. The difference between them is that only one slip system need be involved in Stage I, but at least duplex slip occurs in the Stage II crack plastic zones.

Several authors have published alternative representations of the plastic blunting process (NEUMANN *et al.* [1977]; SHIJVE [1967]; PELLOUX [1969]; KUO and LIU [1976]). They involve the essential "slipping-off" process of the plastic blunting mechanism. Differences may be perceived because alternating slip on specific intersecting slip planes has been proposed. In special, high symmetry orientations of the crystal with respect to the stress axis, the detailed crystallography of the slip may influence the striation morphology. The direct observations of DAVIDSON [1979] using the SEM to examine straining behavior at a crack tip are particularly worthy of reference.

There have been advances which have been helpful in describing how partial cleavage or corrosion enhanced crack growth affect the purely plastic aspects of Stage II growth. It was pointed out in early work (LAIRD [1962]) that the ratio between crack growth per cycle and the plastic crack tip opening should be a constant. VEHOFF and NEUMANN [1980] have verified this, and also have shown how this ratio depends both on the angle between the two slip bands emanating from the crack tip and the coarseness of slip. Furthermore, by varying both temperature and the crack tip opening velocity, they have found a transition from ductile to brittle fracture, with associated marked changes in striation morphology. This behavior of course applies only to material in which brittle failure is readily accessible (e.g., bcc metals). The evidence by Vehoff and Neumann still

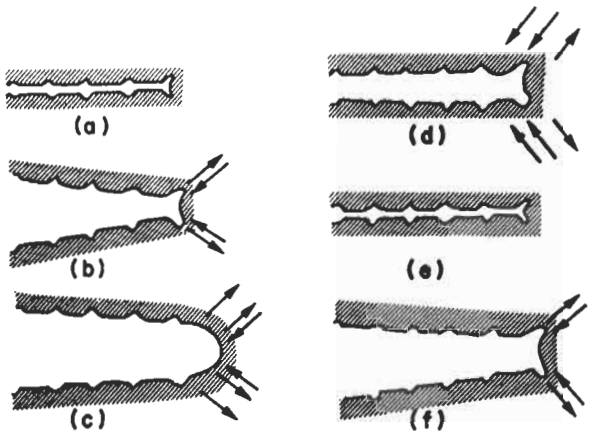

Fig. 63. Schematic representation of the plastic blunting process of fatigue crack propagation in Stage II (a) zero load; (b) small tensile load; (c) maximum tensile load of the cycle; (d) closure; (e) maximum compression load of the cycle (f) small tensile load in the succeeding cycle. The double arrowheads in (c) and (d) signify the widening of slip bands at the crack in these stages of the process. LAIRD [1967].

References: p. 2391.

appears to be the most convincing for the formation of brittle, as opposed to ductile, striations by a cleavage mechanism in metals subject to this type of failure.

Typical brittle striations are shown in fig. 64. The Vehoff and Neumann experiments have led to the following picture for the initiation of cleavage at an atomically sharp crack: the local stress increases at such a high rate that the crack cannot be blunted by thermally activated dislocation glide. This leads to cleavage. If on the other hand the local stress increases at a low enough rate, the crack blunts and remains ductile. VEHOFF and NEUMANN report [1980] that the ratio of the crack advance per cycle to the plastic crack tip opening is definitely higher for quasi brittle fracture (up to a factor of 5). Quasi-brittle cracks do show a small crack tip angle, however, and this indicates that some plasticity accompanies the crack growth. It remains extremely difficult to develop theories of crack growth for such complicated mechanisms.

One purpose of a crack propagation theory is to describe accurately the kinetics of crack propagation of the type shown in fig. 55 and there have been many theoretical studies resulting in equations of the form of the Paris relation. Essentially, there are two classes of problem to handle: 1) the crack propagation rate is proportional to the square of the stress intensity range, which corresponds to ductile Stage II growth, and 2) the rate is proportional to the stress intensity range to a power greater than two, of which four is a popular value, but still higher values have been observed when static failure mechan-

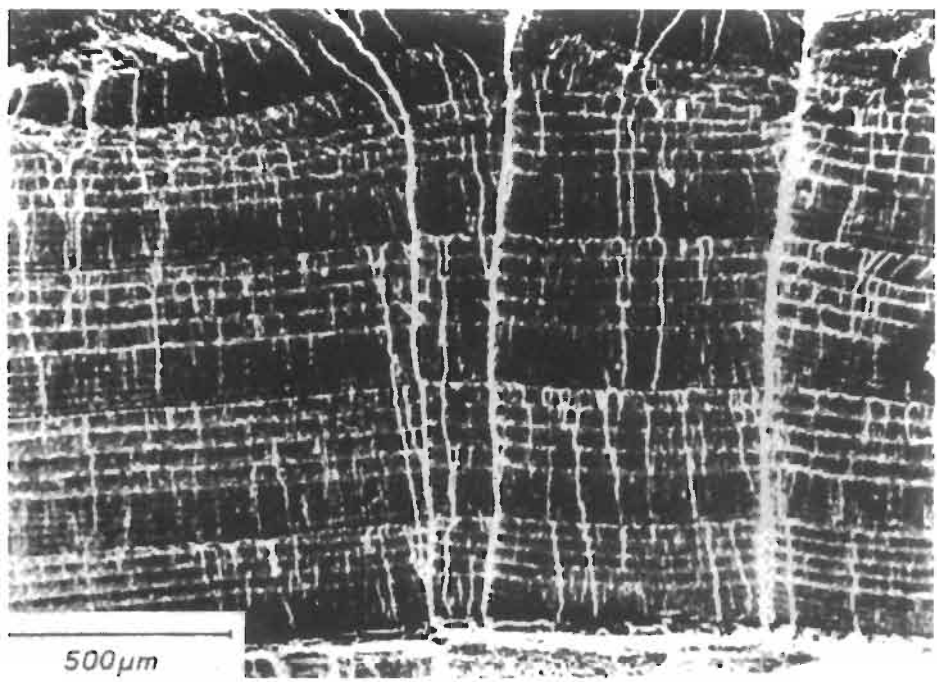

Fig. 64. Fracture surface striations, brittle type, obtained by quasi-brittle crack propagation in program loading at a high crack tip opening velocity. The program consisted of five cycles at large strain amplitude and then five cycles at an amplitude one third of the previous value. Courtesy of VEHOFF and NEUMANN [1980].

isms assist the ductile growth mechanism.

The square law comes about from assuming that the crack growth per cycle is proportional to the crack opening displacement. This type of relation was derived by LAIRD [1962] and there have been many similarly-based derivations since, of which that by MCEVILY [1973] is a typical example. The problem has also been handled by finite element methods (KUO and LIU [1976]; YANG and LIU [1980]; NEWMAN [1977]), and the approach continues to be applied up to the present (MARGOLIN [1995]).

Obtaining Paris relations with a power higher than two is an extremely difficult problem. Many workers assume a ductility exhaustion approach for a ligament at the crack tip. Although such an approach can yield correct answers for sufficiently ingenious theorists, it is unlikely to be very close to reality. Other workers beg the question of mechanism, and derive relations based on the concept that plastic work must be provided to advance the crack (FINE [1980]). The interested reader is directed to WEERTMAN's excellent review for further details on theory [1979], and to MARCUS' for environmental effects [1979].

The advances obtained in understanding fatigue behavior in the last ten years have been considerable and new opportunities are available from new techniques, such as *atomic force microscopy* and *scanning tunneling microscopy* to solve the difficult problem of crack initiation. Non-linear dynamical methods and numerical simulations also offer exciting opportunities.

Acknowledgements

During preparation of this chapter, the writer received support from the Airforce Office of Scientific Research, the Department of Energy and the National Science Foundation, for which he gives warm thanks. He is also most grateful to numerous generations of graduate students who have provided unremitting stimulation.

References

ABEL, A., WILHELM, M. and GEROLD, V., 1979, Mat. Sci. Eng. **37**, 187.
ACKERMANN, F., KUBIN, L.P., LEPINOUX, J. and MUGHRABI, H., 1984, Acta Met. **32**, 715.
AIFANTIS, E.C., 1986, Mat. Sci. Eng. **81**, 563.
ALBERT, W.A.J., 1838, Archiv für Mineralogie, Geognosie, Bergbau und Hüttenkunde **10**, 215.
AMERICAN SOCIETY FOR TESTING AND MATERIALS:
Spec. Tech. Pub., No. 590, 1976;
Spec. Tech. Pub., No. 631, 1977;
Spec. Tech. Pub., No. 637, 1977;
Spec. Tech. Pub., No. 675, 1979.
ANTONOPOULOS, J.G., BROWN, L.M. and WINTER, A.T., 1976, Phil. Mag. **34**, 549.
BASINSKI, S.J., BASINSKI, Z.S. and HOWIE, A., 1969, Phil. Mag. **19**, 899.
BASINSKI, Z.S. and BASINSKI, S.J., 1984, Scripta Met. **18**, 851.
BASINSKI, Z.S. and BASINSKI, S.J., 1992, Progress in Materials Science **36**, 89.
BASINSKI, Z.S., KORBEL, A.S. and BASINSKI, S.J., 1980, Acta Met. **28**, 191.
BAUSCHINGER, J., 1886, Mitt. mech. tech. Lab., München, **13**, pp. 1–115.

BÄUMEL, A., JR. and SEEGER, T., 1990, "Materials Data for Cyclic Loading", Supplement 1, Elsevier, Amsterdam.
BHAT, S. P. and LAIRD, C., 1978, Scripta Metall. **12**, 687.
BHAT, S. P. and LAIRD, C., 1979a, Acta Met. **27**, 1861.
BHAT, S. P. and LAIRD, C., 1979b, Fatigue of Eng. Mater. & Structures **1**, 59.
BLOCHWITZ, C. and KAHLE, E., 1980, Cryst. Res. Tech. **15**, 977.
BOLLER, CHR. and SEEGER, T., 1987, "Materials Data for Cyclic Loading", Materials Sciences Monographs, Vols. 42 A–E, Elsevier, Amsterdam.
BONDA, N. R., POPE, D. P. and LAIRD, C., 1987, Acta Metall. **35**, 2371 and 2385.
BOWLES, C. Q. and SCHIJVE, J., 1983, in "Fatigue Mechanisms", Am. Soc. Test. Mater., Spec. Tech. Publ. **811**, pp. 400–425.
BROOM, T. and HAM, R. K., 1959, Proc. Roy. Soc. **A251**, 186.
BROWN, L. M., 1977, Metal Sci. **11**, 315.
BROWN, L. M., June 1980, in Proc. of Int. Conf. on Dislocation Modelling in Physical Systems, Gainesville, Florida.
BROWN, M. W., 1986, in "The Behavior of Short Fatigue Cracks", Eds.: K.J. Miller and E.R. de los Rios, M.E.D., Inst. of Mech. Engrs., London, pp. 423–439.
BUCHINGER, L., CHENG, A. S., STANZL, S. and LAIRD, C., 1986, Mat. Sci. Eng. **80**, 155.
BUCHINGER, L., STANZL, S. and LAIRD, C., 1984, Phil. Mag. A. **50**, 275.
CALABRESE, C. and LAIRD, C., 1974, Mat. Sci. and Eng. **13**, 141.
CHARSLEY, P., 1981, Mat. Sci. Eng. **47**, 181.
CHENG, A. S. and LAIRD, C., 1981a, Mat. Sci. Eng. **51**, 111.
CHENG, A. S. and LAIRD, C., 1981b, Mat. Sci. Eng. **51**, 55.
CHENG, A. S. and LAIRD, C., 1981c, Fat. Eng. Materials & Structures **4**, 331 and 343.
CHENG, A. S. and LAIRD, C., 1983, Mat. Sci. Eng. **60**, 177.
COFFIN, L. F., 1956, Trans. Am. Soc. Mech. Eng. **78**, 527.
COFFIN, L. F. and MCMAHON, C. J., 1979, Met. Trans. **1**, 3443.
COFFIN, L. F. and READ, J. H., 1956, Int. Conf. on Fatigue of Metals, Inst. of Mech. Engrs., London.
COFFIN, L. F. and TAVERNELLI, J., 1958, Gen. Elec. Co., Research Lab. Rep. No. 58–RL–2100.
COTTRELL, A. H. and HULL, D., 1957, Proc. Roy. Soc. **A242**, 211.
DAVIDSON, D. L. and LANKFORD, J., 1984, in IUTAM Eshelby Memorial Symposium, Eds., B.A. Bilby, K. J. Miller and J.R. Willis, Cambridge University Press, pp. 559–572.
DICKSON, J. I., BAILON, J. P., XIA, J. and BUREAU, M., 1993, in "Fatigue 93", Vol. III, EMAS, Warley, W. Midlands, pp. 1883–1892.
DICKSON, J. I., BANDE, HONG and L'ESPERANCE, G., 1988, Acta Met. **A101**, 75.
DICKSON, J. I., HANDFIELD, L. and L'ESPERANCE, G., 1986, Mat. Sci. Eng. **81**, 477.
ESSMANN, U., 1982, Phil. Mag **45**, 171.
ESSMANN, U., GÖSELE, U. and MUGHRABI, H., 1981, Phil. Mag. **A44**, 405.
EWING, J. A. and HUMPHREY, J. C. W., 1902, Phil. Trans. (A) **200**, 241.
FATIGUE DESIGN HANDBOOK, 1988, Ed. R.C. Rice, Soc. of Automotive Engineers, Inc., Warrendale, PA., Second Edition.
FELTNER, C. E. and LAIRD, C., 1967, Acta Metall. **15**, 1621 and 1633.
FIGUEROA, J. C., BHAT, S. P., DE LA VEAUX, R., MURZENSKI, S. and LAIRD, C., 1981, Acta Metall. **29**, 1667.
FIGUEROA, J. C. and LAIRD, C., 1981, Acta Met. **29**, 1679.
FINE, M. E., 1980, Met. Trans. **11A**, 365.
FINE, M. E. and RITCHIE, R. O., 1979, in "Fatigue and Microstructure", Am. Soc. Metals., pp. 245–278.
FINNEY, J. M., 1974, Ph.D. Thesis, University of Pennsylvania.
FINNEY, J. M. and LAIRD, C., 1975, Phil. Mag. **31**, 339.
FORREST, P. G., 1962, "Fatigue of Metals", Pergamon, Oxford.
FORSYTH, P. J. E., 1953, Nature **171**, 172.
FORSYTH, P. J. E., 1956, Int. Conf. on Fatigue, Inst. of Mech. Engr. and Am. Soc. Mech. Engrs., Paper 6.5, pp. 537–537.
FORSYTH, P. J. E., 1957, Proc. Roy. Soc. **A242**, 198.

FORSYTH, P.J.E. and STUBBINGTON, A., 1955, J. Inst. Met. **84**, 173.
FORSYTH, P.J.E. and RYDER, D.A., 1961, Metallurgia **51**, 117.
GARBACZ, A., RALPH, B. and KURZYDLOWSKI, K.J., 1995, Acta Metall. Mater. **43**, 1541.
GEROLD, V. and MEIER, B., 1987, Fatigue 87, Ed., R.O. Ritchie, West Midlands, Vol. 3, pp. 1517–1540.
GEROLD, V. and STEINER, D., 1982, Scripta Met. **16**, 405.
GLAZOV, M.V., 1995, "Self-Organization and Temporal Dissipative Structures in Fatigued Metals", Submission to A.S.M. International.
GLAZOV, M.V. and LAIRD, C., 1995a, Acta Metall. Mater. **43**, 2849.
GLAZOV, M.V. and LAIRD, C., 1995b, Phys. Stat. Sol., A., in press.
GOUGH, H.J., 1933, Proc. Am. Soc. Test Mater. **33**, 3.
GOUGH, H.J. and SOPWITH, D.G., 1932, J. Inst. Metals. **49**, 93.
GROSSKREUTZ, J.C., 1971, Phys. Stat. Sol. **47**, 11.
GROSSKREUTZ, J.C. and MUGHRABI, H., 1975, "Constitutive Equations in Plasticity", Ed. A.S. Argon, MIT Press, Cambridge, Mass., p. 251.
GU, H., GUO, H., CHANG, S. and LAIRD, C., 1994, Mat. Sci. Eng. **A188**, 23.
HANCOCK, J.R. and GROSSKREUTZ, J.C., 1969, Acta Met. **17**, 77.
HODGSON, B., 1968, Met. Sci. J. **2**, 235.
HOLT, D.L., 1970, J. Appl. Phys. **41**, 3197.
HONG, S.I., 1989, Ph.D. Thesis, University of Pennsylvania.
HONG, S.I., INUI, H. and LAIRD, C., 1992, Acta Metall. Mater. **40**, 394.
HONG, S.I. and LAIRD, C., 1990a, Acta Metall. Mater. **38**, 1581.
HONG, S.I. and LAIRD, C., 1990b, Mat. Sci. Eng. **A124**, 183.
HONG, S.I. and LAIRD, C., 1990c, Mat. Sci. Eng. **A128**, 55, 155.
HONG, S.I. and LAIRD, C., 1990d, Acta Metall. Mater. **38**, 2085.
HONG, S.I. and LAIRD, C., 1991a, Fatigue Fracture Eng. Mater. Struct. **14**, 143.
HONG, S.I. and LAIRD, C., 1991b, Mat. Sci. Eng. **A142**, 1.
HONG, S.I. and LAIRD, C., 1991c, Met. Trans. **22A**, 415.
HORIBE, S. and LAIRD, C., 1983, Acta Met. **31**, 1567.
HORIBE, S. and LAIRD, C., 1985a, Acta Met. **33**, 819.
HORIBE, S. and LAIRD, C., 1985b, Mat. Sci. Eng. **72**, 149.
HORIBE, S. and LAIRD, C., 1987, Acta Metall. **35**, 1919.
HUNSCHE, A. and NEUMANN, P., 1986, Acta Metall. **34**, 207.
IKEDA, S., 1980, in 5th Int. Congress on Strength of Metals and Alloys, Eds., P. Haasen, V. Gerold and G. Kostorz, Pergamon Press, Oxford, pp. 1157–1162.
INUI, H., HONG, S.I. and LAIRD, C., 1990, Acta Metall. Mater. **38**, 2261.
JIN, N.Y. and WINTER, A.T., 1984, Acta Metall. **32**, 989.
KATAGIRI, K., AWATANI, J., OMURA, A., KOYANAGI, K. and SHIRAISHI, T., 1979, in "Fatigue Mechanisms", Am. Soc. for Test. Mater., Spec. Tech. Publ. **675**, pp. 107–123.
KATAGIRI, K., OMURA, A., KOYANAGI, K., AWATANI, J., SHIRAISHI, T. and KANESHIRO, H., 1977, Met. Trans. **8A**, 1769.
KENNEDY, A.J., 1962, "Processes of Creep and Fatigue in Metals", J. Wiley and Sons, London.
KETTUNEN, P. and TIAINEN, T., 1981, in "Deformation of Polycrystals", Eds., N. Hansen, A. Horsewell, T. Leffers and H. Lilholt, Risø, Denmark, pp. 437–444.
KIM, C.S., CHUNG, Y.W. and FINE, M.E., 1987, in "Fatigue 87", Vol. 1, EMAS, Warley, W. Midlands, pp. 73–72.
KIM, W.H. and LAIRD, C., 1978a, Mater. Sci. Eng. **33**, 225.
KIM, W.H. and LAIRD, C., 1978b, Acta. Metall. **26**, 777.
KIM, W.H. and LAIRD, C., 1978c, Acta Metall. **26**, 789.
KITAGAWA, K., ASADA, H., MONZEN, R. and KIKUCHI, M., 1986, Sup. Trans. Jap. Inst. of Metals **27**, 827.
KITAGAWA, H. and TAKAHASHI, S., 1976, in Int. Conf. Mech. Behavior of Materials (ICM2), Am. Soc. of Metals, pp. 627–631.
KLESNIL, M. and LUKÁŠ, P., 1980, "Fatigue of Metallic Materials", Elsevier, Amsterdam.
KOCANDA, S., 1978, "Fatigue Failure of Metals", Sijthoff and Noordhoff Int. Publishers, Amsterdam.

KOCKS, U.F., 1970, Metall. Trans. **1**, 1121.
KOCKS, U.F., 1985, in Dislocations and Properties of Real Materials, The Inst. of Physics, London, pp. 125–143.
KUBIN, L., 1993, in "Materials Science and Technology, Vol. 6", Ed., H. Mughrabi, VCH, Weinheim, FRG, pp. 137–190.
KUBIN, L. and ESTRIN, Y., 1992, Phys. Stat. Sol., B **172**, 173.
KUHLMANN–WILSDORF, D., 1975, in "Work Hardening in Tension and Fatigue", Ed. A.W. Thompson, The Metallurgical Soc., AIME, pp. 1–43.
KUHLMANN–WILSDORF, D., 1979a, Mat. Sci. Eng. **39**, 127.
KUHLMANN–WILSDORF, D., 1979b, Mat. Sci. Eng. **39**, 231.
KUHLMANN–WILSDORF, D. and CHARSLEY, P., 1981, Phil. Mag. **44**, 1851.
KUHLMANN–WILSDORF, D. and LAIRD, C., 1977, Mat. Sci. Eng. **27**, 137.
KUHLMANN–WILSDORF, D. and LAIRD, C., 1979, Mat. Sci. Eng. **37**, 111.
KUHLMANN–WILDORF, D. and LAIRD, C., 1980, Mat. Sci. Eng. **46**, 209.
KUO, A.S. and LIU, H.W., 1976, Scripta Met. **10**, 723.
KWADJO, R. and BROWN, M., 1978, Acta Metall. **26**, 1117.
KWON, I.B., WEERTMAN, J. and FINE, M.E., 1987, in "Fatigue 87", Vol. 1, EMAS, Warley, W. Midlands, pp. 261–270.
LAIRD, C., 1962, Ph.D. Thesis, University of Cambridge.
LAIRD, C., 1967, in "Fatigue Crack Propagation", Am. Soc. Test. Mater., Spec. Tech. Publ. **415**, pp. 131–180.
LAIRD, C., 1976, Mater. Sci. Eng. **22**, 231.
LAIRD, C., 1977, in "Work Hardening in Tension and Fatigue", Ed. A.W. Thompson, The Metallurgical Soc., AIME, p. 150.
LAIRD, C., 1977b, in Spec. Tech. Publ. 637, Am. Soc. Test. Mater., pp. 3–35.
LAIRD, C., 1979, "Mechanisms and Theories of Fatigue", Am. Soc. of Metals, pp. 149–204.
LAIRD, C., 1981, "Metallurgical Treatises", Ed. J.K. Tien and J.F. Elliott, The Metallurgical Soc., AIME, pp. 505–527.
LAIRD, C., 1983, "Dislocations", Ed. F.R.N. Nabarro, Vol. 6, pp. 55–120, North-Holland Co., Amsterdam.
LAIRD, C. and BUCHINGER, L., 1985, Met. Trans. **16A**, 2201.
LAIRD, C., CHARSLEY, P. and MUGHRABI, H., 1986, Mater. Sci. Eng. **81**, pp. 433–450.
LAIRD, C. and DE LA VEAUX, R., 1977, Met. Trans. **8A**, 657.
LAIRD, C. and DUQUETTE, D.J., 1972, in "Corrosion Fatigue", NACE–2, Eds: A.J. McEvily, O. Devereux and R.J. Staehle, pp. 88–117.
LAIRD, C. and FELTNER, C.E., 1967, Trans. Am. Inst. Met. Engrs. **239**, 1074.
LAIRD, C., FINNEY, J.M. and KUHLMANN–WILSDORF, D., 1981, Mat. Sci. Eng. **50**, 127.
LAIRD, C., LANGELO, V.J., HOLLRAH, M., YANG, N.C. and DE LA VEAUX, R., 1978, Mater. Sci. Eng. **32**, 137.
LAIRD, C. and KRAUSE, A.R., 1968, Trans. Am. Inst. Met. Engrs. **242**, 2339.
LAIRD C. and SMITH, G.C., 1962, Phil. Mag. **7**, 847.
LAIRD C. and SMITH, G.C., 1963, Phil. Mag. **8**, 1945.
LAIRD, C., STANZL, S., DE LA VEAUX, R. and BUCHINGER, L., 1986, Mater. Sci. Eng. **80**, 143.
LANDGRAF, R.W., 1977, "Cyclic Deformation Behavior of Engineering Alloys", Proc. of Fatigue Seminars — Fundamental and Applied Aspects, Saabgarden, Remforsa, Sweden, pp. 15–18.
LEE, J.K., 1980, Ph.D. Thesis, University of Pennsylvania.
LEE, J.K., BHAT, S.P., DE LA VEAUX, R. and LAIRD, C., 1981, Int. J. of Fracture **17**, 121.
LEE, J.K. and LAIRD, C., 1982, Mater. Sci. Eng. **54**, 39 and 53.
LEE, J.K. and LAIRD, C., 1983, Phil. Mag. **47**, 579.
LEPISTÖ, T.K., 1984, Doctor of Technology Thesis, Tampere Univ. of Technology.
LEPISTÖ, T.K., KUOKALA, V-T. and KETTUNEN, P.O., 1986, Mat. Sci. Eng. **81**, 457.
LERCH, B. and GEROLD, V., 1985, Acta Met. **33**, 1709.
LI, Y.F., FARRINGTON, G.C. and LAIRD, C., 1993, Acta Metall. **41**, 693, 709 and 723.
LI, Y.F. and LAIRD, C., 1994, Mater. Sci. & Eng. **A186**, 65, 87.
LIU, T.H. and ITO, Y.M., 1969, J. Mechs. Phys. Solids **17**, 511.

LIU, T.H. and LIN, S.R., 1979, in "Fatigue Mechanisms", Spec. Tech. Pub., 675, Am. Soc. Test Mater., Philadelphia, pp. 707–728.
LLANES, L., 1992, Ph.D. Thesis, University of Pennsylvania.
LLANES, L. and LAIRD, C., 1992, Mater. Sci. Eng. **A157**, 21.
LLANES, L., ROLLETT, A.D., BASSANI, J.L. and LAIRD, C., 1993, Acta Metall. Mater. **41**, 2667.
LORENZO, F., 1983, Ph.D. Thesis, University of Pennsylvania.
LORENZO, F. and LAIRD, C., 1984, Acta Metall. **32**, 681.
LUKÁŠ, P. and KLESNIL, M., 1970, Phys. Stat. Sol. **37**, 833.
LUKÁŠ, P. and KLESNIL, M., 1971, Phys. Stat. Sol. **A5**, 247.
LUKÁŠ, P. and KLESNIL, M., 1973, Mater. Sci. & Eng. **11**, 345.
LUKÁŠ, P., KLESNIL, M., KREJCI, J. and RYS, P., 1966, Phys. Stat. Sol. **15**, 71.
LUKÁŠ, P. and KUNZ, L., 1994, Mat. Sci. Eng. **A189**, 1.
LUKÁŠ, P., KUNZ, L. and KREJČI, J, 1993, in Fatigue '93, Eds., J-P. Bailon and J.I. Dickson, EMAS, Warley, W. Midlands, Vol. 1, pp. 71–76.
MA, B.T. and LAIRD, C., 1986, in Small Fatigue Cracks, Eds. R.O. Ritchie and J. Lankford, The Metallurgical Soc., Warrendale, PA, pp. 9–28.
MA, B.T., 1987, Ph.D. Thesis, University of Pennsylvania.
MA, B.T. and LAIRD, C., 1988, Mat. Sci. Eng. **A102**, 247.
MA, B.T. and LAIRD, C., 1989(a), Acta Met. **37**, 349, 357.
MA, B.T. and LAIRD, C., 1989(b), Acta Met. **37**, 325, 337 and 369.
MAGNIN, T., 1983, in "Fatigue 93", Eds., J.P. Bailon and J.I. Dickson, EMAS, Warley, W. Midlands, Vol. II, 733–744.
MANN, Y.F., 1970, Bibliography on the Fatigue of Materials, Components and Structures, Vol. 1, 1838–1950, Pergamon, Oxford.
MANN, Y.F., 1978, Bibliography on the Fatigue of Materials, Components and Structures, Vol. 2, 1951–60, Pergamon, Oxford.
MANSON, S.S., 1953, N.A.C.A. Tech. Note 2933.
MARCUS, H.L., 1979, in "Fatigue and Microstructure", Am. Soc. Met., pp. 365–384.
MARGOLIN, H., 1995, Private Communication.
MAY, A.N., 1960a, Nature **185**, 303.
MAY, A.N., 1960b, Nature **186**, 573.
MCCAMMON, R.D. and ROSENBERG, H.M., 1957, Proc. Roy. Soc. **A242**, 203.
MCEVILY, A.J., 1973, Proc. 3rd Int. Conf. on the Strength of Metals and Alloys, Cambridge.
MECKE, K., 1974, Phys. Stat. Sol. **25A**, K93.
MECKE, K., BLOCHWITZ, C. and KREMLING, U., 1982, Cryst. Res. Tech. **17**, 1557.
MILLER, K.J., 1987, Fatigue Fract. of Eng. Mater. and Struct. **10**, 75.
MILLER, K.J. and DE LOS RIOS, E.R., 1986, Editors, "The Behavior of Short Cracks", Inst. of Mech. Engrs., London, 560.
MITCHELL, M., 1979, "Mechanisms and Theories of Fatigue", Ed. M. Meshii, Am. Soc. Metals, pp. 385–437.
MOORE, H.F. and KOMMERS, J.B., 1927, "The Fatigue of Metals", McGraw–Hill, New York.
MORRISON, D.J., 1995, Materi. Sci. Eng., in press.
MORRISON, D.J. and CHOPRA, V., 1994, Mater. Sci. Eng. **A177**, 29.
MUGHRABI, H., 1975, Zeit. für Metallk. **66**, 719.
MUGHRABI, H., 1977, in "Surface Effects in Crystal Plasticity", Eds. R.M. Latanision and J.T. Fourie, Noordholt, Leyden, pp. 479–485.
MUGHRABI, 1978, Mat. Sci. Eng. **33**, 207–223.
MUGHRABI, H., 1980, 5th Int. Conf. on Strength of Metals and Alloys, Eds. P. Haasen, V. Gerold and G. Kostorz, pp. 1615–1638, Pergamon Press, Oxford.
MUGHRABI, H., 1981, in "Continuum Models of Discrete Systems", Eds. O. Brulin and R.K.T. Hsieh, North-Holland Publishing Co., Amsterdam, pp. 241–257.
MUGHRABI, H., 1983, 4th Risø Int. Symposium on Metallurgy & Mat. Sci., Roskilde, Denmark, pp. 65–82.
MUGHRABI, H., 1985a, Proc. 7th Int. Conf. on Strength of Metals & Alloys, Montreal, Canada, Pergamon Press, Vol. 3, 1917–1942.

MUGHRABI, H., 1985b, Conf. Proc. on Dislocations and Properties of Real Materials, Book No. 323, Inst. of Metals, London, pp. 244–262.
MUGHRABI, H., ACKERMANN, F. and HERZ, K., 1979, in "Fatigue Mechanisms", Am. Soc. Test. Mater. S.T.P. No. 675, pp. 69–94.
MUGHRABI, H., HERZ, K. and STARK, X., 1976, Acta Metall. **24**, 659.
MUGHRABI, H. and WANG, R., 1982, Symposium on "Defects and Fracture", Tuczno, Poland, Eds. G.C. Sih and H. Zovski, Martinus Nijhoff Publishers, The Hague, pp. 15–28.
MUGHRABI, H., WANG, R., DIFFERT, K. and ESSMANN, U., 1983, in "Fatigue Mechanisms", Am. Soc. Test. Mater., Spec. Tech. Publ. **811**, pp. 5–45.
MUGHRABI, H. and WÜTHRICH, C., 1976, Phil. Mag. **33**, 963.
NEUMANN, P., 1968, Z. Metallkunde **59**, 927.
NEUMANN, P., 1986, Mat. Sci. Eng. **81**, 465.
NEUMANN, R., 1975, Zeit. für Metallkunde **66**, 26.
NEUMANN, P. and TÖNNESSEN, A., 1987, in "Fatigue 87", Eds., R.O. Ritchie and E.A. Starke, EMAS Warley, W. Midlands, pp. 3–22.
NEUMANN, P., VEHOFF, H. and FUHLROTT, H., 1977, in "Fracture 77", ICF 4, Vol. 2, Univ. of Waterloo Press, pp. 1313–1324.
NEWMAN, J.C., 1977, in Am. Soc. Test. Mater., Spec. Tech. Pub. **637**, pp. 56–80.
NINE, H., 1970, Scripta Met. **4**, 887.
NINE, H., 1972, Phil. Mag. **26**, 1409.
ORTNER, S., LAIRD, C. and FARRINGTON, G.D., 1987, Acta Metall. **35**, 867.
PAGE, R. and WEERTMAN, J.R., 1981, "Dislocation Structures in Copper Cycled at High Temperatures", AIME Annual Meeting, Chicago.
PAN, Y. and ADAMS, B.L., 1994, Scripta Metall. Mater. **30**, 1055.
PARIS, P.C. and ERDOGAN, F., 1963, J. Basic Engineering **85**, 528.
PARIS, P.C., GOMEZ, M.P. and ANDERSON, W.P., 1961, The Trend in Engineering **13**, 9.
PELLOUX, R.M.N., 1969, in "Fracture 1969", ICF 2, Brighton, pp. 731–744.
PERALTA, P., LI, Y.F., LLANES, L. and LAIRD, C., 1995, "Localized Strain and the Cyclic Stress–Strain Response of Polycrystals", in press, J.C.M. Li Celebration Symposium, Cleveland, Ohio.
PERALTA, P., LLANES, L., BASSANI, J. and LAIRD, C., 1994, Phil. Mag. **A70**, 219.
PERALTA, P., LLANES, L., CZAPKA, A. and LAIRD, C., 1994, "Microstructural Effects on the Cyclic Deformation of Polycrystalline FCC Materials", MRS Fall Meeting.
PERALTA, P., LLANES, L., CZAPKA, A. and LAIRD, C., 1995, Scripta Metall. Mater. **32**, 1877.
PERALTA, P., SCHOBER, A. and LAIRD, C., 1993, Mater. Sci. and Eng. **A169**, 43.
POHL, K., MAYER, P. and MACHERAUCH, E., 1980, Scripta Metall. **14**, 1167.
POLÁK, J., OBRTLÍK, K. and HÁJEK, M., 1994, Fatigue Fract. Eng. Mater. Struct. **17**, 773.
POLÁK, J., 1970, Scripta Met. **4**, 761.
PURUSHOTHAMAN, S. and TIEN, J., 1978, Mat. Sci. Eng. **34**, 241.
RAJAN, K., RAMASWAMI, B. and SASTRY, S.M.L., 1975, Metall. Trans. **64**, 1959.
RASMUSSEN, K.V. and PEDERSEN, O.B., 1980, Acta Metall. **28**, 1467.
RITCHIE, R.O., 1977, Metal. Sci. **11**, 368.
RITCHIE, R.O. and LANKFORD, J., 1986, Editors, "Small Fatigue Cracks", The Metallurgical Soc. Inc., 665 pp.
ROSENBLOOM, S.N., 1990, Ph.D. Thesis, University of Pennsylvania.
ROSENBLOOM, S.N. and LAIRD, C., 1993, Acta Metall. Mater **41**, 3473.
SCHILLER, C., 1989, Ph.D. Thesis, Free Univ. of Brussels.
SCHILLER, C. and WALGRAEF, D., 1988, Acta Metall. **36**, 563.
SHIJVE, J., 1967, in "Fatigue Crack Propagation", Am. Soc. Test. Mater., Spec. Tech. Pub. **415**, pp. 415–459.
STANZL, S.E., 1980, Scripta Met. **14**, 749.
STARKE, JR., E.A. and LÜTJERING, G., 1979, in "Fatigue and Microstructure", Ed. M. Meshii, Am. Soc. Metals, pp. 205–244.
STEINER, D., BEDDOE, R., GEROLD, V. KOSTORZ, G. and SCHMEKZER, R., 1983, Scripta Met. **17**, 733.
STEVENSON, R. and VAN DER SANDE, J.B., 1974, Acta Metall. **22**, 1079.
STOLTZ, R.E. and PINEAU, A.G., 1978, Mater. Sci. Eng. **34**, 275.

SURESH, S., 1991, "Fatigue of Materials", Cambridge University Press.
SUZUKI, H. and MCEVILY, A.J., 1979, Met. Trans. **10A**, 475.
TAN, X., GU, H. and WANG, Z.G., 1995, Mater. Sci. Eng. **A196**, 45.
TAN, X., GU, H., ZHANG, S. and LAIRD, C., 1995, Mat. Sci. Eng. **A189**, 77.
THOMPSON, A.W. and BACKOFEN, W.A., 1971, Acta Metall. **19**, 597.
THOMPSON, N. and WADSWORTH, N.J., 1956, Phil. Mag. **1**, 113.
THOMPSON, N. and WADSWORTH, N.J., 1958, Adv. Physics **7**, 72.
TIEN, J. and PURUSHOTHAMAN, S., 1978, Mat. Sci. Eng. **34**, 247.
TSCHEGG, E. and STANZL, S., 1981, Acta Met. **29**, 33.
TURENNE, S., L'ESPERANCE, G. and DICKSON, J.I., 1988, Acta Met. **36**, 459.
VEHOFF, H. and NEUMANN, P., 1980, Acta Metall. **28**, 265.
VENKATARAMAN, G., CHUNG, Y.W., NAKASONE, Y. and MURA, T., 1990, Acta Metall. Mater. **38**, 31.
VOGEL, W., WILHELM, M. and GEROLD, V., 1980, in Proc. 5th Int. Conf. on Strength of Metals and Alloys, Eds., P. Haasen, V. Gerold and G. Kostorz, Pergamon, Oxford, pp. 1175–80.
VOGEL, W., WILHELM, M. and GEROLD, V., 1982, Acta Metall. **30**, 21.
WALGRAEF, D. and AIFANTIS, E.C., 1985, Int. J. Eng. Sci. **23**, 1351, 1359, 1365.
WANG, R. and MUGHRABI, H., 1984, Mater. Sci. Eng. **63**, 147.
WANG, Z. and LAIRD, C., 1988, Mater. Sci. & Eng. **100**, 57.
WANG, Z. and LAIRD, C., 1989, Met. Trans. A. **20A**, 2033.
WEERTMAN, J., 1979, in "Fatigue and Microstructure", Ed., M.Meshii, Am. Soc. Met., pp. 279–306.
WETZEL, R.M., 1971, Ph.D. Thesis, Univ. of Waterloo, Canada.
WILHELM, M., 1981, Mater. Sci. Eng. **48**, 91.
WILHELM, M. and EVERWIN, P., 1980, in Proc. 5th Int. Conf. on Strength of Metals & Alloys, Aachen, Eds. P. Haasen, V. Gerold and G. Kostorz, Pergamon, Oxford, p. 1089.
WILHELM, M., NAGESWARARAO, M. and MEYER, R., 1979, Am. Soc. Test. Mater., Spec. Tech. Publ. **675**, pp. 214–33.
WILKENS, M., HERZ, K. and MUGHRABI, H., 1980, Z. Metallkunde **71**, 376.
WILKINS, M.A. and SMITH, G.C., 1970, Acta Metall. **18**, 1035.
WINTER, A.T., 1974, Phil. Mag. **30**, 719.
WINTER, A.T., 1975, Phil. Mag. **31**, 411.
WINTER, A.T., PEDERSEN, O.B. and RASMUSSEN, K.V., 1981, Acta Metall. **29**, 735.
WITMER, D.E., FARRINGTON, G.C. and LAIRD, C., 1987b, Acta Metall. **35**, 1895.
WITMER, D.E., FARRINGTON, G.C. and LAIRD, C., 1987a, Acta Metall. **35**, 1911.
WOOD, W.A., 1958, Phil. Mag. **3**, 692.
WOODS, P.J., 1973, Phil. Mag. **28**, 155.
YAN, B., CHENG, A.S., BUCHINGER, L., STANZL, S. and LAIRD, C., 1986, Mater. Sci. Eng. **80**, 129.
YAN, B., FARRINGTON, G.C. and LAIRD, C., 1985, Acta Metall. **33**, 1533 and 1593.
YAN, B.D., HUNSCHE, A., NEUMANN, P. and LAIRD, C., 1986, Mat. Sci. Eng. **79**, 9.
YANG, C.Y. and LIU, H.W., 1980, Scripta Met. **14**, 785.
YOUSSEF, 1970, Phys. Stat. Sol. **A3**, 801.

Further reading

1) S. Suresh, "Fatigue of Materials," Cambridge University Press, 1991 (second edition in preparation).
2) M. Klesnil and P. Lukáš, "Fatigue of Metallic Materials," 2nd Edition, Elsevier, Amsterdam, 1992.
3) "Plastic Deformation and Fracture of Materials", ed. H. Mughrabi, Vol. 6 of "Materials Science and Technology", ed. R.W. Cahn, P. Haasen and E.J. Kramer (VCH, Weinheim, 1993) p. 509.
4) N.E. Frost, K.J. Marsh, L.P. Pook, "Metal Fatigue," Clarendon Press, Oxford, 1974.
5) A.P. Parker, "The Mechanics of Fracture and Fatigue", E. and F.N. Spon, London, 1981.
6) A.J. Kennedy, "Processes of Creep and Fatigue of Metals", J. Wiley & Sons, London, 1962.

CHAPTER 28

RECOVERY AND RECRYSTALLIZATION

R. W. CAHN

Department of Materials Science and Metallurgy
University of Cambridge
Cambridge CB2 3QZ, England

R. W. Cahn and P. Haasen†, eds.
Physical Metallurgy; fourth, revised and enhanced edition

1. Classification of phenomena and terminology

We shall be concerned in this chapter primarily with the mechanisms by which metals and alloys repair the structural damage caused by mechanical deformation, and incidentally with the resulting changes in physical and mechanical properties. These repair mechanisms are thermally activated and thus the deformed material has to be heated: any heat-treatment intended to reduce or eliminate deformation-induced damage is termed *annealing.*

The first distinction to be made is between *recovery* and *recrystallization.* The term *recovery* embraces all changes which do not involve the sweeping of the deformed structure by migrating high-angle grain boundaries. The deformed crystal (or polycrystalline structure) thus retains its identity, while the density of crystal defects and their distribution changes. A special form of recovery occurs when *residual stresses* resulting from metal-working processes are removed by heat-treatment. Where such stresses are *long-range* (i.e., are approximately uniform over distances large compared with the grain size) then their removal is termed *stress-relief.* (We have no space to discuss this last, practically important, topic further.)

In *recrystallization,* the crystal orientation of any region in the deformed material is altered, perhaps more than once. This results from the passage through the material of high-angle grain boundaries.

In *primary recrystallization,* a population of new grains is *nucleated,* often at the grain boundaries of the deformed material, and these then *grow* at the expense of the deformed structure until this is all consumed. Thereafter, grain boundaries continue to migrate, but more slowly: this stage of mutual cannibalism among the new population of grains is termed *grain growth.* Usually all boundaries migrate at roughly equal rates, with the result that at any stage the grains are roughly uniform in size: sometimes, however, migration is restricted to a minority of boundaries only, so that a few grains grow very large at the expense of all the rest. This is termed *secondary recrystallization;* alternative terms in use are *coarsening* and *exaggerated grain growth.*

Boundaries of individual grains in the original deformed structure are sometimes observed to migrate over short distances, leaving in their wake a "healed" crystal of the same orientation as the growing grain. The regions swept by the moving grain-boundary are substantially free of dislocations. This process is called *strain-induced boundary migration.* Another process which can take place in the deformed structure is *subgrain coalescence:* here small-angle (sub) boundaries between sub-grains disappear progressively by the climb and migration of the individual dislocations constituting the sub-boundaries.

The term *recovery* is also often applied in a different sense to the gradual return of physical and mechanical properties to the values characteristic of the undeformed condition, irrespective of the mechanism by which this return is effected. (It is used in this sense in ch. 18, devoted to point defects). In this sense, the yield stress, say, may recover principally as a result of primary recrystallization. The reference state is always the completely recrystallized (fully *annealed*) condition; the material then retains none of the original deformed grains.

2. *Recovery*

2.1. Recovery of electrical properties

Plastic deformation slightly increases the electrical resistivity. A great many investigations have been devoted to the stages by which the electrical resistivity returns to its fully annealed value. This is of interest both because it helps to disentangle the separate contributions made to the resistivity increase by dislocations and by deformation-induced vacancies, and because it helps to cast light on the complex mechanism of the damage caused by neutron irradiation in nuclear reactors; this damage also causes resistivity changes which anneal out in a different manner from those caused by plastic deformation. Further details will be found in ch. 18, §§ 2.2.3.3, 4.3.

2.2. Recovery of stored internal energy

When a piece of metal is plastically deformed, a certain amount of external work has to be expended in the process. A small fraction of this work is retained as stored energy, and on annealing the metal much or all of this is progressively released in the form of heat. The measurement of this released heat requires highly sensitive differential calorimeters, in which the specific heat of a deformed sample is compared over a range of temperature with that of an undeformed sample. These calorimeters either operate at steadily rising temperatures (CLAREBROUGH *et al.* [1955]) or isothermally (e.g., GORDON [1955], BELL and KRISEMENT [1962]). Similar instruments are commercially available as *scanning differential calorimeters*; they are now commonly used to study retained energy as a function of strain and strain rate (SCHÖNBORN and HAESSNER [1982]).

CLAREBROUGH *et al.* [1955, 1956] in a series of classic experiments determined the stages of the release of stored energy for copper and nickel. Figure 1 shows some of their results and correlates the energy release with the change of other physical properties. Pure copper gives off little energy during its recovery stage; only 3–10% of the total stored energy is released, depending on the amount of prestrain; during this stage, most of the vacancies generated by deformation have already diffused out. Most of the energy release and resistivity drop, and all of the hardness drop, are associated with recrystallization. When the copper contains impurities, the recrystallization temperature is raised and more energy is released during recovery. The temperature spectrum of energy release is also altered. – Two quantities are of particular interest. One is the *stored energy fraction*, the fraction of the expended work of plastic deformation (i.e., the area under the stress-strain curve) that is stored in the deformed metal; the other is the *recovered fraction*, the fraction of that stored energy that is released during progressive heating of the deformed metal in the recovery stages (i.e., before recrystallization has begun). Gottstein *et al.* [1975] have compared the stored energy fraction for copper crystals of different orientations deformed at 78K and found it to be 0.07 ± 0.01 for all orientations. The recovered fraction was ≈ 0.3; this is the proportion of the total stored energy that is released owing to point defect annihilation below ambient temperature. – A recent study of stored energy in deformed zinc crystals (ZEHETBAUER *et al.* [1991]) has established that here the stored energy fraction is much lower, only 0.01–0.02; the

References: p. 2492.

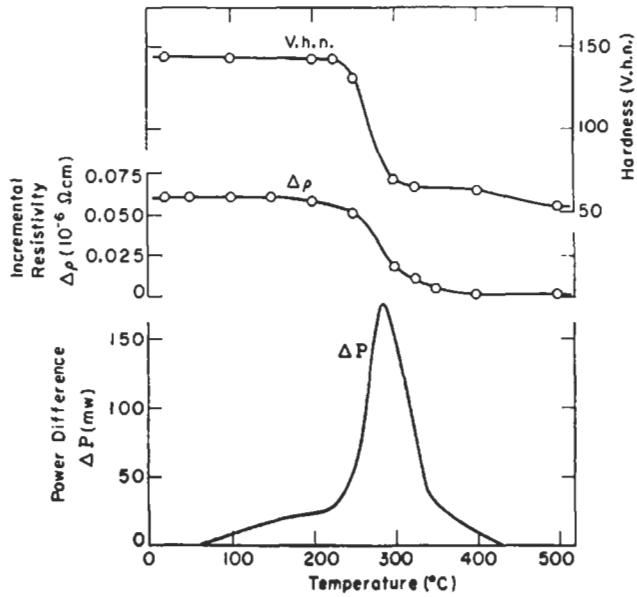

Fig. 1. Power differental, representing released energy, during the uniform heating of plastically twisted pure copper rod. Recovery of resistivity and hardness are also shown. (After CLAREBROUGH *et al.* [1955].).

investigators attribute this to the predominance of basal slip in zinc, which allows most dislocations to pass right through the crystal without being trapped.

An alternative, very sensitive technique for measuring stored energy (not, however, capable of determining a temperature spectrum) is liquid–solution calorimetry. As an example of the application of this technique, SMITH and BEVER [1968] showed that the stored energy in gold after deformation at 78 K is considerably higher than the energy stored after room-temperature deformation to the same strain. The difference is predominantly due to the fact that at 78 K point defects are retained, while at room temperature they anneal out in this metal. (The 78 K sample is held at that temperature until the moment of its dissolution in the liquid metal bath of the calorimeter.) The technique was most recently reviewed by BEVER *et al.* [1973]. Since then, RONNPAGEL and SCHWINK [1978] have developed a sensitive new calorimetric method which operates *during* plastic deformation.

An issue that has attracted a good deal of attention is the question whether any of the stored energy of deformation in copper can be released by true recovery or whether it is only by recrystallization that any of this energy can be released. Published findings differ: a recent set of experiments was by WOLDT and HAESSNER [1991], who established that in the early stages of progressive annealing of copper which had been deformed at room temperature, energy was released considerably faster than in proportion to the micrographically measured fraction recrystallized. This suggests a true recovery stage, but it was also found that this energy release by recovery was not associated with any reduction in hardness. This energy release could not be attributed to point defect

removal, since most of these defects are not stable at room temperature. Because of the low stacking-fault energy of copper, dislocation rearrangement by climb (i.e., cell formation, § 2.4.2) cannot happen, and so the source of this early energy release remains uncertain. Most probably, the finding is a statistical aberration: another recent study by RYDE *at el.* [1990], involving isothermal annealing of deformed copper, found heat release to be strictly proportional to the fraction recrystallized.

In nickel, vacancies do not diffuse as readily as in copper, and here the disappearance of vacancies is represented by the region below about 200°C. The second small peak represents a form of recovery of uncertain origin; BELL and KRISEMENT [1962] regard it as the beginnings of recrystallization. Evidence summarized by CLAREBROUGH *et al.* [1963], however, suggests that this stage is connected in some way with the presence of impurities which slow down the release of vacancies.

The energy released during the recovery of aluminum must be due entirely to dislocation rearrangement and the formation of a cell structure (§ 2.4.2), since vacancies will have migrated out of the lattice at room temperature. Two recovery stages have been found in this metal (VANDERMEER and GORDON [1963]) and have been identified with the processes termed meta- and ortho-recovery (§ 2.3).

Experimental results such as those in fig. 1 can be combined with theoretical values for density, resistivity and stored energy associated with individual vacancies and dislocations and estimates made of the concentration of these defects in the original deformed metal; the overlapping data permit useful cross-checks. Estimates vary somewhat according to the assumptions made. Thus Clarebrough *et al.* found that nickel compressed by 70% contained about 0.01% vacancies and over 10^{11} dislocations/cm^2. Bell and Krisement deduced a higher vacancy concentration and lower dislocation concentration. An uncertainty by a factor of 5–10 must be accepted in this kind of calculation; BROOM and HAM [1957], in an important early paper, discuss the matter in detail. SCHMIDT and HAESSNER [1990], studying high-purity aluminum heavily deformed at 78K, deduced a high vacancy concentration $\approx 0.1\%$, approximately equal to the thermal equilibrium concentration at the melting temperature. The stored energy fraction here was again $\approx$ 0.07. Figure 2 shows some data from this study: the separation between the point-defect peak at ≈ -70°C and the "dislocation peak" at ≈ -20°C is clear; the second peak is taken to include both the extensive dislocation rearrangement (recovery) and recrystallization proper. We discuss this further in relation to primary recrystallization. – A later study by the same authors (HAESSNER and SCHMIDT [1994]), with three grades of aluminum (99.99, 99.999 and 99.9999 % Al), has revealed a surprising feature: the stored energy fraction for small strains was highest for the purest grade of metal (0.06), only 0.02 for the least pure, and for all three grades diminished steadily as the strain was increased, down to ≈ 0.015. The drop was greatest for the purest grade, presumably owing to dynamic recovery.

It is probable (CLAREBROUGH *et al.* [1963]) that at least part of the energy release during the recovery stage is due to changes in the arrangement of dislocations, with or without the formation of a cell structure (§ 2.4.2), as well as some mutual annihilation of dislocations. This consideration complicates the calculation of vacancy and dislocation concentrations from calorimetric measurements. In nickel, the energy, E_{ry}, released in

References: p. 2492.

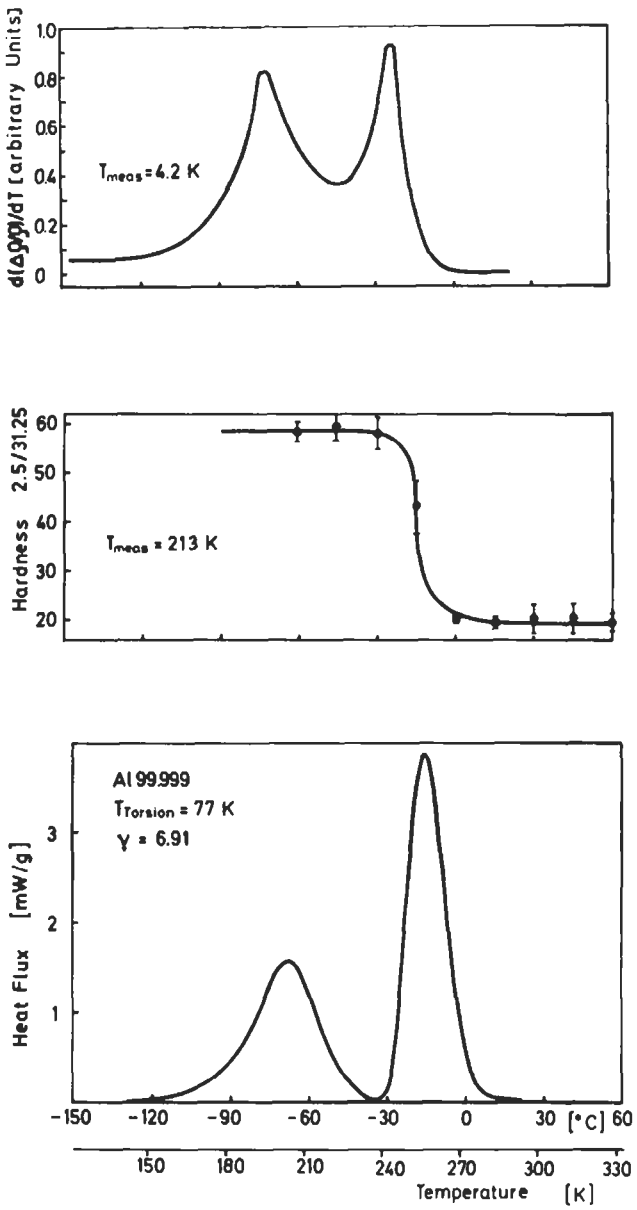

Fig. 2. Comparison of differentiated isochronal resistance (7 min anneals), hardness and heat flux as a function of annealing temperature. (99.999% aluminum, shear strain = 6.91) (after SCHMIDT and HAESSNER [1990]).

recovery is about equal to (Clarebrough *et al.*) or three times greater than (Bell and Krisement) the energy, E_m, released during recrystallization. In aluminum, the proportion of energy released during recovery is again about equal to that released in recrystallization. In fact, the fraction E_{ry}/E_m is an inverse function of the specific energy of stacking faults in the (111) plane of face-centred cubic metals (ch. 3, § 10.2; ch. 20, § 3.3); the lower the stacking-fault energy, the more difficulty dislocations have in *climbing* out of their glide planes (chapter 20, § 5.3) – an important process in recovery – and the more the recovery process is inhibited. In metals with very low stacking fault energy, such as copper, or gold, as we have seen, recovery is largely limited to the diffusion of vacancies out of the deformed metal; dislocations are not substantially rearranged or eliminated until recrystallization begins. (Nevertheless, it has been established by CHERNS *et al.* [1979] that after intense irradiation, when a large supersaturation of point defects is present, dissociated dislocations *can* climb by a special mechanism without the prior formation of a constriction – i.e., without the local disappearance of the stacking fault.

Some attention has been devoted to the stored energy of deformation in two-phase alloys. One recent study is by BAKER and LIU [1994], who compared high-purity copper crystals of the same orientation, with and without a dispersion of SiO_2 created by internal oxidation. Unlike some earlier investigators, they found no enhancement of stored energy on account of the presence of dispersed particles.

2.3. Recovery of mechanical properties

Figure 1, and tests on brass and nickel, shows that no drop in hardness accompanies stress relief or recovery in brass, copper or nickel. These are all metals with low stacking-fault energy, and therefore little climb and rearrangement of dislocations can take place, especially in brass or copper. Since the flow stress and hardness are a function of the concentration and disposition of dislocations, this immutability of dislocation structure prior to recrystallization implies that the mechanical properties also remain fixed. Slight dislocation movements have been postulated to account for considerable stored-energy release during the recovery stage in some metals such as silver (§ 2.2), but such rearrangement must be sufficiently slight to leave the yield stress unaffected. In other metals, of which aluminum and α-iron are the most important, dislocations can climb easily, and correspondingly these soften during a recovery anneal. Under favourable circumstances, the whole of the work-hardening may be recovered without the intervention of recrystallization. Thus a weakly deformed silicon-iron crystal* (DUNN [1946]), and likewise a very slightly deformed iron–aluminum polycrystal (LAWLEY et *al.* [1961]) recovers *completely* at 700–800°C; after heavier deformation, however, iron will recover only partially (fig. 3). Slightly deformed aluminum crystals can recover almost completely at 400–600°C (MASING and RAFFELSIEPER [1950]) while various investigators have found that aluminum single or poly-

* Iron–silicon alloy (3 wt% Si) is often used instead of pure iron in experiments on recovery and recrystallization since this alloy does not undergo a phase transformation on heating.

References: p. 2492.

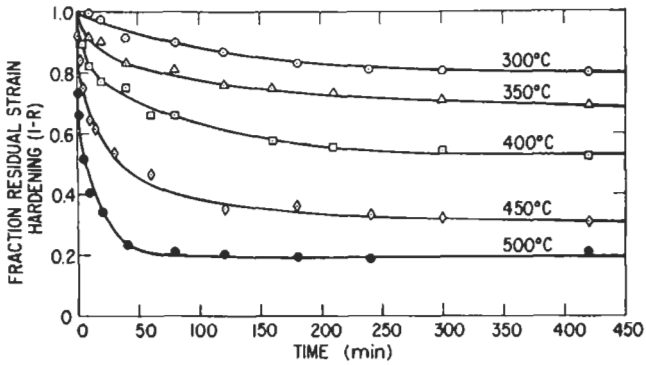

Fig. 3. Recovery kinetics of flow stress of identically strained iron samples at various temperatures. $(1-R)$ represents the fraction of flow stress *increment* which remains after discovery, i.e., $R=(\sigma_m-\sigma_r)/(\sigma_m-\sigma_o)$, where σ_m is flow stress after deformation, σ_r is recovered flow stress, σ_o is fully annealed flow stress. (After LESLIE *et al.* [1962].).

crystals will recover about half the work-hardening at 300–400°C. The general rule is: the larger the deformation, the smaller is the fraction R of the work-hardening that can be recovered by a standard recovery anneal. Crystals of hexagonal metals such as zinc or cadmium are exceptions: these can recover completely even after very large tensile strains by *easy glide* (ch. 19, § 2.2).

Figure 3 depicts softening isothermals for polycrystalline iron prestrained in tension. These show the form characteristic of recovery: the rate of softening is highest at the beginning and then steadily diminishes. Recrystallization-softening isotherms, on the other hand, have a sigmoidal shape: softening (when proportional to fraction recrystallized) is slow at first, accelerates and then slows once more (fig. 16, below, has this shape). The kinetics of recovery in their dependence on prestrain, prestraining temperature and annealing temperature are reviewed by PERRYMAN [1957].

Because of the considerable softening of aluminum by recovery, macrohardness measurements cannot be used to estimate recrystallization in this metal; the technique *can* however be used for copper, in which there is virtually no recovery-softening. For both metals, it is possible to make arrays of microhardness impressions; the histogram of microhardness values then consists of two groupings, one due to unrecrystallized (but possibly recovered) grains and the other to recrystallized ones (GORDON [1955] and LÜCKE and RIXEN [1968]). When this technique was applied to explosively deformed copper, which is intensely hardened but sluggish to recrystallize. then after partial recrystallization it was found that the unrecrystallized grains had somewhat reduced (i.e., recovered) microhardness (fig. 4) (CHOJNOWSKI and CAHN [1973]); the delay in recrystallization gives the copper time to experience some recovery.

Recovery of metals such as aluminum and iron can be considerably accelerated, and the total degree of recovery enhanced, if stress is applied during the anneal (e.g., THORNTON and CAHN [1961]). The stress must be large enough to generate some plastic creep strain, but not so large that the resultant work-hardening outweighs the enhanced

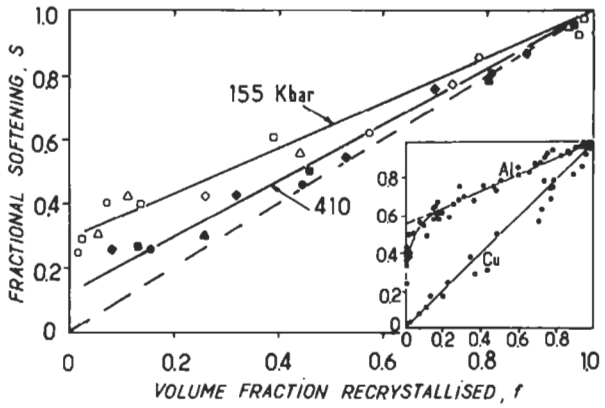

Fig. 4. Softening of copper previously subjected to shock deformation at two different levels of explosive pressure. Fractional softening, $(H_s - H_t)/(H_s - H_o)$, as a function of volume fraction recrystallized. H_s, H_t and H_o are hardness values as shock-deformed, annealed for t and before shock-deformation, respectively. Increasing temperatures in sequence: ◇ ○ □ △, solid symbols at 410 kbar, open symbols at 155 kbar. (After CHOJNOWSKI and CAHN [1973].) Inset: Curve similar to the above for cold-worked copper and aluminum (after LÜCKE and RIXEN [1968]).

recovery. Figure 5 shows stress-enhanced recovery of aluminum; the maximum creep strain generated during the stress-anneal was about 4% in these experiments. Even copper can be made to soften very slightly under these conditions, but the recovery is negligible in comparison with that in aluminum. This effect of stress is due to its accelerating influence on the climb of dislocations, which is an essential part of the recovery mechanism.

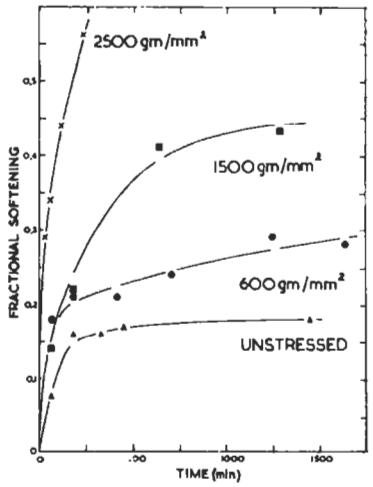

Fig. 5. Fractional recovery of polycrystalline aluminum prestrained 30% and annealed at 255°C (after THORNTON and CAHN [1961]).

References: p. 2492.

Recovery can also proceed *during* hot-working, whether it be rapid or slow. In this case it is denoted *dynamic recovery* *. Under conditions of rapid deformation, this process is again most pronounced in aluminum and α-iron, metals of high stacking-fault energy, in which dislocation climb is rapid. The details of subgrain morphology as affected by dynamic recovery have been extensively studied. McQUEEN and JONAS [1975] have shown that because of continuous growth of subgrains, or cells (§ 2.4.2) during hot-working (the subgrain equivalent of normal grain growth), some sub-boundaries disappear while others are born, and the outcome is that the mean subgrain misorientation remains constant at a few degrees, right up to high strains. TWISS [1977] has made a general study of mean subgrain diameter, d, during hot working, and found that d is related to the applied stress, σ, by:

$$\sigma = kd^{-n},$$

where $n \approx 1$ for many materials. (Twiss has proposed the subgrain size as a means of estimating the pressures that have acted upon rocks in the geological past — a form of "palaeopiezometer"; hence the publication in a geological journal.) Dynamic recovery, and its uses, have been reviewed by McQUEEN [1977].

If a specimen undergoing creep is allowed to recover by temporary removal of the stress, not only is the subsequent creep-rate enhanced but there is evidence that the rupture life may be restored to that characteristic of virgin metals (EVANS and WADDINGTON [1969]; HART and GAYTER [1968]). It appears that this "healing" is associated with the sintering-up and consequent disappearance of grain-boundary cavities formed by creep.

Not only creep strain but also fatigue strains (chapter 27) can assist recovery. Figure 6 shows the change of flow stress when a succession of predetermined strain cycles is imposed on an aluminum sample which had previously been unidirectionally cold-worked. The cold-worked samples recovered extensively under the influence of the fatigue cycles. Presumably, fatigue strain also assists dislocation climb. – A number of other studies have uncovered fatigue-induced recovery. Several of these are cited in a striking study by SCHRANK *et al.* [1985]. These investigators discovered substantial strain-softening (a form of dynamic recovery) in copper rods deformed at room temperature by rotary swaging: they showed that this mode of deformation imposes complex cyclic stresses on the workpiece.

Normally, recovery is measured in terms of the flow stress or hardness. A more fundamental approach is to measure the entire stress-strain curve both before and (on a duplicate sample) after recovery. Thus, fig. 7 shows measurements on aluminum polycrystals by CHERIAN *et al.* [1949]. The stress-strain curves, after recovery at different temperatures and for different periods, of samples prestrained to a standard strain, are compared with the stress-strain curves of samples whose straining has not been interrupted for a recovery anneal. Low-temperature recovery, termed *metarecovery*, is transient in the sense that eventually the sample resumes work-hardening characteristics

* The term "dynamic recovery" is also applied to the reduction of the rate of work-hardening in a stress-strain curve (even at room temperature) (ch. 21, §§ 7.2.4. and 7.3.4).

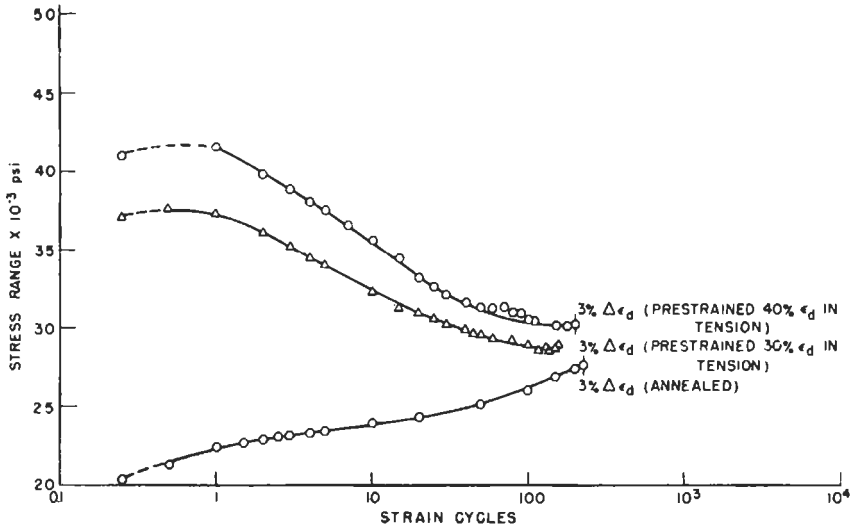

Fig. 6. Aluminum prestrained at 0, 30 or 40% in tension and recovered at room temperature under simultaneous imposed fatigue cycles over a 3% range of strain, $\Delta\varepsilon_d$. The stress range required to maintain this strain range adjusts itself automatically as the material softens or hardens. (After COFFIN and TAVERNELLI [1959].)

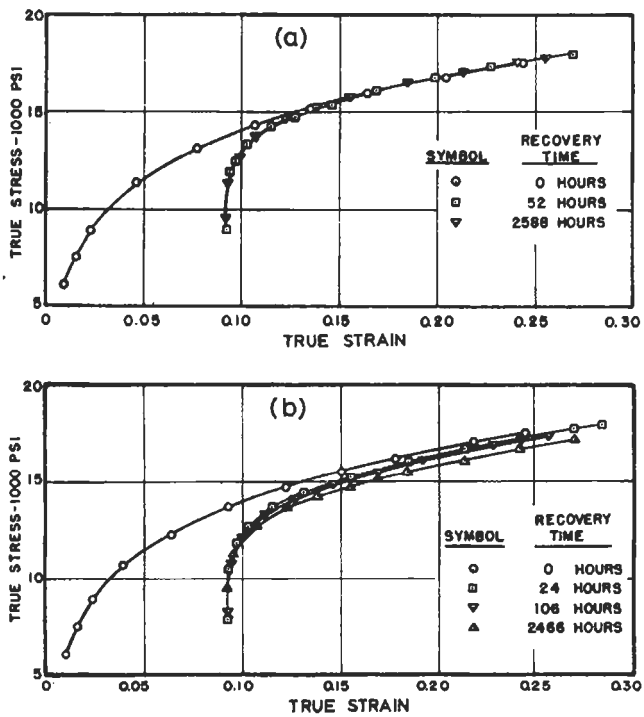

Fig. 7. Aluminum alloy deformed in tension and recovery-annealed (a) at 100°C (metarecovery) and (b) at 150°C (orthorecovery) (after CHERIAN *et al.* [1949]).

References: p. 2492.

identical to those of the sample which has not been annealed; the two stress–strain curves join up. When the temperature of the recovery anneal is sufficiently raised, its effect becomes permanent and the stress–strain curves remain distinct. This is *orthorecovery.* Generally, the work-hardening rate of a recovered metal is greater than it was before recovery at the same total strain.

Mechanical properties of deformed metals or alloys such as flow stress, hardness and ductility normally recover monotonically towards the values characteristic of the fully annealed state. However, there are exceptions: thus brass, copper–aluminum solid solutions (KOPPENAAL and FINE [1961]) and some other similar alloys are subject to slight *anneal-hardening* when annealed at temperatures too low to cause recrystallization; this phenomenon has been thought to be connected with the creation of short-range crystallographic order in the solid solution (ch. 3, § 11.3). WARLIMONT [1979] has found large levels of anneal-hardening in a range of nickel-base solid solutions and found that the magnitude of the effect is well correlated with atomic-size misfit between solvent and solute. He deduces that anneal-hardening (negative recovery as it were) is due to segregation of solute to dislocations, and he holds this to be true for copper alloys also.

2.4. Recovery of microstructure

2.4.1. Polygonization and subgrains

An especially simple form of structural recovery is observed when a crystal is bent in such a way that only one glide system operates, and is subsequently annealed. The crystal breaks up into a number of strain-free *subgrains,* each preserving the local orientation of the original bent crystal, and separated by plane *sub-boundaries* which are normal to the glide vector of the active glide plane. This process is termed *polygonization,* because a smoothly curved lattice vector in the crystal turns into part of a polygon.

The polygonized structure can be seen particularly clearly in fig. 8a, which shows subgrains in a sharply bent and polygonized sapphire (aluminum oxide) crystal, as seen by transmitted polarized light with an appropriately oriented polaroid analyser in front of the eyepiece. The different shades of the subgrains indicate their differing orientations: only those subgrains are seen which have sufficient "extinction". It should be noted that in spite of the sharp curvature of the original crystal, the sub-boundaries are straight. This is in accord with the elastic theory of *bend-gliding* (the process by which a crystal simultaneously glides and becomes bent), which specifies that the bent glide planes have the form of the involute of a cylinder, as indicated in fig. 8b.

In polygonized metals, the sub-boundaries can be revealed by etching; they are normally etched in the form of dense rows of pits (fig. 9) (CAHN [1949]). To understand this, it is necessary to consider the polygonization process in terms of the dislocation distribution. When a crystal undergoes plane gliding, then it is possible for all dislocations, both positive and negative, to pass right through the crystal and out at the surface. To a first approximation this is what happens in easy glide (ch. 21, § 7.2.1). However, in bend-gliding as exemplified in fig. 8b, a number of excess dislocations of one sign must remain in the crystal to accommodate the plastic curvature. This is most readily

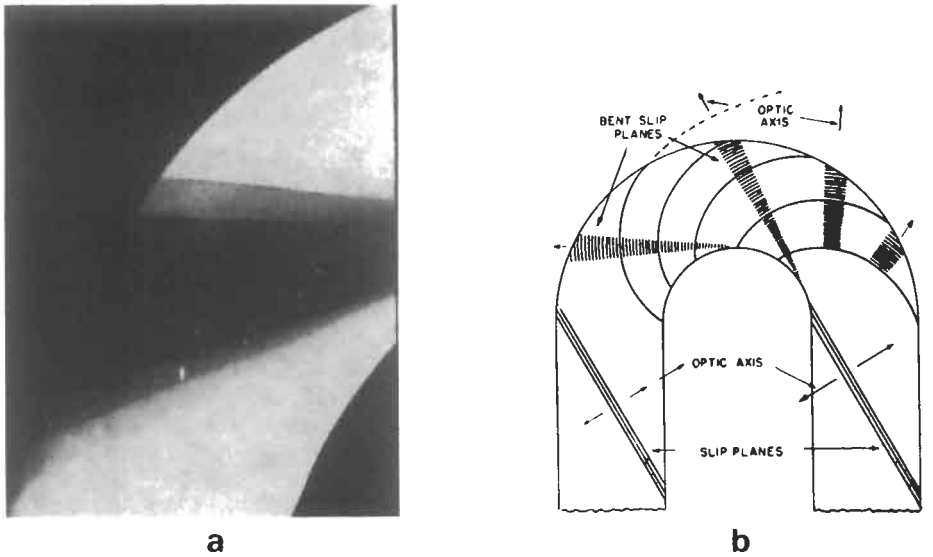

Fig. 8. (a) Single crystal of sapphire bent at 1800°C and then annealed 10 min at 2000°C. Photographed by transmitted polarized light. (b) Diagrammatic representation of plane bending, by glide on a single set of planes. Normals to the curved planes define the positions of the optic axis. (After KRONBERG [1955].)

understood by considering the large difference in dimension between the outer and inner surfaces of a bent crystal. This strain implies the presence of many extra lattice planes near the outer surface, which terminate at edge dislocations within the crystal. The density of these excess dislocations is $1/Rb$, where R is the mean radius of curvature

Fig. 9. Bent, annealed and etched single crystal of aluminum, showing sub-boundaries, 70×. (After CAHN [1949].)

References: p. 2492.

and b is the Burgers vector. When now the bent crystal is annealed, these dislocations rearrange themselves in walls or tilt *boundaries* normal to the Burgers vector, because in this position they largely relieve each other's elastic strain field. This can best be appreciated in terms of the Read–Shockley equation (SHOCKLEY and READ [1950]) for the energy, E_b, of a tilt boundary:

$$E_b = E_{0\theta}\,(A - \ln\theta).$$

This equation, based on the theory of the elastic interaction of edge dislocations, and valid for values of θ up to several degrees, shows that dislocations constituting a tilt boundary progressively relieve each other's energy as θ increases; if there were no such relief then, since the dislocation density in a small-angle boundary $\propto \theta$, E_b would be proportional to θ and there would be no driving force for polygonization. (See also ch. 20, § 6).

Figure 10a shows the structure of a tilt boundary in more detail.

An incipient tilt boundary exerts a small force on isolated dislocations some distance away, sufficient to cause them to glide into the vicinity of the boundary plane. In fact, incipient *glide-polygonization* has been observed even before annealing begins. Each dislocation must then *climb* (ch. 20, § 5.3) sufficiently to find a niche in the boundary. This process requires thermal activation and determines the rate of polygonization. The metastable end state is a tilt boundary with a uniformly spaced array of edge dislocations whose spacing h is given by the relation: $b/2h = \tan(\theta/2)$ or, approximately, $b/h = \theta$, where θ is the relative tilt angle of the two subgrains (fig. 10a). This relation has been verified by counts of etch pits on tilt boundaries, particularly in germanium and silicon, where each etch pit locates an individual dislocation.

Later stages of polygonization take place by the progressive merging of pairs of adjacent sub-boundaries; the driving force for this comes from the progressive reduction of the boundary energy *per dislocation* in the boundary, as the misorientation angle θ increases. The speed of this process (sketched in fig. 10b) is also limited by dislocation climb, since the dislocations in the two merged boundaries will not be uniformly spaced unless some dislocations climb.

A detailed survey of the mechanism and kinetics of polygonization is found in a review by HIBBARD and DUNN [1957]. The elastic theory of tilt boundaries and the consequential properties of such boundaries are treated in detail by LI [1961].

2.4.2. Cell formation

The distribution of dislocations in a piece of plastically deformed metal is not uniform. This was first recognized in a classic research by GAY *et al.* [1954]: they deduced from X-ray microbeam diffraction experiments that grains in various deformed polycrystalline metals consist of subgrains or *cells*, the interiors of which have a comparatively low dislocation concentration while the small-angle cell boundaries are packed with dislocations. During subsequent recovery treatments, the cell boundaries (often called *cell walls*) sharpen and then the cells progressively grow larger while their interiors become further drained of dislocations. The cells, both before and after recovery, are normally roughly equiaxed – i.e., their dimensions a nearly the same in all

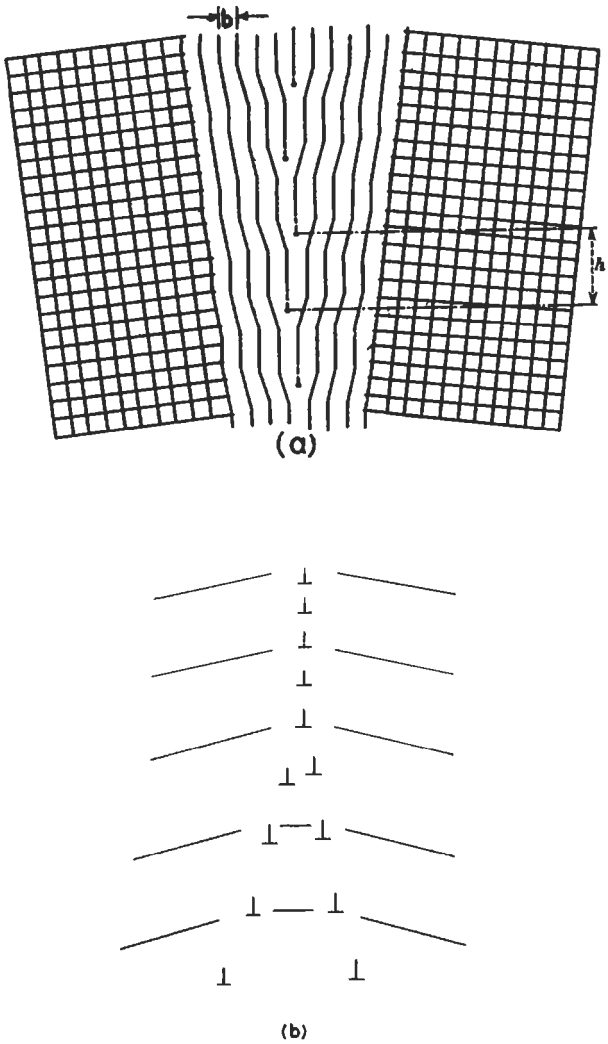

Fig. 10. (a) Structure of a tilt boundary. The two subgrains are mutually tilted through an angle θ. (b) Tilt boundaries meeting at a "triple points". The tilt axis relating the orientations of the two subgrains is normal to the plane of the figure.

directions — although under some circumstances, especially, the deformation of single crystals, cells may be elongated and arranged in bands. Cell formation is characteristic of metals that glide on more than one glide system, so that dislocations with several different Burgers vectors are available to form cell walls. The sharpness of the cell walls formed during plastic deformation varies from metal to metal. There is a clear correlation between stacking-fault energy — and hence the degree of dissociation of dislocations and their ability to climb — and the sharpness of cell walls. Alloys such as α-brass or

References: p. 2492.

austenitic stainless steel after deformation have only the most rudimentary cell structure (dislocation tangles with regions of low dislocation density), copper and silver have recognizable cells with thick tangled boundaries, nickel and especially aluminum have better defined cells which rapidly sharpen and grow during annealing after deformation.

The mechanism by which the diffuse cells present after deformation sharpen and grow is a complex form of polygonization. Since dislocations are present on several glide planes (or, if on a single glide plane, with different glide vectors), the cell walls cannot be simple tilt boundaries. However, where the misorientation across cell walls has been examined, as in zinc (CAHN *et al.* [1954]), it turns out that they are effectively very similar to tilt boundaries. In zinc, each wall contains at least two families of mixed edge-cum-screw dislocations, but so arranged that the misorienting effects of the screw components cancel and the tilt axis is still parallel to the dislocation lines lying in the wall. There is some evidence that cell walls in aluminum have a similar structure. Since a variety of dislocations are available, cell walls have a number of different orientations relative to the crystal axes and can thus completely enclose individual cells.

Further evidence that cell boundaries are similar to sub-boundaries produced by polygonization comes from the observation that the former, like the latter, often appear in the form of rows of etch pits on an etched section. Thus, fig. 11 shows a family of etched cells in annealed aluminum; these have been formed by slight accidental distortion during heating. When aluminum is substantially cold-worked and then given a recovery-anneal, again sharply delineated cells are formed. Since the cold-worked lattice is more sharply distorted, misorientations across cell walls are larger and it becomes convenient to reveal them by an etching process which produces colour contrast by white polarized light (ch. 10, § 2.2.4).

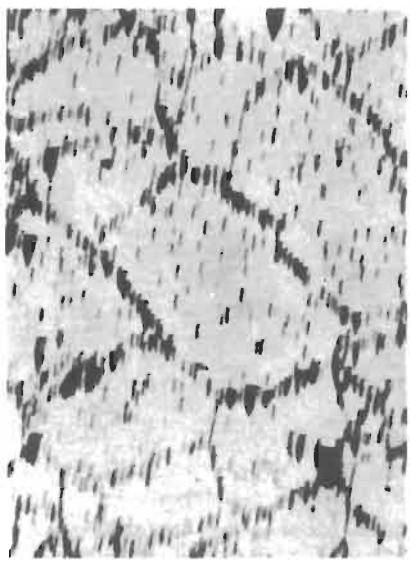

Fig. 11. Subgrains in annealed aluminum sheet. 100×. (After LACOMBE and BEAUJARD [1947].).

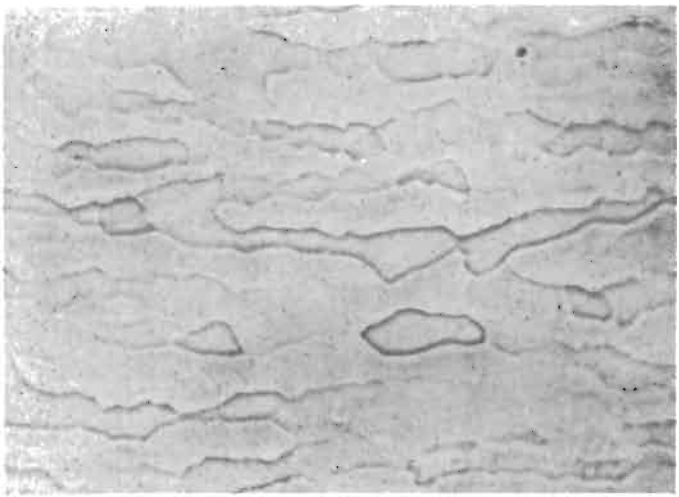

Fig. 12. Cell structure in an aluminum crystal cold-rolled to 20% reduction and annealed at 350%C for 20 s (from PERRYMAN [1954]).

Figure 12 shows such a cell structure in cold-rolled and annealed aluminum.

A number of clear electron micrographs of sub-boundaries in α-iron have been published; sub-boundaries in this metal frequently consist of two-dimensional *networks* of dislocations.

Cell structures are formed most effectively during creep (chapter 22, § 6.1) and fatigue. Here the applied stress both produces the deformation and helps the dislocations to climb into the cell walls; since this is the rate-limiting factor, cell-formation is accelerated. The growth of some cells at the expense of others, which follows on the first formation of sharply defined cell walls, is akin to the growth of polygonized subgrains by the merging of pairs of tilt boundaries (fig. 10b) and is similarly rate-limited by dislocation climb; here again, the effect of stress is to accelerate cell growth.

Cell walls are far more mobile than ordinary large-angle grain boundaries. LACOMBE and BEAUJARD [1947], in a classic study, verified that in aluminum the cell morphology was completely rearranged during an anneal too short to alter the *grain* morphology detectably. This well-established fact is paradoxical, because measurements of the mobility of tilt boundaries of different misorientations, θ, in the range 2–3° (VISWANATHAN and BAUER [1973a]) have established that the smaller θ, the lower the mobility. It may be that mobility reaches a minimum for some value of θ smaller than 2° and again becomes large for misorientations of a few minutes, although no reason for this is apparent. An alternative possibility is that in copper, with its low SFE, the migration of small-angle boundaries is severely inhibited by sluggish climb; whereas in aluminum, with high SFE, small-angle boundaries might move much more easily.

It may be that cell walls, in any metal, move easily under the influence of internal stresses in each grain; it is well established that small-angle tilt boundaries move readily under the influence of an appropriate shear stress (creating thereby a small plastic strain).

References: p. 2492.

This notion has been discussed by EXCELL and WARRINGTON [1972] and is consistent with the observation by CAHN *et al.* [1954] on subgrain behaviour in polycrystalline zinc. On this view, the mobility of very small-angle sub-boundaries (cell walls) under purely thermal activation (i.e., in the absence of stress) may indeed be vanishingly small, but the presence of a suitable small stress may increase apparent mobility by orders of magnitude. This would only be true for pure tilt boundaries, and not for other kinds of small-angle boundaries.

The recovery of the yield stress or hardness of a metal during progressive annealing after plastic deformation is almost certainly correlated with the formation and growth of a sharp cell structure. The interiors of the cells become partially drained of dislocations at an early stage of the process, so it is most unlikely that it is the dislocation concentration in the cells, rather than the cell size, which determines the strength.

We have seen above (§ 2.3) that in hot-worked materials, where the mean mutual misorientation of neighbouring subgrains remains approximately invariant with strain, the subgrain diameter, d, is related to the applied stress, σ, by $\sigma = kd^{-n}$, where $n \approx 1$ for many materials. This relationship was first observed by BALL [1957], who studied aluminum deformed in creep. It seems that in creep or hot-working, rather than the subgrain size defining the strength, the applied stress defines the subgrain size.

For cells formed by recovery from cold work, the subgrain size *does* apparently determine the recovered flow stress. A general relationship has been established:

$$\sigma = \sigma_0 + k_y d^{-m}.$$

When $m = 0.5$, this reduces to the *Hall–Petch relationship*). In the cold-worked, unrecovered state, when cells are ill-defined, $m \approx 1$, but as recovery proceeds, subgrains grow and misorientations increase, m drops towards 0.5. By contrast, in hot-worked metals, m remains close to 1 throughout, as its also does for very small subgrains in recovered metals (MCQUEEN [1977] and THOMPSON [1977]).

Other aspects of the relationship between yield stress and cell structure include:

(a) Metals of low stacking-fault energy, in which dislocations cannot readily climb, do not form sharp cell structures (though diffuse structures are observed). Correspondingly, no recovery of yield stress is observed.

(b) A stress applied during recovery anneal accelerates recovery of mechanical properties and, as we have seen, it also accelerates the growth of the cell structure.

(c) For aluminum, VANDERMEER and GORDON [1973] have proposed that meta-recovery corresponds to the stage at which many dislocations have left the cell interiors but the cell walls have not yet begun to sharpen, while orthorecovery corresponds to the stage when cell walls become more sharply defined and the cells grow; more recent work by HASEGAWA and KOCKS [1979] on aluminum has attributed metarecovery to the sharpening of the cells already created during cold work, whereas orthorecovery is wholly associated with cell growth. A similar correlation has been observed in the case of iron (LESLIE *et al.* [1963]).

(d) A further complication in relating cell size to properties derives from the observation (DILLAMORE *et al.* [1972]) that the mean subgrain size and misorientation within various grains in rolled iron depends on the orientation of individual grains

relative to the rolling plane and direction. This was found to have a pronounced effect on the subsequent formation of annealing textures (§ 3.6).

A general survey of subgrain structures in metals subjected to diverse treatments has been published by DOHERTY [1978].

2.4.3. Quantitative theories of the recovery kinetics of yield strength

At a time when cell formation was still under dispute, early models of recovery were based on the notion that uniform dislocation networks (of the kind revealed in silver and alkali halides by "decoration"), if initially fine enough, would gradually coarsen and thereby soften the material, since the size of the links of the network would determine the operating stress of a Frank–Read source in the network. This idea emerged from a treatment by FRIEDEL [1964] in his celebrated textbook on dislocations: He remarks that "crystals smaller than a few microns seem to be without dislocations; the Frank network of macroscopic crystals seems to be of the order of a few microns. This suggests that *smaller networks are unstable, and grow rapidly by diffusion at high temperatures under the action of their line tension*" (italics in original). His simple quantitative treatment is based on the idea that the total line energy of the network dislocations, for a mean link length of $<\lambda>$, is proportional to $1/<\lambda>^2$, and the driving force for coarsening is inversely proportional to $<\lambda>$, so that $d<\lambda>/dt = 1/<\lambda>$. He estimated the proportionality constant in terms of the self-diffusivity and the jog concentration in the network, and obtained a figure which was of the right order of magnitude.

MCLEAN [1968] made this treatment the basis of a theory of softening by recovery, focusing on the inverse relationship shown by Orowan between flow stress and $1/<\lambda>$. McLean's interest was primarily in creep, which was perceived as being determined by a balance between work-hardening and dynamic recovery (see, for instance, COTTRELL and AYTEKIN [1950]). This approach was gradually developed on the basis of McLean's model, for instance by GITTUS [1974]. The history of this recovery theory and its application to "recovery-creep" has recently been reviewed by SHI and NORTHWOOD [1993].

More recently, and moving away from a specific preoccupation with recovery-creep, theories have been based not on a more or less uniform dislocation network but rather on the formation of a population of cells, as discussed above. BLANK [1989] has examined the formal kinetics of such a process, and compares it with other processes such as the tempering of martensite and the intermediate stage of sintering of ceramics; he concludes that in each instance, the master equation for the property in question, (P), is $P = C/t^m$, with $m = \geq 1$, which leads to a logarithmic kinetics, $P = A + C \ln t$. It was ÅSTRÖM [1956] who pointed out that Cottrell and Aytekin's model, mentioned in the preceding paragraph, and MASING and RAFFELSIEPER's earlier [1949] model of recovery, mentioned in § 2.3 above, in fact both gave a recovery kinetics with a logarithmic form. It seems, then, that formally the network approach and the cell approach yield similar kinetics.

There has been little formal consideration of the process of mutual annihilation of dislocations of opposite sign, which proceeds in parallel with network growth and/or coarsening of the cell structure. One attempt at predicting the kinetics of such annihilation was by SANDSTRÖM [1977]; the form of these kinetics is different from those discussed by Blank. It is not at all clear how important annihilation is in relation to the

other dislocation recovery processes.

One difficulty about the network model is that it would predict a measure of recovery of mechanical properties even in a metal like copper which, because of its low stacking-fault energy, cannot form cells on annealing. It is possible that the disagreement between different investigators on whether or not the flow stress of copper can recover slightly ahead of recrystallization is linked to the coarseness of the dislocation network after deformation, and this will in turn be linked to purity and the degree of deformation.

Recently, computer simulation has begun to be applied to the understanding of recovery. HUMPHREYS [1992] treats a two-dimensional network of cells with variable sizes and orientations. Cell coarsening is assumed to follow $V = M P$, where V is the velocity of a particular cell boundary, M is its mobility and P is the driving pressure, taken as proportional to the local boundary curvature. M is a problem, because there is little information on the dependence of mobiliuty on misorientation; he assumes that $M = K.\theta^n$, where $n = 0.2$. Figure 13 shows the simulated kinetics of mean subgrain size and mean cell misorientation. The process slows down because the driving force dimishes as the mean misorientation increases. Humphreys did not relate this simulation to the kinetics of reduction of the yield strength: this has, however, been attempted in an important theoretical treatment by NES and SAETER [1995]; see also NES [1995].

2.4.4. Effect of prior recovery on textures

It has recently been established (ENGLER *et al.* [1994]), in a study of rolling and annealing textures in cold-rolled Al–Mg–Mn alloy, that during the very early stage of annealing, when no metallographic evidence of recrystallization can yet be seen, the rolling texture *sharpens* considerably. The texture index, an approximate measure of texture sharpness, increases by about 20% at this stage, and then, once visible recrystallization has started and a new annealing texture begins to form, the texture index drops again. It is unclear whether this is a genuine recovery effect or whether measurement of the deformation texture offers a more sensitive indication of the early stages of recrystallization than does metallography. If this is so, it is hard to see why the texture index should first increase and then drop again as recrystallization proceeds.

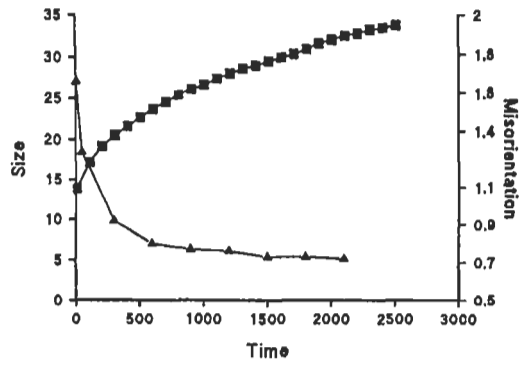

Fig. 13. Effect of annealing on subgrain size and mean sub-boundary misorientation in a computer model (after HUMPHREYS [1992]).

3. Primary recrystallization

3.1. Laws of recrystallization

A very large body of experimental information concerning primary recrystallization, spanning more than seventy years, can be summarized by the following six laws (BURKE and TURNBULL [1952]):

1) Some minimum (critical) deformation is necessary to initiate recrystallization.

2) The smaller the degree of deformation, the higher is the temperature required to initiate recrystallization.

3) Increasing the annealing time decreases the temperature required for recrystallization.

4) The final grain size depends chiefly on the degree of deformation and to a lesser degree on the annealing temperature, normally being smaller the greater the degree of deformation and the lower the annealing ternperature.

5) The larger the original grain size, the greater the amount of deformation required to give equivalent recrystallization temperature and time.

6) The amount of deformation required to give equivalent deformational hardening increases with increasing temperature of working and, by implication, for a given degree of deformation a higher working temperature entails a coarser recrystallized grain size and a higher recrystallization temperature. To this, two more laws can now be added:

7) New grains do not grow into deformed grains of identical or slightly deviating orientation, or into grains close to a twin orientation (TIEDEMA *et al.* [1949]).

8) Recrystallization is slowed if the temperature of deformation is raised while leaving the prestrain the same, but is accelerated if, at the higher temperature, the metal is strained to the same *stress* (GOTTSTEIN *et al.* [1989]).

A ninth law, not strictly concerned with primary recrystallization, is:

9) Continued heating, after primary recrystallization is complete, causes the grain size to increase.

These qualitative laws can be understood in a general manner if they are examined in terms of the component processes of primary recrystallization, i.e., nucleation of the new grains and their growth. Metallographic evidence has established that nuclei are formed in regions where the dislocation concentration and strain-hardening are greatest. A certain local concentration of elastic energy is required to bring about a nucleus, hence the requirement of a threshold strain (law 1). Since the process of nucleation is thermally activated, a longer annealing time and higher temperature increase the probability of producing a nucleus, and correspondingly reduce the threshold strain (laws 2 and 3). The need for thermal activation also accounts for the *induction period* often observed before recrystallization becomes detectable.

The grain size depends on the balance between the nucleation and growth rates; normally the nucleation rate increases faster with increased work-hardening, but the growth rate increases faster with rising temperature (hence law 4). Figure 14 is a micrograph from the *Atlas Metallographicus* published in 1927, which shows a range of grain sizes underneath a Brinell ball impression in a bar of pure otherwise strain-free iron,

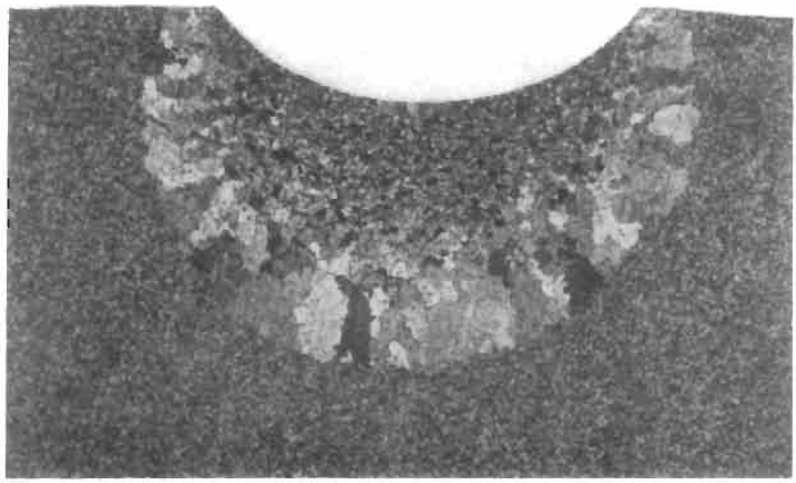

Fig. 14. Wrought low-carbon mild steel, annealed and impressed by a Brinell ball (12 mm diameter), then annealed 30 min at 750°C. The grain size is largest just inside the zone beyond which the critical strain for recrystallization has not quite been attained (after HANEMANN and SCHRADER [1927], courtesy M. Hillert).

after annealing at 750°C for 30 minutes. The grain size rapidly increases further from the face of the impression, which implies decreasing strain. Just beneath the largest grains, there is no recrystallization. This illustrates law 1 and the first half of Law 4. Law 5 is attributed to the fact that most nuclei form at or near grain boundaries, so that a smaller original grain size enhances nucleation, while law 6 results from the reduced dislocation concentration resulting from deformation at elevated temperature. In fact, the acceleration of recrystallization at a given annealing temperature, as the temperature of previous deformation is lowered, can be dramatic. (A general survey of the influence on recrystallization of the conditions of deformation can be found in the book by Cotterill and Mould, see *Further reading* list at the end of this chapter.)

If the threshold strain for recrystallization is only just exceeded then very few nuclei will form, and this can be exploited for the preparation of quite large metal single crystals. Normally, a lightly strained fine-grained sample is heated at a very slowly rising temperature, or alternatively passed slowly through a sharp temperature gradient. In either case, one nucleus will form and grow rapidly enough to consume other potential nucleation sites before they become activated. This method has been applied principally to aluminum, lead, silicon-iron, and some other less common metals. It cannot normally be applied to the hexagonal close-packed metals since the twins which are produced on deformation are too effective as nucleation sites. Copper, silver and gold cannot be grown in this way, because the formation of annealing twins leads to multiple orientations. High purity may be an obstacle, because rapid recovery may impede recrystallization; this is especially a problem with zone-refined iron and aluminum (see below).

The preparation of single crystals by recrystallization is reviewed by AUST [1963] (metals) and THORNTON [1968] (alloys). An early account of this approach and some of its attendant problems can be found in a book by ELAM [1935].

The variation in grain size of a recrystallized metal as a function of prestrain and temperature is apt to be quite complex. This information is sometimes gathered in a single perspective figure, a *recrystallization* (or *Czochralski) diagram.* Figure 15a shows such a diagram for electrolytically refined iron (BURGERS [1941]); some other diagrams are a good deal more complex. A recrystallization diagram is at best approximate: for instance, where new grains nucleate at the boundaries of the deformed grains (VANDERMEER and GORDON [1959] and ENGLISH and BACKOFEN [1964]), the final grain size must evidently depend on the grain size before deformation. Perhaps because of such inadequacies, recrystallization diagrams have gradually fallen out of use in recent years.

A further complication arises when a material is strained in more than one mode, successively, or when strain is inhomogeneous (for instance, on account of friction between a rolled sheet and the rollers). LINDH *et al.* [1993] have recently demonstrated that such "redundant", or auxiliary, deformation is less effective in promoting recrystallization than is the principal mode of strain. This problem can be overcome by using a variant of a recrystallization diagram: thus fig. 15b , from their work, shows the recrystallization temperature plotted, not as a function of strain but instead as a function of (work-hardened) flow-stress. It then does not appear to matter by what path that flow stress was attained.

3.2. Kinetics of primary recrystallization

A great deal of effort has been expended on the analysis of the isothermal kinetics of recrystallization, in the hope that this would cast indirect light on the mechanisms involved. In particular, it was hoped in this way to derive separate values for the nucleation rate, N, and the growth rate, G. Since these quantities themselves are often a function of time and G may be anisotropic, and moreover the analysis must allow for the mutual interference of growing grains in the later stages of recrystallization, this type of analysis has rarely been fruitful. Most investigators agree on a resultant equation of the form

$$X_v = 1 - \exp\left(-Bt^k\right) \tag{1}$$

where X_v is the volume fraction recrystallized, t is time and B and k are constants. Values of k are most commonly in the range 1 to 2; the exact value is sure to vary with the experimental material and circumstances (ch. 15, § 2.4.1). A low value of k implies one- or two-dimensional recrystallization, i.e., new grains growing in the form of rods or platelets. Figure 16 shows typical recrystallization kinetics for isothermal recrystallization, obtained here by the use of quantitative metallography (chapter 10, § 7).

Some kinetic experiments have indicated a nucleation rate which is low at first and then increases, passing through a maximum, while others show a constant rate or else indicate that all nuclei form at zero annealing time; the last of course implies the presence of preformed nuclei. There is more agreement about growth rates; these either

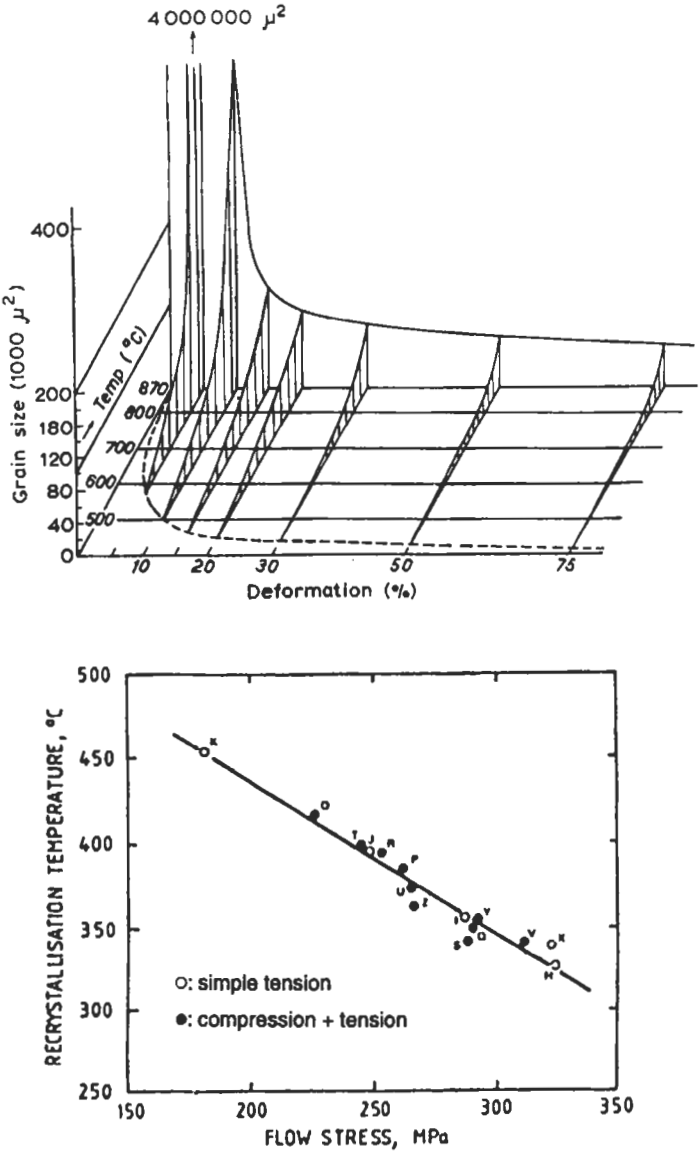

Fig. 15. (a) Recrystallization diagram for electrolytically refined iron annealed 1 h (after BURGERS [1941]). (b) Recrystallization temperatures deduced from differential scanning calorimetry measurements of OFHC copper plotted as a function of final stress at end of the prestraining programme (after LINDH *et al.* [1993]).

remain constant or else slowly diminish as growth continues. Here again, the variation with time and temperature of the constituent processes depends on the purity of the material (a few parts per million of iron dissolved in aluminum drastically reduce the

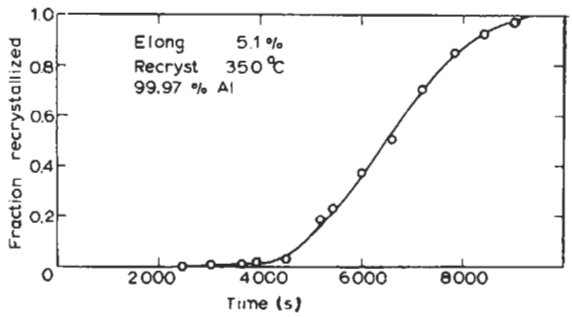

Fig. 16. Recrystallization kinetics for aluminum deformed 50% and annealed at 350%C (after ANDERSON and MEHL [1945]).

value of k, RISSER and CHENAL [1994]), degree of deformation and grain size, and generalizations are dangerous.

One study has been particularly informative, in that the purity of the sample was systematically varied and careful metallographic and calorimetric studies were combined. VANDERMEER and GORDON [1959, 1963] studied the isothermal recrystallization of zone-refined polycrystalline aluminum, with or without small additions of copper, after deformation by 40%. The kinetics for the pure metal followed eq. (1), with $k=2$. All new grains were nucleated in clusters at sites along grain boundaries of the deformed structure. Only a small proportion of the total grain-boundary area produced nuclei, but all those nuclei began to grow at the very beginning of the anneal; there was no induction period. New grains, long and narrow, all grew at a steady rate into the adjoining grains.

If impurity was added or the annealing temperature lowered, or both, deviations were found from the kinetics of eq. (1); these were attributed to a slowing down of the growth of new grains, and this was confirmed by direct measurement. The retardation was attributed to recovery: the authors' own isothermal calorimetric experiments showed that recovery and recrystallization normally overlap in aluminum. Figure 17 shows schematically the kind of calorimetric results obtained, and how they can be decomposed into constituent processes. When the component due to recrystallization has been separated out, it can be used to calculate a recrystallization isotherm like that of fig. 16; the metallographically and calorimetrically derived isotherms then agree well. (If a prolonged low-temperature recovery anneal precedes the recrystallization anneal, the two stages of fig. 17 no longer overlap; there is less energy left to recover when the test temperature is reached, and moreover recrystallization is retarded since the driving force for it has been reduced by the preceding recovery.)

For a given annealing temperature, the deviations due to added impurity are the more pronounced, the greater the impurity content, while for a given composition they are greater for lower annealing temperatures. This correlation is interpreted in terms of the different activation energies for recovery and recrystallization, and the differing effect of copper additions on these activation energies; the activation energy for recrystallization is increased more than that for recovery. As copper is added, therefore, both recovery

References: p. 2492.

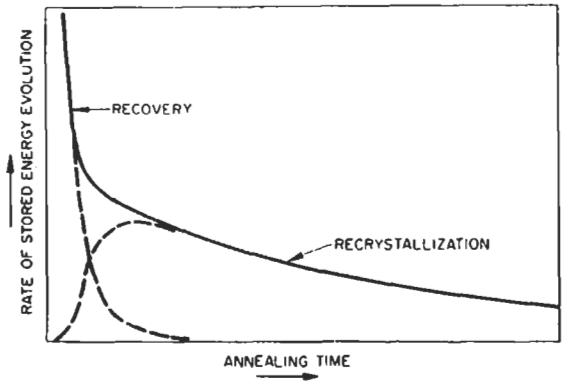

Fig. 17. Schematic illustration of the overlapping of recovery and recrystallization in the isothermal evolution of stored energy (after VANDERMEER and GORDON [1963]).

and recrystallization are slowed down, but recrystallization is slowed down more; as the temperature is lowered, recrystallization is slowed more than recovery since it always has the higher activation energy.

The retarding influence of recovery on recrystallization may go so far as to inhibit growth altogether, especially at the low temperatures which must be used for starting the growth of single crystals. Difficulty has been reported for very pure aluminum, and single crystals of iron cannot be made at all by straining and annealing if the iron is too pure; an intentional carbon contamination must then be added before growth, and removed by gas-phase reaction after the crystal has been grown (TALBOT *et al.* [1957]). Similarly, MONTUELLE [1955] found that superpure (zone- refined) aluminum can only be recrystallized, to make single crystals, if it is doped with 0.04 wt % iron or lithium: but the high purity cannot then be restored. If these observations are taken in conjunction with Vandermeer and Gordon's results, which show that under appropriate experimental conditions impurities depress recovery *less* than they do recrystallization, it can be seen how complex the interaction of recovery and recrystallization is. – A number of recent studies have been made of the recrystallization of highly pure aluminum (though zone-refining is no longer used), e.g., the study already cited by Haessner and Schmidt. A study was performed by KASSNER *et al.* [1994], on metal slowly deformed at 78K to very high strains, and indicates that dynamic recrystallization softens the metal during strain at that low temperature. If the strained metal is taken above room temperature, recovery is so fast that recrystallization is inhibited.

It is not possible to generalize as to recrystallization mechanisms from a single experimental analysis such as Vandermeer and Gordon's. For instance, ANDERSON and MEHL [1945], in a classic study in which they studied polycrystalline aluminum rather less pure and much less heavily deformed than in the work just described, reached the conclusion that the nucleation rate varied with time, that there was an induction period for nucleation, that the growth rate did not diminish with time and that growth of new grains was isotropic. If the amount of strain is even smaller, no proper nuclei arise at all

and some existing grains grow into their neighbours; this is the phenomenon of strain-induced boundary migration, described in § 3.3.

VANDERMEER [1995] describes in detail an analytical, statistical approach to modelling the kinetics of recrystallization.

3.3. Nucleation of primary grains

Few topics in physical metallurgy have generated so much and such prolonged argument as has the nature of the nucleation process in recrystallization; the debate is about sixty years old. HAASEN [1993] has aptly described it as "the eternal struggle"! Only studies undertaken in the past few years have by slow stages been able to resolve the problem and now (1995) there are still occasional mutterings of discord. The difficulty in resolving it has stemmed from two distinct sources. The first is that some investigators rely wholly on micrographic methods of examining the early stages of recrystallization, while others prefer to argue back from detailed studies of the formation of annealing textures. The main disgareement has been between these two groupings, but for the first group of scientists, there has also been the problem that it is very difficult to observe a tiny nucleus (or even a grain which has barely progressed beyond the nuclear stage) under a microscope. Optical microscopy lacks resolution, and electron microscopy normally suffers from a small field of view, so that the statistical chance of hitting on a nucleus is small. There is also the intrinsic problem that, in the words of VATNE and NES [1994], "a successful nucleation event destroys the evidence of the nucleus as well as its neighbourhood". This complex of fundamental difficulties was to some extent bypassed by the use of three techniques:

1) Optical microscopy coupled with the transmission Kossel method of X-ray diffraction (FERRAN *et al.* [1971]).

2) Transmission electron microscopy at 100 kV, using a sample thinned in such a way as to provide a large thinned area, combined with the use of Kikuchi lines as a means of determining local orientation (FAIVRE and DOHERTY [1979]).

3) High-voltage transmission electron microscopy, which provides a large field of view in three dimensions (RAY *et al.* [1975]).

From these studies it became clear that the mechanism of nucleation is intimately linked with the structure of the deformed metal, and specifically with the degree of heterogeneity of orientation *within* each deformed grain. This crucial factor was left out of account during the long debate, which had tended to concentrate on the relationship between the (supposedly uniform) orientation of a deformed grain and that of the recrystallized grain born in it.

Any theory of nucleation must account for the following experimental generalizations:

a) Nuclei form preferentially in regions where the local degree of deformation is highest, such as grain boundaries, deformation bands, inclusions, twin intersections and free surfaces. The rather unexpected conclusion, that strain density and work-hardening just below the free surface of a deformed sample is particularly high and leads to a high nucleation rate, has been proposed (KIMURA *et al.* [1964]) but subsequently was questioned (MUGHRABI [1977]). Figure 18 illustrates nucleation in a region of high disloca-

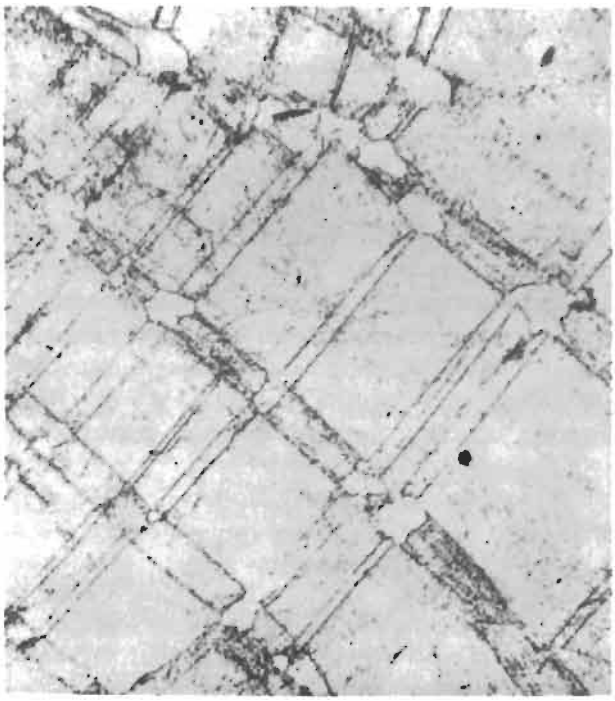

Fig. 18. Nucleation of primary grains at intersection of deformation bands, in a crystal of titanium–molybdenum alloy lightly deformed and annealed. The deformation bands are regions of high dislocation density. 75×. (After SCHOFIELD and BACON [1961].)

tion concentration, seen at low magnification.

b) The nucleation rate increases sharply with increasing strain, above a minimum critical amount*.

c) There is extensive and conclusive evidence that the orientations of nuclei have a statistical connection with the orientations of the deformed regions in which they form, at any rate for moderate degrees of deformation. Formerly, this relationship was deduced indirectly from a comparison of deformation and annealing macrotextures (a process fraught with pitfalls, since no information is available about the orientations of particular regions); recently, it has been established by direct metallographic/diffraction methods.

d) Since, as we have seen, small-angle boundaries are apt to have a very small mobility, a nucleus cannot grow into material of nearly identical orientation.

The stages of development of the modeling of nucleation over the past half century have recently been concisely reviewed by HUTCHINSON [1992].

The older models of nucleation are as follows:

* However, the proclivity to recrystallization depends not only on the amount of strain but also on its nature. RICHARDS and WATSON [1969] have found that cold-swaged iron recrystallizes much more sluggishly than iron cold-rolled to the same strain, and they attribute the difference to the more uniform distribution of stored energy after swaging.

1) *The classical nucleation (or fluctuation) model,* either homogeneous or heterogeneous. This is now recognized to be impracticable, because of the very small driving forces available and the high energy of the large-angle boundary which has to be created. Local elastic strains of the order of 20% over a region some nanometres in diameter would be needed, and this level of stram is not credible. Furthermore (DOHERTY [1974]) because of the small driving force, critical nuclei containing $\approx 10^{10}$ atoms would be required and the probability of so many atoms being combined in the appropriate geometry by classical nucleation is entirely negligible. *It follows logically from this that some preexisting feature must provide the nucleus, and this excludes random orientations of recrystallization nuclei.*

2) *The growth of a locally polygonized reglon of the deformed structure* (a model worked out by CAHN [1950], COTTRELL [1953] and BECK [1954]). The idea was that polygonization would remove the strain energy from a small region which is more severely bent than its environment. The viable nucleus so created would be misoriented relative to its surroundings and can thus grow.

3) A related model based on the hypothesis of *coalescence* of neighbouring subgrains, by the "evaporation" of the dislocations constituting the sub-boundaries between them. (This process must involve both glide and climb.) The enlarged subgrain thus formed, much larger than its neighbours, could grow at their expense – i.e., act as a nucleus. This model was originally advanced by HU [1962, 1963].

4) A model based on the process of *strain-induced boundary migration* (SIBM), in which a subgrain within a deformed grain grows into its neighbour, forming a bulge which has the orientation of the source grain, but is largely free of dislocations. This ballooning subgrain can act as a nucleus. SIBM was first reported by BECK and SPERRY [1949, 1950] and subsequently studied by BAILEY and HIRSCH [1962].

5) A recent model (HUTCHINSON [1992]) based on the idea that material adjacent to *a high-angle boundary, created directly by the deformation process itself,* acts as nucleus, without the need for the processes mentioned in 2) and 3), just above; 5) can be regarded as a variant of 4).

Model 1 having been eliminated, this leaves four contenders. Electron microscopy has proved the validity of models 3 and 4. Model 2, from pre-electron microscopy days, has been overtaken by more precise models based on electron-micrographic observations. The sharply bent lattice region invoked in model 2 is, in fact, most commonly the edge of a deformation band and thus, (as proposed in model 5), it may in fact not be necessary for any polygonization-like process to intervene before a nucleus can become viable, at least in heavily deformed metal. *What is vital is for the potential nucleus to have a sharply defined, high-angle boundary with the adjacent matrix.*

Studies of compressed aluminum polycrystals by FERRAN *et al.* [1971] and BELLIER and DOHERTY [1977] by the Kossel X-ray method, and of rolled or compressed iron by INOKUTI and DOHERTY [1977, 1978], have shown the extreme fluctuation of orientation in the deformed grains. Variations of up to about 45% within a single grain were found after only 40% strain, over distances of often only a few microns. *Deformation bands* are formed, regions which begin by rotating differently from neighbouring regions when deformation starts; such rotational instability, once under way, continues to progress.

References: p. 2492.

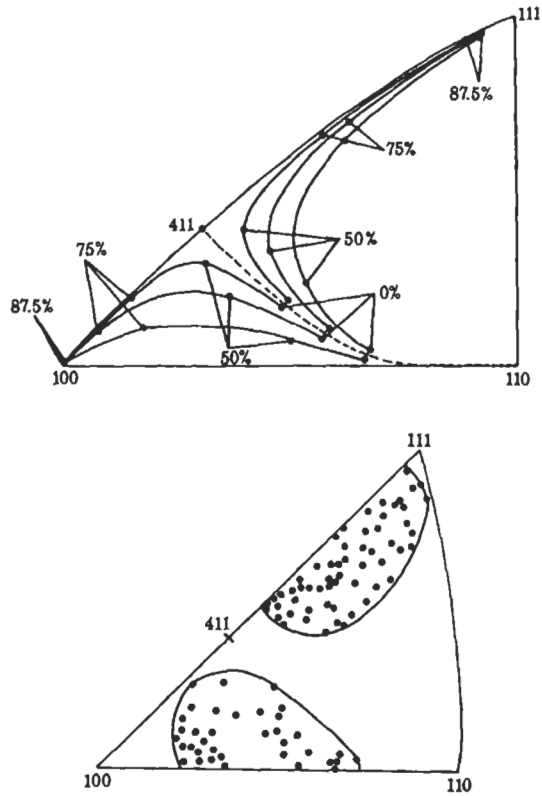

Fig. 19. (a) Slip rotation paths for axisymmetric compressive deformation of a body-centred cubic metal, deforming by pencil glide. Three different initial orientations are indicated, with rotations corresponding to various compressive strains for each initial orientation. (After DILLAMORE and KATOH [1974].) (b) Orientations of various positions in a single grain of polycrystalline iron deformed 40% in compression. Orientations were determined by individual X-ray Kossel diffraction photographs. The two groups of orientations correspond to the matrix and to a series of deformation bands. (After INOKUTI and DOHERTY [1977].)

Figure 19a, due to DILLAMORE and KATOH [1974], shows theoretically predicted orientation changes during uniaxial compression of iron for grains with initial orientations close to the (dashed) instability locus; figure 19b shows corresponding orientations of regions inside and outside deformation bands, as observed by Inokuti and Doherty. While the rotations found by the latter are greater than the computed rotations (presumably individual grains differ in their degree of mean strain), yet the pattern of orientation change is as predicted. Even in the absence of such deformation bands, with their sharp boundaries and extreme orientation gradients, there are still very large orientation gradients, more especially near grain boundaries. (See informative review by HUGHES [1995]).

The studies of annealed specimens, reported in the papers cited at the beginning of the preceding paragraph, showed that new grains are nucleated either at grain boundaries

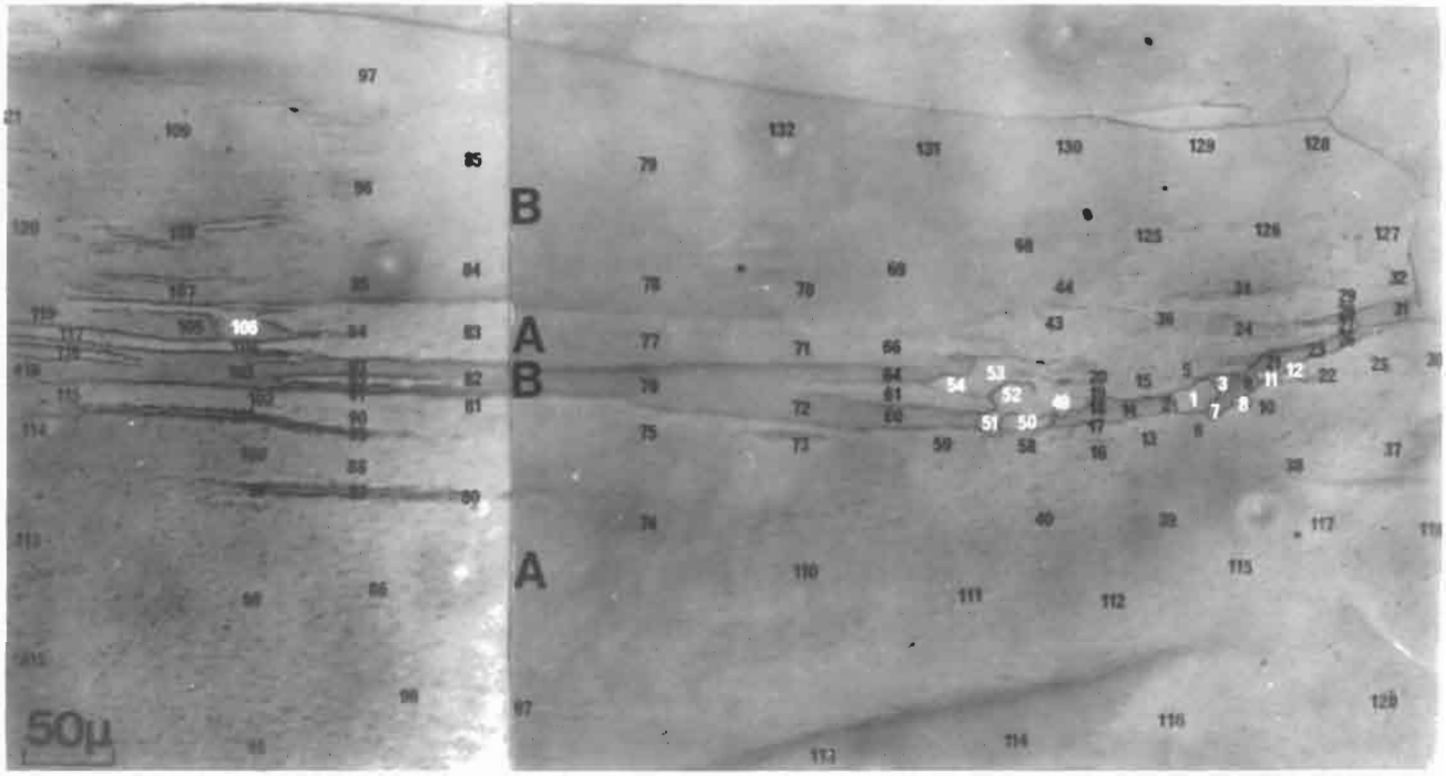

Fig. 20. Part of a large iron grain compressed 40%. The compression axis was vertical in the plane of the micrograph. The sample, which was annealed for 2 h at 500°C and nital-etched, has broken up into two interpenetrating matrix bands, A and B. New grains, numbered in white, have formed at the deformation bands. (After INOKUTI and DOHERTY [1978].)

References: p. 2492.

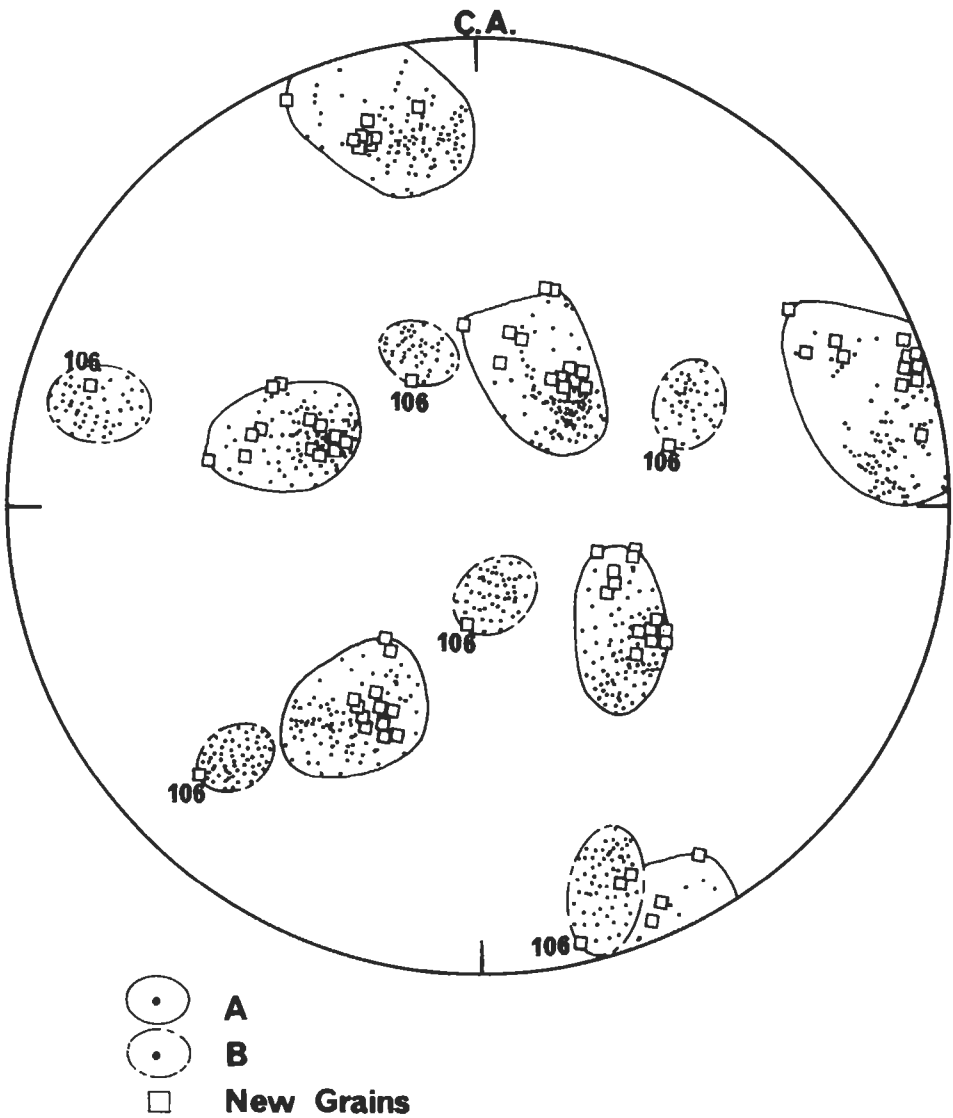

Fig. 21. Stereographic projections of the positions marked in fig. 20. New grain 106 has an orientation within the spread of matrix band B while all the other new grains have an "A" orientation. (After INOKUTI and DOHERTY [1978].)

or at deformation-band limits (which may be characterized as "artificial grain boundaries"). Figure 20 shows a large grain in a compressed iron sample, and fig. 21 is the corresponding stereogram. This shows the distinct orientation clusters in the matrix and deformation bands (black numerals in fig. 20), and of the recrystallized grains after

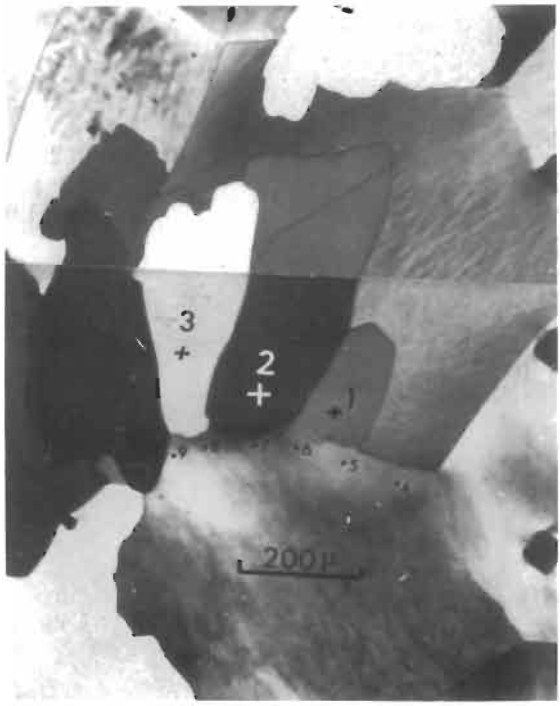

Fig. 22. Cluster of new grains seen at a grain boundary in high-purity aluminum compressed 20% and annealed for 11 min at 395°C. The three new grains were shown by transmission Kossel X-ray diffraction to come from within the orientation spread of the lower grain (4–9), into which they have *not* grown. (After BELLIER and DOHERTY [1977].)

partial recrystallization (white numerals). Figure 22 is a micrograph showing new grains growing from a grain boundary in compressed aluminum. Here again, the original stereogram shows that the new grains have orientations within the spread of the neighbouring deformed region.

Extensive studies of this kind (reviewed by DOHERTY and CAHN [1972] for the earlier studies and, very fully, by DOHERTY [1978] and by DOHERTY *et al.* [1995] for the later ones) all showed the same thing. A subgrain grows slowly at first, either at a grain boundary or at the limit of a deformation band, but if it becomes large enough it will grow fast: it will be able to do so if (and only if) its immediate environment differs in orientation by about 12° or more (the different studies in fact established a critical misorientation which ranged from 9–18°, according to the metal and degree of deformation.

The tendency of a subgrain to grow if it is larger than its neighbours arises from the associated changes in total sub-boundary energy of the configuration. This can be understood by reference to fig. 23, due to DILLAMORE *et al.* [1972]. Fig. 23a represents the limit region of a deformation band with its long narrow subgrains, and at the centre is a larger-than-average subgrain. The orientation gradient vertically is small, while that

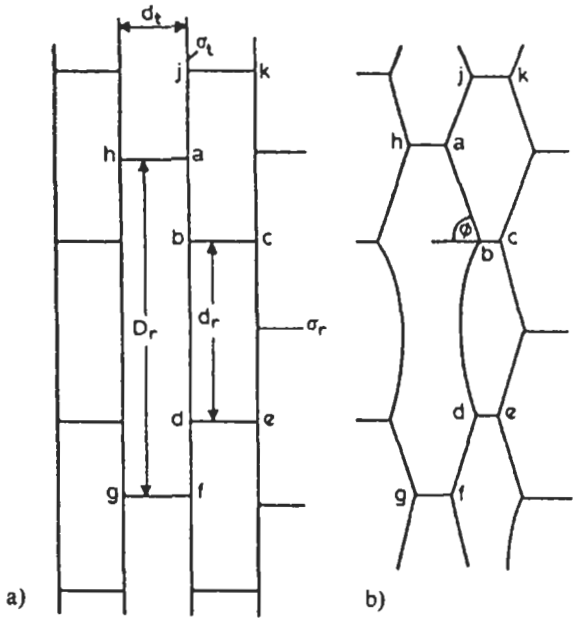

Fig. 23. Schematic representation of a deformation band, (a) as formed by deformation, (b) relaxed to the equilibrium angles on annealing (after DILLAMORE ([1972]).

horizontally, across the band limit, is large. Therefore the specific interfacial energy of the vertical subboundaries (σ_t) is greater than that of the short horizontal boundaries (σ_r).

On annealing, the structure changes to that shown in fig. 23b. The equilibrium configuration at "b" is given by

$$\cos\phi = \sigma_r/2\sigma_t \tag{3!}$$

The large subgrain, abdfgh, can continue to grow if "b" and "c" come into contact before ϕ has decreased sufficiently for the above equilibrium condition to be satisfied. For this to happen, the inequality

$$D_r > \tfrac{4}{3}\left[d_r + d_t\left(\frac{4\sigma_t^2}{\sigma_r^2} - 1\right)^{1/2}\right] \tag{4!}$$

must be satisfied; that is to say, the central subgrain must be sufficiently long.

Just this type of growth was observed in early recrystallization studies from deformation bands (also termed "transition bands") in silicon–iron (WALTER and KOCH [1963], HU [19631). Figure 24 shows an instance of an early stage of nucleus formation at the limit of such a band.

Another kind of deformation band which, unlike those in iron, *runs across a number of grains*, are those found in brass and other copper alloys (GREWEN *et al.* [1977]) and

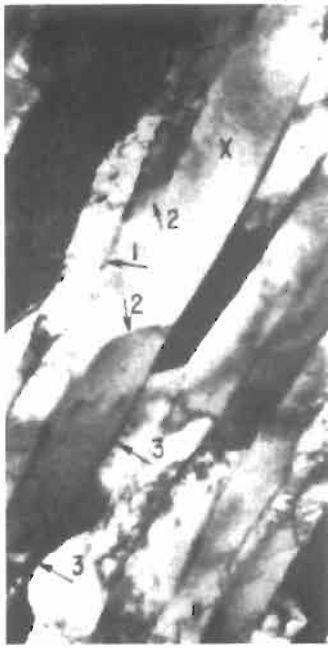

Fig. 24. Electron transmission micrograph showing origin of a recrystallized grain within a transition band, in a silicon–iron crystal rolled 70% and annealed 5 min; at 700°C subgrains are growing to form nuclei at 1, 2 and 3. 50000×. (After WALTER and KOCH [1963].)

DUGGAN *et al.* [1978]). These are likewise the site of nucleation during annealing (HUBER and HATHERLY [1979]). Research into this kind of situation has proliferated during the past few years. Research by Lee, Duggan and Smallman (e.g., LEE, SMALLMAN and DUGGAN [1993]) has worked out in detail the morphology of these deformation bands in copper or brass rolled, typically to 85% reduction or more, the mechanics of their formation and the subsequent behaviour of banded metal on annealing. Figure 25 , from a very detailed paper by SMALLMAN and LEE [1994], shows the sharp discontinuities in orientation in such banded metal, revealed by means of a "crystallographic" etch. (Such a microstructure is a long way, indeed, from the old presumption of uniform orientation in each grain in a deformed metal, and indeed the configurations seen in the figure amount to "deformation-generated grain boundaries"!) The cited papers devote much space to a discussion of how cube texture arises in annealing such metal. That will be briefly discussed below (§ 3.6); here we merely outline the conclusions which have been drawn from this research about the nature of the recrystallization nucleus. For more details, the two cited papers should be consulted. Regions just inside a deformation band act as nucleus and grow into the neighbouring matrix, without necessarily any preliminary recovery stage; the idea of a preexisting nucleus which is "ready to go", as set out by HUTCHINSON [1992], is gaining favour.

References: p. 2492.

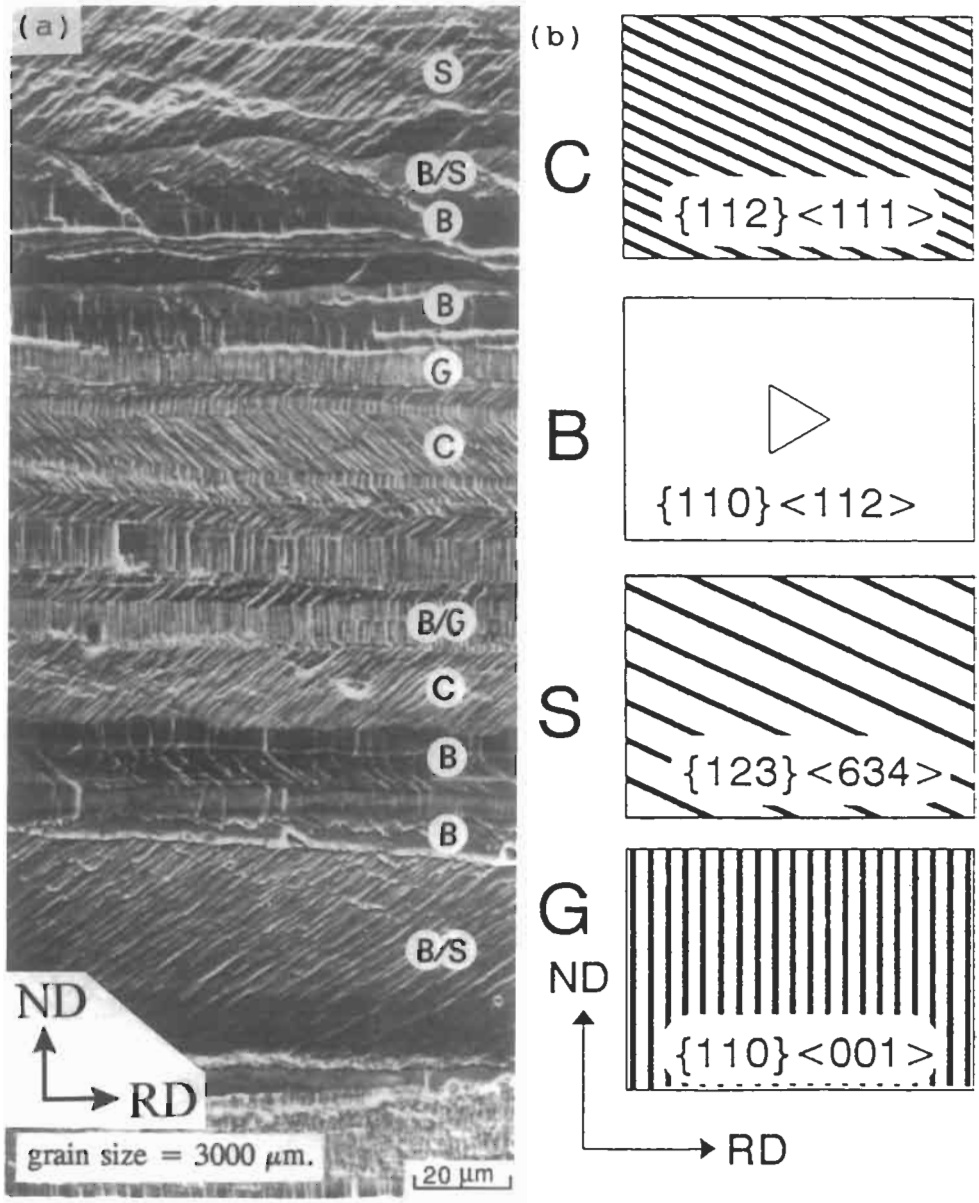

Fig. 25. (a) Scanning electron micrograph of a crystallographically etched longitudinal section of coarse-grained copper (3 mm grain size) after 85% reduction by cold rolling. (b) Schematic diagram of etch patterns in some ideal rolling texture components (after SMALLMAN and LEE [1994]; courtesy R. E. Smallman).

VATNE and NES [1994] have analysed in detail how the existence of a *local* minimum in the plot of grain-boundary energy versus misorientation can enhance the growth rate of such a predetermined nucleus vis-à-vis other, differently oriented nuclei, but only while the new grain is still very small. Once it grows larger, they demonstrate, the preference disappears. The resultant model for texture formation is termed *microgrowth selection* among nuclei of predetermined orientation.

Much of the above-mentioned research has been on copper and brass, but Vatne and Nes's theory springs from detailed analysis of texture formation in aluminum alloys (HJELEN *et al.* [1991], ENGLER *et al.* [1992]). It is quite clear from all this research that nuclei are indeed regions of the deformed microstructure that grow preferentially, with a pronounced microgrowth selection in the early stages of recrystallization. This seems now to be widely agreed (e.g., DUGGAN *et al.* [1993]).

We now have the situation that in some very heavily deformed metals, "nuclei" (deformation-generated grasin boundaries) appear to be ready for action in the as-deformed state; no rearrangement of dislocations is necessary in these cases. In other metals, and generally when the deformation is relatively light so that no large-angle "deformation-generated boundaries" are formed, potential nuclei still have to be rearranged during the first stage of annealing. – For such instances, the question remains by what mechanism the crucial subgrains in fig. 23 and 24 achieve their initial growth, so that they become larger than their neighbours.

Two rival models have been in competition: *strain-induced boundary migration* (SIBM) and *coalescence.* A micrograph showing coarse SIBM in aluminum is shown in fig. 26, and its interpretation by BECK [1954] in fig. 27 . An example from somewhat more recent work is shown in fig. 28 (some of the "tongues" originate from above or below the plane of section and thus appear as islands). The tongues were demonstrated to share the orientation of a nearby region of the deformed structure, below the central band limits.

Coalescence, as originally proposed by Hu, has repeatedly been observed by TEM, mostly in aluminum. Sub-boundaries within a subgrain have been photographed in a state

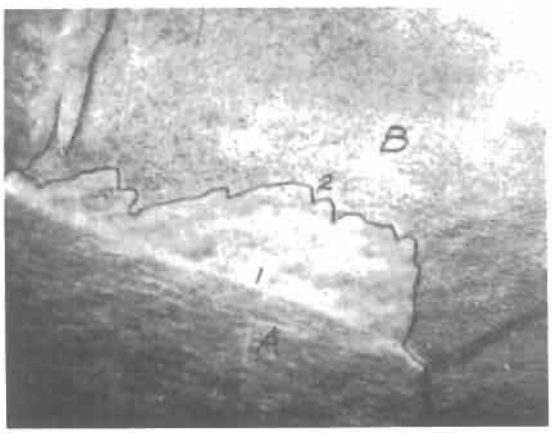

Fig. 26. Strain-induced boundary migrations. 75×. (After BECK and SPERRY [1950].)

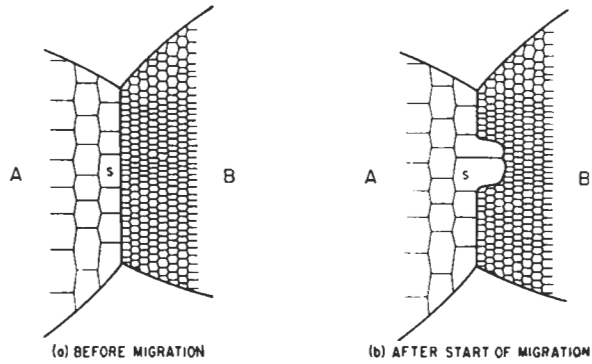

Fig. 27. Model for strain-induced boundary migration (after BECK [1954]).

of partial disappearance. Clear examples are to be found in papers by FAIVRE and DOHERTY [1980] and by JONES *et al.* [1979]. HU [1981] has reviewed the state of knowledge concerning coalescence. Jones *et al.* established very clearly that sub-boundary dislocations link continuously with dislocations in an adjacent high-angle grain boundary; the disappearance of the sub-boundary entails a detectable rearrangement of the dislocations in the grain boundary, and indeed, it was found that grain boundaries act more efficiently as sinks than as sources of dislocations. This is the precondition of coalescence – i.e., the "evaporation" of sub-boundaries. Figure 29 shows a model

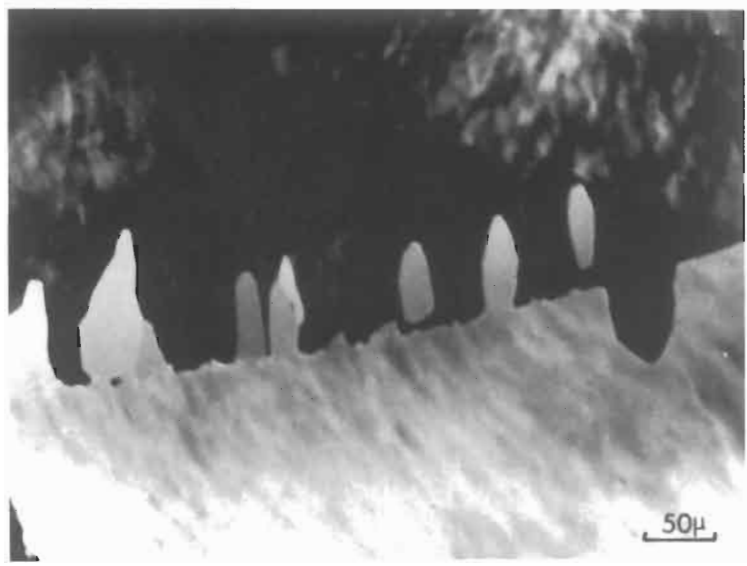

Fig. 28. Aluminum compressed 40% and annealed for 1 h at 328°C, showing strain-induced boundary migration into both grains. The direction of growth is not always parallel to the plane sectioned, as can be seen from the two white "bulges" that do not contact the lower parent grain in the section seen. (After BELLIER and DOHERTY [1977].)

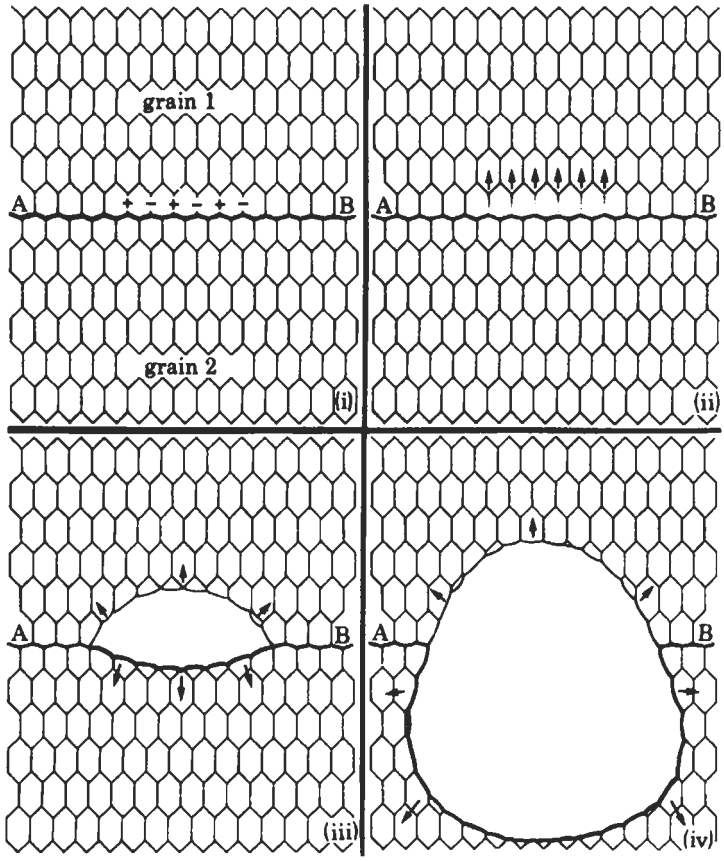

Fig. 29. Nucleation involving subgrain coalescence (after JONES *et al.* [1979a]).

version, due to JONES *et al.* [1979], of nucleus formation based on coalescence. – It is to be noted that, as between SIBM and coalescence, it is only the earliest stage that is different; the later stages of nucleus growth are indistinguishable in the two models. Detailed modelling of the coalescence process, with close attention to the kinetics, to mutual annihilation of dislocations in the early stages and to the role of nearby high-angle boundaries to act as efficient dislocation sinks, has been published by SANDSTRÖM [1977] and by DOHERTY and SZPUNAR [1984].

The HVEM studies of recrystallization in heavily rolled copper (RAY *et al.* [1973]), however, showed no signs of subgrain coalescence; as so often, copper and aluminum behave differently. Long, thin subgrains grow steadily, as indicated in fig. 23, into a strongly misoriented neighbourhood — a pure instance of SIBM. The process was observed in situ, by means of a hot electron microscope stage.

In summary, from studies of aluminum, iron and copper, it would appear that

moderate degrees of deformation favour coalescence as the initial process for turning a subgrain into a nucleus, whereas high strain and low SFE favour SIBM. The reason for this distinction is not clear. What is now established beyond reasonable doubt is that nuclei are always *preformed* — i.e., an existing subgrain, or a deformation-generated grain boundary, turns into a viable nucleus. Therefore, the orientation of a new grain is always already imprinted in the previous deformed microstructure.

The necessary and sufficient condition for nucleus formation is that one subgrain should first grow substantially larger than its neighbours, and that, immediately adjacent, there should be a steep orientation gradient; for this reason, nucleation takes place predominantly at grain boundaries and at deformation bands, i.e., artificial grain boundaries. Where steep orientation gradients are absent, recrystallization is sluggish or impossible. This applies, at one extreme, to crystals of metals such as aluminum and zinc which after very large strains in single glide (as much as 200%) will not recrystallize, for lack of local misorientation; and at the other extreme, to explosively shocked metals which, although much work-hardened, apparently lack orientation gradients and so resist recrystallization (HIGGINS [1971], CHOJNOWSKI and CAHN [1973]). — Different forms of plastic deformation apparently produce quite different misorientation gradients. On present evidence, these gradients diminish in the sequence: compression, rolling, wire drawing or swaging, shock deformation. Correspondingly, recrystallization becomes more sluggish in the same sequence.

One suggested nucleation mechanism has been proposed which is quite distinct from any of those discussed above. Evidence has gradually accumulated that in certain alloys of very low stacking-fault energy, nucleation takes place from very small twins which form during the recovery stage and then grow by a SIBM mechanism. HUBER and HATHERLY [1980] were the first to recognize this clearly on the basis of TEM of rolled brass, and they review earlier observations. They proposed the term *recovery–twins* for this kind of nuclei, to distinguish them from annealing twins formed at a later stage, during grain growth. JONES [1981] provided further micrographic evidence on copper alloys and stainless steels. The formation of such recovery twins at a very early stage of subgrain growth can be rationalized in terms of the misorientation-dependence of the energies of both sub- and grain boundaries: it is possible for a growth accident, creating a twin, to be energetically favoured, if the resulting total boundary energy is thereby reduced; in fact, this is the way annealing twins also form at a later stage (§ 4.2).

A related study by WILBRANDT and HAASEN [1980] was based on HVEM of tensile-deformed and annealed copper single crystals. They claim that the orientations of recrystallized grains found in this study can be interpreted on the basis of multiple twinning (i.e., successive generations of twins), up to at least five generations. The twinning generations were not observed in the HVEM but are deduced from consideration of initial and final orientations. However, later work (see overview by HAASEN [1993]) on Cu–Mn and Cu–P alloys with a much reduced SFE, did uncover successive twin generations in the HV electron microscope (fig. 30). Wilbrandt and Haasen assert that most of the recrystallized orientations are *not* present in the deformed microstructure, having been modified by multiple twinning after nucleation. Another paper by WILBRANDT [1980] comments further on the reliability of the deductive arguments used

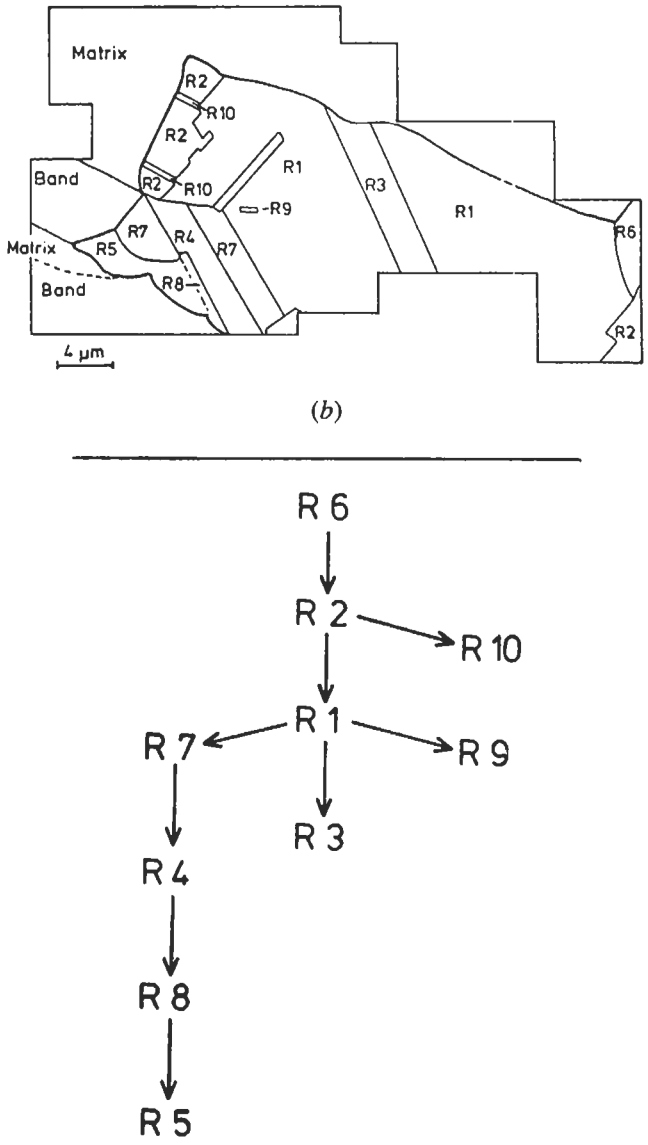

Fig. 30. (a) Recrystallized, multiply twinned grain in Cu-0.03wt% P alloy, diagrammatic, showing microstructure after 80% strain and 20 min annealed at 500°C. (b) The twinning pedigree corresponding to the microstructure (after HAASEN [1993]).

to work out this multiple twinning mechanism, and points out that the successive twinning generations cannot be on random {111} planes, but must in some way be biased so that only particular twinning variants actually operate. This notion is further discussed in a paper by RAE *et al.* [1981], in which it is suggested that twinning

accidents tend to survive if thereby the velocity of a sluggishly moving sub-boundary is increased. An issue of definition arises here, because the later generations of twinning arise long after the initial nucleus became viable (see fig. 30!). A recent paper, discussed again below (GERTSMAN *et al.* [1994]) discusses the grain-boundary misorientation statistics in relation to twinning for low-SFE alloys.

Related evidence comes from the study of recrystallization of non-cubic metals containing *mechanical* twins. A scratch on a zinc single crystal generates many twins, and new grains grow from these in orientations closely related to the twin orientations (CAHN [1964]). In deformed uranium, the orientation of new grains is also very closely related to the twin orientations; one group of recrystallized grains had an orientation accurately identical with the twin, another had a different but closely reproducible orientation (CALAIS *et al.* [1959]). In all these instances, the new grains are evidently produced by oriented nucleation.

3.4. Growth of primary grains and the role of impurities

3.4.1. Impurity drag

We have already discussed in § 3.2 how recovery of the deformed matrix can slow the growth of new grains into it. Here we shall discuss in particular the role of dissolved impurities in controlling the migration rate of boundaries and summarize present theoretical ideas about the process. It is clear that the rate of growth of a new grain into a deformed structure is sensitive to the mutual orientation of the two grains, and moreover, that for a given mutual orientation, the growth rate may be very anisotropic. This first became clear from a classic study by KOHARA, PARTHASARATI and BECK [1958]. (This kind of experiment is now termed a "Beck experiment".) A crystal of aluminum was rolled down by 80% (producing a very sharp deformation texture, almost a single orientation); one side was then abraded lightly with a fine abrasive, and the strip then briefly annealed at 350°C. Copious recrystallization took place in the thin abraded layer (fig. 31a). After a much longer anneal at 350°C, the new grains penetrated to the far side of the strip (fig. 31b). When the grains of fig. 31b were examined by X-ray diffraction, they proved to be related to the texture of the rolled crystal by a rotation of about 38° about several axes common to the deformed orientation and the new grains. This special relationship is best understood by reference to fig. 32; it has so often been found to relate deformation and annealing textures in face-centred cubic metals that it has been given a name of its own, the *Kronberg–Wilson rotation* (KRONBERG and WILSON [1949]). This represents a special instance of a *coincidence lattice,* and the white atoms of fig. 32 are *coincidence sites* (see also § 3.4.2). A more general version of these concepts was developed by CHALMERS and GLEITER [1971], and a fuller account will be found elsewhere in this work (ch. 9, § 2.2). Other rotation angles about a common [111] axis also turn up but $\approx 38°$ is the most common. There is always some scatter about this ideal orientation relationship, but in the sample of fig. 31 the scatter was found to be less on the far side of the strip (fig. 31b) than for the freshly nucleated grains (fig. 31a). A copious supply of randomly oriented nuclei must have been formed in the abraded layer, since abrasion is an intense but isotropic mode of deformation. Among these nuclei, only

(a)

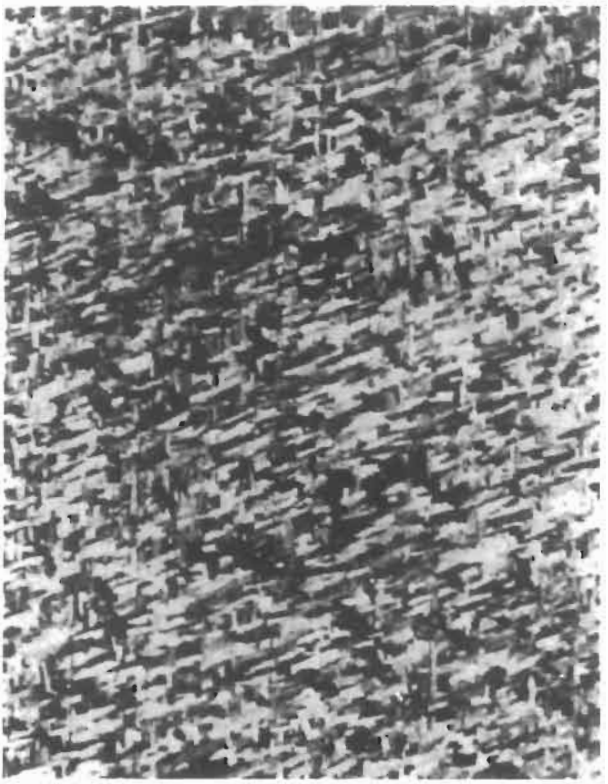

(b)

Fig. 31. (a) Incipient new grains on abraded side of rolled aluminum crystals after 5 s at 750°C. Etched 50×. (b) New grains on far side of rolled aluminum crystal, after 600 s at 350°C. Etched 6×. (After KOHARA *et al.* [1958].)

References: p. 2492.

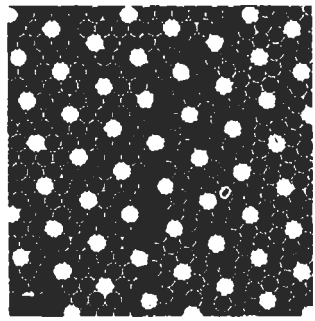

Fig. 32. Coincidence lattice for two grains both of which have [111] parallel to the plane of the figure but which are mutually rotated by 38° about an axis normal to this (111) plane. Only one lattice plane is shown for each grain. (After KRONBERG and WILSON [1949].)

the favourably oriented grew to the stage seen in fig. 31a, the others were consumed by the faster-growing grains. Continuing competition resulted in a sharpening of the texture by the time the grains had grown through to the other side of the strip. The fact that the grains of figs. 31a and b are plate-shaped (seen in cross-section) shows that for the most favourably oriented grains the growth rate was very anisotropic; analysis showed that growth was slow normal to the common (111) plane and fast in directions parallel to this plane. From this it follows further, if fig. 31 is closely examined, that out of the four ⟨111⟩ axes of the deformed crystal, only two acted as rotation axes to produce new grains; only two families of platelets appear in the micrograph. This can most simply be explained by postulating that the nuclei were not in fact randomly distributed in orientation; an alternative explanation is that the growth rate of a new grain depends not only on the mutual orientation of new and deformed grains but also on the inclination of the growing grain's boundaries to the sample surface.

Kohara's experiment has been repeated and extended by HELLER *et al.* [1981]: although grains nucleated after surface abrasion did again show a strong texture, the authors' other evidence indicates that this texture could not be due primarily to selective growth, but rather to oriented nucleation (see § 3.6). The experiments outlined at the end of the preceding section, by Wilbrandt and Haasen, also made extensive use of this "Beck approach".

A number of investigators have performed Beck experiments, but so arranged that the migration of individual primary grain boundaries could be measured over a period of time. This work was first done with strained aluminum monocrystals, squeezed or cut at one end to generate a moderately plentiful supply of nuclei. These were then allowed to compete and the migration rate of the victor determined (fig. 33). These spontaneously selected grains usually had a [111] axis in common with the parent crystal and were rotated with respect to the latter by roughly 38° about the common axis (the Kronberg–Wilson rotation). The extrapolated value for 60° represents the well-established fact that

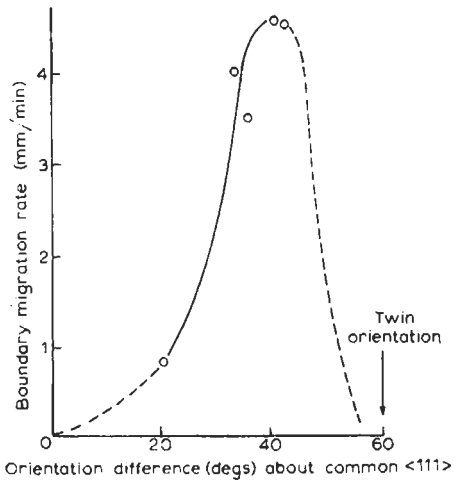

Fig. 33. Growth rates of new grains into a plastically stretched aluminum crystal at 615°C. The common [111] axis is always the same one in the deformed crystal. (After LIEBMANN and LÜCKE [1956].)

an interface between twin-related crystals has zero or very low mobility. These experiments therefore confirm the qualitative conclusions drawn from the work of Kohara *et al.* These results should be considered in conjunction with the recent model by VATNE and NES [1994], mentioned above, which demonstrates that growth selectivity is a maximum when a new grain is still very small. Other investigators found no such distinction in migration rates between differently oriented boundaries. This contradiction was eventually traced to the state of the impurities, especially iron, in the aluminum (GREEN *et al.* [1959]). Growth selectivity according to the Kronberg–Wilson rotation was not found when iron and silicon (0.1% each) were in solution; when some had been precipitated then growth selectivity returned but did not survive for complete precipitation. It appears that when substantial amounts of solute are present they exert such powerful control over boundary motion that orientation differences lose their influence; in a two-phase alloy, again, growth selectivity is prevented. A classic series of experiments on boundary migration kinetics in lead was performed by AUST and RUTTER [1959, 1960]. The metal was zone-refined (ch. 8, § 6.2.6) and thus exceedingly pure. The (small) driving force for boundary migration was provided by *striation substructure* in the lead single crystals into which artificially nucleated new grains were allowed to grow. These striations are a form of sub-boundary introduced during growth of the crystals from the melt; they represent a reproducible dislocation concentration and therefore a small but reproducible driving force. Figure 34 shows some of the results. Two striking conclusions can be drawn: (i) Very small impurity concentrations dramatically retard boundary migration; one part per million of tin will reduce the rate by a factor of four. (ii) Grains with a Kronberg–Wilson or other "special" orientation relationship to the crystal which is being consumed grow much faster than do grains of arbitrary orientation, *but only* if impurity is present. Later experiments with silver or gold as solute led to similar conclusions, except that these

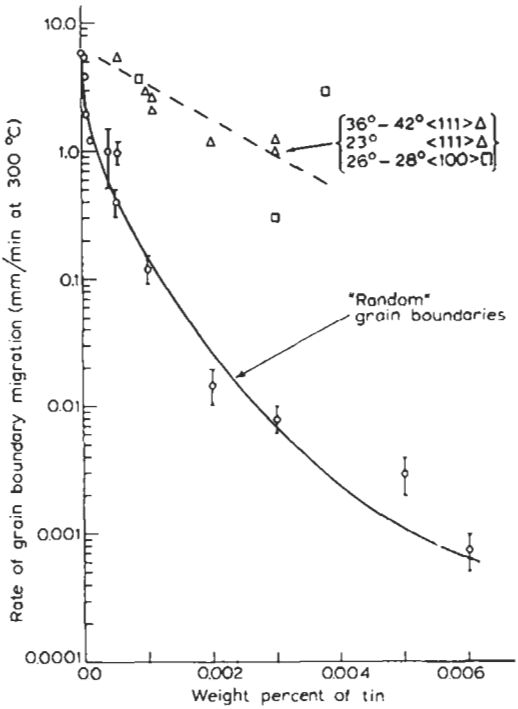

Fig. 34. Plot of log grain-boundary migration rate at 300°C into zone-refined lead crystals doped with various amounts of tin (after AUST and RUTTER [1959]).

solutes were even more effective than tin in slowing down boundary migration. A full account of these important experiments and also of their possible interpretation will be found in a review by AUST and RUTTER [1963] and in the discussion following it. More recent reviews on the same subject have been published by AUST [1969, 1974]. In the second of these, grain-boundary mobility as a function of small deviations from coincidence-orientation relationships is discussed in detail, for various degrees of purity. It must be recognized that these studies refer to experiments with very small driving forces, much smaller than in normal primary recrystallization experiments, and there is no assurance that the orientation-dependence (and purity-dependence) of migration rates is the same for the small and large driving forces. RATH and HU [1972] have assembled comparative data and themselves performed experiments with very small driving forces, for zone-refined aluminum, which show a very steep dependence of boundary velocity on driving force. The most recent examination of the accumulated evidence, by GOTTSTEIN and SHVINDLERMAN [1992a], concludes that the boundary velocity at constant temperature is strictly proportional to the driving force.

A few measurements have been made on iron alloys. LESLIE *et al.* [1963] describe experiments in iron–molybdenum and iron–manganese alloys. 0.01% solute had a

substantial effect on migration rates. Unfortunately the base metal was not zone-refined.

At first sight, the implication of experiments such as those set out in fig. 34 is that a metal entirely devoid of dissolved impurity should have a grain-boundary mobility wholly independent of misorientation (except, presumably, for quite small misorientations as found in the previously discussed experiments of VISWANATHAN and BAUER 1973a]). Figure 35, based on studies by FRIDMAN *et al.* [1975], is consistent with this expectation: a reduction of impurity level in aluminum from 8 ppm to 0.5 ppm greatly reduces the orientation-dependence of mobility. DEMIANCZUK and AUST [1975] found that the activation energy for migration in aluminum containing 40 ppm of copper changes sharply above a certain critical temperature; they suggested that beyond this temperature, boundary motion is no longer controlled by segregated impurity and the boundaries become "intrinsic". The copper microsphere sintering method (HERRMANN *et al.* [1976]) has been effectively used (SAUTTER *et al.* [1977]) to prove that some but not all local minima (cusps) in the plot of boundary energy versus misorientation are sentitive to segregated solute.

The matter is further complicated by the fact that migration rates during primary recrystallization progressively decrease, during an anneal, because of recovery of the deformed matrix (VANDERMEER and GORDON [1959], RATH *et al.* [1979]). The theoretical modelling of this effect is discussed by HU [1981].

The whole topic of the dependence of migration rates on purity, misorientation and driving force is very fully treated by HAESSNER and HOFMANN [1978]. More recently, GOTTSTEIN and SHVINDLERMAN [1992b] have reexamined the available evidence, including Shvindlerman's earlier experiments as shown in fig. 35, and conclude that "the reported segregation dependence of grain-boundary mobility is a segregation effect; 'special' grain boundaries segregate less and thus move faster than random boundaries." They go on to point out that, consequently, most experiments in the literature do not cast

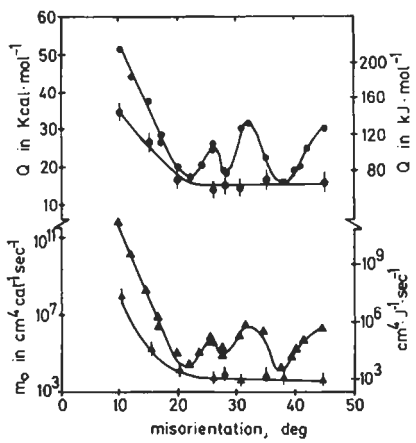

Fig. 35. variation of the activation energy, Q, and the pre-exponential factor of the mobility, m_0, with misorientation for the motion of <100> tilt boundaries in aluminum samples of different purities. ♦, ▲: Al 99.99995 at%; ●, ▲: Al 99.9992 at%. (After FRIDMAN *et al.* [1975].)

References: p. 2492.

light on the *intrinsic* mechanism of grain-boundary migration. They also reach the important conclusion that "the segregation effect is limited to a small interval of total impurity content; at higher and lower impurity levels, the mobility of high-angle boundaries does not depend on misorientation."

It is to be noted that this last conclusion is restricted to "high-angle" boundaries...say, more than a few degrees. The mobility of small-angle boundaries (most work has been done on tilt boundaries) is a murky area, with insufficient experimental evidence for firm conclusions. What information is to hand has enabled HUMPHREYS and HATHERLY [1995] (their figure 4.4) to conclude that, in general, intrinsic mobility varies with misorientation as shown in fig. 36. They agree with Gottstein and Shvindlerman about the independence of mobility on misorientation in domain B (beyond $\approx 20°$). For misorientations in the range 10–20° (domain C1) there is a reasonable amount of evidence for a variation as shown, while for domain C2 there is very little evidence (though the low mobility shown by a solid segment of curve is fairly well established; for domain A there is no evidence. (However, the old work in 1948–50, by Lacombe and Beaujard (§ 2.4.2) and by Guinier, showing that (tilt-type) small-angle subgrains or cell walls in aluminum move about very much faster than grain boundaries, does suggest that the rise from C2 to A is very steep.)

The first attempt to interpret measurements of grain-boundary mobility was due to LÜCKE and DETERT [1957]; improved versions of this theory were published independently by J. W. CAHN [1962] and by LÜCKE and STÜWE [1963]. These are all based on the postulate that *dissolved* impurities retard a moving boundary through an elastic attraction of impurity atoms towards the open structure of the boundary (ch. 13); the boundary must then either drag the impurity atoms along – so that its speed is limited by the

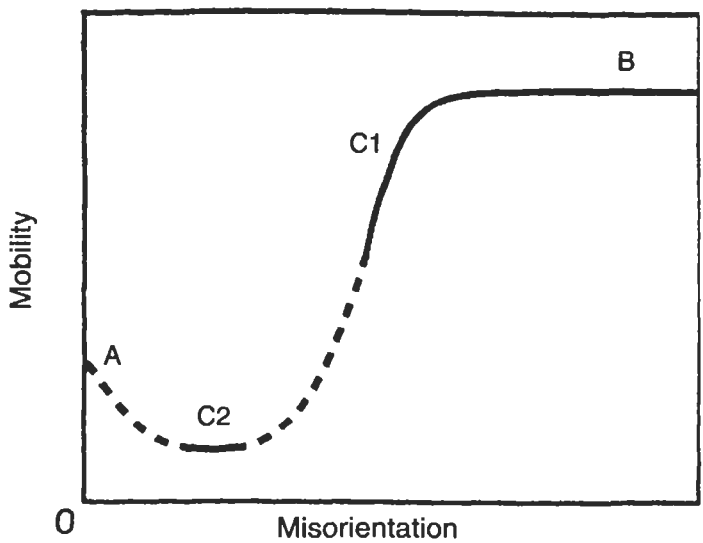

Fig. 36. Schematic diagram of the possible variation of the mobility of general low-angle boundaries with misorientation. The solid lines are regions for which there is some experimental evidence (after HUMPHREYS and HATHERLY [1995]).

diffusion rate of these atoms – or else *break away* if the impurity concentration is small enough, or the driving force or temperature high enough.

In Cahn's revised version of the theory, we have two extreme cases:

(a) For low velocities of the boundary (low driving force P or high solute concentration C_0, or both) the velocity V is given by

$$V = \frac{P}{\lambda + \alpha C_0}, \tag{2}$$

where λ is the reciprocal of the intrinsic mobility (which is determined by the grain-boundary self-diffusion of the solvent, since this is the rate-limiting process in boundary migration in an entirely pure material). α *is* a parameter depending on the variation of the interaction energy $E(x)$ between solute atoms and the boundary, and of the solute diffusivity $D(x)$, as a function distance x from the boundary. The theory predicts that $V \propto P$ at constant composition, that $(1/V)$ is a linear function of C_0, and that a lower diffusivity of the solute will lead to a stronger drag (as would be intuitively expected).

(b) For high boundary velocities, the velocity is given by

$$V = \frac{P}{\lambda} - \left(\frac{\alpha}{\beta^2}\right)\frac{C_0}{P}, \tag{3}$$

where α/β^2 is a different function of $E(x)$ and $D(x)$. Here the velocity is no longer proportional to P unless P is very large or C_0 very small, and in particular a *higher* solute diffusivity generates a stronger drag on the boundary. This is because at high velocities the solute atoms can move very quickly. This last conclusion in particular, that a rapidly diffusing solute will exert more drag on a fast boundary, is in complete agreement with Aust and Rutter's results; the relative efficacy of the solutes, tin, silver and gold, can be explained in terms of this conclusion.

The transition behaviour is complicated, and for certain values of the parameter a breakaway is to be expected: that is, increase of the driving force will cause only gradual change in the boundary velocity until a critical value is reached, when the velocity will suddenly jump to a much larger value; in effect, the solute atmosphere around the boundary evaporates. This kind of abrupt change has been observed in aluminum by DEMIANCZUK and AUST [1975]. In fig. 37 a comparison is made between some of Aust and Rutter's results for tin in lead and the formulae derived from Lücke and Stüwe's version of the migration theory, with two alternative reasonable values for the pre-exponential term D in the diffusivity equation $D = D_0 \exp(-Q/RT)$. An increase in the slope of the experimental relation occurs at about 10^{-3} cm/s.

Ideas concerning the role of vacancies in grain-boundary migration are discussed in § 3.4.3, below.

Two other aspects of grain-boundary migration warrant a brief mention here. One is the curious phenomenon of *diffusion-induced grain-boundary migration*, alternatively known as *chemically induced grain-boundary migration*. This is treated in great detail in ch. 15, § 2.5.5, and so needs no further discussion here. The other phenomenon is grain-boundary migration during high-temperature fatigue. It was shown that during fatigue at

References: p. 2492.

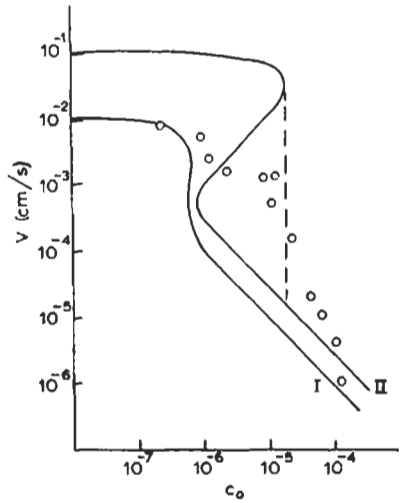

Fig. 37. Comparison of observed boundary migration rates in tin-doped lead as a function of fractional tin concentration c_0 with theory (after LÜCKE and STÜWE [1963]).

573K by cyclic bending, grain boundaries in aluminum undergo both sliding of grain relative to each other and discontinuous boundary migration at a particular stage in the cycle. The sliding is only partly reversed in each cycle, leaving the successive boundary positions (distinct for each successive cycle) clearly visible on the surface (YAVARI and LANGDON [1983]). A model for this migration was put forward in a slightly earlier paper devoted to fatigue in lead (LANGDON and GIFKINS [1983]) and developed in the later paper. It was tentatively suggested that the migration is akin to the stress-induced migration of high-angle tilt boundaries under creep conditions, for instance in aluminum (FUKUTOMI and HORIUCHI [1981]).

3.4.2. Special orientations

It remains to discuss the reason for the remarkable difference in migration rates between the arbitrary or "random" boundaries and the "special" boundaries of fig. 34, and at the same time to interpret the strongly anisotropic migration velocity of such boundaries (fig. 31). Figure 32 shows the structure of an idealized Kronberg–Wilson boundary. The white atoms form a *coincidence lattice,* which continues without disturbance across the boundary. It is intuitively obvious that any boundary which involves the existence of a coincidence lattice will have a less disturbed grain-boundary structure than a random boundary: the average fit between the contiguous grains will be better. The higher the ratio of coincidence lattice sites to total lattice sites (this ratio is 1/7 in fig. 32), the better the boundary fit; for a given coincidence site ratio but for different orientations of the same grain boundary, the fit will be the better, the higher the density of coincidence sites in the plane of the boundary. Thus in fig. 32, the density of coincidence sites is higher along the boundary orientation shown (normal to (111), the plane of the figure)

than it would be if the boundary lay *in* the plane of the figure; that is, the (111) plane normal to the common [111] axis has a comparatively disturbed structure.

The question of the structural disturbance at grain boundaries in relationship to the coincidence lattice structure has been discussed in mathematical terms by BRANDON *et al.* [1964]. In this connection, selective growth of special orientations, akin to the Kronberg–Wilson grains in aluminum, was observed in niobium (a bcc metal) by STIEGLER *et al.* [1963].

AUST [1969] has reported a joint experiment with RUTTER on zone-refined lead, in which they directly confirmed the lower energy of "coincidence boundaries" as compared with random boundaries, in agreement with the lesser structural disturbance of the former. The variation of grain-boundary energy in aluminum with misorientation has been measured over a wide range of angles by HASSO *et al.* [1972] and found to match closely with values computed from the coincidence lattice model (see also ch. 9, § 2.2.1.1).

The observed facts as to both growth selectivity of special grains (those with a high coincidence–site ratio) and *of* the growth-rate anisotropy of each grain, can be explained if it is postulated that a high coincidence–site ratio, by improving lattice fit at the boundary, reduces the interaction energy, E, of solute atoms with the boundary and also the diffusivity of the atoms across the boundary. The reduction of E is to be expected; the reduction of D is not so obvious, since we are concerned with diffusion *across* the boundary, not in its plane. However, the diffusion jumps across the boundary will be impeded if the diffusing impurity atom encounters a host atom in a coincidence site; it will have to wait for a wandering vacancy to remove this atom, whereas elsewhere it can jump into a hole in the boundary itself. If a boundary deviates slightly from an ideal coincidence relationship, the boundary can be regarded as containing some dislocations superimposed on the coincidence sites (BRANDON *et al.* [1964]) and such a boundary should still be unusually mobile so long as its mobility is impurity-controlled.

Field-ion microscopic observations by FORTES and RALPH [1967] have established directly that oxygen atoms segregate to random grain boundaries in iridium, but that "special" boundaries with a high density of coincidence sites are free of oxygen segregation. This was the first direct demonstration of a difference in purity between the two types of boundary. (See also ch. 13, § 4.2.1.)

GLEITER [1969] has published a novel theory of grain-boundary migration in terms of the movement of kinked lattice steps at the boundary (akin to the process of crystal growth from the melt). He is able neatly to relate the migration rate to the degree of misorientation; he obtains good agreement with experiment for small misorientations, but the local variations near critical misorientations do not emerge satisfactorily from the theory as worked out for pure metal.

More recent theories have focused on grain-boundary dislocations and their contribution to boundary migration. Since the process of migration is a diffusive process, thermally activated, one must regard the associated motion of grain-boundary dislocations as climb-like.The most recent discussion of this aspect is by SMITH [1992], and the reader is referred to his study, and to the relevant section of Humphreys's and Hatherly's excellent new book. A more extensive discussion of these aspects can be found in

References: p. 2492.

another new book, on crystal interfaces, by SUTTON and BALLUFFI [1995]. Overall, however, it has to be admitted that the theory of grain-boundary migration is not in a satisfactory state.

3.4.3. Vacancies in grain boundaries

An ordinary high-angle grain boundary is sufficiently imperfect to be regarded as a source of lattice vacancies; indeed, it must be regarded as always containing a certain concentration of vacancies per unit area. However, the effective vacancy concentration in boundaries is strictly limited, and this in turn limits the rate of any process which depends on grain-boundary diffusion (ch. 7, § 7). The pre-exponential term in the diffusivity, which depends directly on the vacancy concentration, is increased if the vacancy concentration is increased. A boundary, as well as being a vacancy source, is also a vacancy sink, and it has in the past been tacitly assumed that the boundary structure is not altered when vacancies are absorbed. There is indirect evidence, however, from grain-boundary migration measurements, that vacancy absorption can so alter a boundary as to increase its migration rate drastically.

MULLINS [1956] first observed a gradual slowing down of grain boundaries in bismuth moving under a very small driving force; the circumstances of the experiment were such that there was no possibility of a reduction of driving force through recovery, and he concluded that vacancies were diffusing out along the boundary to the free surface and thus reducing the boundary mobility. The bismuth had not been deformed and thus the moving boundary could not sweep up any substantial fresh supply of vacancies.

When the driving force is due to plastic deformation, a moving boundary must gather in a steady supply of excess vacancies from the lattice; whether or not it slows down will depend upon the balance between the input and outflow of vacancies. IN DER SCHMITTEN *et al.* [1960] have carried out experiments on deformed aluminum bicrystals to test this idea. Pieces of a deformed crystal were etched down to various diameters and growth rates of primary grains measured for a standard annealing treatment. Figure 38 shows the results. The growth rate varies steeply with diameter; to explain this, the authors developed a theory based on the following structural hypotheses:

(i) Grain-boundary diffusion operates through the migration of vacancies.

(ii) Vacancies above the thermal-equilibrium concentration, and also dislocations, are absorbed by a sweeping boundary so as to produce a steady supply of excess vacancies in the boundary.

(iii) These excess vacancies diffuse along the boundary for a critical distance R_{cr} before they are annihilated by an unspecified mechanism, unless they disappear at a free surface first.

(iv) The degree of disorder of the boundary is not increased during a diffusional vacancy jump, i.e., the entropy of activation is zero.

The quantitative theory shows that below a certain critical sample radius, vacancies will be annihilated at the free surface and migration velocity will depend on the sample radius. Beyond this radius, the velocity should be independent of radius. R_{cr} was estimated by fitting the curve of fig. 38 to a theoretical expression developed by the

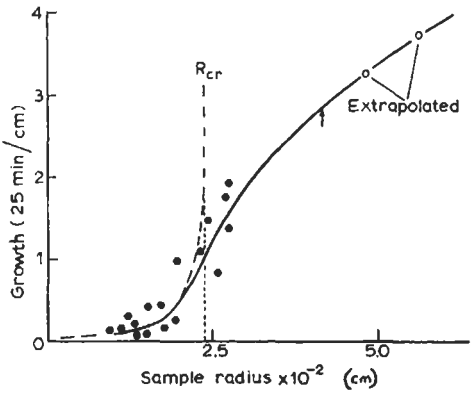

Fig. 38. Aluminum single crystal (normal purity) deformed 10% in tension. Pieces were etched down to different diameters and each annealed 25 min at 616°C. Growth distances of nuclei produced artificially at sample tips were measured. (After IN DER SCHMITTEN *et al.* [1960]).)

authors, and a critical radius R_{cr} of 2.4×10^{-2} cm adopted. With this value, a theoretical curve was calculated. Rough agreement is found for the form of the curves; in view of the simplifications inherent in the derivation of the equations, this offers some support to the underlying idea.

Further evidence of the vital role of vacancies in promoting boundary migration comes from attempts to observe primary recrystallization of thin metal films in situ in an electron microscope. DIMITROV [1960] and his colleagues sought to observe recrystallization in films of heavily rolled zone-refined aluminum, even though this metal in massive form recrystallizes completely below room temperature. Recrystallization detectable by electron microscopy proved to be restricted to film regions which were more than 1500 Å in thickness. Below this thickness, even nuclei which had been previously formed by brief annealing before the metal had been thinned still would not grow. The most straightforward explanation is that both any boundaries present, and the unconsumed cold-worked matrix, are entirely drained of excess vacancies by diffusion to the adjacent surface. Admittedly, the critical half-thickness, 750 Å, is orders of magnitude smaller than the value of R_{cr} derived from the experiment on stretched crystals of aluminum, which was however much less pure than Dimitrov's metal. It is possible that surface grooving where boundaries intersect the surface (§ 4.1) complicates the interpretation of such experiments.

CHRIST *et al.* [1965] have observed a substantial acceleration of recrystallization in heavily rolled copper if the metal had been irradiated with neutrons before rolling. The acceleration was attributed to the cutting of vacancy clusters by the moving boundary and the redistribution of the vacancies. Presumably the transfer of vacancies from the clusters to the boundaries enhances the mobility of the boundaries (HAESSNER and HOFMANN [1971]).

Later experiments (HAESSNER and HOLZER [1974]) on rolled copper crystals which were neutron-irradiated at intervals interspersing the anneal showed a jump in boundary-migration velocity after each irradiation. This finding is again consistent with the idea

References: p. 2492.

that vacancies (or, more generally, point defects) aid migration.

More recently, evidence has been obtained which proves that the vacancy concentration just behind a *moving* grain boundary is strongly enhanced. An important study by GOTTSCHALK *et al.* [1980] showed that Ni_3Al precipitates from a solution supersaturated in vacancies much faster than within a vacancy-equilibrated grain. Figure 39 shows the ratio of precipitation rates, and these indicate that at the lower temperatures, the local vacancy concentration behind the moving boundary is enhanced thousandfold. However, BALLUFFI [1982] has questioned the validity of the conclusions deduced from fig. 39.

GLEITER [1969, 1981] proposed that these findings, and others pointing in the same direction, imply that a moving boundary *generates* vacancies by means of successive growth accidents, and that these vacancies in turn create a vacancy drag, analogous to an impurity drag. Although there is no experimental evidence to test the orientation dependence of the influence of vacancies on migration, in his 1981 paper Gleiter advances arguments for the hypothesis that coincidence boundaries contain localized vacancies whereas random boundaries contain "distributed" vacancies, rather as in metallic glasses (chapter 7, § 9.1.2). The implication seems to be that the migration of random boundaries should be most strongly affected by the presence of vacancies.

Since the work of In der Schmitten *et al.*, discussed above, suggests that vacancies need to be *absorbed* from outside to "lubricate" grain-boundary migration, and Gleiter's arguments indicate that a moving boundary also *rejects* vacancies, it appears that such a boundary must be regarded as a sort of vacancy pump!

The motion of a grain boundary in relation to its intake and rejection of vacancies and of the concentration of vacancies *in* the boundary, has been analyzed quantitatively in a series of theoretical papers by LÜCKE and coworkers (the fifth in the series is by ESTRIN and LÜCKE [1982], and here the new theory is also related to the other ideas mentioned above). In this treatment, the moving boundary is shown to be enriched in vacancies, and the supply of vacancies from the grain being consumed is shown to be an essential feature of rapid migration. This last conclusion is consistent with a number of experimental results cited above.

VAIDYA and EHRLICH [1983] have observed enhancement of recrystallization in

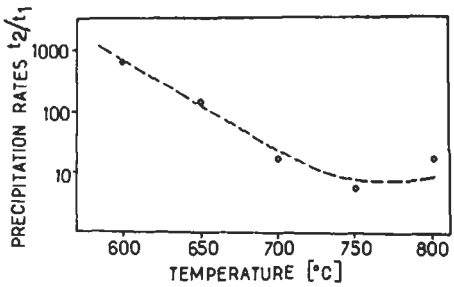

Fig. 39. Measured relative precipitation rates, t_2/t_1 of a Ni_3Al precipitate in a recrystallized (t_2) and in a vacancy-equilibrated (t_1) Ni–12.5 at% Al alloy as a function of the recrystallization temperature. It is seen that the Ni_3Al precipitates form in a recrystalized material up to 1000 times faster than in a vacancy-equilibrated material of the same composition and at the same temperature. (After GOTTSCHALK *et al.* [1980].)

irradiated austenite stainless steel (deformed 20%); they observed that irradiation-induced voids were dissolved by migrating grain boundaries, thereby releasing vacancies which were presumed to be responsible for accelerating recrystallization.

3.5. Recrystallization during hot-working: dynamic recrystallization

In § 2.3, we saw that recovery is accelerated if metal is subjected to strain and high temperature simultaneously. This *dynamic recovery* can be followed by *dynamic recrystallization* if the temperature and strain rate are high enough.

During dynamic recrystallization, nuclei at first grow rapidly but the concurrent deformation steadily increases the dislocation density within the growing grains, so that the driving force for boundary migration is progressively reduced. The new grains reach a limiting size and then stop growing, and a new cycle of nucleation begins. Figure 40 indicates the correlation between this repeated recrystallization and the instantaneous creep rate. For the circumstances illustrated here, the strain ε_x, during the time required for almost complete recrystallization, is less than the critical strain for renewed nucleation, so that there is a necessary interval of further strain before the next cycle of recrystallization can start.

Dynamic recrystallization has been studied since the late 1950s, beginning with a study by ROSSARD and BLAIN [1959]. At first there was uncertainty whether recrystallization as well as recovery was involved in the dynamic softening process, but by the late 1960s this had been resolved. A concise review is by SELLARS [1986], and he

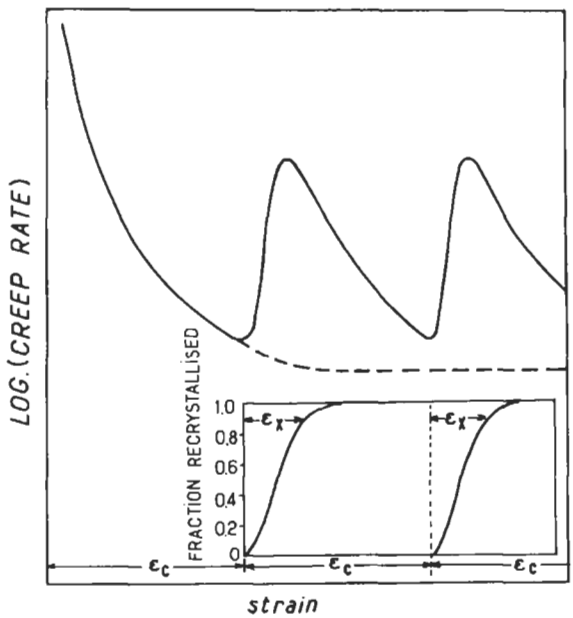

Fig. 40. Schematic behaviour of a metal recrystallizing repeatedly during hot working (after LUTON and SELLARS [1969]).

quotes a few of the early key studies. The subject, induding microstructural aspects, is reviewed by MCQUEEN and JONAS [1975] and by MECKING and GOTTSTEIN [1978]. Both reviews also treat dynamic recovery. J. J. Jonas and H. J. McQueen have been steady contributors over many years, gradually attaining a very profound understanding of the process. Recently, Jonas has published an important practically oriented overview (JONAS [1994]) with special emphasis on steels. Here, there is space only for a concise summary of the present understanding. – Secondary recrystallization associated with hot-working has been investigated by SINGER and GESSINGER [1982].

Jonas makes a distinction between *dynamic recrystallization proper* (completed during the hot deformation process itself) and *metadynamic recrystallization* which immediately follows the cessation of hot deformation (PETKOVIC *et al.* [1975]). Both are to be distinguished from recrystallization that takes place during annealing following low-temperature deformation: this is termed *static recrystallization*. Dynamic recrystallization takes place most readily in metals of low stacking-fault energy in which (because of slow climb of dislocations) dynamic recovery is sluggish, so that the driving force for recrystallization is maintained. In fact, GOTTSTEIN and LEE [1989] showed, by studies with copper single crystals, that an increase of deformation temperature actually promotes recrystallization when deformation is carried out to an equivalent flow stress; this has already been demonstrated in this chapter in fig. 15b, above, taken from the work of LINDH *et al.* [1993]. Gottstein and Lee claim that the segregation of dislocations to cell walls, without annihilation, enhances their power to nucleate recrystallization. Aluminum and its alloys do not recrystallize dynamically at elevated temperature; recovery too quickly gets rid of the necessary stored energy. This has been confirmed in a recent study by MCQUEEN *et al.* [1994], who showed that dynamic grain growth takes place and also causes oscillations in the flow curves like those in fig. 40, but no new grains are formed. Nevertheless, this is clearly not universally true (see next paragraph). The careful study by KASSNER *et al.* [1994] on superpure aluminum did show that some true dynamic recrystallization takes place after heavy strain at room temperature, since recovery is slow there. Dynamic recrystallization of pure magnesium at room temperature has also been demonstrated (KAIBYSHEV and SITDIKOV [1994]).

Attempts have begun recently to computer-model the dynamic recrystallization process. One of these is by DERBY [1992]; he distinguishes between dynamic recrystallization involving nucleation and a variant in which the new grains stem from coalescence and associated subgrain rotation. He models only the former, which he regards as true dynamic recrystallization. (There is an almost religious fervour in the various attempts to distinguish between the true process and less true variants!). Derby's model, applied to a variety of experimental findings, suggests that the deformation temperature makes little difference to his plot of normalised product grain size as a function of deformation stress. A more recent Monte Carlo study by PECZAK [1995] is also focused on the effect of deformation temperature, and claimed good agreement between the elaborate model and a range of observations.

Dynamic recrystallization is apt to produce particularly fine grain sizes, especially in the presence of second phases. This has been exploited industrially to produce superplastic alloys, which deform by diffusional (Herring-Nabarro) creep. In the 1970s

(see review by EDINGTON *et al.* [1976]), a family of Al-Cu-Zr alloys with a very fine dispersion of Al_3Zr were designed which can be (apparently) dynamically recrystallized to give an ultrafine grain size. These alloys are used commercially for superplastic forming. A more recent study by HIGASHI *et al.* [1986] has perfected the dynamic recrystallization process to give even finer grain sizes, allowing faster forming. Recently, a similar finding has been published for an alloy of bcc iron, another metal of high stacking-fault energy. LIN *et al.* [1994] slowly stretched tensile specimens of ternary-alloyed Fe_3Al with a coarse grain size: the alloy recrystallized dynamically to give an extremely fine grain size which permitted large superplastic strains to be imparted.

Precise control of dynamic recrystallization is crucial in thermomechanical processes such as controlled rolling of microalloyed steels. Thus CUDDY [1981] explains how to achieve the finest possible ferrite grain size in Nb-bearing microalloyed steels by controlled rolling: high-temperature deformation with repeated recrystallization, as in fig 40, is used to achieve a uniform fine austenite grain size, followed by further rolling at a temperature below the austenite recrystallization range; the flattened, unrecrystallized austenite grains generate very fine ferrite grains. A general overview of such *controlled rolling* of steels, with special attention to *recrystallization-controlled rolling*, can be found in a book chapter by PICKERING [1992]. Jonas's 1994 review, already cited, is particularly concerned with recrystallization-controlled rolling: he points out that, according to circumstances, the grain refinement in this process can be due entirely to static recrystallization or to various mixes of true dynamic recrystallization and meta-dynamic recrystallization. Dynamic recrystallization can go to completion even during the few milliseconds which may be all that is needed to complete a hot-rolling operation. The strain-rate dependence of dynamic recrystallization is an important parameter and is receiving more attention now (CHEN and KOCKS [1992]). The subject has become exceedingly complex.

Repeated dynamic recrystallization neutralizes incipient grain-boundary cracks in materials of limited ductility, by separating them repeatedly from their associated boundaries, and thus enhances hot-workability (which is likewise enhanced by the repeated softening of the grain interiors).

3.6. Annealing textures

When a piece of metal is deformed by some directional process such as wire-drawing or rolling, the constituent grains acquire a *preferred orientation* or *texture;* the grains approximate, generally with a good deal of scatter, to an *ideal orientation.* In the extreme case the whole sample may turn into a pseudo-single crystal. Sometimes several ideal orientations coexist, so that the total scatter is greater. The actual orientation distribution of grains is termed a *deformation* texture. When such material is recrystallized it again acquires a texture, which may be identical to the previous deformation texture but more often is quite different; this is an *annealing texture.* We shall be concerned here mainly with annealing textures, though it is impossible to understand these properly without reference to their precursor textures. In this outline, we shall be concerned only with the *mechanism* of texture formation. A texture can be described in terms of the ideal

orientation or group of orientations to which it approximates. Thus for a rolled sheet the ideal orientation is quoted as *(hkl)*[*UVW*]; here *(hkl)* is the lattice plane which tends to lie in the rolling plane and [*UVW*] the lattice vector which tends to lie along the rolling direction. (For a drawn wire only a direction [*UVW*] need be specified; the distribution around the wire axis is random). For instance, brass heavily rolled and annealed gives a texture approximating to (113)[211]. Other metals, such as aluminum and iron, have a mixed texture (several ideal orientations coexisting); the texture of rolled and annealed aluminum has been described as a mixture of (100)[001] (the *cube texture),* (110)[011] and (236)[533]; the proportion of the various components varies with purity and annealing temperature.

A clear quantitative expression of the ideal orientation and statistical spread around it, and of the relative proportions of several constituent textures, is provided by a graphical device, the *pole figure,* which is plotted directly from X-ray diffraction data obtained from the sample. To produce a pole figure, imagine all grains concentrated at the centre of a sphere and then construct normals to all the lattice planes of a particular family (say {110}) in all grains, so that each forms a spot where it cuts the sphere. If there is a texture, the spot density varies in different parts of the spherical surface, and contours of equal spot density are drawn to define areas of high and low concentration. The contours on one hemisphere are projected stereographically into a plane parallel to the rolling plane. Figure 41 is a typical pole figure of an annealing texture.

The orientation of a crystallite in a polycrystalline specimen is determined by three orientation angles (α, β, γ). Their choice is somewhat arbitrary; one can, for instance, choose the Eulerian angles. The orientation distribution of all crystals in the specimen, i.e., the texture, may then be defined by the *orientation distribution function* (ODF),

$$\frac{dV}{V} = f(\alpha, \beta, \gamma)d\alpha d\beta d\gamma, \tag{4}$$

giving the relative frequency or volume fraction of crystals having an orientation with respect to the specimen geometry specified by the ranges $\alpha/\alpha + d\alpha$; $\beta/\beta + d\beta$, $\gamma/\gamma + d\gamma$. Straightforwardly one may determine f by X-ray Laue or electron diffraction photographs (LÜCKE *et al.* [1964]). The statistical task is however formidable. It is more promising to start from a pole figure p for a low-index plane *hkl,* which is a two-dimensional projection of the ODF:

$$p_{hkl}(\alpha\beta) = \frac{1}{2\pi}\int f(\alpha\beta\gamma)d\gamma. \tag{5}$$

From many such projections for different *hkl* one then can construct the three-dimensional ODF. Often this is done by series expansions of both functions p and f (BUNGE [1981]), but care has to be taken to avoid "ghosts" in this transformation This error in earlier ODFs has been pointed out by MATTHIES [1979].

An enormous volume of work has been done on annealing textures. It is impossible in a chapter of the length of this one to go into details; one very quickly becomes bogged down in minutiae. All that can be done is to discuss a few key issues. – A very full though somewhat dated account of the subject can be found in the book, in German, by

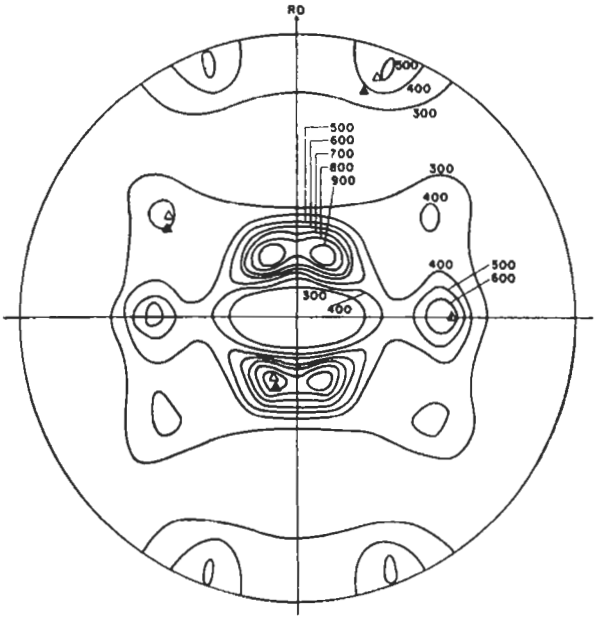

Fig. 41. (111) pole figure of the primary recrystallization texture of rolled brass, showing contours of equal pole density. The normal to the rolling plane is at the centre, RD represents the rolling direction. ▲ represents pole positions for the ideal (113)[$\bar{2}$11] texture; △, (225)[73$\bar{4}$] is a slightly better approximation to the observed texture. There are four symmetrical ideal orientations which are mutually equivalent. (After BECK and HU [1952].)

WASSERMANN and GREWEN [1962]; this also discusses the consequences of annealing texture in generating anisotropy of physical and mechanical properties, which have important technological implications, especially for deep drawing. Later additions can be found in a conference report by the same authors (GREWEN and WASSERMANN [1969]). We shall return to one particular instance of this anisotropy in a later section (§ 4.4.2). A later, concise but very informative review is by GREWEN and HUBER [1978], and a large number of up-to-date papers will also be found in the proceedings of the latest texture conferences (e.g., NAGASHIMA [1981], KALLEND *et al.* [1988], BUNGE [1994]). GREWEN [1994] has a concise overview of texture studies over a period of 25 years, including annealing textures, in the most recent texture conference proceedings. The subtleties of orientation functions and their determination were covered by BUNGE [1987]. A recent, concise overview of the origin and nature of all kinds of textures, including those created by phase transformation, and their effects on mechanical and physical properties, is by CAHN [1992].

There has been much argument concerning the physical origin of recrystallization textures. Opinion has divided into two camps: One group hold that nuclei form only in particular orientations in relation to the deformation texture, and the non-random nuclei then grow to form a preferred orientation of primary grains. This is the *oriented*

nucleation hypothesis. The other view is that such nuclei are so plentiful in a heavily deformed metal that a large range of orientations are present, but only those favourably oriented with respect to the deformation texture grow to a large size. This is the *oriented growth selection* hypothesis. The specific models for oriented nucleation and oriented growth as separate processes are discussed in § 3.3 and § 3.4, respectively.

LÜCKE [1963] described experiments on copper and brass. Pure copper rolled at −196°C (A) produces almost exactly the same texture as a copper–6% zinc alloy rolled at room temperature (B), whereas pure copper rolled at room temperature produces quite a different texture (C)*. On annealing, A and B produced quite different recrystallization textures. If growth selection alone were responsible for determining the texture, then the similar deformation textures of samples A and B should impose a similar growth selection on the new grains growing into these two samples. The difference actually observed can only be attributed to a difference in the supply of nucleus orientations available in the two cases; this may well be due to a difference in fine structure of the twins in samples A and B, or to a variation in the spatial distribution of the different orientations in the two samples.

Oriented nucleation, as we have seen in § 3.3, is now well established. Leaving aside the complications which arise from multiple twinning during the early stages of growth, it is clear that the orientations of nuclei are always present in the deformed structure (which generally, however, has extensive orientation gradients in each grain).

Likewise, we have seen that there is clear evidence of preferential growth of certain orientations only, when a plentiful supply of nuclei is provided by artificial means (fig. 31).

The present consensus, as expressed by GREWEN and HUBER [1978] and more recently in papers such as those by DUGGAN *et al.* [1993] and SMALLMAN and LEE [1994] is that for moderately deformed single crystals (as in the case of Kohara's experiment shown in fig. 31) preferred growth undoubtedly is a determining factor of the resultant texture. But as one goes to a polycrystal, the deformation texture necessarily becomes more scattered and the microstructure more complex, and all the indications are that then the textures are determined largely by preferred nucleation; but there is clearly a residual element of growth selection, acting on available orientations already determined by preferred nucleation. A further subtlety is the recently proposed mechanism of *microgrowth selection*, operating in the early stages only of recrystallization, recently put forward by VATNE and NES [1994].

In the past, attempts were made to draw conclusions about the mechanism involved in texture formation from a critical comparison of deformation and recrystallization textures. This is however a blunt approach, especially if pole figures rather than ODFs are used. It is much more informative to map the behaviour of individual grains both during deformation and subsequent annealing; when this is done for instance by Kossel-type point X-ray diffraction, stereograms like figs. 19b and 21 are obtained, and if this is done for many grains, as for instance was done by INOKUTI *et al.* [1980] for silicon-

* This difference is probably due to the incidence of mechanical twinning in the A and B cases and its absence in C (WASSERMANN [1963]).

iron, then the genesis of an annealing texture can be identified in detail. This approach confirms the primacy of oriented nucleation in many cases. The next section gives a very brief account of the new specialism which has grown up around this kind of approach. — An attempt has also been made to draw conclusions about the relative roles of preferred nucleation and preferred growth by a critical analysis of the experimental kinetics of recrystallization overall (DOHERTY [1985]), but the results were inconclusive, probably because of non-random distribution of nucleation sites.

A topic which has caused much difficulty is the interpretation of the very pronounced *cube texture*, (100)[001], obtainable by annealing heavily rolled copper, aluminum and some alloys; it was long thought that only selective growth of cube-oriented grains could explain this texture, but it was not at all clear why just these grains should grow preferentially. Evidence marshalled by GREWEN and HUBER [1978] then showed that small amounts of material in "cube orientation" have been detected by TEM in rolled sheet, and these can develop by oriented nucleation in the special circumstances that lead to this texture. A whole range of extremely detailed investigations in the last few years (see especially SMALLMAN and LEE [1994]) have focused on this problem, which turns out to be intimately linked to the formation of sharply defined deformation bands, like those shown in fig. 25; even in heavily deformed single crystals, cube texture can form from such deformation bands. It is now established that exceedingly small volume fractions of material in cube orientation are present at the band/matrix interfaces, and that such material can readily form viable nuclei because of the sharp orientation discontinuities adjacent to them, and then grow at an enhanced rate (compared to other orientations) because of microgrowth selection. Taking textures in general, however, there is *still* an apparently irreducible element of disagreement between adherents primarily of preferential nucleation and those who favour selective growth. According to HJELEN *et al.* [1991], in their magisterial overview of recrystallization textures in aluminum, there is no evidence of any preferential growth rates, at least in the later stages, whereas a detailed study of textures in an Al–Cu alloy (ENGLER *et al.* [1995] claims that the whole corpus of observations can be explained on the basis of selective growth! DOHERTY [1995] concludes that cube texture stems from oriented nucleation.

One of the most impressive investigations into the origin of an annealing texture is the study by DILLAMORE *et al.* [1967], set out more fully by HUTCHINSON [1974], to account for the annealing texture of rolled mild steel (of great industrial importance). They showed that differently oriented *deformed* grains incorporated different amounts of strain energy (greatest in (110)[001] and (111)[*UVW*] grains – but the former are only present in trace amounts and do not contribute much to subsequent annealing texture). If a precisely critical dispersion of a second phase such as AlN is present, this can just inhibit the components with smaller stored elastic energy from growing into large recrystallized grains, while allowing the technologically desirable grains with (111) parallel to the sheet plane to grow. The matter is critically discussed by GREWEN and HUBER [1978]. A recent, very full overview of textures in low-carbon steels (RAY *et al.* [1994]) asserts that "the annealing texture... depends significantly on the hot band texture and grain size, as well as on coiling temperature, cold reduction, and alloy chemistry." Grain growth after recrystallization is complete further alters the texture. Detailed

modelling is out of the question in such circumstances.

A critical review of the theories concerning the genesis of recrystallization textures can be found in the book by HUMPHREYS and HATHERLY [1995].

The huge amount of effort which continues to be put into the study of recrystallization textures of aluminum alloys and low-alloy steels in particular is an indication of their industrial importance. Enormous tonnages of aluminum alloys (e.g., Al–Mg–Mn–Fe–Si) are used to make beverage cans: it is essential to prevent "earing", arising from anisotropy of mechanical properties, during the deep drawing operation, and it is also vital to have a uniform reduction of thickness. A reduction of a few percent in can thickness has very great economic consequences, and the possibility of this depends on mechanical isotropy: such isotropy does not necessarily require an absence of textures, but different texture components can be set to neutralise each other's "anisotropising" character. This is fully set out in a review by HUTCHINSON and EKSTRÖM [1990]. With steels, again the "deep drawability" depends intimately on details of the texture, as explained in the review by Ray *et al.*

3.7. Mesotextures

All determinations of "macro-textures", even if the advanced methods involving orientation distribution functions are used, suffer from the weakness that nothing is known about the relative orientations of *neighbouring* grains; the information is purely statistical. For this reason, a number of investigators have in recent years developed techniques for rapidly determining large numbers of such orientation pairs, combining microscopy with crystallography. There is no space here to go into the methods in detail: X-ray microdiffraction, Kossel X-ray diffraction and electron back-scattering patterns have successively held sway. High resolution (of the order of a micron) and high-speed determination of orientations are the chief desiderata. The details of the experimental techniques are exhaustively set out in two reviews (DINGLEY and RANDLE [1992] and RANDLE [1993], and much more briefly in Cahn's 1992 chapter. One generic name for the information given by these techniques is a *mesotexture* (from the Greek root for an intermediate level).

Once the misorientation data for numerous grain boundaries in a particular specimen have been determined, the next problem is to find a manageable way of displaying them. By a process of evolution, three methods of display have found preference. One is a simple stereographic unit triangle in which the misorientation (rotation) axes for each boundary are assembled, as in fig. 42 which shows such a triangle for stainless steel recrystallized in a particular way, showing a non-random distribution of rotation axes (RANDLE and BROWN [1989]). Such a plot gives no information about rotation *angles*. To overcome this, another approach, gradually finding favour, is the use of the *Rodrigues method*, revived by FRANK [1988] from a Victorian precursor. Here, a vector is parallel to the rotation axis in real space, while its length and sense denotes the rotation angle and sense. Any point in Rodrigues space therefore denotes a unique orientation relationship, and this method is thus able to show a full *grain boundary misorientation distribution*, to cite the preferred term. A recent survey of mesotextures in relation to twinning

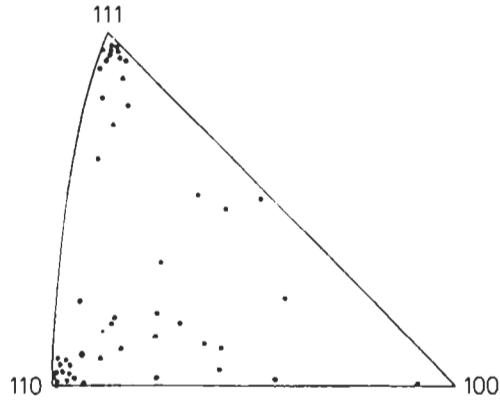

Fig. 42. Mesotextural data for (fcc) stainless steel, recrystallized, lightly strained and reannealed, initiating surface-induced grain growth. The stereographic unit triangle shows the non-random distribution of rotation axes for pairs of contiguous grains (after RANDLE and BROWN [1989]).

(GERTSMAN *et al.* [1994]) shows a such a distribution in terms of a projection of slices in Rodrigues space on to a plane in that space; these authors concluded that such a depiction is not easily understood. They prefer to combine a frequency plot of misorientation angles (without regard to the orientations of the axes), together with a stereographic triangle of axes, like that in fig. 42, as an inset. Figure 43 shows such a

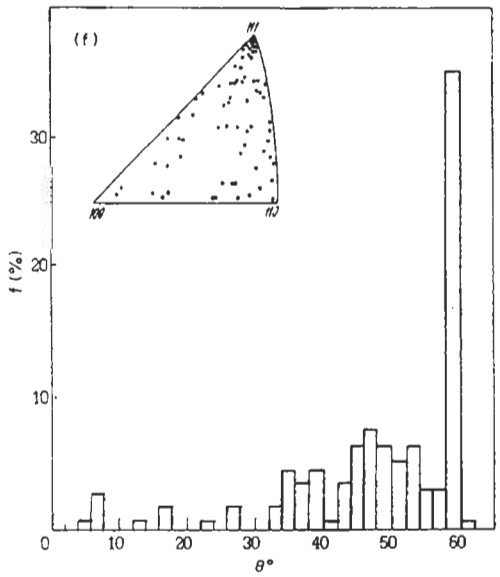

Fig. 43. Grain-boundary misorientation distribution in statically recrystallized Cr–Ni–Mo–Mn stainless steel, of 17 μm grain size. The histogram represents the distribution of boundaries in terms of misorientation angles and the stereographic triangle in the inset shows the distribution of rotation axes (after GERTSMAN *et al.* [1994]).

References: p. 2492.

combined plot, for a stainless steel specimen recrystallized to give a large fraction of twin-related grain pairs (GERTSMAN *et al.* [1994]). The twins are denoted by the 60° bar and, in the stereogram, by the concentration of axes close to [111]. A third method, introduced by WATANABE [1984, 1988] and energetically exploited by him, is the *grain-boundary character distribution*. Here, the focus is on the nature of each grain boundary, as expressed by the Σ figure (ch. 9, § 2.2.2), a measure of "specialness" of the boundary; the lower the value of Σ, the more numerous the coincidence site lattice (CSL) nodes which the two grains have in common and the more orderly the boundary and the lower its specific energy. Thus, a twin of the kind shown plentifully in fig. 43 is denoted by $\Sigma = 3$. Figure 44 (WATANABE *et al.* [1989]) shows a plot of this kind, referring to rapidly solidified and annealed Fe–6.5mass% Si alloy. Here, twins are few (they do not readily form in bcc iron alloys) but instead other special boundaries are plentiful. The specimen to which this plot refers had been heat-treated after quenching to optimise its magnetic properties for use as a transformer lamination, and this state is accompanied by a large fraction of special boundaries. – GERTSMAN *et al.* [1994] have sought to correlate their grain boundary character distributions (mesotextures) with orientation distribution functions (macrotextures) determined from the same specimens, and they found no clear correlation. The two kinds of data are quite distinct.

The information obtained in this kind of study about the orientation of individual grains in a polycrystal, by an automatic computer-steered procedure, can then be displayed in a computer-generated "micrograph" in which the grain boundaries are displayed in different thicknesses according to the degree of misorientation. This procedure has been termed *orientation imaging microscopy* (ADAMS *et al.* [1993, 1994]). An earlier version, using a colour display to denote orientations of individual grains as

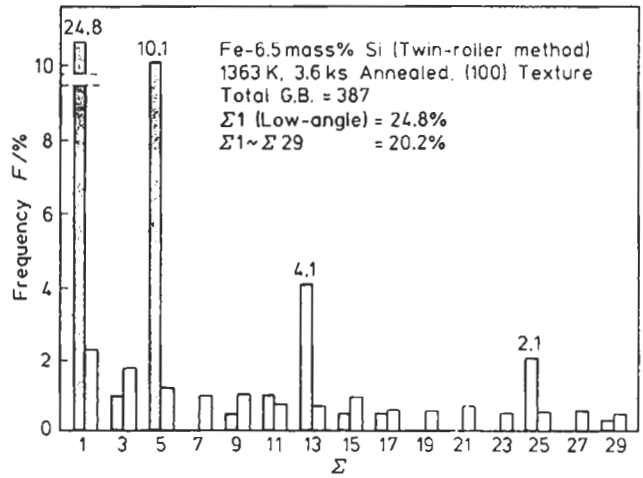

Fig. 44. Grain-boundary character distribution: the frequency of special boundaries as a function of Σ in rapidly solidified and annealed ribbons of Fe-6.5wt% Si alloy, in the state of optimum heat-treatment (after WATANABE *et al.* [1989]).

well as variable grain-boundary thickness display was originated by Y. INOKUTI (see CAHN [1992], fig. 10–11 in colour).

Watanabe termed the kind of work he planned to optimise the distribution of grain boundary misorientations (expressed by him in terms of grain-boundary character), *grain-boundary control* or, rather more grandly, *grain-boundary engineering*. An example of this concept in action is a simulation of the intergranular fracture properties of a simulated polycrystal: a preponderance of low-angle boundaries enhances the fracture resistance (LIM and WATANABE [1990]). The concept has now come of age, as is clear from a splendid overview entitled "Grain Boundary Engineering" by AUST [1994]. He makes clear the precise implications of the Σ-values and the amount of deviation which can be tolerated for any Σ-value without invalidating that value. He goes on to estimate the average crack length in a material subject to intergranular cracking as a function of the volume fraction of grain boundaries with a Σ-value low enough to arrest a crack, and relates this to experimental observations on crack spreading. (This is an example of a grain-boundary percolation issue, which is also important for electrical and electronic properties, for instance, the transmission of superconducting behaviour across grain boundaries in anisotropic superconductors, SMITH and NICHOLS [1991]). Returning to Aust, it appears that a patent has been taken out in Canada for a particular form of thermomechanical treatment of stainless steels and nickel alloys which can increase the percentage of special boundaries to within the 70–90% range; these are highly resistant to intergranular corrosion and stress-corrosion cracking. He goes on to consider the applicability of the concepts of grain-boundary engineering to intermetallics also. The original paper must be consulted for the extensive details.

3.8. Primary recrystallization of two-phase alloys

A dispersed second phase exerts two opposed influences on the progress of primary recrystallization of a deformed alloy:

(i) Nucleation of new grains may be accelerated, especially if the second-phase particles are comparatively large. If they are very small, nucleation is retarded or prevented altogether.

(ii) Growth of new grains is always impeded, because of the drag exerted on a migrating grain boundary by dispersed particles, especially if these are small and numerous.

When dispersed particles are quite coarse (several microns across) it appears that they generate a local concentration of lattice distortion caused by the applied deformation, which in turn enhances the nucleation rate in the matrix close to the inclusions. This has been clearly demonstrated by LESLIE *et al.* [1963], who examined a series of dilute iron–oxygen alloys containing a second phase in various degrees of dispersion. Figure 45a shows clusters of newly nucleated grains near oxide inclusions in cold-rolled iron, briefly annealed, and fig. 45b shows recrystallization isotherms for various alloys. Increase of oxygen content enhances nucleation and thus accelerates the entire recrystallization process, and correspondingly the recrystallized grain size also becomes smaller. Blade (quoted by DOHERTY and MARTIN [1963]) similarly observed that

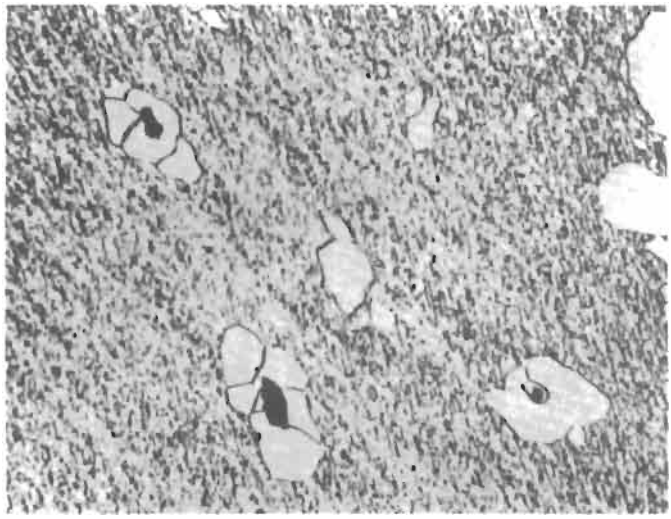

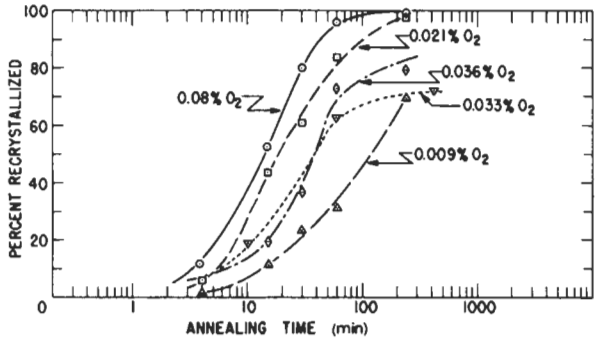

Fig. 45. (a) Initiation of recrystallization at an oxide inclusion in an iron–oxygen alloy (0.033% oxygen). 60% rolling reduction, 2 min at 540°C. 100×. (After LESLIE *et al.* [1963].) (b) Effect of oxygen in iron on recrystallization kinetics at 540°C. 60% rolling reduction. (After LESLIE *et al.* [1963].)

precipitation of $FeAl_3$ particles of about 1 μm diameter in aluminum–iron alloys accelerated nucleation more than it retarded growth of new grains, so that recrystallization as a whole was accelerated. DOHERTY and MARTIN [1963] observed the same in their careful study of the recrystallization of two-phase aluminum–copper alloys. Here the nucleation rate was critically sensitive to particle spacing, while growth rate was much less sensitive to this parameter. Figure 46 illustrates how strongly this extreme sensitivity of nucleation rate on the state of dispersion affects the recrystallization kinetics. The steep softening here is due to recrystallization. There is evidence in Doherty and Martin's work that nucleation becomes very difficult when the particle spacing becomes so small that each developing subgrain collides with a particle before it

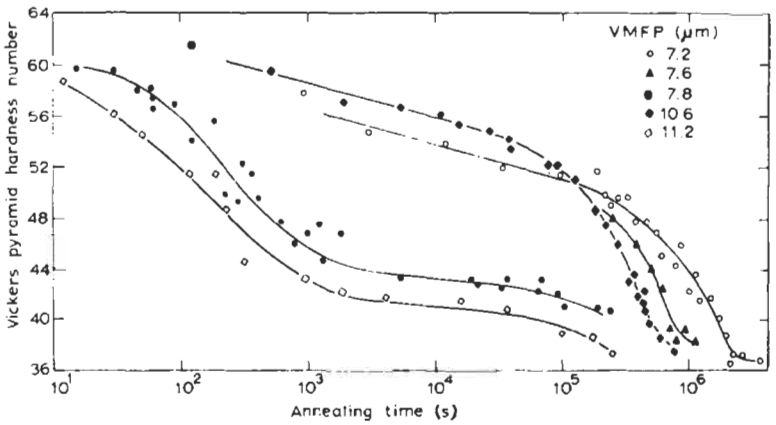

Fig. 46. Hardness–log-term isotherms for aluminum–5% copper alloy heat-treated to different states of dispersion. VMFP is the volumetric mean free path between $CuAl_2$ particles (not the same as the mean particle separation). (After DOHERTY and MARTIN [1963].)

becomes a viable nucleus.

A particularly detailed and thorough study of recrystallization in a two-phase alloy was undertaken by MOULD and COTTERILL [1967], on aluminum–iron alloys heat-treated to give different precipitate morphologies. Nucleation rate was a maximum for a mean particle separation of about 4 μm (the smallest separation studied); taken in conjunction with Doherty and Martin's results, the results suggest that this is the optimum spacing in an aluminum matrix. The authors believe that nucleation becomes difficult when interparticle spacing becomes of the order of twice the mean subgrain diameter in the cold-worked matrix. The same authors discuss the matter in greater detail in their book (see *Further reading*).

GAWNE and HIGGINS [1969] studied recrystallization kinetics in iron containing dispersed Fe_3C particles with a mean separation of about 2 μm, and found a pronounced acceleration compared with unalloyed iron rolled to the same reduction. It thus appears that in iron, the critical interparticle spacing is less than in aluminum (the rolling reductions were similar in the two experiments).

A very detailed TEM study of the role of large particles in stimulating nucleation in deformed two-phase alloys of aluminum and copper has been undertaken by HUMPHREYS [1977, 1979a] and he compares his findings with many other observations in another paper [1979b]. He finds that large particles stimulate nucleation: they do this not only by concentrating deformation locally, but especially by creating surprisingly large local misorientations which can be as large as 45° for 2 μm particles. As strain increases, substantial misorientations, and the associated stimulation of nuclei, were found for particle sizes down to 0.1 μm, for isolated particles; the smaller the particle, the less the limiting misorientation which was observed. This study has established in detail the mechanism of particle-stimulated nucleation in deformed metals. In recent years, Humphreys has continued his use of TEM to characterize particles and their effect on the

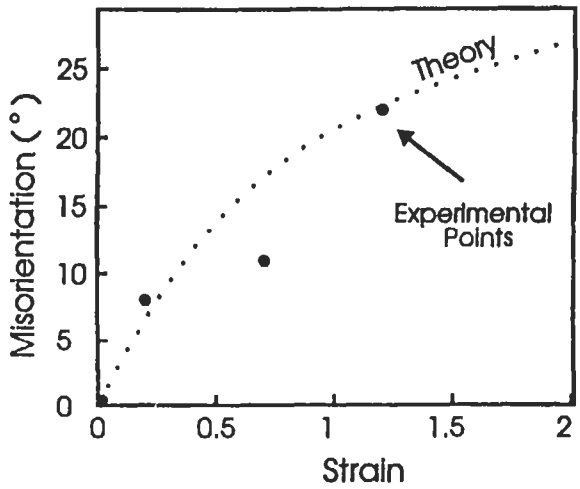

Fig. 47. The misorientation at silicon particles (diameter > 1.5 μm) in polycrystalline aluminum deformed in compression: plot showing the *maximum* misorientation in the zones surrounding the particles (after HUMPHREYS and HATHERLY [1995]).

surrounding matrix and has published a number of key papers. Figure 47, from HUMPHREYS and HATHERLY [1995], shows this misorientation as a function of strain. Experimental points are from HUMPHREYS and ARDAKANI [1994], experimental points from HUMPHREYS and KALU [1990].) The reader is referred to a fine survey of the whole field of the character and recrystallization of multiphase alloys in chapter 8 of the book by HUMPHREYS and HATHERLY [1995]. One consequence of these pronounced misorientations is that the presence of second-phase particles in substantial volume fractions is apt to attenuate recrystallization textures, because new grains are nucleated preferentially in the misoriented zones and, because a new grains shares the orientation of some element of a misoriented zone, the texture becomes broadly scattered. So the texture is not really random *in relation to the orientations present in the deformed alloy.*

RYAN [1967] has studied the recrystallization of chromium containing a fine tantalum carbide dispersion, with a mean interparticle spacing of less than 1 μm, and found that recrystallization was severely inhibited. The presence of the precipitates produced an intractable dislocation substructure and the particles interfered with the migration both of sub-boundaries (fig. 48a) and of high-angle boundaries (fig. 48b).

Extensive work has been done on the annealing characteristics of deformed metals containing dispersed oxide. The extreme case of this is SAP (sintered aluminum powder), a very stable material containing closely-spaced oxide inclusions. These apparently are far too close together to permit any nuclei to develop. Fine oxide dispersions in many other alloy systems behave similarly; thus, internally oxidized alloys (dilute metallic solid solutions in which oxide dispersions are produced in situ by diffusing in oxygen) generally resist not only nucleation, but also the growth into the two-phase region of new grains nucleated in an adjacent region which is still single-

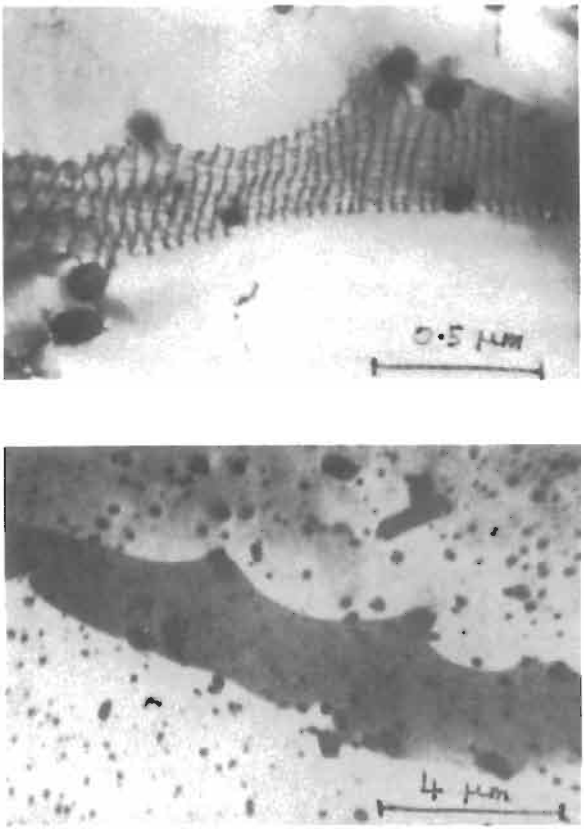

Fig. 48. (a) Sub-boundaries held up by precipitate in deformed chromium annealed at 1300°C (courtesy N. E. Ryan). (b) High-angle boundaries held up by precipitate in deformed chromium annealed at 1300°C (courtesy N. E. Ryan).

phase. These findings are reviewed by BONIS and GRANT [1960] (see also DESALVO and NOBILI [1968]), and JONES *et al.* [1979b].

The problem of the migration of a grain boundary in the presence of finely dispersed particles was first systematically examined in connection with grain growth (§ 4.1), and the fundamental theory was first presented by SMITH [1948], who followed an unpublished treatment due to ZENER. This must be the most quoted unpublished theory in metallurgical history!

Figure 49 represents a grain boundary migrating upwards under the influence of an unspecified driving force, and intersecting a spherical inclusion or pore. The drag exerted by the inclusion on the boundary, resolved in the y direction, is given by:

$$F = \pi r \lambda \sin 2\theta, \tag{6}$$

where λ is the specific interfacial energy of the boundary; this is effectively equivalent to a surface *tension.* The maximum value $F_{max} = \pi\, r\lambda$, for $\theta = 45°$.

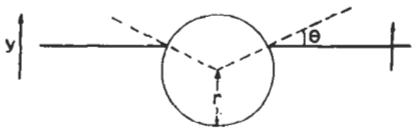

Fig. 49. Spherical inclusion resisting migration of a grain boundary.

If now there are N similar particles per unit volume, randomly distributed, their volume fraction f is $4/3\pi r^3 N$. A boundary of unit area will intersect all particles within a volume of $2r$, that is, $2Nr$ particles. Hence the number, n, of particles intersecting unit area of a boundary is given by:

$$n = \frac{3f}{2\pi r^2}. \tag{7}$$

Now suppose that the boundary is migrating purely under the influence of its own interfacial tension; if the grain periphery has a minimum radius of curvature R, the driving force is simply $2\lambda/R$ (§ 4.1). For a homogeneous grain structure (i.e., one where no grain greatly exceeds its neighbours in size) R approximates to the mean grain diameter D. As the grains grow, R increases and the driving force diminishes, until it is balanced by the drag due to inclusions, and growth suddenly ceases. Assuming that $R \approx D$, the critical diameter, D_{crit}, is given by the condition $nF_{max} \approx 2\lambda/D_{crit}$, or

$$D_{crit} = 2\lambda \frac{2\pi r^2}{3f} \frac{1}{\pi r \lambda} = \frac{4r}{3f}. \tag{8}$$

It is obvious that a given volume fraction of inclusions is much more effective in retarding grain growth when the particles are very small. Thus for $f = 0.01$ and $r = 10^{-4}$ cm (just visible in the *optical* microscope), $D_{crit} \approx 1.3$ cm; in effect, the particles exert no constraint, since homogeneous grain growth does not normally progress to such a large grain size. With $f = 0.01$ but $r = 10^{-6}$ cm (just visible in the *electron* microscope), $D_{crit} \approx 0.013$ cm, which represents effective grain size control. In primary recrystallization, where the driving force is much greater than $2\lambda/D$, the particle drag will be less effective.

HAZZLEDINE *et al.* [1980] have published a more sophisticated version of the Zener treatment, allowing for boundary flexibility and for the fact that not all particles hinder boundary motion. The result is of the same order as Zener's estimate. LOUAT [1981] developed this further and found drag values for $f > 0.001$ which substantially exceed Zener's estimate.

OLSON *et al.* [1982] have established that MnS formed in an ultrafine dispersion by rapid solidification processing leads to exceptional resistance to grain coarsening in a steel even at a temperature as high as 1200°C. They show thermodynamically that other dispersoids such as TiN should be even more effective than MnS in this capacity.

Small bubbles or cavities can act like inclusions in pinning boundaries. Thus, sintered and hot-worked pure platinum (MIDDLETON *et al* [1949]) and copper and silver (BHATIA and CAHN [1978]) recrystallize more slowly than the cast metal, similarly deformed. The general problem of interactions between pores and grain boundaries has been reviewed by CAHN [1980]. Small voids form around ThO_2 particles in thoria-disperse nickel which has been heavily cold-worked, and these voids have been found to hold up grain boundaries and thus impede recrystallization (WEBSTER [1968]). – An industrially very important exemplification of grain stabilisation by fine bubbles is the maintenance of longitudinal grain boundaries in tungsten lamp filaments. The tungsten powder precursor is doped with potassium, silicon and aluminum which form a stable compound that decomposes only at a late stage of sintering, generating cavities filled with potassium vapour that are then drawn down into fine strings of micropores that act to fix the position of grain boundaries and prevent premature failure of the filament. The processing of such filaments is surveyed by WELSCH and WALTER [1990], while a quantitative treatment of the forces acting on the grain boundaries in the filaments was published by STÜWE [1986].

A further complication in connection with particle drag is that small ($<0.5\ \mu$m) particles, especially if their structure is amorphous and has low viscosity, can be dragged bodily through the metal by a moving boundary (ASHBY and CENTAMORE [1968]). The general problem of particle drag has been reviewed by ASHBY [1980].

The general problem of grain-boundary migration in a two-phase alloy in which the precipitate phase is itself liable to form, coarsen or dissolve during the anneal, has received a good deal of attention and has received a masterly survey by HORNBOGEN and KREYE [1969a, b] (see also HORNBOGEN and KÖSTER [1978]). The most important variables are solute concentration and temperature of anneal. At a high concentration or low temperature, precipitate will form *during* recrystallization and strongly impede boundary migration.

A great deal of work has been done on the optimum dispersion of a second phase to achieve specific objectives, especially (for aluminum alloys) the production of the finest possible grain size (e.g., FURRER [1980] and many other papers in the same conference proceedings). Special interest attaches to the behaviour of alloys with a bimodal distribution of particle sizes (a few large, many very fine particles). The complications of recrystallization in such alloys are reviewed by NES [1980]. More recently, NES and HUTCHINSON [1989] have taken the matter further and analysed the ultimate grain size in terms of the ratio f/r. At small values of this ratio, the grains produced by recrystallization are unstable with regard to subsequent grain growth, because the Zener drag can be overcome; the smaller f/r, the smaller the drag and the larger the final grain size. At higher values of the ratio, the number of nuclei determines the grain size, and grain growth is inhibited, so grain size increases as the number of nucleating sites increases; at still higher v alues, recrystallization itself is inhibited. The final grain size is therefore a minimum at the balance point between grain growth control and nucleation control.

In many heat-treatment programmes, precipitation and recrystallization compete with each other; the extent (and mechanism) of recrystallization depends on the temporal

References: p. 2492.

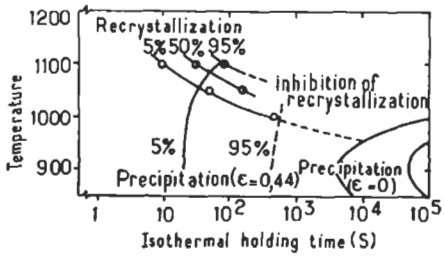

Fig. 50. Interaction of recrystallization and precipitation of an austenitic type-347 stainless steel. Plastic deformation to $\varepsilon = 44\%$ or $\varepsilon = 0$. (After LOMBRY *et al.* [1980].)

balance between the two, and is therefore very sensitive to temperature. Figure 50 (LOMBRY *et al* [1980]) shows an instance of this, for a stainless steel which precipitates NbCN during heat-treatment. The TTT curve shows that, for 44% strain, recrystallization in almost complete at 1100°C but does not proceed far at 1000°C. A similar balance has been studied more recently in a microalloyed steel containing titanium (MEDINA and MANCILLA [1994]). This kind of balance was classified and reviewed by HORNBOGEN and KÖSTER [1978], who also dealt with other aspects of two-phase recrystallization, and by DOHERTY [1982].

Special problems arise if the precipitate is coherent, as for instance in Cu–Co (PHILLIPS [1966]; TANNER and SERVI [1966]), Ni—Al (PHILLIPS [1967]; HAESSNER *et al.* [1966]; OBLAK and OWCARSKI [1968], KREYE and HORNBOGEN [1970]) or Al–Cu (HORNBOGEN and KREYE [1969a, b]). Under these conditions a special form of particle coarsening may be observed: the coherent particles dissolve as the boundary passes and re-precipitate behind the boundary in coarser form. This process can act as equivalent to a driving force, since the interface area is reduced. According to the particle-size distribution, temperature, solute concentration and equilibrium structure, such particles may either retard or accelerate boundary migration, though the former is more frequently observed. Hornbogen and Kreye for the first time succeeded in interpreting in an orderly way the complex situations which arise, and RALPH *et al* [1980] survey the different ways particles react to passing grain boundaries in superalloys. More recently, BOUCHAUD *et al.* [1992] analysed the dissolution/reprecipitation process in terms of the segregation of solute to grain boundaries: when the boundary is moving, the gradient of solute content either side of the boundary becomes unsymmetrical and small particles dissolve when they are bathed by solute-poor matrix adjacent to the advancing boundary. An even more surprising phenomenon has been predicted theoretically by RINGER *et al.* [1992]: when a coherent precipitate is left within a grain of a new orientation during recrystallization, it can seek to reduce its interfacial energy by rotating, via interfacial diffusion, to achieve coherency once again. The authors presented evidence for such a process in austenitic stainless steel containing very fine, coherent TiC precipitates (< 25 nm in diameter).

HOTZLER and GLASGOW [1982] have shown how the dissolution of coherent γ'-phase can be rate-determining for secondary recrystallization (see below). (See also ch. 9, § 4.4.1).

3.9. Recrystallization of ordered alloys (intermetallics)

When an alloy has a long-range ordered crystal structure, its recrystallization behaviour is considerably altered. Such alloys have fallen into two categories: those which become disordered on heating before they melt (reversible ordering), and those which are ordered up to the melting-temperature (permanent ordering). The former are more illuminating, because recrystallization in the same alloy can be compared in the ordered and disordered conditions.

A generalization which can be made with confidence is that when any reversibly ordered alloy is plastically deformed and then annealed above or below the critical ordering temperature and the behaviour compared, recrystallization is severely inhibited when the alloy is ordered. This distinction is particularly striking in alloys such as Ni_3Fe or Cu_3Au which order "discontinuously" at T_c, so that the Bragg order parameter changes abruptly from 0 to ≈ 0.8. The key experiments were done by VIDOZ *et al.* [1963], with Ni_3Fe and by HUTCHINSON *et al.* [1973] with Cu_3Au, and they were followed up by similar experiments on another alloy, $(Co_{78}Fe_{22})_3V$, by CAHN *et al.* [1991]. All these three alloys have the simple cubic $L1_2$ superlattice. In all these experiments the alloy was substantially rolled (50–90% reduction) and isothermally annealed either just below or just above the critical temperature, and in each of these studies the recrystallization was many times more sluggish below T_c. Figure 51 combines the key results of Hutchinson *et al.* with those by Cahn *et al.* The graphs plot the logarithm of the time required to achieve 50% recrystallization against reciprocal temperature: points for several temperatures both above and below T_c are included, and these points generate two straight lines which are extrapolated to T_c. The time taken to reach this level of recrystallization, close to T_c, is $\approx 100\times$ greater for the ordered state of Cu_3Au than for the disordered state; for the other alloy, the factor is $300\times$. The greater factor for the second alloy is presumably connected with the fact that it is more strongly ordered ($T_c = 910°C$) than is Cu_3Au ($T_c = 390°C$). Supplementary experiments in the Cu_3Au study established that the sluggishness in the ordered state was associated specifically with a smaller grain-boundary mobility compared with the disordered state.

The recrystallization behaviour of a range of ordered alloys was comprehensively reviewed by CAHN [1990]. The review includes a discussion of alloys such as FeCo which, in a certain temperature range, order heterogeneously by a "cellular" mechanism originating at grain boundaries; the process is comparable to strain-induced boundary migration, but driven by the ordering energy instead of by strain energy. When such an alloy is deformed in the disordered state and annealed well below T_c, there is competition between ordering and recrystallization and in a certain temperature range, recrystallization is entirely suppressed. Another alloy (Ni_4Mo), crystallographically quite distinct, again behaves quite differently according as the recrystallization temperature is low enough for recrystallization to precede ordering, or so high that ordering happens first (and then recrystallization is sharply braked). Cahn's review should be consulted for the full details of these involved relationships.

There is one other peculiar feature, characteristic of Cu_3Au which has recently been studied. YANG *et al.* [1996] studied the mechanism by which antiphase domains are

References: p. 2492.

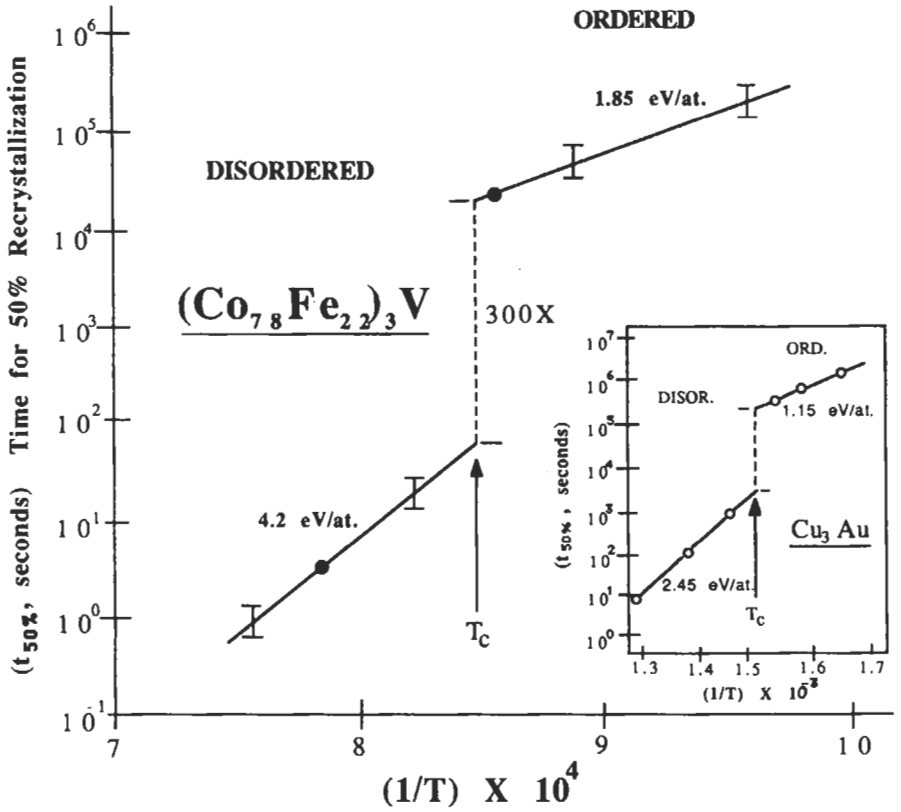

Fig. 51. The time for 50% recrystallization, $t_{50\%}$, versus $1/T$, for a $(Co_{78}Fe_{22})_3V$ alloy rolled 50%. Inset: similar information for Cu_3Au, rolled 50%, from HUTCHINSON *et al.* [1972]. Combined graph after CAHN *et al.* [1991]).

formed during the recrystallization of heavily rolled Cu_3Au. Fig. 52 shows a new grain in the process of growing (left to right) into the deformed matrix, at a temperature 10° below T_c. The domains are very small, of the order of a nanometre, just behind the advancing front of the new grain. The fact that antiphase domains form is proof that somewhere during the growth process, *dis*ordered alloy was present. There is reason to believe (see below) that a thin disordered zone is present around the grain boundary, and the domains form in that zone. This hypothesis at once runs into a difficulty: if the boundary zone itself is disordered, then why does such a boundary move so sluggishly? A simple calculation shows that this conundrum can be resolved by taking into account the energy needed to create the fine antiphase domains as the boundary advances. Indeed, it was shown that there is a critical size of domain, below which the boundary cannot move; it is rather like having a critical nucleus size in a precipitation reaction. If that critical size is larger than the thickness of the putative disordered boundary zone (here,

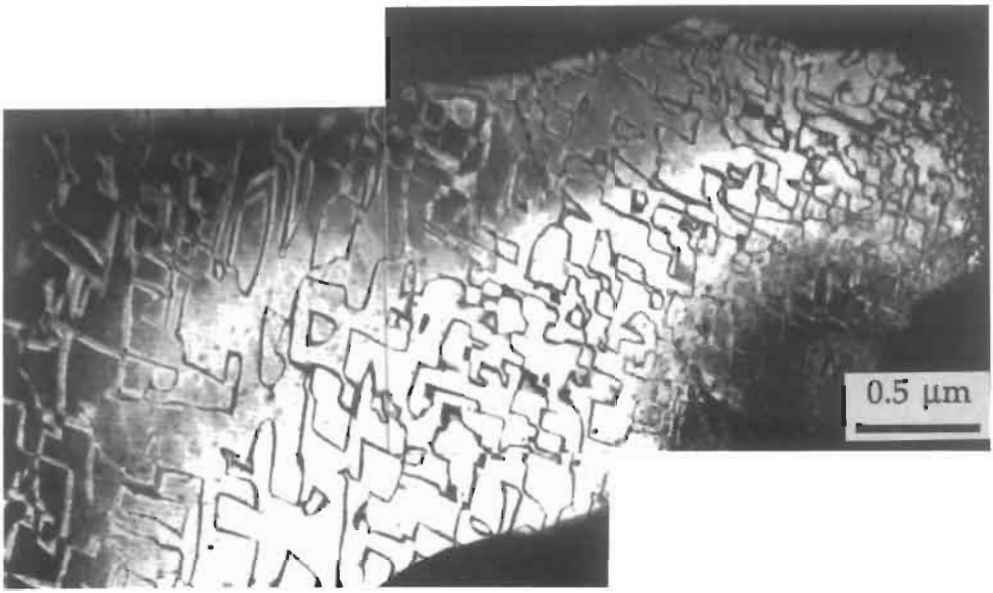

Fig. 52. Antiphase domain boundaries in a growing recrystallized grain in a sample of disordered Cu_3Au rolled to 86% reduction and annealed 96h at 380°C. Transmission electron micrograph (after YANG and CAHN [1995]).

≈ 1 nm), then no domains can form. When an alloy is strongly ordered, like Ni_3Al or $(Co_{78}Fe_{22})_3V$, the critical domain size is larger and this is why no antiphase domains are found in recrystallized grains in these alloys.

The evidence for a disordered boundary zone in Cu_3Au rests on direct electron diffraction with a 1 nm electron probe (YANG *et al.* [1996]). For Ni_3Al, there is extensive recent experimental evidence, though the findings are hotly disputed. Transmission electron microscopy, some of it at high resolution level, was applied to demonstrate that a proportion of boundaries (general high-angle type) in this alloy are disordered; one of the proponents refers to this as a "disordered boundary phase"; the disorder is associated with nickel enrichment, which is itself enhanced if boron is present as a dopant. Important publications on this issue are those by BAKER *et al.* [1990] and by KUNG *et al.* [1991]. It is important for the remaining uncertainty about this finding to be resolved, since the implications for the interpretation of the properties of this intermetallic are important, and it is also desirable for other ordered phases to be examined.

Recrystallization studies of permanently ordered intermetallics, especially Ni_3Al, are now beginning to be performed. The most thorough examination of the recrystallization behaviour of this phase, microstructures and textures included, is by BALL and GOTTSTEIN [1993, 1994]; here of course no comparison can be made between ordered and disordered states of the alloy. A striking feature of these studies is how weak the recrystallization textures are, even after heavy deformation. This is not currently understood. LIN and CAHN [1992] have examined the recrystallization behaviour of a highly alloyed nickel aluminide (containing Cr, Zr and B): this consists of 80% of γ'

References: p. 2492.

phase (i.e., alloyed and ordered Ni_3Al) and 20% of disordered γ, i.e., a nickel primary solid solution, in mutual epitaxy ... a mirror image of a superalloy, as it were. During the recovery stafe after cold work and annealing, it was found that most dislocations had moved from the γ' into the γ-phase; the interface between these acts as a one-way valve for dislocations, because they are paired in γ' but singlets in γ. Recrystallization is retarded in the γ'/γ alloy compared to single-phase γ'; rather surprisingly, nuclei form preferentially in the ordered phase.

4. *Grain growth and secondary recrystallization*

4.1. Mechanism and kinetics of grain growth

When primary recrystallization is complete, the grain structure is not yet stable. The main driving force, associated with the retained energy of deformation, is spent, but the material still contains grain boundaries which have finite interfacial energy. This situation is at best metastable, and ideal thermodynamic stability is only attained when the sample has been converted into a monocrystal. The situation is closely analogous to a froth of soap bubbles, which will gradually coarsen and may finish as a single bubble; indeed, such froths, under reduced pressure to accelerate growth, have been used as quantitative analogue of an unstable grain structure (SMITH [1964]).

Figure 53 serves to explain the instability of grain structures on geometrical grounds. Suppose first that, in two dimensions, the grains were to exist as an array of perfectly regular hexagons. The sides of the grains would then be flat and all triple points would be in equilibrium, because grain boundaries (in two dimensions, strictly grain edges) then all meet at 120°. Since all boundaries are assumed to be high-angle boundaries and thus of equal energy, the triangle of forces at the triple point is stable. If however a "rogue grain" has only, say, five sides, the average internal angle exceeds 120° unless the sides are curved convex outwards; then the sides must be unstable, and in seeking to shorten

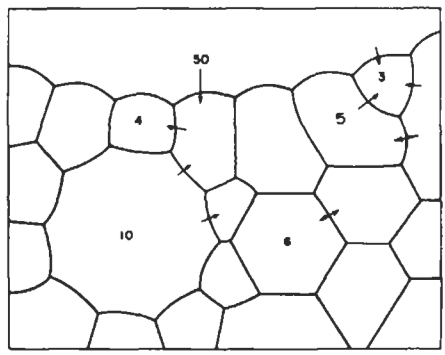

Fig. 53. Schematic diagram showing effect of the number of sides of grains on the curvature of grain boundaries. Six-sided grains are in two-dimensional equilibrium; smaller grains disappear, larger grains grow. (After COBLE and BURKE [1963].)

themselves through straightening, they will disturb the triple-point equilibria at the apices; thus the grain is gradually consumed. The smaller the number of sides, the sharper is the curvature of the sides for a given grain size, and the faster is the process of absorption. Once a rogue grain has vanished, the new neighbours find themselves out of equilibrium, and the process continues. Grains with more than six sides grow, those with fewer vanish. In three dimensions, the topological details are more complex (SMITH [1964]) but the principles are similar. The only entirely stable configuration (never encountered in practice) consists of an array of non-regular 14–sided polyhedra with doubly curved faces. In practice, arrays of grains are always unstable and coarsen continuously, until limited by some counterforce. The detailed grain morphologies that arrive in the course of grain growth are discussed by MCLEAN [1957], in more detail by HILLERT [1965] and most completely by RHINES and PATTERSON [1982].

In a soap-bubble array, it has been experimentally confirmed that the bubble diameter D follows the time law

$$\frac{dD}{dt} = \frac{1}{D}. \tag{9}$$

This law follows directly from the hypothesis that the rate of boundary migration is inversely proportional to the mean radius of curvature and that this in turn is proportional to D.

For this hypothesis to be acceptable, the boundary *mobility* (as distinct from the driving force acting upon it) must be invariant with time; this is reasonable, for the mobility is determined by the diffusivity of gas through the bubble walls, while the driving force is determined by the gas pressure in each bubble, which in turn is fixed by the radius of curvature of its walls. In a metal, correspondingly, either self-diffusion or else impurity diffusion will determine the mobility, while the surface tension of the curved boundary provides the driving force.

From eq. (9) it follows that

$$D - D_0 = Kt^{1/2}. \tag{10}$$

Experimentally, this has been confirmed for a number of pure metals or alloys, though n is usually slightly less than $1/2$. Frequently a value near 0.3 is found.

The simple law can be disturbed by a number of factors. In particular, impurities slow down and may eventually stop grain growth: for instance, a fraction of one per cent of molybdenum or manganese in *solution* in iron reduces the grain growth rate at a given mean grain size and temperature by several orders of magnitude (LESLIE *et al.* [1963]). Here impurities exert their effect through segregation to grain boundaries but without forming precipitates *; indeed, grain growth offers a good way of studying the impurity

* This is why it was long believed that cast structures were intrinsically incapable of grain growth. Geometrically there is no reason why this should be so, but impurities, which segregate at grain boundaries during solidification, slow down the process to vanishing point. Zone-refined cast polycrystalline metals do indeed undergo rapid grain growth (HOLMES and WINEGARD [1960]). A form of grain growth which does not require

drag effect, because the driving force is so well-defined and reproducible. Again, a disperse phase, even in very small quantities, can retard boundary motion as explained in § 3.8, and eventually bring grain growth to a halt. Here the growth law should be controlled not by the instantaneous grain size, but by the difference between this and the final limiting grain size; this, and the experimental evidence generally, are discussed by BURKE and TURNBULL [1952]. This influence is termed *disperse phase inhibition.*

The geometrical theory of grain growth in the presence of a dispersion of second phase particles has been taken to a very detailed level by the work of GLADMAN [1966, 1980] and HELLMAN and HILLERT [1975]. The treatment is based on an idealized grain-shape distribution, and it is assumed that the disperse particles are all the same size.

Only a grain larger than its neighbour, by about 30% at least, can consume the latter with a decrease of total boundary energy. The shrinkage of small grains is energetically favourable, the more so the smaller they become. There are distinct critical particle sizes (for a given volume fraction) to just inhibit growth of large grams and shrinkage of small ones. These critical sizes depend also on the degree of instantaneous heterogeneity of grain sizes. The critical particle size for inhibiting growth of large grains is proportional to the mean grain size, so that it can be seen that grain growth must eventually stop so long as the inhibiting particles do not simultaneously coarsen. An alternative outcome (see next section) is *secondary recrystallization.*

The most remarkable recent study of grain morphology during grain growth is that by RHINES and PATTERSON [1982], following on an earlier study by RHINES and CRAIG [1974]: it is also an excellent demonstration of the power of quantitative metallography (ch. 10, § 7). They demonstrated that the amount of deformation determines the width of the statistical distribution of grain sizes after primary recrystallization. This persists during subsequent grain growth. (The reduced heterogeneity of grain sizes after heavier strain is shown to be consistent with the hypothesis that nucleation centres have a minimum distance of approach) A highly heterogeneous grain-size distribution leads to relatively more small (triangular) grain faces; grains containing these shrink very rapidly, and grain-growth kinetics are thus intimately linked with the initial heterogeneity of grain sizes — and thus with the degree of deformation imparted in the first place.

VARIN and TANGRI [1980] have established that the characteristics of extrinsic boundary dislocations in a stainless steel were different after primary recrystallization and after grain growth. This implies that the grain-boundary structure may not reach a stable state when a boundary migrates rapidly This might affect relative grain-boundary energies, but has not been investigated.

Grain growth can be limited, not only by a particle distribution but also by thickness of the sample when this is in sheet form. The rate of grain growth diminishes sharply

prior deformation has recently come to be of major industrial importance. This is *directional recrystallization*, in which a superalloy (generally strengthened by an oxide dispersion) is passed slowly through a steep temperature gradient in the solid state, and in this way long slender grains are generated. The technique is used where directional solidification is not feasible, as with ODS alloys. Ways are being developed to predetermine the preferred orientation of the long grains, since this has a major effect on elastic and creep properties of the resultant assembly of elongated grains. The technique is reviewed by ROBERTS [1993]. (See also ch. 25, § A6).

once a substantial number of grains span the thickness of the sheet, so that the process becomes two-dimensional and normally growth stops altoghether when the mean grain diameter (as measured in the plane of the sheet) reaches between two and three times the sheet thickness (BURKE [1949]). This is due to the reduced driving force associated with boundaries which are cylindrically rather than spherically curved, and also with the drag caused by the grooves formed on a free surface where grain boundaries emerge; these grooves are formed by a process of surface diffusion and diffuse along with the migrating grain boundaries. This influence is termed *thickness inhibition.*

Finally, grain growth is seriously impeded if the grains resulting from primary recrystallization have a sharp texture (BECK and SPERRY [1949]). This is due to the much reduced grain boundary energy λ associated with grains having mutual misorientations of less than 15° (e.g., MCLEAN [1957]); this in turn reduces the driving force for grain growth, which for a given grain size is proportional to λ. This influence is termed *texture inhibition.*

The above treatment dates back to 1983. Since then, there has been a huge volume of computer simulation, in both 2 and 3 dimensions, of the process of grain growth, based upon a wide variety of models, for both single-phase and two-phase materials. Computer simulation of microstructural evolution, in the widest sense, has burgeoned in the 1980s and 1990s (see an overview by SROLOVITZ [1990]: processes such as sintering, precipitation, solidification and grain growth are all included). In 1991, a major conference on grain growth took place in Rome and the proceedings were published the next year at over 900 pages (see *Further Reading).* Much of this conference was devoted to computer simulation of grain growth. It is clear that the mix of determinisitc and statistical approaches offered by grain growth is irresistible to computer spcialists, though mostly the sheer complexity of the programming has restricted efforts to two dimensions. To a considerably lesser extent, simulation of primary recrystallization and of secondary recrystallization have also "taken off", occasionally in combination with grain growth (e.g., a concise treatment by MARTIN [1994]). This chapter, which is already too long, cannot accommodate a treatment of these approaches, but an excellent critical overview will be found in the book by HUMPHREYS and HATHERLY [1995].

A recrystallization texture can change during grain growth, but generally all that happens is that an existing texture is sharpened (e.g., HUTCHINSON and NES [1992]). This has been particularly demonstrated for the cube texture. This process has also been computer-modelled (TAVERNIER and SZPUNAR [1991]).

4.2. Formation of annealing twins

A commonly observed feature of recrystallized structures in certain face-centred cubic metals (particularly the copper-group metals and their solid solutions, lead and austenitic steels) is the presence of copious parallel-sided *annealing twin* lamellae, as sketched in fig. 54a. These lamellae are always bounded by {111} planes or *coherent boundaries,* apart from short incoherent steps and terminations, which are crystallographically more complicated. The orientation of the lattice within a twin lamella is related to that of the parent grain by reflection in the coherent plane. Immediately after primary

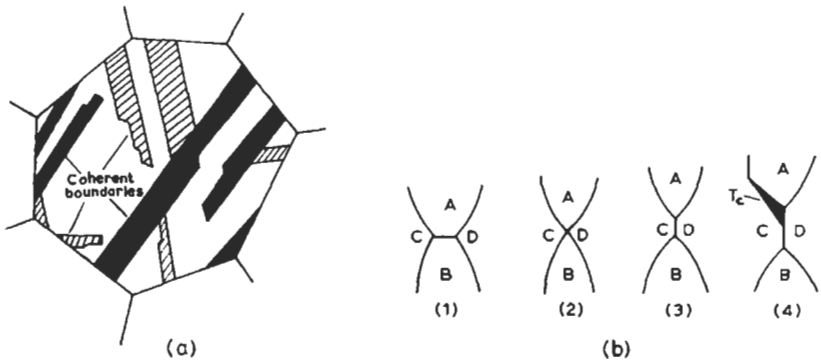

Fig. 54. (a) Annealing twin lamellae in a face-centred cubic metal grain. (b) Stages in the development of a twin during grain growth.

recrystallization there are few lamellae per grain, but their number increases with the progress of grain growth. However, this received truth has been cast into doubt by GINDVAUX and FORM [1973] who established by direct observation that most annealing twins form during primary recrystallization and few additional twins appear during subsequent grain growth.

The genesis of these twin lamellae has been clarified by Fullman, Burke and others (BURKE and TURNBULL [1952], SMITH [1964]). It rests upon the fact that the interfacial energy of coherent interfaces in the above-mentioned metals and alloys is only about 5% of the energy of an arbitrary high-angle grain boundary. If now a region of a grain structure goes through the configurational sequence shown in fig. 44b, then at stage (2) a new grain contact is established between grains C and D. Now it may happen, according to the accident of the particular orientation of these grains, that the twin T_c has an orientation close to that of grain D. Then the T_c–D interface is of lower energy than the C–D interface. C–A and T_c–A on the other hand will in general be of roughly similar energies. In that case the configuration (4) will be of lower energy than configuration (3), in spite of the extra area of interface represented by the coherent twin interface C-T_c; this is only possible because the latter has a very low specific interfacial energy. As growth proceeds, a *growth fault* will sooner or later be generated and a twin will appear at the advancing A–C–D triple point, and such a fault will be stable so that the twin grows as shown in stage (4). When the apex of the growing twin makes contact with a fresh grain, it may become unstable and the original orientation C will again take over; the result will be a parallel-sided twin lamella. On this model, the number of twin lamellae per unit grain boundary area should depend only on the number of new grain contacts (as at stage (2) of the figure) which have been made during growth, irrespective of absolute grain size and temperature; experiments by HU and SMITH [1956] have shown that this is indeed so. This study has established the model beyond doubt. The earlier observations on the balance of grain-boundary energies were extended by VISWANATHAN and BAUER [1973b]; they showed in particular that, as predicted by the theory, the migration of relatively small-angle boundaries does *not* give rise to any twins. A recent review, taking into account

the newer observations, is by GLEITER [1981].

When the coherent twin interfacial energy, γ_T, is higher in relation to the energy of ordinary grain boundaries, γ_B, as in aluminum where $\gamma_T/\gamma_B \approx 0.2$, then annealing twins are very rare.

Annealing twins have also been found in body-centred cubic metals and alloys; here the crystallography is more complicated, and one twin can have three distinct coherent interfaces. Figure 55 shows an example. The low energy of the coherent boundary can be deduced from the fact that the normal grain boundary is only slightly deflected where a coherent boundary abuts on it (at P).

Recently, the methods of mesotextural determination have been applied to the study of twin formation during recrystallization and grain growth, in the already cited study by GERTSMAN *et al.* [1994]. Twin formation has also been adduced in one model of nucleation in primary recrystallization, notably in copper; this model, as already indicated, is fully set out by HAASEN [1993].

4.3. Grain growth in nanostructured materials

The terms *nanostructured* or *nanocrystalline* are applied to polycrystalline materials, metallic or ceramic, in which the grains are a few nanometres across, as distinct from familiar materials in which grain sizes are measured in tens of micrometres or more. The preparation and study of such materials is of recent date: one of the first publications in the field was as recently as 1987 (KARCH *et al.* [1987]); a coauthor, H. Gleiter (one of

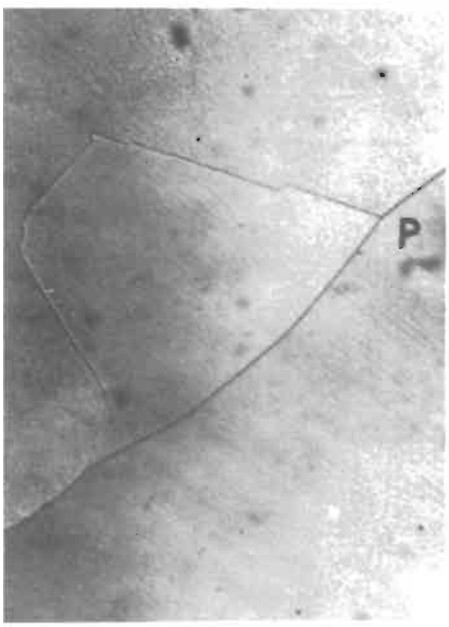

Fig. 55. Annealing twin in an iron–aluminum alloy after prolonged grain growth. 170×. (After CAHN and COLL [1961].

the authors in this work) is generally regarded as the originator of the field, from a materials science perspective (cf. ch. 9, § 5.4). Not long afterwards, a massive review of the field was published by ANDRES *et al.* [1989]; they used the earlier term, "cluster-assembled materials", because it was customary then to make the materials by evaporation into a gas at moderate pressure and "assembling" the smoke by some form of consolidation under pressure. Since then, it has become increasingly common to use prolonged mechanical milling of starting materials with conventional grain sizes to make nanostructured materials (KOCH [1991]). A recent review of these materials in all their ramifications is by SIEGEL [1993]; they now even have their own journal, entitled *Nanostructured Materials.*

It is a common characteristic of nanostructured materials that the proportion of the total volume directly affected by the grain boundaries (or, to use a more common expression, the percentage of "atoms in grain boundaries"), can be several tens of %. There is extensive evidence that these grain boundaries are more disorderly and of lower density than in normal materials; for instance, they lead to a substantial extra specific heat, e.g., 20% for n-platinum (TSCHÖPE and BIRRINGER [1993]). There is thus particular interest in examining the stability of these ultrafine grain sizes, both from a fundamental viewpoint and because some of the proposed applications, in particular superplastic deformation, depends on a stable nanograin structure.

Some nanostructured materials, metals, ceramics and intermetallics alike, especially those made by cluster assembly, show remarkably sluggish grain growth even at temperatures at which the grains in normal equivalent material would grow measurably, whereas one would expect such materials, because of their huge grain-boundary area, to be particularly liable to grain growth at modest temperatures. In others, however, grains grow even at room temperature, but even in these cases, growth soon saturates and the material always remains in the nanocrystalline range. This is exemplified by fig. 56a, from a study of cluster-assembled n-copper (GERTSMAN and BIRRINGER [1994]). This links with a recent observation (DILLE *et al.* [1994]): this referred to electrodeposited copper of 300 nm grain size (rather large by nano standards), strained by 7%. The material recrystallized slowly at room temperature and rapidly at 100°C; the new grains were ≈ 1 μm across, and these tiny new grains were judged large enough to be the product of secondary recrystallization. (This seems to be the only recorded study of recrystallization as distinct from grain growth in a nanostructured material.) N-platinum (TSCHÖPE and BIRRINGER [1993]) coarsened fairly rapidly at 150–200°C (fig. 56b). An intermetallic, TiAl, made by cluster-assembly showed small grain growth up to 800°C and only then breakaway behaviour (fig. 56c) (ALTSTETTER [1993]). Oxides are apt to show even more stability: thus, SIEGEL *et al.* [1988] showed that the grain size in n-TiO_2 was completely unaffected by annealing up to 550°C and runaway increase did not start until 800°C had been reached.

The above examples all refer to cluster-assembled materials. The behaviour of nanocrystalline materials made by mechanical milling is apt to be different from the pure metals described above. Thus n-iron made by milling (MOELLE and FECHT, [1995]) shows little grain growth up to 500°C. Again, ECKERT *et al.* [1993] made Cu-rich n-Fe–Cu alloys (metastable solid solutions) by milling mixed elemental powders and found

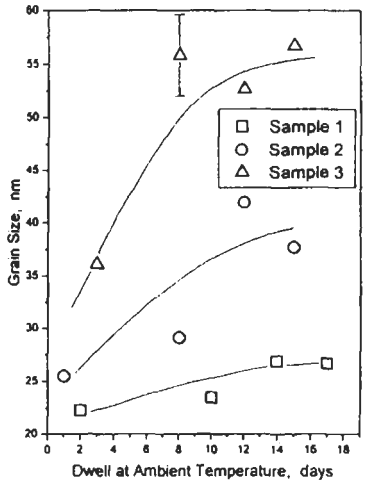

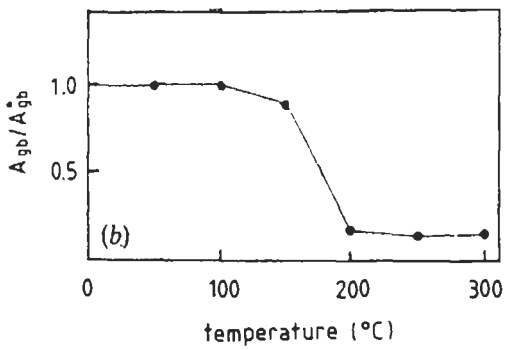

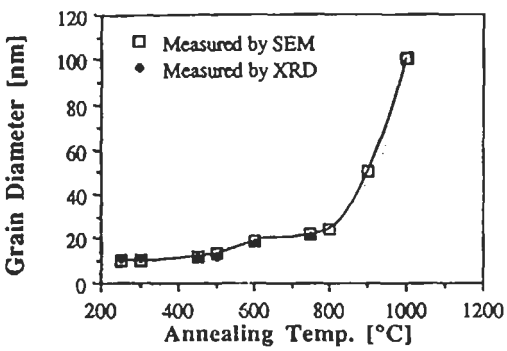

Fig. 56. (a) Grain growth at room temperature in cluster-assembled nanostructured copper, estimated by X-ray diffraction. Sample 1 was consolidated to 93% of theoretical density, sample 2 to 96% and sample 3 to 97% (after GERTSMAN and BIRRINGER [1994]. (b) Grain growth in n-platinum, annealed for unspecified periods at increasing temperatures, depicted in terms of changes in relative total grain-boundary area, estimated from X-ray diffraction (after TSCHÖPE and BIRRINGER [1993]). (c) Grain growth in cluster-assembled-TiAl, caused by two-hour anneals at successively higher temperatures (after ALTSTETTER [1993]).

References: p. 2492.

no detectable grain growth prior to phase separation; they opined that iron atoms metastably enriched at the grain boundaries would prevent these from migrating on account of solute drag. The same kind of behaviour was observed in metastable, milled n-Zr–Al solid solutions (FU and JOHNSON [1993]). The greater grain stability of the milled n-materials seems to be connected with the metastable enrichment of solute in grain boundaries. This can happen even in cluster-assembled n-materials under special circumstances: thus, HÖFLER *et al.* [1993] made n-copper by evaporation and cluster assembly and then diffused in boron, in order to measure its diffusivity. Boron diffusion was measured at 80°C both with and without a prior relaxation anneal at 100–140°C. The diffusivity dropped sharply after the anneal, and there was no grain growth. (Compare this with the R.T. grain growth observed in uncontaminated cluster-assembled copper). Höfler's observation was one of a range of findings which show clearly that grain boundaries in nanostructured materials are in a state of metastably enhanced energy, leading to such properties as increased density (see also LU and SUI [1995]), specific heat and diffusivity; anneals at modest temperatures can modify these properties.

SIEGEL [1993] has discussed the high resistance to grain growth in many nanostructured materials in general terms, and concludes that it is due to what he calls a form of frustration: there is evidence that cluster-assembled materials, at any rate, have flat grain boundaries and a strikingly narrow grain-size distribution, both factors which would make for a modest driving force for grain growth. He compares the materials to fine closed-cell foams with a narrow cell-size distribution, which are "deeply metastable" in spite of their large stored surface energy.

4.4. Secondary recrystallization

4.4.1. General features

When the annealing of an initially deformed sample is continued long beyond the stage when primary recrystallization is complete, the even tenor of grain growth may be interrupted by the sudden very rapid growth of a few grains only, to dimensions which may be of the order of centimetres, while the rest of the grains remain small and are eventually all swallowed by the large grains. This is *secondary recrystallization,* or *coarsening*. Figure 57 shows an instance of incipient secondary recrystallization. The process has the following general characteristics:

(a) The large grains are not freshly nucleated; they are merely particular grains of the primary structure grown large.

(b) The first stages of growth of the large grains are sluggish; there is an induction period before secondary recrystallization gets under way.

(c) The factors governing the choice of the victorious primary grains which are to grow large, and the mechanism of the early stages, are the least understood parts of the process. It is generally agreed that secondary-grains-to-be must be appreciably larger than the mean primary grain size, and they must have orientations which diverge from the main primary texture.

(d) Something must inhibit normal uniform grain growth; it is only when grain growth is very slow that large secondary grains can effectively grow. Inhibition by a

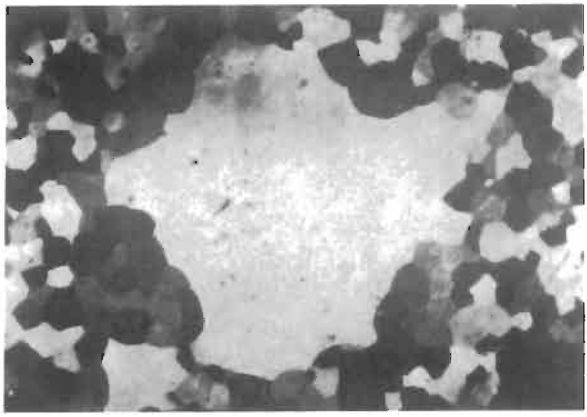

Fig. 57. Incipient secondary recrystallization in zinc sheet. 100×.

dispersed phase, by primary texture or by sheet thickness, may all play a part.

(e) The secondary structure, when complete, sometimes has a pronounced texture. Such a texture always differs from the previous primary texture.

(f) A well-defined minimum temperature must be exceeded for secondary recrystallization. The largest grains are normally produced just above this temperature; at higher annealing temperatures smaller secondary grains result.

(g) The driving force of secondary recrystallization, once the large grains are well launched, normally arises from grain-boundary energy (just as does normal grain growth); under special circumstances, the surface energy of the grains can contribute. Figure 58 exemplifies several of these regularities. Suppose a primary structure contains a grain of roughly twice the average diameter such as the lower left-hand grain of fig. 53. If we assume that the interfacial energy of the boundaries separating this grain from its smaller neighbours (γ_s) is the same as the energy of the boundaries between these neighbours themselves (γ_p), then the sides of the large grain must be convex inwards as shown in the figure, if the triple grain junctions are to be in equilibrium. This configuration, which is clearly recognizable in fig. 57, is evidently unstable, since the curved boundaries will seek to become straight and in the process will upset the equilibrium at the triple points. which thus migrate outwards. The larger the grain grows, the more sharply will its bounding faces become curved and the process is thus self-sustaining. At a certain size a grain has reached "breakaway point", and thereafter grows rapidly, quickly reaching the stage of the grain at the top of fig. 53. There is no mystery, then, about the continuation of secondary growth once it has started; only the first stages are hard to interpret.

Consider a grain such as the ten-sided one in fig. 53. Let its diameter be D while its smaller neighbours have diameter d. Whether or not this grain has reached breakaway point depends on the boundary-energy ratio γ_s/γ_p and on the volume fraction f and radius r of the dispersed-phase particles. When γ_s/γ_p is large (i.e., a grain of divergent orientation surrounded by primary grains with a strong texture) then the critical ratio

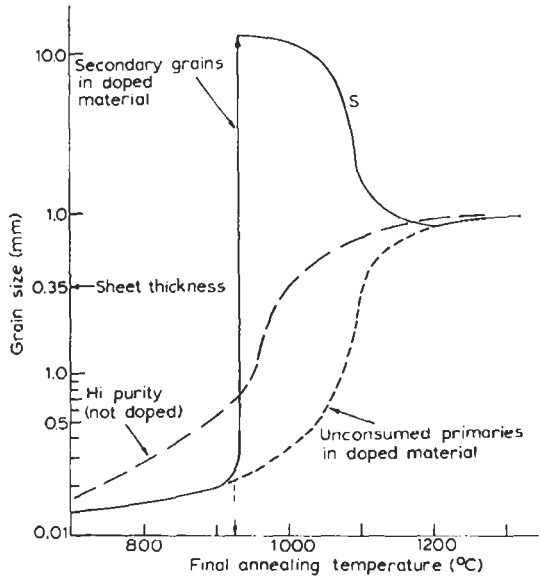

Fig. 58. Grain size (log scale) as a function of temperature for pure and MnS-doped 3% silicon–iron, cold-rolled 50% to 0.35 mm thickness, annealed 1 h. The drop in curve S is due to an increase in the number of secondary grains at higher temperatures, until above 1100°C all grains grow equally to a size limited by the sheet thickness. (After MAY and TURNBULL [1958].)

D_{crit}/d is large (because the equilibrium angle between adjacent sides of the large grains is then greater than 120°). The larger is f and the smaller r, the stronger is the boundary drag. It is only the curvature of the sides of the large grains which drives them to grow and the drag counteracts this driving force. Thus a large f and small r (i.e., an effective dispersion) increase D_{crit}/d. MAY and TURNBULL [1958] have analyzed this problem in detail (fig. 58) and conclude that:

$$\frac{D_{\text{crit}}}{d} = \frac{\frac{3}{4}\left(4\gamma_s/\gamma_p - 1\right)^{1/2}}{1 - \left(\alpha\gamma_s/3\gamma_p\right)f/r}. \tag{11}$$

Once the large grain has somewhat exceeded the critical diameter D_{crit}, then the driving force ΔF per unit volume for boundary migration settles down to a value

$$\Delta F \sim 2\left(\frac{\gamma_p}{d} - \frac{3}{8}\gamma_s\frac{f}{r}\right) \tag{12}$$

and the rate of growth G of the secondary grains is derived by multiplying this term by the mean boundary mobility. This expression for ΔF is most simply regarded as containing an energy term depending on the total area of primary grain boundaries destroyed per unit distance moved by the secondary boundary, and a drag term which counteracts this.

This analysis is qualitatively in agreement with the known facts about secondary recrystallization, but it was subjected to quantitative test until the theory of Thompson *et al.* (see below) and various recent computer simulations.

Three processes suggest themselves that might enable a primary grain to grow to the point of breakaway:

(a) There is a sharp primary texture with only a few sharply deviating primary grains. All or many of these grains grow, not because they have a strong tendency to do so (the large value of γ_s/γ_p indeed discourages them) but only because the small value of γ_p is even more effective in discouraging the normal growth of grains belonging to the sharp texture. Such a situation will not produce a sharply defined secondary texture. This is believed to be the most common source of secondary grains.

(b) There are many deviant primary grains and among them a few are so oriented that their grain-boundary mobility M is particularly high. Then during normal grain growth such grains will forge ahead, not because of a higher driving force but only because of their higher mobility, and eventually they reach the critical diameter for breakaway. KRONBERG and WILSON'S [1949] original discovery of "special orientations" stemmed from a study of secondary grains in copper; here, presumably, growth selectivity operated merely during the very early stages of growth. A sharp texture results from this process.

(c) The successful grains may have a more perfect lattice than their neighbours and thus possess a larger driving force for growth. This has often been suggested but never substantiated. It is hard to see how it can produce a secondary texture.

From the foregoing, it is evident that the nature of the disperse phase is vital in controlling secondary recrystallization; unless there is a very sharp primary texture with a few rogue grains, a properly dispersed second phase is vital for secondary recrystallization. If the dispersion drag is insufficient, too much normal grain growth occurs; if it is too great, the secondary grains cannot grow at all (the right-hand sides of eqs. (11) and (12) are negative). Thus in fig. 58 the primary grain size of the pure alloy increases more rapidly than that of the alloy doped with a manganese sulphide dispersion; the latter undergoes secondary recrystallization, the former does not. GLADMAN [1980] has analyzed the role of the fine-particle dispersion in the light of his (and Hillert's) theory of grain growth in the presence of a dispersion, outlined in § 4.1. When a distribution of grains is just inhibited from growing, then a slight degree of coarsening of the disperse particles by Ostwald ripening (ch. 9, § 4.2.2; ch. 15, § 2.4.2) will unpin the few largest grains only. These can then act as "nuclei" for secondary recrystallization.

This was where the theory of secondary recrystallization stood a few years ago. Since then, it has been recognized that *in the absence of any special features* distinguishing the larger grains (distinct texture, distinct surface energy ... see below), a skewed grain size distribution involving a few large and many small grains is *not* self-sustaining: in other words, under those circumstances, prolonged annealing will tend to restore the grain size distribution back to uniformity, and there can thus be no such thing as a breakaway size for the larger grains. This emerges clearly from a theoretical paper by THOMPSON *et al.* [1987]: they developed two alternative models, one an extrapolation of standard Ostwald ripening theory (grain growth is somewhat analogous to Ostwald ripening), the other based on the average grain-boundary curvature of n-sided grains. In each case, the

References: p. 2492.

explicit conclusion is that "if driven by uniform grain-boundary energy alone, secondary grains do not grow at higher rates than their normal neighbours." It is *essential* that some special feature be present, such as a textural difference (statistical, at the least) between the larger grains and the normal grains, because this affects the relative grain-boundary energies for the two populations ... or a critical degree of dispersion of particles, or an anisotropy of surface energies. To examine how such factors quantitatively affect the development of secondary grains, computer simulation is really indispensable, because so many factors enter into the process. Two such simulations have recently been published for the development of secondary grains with a strong Goss ((110)/[001]) texture in silicon-iron, as observed in practice. It was possible to vary the degree of particle-inhibition, texture sharpness, fractions of texture components, etc. One simulation is by ABBRUZZESE *et al.* [1992], the other by NAKAYAMA and USHIGAMI [1992]. Both found parameters which provided good agreement with the observed extremes of secondary growth and texture sharpening within the secondary grain structure.

Secondary recrystallization can take place during or after hot-working, if normal grain growth is inhibited. A very detailed study on the hot-working of a superalloy (SINGER and GESSINGER [1982]) showed that for large strains and low strain rates, normal grain growth is enhanced by the applied strain and this prevents the "take-off" of secondary grains.

The control of dispersions, especially of manganese sulphide, is evidently of vital importance in producing strip for transformer cores made of iron–3% silicon alloy. This material, when properly treated, consists of secondary grains with the *Goss* texture, (110)[001]. This texture is beneficial because the [001] direction is one of easy magnetization and thus a smaller mass of transformer laminations is required than if the texture were random. While much of this work is subject to commercial secrecy, WASSERMANN and GREWEN [1962] give an extensive survey of the procedures published up to that date. FIEDLER [1964] has illustrated the role of manganese sulphide inclusions in controlling secondary recrystallization in this material. More recent developments concerning texture in iron-silicon alloys are discussed in ch. 29, § 4.2.3.3.

The analysis by DILLAMORE *et al.* [1967] to interpret the primary annealing texture of steel containing an AlN dispersion (§ 3.6) can also serve to explain the development of the Goss texture from a primary annealing texture containing a weak (110)[001] component. That component is weakly represented, because in the deformed structure grains of (110)[001] orientation were few in number, but they did have the largest stored elastic energy; therefore, though few, they began to recrystallize first when the rolled sheet was annealed, and hence grew largest. When the AlN dispersion eventually coarsens, all the largest grains (which then become unpinned) have the (110)[001] orientation. The fact that the secondary texture is so sharp derives from the very sharp variation, in the cold-worked polycrystal, of stored elastic energy with small deviations from the (110)[001] orientation, which in turn implies that the size of the largest primary grains is very sensitive to their exact orientations.

A recent study by INOKUTI *et al.* [1980, 1983], in which orientations of many individual grains were mapped, is consistent with Dillamore's model. (110)[001] grains grow from the surface regions, where they are particularly large after primary

recrystallization (because of a variation, through the thickness, of the degree of dispersion of second-phase particles). This is a particularly comprehensive investigation.

In recent years, major improvements have been achieved in Japan in the secondary recrystallization of iron–silicon transformer alloys: very fine control of dispersed phases has permitted a sharper (110)[001] texture to be obtained (e.g., INOKUTI *et al.* [1980], TAGUCHI and SAKAKURA [1969]; ch. 29, §§ 4.2.3.3, 4.2.4).

A striking illustration of the importance of even very small amounts of disperse phase in promoting secondary recrystallization is provided by the work of CALVET and RENON [1960]. They heat-treated a number of aluminum-copper solid solutions at temperatures close to the solid solubility limit. Effective inhibition of normal grain growth and very rapid secondary recrystallization was observed whenever the annealing temperature was as little as 1–2°C below the temperature at which all the copper present just entered into solid solution; at or above this temperature, only rapid normal grain growth took place. The dividing line between the two modes of recrystallization in alloys of different compositions accurately traced out the known solubility curve. The volume fraction of disperse phase just below the solubility line must be very small, less than 0.1% but this is apparently enough to retard normal grain growth quite brusquely and thus permit secondary recrystallization. This behaviour is the analogue, for secondary recrystallization, of the behaviour in primary recrystallization of an Al–Fe alloy that precipitates and recrystallizes, sluggishly, at the same time (MIKI and WARLIMONT [1968]).

Especially complex behaviour is observed when secondary recrystallization is controlled both by a stable oxide dispersion and by a coherent γ'-dispersion which must dissolve and reprecipitate to allow a grain boundary to pass (HOTZLER and GLASGOW [19821]).

4.4.2. Surface-controlled secondary recrystallization

In 1958 it was discovered independently in several laboratories that after prolonged annealing in the range 1000–1200°C, thin sheets of 3% silicon–iron (the alloy used for transformer cores) sometimes developed a secondary (001)[100] or *cube texture,* as distinct from the normal (110)[001] Goss texture referred to above. DETERT [1959] and WALTER and DUNN [1959], again independently, clarified the necessary conditions: The sheet has to be thin (normally below 0.1 mm in thickness) and the annealing has to be done in an atmosphere containing traces of oxygen. If, after cube texture has been established, the atmosphere is replaced by very dry hydrogen or by high vacuum, the texture disappears and is replaced by the Goss texture. This process has been termed *tertiary recrystallization;* indeed, by repeated changes of atmosphere the texture can be changed repeatedly.

It has been convincingly established that the development of these textures is governed by an anisotropy in surface energy γ_s. The surface energy (surface tension) of a grain at a free surface depends on its orientation; various indirect experiments on copper, silver, iron and other metals show that there is a measurable difference between, for instance, γ_s (100) and γ_s (111); according to the type of experiment, differences of 3–30% have been inferred (SHEWMON and ROBERTSON [1963]). HONDROS and STUART [1968] also made measurements of these energy differences. There is also some

References: p. 2492.

evidence, summarized in the same review, that adsorbed impurities (which are known to change the crystal structure of the surface) considerably reduce the anisotropy. It appears that when the strip surface is comparatively clean, (110) faces have the lower surface energy, while in the presence of adsorbed oxygen, (100) has the lower energy; other orientations are probably intermediate. If the strip is thin enough, this anisotropy of surface energy is sufficient to cause the most favourably oriented grains to grow at the expense of all the others.

If this model is correct, and if moreover the surface energy varies rather sharply with small changes in orientation of a grain, then one would expect the (001) planes to be accurately parallel to the surface, while the parallelism of [100] to the rolling direction might be subject to considerable scatter. This is what is observed: (001) is always parallel to the strip within 5–7° at most, while scatter of up to 40° is observed for the [100] vector in the plane of the strip. This scatter is determined purely by the range of orientations in the primary texture. FOSTER et *al.* [1963] studied the kinetics of the growth of (001)-oriented secondary grains in silicon–iron as a function of primary grain size and sheet thickness. They assumed that the growth rate G is given by the expression

$$G = M\Delta F = M\left(\frac{2\gamma_p}{r} + \frac{2\Delta\gamma_s}{t} - C\right), \tag{13}$$

where M is the mobility of the secondary boundaries, ΔF is the total driving force per unit volume, γ_p is the energy of the boundaries between primary grains, $\Delta\gamma_s$ is the difference between the surface energy of (001)–oriented grains and an "average" orientation, $2r$ is the mean primary grain diameter, t is the sheet thickness and C is the drag force associated with disperse particles. When a secondary grain is big, the driving force for secondary growth is essentially the energy ΔF_p per unit volume associated with primary grain boundaries. For roughly cylindrical primary grains (diameter *d)* spanning the sheet thickness, $\Delta F_p = 2\pi r\gamma_p/\pi r^2 t = 2\gamma_p/r$. The driving surface energy per unit volume of metal in a sheet of thickness t, which is composed entirely of cylindrical (001)-oriented grains, as compared with grains of random orientation) is $\Delta F_s = 2\pi r^2\Delta\gamma_s/\pi r^2 t = 2\Delta\gamma_s/t$. Since $\Delta F = \Delta F_p + \Delta F_s - C$, eq. (13) follows.

From measurements of G in sheets with various r and t, the correctness of the relationship was established. For instance, with a given t, G should vary as $1/r$. Figure 59 shows that this relationship is obeyed, and shows how sensitive secondary grain growth is to primary grain size. Extrapolation shows that above a limiting grain size of about 1 mm, secondary recrystallization could not continue at all; since, however, primary grain size is restricted by thickness inhibition to a maximum of about $3t$, this limiting primary grain size is never reached. Small thicknesses favour surface-induced secondary recrystallization both because it restricts primary grain size and because the surface/volume ratio of secondary grains is greater.

From their measurements, Foster, Kramer and Wiener derived values of $\Delta\gamma_s$ and C in terms of the primary grain boundary energy γ_p. Typically, for $t = r = 0.3$ mm, $\Delta F_p \approx 33\gamma_p$, $\Delta F_s \approx 2\gamma_p$ and $C \approx 14\gamma_p$. Thus $\Delta F = (33 + 2 - 14)\gamma_p = 21\gamma_p$ mJ/m^2. This surface energy term is only 10% of the total resultant driving force. This term decides the

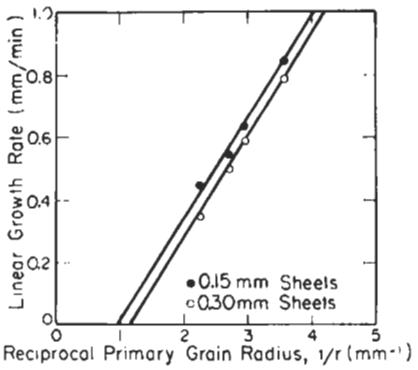

Fig. 59. Effect of primary grain size on growth rate of (001)-oriented secondary grains. Strips of two different thicknesses were used. (After FOSTER *et al.* [1963].)

selection of the orientation which is to grow, but ΔF_p and C together determine the rate of growth of the secondary grains.

Cube texture in silicon–iron would be very desirable for transformer laminations, in spite of the scatter in the texture (ch. 29, § § 4.2.3.3 and 4.2.4), and this is the reason for the considerable effort which has been devoted to attempts to manufacture this material commercially. Up to the present, however, it has not been possible to achieve the necessary rigorous control of processing variables at an economic cost.

It is probable that surface-energy-controlled secondary recrystallization is a good deal more common than has been recognized. Thus DUNN and WEBSTER [1965] have been able to grow (110)-oriented grains in thin tantalum strip by this mechanism: this orientation is particularly favourable if the metal is to be used as an electron emitter in thermionic energy converters. Again, MCLEAN and MYKURA [1965] have found that (111)-oriented grains grow preferentially in thin platinum sheets, and (0001)-oriented grains were found to grow in sheets of zinc (MILLER and WILLIAMS [1964]).

The environmental influence in surface-controlled secondary recrystallization appears to be very subtle in detail. Thus MEE [1968] has found that oxygen and sulphur both have a major effect on the phenomenon, and that moreover the metallic impurities in the alloy and their state of heat-treatment also influence the texture.

The situation concerning secondary recrystallization, overall, has been reviewed in detail by DUNN and WALTER [1966], WALTER [1969] and DETERT [1978], and again in the already cited theoretical paper (THOMPSON *et al.* [1987]).

4.4.3. Thin films

Thin metallic films are used for interconnects in integrated circuits, for superconducting devices, magnetic memories and other advanced applications, and their grain structures and preferred orientations can have a profound effect on their performance. A good example is the performance of interconnects which have the form of narrow strips, which are subject to failue by electromigration. It has been shown that if the grains in

such a strip can attain a "bamboo" configuration, with successive grains occupying the entire cross-section, then the mean life to failure will increase (VAIDYA *et al.* [1980]). A recent modelling study by WALTON *et al.* [1992] has examined the gradual transition of an equiaxed grain strucure in an as-deposited film towards the bamboo configuration as a function of the width-to-thickness ratio (w/t), taking into account the effect of surface grooving which, as shown long ago in a classical study by MULLINS [1956] (see also BROKMAN *et al.* [1995]), restricts the mobility of grain boundaries in thin films. Figure 60 shows the evolution of grain shape for $w/t = 3$. Bamboo formation is not complete, and the simulation showed that for complete conversion, w/t must not exceed 2.

This is an example of the research recently done on grain configurations in thin films, both free-standing and in contact with an epitaxial substrate, by a group led by C. V. Thompson and H. J. Frost. Some of the work is closely related to that described in the preceding Section, but for much smaller thicknesses than the transformer laminations which inspired the work described above. Two of the key papers, dealing with stagnation and abnormal grain growth, are by FROST *et al.* [1990, 1992]. It is simpler, though, to read about the conclusions of these researches in two reviews (THOMPSON [1990, 1992]). The main conclusions are:

a) If the as-deposited grain size (dependent on evaporation rate, substrate temperature, etc.) is less than the film thickness, grain growth proceeds with the usual kinetics.

b) When the mean grain size becomes columnar and reaches about 2.5 times the film thickness, the grain strucrture becomes *stagnant*, and no longer changes unless a special

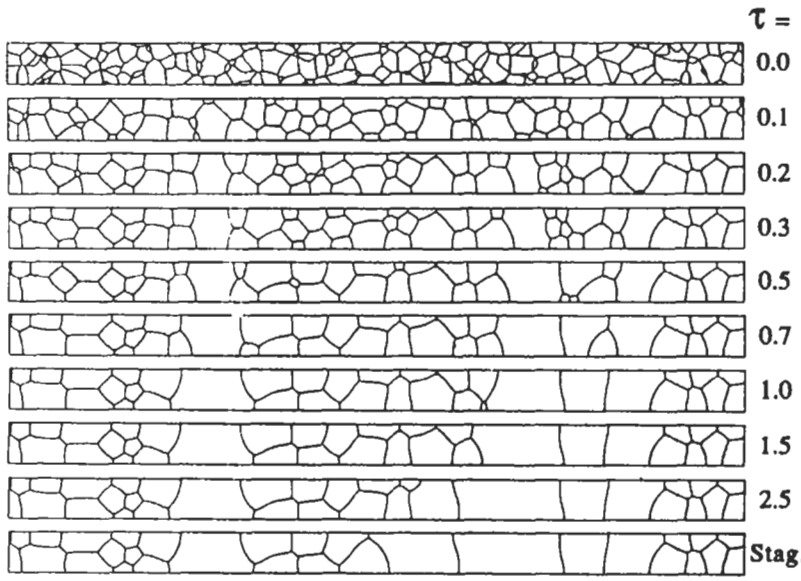

Fig. 60. Evolution of a modelled grain structure in a thin metal strip, width equal 3 times the thickness, taking into account the retarding effect of surface grooves where grain boundaries intersect a free surface. The strip reaches "stagnation" before conversion to a bamboo structure is complete (after WALTON *et al.* [1992]).

stimulus is present.

c) If further grain growth *is* observed, it is secondary recrystallization in which a few grains grow large and the rest remain stagnant. Such growth is driven by orientation anisotropies and a texture thus develops in the lasrge grains. The secondary growth process is the faster, the thinner the film (as with transformer sheets).

Underlying these generalizations is a good deal of experimentation, analytic theory and computer simulation, for details of which the original papers must be consulted.

A good overview of the specific case of surface-controlled (secondary) recrystallization, as modelled by computer, has been published by FROST *et al.* [1992]. It is clear that in this process, a strong preferred orientation arises from an initially randomly oriented polycrystalline film. The stagnant structure before the secondary process begins (allowing for the effects of grooving) is unusual (fig. 61). The distribution of the number of sides per grain is much narrower than in bulk grain growth, and this is accompanied by a clustering of the larger grains and separately of the smaller grains, as seen in the figure. It turns out that quite a small anisotropy of surface energies suffices for a grain to escape stagnation ands grow abnormally. The additional driving force due to surface energy anisotropy need only be 25–50% of the mean driving force from grain boundary curvature, and this means that surface energy differences for different orientations of only a very few per cent should suffice. Indeed, this is positively beneficial, because it will mean that the normal (stagnant) grains all have very similar surface energies, which encourages continued stagnation. If the surface energy anisotropy is too large, there will be numerous local escapes from stagnation, and general grain growth will resume even when the mean grain size has already reached 2.5 times the thickness. Like everything else in the field of grain growth since the introduction of computer modelling, things have become much more complex and finely balanced than they were two decades ago.

A variant of these studies refers to thin films deposited with a preferred orientation by epitaxy on a single-crystal substrate, and then annealed while still in contact with the substrate. Now, an anisotropic interfacial energy replaces, on one side, the anisotropic surface energy. Grain growth under these circumstances is called *epitaxial grain growth* (FLORO *et al.* [1994]). The final preferred orientations are determined by a mixture of the

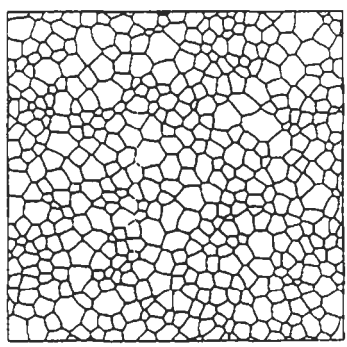

Fig. 61. Modelled grain structure after stagnation, due to grain-boundary grooving (after FROST *et al.* [1992]).

References: p. 2492.

sort of considerations we have met above (surface or interface energy anisotropy) and the need to abate the strain built into an epitaxial deposit. For example, in the cited work, silver films were deposited on a (001) nickel surface and then annealed, and (111) grains replaced the initial population of (100) grains. For further details, the original paper should be consulted.

4.4.4. Secondary recrystallization and sintering

When a compressed compact of metal or ceramic particles is heated, the pores between the particles gradually contract and eventually most of them disappear; this is sintering. It has been established (COBLE and BURKE [1963]) that the essential process is the diffusion of excess vacancies from the immediate neighbourhood of a pore into a nearby grain boundary and rapidly away along the boundary by grain-boundary diffusion (ch. 7, § 7). Complete sintering (i.e., total removal of the pores), which is highly desirable in many applications, thus depends on a plentiful supply of boundaries near all pores. If slow, steady grain growth is maintained, each pore is repeatedly crossed by a migrating grain boundary; a simple statistical calculation (KOOY [1962]) shows that a tenfold increase in grain size by normal grain growth implies that each pore is on the average crossed by seven migrating grain boundaries. This gives plenty of opportunity for substantial sintering.

If, however, secondary recrystallization takes place, then all pores within a secondary grain have been crossed only once by a moving boundary, and moreover one that is moving rapidly. Such pores thus remain stranded within their large grains, far away from the nearest boundary; vacancies then cannot diffuse rapidly away from the pores and sintering virtually comes to a halt. For effective sintering, then, secondary recrystallization must be prevented; this insight has been put to good use by doping aluminum oxide with small quantities of magnesium oxide. This produces a powerful boundary drag, slowing down grain growth without stopping it entirely, and preventing secondary recrystallization. The compressed powder can be completely sintered and the dense product so formed has valuable properties for practical applications.

References

ABBRUZZESE, G., S. FORTUNATI and A. CAMPOPIANO, 1992, Mater. Sci. Forum 94–96, 405.

ADAMS, B. L., S. I. WRIGHT and K. KUNZE, 1993, Met. Trans. **24A**, 819.

ADAMS, B. L., D. J. DINGLEY, K. KUNZE and S. I. WRIGHT, 1994, Mater. Sci. Forum **157–162**, 31.

ALTSTETTER, C., 1993, in Mechanical Properties and Deformation Bahavior of Materials Having Ultra-fine Microstructures, M. Nastasi, D. M. Parkin and H,. Gleiter (eds.), NATO ASI Series, Vol. E-233 (Dordrecht, Kluwer Academic), p. 381.

ANDERSON, W. A. and R. F. MEHL, 1945, Trans. AIME **161**, 140.

ANDRES, R. P. and 12 others, 1989, J. Mater. Research **4**, 704.

ASHBY, M. F., 1980, in: Recrystallization and Grain Growth of Multi-phase and Particle-Containing Alloys, eds. N. Hansen *et al.* (Risø National Laboratory, Denmark) p. 325.

ASHBY, M. F., and R. M. A. CENTAMORE, 1968, Acta Metall. **16**, 1081.

ASSMUS, F., K. DETERT and G. IBE, 1958, Z. Metallk. **48**, 344.

ÅSTRÖM, H. U., 1956, Arkiv för Fysik **10**, 197.

AUST, K.T, 1963, in: Art and Science of Growing Crystals, ed. J. J. Gilman (Wiley, New York) p. 452.
AUST, K.T., 1969, in: Textures in Research and Practice, eds. J. Grewen and G. Wassermann (Springer, Berlin) p. 160.
AUST, K.T., 1974, Canad. Met.all. Quart. **13**, 133.
AUST, K.T., 1994, Canad. Metall. Quart. **33**, 265.
AUST, K.T., and C.G. DUNN, 1957, Trans AIME **209**, 472.
AUST, K.T., and J.W. RUTTER, 1959, Trans. AIME **215**, 119 and 608.
AUST, K.T., and J.W. RUTTER, 1960, Trans. AIME **218**, 682.
AUST, K.T., and J.W. RUTTER, 1963, Recovery and Recrystallization of Metals, ed. L. Himmel (Wiley, New York) p. 131.
BAILEY, J.E., and P.B. HIRSCH, 1962, Proc. Roy. Soc. **267A**, 11.
BAKER, I., E.M. SCHULSON, J.R. MICHAEL and S.J. PENNYCOOK, 1990, Phil. Mag. **B62**, 659.
BAKER, I., and L. LIU [1994] Scripta Metall. et Mater. **30**, 1167.
BALL, C.J., 1957, Phil. Mag. **7**, 1011.
BALL, J. and G. GOTTSTEIN, 1993–1995, Intermetallics, **1**, 171, 191; **2**, 205; **3**, 209 (with B. ZEUMER).
BALLUFFI, R.W., 1982, Metallurg. Trans. **13A**, 2069.
BECK, P.A., 1954, Adv. Phys. **3**, 245.
BECIC, P.A., and H. Hu, 1952, Trans. AIME **189**, 83.
BECK, P.A., and P.R. SPERRY, 1949, Trans. AIME **180**, 240.
BECK, P.A., and P.R. SPERRY, 1950, J. Appl. Phys. **21**, 150.
BELL, F., and O. KRISEMENT, 1962, Z. Metallk. **53**, 115; also F. BELL, Acta Metall. **13** (1965) 363.
BELLIER, S.P., and R.D. DOHERTY, 1977, Acta Metall. **25**, 521.
BEVER, M.B., D.L. HOLT and A.C TITCHENER, 1973, Prog. Mater. Sci., vol. **17** (Pergamon Press, Oxford).
BHATIA, M.L., and R.W. CAHN, 1978, Proc. Roy. Soc. **362A**, 341.
BLANK, H., 1989, Mater. Sci. & Tech. **5**, 1178.
BONIS, L.J., and N.J. GRANT, 1960, Trans. AIME **175**, 151.
BOUCHAUD, E., J.-P. BOUCHAUD, S. NAKA, G. LAPASSET and H. OCTOR, 1992, Acta Metall. Mater. **40**, 3451.
BRANDON, D.G., B. RALPH, S. RANGANTHANAN and M.S. WALD, 1964, Acta Metall. **12**, 813.
BROKMAN, A., R. KRIS, W.W. MULLINS and A.J. VILENKIN, 1995, Scripta Metall. et Mater. **32**, 1341.
BROOM, T., and R.K. HAM, 1957, Vacancies and other Point Defects in Crystals (Inst. Metals, London) p. 41.
BUNGE, H.J., ed., 1981, Quantitative Texture Analysis (Deutsche Gesellschaft fur Metallkunde, Oberursel).
BUNGE, H.J., 1987, Internat. Mater. Rev. **32**, 265.
BUNGE, H.J., 1994, Textures of Materials, ICOTOM–10, Mat. Sci. Forum **157–162**.
BURGERS, W.G, 1941, Rekristallisation, Verformter Zustand und Erholung (Akademische Verlag, Leipzig).
BURKE, J.E., 1949, Trans. AIME **180**, 73.
BURKE, J.E., and D. TURNBULL, 1952, Prog. Met. Phys. **3**, 220.
CAHN, J.W., 1962, Acta Metall. **10**, 789.
CAHN, R.W., 1949, J. Inst. Metals **76**, 121.
CAHN, R.W., 1950, Proc. Phys. Soc. **A63**, 323.
CAHN, R.W., 1964, Deformation Twinning (Wiley, New York) p. 1.
CAHN, R.W., 1980, in: Recrystallization and Grain Growth of Multi-phase and Particle-Containing Alloys, eds. N. Hansen *et al.* (Risø National Laboratory, Denmark) p. 77.
CAHN, R.W., 1992, in Processing of Metals and Alloys (R.W. Cahn, ed.), (Vol. 15 of Materials Science and Technology, R.W. Cahn, P. Haasen and E.J. Kramer, eds.) (Weinheim, VCH), chapter 10.
CAHN, R.W., 1990, in High Temperature Aluminides and Intermetallics, S.H. Whang, C.T. Liu, D.P. Pope and J.O. Stiegler (eds.) (Warrendale, TMS), p. 245.
CAHN, R.W., and J.A. COLL, 1961, Acta Metall. **4**, 683.
CAHN, R.W., I.J. BEAR and R.L. BELL, 1954, J. Inst. Metals **82**, 481.
CAHN, R.W., M. TAKEYAMA, J.A. HORTON and C.T. LIU, 1991, J. Mater. Res. **6**, 57.
CALAIS, D., P. LACOMBE and N. SIMENEL, 1959, J. Nucl. Mater. **1**, 325.
CALVET, J., and C. RENON, 1960, Mém. Sci. Rev. Métallurg. **57**, 347.
CHALMERS, B., and H. GLEITER, 1971, Phil. Mag. **23**, 1541.
CHEN, S.R. and U.F. KOCKS, 1992, Scripta Metall. et Mater. **27**, 1587.

CHERIAN, T. V., P. PEIROKOWSKY and J. E. DORN, 1949, Trans. AIME 185, 948.
CHERNS, D., P. HIRSCH and H. SAKA, 1979, Proc. ICSMA 5, 295.
CHOJNOWSKI, E. H. and R. W. CAHN, 1973, in: Metallurgical Effects at High Strain Rates, eds. Rohde *et al.* (Plenum, New York) p. 631.
CHRIST, W., K. GSCHWENDTER and F. HAESSNER, 1965, Phys. Stat. Sol. **10**, 337.
CLAREBROUGH, L. M., M. E. HARGREAVES and G. W. WEST, 1955, Proc. Roy. Soc. **232A**, 252.
CLAREBROUGH, L. M., M. E. HARGREAVES and G. W. WEST, 1956, Phil. Mag. **1**, 528.
COBLE, R. L., and J. E. BURKE, 1963, Progr. Ceramic Sci. **3**.
COFFIN, JR., L. F., and J. F. TAVERNELLI, 1959, Trans. AIME 215, 794.
COTTRELL, A. H., 1953, Prog. Met. Phys. **4**, 255.
COTTRELL, A. H., and V. AYTEKIN, 1950, J. Inst. Metals **77**, 389.
CUDDY, L. J., 1981, Metallurg. Trans. **12A**, 1313.
DE LIBANATI, N. A., and S. VOLMAN DE TANIS, 1962, Compt. Rend. **252**, 2710.
DEMIANCZUK D. W., and K. T. AUST, 1975, Acta Metall. **23**, 1149.
DERBY, B., 1992, Scripta Metall. et Mater. **27**, 1581.
DESALVO, A., and D. NOBILI, 1968, J. Mater. Sci. **3**, 1.
DETERT, K., 1959, Acta Metall. **7**, 589.
DETERT, K., 1978, in: Recrystallization of Metallic Materials. 2nd Ed., ed. F. Haessner (Dr. Riederer-Verlag, Stuttgart) p. 97.
DILLAMORE, I. L., and H. KATOH, 1974, Met. Sci. **8**, 21 and 73.
DILLAMORE, I. L., C. J. E. SMITH and T. W. WATSON, 1967, Met. Sci. **1**, 49.
DILLAMORE, I. L., P. L. MORRIS, C. J. E. SMITH and B. W. HUTCHINSON, 1972, Proc. Roy. Soc. **329A**, 405.
DILLE, J., J.-L. DELPLANCKE, J. CHARLIER and R. WINAND, 1994, Mat. Res. Soc. Symp. Proc. **362**, p. 231.
DIMITROV, O., 1960, Nouvelles Proprietes Physiques et Chimiques des Métaux de très Haute Pureté (CNRS, Paris) 89 and 103.
DINGLEY, D. J. and V. RANDLE, 1992, J. Mater. Sci. **27**, 4545.
DOHERTY, R. D., 1974, Metal Science **8**, 132.
DOHERTY, R. D., 1978, in: Recrystallization of Metallic Materials, 2nd Ed., ed. F. Haessner (Dr. Riederer-Verlag, Stuttgart) p. 23.
DOHERTY, R. D., 1982, Met. Sci. **16**, 1.
DOHERTY, R. D., 1985, Scripta Metall. **19**, 927.
DOHERTY, R. D., and R. W. CAHN, 1972, J. Less-Common Met. **28**, 279.
DOHERTY, R. D., and J. W. MARTIN, 1963, J. Inst. Metals **91**, 332.
DOHERTY, R. D. and J. A. SZPUNAR, 1984, Acta Metall. **32**, 1789.
DOHERTY, R. D., I. SAMAJDAR, C. T. NECKER, H. E. VATNE and E. NES, 1995, in: 16th Risø Symp., eds. N. Hansen *et al.* (see *Further reading*), p. 1.
DUGGAN, B. J., M. HATHERLY, B. W. HUTCHINSON and P. T. WAKEFIELD, 1978, Met. Sci. **12**, 342.
DUGGAN, B. J., K. LÜCKE, G. KÖHLHOFF and C. S. LEE, 1993, Acta Metall. et Mater. 41, 1921.
DUNN, C. G., 1946, Trans. AIME **167**, 373.
DUNN, C. G., and J. L. WALTER, 1966, in: Recrystallization, Grain Growth and Textures, ed. H. Margolin (ASM, Metals Park, OH) p. 461.
DUNN, C. G., and H. F. WEBSTER, 1964, Trans. AIME **230**, 1567.
ECKERT, J., J. C. HOLZER and W. L. JOHNSON, 1993, J. Appl. Phys. **73**, 131.
EDINGTON, J. W., K. W. MELTON and C. P. CUTLER, 1976, Prog. Mater. Sci. **21**, 61.
ELAM, C. F., 1935, Distortion of Metal Crystals (Clarendon Press, Oxford).
ENGLER, O., C. ESCHER and G. GOTTSTEIN, Materials Science Forum **113–115**, 127.
ENGLER, O., I. HECKELMANN, T. RICKERT, J. HIRSCH and K. LÜCKE, 1994, Mater. Sci. & Tech. **10**, 772.
ENGLER, O., J. HIRSCH and K. LÜCKE, 1995, Acta Metall. et Mater. **43**, 121.
ENGLISH, A. T., and U. A. BACKOFEN, 1964, Trans. AIME **185**, 501.
ESTRIN, Y., and K. LÜCKE, 1982, Acta Metall. **30**, 983.
EVANS, H. E., and J. S. WADDINGTON, 1969, J. Nucl Mater. **30**, 337.
EXCELL, S. F., and D. H. WARRINGTON, 1972, Phil. Mag. **26**, 1121.
FAIVRE, P., and R. D. DOHERTY, 1979, J. Mater. Sci., **14**, 897.

FERRAN, G.L, R.D. DOHERTY and R.W. CAHN, 1971, Acta Metall. **19**, 1019.
FIEDLER, H.C., 1964, Trans. AIME **230**, 95.
FLORO, J.A., C.V. THOMPSON, R. CAREL and R.D. BRISTOWE, 1994, J. Mater. Res. **9**, 2411.
FORTES, M.A., and B. RALPH, 1967, Acta Metall. **15**, 707.
FOSTER, K., J.J. KRAMER and G.W. WIENER, 1963, Trans. AIME **227**, 185.
FRANK, F.C., 1988, Metall. Trans. **A19**, 403.
FRIDMAN, E.M., T.W. KOPEZKII and L.S. SHVINDLERMAN, 1975, Z. Metallk. **66**, 533.
FRIEDEL, J. 1964, Dislocations (Pergamon Press, Oxford, 1964), p. 239.
FROST, H.J., C.V. THOMPSON and D.T. WALTON, 1990, 1992, Acta Metall. Mater. **38**, 1455; **40**, 779.
FROST, H.J., THOMPSON, C.V. and D.T. WALTON, 1992, Mater. Sci. Forum **94–96**, 543.
FU, Z. and W.L. JOHNSON, 1993, Nanostructured Materials **3**, 175.
FUKUTOMI, H. and R. HORIUCHI, 1981, Trans. Japan Inst. Metals **22**, 633.
FURRER, P., 1980, in: Recrystallization and Grain Growth of Multi-phase and Particle-Containing Alloys, eds. N. Hansen *et al* (Risø National Laboratory, Denmark) p. 109.
GAWNE, D.T, and G.T. HIGGINS, 1969, in: Textures in Research and Practice, eds. J. Grewen and G. Wassermann (Springer, Berlin) p. 319.
GAY, P., P.B. HIRSCH and A. KELLY, 1954, Acta Cryst. **7**, 41.
GERTSMAN, V.Y. and R. BIRRINGER, 1994, Scripta Metall. et Mater. **30**, 577.
GERTSMAN, V.Y., K. TANGRI and R.Z. VALIEV, 1994, Acta Metall. et Mater. **42**, 1785.
GINDVAUX, G, and W. FORM, 1973, J. Inst. Met. **101**, 85.
GITTUS, J.H., 1974, Acta Metall. **22**, 789.
GLADMAN, T., 1966, Proc. Roy. Soc. **294A**, 298.
GLADMAN, T., 1980, in: Recrystallization and Grain Growth of Multi-phase and Particle-Containing Alloys, eds. N. Hansen *et al* (Risø National Laboratory, Denmark), p. 183.
GLEITER, H., 1969, Acta Metall. **17**, 853.
GLEITER, H., 1979, Acta Metall. **27**, 1754.
GLEITER, H., 1981, Prog. Mater. Sci. (Chalmers Anniversary Volume) p. 125.
GORDON, P., 1955, Trans. AIME **203**, 1043.
GOTTSCHALK, CHR., K. SMIDODA and H. GLEITER, 1980, Acta Metall. **28**, 1653.
GOTTSTEIN, G. and T. LEE, 1989, Mater. Sci. & Eng. **A114**, 21.
GOTTSTEIN, G. and L.S. SHVINDLERMAN, 1992a, Scripta Metall. et Mater. **27**, 1515.
GOTTSTEIN, G. and L.S. SHVINDLERMAN, 1992b, Scripta Metall. et Mater. **27**, 1509.
GOTTSTEIN, G., T. LEE and U. SCHMIDT, 1989, Mater. Sci. & Eng. **A114**, 21.
GOTTSTEIN, G., J. BEWERUNGE, H. MECKING and H. WOLLENBERGER, 1975, Acta Metall. **23**, 641.
GREEN, R.E., B. LIEBMAN and H. YOSHIDA, 1959, Trans. AIME **215**, 610.
GREWEN, J., 1994, Mater. Sci. Forum **157–162**, 3.
GREWEN, J., and J. HUBER, 1978, in: Recrystallization of Metallic Materials, 2nd Ed., ed. F. Haessner (Dr. Riederer-Verlag, Stuttgart) p. 111.
GREWEN, J., and G. WASSERMANN, eds., 1969, Textures in Research and Practice (Springer, Berlin).
GREWEN, J., T. NODA and D. SAUER, 1977, Z. Metallk. **67**, 260.
HAASEN, P., 1993, Metall. Trans. **24A**, 1001.
HAESSNER, F., and S. HOFMANN, 1971, Z. Metallk. **62**, 807.
HAESSNER, F., and S. HOFMANN, 1978, in: Recrystallization of Metallic Materials, 2nd Edition, ed. F. Haessner (Dr. Riederer-Verlag, Stuttgart) p. 63.
HAESSNER, F. and H.P. HOLZER, 1974, Acta Metall. **22**, 695.
HAESSNER, F., and J. SCHMIDT, 1994, Z. Metallkde. **85**, 324.
HAESSNER, F., E. HORNBOGEN and M. MUKHERJEE, 1966, Z. Metallk. **57**, 270.
HANEMANN, H., and A. SCHRADER, 1927, Atlas Metallographicus (Borntraeger, Berlin), table 101.
HART, R.V., and H. GAYTER, 1968, J. Inst. Metals **96**, 338.
HASEGAWA, T., and U.F. KOCKS, 1979, Acta Metall. **27**, 1705.
HASSON, C., J.T. BOOS, I. HERBEVAL, M. BISCONDI and G. GOUX, 1972, Surf. Sci. **31**, 115.
HAZZLEDINE, P.M., A.B. HIRSCH and N. LOUAT, 1980, in: Recrystallization and Grain Growth of Multiphase and Particle-Containing Alloys, eds. N. Hansen *et al.* (Risø National Laboratory, Denmark) p. 159.

HELLER, H. W. F., J. H. VAN DORP, G. WOLFF and C. A. VERBRAAK, 1981, Met. Sci. **15**, 333.
HELLMAN, P., and M. HILLERT, 1975, Scand. Metall. J. **4**, 211.
HERRMANN, G., H. GLEITER and G. BÄRO, 1976, Acta Metall. **24**, 353.
HIBBARD Jr., W.. A., and C. G. DUNN, 1957, Creep and Recovery (ASM, Metals Park, OH) p. 52.
HIGASHI, K., S. NAGAI, M. MAEDA and T. OHNISHI, 1985, J. Japan Inst. Light Metals **36**, 361.
HIGGINS, G. T., 1971, Metallurg. Trans. **2**, 1271.
HILLERT, M., 1965, Acta Metall. **13**, 227.
HJELEN, J., R. ØRSUND and E. NES, 1991, Acta Metall. et Mater. **39**, 1377.
HÖFLER, H. J., R. S. AVERBACK and H. GLEITER, 1993, J. Appl. Phys. **74**, 3832.
HOLMES, E. L., and W. C. WINEGARD, 1960, J. Inst. Metals **88**, 468.
HONDROS, E. D. and L. E. H. STUART, 1968, Phil. Mag, **17**, 711.
HORNBOGEN, E., and H. KREYE, 1969a, in: Textures in Research and Practice, eds. J. Grewen and G. Wassermann (Springer, Berlin) p. 274.
HORNBOGEN, E., and H. KREYE, 1969b, J. Mater. Sci. **4**, 944.
HORNBOGEN, E., and U. KÖSTER, 1978, in: Recrystallization of Metallic Materials, 2nd Ed., ed. F. Haessner (Dr. Riederer-Verlag, Stuttgart) p. 159.
HOTZLER, R. K. and T. K. GLASGOW, 1982, Metallurg. Trans. **13A**, 1665.
HU, HSUN, 1963, Recovery and Recrystallization of Metals (Interscience, New York) p. 311.
HU, HSUN, 1962, Acta Metall. **10**, 112; Trans. Met. Soc. AIME **224**, 75.
HU, HSUN, 1981, in: Metallurgical Treatises, eds. J. Tien and J. F. Elliott (Met. Soc. AIME) p. 385.
HU, HSUN, and C. S. SMITH, 1956, Acta Metall. **4**, 638.
HUBER, J., and M. HATHERLY, 1979, Met. Sci. **13**, 665.
HUBER, J., and M. HATHERLY 1980, Z. Metallk. **71**, 15.
HUGHES, D. A., 1995, in: 16th Risø Symp., eds. N. Hansen *et al.* (see *Further reading*), p. 63.
HUMPHREYS, F. J., 1977, Acta Metall. **25**, 1323.
HUMPHREYS, F. J., 1979a, Acta Metall. **72**, 1801.
HUMPHREYS, F. J., 1979b, Met. Sci. **13**, 136.
HUMPHREYS, F. J., 1992, Scripta Metall. et Mater. **27**, 1557.
HUMPHREYS, F. J. and M. G. ARDAKANI, 1994, Acta Metall. et Mater. **42**, 749.
HUMPHREYS, F. J. and P. N. KALU, 1990, Acta Metall. et Mater., 1990, **38**, 917.
HUMPHREYS, F. J. and M. HATHERLY, 1995, Recrystallization and Related Annealing Phenomena (Pergamon Press, Oxford).
HUTCHINSON, W. B., 1974, Met. Sci. **8**, 185.
HUTCHINSON, W. B., 1972, Scripta Metall. et Mater. **27**, 1471.
HUTCHINSON, W. B. and H.-E. EKSTRÖM, 1990, Mater. Sci. & Tech. **6**, 1103.
HUTCHINSON, W. B. and E. NES, 1992, Mater. Sci. Forum **94–96**, 385.
HUTCHINSON, W. B., F. M. C. BESAG and C. V. HONESS, 1973, Acta Metall. **21**, 1685.
IN DER SCHMITTEN, W., P. HAASEN and F. HAESSNER, 1960, Z Metallk. **51**, 101.
INOKUTI, Y., and R. D. DOHERTY, 1977, Texture **2**, 143.
INOKUTI, Y., and Rd. DOHERTY, 1978, Acta Metall. **26**, 61.
INOKUTI, Y., Y. SHIMIZU, C. MAEDA, and H. SHIMANAKA, 1980, in: Recrystallization and Grain Growth of Multi-phase and Particle-Containing, Alloys, eds. N. Hansen *et al.* (Risø National Laboratory, Denmark) p. 71. Fuller account (same authors): Trans. Iron & Steel Inst. Japan **23** (1983) 440.
JONAS, J. J., 1994, Mater. Sci. & Eng. **A184**, 155.
JONAS, J. J., C. M. SELLARS and W. J. MCG. TEGART, 1969, Metallurg. Rev. **14**, 1.
JONES, A. R, 1981, J. Mater. Sci. **16**, 1374.
JONES, A. R., B. RALPH and N. HANSEN, 1979a, Proc. Roy. Soc. **368A**, 345.
JONES, A. R., B. RALPH and N. HANSEN, 1979b, Met. Sci. **13**, 149.
KAIBYSHEV, R. and O. SITDIKOV, 1994, Z. Metallkde. **85**, 10.
KALLEND, J. S. and G. GOTTSTEIN (eds.), 1988, Eighth International Conference on Textures of Materials, ICOTOM–8 (Warrendale, TMS).
KARCH, J., R. BIRRINGER and H. GLEITER, 1987, Nature **330**, 556.

KASSNER, M. E., H. J. MCQUEEN, J. POLLARD, E. EVANGELISTA and E. CERRI, 1994, Scripta Metall. et Mater. **31**, 1331.
KIMURA, A., R. MADDIN and H. KIMURA, 1964, Acta Metall. **12**, 1167.
KOCH, C. C., 1991, in Processing of Metals and Alloys, R. W. Cahn (ed.), vol. 15 of Materials Science and Technology, R. W. Cahn, P. Haasen and E. J. Kramer (eds.) (Weinheim, VCH), chapter 5.
KOEHLER, J. S., J. W. HENDERSON and J. H. BREDT, 1957, Creep and Recovery (ASM, Metals Park, OH) p. 1.
KOHARA, S., M. N. PARTHASARATHI and P. A. BECK, 1958, Trans. AIME, 875.
KOOY, C., 1962, Science of Ceramics (Academic, London) p. 21.
KOPPENAAL, T. J., and M. E. FINE, 1961, Trans. Met. Soc. AIME **221**, 178; J. Appl. Phys. **32**, 1781.
KREYE, H., and E. HORNBOGEN, 1970, J. Mater. Sci. **5**, 1.
KRONBERG, M. L., 1955, Science **122**, 599.
KRONBERG, M. L., and H. F. WILSON, 1949, Trans. AIME **185**, 501.
KUNG, H., D., R. RASMUSSEN and S. L. SASS, 1991, Acta Metall. et Mater. **40**, 81.
LACOMBE, P., and L. BEAUJARD, 1947, J. Inst. Metals **74**, 1.
LANGDON, T. G. and R. C. GIFKINS, 1983, Acta Metall. **31**, 927.
LAWLEY, A., A. E. VIDOZ and R. W. CAHN, 1961, Acta Metall. **9**, 287.
LEE, C. S., R. E. SMALLMAN and B. J. DUGGAN, 1993, Scripta Metall. et Mater. **29**, 43.
LESLIE, W. C., J. T. MICHALAK and F. W. AUL, 1963, Iron and its Dilute Solid Solutions (Interscience, New York) p. 119.
LI, J. C. M., 1961, J. Appl. Phys. **32**, 525.
LIEBMANN, B, and K. LÜCKE, 1956, Trans. AIME **209**, 427.
LIM, L. C. and T. WATANABE, 1990, Acta Metall. **38**, 2507.
LIN, Y. and R. W. CAHN, 1992, Phys. Stat. Sol. **131**, 481.
LIN, T. L., A. SHAN, and D. LI, 1994, Scripta Metall. et Mater. **31**, 1455.
LINDH, E., B. HUTCHINSON and S. UEYAMA, 1993, Scripta Metall. et Mater. **29**, 247.
LOMBRY, R., C. ROSSARD and B. THOMAS, 1980, in: Recrystallization and Grain Growth of Multi-phase and Particle-Containing Alloys, eds. N. Hansen *et al.* (Risø National Laboratory, Denmark), p. 257.
LOUAT, N., 1981, Acta Metall. **30**, 1291.
LU, K., and M. L. SUI, 1995, Acta Metall. Mater. **43**, 3325.
LÜCKE, K., 1963, Ecrouissage, Restauration, Recristallisation (Presses Universitaires de France, Paris) p. 1.
LÜCKE, K., and K. DETERT, 1957, Acta Metall. **5**, 628.
LÜCKE, K., and R. RIXEN, 1968, Z. Metallk. **59**, 321.
LÜCKE, K., and H. P. STÜWE, 1961, Recovery and Recrystallization of Metals (Interscience, New York) p. 131.
LÜCKE, K., H. PERLWITZ, and W. PITSCH, 1964, Phys. Stat. Sol. **7**, 733.
LUTON, M. J., and C. M. SELLARS, 1969, Acta Metall. **17**, 1033.
MARTIN, D. G., 1994, Mater. Sci. & Tech. **10**, 855.
MASING, G., and J. RAFFELSIEPER, 1950, Z. Metallk. **41**, 65.
MATTHIES, M., 1979, Phys. Stat. Sol. (b) **92**, K135.
MAY, J. E., and D. TURNBULL, 1958, Trans. AIME **212**, 769.
MCLEAN, D., 1957, Grain Boundaries in Metals (Oxford Univ. Press, Oxford) p. 44 and 87.
MCLEAN, D., 1968, Trans. AIME **242**, 1193.
MCLEAN, M., and H. MYKURA, 1965, Acta Metall. **13**, 1291.
MCQUEEN, H. J., 1977, Metallurg. Trans. **8A**, 807.
MCQUEEN, H. J., and J. J. JONAS, 1975, in: Treatise on Materials Science and Technology, vol. **6**, ed. R. Arsenault (Academic, New York) p. 393.
MCQUEEN, H. J., E. EVANGELISTA, N. JIN and M. E. KASSNER, 1994, in Advances in Hot Deformation Textures and Microstructures, ed. J. J. Jonas, T. R. Bieler and K. J. Bowman (Warrendale: TMS), p. 251.
MECKING, H., and G. GOTTSTEIN, in: Recrystallization of Metallic Materials, 2nd Ed., ed. F. Haessner (Dr. Riederer-Verlag, Stuttgart) p. 195.
MEDINA, S. F. and J. E. MANCILLA, 1994, Acta Metall. et Mater. **42**, 33945.
MEE, P. B., 1968, Trans. Met. Soc. AIME **242**, 2155.
MIDDLETON, A. B., L. B. PFEIL and E. C. RHODES, 1949, J. Inst. Metals **75**, 595.
MIKI, I., and H. WARLIMONT, 1968, Z. Metallk. **59**, 408.

MILLER, W. A., and W. M. WILLLAMS, 1964, J. Inst. Metals **93**, 125.
MOELLE, C. H. and H. J. FECHT, 1995, Nanostructured Materials (in press), **6**, 421.
MONTUELLE, J. 1955, Compt. Rend. Acad. Sci. (Paris) **241**, 1304.
MOULD, P. R., and P. COTTERILL, 1967, J. Mater. Sci. **2**, 241.
MUGHRABI, H., 1977, in: Surface Effects in Crystal Plasticity, eds. R. M. Latanision and J. F. Fourie (Noordhoff, Leyden).
MULLINS, W. W., 1956, Acta Metall. **4**, 431; J. Appl. Phys. **27**, 900.
NAGASHLMA, S., ed., 1981, Proc. 6th Int. Conf. on Textures of Materials (Iron and Steel Institute of Japan).
NAKAYAMA, T. and Y. USHIGAMI, 1992, Mater. Sci. Forum **94–96**, 413.
NES, E., Acta Metall. Mater. **43**, 2189.
NES, E., 1980, in: Recrystallization and Grain Growth of Multi-phase and Particle-Containing Alloys, eds. N. Hansen *et al.* (Risø National Laboratory, Denmark) p. 85.
NES, E. and W. B. HUTCHINSON, 1989, in Proc. 10th Risø Symposium, Bilde-Sørensen (ed.) (Risø National Laboratory, Roskilde, Denmark), p. 233.
NES, E. and J. A. SAETER, 1995, in: 16th Risø Symp., eds. N. Hansen *et al.* (see *Further reading*), p. 169.
OBLAK, J. M., and W. A. OWCARSKI, 1968, Trans. Met. Soc. AIME **242**, 1563.
OLSON, G. B., H. C. LING, I. S. MONTGOMERY, J. B. VANDER SANDE and M. COHEN, 1982, in: Rapidly Solidified Amorphous and Crystalline Alloys, ed. B. H. Kear (North-Holland, Amsterdam) p. 355.
PECZAK, P., 1995, Acta Metall. et Mater. **43**, 1279.
PERRYMAN, E. C. W., 1954, Acta Metall. **2**, 26.
PERRYMAN, E. C. W., 1957, Creep and Recovery (ASM, Metals Park, OH) p. 111.
PETKOVIC, R. A., M. J. LUTON and J. J. JONAS, 1975, Canad. Metall. Quart. **14**, 137.
PHILLIPS, V.A, 1966. Trans. Met. Soc. AIME **236**, 1302.
PHILLIPS, V. A., 1967, Trans. Met. Soc. AIME **239**, 1955.
PICKERING, F. P., 1992, in Constitution and Properties of Steels, ed. F. P. Pickering (Vol. 7 of Materials Science And Technology, ed. R. W. Cahn, P. Haasen and E. J. Kramer) (Weinheim, VCH), pp. 374–381.
RAE, C., C. R. M. GROVENOR and K. M. KNOWLES, 1981, Z. Metallk. **72**, 798.
RALPH, B., C. BARLOW, B. COOKE and A. PORTER, 1980, in: Recrystallization and Grain Growth of Multiphase and Particle-containing Alloys, eds. N. Hansen *et al.* (Risø National Laboratory, Denmark) p. 229.
RANDLE, V., 1993, The Measurement of Grain Boundary Geometry (Institute of Physics Publishing, Bristol).
RANDLE, V. and A. BROWN, 1989, Phil. Mag. **A59**, 1075.
RATH, B. B. and Hsun HU, 1972, in: The Nature and Behaviour of Grain Boundaries, ed. Hsun Hu (Plenum, New York) p. 405.
RATH, B. B., R. T. LEDERICH, C. F. YOLTON and F. H. FROES, 1979, Metallurg. Trans. **10A**, 1013.
RAY, R. K., B. W. HUTCHINSON and B. J. DUGGAN, 1975, Acta Metall. **23**, 83].
RAY, R. K., J. J. JONAS and R. E. HOOK, 1994, Internat. Mater. Rev. **39**, 129.
RHINES, F. N. and K. R. CRAIG, 1974, Metall. Trans. **5**, 413.
RHINES, F. N., and B. P. PATTERSON, 1982, Metallurg. Trans. **13A**, 985.
RICHARDS, C. E., and T. W. WATSON, 1969, J. Iron and Steel Inst. **207**, 582.
RINGER, S. P., W. B. LI and K. E. EASTERLING, 1992, Acta Metall. et Mater. **40**, 275.
RISSER, S. and B. CHENAL, 1994, private communication.
ROBERTS, W. T., 1993, in Supplementary Volume 3 of the Encyclopedia of Materials Science And Engineering, R. W. Cahn (ed.) (Oxford, Pergamon Press), p. 1616.
ROBINSON, P. M., and P. N. RICHARDS, 1965, Phil. Mag. **11**, 407.
RONNPAGEL, D., and C. H. SCHWINK, 1978, Acta Metall **26**, 319.
ROSSARD, C. and P. BLAIN, 1959, Mém. Sci. Rev. Métall. **56**, 285.
RYAN, N. E., 1967, Metallurgy Report ARL/met 64 (Aeronautical Research Laboratories, Australia).
RYDE, L., B. W. HUTCHINSON and S. JONSSON, 1990, in: Recrystallization '90, ed. Chandra, (TMS, Warrendale, PA), p. 313.
SANDSTRÖM, R., 1977, Acta Metall. **25**, 897.
SAUTTER, H., H. GLEITER and G. BÄRO, 1977, Acta Metall. **25**, 467.
SCHMIDT, W., K. LÜCKE and J. POSPIECH, 1974, in: Texture and Properties of Materials, eds. G. J. Davies *et al.* (The Metals Society, London).

SCHÖNBORN, K. H., and F. HAESSNER, 1982, Z. Metallk, **73**, 739.
SCHOFIELD, T. H., and A. E. BACON, 1961, Acta Metall. **9**, 653.
SCHRANK, J., B. ORTNER, H. P. STÜWE and A. GRABIANOWSKI, 1985, Mat. Sci. & Tech. **1**, 544.
SELLARS, C. M., 1986, in Encyclopedia of Materials Science and Engineering, ed. M. B. Bever (Pergamon, Oxford), p. 1270.
SHEWMON, P. G., and W. M. ROBERTSON, 1963, Metal Surfaces (ASM, Metals Park, OH) p. 67.
SHOCKLEY, W., and T. W. READ, 1950, Phys. Rev. **78**, 275.
SHI, Longquan, and D. O. NORTHWOOD, 1993, J. Mater. Sci. **28**, 5963.
SIEGEL, R. W., 1993, in Mechanical Properties and Deformation Bahavior of Materials Having Ultra-fine Microstructures, M. Nastasi, D. M. Parkin and H,. Gleiter (eds.), NATO ASI Series, Vol. E-233 (Dordrecht, Kluwer Academic), p. 509.
SIEGEL, R. W., S. RAMASAMY, H. HAHN, Z. LI and T. LU, 1988, J. Mater. Research **3**, 1367.
SINGER, R. F. and GESSINGER, G. H., 1982, Metallurg. Trans. **13A**, 1463.
SMALLMAN, R. E., and C. S. LEE, 1994, Mat. Sci. & Eng. **A184**, 97.
SMITH, C. S., 1948, Trans. AIME **175**, 151.
SMITH, C. S., 1964, Met. Rev. **9**, 1.
SMITH, D. A., 1992, Materials Science Forum **94–96**, 221.
SMITH, D. A. and C. S. NICHOLS, 1991, in Structure and Property Relations for Interfaces, J. L. Walter *et al.* (eds.) (Metals Park, ASM In ternational), p. 345.
SMITH, J. H., and M. B. BEVER, 1968, Trans. Met. Soc. AIME **242**, 880.
SROLOVITZ, D. J., 1990, in Supplementary Volume 2 of the Encyclopedia of Materials Science and Engineering, R. W. Cahn (ed.) (Oxford, Pergamon Press), p. 845.
STIEGLER, J. O., C. K. H. DUBOSE, R. E. REED and C. J. MCHARGUE, 1963, Acta Metall. **11**, 851.
STÜWE, H. P., 1986, Metall. Trans. **17A**, 1455.
SUTTON, A. P. and R. W. BALLUFFI, 1995, Interfaces in Crystalline Materials (Oxford University Press).
TAGUCHI, S., and A. SAKAKURA, 1969, J. Appl. Phys. **40**, 1539.
TALBOT, J., P. ALBERT and G. CHAUDRON, 1957, Compt. Rend. Acad. Sci. (Paris) **244**, 1577.
TANNER, L. E., and I. S. SERVI, 1966, Mater. Sci. Eng. **1**, 153.
TAVERNIER, Ph. and J. A. SZPUNAR, 1991, Acta Metall. et Mater. **39**, 549.
THOMPSON, A. W., 1977, Metallurg. Trans. **8A**, 833.
THOMPSON, C. V., 1990, Annu. Rev. Mat. Sci. **20**, 245.
THOMPSON, C. V., 1992, Mater. Sci. Forum **94–96**, 245.
THOMPSON, C. V., H. J. FROST and F. SPAEPEN, 1987, Acta Metall. **35**, 887.
THORNTON, P. H., 1968, in: Techniques of Metal Research, ed. R. F. Bunshah (Interscience, New York) vol. 1, part 2, p. 1069.
THORNTON, P. H., and R. W. CAHN, 1961, J. Inst. Metals **89**, 455.
TIEDEMA, T. J., W. MAY and W. G. BURGERS, 1949, Acta Cryst. **2**, 151.
TSCHÖPE, A. and R. BIRRINGER, 1993, Phil. MAG. **68B**, 223.
TWISS, R. J., 1977, Pure and Appl. Geophys. **115**, 227.
VAIDYA, S., T. T. SHENG and A. K. SINHA, 1980, Appl. Phys. Lett. **36**, 464.
VAIDYA, W. V., and K. EHRLICH, 1983, J. Nucl. Mater. **113**, 149.
VANDERMEER, R. A., and P. GORDON, 1959, Trans. **AIME 215**, 577.
VANDERMEER, R. A., and P. GORDON, 1963, in: Recovery and Recrystallization of Metals, ed. L. Himmel (Interscience, New York) p. 211.
VANDERMEER, R. A., 1995. in: 16th Risø Symp., eds. N. Hansen *et al.* (see *Further reading*), p. 193.
VARIN, R. A., and K. TANGRI, 1980, Scripta Metall. **14**, 337.
VIDOZ, A. E., D. P. LAZAREVIĆ and R. W. CAHN, 1963, Acta Metall. **11**, 17.
VISWANATHAN, R., and C. L. BAUER, 1973a, Acta Metall **21**, 1099.
VISWANATHAN, R., and C. L. BAUER, 1973b, Metallurg. Trans. **4**, 2645.
WALTER, J. L., 1969, in: Textures in Research and Practice, eds. J. Grewen and G. Wassermann (Springer, Berlin) p. 227.
WALTER, J. L., and C. G. DUNN, 1959, Acta Metall. **7**, 424; J. Metals **11**, 599.
WALTER, J. L., and G. F. KOCH, 1963, Acta Metall. **11**, 923.

WALTON, D. T., FROST, H. J. and C. V. THOMPSON, 1992, Mater. Sci. Forum **94–96**, 531.
WARLIMONT, H., 1979, Proc. ICSMA **5**, 1055.
WASSERMANN, G., 1963, Z Metallk. **54**, 6L.
WASSERMANN, G., and J. GREWEN, 1962, Texturen Metallischer Werkstoffe (Springer, Berlin).
WATANABE, T., 1984, Res Mechanica **11**, 47.
WATANABE, T., 1988, Materials Forum **11**, 284.
WATANABE, T., H. FUJII, H. OIKAWA and K. ARAI, 1989, Acta Metall. **37**, 941.
WEBSTER, D., 1968, Trans. Met. Soc. AIME **242**, 640.
WELSCH, G. and J. L. WALTER, 1990, in Supplementary Volume 2 to the Encyclopedia of Materials Science and Engineering, R. W. Cahn (ed.), (Oxford: Pergamon Press), p. 1007.
WILBRANDT, P.-J., 1980, Phys. Stat. Sol. (a) **61**, 4H.
WILBRANDT, P.-J. and P. HAASEN, 1980, Z Metallk. **71**, 273 and 385.
WOLDT, E. and F. HAESSNER, 1991, Z. Metallkde. **82**, 329.
YANG, R., G. A. BOTTON and R. W. CAHN, 1996, Acta Metall. Mater. **44**, in press.
YAVARI, P. and T. G. LANGDON, 1983, Acta Metall. **31**, 1595.
ZEHETBAUER, M., J. SCHMIDT and F. HAESSNER, 1991, Scripta Metall. et Mater. **25**, 559.

Further reading

Burgers, W. G., in: The Art and Science of Growing Crystals, ed. J. J. Gilman (Wiley, New York, 1957). (Much older work on recrystallization is summarized here).
Haessner, F., ed., Recrystallization of Metallic Materials, 2nd Ed. (Dr. Riederer-Verlag, Stuttgart, 1978).
Cotterill, P., and P. R. Mould, Recrystallization and Grain Growth in Metals (Wiley, New York, 1976).
Gottstein, G., P. Haasen and N. Hansen (eds.), Fundamentals of Recrystallization (a set of short papers based on a conference), Scripta Metall. et Mater. **27** (1992) pp. 1445 – 1598.
Fuentes, M., and J. Gil Sevillano, Recrystallization '92, Materials Science Forum, Volumes **113–115** (1992).
Hansen, N., A. R. Jones and T. Leffers (eds.), 1st Risø Symposium. Recrystallization and Grain Growth of Multiphase and Particle-Containing Materials (Risø National Laboratory, Roskilde, Denmark, 1980).
Humphreys, F. J., and M. Hatherly, Recrystallization and Related Annealing Phenomena (Pergamon Press, Oxford, 1995).
Hansen, N. *et al.* (eds.), 16th Risø International Symposium, on Microstructural and Crystallographic Aspects of Recrystallization (Risø National Laboratory, Roskilde, Denmark, 1995).
Proceedings of the First International Conference on Grain Growth in Polycrystalline Materials, ed. Abbruzzese, G. And P. Brozzo, Materials Science Forum, **94–96** (1992) pp. 1–913 (2 volumes).
Martin, J. W., and R. D. Doherty, Stability of Microstructure in Metallic Systems (Cambridge University Press, 1976; second edition [with B. Cantor], 1996), ch. 3: Instability due to strain energy.
Dillamore, I. L., and W. T. Roberts, Preferred Orientations in Wrought and Annealed Metals, Metall. Reviews **10** (1965) 271.
Hatherly, M., and W. B. Hutchinson, An Introduction to Textures in Metals (Monograph No. 5; Institution of Metallurgists, London, 1979).
Cahn, R. W., chapter on Measurement and Control of Texture, in: Processing of Metals and Alloys, ed. R. W. Cahn, vol. 15 of MST Series (VCH, Weinheim, 1991), p. 429.
Bunge, H. J. (ed.), Textures of Materials, ICOTOM–10 (Proceedings of the 10th International Conference on textures of Materials), Materials Science Forum, Volumes 157–162 (1994) pp 1–2100.
Ray, R. K., J. J. Jonas and R. E. Hook, Cold rolling and annealing textures in low carbon and extra low carbon steels, International Materials Reviews, **39** (1994) 129.
Randle, V., The Measurement of Grain Boundary Geometry (Institute of Physics Publishing, Bristol, 1993).
Sellars, C. M., and W. J. McG. Tegart, Hot-Workability of Metals, Internat. Metall. Reviews **17** (1972) 1.
McQueen, H. J., and J. J. Jonas, chapter on dynamic recovery and recrystallization, in: Treatise on Materials Science and Technology, ed. R. Arsenault (Academic, New York, 1975) vol. **6**.
Jonas, J. J., Dynamic Recrystallization – Scientific Curiosity or Industrial Tool?, Mat. Sci. Eng. **A184** (1994), 155.
Jonas, John J., T. R. Bieler and K. J. Bowman (eds.), Advances in Hot Deformation Textures and Microstructures (TMS, Warrendale, PA, 1994).

CHAPTER 29

MAGNETIC PROPERTIES OF METALS AND ALLOYS

F. E. LUBORSKY and J. D. LIVINGSTON

Corporate Research and Development
General Electric Company
Schenectady, NY 12301, USA

G. Y. CHIN†

Bell Telephone Laboratories
Murray Hill, NJ 07974, USA

R. W. Cahn and P. Haasen†, eds.
Physical Metallurgy; fourth, revised and enhanced edition

1. Origins of fundamental magnetic properties

In general, there are three kinds of magnetic effects: diamagnetism, paramagnetism, and cooperative magnetism. Cooperative magnetism includes the most important phenomena we have to describe in this chapter, e.g., ferromagnetism, antiferromagnetism and ferrimagnetism. The principal cause of magnetism is to be found in the interactions of electrons with magnetic fields and interaction of electrons with each other. Apart from its orbital motion, the electron possesses a spin which is equivalent to a magnetic moment of the electron itself. Electrons are arranged in energy states of successive order, and for each energy state there can only be two electrons, which must be of opposite spin. In atoms with closed shells of electrons, therefore, the spin magnetism is entirely self-cancelling and the application of a magnetic field has the effect of distorting the electron orbits so that the internal magnetic field remains unchanged. This effect of realignment of electron orbits is very small and is called *diamagnetism*. The substance behaves as though an internal rearrangement opposing the external magnetic field took place. Although this diamagnetism can be used for the examination of materials, it is not of great importance in this connection. It must, however, be noted that the effect is fundamental and occurs in all substances, i.e., diamagnetism is superimposed on any paramagnetic or ferromagnetic effect, but can normally be neglected in comparison.

If within the atomic shells there are some shells which contain electrons whose spin is not compensated by others of corresponding opposite spin, as for instance in the d-shell of the transition metals, we can have atoms which carry a resultant magnetic moment, μ, due to unpaired or uncompensated electron spins (μ is measured by Bohr magnetons). Such atoms are called magnetic atoms, and a dilute assembly of such atoms when exposed to a magnetic field shows a certain degree of magnetic orientation of the atomic magnetic moments. This orientation is opposed by thermal agitation and the law governing the magnetization, M, of the assembly as a function of the strength of the applied magnetic field H is known as the *Langevin law*:

$$M = N\mu \coth \frac{\mu H}{kT} - \frac{kT}{\mu H}, \tag{1}$$

where N is the number of magnetic carriers per cm^3 and k and T have their conventional significance. For low values of $\mu H/kT$ the change of magnetic moment with field is linear ($M = N\mu^2 H/3kT$) and the *magnetic susceptibility*, which is the proportionality constant between field and magnetization, is a constant (*Curie law*):

$$\frac{M}{H} = \chi = \frac{N\mu^2}{3kT} = \frac{\text{const.}}{T}. \tag{2}$$

If we apply very high magnetic fields, this *paramagnetic* magnetization reaches a saturation value which is equal to $N\mu$, the total sum of all the magnetic moments of the carriers. In dilute assemblies. the paramagnetic susceptibility can serve as a measure of the magnetic moment of the individual carriers and can thus give information about the magnetic properties of the atoms of which the assembly is composed. However, in solids

containing many paramagnetic atoms or ions there are usually interactions of the magnetic electrons with either the magnetism arising from neighboring atoms or with the electrostatic fields arising from neighboring atoms. These influences disturb the ideal behavior of the magnetic carriers, and although magnetic effects of a similar nature to those described for the dilute assembly occur, these effects can no longer be used to give simple information about the number of magnetic electrons per atom. Thus, in general, the paramagnetic susceptibility, whilst giving useful information about the substance, is not a direct measure of the metallurgically important factors contributing to the material structure. However, discontinuities which occur in the paramagnetic susceptibility as the composition of a system is systematically changed are of value in the examination of metals and alloys.

If the magnetic atoms are in sufficiently close contact with each other so that the magnetic electrons can exchange between neighboring magnetic atoms, a cooperative phenomenon may occur which spontaneously aligns the spins of all the magnetic carriers in the lattice and binds their moments very strongly. This spontaneous magnetization is characteristic for *ferromagnetic* materials. The spins of neighboring magnetic atoms are aligned by *exchange forces* which are equivalent to magnetic fields of the order of $8–80 \times 10^7$ A/m (1–10 million Oe). However, the coupling is not itself magnetic but is due to a quantum-mechanical interaction between the electrons of neighboring atoms. The exchange interaction between magnetic atoms may often be indirect and take place via an intermediate nonmagnetic atom such as oxygen or sulphur. Under some circumstances, the coupling between magnetic atoms in a substance can cause antiparallel alignment of the spins of neighboring atoms. This is called *antiferromagnetism*. Thus we have substances which consist of two interpenetrating lattices of similar magnetic ions or atoms with magnetizations in exactly opposite directions; these cancel out so that there is no resultant magnetic moment. Finally, the two interpenetrating lattices can have antiparallel magnetizations of unequal magnitude so that there remains a resultant magnetic moment in the direction of the stronger magnetic sub-lattice. This uncompensated antiferromagnetism has been called *ferrimagnetism*.

The saturation magnetization of ferromagnetic materials depends on the number of uncompensated spins in the magnetic atoms. In the ferromagnetic metals — iron, cobalt and nickel — the magnetic moment per atom that is measured is 2.2, 1.7 and 0.6 spin moments (electron units or Bohr magnetons), respectively. The very simple rigid band model (ch. 4, § 5.1) calculation gives values of 2.6, 1.6 and 0.6. The electronic band theory of magnetism is discussed in some detail in ch. 3, § 8.

Ferromagnetic and ferrimagnetic materials are characterized by their high saturation magnetization, M_s, which decreases slowly as the temperature is increased and fairly abruptly disappears at a characteristic temperature known as the *Curie temperature* T_c (fig. 1). The ferrimagnetic substances behave in most respects very similarly to the ferromagnetic substances in showing field-independent magnetization and a definite Curie point. (In what follows the term ferromagnetism will be used for both ferro- and ferrimagnetism.) Antiferromagnetics behave in many respects like paramagnetic substances because the two oppositely directed magnetic lattices compensate each other, showing only a small external magnetic effect which depends on the applied magnetic

References: p. 2560.

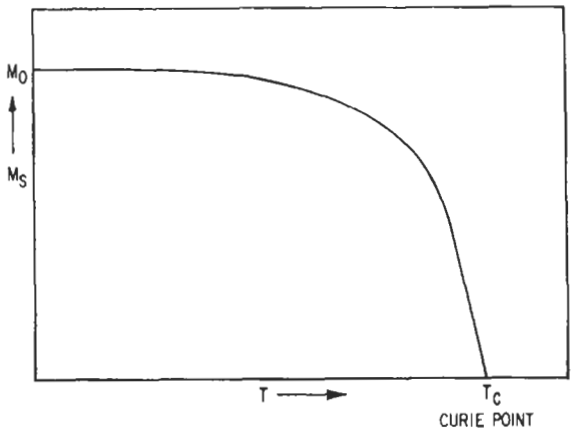

Fig. 1. Variation of saturation magnetic moment M_s with temperature for a ferromagnetic substance.

field. At a given temperature, however, the antiferromagnetic coupling is lost and this is accompanied by an anomaly in the specific heat and by an anomaly in the magnetic susceptibility. The temperature at which antiferromagnetic substances lose their antiparallel alignment and become paramagnetic is called the *Néel point.*

In the paramagnetic region, for a ferromagnet, the variation of susceptibility χ with temperature follows a *Curie–Weiss law* which contains the Curie temperature T_c as the additional constant, $\chi = C/(T-T_c)$. For an antiferromagnetic material above the Néel temperature, T_N, χ is instead given by $\chi = C/(T+T_N)$.

The exchange interaction between the electrons of neighboring magnetic atoms in ferromagnetic and ferrimagnetic materials causes the individual magnetic moments of all atoms in such materials to be aligned, and the material possesses a *spontaneous magnetization* at zero field, M_s. This is in contradiction with the observation that even ferromagnetic materials do not show external polarization under normal circumstances. This apparent paradox is resolved by the fact that a ferromagnet is always subdivided into a number of microscopic *domains.* Inside the domains the magnetization that prevails is equal to M_s but the domains are oriented in different directions so that externally their magnetic moments cancel and no magnetization is observed outside the body. *Domain walls*, i.e., regions which separate domains of different directions of magnetization from each other, can be observed by a variety of methods, and the study of the spontaneous magnetization M_s can give interesting structural information about the materials. The position and density of domain walls as well as their special features can again be of great importance to the study of the structure of materials. The temperature at which the energy of thermal agitation is sufficiently large to overcome the effect of the exchange interaction is the Curie temperature, T_c. The saturation magnetization M_s and the Curie temperature are not dependent on structural imperfections of the material but are characteristic of the atomic constitution and therefore can be used to measure or determine that constitution. In the examination of metals and alloys, observation of M_s

and its variation with temperature can be used for phase diagram investigations.

The exchange interaction between electrons of neighboring atoms which causes the magnetization of all magnetic atoms to be aligned is the principal contribution to the magnetic energy of a specimen. In addition, for crystalline materials the ease with which the magnetization to saturation is achieved differs as we magnetize along different crystal directions (fig. 2). Thus the measurement of this *magnetocrystalline anisotropy energy* can be a sensitive test of the crystal structure. The magnetocrystalline anisotropy energy changes with temperature and, of course, at the Curie point the anisotropy disappears together with the magnetization.

An elastic deformation of the lattice will additionally exert an influence on the magnetization and its symmetry. This effect is called *magnetostriction* and can be expressed as the relation between elastic constants of a material and the strain dependence of the anisotropy energy. The magnetostriction is direction-dependent and can be expressed as a harmonic function of the directions of both the magnetization and the crystal symmetry. The constants of this harmonic series are called *magnetostriction constants* and an accurate analysis of magnetostriction as a function of both field direction and temperature can help in the investigation of structural properties of magnetic materials.

An example of a ferromagnetic material divided into domains to produce no net magnetization is shown at the bottom of fig. 3. Subdivision into domains removes most of the *magnetostatic energy* otherwise associated with surface magnetic poles. The boundaries between domains with different directions of magnetization, called *domain walls*, have a finite thickness and surface energy dependent primarily on the strengths of the exchange interaction and the magnetocrystalline anisotropy energy. For given specimen shape and dimensions, equilibrium domain sizes are determined by a balance between magnetostatic and domain-wall energies. Typical domain sizes range from several μm to several mm. Domain-wall surface energy increases with increasing exchange and anisotropy constants. Domain-wall width increases with increasing exchange constant, but decreases with increasing anisotropy constant, ranging from several hundred nm in low-anisotropy materials down to interatomic distances in very high-anisotropy materials.

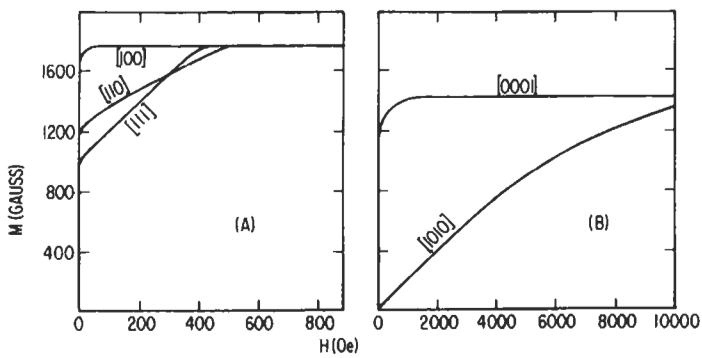

Fig. 2. Magnetization along different crystallographic axes in single crystals of (a) iron and (b) cobalt.

References: p. 2560.

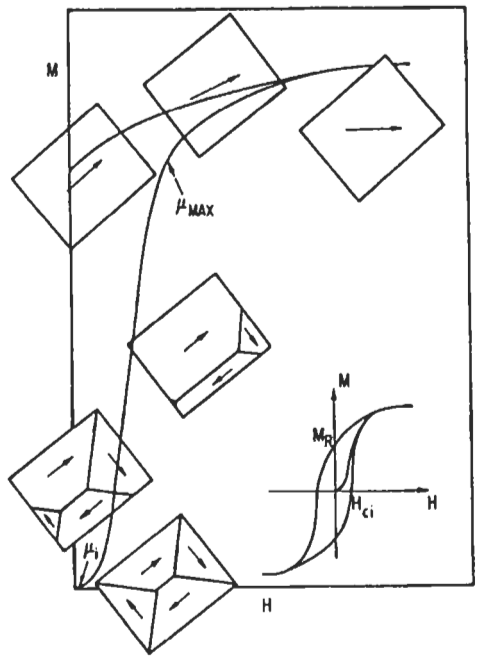

Fig. 3. Schematic diagram of the magnetization process and corresponding changes in domain configuration of a single crystal (inset: hysteresis loop).

Let us now describe the conditions in a magnetic material in low fields where the domain walls play an important role. At first, consider a single crystal. In the demagnetized state, the specimen is sub-divided into domains, each domain magnetized along one of the easy directions of magnetization and the various domains separated by domain walls. The external demagnetizing energy and the domain wall energy as well as the contributions from magnetocrystalline and magnetostrictive energy are minimized by the existence of domain walls. An example of such a demagnetized specimen is shown in fig. 3 where the magnetization process is shown schematically. Upon the application of a magnetic field, initially domain walls will tend to move reversibly, so that the domains which are magnetized with a component in the direction of the field grow at the expense of domains magnetized in opposite directions. The increase in magnetization with field in this region is reversible and the *initial permeability* $\mu_i = (dB/dH)_{H=0}$ and the *initial susceptibility* $\chi_0 = (dM/dH)_{H=0}$. Note that this curve is often plotted as B versus H rather than M versus H, where $B = 4\pi M + H$. Continuing to apply an increasing field the domain walls begin to move from their original positions irreversibly into new positions. Usually in this state the increase in magnetization with field is steeper and reaches a maximum $B/H = \mu_{max}$. Finally, the domain walls have largely moved out of the specimen and the specimen is magnetized in that easy direction which is nearest to that of the applied field; further increase of the field has only the result of rotating the direction of magnetization until it finally coincides with the field direction. This final rotational

change is reversible and the final state is the saturated magnetic state.

Reduction and subsequent reversal of the field produces the *hysteresis curve*, as shown by the inset in fig. 3. The magnetization left in a specimen when the applied field has been removed after full saturation is called *residual magnetization* (M_r) or sometimes *remanence*, and the field required after full saturation to reduce the magnetization M to zero is called the *intrinsic coercivity*, H_{ci}, while the field required to reduce B to zero is called simply the *coercivity*, H_c. Another quantity, commonly used in permanent-magnet technology, is the *maximum energy product*, $(BH)_m$, the maximum of $B \cdot H$ in the second quadrant of the B–H hysteresis curve. The various parameters of the B–H hysteresis curve — χ, M_r, H_c and $(BH)_m$ — are very much dependent on the structural properties of the material and can be used in some instances to obtain information about crystallinity, internal stresses, inclusions, etc., in magnetic materials.

In soft materials, the *core loss* (§ 2.7), or energy loss associated with each cycle of magnetization (as in a transformer core) is of interest. The loss is traditionally separated into two components: a *hysteresis loss* proportional to frequency, and an *eddy-current loss* proportional to the square of the frequency. The latter is, of course, most important in the higher frequency range. It can be reduced by reducing the physical dimensions, for example by using thin films or small particles. Another approach is to increase the resistivity, for example by using ferrites instead of metals. Magnetic aftereffect also gives rise to losses especially at higher frequency. *Magnetic aftereffect* is the delayed change in magnetization after a change in magnetic field. This does not include delays due to eddy currents, or to changes in structure. This aftereffect may arise from many different physical processes; for example, it is due to ion diffusion in ferrites occurring at frequencies of a few Hz or to electron diffusion between Fe^{+2} and Fe^{+3} at a frequency of several hundred MHz.

2. *Magnetic measurements*

This discussion is limited to strongly magnetic materials, especially materials with engineering applications with emphasis on the physical principles involved and on the relative ease and accuracy of the various methods. For more details see CULLITY [1972] or ZIJLSTRA [1967].

2.1. Magnetization

The maximum value of the magnetic moment per unit volume, or *magnetization*, is called the *saturation magnetization*, M_s; it is temperature-dependent, and its value at absolute zero is M_0. In SI units, magnetization may be measured in A/m, M, or in tesla, J. In this convention, $J = \mu_0 M$, where μ_0 is the magnetic constant or the permeability of free space, and J is known as polarization. In cgs units, magnetization is measured in erg oersted/cm^3, or emu/cm^3. (Both kinds of units are used in this chapter, reflecting current practice among specialists.) Absolute measurements of magnetization are notoriously difficult, so that almost always the measuring apparatus is calibrated with a standard sample of nickel or iron.

References: p. 2560.

There are two basic methods for determining magnetization. The first depends on the fact that a magnetic moment experiences a force in a field gradient: $F = M\ \mathrm{grad}(H)$. The resulting force is measured with a chemical balance or equivalent force detector. This method is especially useful for measurements on very small or very weakly magnetic samples; it is also good for measurements at high and low temperatures, since the only connection to the sample is a single supporting wire.

The second basic method relies on the voltage generated in a coil by a changing magnetic flux: $E = -N\,\mathrm{d}\phi/\mathrm{d}t$, giving the magnetic moment per unit volume or equivalently lines of magnetic flux per unit area. This voltage, proportional to the time derivative of the flux in the sample, can be integrated to give the change in flux. Its disadvantages are that only changes in flux can be measured, not the magnetization in constant field; and the measured quantity is actually the sum of the sample flux plus the flux from the field acting on the sample. At high fields, the flux from the applied field is large, so the method is usually used for materials that do not require high magnetizing fields.

Measurement of the field at a fixed distance from the sample can also be used to measure the moment of the sample. The sample is normally oscillated at a fixed frequency (usually below 100 Hz) through a small amplitude. The field at a coil fixed in space near the sample then varies at the frequency of the oscillation, producing an ac voltage in the coil. The ac signal is amplified, normally with a lock-in amplifier, and converted to a dc signal which is proportional to the magnetic moment of the sample. This *vibrating-sample magnetometer* can be made very sensitive, and can operate over a wide temperature range. It is limited to small samples.

A problem that may be severe in high-field measurements is the *image effect*. The local magnetic field around a magnetized sample is distorted if there are nearby masses of high-permeability material, such as the pole pieces of an electromagnet. At high fields, the iron of the pole pieces becomes saturated so that its permeability decreases and the image weakens. The calibration constant relating the sample magnetization to the output signal will thus vary with field. A similar problem exists in a superconducting solenoid. The only solution is to calibrate with a sample whose moment is known as a function of field.

2.2. Magnetic field

The most convenient way to measure magnetic fields is with a *Hall-effect probe*. This instrument gives a dc signal proportional to the field component perpendicular to a semiconductor plate. Fields less than the earth's field (25 A/m ≈ 0.3 oersted) and up to the highest steady fields attainable in the laboratory (8 MA/m ≈ 100 kOe) can be measured, with an accuracy generally of the order of 1%.

Time-varying fields can be measured easily by observing the output voltage from a coil in the field. In practice, this is most useful for sinusoidally varying fields. Steady fields can be measured with a coil by rotating the coil to generate an ac voltage. This device, known as a *rotating-coil gaussmeter*, provides a signal that is accurately linear with field, but the equipment is bulky and inconvenient for routine use.

Very accurate field measurements can be made using nuclear magnetic resonance.

The resonance frequency of a nucleus, usually hydrogen, is directly proportional to the applied field, and the proportionality constant is known with great accuracy. The field, however, must be highly uniform and stable, so this method is mainly used for the calibration of other field-measuring instruments.

2.3. Demagnetizing field

Any magnetized sample not infinitely long sets up a field inside the sample as well as outside it. In the sample it is always directed opposite to the magnetization. It is therefore called the *demagnetizing field.*

There are four basic ways to deal with the demagnetizing field. First, one can try to make it negligibly small, by using a very long sample, or, more commonly, a ring-shaped sample. Second, the demagnetizing field can in principle be calculated if the magnetization is known and the sample is ellipsoidal in shape, on the assumption that the magnetization is uniform throughout the sample. Ellipsoidal samples are difficult to make, so often a simpler shape, such as rod or disk, is assumed to be ellipsoidal. Third, one can attempt to measure the field as near as possible to the surface of the sample. Since the tangential component of the field does not change across the surface, this measurement gives the true field acting on the sample, including the demagnetizing field. Finally, one can determine the demagnetizing field experimentally. A sample of the same shape as the real sample, but made from a material with negligibly small coercivity, is measured. The demagnetizing field is equal and opposite to the applied field and the sample magnetization is linear with applied field. The slope of this line is inversely proportional to the demagnetizing factor, which should be the same for all samples of the same shape.

2.4. Curie temperature

The Curie temperature is the temperature at which ferromagnetic behavior disappears. Its approximate value can be obtained from the temperature dependence of the magnetization measured at any field. At high fields, however, the transition is often not sharply defined, so that low-field determination is more accurate, or at least more reproducible.

2.5. Magnetic anisotropy

Magnetic anisotropy is expressed in terms of a series of *anisotropy constants.* Magnetization curves measured with the field applied in different crystallographic directions can be interpreted to give anisotropy data, but the best method is to use a spherical or disk-shaped crystal and measure the torque exerted on the sample by a magnetic field as a function of the angle between the field and a major crystallographic direction. The major difficulty is that the measured anisotropy constants usually depend slightly on the field, and the proper extrapolation is not clear on theoretical grounds. The dependence of the ferromagnetic resonance frequency on crystallographic direction can also be interpreted to give anisotropy data.

References: p. 2560.

2.6. Magnetostriction

Magnetostriction refers to changes in dimensions with state of magnetization. The term is applied to two rather different phenomena. In engineering usage, magnetostriction means the change in length when a demagnetized polycrystalline sample is magnetized. Scientifically, magnetostriction refers to the change in dimensions resulting from the rotation of the saturation magnetization from one crystallographic direction to another in a single crystal. The strains are usually small, typically 10^{-5}, and the standard measuring technique makes use of resistance strain gages. For routine ac measurements on commercial materials, where long samples are available, phonograph pickups or other displacement transducers can be used.

2.7. Core loss

The principal quantity of interest for soft magnetic materials is the *power loss* under ac excitation. This is specified at a particular operating frequency, at a particular maximum flux density. The sample is usually made into the core of a small transformer; if the material is available in sheet form, a standard test geometry called the *Epstein test* is used. The procedure is equivalent to determining the area of the ac hysteresis loop, which can now also be done by digital data recording and computation. (See also § 4.2.3.)

3. *Permanent-magnet materials*

Permanent-magnet or "hard" magnetic materials, as their name implies, strongly resist demagnetization once magnetized. As used in motors, loudspeakers, meters. holding magnets, etc., permanent-magnet materials usually have coercivities ranging from about 10 kA/m to over 100 kA/m (several hundred to many thousand Oersteds). Properties of some representative materials are shown in table 1. More detailed data and information have been presented by McCaig [1977]. Some applications require coercivities in the 800–8000 A/m (10–100 Oe) range, and such materials are sometimes called "semi-hard" materials. Magnetic-recording materials are permanent-magnet materials whose direction of magnetization can be varied over short distances, thereby recording information. These have typically consisted of dispersions of magnetic oxide particles, but there has been growing interest in metallic recording media.

3.1. Reversal mechanisms and coercivity

To understand the connection between coercivity and metallurgical microstructure, it is necessary to consider the microscopic mechanisms of magnetization reversal. Consider a region of magnetic material initially magnetized along an "easy" or low-energy direction and then subjected to a reverse magnetic field. Figure 4 shows several alternative mechanisms whereby the material can reverse its magnetization. These include *coherent rotation* of all the atomic moments (fig. 4a), *non-coherent rotation* modes such as curling (fig. 4b), and *nucleation and growth of reverse domains* (fig. 4c). Coercivity

Table 1
Representative permanent-magnet properties.

Material	H_c		B_r		$(BH)_m$	
	(kA/m)	(Oe)	(T)	(G)	(kJ/m^3)	(MGOe)
ESD * Fe-Co	70	870	0.8	8 000	25	3.2
Alnico 5	58	620	1.25	12 500	42	5.3
8	130	1 600	0.83	8 300	40	5.0
9	120	1 450	1.05	10 500	68	8.5
$Fe_{65}Cr_{32}Co^3$	40	500	1.25	12 500	34	4.3
$Fe_{63}Cr_{25}Co_{12}$	50	630	1.45	14 500	61	7.7
Cunife	44	550	0.54	5 400	12	1.5
Co_5Sm	760	9 500	0.98	9 800	190	24
$(Co, Fe, Cu, Zr)_8Sm$	800	10 000	1.20	12 000	260	33
Ba ferrite	170	2 100	0.43	4 300	36	4.5
Sr ferrite	250	3 100	0.42	4 200	36	4.5
Mn–Al–C	220	2 700	0.61	6 100	56	7.0
Co – Pt	360	4 500	0.65	6 500	73	9.2
$Fe_{14}Nd_2B$	900	11 000	1.3	13 000	300	37

* Elongated Single Domain (§ 3.3.1)

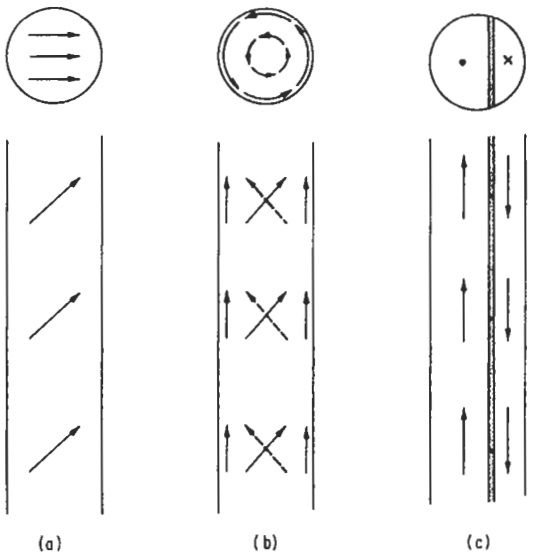

Fig. 4. Schematic representation of magnetization reversal mechanisms. Top and side views of cylindrical region changing from upward to downward magnetization: (a) by coherent rotation: (b) by incoherent rotation (curling); (c) by domain-wall motion.

References: p. 2560.

will be determined by the easiest of these reversal mechanisms.

To impede coherent rotation, the material must possess magnetic anisotropy that will provide an energy barrier to rotation of the magnetization. One possibility is the shape anisotropy of non-spherical particles. A rod-shaped particle has a much lower demagnetizing energy (magnetostatic energy associated with surface magnetic poles) when magnetized along its length than when magnetized across its width (because the demagnetizing field is lower). The resulting energy barrier can be overcome by coherent rotation only for a reverse field given by $(N_t - N_l)M_s$, where N_t and N_l are the transverse and longitudinal demagnetizing factors, respectively. In the limit of infinite length/width ratio, $N_t = 2\pi$ and $N_l = 0$, leading to a predicted coercivity of $2\pi M_s$. A second possibility to provide the energy barrier is *crystal anisotropy*. The simplest case is that of a *uniaxial* crystal anisotropy given by an energy per unit volume of $K \sin^2\theta$, where θ is the angle between the magnetization and the low-energy crystal direction. For this case, a coercivity of $2K/M_s$ is predicted for coherent rotation. Real magnetic materials generally have coercivities far below those predicted for coherent rotation, indicating that other reversal mechanisms are dominant.

Non-coherent rotation modes such as curling (fig. 4b) can significantly lower the energy barrier associated with *shape* anisotropy by lowering the transverse demagnetizing fields. The non-parallel magnetization configurations are opposed by the exchange forces between neighboring moments, but this constraint becomes less important as the size of the independent magnetic regions increases. Thus these theories predict coercivities that decrease with increasing particle size, and curling or other non-coherent rotation modes are believed to control coercivity in some shape-anisotropy materials. However, where *crystal* anisotropy is dominant, noncoherent rotation cannot contribute to lowering the energy barrier or coercivity.

It is now believed that most crystal-anisotropy materials reverse primarily through nucleation and growth of reverse domains. In this process, magnetization rotation is discontinuous, confined to the narrow region within the domain wall. Coercivities for this process can be far lower than for continuous rotation processes, and will be determined by the more difficult of the two necessary steps, reverse-domain nucleation or domain-wall motion. The former becomes more difficult in finer particles, leading to a size-dependence of coercivity when that step is dominant.

In discussing size dependence of coercivity, there are three different size parameters of significance. These are $\delta = \pi(A/K)^{1/2}$, $b_c = 2A^{1/2}/M_s$, and $D_c = 1.4\gamma/M_s^2$, where A is the exchange constant and $\gamma = 4(AK)^{1/2}$ is the domain-wall energy per unit area.

The parameter δ is the width of a domain wall. The parameter b_c is the scaling factor in curling theory, and represents the cylinder diameter below which coherent rotation is favored over curling. It is related to the other parameters through $b_c \approx \frac{1}{2}(\delta D_c)^{1/2}$. The ratio $D_c/\delta \approx 2K/M_s^2$ is a measure of the relative importance of crystal and shape anisotropies. Where $D_c \gg \delta$, the parameter D_c represents the diameter of a sphere below which a single-domain structure is of lower energy at zero field than a two-domain structure. Although particles both above and below D_c may reverse by domain nucleation and growth, domain nucleation becomes increasingly difficult in particles approaching this size range.

In high-anisotropy compounds like Co_5Sm, typical values may be $\delta \sim 5$ nm and $D_c \sim 1$

μm. In pure cobalt, all three size parameters are of the same order of magnitude, about 15–30 nm. In iron and nickel, $\delta > D_c$.

The increase in coercivity with decreasing particle size expected from curling or domain-nucleation theories does not continue indefinitely. For extremely small particles, magnetization rotation over the energy barrier can be thermally activated, leading to *superparamagnetism* (BEAN and LIVINGSTON [1959]) and a decrease of coercivity at small sizes. For a given anisotropy and temperature, there may thus be an optimum particle size for peak coercivity. A more detailed review of coercivity models has recently been prepared by ZIJLSTRA [1983].

3.2. Microstructure and properties

Since dimensions and morphology play such a direct role in reversal mechanisms, coercivity can be extremely sensitive to metallurgical microstructure (LIVINGSTON [1981a,b]). However, satisfactory quantitative correlation of observed microstructure-coercivity relationships and theoretical models of reversal has been achieved only in a few model materials.

Model shape-anisotropy materials have been produced by multiple drawing of compacts of ferromagnetic wires in a nonmagnetic ductile matrix. By drawing down nickel wires in a silver matrix, NEMBACH *et al.* [1977] were able to demonstrate an increase in coercivity with decreasing wire diameter, consistent with the theory of magnetization reversal by *curling* (fig. 5).

In single-phase materials dominated by crystal anisotropy, coercivity is usually

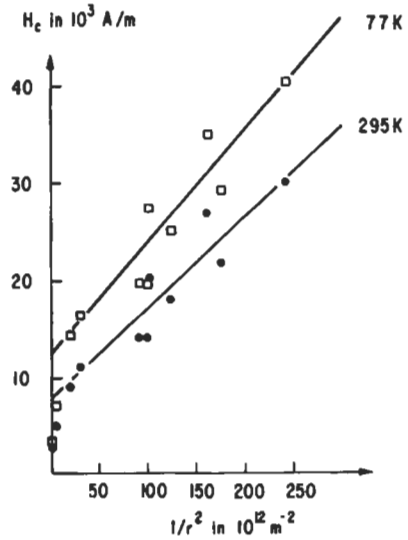

Fig. 5. Variation of coercivity (10^3 A/m$=4\pi$ Oe) of drawn composite of Ni filaments in Ag with inverse square of filament radius. Linear dependence predicted by theory of magnetization-reversal by curling. (From NEMBACH *et al.* [1977].)

References: p. 2560.

determined by *reverse-domain nucleation* at defects such as low-anisotropy regions produced by chemical inhomogeneity. Coercivity can be increased by minimizing the size and density of nucleating defects and by subdivision into fine regions in which the probability of such defects is small. Thus, coercivity in such materials generally increases with decreasing particle size or, in fully dense materials, with decreasing grain size. Apparently grain boundaries frequently provide sufficient magnetic isolation from neighboring grains that separate nucleation events are required for magnetic reversal in each grain. Although theories of the size dependence of coercivity based on domain nucleation have been developed (e.g., BROWN [1962], MCINTYRE [1970], ROWLANDS [1976]), quantitative comparison of theory and experiment has been hampered by inadequate characterization of the nucleating defects.

In many hard and semi-hard materials, coercivity is not determined by curling or by domain nucleation, but by microstructural resistance to domain-wall motion, i.e., by *pinning*. Any local variation in magnetic properties can produce local variations in domain-wall energy and thereby produce forces that resist wall motion. The case most studied by theory and experiment is that of domain-wall pinning by second-phase particles, usually nonmagnetic. Optimum pinning is believed to occur for particle sizes comparable with the domain-wall width δ. For particles smaller than δ, a linear dependence of coercivity on particle diameter has been observed for Co_3Ti precipitates in a Co–Fe–Ti alloy (fig. 6), with the experimentally measured slope in good agreement with that predicted by theory (SHILLING and SOFFA [1978]).

For high-anisotropy materials, domain walls become very narrow, and finer defects become important for pinning. In such cases, planar defects such as grain boundaries and anti-phase boundaries can produce pinning (HILZINGER [1977]), as can point defects and even, in some cases, the discrete nature of the crystal lattice itself (HILZINGER and KRONMÜLLER [1973]). Domain-wall pinning by the lattice structure itself can be viewed as analogous to the Peierls resistance to dislocation motion.

More generally, magnetic "hardening" through domain-wall pinning by defects is analogous in several ways to mechanical hardening by dislocation pinning, (and "hardening" of type II superconductors through vortex pinning) (HAASEN [1972, 1977] and ch. 27, § 4.3). In many alloys, thermal or mechanical treatments that lead to increases in coercivity, e.g., by precipitation, also lead to increases in yield stress. However, because of the different dependence of domain-wall pinning and dislocation pinning on defect size, magnetic and mechanical hardness are not always concurrent. For example, solid-solution alloying elements in iron or nickel can produce mechanical hardening without producing magnetic hardening. An extreme example is that of amorphous alloys, which are mechanically very hard but magnetically very soft.

The general effect of defects depends on which mechanism is controlling coercivity. Defects may *lower* coercivity by serving as nucleation sites for reverse domains or *raise* coercivity by pinning domain walls. Whereas a defect size of the order of δ is effective for pinning, the defect size effective for reverse-domain nucleation is closer to D_c, i.e., much larger for the case of high-anisotropy materials.

The other magnetic properties are much less sensitive to microstructure than is coercivity. Saturation magnetization depends of course on the volume fraction of the

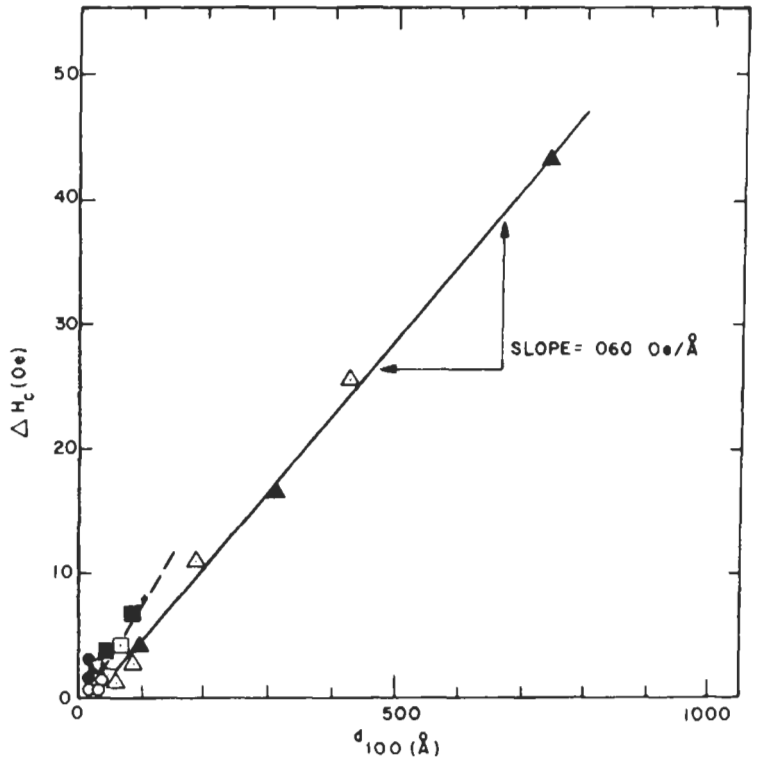

Fig. 6. Variation of coercivity-increment with average diameter of δ' precipitates in Co–Fe–Ti alloy. Linear dependence predicted by theory of domain-wall pinning by nonmagnetic precipitates. (From SHILLING and SOFFA [1978].)

ferromagnetic phase. The remanence-to-saturation ratio depends on the degree of alignment of the easy magnetic axes. Where crystal anisotropy is dominant, it will depend therefore on crystallographic texture. Where shape anisotropy is dominant, it will depend on the alignment of the rod axes. Materials with a high degree of alignment, sometimes called "oriented" magnets, are generally highly anisotropic in properties, with a greatly reduced remanence and energy product in the transverse direction. This is undesirable for some applications, for which "isotropic" magnets, with a random distribution of magnetic easy axes, are more suitable. In such materials, magnetic reversal may occur by domain nucleation and growth or by non-coherent rotation, but full saturation will require higher fields and occurs by coherent rotation from the various easy-axis directions to the field direction.

3.3. Shape-anisotropy materials

Iron and its solid-solution alloys generally have moderate to low crystal anisotropy and usually serve as soft, rather than hard, magnetic materials. However, when processed

to produce fine microstructures with elongated morphologies, useful coercivities can be achieved with these materials through shape anisotropy. Commercial permanent-magnet materials based on shape anisotropy include *elongated-single-domain* (ESD) magnets and various alloys, like the alnico series, produced by spinodal decomposition.

3.3.1. ESD magnets

Development of these materials (LUBORSKY [1961]) was inspired by the theoretical predictions of high coercivity ($2\pi M_s$) for coherent rotation in rod-shaped particles. Elongated particles of iron–cobalt alloy about 10–20 nm in diameter are formed by electrodeposition from an aqueous electrolyte into a mercury cathode. Further processing steps include aging at ~ 200°C to remove dendritic branches from the particles, addition of lead-antimony to provide the matrix metal in which particles are dispersed, removal of the mercury, pressing, grinding, etc. For oriented magnets, a magnetic field is applied during the final processing steps to align the particles.

The coercivities and energy products of ESD magnets, although commercially useful, fall far short of the predictions of coherent-rotation theory. The maximum coercivities attained (about 160 kA/m = 2 kOe) are believed to be limited by a non-coherent mode of rotation, influenced by shape irregularities of the particles. Further, coercivity decreases with increasing volume fraction of the iron–cobalt because of magnetic interactions between particles, thereby limiting energy products.

In later work (LUBORSKY and MORELOCK [1964a,b]), vapor-grown whiskers of iron, iron–cobalt, and cobalt, were produced with more perfect shapes than the electrodeposited particles. Higher coercivities were achieved, but these whiskers could not be developed into a commercial product.

3.3.2. Spinodal alloys

Although the important *alnico* series of permanent-magnet alloys was originally developed empirically, it is now understood in terms of fine (~ 20 nm) elongated particles produced by spinodal decomposition (ch. 14, § 3.1) of a high-temperature body-centered-cubic (bcc) phase into two coherent bcc phases. The earliest alloys in this series contained only Fe, Ni, and Al, and the decomposition resulted from a miscibility gap that developed at low temperatures between the Fe-rich bcc phase (α_1) and the NiAl-rich ordered bcc phase (α_2). Alloys were later improved by major additions of Co and minor additions of Cu, Ti, and other elements.

The Co raised the saturation magnetization and Curie temperature of the α_1 phase, and made the alloy more susceptible to property improvement through *magnetic annealing*, i.e., annealing in a magnetic field. The phases usually are elongated in ⟨100⟩ directions, and magnetic annealing causes preferential growth along the ⟨100⟩ direction nearest the field direction. Most of this preferential alignment appears to occur during the coarsening of the precipitate. The development of ⟨100⟩ rods from coherent precipitation is believed to be related to lattice-misfit strains and anisotropy in the elastic moduli. This ⟨100⟩ alignment appears to be accentuated by increases in the Co and Ti content. Alloying additions also alter the volume fractions of the α_1 and α_2 phases and their magnetic properties. For maximum alignment of the microstructure, directional solidifi-

cation has been used to produce a strong ⟨100⟩ fibre texture. The relations between microstructure and properties in alnico alloys have been reviewed by DE VOS [1969], PFEIFFER [1969], and MCCURRIE [1982].

After initial decomposition of alnico alloys, both α_1 and α_2 phases are ferromagnetic. However, after subsequent lower-temperature aging to increase coercivity, the composition difference between the two phases increases, and the α_2 phase usually becomes nonferromagnetic at room temperature. The microstructure is often modelled as consisting of isolated ferromagnetic α_1 rods in a nonferromagnetic α_2 matrix, and coercivity is interpreted by non-coherent rotation theory, usually curling, modified by interparticle interaction. However, micrographs in some alloys indicate a more complex microstructure, with both α_1 and α_2 phases continuous and interconnected, suggesting the possibility of extended domain walls in the α_1 phase and a coercivity controlled by domain-wall pinning. A similar uncertainty of the operative reversal mechanisms exists in the analogous Fe–Cr–Co alloys.

Guided by the growing understanding of alnico alloys in terms of spinodal decomposition and the Fe–Ni–Al miscibility gap, KANEKO *et al.* [1971] initiated the development of a series of permanent-magnet alloys based on the Fe–Cr miscibility gap. Additions of Co were found to raise the decomposition temperatures and increase the composition spread between the Fe-rich α_1 phase and the Cr-rich α_2 phase (fig. 7). Other alloying additions have been used to avoid the formation of the unwanted γ (fcc) and σ phases, and to modify precipitate morphology. Although precipitates are often nearly spherical, ⟨100⟩ elongated morphology can be enhanced, for example, by Mo additions (HOMMA *et al.* [1980]).

As with the alnicos, magnetic annealing to improve alignment, and subsequent aging at lower temperatures to increase the composition difference between α_1 and α_2 phases,

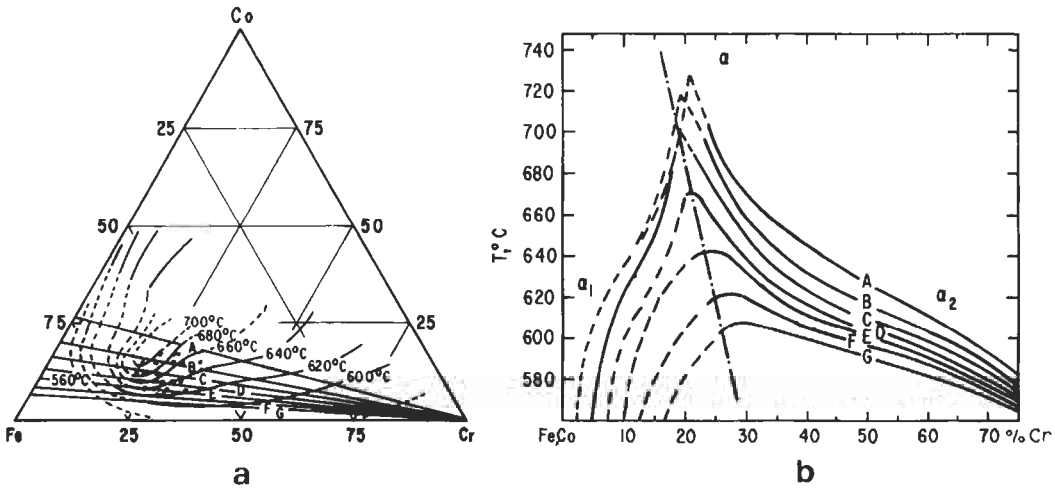

Fig. 7. Miscibility gap in Fe–Cr–Co system: (a) at various temperatures; (b) at various Co/Fe ratios. (From MINOWA *et al.* [1980].)

References: p. 2560.

improve the magnetic properties. A major advantage of the Fe–Cr–Co alloys over the alnico series is that most compositions retain some ductility even after spinodal decomposition has occurred. This allows enhancement and alignment of the shape anisotropy by uniaxial plastic deformation, which can produce significant increases in coercivity and energy product (KANEKO *et al.* [1976]). JIN [1979] developed a "deformation-aging" technique in which this particle elongation is accomplished before the final aging. The dependence of magnetic properties on this intermediate deformation is shown for one alloy composition in fig. 8.

Another advantage of the Fe–Cr–Co alloys over the alnicos is that they can achieve comparable magnetic properties at lower percentages of cobalt (HOMMA *et al.* [1981], CHIN *et al.* [1981]). Recent price and supply problems with cobalt have made this an important consideration. Work has also progressed on other elements that raise the Fe–Cr miscibility gap, and promising Fe–Cr–V alloys have recently been reported (INOUE and KANEKO [1981]).

In some Fe–Cr–Co alloys at peak coercivity, both α_1 and α_2 phases appear to be ferromagnetic, and domain walls have been seen by Lorentz electron microscopy (BELLI

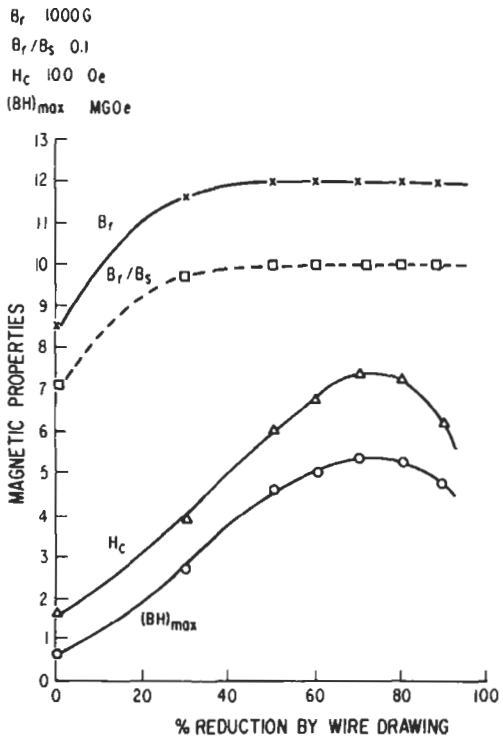

Fig. 8. Magnetic properties of Fe–Cr–Co alloy versus degree of plastic deformation. Alloy was aged before deformation to produce precipitation, and after deformation (at a lower temperature) to increase the composition difference between the phases. (From JIN [1979].)

et al. [1978], MAHAJAN *et al.* [1978]). Such results suggest that, at least for some compositions and heat treatments, domain-wall pinning is a more appropriate model for magnetization reversal than rotation processes in single-domain particles.

Face-centered-cubic spinodal alloys have also found use as permanent-magnet materials. In the Cu–Ni–Fe and Cu–Ni–Co systems, a high-temperature fcc phase decomposes on aging into two coherent fcc phases, one Cu-poor and ferromagnetic and the other Cu-rich and nonferromagnetic. Phases are elongated along ⟨100⟩ directions, and the extensive ductility of these alloys allows enhancement and alignment of the shape anisotropy. Magnetization reversal is believed to occur by curling (KIKUCHI and ITO [1972]).

3.4. Crystal-anisotropy materials

Crystal anisotropy provides an energy barrier that impedes both coherent and noncoherent rotation processes, independent of particle size and volume fraction. Permanent-magnet materials based on crystal anisotropy generally possess hexagonal or tetragonal crystal symmetry with the hexagonal or tetragonal axis the magnetic easy axis. Since experimental coercivities are always well below the $2K/M_s$ predicted by coherent or noncoherent rotation, magnetization in these materials clearly occurs by nucleation and growth of reverse domains. The materials differ, however, in the relative importance of domain nucleation and domain-wall pinning in determining coercivity.

3.4.1. Cobalt–rare earths

The permanent-magnet materials with the highest intrinsic coercivities are the cobalt–rare earth compounds, which have crystal anisotropy constants as high as 10^7 J/m^3 (10^8 erg/cm^3). These magnets can be divided into four types, depending on whether the primary phase is of the Co_5R (R = rare earth, usually Sm), or $Co_{17}R_2$ type, and whether the magnet has a predominantly single-phase or two-phase microstructure. All four types generally consist of a sintered compact of magnetically aligned powders of the order of 10 μm in diameter. Coercivities are usually higher in Co_5R-based magnets, because of the higher anisotropy constants associated with this phase. Magnetizations are generally higher in $Co_{17}R_2$-based magnets, leading to higher remanence and the potential of higher energy products. Coercivity mechanisms in these materials have been reviewed by several authors (LIVINGSTON [1973], MENTH *et al.* [1978], KRONMÜLLER [1978]).

The two-phase magnets generally contain Cu, which enhances the formation of fine coherent precipitates, either of Co_5R phase in a $Co_{17}R_2$ matrix or vice versa. Another common alloying element is Fe. The precipitates sometimes form a cellular microstructure, as in fig. 9. As with the alnicos and Fe–Cr–Co alloys, optimum properties are often obtained by achieving phase separation at one temperature and subsequently aging at a lower temperature (or temperatures) to increase the composition difference between the two phases. Both phases remain ferromagnetic, and coercivity is controlled by the pinning of domain walls. Lorentz electron microscopy of magnets has directly demonstrated the pinning of domain walls by the cellular microstructure (MISHRA and THOMAS [1979]).

In single-phase Co_5R or $Co_{17}R_2$ magnets, coercivity is controlled largely by the

References: p. 2560.

Fig. 9. Transmission electron micrograph of cellular precipitation structure within single-grain-sintered Co–Cu–Fe–Sm aged to peak coercivity (560 kA/m = 7 kOe). Section normal to easy magnetic axis (hexagonal axis). Cell interiors have 17–2 structure, cell boundaries have 5–1 structure, fully coherent. Coercivity controlled by domain-wall pinning by cell boundaries. (From LIVINGSTON and MARTIN [1977].)

nucleation of reverse domains, although domain-wall pinning by grain boundaries is also important. The difference between pinning-controlled and nucleation-controlled behavior can be seen clearly by observing the initial magnetization curve of thermally demagnetized samples. Thermal demagnetization generally leaves the samples with several domains per grain. In the two-phase, pinning-controlled magnets, the existing domain walls cannot move easily, and permeability remains low until the applied field approaches the coercivity (solid curve of fig. 10). In the single-phase, nucleation-controlled magnets, the existing walls move easily within the grains and initial permeability is high, the magnet approaching saturation at low fields (dashed curve of fig. 10). However, once saturated, i.e., once reverse domains are removed, this magnet acquires considerable coercivity. The variation of coercive force with magnetizing field for the two magnets is shown as an inset in the figure.

Reverse-domain nucleation is generally believed to occur at regions of lowered crystal anisotropy, such as $Co_{17}R_2$ precipitates. Co_5Sm, for example, is unstable to eutectoid decomposition below about 800°C (DEN BROEDER and BUSCHOW [1980]) and aging at too low a temperature can produce large $Co_{17}Sm_2$ particles, particularly along grain boundaries. (It is interesting that multi-micron $Co_{17}Sm_2$ particles decrease coercivity in Co_5Sm through domain nucleation, whereas coherent ~ 10 nm $Co_{17}Sm_2$ particles

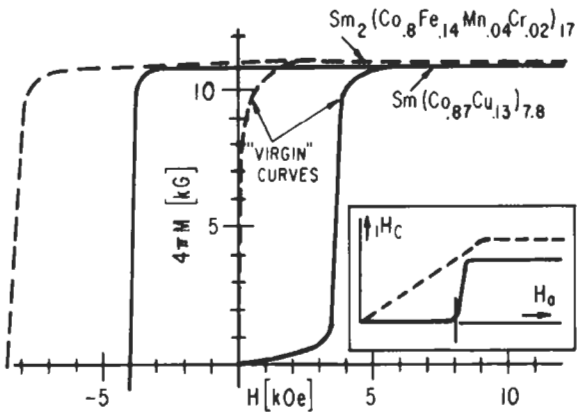

Fig. 10. "Virgin" magnetization curves for precipitation-hardened (solid line) and single-phase (dashed line) $Co_{17}R_2$ permanent magnets. Characteristic, respectively, of pinning-controlled and nucleation-controlled coercivity. Insert shows schematic dependence of coercive field on magnetizing field for the two coercivity mechanisms. (From MENTH *et al.* [1978].)

formed in Cu-containing Co_5Sm alloys increase coercivity through domain-wall pinning.) In some cases, experimentally-defined "nucleation" may not correspond to the initial formation of a reverse domain, but to its irreversible breakaway from its nucleation site, generally to reverse the entire grain. Thus residual reverse domains resulting from incomplete saturation can serve as "nuclei" (BECKER [1973]). Preferential oxidation in grain-boundary regions has been suggested as a source of low-anisotropy nucleation sites (BARTLETT and JORGENSON [1974]).

Domain studies of magnetic reversal in sintered Co_5Sm magnets (LIVINGSTON [1973b], DEN BROEDER and ZIJLSTRA [1976]) show that grain boundaries serve to block the propagation of magnetic reversal from grain to grain. This pinning of domain walls by grain boundaries is important, because otherwise one nucleating defect would lead to the reversal of an entire magnet. The effectiveness of grain boundaries as domain-wall pins is probably sensitive to the physical and chemical state of the boundary. Annealing at too high a temperature has been shown to decrease the pinning effectiveness of grain boundaries in Co_5Sm (DEN BROEDER and ZIJLSTRA [1976]). Cobalt–rare earth magnets have been reviewed by STRNAT [1988].

3.4.2. Iron-rare earths

A major advance in permanent-magnet materials occurred when two companies announced the development of magnets based on a newly-recognized ternary compound, $Fe_{14}Nd_2B$ (SAGAWA *et al.* [1984], CROAT *et al.* [1984]). Although crystal anisotropy constants and coercivities were not as high as those of the Co_5R compounds, $Fe_{14}Nd_2B$ had a higher saturation magnetization, which soon led to higher energy products than obtainable with cobalt-rare earth compounds. Equally if not more important, iron was cheaper and much more plentiful than cobalt, and neodymium was much more plentiful, and potentially cheaper, than samarium. With a Curie temperature of only 312°C

compared to 747°C for Co_5Sm and 917°C for $Co_{17}Sm_2$, $Fe_{14}Nd_2B$ magnets have more limited temperature capability than cobalt-rare earth magnets. They also appear to be more susceptible to some forms of corrosion. However, their higher energy products and lower cost have allowed them to seize a rapidly-growing fraction of the permanent-magnet market. The processing, structure, and properties of Fe–Nd–B and related magnets have been comprehensively reviewed by HERBST [1991] and by BUSCHOW [1988]. Most Fe–Nd–B magnets are made either by sintering of milled and magnetically-aligned powder (a process analogous to that used for most Co–R magnets), or by rapid-solidification.

The grain size of sintered magnets is typically 5–10 μm, and TEM studies indicate that a thin Nd-rich layer is present along most grain boundaries. This layer magnetically decouples neighboring grains, and is believed to be necessary to achieve high coercivities. As with Co_5Sm magnets, magnetization behavior suggests that coercivity is nucleation-controlled. Many alloying additions have been studied, including Co to increase Curie temperature and Dy, Al, Ga and other elements to improve coercivity, either through enhancement of crystal anisotropy or through alteration of microstructure.

Rapid solidification of Fe–Nd–B is usually achieved by melt-spinning, a process commonly used to produce amorphous metals and described in section 5.2. Optimum as-solidified coercivity occurs at an intermediate quench rate that yields grains less than 100 nm in diameter, about 100 times finer than the grains in sintered magnets. Polymer-bonded magnets are made directly from melt-spun flakes, and are isotropic in texture and magnetic properties, with a volume fracture of $Fe_{14}Nd_2B$ of about 80%. Alternatively, magnets of nearly 100% $Fe_{14}Nd_2B$ can be produced by hot pressing of melt-spun flakes. Since some grain growth occurs at the pressing temperature, overquenched ribbon is used so that optimum grain size and coercivity are obtained after pressing.

Observation of slight texture development during hot pressing led to studies of the effects of compressive deformation at temperatures above 700°C. This "die upsetting" process produced substantial alignment of the magnetic easy axis along the compression direction, yielding increases in remanence and energy product. This process typically produces platelike grains about 60 nm thick and 300 nm in diameter.

The successful development of $Fe_{14}Nd_2B$ magnets generated a widespread search for other ternary or higher-order compounds with promising magnetic properties. Emphasis has been on compounds containing Fe and Co (for high saturation magnetization and Curie temperature) and Sm, Nd, or Pr (for high crystal anisotropy). Considerable interest was generated by the discovery that $Fe_{17}Sm_2N_{3-\delta}$ has a higher Curie temperature than $Fe_{14}Nd_2B$ with comparable saturation magnetization and anisotropy. It is, however, unstable at high temperatures, precluding sintering or hot-working as means to produce dense aligned magnets. Properties of $Fe_{17}Sm_2N_{3-\delta}$ and other promising magnetic compounds, some containing nitrogen, have been reviewed by COEY [1991], BUSCHOW [1991], and WALLACE and HUANG [1992].

3.4.3. Hard ferrites

The hexagonal barium and strontium ferrites are today the most used permanent-magnet materials. These oxides are ferrimagnetic rather than ferromagnetic, i.e., some of

the atomic moments are oriented opposite to the remaining moments. This significantly limits the magnetizations and attainable energy products. However, they have a significant crystal anisotropy (about 3×10^5 J/cm^3 = 3×10^6 erg/cm^3), and high coercivities (160–400 kA/m = 2–5 kOe) can be achieved by sintering aligned particles about 1 μm in diameter. Their development and properties have been reviewed by VAN DEN BROEK and STUIJTS [1977].

These magnets appear to be predominantly single phase, and magnetization curves of thermally-demagnetized samples resemble the behavior of single-phase cobalt–rare earth magnets (dashed curves, fig. 10). These results plus direct domain observations of magnetic reversal indicate that coercivities are controlled by domain nucleation, with grain-boundary pinning isolating grains from their neighbors (CRAIK and HILL [1977]).

3.4.4. Mn–Al–C

None of the equilibrium phases in the Mn–Al alloy system are ferromagnetic. The ferromagnetic near-equiatomic τ-phase is metastable, formed from the high-temperature hexagonal phase by an ordering followed by a martensitic shear transformation (KOJIMA *et al.* [1974]). It can be formed by quenching and aging, or by cooling at moderate rates. At long aging times or slow cooling rates, it decomposes eutectoidally into the low-temperature equilibrium phases.

The ferromagnetic phase has the face-centered-tetragonal CuAu(I) structure, which imparts a uniaxial crystal anisotropy of about 10^6 J/m^3 (10^7 erg/cm^3). If grain size is 1 μm or finer, coercivities of 240 kA/m (3 kOe) or more can be attained. However, production of an aligned magnet is difficult, because the instability of the τ-phase at elevated temperatures precludes the sintering of aligned powder. Additions of carbon have been formed to stabilize the τ-phase up to 700°C for extended times. This permits high-temperature extrusion, which produces a texture with significant alignment of the [001] magnetic easy axes. This alignment enhances remanence and energy product (OHTANI *et al.* [1977]).

Transmission electron microscopy reveals an essentially single-phase microstructure, suggesting that, as in the hard ferrites and single-phase cobalt-rare earths, coercivity is controlled by reverse-domain nucleation, with grain-boundary pinning serving to magnetically isolate grains from their neighbors. Micrographs also reveal a significant volume fraction of twins, which is probably a major factor limiting alignment.

The high coercivities of "silmanal" (Ag–Mn–Al) magnets apparently derive from fine precipitates of MnAl τ-phase dispersed in a nonmagnetic Ag-rich matrix (MCCURRIE and HAWKRIDGE [1975]).

3.4.5. Co–Pt and related alloys

Below 825°C, Co–Pt alloys near the equiatomic composition undergo an ordering reaction from a disordered fcc solid solution to an ordered fc tetragonal CuAu(I) phase. This structure imparts a crystal anisotropy of 5×10^6 J/m^3 (5×10^7 erg/cm^3), and Co–Pt alloys with coercivities over 500 kA/m (6 kOe) and energy products over 95 kJ/m^3 (12 MGOe) have been produced (KANEKO *et al.* [1968]). Peak coercivity appears to occur before ordering is complete, and the microstructure consists of a fine coherent mixture

References: p. 2560.

of ordered and disordered phases. Coercivity appears to be governed by domain-wall pinning (GAUNT [1966]).

Fe–Pt and Fe–Pd alloys, and related ternaries, also go through an ordering reaction to a CuAu(I) tetragonal phase with high crystal anisotropy. Since each disordered fcc grain usually yields three tetragonal variants, Co–Pt and related magnets are usually isotropic. However, application of a stress or magnetic field during the order reaction can favor one of the three variants, leading to alignment of the [001] magnetic easy axes. Stress-assisted ordering has been used to produce an 64 kJ/m^3 (8 MGOe) FePd magnet (YERMAKOV *et al.* [1978]).

4. *Soft magnetic materials*

Soft magnetic materials are characterized by high permeability, low coercive force, and low core loss. They are widely used industrially as pole pieces in electric motors and generators, laminations in transformer and inductor cores, and in a variety of electromagnetic devices. There are six major groups of commercially important soft magnetic materials: iron and low-carbon steels, iron–silicon alloys, iron–aluminium and iron–aluminium–silicon alloys, nickel–iron alloys, iron–cobalt alloys, and ferrites. Ferrites are oxide ceramics and hence will not be discussed in the present context of metals and alloys. Because of their high electrical resistivity, ferrites are used at high frequencies ($\geq$ 100 kHz) where eddy-current losses limit the usefulness of metallic magnets. An emerging group of new soft magnetic alloys are the amorphous magnetic alloys which will be discussed in § 5.

In general, the magnetic behavior of soft magnetic materials is governed by domain-wall pinning at heterogeneities such as grain boundaries, surfaces, precipitates and inclusions. Hence, a major common goal in the metallurgy of soft magnetic materials is to minimize such heterogeneities through the use of high-purity starting materials, improved melting and casting practice as well as subsequent fabrication. In addition, eddy-current loss is minimized through alloying additions which increase the electrical resistivity. Initial permeability, a useful parameter in the design of electronic transformers and inductors, is improved by minimizing all sources of magnetic anisotropy energy. Indeed, as will be discussed in § 4.4, the successful development of the high-permeability nickel–iron alloys is primarily the result of the scientific understanding and technical exploitation of the various types of magnetic anisotropy energy and their minimization based on composition and degree of atomic order. On the other hand, a high maximum permeability, useful for power transformer applications, is increased through the alignment of a strong anisotropy. In iron–silicon alloys, where magnetocrystalline anisotropy is dominant, crystallographic texture control is most important. In nickel–iron alloys, where several types of anisotropy can be dominant, the situation is much more complex and the interplay between structure and processing becomes more intricate. Finally, since most soft magnetic materials are processed to thin strips or fine wires, ductility control often becomes as important as magnetic control.

Thus a discussion of soft magnetic materials, as constituted in this section, must

necessarily be linked to each material in accordance with its intended applications, with production and processing playing a major role. For a more complete treatment, the reader is referred to the articles by CHIN and WERNICK [1980] and FISH [1990] and the book by CHEN [1977].

4.1. Iron and low-carbon steels

Commercially pure iron, generally of 99.9 + % purity, is used in dc applications such as pole pieces of electromagnets. The value of saturation magnetization is high, and coercivity low, but the electrical resistivity is also low. Low-carbon steel has higher resistivity and is thus more suitable for ac applications such as small motors.

Chief impurities in iron are C, Mn, Si, P, S, O and N, with C, O, S, and N having the greatest detrimental effect on the magnetic properties as they enter the iron lattice interstitially. These impurities strain the lattice and interfere with domain wall motion. By annealing in H_2 and in vacuum much of these impurities can be removed and the permeability consequently much improved. Although best results are obtained at very high temperatures (1200–1300°C), the usual commercial practice is to anneal at ~ 800°C.

The carbon and nitrogen contents can also be lowered by treating molten iron with titanium and aluminium. The remaining carbon and nitrogen are then tied up as second phase compounds of titanium and aluminium. Such treatment has the further beneficial effect of "stabilizing" the iron, since any appreciable dissolved amounts of carbon and nitrogen can lower the permeability with time by precipitation of carbides and nitrides, resulting in magnetic aging.

Systematic investigations by SWISHER *et al.* [1969] and SWISHER and FUCHS [1970] have clarified the influence of impurities on the magnetic properties and susceptibility to aging of low-carbon steels. Carbon and nitrogen have similar effects on initial magnetic properties, but only nitrogen promotes aging at 100°C. Second phases also increase the coercivity significantly. However, the morphology of the second phase is important. In SAE1010 steel, for example, cementite (Fe_3C) is generally present as fine lamellae or as a grain-boundary network, resulting in high coercivity. On the other hand, a spheroidizing heat treatment can markedly decrease the coercive force (SWISHER *et al.* [1969] and SWISHER and FUCHS [1970]). Such treatment could be used to advantage to upgrade the magnetic properties of a normally low-cost, low-grade steel.

In addition to dissolved interstitials, inclusions and second phase, grain size and crystallographic texture have a substantial influence on the magnetic behavior of low-carbon steels. Coercivity generally decreases with increasing grain size, which is obtained by annealing at high temperatures, in higher-purity starting materials, and under conditions where impurities are removed (e.g., decarburization). For iron, ⟨100⟩ is the easy magnetic direction. Here sheet material with a {110} sheet texture has superior soft magnetic properties as compared with that having a {111} texture. In the investigation by RASTOGI [1977], an increased Mn/S ratio was found to increase the {110} component at the expense of {111} in cold-rolled and decarburized low-C steels, resulting in an improvement in permeability at the 1.5–1.8 T level. A previous study (RASTOGI [1976]) indicated that, under otherwise similar conditions, a rephosphorized 0.1% carbon steel

References: p. 2560.

exhibits superior permeability and core loss as compared to a 0.06% C steel as a result of a more favorable {110} texture.

In general, permeability at the 1.5–1.8 T level is quite well correlated with crystallographic texture, while the core loss is a more complex parameter which depends on sheet thickness, electrical resistivity, grain size, inclusion and second-phase content and morphology, and texture. For commercial low-C steels subjected to standard decarburization treatments, RASTOGI and SHAPIRO [1973] have provided an empirical relationship for the 1.5 T/60 Hz core loss as:

$$P_T = 11.33 \frac{t^{1.35} G^{0.065}}{\left(B_{30}/B_s\right)^{3.09} \rho^{0.40}} \left(W/\mathrm{kg}\right),$$

where t is the thickness (m), G is the average number of grain-boundary intercepts/mm, p is the resistivity ($\mu\Omega$ cm), and B_{30}/B_s is a texture-related ratio of induction at 30 Oe (24 A/cm) to that at saturation.

4.2. Iron–silicon alloys

Iron–silicon alloys containing up to about 4% Si used for magnetic applications are known as *silicon steels*. Higher-loss non-oriented silicon steels are generally used in small motors and generators, relays, and small power transformers where efficiency is of less concern, while the low-loss oriented grades tend to be used in large generators and power- and distribution-transformers where weight and efficiency considerations are of paramount importance.

As a result of intense research and development efforts over the years, the quality of silicon steels has been improved continually. Intense studies on the mechanisms of recrystallization textures and of magnetic core loss have led to the development of new grades of high-induction low-loss material of exceptionally sharp {110}⟨001⟩ texture.

4.2.1. Phase diagram and intrinsic magnetic properties

The technical magnetic properties of silicon steels are intimately related to the phase diagram and intrinsic magnetic properties of the Fe–Si system. According to the most recently drawn iron-rich portion of the Fe–Si phase diagram (HULTGREN *et al.* [1973]), the high-temperature γ-loop extends from 912°C to 1394°C, with the tip at 2.5% Si. Thus one of the benefits of Si addition to Fe is to enable high-temperature heat treatment for grain-orientation control without the deleterious effect of the α–γ (bcc–fcc) phase transformation.

The size of the γ-loop, however, is highly sensitive to small additions of carbon. For this reason, carbon is generally suppressed to below 0.01% through a combination of melting control and decarburization heat treatment.

Silicon additions in the 5–6% range lead to the formation of the DO_3 ordered α_1 phase, resulting in a loss of ductility. Thus practically all commercial grades of silicon steels contain less than 3.5% Si.

The four important intrinsic magnetic parameters of Si–Fe, saturation induction, Curie temperature, magnetocrystalline anisotropy constant K_1, and saturation magnetostriction

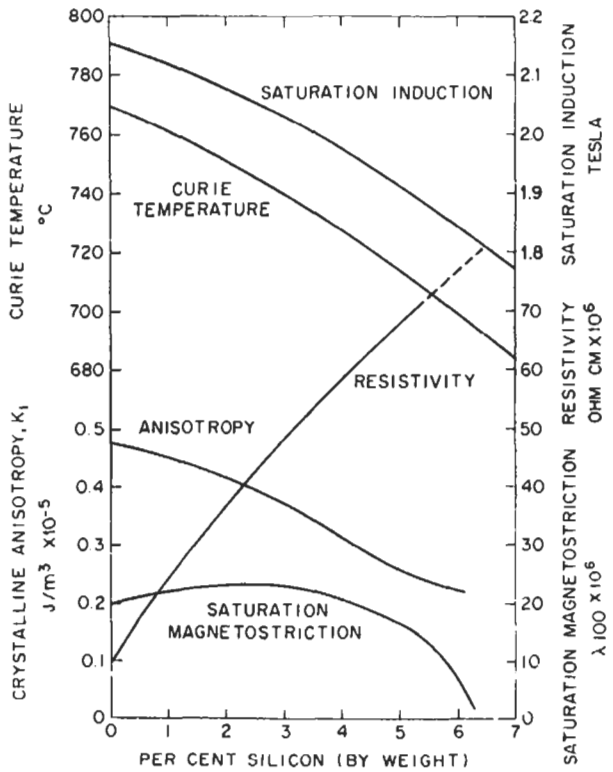

Fig. 11. Effect of silicon on properties of iron.

λ_{100}, are shown in fig. 11 (LITTMANN [1971]). The addition of silicon lowers the saturation induction and Curie temperature and is thus undesirable magnetically. On the other hand, the decrease in K_1 is beneficial. The near-zero value of magnetostriction at 6% Si is highly attractive, but as already noted, material, of this composition is also brittle.

Another benefit of silicon addition, from the magnetic viewpoint, is the increase in electrical resistivity, which helps lower the eddy-current loss.

4.2.2. Magnetic permeability

In general, the value of permeability near the knee of the magnetization curve, typically measured at 10 Oe (800 A/m), is a reasonably sensitive measure of grain orientation and insensitive to other factors. However, experiments by SHILLING *et al.* [1978] on a 3% Si–Fe (110) [001] single crystal revealed that at small misorientations such as a tilt of [001] at 2° from the sheet plane, the magnetization is aligned in the field direction rather than along [001]. Thus in this case $\mu = 2030$ (at $H = 800$ A/m), the same value as for a zero tilt angle.

4.2.3. Core loss

The single most important technical magnetic property of silicon steels is the core loss. The major variables affecting core loss are: composition, impurities, grain orientation, stress, grain size, thickness, and surface condition.

4.2.3.1. Composition. It is well known that the addition of silicon decreases the core loss. The primary reasons for the decrease are the decrease in magnetocrystalline anisotropy, the ability to eliminate harmful impurities through annealing at higher temperature due to the vanishing γ-loop, and the increase in electrical resistivity.

4.2.3.2. Impurities. As stated in the earlier section on iron and low carbon steels, interstitial impurities elastically distort the lattice and impede domain wall motion, and hence cause an increase in core loss. For these reasons, C, S, N and O are generally kept below 0.01% in today's silicon steels. The widespread use of various modern liquid-steel refining techniques has permitted the reduction of carbon levels to as low as 0.005%.

Similarly, insoluble inclusions such as SiO_2 and Al_2O_3 also increase the loss by pinning the moving domain walls and by creating spike domains.

Of the substitutional solid-solution elements, manganese and aluminium are commonly encountered in silicon steels. Manganese increases the loss only slightly and about 0.25% is added to improve workability in non-oriented grades, although the content is kept below 0.1% in oriented grades. Aluminium is also present to about 0.3% in non-oriented grades for improved ductility, but again kept low in oriented grades.

4.2.3.3. Grain orientation. Grain orientation, or texture, is another important variable that affects core loss. The breakthrough by Goss [1934] in the development of the {110} ⟨001⟩, or *cube-on-edge* (COE) texture, is now classic history. It has been estimated (Littmann [1971]) that for COE-textured 3.15% Si-Fe, a 1° smaller average misorientation would improve the total core loss at 1.5 T/60 Hz by 5%.

The relationship of core loss to orientation can be traced to the magnetic domain structure. Shilling and Houze [1974] observed that there are two components of the domain structure in (110)[001] Si–Fe: a main structure consisting of large flux-carrying slab domains with magnetizations along [001], and a supplementary structure which flux-closes along the grain surface with magnetizations along [010] and [001]. Core loss is mainly associated with rearrangement of the supplementary structure during an ac cycle. With increases in misorientation, there is an increase in the supplementary structure and hence an increase in loss.

The above is true for tilts of [001] out of the surface greater than 2°. For lesser tilts, however, the trend is reversed, core loss increasing with decreasing tilt (Shilling *et al.* [1978] and Nozawa *et al.* [1978]). This is shown in fig. 12. Here it was found that the 180° domain wall spacing of the main structure increases rapidly with decreasing tilt, a factor which increases the core loss. Detailed measurements are given in fig. 13, and domain observations are shown in fig. 14.

4.2.3.4. Stress. Since λ_{100} is positive for 3% Si–Fe, the application of a tensile stress near [001] is expected to decrease the core loss by suppressing the supplementary domain structure. The data of fig. 12 show that core loss is indeed lowered by a tensile stress, but the effect is greater for smaller tilts. The domain observations of Shilling *et al.* [1978] indicate that in addition to suppressing the supplementary structure, the applied

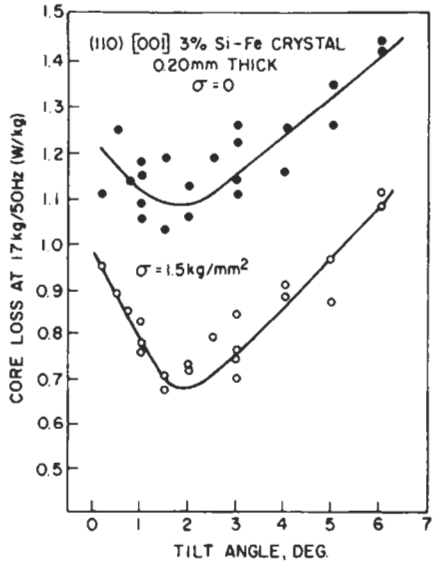

Fig. 12. Core loss versus tilt angle for (100) [001] 3% Si–Fe crystals of 0.20 mm thickness (from NOZAWA *et al.* [1978]).

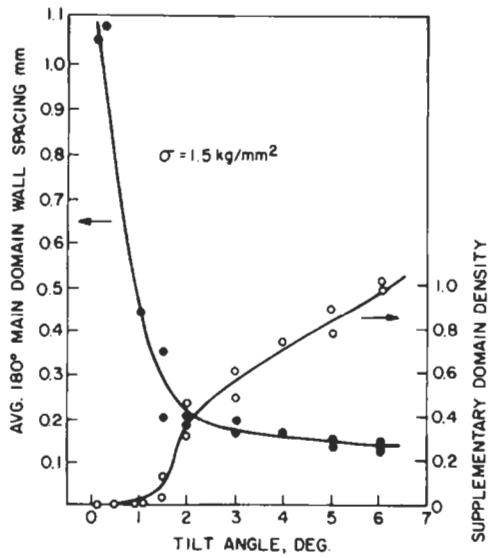

Fig. 13. Dependence of 180° main domain wall spacing and supplementary domain density (normalized at 1 for 6°) on tilt angle for crystals of fig. 12 (from NOZAWA *et al.* [1978]).

References: p. 2560.

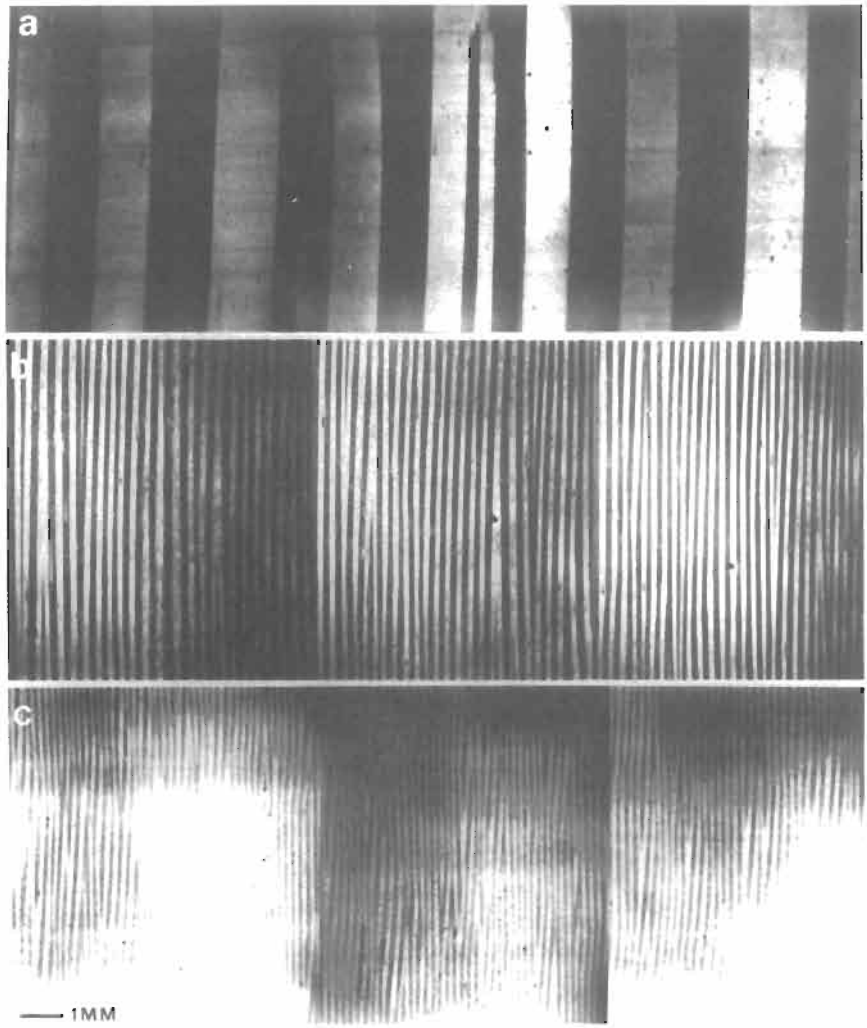

Fig. 14. Domain structure of (100)[001] 3% Si–Fe crystals in the 60 Hz demagnetized and unstressed state: (a) tilt angle $\theta = 0$; (b) $\theta = 2°$; (c) $\theta = 5°$. (From SHILLING *et al.* [1978].)

stress was also effective in refining the spacing of the main structure. Both effects were greater for smaller tilts — hence the larger lowering of core loss there. A stress-inducing surface coat may be applied (§ 4.2.4).

4.2.3.5. Grain size. Everything else being equal, the core loss goes through a minimum with grain size at a grain diameter of about 0.5 mm (LITTMANN [1967]). Domain observations indicate that in the larger grain size range (~ 5 mm), a decrease in grain size results in a decrease in the 180° main domain spacing — hence a decrease in loss. In the finer grain size range (~ 0.05 mm), large magnetostatic energy is expected at

the grain boundaries, causing an increase in loss owing to domain-wall pinning there.

4.2.3.6. Thickness. A decrease in thickness generally leads to a decrease in loss by reducing the eddy-current effects. At very small thicknesses, surface pinning of domain walls becomes dominant and core loss rises again. The core loss minimum, however, is shifted from a thickness of about 0.25 mm for unoriented material to 0.12 mm for oriented material (LITTMANN [1967]). Thus the reduced surface pinning associated with grain orientation drives the thickness minimum to smaller values.

4.2.3.7. Surface morphology. It is well known that surface pinning is more severe at rough spots. Hence it is expected, and generally observed, that a smooth surface, such as that obtained by chemical polishing, leads to lower losses. In commercial production of grain-oriented material a separator such as MgO is applied to the steel surface prior to the final high-temperature (~ 1200°C) hydrogen purification cycle. Depending on the separator material and the details of the heat treatment, a smooth or rough surface can result, leading to changes in core loss (SWIFT *et al.* [1975]).

One conclusion to be drawn from the discussion of the effect of various parameters on core loss is the clear importance of grain orientation. If the grain orientation is sharp, the effects of grain size, thickness, and stress are much more dramatic. Exploitation of such synergistic effects is largely responsible for the design and production of new high-induction steels.

4.2.4. Metallurgy of silicon steels

A major development in silicon steels has been the high-induction material with an exceptionally sharp COE texture. The average misorientation is 3° instead of 7° for conventional oriented grades. The new material exhibits an induction of 1.92 T at $H = 800$ A/m versus 1.83 T for conventional grades, and a 20% lower core loss at high induction (1.7 T).

The new material was first introduced by Nippon Steel in 1968 under the trade name HI-B. Kawasaki Steel introduced its RG-H grade in 1974 and Allegheny Ludlum its Silectperm grade in 1977. Armco Steel produces the TRAN-COR H version of Hi-B in the U.S.

The new high-induction grades differ from conventional grades in the use of grain-growth inhibitors (ch. 25, § 3.7 and 4.1), the processing procedure, and the type of glass coating used.

The conventional process for manufacturing regular grain-oriented material involves hot-rolling a cast ingot near 1370°C to a thickness of about 2 mm, annealing at 800–1000°C, and then cold-rolling to a final thickness of 0.27–0.35 mm in two steps, with a recrystallization anneal (800–1000°C) in-between. The final cold reduction is about 50%. The cold-rolled material is first decarburized to ~ 0.003% C at about 800°C in wet $H_2 + N_2$, a step which also results in primary recrystallization. It is then coated with MgO as separator and annealed in dry hydrogen at 1100–1200°C for about 24 h to form the COE texture via secondary recrystallization (ch. 25, § 4.3). During this anneal the impurities are further removed and inclusions of the grain-growth inhibitors are dissolved and absorbed in the glass film formed on the surface. Manganese sulfide has been the most common grain-growth inhibitor used.

References: p. 2560.

The HI-B process (TAGUCHI [1977]) differs from the conventional process in two major areas: (i) the use of AlN in addition to MnS as grain-growth inhibitor and (ii) a one-stage cold rolling with large thickness reduction (80–85%). Usually a large final cold reduction leads to a sharper COE texture in the finished strip, but it also enhances the undesirable grain growth of the primary grain structure. A strong inhibitor such as AlN thus restrains primary grain growth and permits the large reduction. For the AlN to be effective, however, the anneal after hot-rolling is done at 950–1200°C, higher than conventional, followed by rapid cooling. In addition, the glass film which contains the absorbed aluminium has a smaller coefficient of thermal expansion than the usual glass film, resulting in a larger tensile stress on the strip and a lowering of the core loss.

In addition to these major processing differences, the HI-B process takes into account the effects of silicon content, grain size, inclusion content, etc.

In the Kawasaki RG-H process (GOTO *et al.* [1975]), antimony was added along with MnSe or MnS as a grain-growth inhibitor. It is thought that Sb segregates to the primary recrystallized grain boundaries. The cold rolling is two-stage as in the conventional process, but the final stage is closer to a 60–70% reduction rather than 50%. Finally, the last anneal step is carried out first at 820–900°C for 5–50 h to promote a sharper orientation of the secondary grains, and then at about 1100°C for purification. A low-thermal-expansivity inorganic phosphate coating was also developed to impart a large tensile stress to the finished steel (SHIMANAKA *et al.* [1975]).

In the Allegheny Ludlum Silectperm process (MALAGARI [1977]), boron and nitrogen together with sulfur or selenium are used as grain-growth inhibitors. These are also thought to segregate to the primary recrystallized grains. In addition, since the Mn and S contents are quite low, the MnS solubility temperature is lowered, permitting the hot-rolling operation at 1250°C instead of above 1300°C. This is advantageous in terms of lower fuel costs, added mill life, etc. As in the HI-B process, cold rolling is done in one stage, the reduction exceeding 80%. The Silectperm process is a commercial realization of the laboratory technique developed at General Electric (FIEDLER [1977], GRENOBLE [1977]).

It may be pointed out that the core-loss advantage of the new high-induction material over the conventional oriented material is in the high-induction range only. Below an induction level of 1.5 T, the core-loss difference becomes minimal. In recent years, the sharp increase in energy costs has prompted electric utilities to incur a first-cost penalty for decreased core loss over the working life of transformers. As a result, transformer designers have reduced design induction to the 1.3 T range to minimize the loss penalty, even at the expense of a larger transformer. Consequently, the anticipated large-scale introduction of the high-induction material has been slowed, despite a price premium of only ~ 10%. There is a general tendency in industry to use a thinner-gauge conventional oriented material, at 0.22 mm rather than at 0.27 mm, for lower core loss at the lower design inductions (LITTMANN [1982]). (See also ch. 25, § 4.3.1, and ch. 28, § 4.1 and fig. 28.)

In the 1980s, amorphous metals — with energy losses only one-third or less of the losses of silicon steels — began to replace the steels in several applications, particularly as core materials in utility distribution transformers. This challenge led to increased

efforts in the steel companies and other laboratories to develop improved processing techniques to lower the losses of silicon steels. These approaches have included ceramic coatings to induce tensile stresses (INOKUTI *et al.* [1992]), thinner sections (ARAI *et al.* [1990]), increased purity (ISHIYAMA *et al.* [1991]), and various scribing techniques that produce transverse surface grooves and a resulting reduction in the width of magnetic domains (IUCHI *et al.* [1982], FUKUDA *et al.* [1984]). Although in some cases the beneficial effects of scribing are reduced or disappear on subsequent annealing, with some techniques the loss reduction produced by domain refinement persists after full stress-relief annealing (TAKAHASHI *et al.* [1986], ARAI *et al.* [1989]).

Silicon transformer steels have traditionally been limited to compositions of 3.5% Si or less, because significantly higher silicon contents tend to lead to ordering and loss of ductility. However, it has long been realized that increased silicon concentrations would be desirable because of increased resistivity (and resulting decrease in losses) and decreased magnetostriction. The challenge of amorphous metals stimulated the development of several processing techniques to produce Fe–6.5% Si with promising magnetic (and mechanical) properties. These have included rapid-solidification techniques (ARAI and OHMORI [1986], ALTOE *et al.* [1991]), chemical vapor deposition of silicon on conventional Fe–Si sheet followed by diffusion (TAKADA *et al.* [1988]), and improved rolling and recrystallization techniques (NINOMIYA *et al.* [1991], HONMA *et al.* [1991]).

The ultimate outcome of the competition between silicon steels and amorphous metals for transformer and other applications remains unclear, but one result seems certain — decreased energy losses.

4.3. Iron–aluminium and iron–aluminium–silicon alloys

The iron-rich portion of the Fe–Al phase diagram is similar to that of the Fe–Si diagram. Both Al and Si suppress the formation of the fcc γ-phase and both elements increase the electrical resistivity significantly. The Fe–Al alloys are more ductile than the Fe–Si alloys. Hence Al is added to silicon steel in the unoriented grades to improve ductility.

There has been no extensive commercial development of binary Fe–Al alloys. However, since the magnetocrystalline anisotropy constant K_1 goes to zero at 12–14% Al and the magnetostriction constant λ_{100} is near maximum in this range, alloys near these compositions have some interest as magnetostrictive transducers. In the 14–16% Al range, both K_1 and λ_{100} can be small and thus exhibit high permeability. These alloys have found limited use as recording-head material on account of the additional benefits of high hardness and electrical resistivity.

For recording-head applications, Fe–Al–Si alloys centered around the *Sendust* composition (5.4% Al, 9.6% Si) are more widely used than the binary Fe–Al alloys. Here the $K_1 = 0$ and $\lambda_s = 0$ curves intersect, leading to high values of permeability. The addition of 2–4% Ni, referred to as *Super Sendust* (YAMAMOTO and UTSUSHIKAWA [1976]), reportedly increases the permeability and lowers the coercivity even further.

Because Sendust is brittle, much effort has been expended to shape the alloy for recording-head use. In addition to normal powder-metallurgy techniques, developments

References: p. 2560.

have included "squeeze casting" whereby molten Sendust is forced into a die of predetermined shape (SENNO *et al.* [1977]), sputtered films (SHIBAYA and FUKUDA [1977]), and rapid quenching from the melt (TSUYA and ARAI [1978]). The last technique, patterned after that for producing amorphous metal ribbons from the melt, is interesting in that it provides a ribbon with sufficient ductility to punch out cores for recording-head applications. The enhanced ductility presumably comes from the extremely small grain size (~ 10 μm) of the as-quenched material.

4.4. Nickel–iron alloys

The nickel–iron alloys in the *Permalloy* range, from about 35 to 90% nickel, are probably the most versatile soft magnetic alloys in use today. With suitable alloying additions and proper processing, the magnetic properties can be controlled within wide limits. Some exhibit high initial permeability up to $100\,000\mu_0$ useful for high-quality electronic transformers. Others display a square hysteresis loop ideal for inverters, converters and other saturable reactors. Still others combine low remanence with high constant permeability, ideal for unbiased unipolar pulse transformers. And since these alloys are extremely ductile, material can be precision cold-rolled to thin tapes useful for some magnetic-core components.

4.4.1. Phase diagram and intrinsic magnetic properties

In the nickel–iron system, the fcc γ-phase exists in the 30–100% Ni range at room temperature. At the low-nickel end, the alloy is bcc α, with the α–γ transformation exhibiting considerable hysteresis. Near the Ni_3Fe composition the alloys undergo a long-range-ordered $L1_2$ transformation below about 500°C. This transformation has a significant influence on the intrinsic magnetic parameters and is exploited in the processing of commercial alloys.

Figure 15 shows the major magnetic parameters in the Ni–Fe system: saturation induction B_s, Curie temperature T_c, magnetocrystalline anisotropy constant K_1, and saturation magnetostriction λ_s. Values of B_s, K_1 and λ_s are for room temperature. Highest B_s occurs near 48% Ni and highest T_c is at 68% Ni. The solid K_1 curve is for material quenched from above 600°C to retain a disordered structure. The large dip near 75% Ni in the dashed K_1 curve, for slowly cooled material, is a result of the $L1_2$ ordering.

Magnetic theory indicates that high initial permeability is achieved by minimizing both K_1 and λ_s. Thus a major aim in the development of high-permeability Ni–Fe alloys is to search for compositions and processing conditions whereby K_1 and λ_s are minimized. In the Ni–Fe binary, this occurs at 78.5% Ni in the rapidly-cooled condition, as indicated in fig. 15. With the addition of molybdenum, the kinetics of ordering is slowed and simultaneous attainment of zero K_1 and λ_s is possible with moderate cooling rates for alloys near 4% Mo–79% Ni–17% Fe. The addition of molybdenum confers the additional benefit of increased resistivity, desirable for high frequency usage, but it lowers B_s and T_c. Copper has also been found useful as an addition to minimize K_1 and λ_s. Commercial alloys near the 4% Mo–5% Cu–77% Ni–bal Fe range have been so developed.

In addition to magnetocrystalline anisotropy and magnetostriction, two other sources

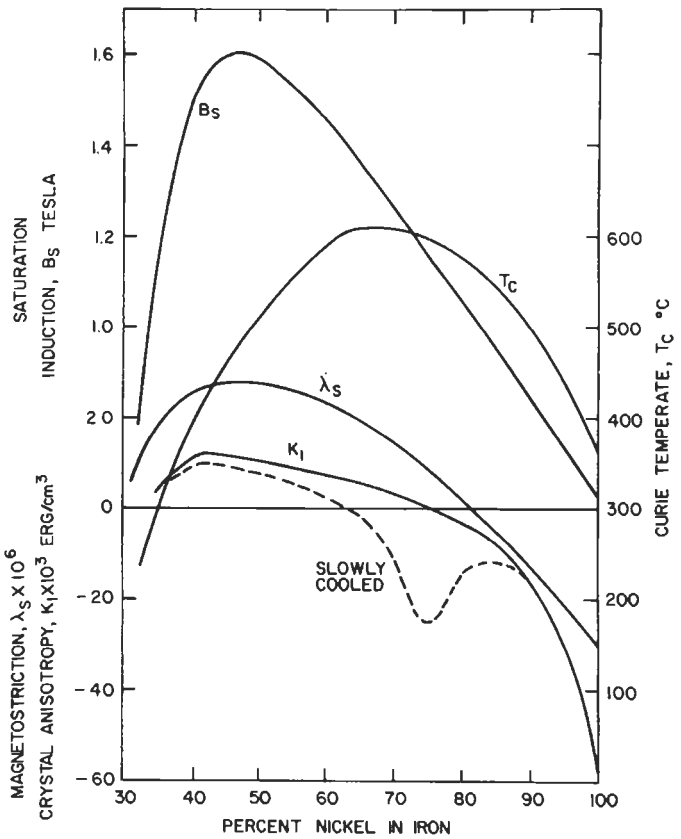

Fig. 15. Magnetic parameters of Ni–Fe alloys.

of magnetic anisotropy are important for Ni–Fe alloys. One is *thermomagnetic anisotropy*, developed by annealing below T_c (GRAHAM [1959], CHIKAZUMI and GRAHAM [1969]). Thermomagnetic anisotropy is most pronounced near 68% Ni where T_c is highest, and is utilized commercially to develop square or skewed hysteresis-loop shaped materials by applying a magnetic field during annealing. If the field is absent, the hysteresis loop becomes constricted. The other is *slip-induced anisotropy*, obtained by cold-working, particularly when the material is atomically ordered prior to deformation (CHIKAZUMI and GRAHAM [1969]; CHIN [1971]).

Both thermomagnetic and slip-induced anisotropies have their origin in the short-range directional ordering of nearest-neighbor atom pairs (NÉEL [1954]). Since the pseudo-dipolar magnetic coupling energy of a pair of atoms depends on the identity of the atoms, e.g., Fe–Fe, Fe–Ni, annealing below T_c in the presence of a magnetic field tends to align in the field direction those pairs with minimum coupling energy. Fast cooling to a low temperature then freezes-in the directional order structure and gives rise

to a uniaxial magnetic anisotropy. Similarly, when material with an atomically ordered structure is deformed, the slip process creates planar anti-phase domain boundaries and establishes a directional-order structure with unequal distribution of atom pairs. For Ni–Fe alloys, the thermomagnetic anisotropy energy is ~ 0.1 kJ/m^3 and the slip-induced anisotropy energy is ~ 10 kJ/m^3, both overlapping the values of K_1 and λ_s.

Thus all four types of anisotropy can be, and have been, manipulated in custom-engineering the magnetic properties of Ni–Fe alloys.

4.4.2. Metallurgy of nickel-iron alloys

Commercial Ni–Fe magnetic alloys are predominantly used for high-permeability and square-loop applications, but some have also been developed for use with skewed-loop characteristics and some for wear-resistant recording-head applications.

4.4.2.1. High-permeability alloys. There are two broad classes of high-permeability Ni–Fe alloys. The low-Ni alloys, near 50% Ni, are characterized by moderate permeability ($\mu_{40} \approx 10\,000\mu_0$, measured at 40 G/60 Hz) and high saturation ($B_s \approx 1.5$ T). This region corresponds to high B_s, low K_1 and λ_{100}. The high-Ni alloys, near 79% Ni and usually combined with Mo and/or Cu, are characterized by high permeability ($\mu_{40} \approx 50\,000$) but lower saturation ($B_s \approx 0.8$ T). This region corresponds to near-zero values of K_1 and λ_s.

Commercial 50% Ni alloys generally range from 45–50% Ni and are of two grades: rotor grade, of $\mu_{40} \approx 6000\mu_0$, useful for rotors and stators where non-direction properties are desired, and transformer grade, of $\mu_{40} \approx 10\,000\mu_0$, where high permeability is achieved both parallel and perpendicular to the rolling direction. To achieve the essentially random texture of the rotor-grade material, the final cold reduction is held low (50–60%). Annealing is done in dry H_2 at 1200°C, followed by furnace cooling (~ 150°C/h). The transformer grade, on the other hand, is produced by severe cold reduction (~ 95%) followed by high-temperature annealing to produce a secondary recrystallization texture of $\{210\}\langle 001\rangle$ type.

A large increase in permeability can be achieved by annealing the alloys, particularly in the 56–58% range, in the presence of a magnetic field after the usual high-temperature anneal. This is the result of the establishment of a thermomagnetic anisotropy by the magnetic annealing.

In the 79% Ni regime, modern alloys contain Mo and Cu as stated earlier. There is a standard grade with $\mu_{40} \approx 30\,000$–$40\,000$, and a very-high-permeability grade with $\mu_{40} \approx 60\,000$. The latter is based on the development of high-purity *Supermalloy* (BOOTHBY and BOZORTH [1947]) with $\mu_{40} > 100\,000$. Today's Supermalloy composition is close to 5% Mo–80% Ni–15% Fe. The attainment of superior permeability requires a simultaneous achievement of zero K_1 and λ_s, which parameters are highly sensitive to composition and heat-treatment conditions. One example is shown in fig. 16 illustrating the effects of annealing temperature and nickel content for alloys containing 4% Mo and 5% Cu (SCHOLEFIELD *et al.* [1967]). It can be understood that as the nickel content is increased, for a given Mo and Cu composition, less atomic ordering is required to achieve $K_1 = 0$ (ENGLISH and CHIN [1967]); hence a higher annealing temperature (i.e., less order) is needed for optimum initial permeability. Figure 16 also shows that the absolute value of μ_i goes down at both the high- and the low-Ni end as a result of

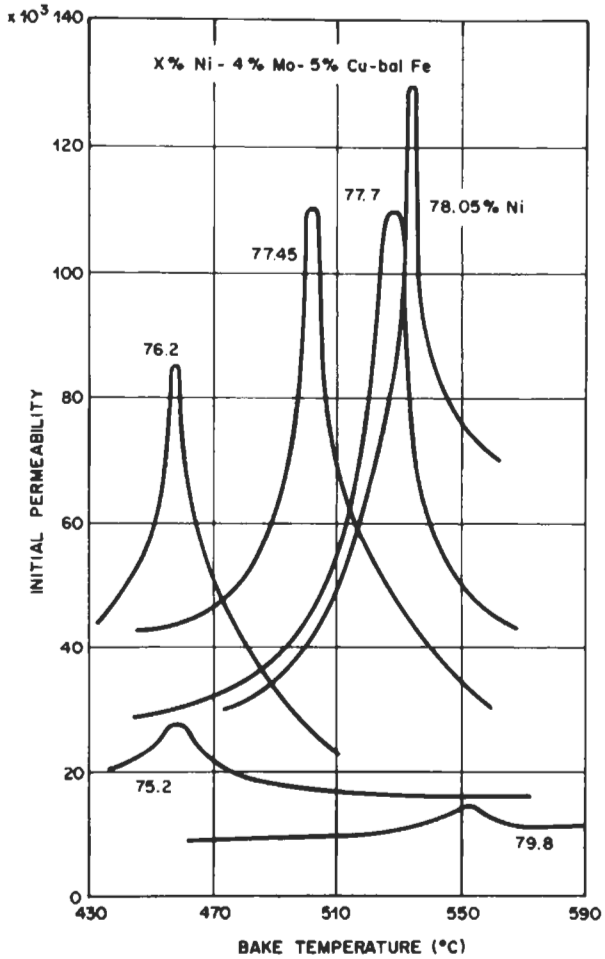

Fig. 16. Influence of annealing ("bake") temperature on initial permeability for alloys of Mumetal type (from SCHOLEFIELD *et al.* [1967]).

deviation from the $\lambda_s = 0$ composition. For a more extended discussion of these complex effects, the reader is referred to the article by CHIN and WERNICK [1980].

In addition to composition selection and heat-treatment control, melting practice and microstructure control are of paramount importance. Today all high-quality Ni–Fe alloys are prepared by vacuum-melting, which minimizes harmful ingredients such as oxygen and sulfur. Figure 17 shows the effect of these two elements on the initial permeability of the two classes of Ni–Fe alloys (COLLING and ASPEN [1969, 1970] and AMES [1970]). In this connection, deoxidation by the use of strong deoxidizers such as Ca, Si and Al has not met with success, primarily because the fine oxide particles left in the matrix restrict grain growth and block domain-wall motion. Figure 18 shows, for example, the

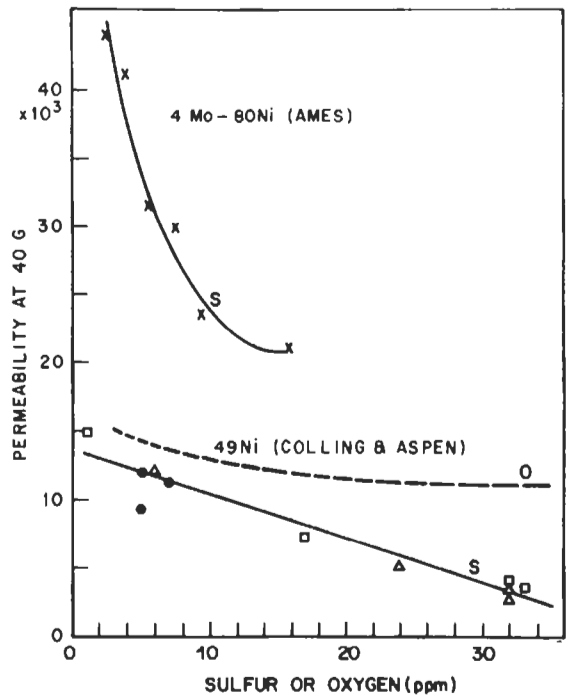

Fig. 17. Influence of sulfur and oxygen on initial permeability (after COLLING and ASPEN [1969, 1970] and AMES [1970]).

initial permeability μ_5, i.e., at $H = 5$ mOe (4 mA/cm), as a function of grain diameter for a 50% Ni alloy with and without Al additions (HOFFMANN [1971]). The lower value of μ_5 for Al-added samples is attributed to the presence of oxide precipitates. A quantitative study by ADLER and PFEIFFER [1974] led to the following expression for the coercivity of 47.5% Ni alloys:

$$H_c = H_{c0} + H_{ci} + H_{cK} = 0.8 + 2.8 \times 10^{-4} N_F + 0.29/d_K (A/m),$$

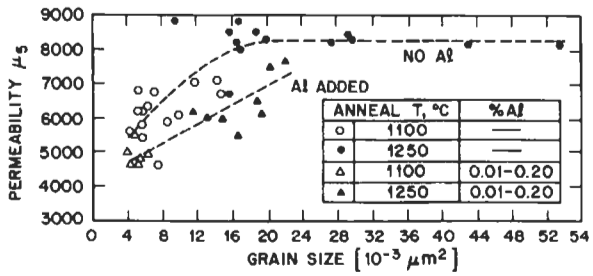

Fig. 18. Dependence of initial permeability on grain size for a commercial 50% Ni alloy with and without Al added as deoxidizer (from HOFFMANN [1971]).

where H_{c0} is the residual coercivity of the pure alloy, H_{ci} is due to inclusions with N_F as the number of particles per mm^2 in the 0.02–0.5 μm range, and H_{cK} represents the grain size effect with d_K as the grain diameter in mm.

A similar study was done on a Mo–Cu–Ni–Fe alloy (KUNZ and PFEIFER [1976]). For a more detailed discussion, see PFEIFER and RADELOFF [1980] and CHIN and WERNICK [1980].

4.4.2.2. Square-loop alloys. A square hysteresis loop is obtained in a material by aligning a nonzero magnetic anisotropy with the easy axis in the direction of magnetization. In 50% Ni alloys, this is primarily achieved through the development of a cube-on-face, {100}⟨001⟩, texture, since $K_1 > 0$ and ⟨001⟩ is the easy direction. The texture is obtained by extensive prior rolling (>95%) followed by primary recrystallization in the vicinity of 1100–1200°C. Among factors favoring texture formation are small penultimate grain size, large cold reduction, and a lowering of impurity elements such as Si and C. For 79% Ni alloys, the situation is more complicated. For weakly textured material normally encountered in commercial processing, a heat treatment to achieve $K_1 < 0$ has been found to provide "quasi-squareness" of the hysteresis loop (PFEIFER [1966a]). This is done by lowering the isothermal annealing temperature or decreasing the cooling rate, as compared to the heat treatment for high μ_i where $K_1 = 0$ is desired. The results are illustrated in fig. 19 for a series of Mo-bearing alloys in which Ni is held at 80%.

The other major technique for achieving a square hysteresis loop is to establish a thermomagnetic anisotropy by magnetic annealing. Here alloys in the 55–65% Ni range are particularly susceptible to magnetic annealing effects as a result of high T_c in this region. The nature of the response, however, is highly dependent on the texture and on annealing conditions under which both magnetocrystalline and thermomagnetic anisotropies compete with each other. For example, to produce maximum squareness in unoriented material, it is important that the magnetic annealing be done such that $K_u \gg K_1$, i.e., aligning the thermomagnetic anisotropy at the expense of crystal anisotropy. Such combination is obtained at a relatively low annealing temperature (~ 430°C) (PFEIFER [1966b]).

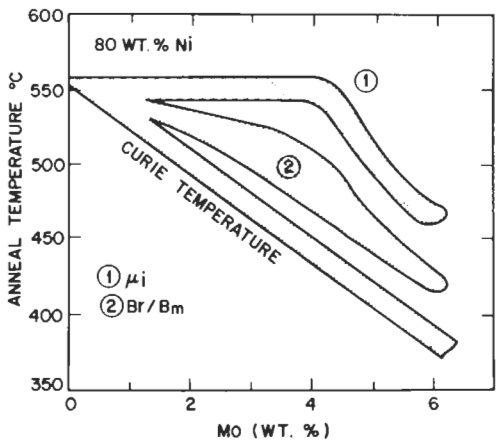

Fig. 19. Optimum annealing temperatures for high μ_i and B_r/B_m in Mo-Permalloys (PFEIFER [1966a]).

References: p. 2560.

4.4.2.3. Skewed-loop alloys. While the alignment of a uniaxial anisotropy, such as by magnetic annealing, results in a square hysteresis loop in the direction of alignment, it also results in a skewed loop in the perpendicular direction. The result is a low-remanence, constant-permeability characteristic highly desirable in loading coil and unipolar pulse transformer applications. Commercial alloys of 2.5% Mo–65% Ni–bal Fe and 4% Mo–79% Ni–bal Fe compositions have been developed with such characteristics. Again there is a complex relationship among texture, K_1 and K_u, which is reasonably well understood.

4.4.2.4. Wear-resistant alloys. For applications such as recording heads, there is a need for high mechanical hardness to reduce wear without sacrifice of magnetic softness. Standard Permalloys have poor wear resistance. It has been found, however, that alloys near 79% Ni with Nb and Ti additions (MIYAZAKI *et al.* [1972]) can greatly enhance the hardness while retaining the high permeability. Figure 20 shows how the mechanical and magnetic parameters change as a function of aging time at 630°C, for a 3% Ti–2.8% Nb–3.8% Mo–10.5% Fe–bal Ni alloy. It may be noted that after aging for 4 h, the permeability goes through a maximum and the coercivity a minimum, but the Vickers hardness is still increasing. This observation is explainable in terms of precipitation where the optimum particle size for blocking dislocation motion differs from that for domain-wall motion.

4.4.2.5. Invar alloys. The thermal expansion coefficient (TEC) of Fe–Ni alloys near room temperature goes through a pronounced minimum near 36% Ni (see ch. 17). In such alloys, the normal thermal expansion resulting from lattice vibrations is compensated by a decrease in volume resulting from loss of ferromagnetism (and "volume magnetostriction") as the Curie temperature is approached. Although the room-temperature TEC of Fe, Ni, and most common metals is over 10^{-5} per °C, it is about 10^{-6} for Fe–36% Ni, the original "Invar", and less than 10^{-7} for an Fe–32% Ni–4% Co alloy called "Super-Invar". The relative invariance of length and volume with temperature of such alloys has many applications in precision instruments, electronic devices, and even large components such as power cables.

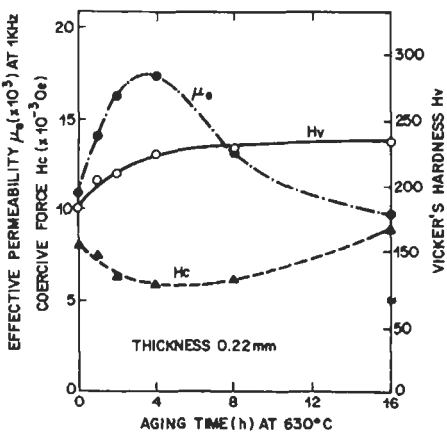

Fig. 20. Magnetic and mechanical properties of a 3% Ti–2.8% Nb–3.8% Mo–10.5% Fe–bal Ni alloy as function of aging time at 630°C (MIYAZAKI *et al.* [1972]).

The Fe–36% Ni composition is in the fcc region of the phase diagram, near the bcc–fcc transition. The TEC can be further decreased by rapid cooling and plastic deformation, which produce nearly perfect disorder. Invar-type alloys also exhibit anomalous temperature dependence of their elastic constants, associated with the loss of ferromagnetism. The alloy Fe–36% Ni–12% Cr, called "Elinvar", has zero temperature coefficient of elastic moduli, and has many applications, including those where a temperature-independent sound velocity is desired. Other variations are precipitation-hardened Invars like Fe–Ni–Co–Ti and "Stainless Invars" like Fe–Co–Cr. Because the classic Invar alloys are ferromagnetic at room temperature, their dimensions are sensitive to a magnetic field. For applications where this is a problem, antiferromagnetic Cr-based Invar alloys have been intensively studied. Invar alloys based on Fe–Pt and Fe–Pd have been developed, and many other alloys — including some intermetallic compounds and amorphous alloys — show a small or even negative TEC in a temperature range below their Curie temperature. A comprehensive review of Invar alloys has recently appeared (SHIGA [1993]).

4.5. Iron–cobalt alloys

Iron–cobalt alloys have the highest value of saturation induction at room temperature, at 2.45 T for the 35% Co alloy. Somewhat lower values of saturation induction but substantially higher permeability are obtained in equiatomic alloys because of their low magnetocrystalline anisotropy. Commercial magnetic alloys are known as *Hiperco*, *Permendur* and *Supermendur*. Because they are relatively costly, these alloys are limited to specialized applications such as aircraft generators where weight and size are important considerations.

The Fe–Co alloys have an fcc structure above 912–986°C to ~ 70% Co. The low-temperature form is bcc. At ~ 50% Co, ordering to the B2 structure sets in below about 730°C and the alloy becomes brittle. Vanadium additions retard the ordering reaction and improve the ductility. An additional benefit is an increase in resistivity.

The magnetocrystalline anisotropy constant K_1 decreases with Co addition to a value near zero at 50% Co, but is sensitive to the degree of order. The magnetostriction constants λ_{100} and λ_{111} increase with Co content, λ_{111} reaching a high value of $\sim 150 \times 10^{-6}$ at 50% Co.

4.5.1. Metallurgy of equiatomic Fe–Co alloys

Since 2V-Permendur and Supermendur, both containing 2% V–49% Fe–49% Co, are the most important Co–Fe soft magnetic alloys, their metallurgy may be discussed in more detail. Preparation of thin sheets of 2V-Permendur involves hot-working in the fcc state, followed by quenching to room temperature for further cold reduction. Optimum magnetic properties are developed by annealing at ~ 850°C, below the fcc–bcc transformation temperature but above the B2 ordering temperature. However, for aerospace high-speed rotor applications, there is a need to develop a high-strength ductile alloy at the sacrifice of maximum magnetic properties. THORNBURG [1969] showed that annealing cold-rolled sheet at 695°C yielded material of high strength and reasonable

References: p. 2560.

ductility and magnetics. The microstructure of this material indicated only partial recrystallization. A similar study by THOMAS [1975] resulted in annealing at 650°C for rotor material and 875°C for stator material, where the high-strength requirement is of less importance.

By adding 4.5% Ni to the 49/49/2 Fe–Co–V alloy, MAJOR *et al.* [1975] were able to enhance the ductility and strength over a wider heat-treating temperature range, thus eliminating the need for relatively close temperature control of the regular alloy. X-ray examination showed that after heat-treatment in the 650–740°C range, some γ-phase and ordered α-phase are present. It is suggested that the enhanced properties stem from the restriction of grain growth owing to the presence of these phases.

Supermendur (GOULD and WENNY [1957]) is essentially of the 2V-Permendur composition, except that the starting ingredients are of higher purity. In addition, the heat-treatment to develop the soft magnetic properties is carried out in a magnetic field of 80 A/m or greater. The result is an extremely square hysteresis loop with a small coercivity, ideal for saturable reactor type applications.

4.6. Nanocrystalline alloys

Most crystalline soft magnetic materials attain their best properties with large grain sizes, typically of the order of millimeters. At the other extreme, as discussed in the next section, excellent soft magnetic properties can also be achieved with amorphous alloys. An interesting recent development is the introduction of "nanocrystalline" soft magnetic materials — alloys with grain sizes of the order of 10 nanometers.

By partially crystallizing melt-spun Fe–B–Si–Cu–Nb alloys, YOSHIZAWA *et al.* [1988] produced Fe–Si-rich grains 10–20 nm in diameter separated by a magnetic amorphous phase. These unusual microstructures have yielded relative permeabilities over 100 000, superior to Fe-based amorphous alloys and with higher magnetizations than Co-based amorphous alloys. In contrast to fine-grained permanent-magnet alloys, which require decoupled grains to achieve high coercivities, these alloys require strong exchange contact between grains to achieve good soft magnetic properties. Evidence for this is a rapid increase in coercivity, and decrease in permeability, at temperatures above the Curie temperature of the amorphous phase separating the grains (YOSHIZAWA and YAMAUCHI [1991], HERZER [1989]). Nanocrystalline alloys of other compositions have also shown good soft magnetic properties (SUZUKI *et al.* [1991]).

The excellent soft magnetic properties of Fe–B–Si–Cu–Nb and similar nanocrystalline alloys are usually explained by the reduction in effective crystal anisotropy expected when grain sizes are reduced below the bulk domain-wall thickness δ (TAKAHASHI and SHIMATSU [1990], DE WIT [1989], HERZER [1990]). Experiments suggest that the variation of coercivity with grain diameter D is roughly as D^{-1} for large grains and D^6 for very fine grains, with maximum coercivities when D is of the order of δ (HERZER [1989]). For good soft magnetic properties, the grain size D should either be very large ($\sim$ 1 mm) or very small ($D \sim$ 10 nm) or the alloy should be amorphous ($D <$ 1 nm).

4.7. Materials for recording heads

Alloys for inductive recording heads have traditionally been crystalline materials with good soft magnetic properties (high magnetization, permeability, and resistivity, low coercivity, magnetostriction, and energy losses) and good resistance to mechanical wear and corrosion. Permalloy (Ni–Fe) and Sendust (Fe–Al–Si) have been widely used in addition to cubic (magnetically soft) ferrites. In recent years, however, amorphous metals have been increasingly used, especially Co-base alloys with low magnetostriction. Future materials for inductive heads may be multilayer thin films in which properties can be engineered independently during fabrication (JAGIELINSKI [1989], [1990]).

There has also been growing interest in "read" heads based on magnetoresistance, the change in electrical resistance produced by a magnetic field. Although Ni–Fe permalloys are widely used in magnetoresistive heads, multilayer films are of growing interest. Great excitement was generated when BAIBICH *et al.* [1988] reported changes in resistance of as much as 50% when magnetic fields were applied to Fe/Cr multilayer films. This "giant magnetoresistance" effect has since been reported in Co/Cu multilayers (PARKIN *et al.* [1991]) and a number of other systems, including granular (non-layered) two-phase systems (XIAO *et al.* [1991]), BERKOWITZ *et al.* [1992], WECKER *et al.* [1993]). The basic physics underlying the effect has been reviewed by WHITE [1992].

5. *Amorphous magnetic materials*

5.1. Introduction

The amorphous magnetic alloys most investigated, and of most interest from the applications viewpoint, are of the type $(Fe, Ni, Co)_{80}$ $(metalloid)_{20}$. The metalloids may be B, Si, C, P or Ge. In the past 20 years research and development on amorphous metals and alloys has increased drastically (ch. 28, § 3). The reasons for this increase are twofold. Firstly, they are a new state of matter, with no long-range order, with many opportunities for scientific investigations. Secondly, many of the properties are of interest in potential applications. For example, the magnetic losses and exciting power are extremely low in alloys with high magnetization, making them of interest in both large and small transformer application. Their hardness, high permeability and zero magnetostriction make them useful for recording heads. The ductility of certain intermetallic alloys makes them extremely useful for brazing alloys. They have excellent corrosion resistance, making them potentially useful for coatings. Their high permeability and toughness make them useful for magnetic shielding applications. Their exceptional magnetomechanical coupling factor and their change in Young's modulus with applied magnetic field make them exceptional electronically controlled delay lines. Finally, the high stress-sensitivity of some of the alloys makes them useful as stress transducers. In addition, there are many other potential applications reported in the literature.

In this section we will describe the preparation and properties of amorphous magnetic materials.

References: p. 2560.

5.2. Preparation

All methods for producing a non-crystalline, i.e., an amorphous or glassy solid, depend on achieving high enough quenching rates so as to prevent crystallization. The quench rate required depends critically on the alloy and alloy composition and its properties, e.g., its melting point and glass temperature. The maximum thickness of ribbon, or splat, which can be cast then is determined by the heat-withdrawal rates achievable through the alloy and across the interface between the alloy surface and quenching surface.

There are a variety of methods available for producing the very rapid quenching necessary to prevent crystallization of a suitable alloy. For example, methods which have been used include sputtering and evaporation methods, chemical and electrodeposition (for a bibliography of glasses prepared by these four methods see DIETZ [1977]), ion implantation (BORDERS [1979]), and various splat-quenching techniques which involve the rapid spreading of a liquid droplet on a surface, or pair of surfaces, by propelling the droplet onto the surface or by propelling the surfaces together with the droplet in between. There are also a variety of methods for the preparation of amorphous metal powders, e.g., gas atomization, centrifugal atomization, or spark erosion. These powders may then be compacted by pressing or extrusion to near-final shapes to obtain bulk amorphous parts (ch. 28, § 4).

Most interest in commercial preparations of amorphous alloys has been concerned with the preparation of continuous tapes or ribbons. Narrow ribbons are prepared by rapidly expelling the molten alloy from a circular orifice onto the surface of a spinning wheel. This is normally called *chill-block melt-spinning* (LIEBERMANN [1980]) (ch. 19, § 3.1). A puddle builds up on the spinning wheel and serves as a reservoir from which ribbon is formed by the solidification of the melt next to the surface of the wheel. The ribbon typically adheres to the wheel for some time before being released, or thrown off, as a continuous filament. A puddle which remains stable in size results in a ribbon with smooth edges and uniform width. Normally casting is done onto the outside rim of a wheel, but casting onto the inside of a wheel, between two rollers or onto belts have also been done in an attempt to improve the ribbon in various respects. For example, casting between two rollers results in ribbon with both surfaces much smoother than casting on a single wheel. This is of particular importance in recording-head applications where it is necessary to achieve the highest permeability and highest packing fraction. However it is a much more difficult process to control and thus is not used by many. Casting onto the inside of a rim results in longer contact with the wheel and therefore a quench to a lower temperature. This results in a ribbon structure with a larger atomic free volume which in term results in more rapid stress-relief, for example. Other methods have also been used to increase the quench rate, for example, by using a gas stream impinging on the ribbon to hold the ribbon down, or by using a secondary roller to hold the ribbon down on the wheel.

The above methods are only suitable for preparing narrow ribbons, i.e., ribbon less than about 2 mm in width. To make wider ribbon an elongated orifice must be used. In order to reduce or eliminate the perturbations caused by the impingement of the air on

the molten metal stream, the casting from wide nozzles must be done at a reduced atmospheric pressure or with the nozzle very close to the wheel. This latter configuration is called *planar flow-casting* and is characterized by the molten metal filling the space between the crucible and wheel. This is the method now used to prepare all wide ribbons (LIEBERMANN [1979]).

Some novel variations of planar flow-casting have been described for particular applications. For example, preparations of wide tapes with teeth or other geometries have been made without the need to punch the teeth out with a die. The teeth were formed by casting onto a wheel with a low-thermal-conductivity pattern. These low-conductivity regions result in slower cooling of the ribbon, causing the ribbon to be brittle and easily separated from the very tough non-brittle remainder of the ribbon.

Another novel variation is the preparation of helical rather than straight ribbons (LIEBERMANN [1981]). The helical ribbon can be wound without producing the degradation in properties associated with the bending stresses produced on winding up straight ribbon into a core. By combining this helical-ribbon technique with the previously described technique for producing a cut-out pattern, electric motor stators or rotors can be prepared directly from the cast ribbon without need for punching.

Another variation of planar flow-casting is the formation of composite layers of ribbons by casting successive layers on top of amorphous ribbons. The problem is to balance the heat transfer against the crystallization of the amorphous alloy being cast on. In this way thick sections of ribbons and combinations of amorphous/crystalline and crystalline/crystalline ribbons have been prepared.

Modeling of the chill-block melt-spinning process has been done both empirically and theoretically (LIEBERMANN [1980], KAVESH [1978], PAVUNA [1982], and VINCENT *et al.* [1982]). Empirical relations have been established, with little scatter, for the ribbon geometry as a function of melt ejection pressure, temperature, flow rate, wheel velocity, atmosphere etc. The theoretical models are all based on the propagation of a solidification boundary which determines the ribbon thickness. Several approaches have evolved, depending whether thermal or momentum boundary layers are the controlling factors. In the thermal boundary-layer propagation, while temperature varies continuously through the melt, there is an abrupt velocity change in the solidification front. This abrupt velocity change is taken as the glass-transition isotherm. A momentum-transfer mode has more recently been proposed to be the dominant process and a combined thermal-momentum transfer process has been worked out. All of these approaches are successful to some extent in describing the experimental results. However, the complex nature of the ribbon-formation process and the factors which control it are still to be described by a physically consistent model.

The modeling of the planar flow-casting process proceeds along the same lines as for chill-block melt-spinning. Empirical relations have also been established using the same parameters as for chill-block melt-spinning. It should be noted that perturbation of the melt on the wheel by the gas boundary-layer and by surface roughness of the wheel, etc., are substantially reduced because of the constraint of the melt imposed by the crucible. The specific effect of the gas on melt-puddle stability and interfacial contact has been studied in detail. The mathematical modeling has been described by characterizing the

References: p. 2560.

fluid dynamics as a laminar-flow process. This can be approximated by lubrication theory. It has been calculated that a momentum, rather than a thermal, boundary layer controls ribbon dimensions.

5.3. Properties

The magnetic properties reflect the short-range order existing in the amorphous alloy. The short-range order, in general, reflects the structure existing at the same composition in the crystalline alloys. The same rules that govern the behavior of the crystalline alloys, appropriately averaged for randomness, also govern the behavior of amorphous alloys. The various magnetic properties will next be discussed in the above terms.

5.3.1. Curie temperature

The simplest system of amorphous alloys is probably the binary iron, cobalt or nickel, FeX, CoX, and NiX alloys, where X is a single metalloid or a combination of metalloid atoms such as B, P, Si, Ge and C. The Curie temperature of these alloys varies with X in a systematic manner as shown in fig. 21a (LUBORSKY *et al.* [1980b], GRAHAM and EGAMI [1978]). It should be noted here, however, that T_c decreases with increase in Fe content, as shown in fig. 21b, suggesting that the structure is behaving like close-packed, rather than bcc iron.

When two transition metal, TM, atoms are present in the amorphous alloy, the change in T_c with variation in the TM ratio can be modeled phenomenologically. On the basis of the coherent potential approximation it can be shown (LUBORSKY [1980a]) that:

$$\alpha^2 T_c^2 + \left\{\alpha(T_{AA} + T_{AB}) - \alpha(1+\alpha)\left[\chi^2 T_{AA} + 2\chi(1-\chi)_{AB}\right]\right\}T_c + \left[(1-\alpha)(1-\chi)^2 - \alpha\right]T_{AA}T_{AB} = 0, \tag{3}$$

where χ is the atom fraction defined by the alloy $A_{x-1}B_x$, T_{AA}, T_{AB}, and T_{BB} are so-called interaction temperatures, $\alpha = (z/2) - 1$, z is the number of nearest neighbors and T_c is the Curie temperature. An *interaction temperature* is an effective temperature for the strength of the interaction of an atom pair. These temperatures involve the exchange coefficients and the atomic moments. Using this relation, the curves in fig. 22 were calculated, giving excellent agreement with the data using only one adjustable parameter, T_{AB}, to fit the data.

5.3.2. Saturation magnetization

5.3.2.1. Dependence of magnetization on alloy composition. The saturation magnetization of Fe_xB_{100-x} varies almost linearly with x at low temperatures, as shown in fig. 23 (LUBORSKY *et al.* [1978]), but at room temperature and above σ_s reaches a peak and then drops with increasing x. This decrease is due simply to the approach of T_c as x increases since T_c is decreasing sharply.

On the replacement of B by another metalloid the magnetization typically decreases as shown by the results in fig. 24 (LUBORSKY [unpublished]) for ternary Fe–B–Si alloys. KAZAMA *et al.* [1978] examined the effect of various metalloids, M, in $Fe_{80}B_{20-x}M_x$ on σ_s

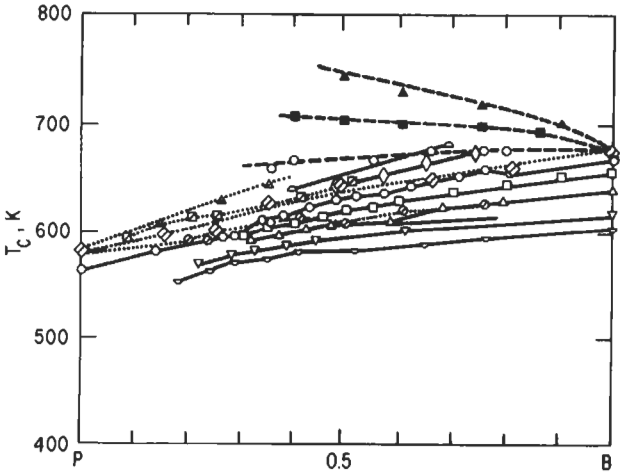

Fig. 21a. Open symbols are for Curie temperatures as a function of P/B fraction for $Fe_x(PB)_{1-x}$ amorphous alloys: ⌓, $Fe_{75}(PB)_{25}$; ◇, $Fe_{77}(PB)_{23}$; ○, $Fe_{79}(PB)_{21}$; □, $Fe_{80}(PB)_{20}$; △, $Fe_{81}(PB)_{19}$; ▽, $Fe_{82}(PB)_{18}$; ⌔, $Fe_{83}(PB)_{17}$ (after GRAHAM and EGAMI [1978]). Solid symbols are for addition of M to $Fe_{80}B_{20-x}M_xN_x$: ▲, Ge; ■, Si; ●, C. Slashed symbol are for additions of N to $Fe_{80}P_{20-x}N_x$: ⧋, Ge; ◈, Si; ⊘, C; ◈, B.

and found that the magnetization in Bohr magnetons per metallic atom, μ_B, varied with P < C < Si < Ge. However, LUBORSKY *et al.* [1978] found P < Si < Ge < C. The reasons for the differences are not known; however, the differences between Si, Ge, and C are quite small.

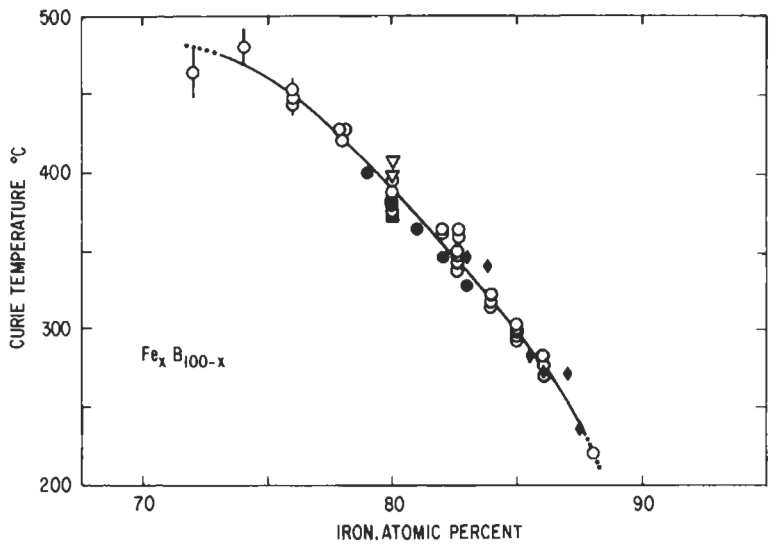

Fig. 21b. Curie temperatures for Fe_xB_{100-x} amorphous alloys (from LUBORSKY *et al.* [1978]).

References: p. 2560.

It would be expected on the basis of charge transfer that P < Si = Ge = C since the effective valency of the metalloid, defined as the number of outer electrons, is 1 for B, 2 for C, Si, and Ge and 3 for P. This is approximately true since the differences between Si, Ge, and C are small.

The effect of changing transition-metal content is shown in fig. 25 (LUBORSKY

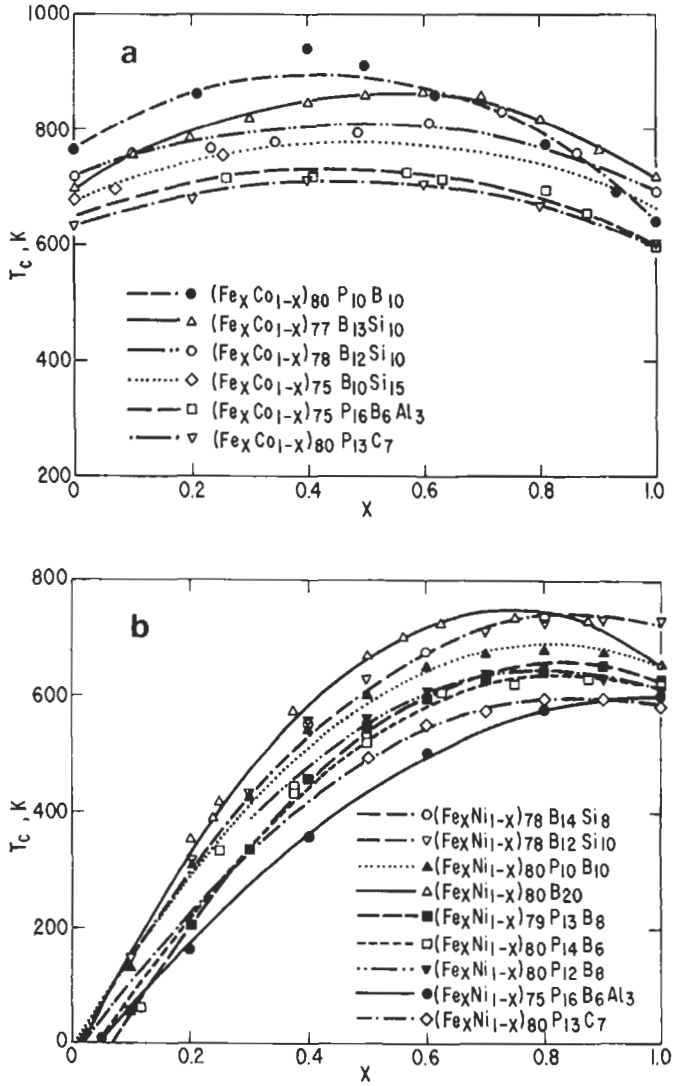

Fig. 22. Composition dependence of the Curie temperature of amorphous alloys. Curves calculated using an equation based on a phenomenological model using the coherent potential approximation: (a) Fe–Co based alloys; (b) Fe–Ni based alloys; (c, on facing page) other alloys.

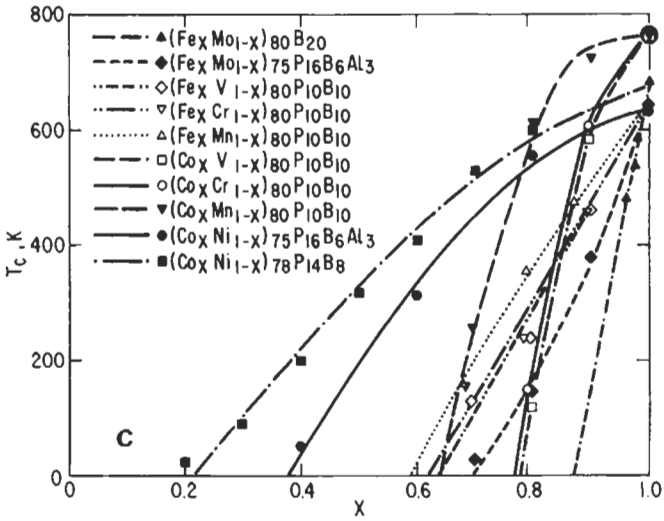

[1980b]) for a variety of metalloid combinations. To a first approximation the μ_B are independent of the metalloids used varying from μ_B for Fe to μ_B for Co or Ni. However, on close examination it is found that alloys containing only boron have slightly higher moments than those containing phosphorus, as would be expected on the basis of the charge transfer model.

5.3.2.2. Temperature-dependence of magnetization and spin waves. The magnetization–temperature curve has been measured for a variety of amorphous alloys. In all cases the decrease in σ is always more rapid than in crystalline metals. This might be predicted from the distribution of exchange interactions resulting from the distribution in atomic spacings. The mean-field model is generally used with a parameter that is a measure of the rms deviation of the nearest-neighbor exchange from its mean value. Values from 0.1 to 0.5 are generally obtained.

The decrease in σ with increasing temperatures can be fitted to the *Bloch law*, $\sigma/\sigma_0 = 1 - \beta(T/T_c)^{3/2}$. For amorphous alloys this law holds up to temperatures as high as $0.5T_c$, much higher than for crystalline alloys. Furthermore, the higher-order terms, e.g., $T^{5/2}$, are much smaller than in crystalline alloys. The reason for these differences is not known. The value of β can be directly related to the quadratic coefficient of the spin-wave dispersion relation, called the *spin-wave stiffness*, D, by an equation $\beta \propto (1/D)^{3/2}$, in which the proportionality constant can be calculated from the material constants. The spin-wave stiffness constant is a measure of the stiffness of the spin-wave system. Experimentally it has been found, in the Fe_xB_{100-x} series, that D is proportional to x, as seen in fig. 26 (LUBORSKY *et al.* [1980]). Furthermore, the replacement of B by C, Si, or Ge increases the value of D in the order C < Si < Ge. It has been shown, on the basis of theoretical arguments, that D should be linearly related to T_c and extrapolate to $D = 0$ at $T_c = 0$. Many of the results reported to date do not extrapolate to zero, as shown in fig. 27 (LUBORSKY *et al.* [1980a]). It has therefore been suggested that the amorphous

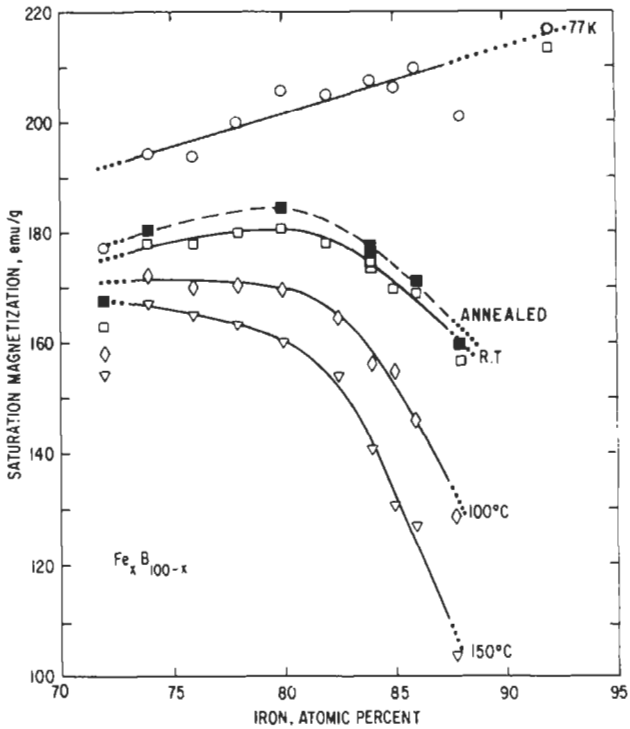

Fig. 23. Saturation magnetization measured at various temperatures for Fe_xB_{100-x} amorphous alloys. Solid symbols measured after annealing at ~ 30° below crystallization temperature for 2 h. (From LUBORSKY and BECKER *et al.* [1979].)

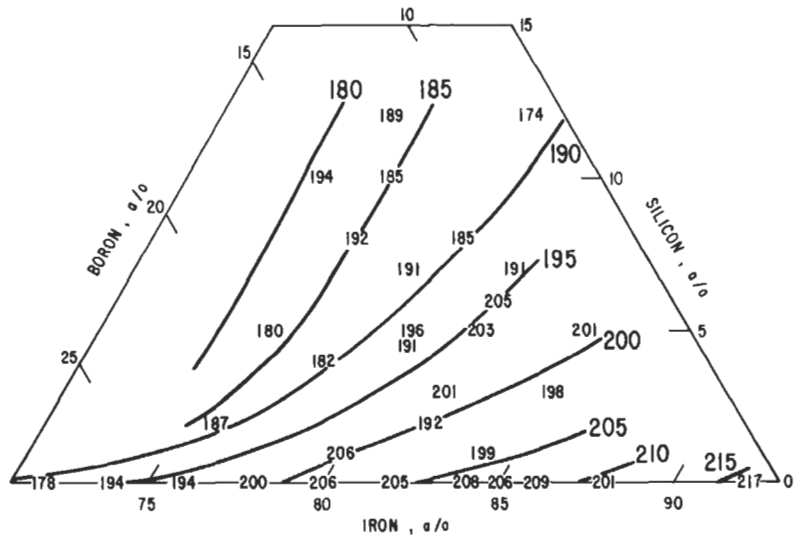

Fig. 24. Saturation magnetization in emu/g measured at 77 K for Fe–B–Si amorphous alloys.

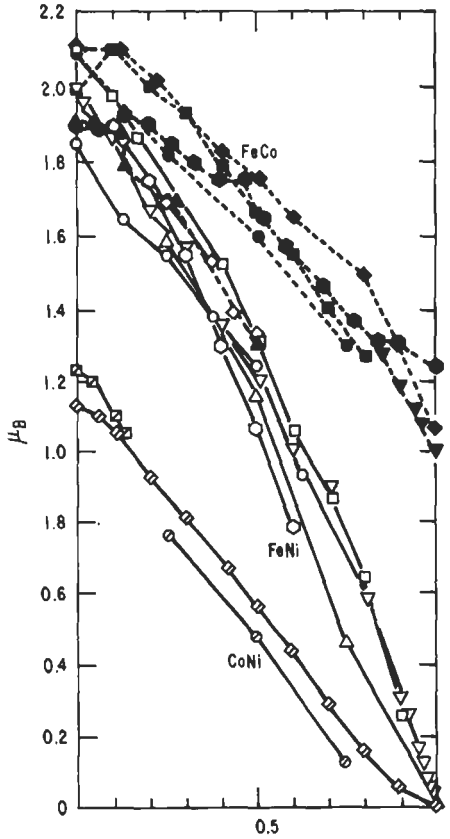

Fig. 25. Magnetization in Bohr magnetons per metallic atom versus atomic percent transition metal. Open symbols for FeNi amorphous alloys: □, $(FeNi)_{80}P_{10}B_{10}$; ○, ◇, $(FeNi)_{80}B_{20}$; ▽, $(FeNi)_{79}P_{13}B_8$; △, $(FeNi)_{80}P_{20}$; ○, $(FeNi)_{80}P_{14}B_6$. Solid symbols for FeCo amorphous alloys: ◆, $(FeCo)_{80}P_{10}B_{10}$; ■, $(FeCo)_{80}B_{20}$; ◆, $(FeCo)_{78}Si_{10}B_{12}$; ●, $(FeCo)_{80}P_{20}$; ▲, $(FeCo)_{80}P_{13}C_7$; ▼, $(FeCo)_{75}Si_{15}B_{10}$. Slashed symbols for CoNi amorphous alloys: ⧄, $(CoNi)_{78}Si_{10}B_{12}$; ⋄, $(CoNi)_{78}P_{14}B_8$; ⊘, $(CoNi)_{80}P_{20}$. (From GRAHAM and EGAMI [1978].)

Fe–B–X alloys do not behave as described by the model but may be regarded as strong ferromagnets, thus predicting that the values of D decrease with increasing T_c and extrapolate to finite T_c.

5.3.3. Anisotropy

Amorphous solids usually are assumed to have no long-range order and thus should be isotropic on a macroscale. However, magnetic anisotropic behavior is observed. Its origin is varied and sometimes not completely understood. In many cases, it reflects the existence of short-range order in the amorphous alloy. In addition, it has become something like folklore that in an ideal amorphous alloy the atomic-scale anisotropy would be averaged away so that there would be no anisotropy effects visible. CHI and

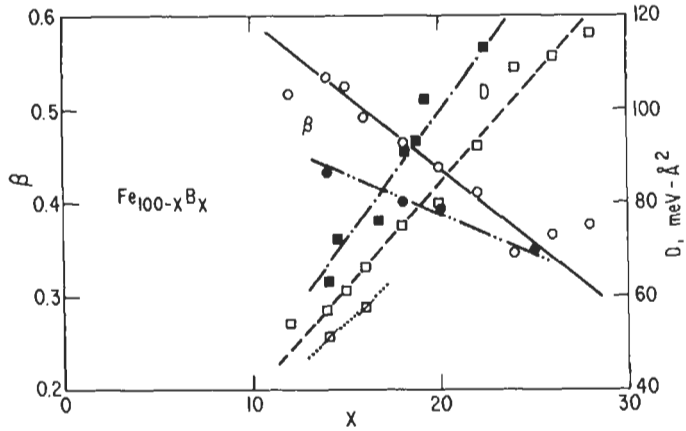

Fig. 26. Slope of the spin wave equation β and the exchange stiffness constant D for Fe_xB_{100-x} amorphous alloys (from LUBORSKY *et al.* [1980a]).

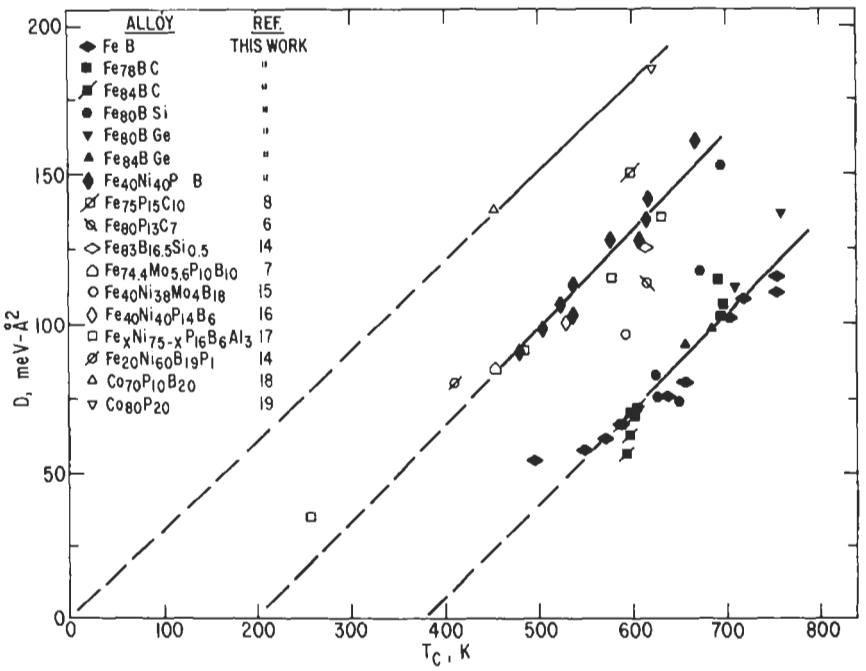

Fig. 27. The exchange stiffness constant D as a function of Curie temperature for various alloys. Solid symbols for D derived from magnetization data: open symbols for D derived from neutron measurements. (From LUBORSKY *et al.* [1980a].)

ALBEN [1976] have shown from a simple model calculation that when the local random anisotropy is small the coercivity is indeed small but high coercivities are abruptly obtained as the local anisotropy increases and dominates the behavior. In the following subsections the various anisotropies existing in amorphous alloys will be described.

5.3.3.1. Structural and compositional anisotropy. Anisotropic microstructures can arise in amorphous alloys owing to their preparation. These microstructures may involve density or compositional fluctuations which produce internal shape effects, that is, variations in magnetization. The resultant anisotropy field can then be no greater than that for long rods, namely $2\pi M_s$. The amorphous electro-deposited Co–P and CoNiP alloys have been studied in some detail. These alloys show a weak perpendicular anisotropy whose origin is believed to be due to such compositional fluctuations. Such fluctuations are often on the scale that can be seen by microprobe analysis or small-angle X-ray scattering, i.e., in the range of 1–1000 nm (10–10 000 Å). Small-angle X-ray-scattering observations on these electrodeposited Co–P films have been interpreted by CHI and CARGILL [1976] as showing the presence of oriented ellipsoidal scattering regions, assumed to be of high Co concentration. Annealing at temperatures well below crystallization reduced the perpendicular anisotropy and the small-angle scattering, suggesting that the annealing resulted in some homogenization of the alloy. In some amorphous alloys of Gd–Co, anisotropy fields greater than $2\pi M_s$ are observed even with no external stresses. The magnitude of K_u depends on the composition and conditions of preparation which influence the quantity of argon incorporated into the film.

5.3.3.2. Strain-magnetostriction anisotropy. Most amorphous ferromagnetic materials have nonzero magnetostriction, λ. Internal stresses, σ, which may be uniform or non-uniform, arise from the original solidification or from subsequent fabrication. These strains couple with λ to produce an anisotropy, K_λ. Uniform strains are often induced in evaporated, sputtered or electrodeposited films due to the differential thermal expansion between the film and the substrate. The magnitude of λ and the direction and magnitude of σ will then determine the direction and magnitude of K_λ. An important example of non-uniform strains is observed in drum-quenched alloys of the $(TM)_{80}(P, B, Al...)_{20}$ type. The non-uniform strains develop during the preparation of the ribbon and result in a periodic fluctuation in the perpendicular component of anisotropy along the length of the tape. Thermal annealing removes the internal strains, causing the anisotropy to disappear. The domain structure and its disappearance on annealing reflect this perpendicular K_λ and its removal.

5.3.3.3. Directional-order anisotropy. Like crystalline alloys, amorphous alloys also order under the influence of a magnetic field or stress, applied at temperatures below the Curie temperature. This results in an *induced uniaxial anisotropy* arising from the ordering of both the magnetic and nonmagnetic atoms in relation to the applied field direction. *Directional-order* theory predicts the dependence of the magnitude of the directional order anisotropy, K_u, on various parameters. It will be seen that the behavior of K_u in amorphous alloys is very similar to the behavior in thin films or bulk alloys of Ni–Fe. Typical results are shown in fig. 28 (LUBORSKY [1978]).

In the case of magnetic ordering, the magnitude of K_u is expected to be a function of the anneal temperature, θ, the magnetization at the anneal temperature, M_θ, at the

References: p. 2560.

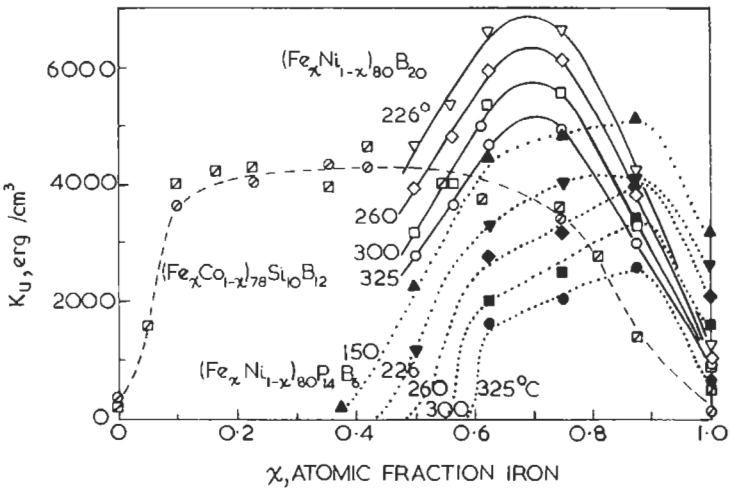

Fig. 28. Magnetically induced anisotropy versus composition. Solid and open symbols both annealed to equilibrium; slashed symbols obtained by heating at successively higher temperatures and on cooling from 380°C at 1.6 K/min.

measurement temperature, M_T, and at 0 K, M_0, and the concentrations of the ordering atoms, c_A and c_B, respectively, as given by:

$$K_u + Af(c)\left(M_T/M_0\right)^2\left(M_\theta/M_0\right)^2/\theta, \tag{4}$$

where A is a constant which depends on the atomic arrangement and the range of interactions considered. For dilute solutions and *monatomic directional order* (i.e., where only one species takes up preferential positions) $f(c) = c$ where c is the concentration of the ordering species. For *di-atomic directional* order (where pairs of distinct atoms arrange themselves in preferential directions), $f(c) = c_a^2$, where c_a is the concentration of the dilute species. If neither constituent is dilute, but assuming ideal solutions, i.e., for negligible nonmagnetic interaction energy, then

$$f(c) = Nnc_a^2c_b^2/2, \tag{5}$$

where N is the number of atoms per unit volume and n is the number of possible orientations of each pair referred to a crystal lattice. For non-ideal solutions the effective nonmagnetic interaction energy must be included in the expression for $f(c)$. In amorphous alloys we expect the interaction energy to be negative, i.e., leading to precipitation. These relations for amorphous Fe–Ni–B alloys were studied in detail by LUBORSKY and WALTER [1977a,b]. The reported values of K_u can be changed reversibly by changing the field direction and anneal temperature. The nonzero value of K_u at $x = 1$ is interpreted as due to ordering of the boron. The temperature-dependence observed fits the theoretically expected dependence on anneal temperature. The dependence of K_u on Fe–Ni composition follows the theoretical dependence for non-ideal solid solutions with a negative

interaction energy, i.e., of the type leading to precipitation, as expected.

There have also been studies of the kinetics of the reorientation of K_u (LUBORSKY and WALTER [1977c]). The time constants for this reorientation for various amorphous alloys show that the amorphous alloys are more closely related in their behavior to the quenched crystalline alloys than to the annealed crystalline alloys. In the quenched crystalline alloys, the rate-determining step in the reorientation has been associated with the excess vacancies present. It has thus been suggested that the disordered structure of the amorphous alloys has produced a similar atomic environment and thus similar kinetics for the reorientation. The $Fe_{40}Ni_{40}P_{14}B_6$ alloy surprisingly exhibited simple first-order kinetics in the reorientation of its anisotropy, as measured by the changes in its remanent-magnetization ratio M_r/M_s. This suggests that a uniform atomic environment exists around the reordering species. On the other hand, the reorientation kinetics of the $Fe_{40}Ni_{40}B_{20}$ alloy did not exhibit simple first-order kinetics; the kinetics could be fitted to a distribution of time constants or by second-order kinetics with equal concentrations of the two species.

Amorphous alloys are also susceptible to stress-induced ordering. As in crystalline alloys, this ordering presumably occurs via the interactions of the strain produced with the magnetostriction. The activation energy for stress-induced ordering is about twice as large as the values for magnetic ordering. It is thus concluded that stress-induced directional ordering involves different atomic species or motions than those involved in magnetically induced ordering. In addition, the final state produced by the two ordering processes must be different.

5.3.4. Magnetostriction

Since amorphous alloys are isotropic on a macroscale, the magnetostriction is expressed as a single saturation constant, λ_s. Measured values of λ_s are comparable to those in the corresponding crystalline phase. Some results are shown in fig. 29, for various series of amorphous alloys. Most measurements were obtained using strain gages but the small size of the ribbons may mean that the gage-backing and cement may not be negligible, meaning that the measurements represent only lower limits. TSUYA *et al.* [1975] have used a capacitance technique to avoid this problem. Note that both positive and negative values of λ_s are achievable.

O'HANDLEY [1977] has explored a wide range of temperatures. Band models which adequately describe the λ_s of crystalline Fe–Ni alloys do not apply to amorphous alloys. A combination of the single-ion and two-ion models does account for the temperature dependence λ_s of amorphous alloys.

5.3.5. Low-field properties

The low-field properties include the coercivity, remanence, losses, and permeability. The very low coercivities and losses make amorphous alloys particularly attractive in many applications, e.g., in transformers of all sizes. The low-field properties are usually the controlling parameters in the applications.

At least five pinning effects have been identified and discussed by KRONMÜLLER [1981] as contributing to the total coercivity. In order of increasing importance these are:

References: p. 2560.

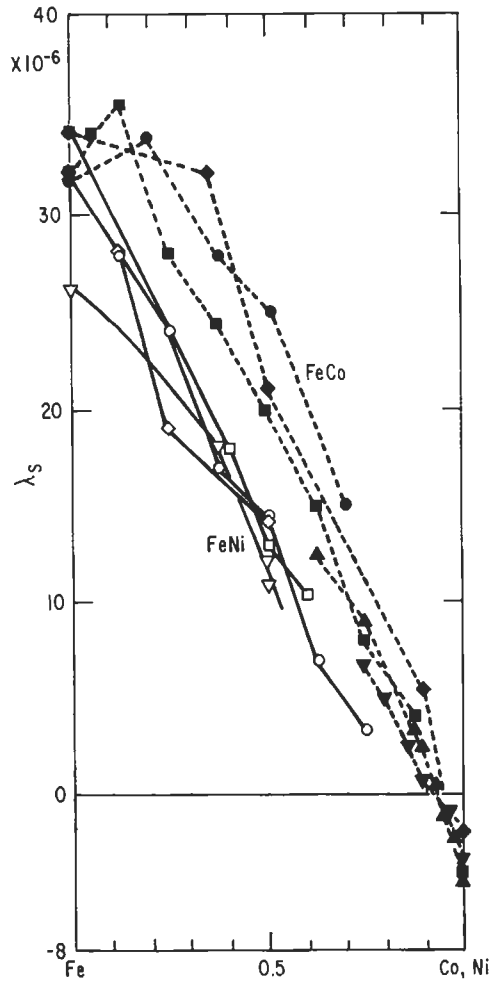

Fig. 29. Saturation magnetostriction measured at room temperature versus atomic percent transition metal. Open symbols for FeNi amorphous alloys; ◇, $(FeNi)_{80}P_{13}C_7$; ○, $(FeNi)_{80}B_{20}$; □, $(FeNi)_{78}B_{14}Si_8$; ▽, $(FeNi)_{80}P_{14}B_6$. Solid symbols for FeCo amorphous alloys: ■, $(FeCo)_{80}B_{20}$; ▲, $(FeCo)_{80}B_{20}$; ◆, $(FeCo)_{78}B_{14}Si_8$; ▼, $(FeCo)_{75}S_{15}B_{10}$; •, $(FeCo)_{80}P_{13}C_7$. (From GRAHAM and EGAMI [1978].)

a) *Intrinsic fluctuations* of exchange energies and local anisotropies (10^{-3}–1 mOe), H_c(i).

b) Clusters of *chemical short-range-ordered* regions (< 1 mOe), H_c(SO).

c) *Surface irregularities* (< 5 mOe), H_c(surf).

d) *Relaxation effects* due to local structural rearrangements (0.1–10 mOe), H_c(rel).

e) *Volume pinning* of domain walls by defect structures in magnetostrictive alloys (10–100 mOe), $H_c(\sigma)$.

Within the framework of the statistical potential theory (KRONMÜLLER *et al.* [1979]), on the basis of which the coercivity has to be determined, the contributions of the different statistically distributed pinning centers must be added quadratically. However, the effect of $H_c(\text{rel})$ has to be added linearly because each domain wall sees a stabilizing energy due to the relaxation with a wavelength of $2\delta_0$, where δ_0 is related to the domain wall width. This wavelength is of the same order of magnitude as the wavelength of the potential due to statistical fluctuations. Thus, the resultant total coercivity is:

$$H_c(\text{total}) = \left[H_c^2(\sigma) + H_c^2(\text{surf}) + H_c^2(\text{SO}) + H_c^2(\text{i})\right]^{1/2} + H_c(\text{rel}). \tag{6}$$

In the special case where the contribution of the pinning due to surface irregularities is larger than all other contributions the various terms add linearly, i.e.:

$$H_c(\text{total}) = H_c(\sigma) + H_c(\text{rel}) + H_c(\text{surf}) + H_c(\text{SO}) + H_c(\text{i}). \tag{5.5}$$

This is so because the wavelength of the surface-pinning is much larger (~ 10 μm) than that of the intrinsic fluctuations (< 0.5 μm). Explicit mathematical expressions have been derived for each of these contributions, giving the limits on H_c shown above.

The question now is how we can minimize the coercivity. Defect structures which give rise to the maximum contribution to the coercivity cannot be completely suppressed. These defect structures are generated during the rapid quenching process by an agglomeration of the free volume. This free volume is stable with respect to annealing and thus cannot be removed completely. Thus, the interaction of domain walls with defects can only be reduced significantly by using nonmagnetostrictive alloys. Then short-range order effects and relaxation effects become important. These latter effects may be minimized by a suitable anneal treatment. The intrinsic coercivity may only be detectable in ribbons with extremely smooth surfaces, with $\lambda = 0$, and after an anneal arranged to avoid relaxation and short range order effects.

It is well established that amorphous alloys with high saturation magnetization have losses at 60 Hz that are smaller than the best commercial grain-oriented Fe–3$\frac{1}{4}$% Si by

Table 2
Some typical magnetic properties of amorphous alloys compared to commercial alloys after optimum magnetic anneals.

Alloy	60 Hz, 1.4 T		50 kHz, 0.1 T	
	Core loss W/kg	Exciting power VA/kg	Core loss W/kg	Exciting power VA/kg
$Fe_{81}B_{13.5}Si_{3.5}C_2$ (METGLAS 2605 SC)	0.20	0.31	6	26
$Fe_{79}B_{16}Si_5$ (METGLAS 2605 S3)	–	–	9	21
Fe–3.2% Si (0.28 mm thick)	0.90	1.1	–	–
Supermalloy	–	–	9.4	–
Ferrite, H7A	–	–	11	–

References: p. 2560.

a factor of three to twenty (LUBORSKY and BECKER [1979]) as indicated in table 2. Since amorphous alloys have four times the resistivity and are about 1/5 the thickness of Fe–$3\frac{1}{4}$% Si we would predict, using a simple classical model, that the eddy-current losses would be reduced by a factor of ten; i.e., eddy-current losses are proportional to the inverse of resistivity and the square root of thickness. Thus the remaining losses at 60 Hz in amorphous alloys, for example in $Fe_{81}B_{13.5}Si_{3.5}C_2$, are due to hysteresis losses associated with domain wall motion. Refining the domain structure, for example by inducing an easy axis at some angle to the length of the ribbon, leads to reduction in losses (LUBORSKY and LIVINGSTON [1982]). The exciting power necessary to achieve a given level of induction remains relatively constant for field angles out to about 30° and then rises rapidly.

The same annealing which minimizes losses for the iron-rich metallic glasses for 60 Hz applications does not minimize losses in the higher frequency region, e.g., from 1 to 100 kHz. Minimum losses in this frequency region are achieved by a higher-temperature anneal which induces a precipitation of fine crystallites (DATTA *et al.* [1982]). These precipitates provide nucleation sites for domain walls, thereby refining the domain structure and reducing losses. Typical results are shown in table 2.

In the early 1980s, 1000 prototype distribution transformers with amorphous-metal cores were installed by utility companies throughout the United States. Field experience showed that the lower core loss and exciting power cited in table 2 did not deteriorate with time, and soon amorphous metals were replacing silicon steels in a growing fraction of this market. Improved steel processing techniques to meet this challenge were discussed earlier. Research on amorphous metals continues, aimed at increasing saturation magnetization and avoiding the embrittlement and increased crystallization encountered in Fe–B–Si alloys with higher iron concentrations. Some of the techniques used to reduce losses in silicon steels by domain refinement, such as laser scribing, have been shown to reduce losses in amorphous metals as well.

6. *Magnetic measurements in metallurgy*

When alloys contain one or more ferromagnetic phases, magnetic measurements can provide significant metallurgical information (HOSELITZ [1952, 1960] and BERKOWITZ [1969]). *Curie temperatures* are characteristic of particular phases and compositions. Therefore, measurement of magnetization versus temperature at fixed field, or *thermomagnetic analysis*, is often used to identify the Curie temperatures of the various phases present, and thereby to identify those phases and their compositions. In special cases, changes in the magnetic symmetry of phases with temperature can lead to discontinuities in magnetization-temperature curves that can also be used to identify the presence of particular phases (BERKOWITZ *et al.* [1979]). Thermomagnetic analysis, of course, is only useful if no metallurgical changes are produced by the heating.

If only one ferromagnetic phase is present, *saturation magnetization* can be used as a measure of the volume fraction of that phase. This is frequently used to study phase transformations, particularly in steels, in which Fe-rich austenite is not ferromagnetic, but

ferrite and martensite are. For example, saturation-magnetization measurements have been used to determine the amounts of retained austenite (KRAWIARZ *et al.* [1979]) or strain-induced martensite (CHANANI *et al.* [1971], LARBALESTIER and KING [1973] and COLLINGS [1979b]) in steels. Measurement of saturation magnetization may require larger fields than are available in some situations, and magnetic quantities that are simpler to measure are often used instead to determine the volume fraction of ferromagnetic phase. *Permeability* is commonly used, as is the *force* exerted by the sample on a standard permanent magnet. Force or permeability measurements are often used, for example, to determine the volume fraction of ferrite in duplex steel castings or welds (RATZ and GUNIA [1969]). Such measurements can be useful, but depend not only on saturation magnetization but also on sample microstructure and on experimental details, making determination of volume fractions less reliable.

Since measurements of Curie temperature and saturation magnetization can be used to identify compositions and volume fractions of ferromagnetic phases, they have frequently been used in phase-diagram determination. It is less well appreciated that the free energies involved in the ferromagnetic (or antiferromagnetic) state can influence phase equilibria and thereby affect the boundaries in the phase diagram (MIODOWNIK [1982]).

The structure-sensitivity of various features of the hysteresis loop, such as permeability, coercivity, approach to saturation, etc., has led to use of these magnetic parameters as measures of microstructural parameters such as grain size, internal stresses, dislocation densities, etc. Coercivity, for example, has been used as a measure of microstructural refinement in Co–WC composites (FISCHMEISTER and EXNER [1966] and FREYTAG *et al.* [1978]). The noise signals produced by irregular domain-wall motion ("Barkhausen noise") have been used to determine internal stresses (GARDNER *et al.* [1977] and JAMES and BUCK [1980]). Many earlier examples have been discussed by HOSELITZ [1952, 1960]. However, such measurements must be used with great care, since these quantities usually depend on more than one microstructural variable.

One special case in which details of the magnetization curve can provide considerable metallurgical information is that of an alloy containing "superparamagnetic" particles (§ 3.1). These are ferromagnetic particles that are sufficiently fine that the assembly is in thermal equilibrium with an applied field. This yields a non-hysteretic, temperature-dependent magnetization curve that can be used to determine not only volume fraction but also average particle size, distribution of sizes, and particle shape (BEAN and LIVINGSTON [1959]).

Another measurement sometimes used to provide metallurgical information is that of *magnetic anisotropy*, frequently determined by *torque* measurements in an applied field. Where the magnetization curve is determined largely by crystal anisotropy, this can be a useful means of *texture* determination. In other cases, shape, or stress, or directional-ordering anisotropies may be dominant, and torque measurements can provide quantitative information about the dominant anisotropy.

Direct metallographic observation of the distribution of ferromagnetic phases can be enhanced with the use of ferromagnetic colloids (GRAY [1974] and GRAY *et al.* [1977]). Magnetic-powder techniques are also used for flaw detection in steels. In special cases, magnetic domain patterns can be revealed using polarized light, aiding phase identific-

References: p. 2560.

ation and orientation determination (LIVINGSTON [1981c]).

The hyperfine magnetic fields experienced by the nuclei in alloys can be analyzed through Mössbauer spectra, nuclear magnetic resonance, and related measurements. Since they are characteristic of particular phases and compositions, they have been used in phase-diagram determination in several alloy systems (RENO *et al.* [1978]) and in determining ferrite content in duplex steels (SCHWARTZENDRUBER *et al.* [1974]).

Finally, magnetic measurements can be used in metallurgical studies even where the phases are paramagnetic rather than ferromagnetic, provided the paramagnetic susceptibilities of the constituent phases are known (COLLINGS [1975, 1979a]). The disturbing effect of ferromagnetic impurities on such measurements is usually surmounted by assuming that the ferromagnetic material saturates in moderate fields, and that the high-field susceptibility is caused by the paramagnetic phase alone. The presence of superparamagnetism or of high anisotropies in the ferromagnetic phase may make this assumption questionable in some cases.

References

ADLER, E., and H. PFEIFFER, 1974, IEEE Trans. Magn. **MAG-10**, 172.

ALTOE, M. V. P., M. S. LANCAROTTE, R. COHEN, F. P. MISSELL, W. A. MONTEIRO, J. DEGAUQUE and M. FAGOT, 1991, IEEE Trans. Magn. **27**, 5325.

AMES, S. L., 1970, J. Appl. Phys. **41**, 1032.

ARAI, K. I. and OHMORI, 1986, Met. Trans. **17A**, 1295.

ARAI, K. I., K. ISHIYAMA and H. MOGI, 1989, IEEE Trans. Magn. **25**, 3949.

ARAI, K. I., H. SATOH, S. AGATSUMA and K. ISHIYAMA, 1990, IEEE Trans. Magn. **26**, 1969.

BAIBICH, M. N., J. M. BROTO, A. FERT, F. NGUYEN VAN DAU, F. PETROFF, P. ETIENNE, G. CREUZET, A. FREDERICK and J. CHAZELAS, 1988, Phys. Rev. Letters **61**, 2472.

BARTLETT, R. W., and P. J. JORGENSON, 1974, J. Less-Common Met. **37**, 21.

BEAN, C. P., and J. D. LIVINGSTON, 1959, J. Appl. Phys. **30**, 120S.

BECKER, J. J., 1973, IEEE Trans. Magn. **MAG-9**, 161.

BELLI, Y., M. OKADA, G. THOMAS, M . HOMMA and H. KANEKO, 1978, J. Appl. Phys. **49**, 2049.

BERKOWITZ, A. E., 1969, in: Magnetism and Metallurgy, vol. 1, eds. A. E. Berkowitz and E. Kneller (Academic, New York) p. 331.

BERKOWITZ, A. E., J. D. LIVINGSTON, B. D. NATHAN and J. L. WALTER, 1979, J. Appl. Phys. **50**, 1754.

BERKOWITZ, A. E., J. R. MITCHELL, M. J. CAREY, A. P. YOUNG, S. ZHANG, F. E. SPADA, F. T. PARKER, A. HUTTEN and G. THOMAS, 1992, Phys. Rev. Letters **68**, 3745.

BOOTHBY, O. L., and R. M. BOZORTH, 1947, J. Appl. Phys. **18**, 173.

BORDERS, J. A., 1979, Ann. Rev. Mater. Sci. **9**, 313.

BROWN, W. F., Jr., 1962, J. Appl. Phys. **33**, 3022.

BUSCHOW, K. H. J., 1988, in: Ferromagnetic Materials, vol. 4, ed. E. P. Wohlfarth and K. H. J. Buschow, (North-Holland, Amsterdam) p. 1.

BUSCHOW, K. H. J., 1991, Rep. Prog. Phys. **54**, 1123.

CHANANI, G. R., V. F. ZACKAY and E. R. PARKER, 1971, Metallurg. Trans. **2**, 133.

CHEN, C. W., 1977, Magnetism and Metallurgy of Soft Magnetic Materials (North-Holland, Amsterdam).

CHI, G. C., and R. ALBEN, 1976, AIP Conf. Proc. **34**, 316.

CHI, G. C., and G. S. CARGILL, 1976, Mater. Sci. Eng. **23**, 155.

CHIKAZUMI, S., and C. D. GRAHAM Jr., 1969, in: Magnetism and Metallurgy, vol. 2, eds. A. E. Berkowitz and E. Kneller (Academic, New York) ch. 12.

CHIN, G. Y., 1971, Adv. Mater. Res. **5**, 217.

CHIN, G. Y., and J. H. WERNICK, 1980. in : Ferromagnetic Materials, vol. 2, ed. E. P. Wohifarth (NorthHolland, Amsterdam) ch. 2.
CHIN, G. Y., S. JIN, M. L. GREEN, R. C. SHERWOOD and J. H. WERNICK, 1981, J. Appl. Phys. **52**, 2536.
COEY, J. M. D., 1991, Physica Scripta **T39**, 21.
COLLING, D. A., and R. G. ASPEN, 1969, J. Appl. Phys. **40**, 1571.
COLLING, D. A., and R. G. ASPEN, 1970, J. Appl. Phys. **41**, 1040.
COLLINGS, E. W., 1975, J. Less-Common Met. **39**, 63.
COLLINGS, E. W., 1979a, Metallurg. Trans. **10A**, 463.
COLLINGS, E. W., 1979b, Cryogenics **19**, 215.
CRAIK, D. J., and E. W. HILL, 1977, J. Physique **38**, C1–39.
CROAT, J. J., J. F. HERBST, R. W. LEE, and F. E. PINKERTON, 1984, J. Appl. Phys. **55**, 2078.
CULLITY, B. D., 1972, Introduction to Magnetic Materials (Addison–Wesley, Reading, MA).
DATTA, A., N. DECRISTOFARO and L. A. DAVIS, 1982, in: Proc. Fourth Int. Conf. on Rapidly Quenched Metals, Sendai, Japan (1981) eds. T. Masumoto and K. Suzuki (Japan. Inst. Metals, Sendai) pp. 1007 and 1031.
DE VOS, K. J., 1969, in: Magnetism and Metallurgy, vol. 1, eds. A. E. Berkowitz and E. Kneller (Academic, New York) p. 473.
DE WIT, J. J., 1989, J. Magn. Magn. Mater. **79**, 167.
DEN BROEDER, F. J. A., and H. ZIJLSTRA, 1976, J. Appl. Phys. **47**, 2688.
DEN BROEDER, F. J. A., and K. H. J. BUSCHOW, 1980. J. Less-Common Met. **70**, 289.
DIETZ, G., 1977, J. Magn. Magn. Mater. **6**, 47.
ENGLISH, A. T., and G. Y. CHIN, 1967. J. Appl. Phys. **38**, 1183.
FIEDLER, H. C., 1977, IEEE Trans. Magn. **MAG-13**, 1433.
FISCHMEISTER, H., and H. E. EXNER, 1966, Arch. Eisenhuttenw. **37**, 499.
FISH, G. E., 1990, Proc. IEEE **78**, 947.
FREYTAG, J., P. WALTER and H. E. EXNER, 1978, Z. Metalik. **69**, 546.
FUKUDA, B., K. SATO, Y. SHIMIZU and Y. ITO, 1984, J. Appl. Phys. **55**, 2130.
GARDNER, C. G., G. A. MATZKANIN and J. LANKFORD, 1977, Int. Adv. Nondestructive Testing **5**, 201.
GAUNT, P., 1966, Phil. Mag. **13**, 579.
GOSS, N. P., 1934, U. S. Patent **1965**, 559.
GOTO, I., I. MATOBA, T. IMANAKA, T. GOTOH and T. KAN, 1975, Proc. 2nd EPS Conf. on Soft Magnet Materials (Wolfson Centre for Magnetic Technology, Cardiff, Wales) p. 262.
GOULD, H. L. B., and D. H. WENNY, 1957, AIEE Spec. Publ. **T-97**, 675.
GRAHAM, C. D., Jr., 1959, Magnetic Properties of Metals and Alloys (ASM, Metals Park, OH) ch. 13.
GRAHAM, C. D., Jr., and T. EGAMI, 1978, Ann. Rev. Mater. Sci. **8**, 423.
GRAY, R. J., 1974, in: Microstructural Science, vol. 1, eds. R. J. Gray and J. L. McCall (American Elsevier, New York) p. 159.
GRAY, R. J., R. S. CROUSE, V. K. SIKKA and R. T. KING, 1977, in: Microstructural Science, vol. 5, eds. J. D. Braun, H. W. Arrowsmith and J. L. McCall (Elsevier, New York) p. 65.
GRENOBLE, H. E., 1977, IEEE Trans. Magn. **MAG-13**, 1427.
GROGER, B., 1979, J. Magn. Magn. Mater. **13**, 53.
HAASEN, P., 1972, Mater. Sci. Eng. **9**, 191.
HAASEN, P., 1977, Contemp. Phys. **18**, 373.
HERBST, J. F., 1991, Rev. Mod. Phys. **63**, 819.
HERZER, G., 1989, IEEE Trans. Magn. **25**, 3327.
HERZER, G., 1990, IEEE Trans. Magn. **26**,1397.
HILZINGER, H. R., and H. KRONMÜLLER, 1973, Phys. Stat. Sol. (b) **59**, 71.
HILZINGER, H. R., 1977, Appl. Phys. **12**, 253.
HOFFMANN, A., 1971, Z. Angew. Phys. **32**, 236.
HOMMA, M., E. HORIKOSHI, T. MINOWA and M. OKADA, 1980, Appl. Phys. Lett. **37**, 92.
HOMMA, M., M. OKADA, T. MINOWA and E. HORIKOSHI, 1981, IEEE Trans. Magn. **MAG-17**, 3473.
HONMA, H., Y. USHIGAMI and Y. SUGA, 1991, J. Appl. Phys. **70**, 6259.
HOSELITZ, K., 1952, in. Ferromagnetic Properties of Metals and Alloys (Oxford Univ. Press, London) ch. 4.

HOSELITZ, K., 1960, in: The Physical Examination of Metals, 2nd Ed., eds. B. Chalmers and A. G. Quarrell (Arnold, London) p. 225.
HULTGREN, R., P. D. DESAI, D. T. HAWKINS, M. GLEISER and K. K. KELLEY, 1973, Selected Values of the Thermodynamic Properties of Binary Alloys (ASM, Metals Park, OH) p. 871.
INOKUTI, Y., K. SUZUKI and Y. KOBAYASHI, 1992, Mater. Trans. JIM **33**, 946.
INOUE, K., and H. KANEKO, 1981, U.S. Patent 4 273 595.
ISHIYAMA, K., ARAI, K. I. and T. HONDA, 1991, J. Appl Phys. **70**, 6262.
IUCHI, T., S. YAMAGUCHI, T. ICHIYAMA, M. NAKAMURA, T. ISHIMOTO and K. KUROKI, 1982, J. Appl. Phys. **53**, 2410.
JAGIELINSKI, T., 1989, Mater. Sci. Eng. **B3**, 467.
JAGIELINSKI, T., 1990, MRS Bulletin, March, p. 36.
JAMES, M. R., and O. BUCK, 1980, CRC Reviews **9**(1), 61.
JIN, S., 1979, IEEE Trans. Magn. **MAG-15**, 1748.
KANEKO, H., M. HOMMA and K. SUZUKI, 1968, Trans. Japan. Inst. Metals **9**, 124.
KANEKO, H., M. HOMMA and K. NAKAMURA, 1971, AIP Conf. Proc. **5**, 1088.
KANEKO, H., M. HOMMA, M. OKADA, S. NAKAMURA and N. IKUTA, 1976, AIP Conf. Proc. **29**, 620.
KAVESH, S., 1978, in: Metallic Glasses, eds. J. J. Gilman and H. I. Leamy (ASM, Metals Park, OH) p. 36.
KAZAMA, N. S., M. MITERA and T. MASUMOTO, 1978, in: Proc. Third Int. Conf. on Rapidly Quenched Metals, Univ. of Sussex, England, 1978, ed. B. Cantor (The Metals Society, London) vol. 2, p. 164.
KIKUCHI, S., and S. ITO, 1972, IEEE Trans. Magn. **MAG-8**, 344.
KOJIMA, S., T. OHTANI, N. KATO, K. KOJIMA, Y. SAKAMOTO, I. KONNO, M. TSUKAHARA and T. KUBO, 1974, AIP Conf. Proc. **24**, 768.
KRAWIARZ, J., T. MALKIEWICZ and A. MAZUR, 1979, M6m. Sci. Rev. Metallurg. **76**, 5.
KRONMÜLLER, H., 1978, in: Proc. 2nd Int. Symp. on Magnetic Anisotropy and Coercivity in Rare-Earth–Transilion-Metal Alloys, ed. K. I. Slrnat (Univ. of Dayton, OH) p. 1.
KRONMÜLLER, H., M. FAHNLE, N. DOMANN, H. GRIMM, R. GRIMMAND and B. GROGER, 1979, J. Magn. Magn. Mater. **13**, 53.
KRONMÜLLER, H., 1981, J. Appl. Phys. **52**, 1859; 1981, J. Magn. Magn. Mater. **24**, 159.
KUNZ, W., and F. PFEIFER, 1976, AIP Conf. Proc. **34**, 63.
LARBALESTIER, D., and H. W. KING, 1973, Cryogenics **13**, 160.
LIEBERMANN, H. H., 1979, IEEE Trans. Magn. **MAG-15**, 1393.
LIEBERMANN, H. H., 1980, Mater. Sci. Eng. **43**, 203.
LIEBERMANN, H. H., 1981, Mater. Sci. Eng. **49**, 185.
LITTMANN, M. B., 1967, J. Appl. Phys. **38**, 1104.
LITTMANN, M. B., 1971, IEEE Trans. Magn. **MAG-7**, 48.
LITTMANN, M. B., 1982, J. Appl. Phys. **53**, 2416.
LIVINGSTON, J. D., 1973a, AIP Conf. Proc. **10**, 643.
LIVINGSTON, J. D., 1973b, Phys. Stat. Sol. (a) **18**, 579.
LIVINGSTON, J. D., and D. L. MARTIN, 1977, J. Appl. Phys. **48**, 1350.
LIVINGSTON, J. D., 1981a, Prog. Mater. Sci., Chalmers Anniversary Volume, 243.
LIVINGSTON, J. D., 1981b, J. Appl. Phys. **52**, 2544.
LIVINGSTON, J. D., 1981c, J. Appl. Phys. **52**, 2506.
LUBORSKY, F. E., 1961, J. Appl. Phys. **32**, 1715.
LUBORSKY, F. E., and C. R. MORELOCK, 1964a, J. Appl. Phys. **35**, 2055.
LUBORSKY, F. E., and C. R. MORELOCK, 1964b, in: Proc. Int. Conf. on Magnetism, Nottingham (The Institute of Physics and The Physical Society, London) p. 763.
LUBORSKY, F. E., 1976, AIP Conf. Proc. **29**, 209.
LUBORSKY, F. E., and J. L. WALTER, 1977a, IEEE Trans. Magn. **MAG-13**, 1635.
LUBORSKY, F. E., and J. L. WALTER, 1977b, IEEE Trans. Magn. **MAG-13**, 953.
LUBORSKY, F. E., and J. L. WALTER, 1977c, Mater. Sci. Eng. **28**, 77.
LUBORSKY, F. E., 1978, J. Magn. Magn. Mater. **7**, 143.
LUBORSKY, F. E., H. H. LIEBERMANN, J. J. BECKER and J. L. WALTER, 1978, in: Proc. Third Int. Conf. on Rapidly Quenched Metals, Univ. of Sussex, England, 1978, ed. B. Cantor (The Metals Society, London) vol. 2, p. 188.

LUBORSKY, F.E., and J.J. BECKER, 1979, IEEE Trans. Magn. **MAG-15**, 1939.
LUBORSKY, F.E., 1980a, J. Appl. Phys. **51**, 2808.
LUBORSKY, F.E., J.L. WALTER, H.H. LIEBERMANN and E.P. WOHLFARTH, 1980a, J. Magn. Magn. Mater. **15–18**, 1351.
LUBORSKY, F.E., 1980b, Amorphous Ferromagnets, in: Ferromagnetic Materials, vol. 1, ed. E.P. Wohlfarth (North-Holland, Amsterdam) ch. 6.
LUBORSKY, F.E., J.L. WALTER and E.P. WOHLFARTH, 1980b, J. Phys. **F10**, 959.
LUBORSKY, F.E., and J. LIVINGSTON, 1982, IEEE Trans. Magn. **MAG-18**, 908.
MAHAJAN, S., E.M. GYORGY, R.C. SHERWOOD, S. JIN, S. NAKAHARA, D. BRASEN and M. EIBSCHUTZ, 1978, Appl. Phys. Lett. **32**, 688.
MAJOR, B.V., M.C. MARTIN and M.W. BRANSON, 1975, in: Proc. 2nd EPS Conf. on Soft Magnetic Materials (Wolfson Centre for Magnetics Technology, Cardiff, Wales) p. 103.
MALAGARI, F.A., 1977, IEEE Trans. Magn. **MAG-13**, 1437.
MCCAIG, M., 1977, Permanent Magnets in Theory and Practice (Wiley, New York).
MCCURRIE, R.A., and D.G. HAWKRIDGE, 1975, Phil. Mag. **32**, 923.
MCCURRIE, R.A., 1982, in: Ferromagnetic Materials, vol. 3, ed. E.P. Wohlfarth (North-Holland, Amsterdam) p. 107.
MCINTYRE, D.A., 1970, J. Phys. **D3**, 1430.
MENTH, A., H. NAGEL and R.S. PERKINS, 1978, Ann. Rev. Mater. Sci. **8**, 21.
MINOWA, T., M. OKADA and M. HOMMA, 1980, IEEE Trans. Magn. **MAG-16**, 529.
MIODOWNIK, A.P., 1982, Bull. Alloy Phase Diagrams **2**, 406.
MISHRA, R.K., and G. THOMAS, 1979, in: Proc. 4th Int. Workshop in Rare-Earth–Cobalt Magnets (Society for Non-Traditional Technology, Tokyo) p. 301.
MIYAZAKI, T., E. SAWADA and Y. ISHIJMA, 1972, IEEE Trans. Magn. **MAG-8**, 501.
NÉEL, L., 1954, J. Phys. Radium **15**, 225.
NEMBACH, E., C.K. CHOW and D. STOCKEL, 1977, Physica B **86–88**, 1415.
NINOMIYA, H., Y. TANAKA, A. HIURA and Y. TAKADA, 1991, J. Appl. Phys. **69**, 5358.
NOZAWA, T., T. YAMAMOTO, Y. MATSUO and Y. OHYA, 1978, IEEE Trans. Magn. **MAG-14**, 252.
O'HANDLEY, R.C., 1977, in: Amorphous Magnetism II, eds. R.A. Levy and R. Hasegawa (Plenum, New York) p. 379.
OHTANI, T., N. KATO, S. KOJIMA, K. KOJIMA, Y. SAKAMOTO, I. KONNO, M. TSUKAHARA and T. KUBO, 1977, IEEE Trans. Magn. **MAG-13**, 1328.
PARKIN, S.S.P., Z.G. LI and D.J. SMITH, 1991, Appl. Phys. Letters **58**, 2710.
PAVUNA, D., 1982, J. Mater. Sci. **16**, 2419.
PFEIFER, F., 1966a, Z. Metalik. **57**, 295.
PFEIFER, F., 1966b, Z. Metalik. **57**, 240.
PFEIFER, F. and C. RADELOFF, 1980, J. Magn. Magn. Mater. **19**, 190.
PFEIFFER, I., 1969, Cobalt **44**, 115.
RASTOGI, P.K., and J.M. SHAPIRO, 1973, IEEE Trans. Magn. **MAG-9**, 122.
RASTOGI, P.K., 1976, AIP Conf. Proc. **34**, 61.
RASTOGI, P.K., 1977, IEEE Trans. Magn. **MAG-13**, 1448.
RATZ, G.A., and R.B. GUNIA, 1969, Met. Prog. **95**(1), 76.
RENO, R.C., L.J. SCHWARTZENDRUBER, G.C. CARTER and L.H. BENNETT, 1978, in: Applications of Phase Diagrams in Metallurgy and Ceramics, ed. G.C. Carter (NBS Special Publication 496) p. 450.
ROWLANDS, G., 1976, J. Phys. **D9**, 1267.
SAGAWA, M., S. FUJIMURA, M. TOGAWA, and Y. MATSUURA, 1984, J. Appl. Phys. **55**, 2083.
SCHOLEFIELD, H.H., R.V. MAJOR, B. GIBSON and A.P. MARTIN, 1967, Brit. J. Appl. Phys. **18**, 41.
SCHWARTZENDRUBER, L.J., L. H. BENNETT, E.A. SCHOEFER, W.T. DE LONG and H.C. CAMPBELL, 1974, Welding J. **53**, 1-S.
SENNO, H., Y. YANAGIUCHI, M. SATOMI, E. HIROTA and S. HAYAKAWA, 1977, IEEE Trans. Magn. **MAG-13**, 1475.
SHIBAYA, H., and I. FUKUDA, 1977, IEEE Trans. Magn. **MAG-13**, 1029.

SHIGA, M., 1993, in: Electronic and Magnetic Properties of Metals and Ceramics (ed. K.H.J. Buschow), vol. 3B of Materials Science and Technology (ed. R.W. Cahn, P. Haasen, and E.J. Kramer), VCH, Weinheim, Germany) p. 159.
SHILLING, J.W., and G.L. HOUZE Jr., 1974, IEEE Trans. Magn. **MAG-10**, 195.
SHILLING, J.W., W.G. MORRIS, M.L. OSBORN and P. RAO, 1978, IEEE Trans. Magn. **MAG-14**, 104.
SHILLING, J W., and W.A. SOFFA, 1978, Acta Metall. **26**, 413.
SHIMANAKA, H., I. MATOBA, T. ICHIDA, S. KOBAYASHI and T. FUNAHASHI, 1975, in: Proc. 2nd EPS Conf. On Soft Magnetic Materials (Wolfson Centre for Magnetic Technology, Cardiff, Wales) p. 269.
STRNAT, K.J., 1988, in: Ferromagnetic Materials, vol. 4, ed. E. Wohlfarth and K.H.J. Buschow (North-Holland, Amsterdam) p. 131.
SUZUKI, K., A. MAKINO, A. INOUE and T. MASUMOTO, 1991, J. Appl. Phys. **70**, 6241.
SWIFT, W.M., W.H. DANIELS and J.W. SHILLING, 1975, IEEE Trans. Magn. **MAG-11**, 1655.
SWISHER, J.H., A.T. ENGLISH and R.C. STOFFERS, 1969, Trans. ASM **62**, 257.
SWISHER, J.H., and E.O. FUCHS, 1970, J. Iron Steel Inst. **208**, 777.
TAGUCHI, S., 1977, Trans. Iron Steel Inst. Japan **17**, 604.
TAKADA, Y., M. ABE, S. MASUDA and J. INAGAKI, 1988, J. Appl. Phys. **64**, 5367.
TAKAHASHI, M., and T. SHIMATSU, 1990, IEEE Trans. Magn. **26**, 1485.
TAKAHASHI, N., Y. USHIGAMI, T. NOZAWA and T. NAKATA, 1986, IEEE Trans. Magn. **MAG-22**, 490.
THOMAS, B., 1975, in: Proc. 2nd Conf. EPS on Soft Magnetic Materials (Wolfson Centre for Magnetics Technology, Cardiff, Wales) p. 109.
THORNBURG, D.R., 1969, J. Appl. Phys. **40**, 1579.
TSUYA, N., K.I. ARAI, Y.Y. SHIRAGA, M. YAMADA and T. MASUMOTO, 1975, Phys. Stat. Sol. (a) **31**, 557.
TSUYA, N., and K.I. ARAI, 1978, Solid State Phys. **13**, 237.
VAN DEN BROEK, C.A.M., and A.L. STUIJTS, 1977, Philips Tech. Rev. **37**, 157.
VINCENT, J.H., J.G. HERBERTSON and H.A. DAVIES, 1982, in: Proc. 4th Int. Conf. on Rapidly Quenched metals, Sendai, Japan, 1981, eds. T. Masumoto and K. Suzuki (Japan. Inst. Metals, Sendai) p. 77.
WALLACE, W.E., and M.Q. HUANG, 1992, IEEE Trans. Magn. **28**, 2312.
WECKER, J., R. VON HELMOLT, L. SCHULTZ and K. SAMWER, 1993, IEEE Trans. Magn. **29**, 3087.
WHITE, R.L., 1992, IEEE Trans. Magn. **28**, 2482.
XIAO, J.Q., J.S. JIANG and C.L. CHIEN, 1991, Phys. Rev. **B43**, 8089.
YAMAMOTO, T., and Y. UTSUSHIKAWA, 1976, J. Japan. Inst. Metals **40**, 975.
YERMAKOV, A.Ye., N.I. SOLOKOVSKAYA, U.A. TSURIN, G.V. IVANOVA and L.M. MAGAT, 1978, Phys. Met. Metallogr. **46**(4), 46.
YOSHIZAWA, Y., S. OGUMA, and K. YAMAUCHI, 1988, J. Appl. Phys. **64**, 6044.
YOSHIZAWA, Y. and K. YAMAUCHI, 1991, Proc. Internat. Symp. on 3d Transition-Semi Metal Thin Films (Japan Soc. for Promotion of Science, Sendai) p. 140.
ZIJLSTRA, H., 1967, Experimental Methods in Magnetism, vol. 2 (North-Holland, Amsterdam; Wiley–Interscience, London).
ZIJLSTRA, H., 1983, in: Ferromagnetic Materials, vol. 3, ed. E.P. Wohlfarth (North-Holland, Amsterdam) p. 37.

Further reading

R.M. Bozorth, Ferromagnetism (Van Nostrand, New York, 1951).
K. Hoselitz, Ferromagnetic Properties of Metals and Alloys (Oxford Univ. Press, London, 1952).
E. Kneller, Ferromagnetismus (Springer, Berlin, 1962).
A.E. Berkowitz and E. Kneller, eds., Magnetism and Metallurgy, vols. I and 2 (Academic, New York, 1969).
R.S. Tebble and D.J. Craik, Magnetic Materials (Wiley–Interscience, London, 1969).
B.D. Cullity, Introduction to Magnetic Materials (Addison–Wesley, Reading, MA, 1972).
C.W. Chen, Magnetism and Metallurgy of Soft Magnetic Materials (North-Holland, Amsterdam, 1977).
E.P. Wohlfarth, ed., Ferromagnetic Materials, vols. 1 and 2 (North-Holland, Amsterdam, 1980; vol. 3, 1982).
G. Conderchon and J.F. Tiers, Some Aspects of Magnetic Properties of Ni–Fe and Co–Fe alloys, J. Magn. Magn. Mater. 26 (1982) 196.

R. Hasegawa, ed., Glassy Metals: Magnetic, Chemical and Structural Properties (CRC Press, Boca Raton, FL, 1983) chs. 4–6.

F. E. Luborsky, ed., Amorphous Metallic Alloys (Butterworths, London, 1983) chs. 14–20.

Novel Magnetic Structures and Properties — a Symposium, Scripta Metall. et Mater. **33** (1995) 1525–1881.

CHAPTER 30

METALLIC COMPOSITE MATERIALS

T. W. CLYNE

Department of Materials Science & Metallurgy
Pembroke Street
Cambridge CB2 3QZ, UK

R. W. Cahn and P. Haasen†, eds.
Physical Metallurgy; fourth, revised and enhanced edition

1. Introduction

Reinforced materials based on metals have long been of technological significance. Dispersion hardened metals and precipitation hardening systems were both developed several decades ago. For both dispersion hardening and precipitation hardening, strengthening is due to dislocation motion in the metal being impeded by the presence of small, hard particles. This mechanism operates efficiently only when they are very closely spaced (<1 μm apart). These materials would not, however, generally be classified as true composites. While there is no universally accepted definition of a composite, it is commonly assumed that it is only when *load transfer* between matrix and reinforcement is significant that the term can properly be applied. When a composite is subjected to an external load, the matrix is relieved of a substantial proportion of that load by the presence of the reinforcement. On this basis, conventional dispersion and precipitation hardened systems are not composites, since they typically contain only around 1% or less of second phase and at such levels the reinforcing constituent cannot significantly reduce the stress borne by the matrix.

Interest in genuine metal matrix composites (MMCs), such as aluminium or copper reinforced with 30–70% of continuous tungsten or boron fibres, grew rapidly in the 1960s. As with most polymeric composites, an applied load is largely borne by the fibres in such a material and the matrix microstructure and strength are relatively unimportant. While commercial interest in such systems has fluctuated somewhat since that period, the attraction of strongly enhanced stiffness and creep resistance has ensured that research activities have continued, particularly for *titanium matrices*. The main problems concern fabrication difficulties and cost, although issues such as interfacial chemical reactions and their effects on properties have also received attention. The most popular reinforcement in such cases is currently *silicon carbide monofilament* with various surface coatings.

Discontinuously reinforced metal composites were developed during the 1980s, with attention focussed on *Al-based matrices* reinforced with *SiC particles*, or Al_2O_3 *particles* or *short fibres*. A combination of good properties, low cost and high workability has made them attractive for many applications. These materials fall somewhere between the dispersion-strengthened and fibre-strengthened extremes. They differ from dispersion hardened systems in having large (~1–100 μm diameter) reinforcing particles, which contribute negligible Orowan strengthening, and in containing a relatively high (5–40%) volume fraction of reinforcement, such that load transfer from the matrix is significant. However, unlike long fibre reinforced systems, the matrix does bear a substantial load and its strength is important. These distinctions are highlighted by the schematic plots (CLYNE and WITHERS [1993]) shown in fig. 1, which illustrate how strengthening is strongly dependent on reinforcement size for dispersion and precipitation hardened metals, but is sensitive to reinforcement content and aspect ratio for MMCs. In some cases, both types of mechanism may be significant, as with particle reinforcement of age-hardening alloys. Furthermore, the reinforcement may itself give rise to both types of strengthening, directly by load transfer and indirectly by stimulating changes in matrix microstructure.

In this review, a summary is given of the main factors responsible for the thermo-

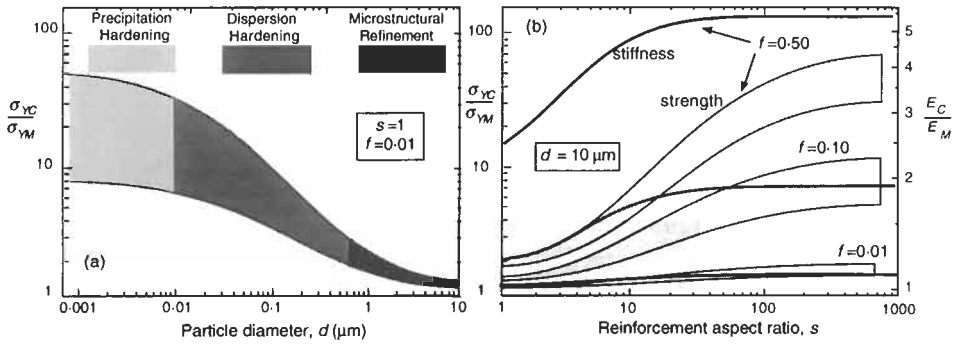

Fig. 1. Depiction (CLYNE and WITHERS [1993]) of strengthening (and stiffening) as a function of inclusion shape, size and volume fraction. (a) Matrix strengthening dominates for dispersion and precipitation hardening systems, with the inclusions constituting too low a volume fraction to carry a significant proportion of the load. (b) Strengthening and stiffening in MMCs are primarily a consequence of load transfer to the reinforcement, which is dependent on volume fraction and aspect ratio.

mechanical characteristics of MMCs. Since the production of material with suitable microstructure is central to any attempt to optimise such characteristics, this is preceded by an outline of the processing methods developed for MMCs.

2. *Material production*

In general, MMCs can offer various attractive combinations of properties. However, their commercial usage has been limited by difficulties in finding technically and economically attractive methods of preparing material and components with appropriate microstructural characteristics. Research on processing of MMCs has therefore assumed considerable importance. A particular aim is often to ensure that the reinforcement is homogeneously distributed, since this tends to improve the fracture characteristics (see § 4).

2.1. Liquid-phase processing

2.1.1. Squeeze infiltration

The squeeze casting process can be applied to MMCs, in the form of reheated powder mixtures or as stir-cast material, but the most common pressure-assisted solidification process for MMC production is usually termed *squeeze infiltration*. This involves the injection of liquid metal into the interstices of an assembly of short fibres, usually called a *preform*. Commonly, the preform is designed with a specific shape to form an integral part of a finished product in the as-cast form (FEEST [1988]). Preforms are commonly fabricated by sedimentation of short fibres from liquid suspension. This procedure has often been carried out with short alumina fibres, such as "Saffil" (STACEY *et al.* [1987]). Various preform shapes are possible, such as hollow tubes made by suction of suspended fibres onto a cylindrical former immersed in a slurry (SAMPLE *et al.* [1988]). Long fibres

can be held in place by filament winding onto a mandrel before infiltration (CHARBONNIER *et al.* [1988]). The process can also be adapted for production of particulate MMCs (KLIER *et al.* [1991]).

In order for the preform to retain its integrity and shape, it is often necessary for a *binder* to be used. Various silica- and alumina-based mixtures have been popular as high temperature binders. The binding agent is normally introduced via the suspension liquid, so that it deposits or precipitates out on the fibres, often forming preferentially at fibre contact points, where it serves to lock the fibre array into a strong network. Typically, a binder might be present in the preform at levels of about 5%-10% by weight. There has been interest in the chemical effects induced by the presence of the binder. For example, it has been shown (CAPPELMAN *et al.* [1985]; LI *et al.* [1989]) in Al-based MMCs that a silica binder is rapidly attacked by Mg in the melt during squeeze infiltration, affecting both interfacial properties and matrix age hardening characteristics (FRIEND *et al.* [1988]).

Squeeze infiltration has also been popular for very fine fibres, such as SiC whiskers, which are difficult to blend with metallic powders because of the size difference and the tendency for tenacious fibre agglomerates to be formed, which also makes stir mixing into a melt impractical. Furthermore, many handling procedures lead to fine fibres becoming airborne, creating a risk of inhalation, which is hazardous for whiskers (BIRCHALL *et al.* [1988]). The preform preparation procedures described above must be carried out within a glove box when whiskers are involved. One problem with fine fibres is that the pressures necessary to ensure that full infiltration occurs can become quite large. The pressure required can readily be calculated (CLYNE and MASON [1987]) on the basis of the necessary meniscus curvature, and corrections can be made (NOURBAKHSH *et al.* [1989]) for melt/fibre wetting which occurs during infiltration. In practice, substantial pressures of at least several MPa are likely to be needed with fine (~1 μm diameter) reinforcement. Hydrodynamic processes occurring during infiltration have also been analysed (LONG *et al.* [1994]). This work has highlighted the significance of inhomogeneities in the fibre distribution, air entrapment and premature solidification in influencing defect formation.

For most cases of interest the fibres do not act as preferential crystal nucleation sites during melt solidification (ROCHER *et al.* [1985]; CLYNE and MASON [1987]; MORTENSEN and CORNIE [1987]; LI *et al.* [1989]; MORTENSEN *et al.* [1993]). One consequence of this is that the last liquid to freeze, which is normally solute-enriched, tends to be located around the fibres. An example of this is shown in fig. 2. Such prolonged fibre/melt contact, often under high hydrostatic pressure and with solute enrichment, tends to favour formation of a strong interfacial bond. Also worth noting in this context is the question of oxide film formation. It might be expected with metals such as aluminium that an oxide film would repeatedly form at the infiltration front and become deposited on the fibres. In fact, at least with relatively fine fibres, it can be shown (CLYNE and MASON [1987]) that films of significant thickness (>atomic monolayer) cannot form because of the limited oxygen availability in the system, and this is consistent with microanalysis data (CAPPELMAN *et al.* [1985]). The absence of oxide films is a noteworthy feature of squeeze cast material, which probably contributes to the high interfacial bond strengths commonly observed. Other forms of defect are, however,

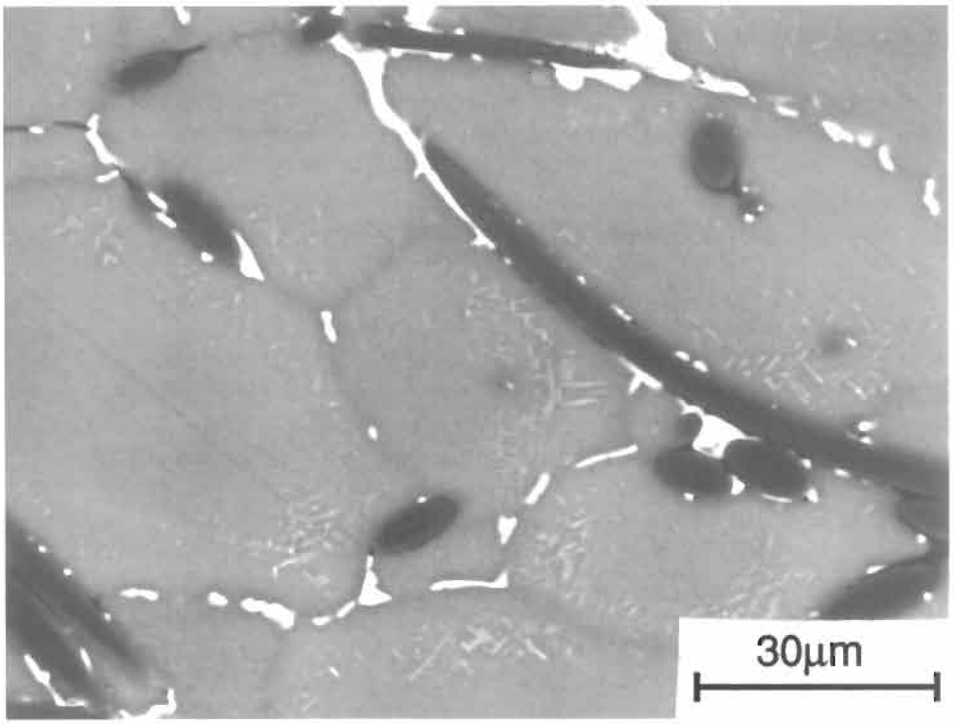

Fig. 2. Back-scattered SEM micrograph (CLYNE and WITHERS [1993]) of an Al–4.5wt%Cu/Saffil composite. The fibres appear dark in this image and the light (copper-rich) regions are concentrated around them (and at grain boundaries). These solute-enriched regions indicate the locations of the last-solidifying liquid, for solutes (such as copper in aluminium) which have a partition coefficient less than unity.

common in squeeze infiltrated composites. These include variations in fibre content and in average alloy composition, which have been correlated with process modelling predictions (JARRY *et al.* [1992]).

2.1.2. Stir casting

An attractively simple method of MMC manufacture involves stirring the liquid metal with solid ceramic particles and then allowing the mixture to solidify. The slurry can be continuously agitated while the ceramic is progressively added. This can in principle be done using fairly conventional processing equipment and can be carried out on a continuous or semi-continuous basis. This type of processing is now in commercial use for particulate Al-based composites (SKIBO *et al.* [1988]) and the material produced is suitable for further operations such as pressure die-casting (HOOVER [1991]). A primary concern during such processing is with ensuring that good particle *wetting* occurs. Various techniques have been developed to improve wetting of ceramic particles by liquid metals (ROHATGI *et al.* [1986]).

Some difficulties can arise from the increase in viscosity on adding particles or,

especially, fibres to a melt. However, this increase is only a factor of 2 or so with up to about 25vol.% particulate, provided the particles remain well-dispersed in suspension (KATTAMIS and CORNIE [1988]; LLOYD [1988]). This viscosity is sufficiently low to allow fairly conventional casting operations to be carried out. Usually of greater concern are the potential sources of microstructural inhomogeneity, including particle agglomeration and sedimentation in the melt and redistribution as a result of *particle pushing* by an advancing solidification front, which is still poorly understood and can be difficult to eliminate. A typical microstructure (LLOYD [1991]) illustrating the effect of particle pushing during solidification is shown in fig. 3.

This type of inhomogeneity is reduced when solidification is rapid, both as a result of a refinement in the scale of the structure and because there is a critical growth velocity, above which solid particles should be enveloped rather than pushed (STEFANESCU *et al.* [1988]; POTSCHKE and ROGGE [1989]). Pushing is caused by a *disjointing force* exerted on the particle by the advancing front if the total interfacial energy would be raised by formation of a solid/particle interface. This is a simple thermodynamic effect, but modelling of the pushing process is complicated by various phenomena which might influence the net retarding force acting on the particle. These include the requirement for liquid to flow around the particle and into the narrow channel between particle and solidification front, which gives rise to a viscous drag force. Other effects include the disturbance to the heat flow and solute redistribution processes and the presence of buoyancy forces. Further complications arise from the presence of neighbouring particles, which is expected to oppose pushing by inhibiting the required liquid flow. A simple correction to the liquid viscosity in the viscous drag term may, however, be inappropriate, depending on whether it is the supply of liquid to the general area of the front or flow within the particle/solid channel which is the critical process. The formation of cells or dendrites is also expected to favour engulfment, although particles may then be pushed laterally by the thickening cells or dendrite arms (see fig. 3).

Several models (UHLMANN *et al.* [1964]; BOLLING and CISSE [1971]; STEFANESCU *et al.* [1988]; POTSCHKE and ROGGE [1989]) have been developed to describe particle pushing, but most of them result in underestimates of the interface velocity needed to cause engulfmant. In practice, ceramic particles in Al can apparently be pushed (KENNEDY and CLYNE [1991]) at surprisingly high velocities, up to the mm s^{-1} range. Other experimental work (LAJOYE and SUERY [1988]; ROHATGI *et al.* [1988]; (STEFANESCU *et al.* [1990]) is broadly consistent with the conclusion that pushing takes place readily in aluminium-based systems. While interfacial energy values are obviously relevant, it seems probable that pushing will also occur quite readily in particulate MMCs based on other metals. It is both predicted and observed (MCCOY and WAWNER [1988]) that finer particles are more readily pushed. (This is in contrast to sedimentation-driven segregation prior to casting, which is less pronounced for finer particles.)

Stir casting usually involves prolonged liquid–ceramic contact, which can cause substantial interfacial reaction. This has been studied in detail (SKIBO *et al.* [1988]; LLOYD [1989]) for Al–SiC, in which the formation of Al_4C_3 and Si can be extensive. This both degrades the final properties of the composite and raises the viscosity of the slurry, making subsequent casting difficult. The rate of reaction is reduced, and can

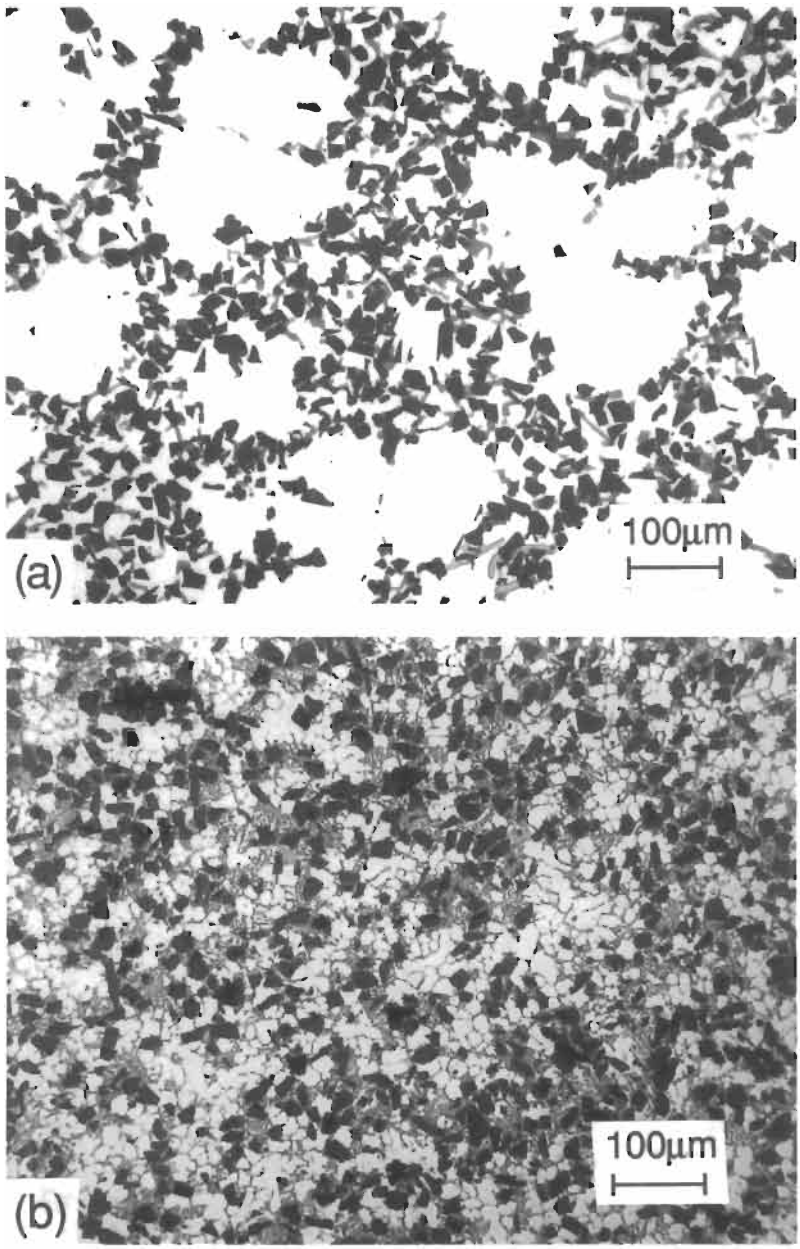

Fig. 3. Microstructures (LLOYD [1991]) of Al–7wt%Si/20vol%SiC particles, (a) investment cast (slow cooling) and (b) pressure die cast (rapid cooling). At the slower cooling rate, the SiC particles have been pushed into the interdendritic regions by the growing dendrites, causing severe clustering.

References: p. 2616.

become zero, if the melt is Si-rich, either by prior alloying or as a result of the reaction. The reaction kinetics and Si levels needed to eliminate it are such that it has been concluded (LLOYD [1989]) that casting of Al–SiC_p involving prolonged melt holding operations is suited to conventional (high Si) casting alloys, but not to most wrought alloys. There are few systematic data available on reaction during stir casting with other systems, but evidently problems would arise in many cases.

2.1.3. Spray deposition

Several processes have evolved in which metallic droplets impinge on a substrate so as to build up a composite deposit. The reinforcement can be fed into the spray, if particulate, or introduced onto the substrate in some way, if fibrous. The techniques employed fall into two distinct classes, depending whether the droplet stream is produced from a molten bath, or by continuous feeding of cold metal into a zone of rapid heat injection. A review is available (SRIVATSAN and LAVERNIA [1992]) covering both types of process and microstructural features of the products. In general, spray deposition methods lead to significant porosity levels and difficulties in obtaining homogeneous distributions of reinforcement.

Spray deposition was developed by Osprey Ltd (Neath, UK) as a method of building up bulk metallic material by directing an atomised stream of droplets onto a substrate. Many such processes are covered by their patents or licences and are now generally referred to as *Osprey Processes* (EVANS *et al.* [1985]; LEATHAM *et al.* [1989]). Adaptation to particulate MMC production by injection of ceramic powder into the spray has been extensively explored (WILLIS [1988]; WHITE *et al.* [1990]), although with limited commercial success. Droplet velocities typically average (GRANT and CANTOR [1989]) about 20–40 $m\,s^{-1}$, giving flight times around a few tens of ms. This is shorter than expected freezing times, so that that most droplets do not freeze in flight and a thin layer of liquid, or semi-solid, is often present on the top of the ingot as it forms. The solidification rate, although high, is therefore considerably lower than in many Rapid Solidification Processes.

MMC material produced by the Osprey route tends to exhibit inhomogeneous distributions of the ceramic particles. Ceramic-rich layers approximately normal to the overall growth direction are often seen. This may be the result of hydrodynamic instabilities in the powder injection and flight patterns or possibly to the repeated pushing of particles by the advancing solidification front (§ 2.1.2) in the liquid or semi-solid layer, until the ceramic content is too high for this to continue. Among the other microstructural features of Osprey MMC material are a strong interfacial bond, little or no interfacial reaction layer and very low oxide content. Porosity in the as-sprayed state is typically about 5–10%.

Thermal spraying differs in several respects from melt atomization processes. Deposition rates (usually ~1 $g\,s^{-1}$) are slower, but particle velocities (~ 100–700 $m\,s^{-1}$) are higher. Quenching rates (MCPHERSON [1981]) for each individual splat are very high ($\geq 10^6 K\,s^{-1}$). Porosity levels are typically at least a few %. Thermal spraying onto arrays of fibres to form MMCs has received quite extensive attention (WESTFALL [1987]; BERNDT and YI [1989]; SMITH [1991]; CANTOR [1993]; ZHAO *et al.* [1993]; CLYNE and

ROBERTS [1995]). An attraction here is the possibility of producing composite material in an operation involving only very brief exposure to high temperatures. Provided the void content and distribution are such that full consolidation could be effected with little further heat treatment, this would allow problems of excessive fibre/matrix chemical reaction during processsing to be avoided — a particularly important objective for titanium-based MMCs.

Unfortunately, it has proved very difficult to spray onto fibre arrays so as to produce MMCs with acceptably low void contents (< 10%). To illustrate this, fig. 4 shows measured void contents in sprayed titanium-based composites as a function of the fibre spacing (ratio between the inter-fibre gap and the average droplet diameter), for three different droplet sizes. Several features are apparent from this plot. Firstly, for each particle size, the void content goes up as the spacing is decreased (fibre content increases). Secondly, this rise becomes pronounced at finer spacings; values of the gap/droplet ratio below about 5 lead to very high porosites. Finally, the void content is greater for the finer droplet sizes. This is because there is less lateral spreading of such droplets after they have passed between fibres.

The distribution of the voids within the composite deposits is illustrated by fig. 5, which shows low magnification SEM micrographs of the specimens with the widest fibre spacings (~ 550 μm gap), produced using coarse and fine powders. Much of the coarse

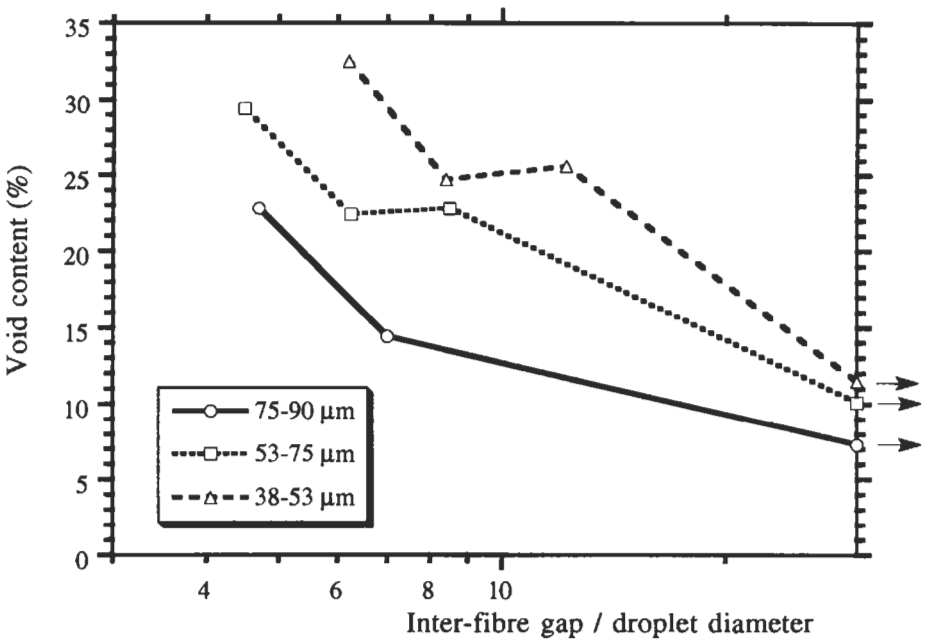

Fig. 4. Plot (CLYNE and ROBERTS [1995]) of measured average void content in vacuum plasma sprayed titanium/tungsten fibre composites, as a function of the ratio of the inter-fibre gap to the average droplet diameter, for three different particle size ranges.

References: p. 2616.

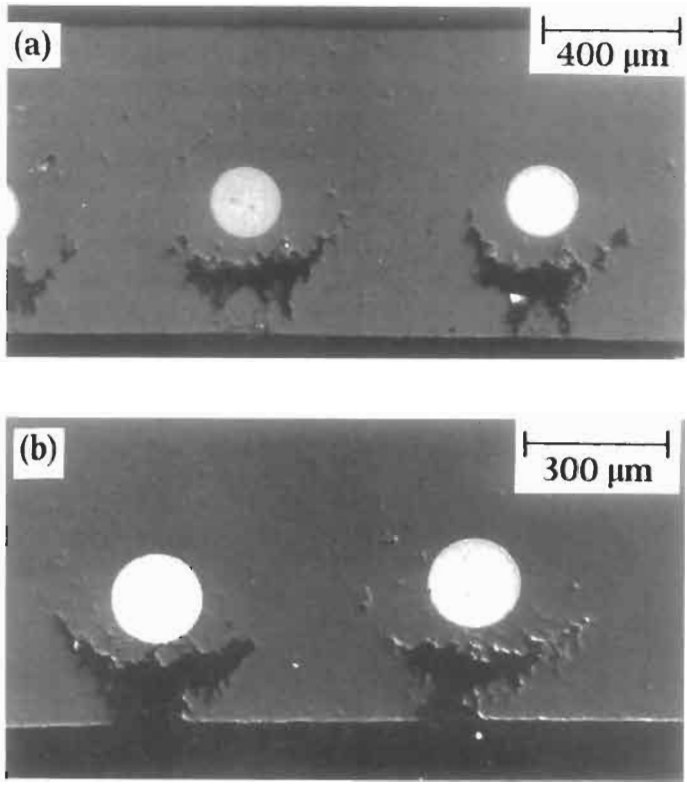

Fig. 5. Scanning electron micrographs (CLYNE and ROBERTS [1995]) of polished transverse sections from sprayed titanium on tungsten fibre specimens having inter-fibre spacings of about 550 μm, with powder sizes of (a) 75–90 μm and (b) 38–53 μm.

porosity is localised in the "shadow" of the fibres, but the fibres themselves appear to have been fairly well enveloped and the large voids are located a few tens of μm below the fibres. This is apparently a consequence (CLYNE and ROBERTS [1995]) of some droplets striking the flanks of the fibres and remaining in contact with the fibre surface as they enter the shadow region. Such large local voids are highly undesirable, since substantial hot pressing operations are required for their removal. In general, the problems of high void contents, fibre damage and inhomogeneous fibre distributions have severely limited the commercial development of this route.

2.1.4. Reactive processing

Several similar processes have been developed in which constituents are brought together under conditions such that a chemical reaction occurs while the mixture consolidates. In many such processes, liquid metal is introduced and progressively

oxidises. For example, the *directional oxidation* of aluminium is exploited in several processes patented under the "XD" tradename. An attraction of such procedures is that, by making a suitable powder compact into which liquid metal is infiltrated, near net shape forming is possible. Levels of internal stresses and porosity can be kept low by control over reaction kinetics, thermal gradients and liquid infiltration rates. In many cases, there is residual unreacted metal, so that an MMC is produced. Various composite systems have been developed, including several based on intermetallic matrices (STOLOFF and ALMAN [1990]). The oxidation reactions exploited by the *Lanxide Corporation* have been described (NEWKIRK *et al.* [1986]) and overviews presented of the materials and components produced by this type of processing (CHRISTODOULOU and BRUPBACHER [1990]; URQUHART [1991]).

2.2. Solid-state processing

2.2.1. Powder blending and consolidation

Blending of metallic powder and ceramic fibres or particulate is a versatile technique for MMC production. Among the obvious advantages is scope for close control over the ceramic content. The blending can be carried out dry or in liquid suspension. This is usually followed by cold compaction, canning, evacuation, degassing and a high temperature consolidation stage such as Hot Isostatic Pressing (HIP) or extrusion. Some information has been published concerning these procedures (JHA *et al.* [1989]; MCLEOD *et al.* [1989]; UPADHYAYA [1989]), with at least one report (NIKLAS *et al.* [1991]) that HIPing gives rise to a higher interfacial bond strength and hence improved properties. It can be difficult to achieve a homogeneous mixture during blending (HAAR and DUSZCZYK [1991]; RACK [1991]), particularly with fibres (and especially whiskers), which tend to persist in the form of tangled agglomerates with interstitial spaces which are too small for the penetration of matrix particles. The relative size of metal and ceramic particles has also been identified (HUNT *et al.* [1987]) as significant during blending of powder route particulate MMCs.

A feature of much powder route material is the presence of fine oxide particles, usually present in Al–MMCs in the form of plate-like particles a few tens of nm thick, constituting about 0.05–0.5vol%, depending on powder history and processing conditions (HANSEN and JENSEN [1990]; WHITEHOUSE *et al.* [1991]). This fine oxide tends to act as a dispersion strengthening agent and often has a strong influence on the matrix properties, particularly at high temperature (see § 5.2).

Extrusion is commonly carried out on discontinuous MMCs produced by powder blending. Generally, extrusion pressures required are higher than for unreinforced material and heating during the process is more rapid, leading to greater limitations on extrusion speed to avoid liquation and surface tearing (BRUSETHAUG *et al.* [1990]). A primary interest centres on the microstructural changes induced during the process. There is scope for alignment of fibres parallel to the extrusion axis, but at the expense of progressive *fibre fragmentation*. It has been shown (STANFORD-BEALE and CLYNE [1989]) that the degree of fibre fracture decreases with increasing temperature and decreasing local strain rate. This can be explained in terms of the kinetics of the stress relaxation

processes, which act to limit the build-up of tensile stress within the fibre.

Other microstructural features of extruded MMCs include the formation in some cases of ceramic-enriched *bands* parallel to the extrusion axis. Examples (SHAHANI [1991]) of slight and more severe banding in particle-reinforced aluminium are shown in fig. 6. The mechanism of band formation is still unclear, but it appears to involve the concentration of shear strain in regions where ceramic particles or fibres accumulate. A proposed mechanism (EHRSTROM and KOOL [1988]) involves migration of particles down gradients

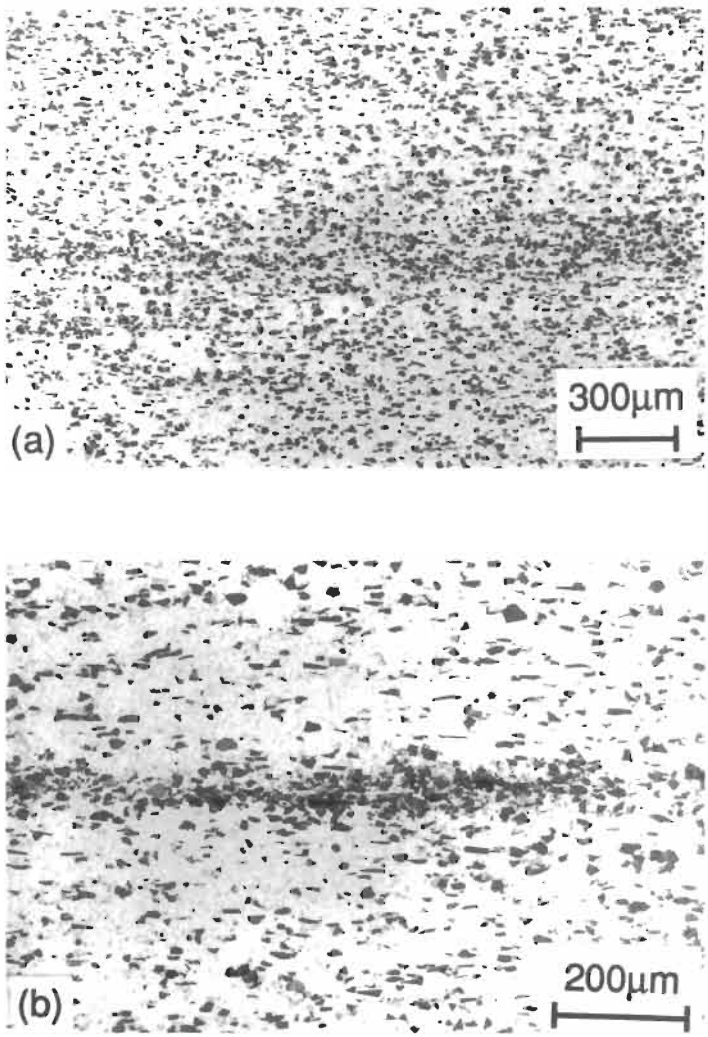

Fig. 6. Formation of ceramic-rich bands during extrusion of particulate composites based on commercial purity aluminium (SHAHANI [1991]). (a) slight banding and (b) a more severe occurrence, with cavitation occurring within the band.

of matrix flow stress, associated with thermal gradients caused by local generation of heat in regions of higher ceramic content. This would amplify existing composition fluctuations, although it is clear that the flow trajectories and local strain rate variations, which are controlled by the die shape and extrusion conditions, strongly affect band formation. However, extrusion of consolidated MMCs, such as castings, can *reduce* the level of clustering and inhomogeneities in the material (DUTTA *et al.* [1990]).

In general, the microstructural effects observed in MMCs after various conventional forming processes are explicable in terms of local temperatures, stresses and strain rates. Processes such as rolling and forging involve high deviatoric strains being imposed quickly, and hence readily cause damage such as cavitation, particle fracture and macroscopic cracking, particularly at low temperature. *Rolling* in particular involves high local strain rates, often with sharp reductions in temperature caused by contact with cold rolls, and is generally unsuitable for consolidation operations. *Forging* is more easily carried out at relatively low strain rates and elevated temperatures. Very high temperatures, and the possibility of matrix liquation, on the other hand, can cause macroscopic defects such as *hot tearing* or *hot shortness*.

In contrast to these forming processes, *Hot Isostatic Pressing* (HIPing) generates no (volume-averaged) deviatoric stresses and so is unlikely to give rise to either microstructural or macroscopic defects. It is an attractive method for removing residual porosity, which can include surface-connected porosity as long as some form of encapsulation is provided. It has been quite widely applied to MMCs (ITO *et al.* [1989]; MORITZ [1989]). However, it can be very difficult to remove residual porosity in regions of very high ceramic content, such as within particle clusters and the absence of any macroscopic shear stresses means that such clusters are not readily dispersed during HIPing.

2.2.2. Diffusion bonding of foils

Titanium reinforced with long fibres is commercially produced by the placement of arrays of fibres between thin metallic foils, often involving a *filament winding* operation, followed by *hot pressing*. The plastic flow taking place during pressing has been analysed (CHANG and SCALA [1974]) and it has been shown both experimentally and theoretically that the pressure required for consolidation is independent of the fibre volume fraction. They also predicted that the pressure required rises with increasing coefficient of friction between the contacting surfaces. Matrix creep characteristics and factors affecting surface oxide film durability are also likely to be important. The procedure is attractive for titanium since it dissolves its own oxide (KASAKOV [1985]) at temperatures above about 700°C and the rapid interfacial chemical reaction (MARTINEAU *et al.* [1984]; WHEATLEY and WAWNER [1985]) caused by contact between liquid Ti and ceramics is avoided.

Progressive removal of porosity during the process is illustrated (GUO and DERBY [1993]) by fig. 7, from which it can be seen that consolidation is typically complete in less than an hour at 870°C. More severe conditions might be required in order to ensure good bonding between foils and at the fibre-matrix interface. In general, one of the main problems lies in avoiding excessive *chemical reaction* at this interface, which tends to lead to embrittlement (see § 4.1). Additions of Al, Mo or V slow the kinetics of

References: p. 2616.

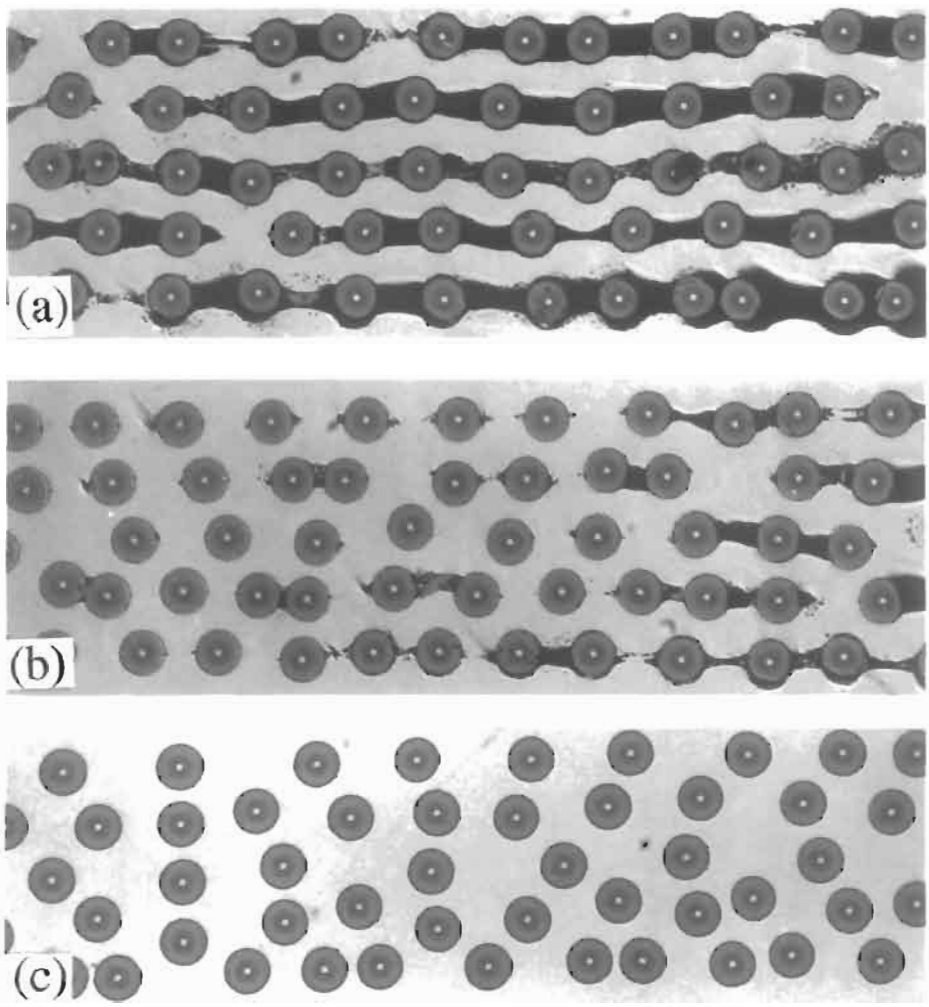

Fig. 7. Optical micrographs (GUO and DERBY [1993]) of a Ti–6Al–4V composite containing about 30 vol% of SiC monofilament, during hot pressing of a five-ply lay-up at 870°C under an applied pressure of 20 MPa. Pressing times were (a) 1 minute, (b) 8 minutes and (c) 40 minutes. The fibres are 100 μm in diameter and have tungsten cores, which appear light in these images.

interfacial reaction (SMITH and FROES [1984]), but also tend to make the rolling of thin foils more difficult. Introduction of nickel allows reduced diffusion bonding temperatures (RHODES *et al.* [1987]), but also leads to formation of coarse intermetallics such as Ti_2Ni, which impairs the mechanical properties. There is considerable interest in *fibre coatings* (KIESCHKE *et al.* [1991]; WARWICK and SMITH [1991]; UPADYAYA *et al.* [1994]) designed to reduce these problems of interfacial attack.

In general the diffusion bonding procedure is rather cumbersome and there can be

difficulties in obtaining very high fibre volume fractions and homogeneous fibre distributions. Good process control is necessary if fibre-fibre contact or close approach (see fig. 7) is to be avoided. This is important in view of the danger of such defects causing premature failure (see §4.1.2). Diffusion bonding has also been used (CHEN and MECHOLSKY [1993]) to fabricate laminates composed of alternate layers of metal and ceramic. These materials offer potential for good combinations of toughness, stiffness and creep resistance.

2.2.3. Physical vapour deposition (PVD)

Several PVD processes have been used in fabrication of MMCs (EVERETT [1991]). All PVD processes are relatively slow, but the fastest is *evaporation* — involving *thermal vaporisation* of the target species in a relatively high vacuum. An evaporation process used (WARD-CLOSE and PARTRIDGE [1990]) for fabrication of long fibre reinforced titanium involves continuous passage of fibre through a region having a high partial vapour pressure of the metal to be deposited, where condensation takes place so as to produce a relatively thick coating on the fibre. The vapour is produced by directing a high power (~10 kW) electron beam onto the end of a solid bar feedstock.

One advantage of the technique is that a wide range of alloy compositions can be used; differences in evaporation rate between different solutes become compensated by changes in composition of the molten pool formed on the end of the bar until a steady state is reached in which the alloy content of the deposit is the same as that of the feedstock. Titanium and aluminium alloys and Ti–Al intermetallic compounds have been deposited (WARD-CLOSE and PARTRIDGE [1990]). A further point worthy of note is that there is little or no mechanical disturbance of the interfacial region; this may be of significance when the fibres have a diffusion barrier layer, or a tailored surface chemistry, which might be degraded by the droplet impacts in spray deposition (§ 2.1.3) or the frictional motion in diffusion bonding (§ 2.2.2). Typical deposition rates are ~5–10 μm min^{-1}. Composite fabrication is usually completed by assembling the coated fibres into a bundle and consolidating this in a hot pressing or HIPing operation. A very uniform distribution of fibres is produced in this way, with fibre contents of up to about 80%. A typical coated fibre and consolidated titanium composite are shown in fig. 8. The fibre volume fraction can be accurately controlled via the thickness of the deposited coatings and the fibre distribution is always very homogeneous. This production route is currently being developed, particularly for hoop-wound components in titanium alloys.

3. *Deformation behaviour*

3.1. Elastic properties

Various models (CLYNE and WITHERS [1993]) have been developed for prediction of the elastic constants of fibre composites. Of the analytical models available, that of *Eshelby* (ESHELBY [1957]) gives predictions which are closest to those from numerical treatments and which can usually be considered as reliable, at least for reinforcement contents up to about 50%. The model is based on assuming the reinforcement to be in

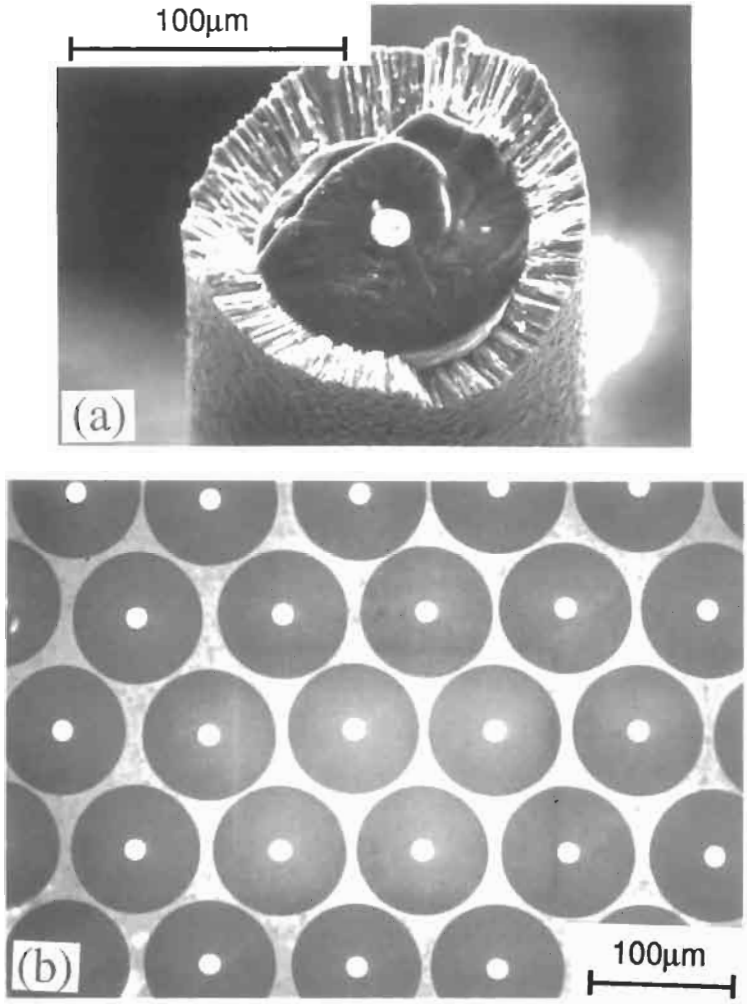

Fig. 8. (a) A SiC monofilament with a 35 μm vapour-deposited layer of Ti–5Al–5V and (b) A Ti–5Al–5V–80 vol%SiC composite produced by HIPing of a bundle of monofilaments with 8μm thick coatings (WARD-CLOSE and PARTRIDGE [1990]).

the shape of an *ellipsoid*. Stresses arise from the imposition of a *misfit strain* between the natural shape of the ellipsoid and that of the hole into which it fits. Such a misfit arises, for example, when an external tensile load is applied, since the natural extension of the (stiffer) reinforcement is less than that of the matrix and hence of the hole. The stress in the reinforcement, which is uniform throughout its volume provided it has an ellipsoidal shape, can be calculated from the misfit strain. Since only the *volume-averaged* partitioning of load between reinforcement and matrix needs to be quantified in order to establish the macroscopic strains, this allows the elastic constants to be established. The resulting equation for the *stiffness tensor* of the composite is

$$C_C = \left[C_m^{-1} - f\{(C_f - C_m)[S - f(S - I)] + C_m\}^{-1}(C_f - C_m)C_m^{-1}\right]^{-1} \quad (1)$$

where C_f and C_m are the stiffnesses of fibre and matrix, f is the fibre volume fraction, I is the identity tensor and S is the *Eshelby tensor* (dependent only on the aspect ratio of the ellipsoid and the Poisson ratio of the matrix).

The elastic constants of metals containing various types of ceramic reinforcement can be explored using this equation. Interest often centres on the *Young's modulus*. Experimental data (McDANELS [1985]) are shown in fig. 9 for the Young's modulus of extruded Al–SiC_p composites loaded in the extrusion direction, together with predictions for aspect ratios of 1 and 2. It can be seen that the experimental data lie between the two predicted plots. Since the particles are not equiaxed, and become aligned with their long axis along the extrusion direction during processing (see fig. 6), these data follow the expected trends. Useful increases in stiffness of 20–30% can be obtained in this system with about 20% of reinforcement, a level at which reasonably high toughness and ductility can be retained (see § 4.1.2 and 4.2.1). It should be mentioned, however, that experimental measurement of Young's modulus requires some care (PRANGNELL *et al.*

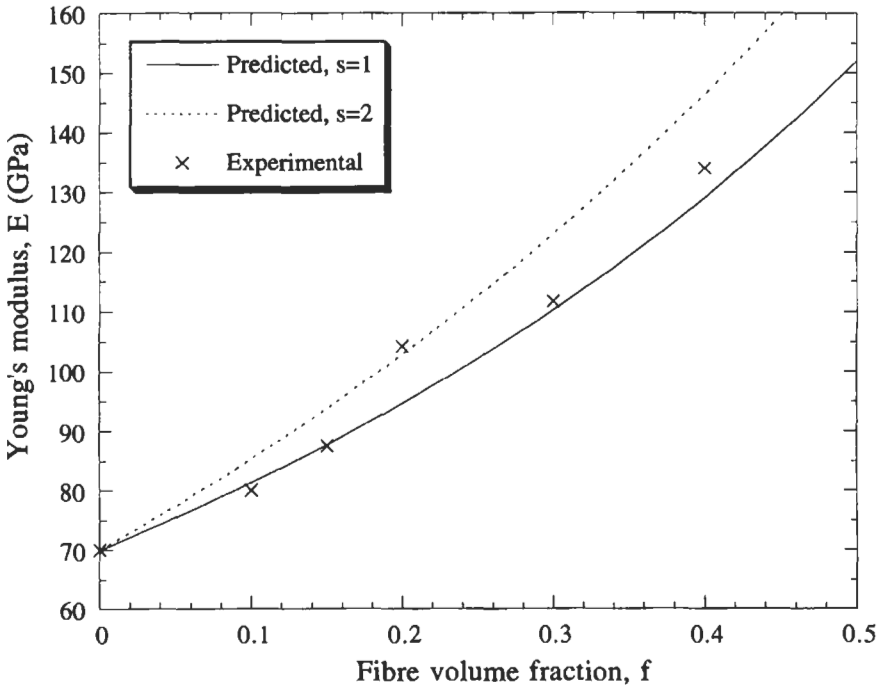

Fig. 9. Comparison between experimental data (McDANELS [1985]) and predictions from the Eshelby model for the Young's modulus of aluminium reinforced with SiC particulate. Experimental results are for the axial stiffness of extruded material. Predictions are shown for aspect ratios of 1 and 2, since the particles usually exhibit values in this range and tend to be aligned in the extrusion direction.

References: p. 2616.

[1994]), since early local yielding (§ 3.2.1) can affect many measurements.

For fibre-reinforced metals, there is interest in the effect of *fibre aspect ratio* and in the *transverse properties*. Predicted plots are shown in fig. 10a for the Young's modulus of aluminium reinforced with SiC whiskers, as a function of fibre aspect ratio. It can be seen that the stiffness rises sharply at first as the aspect ratio is increased. A value of about 10 gives a stiffness quite close to the continuous fibre case. (Higher values than this are needed to reach this regime in polymer composites.) Transverse properties are also of interest. The data in fig. 10b show that the transverse stiffness is much lower than in the axial direction, but is insensitive to fibre aspect ratio. For a *planar random* array, the in-plane stiffness is not very much greater than the transverse stiffness of a unidirectional composite, although it does rise with fibre aspect ratio.

There is sometimes interest in the other elastic constants. For example, monitoring of the *Poisson ratio* values of long fibre-reinforced titanium and aluminium has proved useful for following the development of damage under load (MAJUMDAR and NEWAZ [1992]; MAJUMDAR *et al.* [1993]; SINGH and LEWANDOWSKI [1993]; WATSON and CLYNE [1993]). In fig. 11a, the two shear moduli of long fibre reinforced titanium are shown as a function of fibre content, together with the axial and transverse Young's moduli. It can be seen that the shear moduli are very close to each other, which is usually the case for fibre-reinforced metals. The Poisson ratio data shown in fig. 11b merit a brief discussion. As expected, the presence of the fibres causes a sharp drop in ν_{21} (the contraction parallel to the fibres divided by the transverse extension, when loaded transversely). This arises because the fibres (which are stiffer and have a lower Poisson ratio than the matrix) strongly inhibit this contraction. In compensation for this, however, there is a large contraction in the other transverse direction, giving rise to a relatively high value for ν_{23}. In fact, this effect is often so strong that the addition of fibres to the matrix can cause the value of ν_{23} to rise initially above the value for the unreinforced matrix.

3.2. Yielding and work hardening

3.2.1. Matrix flow

Prediction of the yielding and flow behaviour of a metal composite is relatively complex. One problem is that the presence of the reinforcement is likely to affect the microstructure of the matrix. For example, the *dislocation density* is likely to be higher as a result of the misfit strains from *differential thermal contraction* during cooling after fabrication (ARSENAULT and SHI [1986]; ARSENAULT *et al.* [1991]; ARSENAULT and ZHOU [1993]). This is likely to affect the yield stress directly and also indirectly in some cases via an influence on *precipitation characteristics* in age-hardening systems (MAHON *et al.* [1990]; CHAWLA *et al.* [1991]; PRANGNELL and STOBBS [1991]; LIN *et al.* [1993]) and possibly changes in *recrystallisation* behaviour (HUMPHREYS *et al.* [1990]; MILLER and HUMPHREYS [1991]).

In general, however, the changes induced in the inherent yielding and flow characteristics of the matrix as a result of the presence of the reinforcement are not of over-riding importance. The main features of the composite yielding behaviour can be rationalised

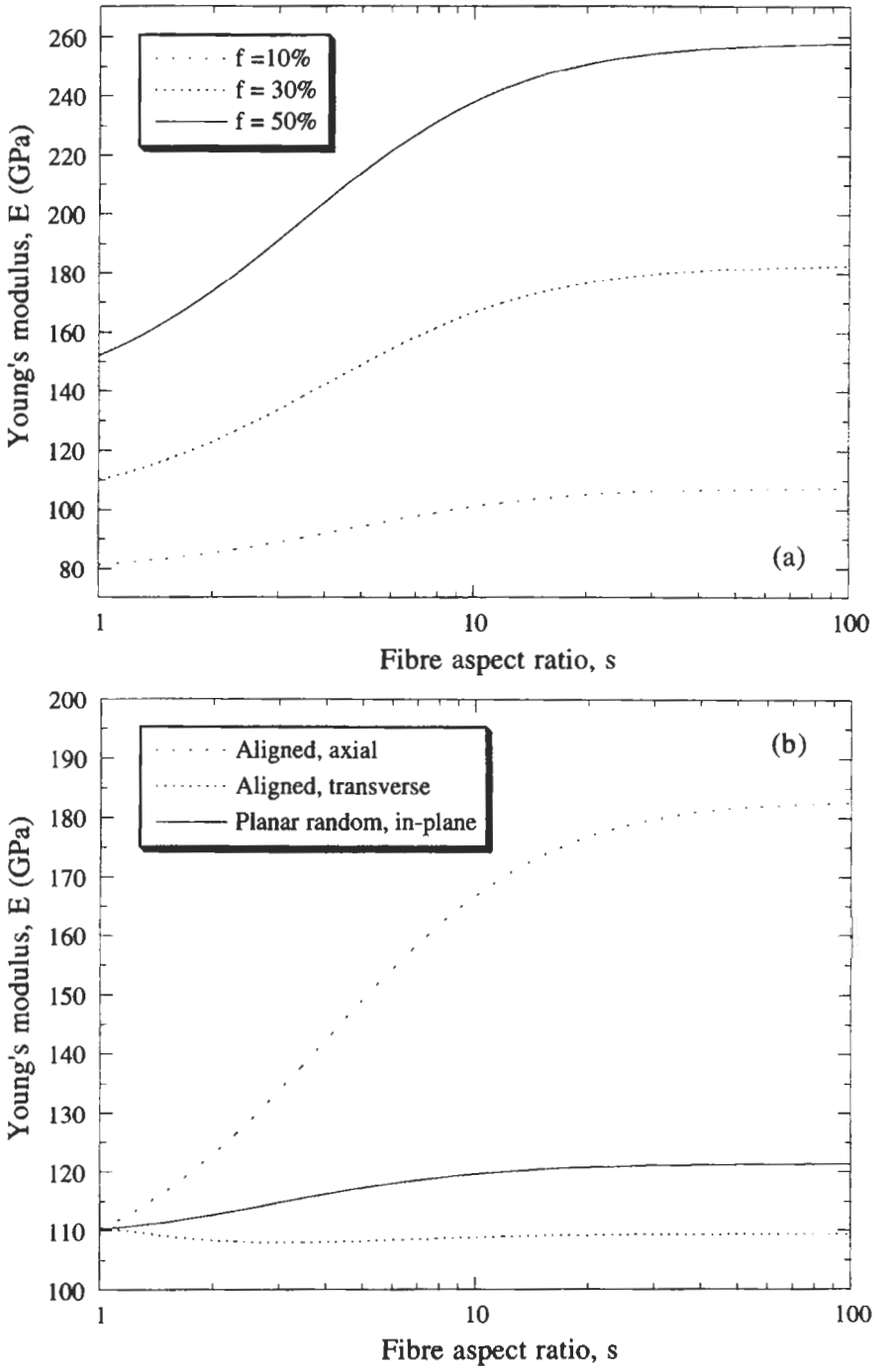

Fig. 10. Predictions from the Eshelby model for the Young's modulus of Al–SiC composites, as a function of the fibre aspect ratio. Plots are shown of (a) axial stiffness with aligned fibres for three fibre contents and (b) axial and transverse stiffness with aligned fibres, and in-plane stiffness with planar random fibres, for a fibre content of 30%.

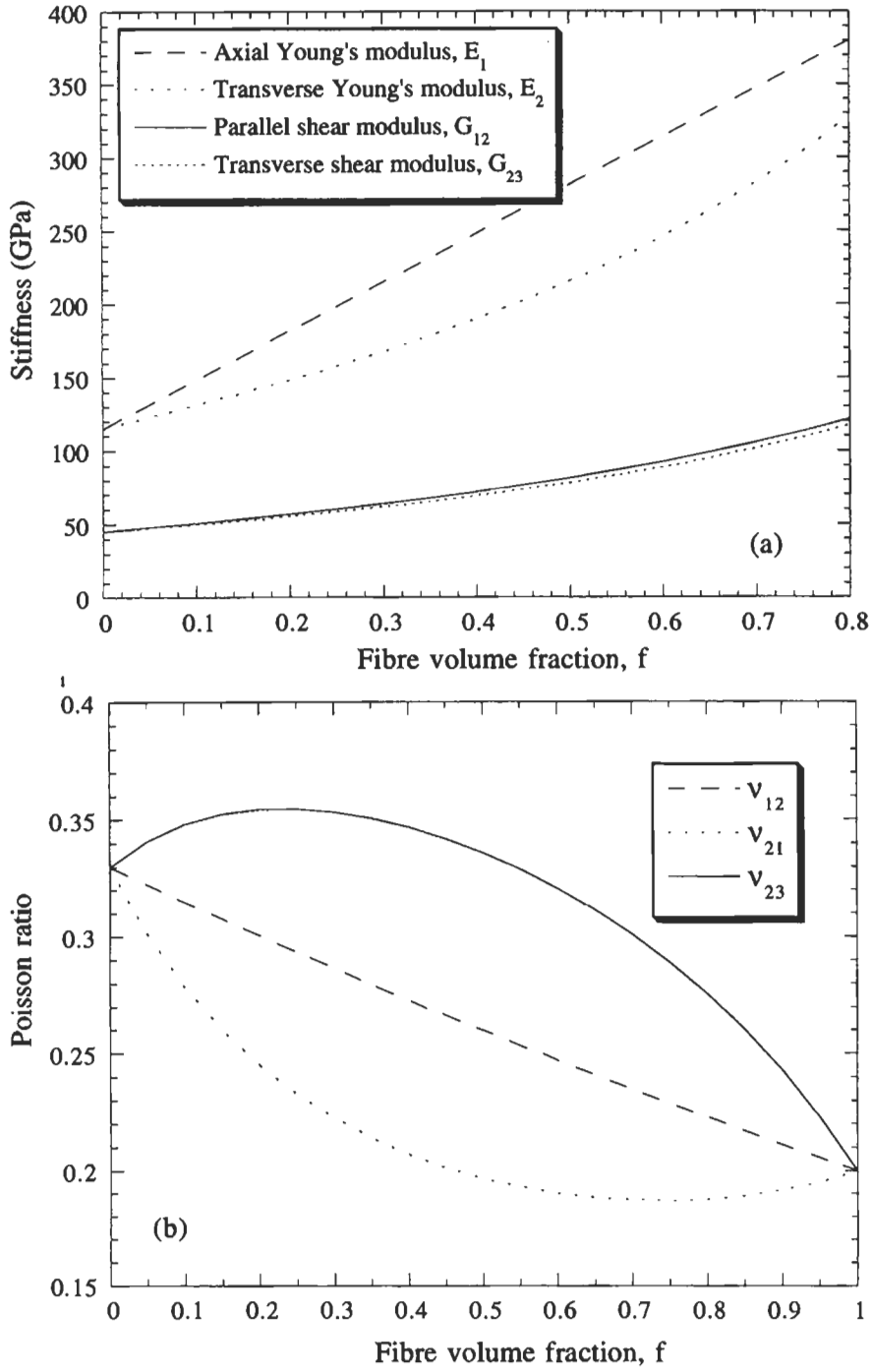

Fig. 11. Predictions from the Eshelby model for elastic constants of titanium reinforced with aligned long fibres of SiC, as a function of the fibre content. Plots are shown of (a) axial and transverse Young's moduli, and the two shear moduli and (b) the three Poisson ratios.

on the basis of the (volume-averaged) matrix stress field, which differs markedly from that in unreinforced metal under the same applied load. Broadly, matrix stresses are expected to be lower than in unreinforced metal, since *load transfer* occurs to the (stiffer) reinforcement. This delays yielding, giving MMCs higher yield stresses than unreinforced metals. However, in practice there are several factors related to matrix stress fields which may alter this simple picture.

The first point is that the stress field is very *inhomogeneous*. High matrix stresses are usually present adjacent to the reinforcement along the loading direction. This often gives rise to early *local plasticity* in such regions. There have been several *finite element method (FEM)* studies (CHRISTMAN *et al.* [1989]; LEVY and PAPAZIAN [1990]; ZAHL and MCMEEKING [1991]; CHOI and TAKAHASHI [1992]) of this effect. A predicted (CHRISTMAN *et al.* [1989]) plastic strain field adjacent to a short fibre is shown in fig. 12. Local plastic flow often starts at very low macroscopic strains (NIEH and CHELLMAN [1984]) — well below those at which the unreinforced matrix would start to yield. This effect can be accentuated by thermal residual stresses, since these are often tensile in the matrix (see § 3.2.2).

However, *macroscopic yielding* of the composite requires flow in large, contiguous volumes of matrix and usually occurs at appreciably higher loads than that at which local plasticity is initiated (PRANGNELL *et al.* [1994]). Moreover, while numerical modelling (CHRISTMAN *et al.* [1989]) has shown that *clustering* affects the work hardening behaviour, it is predicted to have little effect on yielding. It is therefore acceptable to treat macroscopic yielding on the basis of volume-averaged stresses in the matrix, as predicted, for example, using the Eshelby method. Under an applied load, σ_A, the average matrix stress is readily obtained from the (uniform) value in the reinforcement,

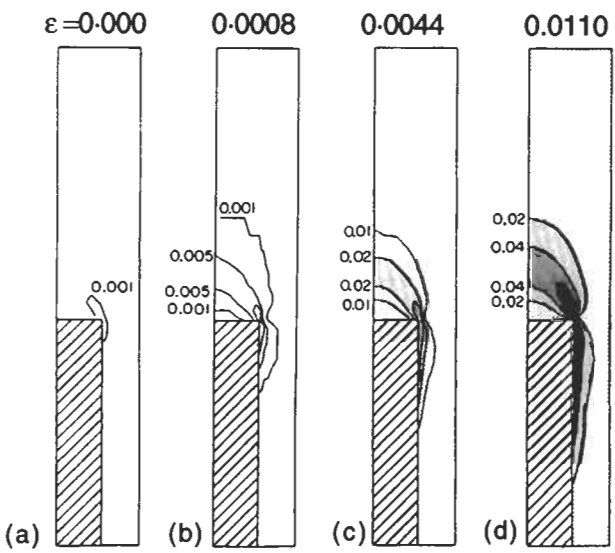

Fig. 12. Contours of plastic strain around the end of a short cylindrical fibre in an MMC, for different applied macroscopic strains, as predicted by finite element method (FEM) modelling (CHRISTMAN *et al.* [1989]).

by applying a simple force balance. This leads to the following expression (CLYNE and WITHERS [1993])

$$\sigma_m = \sigma_A - fC_m(S-I)\{(C_m - C_f)[S - f(S-I)] - C_m\}^{-1}(C_f - C_m)C_m^{-1}\sigma_A. \quad (2)$$

These matrix stresses scale with the applied stress and can therefore be plotted as ratios. Application of eq. (2) to particular systems allows the construction of graphs such as that shown in fig. 13, which refers to axial loading of an Al–SiC whisker composite having aligned fibres with an aspect ratio of 5. In the loading (1) direction, the ratio σ_m/σ_A falls below unity as the volume fraction of fibre rises, since the fibres are taking an increasing proportion of the applied load. In the transverse directions, however, the matrix stress rises slowly above zero as fibres are introduced, as a result of *differential Poisson contraction* effects. Using such plots, and applying a suitable yield criterion, an estimate can be made of the applied load at which macroscopic yielding would occur.

The case of *transverse loading* is slightly more complex, since the matrix stresses in the three principal directions are all different. A plot of these is shown in fig. 14, again for an Al–SiC ($s=5$) composite. The stress in the loading (2) direction is higher than for the axial loading case, since the fibres now take up the load less efficiently. The stresses in the other two directions again arise from inhibition of the matrix Poisson contraction, but this constraint occurs more strongly in the direction (1) of fibre alignment (cf fig. 11b), so that the matrix stress is higher in this direction. Again the onset of yielding can be predicted from such plots, assuming the in situ yield stress of the matrix is the same as that when unreinforced. An example of such a calculation is given in the next section.

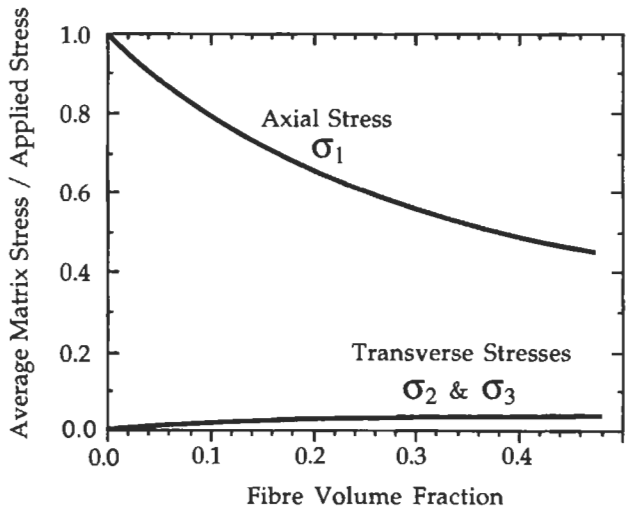

Fig. 13. Predictions from the Eshelby model for the volume-averaged matrix stresses in an Al–SiC composite, with fibres of aspect ratio 5, under an applied load along the direction (1) of fibre alignment. The matrix stresses are plotted as a ratio to the magnitude of the applied stress in the 1 direction.

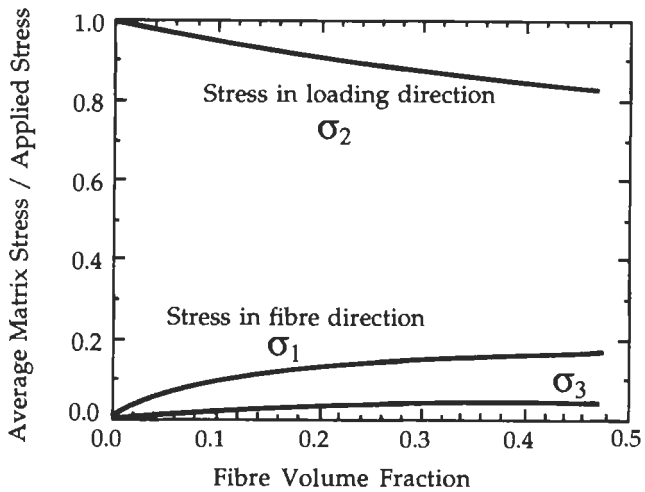

Fig. 14. Predictions from the Eshelby model for the volume-averaged matrix stresses in an Al–SiC_w composite, with fibres of aspect ratio 5, under an applied load in a direction (2) which is normal to that of fibre alignment. The matrix stresses are plotted as a ratio to the magnitude of the applied stress in the 2 direction.

3.2.2. Thermal stresses

It is well established (DESILVA [1969]; ARSENAULT and TAYA [1987]; WITHERS *et al.* [1989]; LEVY and PAPAZIAN [1990]) that the *residual stresses* from *differential thermal contraction* can affect the yielding behaviour of MMCs. Usually, the matrix is in residual tension overall at room temperature, since its contraction will have been inhibited by the reinforcement (assuming it to have the lower expansivity, i.e., $\alpha_m > \alpha_f$). If the reinforcement is in the form of equiaxed particles or randomly oriented fibres, then the volume-averaged matrix stress field will be isotropic. In such cases, thermal stresses cannot influence global yielding (although they can affect local plastic flow). However, if aligned fibres are present, then the average matrix stresses will be anisotropic and will thus affect the overall deviatoric stress and influence the yielding behaviour.

The average matrix stresses can again be evaluated using the Eshelby method, assuming elastic behaviour over a specified cooling interval. These stresses are given by the following equation (CLYNE and WITHERS [1993])

$$\sigma_m = -fC_m(S - I)\{(C_m - C_f)[S - f(S - I)] - C_m\}^{-1} C_f(\alpha_m - \alpha_f)\Delta T \tag{3}$$

in which ΔT is the temperature change to which the composite has been subjected. Predicted matrix stresses (per unit temperature drop) obtained using this equation are shown in fig. 15 for a Al–SiC ($s = 5$) system. Both axial and transverse matrix stresses are positive, since the fibres inhibit matrix contraction. The axial stresses are higher, since the fibres inhibit the contraction more effectively in the alignment direction.

In order to predict the effect on yielding, matrix stresses from a specified temperature change are superimposed on those from an external load. The applied stress level at

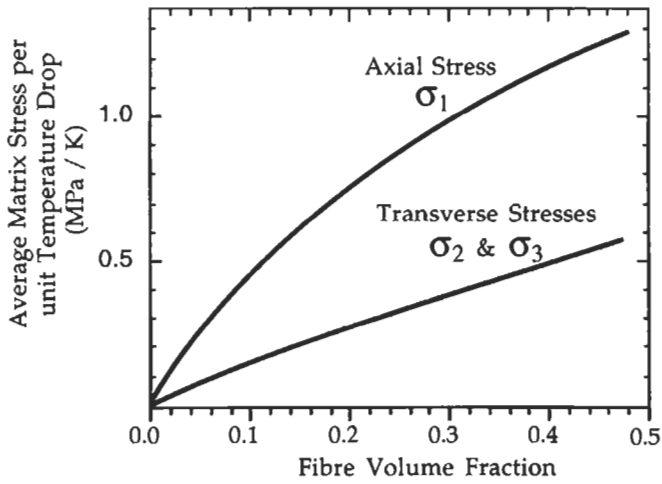

Fig. 15. Predictions from the Eshelby model for the volume-averaged matrix stresses in an Al–SiC composite, with fibres of aspect ratio 5, as a result of differential thermal contraction. The matrix stresses are given per degree of temperature decrease.

which a yielding criterion is satisfied may then be taken as the composite yield stress. Some values obtained in this way are shown in fig. 16, which compares measured (LEDERICH and SASTRY [1982]) and calculated yield stress data for an Al–20%SiC (whisker) composite loaded axially or transversely in tension or compression. The calculated values can be obtained by inspection of the plots in figs. 13–15. For example, consider the case of the transversely-oriented specimen under tensile load. The matrix stresses are obtained from fig. 14 and fig. 15 as

$$\sigma_1 \approx 0.13\sigma_A + 0.75\Delta T \tag{4}$$

$$\sigma_2 \approx 0.91\sigma_A + 0.28\Delta T \tag{5}$$

$$\sigma_3 \approx 0.04\sigma_A + 0.28\Delta T \tag{6}$$

These values are then substituted into the *von Mises yielding criterion*

$$(\sigma_1 - \sigma_2)^2 + (\sigma_2 - \sigma_3)^2 + (\sigma_3 - \sigma_1)^2 = 2\sigma_Y \tag{7}$$

where σ_Y is the yield stress of the unreinforced matrix. The actual temperature drop after fabrication of the composite was several hundred degrees. However, it is well established that stress relaxation processes (see § 3.2.3) act to reduce the thermal stresses, so that they correspond to a lower value than this. In the case of aluminium, an effective value of about 100 K is thought to be appropriate (WITHERS *et al.* [1989]). Solving eq. (7) on this basis then leads to an estimate for σ_A at yield of about 418 MPa, as shown in fig. 16. The other values were obtained similarly, using measured matrix yield stresses for corresponding unreinforced material (~ 340 MPa, except for transverse compression,

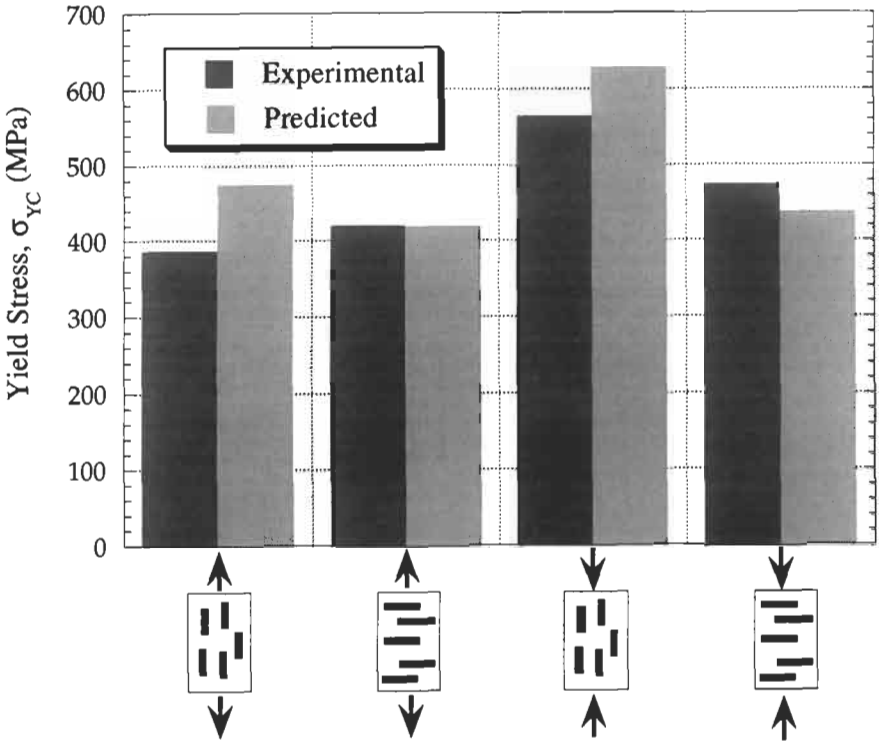

Fig. 16. Comparison between experimental yield stress data (LEDERICH and SASTRY [1982]) for Al(2024)–20 vol%SiC whisker composites, under four different loading geometries, and predictions obtained using the Eshelby model. The latter are based on application of the von Mises yield criterion to the volume-averaged matrix stresses, resulting from the applied load and from thermal mismatch strains corresponding to a temperature drop of 100 K. The whisker aspect ratio was taken as 5. The yield stress of the unreinforced matrix was ~ 340 MPa in (axial or transverse) tension and in axial compression and ~ 360 MPa in transverse compression.

which was ~ 360 MPa). The axial values are higher because of the more efficient load transfer. They show *tension/compression asymmetry*, since matrix thermal stresses are tensile in this direction. Under transverse loading, on the other hand, there is no asymmetry between tensile and compressive loading (except for that due to the difference in matrix yield stress).

In view of the various sources of error involved, the agreement shown in fig. 16 is quite encouraging. The comparison is, however, rather limited. Unfortunately, experimental data of this type, covering a range of loading geometries, are in short supply. There are often difficulties in carrying out the compression testing and in obtaining specimens suitable for transverse testing. It may also be noted that some FEM modelling (POVIRK *et al.* [1991]; ZAHL and MCMEEKING [1991]; POVIRK *et al.* [1992]) has suggested that the effect of thermal stresses on the onset of global yielding should be relatively small. Such

predictions are not strongly supported by experimental data, although there is good agreement with neutron diffraction data for residual strains, at least for fibrous MMCs (POVIRK *et al.* [1992]). It has been confirmed (DAYMOND and WITHERS [1995]) by FEM calculations oriented towards experimental data for whisker-reinforced aluminium that thermal stresses do make a significant contribution to the tensile/compressive asymmetry in global yielding. Discrepancies between FEM and ESHELBY predictions may highlight a limitation of using volume-averaged stresses to predict the behaviour. A general conclusion, however, is that the introduction of reinforcement can raise the yield stress significantly and that this strengthening is broadly predictable, provided that loading geometry and residual stresses are taken into account.

3.2.3. Work hardening and stress relaxation

The presence of reinforcing particles or fibres can have a substantial effect on the way that the applied load changes with strain after the onset of macroscopic yielding. In general, assuming that the reinforcement remains elastic, the work hardening rate exhibited by the composite is appreciably higher than that of the corresponding unreinforced metal. In exploring this, it is convenient to assume that the matrix itself has *no work hardening capacity*, so that it deforms in an elastic/perfectly plastic manner. In practice, this will be inaccurate, but inherent matrix work hardening can be taken into account as a contribution which is additive to that caused by the presence of the reinforcement. On this basis, the behaviour can be examined in terms of the matrix stress field during plastic deformation, in a similar manner to that of the previous two sections concerned with yielding. As in that case, differences in matrix microstructure attributable to the presence of the reinforcement may complicate the issue, but such effects are usually of secondary importance.

The following treatment is concerned with the volume-averaged stress in the matrix, which is again conveniently obtained by using the Eshelby method. Consider the case of a composite reinforced with an array of spheres being subjected to uniaxial tension. After the onset of global yielding, it may be assumed that deformation occurs only by plastic deformation of the matrix, the strain being homogeneously distributed throughout the matrix. A finite (plastic) extension of the composite as a whole will involve corresponding extensions to the holes containing the reinforcement. These holes will therefore tend to become ellipsoidal in shape. If the interface is to remain intact, the spheres must therefore become (elastically) extended, so that a tensile stress is generated in them. In order to satisfy the *force balance*, the matrix must be subject to a stress which is compressive when averaged over its volume (although regions adjacent to the spheres along the direction of straining will be under tension). This load transfer is analogous to that which occurs elastically as a result of *modulus mismatch* under an applied load. Its effect is to reduce the overall tensile stress in the matrix (which was responsible for the plastic flow) and hence to postpone further plastic deformation to higher applied loads — i.e., to promote work hardening. As with the elastic case, this load transfer is more efficient if the reinforcement is in the form of fibres aligned parallel to the applied stress.

Quantification of this effect is based on the following expression for the change in matrix stress as a result of an imposed plastic strain, ε_{mp}

$$\Delta\sigma_{mp} = -fC_m(S-I)\{(C_m - C_f)[S - f(S-I)] - C_m\}^{-1} C_f \varepsilon_{mp}. \quad (8)$$

Note the similarity to eq. (3), with the plastic strain being analogous to a thermal misfit strain given by $(\alpha_m - \alpha_f)\Delta T$. Predictions from this equation are shown in fig. 17, for an aluminium matrix reinforced with SiC fibres having an aspect ratio, s, of 5, being loaded in the fibre (1) direction. It can be seen that, as plastic deformation occurs, the matrix stress becomes highly compressive in the fibre direction, with the fibres correspondingly loaded in tension. Stresses in the transverse directions, which are due to Poisson effects, are relatively low.

These data are readily translated into predictions of *work hardening rates*. For example, consider the Al–20%SiC ($s=5$) composite taken above as an example case. By combining data from figs. 13 and 17, the matrix stresses under an applied load σ_A after a matrix plastic strain of ε_{mp} in the 1 direction can be written as

$$\sigma_1 \approx 0.63\sigma_A - 37\varepsilon_{mp} \quad (9)$$

$$\sigma_2 = \sigma_3 \approx 0.015\sigma_A + 2\varepsilon_{mp} \quad (10)$$

where the units are such that the stresses are in GPa. Application of the von Mises criterion (eq. 7) then leads to

$$\sigma_Y = 0.615\sigma_A - 39\varepsilon_{mp}. \quad (11)$$

Rearranging this equation and differentiating then leads to an expression for the work hardening rate

$$\frac{\partial\sigma_A}{\partial\varepsilon_{mp}} = \frac{39}{0.615} = 63\text{GPa} \quad (12)$$

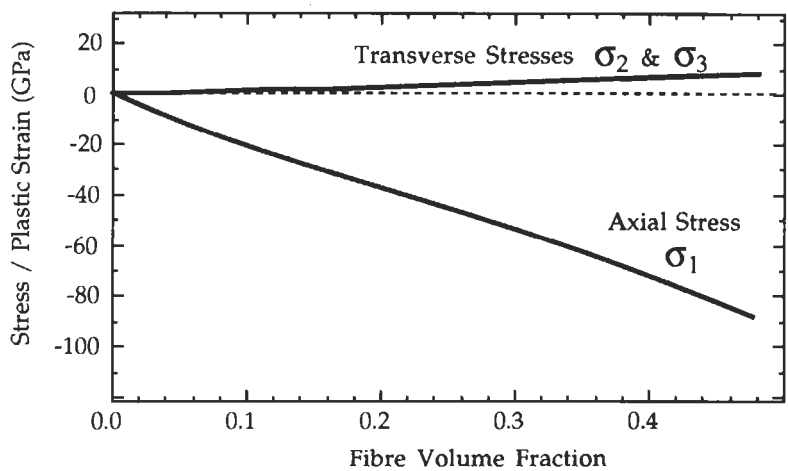

Fig. 17. Predictions from the Eshelby model for the volume-averaged matrix stresses in an Al–SiC_w composite, with fibres of aspect ratio 5, as a result of plastic deformation of the matrix. The matrix stresses are given per unit plastic strain in the loading (1) direction, which is that in which the fibres are aligned.

References: p. 2616.

Strictly, a correction involving the fibre volume fraction is needed in order to convert this to a rate of increase of applied stress per unit composite strain. However, such details are of secondary importance, since they do not affect the obvious conclusion that this is an extremely high work hardening rate (about half of the elastic modulus). Lower values would be obtained for particles and for lower volume fractions, but calculation for those cases still indicates much higher rates than are actually observed, at least when evaluated over appreciables ranges of plastic strain. Typical experimental work hardening rates for Al-based particulate MMCs, with a soft matrix showing little or no intrinsic work hardening capacity, are of the order of 1 GPa.

Experimentally observed work hardening rates are usually much lower than those suggested by these calculations as a result of the operation of various *stress relaxation mechanisms*. These include *fibre fracture*, *interfacial debonding*, *interfacial sliding*, *matrix cavitation* and *matrix creep processes*. *Plastic punching* of dislocations (DUNAND and MORTENSEN [1991]; DUNAND and MORTENSEN [1991]; TAYA *et al.* [1991]) also has the effect of reducing the misfit strain around the reinforcement. These phenomena all reduce the tensile stress in the fibre and hence the associated matrix compression and the work hardening rate. It is not surprising that such processes tend to be triggered, since the fibre stresses, and the stress gradients in the matrix, associated with matrix plasticity can easily become very large. In the example composite cited above, a matrix plastic strain of 1% would generate a fibre stress of 1.48 GPa. This is a large stress and, since the matrix stress at the fibre ends must be similar, it is not surprising that various inelastic processs are likely to be triggered at low plastic strains. The net effect is to produce a stress/strain plot of the form shown schematically in fig. 18.

Experimental work hardening data for MMCs are generally consistent with this

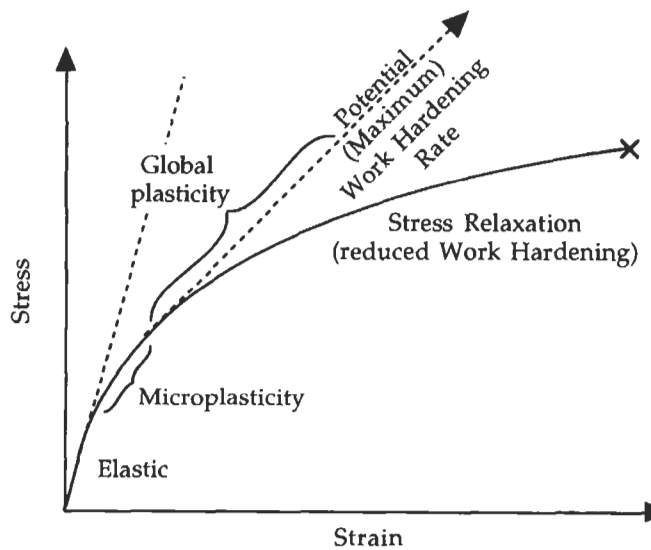

Fig. 18. Schematic depiction of the different regimes of the stress–strain curve.

picture. Work hardening rates are usually significantly higher than for the corresponding unreinforced metal, but are well below the calculated maximum, at least for appreciable plastic strains. However, there have to date been virtually no quantitative comparisons made between theory and experiment for discontinuously-reinforced MMCs, since the stress relaxation processes are usually complex and difficult to model. The case of long fibre composites, loaded along the fibre axis, is simpler, since the absence of high interfacial stresses or high stress gradients in the matrix means that stress relaxation is usually very limited up to the onset of fibre fracture. It is well established (CHESKIS and HECKEL [1970]; LILHOLT [1977]) that yielding in such cases is followed by a very high work hardening rate, which remains linear over an appreciable range of strain. These work hardening rates are usually fairly close to those predicted using these stress transfer concepts, often representing a substantial fraction of the elastic modulus. It may, however, be noted as a general point that the limited ductility of many MMCs (§ 4.1.2) is something of a handicap for detailed investigation of work hardening characteristics.

3.3. Wear

The wear resistance of MMCs can be excellent and the scope for attainment of good tribological properties is one of the reasons for industrial interest in these materials. Despite this, understanding of their wear characteristics is still far from complete. This is due in part to the inherent complexity of many wear processes, but the problem is compounded by a possible interplay with microstructural variables such as fibre content, size, orientation, bond strength etc., which can influence wear behaviour.

Several studies (HOSKING *et al.* [1982]; PAN *et al.* [1990]; HUTCHINGS [1991]) have demonstrated an improved wear resistance for aluminium, steel etc., in both lubricated and dry conditions, after incorporation of SiC or Al_2O_3 particles or fibres. These reductions in wear rate are in most cases not due to a reduction in the coefficient of friction. The improvement can be attributed to the hard particles or fibres remaining intact when struck by asperities or abrading particles, under conditions such that material would have been ploughed out from unreinforced metal. The limited data currently available (BHANSALI and MEHRABIAN [1982]; WANG and HUTCHINGS [1989]; PAN *et al.* [1990]) suggest that fibres do not offer dramatically greater improvement in wear resistance than do particles of the same material and diameter. Consistent with this is the observation (WANG and HUTCHINGS [1989]) that composites having a planar random distribution of fibres exhibit similar wear behaviour on surfaces normal and parallel to the fibre plane.

The diameter (smallest dimension) of the reinforcement, relative to the size of the abrading particles, is apparently important (HUTCHINGS [1991]). This is illustrated by the data (WANG and HUTCHINGS [1989]) shown in fig. 19. Improvements in wear resistance are clear-cut for fine abrading particles, but less obvious when they are larger. Fibres become fractured under the higher loads to which they are subjected with larger abrading particles, after which they become excavated along with plastically deformed matrix. A model has been proposed (WANG and HUTCHINGS [1989]) to quantify this size effect.

The incorporation of a soft constituent into a harder matrix has long been used in

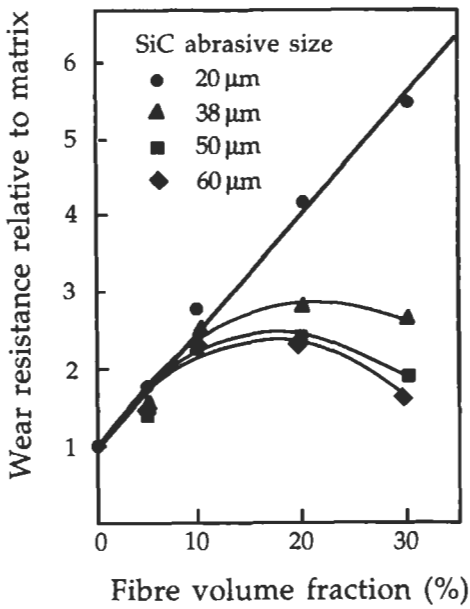

Fig. 19. Pin-on-disk data showing the dependence of wear resistance ratio on fibre content for 6061 Al–Saffil (Al_2O_3) composites subjected to abrasive wear (WANG and HUTCHINGS [1989]). Curves are shown for four grades of paper, each having SiC particles of different average size.

tribological materials such as bearing alloys. Superior sliding wear performance is obtained as a result of improved lubrication, either due to shearing of the soft phase located between the sliding surfaces or by improved retention of an added lubricant in surface depressions left in the harder matrix. When improvements to the wear resistance are obtained in this way, it is normally accompanied by a reduction in the coefficient of friction. Several materials conventionally regarded as MMCs apparently exhibit improved wear resistance as a result of this effect (ROHATGI *et al.* [1988]). The factors favouring good wear resistance with hard reinforcing constituents, *viz.* large reinforcement size, high reinforcement strength (fracture toughness), strong interfacial bonding etc., are not relevant in this case. Rather, the critical parameters are likely to be those dictating the efficiency of lubrication. These may be highly specific both to the imposed conditions and to the microstructure of the soft constituent.

4. *Fracture*

It has long been clear that the strength of metals can be considerably enhanced by the introduction of fibres. For example, fig. 20 shows how the failure stress of copper

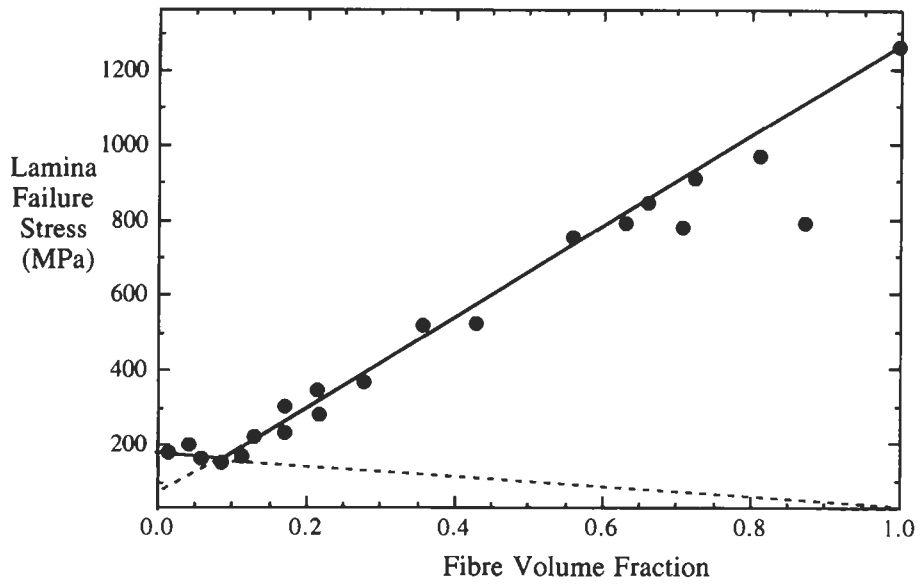

Fig. 20. Strength data for axial loading of copper reinforced with tungsten fibres (KELLY [1966]; KELLY [1972]). Also shown are predictions from a simple model based on the stress levels in the two constituents.

reinforced with long tungsten fibres rises with fibre content. The behaviour conforms well to predictions from simple composite theory based on load partitioning between the two constituents and measured fracture stresses for them.

The situation is more complex when attention is directed towards ductility and toughness, particularly for discontinuously-reinforced MMCs. A predominant factor inhibiting increased industrial usage has been concern about low levels of ductility, damage tolerance and fracture toughness. In general terms, the origins of this impairment of fracture properties are fairly well understood. The high ductility of metals is largely a consequence of the ease with which plastic deformation can occur via dislocation glide. When significant proportions of ceramic are present, constraint on matrix plasticity is introduced. What still remains somewhat unclear, however, is the precise degree to which this is expected to affect the relevant properties. Also, there is uncertainty about the effects of factors such as reinforcement size and shape, interfacial bond strength and matrix microstructure. It is, however, widely recognised that there are important differences between MMCs and brittle matrix composites (including most PMCs). While processes such as interfacial debonding and sliding can make important contributions to the toughness of such composites, the potential for ductility and energy absorption in MMCs lies mainly in the scope for promotion of matrix plasticity. Detailed understanding of the deformation mechanisms is clearly necessary. Fracture is sensitive to local events, so that stress analysis approaches have tended to be based on FEM analysis of local fields, rather than examination of volume-averaged matrix stresses.

References: p. 2616.

4.1. Damage development and ductility

4.1.1. Damage mechanisms

Several types of microstructural damage can develop in MMCs under applied loads. These include *fracture of the reinforcement*, *interfacial debonding* and *matrix cavitation*. For particulate MMCs, fracture of the reinforcement is relatively rare. It is more common with larger particles. For Al-based MMCs reinforced with relatively weak ZrO_2 particles, particle fracture has been analysed using a Weibull approach to predict the size effect (LEWIS and WITHERS [1995]). In Al–SiC particulate composites, particle cracking was reported (LLOYD [1991]) to be important only for particle sizes above about 20 μm. Even with SiC whiskers, which become much more highly stressed than particles, fibre fracture is rare. In many discontinuously-reinforced systems, specimen failure arises from the *formation and growth of voids* at the reinforcement-matrix interface (HUNT *et al.* [1987]; LEWANDOWSKI *et al.* [1989]; WHITEHOUSE and CLYNE [1993]; WHITEHOUSE and CLYNE [1995]). Typical voids forming adjacent to reinforcements in particulate and short fibre-reinforced aluminium are apparent in the micrographs shown in fig. 21. These voids subsequently coalesce by a ductile tearing mechanism, resulting in failure of the composite.

It is commonly assumed that cavity formation will occur when a *critical stress criterion* is satisfied. This may be questionable, since energy-based approaches (MARSHALL and EVANS [1985]; HE and HUTCHINSON [1989]; EVANS *et al.* [1991]) are sometimes more successful in describing interfacial debonding. However, such approaches are in general more applicable to stable propagation of interfacial cracks, usually in brittle systems. Satisfaction of an energy balance is necessary, but not sufficient, for an initial cavity formation event. In any event, calculation of the strain energy release rate within an MMC when an interfacial cavity starts to form is difficult and attention has in practice been concentrated on stress-based analyses. There have been a number of finite element method (FEM) investigations of stress fields around reinforcements in MMCs. Assumptions have been made that cavitation required attainment of a critical normal stress (NUTT and NEEDLEMAN [1987]) or a critical hydrostatic stress (CHRISTMAN *et al.* [1989]; LLORCA *et al.* [1991]) at the interface. Hydrostatic stress fields from FEM calculations are shown in fig. 22 around spherical and short fibre reinforcements. On comparing these with micrographs in fig. 21, it can be seen that the voids do seem to form at the locations of peak hydrostatic stress. This was confirmed by a detailed study (WHITEHOUSE and CLYNE [1995]) covering a range of temperatures and reinforcement shapes. For example, it can be seen from the plot of fig. 23 that the observation of voids forming in the "polar" location (along the loading axis) for spherical reinforcement is consistent with attainment of a critical hydrostatic stress being necessary, whereas the peak in normal stress at the interface occurs off-axis.

Few data are available concerning values of the critical stress levels for particular cases. Direct measurements of interfacial bond strength have been largely confined to pure shear loading, as in the single fibre push-out (MARSHALL and OLIVER [1987]; SHETTY [1988]; YANG *et al.* [1990]; KIM *et al.* [1992]) test, whereas a normal (opening mode) component is probably needed for cavity formation. The tensioned push-out test

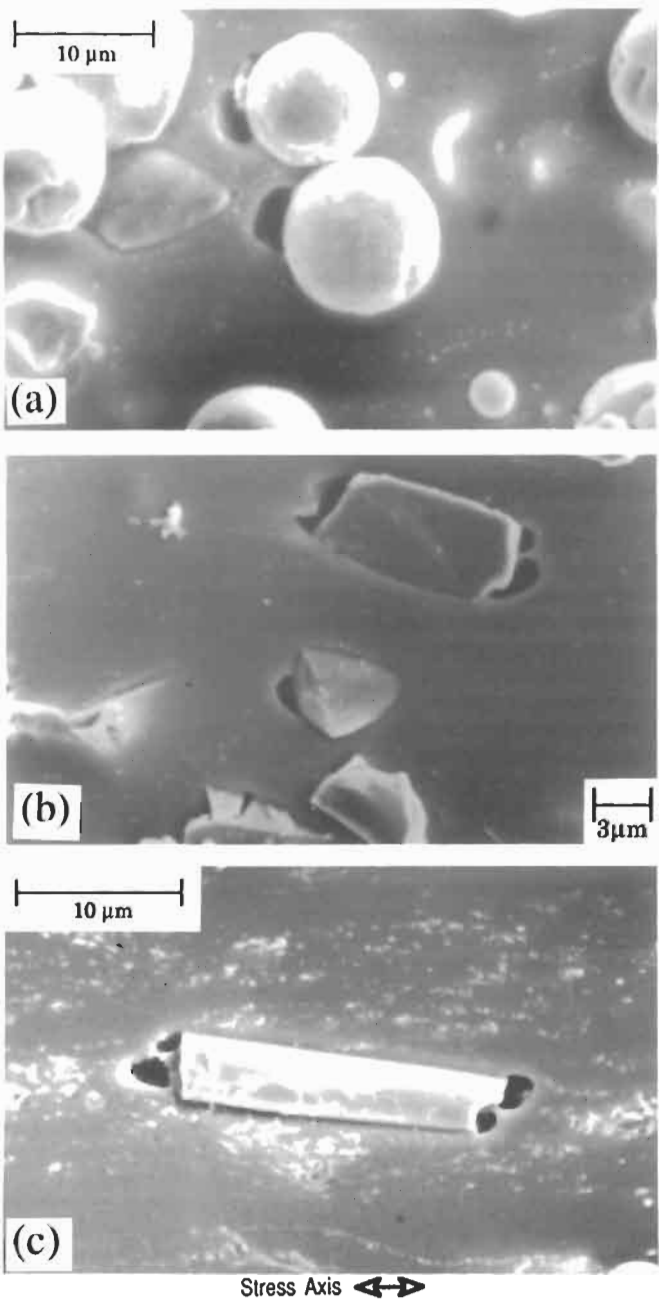

Fig. 21. SEM micrographs of aluminium-alumina composites after tensile loading at room temperature, showing typical void nucleation sites with (a) spherical (b) angular and (c) short fibre reinforcements.

References: p. 2616.

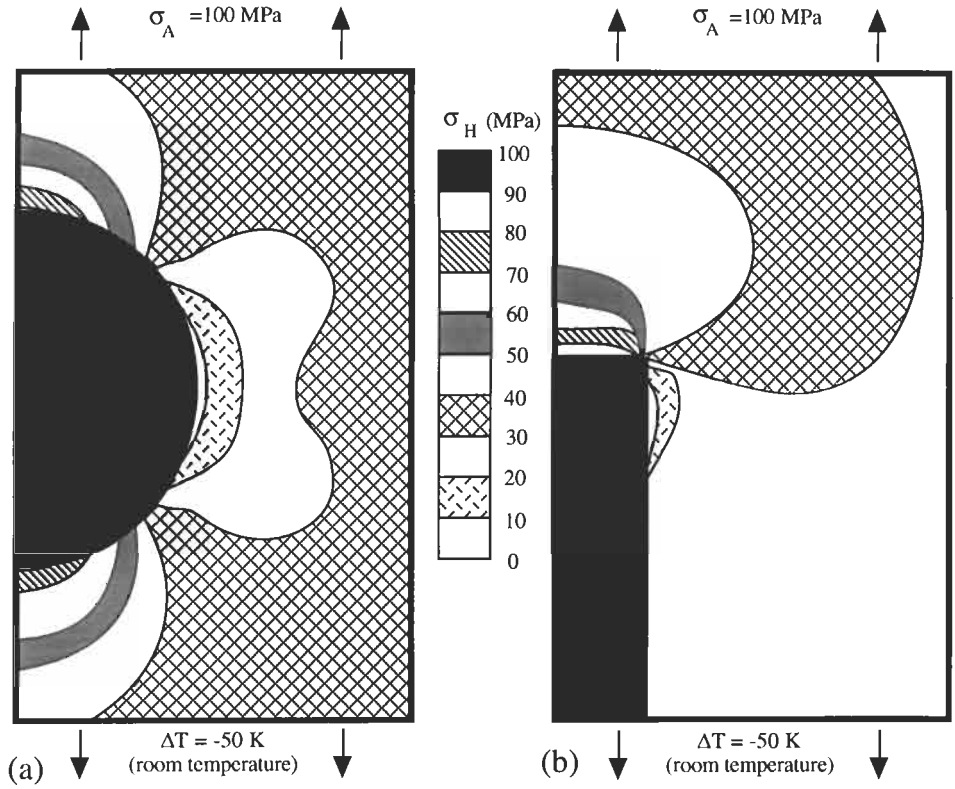

Fig. 22. Contours of hydrostatic stress, σ_H, obtained by FEM modelling (WHITEHOUSE and CLYNE [1995]) for (a) spherical and (b) short fibre (s = 5) alumina reinforcement in an aluminium matrix, generated by an applied load of 100 MPa at room temperature. The thermal stresses were taken as those corresponding to a temperature drop of 50 K.

(WATSON and CLYNE [1993]; KALTON *et al.* [1994]) could be used to explore the onset of debonding with applied opening mode stresses, but few data are available as yet (and the test is not applicable to particle-reinforced material). For titanium reinforced with SiC monofilaments, observations have been made about the ease of interfacial debonding and void formation under transverse loading. These suggest (WRIGHT *et al.* [1990]; JANSSON *et al.* [1991]; CLYNE *et al.* [1995]) that debonding occurs soon after the net normal stress across the interface becomes tensile (i.e., the compressive stress from diferential thermal contraction is offset by the applied tension). These observations are, however, limited to material in which the fibres have graphitic coatings, which might be expected to offer little resistance to debonding. For commercial purity Al reinforced with alumina, data such as those in fig. 23, combined with the observation (WHITEHOUSE and CLYNE [1995]) that voids started to form in this system under applied stresses of around 100 MPa, suggest that a hydrostatic stress of around 80–100 MPa was sufficient for cavity formation. However, there are many sources of error in this estimate and there

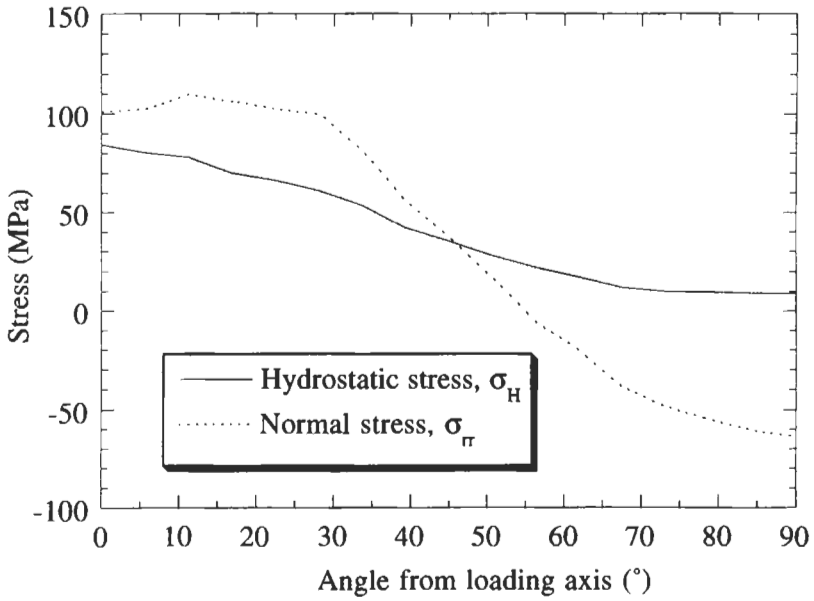

Fig. 23. Predicted (WHITEHOUSE and CLYNE [1995]) hydrostatic and normal stress components in the matrix at the interface around a spherical particle, as a function of the angle between the loading direction and the line joining the centre of the particle to the point concerned, with an applied load of 100 MPa. The thermal stresses were taken as those corresponding to a temperature drop of 50 K.

may well be a high sensitivity to system chemistry and to the processing conditions. Certainly a higher interfacial strength than this is likely to be desirable in particulate and short fibre MMCs designed to operate under high applied loads.

4.1.2. Ductility

Whatever the mechanism of micro-damage initiation, the ductility is expected to be sensitive both to the strain at which damage nucleates and to the rate at which it accumulates and causes failure. It is also expected to be sensitive to the prior presence of gross defects generated during the manufacturing process. Since the fracture toughness of MMCs tends to be appreciably lower than for unreinforced metals (see § 4.2.1), such defects can rapidly lead to brittle fracture. This has been troublesome in the industrial application of MMCs and has also caused confusion during attempts to develop reliable scientific models for failure of these materials. The situation has improved recently with advances in quality control and inspection procedures during manufacture of MMCs, but prediction of ductility from identifiable microstructural features is still rather unreliable.

It is well established that, provided no gross flaws are present, void formation and growth (and/or reinforcement cracking) can occur progressively over an appreciable range of plastic strain. There have been several attempts (EVENSEN and VERK [1981]; BRECHET *et al.* [1991]; THOMASON [1993]; WHITEHOUSE and CLYNE [1993]) to predict the ductility by specifying some saturation condition under which this process becomes

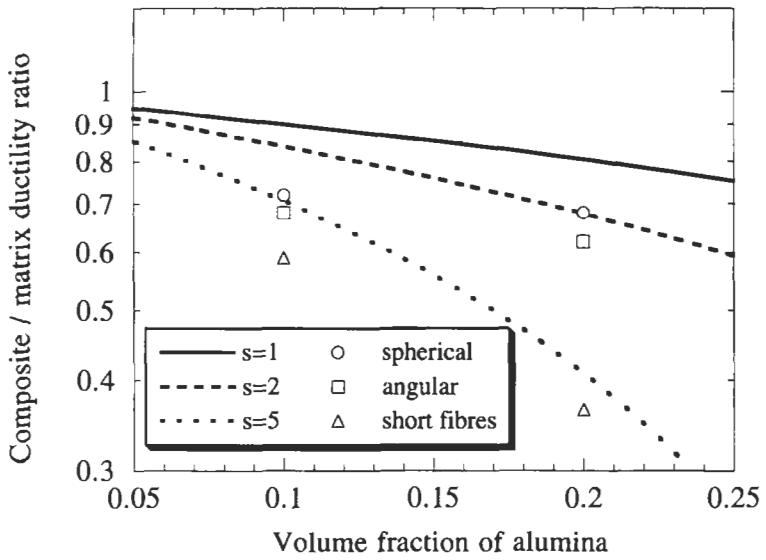

Fig. 24. Comparison between experimental and predicted ductilities (WHITEHOUSE and CLYNE [1993]) for extruded powder route Al–Al_2O_3 composites, expressed as a ratio to the value for unreinforced Al made in the same way (=24.5%).

unstable and leads to failure. These are based on geometric models of the *void coalescence* process. An example of the type of predictions obtained in this way is shown in fig. 24, in which a comparison is presented between the observed and predicted dependence of the ductility on the volume fraction and aspect ratio of the reinforcement. In this case, the model (WHITEHOUSE and CLYNE [1993]) is based simply on the constraint imposed by the presence of the reinforcement on the plastic strain of the matrix. The predictions are therefore in the form of a ductility relative to that of the unreinforced matrix.

The agreement shown in fig. 24 is encouraging, although based on limited experimental data. These data suggest that the ductility of discontinuous MMCs can be quite respectable. For example, even with 20% of short fibres, the ductility has only been reduced to just under half that of the matrix. Since the ductility of many metals is considerably greater than is strictly necessary for most engineering purposes, this suggests that acceptable ductilities should be achievable for many MMCs. However, it should be recognised that these predicted levels of ductility are effectively upper bounds. Some constraint on matrix plasticity is inevitable, but there may be further reductions in ductility if certain microstructural features are present. Gross flaws such as cracks or large pores are obvious examples, but features such as *clustering* of reinforcement are also thought to be detrimental. This is because the degree of *triaxial constraint* on the matrix is appreciably higher within such clusters, so that cavitation and void coalescence will readily occur in that region. If the cluster is sufficiently large, then a defect of critical size will tend to form there at a low macroscopic strain. From arguments along

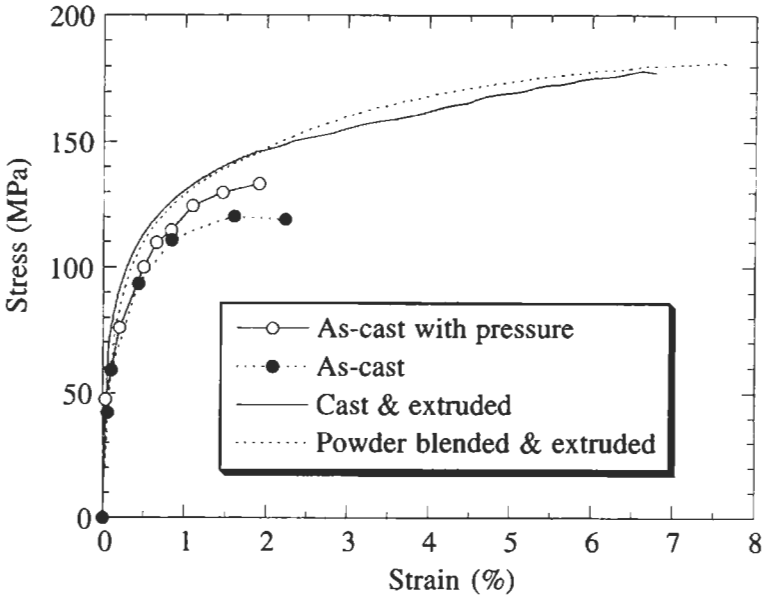

Fig. 25. Tensile stress/strain curves (MURPHY *et al.* [1995]) for four Al–Al_2O_3 composites. Two were cast, by squeeze infiltration, one with a pressure intensification stage, while the other two were extruded, one from a casting and the other from a powder blend.

these lines, and from general experimental observation, it seem likely that homogeneity of reinforcement distribution is critical if the maximum ductility is to be obtained.

Some further points concerning ductility are illustrated by the plots shown in fig. 25. This shows stress/strain curves (MURPHY *et al.* [1995]) for four MMCs, each based on Al with 20% of "Saffil" alumina fibres. The two in the as-cast state have similar ductilities (~ 2%), while the two in the as-extruded form both failed at higher strains (~ 7%). Of the two as-cast composites, both had been produced by squeeze infiltration (§ 2.1.1), but one had been subjected to a pressure intensification stage which removed all of the porosity. It can be seen that this had little effect on the stress/strain curve, although it was confirmed by gravimetric measurements that it did reduce the porosity to a very low level. The extrusion process produces material with a relatively low fibre aspect ratio (~ 5 in this case) and a good homogeneity of fibre distribution. The ductilities of these two extruded materials were both close to the upper bound predicted by the geometric model (fig. 24), even though the one which had been cast first had a higher interfacial bond strength than the powder route material. This difference in bond strength is reflected in the data shown in fig. 26, indicating that voids formed at much lower strains in the powder material. These results confirm that the shape, content and distribution of the reinforcement largely dictates the ductility, provided gross defects are not present. The low ductilities of the as-cast composites are thought to be due partly to the high fibre aspect ratio and partly to a degree of clustering. (Predictions cannot be made with the current simple version of the geometric model, since it applies only to

References: p. 2616.

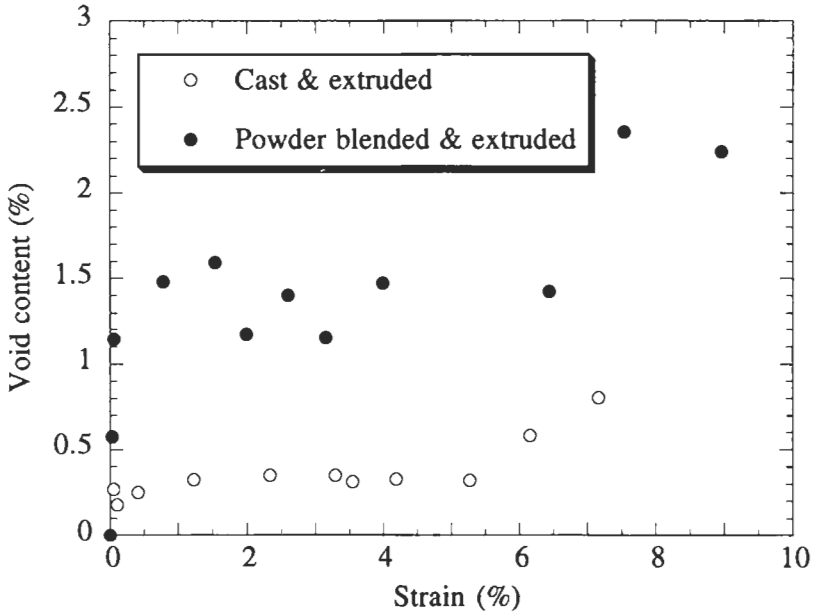

Fig. 26. Gravimetric data from interrupted tensile tests (MURPHY *et al.* [1995]) on the two extruded materials referred to in fig. 25. Density measurements have been converted to porosity levels, assuming zero porosity initially.

aligned fibres, whereas in the as-cast material the fibre arrangement was approximately planar random.)

4.2. Fracture toughness and fatigue

4.2.1. Fracture toughness

The development of models for prediction of the fracture toughness of MMCs is still at an early stage. Examples of attempts made hitherto include some based on the way that the geometry of the crack path affects the crack opening displacement (HAHN and ROSENFIELD [1975]), on observations of the dimple height on fracture surfaces (THOMPSON and ASHBY [1984]; RITCHIE and THOMPSON [1985]) and on the energy absorption associated with fracture processes which occur in the presence of reinforcement (DAVIDSON [1987]). None of these models are really very satisfactory in terms of agreement between predicted and observed trends on changing reinforcement variables. Evaluation of energy absorption is probably the most promising approach, but the most important contribution comes from matrix plasticity and the effect of constraint on this due to the presence of the reinforcement is rather difficult to model, at least for discontinuous MMCs. There is, however, current interest in modelling of stress and strain fields around cracks in long fibre (HE *et al.* [1993]) and layered (HE *et al.* [1993]; SHAW *et al.* [1994]) MMCs and this could be extended to predictions of energy absorption.

Some of the experimental characteristics are, however, fairly well established. For example, the fracture toughness usually falls with increasing ceramic content. Of course, this is entirely as expected and is consistent with the associated increase in constraint on matrix deformation and the consequent reduction in ductility. Furthermore, an increase in ceramic content effectively raises the degree of prior cold work imposed on the matrix (both as a result of differential thermal contraction and during loading), which is known to reduce the toughness of metals. The precise way in which fracture toughness falls as the ceramic content increases is, however, not well established. This is illustrated by the data (FLOM and ARSENAULT [1989]; KAMAT *et al.* [1989]) in fig. 27, which show the effect of volume fraction for two particulate MMCs. While both plots show the same general trend, the details of the dependence appears to differ between the two cases. It should also be mentioned that particle size has often been observed to have an appreciable effect (PADKIN *et al.* [1987]; LEWANDOWSKI *et al.* [1989]; MANOHARAN and LEWANDOWSKI [1990]; LLOYD [1991]), with larger particles both more likely to fracture and tending to cause a greater reduction in the fracture toughness of the composite. The data of FLOM and ARSENAULT (FLOM and ARSENAULT [1989]) indicate that the effect on fracture toughness is only significant when the particle size becomes large enough for them to be likely to fracture (> 20 μm). It may, in any event, be noted that the fracture toughness values shown in fig. 27 are quite adequate for many engineering applications.

In general, fracture toughness tends to vary inversely with tensile strength. This trend is usually observed with MMCs, but certain qualifications should be made. For example, consider the data (KLIMOWICZ and VECCHIO [1989]; LEWANDOWSKI *et al.* [1989]) in fig. 28. This shows measured fracture toughness and tensile strength as a function of heat

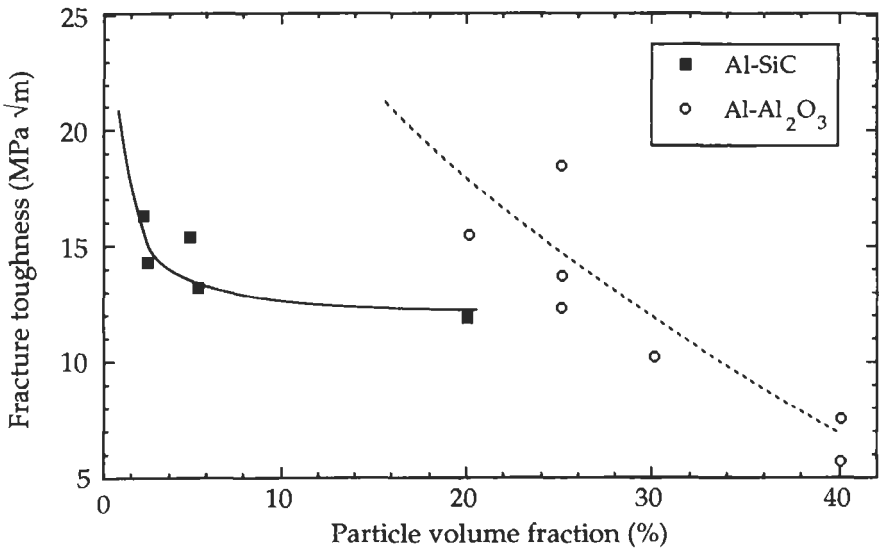

Fig. 27. Experimental fracture toughness data (FLOM and ARSENAULT [1989]; KAMAT *et al.* [1989]) for Al–SiC and Al–Al_2O_3 particulate composites, plotted as a function of particle volume fraction.

References: p. 2616.

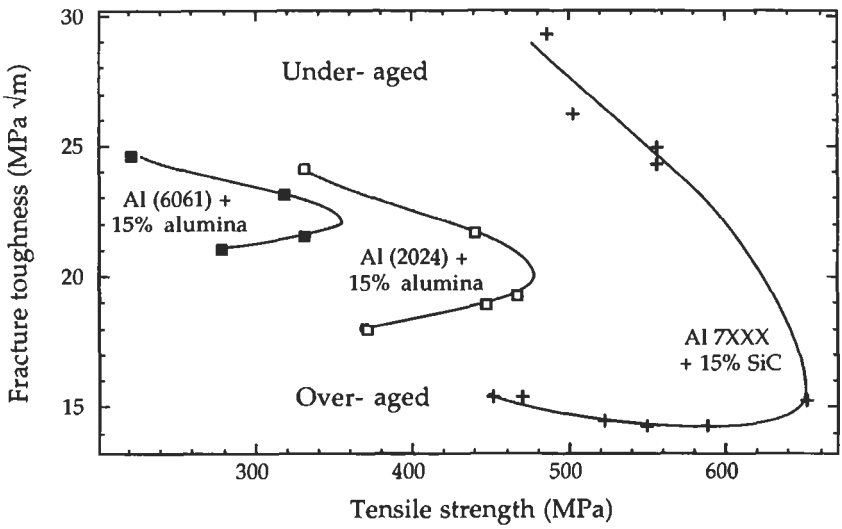

Fig. 28. Experimental data (KLIMOWICZ and VECCHIO [1989]; LEWANDOWSKI *et al.* [1989]) for fracture toughness and tensile strength, measured after various heat treatments, for Al–SiC and Al–Al_2O_3 particulate MMCs, based on three different age-hardening alloys.

treatment for MMCs based on three different age-hardening Al alloys. As ageing is continued to give peak hardness, there is a decrease in fracture toughness and an increase in tensile strength, as expected. On extending the ageing treatment to give an over-aged matrix with a lower tensile strength, however, the fracture toughness does not recover significantly and remains low. This may be the result of precipitates forming preferentially at the interface, where they cause embrittlement, but this has not yet been confirmed.

4.2.2. Fatigue of discontinuous composites

Fatigue characteristics are conveniently represented on a plot of crack growth increment per cycle against driving force as represented by change in *stress intensity factor*. The fatigue response of discontinuous MMCs tends to differ from that of the unreinforced metal in the manner shown schematically in fig. 29. The fracture toughness of the composite is usually lower, for the reasons outlines in § 4.2.1, which leads to the onset of fast fracture at lower applied ΔK. Growth rates at low ΔK levels, on the other hand, are usually slower for the composite. Furthermore, the *threshold level*, ΔK_{th}, below which no crack growth occurs, is often appreciably higher for an MMC than for the metal. Data are often presented in the form of the number of cycles to failure as a function of the applied stress level (S/N curves). Improvements in *fatigue limit* (stress below which failure does not occur, even for large numbers of cycles) are equivalent to increases in ΔK_{th}. Data for welded components in aluminium alloys with and without particulate reinforcement (HARRIGAN [1994]) confirmed the superior fatigue limits of MMCs.

The good fatigue resistance of MMCs at low driving forces is usually explained (WILLIAMS and FINE [1985]; PADKIN *et al.* [1987]; CHRISTMAN and SURESH [1988]) in

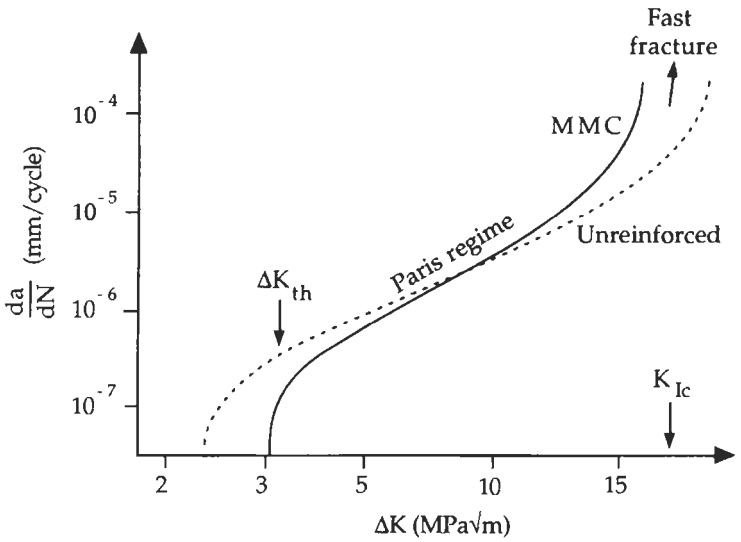

Fig. 29. Schematic depiction of fatigue crack growth rate as a function of applied stress intensity factor, for a typical discontinuous MMC and the corresponding unreinforced alloy.

terms of reduced matrix stress levels, crack deflection by particles or reduced crack opening displacement because of higher stiffness and work hardening rates. The significance of the value of ΔK in this context is that the plastic zone at the crack tip is small at low ΔK. This zone may therefore encompass few, or no, ceramic particles. Under these circumstances, crack deflection at interfaces is easier and fracture of particles ahead of the crack tip is less likely. It has also been observed (LUKASAK and KOSS [1993]) that fatigue crack initiation is easier when larger ceramic particles are present. Improvements in fracture properties on keeping the reinforcement size down are sometimes taken to be universal for discontinuous MMCs. However, there has been some success (DAVIDSON [1993]) in predicting ΔK_{th} from yield stress, particle content and particle size values, with ΔK_{th} predicted to be higher with larger particles. Clearer benefits are expected from ensuring that the reinforcement is homogeneously distributed, since clustering has often been observed (CROWE *et al.* [1985]; HUNT *et al.* [1987]) to promote fatigue crack growth.

4.2.3. Fatigue of long fibre and layered composites

There has been extensive study of the fatigue resistance of long fibre MMCs loaded in tension along the fibre axis. Much of the interest has centred on titanium alloys reinforced with SiC monofilaments, although other (model) systems have also been used. In general, the performance is markedly superior to that of the unreinforced metal (DVORAK and JOHNSON [1980]; DVORAK and JOHNSON [1980]; NUNES *et al.* [1985]; TSANGARAKIS *et al.* [1985]; JOHNSON [1993]). This is expected on the basis of load transfer to the fibres from the matrix. Under transverse loading, on the other hand, the

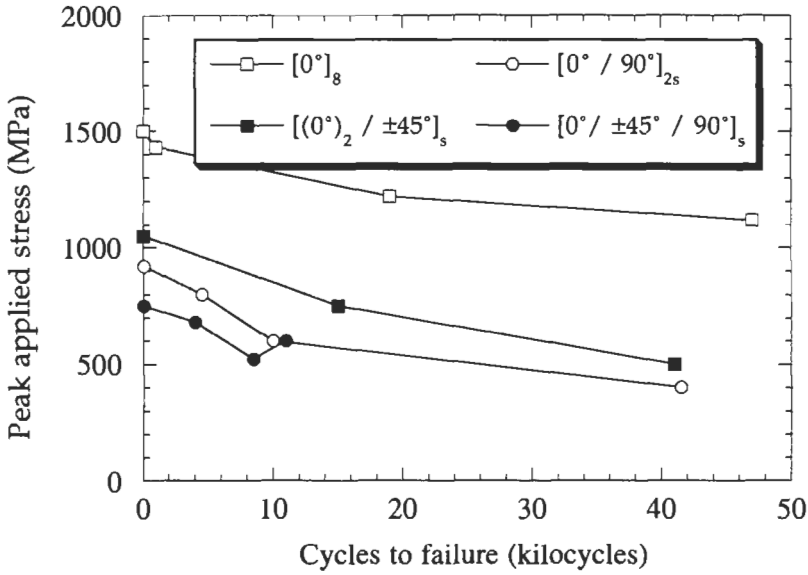

Fig. 30. S/N curves (JOHNSON [1993]) for several Ti–15–3/35% SCS–6 SiC monofilament laminate composites. The suffices refer to the lay-up sequences of the laminates, with "s" meaning "symmetrical". Testing was done at room temperature with a stress ratio, R, of 0.1.

fatigue resistance of such composites is often very poor. The data in fig. 30 illustrate some of the effects observed. This shows S/N plots for several Ti MMC laminates. The best performance is shown by the unidirectional laminate, having the fibres parallel to the applied load. It can be seen that this composite showed a fatigue limit well above 1000 MPa, a level at which the unreinforced matrix would fail in tension immediately. The performance of the different laminates in fig. 30 can be rationalised by calculating the range of stress to which the 0° ply (parallel to the applied load) is subjected during loading. When this is plotted against the number of cycles to failure (fig. 31), then the data for the different laminates fall on a common curve. This highlights the point that the laminate does not fail until the fibres in the 0° ply become fractured.

There are, however, a few points which should be noted concerning the behaviour of such composites. Firstly, the good fatigue resistance which is often observed is largely dependent on the crack being bridged by intact fibres (SENSMEIER and WRIGHT [1990]). This depends to some extent on interfacial properties and crack deflection characteristics. The length of the debonded zone is also relevant, since it influences the region over which the fibre is overloaded and tends to become damaged. Interfacial reaction is often deleterious, since it tends to inhibit deflection of matrix cracks, to raise the interfacial frictional sliding stress (generating high fibre stresses close to the crack plane) and to promote crack initiation in the matrix via slip band formation. Some of these effects have been considered by Majumdar and Newaz (MAJUMDAR and NEWAZ [1995]) and by Robertson and Mall (ROBERTSON and MALL [1994]). Fatigue crack growth has also been examined (SHAW *et al.* [1994]) in layered metal/ceramic composites. This work

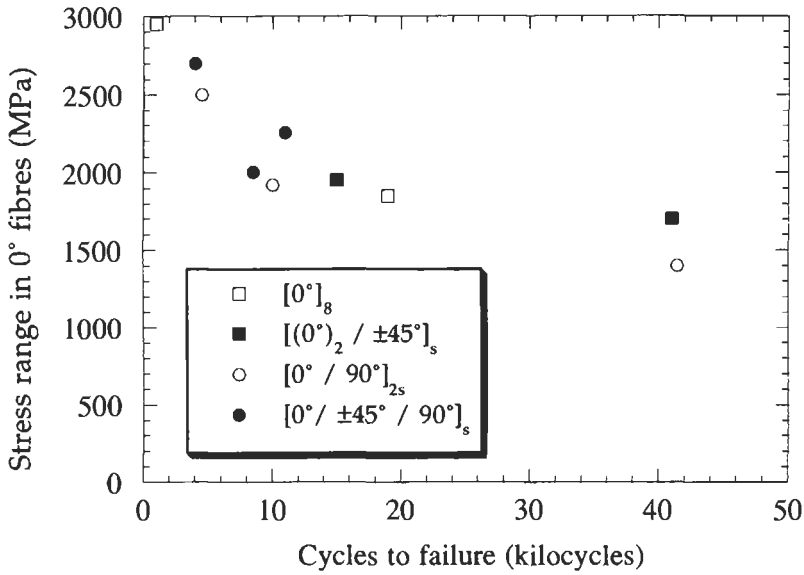

Fig. 31. Data of fig. 30, replotted (JOHNSON [1993]) with the stress range to which fibres in the 0° ply were subjected during each cycle as the vertical axis.

confirmed the importance of interfacial debonding in reducing the stress concentration ahead of the crack, and hence improving the fatigue resistance. This is more effective than matrix plasticity, even with a low flow stress.

5. *High temperature behaviour*

One of the attractions of MMCs is centred on their high temperature properties. The presence of ceramic reinforcement in metals can certainly improve their strength at elevated temperature. There is also interest in the changes induced in thermal expansion characteristics. A study of thermal expansion is instructive, since it highlights the importance of the stresses which result from differential thermal expansion between the two constituents. These strongly affect the deformation characteristics, as well as the expansion behaviour.

5.1. Thermal expansion and thermal stresses

For most MMC systems, the matrix expansivity, α_m, is appreciably higher than that of the reinforcement, α_f. A temperature change ΔT will produce a misfit strain $\Delta\alpha\Delta T$, which, if elastically accommodated, will give rise to a set of internal stresses. For example, cooling after fabrication of a fibre composite will put the matrix into tension, particularly along the fibre direction (see fig. 15). These stresses will have associated strains and the net effect of these on the length of the composite in any given direction

can be calculated or estimated. This net length change arising from the internal stresses is simply added to the natural thermal expansion of the matrix to give the overall length change and hence the composite expansivity. This simple view of thermal expansion allows certain points to be identified immediately. For example, a porous material, regarded as a composite of voids in a matrix, will not develop any internal stresses on heating because the "inclusions" have zero stiffness. Hence, the presence of pores (of whatever shape, size and volume fraction) will not affect the expansivity, although they will evidently give rise to sharp reductions in stiffness.

Quantitative prediction of composite expansivity requires some sort of modelling of the thermal stresses and strains. Various approaches have been used (SCHAPERY [1968]; HALE [1976]; BOWLES and TOMPKINS [1989]), and analytical solutions are available for spherical and long fibre reinforcement which are fairly reliable. However, the Eshelby method is again very convenient, since it is both reasonably accurate and applicable to a range of fibre aspect ratios. The appropriate expression (CLYNE and WITHERS [1993]) for the expansivity of the composite is closely linked to that given as eq. (3) for the matrix stress arising from a thermal misfit strain of $(\alpha_m - \alpha_f)\,\Delta T$

$$\alpha_c = \alpha_m - f\{(C_m - C_f)[S - f(S - I)]C_m\}^{-1} C_f(\alpha_m - \alpha_f). \tag{13}$$

Predictions from this equation are shown in fig. 32 for Al–SiC composites. The increase in transverse expansivity on adding a small volume fraction of fibres is worthy

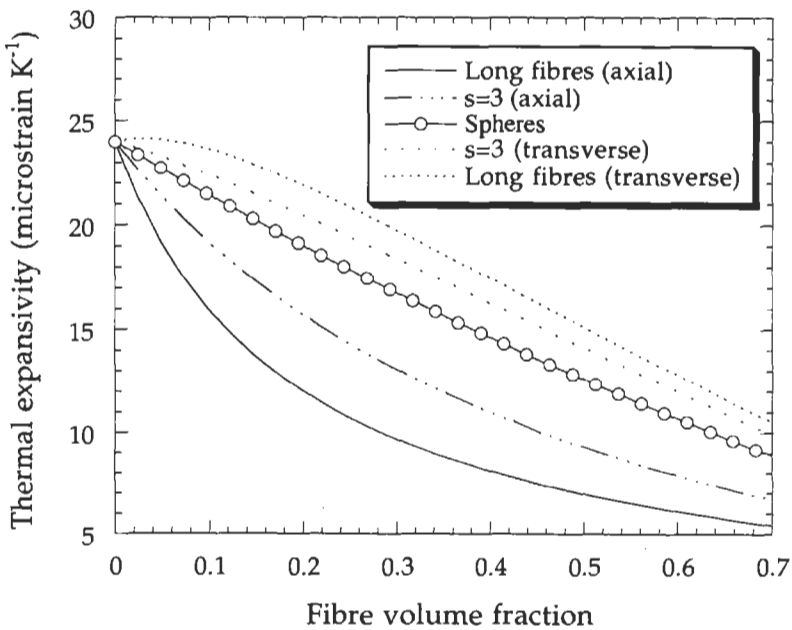

Fig. 32. Predicted dependence of composite expansivity on reinforcement content for Al-SiC composites, obtained using eq. (13). The aspect ratio, s, has a value of 1, 3 or ∞.

of note. This arises because, on heating the composite, axial expansion of the matrix is strongly inhibited and the resultant axial compression of the matrix generates a Poisson expansion in the transverse direction, which more than compensates for the reduction in natural transverse thermal expansion induced by the presence of the fibres. Such effects should be borne in mind when designing MMCs for controlled thermal expansion applications. Experimental data for both axial (WOLF *et al.* [1980]) and transverse (KREIDER and PATRANI [1970]) expansivity of long fibre MMCs are consistent with these predictions.

5.2. Creep and thermal cycling effects

Creep of MMCs has received extensive attention. The main features are fairly easy to summarise. Usually, the ceramic reinforcement remains elastic, while the metal undergoes plastic deformation in response to a stress field which is strongly affected by the presence of the ceramic. Contributions to this stress field come from thermal expansion mismatch (§ 3.2.2), from elastic modulus mismatch (§ 3.1), from plastic flow of the matrix (§ 3.2.3) and from stress relaxation processes (§ 3.2.3). For long fibre composites loaded along the fibre axis (ENDO *et al.* [1991]), the creep rate is low and falls to zero as the fibres gradually take all of the applied load (provided they do not fracture). This behaviour is a major attraction of long fibre MMCs, but other aspects of MMC creep characteristics are of some concern. With discontinuous reinforcement, or with long fibres under transverse load, a steady state is often set up in which the matrix creeps in such a way that its stress state remains relatively unchanged. This creep rate is usually lower when the reinforcement is elongated in the direction of applied stress, which is expected from simple load transfer arguments. The inherent creep resistance of the matrix, particularly when raised by fine dispersions, affects the composite creep rate. Finally, the presence of the reinforcement may accelerate the onset of damage development and creep rupture, especially if interfacial debonding occurs easily.

Some of these features are illustrated by the data (FURNESS [1991]) shown in fig. 33. These refer to isothermal loading of aluminium, with or without alumina reinforcement. The unreinforced aluminium has fairly good creep resistance, as a result of the presence of a small volume fraction of very fine alumina particles (from the surface of the original aluminium powder particles). While the presence of aligned alumina fibres led to a reduced steady state creep rate and delayed onset of stage III damage and rupture, addition of (relatively large) alumina particles had a deleterious effect. In the latter case, the enhanced cavitation (§ 4.1.1) resulting from the presence of the (large) particles masks any benefit from the reduction of load on the matrix. It may be noted that stress relaxation processes (§ 3.2.3) occur very rapidly during creep, largely via diffusive processes. This tends to unload the reinforcement, particularly if it has a low aspect ratio. Such unloading is much harder with fibres.

Various other features of the creep of MMCs have been noted. For example, while steady state creep rates are often lower than for the corresponding unreinforced metals (at least with fibrous reinforcement), sensitivity of the creep rate to the level of applied stress (i.e., the *stress exponent*) is often greater (NIEH [1984]; NARDONE and STRIFE

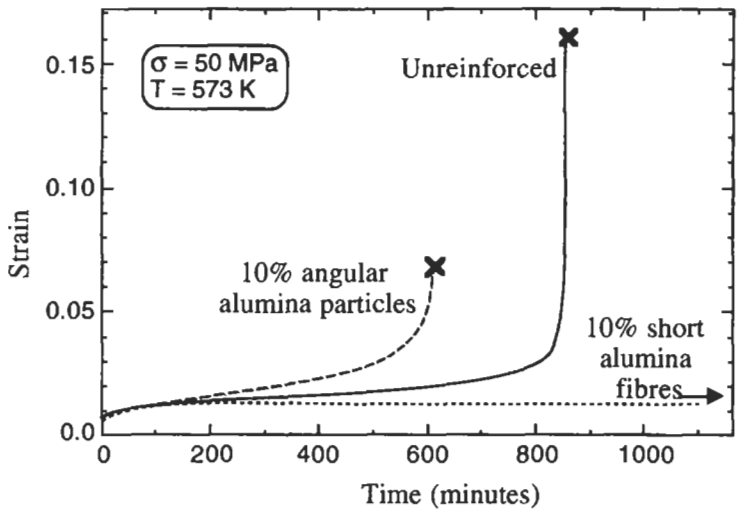

Fig. 33. Creep curves (FURNESS [1991]) for materials produced by consolidation of Al powder by extrusion, with and without Saffil short fibres (3 μm diameter, aspect ratio about 5) or alumina particles (diameter about 15 μm).

[1987]; XIONG *et al.* [1990]). High *apparent activation energies* for steady state creep rates have also been widely reported. These effects may be partly due to differences in matrix microstructure between MMC and unreinforced metal (PARK *et al.* [1990]). However, it seems probable that changes in matrix stress state on altering the temperature (NARDONE and TIEN [1986]; JARRY *et al.* [1987]) are also partly responsible.

There have been a number of attempts (LILHOLT and TAYA [1987]; DRAGONE and NIX [1990]; WAKASHIMA *et al.* [1990]; GOTO and MCLEAN [1991]; SØRENSEN [1991]; TAYA *et al.* [1991]) to model the creep behaviour of MMCs, using analytical or numerical methods. These have usually focussed on prediction of the stress state in the matrix, which is then assumed to creep in a similar manner to the unreinforced metal. There are two main sources of complication. The first is that the spatial variation of matrix stress state is substantial; this variation introduces errors into analytical models, which are usually based on volume-averaged stresses. This difficulty can be resolved by using numerical methods. The second problem, however, is more intractable. This centres on stress relaxation phenomena, which are difficult to model from a mechanistic point of view. It may be possible to take them into account empirically, for example via adjustments to a constitutive equation, but this will not represent correctly the dependence on local geometry etc. In any event, while models often faithfully reflect several features of the isothermal creep behaviour of MMCs, quantitative prediction of creep rates has proved quite difficult and creep rupture has not hitherto been reliably modelled.

There has been extensive interest in the creep behaviour of MMCs under conditions of *thermal cycling*. Concern was stimulated by observations of a strong enhancement of average creep rates when the specimen is thermally cycled (WU and SHERBY [1984];

HONG *et al.* [1988]; PICKARD and DERBY [1988]; DAEHN and GONZÁLEZ-DONCEL [1989]) and by reports (PATTERSON and TAYA [1985]; LE FLOUR and LOCICÉRO [1987]; WARWICK and CLYNE [1990]; TOITOT *et al.* [1991]; WAKASHIMA *et al.* [1991]) that short fibre composites tend to elongate along the fibre direction even without any applied load (*strain ratchetting*). The mechanisms responsible for these effects are now fairly well established (DERBY [1991]; FURNESS and CLYNE [1991]; TOITOT *et al.* [1991]; ZHANG *et al.* [1991]), at least in general terms. Changes in temperature lead to thermal stresses, which affect the matrix creep rate. These are more significant when thermal cycling is imposed, since they are continuously regenerated. During isothermal creep, on the other hand, thermal stresses tend to be relaxed away after a time and therefore often exert only limited influence on the behaviour. The effect during thermal cycling is often such that thermal stresses which act to supplement those from the applied load occur during parts of the cycle when creep is most rapid. These thermal stresses are often sufficient to promote matrix creep in the absence of any external load, giving rise to the strain ratchetting effect.

An illustration of the nature of thermal cycling-enhanced creep is given by fig. 34, which shows predicted and measured strain histories during thermal cycling of long fibre reinforced titanium under transverse load (GORDON and CLYNE [1993]). The predictions were obtained from volume-averaged matrix stresses, using a creep rate equation obtained experimentally for the unreinforced alloy. These data were obtained during steady state creep under a small applied load of 20 MPa. It can be seen that average creep rates are substantially higher than under isothermal conditions (at the "*diffusional*

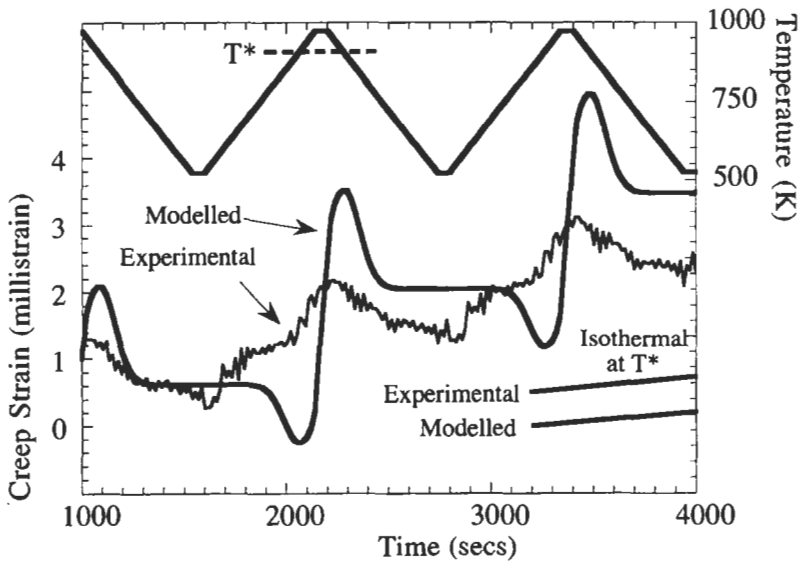

Fig. 34. Comparison between measured and modelled creep strain data (GORDON and CLYNE [1993]) for a Ti–6Al–4V/30% SiC monofilament composite under a transverse 20 MPa load. Data are shown for both a thermally cycled specimen and one held at the diffusional mean temperature.

References: p. 2616.

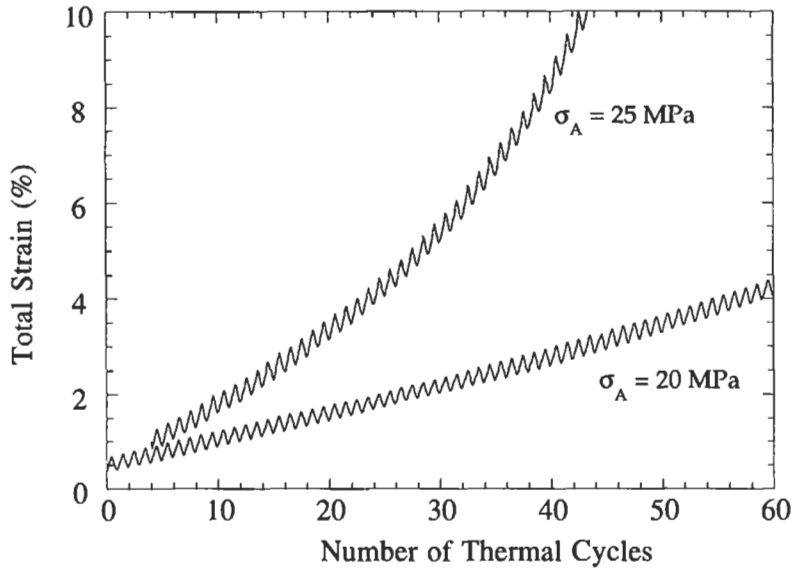

Fig. 35. Complete strain histories (CLYNE *et al.* [1995]) for Ti–6Al–4V/30% SiC monofilament composite, under applied transverse loads of 20 and 25 MPa, as a function of the number of imposed thermal cycles. The temperature profile employed was of the same form as that shown in fig. 34, but with higher heating and cooling rates of 100°C per minute (so that each cycle was of about 10 minutes duration).

mean" temperature, for which the creep rate would be the same as that with cycling if there were no thermal stresses during cycled testing).

Thermal cycling can also have a strong effect on the development of damage during creep loading. An example of the type of effect involved is shown in fig. 35, which gives total strain history curves for the Ti/SiC MMC referred to above, for two levels of applied load (CLYNE *et al.* [1995]). Under the higher load, there is virtually no steady state regime, since damage processes set in at an early stage. This predominantly takes the form of interfacial debonding, leading to formation of large cavities. This is illustrated by the micrographs in fig. 36. These show that debonding takes place through the graphitic layer of the fibre surface, followed by the formation of large voids as the matrix experiences accelerated creep under the influence of the thermal cycling and the transfer of load from the fibres. The early onset of this damage, under a relatively low applied load, is a consequence of the fact that the graphitic layer has virtually no resistance to a tensile stress, once the thermal clamping stress normally present at room temperature is largely removed by heating. The plots shown in fig. 37 illustrate that resistance to this damage is considerably enhanced by a prior heat treatment which consumes the graphitic layer, albeit at a cost in room temperature strength and fatigue resistance. The very poor creep behaviour of these composites under transverse load with thermal cycling remains a cause for concern, since hoop-wound rotating turbine components would be subjected to such conditions during service.

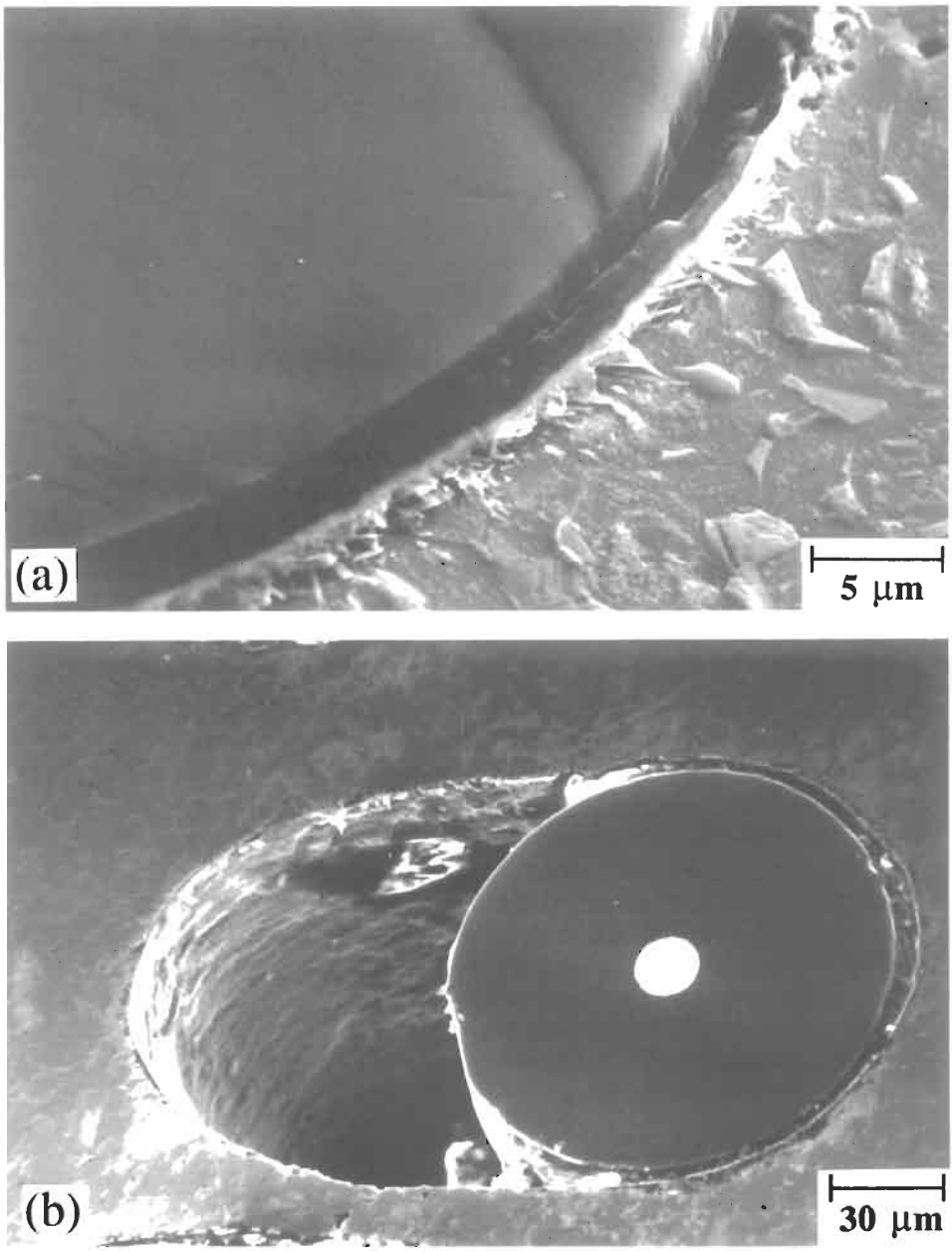

Fig. 36. SEM micrographs showing transverse sections from Ti–6Al–4V/30% SiC monofilament composite, after different periods under 25 MPa applied load, under the thermal cycling conditions referred to in fig. 35. (a) interfacial region after a few cycles, showing debonding within the graphitic layer of the duplex (C/TiB_2) fibre coating and (b) low magnifaction view after failure, showing extensive formation of large interfacial cavities. (Courtesy of P.Feillard).

References: p. 2616.

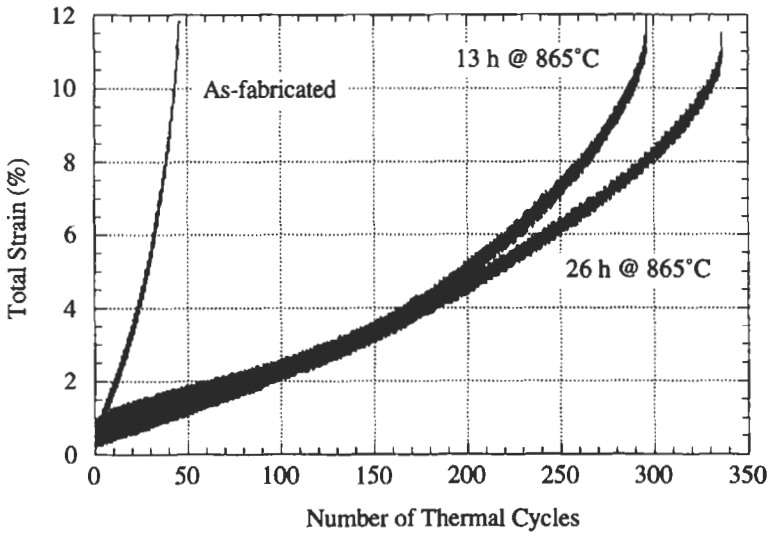

Fig. 37. Complete strain histories (CLYNE *et al.* [1995]) for Ti–6Al–4V/30% SiC monofilament composite, with and without prior heat teatments, under an applied transverse load of 25 MPa, as a function of the number of imposed thermal cycles. The thermal conditions during cycling were the same as in fig. 35.

References

ARSENAULT, R.J. and SHI, N., 1986, Dislocation Generation due to Differences between Coefficients of Thermal Expansion. Mat. Sci. and Eng. **81,** 175–87.

ARSENAULT, R.J. and TAYA, M., 1987, Thermal Residual Stress in Metal Matrix Composite. Acta Met. **35,** 651–9.

ARSENAULT, R.J., WANG, L. and Feng, C.R., 1991, Strengthening of Composites due to Microstructural Changes in the Matrix. Acta. Met. **39,** 47–57.

ARSENAULT, R.J. and ZHOU, X., 1993, Effect of Thermal-History on the Strengthening of SiC/Al Composites. Scripta Met. **28,** 875–8.

BERNDT, C.C. and YI, J.H., 1989, The Manufacture and Microstructure of Fiber Reinforced Thermally Sprayed Coatings. Surf. and Coat. Techn. **37,** 89–110.

BHANSALI, K.J. and MEHRABIAN, R., 1982, Abrasive Wear of Aluminium Matrix Composites. J. Metals **32,** 30–4.

BIRCHALL, J.D., STANLEY, D.R., MOCKFORD, M.J., PIGOTT, G.H. and PINTO, P.J., 1988, The Toxicity of Silicon Carbide Whiskers. J. Mater. Sci. Lett. **7,** 350–2.

BOLLING, G.F. and CISSE, J., 1971, A Theory for the Injection of Particles with a Solidifying Front. J.Cry.Gr. **10,** 56–66.

BOWLES, D.E. and TOMPKINS, S.S., 1989, Predictions of Coefficients of Thermal Expansion for Unidirectional Composites. J. Comp. Mat. **23,** 370–88.

BRECHET, Y., EMBURY, J.D., TAO, S. and LUO, L., 1991, Damage Initiation in MMCs. Acta Metall. et Mater. **39,** 1781–6.

BRUSETHAUG, S., REISO, O. and RUCH, W., 1990, Extrusion of Particulate-Reinforced Aluminium Billets Made by DC Casting. Fabrication of Particulates Reinforced Metal Composites, ASM, J. Masounave and F.G. Hamel (eds.), 173–80.

CANTOR, B., 1993, Optimising Microstructure in Spray Formed and Squeeze Cast Metal Matrix Composites. J. Microscopy **169,** 97–108.

CAPPELMAN, G.R., WATTS, J.F. and CLYNE, T.W., 1985, The Interface Region in Squeeze-Infiltrated Composites containing δ-alumina Fibre in an Aluminium Matrix. J.Mat.Sci. **20,** 2159–68.

CHANG, M. and SCALA, E., 1974, Plastic Deformation Processing Compressive Failure Mechanism in Al Composite Materials. Composite Materials: Testing and Design, ASTM STP **546,** 561–79.

CHARBONNIER, J., DERMARKAR, S., SANTARINI, M., FAGES, J. and SABATIE, M., 1988, High Performance Metal Matrix Composites Manufactured by Squeeze Casting. Cast Reinforced Metal Composites, S.G. Fishman and A.K. Dhingra (eds.), 127–32, ASM.

CHAWLA, K.K., ESMAEILI, A.H., DATYE, A.K. and VASUDEVAN, A.K., 1991, Effect of Homogeneous/ Heterogeneous Precipitation on Aging Behavior of SiC_p/Al 2014 Composite. Scripta Metall. Mater. **25,** 1315–9.

CHEN, Z. and MECHOLSKY, J.J., 1993, Control of Strength and Toughness of Ceramic/Metal Laminates Using Interface Design. J. Mat. Res. Soc. **8,** 2362–9.

CHESKIS, H.P. and HECKEL, R.W., 1970, Deformation Behaviour of Continuous-Fibre MMC Materials. Met. Trans. **1,** 1931–42.

CHOI, N.S. and TAKAHASHI, K., 1992, Stress Fields on and Beneath the Surface of Short-Fiber-Reinforced Composites and their Failure Mechanisms. Comp. Sci. and Tech **43,** 237–44.

CHRISTMAN, T., NEEDLEMAN, A. and SURESH, S., 1989, An Experimental and Numerical Study of Deformation in MMCs. Acta Metall. **37,** 3029–50.

CHRISTMAN, T. and SURESH, S., 1988, Effects of SiC Reinforcement and Aging Treatment on Fatigue Crack Growth in an Al-SiC Composite. Mat. Sci. and Eng. **102A,** 211–6.

CHRISTODOULOU, L. and BRUPBACHER, J.M., 1990, Metal Matrix Composites: XD™ Materials for Aerospace Applications. Materials Edge **20,** 29–33.

CLYNE, T.W., FEILLARD, P. and KALTON, A.F., 1995, Interfacial Mechanics and Macroscopic Failure in Titanium-based Composites. Life Prediction Methodology for Titanium Matrix Composites, ASTM STP, W.S. Johnson (ed.), in press.

CLYNE, T.W. and MASON, J.F., 1987, The Squeeze Infiltration Process for Fabrication of Metal Matrix Composites. Metall. Trans. **18A,** 1519–30.

CLYNE, T.W. and ROBERTS, K.A., 1995, The Influence of Process Parameters on Consolidation Efficiency when Forming Titanium Composites by Spraying onto Monofilaments. Acta Metall Mater., **43,** 2541–50.

CLYNE, T.W. and WITHERS, P.J., 1993, An Introduction to Metal Matrix Composites. Cambridge University Press, Cambridge.

CROWE, C.R., GRAY, R.A. and HASSON, D.F., 1985, Microstructure controlled fracture toughness of SiC/Al Metal Matrix Composites. 5th Int. Conf. Comp. Mats., W.C. Harrigan, J. Strife and A.K. Dhingra (eds.), 843–66, TMS-AIME.

DAEHN, G.S. and GONZÁLEZ-DONCEL, G., 1989, Deformation of Whisker-Reinforced Metal-Matrix Composites under Changing Temperature Conditions. Metall. Trans. **20A,** 2355–68.

DAVIDSON, D.L., 1987, Fracture Characteristics of Al–4%Mg Mechanically Alloyed with SiC. Metall. Trans. **18A,** 2115–28.

DAVIDSON, D.L., 1993, Fatigue and Fracture Toughness of Aluminium Alloy Reinforced with SiC and Alumina Particles. Composites **24,** 248–55.

DAYMOND, M.R. and WITHERS, P.J., 1995, An Examination of Tensile / Compressive Loading Asymmetries in Aluminium-based MMCs using the Finite Element Method. Mater. Sci. and Techn., **11,** 228–35.

DERBY, B., 1991, Thermal Cycling of Metal Matrix Composites. Risø 12th Int. Conf. on Metal Matrix Composites - Processing, Microstructure and Properties, N. Hansen, D.J. Jensen, T. Leffers, H. Lilholt, T. Lorentzen, A.S. Pedersen, O.B. Pedersen and B. Ralph (eds.), 31–50, Risø Nat. Lab., Roskilde, Denmark.

DESILVA, A.R.T., 1969, Thermal Stresses in Fibre Reinforced Composites. J. Mech. Phys. Solids **17,** 387–403.

DRAGONE, T.L. and NIX, W.D., 1990, Geometric Factors Affecting the Internal Stress Distribution and High Temperature Creep Rate of Discontinuous Fibre Reinforced Metals. Acta Metall **38,** 1941–53.

DUNAND, D.C. and MORTENSEN, A., 1991, Dislocation Emission at Fibres - II. Experiments and Microstructure of Thermal Punching. Acta Metall. et Mater. **39,** 1417–29.

DUNAND, D.C. and MORTENSEN, A., 1991, On Plastic Relaxation of Thermal Stresses in Reinforced Metals. Acta Metall. et Mater. **39,** 127–39.

DUTTA, I., TIEDEMANN, C.F. and MCNELLEY, T.R., 1990, Effect of Hot Working on the Microstructure and Properties of a cast 5083 Al-SiC_p MMC. Scripta Metall. Mater. **24,** 1233–8.

DVORAK, G.J. and JOHNSON, W.S., 1980, Fatigue Damage Mechanisms in Boron-Aluminium Composite Laminates. Advances in Composite Materials, A.R. Bunsell, C. Bathias, A. Martrenchar, D. Menkes and G. Vercher (eds.), 1117–90, Pergamon, Oxford.

DVORAK, G.J. and JOHNSON, W.S., 1980, Fracture of Metal Matrix Composites. Int. J. Fract **16,** 585–602.

EHRSTROM, J.C. and KOOL, W.H., 1988, Migration of Particles during Extrusion of Metal Matrix Composites. J. Mat. Sci. Letts. **7,** 578–80.

ENDO, T., CHANG, M., MATSUDA, N. and MATSUURA, K., 1991, Creep behaviour of SiC/Al Composite at Elevated Temperatures. Risø 12th Int. Conf. on Metal Matrix Composites - Processing, Microstructure and Properties, N. Hansen, D.J. Jensen, T. Leffers, H. Lilholt, T. Lorentzen, A.S. Pedersen, O.B. Pedersen and B. Ralph (eds.), 323–8, Risø Nat. Lab., Roskilde, Denmark.

ESHELBY, J.D., 1957, The Determination of the Elastic Field of an Ellipsoidal Inclusion and Related Problems. Proc. Roy. Soc. London, Ser. A **241,** 376–96.

EVANS, A.G., Zok, F.W. and Davis, J., 1991, The Role of Interfaces in Fiber-Reinforced Brittle Matrix Composites. Comp. Sci and Tech. **42,** 3–24.

EVANS, R.W., Leatham, A.G. and Brooks, R.G., 1985, The Osprey Preform Process. Powder Metallurgy **28,** 13–9.

EVENSEN, J.D. and VERK, A.S., 1981, The Influence of Particle Cracking on the Fracture Strain of some Al-Si Alloys. Scripta Metall. **15,** 1131–3.

EVERETT, R.K., 1991, Deposition Technologies for MMC Fabrication. Metal Matrix Composites: Processing and Interfaces, R.K. Everett and R.J. Arsenault (eds.), 103–19, Academic Press, Boston.

FEEST, E.A., 1988, Exploitation of the Metal Matrix Composites Concept. Metals and Mats. **4,** 273–8.

FLOM, Y. and ARSENAULT, R.J., 1989, Effect of Particle Size on Fracture Toughness of SiC/Al Composute Material. Acta Met. **37,** 2413–23.

FRIEND, C.M., HORSEFALL, I., LUXTON, S.D. and YOUNG, R.J., 1988, The Effect of Fibre/Matrix Interfaces on the Age-Hardening Characteristics of δ-alumina fibre Reinforced AA6061. Cast Reinforced Metal Composites, S.G. Fishman and A.K. Dhingra (eds.), 309–15, ASM.

FURNESS, J.A.G., 1991, Thermal Cycling Creep of Aluminium-Based Composites. PhD thesis, Cambridge University, UK,.

FURNESS, J.A.G. and CLYNE, T.W., 1991, Thermal Cycling Creep of Short Fibre MMCs - Measurement and Modelling of the Strain Cycle. Metal Matrix Composites - Processing, Microstructure and Properties. 12th Riso International Symposium, N. Hansen, D.J. Jensen, T. Leffers, H. Lilholt, T. Lorentzen, A.S. Pedersen, O.B. Pedersen and B. Ralph (eds.), 349–54, Risø Nat. Lab., Roskilde, Denmark.

GORDON, F.H. and CLYNE, T.W., 1993, Thermal Cyling Creep of Ti-6Al-4V/SiC Monofilament Composites under Transverse Loading. Residual Stresses in Composites: Modelling, Measurement and Effects on Thermomechanical Properties, E.V. Barrera and I. Dutta (eds.), 293–304, TMS, Warrendale.

GOTO, S. and MCLEAN, M., 1991, Role of Interfaces in Creep of Fibre-Reinforced Metal-Matrix Composites-I Continuous Fibres. Acta Met. **39,** 153–64.

GRANT, P.S. and CANTOR, B., 1989, Modelling of Spray Forming. Cast Metals **4,** 140–51.

GUO, Z.X. and DERBY, B., 1993, Microstructural Characterization in Diffusion Bonded SiC/Ti-6Al-4V Composites. J. Micros. **169,** 269–77.

HAAR, J.H.T. and DUSZCZYK, J., 1991, Mixing of Powder Metallurgical Fibre-reinforced Aluminium Composites. Mat. Sci. and Eng. **A135,** 65–72.

HAHN, G.T. and ROSENFIELD, A.R., 1975, Metallurgical Factors affecting Fracture Toughness of Al Alloys. Met. Trans. **6A,** 653–70.

HALE, D.K., 1976, The Physical Properties of Composite Materials. J. Mat. Sci. **11,** 2105–41.

HANSEN, N. and JENSEN, D.J., 1990, Recrystallization of Metals Containing Particles and Fibres. Recrystallization '90, T. Chandra (ed.), 79–88, TMS, Warrendale.

HARRIGAN, W.C., 1994, Fatigue Testing Welded Joints for P/M Al Matrix Composites. J. of Metals **46,** 52–4.

HE, M.-Y. and HUTCHINSON, J.W., 1989, Crack Deflection at an Interface between Dissimilar Elastic Materials. Int. J. of Solids and Structures **25,** 1053–67.

HE, M.Y., EVANS, A.G. and Curtin, W.A., 1993, The Ultimate Tensile Strength of Metal and Ceramic Matrix Composites. Acta. Metall.et. Mater. **41,** 871–8.

HE, M.Y., Heredia, F.E., Wissuchek, D.J., Shaw, M.C. and Evans, A.G., 1993, The Mechanics of Crack Growth in Layered Materials. Acta. Metall.et. Mater. **41,** 1223–8.

HONG, S.H., SHERBY, O.D., DIVECHA, A.P., KARMARKAR, S.D. and MACDONALD, B.A., 1988, Internal Stress Superplasticity in 2024 Al-SiC Whisker Reinforced Composites. J. Comp. Mat. **22,** 102–23.

HOOVER, W.R., 1991, Die Casting of Duralcan Composites. Metal Matrix Composites - Processing, Microstructure and Properties, N. Hansen, D.J. Jensen, T. Leffers, H. Lilholt, T. Lorentzen, A.S. Pedersen, O.B. Pedersen and B. Ralph (eds.), 387–92, Risø Nat. Lab., Roskilde, Denmark.

HOSKING, F.M., FOLGAR-PORTILLO, F., WUNDERLIN, R. and MEHRABIAN, R., 1982, Composites of Aluminium Alloys: Fabrication and Wear Behaviour. J.Mat.Sci. **17,** 477–98.

HUMPHREYS, F.J., MILLER, W.S. and DJAZEB, M.R., 1990, Microstructural Development During Thermomechanical Processing of Particulate Metal Matrix Composites. Mater. Sci. Tech. **6,** 1157–66.

HUNT, W.H., RICHMOND, O. and YOUNG, R.D., 1987, Fracture Initiation in Particle Hardened Materials with high Volume Fraction. Proc. ICCM6/ECCM2, F.L. Matthews, N.C.R. Buskell, J.M. Hodgkinson and J. Morton (eds.), 209–23, Elsevier.

HUTCHINGS, I.M., 1991, Abrasive and Erosive Wear of Metal Matrix Composites. 2nd European Conference on Advanced Materials, Euromat'91, T.W. Clyne and P.J. Withers (eds.), vol. 2, 56–64, Institute of Metals, London.

ITO, S., MIYAZAKA, K., YONEDA, N. and ASAKA, K., 1989, Preparation of SiC-Fe composite using HIP. J. Jap. Soc. Powder Metall. **36,** 831–6.

JANSSON, S., DEVE, H.E. and EVANS, A.G., 1991, The Anisotropic Mechanical Properties of a Ti matrix Composite Reinforced with SiC Fibres. Metall.Trans. **22A,** 2975–84.

JARRY, P., LOUÉ, W. and BOUVAIST, J., 1987, Rheological Behaviour of SiC/Al Composites. ICCM VI/ECCM 2, F.L. Matthews, N.C.R. Buskell, J.M. Hodgkinson and J. Morton (eds.), 2.350–2.61, Elsevier, London.

JARRY, P., MICHAUD, V.J., MORTENSEN, A., DUBUS, A. and TIRARD-COLLET, R., 1992, Infiltration of Fiber Preforms by an Alloy: Part III. Die Casting Experiments. Metall. Trans. **23A,** 2281–9.

JHA, A.K., PRASAD, S.V. and UPADHYAYA, G.S., 1989, Preparation and Properties of 6061 Aluminium Alloy /Graphite Composites by PM Route. Powder Metall. **32,** 309–12.

JOHNSON, W.S., 1993, Damage Development in Titanium Metal Matrix Composites Subjected to Cyclic Loading. Composites **24,** 187–96.

KALTON, A.F., WARD-CLOSE, C.M. and CLYNE, T.W., 1994, Development of the Tensioned Push-out Test for Study of Fibre-Matrix Interfaces. Composites **25,** 637–44.

KAMAT, S., HIRTH, J.P. and MEHRABIAN, R., 1989, Mechanical Properties of Particulate Reinforced Al-matrix Composites. Acta Metall. **37,** 2395–402.

KASAKOV, N.F., 1985, Diffusion Bonding of Materials. Pergamon, Oxford.

KATTAMIS, T.Z. and CORNIE, J.A., 1988, Solidification Processing of Particulate Ceramic-aluminium Alloy Composites. Cast Reinforced Metal Composites, S.G. Fishman and A.K. Dhingra (eds.), 47–52, ASM.

KELLY, A., 1966, Strong Solids. Oxford University Press, Oxford.

KELLY, A., 1972, Reinforcement of Structural Materials by Long Strong Fibres. Metall. Trans. **3,** 2313–25.

KENNEDY, A.R. and CLYNE, T.W., 1991, Particle Pushing during the Solidification of Metal Matrix Composites. Cast Metals J. **4,** 160–4.

KIESCHKE, R.R., SOMEHK, R.E. and CLYNE, T.W., 1991, Sputter Deposited Barrier Coatings on SiC Monofilaments for Use in Reactive Metallic Matrices - Part I Optimization of Barrier Structure. Acta Metall. **39,** 427–36.

KIM, J.K., BAILLIE, C. and MAI, Y.W., 1992, Interfacial Debonding and Fibre Pull-out Stresses. Part II - A New Model Based on the Fracture Mechanics Approach. J. Mat. Sci. **27,** 3155–66.

KLIER, E.M., MORTENSEN, A., CORNIE, J.A. and FLEMINGS, M.C., 1991, Fabrication of Cast Particle-Reinforced Metals via Pressure Infiltration. J. Mat. Sci. **26,** 2519–26.

KLIMOWICZ, T.F. and VECCHIO, K.S., 1989, The Influence of Aging Condition on the Fracture Toughness of Al_2O_3–Reinforced Al Composites. Fundamental Relationships between Microstructure and Mechanical Properties of MMCS, P.K. Liaw and M.N. Gungor (eds.), 255–67, TMS, Warrendale.

KREIDER, K.G. and PATRANI, V.M., 1970, Thermal Expansion of Boron Fiber-Aluminium Composites. Metall. Trans. **1,** 3431–5.

LAJOYE, L. and SUERY, M., 1988, Modelling of Particle Segregation during Centrifugal Casting of Al-matrix Composites. Cast Reinforced Metal Composites, S.G. Fishman and A.K. Dhingra (eds.), 15–20, ASM.

LE FLOUR, J.C. and LOCICÉRO, R., 1987, Influence of Internal Stresses Induced by Thermal Cycling on the Plastic Deformation Resistance of an Al/SiC Composite Material. Scripta Met. **21,** 1071–6.

LEATHAM, A.G., OGILVEY, A., CHESNEY, P.F. and WOOD, J.V., 1989, Osprey Process - Production Flexibility in Materials Manufacture. Metals and Materials **5,** 140–3.

LEDERICH, R.J. and SASTRY, S.M.L., 1982, Deformation Behaviour of SiC_w Reinforced Al Composites. Mat. Sci. and Eng. **55,** 143–6.

LEVY, A. and PAPAZIAN, J.M., 1990, Tensile Properties of Short fibre-reinforced SiC/Al Composites, part II. Finite Element Analysis. Metall Trans. **21A,** 411–20.

LEWANDOWSKI, J.J., LIU, C. and HUNT, W.H., 1989, Effects of Matrix Microstructure and Particle Distribution on Fracture of an Al MMC. Mat. Sci. and Eng. **A107,** 241–55.

LEWIS, C.A. and WITHERS, P.J., 1995, Weibull Modelling of Particle Cracking in Metal Matrix Cracking. Acta Metall. et Mater., **43,** 3685–99.

LI, C.H., NYBORG, L., BENGTSSON, S., WARREN, R. and OLEFJORD, I., 1989, Reactions between SiO_2 binder and matrix in δ-Al_2O_3/Al-Mg Composites. Interfacial Phenomena in Composite Materials 1989, F.R. Jones (ed.), 253–7, Butterworths.

LILHOLT, H., 1977, Hardening in two-phase materials - I Strength Contributions in Fibre-reinforced Cu-W. Acta Metall. **25,** 571–85.

LILHOLT, H. and TAYA, M., 1987, Creep Behaviour of the Metal Matrix Composite Al 2124 with SiC Fibres. ICCM-6/ECCM-2, F.L. Matthews, N.C.R. Buskell, J.M. Hodgkinson and J. Morton (eds.), 2.234–2.44, Elsevier, London.

LIN, J.S., LI, P.X. and WU, R.J., 1993, Aging Evaluation of Cast Particulate-Reinforced SiC/Al(2024) Composites. Scripta Met. **28,** 281–6.

LLORCA, J., NEEDLEMAN, A. and SURESH, S., 1991, An Analysis of the Effects of Matrix Void Growth on Deformation and Ductility in Metal-Ceramic Composites. Acta.Metall. **39,** 2317–35.

LLOYD, D., 1991, Aspects of Fracture in Particulate Reinforced Metal Matrix Composites. Acta Metall. **39,** 59–71.

LLOYD, D.J., 1988, Properties of Shape Cast Al-SiC Metal Matrix Composites. Cast Reinforced Metal Composites, S.G. Fishman and A.K. Dhingra (eds.), 263–9, ASM.

LLOYD, D.J., 1989, The Solidification Microstructures of Particulate Reinforced Al/SiC Composites. Comp. Sci. and Tech. **35,** 159–80.

LLOYD, D.J., 1991, Factors influencing the Properties of Particulate Reinforced Composites Produced by Molten Metal Mixing. Metal Matrix Composites - Processing, Microstructure and Properties, N. Hansen, D.J. Jensen, T. Leffers, H. Lilholt, T. Lorentzen, A.S. Pedersen, O.B. Pedersen and B. Ralph (eds.), 81–99, Risø Nat. Lab., Roskilde, Denmark.

LONG, S., ZHANG, Z. and FLOWER, H.M., 1994, Hydrodynamic Analysis of Liquid Infiltration of Unidirectional Fibre Arrays by Squeeze Casting. Acta Metall. et Mater. **42,** 1389–97.

LUKASAK, D.A. and KOSS, D.A., 1993, Microstructural Influences on Fatigue Crack Initiation in a Model Particulate-Reinforced Aluminium Alloy MMC. Composites **24,** 262–9.

MAHON, G.J., HOWE, J.M. and VASUDEVAN, A., 1990, Microstructural Development and the Effect of Interfacial Precipitation on the Tensile Properties of a Al/SiC Composite. Acta Metall. **38,** 1503–12.

MAJUMDAR, B.S. and NEWAZ, G.M., 1992, Inelastic Deformation of Metal Matrix Composites: Plasticity and Damage Mechanisms. Phil. Mag. **66,** 187–212.

MAJUMDAR, B.S. and NEWAZ, G.M., 1995, Constituent Damage Mechanisms in MMCs under Fatigue Loading, and their Effects on Fatigue Life. Mat. Sci. and Eng., in press.

MAJUMDAR, B.S., NEWAZ, G.M. and ELLIS, J.R., 1993, Evolution of Damage and Plasticity in Titanium-Based, Fiber-Reinforced Composites. Metall. Trans. **24A,** 1597–610.

MANOHARAN, M. and LEWANDOWSKI, J.J., 1990, Crack Initiation and Growth Toughness of an Al MMC. Acta Metall. et Mater. **38,** 489–96.

MARSHALL, D.B. and EVANS, A.G., 1985, Failure Mechanisms in Ceramic-Fibre/Ceramic-Matrix Composites. J. Amer. Ceram. Soc. **68,** 225–31.

MARSHALL, D.B. and OLIVER, W.C., 1987, Measurement of Interfacial Mechanical Properties in Fiber-reinforced Ceramic Composites. J. Amer. Ceram. Soc **70,** 542–8.

MARTINEAU, P., LAHAYE, M., PAILLER, R., NASLAIN, R., COUZI, M. and CRUEGE, F., 1984, SiC Filament/Titanium Matrix Composites Regarded as Model Composites. Part2: Fibre/Matrix Chemical Interactions at High Temperatures. J. Mat. Sci **19,** 2749–70.

MCCOY, J.W. and WAWNER, F.E., 1988, Dendritic Solidification in Particle-reinforced Cast Aluminium Composites. Cast Reinforced Metal Composites, S.G. Fishman and A.K. Dhingra (eds.), 237–42, ASM.

MCDANELS, D.L., 1985, Analysis of Stress-Strain, Fracture, and Ductility of Aluminium Matrix Composites Containing Discontinuous Silicon Carbide Reinforcement. Metall.Trans. **16A,** 1105–15.

MCLEOD, A.D., GABRYEL, C., LLOYD, D.J. and MORRIS, P., 1989, Particle Incorporation Studies in Support of the Dural Process. Processing of Ceramic and Metal Matrix Composites, 228–35, Pergamon, Oxford.

MCPHERSON, R., 1981, The Relationship between the Mechanism of Formation, Microstructure and Properties of Plasma-sprayed Coatings. Thin Solid Films **83,** 297–310.

MILLER, W.S. and HUMPHREYS, F.J., 1991, Stengthening Mechanisms in Particulate MMCs. Scripta Metall. Mater. **25,** 33–8.

MORITZ, R., 1989, Steel Matrix - Titanium Carbide Composite Materials by Hot Isostatic Pressing (HIP), 12th International Plansee Seminar, H. Bildstein and H.M. Orter (eds.), 847–62, Metallwerk Plansee GmbH.

MORTENSEN, A. and CORNIE, J.A., 1987, On the Infiltration of Metal Matrix Composites. Metall.Trans. **18A,** 1160–3.

MORTENSEN, A., MICHAUD, V.J. and FLEMINGS, M.C., 1993, Pressure-Infiltration Processing of Reinforced Aluminium. J. of Metals **45,** 36–43.

MURPHY, A.M., WHITEHOUSE, A.F. and CLYNE, T.W., 1995, Tensile Failure of Cast and Extruded Fibre Reinforced Aluminium Composites. Advanced Structural Fibre Composites, P. Vincenzini (ed.), Techna Srl., 653–60.

NARDONE, V.C. and STRIFE, J.R., 1987, Analysis of the Creep Behaviour of SiC Whisker-Reinforced 2124 (T4, Metall. Trans. **18A,** 109–14.

NARDONE, V.C. and TIEN, J.K., 1986, On the Creep Rate Dependence of Particle Strengthened Alloys. Scripta Met. **20,** 797–802.

NEWKIRK, M.S., URQUHART, A.W., ZWICKER, H.R. and BREVAL, E., 1986, Formation of Lanxide Ceramic Composite Materials. J. Mat. Res. **1,** 81–9.

NIEH, T.G., 1984, Creep Rupture of a Silicon Carbide Reinforced Aluminium Composite. Metall. Trans. **15A,** 139–46.

NIEH, T.G. and CHELLMAN, D.J., 1984, Modulus Measurements in Discontinuous Reinforced Al Composites. Scripta Met. **18,** 925–8.

NIKLAS, A., FROYEN, L., DELAEY, L. and BUEKENHOUT, L., 1991, Comparative Evaluation of Extrusion and Hot Isostatic Pressing as Fabrication Techniques for Al-SiC Composites. Mat. Sci. and Eng. **A135,** 225–9.

NOURBAKHSH, S., LIANG, F. and MARGOLIN, H., 1989, Calculation of Minimum Pressure for Liquid Metal Infiltration of a Fiber Array. Metall. Trans. **20A,** 1861–6.

NUNES, J., CHIN, E.S.C., SLEPETZ, J.M. and TSANGARAKIS, N., 1985, Tensile and Fatigue Behavior of Alumina Fiber Reinforced Magnesium Composites. 5th Int. Conf. on Comp. Mats. (ICCM 5), W. Harrigan, J. Strife and A.K. Dhingra (eds.), 723–45, TMS-AIME.

NUTT, S.R. and NEEDLEMAN, A., 1987, Void Nucleation at Fibre Ends in Al-SiC Composites. Scripta. Met. **21,** 705–10.

PADKIN, A.J., BORETON, M.F. and PLUMBRIDGE, W.J., 1987, Fatigue Crack Growth in Two-phase Alloys. Mat. Sci. and Tech. **3,** 217–23.

PAN, Y.M., FINE, M.E. and CHENG, H.S., 1990, Wear Mechanisms of Aluminium-based Metal Matrix Composites under Rolling and Sliding Contact. Tribology of Composite Materials, P.K. Rohatgi, B.G. Blau and C.S. Yust (eds.), 93–101, ASM.

PARK, K.T., LAVERNIA, E.J. and MOHAMED, F.A., 1990, High Temperature Creep of Silicon Carbide Particulate Reinforced Aluminium. Acta Metall. **38,** 2149–59.

PATTERSON, W.G. and TAYA, M., 1985, Thermal Cycling Damage of SiC Whisker/2124 Aluminium. ICCM V, W.C. Harrigan, J. Strife and A. Dhingra (eds.), 53–66, TMS, Warrendale.

PICKARD, S.M. and DERBY, B., 1988, Thermal Cycle Creep of Al/SiC Particulate Composite. Mechanical and Physical Behaviour of Metallic an Ceramic Composites. 9th Risø Int. Symp. on Met. and Mat. Sci., S.I. andersen, H. Lilholt and O.B. Pedersen (eds.), 447–52, Risø Nat. Lab., Roskilde, Denmark.

POTSCHKE, J. and ROGGE, V., 1989, On the Behaviour of Foreign Particles at an Advancing Solid-Liquid Interface. J. Cry. Growth **94,** 726–38.

POVIRK, G.L. et al., 1991, Mechanically Induced Residual Stresses in Al-SiC Composites. Scripta Metall. **25,** 1883–8.

POVIRK, G.L. et al., 1992, Thermally and Mechanically Induced Residual Strains in Al-SiC Composites. Acta. Metall. **40,** 2391–412.

PRANGNELL, P. and STOBBS, W.M., 1991, The Effect of Internal Stresses on Precipitation Behaviour in Particulate Reinforced Al Matrix MMCs. Metal Matrix Composites - Processing, Microstructure and Properties, 12th Risø Int. Symp. on Materials Sci., N. Hansen, D.J. Jensen, T. Leffers, H. Lilholt, T. Lorentzen, A.S. Pedersen, O.B. Pedersen and B. Ralph (eds.), 603–10, Risø Nat. Lab., Roskilde, Denmark.

PRANGNELL, P.B., DOWNES, T., STOBBS, W.M. and WITHERS, P.J., 1994, The Deformation of Discontinuously Reinforced MMCs. Part I: The Initial Yielding Behaviour. Acta Metall. et Mater. **42,** 3425–36.

PRANGNELL, P.B., DOWNES, T., STOBBS, W.M. and WITHERS, P.J., 1994, The Deformation of Discontinuously Reinforced MMCs. Part II: The Elastic Response. Acta Metall. et Mater. **42,** 3437–42.

RACK, H.J., 1991, Processing of Metal Matrix Composites. Metal Matrix Composites: Processing and Interfaces, R.K. Everett and R.J. Arsenault (eds.), 83–101, Academic Press, Boston.

RHODES, C.G., GOSH, A.K. and SPURLING, R.A., 1987, Ti-6Al-4V-2Ni as a Matrix for a SiC Reinforced Composites. Metall. Trans. **18A,** 2151–6.

RITCHIE, R.O. and THOMPSON, A.W., 1985, On Macroscopic and Microscopic Analyses for Crack Initiation and Crack Growth Toughness in Ductile Alloys. Metall. Trans. **16A,** 233–48.

ROBERTSON, D.D. and MALL, S., 1994, A Non-linear Micromechanics-based Analysis of Metal Matrix Composite Laminates. Comp. Sci. and Techn. **52,** 319–31.

ROCHER, J.P., QUENISSET, J.M. and NASLAIN, R., 1985, A New Casting Process for Carbon (or SiC-based) fibre-aluminium Low Cost Composite Materials. J.Mat.Sci.Letts. **4,** 1527–9.

ROHATGI, P.K., ASTHANA, R. and DAS, S., 1986, Solidification, Structures and Properties of Cast metal-Ceramic Particle Composites. Int. Met. Reviews **31,** 115–39.

ROHATGI, P.K., DAHOTRE, N.B., LIU, Y., LIN, M. and BARR, T.L., 1988, Tribological Behaviour of Al alloy-Graphite and Al Alloy-Microcrystalline Carbon Particulate Composites. Cast Reinforced Metal Composites, S.G. Fishman and A.K. Dhingra (eds.), 367–74, ASM.

ROHATGI, P.K., YARANDI, F.M. and LIU, Y., 1988, Influence of Solidification Conditions on Segregation of Aluminium-silicon Carbide Particle Composites. Cast Reinforced Metal Composites, S.G. Fishman and A.K. Dhingra (eds.), 249–55, ASM.

SAMPLE, R.J., BHAGAT, R.B. and AMATEAU, M.F., 1988, High Pressure Squeeze Casting of Unidirectional Graphite Fiber Reinforced Aluminium Matrix Composites. Cast Reinforced Metal Composites, S.G. Fishman and A.K. Dhingra (eds.), 179–83, ASM.

SCHAPERY, R.A., 1968, Thermal Expansion Coefficients of Composite Materials based on Energy Principles. J. Comp. Materials **2,** 380–404.

SENSMEIER, M.D. and WRIGHT, P.K., 1990, The Effect of Fiber Bridging on Fatigue Crack Growth in Titanium Matrix Composites. Fundamental Relationships Between Microstructures and Mechanical Properties of Metal-Matrix Composites, P.K. Liaw and M.N. Gungor (eds.), 441–57, TMS, Warrendale.

SHAHANI, R.A., 1991, Microstructural Development during Thermomechanical Processing of Aluminium-based Composites. PhD thesis, Cambridge University, UK.

SHAW, M.C., MARSHALL, D.B., DALGLEISH, B.J., DADKHAH, M.S., HE, M.Y. and EVANS, A.G., 1994, Fatigue Crack Growth and Stress Redistribution at Interfaces. Acta Metall. et Mater. **42,** 4091–9.

SHETTY, D.K., 1988, Shear Lag Analysis of Fibre Push-out (Indentation) Tests for estimating Interfacial Friction Stress in Ceramic-Matrix Composites. J.Amer. Ceram. Soc. **71,** C107–9.

SINGH, P.M. and LEWANDOWSKI, J.J., 1993, Poisson Ratio Measurements for an Al-Based Metal Matrix Composite During Elastic and Plastic Deformation. Scripta Met. **29,** 199–204.

SKIBO, M., MORRIS, P.L. and LLOYD, D.J., 1988, Structure and Properties of Liquid Metal Processed SiC Reinforced Aluminium. Cast Reinforced Metal Composites, S.G. Fishman and A.K. Dhingra (eds.), 257–61, ASM.

SMITH, P.R. and FROES, F.H., 1984, Developments in Titanium MMCs. J. Metals **36,** 19–26.

SMITH, R.W., 1991, Plasma Spray Processing - The State of the Art and Future - From a Surface to a Materials Processing Technology. 2nd Plasma Technik Symposium, S. Blum-Sandmeier, H. Eschnauer, P. Huber and A.R. Nicoll (eds.), 17–38, Plasma Technik, Wohlen, Switzerland.

SØRENSEN, N., 1991, Effects of Clustering on the Creep Properties of Whisker Reinforced Al. Metal Matrix Composites - Processing, Microstructure and Properties, 12th Risø Int. Symp. on Materials Sci., N. Hansen, D.J. Jensen, T. Leffers, H. Lilholt, T. Lorentzen, A.S. Pedersen, O.B. Pedersen and B. Ralph (eds.), 667–74, Risø Nat. Lab., Roskilde, Denmark.

SRIVATSAN, T.S. and LAVERNIA, E.J., 1992, Use of Spray Techniques to Synthesize Particulate-Reinforced Metal-Matrix Composites. J. Mat. Sci. **27,** 5965–81.

STACEY, M.H., TAYLOR, M.D. and WALKER, A.M., 1987, A new Alumina Fibre for Advanced Composites. 6th Int. Conf. on Composite Materials (ICCM6), F.L. Matthews, N.C.R. Buskell, J.M. Hodgkinson and J. Morton (eds.), 5.371–5.81, Elsevier, London.

STANFORD-BEALE, C.A. and CLYNE, T.W., 1989, Extrusion and High Temperature Deformation of Fibre-reinforced aluminium. Comp. Sci. and Tech. **35,** 121–57.

STEFANESCU, D.M., DHINDAW, B.K., KACAR, S.A. and MOITRA, A., 1988, Behaviour of Ceramic Particles at the Solid-Liquid Metal Interface in MMCs. Metall. Trans. **19A,** 2847–55.

STEFANESCU, D.M., MOITRA, A., KACAR, A.S. and DHINDAW, B.K., 1990, The Influence of Buoyant Forces and Volume Fraction of Particles on the Particle Pushing/entrapment Transition During DS of Al/SiC and Al/graphite Composites. Metall. Trans. **21A,** 231–9.

STOLOFF, N.S. and ALMAN, D.E., 1990, Innovative Processing Techniques for Intermetallic Matrix Composites. MRS Bulletin **15,** 47–53.

TAYA, M., DUNN, M. and LILHOLT, H., 1991, Long Term Properties of Metal Matrix composites. Risø 12th Int. Conf. on Metal Matrix Composites - Processing, Microstructure and Properties, N. Hansen, D.J. Jensen, T. Leffers, H. Lilholt, T. Lorentzen, A.S. Pedersen, O.B. Pedersen and B. Ralph (eds.), 149–72, Risø Nat. Lab., Roskilde, Denmark.

TAYA, M., LULAY, K.E. and LLOYD, D.J., 1991, Strengthening of a Particulate Metal Matrix Composite by Quenching. Acat Metall. et Mater. **39,** 73–87.

THOMASON, P.F., 1993, Ductile Fracture by the Growth and Coalescence of Microvoids of Non-uniform Size and Spacing. Acta Metall. et Mater. **41,** 2127–34.

THOMPSON, A.W. and ASHBY, M.F., 1984, Fracture Surface Micro-roughness. Scripta Metall. **18,** 127–30.

TOITOT, D., ANDRIEU, E. and JARRY, P., 1991, Dimensional Changes and Transient Deformations Affecting a Metal Matrix Composite during Thermo-Mechanical Loadings. Metal Matrix Composites - Processing, Microstructure and Properties. 12th Riso International Symposium, N. Hansen, D.J. Jensen, T. Leffers, H. Lilholt, T. Lorentzen, A.S. Pedersen, O.B. Pedersen and B. Ralph (eds.), 695–700, Risø Nat. Lab., Roskilde, Denmark.

TSANGARAKIS, N., SLEPETZ, J.M. and NUNES, J., 1985, Fatigue Behaviour of Alumina Fiber Reinforced Aluminium Composites. Recent Advances in Composites in the United States and Japan, ASTM STP 864, J.R. Vinson and M. Taya (eds.), 131–52, ASTM, Philadelphia.

UHLMANN, D.R., CHALMERS, B. and JACKSON, K.A., 1964, Interactions between Particles and Solid-Liquid Interface. J. Appl. Phys. **35,** 2986–93.

UPADHYAYA, G.S., 1989, Powder Metallurgy Metal Matrix Composites: an Overview. Met. Mater. Process **1,** 217–28.

UPADYAYA, D., WOOD, M., WARD-CLOSE, C.M., TSAKIROPOULOS, P. and FROES, F.H., 1994, Coating and Fiber Effects on SiC-reinforced Titanium. J. of Metals **46,** 62–7.

URQUHART, A.W., 1991, Novel Reinforced Ceramics and Metals: A Review of Lanxide's Composite Technologies. Mat. Sci. and Eng. **A144,** 75–82.

WAKASHIMA, K., CHOI, B.H. and MORI, T., 1990, Plastic Incompatibility and its Accommodation by Diffusional Flow: Modelling of Steady State Creep of a Metal Matrix Composite. Mat. Sci. and Eng. **A127,** 57–64.

WAKASHIMA, K., TSUKAMOTO, H. and CHOI, B.H., 1991, A Mechanism of Thermal Cycling-induced Superplasticity in Discontinuous Fibre Reinforced MMCs. Metal Matrix Composites - Processing, Microstructure and Properties, 12th Risø Int. Symp. on Materials Sci., N. Hansen, D.J. Jensen, T. Leffers, H. Lilholt, T. Lorentzen, A.S. Pedersen, O.B. Pedersen and B. Ralph (eds.), 725–34, Risø Nat. Lab., Roskilde, Denmark.

WANG, A.G. and HUTCHINGS, I.M., 1989, Wear of Alumina fibre-Aluminium Matrix Composites by Two-Body Abrasion. Mat.Sci.Tech. **5,** 71–5.

WARD-CLOSE, C.M. and PARTRIDGE, P.G., 1990, A Fibre Coating Process for Advanced Metal Matrix Composites. J. Mat. Sci. **25,** 4315–23.

WARWICK, C.M. and CLYNE, T.W., 1990, The Micromechanisms of Strain Rachetting During Thermal Cycling of Fibrous MMCs. Fundamental Relationships Between Microstructures and Mechanical Properties of Metal-Matrix Composites, P.K. Liaw and M.N. Gungor (eds.), 209–23, TMS, Warrendale.

WARWICK, C.M. and SMITH, J.E., 1991, Interfacial Reactions in Ti Alloys Reinforced with C/TiB_2 - Coated SiC Monofilament. Metal Matrix Composites - Processing, Microstructure and Properties, 12th Risø Int. Symp. on Met. and Mat. Sci., N. Hansen, D.J. Jensen, T. Leffers, H. Lilholt, T. Lorentzen, A.S. Pedersen, O.B. Pedersen and B. Ralph (eds.), 735–40, Risø Nat. Lab., Roskilde, Denmark.

WATSON, M.C. and CLYNE, T.W., 1993, Reaction-Induced Changes in Interfacial and Macroscopic Mechanical Properties of SiC Monofilament Reinforced Titanium. Composites **24,** 222–8.

WATSON, M.C. and CLYNE, T.W., 1993, The Tensioned Push-Out Test for Measurement of Fibre/Matrix Interfacial Toughness under Mixed Mode Loading. Mat. Sci. and Eng. **A160,** 1–5.

WESTFALL, L.J., 1987, Composite Monolayer Fabrication by an Arc Spraying Process. Nat. Thermal Spray Conf. - Thermal Spray : Advances in Coating Technology, D.L. Houck (ed.), 417–26, ASM.

WHEATLEY, W.J. and WAWNER, F.W., 1985, Kinetics of the reaction between SiC (SCS-6) filaments and Ti-6Al-4V matrix. J. Mat. Sci. Lett. **4,** 173–5.

WHITE, J., DARBY, N.A., HUGHES, I.R., JORDAN, R.M. and WILLIS, T.C., 1990, Metal Matrix Composites produced by Spray Deposition. Adv. Mater. Technol. Int., 96–9.

WHITEHOUSE, A.F. and CLYNE, T.W., 1993, Cavity Formation during Tensile Straining of Particulate and Short Fibre Metal Matrix Composites. Acta Metall. et Mater. **41,** 1701–11.

WHITEHOUSE, A.F. and CLYNE, T.W., 1995, Critical Stress Criteria for Cavitation in MMCs. Acta Metall. et Mater., **43,** 2107–14.

WHITEHOUSE, A.F., SHAHANI, R.A. and CLYNE, T.W., 1991, Cavitation during Tensile Deformation of Powder route Particle-Reinforced Aluminium. Metal Matrix Composites: Processing, Microstructure and Properties, N. Hansen, D.J. Jensen, T. Leffers, H. Lilholt, T. Lorentzen, A.S. Pedersen, O.B. Pedersen and B. Ralph (eds.), 741–8, Risø Nat. Lab., Roskilde, Denmark.

WILLIAMS, D.R. and FINE, M.E., 1985, Quantitative Determination of Fatigue Microcrack Growth in SiC_w Reinforced 2124 Al alloy Composite. ICCM V, W.C. Harrigan, J. Strife and A. Dhingra (eds.), 639–70, TMS, Warrendale.

WILLIS, T.C., 1988, Spray Deposition Process for Metal Matrix Composite Manufacture. Metals and Materials **4,** 485–8.

WITHERS, P.J., STOBBS, W.M. and PEDERSEN, O.B., 1989, The Application of the Eshelby Method of Internal Stress Determination for Short Fibre Metal Matrix Composites. Acta Metall. **37,** 3061–84.

WOLF, E.E., KENDALL, E.G. and RILEY, W.C., 1980, Thermal Expansion Measurements of MMCs. 3rd Internat. Conf. on Composite Materials (ICCM3), A.R. Bunsell and C. Bathais (eds.), 1140–52, Pergamon, Oxford.

WRIGHT, P.K., NIMMER, R., SMITH, G., SENSMEIER, M. and BRUN, M., 1990, The Influence of the Interface on Mechanical Behaviour of Ti-6Al-4V/SCS6 Composites. Interfaces in Metal-Ceramic Composites, R.Y. Lin, R.J. Arsenault, G.P. Martins and S.G. Fishman (eds.), 559–81, TMS, Warrendale.

WU, M.Y. and SHERBY, O.D., 1984, Superplasticity in a Silicon Carbide Whisker Reinforced Aluminium Alloy. Scripta Met. **18,** 773–6.

XIONG, Z., GENG, L. and YAO, C.K., 1990, Investigation of High-Temperature Deformation Behaviour of a SiC Whisker Reinforced 6061 Aluminium Composite. Comp Sci and Tech **39,** 117–25.

YANG, C.J., JENG, S.M. and YANG, J.M., 1990, Interfacial Properties Measurement for SiC fiber-reinforced Titanium Alloy Composites. Scripta Met. et Mat. **24,** 469–74.

ZAHL, D.B. and MCMEEKING, R.M., 1991, The Influence of Residual Stress on the Yielding of MMCs. Acta Metall. et Mater. **39,** 1117–22.

ZHANG, H., DAEHN, G.S. and WAGONER, R.H., 1991, Simulation of the Plastic Response of Whisker Reinforced Metal Matrix Composites under Thermal Cycling Conditions. Scripta Met. **25,** 2285–90.

ZHAO, Y.Y., GRANT, P.S. and CANTOR, B., 1993, The Microstructure of Spray Formed Ti-6Al-4V/SiCf Metal Matrix Composites. J. of Microscopy **169,** 263–7.

Further reading

Metal Matrix Composites: Thermomechanical Behaviour, 1989, Taya, M. and Arsenault, R.J., Pergamon.

Metal Matrix Composites: Processing and Interfaces, 1991, Everett, R.K. and Arsenault, R.J. (eds.), Academic.

Metal Matrix Composites: Processing, Microstructure and Properties, 1991, Hansen, N., Juul Jensen, D., Leffers, T., Lilholt, H., Lorentzen, T., Pedersen, A.S., Pedersen, O.B. and Ralph, B. (eds.), Risø Nat. Lab., Denmark.

Metal Matrix Composites, 1991, Chadwick, G. and Froyen, L. (eds.), North Holland, Amsterdam.

An Introduction to Metal Matrix Composites, 1993, Clyne, T.W. and Withers, P.J., Cambridge Univ. Press.

CHAPTER 31

SINTERING PROCESSES

H. E. EXNER and E. ARZT

Technische Hochschule, Fachbereich Materialwissenschaft
D-64287 Darmstadt, FRG
and Max–Planck–Institut für Metallforschung
Institut für Werkstoffwissenschaft, D-70174 Stuttgart, FRG

R. W. Cahn and P. Haasen†, eds.
Physical Metallurgy; fourth, revised and enhanced edition

Introduction

The technique of forming metal parts from powders by pressing and sintering dates back to the beginning of human civilization. Almost every metal or ceramic material was initially made via the powder route. Modern applications of sintering in materials technology are widespread: powder-technological production of structural steel parts, self-lubricating bearings, porous metals for filtering, tungsten wires for lamp filaments, soft and hard magnetic materials, electrical contacts, composite packages for highly integrated electronic devices, oxide-dispersion strengthened superalloys for high temperature motors, amalgams for dental applications, metallic and ceramic materials for medical applications, cemented carbides for cutting tools and a large variety of ceramic components are only a few of the many technical production processes involving sintering as an important step. A book by LENEL [1980] gives a comprehensive review. Sintering processes are also important in a number of other fields of materials technology. One example is sintering of finely ground ores into pellets, thereby preparing them for smelting. On the other hand, sintering of finely dispersed catalyst materials at operating temperatures is undesirable since it lowers their activity. Pore closure or formation during diffusion bonding, during chemical reactions, during creep and during superplastic deformation follow the same physical principles as sintering, reaction sintering, hot pressing or rapid densification during sinterforging (for references see SCHATT [1992]) and can be formally described by similar models and equations. This is particularly true for creep processes (see ch. 22) which can be seen as reversed hot-pressing (power law creep) or sintering (diffusional creep).

The consolidation of powders and densification of porous solids is possible by pressing and subsequent pressureless heat-treatment (*solid-state sintering*), by simultaneous application of pressure and heat (*hot-pressing* or *pressure-sintering*) or with the aid of a limited amount of melt (*liquid-phase sintering*). The technology of sintering and hot-pressing has been thoroughly developed down to minute details. Physicists, chemists, metallurgists and ceramists have worked together to establish the theoretical basis for understanding the complex interaction of geometrical and thermodynamic factors and the effects of a number of mechanisms which occur simultaneously or in sequence. Some of these results are discussed in the following.

1. Solid-state sintering

In the majority of technical applications, powders are compacted into shaped parts which then are heat-treated in order to give them the required mechanical and physical properties. The essential difference between a powder (or a porous body) and a dense solid body of exactly the same material and identical mass is, from the energetic point of view, the excess free energy due to the broken atomic bonds at the surface. Stressing this fundamental aspect, we can define *pressureless sintering* as material transport driven by surface energy or, in other words, by capillary forces. This material transport involves several basic mechanisms, essentially of diffusional-flow type. By filling in the necks at the points of contact between the powder particles and, at a later stage, the pore space,

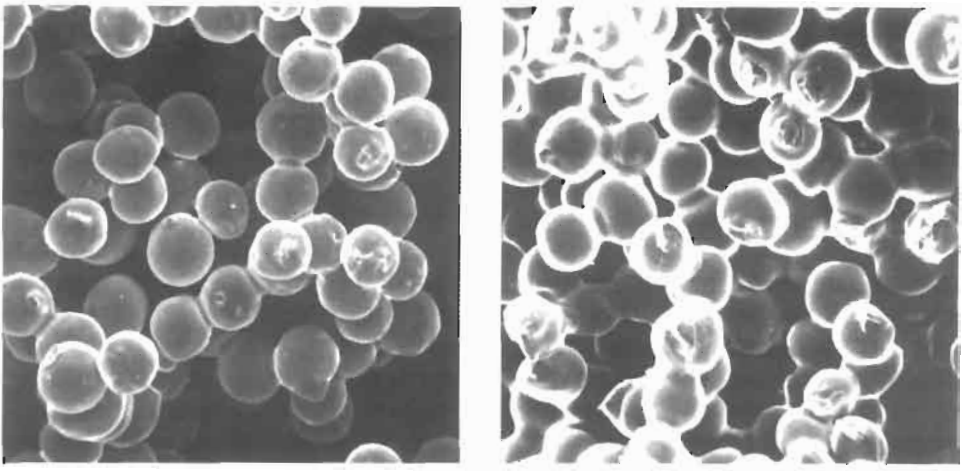

Fig. 1. Neck formation between loosely packed spherical copper particles during sintering at 1300 K for 1 h (left) and 8 h (right). 150×.

sintering increases density and strength of the compacted powders.

Figure 1 shows neck formation between spherical copper particles, and fig. 2 shows the geometrical changes taking place during sintering of tungsten powder. There are numerous experimental methods for studying the progress of sintering in laboratory experiments (see, for example, EXNER [1980]). Table 1 gives a summary of the frequently used techniques. In the following we will focus on experimental facts elucidating the basic phenomena and on the theoretical concepts for quantifying sintering mechanisms.

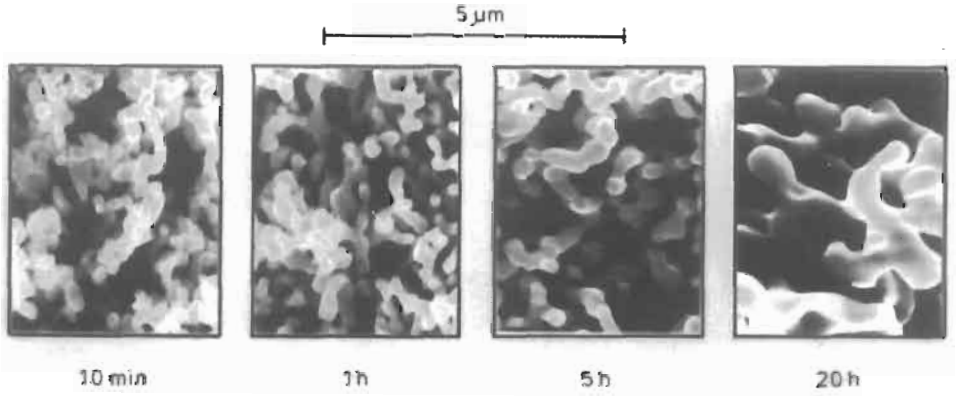

Fig. 2. Fine tungsten powder sintered in hydrogen at 1470 K for 10 min, 1 h, 5 h, and 20 h (from left to right). (From EXNER [1979a].)

Table 1
Experimental method for deriving quantitative information on changes of pore geometry during sintering.

Method	Quantity measured	Remarks
Dilatometry	Length change	Shrinkage may vary in different directions. Relative precision approximately 10^{-6} of sample length.
Buoyancy	Density	Impregnation or pore sealing necessary. Relative precision approximately 10^{-3}.
Gas adsorption	Solid-pore interface	Only for high specific interfaces (>0.1 m^2/cm^3). Closed pores not included. Relative precision approximately 10^{-2} for total areas >0.5 m^2.
Mercury porosimetry	Accessible pore volume	For open and fine pore systems. Interpretation of pressure-volume diagrams difficult.
Indirect methods	Physical properties	Exact relationships between pore geometry and properties usually not known.
Quantitative microscopy	Direct geometric parameters	Tedious but most effective method for complete characterization of pore geometry.

1.1. Driving energy

Surface energy provides the motivation of material transport during pressureless sintering. Its magnitude can be estimated theoretically by approximative equations from other physical data (as, for example, from the melting temperature and the molar volume by a simple relationship derived by SCHYTIL [1949] (see also SCHATT [1992]), or by ab-initio calculations from the interaction potentials of individual atoms or ions, or determined experimentally in various ways, ranging for metals, alloys, intermetallic compounds and nonmetallic crystalline solids from a tenth to a few J/m^2 (for references see ROTH [1975] and EXNER [1982]). The most reliable and instructive technique of visualizing the effect and measuring the value of surface energy is the so-called zero-creep technique first used by UDIN *et al.* [1949]. This technique is outlined in ch. 13, § 3.1.

Depending on the size of the powder particles or the amount and dispersion of porosity in a compact, the total excess energy of the surface amounts to 0.1–100 J per mole of solid where the smaller number applies to coarse powders (~ 100 μm diameter) and to low-porosity material and the larger number to submicron powders or highly dispersed porosity. With nanoparticles made by vapour decomposition or sol–gel processes, even higher values of excess energies are obtained (GRYAZNOV *et al.* [1992]), leading to spontaneous compaction at temperatures as low as room temperature and below (but also to self-ignition of metallic particles in air).

Grain-boundary energy usually provides a back-driving force because, at least in the early stages, new grain boundaries are formed while the particle contacts are being filled in (fig. 3). For most materials (especially metals) grain-boundary energies are lower (approximately by a factor of three) than surface energies, and the dihedral angle is of the order of 160°. Therefore the back-driving effect is not very pronounced. However, as pointed out by HOGE and PASK [1977], material transport during sintering may cease because of the establishment of local equilibrium between grain-boundary and surface

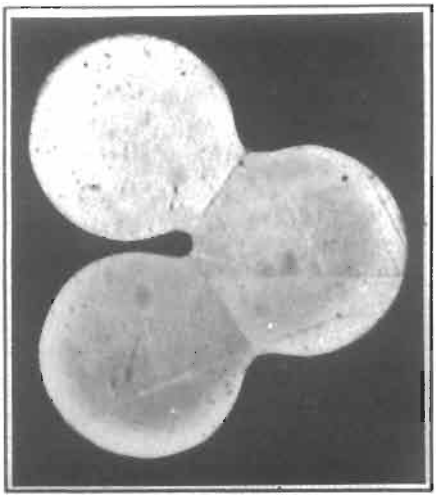

Fig. 3. Metallographic cross-section through an arrangement of three copper particles sintered at 1300 K for 8 h. Note the grain boundaries in the necks. 500×. (From EXNER [1979a].)

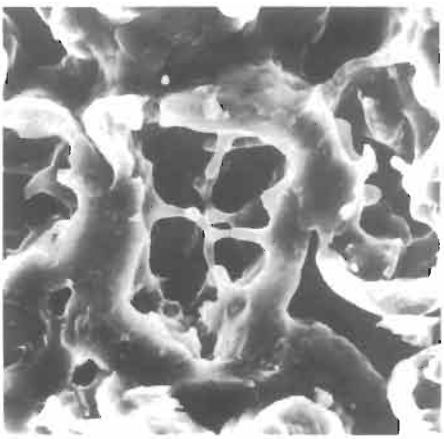

Fig. 4. High-porosity beryllium alloy produced from cobalt-coated beryllium particles by sintering. 1000×. (From ALDINGER [1974].)

energy in cases where the grain-boundary energy is high (dihedral angle $< 120°$).

If a volume element dV is removed from ($dV < 0$) or added to ($dV > 0$) a surface with the principal radii of curvature r_1 and r_2, the energy change, dE, involved is

$$\frac{dE}{dV} = \gamma \frac{dA}{dV} = \gamma\left(\frac{1}{r_1} + \frac{1}{r_2}\right), \tag{1}$$

where γ is the (isotropic) surface energy and dA is the change in surface area. dE/dV formally corresponds to a stress, σ, which leads to the well-known Laplace equation

$$\sigma = \gamma\left(\frac{1}{r_1} + \frac{1}{r_2}\right). \tag{2}$$

Under a concave surface, this stress is tensile and under a convex surface, compressive. Therefore, a stress gradient exists between the particle interior and the neck. Similarly, a gradient in chemical potential can be defined which, in turn, corresponds to a gradient of vapour pressure (Kelvin equation) or vacancy concentration (Thomson–Freundlich equation, see ch. 5, § 9.3). Owing to the stress gradient, the difference in vapour pressure, or the gradient in vacancy concentration, material is transported by viscous flow (in amorphous materials), by plastic flow, evaporation/vapour transport/condensation, diffusion along the surface and grain boundaries, or volume diffusion (in crystalline materials).

Chemical effects, which play a major role in most real systems, must clearly be differentiated from ideal surface-energy controlled sintering. Chemical driving forces (heat of solution, reaction enthalpies) due to nonequilibrium composition of powders

(e.g., mixture of elemental powders which react at sintering temperature) are usually much higher than capillary forces. This fact, which becomes apparent by merely comparing the molar surface energies with energies of mixing or compound formation, has been demonstrated in models, e.g., by sintering a cobalt sphere to a nickel plate (THÜMMLER and THOMMA [1966]). The same effect causes the well-known Kirkendall porosity (ch. 5, § 5.3) and has been used to prepare highly porous bodies from nickel or cobalt-covered beryllium spheres, as shown in fig. 4. However, in special cases chemical driving forces can be overcome by capillary forces: owing to the higher diffusivity of indium, an intermetallic compound is formed at the neck region between two wires of an originally homogeneous solid solution of copper–indium (KUCZYNSKI *et al.* [1960]), and silver is enriched in the neck region between initially homogeneous Ag–Au spheres (MISHRA *et al.* [1975]). However, rehomogenization occurs as soon as the sharp curvatures at the neck surface are filled in and capillary forces are reduced.

In some instances, chemical reactions aid densification. This fact can be utilized in the preparation of intermetallic compounds (see, for example, WANG and DAHMS [1992] and WANG *et al.* [1994]) or of special ceramics (like high-temperature superconductors). Also, ceramic materials may be produced by reaction sintering, i.e., by sintering in a reactive atmosphere (like reaction-bonded silicon nitride). Reviews of phenomena occurring during heat-treatment of powder mixtures which are far away from chemical equilibrium are available (see, for example, SKOROKHOD and SOLONIN [1984], GERMAN [1984], FEDORCENKO and IVANOVA [1987], EXNER [1988a], KAYSSER [1992], and SCHATT [1992]). The interaction of capillarity and chemically driven processes leads to a very complex behaviour which may vary significantly from one powder mixture to another, depending on a large number of influencing parameters like the underlying equilibrium phase diagram, the enthalpies of solution and reaction processes, the partial diffusion coefficients, the relative size and shape of the particles and particularly the mutual arrangement of the powder components, pre-homogenization, if used, etc. Owing to the difficulties in finding physical principles which are sufficiently general and reliable for a quantitative prediction, these phenomena (which are well-covered by the references given above) will not be discussed here any further.

1.2. Material sinks and sources

Possible sinks and sources for material (or vice versa for vacancies) are the surface (pore–solid interface), grain boundaries, and dislocations. The role of the surface is clear: Since surface energy is reduced when concave regions are filled in, these regions (in the early stages predominantly the highly concave neck surface, in the later stages the concave parts of the pore–solid interface) are the sinks for material (or the sources of vacancies). The convex part of the particle surface or solid–pore interface is one of the material sources. It is obvious that redistribution of material over the surface by surface and/or volume diffusion will not result in shrinkage of the compact or reduction of pore space (i.e., densification) but can only increase strength by enlarging the contact areas and reducing the notch effect of sharp pore contours.

Densification occurs when material is removed from the volume between the particle contacts. In numerous experiments, the decisive role of grain boundaries as sinks for vacancies arriving from the neck surface or pores has been demonstrated (ALEXANDER and BALLUFFI [1957]), ICHINOSE and KUCZYNSKI [1962]; for further references see GEGUZIN [1973], USKOKOVIC and EXNER [1977], and EXNER [1979a].

Pores shrink only when attached to or located very close to grain boundaries, and particle centres approach each other only when the particles are separated by at least one grain boundary. A most convincing experiment is the comparison of shrinkage rates of sintered copper with a high density of grain boundaries, resulting in pronounced shrinkage, with that of dezincified brass with a low density of grain boundaries, showing virtually no shrinkage (BRETT and SEIGLE [1963]).

Grain boundaries are usually assumed to be perfect vacancy sinks at the supersaturation levels caused by capillarity, but most models for the structure of grain boundaries (ASHBY *et al.* [1978], BALLUFFI [1980], ch. 9, § 2.2) assume a fairly well-defined structure that would be disrupted if atoms were removed. This leads to the suggestion (see, for example, ASHBY [1972], ARZT *et al.* [1983b]) that a divergence of the diffusive flux of matter can occur only at dislocation-like defects (grain-boundary dislocations as observed, for example, by GLEITER [1969, 1979], SCHOBER and BALLUFFI [1970], NILSSON *et al.* [1979] and KING and SMITH [1980]). The details of these dislocation structures (ch. 9, § 2.2) can depend on the misorientation of the adjacent grains. By emitting atoms, these defects move in a non-conservative way in the boundary plane. The effectiveness of a grain boundary as a source for atoms or sink for vacancies is thus determined by the number and the mobility of the grain-boundary dislocations, which may be reduced by solute atoms exerting a viscous drag, or by grain-boundary particles pinning the dislocations. A large number of unexpected effects and phenomena observed in sintering experiments can be explained in these terms: Neck growth between single-crystal zinc rods (NUNES *et al.* [1971]) and between single-crystal copper spheres and a single-crystal copper plate (see SCHATT [1992]) shows a pronounced dependence upon the mutual orientation with an exact correlation of small energy grain-boundary orientations and small neck sizes. Characteristic non-circular cross sections of the necks were found in copper sphere-copper plate models (SCHATT [1992]). A wide variation of neck sizes was measured and surprisingly low diffusivities were calculated from neck size data in closely controlled sintering experiments with planar arrays of copper spheres (for references, see EXNER [1979a]). When inert particles are dispersed in metals, shrinkage can be completely suppressed (ASHBY *et al.* [1980]). A pronounced effect of the grain-boundary structure on neck growth rates was also observed in zero-creep experiments (JAEGER and GLEITER [1978]).

There is more or less general agreement that lattice dislocations cannot be generated under the action of capillary stresses prevailing during sintering. Nevertheless, high densities of lattice dislocations have been observed in regions close to the grain boundary of a particle sintered to a plate and it has been suggested that these dislocations may contribute to the shrinkage in various ways (SCHATT *et al.* [1986]).

References: p. 2654.

For example, diffusion can take place from one dislocation to another, which can result in removal of atomic planes in the direction of compressive stress and insertion of those under tension. Lattice dislocations then act both as vacancy sources and sinks, and move non-conservatively by climb (NABARRO [1967], SCHATT [1981] and SCHATT *et al.* [1982, 1986]). Obviously, an increased dislocation density in the neck region also provides short-circuits for diffusion and thus reduces the effective diffusion distance between material sinks and sources. Detailed discussions of the experimental evidence for the formation of dislocations increasing the dislocation density in crystals of ionic and metallic materials, the width of the dislocation-enriched zones, the dependence of these zones on the heating rates and their influence on the sintering rates (with effective diffusivities orders of magnitude higher than that measured by tracer techniques) were presented by LENEL [1980] and by SCHATT [1992] together with reviews of many related references.

1.3. Neck growth and center approach in two-particle models

There have been a large number of attempts to quantify the kinetics of neck growth and shrinkage. Early work dating back to the time between the two World Wars (TAMMANN [1926], HEDVALL and HELIN [1927] and BALSHIN [1936]) is characterized by intuition rather than by physical reasoning (GEGUZIN [1973]). Some of the important fundamental ideas can be found in papers published around 1950 (e.g., FRENKEL [1945], JONES [1946], PINES [1946], HÜTTIG [1948], SHALER and WULFF [1948], MACKENZIE and SHUTTLEWORTH [1949] and CLARK and WHITE [1950]). In particular. the work by FRENKEL [1945], PINES [1946], KUCZYNSKI [1949] and HERRING [1950] marks the beginning of a quantitative modelling of sintering processes. Several research schools have developed since then in the various parts of the world (for reviews see FISCHMEISTER and EXNER [1964], THÜMMLER and THOMMA [1967], GEGUZIN [1973], IVENSEN [1973], EXNER [1979a], SHAW [1989], HANDWERKER *et al.* [1989], SKOROKHOD [1989], SOMIYA and MORIYOSHI [1990], or SCHATT [1992]). The classical approach has been the study of two coalescing particles (Frenkel–Kuczynski model), usually spheres or rods, in order to reduce problems inherent in the highly complicated geometry of powder compacts. Using idealized neck shapes (cylindrical or toroidal necks which result in contours formed by tangent circles, see fig. 5), analytical relationships were derived for the time- and particle-size dependence of neck size, x, during isothermal sintering. These equations are generally of power-law type

$$(x/a)^n = Ca^{-m}t \tag{3}$$

where a is the radius of the spherical or cylindrical particles in contact with each other, t is the time of isothermal sintering, and n, m and C are constants which are typical for the individual transport mechanism. Table 2 (see also COBLENZ *et al.* [1980], and GERMAN [1982]) lists the range of values of n and m given in the literature and plausible values for n, m and C following derivations by FRENKEL [1945] for viscous flow, by KINGERY and BERG [1955] for evaporation and condensation, and by ROCKLAND [1967] for the diffusional transport mechanisms. From the neck growth the amount of interpen-

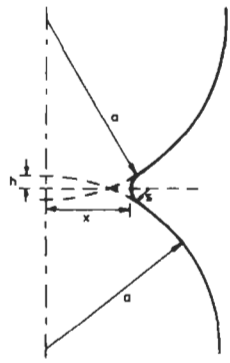

Fig. 5. Geometry of an idealized neck contour between two spherical particles (a = particle radius, x = neck radius, s = radius of neck curvature for a tangent circle, h = half of the centre approach and particle interpenetration).

etration of the two particles, and thus the centre approach between the two particles, can be estimated. Evaporation and condensation, volume diffusion from the surface, and surface diffusion cannot produce centre approach. For the other mechanisms it is assumed

Table 2
Constants appearing in eqs. (3) and (5) (after EXNER [1979a])

Transport mechanism	Range		Plausible values [b]		
	n	m	n	m	C
Viscous flow	2	1	2	1	$\frac{3\gamma}{2\eta}$
Evaporation and recondensation [a]	3–7	2–4	3	2	$3 \cdot \sqrt{\frac{2}{\pi}} \frac{\nu\gamma p M^{3/2} \rho^{1/2}}{(RT)^{3/2}}$
Grain-boundary diffusion	6	4	6	4	$\frac{48\gamma \cdot D_b \cdot b \cdot M}{RT}$
Volume-diffusion from the grain boundary	4–5	3	5	3	$\frac{16 D_v \cdot \gamma \cdot M}{RT}$
Volume diffusion from the surface [a]	4	3	4	3	$\frac{20 D_v \cdot \gamma \cdot M}{RT}$
Surface diffusion [a]	3–7	2–4	7	4	$\frac{23\gamma \cdot D_s \cdot w \cdot M}{RT}$

[a] No centre approach, $h/a \equiv 0$.
[b] With the symbols in the expressions for C denoting:

D_b, D_S, D_v = diffusion coefficients for grain-boundary, surface and volume diffusion; M = molar volume; R = gas constant; T = absolute temperature; b = grain-boundary width; p = gas pressure; w = width of surface atom layer; γ = specific surface energy; η = viscosity constant; ν = accommodation coefficient for gas transport; ρ = specific gravity.

References: p. 2654.

that all the material filling the neck comes from the grain boundaries in contact regions, and using again the idealized geometry and neglecting second-order terms, the approach of the two particle centres, $2h$, (see fig. 5) can be estimated from the neck size, x:

$$h = x^2/4a. \tag{4}$$

Using eq. (3), the time- and temperature dependence of the relative centre approach, h/a, is:

$$(h/a)^{n/2} = 2^{-n} C a^{-m} t, \tag{5}$$

with C, n and m shown in table 2 for the relevant mechanisms.

Viscous flow and volume diffusion can act on their own to remove material from regions between the particle centres while grain-boundary diffusion obviously needs the cooperation of another process, e.g., surface- or volume diffusion, to distribute the material reaching the surface at its intersection with the grain boundary. The major role of material redistribution over the surface is to reshape the surface in such a way that the curvature gradient (and thus the chemical potential gradient) changes continuously over the surface and sharp curvatures are reduced quickly. This effect, termed *undercutting* (NICHOLS and MULLINS [1965]), is particularly pronounced at the early stages of contact formation, producing a bulb-shaped neck contour (see also EXNER [1979a]). It has been suggested that the surface redistribution processes may be rate-controlling (COBLE [1958], GESSINGER [1970], JOHNSON [1970]) and it has indeed been quantitatively demonstrated by an approximative analytical solution (SWINKELS and ASHBY [1980]) as well as by numerical simulations (EXNER [1987]) that there is a limit of the ratio of transport coefficients $A = b \cdot D_{gb}/a \cdot D_s$ (where a and b are the atomic distance and the grain boundary width, and D_{gb} and D_s are the coefficients of grain-boundary and surface diffusion, respectively) above which neck shape, neck growth and shrinkage are not affected by a further enhancement of grain-boundary diffusivity.

There have been numerous attempts to derive equations for neck growth and centre approach for more realistic neck geometries. Reviews and detailed discussions have been published (EXNER [1979a] and COBLENZ *et al.* [1980]). Analytical solutions are still possible for neck geometries with elliptical or catenoid-shaped contours (SWINKELS and ASHBY [1980] and GERMAN and MUNIR [1975]). Frequently, numerical techniques have been applied for assumption-free modelling of neck shapes (NICHOLS and MULLINS [1965], NICHOLS [1968, 1980], ROSS *et al.* [1982], GERMAN and LANTHROP [1978], BROSS and EXNER [1979], EXNER [1979a], SVOBODA and RIEDEL [1992, 1995], ZHANG and SCHNEIBEL [1994], RIEDEL *et al.* [1994], and VAN DE VORST [1994]). For example, it has been demonstrated (EXNER [1979a]) that the shape of the neck region predicted by numerical simulation of simultaneous grain-boundary and surface transport conforms much more closely to the experimentally observed shape than the simple geometries assumed in analytical modelling.

A further complication adds up to the fact that analytical equations do not give a realistic description of neck growth and sintering rates: the superposition of two or more of the transport mechanisms mentioned in table 2 is not only possible but to be expected

in most real situations. Numerical approaches are available (JOHNSON [1972, 1990], ASHBY [1974], BROSS and EXNER [1979], SWINKELS and ASHBY [1981], EXNER [1979a]). However, the results of these complex calculations are not as easily visualized or applied as the simple power laws [eqs. (3) and (5)] and, therefore, have not gained much popularity. Usually, however, application of the simple equations is taken too far in interpreting experimental work quantitatively, considering the severe geometric simplifications and the problems connected with superimposed mechanisms (in addition to chemical effects due to impurities, among other divergences between theoretical assumptions and real systems). The same restrictions must apply to *sintering maps* delineating the temperature and neck-size regions in which a specific material transport mechanism is predominant (ASHBY [1974] and SWINKELS and ASHBY [1981]). Unlike the *hot-pressing maps* discussed below (see figs. 10 and 11), these sintering-mechanism diagrams are rather limited for quantifying the effects of various sintering parameters for practical purposes owing to the severe simplifications they are based on. Nevertheless, they provide a convenient means of visualizing the results of theoretical calculations.

1.4. Shrinkage of particle arrays and powder compacts

In spite of these principal deficiencies, the theoretical treatments and experiments based upon the two-particle approach have been highly successful in categorizing the active material-transport processes. There is general agreement that sintering of most metals and ceramics can be understood on the basis of *diffusional or Herring–Nabarro–Coble and Coble creep* (ch. 22, § 7) with surface diffusion playing a major role, while vapour transport and plastic flow play a minor part which, however, cannot be neglected in all cases. Most of the basic phenomena occurring in the early stages of solid-state sintering are now well understood, and the general findings give a sound basis for a qualitative understanding of the later stages and more complex geometries as, for example, for contacts between pressed spheres (WELLNER *et al.* [1974]), spheres of different diameter (COBLE [1973]), for nonspherical geometries (USKOKOVIC and EXNER [1977]) and for models consisting of three or more particles (EXNER [1979a]).

Nearly unsurmountable problems are present when a concise quantitative description of the sintering behaviour of real powder compacts is attempted by extrapolating the results derived for two-particle models to multiparticle systems. Shrinkage equations have been derived in a straightforward way by simply assuming that the relative linear shrinkage, $\Delta L/L$, is equal to the ratio of centre-approach and particle diameter, h/a. Thus, the well-known and frequently applied power-law shrinkage relationship dating back to KINGERY and BERG [1955] is obtained:

$$\Delta L/L = h/a = ct^n, \tag{6}$$

where: $\Delta L/L$ = relative linear shrinkage, c, n = constants, t = sintering time. However, this extrapolation has no relevance and determination of the exponent n from shrinkage experiments with powder compacts (which was highly popular during at least three decades) is of no use for identifying the dominant sintering mechanism. To prove this fact, fig. 6 shows the pronounced difference of individual relative centre approach and

References: p. 2654.

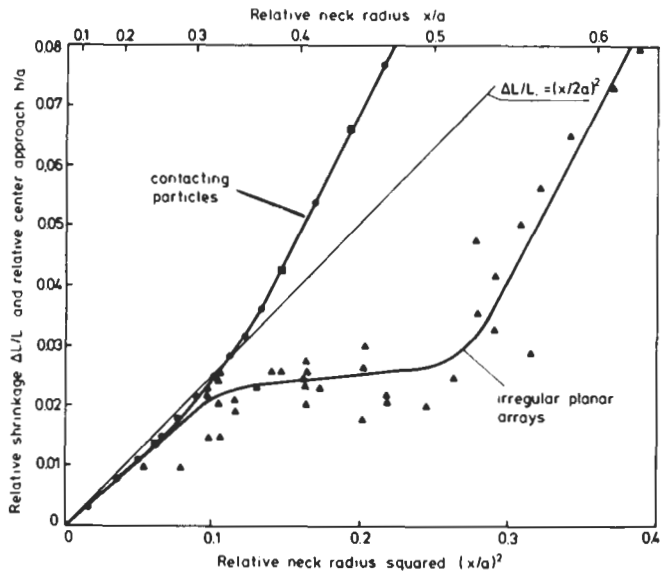

Fig. 6. Centre approach between contacting particles and overall shrinkage in an irregularly packed planar array of equally sized copper spheres sintered at 1300 K. The straight line corresponds to eq. (2). Note the pronouncedly lower shrinkage for the irregular array than predicted from centre approach. (From EXNER [1979a].)

shrinkage values measured for irregular planar arrays of copper spheres. The reason is that particles shift positions, contacts form or break up, and pores open up owing to rearrangement processes (fig. 7). Though uniform packing and pressing reduce these differences (EXNER *et al.* [1973] and EXNER [1979a]), particle shapes typical for technical powders, local variations in packing, asymmetric contact geometry, and stresses induced by nonuniform particle size and packing may cause pronounced rearrangement and

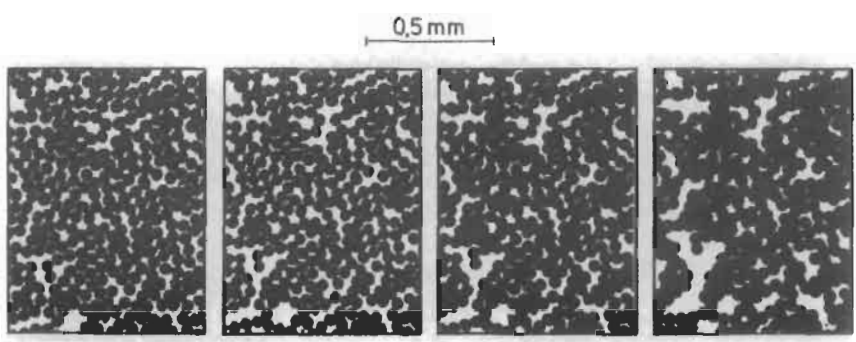

Fig. 7. Planar array of spherical copper particles (diameter approx. 60 μm) sintered at 1300 K. Identical field at different stages (from left to right: presintered for 1 min, sintered for 2, 5 and 25 h). Note the local shrinkage and opening of large void regions. (From EXNER [1979a].)

deviations from uniform shrinkage. These effects, adding up to the deviations from the ideal two-particle models discussed above, invalidate eq. (6) for most practical applications. EVANS [1982] has shown that the stresses induced by inhomogeneous shrinkage may be large enough to open cracks as frequently observed in sintered ceramic compacts.

The decisive part of shrinkage takes place during a sintering stage where the individual necks and powder particles grow together and cannot be clearly identified any longer. The pore space then is still a continuous network embedded in an (obviously) continuous solid. During this stage, porosity is attached to the grain boundaries (or vice versa). Simple geometric, statistical and stereological models have proven useful for describing this situation (see EXNER [1980]). The most successful model, designed by COBLE [1961], has been a geometrically simple arrangement of cylindrical pores situated along the edges of regularly polyhedral grains. The flow of vacancies to each of these cylindrical pores is independent of its radius, r, because the higher curvature of a thin pore channel (proportional to $1/r$) is compensated by its smaller area for the arriving atoms (proportional to r). A cubic time-dependence for grain growth (increase of edge length of the polyhedral grains) and diffusional creep as rate-controlling mechanisms are assumed. This model yields a logarithmic dependence of porosity, P, upon sintering time t:

$$P_0 - P = k \ln t/t_0, \tag{7}$$

where P_0, and t_0 are porosity and time at the beginning of isothermal sintering, respectively. The cubic relationship for grain growth has repeatedly been confirmed for porous materials while, as pointed out in ch. 28, § 4.1, a quadratic relationship is typical for pure dense metals. The linear dependence of porosity on the logarithm of time has been found to fit many of the experimental results obtained with powders of alumina, copper, silver iron, cobalt and nickel (for references see EXNER [1979a]). The interesting aspects of this model are the very clear connection between grain growth and densification and the extreme simplicity of the geometric and thermodynamic reasoning. More recently, refined versions have been published (e.g., BEERE [1975], KUCZYNSKI [1975, 1976, 1978], EADIE *et al.* [1978] and WONG and PASK [1979]).

The modelling of densification kinetics of loose or compacted amorphous powders is well advanced (for references see EXNER and GIESS [1989], BRINKER and SCHERRER [1993], or VAN DE VORST [1994]). Going beyond the extrapolation of the relationships derived on the basis of two-particle or single-pore models (FRENKEL [1945], MACKENZIE and SHUTTLEWORTH [1949], KINGERY and BERG [1955]), SCHERRER [1977] developed a versatile model on the basis of a simple geometry (unit cell composed of a three-dimensional arrangement of interconnected rods) and the elasticity analogon for the constitutive equations. The resulting equations were successfully applied to describe the sintering of glass powders during the preparation of optical waveguides (SCHERRER and BACHMAN [1977], WALKER *et al.* [1980]) and elegantly extended to the sintering behaviour of compacts containing two different sizes or an arbitrary size distribution of pores (SCHERRER [1979, 1984, 1988]), to the sintering of a powder film on a rigid substrate (SCHERRER and GARINO [1985], SCHERRER [1987, 1988] or BORDIA and SCHERRER [1988a, b]) and to the viscoelastic densification of gels (BRINKER and

References: p. 2654.

SCHERRER [1993]). Another, more recent, approach relies on the observation that the shape of the pores in sintering glass powders remains constant. Based on stereological reasoning, this results in an Avrami-type shrinkage equation (EXNER and GIESS [1989]) which is well supported by experimental evidence (GIESS *et al.* [1984], EXNER and GIESS [1989], BOCCACCINI [1993], BOCCACCINI and KRAMER [1995]).

Table 3 shows a systematic survey of these and other popular concepts for deriving equations for isothermal shrinkage (linear or volume shrinkage, increase of density or decrease of porosity) together with some major objections. Each of these concepts has merits in focusing attention on particular aspects of the sintering process. The equations derived analytically or empirically were often applied to a variety of materials with little awareness of the critical assumptions implied. Nevertheless excellent agreement with experimental data has been obtained. This is due to the fact that most equations contain more than one adjustable parameter which makes it difficult to reach conclusive differentiation of the quality of different sintering equations (and the underlying ideas) on the basis of quality of fit (PEJOVNIK *et al.* [1979]). However, since the effects of compacting, density distribution, contact geometry, structural defects, impurities and other factors of influence are understood for specific cases but not in terms of a general theory, further work will be needed to close some of these gaps. First attempts to model the effect of pressing on the density distribution and its influence on local shrinkage and distortion during sintering were successfully made by SUN and RIEDEL [1995].

1.5. Factors accelerating or retarding shrinkage

In the very late stages of sintering (below 10% porosity), when isolated and geometrically well defined pores are present, a more realistic modelling of the behaviour of real materials is possible. The classical shrinkage equations for viscous sintering (FRENKEL [1945], MACKENZIE and SHUTTLEWORTH [1949]) have been followed up for crystalline materials by numerous equations for shrinkage and growth during powder sintering, diffusional bonding and creep based on the treatment of diffusional mechanisms, power law creep and their combination (for references see TAKAHASHI and INOUE [1992]). These approaches are also the basis for understanding and quantitatively describing densification during hot-pressing (see § 2.2). Especially in ceramics, where high density values are striven for, breakaway of grain boundaries from the pores is the pre-eminent barrier to complete densification (see next section). In the light of the extensive efforts to give a proper theoretical basis to sintering processes, it is interesting to note that the techniques for improving sintering behaviour of materials which are difficult to densify have been developed essentially by trial and error.

There is general agreement that a large density of grain boundary area should be advantageous for the elimination of porosity. Grain growth is strongly retarded by disperse particles, but these may have a detrimental effect on the effectivity of the grain boundaries in their role as vacancy sinks as discussed earlier. The effects of dopants, such as transition metals (Ni, Fe) in tungsten or molybdenum (KAYSSER [1992]), phosphorus in iron (GOWRI and LUND [1989]) or MgO in Al_2O_3 (for references see HANDWERKER *et al.* [1989]) making it possible to attain close to full density at compara-

Table 3
Basic concepts for deriving quantitative relationships for shrinkage kinetics of powder compacts.

Basic concept	Authors	Critical remarks
Extrapolated two-particle model	KINGERY and BERG [1955] COBLE [1958, 1970] ROCKLAND [1967]	Nonrealistic assumptions on neck shape. Effects of asymmetry and rearrangement not considered. Explicit equations valid only for single mechanism. Not applicable to later sintering stages.
Extrapolated simple-pore model	COBLE [1961]	Geometry oversimplified. Empirical grain-growth relationship
Unit cell model	SCHERRER [1977]	Versatile for many applications. Highly idealized geometry.
Statistical approach	KUCZYNSKI [1975, 1976, 1978]	Simplifying geometric assumption on pore shape (no convex interfaces).
Rheological approach	SKOROKHOD [1972, 1989] SKOROKHOD *et al.* [1991, 1993]	Defect geometry and interaction porosity-defects not clearly defined. Phenomenological definition of viscosity.
Stereological approaches	JOHNSON [1972] AIGELTINGER and DROLET [1974] DE HOFF [1989] EXNER and GIESS [1989]	Integration of rate equation only possible with additional assumptions (e.g., geometric similarity). Phenomenological introduction of geometric parameters.
Empirical approaches	TIKKANEN and MÄKIPIRTTI [1965]	Posterior motivation of empirical equation on basis of vacancy-dislocation interaction.
	IVENSEN [1973]	Posterior motivation of ad hoc equation based on non-defined defects. Three adjustable parameters.
	Other authors (for references see EXNER [1979a, 1980]	Mathematical derivations or phenomenological and purely pragmatic equations without reasonable physical support.
Numerical approaches	JOHNSON [1972, 1990] EXNER [1988b] RIEDEL [1990] SVOBODA and RIEDEL [1992, 1995] RIEDEL *et al.* [1994] MC MEEKING and KUHN [1992], SVOBODA *et al.* [1994]	First attempts for assumption-free modelling using constitutive equations for material transport and thermodynamic reasoning for evolution of pore geometry. Presently not fully developed, highly simplified physical approaches.

tively low temperatures without applying an external pressure. The understanding of these effects or that of the influence of the composition of sintering atmospheres, are still a matter of controversy (see, for example, GERMAN and MUNIR [1982]). This field is characterized by an astonishing predominance of empiricism and variety of unproven

References: p. 2654.

explanations of the various phenomena, and only recently have systematic and critical reviews on the effects of small additions been published (KAYSSER [1992], SCHATT [1992]).

For effective sintering to high densities and for achieving homogeneous microstructures it is important to control the density distribution in the unsintered compact in such a way that a narrow pore size distribution and a narrow distribution of particle coordination number are obtained (HARE [1980], LANGE [1984], KELLETT and LANGE [1984], FANG and PALMOUR [1989], GEHO and PALMOUR [1992]). It was thought that this could be achieved by monosized particles which were successfully produced by chemical techniques (OKAMURA *et al.* [1986], BARRINGER and BOWEN [1982], see also HANDWERKER *et al.* [1989] for references). However, in technical processing, regular packing is difficult if not impossible to obtain, and a wide pore size distribution may be expected even with uniform particle sizes for random dense packing (EXNER [1988a], GERMAN [1989]). As observed by CLAUSSEN and EXNER [1972], LANGE [1984], DE JONGHE *et al.* [1987], HANDWERKER *et al.* [1989], and WHITTEMORE and VARELLA [1990] and discussed extensively by EXNER [1979a], large pores can open up at locations of low density in irregular stackings of fine particles (see also fig. 7). Additionally, a more long-ranged uneven density distribution may lead to severe shape changes of sintered parts being detrimental to technical use. Anisotropic shrinkage (i.e., significant differences in length change in different directions) has been observed in most powder compacts. Rather than gravity (which has a negligible effect for small particle sizes), the anisotropic pore shape is responsible for this usually disadvantageous effect (EXNER [1977], MITKOV [1978], MITKOV *et al.* [1979], KUROKI and HIRAISHI [1989] or EXNER and GIESS [1988], see also EXNER [1979a]. Computer simulations (e.g., HARE [1980], SVOBODA and RIEDEL [1992]) can be used to predict these effects and the optimum design of pressing dies achieving precise shape control of sintered parts. In any case, the care taken in de-agglomerating fine powders and close processing control during compacting is one of the prerequisites for sound ceramic parts.

Particularly with the upcoming packaging technology for electronic components, the effects of stresses and constraints related to uneven packing density, wide particle and pore size distributions, and rigid inclusions, fibres or substrates have been carefully analysed theoretically as well as studied experimentally by numerous authors (SCHERRER [1984, 1987, 1988], DE JONGHE *et al.* [1986, 1987], EVANS and HSUEH [1986], HSUEH *et al.* [1986], LANGE [1987], RAHAMAN and DE JONGHE [1987, 1988], BORDIA and SCHERRER [1988a,b], HSUEH [1988], DE JONGHE and RAHAMAN [1988], WEISER and DE JONGHE [1988], OSTERTAG [1989], see also HANDWERKER *et al.* [1989]). The controversial discussions, particularly on the magnitude of stresses developing in powder compacts during sintering of composites and the origin of cracks and other damages in ceramic materials have, more recently, resulted in a general understanding of many details. However, a simple and generally valid theoretical description is not in sight at present, and the various origins of constraints and resulting stresses counteracting the capillary stresses must be analysed carefully for each situation when theoretically derived shrinkage equations are used to predict the shrinkage of a powder compact.

1.6. Development of microstructure and grain growth

The initial state of microstructure in a pressed compact is characterized by the microstructure of the individual particles and the shape of the pore space which, in turn, is determined by the shape and the arrangement of the particles. During the initial stage of sintering, grain boundaries develop at the contact regions, and the grain structure in the particles changes quickly by recrystallization if deformation during pressing has exceeded a critical value. The microstructure is then characterized by a continuous pore space with grain boundaries located at the small cross-sections of the solid. Further development of microstructural geometry (i.e., shape, dimensions and topological arrangement of porosity and grain-boundary network) can be assessed by quantitative microscopy (ch. 10, § 7). Descriptive work using stereological and topological parameters (DE HOFF and AIGELTINGER [1970], AIGELTINGER and EXNER [1972], JERNOT *et al.* [1980], CHERMANT *et al.* [1981], RHINES and DE HOFF [1971, 1984] and EXNER [1994]) shows that the geometric changes related to the reduction of pore volume are fairly similar for most materials. During the intermediate stage, the pore space forms a continuous network attached to grain boundaries, and the dimensions of the pore cross-section and the grains are related in much the same way as predicted by the Zener relationship (KUCZYNSKI [1975]):

$$R = k\frac{r}{p}, \tag{8}$$

where R and r are typical average dimensions of the grains and the porosity, respectively (e.g., mean linear intercepts or area-equivalent radii of planar cross-sections). The constant k is of the order of unity and related to the shape and to the size-distribution of the grains and the cross-sections of the pore network. The stereological approach taken by AIGELTINGER and EXNER [1979] and LIU and PATTERSON [1993] showed, for copper and for (doped and undoped) alumina respectively, that the ratio of grain boundary/pore surface intersection lengths remains constant throughout major periods of sintering in spite of large changes in pore volume and pore shape. This can be seen as a generalisation of Zener's relationship (which only applies for constant pore volume and shape), and validates the assumptions made by KUCZYNSKI [1978] in his statistical sintering model.

Only later in the sintering process, when the continuous pore system breaks down, are more or less equilibrium-shaped isolated pores formed at the grain boundaries (fig. 8). Theoretical studies show how the grain-growth kinetics are influenced by pores (MOCELLIN and KINGERY [1973], CARPAY [1977], CAHN [1980], HSUEH *et al.* [1982], SPEARS and EVANS [1982] and WEI and GERMAN [1982]). Pores can be dragged by grain boundaries and coalesce when meeting at grain edges or corners until they break away from the grain boundaries. The separation limits final densification since volume diffusion is usually much slower than grain-boundary diffusion. Additionally, local breakaway results in exaggerated grain growth or secondary recrystallization (ch. 28, § 4.4). Thus, the separation process is a decisive step in final-stage sintering, determining the microstructural details as well as the remaining porosity.

References: p. 2654.

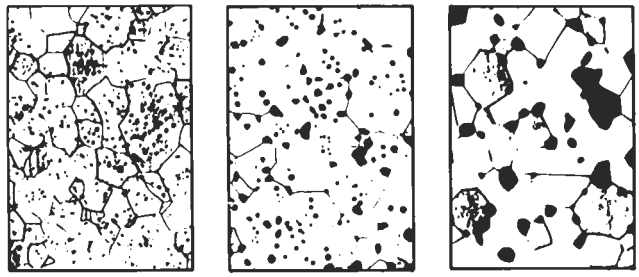

Fig. 8. Typical microstructures of sintered materials at late sintering stages. In carbonyl iron (left) the pores are mostly separated from grain boundaries, in magnesia (middle) small pores lie inside grains and the larger ones on grain boundaries, and in zinc oxide (right) most pores are on grain boundaries and corners. (From EXNER [1979b].)

Grain-boundary motion, pore drag, pore shrinkage, pore coalescence, and pore detachment from grain corners, edges and facets have been modelled in order to explain the effects of process variables as heating rate, sintering time, sintering temperature, dopants etc. (COBLE and CANNON [1978], HSUEH *et al.* [1982] and SPEARS and EVANS [1982], see also HANDWERKER *et al.* [1989]). Figure 9 shows schematically the dependence of pore size on grain size and the conditions under which the pores become separated from the grain boundaries. Two pore-grain trajectories are indicated, one of

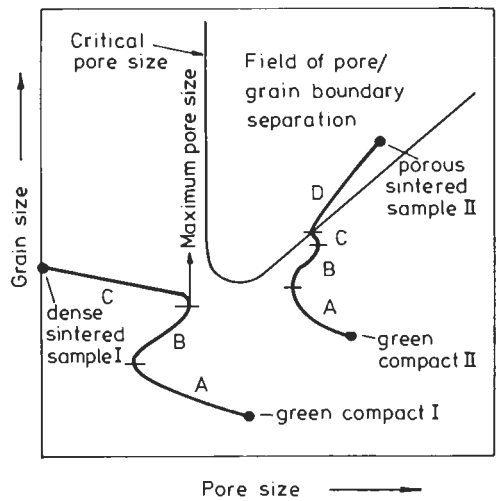

Fig. 9. Schematic plot of theoretical results indicating the relationship between pore and grain size in the final sintering stages. Sample I: favourable path for high final density. Sample II: path for porous product. A: rearrangement and densification by contact formation. B: intermediate stage shrinkage and coarsening. C: normal grain growth and final densification. D: pore-grain boundary separation, exaggerated grain growth, Ostwald ripening of isolated pores and cease of densification. (After SPEARS and EVANS [1982].)

which indicates a technically advantageous sintering route leading to full densification and a fine grain microstructure, while the second one enters the pore-detachment region resulting in residual porosity and coarse microstructure. In spite of the detailed models and derivations, equations describing these processes and their interactions, care must be taken not to carry the conclusions too far for practical cases. There are still many assumptions unproven by experimental facts (see, for example, CAHN [1980]). On the other hand, however, one should be able to optimize sintering conditions on this basis in order to obtain taylor-made microstructures in sintered materials, and to better understand the pronounced effects of special heating schedules such as rate-controlled heating (HUCKABEE *et al.* [1978], PALMOUR *et al.* [1979], PALMOUR and HARE [1987], PALMOUR [1989], microwave sintering (TIAN *et al.* [1988]), rapid and high-temperature sintering (BROOK [1969], SANDEROW [1989], ARNHOLD [1989], DUSTOOR *et al.* [1989]), plasma sintering (JOHNSON *et al.* [1984]), quasi-isothermal heating (SOERENSEN [1980]) etc., by comparing the experimental findings with theoretical approaches and ideas.

2. *Hot pressing (pressure-sintering)*

Powders which are difficult to sinter can be consolidated to high density and strength by simultaneous application of heat and pressure. Such a process may be thought of as sintering enhanced by a pressure (*pressure-sintering*) or as a pressing operation activated by high temperatures (*hot-pressing*). The pressure allows lower temperatures than in pressureless sintering to be employed with no extra heating at extremely high pressures, as in explosive densification (PRÜMMER [1989]). Thus normal grain growth can be reduced and abnormal or exaggerated grain growth, caused by breakaway of grain boundaries from pores, may be avoided. If the pressure is applied uniaxially, the process is commonly referred to as hot-pressing, while *hot isostatic pressing* (HIP, for short) utilizes hydrostatic pressure. The HIP process in particular has attained the position of the leading hot consolidation process; presses are commercially available which allow hydrostatic pressure, transmitted by gas, to be applied to a large heated volume (HANES *et al.* [1977] and FISCHMEISTER [1978]). Examples of its successful application are the production of tool steels, of superalloys, of alumina (e.g., for nuclear waste encapsulation), and of ceramic cutting tools. More recently, hot isostatic pressing has been successfully employed to densify intermetallics and to produce metal-matrix composites, e.g., by consolidating monotapes of ceramic fibers embedded in a plasma-sprayed metal (ELZEY and WADLEY [1993]). Furthermore, sinter-HIP, i.e., a combination of pressureless sintering with or without a liquid phase (closing open porosity) and of subsequent hot isostatic pressing (HIP, eliminating residual porosity), has found widespread technical application for high-density products (see, for example, FRISCH *et al.* [1989]).

2.1. Stresses and mechanisms

When an external pressure is applied to a hot powder compact, it is transmitted through the powder bed as a set of forces acting across the particle contacts. The exact force distribution depends on the stress state: in uniaxial hot-pressing some of the

pressure is dissipated by die-wall friction. while HIP produces a uniform distribution resulting in more homogeneous densification. The local contact force per unit contact area (the "effective pressure") may exceed the capillary stress by several orders of magnitude, especially in the early stages of densification. This high stress not only enhances the diffusional processes contributing to pressureless sintering, but also introduces new densifying mechanisms. When the pressure is first applied, the contacts between the particles are small and the effective pressure will be sufficient to cause instantaneous plastic yielding in the contact zone. The resulting contact flattening leads to a rapid attenuation of the effective pressure until yielding stops. Then time-dependent deformation mechanisms determine the rate of further densification: power-law creep and stress-enhanced diffusion from a grain-boundary source to the neck surface, as in pressureless sintering. The contribution of vapour transport is even more insignificant than in pressureless sintering because it is not enhanced by the applied pressure.

It is convenient to divide the densification process into two stages (sometimes a third, intermediate stage is assumed which bridges the two mentioned here). During stage 1 the individual particles, which are commonly assumed to be spherical, can still be distinguished. The densification is determined by the deformation of the particle contacts caused by the local effective pressure acting on the contact area. In isostatic compaction, this effective pressure, σ, is proportional to the applied pressure, p (KAKAR and CHAKLADER [1968], COBLE [1970], MOLERUS [1975] and KISLY [1989], e.g.:

$$\sigma = \frac{4\pi a^2}{AZ\rho} p, \tag{9}$$

where a is the particle radius, ρ the relative density of the compact (volume fraction of the solid), and A and Z are the average contact area and number of contacts per particle, respectively. Under certain assumptions concerning the structure of the particle packing and the contact geometry, A and Z can be expressed as functions of ρ (ARZT [1982], FISCHMEISTER and ARZT [1983] and HELLE *et al.* [1985]).

During stage 2 at relative densities greater than roughly 90%, the compact is usually modelled as a homogeneous solid containing isolated spherical pores. The effective pressure causing densification is then identical with the applied pressure, unless gas trapped in the pores causes a back-pressure which may prevent the compact from reaching full density.

2.2. Densification models

The theoretical models which have been developed for describing the densification mechanisms reflect the processes by which deformation can occur in a solid at elevated temperature (fig. 10). The initial densification upon application of the pressure is usually due to instantaneous *plastic yielding* of the contact zones because the effective pressure is high at this stage. As the appropriate slip-line field is similar to that of a hardness indentation (HILL [1960]), the following relationship between the effective pressure σ and the yield stress σ_y of the powder material is normally assumed if yielding is to occur:

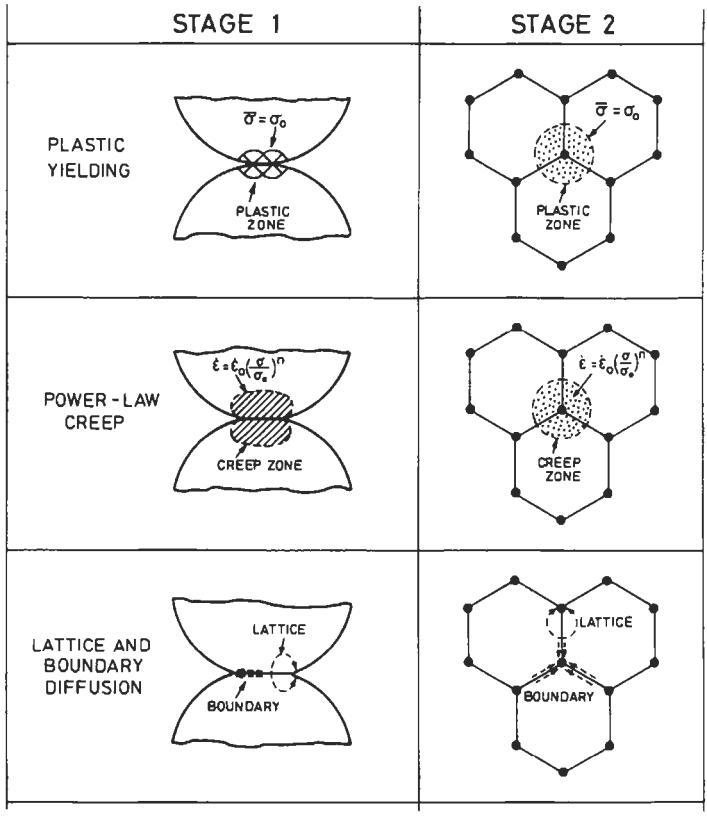

Fig. 10 Mechanisms of densification by hot pressing. In stage 1 (relative density below 90%) densification occurs by deformation processes in the zones of contact between particles; in stage 2 shrinkage of isolated pores is effected by similar deformation mechanisms (after ASHBY [1990a]).

$$\sigma \geq 3\sigma_y. \tag{10}$$

Yielding enlarges the areas of contact between the particles and, as a consequence of the resulting densification, increases the number of contacts per particle. This "geometrical" hardening, possibly combined with work-hardening of the material, limits the extent of densification that can occur by yielding. Once the effective pressure no longer satisfies eq. 10, yielding stops. If the pressue is high enough for the compact to enter stage 2 by plasticity alone, its behaviour is better modelled as the plastic collapse of a thick spherical shell (TORRE [1948], HEWITT *et al.* [1973]).

Further densification is effected by time-dependent mechanisms. One important mechanism is *power-law creep* in the zone of contact between the particles, resulting in a power-law dependence of the densification rate on the applied pressure (WILKINSON and ASHBY [1975], MATTHEWS [1980], ARZT *et al.* [1983a]). Another mechanism is

diffusional densification, governed by diffusion either along the interparticle boundary or through the volume. This mechanism is, vis-a-vis pressureless sintering, enhanced in hot-pressing because the additional energy $\sigma\Omega$ is gained on moving an atom with volume Ω from the interparticle boundary which is acted on by a compressive traction σ into the pore space or to the surface (HERRING [1950], COBLE [1970]). Compared to this external stress effect, the capillary stress is negligible and hence hot-pressing, unlike pressureless sintering, is not sensitive to the exact shape and curvature of the contact necks, and simplifying assumptions about the contact geometry are less critical. If the powder particles are polycrystalline, they can in addition densify by deformation through *diffusional creep* (Nabarro-Herring-Coble creep, see ch. 22, § 7). A common feature of these diffusional mechanisms is their linear dependence on external pressure and their sensitivity to scale, i.e., to particle size and grain size, respectively.

For these mechanisms, constitutive equations have been developed and refined (WILKINSON and ASHBY [1975], ARZT *et al.* [1983a, b], SWINKELS *et al.* [1983], HELLE *et al.* [1985]). They relate the densification rate to materials parameters M (diffusivities, creep parameters), processing conditions (HIP pressure P and temperature T), particle radius R and current density ρ in the following form:

$$\left(\frac{\mathrm{d}\rho}{\mathrm{d}t}\right)_i = K_i(P, T, R, M) \cdot f_i(\rho). \tag{11}$$

The functions K_i and f_i for the different mechanisms and stages of densification are listed in LI *et al.* [1987] and ASHBY [1990a].

One complication, which affects densification by diffusional mechanisms, is the tendency to grain growth in the powder compact during pressing. This can result in pore separation from grain boundaries, which suppresses densification by diffusion. Pores can also be dragged by moving grain boundaries, causing them to agglomerate, which again slows down the densification. This interaction between densification and grain growth can be incorporated in the governing equations (ASHBY [1990a]).

Another difficulty arises in modelling the fabrication of composites by hot isostatic pressing, where densification is constrained by reinforcing phases, e.g., fibers or particles. More advanced concepts have been developed for these cases (TURNER and ASHBY [1993], LI and FUNKENBUSCH [1993], ELZEY and WADLEY [1993]). The major result is that the densification behaviour is largely controlled by the contacts between the rigid inclusions resulting in a reduced effectiveness of grain boundaries as vacancy sinks (or atom sources).

2.3. HIP (hot isostatic pressing) maps

The competition among the densification mechanisms depends in a complicated way on material and process parameters. In order to illustrate these dependencies, theoretical "HIP maps" have been constructed, e.g., for tool steel, superalloys, copper, silicon nitride etc. (ARZT *et al.* [1983a] and HELLE *et al.* [1985]). A typical, generic example is shown in fig. 11.

Such HIP maps exhibit the field of dominance for each mechanism (i.e., the range of

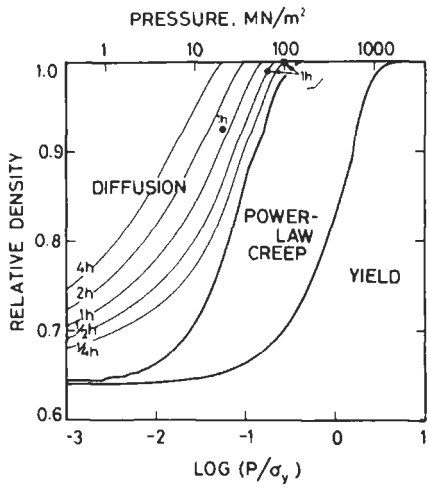

Fig. 11. A density-pressure diagram for hot isostatic pressing (HIP) of a tool-steel powder with a particle radius of 25 μm, at a temperature of 1200°C. σ_y is the yield stress of the powder material. Data points correspond to typical industrial HIP cycles (with time marked in hours). Follow a vertical line (at a given external pressure p) in the direction of increasing density: the initial densification is due to plastic yielding of the particle contacts; at intermediate densities power-law creep in the contact zone dominates; diffusion may finally achieve full density. The thin lines are contours of constant time. (After ARZT *et al.* [1983a].)

pressure or temperature and density in which a given mechanism contributes more to the densification than the others). The field boundaries (heavy lines in fig. 11) are the lines along which two mechanisms contribute equally. Superimposed on the fields are contours of constant time; they predict the HIP processing time necessary for reaching a given compact density.

Considerable insight into the HIP process is provided by HIP maps. The mechanism fields, for example, depend critically on the HIP parameters: at relatively low pressure, the diffusion mechanisms tend to contribute more to densification than yielding and power-law creep which, in turn, dominate at high pressures. This reflects the much higher stress dependence of the latter processes. Another characteristic concerns the role of powder-particle or grain size: as diffusional densification processes depend critically on these microstructural parameters, their contribution is significantly enhanced in fine, polycrystalline powder particles.

2.4. Technological considerations

In the practice of powder consolidation, transient effects can occur which influence the quality of the HIPed product. Most importantly, the HIP parameters, temperature and pressure, are not constant over the dimensions of the compact; as heat diffuses into the powder, the hotter surface layers densify more rapidly than the interior. Heat is conducted through the dense skin faster than through the less dense center, further adding to the temperature difference between surface and interior where, in addition, the effective pressure is reduced compared to the skin of the compact. Under these con-

References: p. 2654.

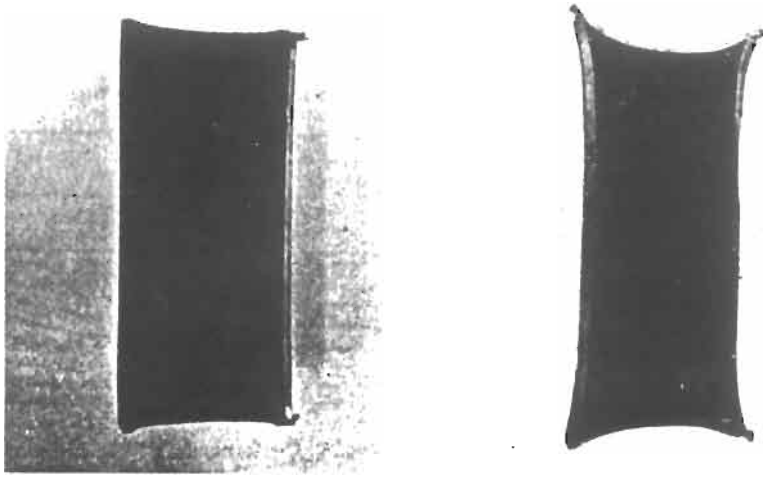

Fig. 12. Model experiments with rectangular compacts to minimize the shape change due to transient effects during HIP. Pre-heating before application of pressure (left) results in small shape changes, whereas simultaneous application of pressure and temperature gives rise to significant shape distortions (after Li *et al.* [1987]).

ditions, densification will no longer be isotropic but will lead to severe shape distortions. This effect is illustrated in fig. 12.

In a numerical analysis of the coupling between heat flow and densification, the conditions to be avoided have been identified (Li *et al.* [1987]). Also, the residual stresses resulting from non-uniform densification have been calculated (Li *et al.* [1991]). During the "unloading process" following the HIP treatment, tensile surface stresses can cause cracking. This risk is reduced by controlling the rate of reduction of pressure and temperature at levels predicted by numerical simulation.

The modelling of densification mechanisms has recently been developed into a useful tool for optimizing HIP process cycles. A commercial software package for constructing HIP maps is now available (Ashby [1990b]). It allows sintering, cold and hot isostatic pressing, and combinations of these processes to be modelled. It also incorporates grain growth and pore dragging effects and allows kinetic data, such as TTT curves, to be superimposed on the densification contours. Similar maps have been constructed to identify process windows for consolidation of amorphous powders without inducing crystallization (Fischmeister and Arzt [1986]).

The precision of HIP maps has been greatly improved by "tuning" the material parameters (which for many materials are only approximately known) to calibrate the equations to be results of real HIP runs. These efforts have profited from the development of sensitive eddy-current sensors which measure changes of compact dimensions *in situ* (e.g., Schaefer and Kushner [1990]). This development has led to implementation

of a workstation which provides a HIP operator with the ability to control the densification of a powder compact on-line and to improve component yields by HIP (WLASSICH *et al.* [1990]). Hot isostatic pressing has thus become a prime example for "intelligent processing", that is, the support of industrial production by fundamental insight.

3. *Sintering with a liquid phase*

High-quality technical products can be made from mixed powders by cold compacting and then heating above the melting temperature of the lower-melting, low-volume-fraction (1–40 vol%) component. The shape of the compact is maintained, though usually not as closely as in solid state sintering, but higher densification levels are obtained as a rule.

Heavy metals (W with Cu, Fe, Ni), cemented carbides (WC, TiC with Co), ceramics containing glassy phases, aluminium alloys, superalloys, cobalt-rare-earth magnets, and a variety of sintered steels on the basis of Fe-Cu or Fe-Cu-C are prominent examples of materials produced by liquid-phase sintering, the basic principles of which have been extensively studied and are quite well understood (for reviews see, for example, LENEL [1980], GERMAN [1985], MARION *et al.* [1987], HANDWERKER *et al.* [1989], KAYSSER [1992] or SCHATT [1992]). The technical or economic reasons for applying this production process vary largely for these materials; reasons include the incapacity of other processes to produce optimized microstructures with specified compositions and density, a need for reduced shaping cost, or a need for improved homogeneity. Usually, the original powder mixtures are not in chemical equilibrium at sintering temperature, at least in early stages, and chemical driving forces are present. Owing to the very low stresses needed for activating the flow of liquids, capillary forces play a major role even in non-equilibrium systems.

The shrinkage processes occurring during isothermal liquid state sintering are usually divided into three stages as suggested in early work (for reviews see FISCHMEISTER and EXNER [1964], HUPPMANN [1975, 1979], LENEL [1980], PETZOW and KAYSSER [1984, 1987, 1990], GERMAN [1985], KAYSSER [1988, 1992] and SCHATT [1992]):

(i) Rearrangement by liquid flow, retarded by friction between the solid particles. This stage requires good wetting since capillary forces acting at the liquid bridge are determined by the wetting angle (CAHN and HEADY [1970]).

(ii) Dense packing by shape-accommodation of particles separated by liquid films through solution and reprecipitation. This stage requires that the solid phase has a finite solubility in the liquid. In most systems this stage is connected with pronounced structural coarsening.

Neglecting all complicating factors (e.g., chemical driving forces, size and shape distribution of particles, bridging and coarsening effects), KINGERY [1959] has derived a quantitative description of shrinkage during isothermal liquid-phase sintering which results in equations of the type

$$\Delta V/V \approx 3\Delta L/L = kt^n, \tag{12}$$

References: p. 2654.

where ΔV and V are the volume change and the initial volume, ΔL and L length change and initial length of the sample and k and n constants typical for each stage and mechanism involved. Application of this equation to compacts of metal and ceramic powder mixtures showed reasonable agreement, and conclusions on the rate-controlling steps were made on the basis of experimental values of n (approx. 1 for the rearrangement stage, 0.5 for reaction-controlled and 0.33 for diffusion-controlled solution/reprecipitation and slopes as discussed for solid state sintering in § 1.4 for the final stage.) In the light of later work (for references see HUPPMANN and PETZOW [1980] and LENEL [1980], GERMAN [1985], PETZOW and KAYSSER [1990], KAYSSER [1992]), this agreement must be considered fortuitous or, by analogy with observations made with powders and solid-state sintering equations, due to a convenient fitting of two-parametric equations rather than to physical relevance.

In systems with appreciable solubility of the solid in the liquid phase (as in virtually all materials produced by liquid-phase sintering), the liquid penetrates particle bridges and grain boundaries in the early stages. Disintegration of polycrystalline particles into small grains has been overlooked by early authors but was clearly demonstrated for metals (e.g., tungsten with nickel melt) as well as ceramics (e.g., alumina with melted glass), and discussed in detail, for example, by KAYSSER [1992] among many others. It is an important process occurring during particle rearrangement (stage [i]) and, owing to the high driving forces involved, between stages [i] and [ii]. There is some discrepancy why liquid films separating solid particles are stable during most of the sintering process and why they assume an equilibrium thickness for a given volume fraction of liquid. Convincing experimental evidence is available for this fact (see, for example, GREIL and WEISS [1982]) and a quantitative theoretical explanation was offered by CLARK [1987]. Later in the process, the melt is redistributed among fine and large pores, following the local differences of capillary forces depending on the distribution of interface curvature filling even the larger pores (KWON and YOON [1980], KAYSSER *et al.* [1982], KANG *et al.* [1984], PARK *et al.* [1984], SHAW [1986]). Finally, when all pores are eliminated (which is sometimes the case long before the sintering temperature is taken back below liquidus), liquid may be squeezed out to the surface where it evaporates as in the case of nickel during vacuum sintering of tungsten-nickel composites (RIEGGER *et al.* [1980]). On the other hand, penetration of liquid into the grain boundaries may cause swelling if shrinkage by rearrangement is not rapid enough as, for example, in iron-copper alloys (BERNER *et al.* [1974], KAYSSER *et al.* [1980], LENEL [1980], TABESHFAR and CHADWICK [1982], GERMAN[1985], KAYSSER [1992] and SCHATT [1992]). According to the classical second-stage mechanism (KINGERY [1959]), the capillary pressure at the contact points of the solid particles increases solubility and causes solution, transport through the liquid and reprecipitation at pressure-free solid-liquid interfaces. Additional and in most cases dominating driving forces for material transport through the liquid are caused by differences in surface curvature when irregular powders are concerned, and variations of defect densities or composition not only due to variations in the original powder particles but also due to the low defect density and the equilibrium composition of the reprecipitated parts (HUPPMANN and PETZOW [1980], PETZOW and KAYSSER [1984, 1987, 1990], and KAYSSER [1992]). Though these effects do not directly affect the driving force for

shrinkage exerted by porosity, they may contribute to densification and particle accommodation indirectly (HUPPMANN and PETZOW [1980], LENEL [1980] and KAYSSER [1992]). Finally, when a solid skeleton forms, shrinkage depends on solid state sintering mechanisms and follows the lines described in § 1.

Owing to the rapid material transport in liquids, coarsening of the microstructure is usually pronounced in liquid-phase sintering. Theories developed for coarsening (ripening) in dispersed systems (Wagner-Lifshitz-Ardell theory for Ostwald ripening, see. ch. 10, § 3.2.2) apply to systems in which the amount of liquid is high (e.g., EXNER [1973] and GERMAN [1985]). In the typical range for liquid-phase sintering (volume fractions < 30%) or for systems with incomplete wetting of the solid by the liquid experienced with most combinations used in technical materials,, the particles are in contact and coarsening will be effected by coalescence, i.e., grain-boundary movement assisted by reprecipitation of material into the energetically unfavourable grooves left behind.

A concise theoretical treatment of liquid-phase densification and microstructural development, during sintering of technically important powder mixtures is difficult. This is particularly true for the varying nonisothermal heating schedules used in industry owing to the complex interaction of mechanisms involved in the superposition of parallel and in the sequence of consecutive processes. For example, for slow heating rates a large part of the total shrinkage may occur before a liquid phase is formed as, for example, observed for WC-Co hard metals (fig. 13). Small additions may change the onset and the course of shrinkage and particularly the size, the shape and the contiguity of the majority phase in a generally unpredictable way. For most metallic and ceramic systems which are presently of technical importance the basic phenomena are now well understood and

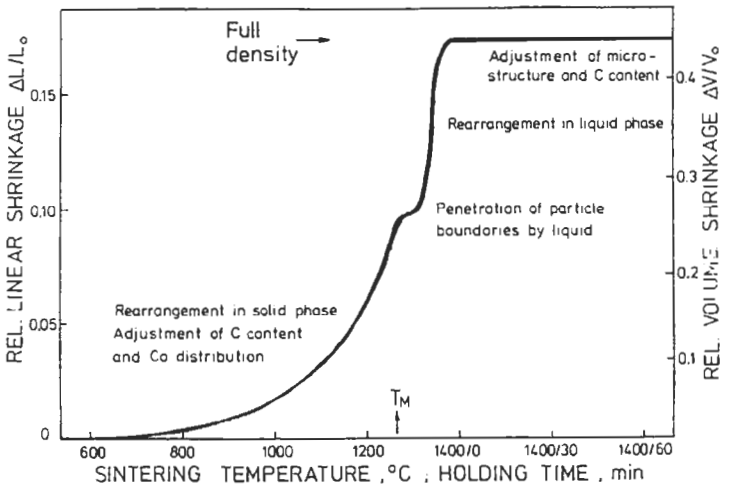

Fig. 13. Nonisothermal shrinkage of a 90 wt% tungsten carbide — 10 wt% cobalt alloy (semischematic, T_M = melting temperature of the Co-W-C eutectic). The various contributions to shrinkage are indicated. The effect of swelling due to particle agglomerate disintegration by liquid penetration is exaggerated. Chemical changes of the cobalt phase taking place in the solid as well as in the liquid phase are due to the large differences of solubilities of carbon (as well as tungsten) at different temperatures (From EXNER [1979c]).

References: p. 2654.

adequately covered in text books such as those by LENEL [1980], GERMAN [1985] or SCHATT [1992] (see also further reading and KAYSSER *et al.* [1984] or TAKAJO *et al.* [1984] for reviews). Discontinuous grain growth is frequently observed in liquid phase sintered materials, particularly in cemented carbides, and attributed to impurities (EXNER [1983] and GERMAN [1985]). Continuous as well as discontinuous coarsening processes have also been studied for liquid-phase sintering of ceramics where a number of additional phenomena occur, e.g., chemical reactions causing transient liquid phases and pronounced atmosphere effects (GERMAN [1985] and HANDWERKER *et al.* [1989]).

Quantitative description of liquid-phase sintering for adequately realistic models seems feasible in the near future. First attempts were recently made by computer simulation, e.g., by RIEDEL [1990], by RIEDEL and SUN [1992], SWOBODA *et al.* [1994] or by SUN and RIEDEL [1995] using constitutive equations and, again, simplified geometries as well as unrealistic assumptions on the mechanisms involved. Nevertheless, predictions of stresses and distortions of hardmetal parts agree to experimental observations. It seems that the results are not very sensitive to such simplifications which are allowable in these early stages of development but should be avoided when work goes on.

4. *Outlook*

Powder metallurgical and ceramic production includes sintering or hot pressing as an essential step in the processing route. Since the beginning of modern physical metallurgy, theoretical concepts have accompanied technical progress. Usually, however, researchers have pursued esoteric directions which hardly contributed to decisive advances in industrial techniques or technical products. Sometimes, simplified approaches even have obscured recognition of the complexity of real powder systems, and quite frequently, researchers worked in fields which are of little or no practical interest. On the other hand, theoretical concepts have made investigators aware of some important mechanisms underlying solid- and liquid-state sintering, and particularly hot pressing. Hot-pressing diagrams are at the verge of being used widely for process optimisation. It is now timely to take the principal ideas to application so as to produce better products from powders. However, we will have to deal with such impure, irregular, inhomogeneous and anisotropic powders, powder mixtures and powder compacts as are typically used in powder technology rather than with idealized geometries and high-purity substances. Some interesting routes have already been demonstrated to be successful, and more will be known by the time of the next edition of this book.

References

AIGELTINGER, E. H., and J. P. DROLET, 1974, in: Modern Developments in Powder Metallurgy, vol. 6, eds. H. H. Hausner and W. E. Smith (Metal Powder Industries Federation, Princeton) p. 323.

AIGELTINGER, E. H., and H. E. EXNER, 1972, J. Mater. Techn. **3**, 425.

AIGELTINGER, E. H., and H. E. EXNER, 1977, Metall. Trans. A, **8A**, 421.

ALDINGER, F., 1974, Acta Metall. **22**, 923.

ALEXANDER, B. H., and R. W. BALLUFFI, 1957, Acta Metall. **5**, 666.

ARNHOLD, V., 1989, in: Advances in Powder Metallurgy, Vol. 1, eds. F. Gasbarre and W.F. Jandeska (Metal Powder Industry Federation, Princeton) p. 175.
ARZT, E., 1982, Acta Metall. **30**, 1883.
ARZT, E., M.F. ASHBY and K.E. EASTERLING, 1983a, Metallurg. Trans. **14A**, 211.
ARZT, E., M.F. ASHBY and R.A. VERRALL, 1983b, Acta Metall. **31**, 1977.
ASHBY, M.F., 1972, Surf. Sci. **31**, 498.
ASHBY, M.F., 1974, Acta Metall. **22**, 275.
ASHBY, M.F., 1990a, "HIP 6.0: Background Reading: Sintering and Isostatic Pressing Diagrams", Technical Report (Department of Engineering, University of Cambridge).
ASHBY, M.F., 1990b, "Operating Manual for HIP 6.0 - Software for Constructing Maps for Sintering and Hot Isostatic Pressing", Technical Report (Department of Engineering, University of Cambridge).
ASHBY, M.F., S. BAHK, J. BEVK and D. TURNBULL, 1980, Prog. Mater. Sci. **25**, 1.
ASHBY, M.F., F. SPAEPEN and S. WILLIAMS, 1978, Acta Metall. **26**, 1647.
BALLUFFI, R.W., 1980, Grain-Boundary Structure and Kinetics (ASM, Metals Park, OH).
BALSHIN, J.M., 1936, Vestn. Metalloprom. **16**, No. 17, 87.
BARRINGER, E.A., and H.K. BOWEN, 1982, J. Amer. Ceram. Soc. **65**, C 199.
BEERE, W., 1975, Acta Metall. **23**, 139.
BERNER, D., H.E. EXNER and G. PETZOW, 1974, in: Modern Developments in Powder Metallurgy, vol. 6, eds. H.H. Hausner and W.E. Smith (Metal Powder Industries Federation, Princeton) p. 237.
BOCCACCINI, A.R., 1993, J. Mat. Sci. Lett. **12**, 943.
BOCCACCINI, A.R., and R. KRAMER, 1995, Glass Technol. (in print).
BORDIA, R.K., and G.W. SCHERRER, 1988a, Acta Metall. **36**, 2393.
BORDIA, R.K., and G.W. SCHERRER, 1988b, in: Ceramic Transactions, Vol. 1, eds. G.L. Messing, R.L. Fuller and H. Hausner (American Ceramic Society, Westerville) p. 1988.
BRETT, J., and L.L. SEIGLE, 1963, Acta Metall. **11**, 467.
BRINKER, C.J. and G.W. SCHERRER, 1993, Sol-Gel-Processing (Academic Press, London).
BROOK, R.J., 1969, J. Amer. Ceram. Soc. **52**, 56 and 339.
BROSS, P., and H.E. EXNER, 1979, Acta Metall, **27**, 1013.
CAHN, J.W., and R.B. HEADY, 1970, J. Amer. Ceram. Soc. **53**, 406.
CAHN, R.W., 1980, in Recrystallization and Grain Growth of Multi-Phase and Particle Containing Materials, eds. N. Hansen, A.R. Jones and T. Leffers (Risø National Laboratory, Roskilde, Denmark) p. 77.
CARPAY, F.M.A., 1977, J. Amer. Ceram. Soc. **60**, 82.
CHERMANT, J.L., M. COSTER, J.P. JERNOT and J.L. DUPAIN, 1981, J. Microsc. **121**, 89.
CLARK, D.R., 1987, J. Amer. Ceram. Soc. **70**, 15.
CLARK, P.W., and J. WHITE, 1950, Trans. Brit. Ceram. Soc. **49**, 305.
CLAUSSEN, N., and H.E. EXNER, 1972, Powder Metall. **15**, 201.
COBLE, R.L., 1958, J. Amer. Ceram. Soc. **41**, 55.
COBLE, R.L., 1961, J. Appl. Phys. **32**, 787.
COBLE, R.L., 1970, J. Appl. Phys. **41**, 4798.
COBLE, R.L., 1973, J. Amer. Ceram. Soc. **56**, 461.
COBLE, R.L., and R.M. CANNON, 1978, in: Processing of Crystalline Solids, Materials Science Research, vol. 11, eds. H. Palmour, R.F. Davis and T.M. Hare (Plenum Press, New York) p. 151.
COBLENZ, W.S., J.M. DYNYS, R.M. CANNON and R.L. COBLE, 1980, in: Sintering Processes, Materials Science Research, vol. 13, ed. G.C. Kuczynski (Plenum Press, New York) p. 141.
DE HOFF, R.T., 1989, in: Science of Sintering: New Directions for Materials Processing and Microstructural Control, eds. H. Palmour and R.M. Spriggs (Plenum Press, New York) p. 55.
DE HOFF, R.T., and H.E. AIGELTINGER, 1970, in: Advanced Techniques in Powder Metallurgy, Perspectives in Powder Metallurgy, vol. 5, eds. J.S. Hirschhorn and K.H. Roll (Plenum Press, New York) p. 81.
DE JONGHE, L.C., and M.N. RAHAMAN, 1988, Acta Metall. **36**, 223.
DE JONGHE, L.C., M.N RAHAMAN and C. H. HSUEH, 1986, Acta Metall. **34**, 1467.
DE JONGHE, L.C., M.N. RAHAMAN and M. LIN, 1987, in: Ceramic Microstructures '86, Role of Interfaces, eds. J.A. Pask and A.G. Evans (Plenum Press, New York) p. 447.

DUSTOOR, M. R., A. C. TAYLOR and R. M. GERMAN, 1989, in: Advances in Powder Metallurgy, Vol. 1, eds. F. Gasbarre and W. F. Jandeska (Metal Powder Industry Federation, Princeton) p. 203.
EADIE, R. L., G. C. WEATHERLY and K. T. AUST, 1978, Acta Metall. **26**, 759.
ELZEY, D. M. and H. N. G. WADLEY, 1993, Acta Metall. Mater. **41**, 2297.
EVANS, A. G., 1982, J. Amer. Ceram. Soc. **65**, 497.
EVANS, A. G., and C. H. HSUEH, 1986, J. Amer. Ceram. Soc. **69**, 444.
EXNER, H. E., 1973, Z. Metallk. **64**, 273.
EXNER, H. E., 1977, in: Science of Sintering, ed. D. P. Uskokovic (International Institute for the Science of Sintering, Beograd) p. 8.
EXNER, H. E., 1979a, Rev. Powder Metallurg. Phys. Ceram. **1**, 7.
EXNER, H. E., 1979b, J. Microsc. **116**, 25.
EXNER, H. E., 1979c, in: Proceedings Recent Advances in Hard Metal Production, Vol. 2 (Metal Powder Report, London) p. 13–1.
EXNER, H. E., 1980, Powder Metallurg. **23**, 203.
EXNER, H. E., 1982, Met. Sci. **16**, 451.
EXNER, H. E., 1983, in: Science of Hard Materials, eds. R. K. Viswanadham, D. J. Rowcliff and J. Gurland (Plenum Press, New York) p. 233.
EXNER, H. E., 1987, Acta Metall. **35**, 587.
EXNER, H. E., 1988a, in: Jahrbuch Technische Keramik (Vulkan Verlag, Essen). p. 28.
EXNER, H. E., 1988b, in: Sintering 87, Vol. 1, eds. S. Somiya, M. Shimeda, M. Yoshimura and R. Watanabe (Elsevier Applied Science, London) p. 291.
EXNER, H. E., 1994, in: Materials Science and Technology, Vol. 2B, ed. E. Lifshin (VCH, Weinheim) p. 281.
EXNER, H. E., and E. A. GIESS, 1988, J. Mater. Research **3**, 122.
EXNER, H. E., and E. A. GIESS, 1989, in: Science of Sintering: New Directions for Materials Processing and Microstructural Control, eds. D. P. Uskokovic, H. Palmour and R. M. Spriggs (Plenum Press, New York) p. 73.
EXNER, H. E., G. PETZOW and P. WELLNER, 1973, in: Sintering and Related Phenomena, Materials Science Research, vol. 6, ed. G. C. Kuczynski (Plenum Press, New York) p. 351.
FANG, T. T., and H. PALMOUR, 1989, Ceramics Intern. **15**, 329.
FEDORCENKO, I. M., and I. I. IVANOVA, 1987, Teorija i technologija spekanija (Theory and Technology of Sintering) in Russian (Naukova Dumka, Kiev).
FISCHMEISTER, H. F., 1978, Powder Metallurg. Int. **10**, 119.
FISCHMEISTER, H. F. and E. ARZT, 1983, Powder Metallurg. **26**, 82.
FISCHMEISTER, H. F. and E. ARZT, 1986, in: Science and Technology of the Undercooled Melt, eds. P. R. Sahm, H. Jones and C. M. Adam (M. Nijhoff Publishers, Dordrecht) p. 137.
FISCHMEISTER, H. F. and H. E. EXNER, 1964, Metall 18, 932; 1965, Metall **19**, 113.
FRENKEL, J., 1945, J. Phys. USSR **9**, 385.
FRISCH, A., W. A. KAYSSER and G. PETZOW, 1989, Science of Sintering: New Directions for Materials Processing and Control, eds. D. P. Uskokovic, H. Palmour, R. M. Spriggs (Plenum Press, New York) p. 311.
GEGUZIN, J. A., 1973, Physik des Sinterns (Physics of Sintering) in German (VEB Deutscher Verlag für Grundstoffindustrie, Leipzig).
GEHO, M., and H. PALMOUR, 1992, Paper presented at the Symposium on Manufacturing, Third International Ceramic Science and Technology Congress, San Francisco (Am. Ceram. Soc., Philadelphia).
GERMAN, R. M., 1982, Sci. Sint. **14**, 13.
GERMAN, R. M., 1984, Powder Metallurgy Science (Metal Powder Industry Federation, Princeton).
GERMAN, R. M., 1985, Liquid Phase Sintering (Plenum Press, New York).
GERMAN, R. M., 1989, Particle Packing Characteristics (Metal Powder Industry Federation, Princeton).
GERMAN, R. M., and J. E. LANTHROP, 1978, J. Mater. Sci. **13**, 921.
GERMAN, R. M., and Z. A. MUNIR, 1975, Metallurg. Trans. **6A**, 2223.
GERMAN, R. M., and Z. A. MUNIR, 1982, Rev. Powder Metallurg. Phys. Ceram. **2**, 9.
GESSINGER, G. H., 1970, Scripta Metall. **4**, 673.
GIESS, E A., J. P. FLETCHER and L. W. HERRON, 1984, J. Amer. Ceram. Soc. **77**, 549.

GLEITER, H., 1969, Acta Metall. **17**, 565.
GLEITER, H., 1979, Acta Metall. **27**, 187.
GOWRI, S., and J. A. LUND, 1989, in: Advances in Powder Metallurgy, Vol. 1, eds. F. Gasbarre and W. F. Jandeska (Metal Powder Industry Federation, Princeton) p. 139.
GREIL, P., and J. WEISS, 1982, J. Mater. Sci. **17**, 1571.
GRYAZNOV, V. G., M. Y. TANAKOV and L. I. TRUSOV, 1992, J. Mater. Sci. **27**, 4829.
HANDWERKER, C. A., J. E. BLENDELL and R. L. COBLE, 1989, in: Science of Sintering: New Directions for Materials Processing and Microstructural Control, eds. D. P. Uskokovic, H. Palmour and R. M. Spriggs (Plenum Press, New York) p. 3.
HANES, H. D., D. A. SEIFERT and C. R. WATTS, 1977, Hot Isostatic Processing (Metals and Ceramics Information Center, Columbus).
HARE, T. M., 1980, in: Sintering Processes, Materials Research, Vol. 13, ed. G. C. Kuczynski (Plenum Press, New York) p 77.
HEDVALL, J. A., and E. HELIN, 1927, Jernkont. Ann. **82**, 265.
HELLE, A. S., K. E. EASTERLING and M. F. ASHBY, 1985, Acta metall. mater. **33**, 2163.
HERRING, C., 1950, J. Appl. Phys. **21**, 437.
HEWITT, R. L., W. WALLACE and M. C. DE MALHERBE, 1973, Powder Metallurg. **16**, 88.
HOGE, C. E., and J. A. PASK, 1977, Ceramurgia Int. **3**, 95.
HSUEH, C. H., 1988, J. Amer. Ceram. Soc. **71**, C 314.
HSUEH, C. H., A. G. EVANS and R. L. COBLE, 1982, Acta Metall. **30**, 1281.
HSUEH, C. H., A. G. EVANS, R. M. CANNON and R. J. BROOK, 1986, Acta Metall. **34**, 927.
HUCKABEE, M. L., T. M. HARE and H. PALMOUR, 1978, in: Processing of Crystalline Solids, Materials Science Research, vol. 11, eds. H. Palmour, R. F. Davis and T. M. Hare (Plenum Press, New York) p. 205.
HUPPMANN, W. J., 1975, in: Sintering and Catalysis, Materials Science Research, vol. 10, ed. G. C. Kuczynski (Plenum Press, New York), p. 359.
HUPPMANN, W. J., 1979, Z. Metallkde. **70**, 792.
HUPPMANN, W., and G. PETZOW, 1980, in: Sintering Processes, Materials Science Research, vol. 13, ed. G. C. Kuczynski (Plenum Press, New York) p. 189.
HÜTTIG, G. F., 1948, Arch. Metallk. **2**, 93.
ICHINOSE, H., and G. C. KUCZYNSKI, 1962, Acta Metall. **10**, 205.
IVENSEN, V. A., 1973, Densification of Metal Powders during Sintering (Consultants Bureau, New York, London).
JAEGER, W., and H. GLEITER, 1978, Scripta Metall. **12**, 675.
JERNOT, J. P., J. L. CHERMANT, P. MAIRE and P. GILES, 1980, Mikroskopie **37**, (Suppl.) 331.
JOHNSON, D. L., 1970, Scripta Metall. **4**, 677.
JOHNSON, D. L., 1972, in: Powder Metallurgy for High Performance Applications, eds. J. J. Burke and V. Weiss (Syracuse University Press, Syracuse) p. 139.
JOHNSON, D. L., 1990, in: Sintering Key Papers, eds. S. Somiya and Y. Moriyoshi (Elsevier Appl. Sci., London) p. 357.
JOHNSON, D. L., V. A. KRAMB and D. C. LYNCH, 1984, in: Emergent Process Methods for High-Technology Ceramics, Materials Science and Research, Vol. 17 (Plenum Press, New York), p. 207.
JONES, W. D., 1946, Metal Treatment **13**, 265.
KAKAR, A. K., and A. C. D. CHAKLADER, 1968, Trans. AIME **242**, 1117.
KANG, S. J. L., W. A. KAYSSER, G. PETZOW and D. N. YOON, 1984, Powder Metall. **27**, 97.
KAYSSER, W. A., 1988, in: Ceramic Transactions Vol. 1, eds. G. L. Messing, E. R. Fuller and H. Hausner (American Ceramic Society, Westerville) p. 955.
KAYSSER, W. A., 1992, Sintern mit Zusätzen (Sintering with Additions), in German, Materialkund.-Technische Reihe, Vol. 11 (Gebr. Borntraeger, Berlin, Stuttgart).
KAYSSER, W. A., W. J. HUPPMANN and G. PETZOW, 1980, Powder Metallurg. **23**, 86.
KAYSSER, W. A., O. J. KWON and G. PETZOW, 1982, in: P/M-82 in Europe, Preprints Intern. Powder Metallurgy Conference (Assoc. Italiana di Metallurgia, Milano) p. 23.
KAYSSER, W. A., S. TAKAJO and G. PETZOW, 1984, Acta Metall. **32**, 115.
KELLETT, B., and F. F. LANGE, 1984, J. Amer. Ceram. Soc. **67**, 369.

KING, A. H., and D. A. SMITH, 1980, Phil. Mag. **42**, 495.
KINGERY, W. D., 1959, J. Appl. Phys. **30**, 301.
KINGERY, W. D., and M. BERG, 1955, J. Appl. Phys. **26**, 1205.
KISLY, P. S., 1989, in: Science of Sintering: New Directions for Materials Processing and Control, eds. D. P. Uskokovic, H. Palmour, R. M. Spriggs (Plenum Press, New York) p. 279.
KUCZYNSKI, G. C., 1949, Metallurg. Trans. AIME **185**, 169.
KUCZYNSKI, G. C., 1975, in: Sintering and Catalysis, Materials Science Research, vol. 10, ed. G. C. Kuczynski (Plenum Press, New York) p. 325.
KUCZYNSKI, G. C., 1976, Z. Metallkde. **67**, 606.
KUCZYNSKI, G. C., 1978, Science of Sintering, Monograph 17 (The Serbian Academy of Science and Arts, Beograd).
KUCZYNSKI, G. C., G. MATSUMURA and B. B. CULLITY, 1960, Acta Metall. **8**, 205.
KUROKI, H., and M. HIRAISHI, 1989, in: Science of Sintering: New Directions for Materials Processing and Microstructural Control, eds. D. P. Uskokovic, H. Palmour and R. M. Spriggs (Plenum Press, New York) p. 91.
KWON, O. J., and D. N. YOON, 1980, in: Sintering Processes, Materials Science Research, vol. 13, ed. G. C. Kuczynski (Plenum Press, New York) p. 203.
LANGE, F. F., 1984, J. Amer. Ceram. Soc. **67**, 83.
LANGE, F. F., 1987, J. Mater. Res. **2**, 59.
LENEL, F. V., 1980, Powder Metallurgy - Principles and Applications (Metal Powder Industries Federation, Princeton).
LI, E. K. H. and P. D. FUNKENBUSCH, 1993, Metall. Trans. **24A**, 1345.
LI, W.-B., K. E. EASTERLING and M. F. ASHBY, 1991, Metall. Trans. **22A**, 1071.
LI, W.-B., M. F. ASHBY and K. E. EASTERLING, 1987, Acta metall. mater. **35**, 2831.
LIU, Y., and B. R. PATTERSON, 1993, Metall. Trans. A. **24A**, 1497.
MACKENZIE, J. K., and R. SHUTTLEWORTH, 1949, Proc. Phys. Soc. **62**, 833.
MARION, J. E., C. H. HSUEH and A. G. EVANS, 1987, J. Amer. Ceram. Soc. **70**, 708.
MATTHEWS, J. R., 1980, Acta Metall. **28**, 311.
MC MEEKING, R. M., and L. T. KUHN, 1992, Acta Metall. Mater. **40**, 961.
MISHRA, A., F. V. LENEL and G. S. ANSELL, 1975 in: Sintering and Catalysis, Materials Science Research, vol. 10, ed. G. C. Kuczynski (Plenum Press, New York) p. 339.
MITKOV, M., 1978, Proc. 5th European Symp. Powder Metall., Vol. 3 (Jernkontoret, Stockholm) p. 379.
MITKOV, M., H. E. EXNER and G. PETZOW, 1979, in: Sintering - New Developments, ed. M. M. Ristic, Materials Science Monographs 4 (Elsevier Scient. Publ. Corp., Amsterdam).
MOCELLIN, A., and W. D. KINGERY, 1973, J. Amer. Ceram. Soc. **56**, 309.
MOLERUS, O., 1975, Powder Techn. **12**, 259.
NABARRO, F. R. N., 1967, Phil. Mag. **16**, 231.
NICHOLS, F. A., 1968, Acta Metall. **16**, 103.
NICHOLS, F. A., 1980, Scripta Metall. **14**, 951.
NICHOLS, F. A., and W. W. MULLINS, 1965, J. Appl. Phys. **36**, 1826.
NILSSON, J.-O., P. R. HOWELL and G. L. DUNLOP, 1979, Acta Metall. **27**, 179.
NUNES, J. J., F. V. LENEL and G. S. ANSELL, 1971, Acta Metall. **19**, 107.
OKAMURA, E., A. BARRINGER, and H. K. BOWEN, 1986, J. Amer. Ceram. Soc. **69**, C22.
OSTERTAG, C. P., 1989, in: Science of Sintering: New Directions for Materials Processing and Control, eds. D. P. Uskokovic, H. Palmour, R. M. Spriggs (Plenum Press, New York) p. 453.
PALMOUR, H., 1989, in: Science of Sintering: New Directions for Materials Processing and Microstructural Control, eds. H. Palmour and R. M. Spriggs (Plenum Press, New York) p. 337.
PALMOUR, H., and T. M. HARE, 1987, in: Sintering 85, eds. G. C. Kuczynski, D. P. Uskokovic, H. Palmour and M. M. Ristic (Plenum Press, New York) p. 17.
PALMOUR, H., M. L. HUCKABEE and T. M. HARE, 1979, in: Sintering - New Developments, ed. M. M. Ristic (Elsevier Science Publ., Amsterdam) p. 46.
PARK, H. H., S. J. CHO and D. N. YOON, 1984, Metall. Trans. A., **15 A**, 1075.
PEJOVNIK, S., V. SMOLEJ, D. SUSNIK, and D. KOLAR, 1979, Powder Metallurg. Int. **11**, 22.

PETZOW, G., and W. A. KAYSSER, 1984, in: Sintered Metal-Ceramic Composites, ed. G. S. Upadhyaya (Elsevier Science Publ., Amsterdam) p. 51.

PETZOW, G., and W. A. KAYSSER, 1987, J. Japan. Soc. Powder Metall. **34**, 235.

PETZOW, G., and W. A. KAYSSER, 1990, in: Sintering Key Papers, eds. S. Somiya and Y. Moriyoshi (Elsevier Applied Science, London) p. 595 and p. 615.

PINES, B. J., 1946, Zh. Tekh. Fiz. **16**, 737.

PRÜMMER, R., 1989, in: Science of Sintering: New Directions for Materials Processing and Control, eds. D. P. Uskokovic, H. Palmour, R. M. Spriggs (Plenum Press, New York) p. 267.

RAHAMAN, M. N., and L. C. DE JONGHE, 1987, J. Amer. Ceram. Soc. **70**, C 348.

RAHAMAN, M. N., and L. C. DE JONGHE, 1988, in: Ceramic Transactions, Vol. 1, eds. G. L. Messing, R. L. Fuller and H. Hausner (American Ceramic Society, Westerville) p. 887.

RHINES, F. N., and R. T. DE HOFF, 1971, in: Modern Developments in Powder Metallurgy, Vol. 4, ed. H. H. Hausner (Plenum Press, New York) p. 173.

RHINES, F. N., and R. T. DE HOFF, 1984, in: Sintering and Catalysis, ed. G. C. Kuczynski (Plenum Press, New York) p. 43.

RIEDEL, H., 1990, in: Ceramic Powder Science III, eds. G. L. Messing *et al.* (American Ceramic Society, Westerville) p. 619.

RIEDEL, H., and D. Z. SUN, 1992,in: Numerical Methods in Industrial Forming Processes, Proceedings NUMIFORM '92, eds. J. L. Chenot, R. D. Wood and O. C. Zienkiewicz (A. A. Balkema, Rotterdam) p. 883.

RIEDEL, H., H. ZIPSE and J. SVOBODA, 1994, Acta Metall. Mater. **42**, 445.

RIEGGER, H., J. A. PASK and H. E. EXNER, 1980, in: Sintering Processes, Materials Science Research, vol. 13, ed. G. C. Kuczynski (Plenum Press, New York) p. 219.

ROCKLAND, J. G. R., 1967, Z. Metallk. **58**, 467 and 564.

ROSS, J. W., W. A. MILLNER and G. S. WEATHERLY, 1982, Z. Metallk. **73**, 391.

ROTH, T. A., 1975, Mater. Sci. Eng. **18**, 183.

SANDEROW, M. I., 1989, in: Advances in Powder Metallurgy, Vol. 1, eds. F. Gasbarre and W. F. Jandeska (Metal Powder Industry Federation, Princeton) p. 175.

SCHAEFER, R. J. and B. G. KUSHNER, 1990, in: Intelligent Processing of Materials, eds. H. N. G. Wadley and W. E. Eckhardt (The Minerals, Metals and Materials Society, London) p. 55.

SCHATT, W., ed., 1981, Einführung in die Werkstoffwissenschaft (Introduction to Materials Science) in German (VEB Deutscher Verlag für Grundstoffindustrie, Leipzig).

SCHATT, W., 1992, Sintervorgänge - Grundlagen (Sintering Processes-Fundamentals) in German (VDI-Verlag, Düsseldorf).

SCHATT, W., E. FRIEDRICH and K. P. WIEST, 1986, Rev. Powder Metallurg. Phys. Ceram. **3**, No. 1, 1.

SCHATT, W., H. E. EXNER, E. FRIEDRICH and G. PETZOW, 1982, Acta Metall. **30**, 1367.

SCHERRER, G. W., 1977, J. Amer. Ceram. Soc. **60**, 236.

SCHERRER, G. W., 1979, J. Non-Crystall. Sol. **34**, 239.

SCHERRER, G. W., 1984, J. Amer. Ceram. Soc. **67**, 709.

SCHERRER, G. W., 1987, J. Amer. Ceram. Soc. **70**, 719.

SCHERRER, G. W., 1988, J. Amer. Ceram. Soc. **71**, C. 447.

SCHERRER, G. W., and D. L. BACHMAN, 1977, J. Amer. Ceram. Soc. **60**, 239.

SCHERRER, G. W., and T. A. GARINO, 1985, J. Amer. Ceram. Soc. **68**, 216.

SCHOBER, T., and R. W. BALLUFFI, 1970, Phil. Mag **21**, 109.

SCHYTIL, F., 1949, Z. Naturforsch. **4, A1**, 191.

SHALER, A. J., and J. WULFF, 1948, Ind. Eng. Chem. **40**, 838.

SHAW, N., 1989, Powder Metall. Intern. **21**, No. 3, 16, No. 5, 31 and No. 6, 25.

SHAW, T. M., 1986, J. Amer. Ceram. Soc. **69**, 27.

SKOROKHOD, V. V., 1972, Rheologischeskie Osnovy Teorii Spekania (Rheological Theory of Sintering) in Russian (Izd. Naukovaya Dumka, Kiew).

SKOROKHOD, V. V. 1989, in: Science of Sintering: New Directions for Materials Processing and Microstructural Control, eds. D. P. Uskokovic, H. Palmour and R. M. Spriggs (Plenum Press, New York) p. 39.

SKOROKHOD, V. V., and S. M. SOLONIN, 1984, Fisiko-metallurgisceskije osnovi spekanija proskov (Physical-Metalurgical Phenomena in Powder Sintering) in Russian (Metallurgija, Moscow).

SKOROKHOD, V. V., E. A. OLEVSKI and M. B. SHTERN, 1991, Science of Sintering **23**, No. 2, 79.

SKOROKHOD, V. V., E. A. OLEVSKI and M. B. SHTERN, 1993, Sov. Powder Metall.Phys. Ceram. **21**, 21, 112 and 208.

SOERENSEN, O. T., 1980, in: Thermal Analysis (Birkhauser, Basel) p. 231.

SOMIYA, S., and Y. MORIYOSHI, eds., 1990, Sintering Key Papers (Elsevier Applied Science, London, New York).

SPEARS, M. A. and A. G. EVANS, 1982, Acta Metall, **30**, 1281.

SUN, D. Z., and H. Riedel, 1995, in: Simulation of Materials Processing, eds. S. F. Shen and P. R. Dawson, Proceedings NUMIFORM 95 (A. A. Balkema, Rotterdam) p. 881.

SVOBODA, J., and H. RIEDEL, 1992, Acta Metall. Mater. **40**, 2829.

SVOBODA, J., and H. RIEDEL, 1995, Acta Metall. Mater. **43**, 1.

SVOBODA, J., H. RIEDEL and H. ZIPSE, 1994, Acta Metall. Mater. **42**, 435.

SWINKELS, F. B., and M. F. ASHBY, 1980, Powder Metallurg. **23**, 1.

SWINKELS, F. B., and M. F. ASHBY, 1981, Acta Metall. **29**, 259.

SWINKELS, F. B., D. S. WILKINSON, E. ARZT and M. F. ASHBY, 1983, Acta Metall. **31**, 1829.

TABESHFAR, K., and G. A. CHADWICK, 1982, in: P/M-82 in Europe, Preprints Intern. Powder Metallurgy Conference (Assoc. Italiana di Metallurgia, Milano) p. 693.

TAKAHASHI, Y., and K. INOUE, 1992, Mater. Sci. Techn. **8**, 953.

TAKAJO, S., W. A. KAYSSER and G. PETZOW, 1984, Acta Metall. **32**, 107.

TAMMANN, G., 1926, Z. Anorg. Allg. Chem. **157**, 321.

THÜMMLER, F., and W. THOMMA, 1966, in: Modern Developments in Powder Metallurgy, vol. 12, ed. H. H. Hausner (Plenum Press, New York) p. 3.

THÜMMLER, F., and W. THOMMA, 1967, Metallurg. Rev. **12**, 69.

TIAN, Y. L., D. L. JOHNSON and M. E. BRODWIN, 1988, in: Ceramic Transactions, Vol. 1, eds. C. L. Messing, E. R. Fuller and H. Hausner (American Ceramic Society, Westerville) p. 933.

TIKKANEN, M. H., and S. A. MÄKIPIRTTI, 1965, Int. J. Powder Metallurg. **1**, No. 1, 15.

TORRE, C., 1948, Berg- u. Hüttenm. Mh. **93**, 62.

TURNER, C. D. and M. F. ASHBY, 1993, Paper presented at the HIP Conference, Antwerp.

UDIN, H., A. J. SHALER and J. WULFF, 1949, Metallurg. Trans, AIME **185**, 186.

USKOKOVIC, D., and H. E. EXNER, 1977, Phys. Sint. **9**, 265.

VAN DE VORST, G. A. L., 1994, Modelling and Numerical Simulation of Viscous Sintering (University of Technology, Eindhoven)

WALKER, K. L., J. W. HARVEY, F. T. GEYLING, and S. R. NAGEL, 1980, J. Amer. Ceram. Soc. **63**, 96.

WANG, G. X., and M. DAHMS, 1992, Scripta Metall. Mater. **26**, 1469.

WANG, G. X., U. BOHNENKAMP and M. DAHMS, 1994, Pract. Metallogr. **31**, 234.

WEI, T. S., and R. M. GERMAN, 1982, in: P/M-82 in Europe, Preprints Intern. Powder Metallurgy Conference (Assoc. Italiana di Metallurgia, Milano) p. 239.

WEISER, M. W., and L. C. DE JONGHE, 1988, J. Amer. Ceram. Soc. **71**, C 125.

WELLNER, P., G. H. GESSINGER and H. E. EXNER, 1974, Z. Metallk. **65**, 602.

WHITTEMORE, O. J. and J. A. VARELA, 1990, in: Sintering Key Papers, eds. S. Somiya and Y. Moriyoshi (Elsevier Applied Science, London, New York) p.777.

WILKINSON, D. S. and M. F. ASHBY, 1975, Acta Metall. **23**, 1277.

WLASSICH, J. J., M. F. ASHBY, D. R. BLANCHARD, B. L. HENNIGES and D. W. O'BRIEN, 1990, in: Intelligent Processing of Materials, eds. H. N. G. Wadley and W. E. Eckhardt (The Minerals, Metals and Materials Society, London) p. 207.

WONG, B., and J. A. PASK, 1979, J. Amer. Ceram. Soc. **62**, 138.

ZHANG, W., and J. H. SCHNEIBEL, 1994, preprint (private communication).

Further reading

Books, Proceedings and Monographs

4th International Conference on Hot Pressing (Metal Powder Report, London, 1992).
Brinker, C. J., and G. W. Scherer, Sol-Gel Processing (Academic Press, London, 1993).
Burke, J. J., and V. Weiss, eds., Powder Metallurgy for High-Performance Application (Syracuse University Press, Syracuse, 1972).
Exner, H. E., Grundlagen von Sintervorgängen (Gebr. Borntraeger Verlag, Stuttgart, 1978), in German, English translation by V. F. Lenel published 1980, Rev. Powder Metallurg. Phys. Ceram. **1**, 7.
Exner, H. E., Powder Metallurgy of Steel, in: Gmelin Handbook of Inorganic and Organometallic Chemistry, 8th ed., Vol. 10, Practice of Steelmaking (Springer Verlag, Berlin, 1991), p. 129a and p. 72b.
Geguzin, J. E., Physik des Sinterns (VEB Deutscher Verlag für Grundstoffindustrie, Leipzig, 1973).
German, R. M., Powder Metallurgy Science (Metal Powder Industry Federation, Princeton, 1984).
German, R. M., Liquid Phase Sintering (Plenum Press, New York, 1985).
German, R. M., Particle Packing Characteristics (Metal Powder Industry Federation, Princeton, 1989).
Hanes, H. D., D. A. Seiffert and C. R. Watts, Hot Isostatic Processing (Metals and Ceramics Information Center, Columbus, 1977).
Hench, L. L., and D. R. Ulrich, Ultrastructure Processing of Ceramics, Glasses and Composites (John Wiley Publ., New York, 1984).
Hot Isostatic Pressing (Adam Hilger, IOP Publishing, Bristol, 1991).
Jenkins, I. and J. V. Wood, eds., Powder Metallurgy – An Overview (The Institute of Metals, London, 1991).
Kaysser, W. A., Sintern mit Zusätzen (Sintering with Additions) in German, Materialkundl. Techn. Reihe Vol. 11 (Gebr. Borntraeger, Berlin, Stuttgart, 1992).
Lenel, V. F., Powder Metallurgy – Principles and Applications (Metal Powder Industries Federation, Princeton, 1980).
Schatt, W., ed., Pulvermetallurgie, Sinter- und Verbundwerkstoffe (VEB Deutscher Verlag für Grundstoffindustrie, Leipzig and Hüttig-Verlag, Heidelberg, 1986).
Schatt, W., Sintervorgänge – Grundlagen (Sintering Processes-Fundamentals), in German (VDI-Verlag, Düsseldorf, 1992).
Schatt, W., and K. P. Wieters, Pulvermetallurgie – Technologie und Werkstoffe (Powder Metallurgy – Technology and Materials) in German (VDI-Verlag, Düsseldorf, 1994).
Sintering, Advances in Powder Metallurgy 1991, Vol. 3 (Metal Powder Industry Federation, Princeton, 1991).
Sintering, Advances in Powder Metallurgy 1992, Vol. 4 (Metal Powder Industry Federation, Princeton, 1992).
Somiya, S. and Y. Moriyoshi, Sintering Key Papers (Elsevier Applied Science, London, New York, 1990).
Thümmler, F., and W. Thomma, 1967, Metallurg. Rev. **12**, 69.
Thümmler, F., and R. Oberacker, An Introduction to Powder Metallurgy (The Institute of Materials, London, 1993).
Uskokovic, D. P., H. Palmour and R. M. Spriggs, (eds.), Science of Sintering: New Directions for Materials Processing and Microstructural Control (Plenum Press, New York, 1989).

The following book series are specialized in powder metallurgy and topics treated in this chapter are frequently discussed:

Book Series

Materials Science Research (Plenum Press, New York, London): Vol. 6, 1973, G. C. Kuczynski, ed., Sintering and Related Phenomena. Vol. 9, 1975, A. R. Cooper and A. H. Heuer, eds., Mass Transport Phenomena in Ceramics. Vol. 10, 1978, G. C. Kuczynski, ed., Sintering and Catalysis. Vol. 13, 1980, G. C. Kuczynski, ed., Sintering Processes. Vol. 14, 1981, J. Pask and A. Evans, eds., Surfaces and Interfaces in Ceramic and Ceramic Metal Systems.

Modern Developments in Powder Metallurgy, Proceedings of the International Powder Metallurgy Conferences (Metal Powder Industries Federation, Princeton, NJ, USA).

Perspectives in Powder Metallurgy – Fundamentals, Methods and Applications (Plenum Press, New York, London).

New Perspectives in Powder Metallurgy (Metal Powder Industries Federation, Princeton, NJ, USA).

Progress in Powder Metallurgy, Proceedings of the National US Powder Metallurgy Conferences (Metal Powder Industries Federation, Princeton, NJ, USA).

"Materials Science and Technology", ed. R. W. Cahn *et al.*, Vol. 17b, Processing of Ceramics Part II, ed. R. J. Brook (VCH, Weinheim , 1996): chapter 13 (Eisele: Sintering and Hot Pressing); 14 (Kwon: Liquid–phase sintering); 15 (Cambler & Leriche: Vitrification); 16 (Larker & Larker: Hot isostatic pressing).

CHAPTER 32

A METALLURGIST'S GUIDE TO POLYMERS

A. H. WINDLE

Department of Materials Science and Metallurgy
Cambridge University
Pembroke Street
Cambridge, CB2 3QZ
UK

R. W. Cahn and P. Haasen†, eds.
Physical Metallurgy; fourth, revised and enhanced edition

Preface

The development of the discipline of Materials Science owes a great deal to Metallurgy; indeed many university departments which now thrive under the Materials banner were once departments of metallurgy. Professional Institutes also reflect this change, with the Materials Research Society in the US and the Institute of Materials in the UK catering for the catholic interests of the new Materials Discipline. At the centre of this applied science is the interrelation of the internal structure of materials with their properties, particularly their useful properties. It is to physical metallurgy that we owe this science, which applies now to polymers and ceramics alike. Indeed, this author recalls an erstwhile professor of physical metallurgy proposing a new course entitled "The Physical Metallurgy of Polymers". So, is it straightforward for one schooled in physical metallurgy to move into the polymer domain, learn some new vocabulary and be airborne in the research and teaching of this different class of material? The answer is yes and no. There is no doubt that the intellectual discipline of physical metallurgy stands one in good stead in understanding many of the issues of polymer science. There are areas of Materials Science which are comparatively 'materials-independent', fields such as fracture mechanics, X-ray crystallography and composites which can provide a unifying influence across materials types. On the other hand, polymer science has its origins in chemistry and it attracted physicists, who addressed issues of microstructure well before the metallurgical community had broadened towards it. However, irrespective of the origins of the science there are some central areas of the polymer field which are really quite alien to the discipline of physical metallurgy. It is not that they are in any sense inaccessible, it is just that they can in no way be seen as an extrapolation of metallurgical thinking.

One way to learn the way around a big city is to use the underground railway (metro, subway or whatever). One gradually builds up pools of knowledge about the areas surrounding the stations, and with time these connect up. Physical metallurgy is a good

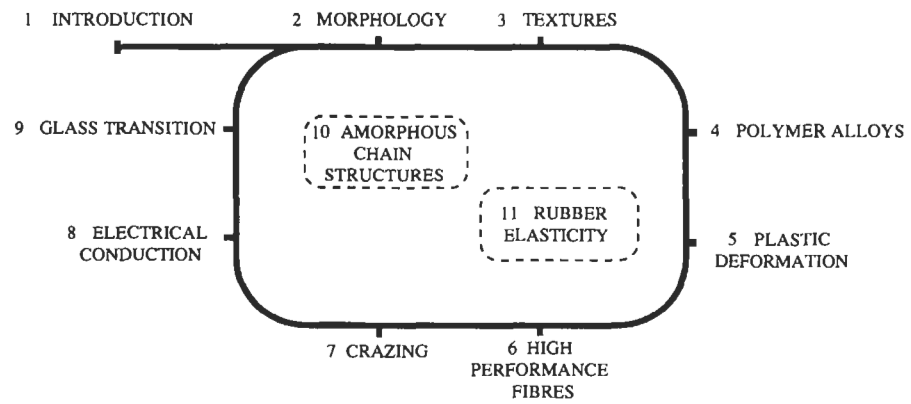

underground system for 'polymer city', and much of this article is structured along these lines. Section 1 is an 'above-ground' introduction to the broad classification of polymer types, the new language that is involved and the way in which polymers are named. Sections 2–9 deal with topics which can be usefully accessed via physical metallurgy. In these cases polymers show new and interesting aspects, and as ever the language is sometimes different, yet the physical metallurgist has a distinct advantage over other physical scientists in approaching them. The map illustrates the metallurgical route to these key topics.

Two topic areas have been selected in which an approach through metallurgy is of no special advantage. These are of central importance to polymer science nevertheless, and a good understanding of them is taken for granted within the polymer materials community. They are put in the centre of the map, not served by the railway.

1. Introduction to synthetic polymers

Synthetic, organic polymers first made a major impact in the 1930s, with the addition of a range of thermoplastic materials such as 'polythene', 'perspex' and 'nylon', to the earlier thermosetting resins such as 'bakelite'. The division of polymers into thermoplastics and thermosets is a fundamental one (fig. 1).

1.1. Thermosets (network polymers)

Once polymerised, *thermosets* cannot be subsequently melted, for the molecules are connected together into a three-dimensional network, rather like the SiO_4^- tetrahedra in a silica glass. 'Araldite', an epoxy resin, is an example of a thermosetting resin which once set cannot be subsequently melted. Networks which have rather longer runs of molecular chains connecting the network points show a glass transition temperature (T_g). Below this temperature they behave as a glass — hard, transparent, tending to be brittle — while above it they are rubbery, with an elastic modulus perhaps 1% that of the glass. The lower the number of network points per unit volume, the softer the rubber.

1.2. Thermoplastics: (a) Non-crystalline polymers

Thermoplastics are not covalently bonded networks, but assemblies of long, linear chain molecules. Typically, the chains contain between 100 and 10000 monomer units connected end to end, and they may sometimes have short side chains attached. Most types of chain wander in three dimensions and are extensively entangled, a proverbial 'can of worms'. Below their glass transition temperature, thermoplastics form a glassy phase, similar to that seen in thermosets. In the temperature range immediately above the glass transition, thermoplastics show rubbery behaviour too. In this case the physical entanglements of the chains act in much the same way as the chemical network points did for the thermosets, at least if the chains are sufficiently long. However, as the temperature is increased further the thermoplastic shows increasing amounts of viscous flow and can now be readily sheared, moulded or extruded. Many polymer articles are thermoplastically formed in this state. Probably the most important 'non-crystalline'

References: p. 2740.

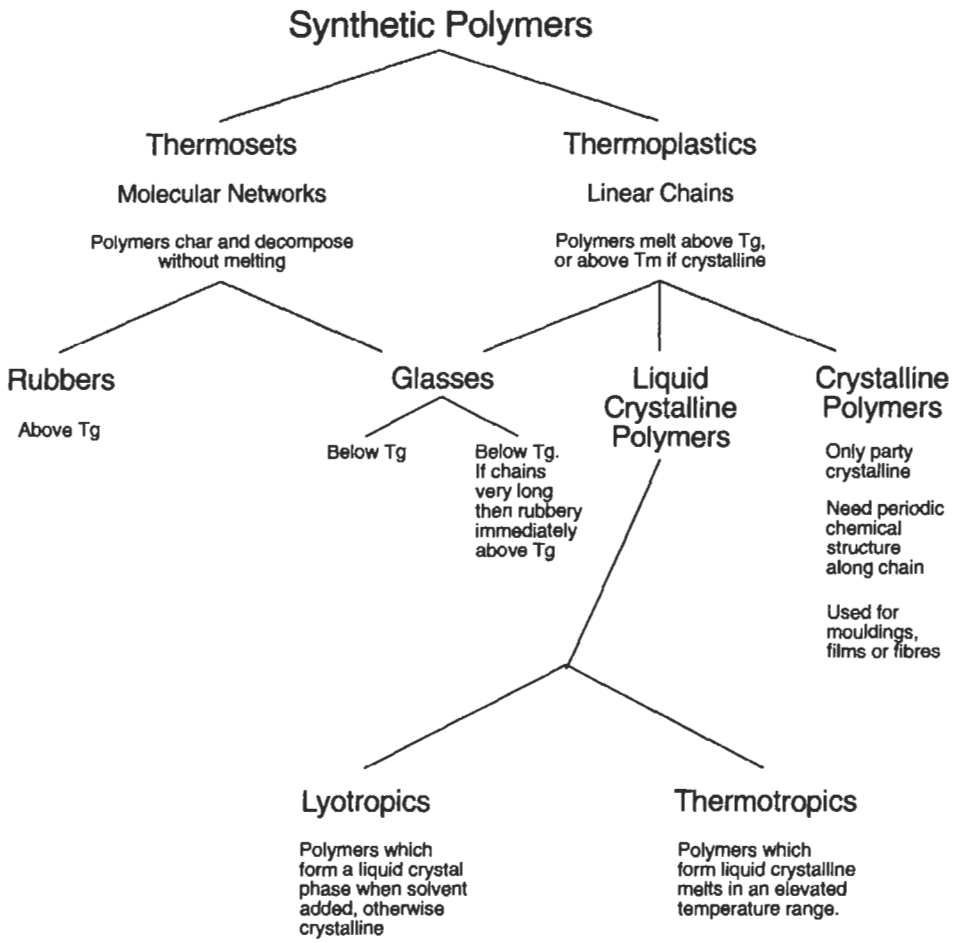

Fig. 1. Outline of different broad classes of polymers

thermoplastic is poly(vinyl chloride) (PVC) which is a glass with a glass transition temperature (T_g) of 80°C. It often used in a 'rubberised' form made by adding a non-polymeric compound known as a *plasticiser*. Other important examples of polymer glasses are 'Perspex' and poly(styrene), with T_gs around 100°C, and poly(carbonate) which is one of the toughest glasses known and has a higher T_g of 150°C.

1.3. Thermoplastics: (b) Semi-crystalline polymers

The linear polymer chains of a thermoplastic can sometimes crystallise. The entanglements are not eliminated by the formation of crystals, but instead, are squeezed into the regions between the crystals which remain amorphous. The crystallinity of a polymer is never 100%, but is usually in the range 30–80%. If the amorphous 'phase' is below its

glass transition, then the crystals have relatively little influence on strength although the fact that they can deform plastically improves the toughness. When the amorphous phase is above its glass transition, the embedded crystals contribute to the stiffness of the rubber and also prevent the onset of viscous flow. With increasing temperature, the crystals will melt and the rapid onset of flow means that the polymer can be processed.

The crystals in a polymer are very small, often only 10 nm thick in the chain direction, and a given chain may form part of one crystal, then wander through the amorphous phase before being incorporated in another, and so on. By convention, the axis of the crystal unit cell which is parallel to the chain axis of the molecule is designated the *c* axis. Polymer crystals are organised on a micron scale into microstructures, such as spherulites, which scatter light readily. Crystalline polymers thus appear translucent rather than transparent. The most widely used crystalline polymers are poly(ethylene), poly(propylene), *nylon* [poly(amide)] and PET [poly(ethylene terephthalate)], the last three also being important as fibers. They maintain their mechanical properties up to the crystal melting point, which in the case of molecules with stiff chains such as PTFE [poly(tetrafluorethylene)] can be as high as 325°C.

1.4. Thermoplastics: (c) Liquid crystalline polymers

The liquid-crystalline state is characterised by long-range *orientational order* of rod-shaped molecules, but only short-range positional order, as one might find in any liquid. The phase, while behaving as a fluid, shows physical phenomena associated with the orientational order such as optical anisotropy (birefringence). The influence of electric and surface fields on the direction of preferred orientation is the basis of the ubiquitous liquid-crystal display. The question as to what would happen if a short rod molecule was extended into a long rod, or stiff polymer, was first asked by Vorlander, a brilliant German synthetic chemist, in the 1920s. He tried to make the first liquid-crystalline polymers but ran into the problem that the crystal melting point of long, stiff polymer molecules becomes very high, frequently exceeding the decomposition temperature of the polymer. There are two ways round this difficulty. Either the crystal melting point can be reduced by adding a solvent, which leads to the formation of a solvent-containing liquid-crystalline phase called a *lyotropic* phase, or through molecular engineering of the chain molecules to reduce the crystal melting point without compromising the chain rigidity and straightness to any great extent. Such liquid-crystalline polymers are called *thermotropic*. The special properties of liquid-crystalline polymers are achieved by processing the liquid-crystal phase. They are not used as structural materials in this state but after crystallisation and glass formation, either through solvent removal in the case of the lyotropics or cooling in the case of thermotropics. The need for solvent removal means that the lyotropic route is confined to thin-section materials such as fibers and films. *Kevlar*, the high performance poly(aramid) fiber achieves is properties by being spun from a lyotropic solution. On the other hand, *Vectra*, a random copolymer of hydroxybenzoic and hydroxynaphthoic acids, is a thermotropic liquid-crystalline material and thus available for both molding and fibers. It prime application is in very high-precision mouldings which show exceptional levels of thermal and environmental stability.

References: p. 2740.

1.5. Naming of plastics

Polymers have different classes of names. Firstly, there is the full chemical name which should enable a chemist to work out the actual structure of the polymer. These can follow the IUPAC (International Union of Pure and Applied Chemists) convention, which although taught in schools is not widely adopted in either practice or in research science. The more traditional full names are still in general use. Next there is an abbreviated name, often a series of letters which remind one of the full name, such as PP for poly (propylene) or PET for poly(ethylene terephthalate). Finally, many polymers are known by the trade names under which they are marketed. For example, *Perspex* is ICI's trade name for sheets of poly(methylmethacrylate) (PMMA), *Lucite* is Dupont's, and *Plexiglas*, Rohm & Haas's. Of course, in this day of word processor software designed to draw chemical formulae, it is often much more straightforward to draw a repeat unit of a polymer structure, rather than refer to it by name, especially if it is complex.

Another aspect in naming is the form the polymer is marketed in. For example, *Terylem*, ICI's PET, was marketed by them as *Terelene* as a fiber, and is *Melinex* when in film form.

So far polymers have been referred to by their most familiar names. For these polymers, the various classes of name are as presented in table 1:

2. *Crystal morphology of polymers and the concept of crystallinity*

2.1. Crystalline or non-crystalline?

Metals form crystalline solids. Only with considerable difficulty is it possible to quench them to the glassy state, and then only for particular alloys. In a polycrystalline metal, one can identify thin grain-boundary regions where there is disorder, but they are exceedingly thin. A polymer scientist faced with this information might reckon that a metal with a grain size of 100 μm is about 99.995% crystalline! To understand this rather strange way of looking at things it is helpful to look at crystallisation from a polymeric perspective.

To start with, it is much more common to find non-crystalline polymers, whether as glasses or rubbers, than it is to meet a metallic glass. There are a number of reasons why, in practice, polymers may not be crystalline:

Firstly, as rubbers, they are still useful materials above their crystalline melting points, although this will only be the case when the chains are especially long or joined together at occasional cross-link points by strong covalent bonds.

Secondly, polymers can be very slow to crystallise. Compared with metals, rather long-range adjustments are required before one chain can be straightened out and fitted exactly onto its neighbour. Some polymers such as poly(ethylene) crystallise so quickly that it is all but impossible to quench them quickly enough to prevent crystallisation; others, such as poly(carbonates), need extended anneals for several days before they will crystallise.

Thirdly, many polymer molecules do not have chemical periodicity along the chain.

Table 1
Some examples of polymer names and chemical structures

Chemical Name	Abbreviation	Trade Name(s)	Monomer Unit(s)
Thermosets (rubbers)			
Poly(dimethyl siloxane)	PDMS	*Silocet, Silopren*	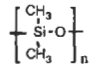
Poly(butadiene)	BR	*Budene, butadiene*	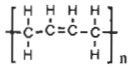
Thermosets (glasses)			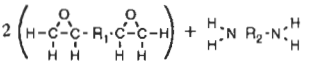
Epoxy	EP	*Araldite*	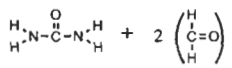
Urea/formaldyhyde resin	UF	*Resolite, Stypol*	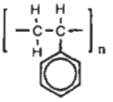
Thermoplastics (glasses)			
Poly(styrene)	PS	*Styron, Bextrene*	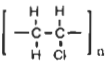
Poly(vinyl chloride)	PVC	*Corvic, Elvic*	
Poly(methyl methacrylate)	PMMA	*Perspex, Lucite, Plexiglas*	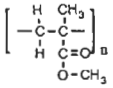
Thermoplastics (crystalline polymers)			
Poly(ethylene)	PE	*Alkathene*	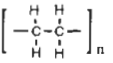
Poly(propylene)	PP	*Propathene, Courlene*	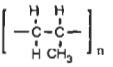
Poly(ethylene terephthalate)	PET	*Dacron, Terelem*	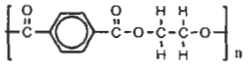
Poly(amide) 6	Nylon 6	*Akulon, Perlenka*	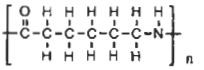
Liquid crystalline polymers			
Poly(paraphenylene terephthalamide)	PPTA	*Kevlar, Tweron* (fibers)	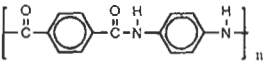
Poly(co-hydroxy benzoic-hydroxy naphthoic acid)	BN	*Vectra, Vectran* (as fiber)	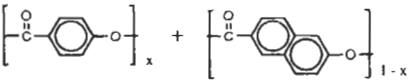

References: p. 2740.

This may be because they are random copolymers, being built from two or more chemically different monomer units joined together in no particular order. A variant of this is that there are different geometric ways in which a particular monomer unit might be organised at the point of its incorporation into a chain. These variants are known as *stereoisomers*, and a chain consisting of different stereoisomers joined at random is called *atactic*. Atactic polymers, precisely because of their chemical randomness, cannot form properly periodic crystals. Well known polymer glasses such as poly(styrene), unplasticised PVC and poly(methyl methacrylate), *Perspex*, are atactic, although in the latter example the reason why crystallinity is prevented is rather more subtle.

Fourthly, polymerisation of monomers which contain three or more active groups to give connections to other similar monomers creates a series of three-dimensional branching points and thus a network. Networks fill space in a rather disordered fashion and they therefore prevent crystallisation also. Glasses such as phenolic resins (once known as *Bakelite*), epoxy resins and the polyester resins which are used as matrices in 'fiberglass' repair kits, are all based on such chemical networks.

In short, the polymer scientist has the option, through careful choice of chemistry, to determine whether the material will be a glass, a rubber or a crystalline solid. But there is more to it than this.

2.2. Crystallinity

Take for example poly(ethylene). On cooling the melt below 130°C it crystallises very readily. However, *it does not crystallise completely*. The crystals are in the form of very thin (≈ 10 nm thick) platelets with a sandwich of non-crystalline material between them. This mixture of crystalline and non-crystalline phases is typical of virtually all polymers which can crystallise. It means that the *crystallinity* is one of the most important parameters used in characterising a polymer. The *percentage crystallinity* can be measured by any technique which can distinguish between the phases. X-ray diffraction shows the crystalline phase as sharp Bragg peaks superimposed on a broad halo characteristic of the non-crystalline phase (often called the 'amorphous' phase). A simple assessment of the relative areas of these two components of a 'powder' photograph gives a reliable indication of the percentage crystallinity: fig. 2 is an example of an x-ray diffraction pattern of a polymer which is 20% crystalline. Other approaches involve the measurement of density enabling the crystallinity to be obtained on a *pro-rata* basis if the densities of the amorphous and crystalline components are known, and also IR spectroscopy, where it is possible to recognise absorption peaks which are characteristic of each of the phases.

2.3. Chain folding

The next question is 'why'? and it has two aspects. Why should polymers not fully crystallise, and why are the crystallites thin platelets, as is usually observed? The basic reason is that in forming a series of perfectly aligned chains in a crystal from an amorphous tangled mass, there is generally no need to turn each of the molecules around to ensure that they all point up or all point down, up or down serving equally well. One

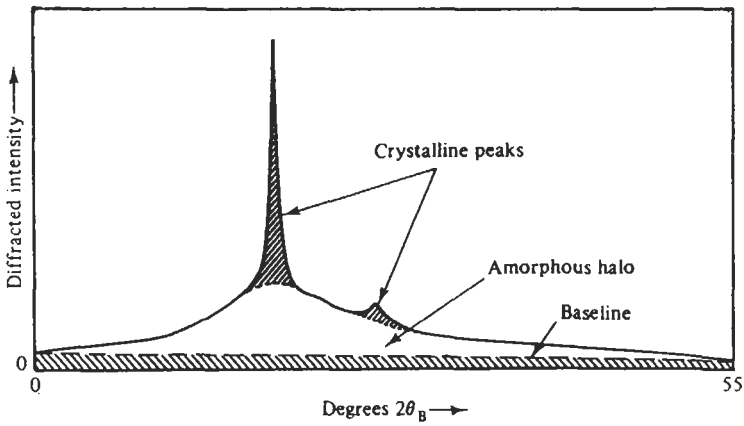

Fig. 2. The wide-angle diffraction of a powder of a polymer which is about 20% crystalline. The area under the sharp peaks divided by the total area under the plot, including the broad halo, is one measure of the crystallinity. In this case it is 20%. (Courtesy Dr. T.J. Lemmon)

might imagine that such leeway would make crystallisation even easier, but as successive stems attached to the crystal can be different parts of the same molecular chain, the growth surfaces normal to the chains become 'poisoned' by folds. Their development is prevented and the crystals remain thin in that direction.

At the time when metallurgists were first turning their hand to electron microscopy and seeing dislocations and GP zones, polymer people were doing the same and looking at very thin single crystals of poly(ethylene) (in fact precipitated from solution) and noting with incredulity that the long chains organise themselves parallel to the uniquely *thin* direction of the crystals. These observations led Keller in 1955 to propose the *chain-folded model of polymer crystallisation*, which is now the accepted view. It is important to appreciate that not all the chains necessarily fold at the crystal surface, and that other defects, especially those associated with topological entanglements of the chain, and short-branched sections, will also poison growth in the chain direction and effectively contribute to the non-crystalline phase between the crystal platelets. A picture of this simple two-phase model of polymer crystallisation is shown in fig. 3. (See also ch. 9, § 5.3).

2.4. Annealing

The grain structure of a metal is often seen to coarsen on annealing. A similar effect can be seen in the case of polymer crystallites which thicken when annealed for long periods close to their melting point. Typically, poly(ethylene) crystals may increase in thickness from 10 nm to perhaps 40 nm. The process is intriguing in that it is not obvious at first sight how the fold surfaces of a given crystal can move apart without running into those of its neighbours. However, there are possible mechanisms which involve multiples of the original crystal thickness, crystals expanding into space vacated by the sideways contraction of the next crystal in the stack and so on. Annealing can also affect properties and is more likely to embrittle than toughen the polymer.

References: p. 2740.

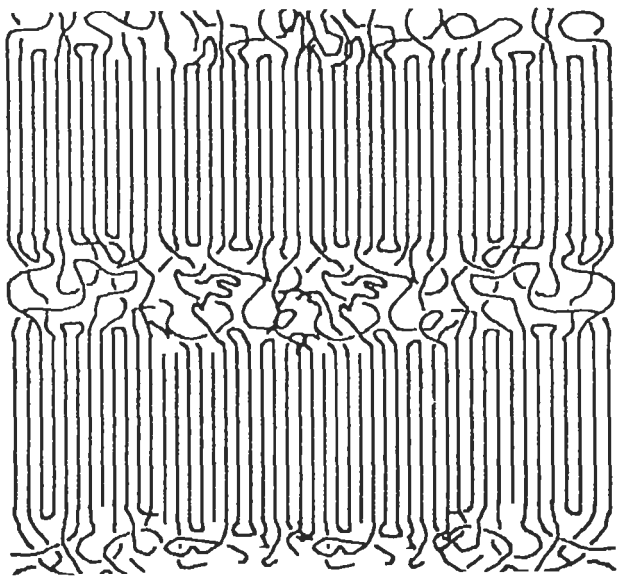

Fig. 3. A diagrammatic view of a crystalline polymer showing chain folding and the presence of entanglements within the non-crystalline phase. The crystals occur as platelets, 5–50 nm thick.

2.5. Special cases

It is always instructive to look at exceptions. In the case of some poly(diacetylenes), it is possible to grow well formed single crystals of the monomer, much as one might of alum or copper sulphate, and then polymerise the monomer in the solid state by means of irradiation. As no condensates are evolved from the reaction, it can be completed without disturbing the long-range periodicity of the lattice. Of course, the chains are perfectly straight and fully extended without folds. A similar and equally unusual state of affairs can be achieved in a fiber which has been crystallised from an oriented liquid-crystalline phase. Liquid crystallinity, in which there is long-range orientational order without long-range positional periodicity, is often achieved by synthesising molecules which are stiff and straight, and bringing down their (inevitably) high crystal melting point by adding solvent or forming the rods as random copolymers. In these cases it is the intrinsic rigidity of the chains which prevents them folding both in the liquid crystalline melt and on subsequent crystallisation. While not as perfectly organised as in the case of the poly(diacetylenes), the extended chains give great stiffness and strength along the fiber axis. This approach is used in the manufacture of *Kevlar* fibers (*Kevlar* is the Dupont trade name for fibers of poly(paraphenylene terephthalamide)), the solvent used being concentrated sulphuric acid.

The crystal morphology of poly(ethylene) can be modified in several ways. If it is heated to between 235°C and 240°C at a pressure of 5 kbar, then a different crystal phase appears. The molecular packing in this case is hexagonal rather than orthorhombic

and there is little or no correlation between the rotational settings of neighbouring molecules about their chain axes. The significance of this phase is that it is a *mesophase* (*meso* = middle) which has order intermediate between that of a crystal and a melt. (Note that a liquid-crystalline phase is another form of mesophase). Crystals held under these conditions appear to anneal very quickly, thickening rapidly along the chain direction as the inter molecular mobility enables the folds to move outwards away from the crystal. Figure 4 is an electron micrograph of a replica of an etched fracture surface showing cross-sections of such chain-extended crystals. They are of the order of 1 μm thick — some 100 times thicker than the crystal platelets of the conventionally crystallised material. Recent studies have indicated that this mesophase plays a key role in the nucleation of poly(ethylene) crystals under more usual conditions, but that in this more normal case, it is a transient phenomenon, and the crystals lock into the orthorhombic phase once they have reached the thickness of a few nanometers.

2.6. Spherulites

The archetypical metal microstructure seen in a light microscope consists of grains and grain boundaries. A comparable examination of a polymer sample in such a microscope is likely to show a microstructure of impinging spherulites. Often the observations are made on thin films in transmitted polarised light, and under these conditions the Maltese cross contrast such as that in fig. 5 testifies to the radial structure of the spherulites. The thin, chain-folded crystallites, once nucleated, grow radially outwards as thin ribbons, known as *fibrils*. The fibrils, separated by non-crystalline polymer, continually branch in order to fill space, and sometimes they twist also. As the chains lie parallel to the thin dimension of the ribbons, they will, for this simple model, lie normal to the growth direction, in accord with most observations.

It is possible to follow the crystallisation process by measuring some property of

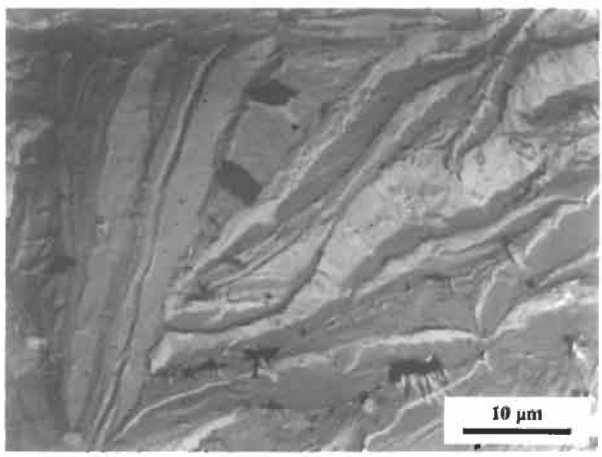

Fig. 4. Etched surface of polyethylene which had been treated to grow chain-extended crystals. The etching solution contains permanganate as the active oxidising ingredient. (Courtesy Professor D.C. Bassett)

References: p. 2740.

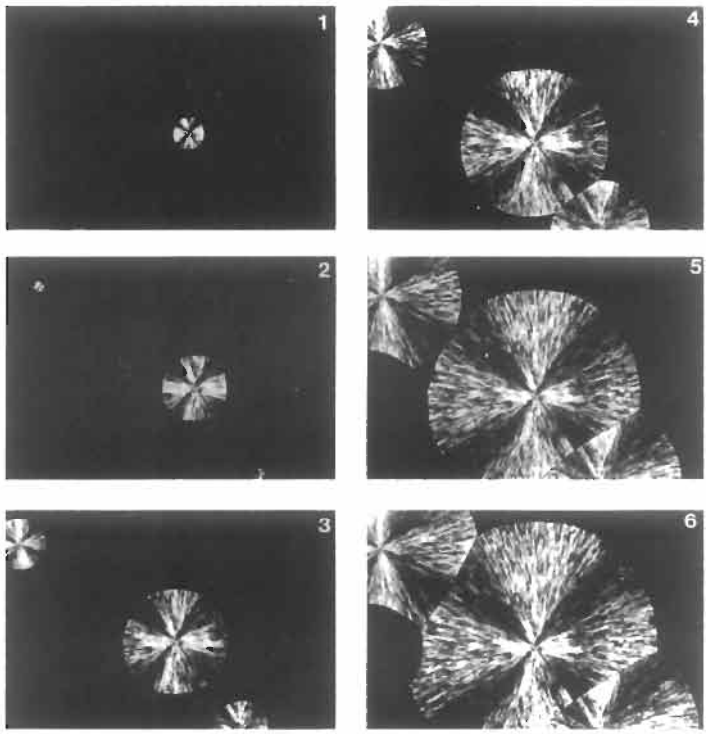

Fig. 5. A time sequence showing spherulites of poly(ethylene oxide) growing from the melt. They are viewed in transmitted light between crossed polars.

state, χ, such as density or heat flow. Such data will tend to fit the standard Avrami equation:

$$\chi(t) = 1 - \exp\left(-kt^{-n}\right). \tag{1}$$

For a constant radial growth rate, as observed for polymers, the equation relates the overall progress of the crystallisation to a rate constant, k, and an exponent, the Avrami exponent n, which is related to the shape of the growing entities. An important property of such a type of function is that it takes into account the decrease of the overall rate as the process approaches completion and the spherulites run into each other. If the growth is spherulitic and nucleation is assumed to occur at random times, then n is predicted to be 4.

For polymers, n is hardly ever 4, and values between 2 and 3 are usually seen. The reason for this is that the spherulites do not reach their full crystalline density at the spherical growth surface. Much of the crystallisation is associated with secondary crystals filling-in between the fibrils behind the advancing front, while the derivation of the

equation assumes that the full density is achieved immediately behind the growth front. Furthermore, the crystallites also undergo some thickening with time, which is also not accounted for by the equation.

3. *Textures*

3.1. Wire textures in metals — an overview

The deformation of a metal as it is drawn into a wire leads to preferred orientation of the grains known as *texture*. Wire texture is usually determined by X-ray diffraction and the nature of the preferred orientation expressed on a pole figure.

The development of wire texture leads to bunching or 'arcing' of the continuous diffraction rings seen in an X-ray transmission photograph. If the texture were perfectly developed, the arcs would be concentrated into spots, and the diffraction pattern would be equivalent to a rotating crystal pattern with the rotation axis of the crystal corresponding to the wire axis. When a low index direction is well aligned with the fiber axis, the reflections will tend to lie on lines or arcs. Figure 6 shows a diffraction pattern of cold-drawn aluminium wire in which the ⟨111⟩ axes of the crystals are tending to align with the wire axis.

The degree of preferred orientation is represented on a pole figure which is a stereographic plot of the orientational probabilities of *a particular* set of plane normals. Figure 7 is one such example. The dark bands represent the preferred orientation of the normals to the (100) planes with respect to the wire axis. Note that the normals to the these planes tend to lie at about 54° to the points representing the wire axis. If one had

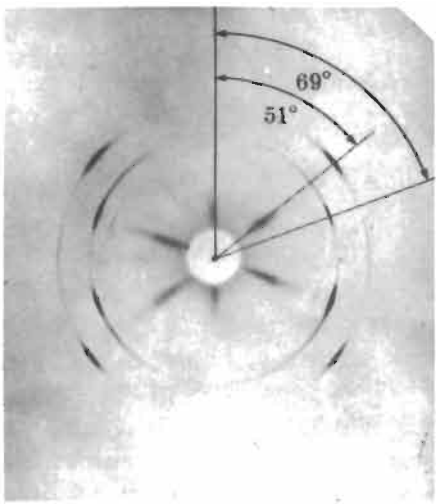

Fig. 6. A transmission X-ray diffraction photograph of a cold-drawn aluminium wire with the axis vertical. The concentration of the diffraction rings into arcs is a measure of the preferred crystal orientation (texture) in the wire in which ⟨111⟩ tends to align with the wire axis. (From B. D. Cullity, "Elements of X-ray Diffraction", Addison-Wesley, Mass.).

References: p. 2740.

Fig. 7. A pole figure drawn for the {100} planes of drawn aluminium wire. The dark bands on the stereogram represent orientations of high probability of the plane normals for the 111 wire texture. The wire axis corresponds to the top and bottom poles of the stereogram.

chosen another set of plane normals the pole figure would appear different but it would contain, for the case of wire textures which have uniaxial symmetry, the same orientational information. With the availability of automated X-ray texture goniometers, it is now common to expect a pole figure to be plotted by the machine, with the possible advantage that the desired information can be extracted without the need for an intimate understanding of diffraction.

3.2. Fiber textures in polymers

While the development of wire textures in metals is significant and can lead to particular property–structure relationships, the importance of the development of similar textures in drawn polymer fibers is much more obvious. In polymers, one crystallographic orientation is of prime importance, that is, the direction of the chain axis. Protocol deems that the chain axis is the *c* axis of the unit cell, the [001] direction, although it should be mentioned that where the crystal structure is monoclinic there is a clash of cultures, and the chain axis, as the diad axis, is usually defined as [010] in deference to crystallographic convention. It is the orientation of the chain axis along the fiber axis which endows polymer fibers with their special stiffness and strength. Figure 8 is an X-ray diffraction pattern taken from a poly(ethylene) fiber with the fiber axis vertical. (When there is little 'arcing' of the crystal reflections, this indicates near perfect alignment of the molecular chains *in the crystals* with the fiber axis.) The uniqueness of the chain axis means that the 'fiber texture' of a polymer implies simply the quality of the alignment of the chains with respect to the fiber axis. One might choose to draw a 001 pole figure for a polymer fiber but this is seldom done as there are neater and more powerful methods of describing alignment quality.

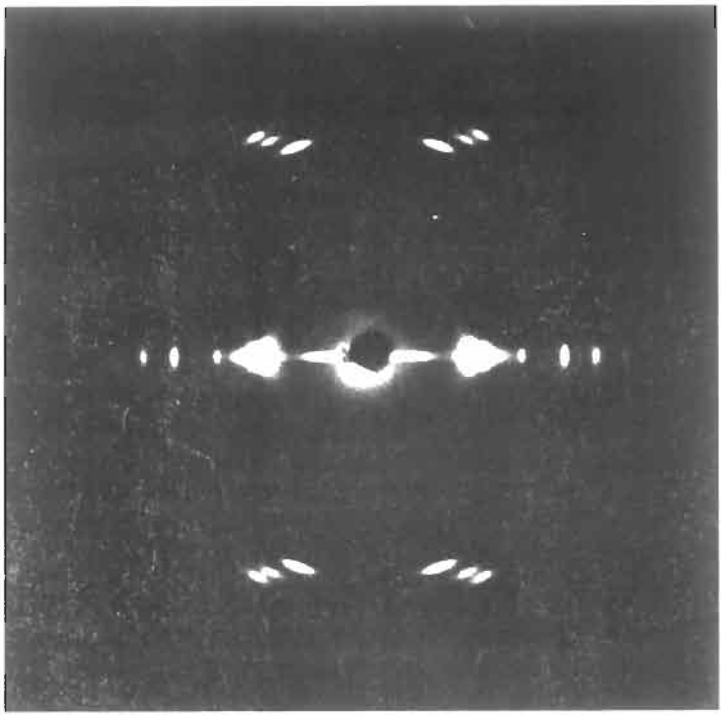

Fig. 8. Diffraction pattern of a fiber of polyethylene (fiber axis vertical). Note the excellent alignment of the crystals, but the very weak orientation of the diffuse halo.

For the case of the flat film held normal to the X-ray beam 'downstream' from the sample, the rows of spots are generally hyperbolae, with the exception of the one passing through the centre which is straight. If the film had been wrapped into a cylinder with its axis coincident with the wire axis, all the rows would be straight, as in the case of the layer lines of a rotating crystal photograph.

3.3. Alignment of non-crystalline polymers

When a rubber band is stretched, or a non-crystalline polymer glass such as polystyrene extruded, the chain molecules align with the extension axis. As with aligned crystals, the mechanical properties are affected. In particular, the increasing stiffness of rubber as it is stretched towards its fracture strain is the result of the chains becoming sufficiently well aligned so that the stiff covalent backbone bonds make their presence felt.

While X-ray diffraction is clearly the most appropriate method for measuring the texture in crystals, the method of determining orientation in non-crystalline polymers is not as obvious. The diffraction pattern consists of diffuse maxima rather than discrete reflections, and while orientational information can be extracted from oriented diffuse halos such as those in fig. 9, for PMMA, the analysis is far from straightforward. Other

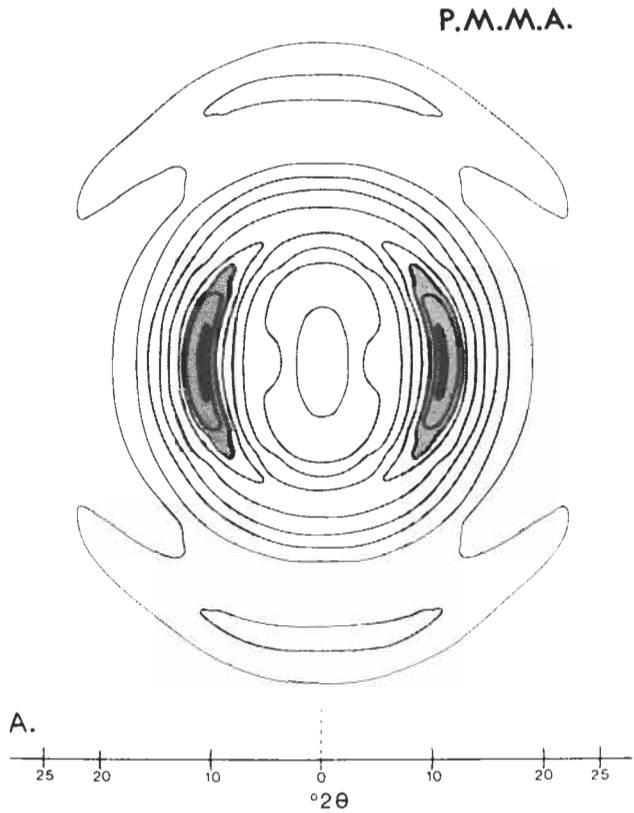

Fig. 9. Transmission diffraction pattern of a sample of PMMA which has been aligned in the glassy state. The alignment axis is vertical. Note that there is arcing of the diffuse haloes.

approaches are through the measurement of optical birefringence, infrared dichroism — the anisotropy of IR absorption by an oriented sample and nuclear magnetic resonance. In each case, the important question is the identity of the unit the orientation of which is being measured. In the case of the spectroscopic methods it is likely to be a single bond or the local environment of an atom, and it will be necessary to relate the orientation of this 'unit' to that of the local chain axis. Both the X-ray and birefringence methods need information about the hypothetical, perfectly aligned state, which is difficult, but not impossible to obtain.

In the case of the amorphous component of a semi-crystalline polymer, the methods mentioned above will apply, as long as it is possible to separate the signal due to the crystals from that from the non-crystalline phase. In the case of diffraction, the diffuse nature of the non-crystalline peaks makes separation easy. From a very highly orientated crystalline polymer the sharp crystalline reflections show very good orientation (they are spots rather than arcs), whereas the amorphous scattering shows virtually no orientation at all, it is a ring. The failure of the non-crystalline component of semi-crystalline

polymers to orient on drawing into a fiber is fairly typical, and is associated with the identity of the non-crystalline component with chain entanglements and folds.

3.4. A parameter to describe the quality of fiber texture

In polymer science it is much more common to hear orientation described in terms of a single parameter, called P_2, than to see pole figures plotted, the fact that the orientational relationship is that between the fiber axis and the chain axis being taken as read. P_2 can be described as the second harmonic coefficient of the Legendre polynomial series, but it is quite easy to understand and use. Consider the distribution of chain axes in relation to the fiber axis. The most probable orientation is aligned with the fiber axis and the distribution has axial symmetry about this axis and a mirror plane normal to it. For this situation the symmetry axis is known as the *director*. In polar co-ordinates the probability ellipsoid is a volume of revolution as shown in fig. 10a. The higher the quality of the alignment, the longer and thinner the ellipsoid; the lower, the more it approaches a sphere. If the shape of the ellipsoid represents the distribution of orientation (the wire texture, in metallurgical parlance), then the challenge is to describe this shape. This can be done mathematically by a harmonic method similar to Fourier analysis. The shape is broken down into harmonic components. In the case of a periodic wave of arbitrary

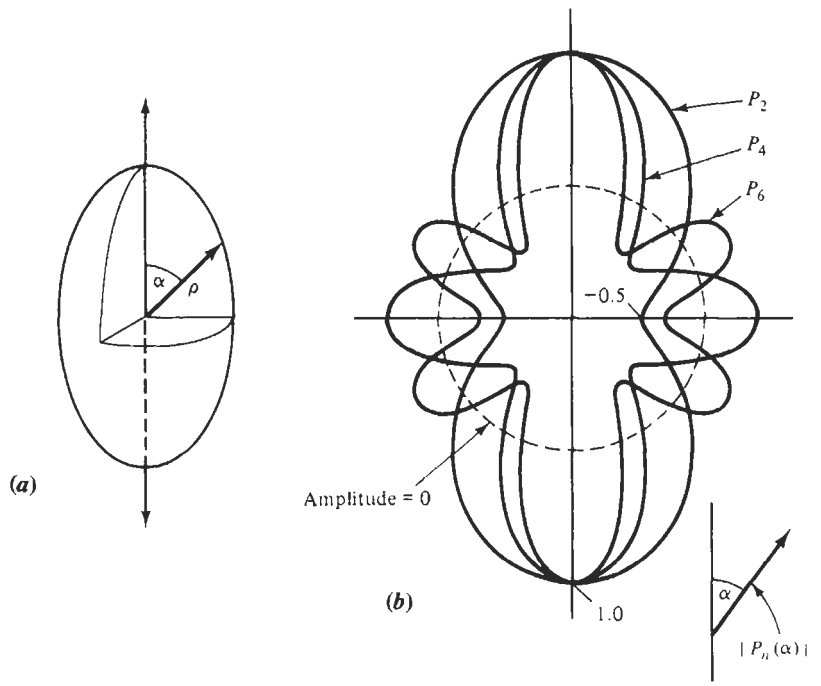

Fig. 10. (a) The probability ellipsoid for a distribution about a symmetry axis, the director. The ellipsoid describes the probability in polar coordinates, (P,α). (b) The harmonic functions which can be summed, with particular weightings, to form any symmetrical ellipsoid.

References: p. 2740.

shape, these would be sinusoidal waves, in the case of an ellipsoidal shape, they are a series of 'spherically harmonic' functions which correspond to the terms of a Legendre series. The even-order components have shapes shown in fig. 10b, the odd-order components do not have mirror symmetry normal to their principal axis and are not of interest here. Any ellipsoidal form can be described in terms of a weighted summation of these component function. If the orientation were perfect, the ellipsoidal would reduce to a thin line along its axis which could be made from summing all harmonic components (strictly to $n=\infty$) with equal amplitude. For a more general ellipsoid, the amplitude of the components would reduce as the order increases. Hence the harmonic coefficients might read: $P_0=1$ (it always is), $P_2=0.62$, $P_4=0.29$, $P_6=0.08$ ... and so on. In the absence of orientation, all coefficients except P_0 are zero. Now, the general level of preferred orientation is contained in the single parameter P_2, while the higher coefficients serve to describe the shape of the distribution. Not surprisingly, P_2 is overwhelmingly popular, and reference is only made to the higher harmonic coefficients in special cases. For axial orientation, P_2 ranges from 0 for the isotropic case to 1 for perfect alignment There is also the possibility of oblate distributions where the orientation tends to lie in a plane normal to the symmetry axis, while being random within that plane. For perfect 'in-plane' orientation, P_2 has the value of –0.5.

Another great advantage of using orientation parameters is that they can handle orientational convolutions with ease. Imagine a series of grains or domains, within each of which the orientation of the units is distributed about a director. The quality of orientation about the director assignable to each grain might be described, say, by $P_2=0.8$. On the other hand the grains themselves may exhibit a texture, and thus their individual directors may be distributed about a global director with a perfection described by a second P_2 which might have the value of 0.4, say. The situation is sketched in fig. 11. Now, the orientation of the units with respect to the global director is given simply by the product of the two individual P_2s, i.e., $0.8\times0.4=0.32$. This property of harmonic orientation parameters is useful when determining the chain orientation from absorption measurements which may give the orientation of a particular chemical group with respect to the fiber axis, P_2', while the orientation distribution of that group with respect to the polymer chain, P_2'' is obtained by other means such as conformational calculations. The orientation of the chains to the fiber axis, P_2, is then given simply by the division: P_2'/P_2''.

It is interesting to note that another important application of spherical harmonics is in the description of preferred molecular orientation in liquid crystals. However, such was the independence of this field from polymers over several decades, that a different nomenclature arose. Instead of 'P_2', the same orientational parameter was designated S and called the *order parameter*. The absence of a subscript indicates that higher order parameters were rarely used.

3.5. Rolling textures

While rolling, as such, is not used in polymer processing, there are a number of processes by which polymer film or sheet is made from the molten material. Examples

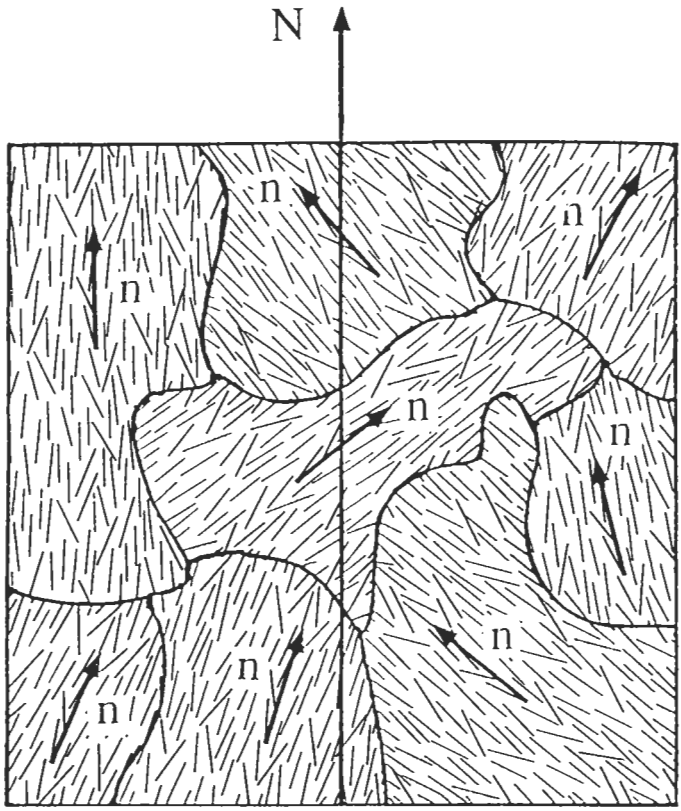

Fig. 11. Diagram to illustrate that the global quality of orientation can, for well behaved systems, be expressed as the products of the two orientation functions, one, that of the orienting units with respect to the local director, **n**, and the second that of the local directors with respect to the global director, **N**.

of these are the extrusion or callandering of sheet, and the manufacture of polymer film by either bubble blowing, or the forward and sideways extension of extruded sheet. The film methods usually involve semi-crystalline polymers, and the texture of the crystallites is of considerable significance. There is no easy method of using spherical harmonic coefficients to define orientational distributions which are not axially symmetric, and polymer research reverts to pole figures to communicate multiaxial orientation. Another consequence of the absence of axial symmetry is that more than one pole figure may be needed to define the texture fully. Figure 12 shows the $\bar{1}10$ pole figure from a piece of PET [poly(ethylene terephthalate)]film. The fact that the (100) planes lie parallel to the plane of the film is not obvious from this figure. The direction in which the film passes through the process is known as the *machine direction* and is equivalent to the rolling direction familiar in metallurgy.

References: p. 2740.

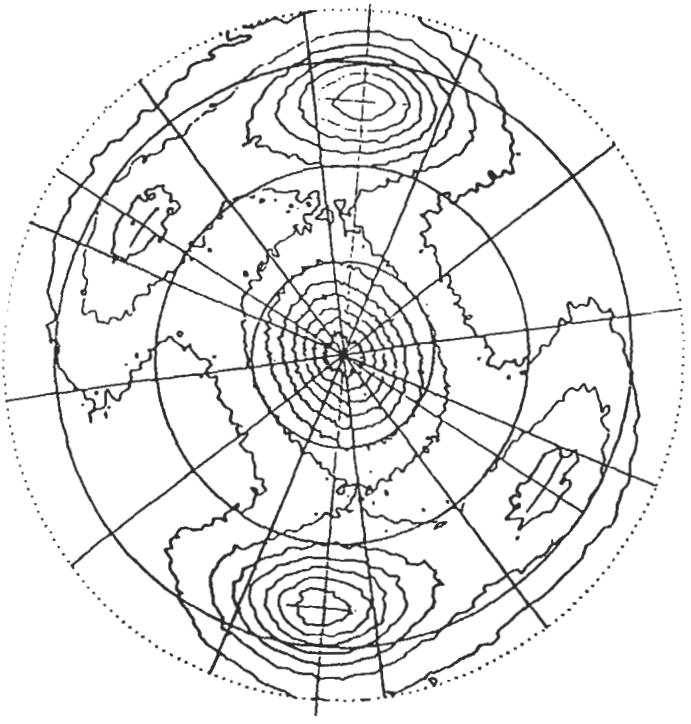

Fig. 12. A $\bar{1}10$ pole figure of biaxially drawn poly(ethylene terephthalate) film. The extrusion direction is near to the vertical and the plane of the film normal to the plane of the diagram i.e., the central pole of the stereogram. This pole figure has been generated automatically using a computer-controlled texture goniometer. (Courtesy L. M. Nicholson.)

4. *Polymer alloys: phase diagrams in macromolecular systems*

4.1. General

Metallurgy is above all the science of alloying. From the big three: iron, copper and aluminium, and perhaps twenty other elements which are also household names, it is possible to generate more or less the complete range of alloys in common use. Of course, the interaction between pairs, or larger numbers, of elements is described, as a function of temperature and compositions, by a *phase diagram*. The understanding of these diagrams is as mother's milk to a metallurgist, and their importance cannot be questioned.

Phase diagrams do exist in polymer science, but their significance is not pre-eminent, and there are many involved with polymeric materials who can ply their trade without ever having to encounter one. Why the difference?

In the first instance, the number of polymers which can be envisaged and synthesised is semi-infinite. There is a huge number of ways in which carbon, oxygen, nitrogen and hydrogen atoms can be put together to make different chains or networks. So it could be

argued that instead of trying to mix different types of chains to make materials with different properties, the polymer chemist merely dreams up and synthesises another molecule. There may be something in this view; however the central reason why polymer alloys are not centre stage is that they are reluctant to form solutions or compounds with each other. *They simply do not alloy very well.*

The word 'alloy' is not used by the polymer scientist (this chapter excepted). The closest equivalent is *blend*. In general, solid solutions of polymers are referred to as *miscible blends* while two-phase mixtures where there is effectively no terminal or liquid–liquid solubility, such as in the copper–lead system, are referred to as *immiscible blends*.

4.2. Entropy and enthalpy of mixing

We will consider solution first. Where one has a random solution of two atom types, 1 and 2, it is a familiar calculation to arrive at the entropy of mixing. For mole fractions x_1 and x_2, the entropy of mixing per one total mole is given by:

$$\Delta S/\text{mole} = -R[x_1 \ln x_1 + x_2 \ln x_2]. \tag{2}$$

However, in the case of intermingled polymer chains, one type dissolved in the other, there is less freedom of action, for the movement of a unit of one chain with respect to a unit of another chain is hindered by its connectivity with its own chain, and vice versa. The calculation of the entropy of mixing is more complicated than for atoms, and was first carried out independently by Flory and by Huggins in 1942. The result is interesting and the equation is related to the one above; it is:

$$\Delta S/\text{mole} = -R[(\phi_1/X_1) \ln \phi_1 + (\phi_2/X_2) \ln \phi_2]. \tag{3}$$

Here ϕ_1 and ϕ_2 are the volume fractions of the *monomer units* comprising the different chains, and X_1 or X_2 the number of monomer units in each polymer chain, assuming that each polymer chain is a *homopolymer* chain, that is, containing only a single type of monomer. The entropy of mixing is per mole of monomer units comprising the chains, not per mole of polymer molecules.

Taking the mole fraction of atoms and volume fraction of monomer units to be broadly equivalent, the major difference between the polymer equation and the atomistic one (which would equally apply to mixing of monomer molecules) is in the pre-log terms. In the polymer case they are divided by the number of monomer units in each polymer chain. For most polymers this is a big number, extending from 100 to 10,000 or more. Hence, volume for volume, the entropy of mixing of polymer molecules will be several orders of magnitude less than in the case of atoms of a metal solution. The entropic driving force for solution is therefore negligible in comparison with a metallic solution.

Before one can predict the phase diagram of a metallic system one needs to consider the enthalpy (or heat) of mixing, ΔH. For a strictly regular solution of equal-sized molecules, the enthalpic term can be written:

References: p. 2740.

$$\Delta H/\text{mole} = zN_a\left(\varepsilon_{12} - 0.5(\varepsilon_{11} + \varepsilon_{22})\right)x_1x_2 \tag{4}$$

where z is the coordination number, N_a is Avogadro's number and ε_{11}, ε_{22} and ε_{12} the interatomic bonding energies, per atom.

A very similar relation holds for the enthalpic reactions between the chemical units of the polymer chain, except that as above mole fractions are replaced by volume fractions. However, here the terminology used in polymers changes a little.

4.3. The Flory–Huggins equation

While the free energy of a metal solution is written as:

$$\Delta G/\text{mole} = zN_a\left(\varepsilon_{12} - 0.5(\varepsilon_{11} + \varepsilon_{22})\right)x_1x_2 + RT\left[x_1 \ln x_1 + x_2 \ln x_2\right] \tag{5}$$

that of a solution between two polymers is usually expressed as:

$$\Delta G/\text{mole} = RT\left[\chi\phi_1\phi_2 + (\phi_1/X_1)\ln\phi_1 + (\phi_2/X_2)\ln\phi_2\right]. \tag{6}$$

This is the *Flory–Huggins equation*, and the Flory–Huggins 'χ' is a famous term in polymer science and, in the field, this Greek letter is dedicated to this particular meaning. χ is essentially:

$$zN_a\left(\varepsilon_{12} - 0.5(\varepsilon_{11} + \varepsilon_{22})/RT\right). \tag{7}$$

Note that the enthalpic terms are similar for both metallic and polymeric cases (assuming that it is expressed per mole of monomer repeat units for polymers), but the entropic terms are very different.

Hence for polymeric alloy systems where the molecular weights of the chains are high, the enthalpic term will be very dominant. Given that, in bonding terms, like tends to prefer like, and thus the enthalpic term will usually be positive, solubility, or *miscibility* as it is known in polymeric parlance, will be unlikely. This is in accord with observation. In general, dissimilar polymers are insoluble in each other. There are however, important and interesting exceptions.

4.4. Polymer–polymer miscibility

(i) Two polymers which are very similar chemically. Perhaps the best example is a polymer such as poly(butadiene) and its deuterated equivalent in which the hydrogen atoms have been replaced by deuteriums. Polymer scientists are keen to work with deuterated molecules because they give excellent contrast with the normal (hydrogenated) ones in neutron scattering experiments while having nominally the same chemical behaviour. However, the enthalpy of mixing is still slightly positive and thus the system is immiscible at low temperatures as shown in the phase diagram of fig. 13, based on experimental measurements. In this case, however, the small entropy of mixing term is able to make its presence felt at higher temperatures and one has a typical solvus with complete miscibility being observed above about 240°C. This temperature, which is

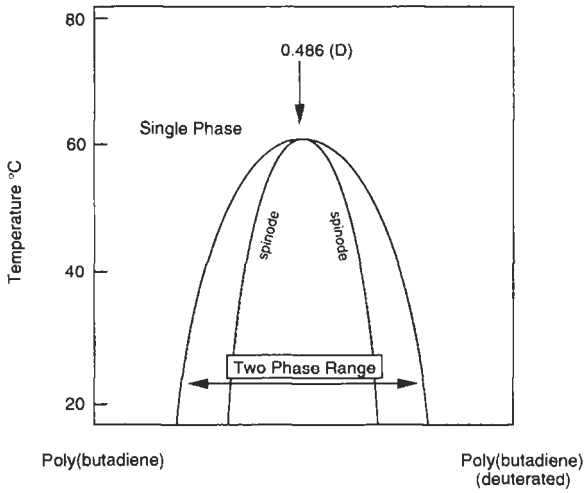

Fig. 13. A sketch of a phase diagram for the mixing of poly(butadiene) and its deuterated analogue. Note how the miscibility (solubility) is achieved only at higher temperatures. The diagram is said to exhibit an Upper Critical Solution Temperature (UCST). [Redrawn from F.S. Bates and P. Wietzins, *J. Chem. Phys.*, **91** (5), 1989, p. 3258].

known as the *Upper Critical Solution Temperature* (UCST), would obviously be very dependent on molecular weight, increasing with increasing molecular weight (the x_1 and x_2 terms of equation (2)). Note how polymer scientists usually put the spinodal curve in as well.

(ii) Polymer systems in which there is a negative enthalpic interaction. In these systems one has a specific attractive bonding between groups on neighbouring, but chemically different, chains. These specific bonds are in some ways akin to those which would stabilise an intermetallic compound, although in this case without the crystal lattice. Hence, A–B ordering is in essence the driving force for miscibility. As such systems are heated, the specific juxtaposition of the groups which are forming the bonds between the neighbouring chains, becomes more costly in entropic terms, and they 'boil off'. Robbed of its strong negative and thus favourable enthalpic interactions, the chains then phase-segregate. Such behaviour is shown by the sketch in fig. 14 which corresponds to the system poly(styrene) and poly(vinylmethylene). Such a system is said to exhibit a *Lower Critical Solution Temperature* (LCST). The only way of rationalising such behaviour in terms of the Flory–Huggins equation is to have a χ term which is temperature-dependent, and various modelling protocols depend on the choice of an *effective* χ which is given an appropriate temperature dependence to enable the model to fit the data.

(iii) Polymer systems showing both lower and upper critical solution temperatures. Figure 15 is a representative phase diagram. As the specific interactions between the two

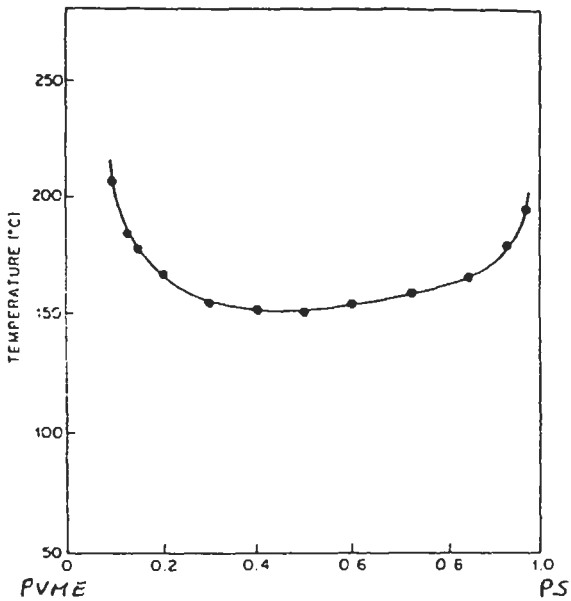

Fig. 14. Equilibrium diagram for two polymers, poly(styrene) and poly(vinyl methylene), which are miscible at low temperatures on account of favourable enthalpic interactions. The diagram is said to exhibit a Lower Critical Solution Temperature.

molecules are first lost on heating, the single phase splits into two only to revert back to a single phase at a higher temperature as the very modest entropy of mixing of the molecules is able to make its presence felt.

(iv) Polymer-solvent systems. The thermodynamics of these systems will follow similar equations to the polymer–polymer case, although the entropy of mixing will not be as small. Put another way, the value of X_1, the number of chemical units in the chain, in equation (3) will no longer be large, tending in this case to unity and thus the $\ln\phi_1$ term will make a significant contribution to the entropy. (Note that it is standard practice to assign the index $_1$ to the solvent and the index $_2$ to the polymer) In this case one might expect to encounter a normal solidus with a UCST, and that is often indeed the case. However, in some situations both a UCST and a LCST are present, the former being at a lower temperature than the latter! Such behavior is shown in fig. 16 for poly(styrene) of different molecular weights dissolved in cyclohexane. The system is two-phase at low temperatures, single phase in an intermediate region, and two-phase again at higher temperatures. A rational explanation of such behavior is that the chain molecules are quite closely associated with the solvent molecules which effectively bond to them and coat them, so in effect the coated surface of the chain is similar to the surrounding solvent. At low temperatures, the entropy of mixing term is insufficient to cause mixing and the (coated) chains phase-segregate. With increasing temperature the mixing term leads to a single-phase region. At still higher temperatures the specific association

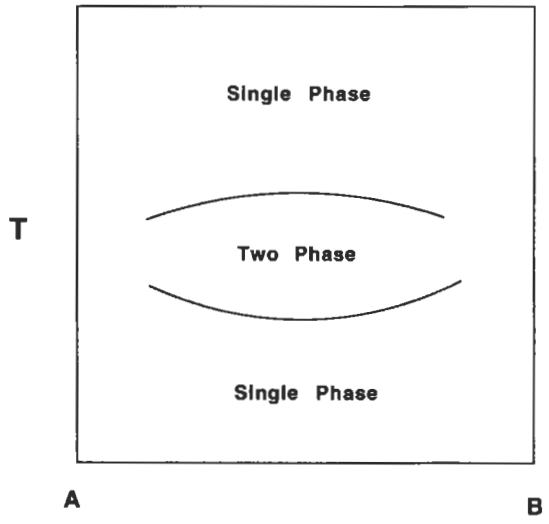

Fig. 15. A sketch of a polymer–polymer phase diagram which shows both a LCST and HCST. Note the comparatively narrow temperature range of this effect, and the discrete two-phase field.

between the chains and the coating layer of solvent molecules is lost, the chains are now, in effect, more dissimilar from the solvent and they choose to aggregate, leading again to phase separation.

(v) The phase diagram of a lyotropic system. A *lyotropic system* is a polymer-solvent combination which shows a liquid crystalline phase in particular composition and temperature ranges. Figure 17 shows an equilibrium diagram of such a system, as predicted by Flory in 1955 which was long before any experimental observations were reported. The narrow two-phase near-vertical region towards the left of the diagram is known as the 'Flory chimney', and separates the isotropic from the liquid crystalline phases. To the right of this chimney is a monotectic which is intrinsically the same as that seen, for example, in the copper–lead system. The diagram, as drawn, assumes a non-crystallisable polymer. In systems such as sulphuric acid–poly paraphenylene terephthalate (which is used to make Kevlar fiber) there are extra features as sketched in fig. 18. Firstly, the polymer is crystalline so there is a high melting point crystal phase to the right of the diagram. There is also a *crystallosolvate* phase which is a crystal containing both polymer and solvent molecules in the lattice. It appears on the diagram much as an intermetallic compound would in a metallic system, and the monotectic of fig. 17 is replaced by a peritectic and a eutectic.

References: p. 2740.

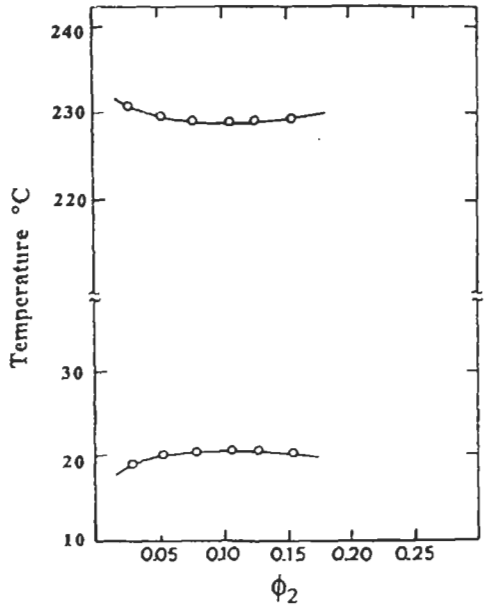

Fig. 16. Phase diagram for polystyrene of molecular weight 37,000 in cyclohexane. Note that the concentration range of the diagram is from 0–25% polymer, and also how the single-phase region is now between the curves (Boyd and Phillips).

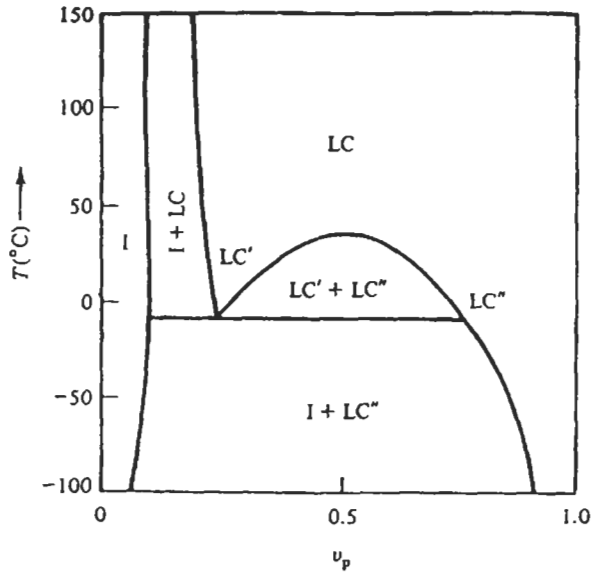

Fig. 17. Representative phase diagram for a rigid-chain polymer and a solvent which shows a lyotropic liquid crystalline phase.

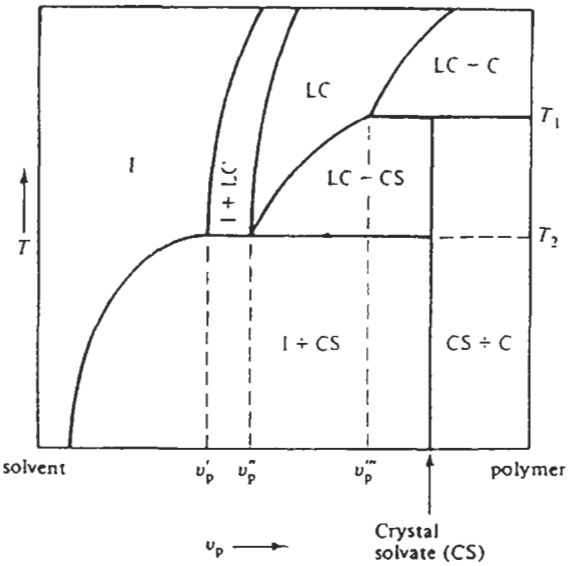

Fig. 18. Representative phase diagram of a lyotropic polymer-solvent system showing both the crystalline (pure polymer) and crystallosolvate phases.

4.5. Copolymers

Polymers may interact with each other in less comprehensive ways than metal atoms, yet they have a trick up their sleeve which opens up unique additional potential. It is possible to polymerise multicomponent chain molecules. Examples of these are illustrated in fig. 19.

(i) Block copolymers. In a block copolymer, there are runs of one monomeric species followed by runs of second, and so on along the chain. At its simplest level, such a structure enables a chain to show something of the properties of each type of unit. One, for example, may be rubbery, the other glassy, but because each chain is nominally the same there is no driving force for macro segregation into separate phases. On the other hand micro segregation of the different sequences does occur, and fascinating microstructures can be generated on the 100 Å scale. One of the most striking examples comes from tri-block chains which are essentially rubber (poly(butadiene)) with lengths of glassy polymer (poly(styrene)) attached to each end. The polymer is referred to as an SBS block copolymer (for styrene–butadiene–styrene). In the melt phase, the poly(styrene) ends segregate to be next to each other as do the poly(butadiene) segments. If the melt is extruded, then the poly(styrene) chains organise themselves into minute rods, which are attached via covalent bonds to the surrounding poly(butadiene) matrix. At room temperature the poly(styrene) rods are glassy, and one has, in effect, a micro fiber composite. A cross-section of this microstructure is shown in fig. 20. Changing the relative sequence lengths of the different components in the chain can have a radical

a *random copolymer*

- AABBABABBBAAAABABABAAAAAABBBBABABAABAABBB -

a *block copolymer*

- AAAAAAAAABBBBBBBAAAAAAAAABBBBBAAAAAAAAAAAA -

a *triblock copolymer*

AAAAAAAAAAAAABBBBBBBBBBBBBBBBAAAAAAAAAAAAA

a *graft copolymer*

- AAAAAAAAAAAAAAAAAAAAAAAAAAAAAAAAAAAAAAAAA-
B B B
B B B
B B B
B B B
B B B
B B B

Fig. 19. Examples of copolymers.

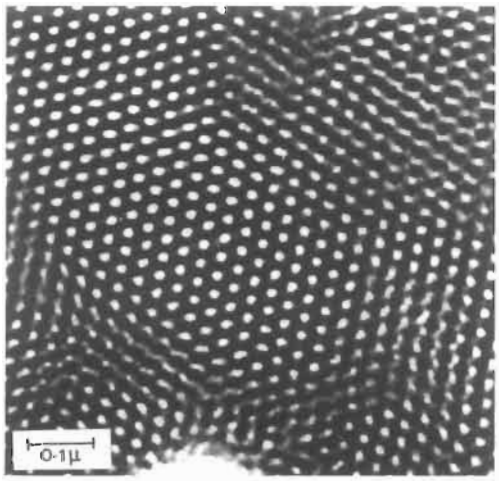

Fig. 20. A thin section cut through an aligned SBS polymer showing the poly(styrene) rods set in a poly(butadiene) matrix which has been stained by osmium tetroxide to appear black. The stain attaches itself to the double bonds of the poly(butadiene) sequences and renders the rubber electron-opaque. (Courtesy Prof. M.J. Folkes.)

influence on the microstructures, with one microphase distributed as plates, or as spheres. In the case of poly(styrene) and poly(butadiene) neither will crystallise (at least at room temperature), but where one or more of the block types can crystallise, then the micro segregated structures present in the melt control the morphology of the subsequent crystallisation.

Another application of block copolymers is as *surfactants*. A molecule which has a chain of one type of units at one end joined to a chain of different type at the other, can form an excellent compatibility bridge between two immiscible phases. For example, poly(butadiene) and poly(styrene) are completely immiscible in each other, yet either an BS block copolymer molecule or a graft polymer where a poly(butadiene) backbone has poly(styrene) side chains grafted on to it, will tend to lie in the interface with one end in each phase. The result is that the interface energy is lowered and the surfactant behaviour means that the size distribution of the phase regions can be refined. In this role the surfactants are referred to as *compatabilisers*. Furthermore, the mechanical properties of the interface are enhanced, and the approach is used widely in the production of rubber-toughened polymer glasses. (See also ch. 9, § 5.3).

(ii) Random copolymers Random copolymers provide an example of how it is possible to 'cheat' the thermodynamics of mixing. Two different types of monomer units, which would be wholly incompatible if each were polymerised as their respective chain molecules, will, if polymerised together in random order in each chain, form a polymer system in which miscibility is assured as the chains are indistinguishable. Such a system enables some degree of independent control of both the glass transition temperature and the melting point as shown in fig. 21. The glass transition temperature is controllable pro rata as a function of composition. On the other hand, the crystal melting points of each homopolymer component are much reduced by random copolymerization, and at intermediate compositions the crystallinity is often destroyed altogether. One might

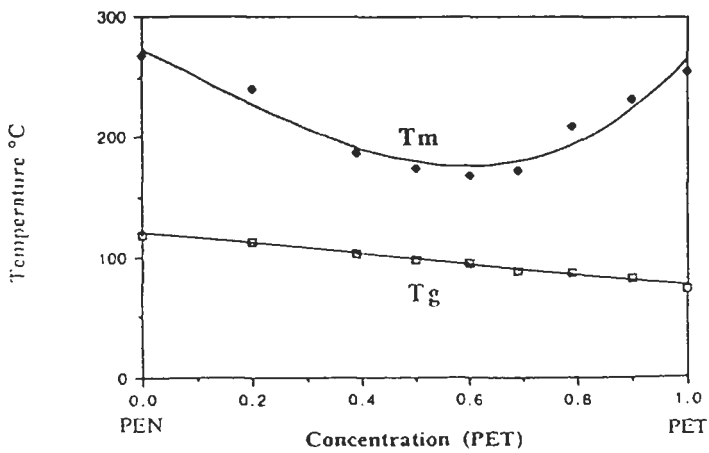

Fig. 21. Plot of the glass transition temperature and the crystal melting point as a function of the composition of random copolymers based on poly(ethylene terephthalate) (PET) and poly(ethylene naphthoate) (PEN).

References: p. 2740.

expect this, as it is difficult to see how chains which do not have chemical periodicity along their length can contribute to a crystal which is defined in terms of periodicity in three dimensions! There are however surprises. The random copolymer of hydroxy benzoic and hydroxy naphthoic acids shows some crystallinity over its full composition range, with a crystallinity of 20% for the 50:50 composition. The reason this can occur is because of the segregation of identical yet random sequences alongside each other where they are able to form, in effect, thin mixed crystals. Such are known as a *non-periodic layer crystals*, and their structure is illustrated in fig. 22 They are very thin as the concentration of longer predefined sequences will be very low. This matching of particular molecular sequences to form order is very reminiscent of biology in which structure at larger size scales is molecularly encoded. Controlled-sequence synthetic co-polymers, which are neither random nor block, remain a challenge to the polymer scientist. There is much to be gained by learning from biology, even though one is taken still further from the home ground of metallic alloy systems.

5. *Plastic deformation and yielding*

5.1. Metals and polymers

In metals, plastic flow is the dominant process of crystal deformation. It is well understood in terms of dislocation mechanisms and is close to the heartland of metallurgy. The transition from elastic behaviour to plastic at the yield is of quite exceptional significance as it is, at the same time, the effective upper stress limit for structural performance, and the lower limit for mechanical processing. Polymers are different

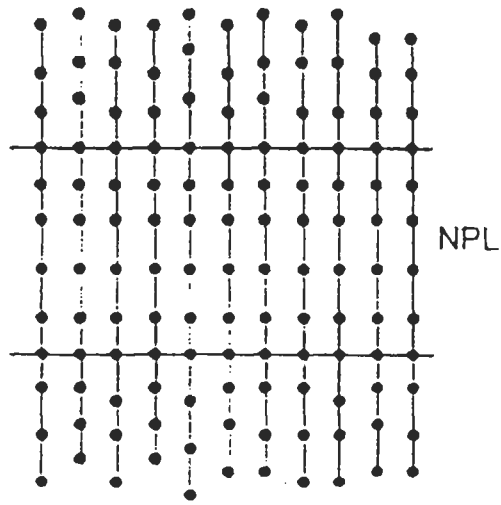

Fig. 22. Idealised sketch of a Non-Periodic Layer (NPL) crystal showing how the segregation of short sequences on adjacent chains can lead to limited crystallinity in random copolymers.

enough to be interesting, although in most respects the same principles apply. In polymers there is a yield stress, followed by an extensive region of plastic flow, and one may comfortably think in terms of pre-yield plasticity, yield drops, work-hardening rate, hysteresis and so on. However, there are two key distinctions. The first is qualitative, in that the strains observed, both elastic and plastic, are usually much higher than in metals. One might have a yield strain as high as 40% and a strain to failure of perhaps 600%, and the difference between true stress and nominal stress is correspondingly more significant. The other distinction, not totally unconnected from the first, is that for polymers at very high strains, the work-hardening rate actually begins to increase again. Figure 23a compares the true stress–strain curves for nickel and nylon 6, and fig. 23b the nominal stress–strain curves. Note how the nickel curve is interrupted by fracture at what for a polymer is a comparatively low strain.

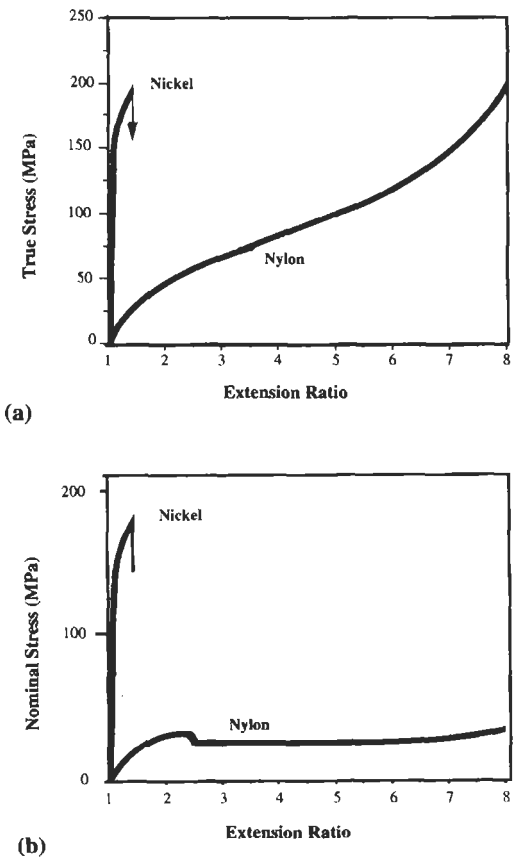

Fig. 23. (a) True stress–strain curves for annealed nickel and for nylon 6. (b) Nominal stress–strain curves for the same data. Most polymer plots use the extension ratio or 'draw ratio', λ, instead of engineering strain ε. Note that while ε is $(l - l_0/l_0)$, λ is (l/l_0).

References: p. 2740.

5.2. True stress–strain relations

Compare nickel and nylon 6 in fig. 1a. The elastic modulus of the polymer is approximately 2 orders of magnitude less than that of the metal, 2 GPa for the Nylon compared with 200 GPa for nickel. Firstly, a polymer is never 100% crystalline and the crystals are set in an 'amorphous' matrix which, if it is a glass — which is the case for nylon 6 at room temperature — will have a stiffness of around 1 GPa. Secondly, the polymer crystals themselves are none too stiff. While values of tensile modulus along the chain directions may rival, or even exceed, those of metals, the bonding between the chains is comparatively weak, the tensile and shear moduli which involve interchain deformation being both in the 1 GPa range. Of course, if the amorphous material is above its glass transition temperature it will be rubbery, with much lower moduli of between 10 and 100 MPa, and in this case the pre-yield deformation will seem quite excessive in relation to metals. In each case the yield stresses are associated with the onset of plastic deformation of the crystals, although it is rather difficult to identify where exactly this happens in the polymer, bearing in mind that the process involves the yielding of both glassy and crystalline phases, and is exceedingly complex. It is interesting that on moving to the nominal stress relation, the definition of the yield stress becomes rather easier.

The increase in slope of the polymer curve at very high strains is a unique property. In most general terms it can be identified with the completion of the chain-unravelling process, and the assertion of the axial stiffness of straightened chains. In effect, one begins to 'feel' the covalent carbon–carbon bonds of the chain backbones. Of course, it could be argued that the real difference is that the metal curve is interrupted by 'premature' fracture, albeit ductile fracture. The understanding of this failure, which is initiated by the onset of plastic instability, is a familiar aspect of physical metallurgy, and the application of *Considère's criterion* is a standard topic at undergraduate level. However, this relation is of central importance to the tensile behaviour of polymers too. It is perhaps useful first to rehearse this criterion using strain parameters which are particularly convenient to the polymer case.

5.3. Considère's criterion

The unit of strain used will be the extension ratio, λ, which is known to the polymer community as the *draw ratio*. It is defined as:

$$\lambda = l/l_0, \text{ the ratio of new to original lengths.} \tag{8}$$

Furthermore, the ratio of the true stress σ_T to the nominal stress σ_n is:

$$\begin{aligned} \sigma_T/\sigma_n &= A_0/A \quad \text{(ratio of cross-sectional areas)} \\ &= l/l_0 \quad \text{(for constant volume)} \\ &= \lambda \end{aligned} \tag{9}$$

Plastic instability occurs when the increase in flow stress due to work-hardening over a small strain increment is no longer able to compensate for the increase in true stress due to the reduction in cross-sectional area caused by that strain increment. In other words, plastic instability occurs at the strain when the slope of the nominal stress–strain curve has decreased to zero, i.e., when:

$$\left(d\sigma_n/d\lambda\right) = 0. \tag{10}$$

Putting in terms of true stress, then

$$\left(d\sigma_T/\lambda\right)/d\lambda = 0 = \left(\left(d\sigma_T/d\lambda\right)/\lambda - \sigma_T/\lambda^2\right). \tag{11}$$

Hence,

$$d\sigma_T/d\lambda = \sigma_T/\lambda, \tag{12}$$

which is *Considère's relation.*

On the true stress–strain relation, plastic instability commences when the slope of the curve $=\sigma_T/\lambda$. The relation is represented as a well-known construction in fig. 24. Note also that any line drawn from the point at $\lambda = 0$ is a line of constant nominal stress.

If the work-hardening rate immediately on yield is less than the yield stress (assuming small elastic strain), then plastic instability will occur immediately and the material will not deform plastically in the macroscopic tensile sense. Such behaviour is seen in extensively drawn wires where the tensile extension generated in the die exceeds the plastic strain for instability which would be seen in an annealed sample.

5.4. Yield drops and Lüders bands

Metallic alloys which show yield drops take us one stage nearer to polymeric behaviour. The fact that dislocations are locked up by alloying elements means that yielding occurs only when new ones are liberated from a source. The sudden increase in number of dislocations at the yield stress causes a yield drop as the mean velocity of the dislocations necessary to satisfy the applied strain rate decreases. Further multiplication with increased strain, and further reduction in required velocity, initially compensate for

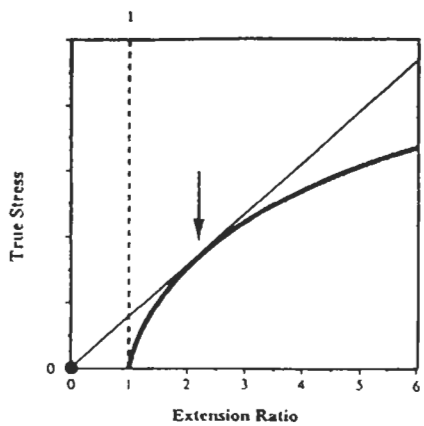

Fig. 24. The graphical representation of Considère's criterion. When the slope at a point on a true stress–true strain curve drops below that of a tangent drawn to the curve from $\sigma_T = 0$, $\lambda = 0$, necking or plastic instability occurs.

References: p. 2740.

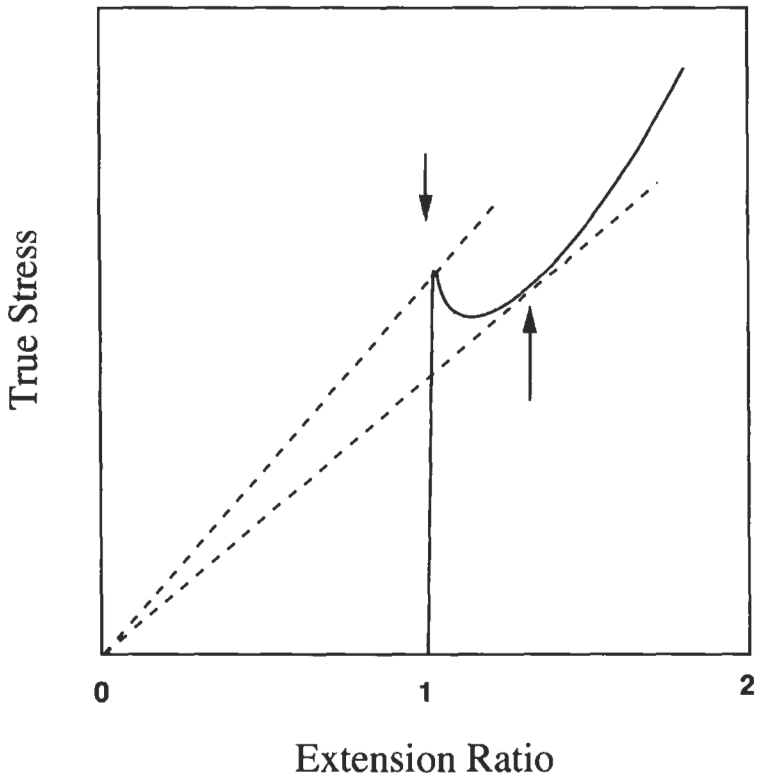

Fig. 25. Double tangents drawn to a true stress–strain curve showing a yield drop. The two tangent slopes define the upper and lower yields stress (nominal stresses) respectively, and the difference in strain between the two tangent points is the strain associated with the propagation of the Lüders band.

the work-hardening due to the developing dislocation interactions, and thus the apparent work hardening only builds up slowly to give a true stress–strain curve such as that of fig. 25. Considère's criterion would suggest plastic instability at the yield point. But it is possible to draw a second tangent to the underside of the curve. Hence plastic instability develops at one point on the gauge length, is stabilised when the strain in that one region reaches the second tangent point and then a plastic strain increment propagates down the specimen as a *Lüders band,* the propagation being at constant nominal stress which is given by the slope of the second tangent. The same effect occurs in the extension of thermoplastics when it is known as *drawing*, but it is very much more strident.

5.5. Drawing of polymers

As the work-hardening rate for a polymer such as nylon 6 increases again at high strains it is possible to construct two Considère tangents to the true stress–strain relationship in fig. 23a. However, the strain at the first tangent point would be at about 100% strain while that of the second several hundred percent. The strain differential between the drawn and undrawn parts of the specimen is thus very much greater than in the case of the Lüders band of a metal. (The term 'Lüders band' is not generally applied in the drawing of polymers although the principles are exactly parallel). The ratio of the two strains is called the *natural draw ratio*. The neck propagates along the length of the sample at a constant nominal stress as to give the long horizontal region of the curve in fig. 23b. A partially drawn specimen is shown in fig. 26. Commercial fibers are first *spun*, which means they are extruded through a spinneret of minute holes, and then drawn down to give a finer fiber with improved axial stiffness and yield strength. The drawing is achieved by passing the thread over two rollers in sequence, the second set rotating more rapidly than the first. Drawing can be experienced by stretching a strip of polymer film cut from a plastic bag, or better, from the rather thicker poly(ethylene) sheet used to hold 'six packs' together.

There are true stress–strain curves to which it is impossible to draw a Considère tangent. In the polymer realm, rubber is an example. There is of course no yield point and the slope of the stress strain curve increases continually with strain as shown in fig. 27. Rubber can thus be strained to high deformations without any non-uniformity or drawing occurring.

Fig. 26. A polymer sample which has been partially drawn.

References: p. 2740.

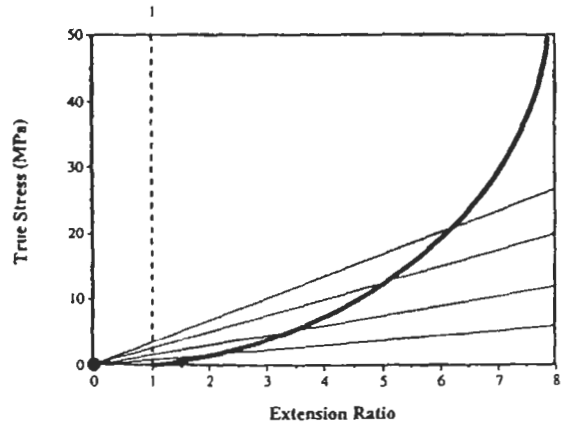

Fig. 27. A true stress–strain curve of natural rubber. There is no tangent point for the Considère construction which is the reason why rubber does not neck or draw.

5.6. Structural control of the natural draw ratio

Some non-crystalline, glassy polymers such as poly(styrene) are quite brittle and cannot be drawn plastically. On the other hand, poly(carbonate) can be drawn extensively. While one might be impressed by such plasticity in a glass, it should be noted that the natural draw ratio is significantly less than in nylon 6 and in semi-crystalline polymers in general. Why should this be? Imagine a tangled mass of wool. If it is held firmly with two hands and stretched, the extension will not be very high, even though individual strands may be pulled taut. If however the wool is carefully folded to start with, it is possible for it to become extensively 'undone' on stretching. If one is to equate chain-folded polymer crystallites with some measure of disentanglement, then the reason for the higher drawability of chain folded crystals, compared with the non-crystalline phase, can be grasped. One can throw a rope from a boat further, if it is neatly coiled or folded on deck, than if it were left in a tangle. The fact that drawing leads to an improvement of fiber properties, and the greater the natural draw ratio the greater the improvement, has encouraged polymer scientists to try to manipulate the microstructure to gain even greater extensions. One successful route, *super drawing*, is described in section 6.4(c) below.

5.7. Yield criteria

The yielding response of materials to three-dimensional stress states is described by the well known yield criteria, the *Tresca criterion*, where yielding is taken to occur at a critical value of the largest principal stress difference, and the *von Mises criterion* which suggests that yielding occurs when a critical value is reached in a parameter which is a form of geometric mean of the three principal stress differences. These criteria can be represented in three-dimensional stress space as yield surfaces, for Tresca it is a hexagonal prism with its axis along the $\sigma_1 = \sigma_2 = \sigma_3$ axis, for von Mises a cylinder also

aligned along this axis. These criteria are appropriate for unoriented polymers too, but with one significant difference. The ease with which polymers yield depends on the hydrostatic stress state also. Hydrostatic pressure increases the principal stress differences needed to achieve yielding, while hydrostatic tension has the opposite effect. In very simple terms, the reason for this dependence on pressure is that the deformation of a polymer glass, or the glassy phase of semi-crystalline polymer, involves what is called *free volume*. Any reduction in this internal space as a result of hydrostatic pressure drastically increases the yield stress of the polymer at the applied strain rate and vice versa for hydrostatic tension. Figure 28 shows that the yield surface, using the von Mises criterion, is now a cone rather than a cylinder. The diagram begs the question as to what happens at the apex of the cone. The stress differences for yield are here zero, which

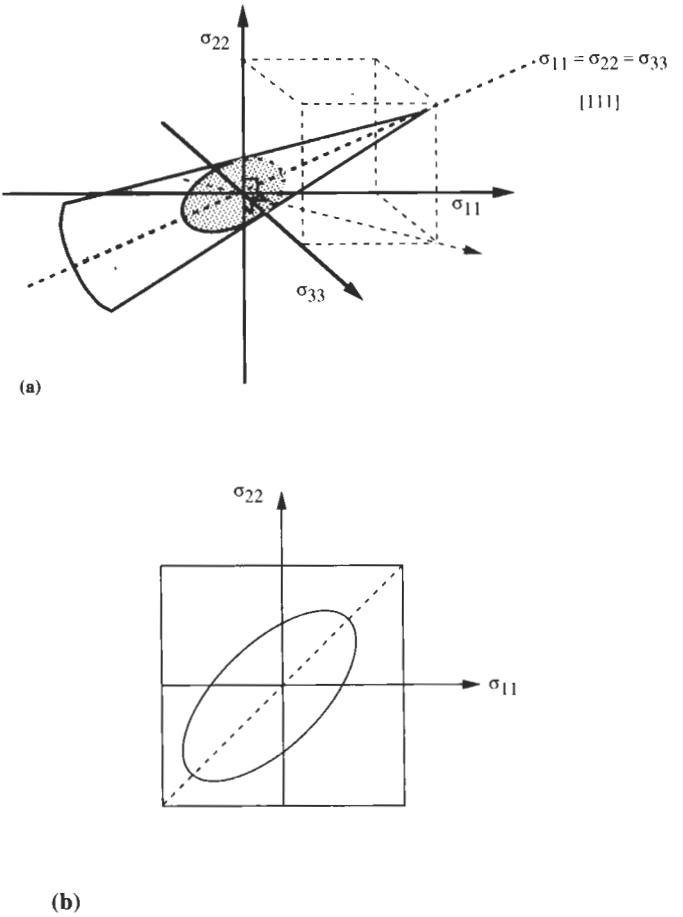

Fig. 28. The σ_1, σ_2 section through a polymer yield surface. The fact that the surface is a cone in stress space means that the ellipsoidal section is not centred on the origin, but displaced towards the compressive side of the diagram.

implies a zero yield stress. One can understand the effect by noting that the glass transition of a polymer is also dependent on the hydrostatic component of stress, decreasing with increasing hydrostatic tension. Hence the apex seems to suggest a stress state which reduces the glass transition to the testing temperature and thus changes the glass into a rubber. Of course such an explanation is compromised for semi-crystalline systems where the presence of crystals would still ensure some sort of yielding behaviour, albeit at higher strains.

6. *High-performance polymer fibers*

6.1. Diamond — the ultimate polymer?

A metallurgist steeped in face-centered cubic packing and its tetrahedral interstices is readily at home with diamond. The structure can be viewed as fcc with additional carbons in one half of the tetrahedral interstices, or as having an fcc lattice with a motif of carbon atoms at $\pm(1/8, 1/8, 1/8)$.

On the other hand, from the perspective of a polymer scientist, diamond can be viewed rather differently. It is certainly the ultimate cross-linked polymer, one might even argue that it is organic. But the crystal structure appears as a series of planar zig-zag chains, exactly the same as the backbone of poly(ethylene) in crystalline form, lying along [110]. But instead of there being two hydrogens attached to each carbon, the spare 'non-backbone' bonds form the covalent links to neighbouring chains. In fig. 29a such a series of chains is highlighted within the diamond structure; of course one could have identified a set of such 'chains' along any of the $\langle 110 \rangle$ directions, in which case backbone and cross-linking bonds would have been differently identified. Figure 29b is an endwise projection of the selected set of chains onto the $[1\bar{1}0]$ plane normal to them. Imagine that the cross-linking bonds are cut (fig. 29c) and the severed ends capped with hydrogen (fig. 29d). The chains had to be moved further apart because of the bulk of the new atoms, and packing is enhanced if the chains of the group rotate about their chain axes, fig. 29e. The structure is now crystalline poly(ethylene).

6.2. Theoretical axial modulus of polymer crystals

Given the similarity between polymer crystals and diamond, it is not surprising that the tensile modulus in the chain direction should be impressive. In the case of poly(ethylene) it is possible to calculate an ideal axial modulus from a knowledge of the energies required to distort bond lengths and bond angles in the backbone as well as the packing density in the crystal. This value comes out to be 350 GPa, which is more than 50% higher than the stiffness of steel (210 GPa), and higher by an even greater factor if one divides the stiffnesses by the specific gravity, which is close to unity for poly(ethylene), to give the *specific stiffness*. The use of so-called 'specific' properties tends, of course, to put polymer properties in a good light when compared with metals. It is particularly relevant when considering materials in applications where weight is a penalty, such as transport and especially aerospace. On the other hand, it should be emphasised that these

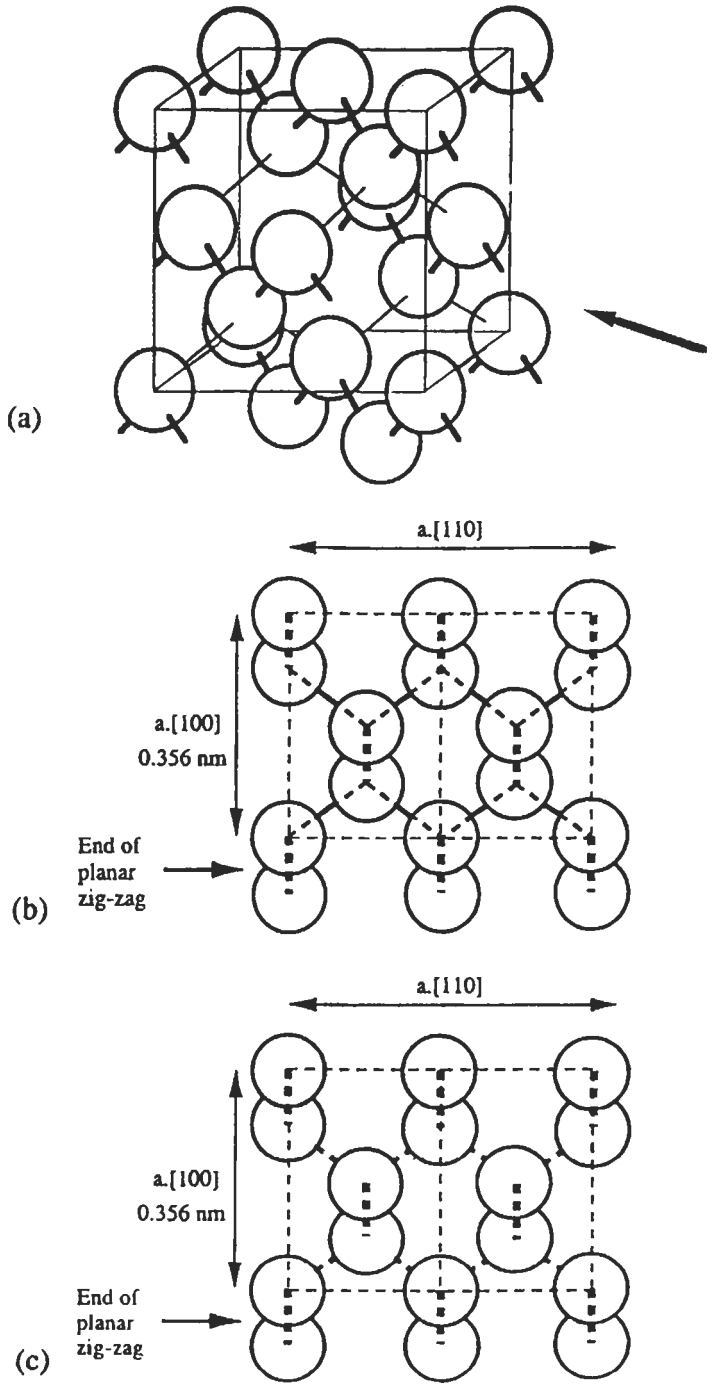

References: p. 2740.

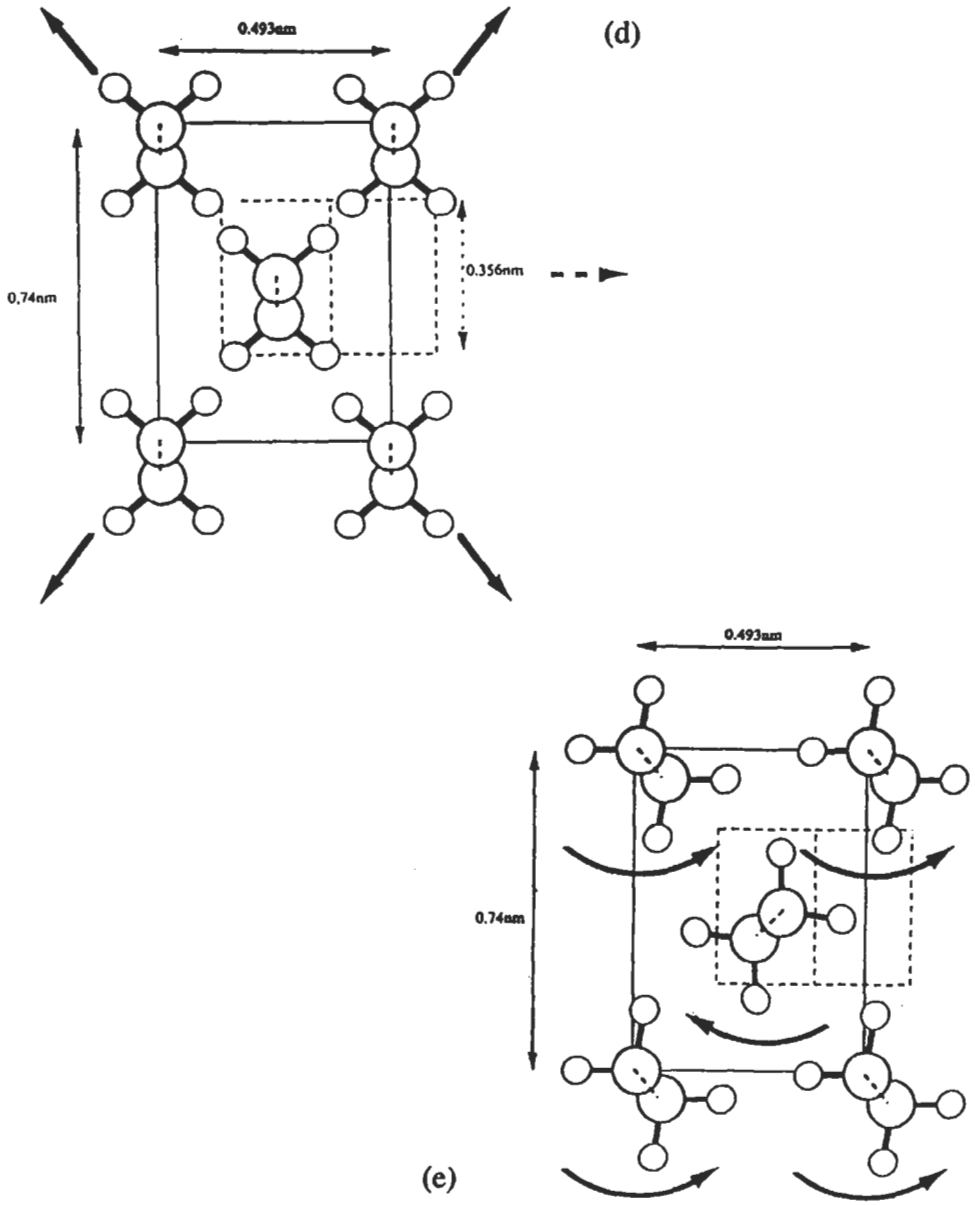

Fig. 29. The relationship between the unit cellls of diamond and polyethylene (see text).

polymer fiber moduli are only tensile, and only apply to loading along the fiber axis! Polymers which crystallise with the molecule in a conformation which is not the one which will give the maximum chain length, for example a helix, will show rather lower

theoretical moduli. For example, the theoretical axial modulus of crystalline poly(propylene), in which the chain has a helical conformation, is only 46 GPa.

The fact that the axial stiffness of poly(ethylene) is only about 25% that of diamond (1200 GPa) can be accounted for by the fact that the chains are significantly further apart in poly(ethylene) to provide space to accommodate the hydrogens. The expansion shown in fig. 29d was of the order of times 4 in area terms, which almost completely accounts for the lower modulus of poly(ethylene) compared with diamond. In fact, the ultimate stiffness achievable in a polymer crystal where the chain is not coiled or corrugated, is primarily related to the number of backbone bonds per unit area. The greater the bulk of the substituted atoms on a molecule, the fewer chains that can be packed within a unit cross-sectional area and the lower the axial mechanical properties. Figure 30 shows a plot of the calculated axial moduli against the density of packing of the chains. The poly(diacetylenes) have very high-modulus backbones, yet the bulky side groups effectively 'dilute' these to give rather ordinary moduli.

6.3. Axial properties of conventionally drawn fibers

Polymer fibers, spun conventionally from the melt and then drawn, show almost perfect axial orientation of the crystallites (see fig. 8). However, the axial moduli of a range of such fibers are typically between 1/20 and 1/50th of that calculated for the crystals alone. The reason is that the microstructure of a conventional fiber consists of

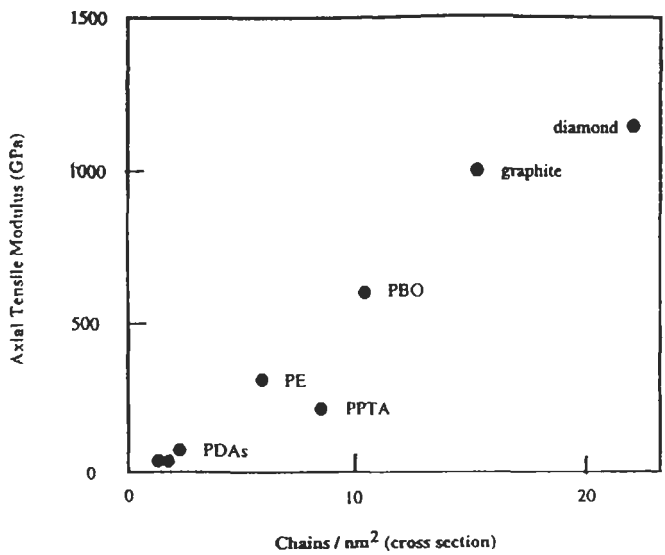

Fig. 30. Plot of the calculated axial modulus against the effective chain density (density in which only the atoms comprising the chain backbones are counted for mass) of a range of materials. PBO is poly(benzobisoxazole), a highly aromatic rigid chain polymer, PPTA is Kevlar, and the PDA's are polydiacetylenes which have rigid aliphatic backbones but large side groups which effectively dilute the number of load-bearing chains per unit area.

References: p. 2740.

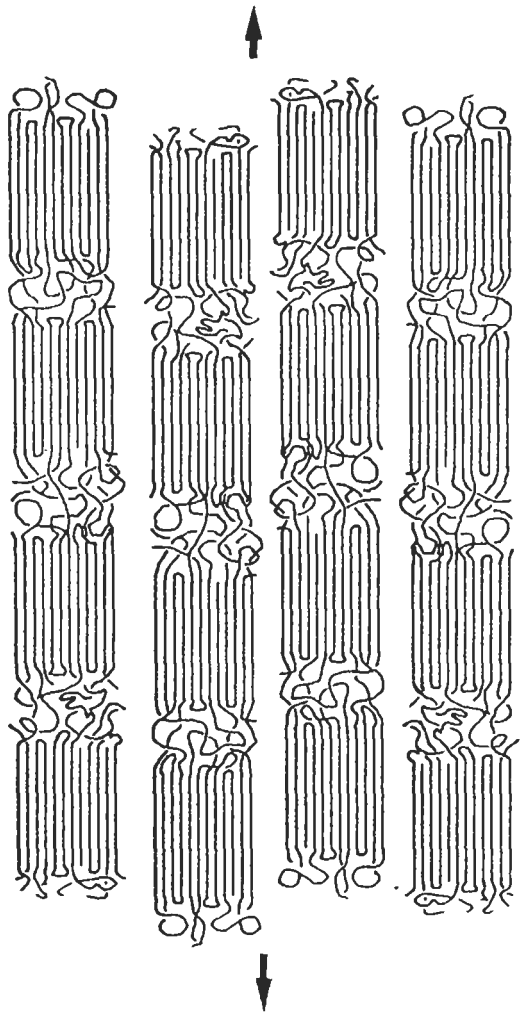

Fig. 31. Schematic diagram of the microstructure of a drawn polymer fiber. The modulus of the crystal along the direction of the fiber axis will be between 50 and 300 GPa while that of the interspersed 'amorphous' regions will be only in the range of 0.1–5 GPa.

the oriented crystals interspersed with non-crystalline regions involving entanglements and folds, as sketched in fig. 31. In polymers such as poly(ethylene) where the glass transition temperature is below room temperature, the amorphous regions are rubbery with modulus in the region of 0.1–0.05 GPa. As the strains are additive, the axial modulus of the fiber, E_f, is given by:

$$E_f = 1/\{(\chi/E_c) + (1-\chi)/(E_a)\} \tag{13}$$

where E_c is the axial modulus of the crystals, E_a the axial modulus of the amorphous region, and χ the crystallinity.

The large differences in the moduli of the components means that the stiffness of the fiber is approximately, $E_a/(1-\chi)$. Hence, even for high crystallinities, ($\chi > 0.8$), the stiffness of conventionally drawn poly(ethylene) fibers is unlikely to exceed 1 GPa, despite an axial crystal stiffness of 250 GPa. Fibers such as PET in which the amorphous phase is below its glass transition at ambient, i.e., a glass, will show higher moduli of a few GPa.

The challenge is to make fibers having microstructures which do not contain amorphous regions between the crystals.

6.4. Making high-performance fibers

To achieve an elastic modulus approaching that of a the polymer crystal in the direction of the chain axis, it is necessary to remove the amorphous component and by implication the entanglements and folds which stabilise it. Once such a 'supercrystal' has been created, its ultimate strength will depend largely on the concentration of chain ends within it. Each chain end leads to a stress concentration which detract from the ultimate strength of the crystal along the chain axis which is related directly to the strength of the carbon–carbon backbone bonds in the chains. Hence, high strength will require high molecular weight.

(i) The liquid–crystalline route. Suitably stiff chain molecules are able to form a liquid-crystalline phase in which they will be pre-aligned, at least with respect to their immediate environment. In this state the number of entanglements is much reduced; uncooked spaghetti in their jar, an example of a liquid–crystalline phase, will have few if any entanglements, with their inherent stiffness ruling out the possibility of hairpin folds. When cooked and soft, however, the spaghetti will entangle and fold. The drawing of a polymer fiber directly from the liquid crystalline phase will thus reduce the possibility of entanglements and folds and thus eliminate the primary cause the amorphous component. When fibers are spun from a *lyotropic* phase the solvent has to be removed to enable the fiber to crystallise. In the case of polyaramid fibers such as *Kevlar*, the solvent which is neat sulphuric acid is washed out by passing the fiber through a water bath. There are various grades of *Kevlar* with stiffness ranging from 60 GPa up to 185 GPa, while the strengths are in the 2–3.5 GPa range (see table 2). Fibers, such as *Vectran*, which are spun from thermotropic liquid-crystalline melts, show somewhat inferior stiffnesses to Kevlar, possibly as the crystallinity is low on account of the random copolymer chains used to bring the crystal melting point within bounds (table 2). Nevertheless, the non-crystalline component, which is, in essence, a liquid-crystalline glass with excellent chain alignment and a density not much less than that of the crystal, has axial mechanical properties to match.

(ii) The gel-drawing route. *Gel-drawing* is an approach entirely different from the removal of the non-crystalline phase through the reduction of the entanglement density. It is applied to conventional (non liquid-crystalline) thermoplastics, typically poly(ethylene). The method involves the creation of a very dilute gel in which the especially high

Table 2
Properties of fibers

Material	Elastic modulus E (GPa)	E/SG	Tensile strength σ (GPa)	σ/SG	Compressive strength (GPa)
Steel	210	25	4.2	0.5	
Glass	65	25	4.5	1.8	
Nylon	6	5	1.0	0.9	
PE (Ultra)	170	170	3.0	3.0	
Vectran	80	55	3.2	2.3	0.20
Kevlar (149)	185	123	2.0	1.3	0.48
PBO	365	230	5.8	3.6	0.40
Carbon (HT)	230	130	3.2	1.8	2.80
Carbon (HM)	720	320	2.2	1.05	0.48
Diamond	1100	380			

SG = specific gravity

molecular weight of the poly(ethylene) ensures that there are still the required stable entanglements despite polymer concentrations of only a few percent. The low density of the entanglement points ensures that there are large number of chain links in each of the molecular segments joining them. If the gel is now stretched, not only will it extend by a very high ratio, possibly as high as 50 times, but the entanglement density will remain low, and this state will be maintained as the solvent is dried off. One of the first such fibers to be marketed commercially was *Spectra*, from Allied Signal. Its properties appear in table 2 too under "PE (Ultra)". Note its especially high strength, a consequence, in part, of the very high molecular weight, and the fact that its axial modulus is of the order of the theoretically determined value of 300 GPa. The specific properties of this fiber are especially good as the density of poly(ethylene) crystals is low, in fact almost the same as that of water.

(iii) Super-drawing. It is possible to enhance the natural draw ratio (see section 5.6) and thus improve the stiffness of the drawn fiber by manipulating the microstructure prior to drawing. The polymer is heat-treated to grow well formed crystals within the 'amorphous' surrounds. The chains in the well-formed crystals are thus able to unravel well with the results that natural draw ratios in poly(ethylene) in excess of 50 have been achieved. This *super-drawing* can give axial stiffnesses in excess of 100 GPa. The drawback however is that it is necessary to keep the molecular weight comparatively low, at least by the standards of gel drawing, in order to achieve the desired high draw ratio. The consequence is that the strength is not significantly enhanced.

6.5. The Achilles' heel and the diamond challenge

A significant limitation of high-modulus polymer fibers for composite applications is that their compressive strength (see table 2) is rarely more than 10% of the tensile value! This is the telephone directory effect: it is impossible to stretch a directory along an axis parallel to the page, yet it will buckle under even modest compressive force. This

behaviour is the result of the low resistance to shear between the pages. If they were to be individually glued together, then we would have a block rather like wood, good in compression as well as tension. By analogy, the answer is to cross-link the poly(ethylene) molecules together, which of course takes us back to diamond as the ultimate example. There is thus a very clear challenge to the materials scientist: he must learn to make diamond fibers for a sensible cost. We would then have the ultimate material for fiber-composite work, and probably much else besides.

7. *Crazing*

7.1. Introduction to a craze

The science of fracture mechanics embraces polymers quite naturally. Griffith's criterion is perfectly appropriate, giving the condition for when stored elastic energy in the stressed material is sufficient to feed the plastic and surface energies necessary for crack growth. The non-brittle propagation of cracks, where work done by the applied load in extending the sample is able to supply very considerable energy to the region of the crack, and thus enable really rather ductile propagation mechanisms to occur, is also common to both metals and polymers.

In metals these more ductile mechanisms might be described as ductile tearing, or involve the sequential nucleation of voids ahead of the crack which then grow by plastic flow to coalesce into the advancing crack.

In polymers, especially glassy polymers, a particular mechanism of void formation operates which is known as *crazing*. It is often associated with an advancing crack and is quite unique in its structural characteristics. The voiding is on a nano scale, and thus quite invisible in the light microscope. However, the crazed region itself is visible as the distribution of invisible voids reduces the effective density and refractive index of the polymer, while the high degree of localised extension will mean that the polymer within the craze will also be highly birefringent. Figure 32a shows crazes in a poly(styrene) specimen viewed in oblique light and made visible by the reflection of light at the refractive index discontinuity. The craze ahead of a crack seen in the light microscope in fig. 32b is visible owing to the localised surface rumpling associated with the deformation in the craze. Note that the craze has the geometry of a crack; it is coplanar with the crack and is capable of propagating in a crack-like manner, but also that as in fig. 32a it does not necessarily have to be associated with a crack. However, the craze is not a crack, the microvoided material is capable of bearing a tensile load, and its development is a potent, albeit localised, energy absorption mechanism which makes an effective contribution to resisting the propagation of a crack which follows it. A craze is thus both an incipient fracture and a toughening mechanism.

7.2. Craze criteria

Series of experiments in which polymers have been exposed to multiaxial stress states demonstrate that, as with plastic yielding, crazes require a shape-changing (deviatoric)

References: p. 2740.

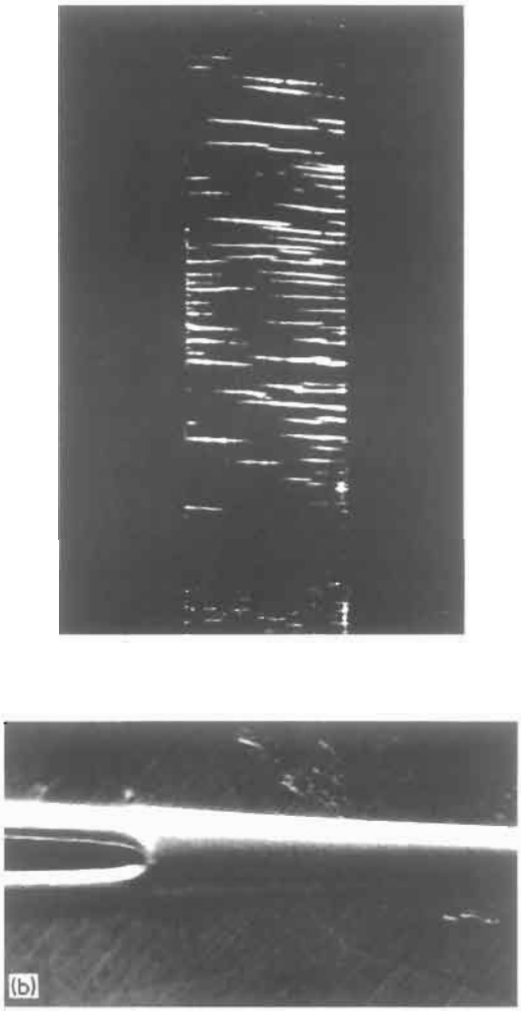

Fig. 32. (a) Crazes seen in a specimen of polystyrene, by the internal reflection of light at the refractive index discontinuity. (b) Craze made visible through associated surface distortion [Kinloch and Young].

stress component, but in addition, the overall hydrostatic component must be tensile. Crazing, which involves microvoid formation and a volume increase, will not occur during any compressive deformation process. On the other hand, simple axial tension is close to the most potent stress state for craze formation. In fact there appears to be a critical tensile strain for craze initiation, which is reduced as the hydrostatic tensile stress increases. An expression for the critical tensile strain, ε_{11}, based on the work of Bowden and Oxborough in 1973, is:

$$\varepsilon_{11} = (1/E)\left[C(t,T) + D(t,T)/(\sigma_{11} + \sigma_{22} + \sigma_{33})\right] \tag{14}$$

E is Young's modulus, C and D constants dependent on time and temperature, and the sum of the three principal stresses gives the hydrostatic stress component.

The same principle can be expressed in stress space. Figure 33 is a σ_{11}, σ_{22} section showing the trace of the von Mises yield envelope for the onnset of plastic flow, in this case off set from the origin relecting the fact that plastic flow in a polymer is rendered more difficult as the hydrostatic component shifts from tensile to compressive. Also on the plot, is a section through the craze criterion envelope. In three dimensions it has the form of coolie hat, lying parallel to the deviatoric plane (where hydrostatic stress is zero) but cusped to a spike parallel to the $\sigma_{11}=\sigma_{22}=\sigma_{33}$ axis. Note that where the hydrostatic tension is reducing towards zero, the craze surface passes through the yield surface, indicating that shear yield has become the preferred deformation mode. The craze surface never moves into the hydrostatic compression half of stress space.

Once a craze is initiated, its subsequent growth is determined only by the value of the maximum principal tensile stress. It follows that a craze could continue to grow even though its propagation moves it into an area where the hydrostatic stress component is zero. The implication is either that the front of a crack itself leads to a hydrostatic tension ahead of its tip, much as a for a crack in metal, or that the microvoid nucleation is no longer necessary to extend an established craze, as the craze develops by a process of meniscus instability at its tip. The argument is unresolved, for while there will be a hydrostatic tensile stress component ahead of the tip, it is calculated to be rather small,

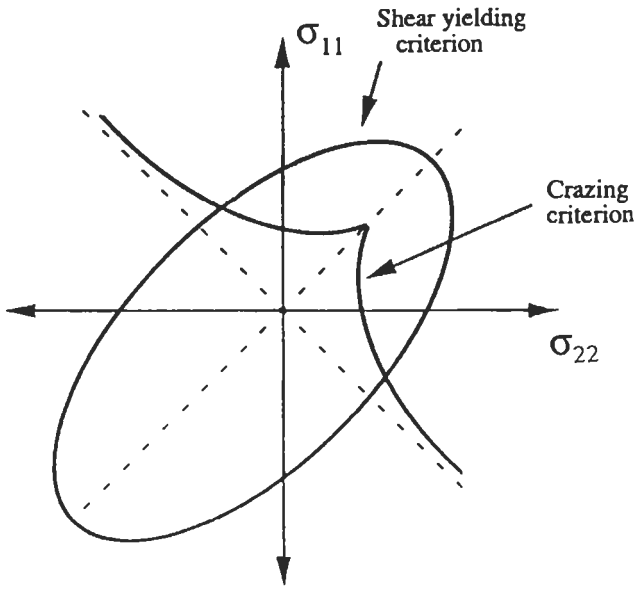

Fig. 33. Shear yielding (von Mises) and crazing criterion on a σ_{11}, σ_{22} section through stress space.

References: p. 2740.

and the possibility of a mechanism not requiring ongoing microvoid nucleation is supported by both experiment and theory.

The rate of propagation of a craze under constant applied stress conditions is controlled by the relaxation (creep) rate of the polymer. Craze length as a function of time is not a simple relation and is described by a power law with an exponent which depends on the polymer type. Nevertheless, the length after a particular time is proportional to the stress intensity factor squared. The development of a craze can be very slow with propagation rates of the order of mm/day under some circumstances. It can also be influenced quite drastically by the presence of solvents.

7.3. Materials factors

Polymer samples which have been preoriented, possibly as a result of injection moulding or extrusion forming, show a marked anisotropy in the ease of craze formation. For the case of a simple tensile stress, craze formation is more difficult when the stress is applied parallel to the preferred chain orientation, and easier when applied normal to this direction. Crazes formed across the direction of the pre-orientation (tensile stress parallel to orientation) tend to be short, thin and of a density closer to that of the bulk polymer, while those forming along the preorientation axis are much longer, thicker and less dense.

The molecular weight of a polymer appears to have little influence on the stress to form a craze, even though the it is generally true that low molecular weight reduces fracture strength of polymers in general. Crazes do not form in very low molecular weight polymers simply because the fracture stress is lower than the craze initiation stress.

The presence of an organic solvent can have a profound effect on the ease of formation of crazes in a polymer. Plastic jugs which have crazed as a result of the action of detergents in the presence of internal stress are a familiar sight (fig. 34). It is probably the flow direction in the moulding and the resultant preferred chain orientation, which determines the pattern of the crazing more than then the distribution of internal stress, although the two factors will be related. A solvent obviously has the ability to speed up relaxation processes at the craze tip through its plasticising action in lowering the glass transition temperature, although it appears that at higher growth speeds the solvent is not able to diffuse through the voided craze material rapidly enough to actually be present at the craze tip. However, it is still able to influence the widening of the craze which occurs over some distance behind the propagating tip.

7.4. Microstructure and micromechanisms

Figure 35 shows a transmission electron micrograph of a thin section of poly(styrene) containing a craze. Note that the scale of the structure is far too fine to be resolvable by light. A forest of nanofibrils, some 5–10 nm in diameter, is clearly apparent. While the initiation of the craze itself requires the nucleation of minute voids, in fact *nanovoids*, the propagation of an established craze occurs by the process of meniscus instability, in which voided material at the tip effectively propagates forward as highly localised 'fingers', the material between these fingers becoming isolated and drawing out into the

Fig. 34. Crazes in an injection-moulded polymer jug.

microfibrils. This mechanism is illustrated in fig. 36. Such instability is typical of advancing fluid/fluid interfaces under the influence of a negative pressure (suction). The hydrostatic tension will only develop a little ahead of the first void at the craze tip and thus a void finger moving forwards will be entering material stressed increasingly favourably to its continuing propagation. This is the basis for instability. The material left in the proto-microfibrils bears no hydrostatic component, except locally at the craze margins where it is connected to the bulk polymer.

The extension of the the microfibrils is the main mechanism through which energy is absorbed in craze formation, and thus vital to the toughening contribution which

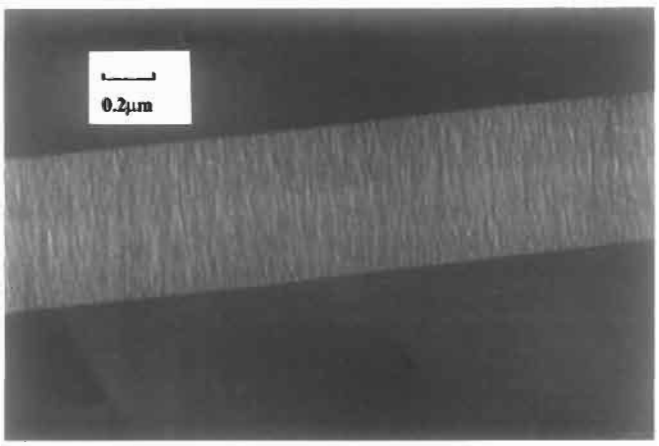

Fig. 35. Craze in polystyrene seen in transmission electron microscopy. (Courtesy Dr. A.M. Donald)

References: p. 2740.

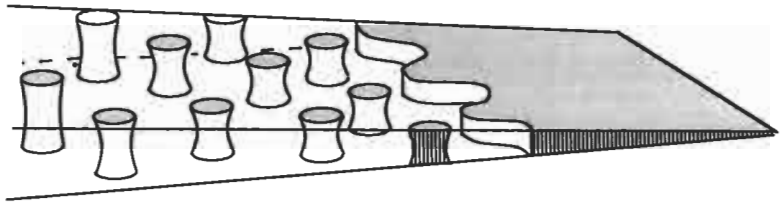

Fig. 36. The mechanism of meniscus instability by which the microvoids propagate at the craze tip.

crazing make to the polymer as a whole. The microfibrils draw down to a point where the neck is stabilised in much the same way as in drawing bulk fibers (c.f section 5). The draw ratio at which the microfibrils 'stabilise' depends on the entanglement density of the chain molecules in the polymer, the higher the entanglement density, the lower the draw ratio needed for stabilisation. The thickening of the craze behind its tip occurs mainly through more material being drawn into the microfibrils. The material within the microfibrils is not totally stable however and it is subject to creep as the entanglements unravel or the chains themselves break. Microfibril failure is the process by which a craze becomes a crack, the stress concentration associated with the crack geometry enhancing the fracture processes at the tip.

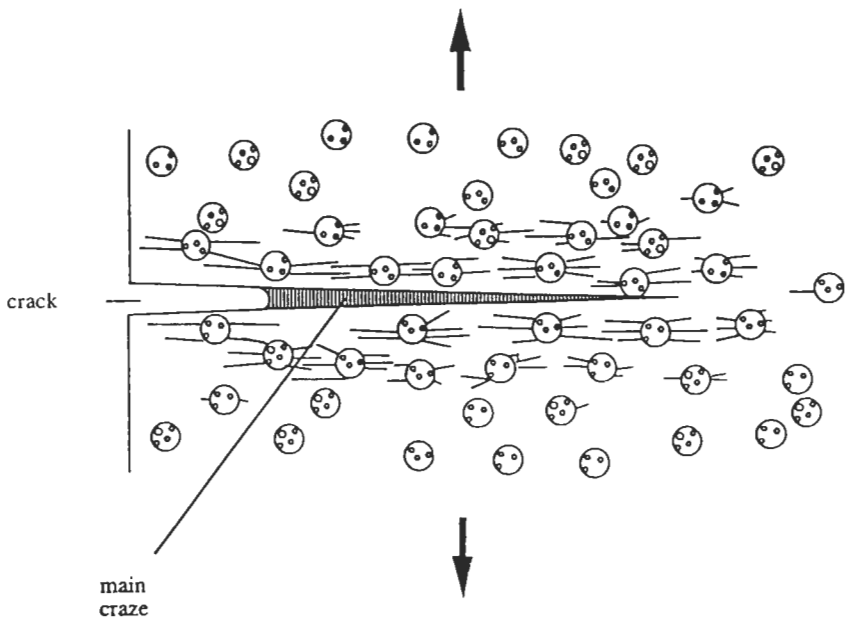

Fig. 37. Subsidiary crazes forming around rubber particles introduced into a polymer glass. The crazing increases the amount of energy absorbed in the plastic zone ahead of the crack.

7.5. Multiply induced crazing

Crazing can be viewed as an internal mechanism which enables plastic deformation to occur at stress levels below those necessary for shear yielding. It is also, unlike shear yielding, enhanced by modest degrees of hydrostatic tension added to a given deviatoric component. The promotion of subsidiary, multiple crazing through the addition of micro-stress concentrators within a polymer glass, is a major method of toughening polymer glasses. Small (10–100 μm) rubber particles dispersed in the glassy polymer are the most common form of stress concentrator, and form the basis of well known materials such as High Impact Poly(styrene) (HIPS) and Acrylic Butadiene Styrene (ABS). The rubber, which is dispersed during polymerization, has its adhesion to the glass promoted by compatabilising molecules in the interface, and it produces a local stress concentration on account of its much lower tensile modulus than the surrounding glass. The rubber particles which fall within the zone of stress concentration at the tip of the advancing crack nucleate crazes in their equatorial zones. These contribute to a 'plastic zone' around the crack tip which absorbs significantly more energy than the single craze at the crack tip itself. The mechanism is shown diagramatically in fig. 37. Recent work has shown that the formation of internal voids in the rubber particles makes a big contribution to the nucleation of subsidiary crazes.

8. *Electrically conducting polymers*

While it is a characteristic of a metal to conduct electricity, it is rather unusual for a polymer to do so. In fact some of the earliest polymers to be synthesised, made a major contribution to electronics as insulators with exceptionally low dielectric loss. Nevertheless, some specialised polymers are now available that have electrical conductivities which approach those of metal, and others that show many of the features of semiconductors.

8.1. Conjugated polymers

The carbon atoms in a sheet of graphite are held together by two different types of bonds: the directional bonds in the plane resulting from the so-called sp_2 hybridization, three joining each carbon atom, and the π bonding which is delocalised, puts an electron cloud between each adjacent sheet and holds the sheets together. In a polymer chain which is 'unsaturated', there are both localised and π bonds along the backbone. The presence of a π bond in addition to a localised, σ, one is represented as a double bond. In the chain of poly(acetylene), every second backbone bond is double (fig. 38a). In chains incorporating phenyl rings such as poly(*para* phenylene) (fig. 38b), or heterocyclic rings such as poly(thiophene) (fig. 38c), the ring structures are unsaturated and contain double bonds, although they are connected together through single ones. The delocalised π bonds, if they are separated by only one single bond as in the examples of fig. 38, can in effect, 'talk' to each other and produce some linking which spans the single bonds. Another way of expressing this behaviour is to consider that each single bond has some

References: p. 2740.

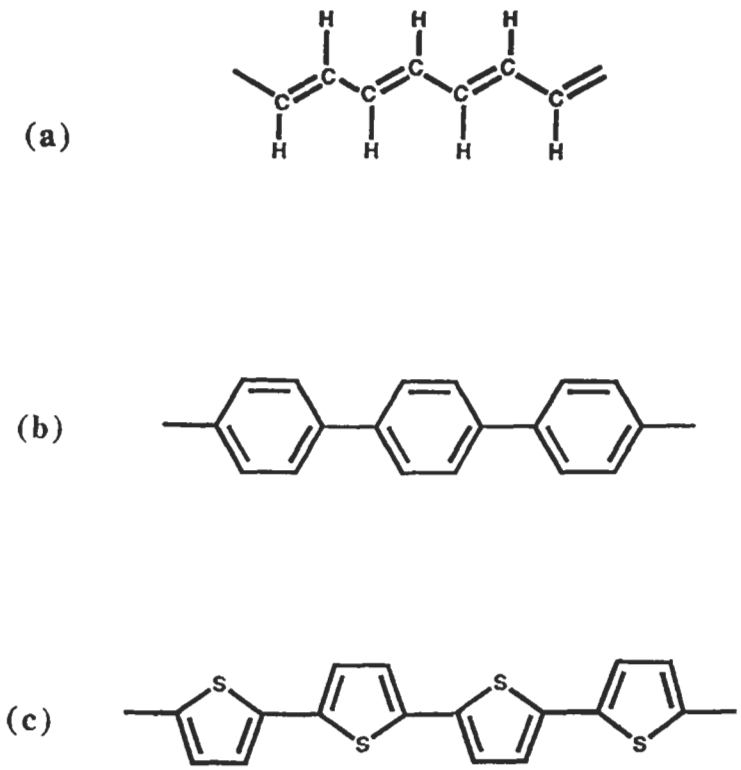

Fig. 38. Examples of conjugated polymers. (a) poly(acetylene), (b) poly(para phenylene), (c) poly(thiophene).

double bond character. This linking is called *conjugation*. One might immediately suppose that the presence of delocalised electrons which are conjugated, will give rise to electrical conductivity, just as in graphite. However, aligned, conjugated polymers have conductivities along the chain direction which are typical of a semiconductor at best. Poly(acetylene), for example has a band gap of 1.4eV, slightly greater than that of pure silicon. It is important to understand why this should be.

8.2. Band structure

Consider the simplified structure of poly(acetylene) in fig. 38a. One can consider the movement of charge along the molecule under the influence of a field, by the stepwise movement of the double bonds from (say) right to left. For this case the chain would be an electrical conductor, with charge flowing in one end and out of the other. However, an absolute key factor (and it is here that the behaviour is distinctly different from metals or inorganic semiconductors) is that the double C=C bond is shorter than the single one. The difference is only of the order of 0.003–0.004 nm, yet it is very significant. It is

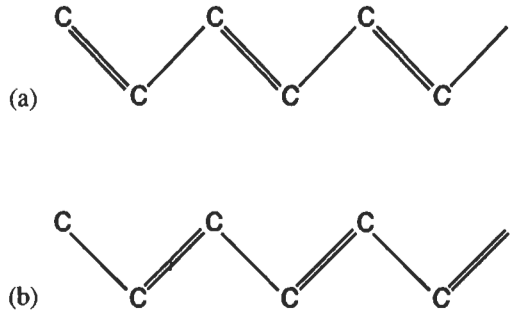

Fig. 39. (a) The structure of poly(acetylene) illustrating and (exaggerating) the difference in bond lengths between the single and double bonds. (b) The movement of the double bonds without a readjustment in the atom positions. The bond lengths are now wrong.

illustrated schematically in fig. 39a. Imagine the movement of double bonds to the left, as indicated in fig. 39b. They are now occupying positions where the atom spacing is that characteristic of a single bond, and the energy will thus be greater. Of course the atom can move so that the correct spacing catches up with the electron, but this process, a phonon process, is many orders of magnitude slower, and the electron will not wait. It is this energy difference which is the origin of the band gap. As with metals and inorganic semiconductors, one can think of the band gap as arising from the electrons being diffracted by the lattice, to give two standing waves of electron density, one leading to the maximum density in the region of the atomic nuclei, (or the bonds of the correct length in the polymer case), giving the lower-energy state and corresponding to the top of the valence band, while the other puts the electron density between the nuclei (or on the bonds of incorrect length), has the higher energy and corresponds to the bottom of the conduction band. The same arguments apply to other more complicated polymer molecules as illustrated for poly(*para* phenylene) in fig. 40. In this case there are three energies to consider: the lowest, ground state with single bonds between the rings, the excited state in which the bond between the rings is now double with a lower π electron concentration in the ring, but without any adjustment in bond lengths, and the relaxed state in which the bond lengths have now adjusted by relaxation to give a situation in which the energy is between the ground and excited states. For the poly-(acetylene) case the ground and relaxed states are equivalent with the same energy, and correspond to the valence band, whereas the excited state is the conduction band (fig. 41).

8.3. Solitons

For the case of poly(acetylene), a *soliton* is an antiphase boundary within the chain. It is illustrated in fig. 42a. The soliton is stabilised by the lattice relaxation, in that its movement will require repositioning of the atoms to keep the bond lengths right. The electron on the carbon atom at the centre of the defect which is not incorportated into any bond will occupy a state at the centre of the band gap. The central position of the

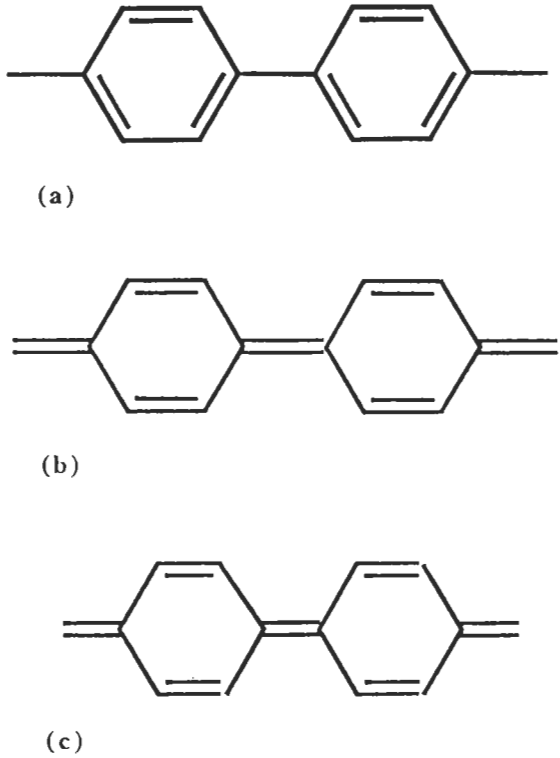

Fig. 40. The three states of poly(para phenylene).

state representing the equal amounts of the in-phase and anti-phase chain in the model.

In the case of other chains where the in-phase and anti-phase structures have different

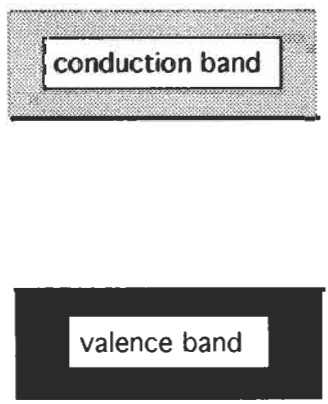

Fig. 41. A schematic band structure for poly(acetylene).

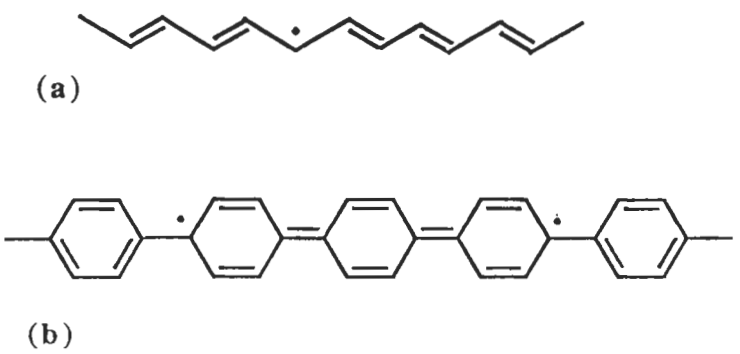

Fig. 42. (a) A soliton in poly(acetylene). (b) A soliton pair in poly(para phenylene).

energies. The solitons will occur in pairs bound together by the higher energy of the anti-phase material between them. An example of such a soliton pair in poly(para phenylene) is shown in fig. 42b. Their role in conduction involves the formation of charged solitons or *polarons.*

8.4. Polarons

The existence of a band gap in the electronic structure of conjugated polymers means that conductivity will require ionization of the molecule, in other words, insertion of electrons into the conduction band or holes into the valence band. The mechanisms by which ionization is achieved in practice are outlined in the next section, but at this point we note its effect on the band structure. The main point is that an electron or a hole will bind themselves weakly to a soliton to form a charged soliton, or in the case of polymers other than poly(acetylene), to a soliton pair to form what is known as a *polaron.* The presence of a charge, stabilises the antiphase distribution of the bonding and bond lengths between the bounding solitons. The localization of charge in the region of the defect, means that it is not in either the conduction band or in the valence band (for the hole case) but in localised states within the gap, as depicted in fig. 43. For the case of n-type polarons, the states are donor levels, while in the p-type case, they are acceptor levels. The pairs of states are symmetrical about the Fermi level which is in the middle of the gap. The analogy with extrinsic semiconductivity in inorganic crystals is helpful, but it must be emphasised that while doping levels in conventional semiconductors are of the order of parts per million, the levels in conducting polymers are several percent! It is thus not possible to consider the charged defects in isolation. Firstly a soliton pair will accept two electrons (or holes) to form a *bipolaron.* which gives rise to different states within the band. More generally, it is thought that at higher doping levels (>7%), the interaction between the defects means that there is a defect band, within the gap which broadens to merge with either the conduction or valence bands rendering the polymer a conductor rather than a semiconductor. Put another way, the charge carriers are able to move along the chain by hopping from soliton to soliton.

References: p. 2740.

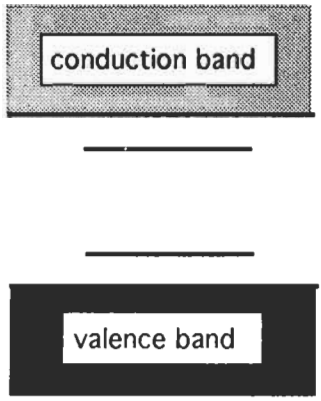

Fig. 43. Polaron states in the band gap.

8.5. Materials

The chemical synthesis of highly conjugated polymers is demanding, and the rapid growth in the development of this branch of materials science over the past decade has been measured by the availability of suitable polymers as much as the development of the physical theory. One of the major challenges is that conjugated polymers have very high melting points and thus cannot be processed in the melt state without degrading chemically. The routes around this depend on either the addition of extra groups to the chain, or the formation of some related precursor polymer which make the molecule tractable either in solution or in the melt. The molecule is converted to that desired after the processing is completed.

Doping, the insertion of charge carriers into the polymer chains, is achieved by adding either oxidising or reducing agents to the polymer, often at some stage during the chemical formation of the chains themselves, although the chemical agents are not incorporated within the chains but lie between them, often within preferred channels or as sheets. Oxidation, which is electron withdrawal from the chains, uses halogens (the combination of iodine and poly(acetylene) is particularly successful) or compounds such as $FeCl_3$ or AsF_5. Reduction, which adds electrons to the chains, is achieved by means of the alkali metals.

The conductivity mechanisms are essentially along the polymer chains, and thus properties can be enhanced, in one dimension, by drawing the polymer chains to align them macroscopically. Another advantage of alignment is that the extent of lateral coherence between the chains is enhanced. The ability of charge carriers to hop between chains is important as any one molecule is very much shorter than the macroscopic dimensions of the sample.

8.6. Applications

There are three major areas in which conducting polymers are of utility:

(i) As electrical conductors. The vision here is of the polymer wire, easily formed

and joined, light in weight and environmentally resistant. The highest polymeric conductivity reported to date is 10^5 S/cm in oriented, doped poly(acetylene). The measure of the achievement is that this value is in the metallic range and approaches that of copper (6.5×10^5 S/cm). Furthermore, there are reasons to believe that the resistivity mechanisms involving the scattering of electrons by lattice vibrations (phonons), are not as potent in conducting polymers as in metals; so there is the possibility of materials that are actually better electrical conductors than any metal. But that is in the future. Probably the most serious limitation in the widespread application of polymeric conductors to the electrical industry stems from the fact that the polymers in which these properties can be achieved, are amongst the most difficult of all polymers to process and their environmental stability is limiting on two accounts. The first is that of photo-oxidation: illumination in the presence of air does pose a problem for almost all types, although it is possible to achieve oxidative resistance in the absence of light and vice versa. The second concerns the stability of the doping additions. It is perhaps not surprising that polymers doped with alkali metals will react with moisture to the detriment of their electrical properties. Oxidative dopants such as halogens or their salts are rather more resistant in some cases, performance being maintained in damp air over useful periods.

(ii) As devices. The presence of localised electron and hole states within the band gap of the undoped polymers has opened up their potential for semiconductor devices. In particular the Metal-Insulator-Semiconductor (MIS) device, with poly(acetylene) as the semiconductor, has been the subject of detailed investigation. Not only does the device show intrinsic promise, with the usual caveat about environmental stability, but the investigation of its properties has considerably added to the understanding of the physics of the polymer where the charge carriers are injected, rather than being generated by doping. Another very important device application is as light-emitting diodes. A thin sample of polymer held between conducting electrodes, one of which is transparent, is subject to the injection of charge carriers when the electric field is above 10^5 V/cm. The injection of electrons from the negative electrode forms n-type polarons, while holes from the positive electrode, forms p-type polarons. The two types of polaron migrate across the polymer and annihilate on meeting to emit light. The beauty of using a polymer as an active element, is that the position of the states within the band gap can be tailored by choosing different chemical structures at the point of synthesis. A wide range of emitted colours are thus available, almost at will, while the efficiency of the devices matches those based on inorganic semiconductors. Other applications are in capacitors, batteries, and chemical sensors

(iii) For conductivity enhancement. There are a number of applications in which a degree of electrical conductivity is desirable in polymer products. One of the most significant is to prevent the build-up of static charge on polymers. Here the conductivities required are very modest, say 10^{-5} S/cm. They can be achieved either through the application of a conducting polymer as an antistatic coating, or through the dissolution of a conducting polymer within a conventional one. The dissolution approach can be viewed as a molecular-scale equivalent of the technology of achieving modestly conducting polymers by adding conducting particles as fillers. The so-called percolation threshold, the volume fraction at which there are sufficient interparticle contacts to

References: p. 2740.

provide an electrical path across the polymer, is reduced as the axial ratio of the particles is increased. Hence for fibers and for dissolved conducting molecules alike, a smaller volume fraction is needed to achieve a given effect.

9. *The glass transition: to melt and rubber*

Basically a glass, whether metallic or inorganic or polymeric, is a frozen version of a liquid, frozen in time and space as far a the molecular structure is concerned. In order to achieve a glass, the alternative route to solidification, crystallization, must be suppressed on cooling. The avoidance of crystallization in both metals and polymers can achieved by quenching. It works for many but not all polymers — poly(ethylene) is a notable exception. Polymers provide a totally unique route to the promotion of glass formation, namely through the control of the chemical organization of the chain. Random sequences of stereoisomers along the chain, the *atactic* configuration, or random sequences of two or more different types of monomer along the chain forming a *random copolymer*, both serve to prevent crystallization. Chemical cross-linking to form molecular networks frustrates crystallization too.

9.1. Formation of a polymer glass

Given that crystallization is prevented from occurring on cooling, for whatever reason, the polymer solidifies by forming a glass at the *glass transition temperature*. A useful basis for thinking about the glass transition is the plot of a specific physical quantity, such as density, or enthalpy, against temperature. Figure 44 is such a plot, in this case of specific volume, the volume of a given mass of polymer. Above the glass

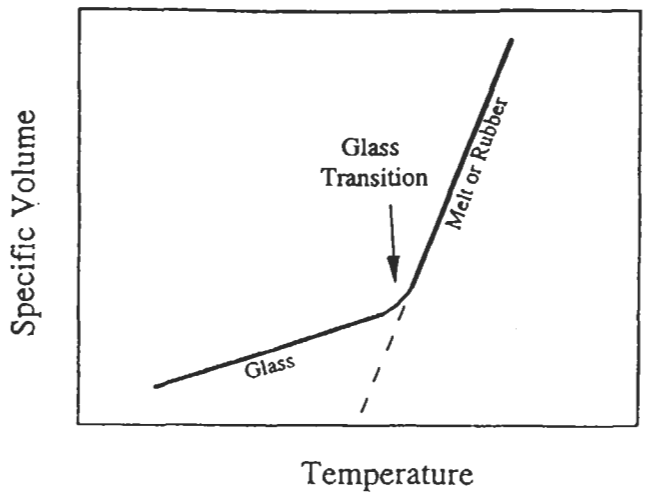

Fig. 44. Plot of the volume of a given mass of polymer against temperature. The change in slope marks the glass transition temperature.

transition temperature, the polymer contracts at a greater rate with cooling than below this temperature which is defined by the discontinuity in slope.

A central aspect to appreciate about any glass is that it is not an equilibrium phase in any thermodynamic sense. It is a phase which is prevented from reaching its thermodynamic equilibrium by kinetic constraints. The dashed line on fig. 44 represents the equilibrium condition for the non-crystalline state. Note that the lower the temperature below the glass transition, the further the glass is from equilibrium. It follows that, as the glass is not a stable phase, the glass transition is not a thermodynamic transition, and attempts to describe it as pseudo second order, which have appeared in the literature on occasions, must be viewed with the utmost circumspection. The glass transition is a kinetic one, and it follows that it will be intrinsically dependent on the time scale of experiment used to observe it. (See also ch. 19, § 2.1).

9.2. Rate effects

Focus on the region of fig. 44 just above the glass transition, and consider cooling at a fixed rate. As a small group of molecules contract, they are continually having to reorganise their arrangement to use the ever decreasing space available to them more efficiently. The ability to reorganise, needs available intermolecular space as well as thermal activation. Hence the ability to reorganise at a rate sufficent to keep the structure in equilibrium, decreases on cooling on two counts, firstly the amout of thermal energy available is decreasing, but secondly, and more significantly, the space or *free volume* as it is known, is decreasing too. There comes a point where the required rate of positional adjustment can no longer keep pace with the cooling rate, and the structure reached becomes frozen in. That point is the *glass transition.*

It follows that if the cooling rate is very slow, then the equilibrium contraction can proceed to a lower volume and temperature until things lock up, and vice versa. The glass transtion temperature, as well as the density of the glass formed, is thus dependent on cooling rate as shown in fig. 45. Fast cooling rates give high glass transition temperatures and low density glasses, slow cooling rates give lower transition temperatures and denser glasses. Another aspect of the family of plots on this figure, is that if a glass is held at a given temperature below the transition, then it will densify with time. This densification of polymer glasses with annealing can have a profound influence on its mechanical properties. In general the more dense a glass the more brittle it will be. Poly(carbonate) cooled at normal processing rates is one of the toughest polymer glasses and it can be plastically deformed several hundred percent. However, annealing for a few hours in the region of 10°C below the glass transition, renders poly(carbonate) sufficiently brittle to ensure that it will shatter when hit by a hammer. Densification of polymer glasses on annealing will also reduce their mechanical creep rates by several order of magnitude, and also, equally drastically in some cases, the rates of penetration of organic solvents.

There is continued contraction below the glass transition, albeit at a reduced rate. This limited contraction is associated with the reduction, with temperature, in amplitude of atomic vibrations as well as other localised rotational and conformational transitions

References: p. 2740.

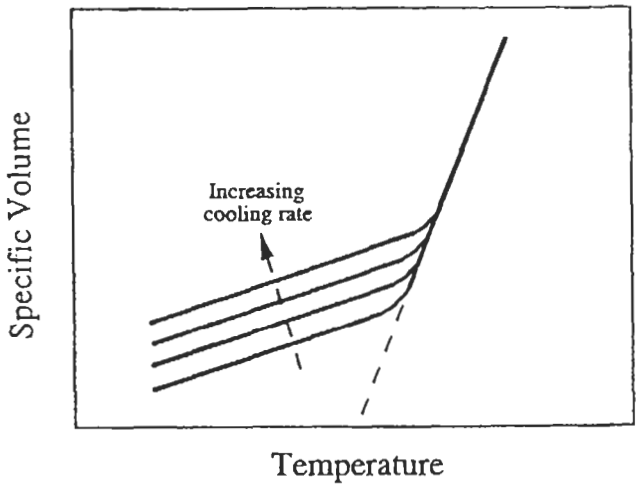

Fig. 45. Specific volume vs. temperature curves for different cooling rates.

on the chain. Some of these transitions may well 'freeze out' at lower temperatures, contributing to a further reduction in the slope of the line.

9.3. Observation of the glass transition using differential scanning calorimetry (DSC)

Of the various types of thermal analysis used to examine transitions in polymers, DSC is probably the most widely available and easy to use. The internal energy of a polymer as a function of temperature spanning the glass transition temperature is an analogue of the volume/temperature relationship considered above (fig. 44). Ignoring work against atmospheric pressure on heating, the energy is referred to as the enthalpy, H, as in fig. 46a. Differential scanning calorimetry plots the heat capacity, dH/dT, against temperature, so that a typical DSC plot is the differential of the enthalpy plot and is illustrated in fig. 46b. The glass transition temperature appears as a step on the calorimeter trace. In reality the step is not sharp and is often complicated by overshoot effects. Consider reheating a glass more rapidly than it had been cooled. The reheat curve on the enthalpy plot will follow the cooling curve in the glassy state, but when the glass transition is approached the molecular rearrangements required for equilibrium increase in enthalpy will not initially be able to keep pace with the fast heating rate and overshoot occurs as sketched in fig. 47a. A result of the overshoot is that the enthalpy curve becomes transiently steeper than the equilibrium line before it catches up. The consequences for the heat capacity plot logged by the machine are that the onset of the glass transition is delayed, and that the transition appears to be marked by a peak (fig. 47b). It is vital that the appearence of a DSC peak at a glass transition does not tempt one to think in terms of a first-order transition, the transition is *not* a thermodynamic one. Despite overshoot, it is apparent from fig. 47a that the transition temperature can still be

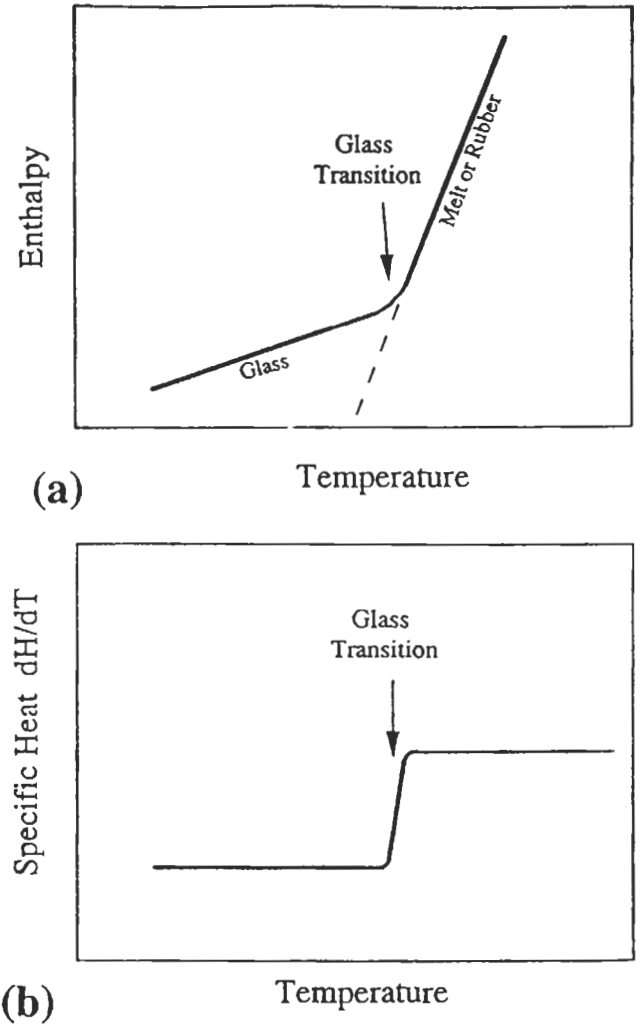

Fig. 46. Plots of: (a) Enthalpy vs. temperature; (b) Heat capacity vs. temperature. In reality, the step is not so sharp (dashed line).

assessed by extrapolating both linear parts of the plot to their intersection. The consequences of this construction for the differential plot of fig. 47b are interesting. Basically, one is fitting this curve to a step function with the temperature of the step determined by the necessity of the two types of cross hatched areas to balance as shown in fig. 47c. The glass transition temperature determined in this way has bee referred to as the *fictive* temperature within the polymer community, although it is recognised that the parallels with the use of this term in the inorganic glass field are not very close. Other definitions

References: p. 2740.

of the transition temperature from DSC heating plots (T_{peak} and $T_{extrapolated}$) are shown too in fig. 47c.

9.4. Control of the glass transition temperature (T_g)

The glass transition temperature is the single most important parameter when considering the performance of structural polymers at elevated temperatures. There appear to be two key features of the chemical structure of the chain which determine the T_g. One is the intrinsic stiffness of the molecule, determined by the ease of rotation about the backbone bonds. It is possible to design molecules in which such rotations are very difficult and T_gs can be moved up into the region, perhaps above 350°C where chemical

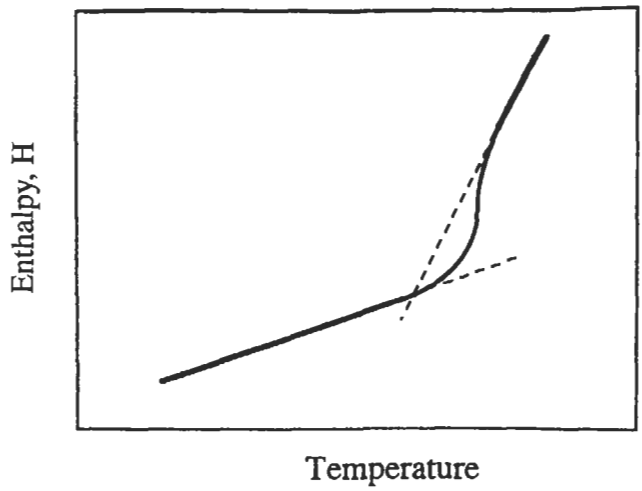

(a)

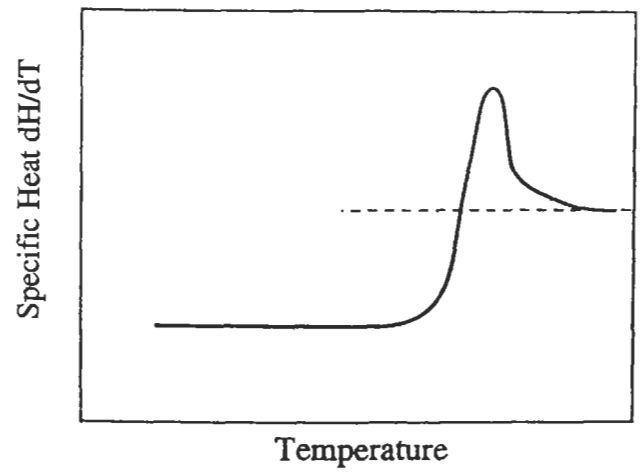

(b)

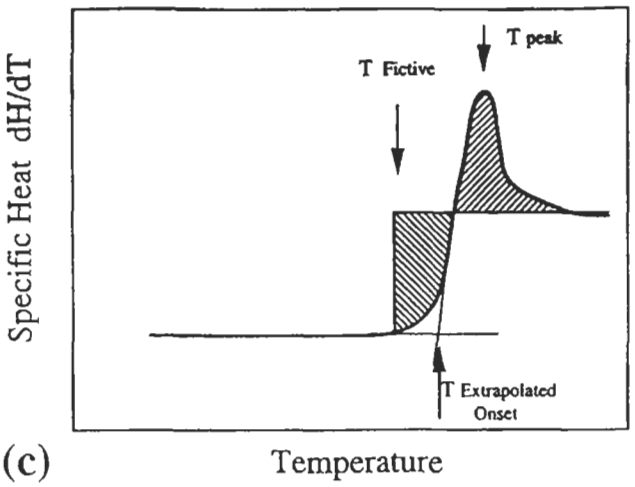

Fig. 47. Plots showing the efects of 'overshoot' on heating. (a) enthalpy v. temperature; (b) heat capacity v. temperature showing the peak; (c) 'fictive' and other constructions.

degradation will almost certainly occur. There is however another factor. The molecular readjusting movements necessary for a polymer melt to contract along the equilibrium line, the ones which 'freeze' at T_g', are highly cooperative in nature. That means that for one chain unit to move towards a better packing position, several other neighbouring units, whether on the same molecule or on different ones, will have to move too in a synchronised fashion. Waiting on thermal activation to achieve the movement will thus take considerably longer, as several neighbouring units, will thus have to be 'kicked' in the appropriate direction at the right moment. Hence a chain which will, as a result of its chemical design, involve a considerable swept volume and thus great cooperation from its neighbours to achieve a transition, will thus tend to have a higher glass transition, for a given backbone stiffness, than for a chain which can change its shape without requiring so much elbow room. For example, poly(ethylene terephthalate) (PET) has a T_g of 65°C, with most of the chain flexibility coming from the two (CH_2) units between the phenyl rings (see fig. 21). On the other hand poly(ethylene naphthoate) (PEN), has a T_g of 115°C, despite having equivalent flexible groups. The difference is that a rotational transition around one of the backbone bonds in the (CH_2) unit will require a greater swept volume than for PET on account of the greater length of the rigid (naphthoic) unit. The lower T_g of PET is a limitation in the plastic bottle industry as it severely limits hot-fill and hot-wash recycling options. PEN is a serious candidate despite its additional cost.

9.5. Melt or rubber?

The issues associated with the glass transion temperature are essentially those of the local packing and associated dynamics of units of the polymer chains. The polymer above the glass transition temperature has so far been referred to as a melt however, if

References: p. 2740.

the chains are lightly cross-linked, or of sufficiently high molecular weight so that chain entanglements are stable on the time scale of observation, then the polymer will behave as a rubber not as a melt. The cross-link points, whether they are permanent covalent bonds or semi-permanent entanglements, form a molecular *network*. While the interchain mobility is little influenced by a low concentration of cross-link points, viscous flow, the relative motion of the centres of gravity of the molecules, is effectively suppressed. It should be added that where the density of cross-link points is high, the reduction in interchain mobility does become important and the glass transition temperature will be increased. An extreme case is natural rubber, which can be cross-linked with sulphur (*vulcanization*) to such a degree that the glass transition is increased to above room temperature, turning the polymer effectively into a glass, which was marketed at one time as 'ebonite'.

Another type of cross-link point is formed by the crystals of a semicrystalline polymer. The rubbery properties of low-density poly(ethylene), which has a crystallinity of about 40%, are due to the fact that the crystals act as super cross-link points, as a proportion of molecules have a part of their length in the amorphous phase and other parts incorporated into one or more crystals. The reduction of interchain mobility in the rubbery phase on account of the crystal cross-links is shown as an increase in T_g with increasing crystallinity. Whereas the T_g of non-crystalline poly(ethylene) (very difficult to make) is likely to be around −100°C, that of the amorphous component of the low-density material is closer to −40°C, while that of higher-density poly(ethylenes) with crystallinities exceeding 60% approaches 0°C.

9.6. Viscoelasticity

A high molecular weight polymer is effectively cross-linked through the chain entanglements. However, these cross-links are subject to thermally activated disentanglement. In other words, a rubber without chemical cross-links will creep when held under constant load, so that at very long time scales it is effectively a viscous melt. For lower molecular weights, the rubbery properties are only apparent at short, transient time scales. With increasing temperature, the rate of thermal unravelling of the entanglements will become more significant, and thus properties will shift from elastic towards viscous. One therefore has a material which has both viscous and rubbery properties, the dominance of either being dependent on the time scale and the temperature. This behaviour is known as *viscoelasticity*.

Viscoelasticity can be described by a mechanical analogue model known as a *Maxwell element*, fig. 48. It consists of a dashpot and spring connected in series. The model leads simply to a constitutive equation:

$$\dot{\varepsilon} = \dot{\sigma}/G + \sigma/\eta \tag{15}$$

Where, $\dot{\varepsilon}$ is the strain rate
$\dot{\sigma}$, the rate of stress application
G the rubber modulus
and η the viscosity

Fig. 48. A Maxwell element describing viscoelasticity. The spring represents the rubber modulus, and the dashpot the viscosity. The dashpot becomes 'stiffer' with decreasing temperature and/or increasing molecular weight. For a chemically crosslinked rubber it will be locked solid.

The use of this model, or rather its constitutive equation, enables one to calculate the mechanical behaviour for simple consitions.

If a stress was added instantaneously and then held constant (fig. 49a), there would be an instantaneous strain of σ/G, followed by a constant strain rate given by σ/η. The strain would thus increase constantly with time. On the other hand, if the strain was held constant after an instantaneous extension (fig. 49b), then $\dot{\varepsilon} = 0$, and so the solution of the simple differential equation follows as:

$$d\sigma/\sigma = -(G/\eta)dt. \tag{16}$$

Integrating and putting $\sigma = \sigma_o$ for $t = 0$ we get:

$$\sigma = \sigma_o \exp-(G/\eta)t. \tag{17}$$

The ratio η/G has the dimensions of time, and is known as the *relaxation time*, τ, and

References: p. 2740.

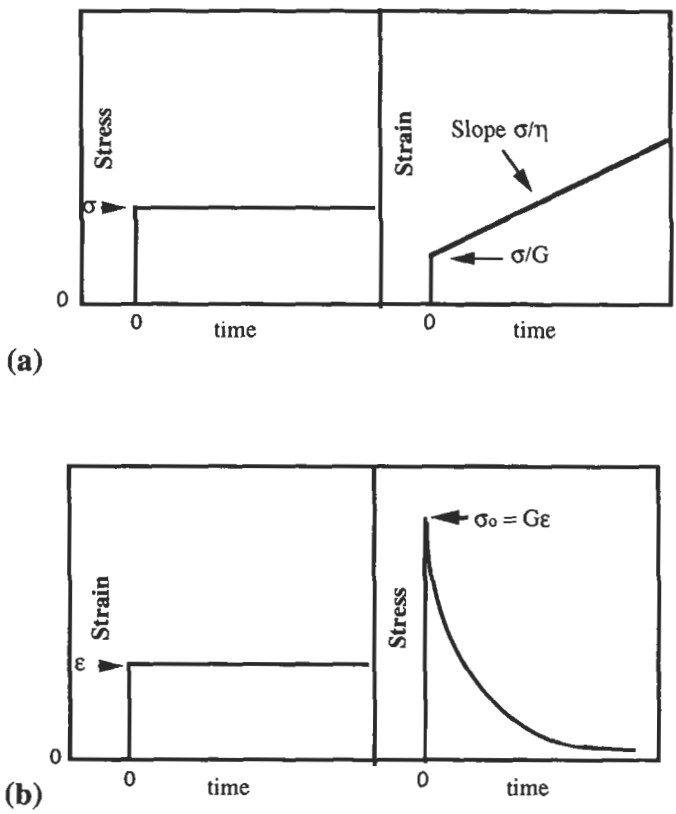

Fig. 49. The response of a Maxwell element to stress and strain pulses (see text).

represents the rate constant for the exponential decay of stress at constant strain, illustrated in fig. 49b and known as *stress relaxation*.

It is also possible to investigate the behaviour under conditions of oscillating stress. Under these conditions the viscoelastic behaviour of the polymer is described by the *complex modulus* G^*, which is the ratio of stress to strain at any point in the cycle.

$$G^* = G' + iG''. \tag{18}$$

G' is the *storage modulus* or *elastic modulus*, and represents the elastic component of the deformation, that is the component of load which is in phase with the strain.

G'' is the *loss modulus*, representing the component of stress which leads the strain by 90° as indicated by the vector operator, i.

The ratio, of G''/G' is $\tan\delta$, where δ is the angle by which strain lags stress in the experiment as a whole. $\tan\delta$ shows a maximum at transitions such as the glass

transition, and dynamic (oscillating) measurements are used to detect both the glass and subsidiary transitions.

9.7. Model description of non-crystalline polymers

It is possible to extend the dashpot and spring description to cover the total behaviour of a non-crystalline polymer. The model of fig. 50 shows how this is done. The spring at the top is a stiff one and represents the elastic modulus of the polymer glass, typically 1 GPa. The dashpot on the left, represents the onset of intersegmental motion which occurs at the glass transition temperature. Its behaviour is thus very temperature dependent, describing creep in the glass below T_g, as well as the onset of viscoelasticity above T_g. The creep of the glass will be limited by the Maxwell element on the right, although

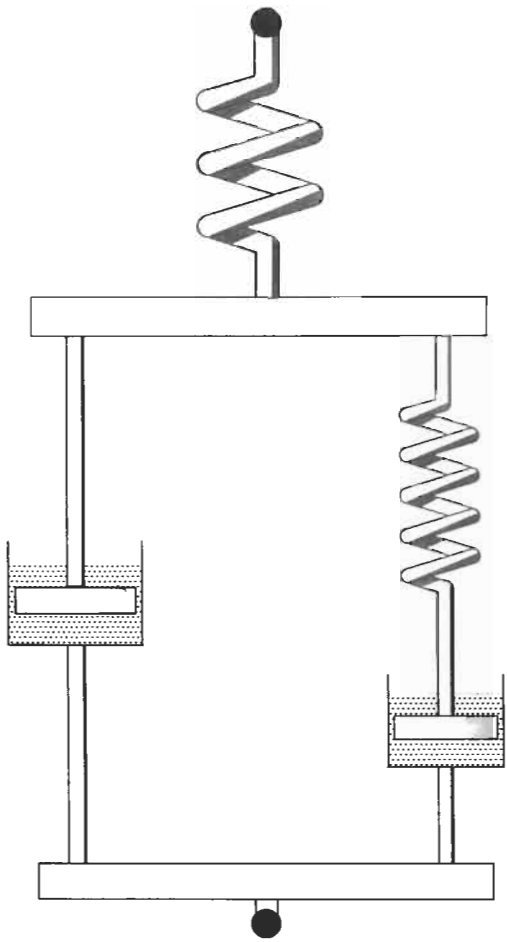

Fig. 50. A spring-dashpot system to represent the behaviour of a non-crystalline polymer in glassy, rubbery and viscous states.

References: p. 2740.

the influence will only be significant at higher strains. With the 'glassy' dashpot effectively free above T_g, the behaviour is described by the Maxwell element. For high molecular weights and short times, or for chemically cross-linked networks, the rubbery spring will operate, with an elastic modulus of approximately 0.01 GPa. The viscous creep of the rubbery network will be described by the Maxwell dashpot as appropriate.

The final two sections (10 and 11)

The two sections which follow "Amorphous Chain Structures" and "Rubber Elasticity", represent the central areas of polymer science which are relatively unique to the field. It is not clear that physical metallurgy will give any special 'head start' to the reader, yet they are central areas none the less, and a basic understanding of them is seen as a *sine qua non* for any one who wishes to be well informed on the polymer front.

10. Amorphous chain structures

10.1. Simple statistical chains

The basic structural building block of metals and crystalline ceramics is the unit cell. For crystalline polymers, the unit cell is still important, but for polymer glasses, rubbers and also the non-crystalline phase of crystalline polymers, one needs another starting point. The best basic unit is the randomly coiled chain. The most simple chain one can consider, which is a useful model of a real polymer molecule, is the *freely jointed chain*. This chain consists of n units each of length l, with there being no restriction on the freedom of the joints to take up any angle. Such a chain is an example of a random walk in three dimensions. Imagine such a chain squirming about in space. A snap-shot of it would correspond to a particular *conformation*, that is a particular angular relationships between the adjacent links at each joint. One of the most basic parameters of the chain in the snap-shot is the end-to-end length. It may have a wide range of values ranging from zero, if the two ends happened to be next to each other, to nl, the stretched-out-straight length of the chain. One of the most basic relations in polymer science is the end-to-end length averaged over time, or over all possible conformations which amounts to the same thing. It is:

$$\langle R^2 \rangle = nl,^2 \tag{19}$$

where $\langle R^2 \rangle$ is the mean square end-to-end length.

In addition to the assumptions about free joint rotation, this simple relation also neglects the fact that different parts of the chain cannot occupy the same region of space more than once. It thus describes a *phantom chain*, a chain which can intersect itself and thus has no *excluded volume*.

10.2. Real chains

A real chain molecule will differ from a freely jointed chain in a number of respects. Their consideration, in turn, is the next step in understanding amorphous structure. Firstly, the freely jointed assumption must be challenged on two counts. There are fixed bond angles at the (typically) carbon atoms forming the backbone, and there is hindered rotation about the bonds themselves. In the simple example of poly(ethylene) the bond angles are near to tetrahedral, which means that the angle between adjacent bonds, θ, is 71°. The mean square end-to-end length is now given by:

$$\langle R^2 \rangle = nl^2(1 + \cos\theta)/(1 - \cos\theta). \tag{20}$$

For $\theta = 71°$, $\cos\theta$ is approximately $1/3$, and thus $\langle R^2 \rangle$ is double that of the freely jointed chain.

A further restriction is the freedom which the bonds have to rotate around their axes. The rotation is restricted as the *staggered* bond positions are some 12 KJ/mole lower in energy than the *eclipsed* positions. Looking along one bond at the adjacent bonds on the same atom, one of which continues the chain while the other two are bonds to hydrogens, when the three are symmetrically projected between the equivalent three bonds on the second atom, the conformation is *staggered*. For the *eclipsed* case, the two sets of three bonds map onto each other. The energy as a function of bond rotation angle in poly(ethylene) is shown in fig. 51. Note that the staggered state, called *trans*, is lower than either of the other two *gauche* states. If all the bonds were in the staggered setting, then the chain would be straight in the planar zig-zag conformation, which gives the

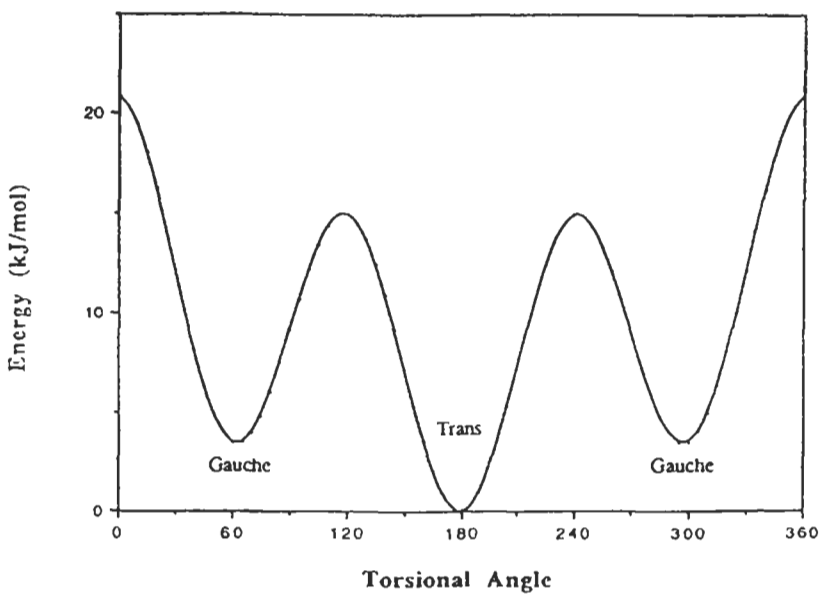

Fig. 51. Energy of rotation about a backbone bond in poly(ethylene).

References: p. 2740.

greatest chain length per monomer unit, and is, in fact, the conformation in the poly(ethylene) crystal. For the random chain, however, there is simply a statistical preference for the staggered states, and a weaker preference for the trans over the gauches. The higher the temperature, the more the staggered states become equivalent, and eventually, at admittedly unrealistically high temperatures, all states, staggered and eclipsed will become equivalent, and the hindered rotation will be swamped by the thermal energy. The degree of hindered rotation is handled by a mean rotation angle parameter, $\langle \cos \phi \rangle$, where ϕ is 180° for the trans setting and 60° and 300° for the two gauches. The higher the temperature, the more the mean cosine tends towards zero. $\langle R^2 \rangle$ is now given by:

$$\langle R^2 \rangle = nl^2(1 + \cos\theta)/(1 - \cos\theta).(1 - \langle \cos\phi \rangle)/(1 + \langle \cos\phi \rangle). \tag{21}$$

The ratio $\langle R^2 \rangle / nl^2$ is known as the *characteristic ratio*, C. It describes the degree to which the mean square end-to-end length of a real chain deviates from that of an 'ideal' freely jointed chain.

The correction for excluded volume is usually expressed by raising the value of n to the power of 1.2, although this only applies when n is large. Hence, for a freely jointed chain:

$$\langle R^2 \rangle = n^{1.2} l^2. \tag{22}$$

10.3. The Gaussian approximation

Imagine viewing a high molecular weight chain molecule from a large distance. The individual details of the chain would be lost, and one would see but a blob with a somewhat greater density towards the centre. If one were to average many such observations, then the blobs would become equiaxed, with a higher density core gradually fading towards the periphery. This distribution of density can be approximated by a Gaussian function, as shown in fig. 52. As the chain ends are not constrained to be in any special part of the envelope, their probability of occurrence will scale with the chain density. Hence the distribution of end-to-end lengths will follow the Gaussian function also; in this case, the function represents the probability distribution of the position of one end a chain with the other held at the origin. It follows that the most probable position of the 'far' end of the chain will be at the origin, next to the other end. The Gaussian function can be scaled to $\langle R^2 \rangle$ when it takes the following form:

$$P(R) = (B/\pi)^{3/2} e^{-BR^2} \tag{23}$$

where $B = 3/(2\langle R^2 \rangle)$.

Note that the Gaussian decays continuously as R tends to ± infinity, whereas the dimensions of a random coil will have a distinct limit as the diameter of the true distribution cannot exceed the stretched-out-straight length of the chains.

The Gaussian approximation is the basis for calculating the mechanical properties of rubber, and will be used in this role in the next section.

A further parameter of the Gaussian approximated chain is the *radius of gyration*. The

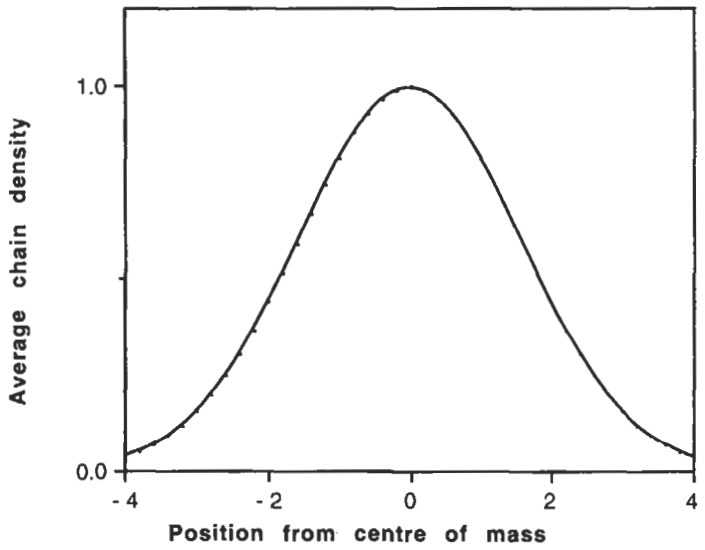

Fig. 52. Gaussian function representing the distribution of mass of a randomly coiled chain.

radius of gyration is the second moment of the chain mass referred to the centre of its distribution. For the Gaussian case, the mean square radius of gyration, $\langle R_g^2 \rangle$, is related to the mean square end-to-end length by:

$$\langle R_g^2 \rangle = \langle R^2 \rangle / 6. \tag{24}$$

Where chain dimensions are measured using small-angle X-ray or neutron scattering techniques, it is the radius of gyration which is most directly related to the angular distribution of the recorded scattering.

10.4. The chain environment

It is all very well to describe the statistical properties of real polymer chains on the assumption that they are isolated, and that there are no possible interactions between different parts of the same chain. In fact a chain suspended in free space would collapse on itself as the van de Waals forces came into play, with considerable consequences for the parameters such as $\langle R^2 \rangle$. On the other hand, if the chain is dissolved in what is called a *good solvent*, where the attraction of the solvent molecules for the polymer chain exceed the attraction of the chain for itself, then the chain is in effect opened out in order to maximise the access of solvent molecules to its surface. The effect of a good solvent is thus to increase the characteristic ratio. Conversely, a *bad solvent* will tend to cause the molecule to bunch up, rather as in the vacuum case, and have the effect of reducing the characteristic ratio below unity. The question now arises, if a solvent with just the right properties can be found, would it be possible to achieve chain dimensions in solu-

tion which exactly match those predicted by chain statistics, that is, achieve a situation in which the potential interchain bonds are exactly balanced out by the solvent molecules? The answer is 'yes', and such a solvent is known as a θ *solvent*. A given solvent will only show 'θ conditions' at one temperature which is known as the θ *temperature*. The effect of environment on chain dimensions is illustrated in fig. 53. It should be noted that in all but the most dilute of solutions, a bad solvent will also cause the chains to aggregate, for if two parts of one chain would bond to each other in preference to their environment, then it follows that different chains will similarly tend to bond. In fact the chains will precipitate out. This effect, which is called the *cloud point* (since precipitated chains scatter light effectively), occurs once conditions stray, even marginally, to the *bad* side of θ, and is used to determine when θ conditions have been achieved.

10.5. The condensed phase

The structure of rubbers and polymer glasses has been the subject of energetic debate, especially in the 1970s when reputations were bruised and a Nobel prize won. Basically, the issue is one of perception. How can randomly writhing molecules pack to fill space to give densities as high as 90% that of the corresponding crystal? Surely there must some degree of order to achieve the packing. The answer is that, to a first approximation, chains in a glass or rubber do have their random coil dimensions. In fact the surrounding and interweaving neighbouring molecules act exactly as a θ solvent, as chemically they are indistinguishable from any part of the central molecule. Both ΔH_{mix} and ΔS_{mix} are zero as a result. This prediction was beautifully confirmed by the application of neutron scattering to amorphous polymers in which a fraction of the molelcules had been tagged by substituting deuterium for the hydrogens. It thus proved possible to measure the dimensions of a particular molecule and demonstrate that this value was identical for the same polymer in a θ solvent.

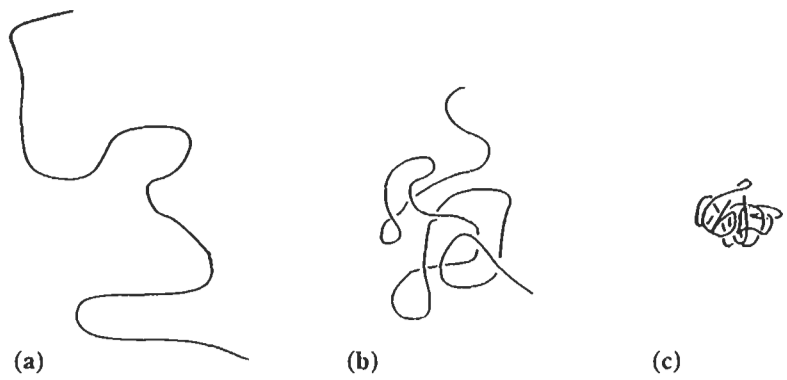

Fig. 53. Schematic diagram of a polymer chain in (a) a good solvent, (b) a θ solvent and (c) a poor solvent.

11. Rubber elasticity

The relatively straightforward calculation of the stress–strain relationship for rubber for extensions of several hundred percent is one of the more significant achievements of materials science, (or physics, or chemistry — depending on one's point of view). The fact that the principles governing rubber elasticity are more akin to the compression of an ideal gas than to any other aspect of science, sets this corner of the mechanical properties field utterly apart from the main stream. It is thus especially inviting.

11.1. The network

A rubber is an amorphous polymer above its glass transition temperature, in which the chains are associated as a *network*. The network points are generally chemical cross-links, in which case a rubber is technically a thermoset, although for linear polymers of sufficiently high molecular weight, the entanglements are sufficiently stable to suppress viscous flow and thus enable rubbery properties to dominate, at least at short times. The chains which join the network points are known as *network segments*. A very useful first-order assumption is that as the rubber is deformed, the network points move *pro rata* with the overall shape change. This deformation is described as *affine*, and is illustrated in fig. 54. The fact that the points move in this simple way does not imply anything about the movement of the molecular chains connecting them. In fact at a fixed overall strain, the network segments will be continually on the move, exploring the multitude of different routes which they can take between the network points. It is this constant, thermally driven motion which is the source of rubber elasticity.

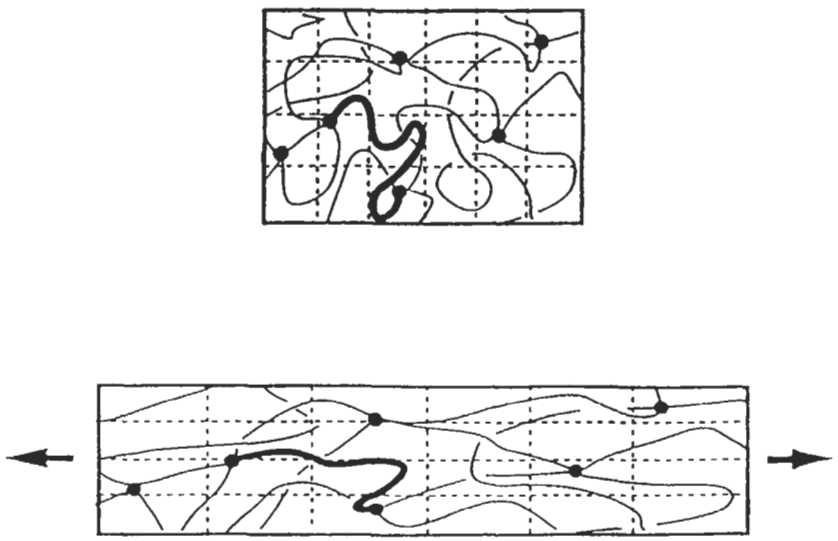

Fig. 54. Illustration of affine deformation. The positions of the cross link points move pro-rata with extension of the specimen, although the connecting chain segments do not.

References: p. 2740.

11.2. The entropy spring

Consider a network segment, with the cross-link point at one end fixed at the origin, and the other cross-link point at x, y, z as shown in fig. 55a. The affine deformation of the network, fig. 55b, moves the far end of the segment from x, y, z to x', y', z' where the external deformation ratios, $\lambda_x, \lambda_y, \lambda_z$, are given by x'/x, y'/y, and z'/z. We now need to be able to calculate the force to stretch the chain by a given amount, which then, through a knowledge of the number of segments per unit volume, will give the overall stress on the sample. As the network points at either end of a given segment are moved apart, the number of routes which the chain can take between the two (fixed) ends decreases. In the ultimate, when the chain is fully stetched, there is only one route, a straight line. The reduction of the number of conformations the chain can adopt with increasing strain, decreases the entropy of the chain, and thus increases its free energy. There will be an increase in the enthalpy, ΔH_λ, of a chain on stretching, but this is a second order term, and will for now be neglected. The fact that the prime source of rubber elasticity is the decrease in entropy with increasing deformation, is absolutely central, and the assumption that $\Delta H_\lambda = 0$ is flagged, by analogy to the gas laws, with the reference to an *ideal rubber.*

11.3. Thermodynamics

Before continuing with the calculation of the stress–strain curve, it is worth reflecting on the consequences of the fact that the origin of rubber elasticity is entropic. An

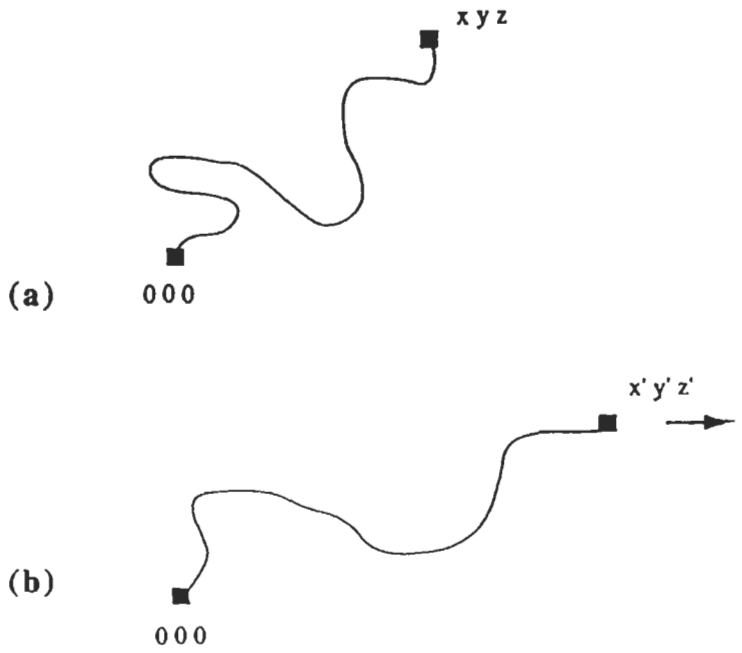

Fig. 55. Relative displacements of network points on deformation, ($x' = \lambda_x$, etc.)

implication of the statement that $\Delta H_A = 0$, is that the rubber does not store any of the work done on it to deform it. The mechanical work which goes in is released immediately as heat (fig. 56). The analogy with the compression of an ideal gas is compelling, as the volume of gas is reduced its entropy decreases, but the work of deformation is released as heat, at least for isothermal conditions. The same applies to the stretching of a rubber band; it gets hot, by only a few degrees but sufficient to be detected by holding it against the lips. What is more, if the rubber is allowed to relax, the entropy now increases and so the mechanical work it is now doing is supplied by the rubber drawing in heat from its surroundings. If the stretched band is relaxed (smoothly) it cools, and this can be felt too. A further consequence of the entropic origins of its elasticity, is that, as the temperature of a piece of rubber, stretched to a constant length, is increased, it will tend to contract more strongly, again analogous to the increase in pressure of a gas with increasing temperature at constant volume. The implication is that the *elastic modulus of rubber increases with increasing temperature* in contrast to virtually all other materials, where elasticity is energetically based, and the elastic modulus decreases with increasing temperature.

One can write, where f is the applied force and l the length of a sample:

$$f = \left(\mathrm{d}G/\mathrm{d}l\right)_{T,P} \tag{25}$$

where $\mathrm{d}G = -T\mathrm{d}S$, because $\Delta H = 0$, and the use of the Gibbs free energy, G, is possible only because of the assumption that $(\Delta V)_e = 0$.

11.4. Dependence of entropy on strain

The Gaussian distribution function describing the position of one end of the chain when the other is at the origin has been derived (eq. 26) as:

$$P(\boldsymbol{R}) = \left(B/\pi\right)^{3/2} e^{B\boldsymbol{R}^2} \tag{26}$$

where $B = 3/(2\langle \mathbf{R}^2 \rangle)$.

The entropy of a chain is then given by substituting the above relation in the Boltzmann relation:

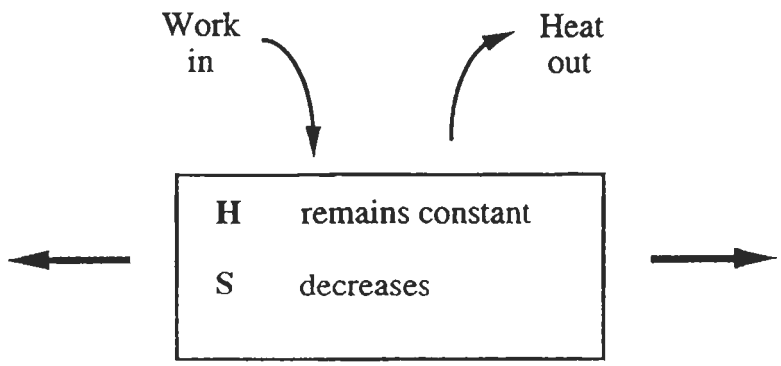

Fig. 56. When an ideal rubber is deformed, all of the work done on it is turned into heat.

References: p. 2740.

$$S = k \ln\big(CP(R)\big), \tag{27}$$

where C is the number of conformations possible with the ends of the chain fixed at cross-link points in the underformed rubber.

Hence from eqs. 27 and 26,

$$S = k\Big(\ln C + \ln\big(B/\pi\big)^{3/2} - BR^2\Big). \tag{28}$$

It is now necessary to obtain the chainge in entropy on elongation by calculating the entropy for the cases of zero and finite strain.

It helps to write that $R^2 = \lambda_x{}^2 x_o{}^2 + \lambda_y{}^2 y_o{}^2 + \lambda_z{}^2 z_o{}^2$, so that the change in entropy between the deformed and undeformed ($\lambda_x = \lambda_y = \lambda_z = 1$) states is given by:

$$\Delta S/\text{chain} = -kB\Big[\big(\lambda_x^2 - 1\big)x_0^2 + \big(\lambda_y^2 - 1\big)y_0^2 + \big(\lambda_z^2 - 1\big)z_0^2\Big]. \tag{29}$$

Summation over all network segments gives spherical symmetry and hence the mean values are:

$$\langle x_0^2\rangle = \langle y_0^2\rangle = \langle z_0^2\rangle = \big(1/3\big)\langle r^2\rangle = 1/(2B). \tag{30}$$

Hence for n network segments:

$$\Delta S = -(1/2)nk[\lambda_x^2 + \lambda_y^2 + \lambda_z^2 - 3]. \tag{31}$$

This relation is of central importance, and it is the basis for the calculation of the stress/strain curves for a whole range of three-dimensional stress states. We will look at the simplest case of uniaxial tension.

11.5. The stress–strain curve

The assumption of constant volume under deviatoric deformation is reasonable for rubbers, as their shear moduli are of the order of two orders of magnitude less than bulk moduli. Hence:

$$\lambda_x\lambda_y\lambda_z = 1. \tag{32}$$

So a uniaxial strain, λ_x, will mean that

$$\lambda_y = \lambda_z = \big(1/\lambda_x\big)^{1/2}. \tag{33}$$

Now, we have already seen from eq. (25) that: $f = (\mathrm{d}G/\mathrm{d}l)$, so:

$$f = -T\big(\mathrm{d}S/\mathrm{d}l\big). \tag{34}$$

Taking a unit cube of material, so that n now becomes the number of segments per unit volume, N, and $l = 1$ so that $\mathrm{d}l$ becomes $\mathrm{d}\lambda$:

$$f = Td/d\lambda\left[(1/2)Nk\left[\lambda_x^2 + 2/\lambda_x - 3\right]\right]$$
$$= NkT\left[\lambda_x - 1/\lambda_x^2\right]. \tag{35}$$

This curve, based on the Gaussian approximation, is plotted in fig. 57a. The term NkT is commonly called the *rubber modulus*. Note also the structural similarity between the relation and the gas law, P = NkT(1/V).

11.6. The high-strain discrepancy

It is common experience that when a rubber band is extended towards its limit, it becomes 'hard'. Basically, this effect arises because many of the network segments are being stretched out straight and thus one is beginning to experience the stiffness of the covalent bonds in the chain backbone, rather than the effect of entropic elasticity. The fact that the Gaussian theory of rubber elasticity is unable to predict that upturn in load stems from the approximation of treating the end-to-end distribution function as a Gaussian curve. The Gaussian function decays gradually towards infinity, yet the maximum end-to-end distance must be limited to the length of a straightened chain. One way in which the true behaviour at high strains can be modelled is by substituting for the Gaussian distribution, a modified function which, while having the characteristics of a Gaussian at modest end-to-end lengths, intersects the displacement (R) axis at a distance corresponding to the maximum length (nl). One such function is the inverse Langevin function which has the form of a series, the first term being the Gaussian case:

$$\ln P(\boldsymbol{R}) = \text{constant} - n\left[3/2(\boldsymbol{R}/nl)^2 + 9/20(\boldsymbol{R}/nl)^4 + 99/350(\boldsymbol{R}/nl)^6 + \ldots\right]. \tag{36}$$

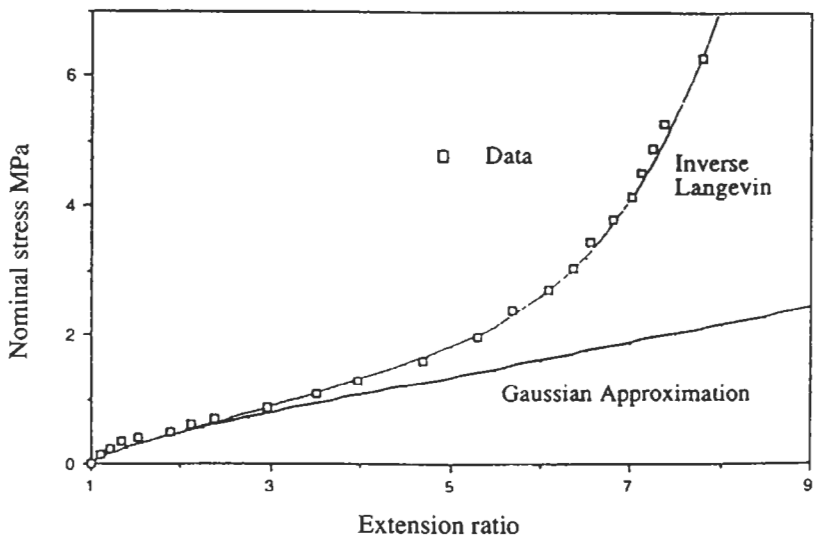

Fig. 57. Predicted load/extension plots from the Gaussian function and the inverse Langevin modification, compared with experimental data from L. R. G. Treloar.

References: p. 2740.

Figure 57 shows the inverse Langevin function compared with the Gaussian and with typical experimental curves. The maximum strain with the nl limitation is $nl/n^{1/2}l$ which equals $n^{1/2}$. Hence the maximum strain achievable in a piece of rubber is, to a first approximation, equal to the square root of the mean number of links in each network segment. Putting it another way, stretching a piece of rubber should provide an estimate of this rather basic molecular parameter! The only problem is that natural rubber stress-crystallises, and it is this phenomenon which limits the mechanical extension as well as overlaying the subtle thermal effects associated with the random chain.

11.7. Summary

The fact that the essentials of a stress–strain curve are in the hands of a single, sweeping algebraic expression is eye-catching, if only because the prediction of curves to similar strains in most other materials involve the complexities of plasticity, where the properties are largely controlled by defect interactions. However, the abiding novelty of rubber elasticity is its entropic origin and its relationship to the gas laws. Rubber is actually an excellent illustrative material for a fundamental course of thermodynamics.

References

ALFREY, T. and E. GURNEE, 1967, Organic Polymers, Prentice Hall. A brief introduction to polymers, difficult to buy now but still on some library shelves.

FLORY, P., 1953, Principles of Polymer Chemistry, Cornell. A classic text.

BOYD, R.H. and P.J. PHILLIPS, 1993, The Science of Polymer Molecules, Cambridge Solid State Science Series (Cambridge University Press).

BASSETT, D.C., 1981, Principles of Polymer Morphology, Cambridge Solid State Science Series (Cambridge University Press).

DONALD, A.M. and A.H. WINDLE, 1992, Liquid Crystalline Polymers, Cambridge Solid State Science Series (Cambridge University Press).

CIFERRI, A. and I.M. WARD (eds.), 1979, Ultra-High Modulus Polymers, Applied Science Publishers, London.

KINLOCH, A.J. and R.J. YOUNG, 1983, Fracture Behaviour of Polymers, Applied Science Publishers, London.

BLOOR, D., M.R. PRYCE and M.C. PETTY (eds.), 1994, An Introduction to Molecular Electronics, Edward Arnold, London.

HAWARD, R.N., (ed.), 1973, The Physics of Glassy Polymers, Applied Science Publishers, London.

TRELOAR, L.R.G., 1958, The Physics of Rubber Elasticity, Oxford University Press.

– AUTHOR INDEX –

1st Volume: Pages 1–942
2nd Volume: Pages 943–1830
3rd Volume: Pages 1831–2740

The labour and patience, the judgment and the penetration, which are required to make a good index, is only known to those who have gone through this most painful, but least praised part of a publication. But laborious as it is, I think it indispensably necessary, to manifest the treasures of any multifarious collection, facilitate the knowledge of those who seek it, and invite them to make application thereof. — **William Oldys (1696–1761)**

(With acknowledgment to J. H. Westbrook and R. L. Fleischer, who recently resurrected this ancient quotation).

– SUBJECT INDEX –

1st Volume: Pages 1–942
2nd Volume: Pages 943–1830
3rd Volume: Pages 1831–2740

"page number ff" signifies that treatment of the topic continues on the following page(s).

The late Prof. Peter Haasen

Colour picture on front cover:

Simulation of an alloy dendrite growing into a supercooled liquid using the phase-field method. The colours show variation of composition (atomic fraction Cu) in the liquid and solid for parameters approximating a Ni-Cu alloy with 0.41 atomic fraction Cu. See ch. 8, par. 7.5 (Courtesy of William J. Boettinger and James A. Warren).

ISBN 0 444 89875 1